JP0450776

JAERI-Review
2004-016

研究炉利用における研究成果集（平成14年度）

2004年8月

（編）研究炉利用課

日本原子力研究所
Japan Atomic Energy Research Institute

本レポートは，日本原子力研究所が不定期に公刊している研究報告書です。
入手の問合わせは，日本原子力研究所研究情報部研究情報課（〒319-1195　茨城県那珂郡東海村）あて，お申し越しください。なお，このほかに財団法人原子力弘済会資料センター（〒319-1195　茨城県那珂郡東海村日本原子力研究所内）で複写による実費頒布をおこなっております。

This report is issued irregularly.
Inquiries about availability of the reports should be addressed to Research Information Division, Department of Intellectual Resources, Japan Atomic Energy Research Institute, Tokai-mura, Naka-gun, Ibaraki-ken, 319-1195, Japan.

© Japan Atomic Energy Research Institute, 2004

編集兼発行　　日本原子力研究所

JAERI-Review 2004-016

Activity Report on the Utilization of Research Reactors (Japanese Fiscal Year, 2002)

(Ed.) Research Reactor Utilization Division

Department of Research Reactor
Tokai Research Establishment
Japan Atomic Energy Research Institute
Tokai-mura, Naka-gun, Ibaraki-ken

(Received June 1, 2004)

During the fiscal year 2002, the Tokai Research Establishment research reactors carried out 7 cycles of joint use reactor operation at JRR-3 and 39 cycles at JRR-4.
The research reactors are being utilized for various purposes including experimental studies such as neutron scattering, prompt gamma analysis, neutron radiography and medical irradiation (BNCT), and irradiation utilization such as neutron activation analysis of various samples, Irradiation Test of Reactor Materials and fission track.
This volume contains 279 activity reports, which are categorized into the fields of neutron scattering (9 subcategories), neutron radiography, neutron activation analysis, reactor materials, prompt gamma analysis, and others, submitted by the users in JAERI and from other organizations.

Irradiation Test of Reactor Materials

Keywords: JRR-3, JRR-4, Research Reactor, Neutron Scattering, Neutron Radiography, Neutron Activation Analysis, Neutron Beam, Irradiation

JAERI-Review 2004-016

研究炉利用における研究成果集（平成１４年度）

日本原子力研究所東海研究所研究炉部
（編）研究炉利用課

（2004年6月1日受理）

平成14年度、東海研究所研究炉においてはJRR-3の7サイクルとJRR-4の39サイクルの共同利用運転が行われた。

研究炉は、中性子散乱、即発ガンマ線分析、中性子ラジオグラフィ、医療照射（ＢＮＣＴ）などの実験利用及び、各種試料の放射化分析、原子炉材料の照射試験、フィッショントラックの照射利用など、様々な目的に利用されている。

本報告書は、研究炉の利用者（原研外を含む）から成果の提出279件を受け、中性子散乱（９分野）、中性子ラジオグラフィ、放射化分析、原子炉材料照射試験、即発ガンマ線分析、その他の分野別に取りまとめたものである。

東海研究所：〒319-1195　茨城県那珂郡東海村白方白根2-4

Contents

Preface 1
Research Reports 3
1. Neutron Scattering 25
1) Structure・Excitation 25
2) Magnetism 83
3) Superconductivity 183
4) Amorphous・Liquid 221
5) Polymer 241
6) Biology 303
7) Fundamental Physics・Neutron Optics 319
8) Instrument 329
9) Others 347
2. Neutron Radiography 367
3. Neutron Activition Analysis 391
4. Irradiation Test of Reactor Materials 513
5. Prompt Gamma-ray Analysis 517
6. Others 529
Acknowledgments 537
Appendix 539

目　次

はじめに 1
研究成果一覧 3
1. 中性子散乱 25
1) 構造・励磁 25
2) 磁　性 83
3) 超伝導現象 183
4) 非晶質・液体 221
5) 高分子 241
6) 生物学 303
7) 基礎物理学・中性子光学 319
8) 装　置 329
9) その他 347
2. 中性子ラジオグラフィ 367
3. 放射化分析 391
4. 原子炉材料照射試験 513
5. 即発ガンマ線分析 517
6. その他 529
謝 辞 537
付 録 539

はじめに

平成１４年度には、ＪＲＲ－３において７サイクルの共同利用運転、ＪＲＲ－４において３９サイクルの共同利用運転が行なわれ、これに伴いさまざまな利用が行われた。

本報告書は、利用者（原研外利用者を含む）から当該利用の成果の提出を受け、取りまとめたものである。

提出して頂いた成果の件数は、中性子散乱２２９件、中性子ラジオグラフィ８件、放射化分析３４件、原子炉材料照射試験１件、即発ガンマ線４件、その他３件で合計２７９件であった。なお、本報告書の一部は下記報告書の中から転載させて頂いた。

最後に、原稿を提出して頂いた利用者の皆様のご協力に感謝するとともに、今後も研究炉が有効に利用され、種々の研究がさらに進展されることを期待します。

研究炉利用課長
佐川　尚司

---

1)標　　題　：ACTIVITY REPORT ON NEUTRON SCATTERING RESEARCH issued by ISSP-NSL,University of Tokyo
（東京大学物性研究所発行）
レポート番号：Vol.10（第１０巻）
編　　者　：東京大学物性研究所
発 行 年　：２００３年

2)標　　題　：原研施設利用共同研究成果報告書（平成１４年度）
レポート番号：UTRCN-G-32
編　　者　：東京大学原子力研究総合センター
発 行 年　：２００３年

This is a blank page.

研 究 成 果 一 覧

Research Reports

This is a blank page.

No.	「 Title 」	Page
	Neutron Scattering - Structure · Excitation -	
1-1-1	**Magnetic Excitation in the Long Periodic Magnetic State of ErB_2C_2** K. Ohoyama, A. Todo, H. Hiraka, K. Hirota, T. Matsumura, H. Onodera, Y. Yamaguchi	27
1-1-2	**Neutron Diffraction and X-ray Absorption Study of Silver-Lead Oxide $Ag_5Pb_2O_6$ Synthesized from Fused Nitrates** K. Yoshii, H.Abe, M.Mizumaki, A. Nakamura, Y. Shimojyo, Y. Ishii, Y. Morii, K. Kato, T. Uruga	28
1-1-3	**Second Magnetic Excitation in CoO With Unquenched Orbital Angular Momentum** K.Tomiyasu, Y. Tsunoda	29
1-1-4	**Structure Analysis of MeHPLN at Low Temperature and the Measurement of the Order Parameter** R. Kiyanagi, H. Kimura, M. Watanabe, Y. Noda, T. Sugawara, T. Mochida	30
1-1-5	**Martensitic Transformation of Heusler-Type $Ni_{2.18}Mn_{0.82}Ga$ Single Crystal** K.Inoue, Y. Noda, H. Kimura, Y. Yamaguchi	31
1-1-6	**Crystal Structure in the Martensitic Phase of $Ni_{2.18}$ $Mn_{0.82}Ga$ with Small Amount of B** K. Inoue, T. Masuda, H. Maeda, K. Enami, Y. Yamaguchi	33
1-1-7	**Preliminary Report on Precise Hydrogen Content in Hydrogen Absorbing Materials Using Neutron Spin Interferometry** S. Tasaki, T. Ebisawa, D. Yamazaki, M. Hino, Y. Kawabata	35
1-1-8	**Neutron Diffraction Analysis of Hydrogen Bonding Networks of the Inosine 5'-Monophosphate Hydrate Stable in Medium Humidity Range** Y. Sugawara, S. Yamamura, H. Osamura, H. Kimura, Y. Noda	36
1-1-9	**Temperature Dependence of Diffuse Scattering from Crystalline Ge** M. Arai, A. Thazin, Y. Fujishima, T. Sakuma, H. Takahashi, Y. Ishii	38
1-1-10	**Zero Point Distribution of Protons and Deuterons in $(NH_4)_2SnCl_6$ and $(ND_4)_2SnCl_6$ by Single Crystal Neutron Diffraction** T. Matsuo, N. Onoda-Yamamuro, O. Yamamuro, A. Inaba, R. Kiyanagi, H. Kimura Y. Noda	39
1-1-11	**Correlation Among Thermal Displacements of Atoms in Crystalline AgCl** M. Arai, A. Thazin, Y. Fujishima, T. Sakuma, H. Takahashi, Y. Ishii	41
1-1-12	**Analysis of Deuterium Migration Process in Chiral Thiolactam Formation by Neutron Diffraction** T. Hosoya, H. Uekusa, Y. Ohashi, T. Ohhara, H. Kimura, Y. Noda	42
1-1-13	**Structural Phase Transition for Ternary Iridium Oxide Pr_3IrO_7** H. Nishimine, M. Wakeshima, Y. Hinatsu, Y. Ishii	44
1-1-14	**Observation and Calculation for Phonon Density of States in the Filled Skutterudite, $Ba_{0.1}CoSb_3$** T. Kajitani, Y. Ono, Y. Miyazaki, T. Goto, M. Sluiter, Y. Kawazoe	45
1-1-15	**Crystal Structure and Physical Properties of Pseudo-one-dimensional Calcium Iridate $Ca_5Ir_3O_{12}$** M.Wakeshima, Y. Hinatsu, Y. Ishii	46
1-1-16	**Behavior of Σ_2-Σ_3 Phonon Branches of $KRbSeO_4$** H. Shigematsu, T. Matsui	47
1-1-17	**Crystal Structure of Perovskite $Ba_3Tb_2Wo_9$** S. Oyama, Y. Doi, Y. Hinatsu, Y. Ishii	48
1-1-18	**Atomic Density and Polarization of $NaNO_2$** H. Mashiyama, T. Asahi, H. Kasano, Y.Noda, H. Kimura	49
1-1-19	**Lattice Dynamics of Tetragonal $PbTiO_3$** I. Tomeno, Y. Ishii, Y. Tsunoda	50
1-1-20	**Crystalline Structural Analysis of the Lattice Dimerization in Pyroxene Compounds** E.Ninomiya, M. Isobe, Y. Ueda, M. Nishi, K. Ohoyama	51

1-1-21	**Crystal Structure Study on Defective Silicalite by Neutron Diffraction** T. Suzuki, M.Inui, K. Sugita, Y. Ishii	52
1-1-22	**Relation Between Crystal Structure, Thermodynamic Stability, Electronic Structures and Electrode Characteristics of $LiMn_{2-x}MxO_4$(M=Co,Ni,Zn)as a Cathode Active Material for the 4V Class Lithium Secondary Battery** Y.Idemoto, Y. Ito, Y. Tsunoda, N. Koura	53
1-1-23	**Deuterium Migration Mechanism in Chiral Thiolactam Formation by Neutron Diffraction Analysis** T. Hosoya, H. Uekusa, Y. Ohashi, T. Ohhara, I. Tanaka, N. Niimura	55
1-1-24	**Structure Analysis of $Sr_3Ru_2O_7$ under the Ambient Pressure at Room Temperature** R. Kiyanagi, N. Aso, H. Kimura, Y. Noda, S. Ikeda, Y. Yoshida, M. Uwatoko	57
1-1-25	**Structure Refinements for Single Crystalline $Sr_3Ru_2O_7$ Under Magnetic Field** Y. Yoshida, S. Katano, N. Aso, S.I. Ikeda, N. Shirakawa, M. Nishi, Y. Uwatoko	58
1-1-26	**Structural Phase Transition of Superconductor $La_{2-x}SrxCuO_4$;=0.17** M. Hidaka, N. Tokiwa, S. Takahashi, T. Matsumoto, K. Oda	59
1-1-27	**Modulated Structure of the Composite Crystal $(Ca_{0.80}Y_{0.20})_{0.82}Cuo_2$** Y. Miyazaki, Y. Ishii, Y. Morii, T. Kajitani	61
1-1-28	**High-temperature Neutron Powder Diffraction Study of Crystal Structure and Disorder of δ-Bi_2O_3** D. Ishimura, M. Yashima, A. Sakai, M. Mori, K. Oh-uchi, K. Ohoyama, Y. Yamaguchi	62
1-1-29	**Modulated Structure of the Composite Crystal $(Ca_2(Co_{0.65}Cu_{0.35})_2O_4)_{0.63}CoO_2$** Y.Miyazaki, Y. Miura, M. Onoda, Y. Ishii, Y. Ono, Y. Morii, T. Kajitani	64
1-1-30	**High-temperature Neutron Powder Diffraction Study of Structural Changes in Strontium Zirconate** K. Oh-uchi, M. Yashima, M. Mori, A. Sakai, D. Ishimura, K. Ohoyama, Y. Yamaguchi	65
1-1-31	**Determination of the Structure of a Molecular Ice that Forms within a Molecular Cage** M. Yoshizawa, T. Kusukawa, M. Kawano, M. Fujita, T. Ohhara, I. Tanaka, K. Kurihara N. Niimura	66
1-1-32	**Study of Structure and Soft Phonon Mode of $SrTi^{18}O_3$ on the Ferroelectric Phase Transition at 23K** Y. Noda, K. Mochizuki, H. Kimura, T. Kyomen, M. Itoh	67
1-1-33	**Crystal Structures of γ-Na_xCoO_2(x=0.67,0.71,0.73 and 0.75)** Y. Ono, N. Kato, Y. Ishii, Y. Miyazaki, T. Kajitani	69
1-1-34	**Neutron Diffraction Study of Field Cooling Effects on Relaxor Ferroelectrics $Pb[(Zn_{1/3}Nb_{2/3})_{0.92}Ti_{0.08}]O_3$** K. Ohwada, K. Hirota, P.W. Rehrig, Y. Fujii, G. Shirane, H. Kimura, Y. Noda	70
1-1-35	**Neutron Stress Measurement of Composite and Film Materials** T. Hanabusa, K. Kusaka, M. Nishida, N. Minakawa, A. Moriai	72
1-1-36	**High-Temperature Neutron Diffraction Study on Fast Oxide Ion Conductor $(La_{0.8}Sr_{0.2})(Ga_{0.8}Mg_{0.15}Co_{0.05})O_{3-\delta}$** K. Nomura, H. Kageyama, Y. Miyazaki, M. Yashima, N. Chitose, K. Hoshino	74
1-1-37	**Residual Stress in the Induction Hardened S45C Round Bar** K. Inoue, M. Sugimoto, H. Maeda, T. Horikawa, T. Tsujikami, N. Minakawa, A. Moriai, F. Ikuta	75
1-1-38	**Neutron Diffraction Study on Nano-size Perovskite $KNbO_3$** K. Toda, S. Tokuoka, M. Kawakami, K. Uematsu, M. Sato	77
1-1-39	**HRPD Study on FeCo-Zr-O Soft Magnetic Films** M. Ohnuma, J. Suzuki, Y. Ishii	78
1-1-40	**Crystal Structure in $(La_{0.55}{}^7Li_{0.35})_{0.95}Sr_{0.05}TiO_3$** H. Shigematsu, S. Shioya, A.Tobo, T. Matsui	79
1-1-41	**Cooperative Jahn-teller Structural Phase Transitions of $PrAlO_3$** M. Hidaka, S. Takahashi, S. Watanabe	80

No.	「 Title 」	Page
	Neutron Scattering - Magnetism -	
1-2-1	**Magnetic Properties of Perovskite Manganites $L_{0.5}A_{0.5}MnO_3$** K.Yoshii, Y. Hiramitsu, Y. Nishihata, J. Mizuki, A. Nakamura, Y. Shimojo, Y. Ishii Y. Morii, H. Abe, K. Nishida	85
1-2-2	**Estimation of Magnetic Structure of Co_2Z-type Hexaferrite by Powder Neutron Diffraction** Y. Takada, T. Nakagawa, T. Tachibana, T. Ino, T.A. Yamamoto, S. Kawano	86
1-2-3	**Low-temperature Magnetic Properties in the Non-kramers System TmM_2Si_2 (M:Transition Metals)** H.Amitsuka, M. Yokoyama, J. Nozaki, T. Sakakibara, A. Tobo, K. Ohoyama	88
1-2-4	**Antiferromagnetic Ordering of $Ce(Ni_{1-x}Pdx)_2Ge_2$** T. Fukuhara, H. Kadowaki	89
1-2-5	**Irreversible Magnetization Process and Magnetic Transitions of $PrCu_2Ge_2$** T.Shigeoka, K. Ohishi, M. Nishi, Y. Uwatoko	90
1-2-6	**Neutron Diffraction Study on YbPdGe** M. Kurisu, G. Nakamoto, Y.Andoh, T. Tsutaoka, S. Kawano	91
1-2-7	**Neutron Diffraction Studies on Tb_7Rh_3 Single Crystals** T. Tsutaoka, T. Tokunaga, Y. Andoh, S.Kawano, G. Nakamoto, M. Kurisu	92
1-2-8	**Magnetic Structure of HoPdSn** Y. Andoh, G. Nakamoto, M. Kurisu, T. Tsutaoka, S. Kawano	93
1-2-9	**The Magnetic Structure of $Pt_{67}Fe_{33}$** Y. Higashiyama, Y. Tsunoda	94
1-2-10	**Magnons in Ordered PtFe Alloy** H. Kobayashi, Y. Tsunoda	95
1-2-11	**Magnetic Structure of MnPt Alloy** H. Hama, T. Ikeda, Y. Tsunoda	96
1-2-12	**Magnetic Structure in Pt-rich Pt-Mn Alloys** M. Takahashi, K. Ohshima, T. Shishido, Y. Noda	97
1-2-13	**Magnetic Fluctuation in Ordered Pt-14.4 at.% Mn** M. Takahashi, K. Ohshima, T. Shishido, K. Hirota	98
1-2-14	**Growth-orientation Dependence of Spin Structures of Epitaxial Cr/Sn Multilayers with Monatomic Sn Layers** K. Mibu, N. Jiko, J. Suzuki, M. Takeda	99
1-2-15	**New Magnetic Excitations in the Spin-density Wave of Cr** H. Hiraka, Y. Endoh, M. Fujita, K. Yamada, G. Shirane	100
1-2-16	**Structural Analysis of Magnetically Oriented Samples of $Ba_3Co_2Fe_{24}O_{41}$ by Neutron Diffraction** Y. Takada, T. Nakagawa, T. Tachibana, T. Ino, T.A. Yamamoto, S. Kawano	101
1-2-17	**Crystal and Magnetic Structures of $BaNd_2FeS_5$** M. Wakeshima, Y. Hinatsu, A. Tobo, K. Ohoyama, Y. Yamaguchi	102
1-2-18	**Doping-Dependent Magnetic Structure of $Tb_{1-x}Ca_xMnO_3$** A. Machida, Y. Moritomo, K. Ohoyama	103
1-2-19	**Magnetic Phase Diagrams of $Nd_{1/2}Ca_{1/2}(Mn_{1-y}M_y)O_3$(M=Ru,Cr and Sc)** Sh.Xu, A.Machida, Y. Moritomo, K. Ohoyama	104

1-2-20	**Magnetic Properties of Perovskite Mangnites $L_{0.5}A_{0.5}MnO_3$ (L=Eu,Gd,Tb and Dy, A=Ca and Sr)** K. Yoshii, Y. Hiramitsu, Y. Nishihata, J. Mizuki, A. Nakamura, Y. Shimojo, Y. Ishii Y. Morii, H. Abe, K. Nishida	105
1-2-21	**Magnetic Structure and Excitations of Metallic $(V_{1-x}Ti_x)_2O_3$** J. Kikuchi, K. Motoya, S. Tabaru	106
1-2-22	**Spin Structure of the Impurity-induced Antiferromagnetic Ordered Phase in the Doped Spin Gap System $Tl(Cu_{1-x}Mg_x)Cl_3$** A. Oosawa, M. Fujisawa, K. Kakurai, H. Tanaka	108
1-2-23	**Magnetic Structure of TbB_6** Y. Yamaguchi, K. Ohoyama, S. Kunii	110
1-2-24	**Magnetic Excitations in the Impurity-induced Antiferromagnetic Ordered Phase of the Doped Spin Gap System $Tl(Cu_{1-x}Mg_x)Cl_3$** A.Oosawa, M. Fujisawa, K. Kakurai, H. Tanaka	111
1-2-25	**Antiferro-quadrupoiar Ordering of Pr-ion 4f-Electron State in $PrFe_4P_{12}$** K. Iwasa, L. Hao, M. Nakajima, M. Kohgi, H. Sugawara, Y. Aoki, T.D. Matsuda, H. Sato	113
1-2-26	**Coexistence of the Spin Gap and the Magnetic Ordering in the Impurity-induced Antiferromagnetic Ordered Phase of the Doped Spin Gap System $Tl(Cu_{1-x}Mgx)Cl_3$** A. Oosawa, M. Fujisawa, K. Kakurai, H. Tanaka	115
1-2-27	**Neutron Scattering Studies of the Flux Line Lattice $ErNi_2B_2C$** T. Nagata, F. Yano, E. Habuta, H. K. Furukawa, M. Nagao, H. Yoshizawa, N. Furukawa H. Takeya, K. Kadowaki	117
1-2-28	**Spin Structure of the Pressure-induced Magnetic Ordered Phase in the Spin Gap System $TlCuCl_3$** A. Oosawa, M. Fujisawa, T. Osakabe, K. Kakurai, H. Tanaka	119
1-2-29	**Successive Phase Transitions of $TbBaCo_2O_{5.5}$** M. Soda, Y. Yasui, T. Fujita, T. Miyashita, M. Ito, S. Iikubo, M. Sato, K. Kakurai	121
1-2-30	**Long Periodic Magnetic Phase of $Ho_{1-x}Tb_xB_2C_2$** K. Ido, A. Tobo, K. Ohoyama, H. Onodera, Y. Yamaguchi	123
1-2-31	**Static Spin Correlations in Lightly-doped $La_2CuO_{4+\delta}$** M. Matsuda, M. Fujita, K. Yamada	124
1-2-32	**Unusual Magnetic Diffuse Scattering in the Tetragonal TbB_2C_2** K. Kaneko, K. Ohoyama, R. Kiyanagi, H. Kimura, Y. Noda, H. Onodera, Y. Yamaguchi	126
1-2-33	**Magnetic and Crystal Structure of $CeAgSb_2$** S. Araki, N. Metoki, A. Thamizhavel, Y. Onuki	127
1-2-34	**Thermal Neutron Spin Echo study on the Magnetic Diffuse Scattering in $LuFe_2O_4$** K. Kakurai, M. Nishi, K. Nakajima, Y. Ishii, S. Nagai, N. Ikeda, H.kito, Y. Yamada	129
1-2-35	**Magnetic Excitations in $CeAgSb_2$** S. Araki, N. Metoki, A. Thamizhavel, Y. Onuki	130
1-2-36	**Anomalous Magnetic Excitation on a Triangular Lattice Antiferromagnet $CuFeO_2$** N. Terada, S. Mitsuda	132
1-2-37	**Polarized Neutron Scattering Study of the Edge-Sharing CuO_2 Chains in $Ca_2Y_2Cu_5O_{10}$** M. Matsuda, M. Nakamura, M. Takeda, K. Kakurai, H. Yamaguchi, T. Ito, K. Oka	133
1-2-38	**Mgnetic Excitation of $S=1/2$ Quasi Two Dimensional Quantum Spin System Cs_2CuBr_4** T. Ono, H. Tanaka, A. Oosawa, Y. Koike, K. Kakurai, K. Nakajima	135
1-2-39	**Ferromagnetism in CeP under High Pressure** D. Kawana, T. Osakabe, A. Hannan, M. Kohgi	136
1-2-40	**Neutron Diffraction Study of Distorted-Triangular-lattice Ising-like Antiferromagnet $RbCoBr_3$** T. Kato, Y. Nishiwaki, K. Iio, Y. Oohara	137

1-2-41	**Anomalous Phase Transition in the Pressure-induced Magnetic Ordered Phase of the Spin Gap System $TlCuCl_3$: Polarized Neutron Scattering Study** A. Oosawa, K. Kakurai, T. Osakabe, M. Nakamura, M. Takeda, H. Tanaka	138
1-2-42	**Magnetic Excitations in Halogen-bridged Nickel Complex** S. Itoh, S. Takaishi, R. Ikeda, K. Nakajima	140
1-2-43	**Diffuse Scattering of $ZnFe_2O_4$ Under High Pressure** Y. Tsunoda, K. Kamazawa, S. Katano	141
1-2-44	**Neutron Diffraction of $BaVS_3$ Oriented Single Crystals** H. Nakamura, K. Matsui, M. Shiga, T. Yamasaki, M. Nishi, K. Kakurai	143
1-2-45	**Magnetic Order of UGa_3 Investigated by Neutron Scattering Under Uniaxial Pressure** M. Nakamura, T.D. Matsuda, K. Kakurai, G.H. Lander, S. Kawarazaki, Y. Onuki	144
1-2-46	**Partial Frustration System in the Ordered Mn_3Pt Alloy** T. Ikeda, Y. Tsunoda	146
1-2-47	**Spin Structure and Magnetic Excitation of *S=1/2* Quasi Two-dimensional Triangular Antiferromagnet Cs_2CuBr_4** T. Ono, H. Tanaka, A. Oosawa, Y. Koike, K. Kakurai	147
1-2-48	**3*d* Orbital Configuration in Ferromagnetic Mott Insulator $Lu_2Cr_2O_7$** S. Shamoto, S. Takeda, T. Kajitani, M. Azuma, M. Takano	149
1-2-49	**Magnetic Ordering Process in the Charge Ordered $LuFe_2O_4$** S. Nagai, M. Matsuda, Y. Ishii, K. Kakurai, H. Kito, N. Ikeda, Y. Yamada	150
1-2-50	**Neutron Diffraction Study on β-MnCoZn Alloys** T.Hori, H. Shiraishi, Y. Ishii	152
1-2-51	**Neutron Scattering Study of Pyrochlore Compound $Yb_2Ti_2O_7$** Y. Yasui, M. Soda, S. Iikubo, M. Ito, M. Sato, N. Hamaguchi, T. Matsushita, N. Wada N. Aso, K. Kakurai	153
1-2-52	**Magnetic Structure of GeV_4S_8 with V_4 Tetrahedral Clusters** H. Nakamura, H. Chudo, Y. Shimojo, Y. Ishii, K. Kakurai	155
1-2-53	**Detailed Studies on the Anomalous Hall Effects and Magnetic Structure of $Nd_2Mo_2O_7$** Y. Yasui, T. Kageyama, S. Iikubo, M. Ito, M. sato, K. Kakurai	156
1-2-54	**Spin Orientation of Exotic Spin-density Waves in Cr(001)/Sn Epitaxial Films** M. Takeda, K. Mibu, J. Suzuki, M. Nakamura, M. Matsuda, K. Kakurai, Y. Endoh	158
1-2-55	**Magnetic Structure of $Cu_{0.3}Zn_{0.7}Cr_2Se_4$** S. Iikubo, Y. Yasui, Y. Kobayashi, Y. Ohno, M. Ito, M. Soda, M. Sato, K. Kakurai	160
1-2-56	**Crystal Field Excitation in Rare Earth Er-based Antiferromagnet $ErAg_2$** I. Umehara, K. Sato, N. Metoki	162
1-2-57	**Magnetic Structure and Magnetic Short Range Order in $CoCr_2O_4$** K. Tomiyasu, J. Fukunaga, Y. Tsunoda	163
1-2-58	**Structural Study of Itinerant 5f Antiferromagnet $UTGa_5$(T:Ni,Pd,Pt) by Neutron Diffraction** K. Kaneko, N. Metoki, N. Bernhoeft, G. H. Lander, Y. Ishii, Y. Tokiwa, S. Ikeda, Y. Haga Y. Onuki	164
1-2-59	**Field Cooling Effect Magnetic Neutron Scattering of Zn Cr_2O_4 Crystal** I. Kagomiya, M. Toki, Y. Hata, K. Kohn, K. Nakajima, E. Kita, K. Kakurai, K. Siratori	166
1-2-60	**Unusual Antiferromagnetic Properties Affected by Antiferroquadrupolar Interaction in TbB_2C_2** K. Kaneko, N. Metoki, K. Ohoyama, H. Onodera, Y. Yamaguchi	168
1-2-61	**Structural and Magnetic Transitions of Spinel Oxide ZnV_2O_4** M. Isobe, M. Nishi, Y. Ueda, T. Ohyama	170

1-2-62	**The Neutron Small-angle Diffraction Study of an Itinerant Electron Metamagnet MnSi** M. Yamada, T. Goto, J. Suzuki, M. Takeda, K. Kakurai	171
1-2-63	**Diffuse Scattering due to Geometrical Frustration in Mn_3O_4** A. Kuriki, Y. Moritomo, K. Ohoyama	173
1-2-64	**Magnetic Form Factors of 5f Itinerant Antiferromagnetic Compound $UTGa_5$(T:Ni,Pt)** K. Kaneko, N. Metoki, N. Bernhoeft, G. H. Lander, Y. Ishii, Y. Tokiwa, S. Ikeda, Y. Haga Y. Onuki	174
1-2-65	**High-Q-Resolution Neutron Scattering Study on Temperature Dependence of Magnetic Diffuse Scattering in a Frustrated $^{110}CdFe_2O_4$** K. Kamazawa, S. Park, T. J. Sato, S.-H. Lee, Y. Tsunoda	176
1-2-66	**Neutron Diffraction Study on the Antiferroquadrupolar Order of DyB_2C_2 under the Magnetic Field** H. Yamauchi, S. Katano, M. Matsuda, K. Ohoyama, K. Indoh H. Onodera, Y. Yamaguchi	177
1-2-67	**High Magnetic Field Susceptibility and Neutron Scattering Measurements for $ZnFe_2O_4$ Single Crystal** K. Kamazawa, K. Nakajima, K. Kohn, Y. Tsunoda	179
1-2-68	**Spin Reorientation in $SrNdFeO_4$** S. Oyama, M. Wakeshima, Y. Hinatsu, A. Tobo, K. Ohoyama, Y. Yamaguchi	181

No.	「 Title 」	Page
	Neutron Scattering - Superconductivity -	
1-3-1	**Observation of Magnetic Form Factor in $Nd_2Mo_2O_7$** L. Kano, M. Saitoh, M. Togasaki, T. Sasaki, T. Matsumura, M. Fujita, H. Hiraka K. Nakajima, K. Hirota, J. Akimitsu	185
1-3-2	**Observation of the Spin Density Distributions in PrB_6 and NdB_6** Y. Kousaka, M. Saitoh, M. Togasaki, Y. Kawaguchi, M. Sera, M. Nishi, J. Akimitsu	186
1-3-3	**Study of β-$Na_{0.33}V_2O_5$(I); Lattice Instability at MI Transition** S. Nagai, J. Muraoka, M. Nishi, Y. Fujii, Y. Oohara, H. Yoshizawa, K. Kakurai T. Yamauchi, J. Yamaura, M. Isobe, Y. Ueda	187
1-3-4	**Study of β-$Na_{0.33}V_2O_5$(II); Detection of Field-induced Ferromagnetic Component in the Paramagnetic Phase** S. Nagai, M. Nishi, Y. Fujii, K. Nakajima, K. Kakurai, T. Yamauchi, J. Yamaura, M. Isobe, Y. Ueda	188
1-3-5	***A*-site Ordered Manganese Perovskites *R*$BaMn_2O_6$** T. Nakajima, H. Kageyama, M. Ichihara, H. Yoshizawa, K. Ohoyama, Y. Ueda	189
1-3-6	**Spin Wave in the C-type Antiferromagnetic Phase of $Nd_{1-x}Sr_xMnO_3$** R. Kajimoto, H. Yoshizawa, R. Kawasaki, K. Noda, H. Kuwahara	190
1-3-7	**Ferromagnetic Insulating Phase in $Pr_{1-x}Ca_xMnO_3$** R. Kajimoto, H. Mochizuki, H. Yoshizawa	191
1-3-8	**The Evidence of the Suppression of Ferromagnetic State in $Sr_{1-x}La_xRuO_3$ ($0.0 \leqq x \leqq 0.5$)** H. Nakatsugawa, Y. Oohara	192
1-3-9	**Observation of Magnetic order Associated with Charge order in single Crystal CuO** X. G. Zheng, M. Togasaki, M. Saitoh, T. Sasaki, M. Nishi, J. Akimitsu	193
1-3-10	**Studies on the Magnetic Excitation Spectra of $La_{1.48}Nd_{0.4}Sr_{0.12}CuO_4$** M. Ito, Y. Yasui, S. Iikubo, M. Soda, M. Sato, K. Kakurai, M. Nishi	194
1-3-11	**Spin Pseudo Gap in $La_{2-x}Sr_xCuO_4$ Studied by Neutron Scattering** C. H. Lee, K. Yamada, H. Hiraka, C.R. Venkateswara Rao, Y. Endoh	196
1-3-12	**Magnetic Field Effect on Low-energy Spin Excitatione in Zn-doped $La_{1.85}Sr_{0.15}CuO_4$** H. Kimura, M. Kofu, K.Hirota, K. Nakajima	197
1-3-13	**Study of Stripe Fluctuation in High-Tc Cuprate $La_{1.875}Ba_{0.125}CuO_4$** M. Fujita, H. Goka, K. Yamada	198
1-3-14	**Competitive Relation Between Stripe Order and Superconductivity in $La_{2-x}Ba_xCuO_4$** H. Goka, M. Fujita, T. Adachi, N. Kitajima, Y. Koike, K. Yamada	199
1-3-15	**Magnetic Excitations in a Singlet-ground-state Magnet $PrPd_2Al_3$** N. Aso, G. Motoyama, N.K. Sato, H. Kadowaki	200
1-3-16	**Low-energy Spin Fluctuations of $CeNi_2Ge_2$: Origin of non-fermi Liquid Behavior** H. Kadowaki, T. Fukuhara, K. Maezawa	201
1-3-17	**Studies on the in Plane Phonons of $YBa_2Cu_3O_y$ and $La_{1.48}Nd_{0.4}Sr_{0.12}CuO_4$** M.Ito, Y. Tasui, S. Iikubo, M. Soda, M. Sato, K. Kakurai	203
1-3-18	**Instability of Magnetic Order in Kondo-lattice System: Neutron Diffraction Study of the Pseude-binary Alloy System $Ce(Ru_{0.90}Rh_{0.10})_2(Si_{1-y}Ge_y)_2$** S. Kawarazaki, K. Watanabe, Y. Tabata, Y. Okita, H. Kadowaki, Y. Uwatoko	205
1-3-19	**Magnetic-field-induced Quadrupolar Ordering in the Heavy-fermion Superconductor $PrOs_4Sb_{12}$** M.Kohgi, K.Iwasa, M.Nakajima, N.Metoki, S.Araki, N.Bernhoeft, H.Sato, Y.Aoki, H.Sugawara	207
1-3-20	**Phonon Dispersion Relations of UGe_2** H. Sagayama, K. Kuwahara, K. Iwasa, M. Kohgi, T. D. Matsuda, E. Yamamoto, Y. Haga Y. Onuki	209

1-3-21	**Development of Neutron Detector by Using a Novel Metallic High-Tc Superconductor MgB_2** T. Ishida, K. Takahashi, T. Yotsuya, K. Satoh, A. Saito, A. Kawakami, H. Shimakage Z. Wang, S. Okayasu, K. Hojyou, M. Katagiri, Y. Morii, N. Niimura	210
1-3-22	**Anisotropic Lattice Distortion of UGe_2** H. Sagayama, K.Kuwahara, K. Iwasa, M. Kohgi, T. Osakabe, T.D. Matsuda, E. Yamamoto Y. Haga, Y. Onuki	212
1-3-23	**Magnetic Excitations in Ni-substituted $La_{2-x}Sr_xCuO_4$** H. Hiraka, T. Churei, Y. Endoh, K. Yamada, M. Matsuda	213
1-3-24	**Spin Fluctuations in UGe_2** H. Sagayama, K. Kuwahara, K. Iwasa, M. Kohgi, M. Nishi, K. Nakajima, T. D. Matsuda E. Yamamoto, Y. Haga, Y. Onuki	214
1-3-25	**Neutron Scattering Study of Spin Correlations in Electron -doped $Pr_{0.89}LaCe_{0.11}CuO_{4+\delta}$ Single Crystals** M. Fujita, S. Kuroshima, T. Uefuji, M. Matsuda, K. Kakurai, K. Yamada	215
1-3-26	**Magnetic Form Factor in the Heavy-electron System URu_2Si_2** K. Kuwahara, H. Sagayama, M. Kohgi, M. Nishi, K. Nakajima, H. Amitsuka	217
1-3-27	**Search for Antiferromagnetic Fluctuations in Bismuth-based Superconductors** N. Kaneko, M. Matsuda, K. Kakurai, M. Greven	218
1-3-28	**Competition Between Hidden Order and Antiferromagnetism in URu_2Si_2** H. Amitsuka, M. Yokoyama, S. Itoh, S. Kawarazaki, H. Yoshizawa	220

No.	「 Title 」	Page
	Neutron Scattering -Amorphous・Liquid-	
1-4-1	**Structural Changes in Liquid As-Te Mixtures around Semiconductor-Metal Transition** K. Maruyama, T. Shibuya	223
1-4-2	**Quasi Elastic Neutron Scattering Measurements on the Liquid Mixture Having Closed** K. Maruyama, S. Kawase	224
1-4-3	**Molecular-level Structure of 1-propanol Aqueous Solution** T. Sato, M. Misawa	225
1-4-4	**Hydration Structure around the Methylene-hydrogen Atom of Glycine Molecule** Y. Kameda, M. Sasaki, M. Yaegashi, K. Tsuji, S. Ohmori, T. Usuki	226
1-4-5	**Concentration Fluctuations and Slow Dynamics of 2-Butoxyethanol-water Mixtures** K. Yoshida, T. Yamaguchi	228
1-4-6	**Small-angle Neutron Scattering of Supercritical Water-alcohol Binary Fluids** M. Shimohira, K. Yoshida, M. Nagao, T. Yamaguchi	230
1-4-7	**Small-angle Neutron Scattering Study on Cluster Formation in TFE-water Mixtures** T. Takamuku, T. Kumai, K. Yoshida, T. Yamaguchi, M. Nagao	232
1-4-8	**Alkali Chlorides-Induced Phase Separation of Acetonitrile-water Mixtures Studied by Neutron Scattering Technique** T. Takamuku, Y. Noguchi, E. Yoshikawa, T. Kumai, M. Nagao	234
1-4-9	**Effects of Surface State on Dynamics of Water Molecules in Mesopores of MCM-41** S. Kittaka, S. Takahara, Y. Kuroda, T. Mori, T. Yamaguchi	236
1-4-10	**Small Angle Neutron Scattering from Superionic Conducting Glasses** H. Takahashi, T. Ogihara, T. Sakuma, Y. Ishii, J. Suzuki	237
1-4-11	**Quasielastic Neutron Scattering Study on Diffusive Motions of Water Molecules in Some Clathrate Aqueous Solutions** O. Yamamuro, N. Tanaka, T. Matsuo, N. Onoda-Yamamuro	238

No.	「 TItle 」	Page
	Neutron Scattering - Polymer -	
1-5-1	**Neutron Qausielastic Scattering Study on 'Rotator' Phase of Heptadecane** N. Achiwa, K. Kumagai	243
1-5-2	**Doppler Shift Neutron Spin Echo at Bragg Reflection of Magnetite Particle in Ferrofluid** N. Achiwa, H. Nishioka, T. Ebisawa, M. Nishi, K. Nakajima, K. R. Maruyama	244
1-5-3	**Effects of Guest Hydrophobic Molecule on Stability of Ordered Meso Structure of a Surfactant/Water System** M. Imai, I. Takahashi, K. Nakaya	245
1-5-4	**Change in Lamellar Spacing in Nonionic Surfactant/Water System by Shear Flow** T. Kato, K. Minewaki, K. Miyazaki, Y. Kawabata, M. Imai	246
1-5-5	**A Dynamic Behavior of a Semi-dilute Droplet Phase in a Ternary Microemulsion Consisting of AOT** M. Nagao, H. Seto, N. L. Yamada, M. Shibayama	247
1-5-6	**Pressure-Induced Phase Transition in a Microemulsion Composed of Non-ionic Surfactant, Water, and Oil** M. Nagao, D. Ihara, H. Seto, T. Takeda	249
1-5-7	**Dynamical Neuture of Least Stable Fluctuation Modes of Lamellar Structure Observed in a Nonionic Surfactant/Water System** M. Imai, K. Nakaya, T. Kawakatsu, H. Seto	251
1-5-8	**Pressure Effects on the Dynamical Properties of the Lamellar Structure in a Ternary Microemulsion** M. Nagao, D. Ihara, H. Seto, T. Takeda	252
1-5-9	**A Swollen Gel Phase Neighboring the Interdigitated Phase Observed in Aqueous Solution of DPPC with or Without Ethanol** H. Seto, N. L. Yamada, H. Nobutou, M. Nagao, T. Takeda	253
1-5-10	**Neutron Spin Echo Study on Slow Dynamics of Lipid Bilayers in the DPPC/D_2O/$CaCl_2$ System** T. Takeda, N. L. Yamada, Y. Kawabata, H. Seto, M. Nagao	255
1-5-11	**Study of Pressure Effect with Small-angle Neutron Scattering in DPPC/D_2O/$CaCl_2$ System** N. L. Yamada, T. Takeda, H. Seto, M. Nagao	257
1-5-12	**Dynamical Analysis of Triacylglycerol with *cis* Unsaturated Acyl Chain** C. Akita, T. Kawaguchi, F. Kaneko	259
1-5-13	**Structural Analysis of Metastable Phase of Triacylglycerols; the Order of the Acyl Chain Packing** C. Akita, T. Kawaguchi, F. Kaneko	260
1-5-14	**Structure Transition of Amphiphilic Block Copolymer Micelles Induced by Solubilization of Hydrophobic Small Molecules** K. Matsumoto, H. Mazaki, T. Ishizuka, S. Maeda, P. Kaeusaiha, H. Matsuoka	261
1-5-15	**Annealing Effects on Thickness of Polystyrene Thin Films As Studied by Neutron Reflectivity** T. Kanaya, T. Miyazaki, H. Watanabe, K. Nishida, H. Yamano, S. Tasaki, D.B. Bucknall	263
1-5-16	**Time Evolution of Interfacial Thickness in Polymer Bilayers Below Its Bulk Glass Transition Temperature by Neutron Reflectivity** K. Tanaka, D. Kawaguchi, S. Tasaki, A Takahara, T. Kajiyama	264
1-5-17	**Neutron Reflectivity Studies on Interfacial Composition in Blend Films of Polystyrene and Poly(vinyl methyl ether)** A. Takahara, D. Kawaguchi, K. Tanaka, S. Tasaki, T. Kajiyama	265

1-5-18	**Structure of Immiscible Polyolefin Blends Under Steady Shear Flow Studied by Small Angle Neutron Scattering** Y. Takahashi, Y. Ukai, M. Seki, Y. Matsushita	266
1-5-19	**Molecular Interaction Analysis on Crystalline-amorphous Polypropylene Blends** K. Abe, S. Okabe, M. Shibayama	267
1-5-20	**Shish-kebab Structure of Polyethylene** T. Kanaya, Y. Ogino, H. Fukushima, N. Takahashi, K. Nishida	268
1-5-21	**Structural Analysis of the Clathrate δ form Syndiotactic Polystyrene Containing Toluene** T. Kawaguchi, Y. Uda, F. Kaneko	269
1-5-22	**Complex Microphase Transitions in an ABC Triblock Terpolymer** K. Yamauchi, H. Hasegawa, T. Hashimoto, M. Nagao	270
1-5-23	**Characterization of Structure Inhomogeneities in Polymer Gels** M. Shibayama, T. Norisuye, N. Masui, S. Okabe	272
1-5-24	**Microstructure of Poly(12-acryloyloxydodecanoic acid-co-acrylic acid)Gels in Ethanol/Water System** F. Ikkai, N. Masui, T. Karino, S. Naito, K. Kurita, M. Shibayama	273
1-5-25	**Viscoelastic Effects on the Nucleation and Growth in Dynamically Asymmetric Mixtures** M. Takenaka, N. Iwase, T. Hashimoto, S. Koizumi	275
1-5-26	**Dynamic Fluctuations in Chemically Cross-liked PVA Gels** N. Takahashi, K. Nishida, T. Kanaya, M. Nagao, H. Seto, T. Takeda	276
1-5-27	**Small-angle Neutron Scattering Study on In-site Observation of NIPA-*block*-PEG Qiasi-living Polymerization** R. Motokawa, M. Annaka, T. Nakahira, S. Koizumi	277
1-5-28	**Inhomogeneities and Sol-gel Transition of Topological Gels** M. Shibayama, S. Okabe, T. Karino, Y. Okumura, Y. Domon, K. Ito	278
1-5-29	**Direct Extraction of Hydrogen Atoms in the Crystal Structure Analysis of Synthetic Polymers by Utilizing 2-Dimensional Neutron Imaging Plate System** K. Tashiro, N. Niimura, I. Tanaka, S. Fujiwara	279
1-5-30	**Morphological Transition Induced by Confinement the Polymer Chains in a Dilute Microemulsion Droplet System** K. Nakaya, M. Imai	281
1-5-31	**Elastic Incoherent Scattering Studies of Poly(Styrne) and Poly(Vinyl Methyl Ether) Mixtures** H. Takeno, S. Koizumi	282
1-5-32	**Viscoelastic Effects on the Dynamics of Concentration Fluctuations in Dynamically Asymmetric Semi-dilute Polymer Solutions** M. Takenaka, K. Tada, N. Iwase, T. Hashimoto, M. Nagao	284
1-5-33	**Dynamical Asymmetry Effect of Long-chain Branching in Polyethylene Blends** T. Kasahara, S. Utsumi, T. Sakurai, N. Yamaguchi, S. Koizumi	285
1-5-34	**Pressure-induced Phase Separation of Poly(*N*-isopropylacrylamide) Aqueous Solutions** M. Shibayama, K. Isono, S. Okabe, S. Takata, M. Nagao	287
1-5-35	**Small-angle Neutron Scattering Study on Living Anionic Polymerization Process of Styrene** K. Yamauchi, H. Hasegawa, T. Hashimoto, S. Koizumi	288
1-5-36	**Rheo-SANS Study on Gelation of Poly(vinyl Alcohol)** N. Takahashi, T. Kanaya, K. Nishida, Y. Takahashi	289
1-5-37	**Small-angle Scattering on Polystyrene/Poly(vinyl methylether) Mixture I-anomalous Suppression of Small-angle Scattering in Quiescent State-** S. Koizumi, H. Takeno	291

1-5-38	**Chain Dimension of Ring-shaped Polystyrene in Dilute Solution Investigated by Small-angle Neutron Scattering** A. Takano, T. Nakano, Y. Matsushita	293
1-5-39	**Small-angle Scattering on Polystyrene/Poly(Vinyl Methylether) Mixture II Competition Between Rheological and Concentration Fluctuation Relaxations-** S. Koizumi	295
1-5-40	**Investigation of Living Polymerization Mechanism by Neutron Scattering** K. Matsumoto, H. Matsuoka	297
1-5-41	**Small-angle Scattering on Polystyrene/Poly(vinyl methylether) Mixture III Shear-induced Phase Separation-** S. Koizumi	298
1-5-42	**Small-angle Neutron Scattering on Polystyrene Microsphere Formation Induced by In-situ Radical Polymerization** S. Koizumi, R. Motokawa, M. Annaka	300

No.	「 Title 」	Page
	Neutron Scattering - Biology -	
1-6-1	**Neutron Scattering Study on Self-assembly of Keratin molecules in Water** S. Naito, T. Karino, M. Furusaka, S. Fujiwara, N. Niimura	305
1-6-2	**Neutron Diffraction Experiment of DsrD Protein** T. Chatake, N. Mizuno, G. Voordouw, Y. Higuchi, I. Tanaka, N. Niimura	307
1-6-3	**Neutron Crystallography of B-DNA Decamer d(CCATTAATGG)** S. Arai, T. Chatake, T. Ohhara, K. Kurihara, I. Tanaka, N.Niimura	308
1-6-4	**Neutron Diffraction Experiment of Cubic Insulin Crystal** M. Maeda, T. Chatake, I. Tanaka, A. Ostermann, N. Niimura	310
1-6-5	**Crystal Structure of Polymer(Cellulose)** Y. Takahashi	311
1-6-6	**Neutron Diffraction Measurements of Single Crystals of Hen Egg White Lysozyme under Various Conditions** S. Fujiwara	312
1-6-7	**Neutron Fiber Diffraction of the Muscle Thin Filaments** S. Fujiwara, F. Matsumoto, S. Deshimaru	313
1-6-8	**Dynamics of the Hydration Cluster Distributed on the Protein Surface** H. Nakagawa, H. Kamikubo, I. Tukushi, T. Kanaya, M. Kataoka	314
1-6-9	**Small-Angle Neutron Scattering Measurements of TroponinC on the Thin Filament** F. Matsumoto, K. Makino, K. Maeda, Y. Maeda, S. Fujiwara	315
1-6-10	**Strcutre and Dynamics of Ganglioside/Cholestrol/DPPC Mixed Vesicle** M. Hirai, T. Hayakawa, K. Koisumi	316
1-6-11	**Association of the Amyloid Protofilaments of Hen Egg White Lysozyme Studied by Time-Resolved Neutron Scattering** S. Fujiwara, F. Matsumoto, Y. Yonezawa	317
1-6-12	**Solution Structure of Ca^{2+} -Saturated Calmodulin Complexed with N^{α} myristoylated NAP-22** Y. Izumi, N. Hayashi, Y. Jinbo, T. Matsufuji, N. Matsushima	318

No.	「 Title 」	Page
Neutron Scattering - Fundamental Physics · Neutron Optics -		
1-7-1	**Phase Transformation in Smooth Specimen and at Notch Root in Shape Memory Alloy TiNi** Y. Akiniwa, H. Kimura, K. Tanaka, N. Minakawa, Y. Morii	321
1-7-2	**Development of a 5Qc Ni/Ti Supermirror Using Ion Beam Sputter Instrument** M. Hino, S. Tasaki, H. Yoshino, Y. Kawabata	323
1-7-3	**Neutron Diffraction Measurement of Residual Strain of Partial Penetration Welds for ITER Vacuum Vessel** M. Nakahira, A. Moriai, N. Minakawa	324
1-7-4	**Direct Measurement of the Transverse Coherence Length of Cold Neutron Beam** M. Kitaguchi, H. Funahashi, T. Nakura, K. Taketani, M. Hino, H. M. Shimizu	325
1-7-5	**Compatibility study of SS316 with Pb-Bi by Neutron Diffraction Method** K. Kikuchi, N. Minakawa, A. Moriai, Y. Morii	326
1-7-6	**A Tiny Velocity Change of Neutrons Through Si Crystal by Time Beat Neutron Interferometer due to Refractive Index** N. Achiwa, T. Ebisawa, M. Hino, D. Yamazaki, R. Maruyama, S. Tasaki	328

No.	「 Title 」	Page
	Neutron Scattering - Instrument -	
1-8-1	**Development of an Electrostatic Levitation Furnace for Neutron Scattering Experiments of High Temperature Liquids** T. Masaki, T. Isihikawa, P.-F. Paradis, H. Aoki, T. Aoyama, Y. Arai, Y. Ishii, S. Yoda	331
1-8-2	**2-Dimesional Characteristics of $SrBPO_5:Eu^{2+}$ Photostimulable Phosphor** K. Sakasai, M. Katagiri, K. Toh, H. Takahashi, M. Nakazawa, Y. Kondo	332
1-8-3	**High Contrast Neutron Imaging Using Low Energy Neutrons** Y. Kawabata, M. Hino, H. Sunohara, S. Tasaki, T. Nakano	333
1-8-4	**An Elastically Bent Si Monochromator to Share the Whole Beam Neutron Size Tandem Among Three Diffractometers** I. Tanaka, M. Refai-Muslih K. Kurihara, N. Niimura	334
1-8-5	**Preliminary Results on Remanent Neutron Polarizer with Vacuum Evaporation** S. Tasaki, Y.Yoshimura, M. Hino, T. Ebisawa, R. Maruyama, Y. Kawabata	336
1-8-6	**Neutron Beam Enhancement with a HOPG Pre-crystal** H. Tomimitsu, Y. Hasegawa, K. Aizawa	337
1-8-7	**Measurement of Spin-flip Probabilities of N=10 Drabkin Spin-flipper** S. Tasaki, D. Yamazaki, K. Soyama, T. Ebisawa	339
1-8-8	**Performance of the Renewed Polarization Analysis Option on TAS-1** M. Nakamura, M. Takeda, Y. Shimojo, K. Kakurai	340
1-8-9	**Development of the Modified Neutron Spin Echo Spectrometer "MIEZE"** T. Kawai, R. Maruyama, T. Ebisawa	342
1-8-10	**High-Pressure Apparatus for Magnetic Neutron Diffraction Beyond 3 Gpa at Low Temperature** T. Osakabe, M. Kohgi, D. Kawana, A. Hannan, K. Soyama, H. Kitazawa	343
1-8-11	**Development of Spin Flippers with Steady Current for the TOF-NSE Spectrometer** T. Takeda, N. L. Yamada, H. Seto, Y. Kawabata	345

No.	「 Title 」	Page
	Neutron Scattering - Others -	
1-9-1	**Development of A Method for Determining Residual Stress Using Diffraction Ring Detected with Neutron Image Plate** T. Sasaki, N. Minakawa, Y. Morii, N. Niimura, Y. Hirose	349
1-9-2	**Development of Optical Devices for Cold Neutrons** H.M. Shimizu, T. Adachi, T. Oku, K. Ikeda, H. Sato, Y. Takizawa, K. Morimoto, S. Morita, H. Ohmori, K. Sakai, F. Tokanai, K. Sasaki, Y. Kiyanagi, J. Suzuki	350
1-9-3	**Study of Residual Stress for Carbon/Carbon Composite by Neutron Scattering** S. Baba, M. Ishihara, N. Minakawa, J. Suzuki	352
1-9-4	**Diffraction Angle Error Investigation of the Sample Surface Measurement by the Small Neutron Beam** N. Minakawa, A. Moriai, Y. Morii	354
1-9-5	**The Comparison Measurement of the Strain Gauge Method and the Neutron Diffraction Methods by the Automobile Aluminum Engine** N. Minakawa, A. Moriai, Y. Morii, K. Goto, S. Nishii, S. Yamada, H. Hosoda, A. Nomura T. Hamamoto	356
1-9-6	**Residual Stress Measurement of Peened Material by Neutron Diffraction Method** S. Okido, T. Machida, M. Hayashi, Y. Morii, N. Minakawa, A. Moriai	358
1-9-7	**Anisotropy in Residual Phase Stresses in a Pearlitic Steel Subjected to Tensile Deformation** T.Suzuki, Y. Tomota, A. Moriai, N. Minakawa, Y. Morii	359
1-9-8	**Strengthening Mechanism of a Heavily Drawn Pearlite Wire with 4 Gpa -*In Situ* Neutron Diffraction under Tensile Loading-** Y. Tomota, A. Kanie, Y. Shiota, T. Suzuki, A. Moriai, N. Minakawa, Y. Morii	361
1-9-9	**Residual Grain Stress and Ultra-high Strength of a Heavily Drawn Ferrite Steel** Y. Tomota, M. Uno, T. Suzuki, A. Moriai, N. Minakawa, Y. Morii	363
1-9-10	**Inside Residual Stress Measurement of Quenched Steel by Neutron Diffraction Method** R. Mukai, D.Y. Ju, N. Minakawa, Y. Morii, A. Moriai	365

No.	「 Title 」	Page
	Neutron Radiography	
2-1	**Research and Development on Neutron Beam Utilization** M. Matsubayashi, M. Katagiri, K. Kikuchi, M. Kashiwagi	369
2-2	**Development and Application of Neutron Radiography Techniques with High Temporal Resolution** K. Mishima, T. Hibiki, Y. Saito, M. Matsubayashi	370
2-3	**Analysis of Hydrogen and Lithium in Ion Conducting Solid-State Materials** H. Sakaguchi, S. Takai, M. Matsubayashi, T. Esaka	371
2-4	**Image Analysis of Biomedical Tissues by Neutron Radiography** T. Takeda, Y. Tsuchiya, M. Matsubayashi, J. Wu, T. T. Lwin, A. Yoneyama, Y. Itai	375
2-5	**Qualitative Measurements of Gas-solid Two-phase Flow by using Thermal Neutron Radiography** H. Umekawa, M. Ozawa, S. Furui, K. Hayashi, M. Tsuzuki, Y. Oshima,	376
2-6	**Visualization study for Oscillation Heat Pipe by Using Neutron Radiography** S. Toyama, R. Futamata, H. Nagai, M. Matsubayashi	379
2-7	**Precision Measurement of the Neutron Lifetime** A. Maki, H. Maezawa, S. Yasumi, Y. Sakamoto, S. Kobayashi, Y. Inagaki, S. Mori	381
2-8	**Void Fraction Measurement of Boiling Flow in a Tight-lattice 7-rod Bundle by Neutron Radiography** M. Kureta, H. Akimoto	390

No.	「 Title 」	Page
	Neutron Activation Analysis	
3-1	**Cadmium Binding Protein in Scallop Mizuhopecten Yessoensis** T. Ohnishi, G. Ohnishi, Y. Noya	393
3-2	**Quantitative Analysis of Trace Elements in the Brain Tissue of Patients with Dementia** Y. Ueda, A. Nakajima	397
3-3	**The Activation Analysis of Phosphorescent Phosphor(II)** K. Moriwaki, Y. Hagiwara, J. Obata, S. Furuyama	400
3-4	**Neutron Activation Analysis of Trace Elements in Carbonate Rocks by Using a Ko Standardization Method** S. Aizawa, H. Sawahata, M. Kawate	404
3-5	**Evaluation and Database of Ko-standardization Neutron Activation Analysis System** Y. Ito, H. Ozaki, H. Sawahata, M. Kawate, S. Aizawa, T. Fukuoka, Y. Katayama, M. Matsuo, T. Nakanishi, M.Ebihara	410
3-6	**Application of Carbon Fiber for Environmental Monitor** Y. Maeda, S. Sugihara, S. Kameda, K. Kawamura	417
3-7	**Study of Metallofullerenes with Neutron Activation(II)** K. Sueki, Y. Zhao, K. Akiyama, W. Sato, K. Kikuchi, M. Katada	420
3-8	**Development of Neutron Activation Analysis for Ultra-trace Elements in High Purity Materials and Metals** Y. Okada, S. Hirai	424
3-9	**Study on Trace Elements in Physiologically Active Substances** Y. Morita, I. Murakami, S. Iijima	428
3-10	**Dynamics of Transition Elements in Antioxidant Networks of Selenium Deficient Rat** K. Endo, I. Ui, K. Matsumoto	431
3-11	**Detection of Extractable Organic Iodine in Biological Samples Using Instrumental Neutron Activation Analysis** Y. Kashima, M. Aoyagi, H. Sakai, M. Matsui, T. Okabe	436
3-12	**Instrumental Neutron Activation Analysis of Drill-core Samples in Coral Reefs** S. Ohde, M. M. M. Hossain, H. Ozaki	443
3-13	**Determination of Trace Elements in Tree Rings as Environmental Monitors** Y. Katayama, M. Nagai, N. Okada, S. Ko, T. Aoki, J. Takada, Y. Kawabata	447
3-14	**Effects of Zn Deficiency During the Pregnant and Lactating Period on Growth of Mice(II)** M. Yanaga, H. Suganuma, M. Noguchi, T. Yoshida, T. Ohyama, H, Maetsu, T. Oida, T. Ogi, Y. Kawamoto, M. Koike, Y. Kajita, N. Kinugawa	452
3-15	**Study on Element Concentrations in Aerosol in Ambient air from Phnom Penh, Cambodia** Y. Kashima, H. Sakai, M. Matsui	456
3-16	**Determination of As and Sb in Iron and Steel by Neutron Activation Analysis with Multiple Gamma-ray Detection** A. Kimura, Y. Toh, Y. Hatsukawa, M. Oshima	462
3-17	**Capture Capability and Residence Time of Atmospheric Aerosols in the plant** S. Osaki, S. Sugihara, S. Kameda,	463
3-18	**Field Application of the Measuring Method Using Bromine Isotope Ratio in Order to Trace Soil Water** N. Kihou, H. Fujiwara	466
3-19	**Activation Analysis of River and Estuarine Sediments** M. Matsuo, A. Kuno, M. Kataoka, Y. Tanaka, K.Seimiya, O. Takahashi	468
3-20	**Research on Estimation of Generated Amount of Trace Gas in the Atomosphere by Biomass Combustion** S. Sudo	472

3-21	**Geochemical Studies on Submarine Hydrothermal Deposits by Neutron Activation Analysis** C. Sato, K. Nakashima	474
3-22	**Labeling of Heavy Metals in Soil Organic matter with Stable Isotopes** Y. Sakurai, N. Kihou	479
3-23	**Distributions and Characteristics of Trace Elements in Marine Sediment Core Samples** T. Honda, T. Nozaki, Y. Kikawada, T. Morimoto	480
3-24	**Determination of Several Elements of Soil in Feces of Domestic Animal by Activation Analysis** K. Nishimura, N. Kihou, S. Miyamoto	487
3-25	**Neutron Activation Analysis of U and Th for Annual Dose Measurement** Y. Ganzawa	488
3-26	**Minor and Truce Elements Determination of Environmental Samples(III)** Y, Miyamoto, Y. Saito, M. Magara, S. Sakurai, S. Usuda	491
3-27	**High Sensitive Iridium Determination in Deep Sea Sediment Using Multiparameter Coincidence Method** Y. Hatsukawa, Y. Toh, A. Kimura, G. Hosein, M. Oshima, T. Noguchi, K. Toyoda	493
3-28	**Determination of Sodium and Copper in Saltwater Clam Shell by Activation Analysis** H. Kamioki	494
3-29	**Geochemical Study of the Setouchi Volcanic Rocks Around the Sanuki Plain** H. Shinjoe, T. Sumii	495
3-30	**Detection of the Particles Containing Natural Uranium by Fission Track Method** K. Esaka, F. Esaka, H. Fukuyama, T. Onodera, J. Inagawa, C. G. Lee, K. Iguchi, S. Sakurai, S. Usuda, K. Watanabe	498
3-31	**Mossbauer Spectroscopic Studies on Inorganic Compounds IV** M. Takahashi, J. Wang, T. Nishimura, K. Suziki, T. Kitazawa, M. Takeda, H. Sawahata Y. Ito	500
3-32	**Distribution Coefficient Kd of Chlorine in Soil Groups in Aomori Prefecture** H. Tsukada, A. Takeda, S. Hisamatsu, J. Inaba,	507
3-33	**Chemical State Analysis by Means of Nuclear Decay** Y. Tamaki	509
3-34	**Neutron Activation Analysis of Trace Elements in Rice** K. Kushita, H. Kamioki	512

No.	「 Title 」	Page
	Irradiation Test of Reactor Materials	
4-1	**Tritium Release from Neutron-Irradiated Porous Li_2O Sintered Pellets:Isothermal Annealing of Tritum Trap** T. Tanifuji, D. Yamaki, S. Jitsukawa	515

No.	「 Title 」	Page
	Prompt Gamma-ray Analysis	
5-1	**Contents of Boron and Phosphorus in the Nickel Alloy Films Deposited by Electroplating and Electroless Plating** S. Morisaki, T. Nagano, K. Sunohara	519
5-2	**Study on Neutron Activation and Prompt Gamma-ray Analyses** C. Yonezawa, H. Matsue	522
5-3	**Prompt Gamma-ray Analysis of Large and Volumious Samples. III** Y. Oura, S. Enomoto, E. Hirunuma	524
5-4	**The Analysis of Cadmium-polluted Rice Multiple Gamma-ray Detecting Method** Y. Toh, M. Oshima, Y. Hatsukawa, M. Koizumi, A. Osa, A. Kimura, J. Goto	528

No.	「 Title 」	Page
	Others	
6-1	**Evaluation of DNA Damage of the Rat 9L Gliosarcoma After Boron Neutron Capture Therapy by use of Single Cell Electrophoresis (Comet) Assay** K. Nakai, F. Yoshida, M. Endo, T. Yamamoto, A. Matsumura	531
6-2	**Neutron Irradiation Effects on Electrical Properties of LiAl:III** M. yahagi, T. Hashimoto, K. Kuriyama, H. Hamanaka, H. Sugai	532
6-3	**Automatic Counting of Fission Tracks in a DAP Plastic Detector** H. Iwano, T. Yoshioka, T. Danhara, T. Tsuruta	536

1. 中性子散乱 1)構造・励磁

1. Neutron Scattering 1) Structure・Excitation

This is a blank page.

研究テーマ： 正方晶四極子秩序化合物 RB_2C_2 でのスピン格子ダイナミクス
表題： ErB_2C_2 の長周期磁気秩序相での磁気励起

Magnetic excitation in the long periodic magnetic state of ErB_2C_2

1-1-1

K. Ohoyama[1], A. Tobo[1], H. Hiraka[1], K. Hirota[2], T. Matsumura[3], H. Onodera[1], Y. Yamaguchi[1]

[1] *Institute for Materials Research, Tohoku Univ. 1-2-1 Katahira, Sendai, 980-8577*

[2] *Institute for Solid State Physics, The University of Tokyo, 106-1 Shirakata, Tokai, 319-1106*

[3] *Fac. of Science, Tohoku Univ., Aramaki, Sendai, 980-8578*

The tetragonal RB_2C_2 (R=rare earth) system shows characteristic magnetic and quadrupolar behaviour caused by competition between antiferroquadrupolar (AFQ) and antiferromagnetic (AFM) interactions [1, 2]. AFQ orderings in RB_2C_2 are unique phenomena, because the strict $4f$ ground states by crystal electric field with tetragonal symmetry have no degree of freedom on quadrupolar moments; therefore, it was thought that quadrupolar orderings can never be realised in rare earth tetragonal compounds before the discovery of AFQ orderings in RB_2C_2.

The RB_2C_2 compounds which have long periodic magnetic structure phases, HoB_2C_2, TbB_2C_2 and ErB_2C_2, show anomalous magnetic diffuse scattering in the long periodic states; the diffuse scattering can not be understood in terms of magnetic correlations.

Although the origin of the magnetic diffuse scattering in RB_2C_2 is unknown yet, we expect that spin-lattice dynamics probably plays important roles. Therefore, we performed inelastic scattering experiments on a single crystalline sample of $Er^{11}B_2C_2$ on the triple axis spectrometer TOPAN at 6G beam hole of JRR3-M of JAERI(Tokai). The experimental conditions were as follows; collimation was B-60′-S-PG-60′-B, E_f=14.7 meV, the sample dimension was $3\times4\times0.5$ mm^3.

ErB_2C_2 exhibits a magnetic transition at T_N=15.9 K and a successive magnetic order-order transition at T_t = 13.0 K [3]. The magnetic structure between T_N and T_t is a sinusoidal modulation type one with k=(1+δ, δ, 0), where δ=0.112 [3].

Fig.1 shows spectra at T=15.0 K where the satellite peaks due to the long periodic ordering do not exist. The open and closed circles indicate the spectra at (1, 0.025, 0), and at (1, 0.11,0), respectively; the farmer and the later points exist at the centre and at the edge of the region in which the anomalous diffuse scattering is observed. As shown in Fig.1, a broad excitation was observed around 10meV at (1, 0.025, 0). Since no obvious structure was observed around (3,0,0) at T=15K, the peak around 10meV at (1, 0.025, 0) must be magnetic. Though the broad peak disappears at the edge of the diffuse scattering region, detailed Q dependence is unknown yet.

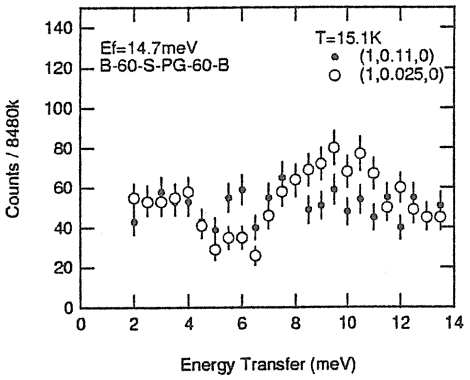


Fig. 1. Spectra at T=15K of ErB_2C_2 on TOPAN. The open and closed circles indicate the spectra at the (1,0.025,0), and (1, 0.11,0).

The present work was the first experiments on dynamics in RB_2C_2. To understand dynamic characters in RB_2C_2, more detailed experiments are in progress.

References

[1] H. Yamauchi *et al.*: J. Phys. Soc. Jpn. **68** (1999) 2057.

[2] H. Onodera *et al.*: J. Phys. Soc. Jpn. **68** (1999) 2526.

[3] K. Ohoyama *et al.*: J. Phys. Soc. Jpn. **71** (2002) 1746.

使用施設：JRR-3 ., 装置： 6G(TOPAN) , 分野： 1.Structure and Excitation

研究テーマ：アクチノイド及び関連イオン性化合物の構造・物性研究
表　　題：硝酸塩から合成した $Ag_5Pb_2O_6$ の中性子散乱およびX 線吸収分光による研究
1-1-2

NEUTRON DIFFRACTION AND X-RAY ABSORPTION STUDY OF SILVER-LEAD OXIDE $Ag_5Pb_2O_6$ SYNTHESIZED FROM FUSED NITRATES

K. YOSHII, H. ABE[1], M. MIZUMAKI[2], A. NAKAMURA[3], Y. SHIMOJO[3], Y. ISHII[3], Y. MORII[3], K. KATO[2], T. URUGA[2]

Synchrotron Radiation Research Center, Japan Atomic Energy Research Institute (JAERI), Mikazuki, Sayo-gun, Hyogo, 679-5148

[1]*National Institute for Materials Science, Tsukuba, Ibaraki 304-0047*

[2]*Japan Synchrotron Radiation Research Institute, Mikazuki, Sayo-gun, Hyogo, 679-5198*

[3]*Advanced Science Research Center, JAERI, Tokai, Ibaraki, 319-1195*

A silver-lead oxide $Ag_5Pb_2O_6$ shows metallic conductivity below room temperature.[1)] Its crystal structure is a trigonal type of *P*-31*m*, which has a two-dimensional Ag layer and a Pb_2O_6 network. [1,2)] So far, this material has been synthesized by a solid-state reaction under high-pressure oxygen.

Recently, we reported that single crystals of this material can be grown in the fused mixture of nitrates at an ambient pressure.[3)] In this work, neutron diffraction and X-ray absorption measurements were carried out to obtain detailed information on the crystal structure and the valence state of each ion. Neutron diffraction experiments were conducted with a high-resolution powder diffractometer (HRPD) at the JRR-3 reactor. X-ray absorption measurements were carried out using synchrotron radiation at the BL01B1 beamline of SPring-8.

Figure 1 shows the neutron diffraction patterns at room temperature. It was found that the experimental pattern could be fitted to the *P*-31*m* structure by the Rietveld analysis (RIETAN-2000). The structural parameters such as bond lengths were well close to those reported previously.[1)] Thus, $Ag_5Pb_2O_6$ is actually synthesized by the present method. The absorption measurements showed also that the valence of Pb stands between +3 and +4. This result implies that atomic orbitals of Pb play an important role in the conductivity.

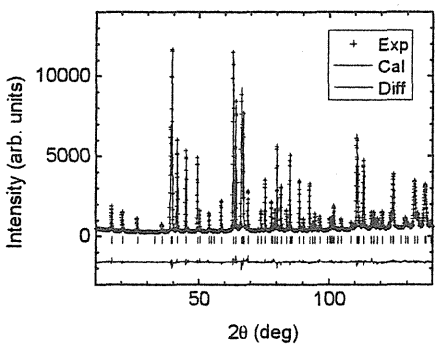


Fig. 1 Neutron powder diffraction patterns of $Ag_5Pb_2O_6$ at room temperature.

References

1) M. Jansen *et al.*, L. Less-Common Met. 161 (1990) pp. 17-24.
2) T. D. Brennan and J. K. Burdett: Inorg. Chem. 33 (1994) pp. 4794-4799.
3) H. Abe *et al.*, J. Cryst. Growth 241 (2002) pp. 347-351

原子炉：JRR-3　　装　置：HRPD　　分　野：中性子散乱（構造）

研究テーマ:CoO の軌道角運動量が磁気励起におよぼす影響
表題:凍結していない軌道角運動量を持つ系 CoO の第二磁気励起

Second magnetic excitation in CoO with unquenched orbital angular momentum

1-1-3

K. Tomiyasu and Y. Tsunoda

School of science and engineering, Waseda University, 3-4-1, Ohkubo, Shinjuku-ku, Tokyo, 169-8555, Japan

CoO has a NaCl-type crystal structure in the paramagnetic phase and tetragonally distorts below T_N = 290 K. The magnetic structure is the antiferromagnetic type-fcc I, in which ferromagnetic sheets of magnetic moments on the (111) planes are antiferromagnetically stacked along the [111] direction. Sakurai et al investigated the dispersion curve of the spin wave by means of neutron-scattering used a single crystal, and they found that it is almost flat. However, we performed neutron-scattering experiments using a single crystal, and found that it has a large slope. We consider that Sakurai et al measured the inelastic incoherent scattering, and misunderstood the scattering from the density of the phonon as that from the spin-wave.

In CoO, Co^{2+} ion has unquenched orbital angular momentum **L**, and the **L** should influence the magnetic excitation. Figure 1 shows our raw data of the inelastic neutron-scattering experiments at 150 K. All the experiments were performed at the triple axis spectrometer PONTA(5G) installed at JRR-3M in JAERI (Tokai). The lower peaks indicate the scattering of the spin-wave, however, another magnetic branch was also observed, which is different from the spin-wave and Sakurai's branches. In $KCoF_3$ and CoF_2, Co^{2+} ion also has unquenched **L** and second magnetic branch, which is different from the spin wave. The unquenched **L** is considered to cause the second excitation through the spin-orbit coupling. The analysis of the raw data is under investigation.

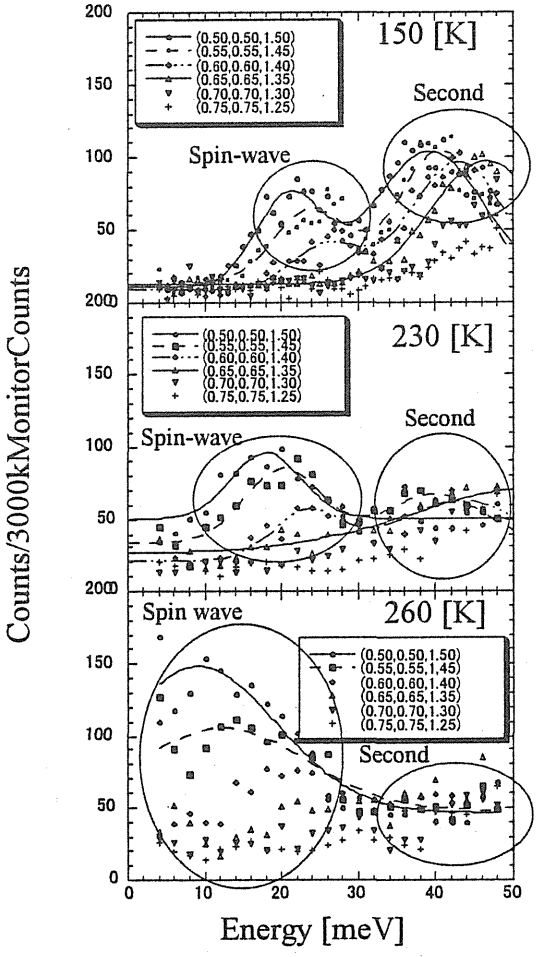


Fig.1 Raw data of our neutron-scattering experiments are shown. These data were taken by operating the constant-Q mode around 1/2 1/2 3/2 reciprocal lattice point at 150, 230 and 260 K.

使用施設:JRR-3 in JAERI (Tokai), 装置:PONTA(5G), 分野 Structures&Excitations

研究テーマ： 孤立水素結合型物質 BrHPLN(C13O2H7Br) の水素結合間距離の温度特性と水素の核密度分布
表題： MeHPLN の低温構造解析及び秩序変数の測定

Structure Analysis of MeHPLN at low temperature and the measurement of the order parameter

1-1-4

R. Kiyanagi, H. Kimura, M. Watanabe, Y. Noda, T. Sugawara[1] and T. Mochida[2]
Institute of Multidisciplinary Research for Advanced Materials, Tohoku University, 2-1-1 Katahira, Aoba-ku, Sendai 980-8577
[1] *Department of Basic Science, Graduate School of Arts and Science, The University of Tokyo 3-8-1 komaba, meguro-ku 153-8902*
[2] *Department of Chemistry, Faculty of Science, Toho University 2-2-1 miyama, funabashi 273-8510*

Some ferro- or antiferroelectric materials containing hydrogen-bonds show various physical property. In particular, when the hydrogen atom in the hydrogen-bond is replaced with a deuteron atom, they show drastic changes of the ferro- or antiferroelectric phase transition temperature.

5-methyl-9-hydroxyphenalenon($C_{14}H_{10}O_2$, MeHPLN) has an intra-molecular hydrogen-bond and has no hydrogen-bond network between the molecules. The material undergoes an antiferroelectric phase transition around Tc (= 42K), without reference to the sort of the atom in the hydrogen-bond. We have already performed the structure analyses at room temperature and below the transition temperature. During the present experiment, we performed the structure analysis at 50K and 150K.

The experiment was performed at T2-2 beam port at JRR-3M in JAERI(Tokai), utilizing the four circle neutron diffractometer, FONDER. The wavelength of the neutron beam was 1.5656Å , and the sample size was $1.0\times1.0\times5.0[mm^3]$. The data collection for the structure analyses was carried out with $\theta - 2\theta$ scan mode at 50K, and with ω scan mode at 150K, respectively. The total observed data number was 934 at 50K, and 960 at 150K, respectively. The obtained lattice parameters were, a = 11.882(2)Å, b = 11.091(3)Å, c = 7.253(3)Å, α = 89.99(4), β = 93.79(3), γ = 90.00(2) at 50K, a = 11.983(3)Å, b = 11.116(3)Å, c = 7.277(3)Å, α = 90.02(3), β = 94.14(3), γ = 90.02(2) at 150K, respectively.

Least-square fitting analyses and Maximum Entropy Method analyses were carried out after applying absorption correction. As a result, it was found that the hydrogen atom in the hydrogen-bond region is in a disordered state, occupying two equivalent sites by a 50 : 50 ratio at both 50K and 150K. This feature is same as that in the room temperature phase.

We also measured the temperature dependence of a superlattice reflection around the transition temperature. The result is shown in Fig. 1. The intensity of the superlattice reflection obviously increases from Tc, indicating the breaking down of C-lattice symmetry. The space group of MeHPLN, indeed, turns into $P2_1/c$ from $C2/c$ at Tc with the cell doubling along the b-axis.

We will perform similar and systematic experiment on 5-Br-9-hydroxyphenalenon at the next stage, to understand the similarity and the difference of the phase transition scheme.

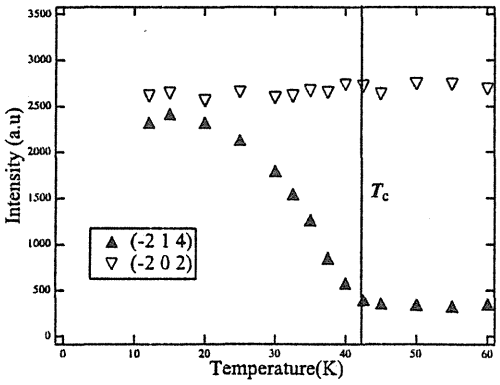


Fig. 1. Temperature dependence of the superlattice reflection (-2 1 4) and the fundamental reflection (-2 0 2).

使用施設：JRR-3 ， 装置： T2-2 (FONDER) ， 分野： 1. Structures & Excitations

研究テーマ：ホイスラー型 $Ni_{2.18}Mn_{0.82}Ga$ 単結晶のマルテンサイト変態
表題：ホイスラー型 $Ni_{2.18}Mn_{0.82}Ga$ 単結晶のマルテンサイト変態

1-1-5 Martensitic Transformation of Heusler-type $Ni_{2.18}Mn_{0.82}Ga$ Single Crystal

K. Inoue, Y. Noda*, H. Kimura* and Y. Yamaguchi**

Faculty of Science and Technology, Ryukoku University, Seta, Otsu 520-2194, Japan;
**IMRAM, Tohoku University, Aoba-ku, Sendai 980-8577, Japan;*
***IMR, Tohoku University, Aoba-ku, Sendai 980-8577, Japan*

A Heusler-type $Ni_{2.18}Mn_{0.82}Ga$ alloy has a thermo-elastic martensitic transformation temperature of around 330 K, which is nearly coincident with the Curie temperature. It is ferromagnetic in the martensitc phase and paramagnetic in the mother phase. The crystal structure in the martensitic phase was previously determined by Rietveld analysis of the powder neutron diffraction patterns [1]. The martensitic phase contains two crystal structures, one is an orthorhombic structure and the other is a tetragonal structure. This tetragonal structure is quite different from the tetragonal structure in the martensitic phase of stoichiometric Ni_2MnGa [2].

A single crystal of $Ni_{2.18}Mn_{0.82}Ga$ alloy shows a shape memory effect, when we increase the temperature [3]. The shape memory effect observed with increasing temperature is shown in Fig. 1.

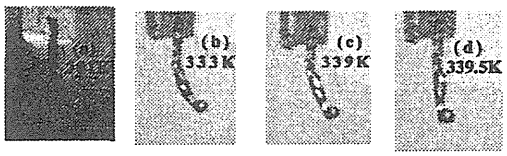


Figure 1: Shape memory effect of a $Ni_{2.18}Mn_{0.82}Ga$ single crystal observed with increasing temperature. It was bent from the straight bar at room temperature of 301 K. T the shape was suddenly recovered at the temperature above 339 K.

In the present experiment, we have observed the change of crystal structure of $Ni_{2.18}Mn_{0.82}$ Ga single crystal with decreasing temperature. It is expected that the crystal structure in the martensitic phase of single crystal is determined and the structure change accompanied by shape memory effect becomes clear. The four circle diffractometer, FONDER, installed at T2-2 port of JRR-3M reactor was used.

The SEM image of the crystal used for neutron diffraction in the present experiment is shown in Fig. 2. The length of the crystal is about 6 mm.

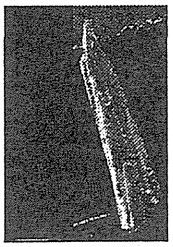


Figure 2: SEM image of the single crystal used for neutron diffraction.

The intensity maps on the reciprocal plane observed by neutron diffraction are shown in Figs. 3, 4 and 5. By neutron diffraction at 415 K, we found that it is almost a single crystal with a cubic Heusler structure, however, we see slightly split two (002) peaks in Fig. 3(a) and two (200) peaks in Fig. 5(a). This fact indicates that the crystal in the mother phase consists of two single crystals, with only slightly slipped axes. The direction of crystal growth is [001] of cubic structure. In Figs. 3 (a), (b) and (c), the intensity maps on the (h0l)-reciprocal plane around cubic (002) point at 415 K, 330 K and 298 K are shown. In Fig.4, the map at 330 K is shown again, in which the scale of the vertical axis are extremely expanded. We do not observe any remarkable peak in Fig. 3(b). However, when the vertical axis is expanded as shown in Fig. 4, we can observe many peaks beginning to appear. In Fig. 4 we observe the

使用施設：JRR-3　in JAERI (Tokai)，装置：FONDER，分野 Structure & Excitation

peaks characteristic of orthorhombic structure and the tetragonal structure in addition to the small cubic (002) peak. However, as shown in Fig. 3(c), at 298 K the peaks characteristic of orthorhombic structure and cubic structure disappear and the three slightly split tetragonal (002) peaks appear. The fact means that only the tetragonal structure remains at low temperature. The [001] direction of tetragonal structure is almost along the direction of crystal growth. It suggests that in the martensitic phase at low temperatures, the tetragonal structure is more stable than the orthorhombic structure as we see in the powder case [1]. In Figs. 5(a), (b) and (c), the intensity maps of (hk0)-reciprocal plane around cubic (200) point at 415 K, 340 K and 303 K are shown. We see that the intensity of cubic (200) peak observed at 415 K decreases at 340 K and the peaks corresponding to tetragonal (200) or orthorhombic (002) begin to appear. At 303 K, only these newly appeared peaks grow up. They are presumably tetragonal (200) peaks, because at 303 K the orthorhombic structure is expected to disappear as shown in Fig. 3(c).

As a result, the structure of single crystal seems to elongate along the cubic [001] direction and shrink along the cubic [100] and [010] direction and finally to form the tetragonal structure (a=b<c) at low temperature.

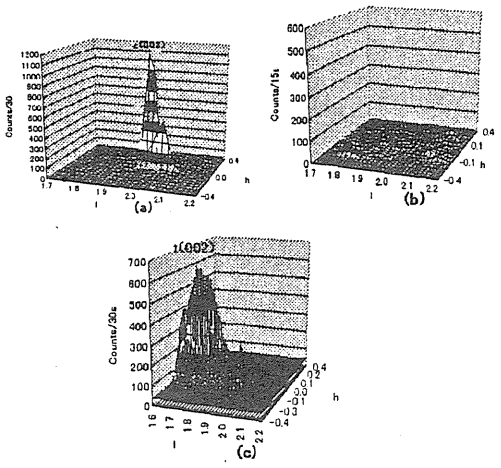


Figure 3: Intensity maps on (h0l)-reciprocal plane around cubic (002) point, (a) at 415K, (b) at 330 K and (c) at 298 K.

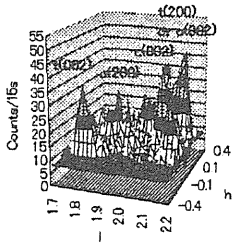


Figure 4: Intensity map on (h0l)-reciprocal plane around cubic (002) point at 330 k, where the scale of vertical axis is expanded.

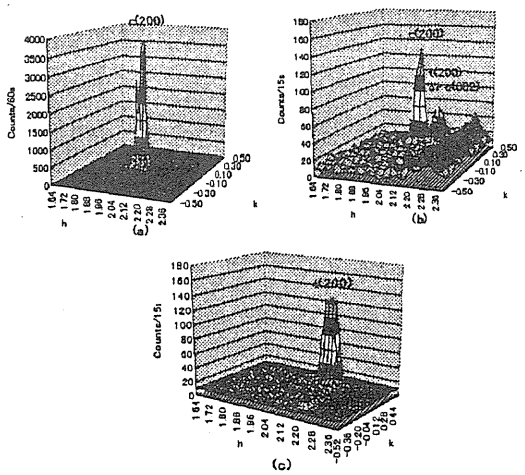


Figure 5: Intensity maps on (hk0)-reciprocal plane around cubic (200) point, (a) at 415 K, (b) at 340 K and (c) at 303 K. The long slender peak in Fig. (b) is due to the diffraction of Al sample holder.

References

[1] K. Inoue et al., Activity Report on Neutron Scattrering Research, 9 (2002) 64.
[2] P. J. Brown et al., J. Phys: Condens. Matter 14 (2002)10159.
[3] K. Inoue et al., *Proc. Forth Pacific Rim Int. conf. on Advanced Materials and Processing*, (The Japan Institute of Metals,2001) **Vol.II** (2001) 1689.

研究テーマ：形状記憶合金の中性子回折
表題：少量の B を含む $Ni_{2.18}Mn_{0.82}Ga$ のマルテンサイト相における結晶構造

Crystal Structure in the Martensitic Phase of $Ni_{2.18}Mn_{0.82}Ga$ with Small Amount of B

1-1-6

K. Inoue, T. Masuda, H. Maeda, K. Enami and Y. Yamaguchi *

Faculty of Science and Technology, Ryukoku University, Seta, Otsu 520-2194, Japan;
**IMR, Tohoku University, Aoba-ku, Sendai 980-8577, Japan*

A Heusler-type $Ni_{2.18}Mn_{0.82}Ga$ alloy has a thermo-elastic martensitic transformation temperature of about 340 K, which is coincident with Curie temperature. The alloy is expected as a material showing a shape memory effect caused by external magnetic field [1]. A single crystal of the alloy shows a shape memory effect, when we increase the temperature. However, a poly-crystal of the alloy did not show a shape memory effect, because of the brittleness of the alloy.

Recently, we have found that the addition of small amount of B to the alloy improves the brittleness marvelously and the thin plate of the poly-crystal of the alloy exhibits a shape memory effect. To investigate the origin of this improvement, we have made the neutron diffraction of the powder sample to know the change of crystal structure according to the temperature change. We also made surface analysis by EPMA to know the position of B in the poly-crystal.

The samples, $(Ni_{2.18}Mn_{0.82}Ga)_{99.6}B_{0.4}$ and $(Ni_{2.18}Mn_{0.82}Ga)_{98.8}B_{1.2}$ were prepared by non-contact float-melting furnace under Ar atmosphere. After melting of two times with upside down, they were annealed at 850 ℃ for 24 hours. The martensitic transformation temperature and the Curie temperature were determined by electrical resistivity measurement and the magnetization measurement. We found that the addition of B decreases the martensitic transformation temperatures (M_S, M_f, A_S and A_f points) extremely. For instance, in case of $(Ni_{2.18}Mn_{0.82}Ga)_{98.8}B_{1.2}$, they decrease about 100 K from about 340K to about 240 K.

For neutron diffraction, after crushing the sample to the powder, we annealed them for 1 hour to remove the strain. The size of the powder was not so small as that for X-ray diffraction, because the size effect changes the transformation temperature extremely. The diffractometer, HERMES, installed on T1-3 port of JRR-3M was used for powder neutron diffraction. We perform Rietveld analysis of the diffraction patterns using the computer program, RIETAN-2000. To exclude the effect of magnetic scattering, we made the analysis using the scattering angle, 2θ, over 70° .

We found that in the martensitic phase of $(Ni_{2.18}Mn_{0.82}Ga)_{99.6}B_{0.4}$ and $(Ni_{2.18}Mn_{0.82}Ga)_{98.8}B_{1.2}$, a tetragonal structure and an orthorhombic structure coexist as in case of $Ni_{2.18}Mn_{0.82}Ga$ alloy [3]. The two structures are all Heusler structures, which are constructed only by changing the length of axis of cubic Heusler structure. In the orthorhombic structure, the length of b-axis is nearly the same as that of a, b and c-axes of cubic structure. The length of a-axis of orthorhombic structure is about 5 % longer than that of cubic axis, and that of c-axis is about 5 % shorter. The length of tetragonal a- and b-axes is the same as that of orthorhombic c-axis, and that of tetragonal c-axis is longer than that of orthorhombic a-axis. These relations are shown in Fig. 1. The volume of the unit cell of two structures is the same as that of cubic structure. The situation is similar to that of $Ni_{2.18}Mn_{0.82}Ga$ [3]. However, the structures are quite different from that in the martensitic phase of stoichiometric Ni_2MnGa [4].

For $(Ni_{2.18}Mn_{0.82}Ga)_{98.8}B_{1.2}$, mass fractions of each structure obtained by Rietveld analysis are shown in Fig. 2, where Fig. 2 (a) shows the mass fractions with increasing temperature and Fig. 2 (b) shows

使用施設：JRR-3 in JAERI (Tokai)，装置：HERMES，分野 Structure & Excitation

ing temperature and Fig. 2 (b) shows those with decreasing temperature. It was found that martensitic transformation temperature decreases down to around 240 K, which is low with amount of about 100 K compared to the case of $Ni_{2.18}Mn_{0.82}Ga$ alloy with no B. We see that the behavior around transformation temperature is different for increasing temperature and for decreasing temperature. Moreover, the mass fraction of the orthorhombic structure is larger than that of tetragonal structure. This situation is opposite to the case of $Ni_{2.18}Mn_{0.82}Ga$.

To investigate the role of B, we have made the surface analysis using EPMA. The obtained result is shown in Fig. 3. We recognize the existence of grain boundary. We see that B and Ni elements exist on the grain boundary. There is almost no B element in the grain. This is the reason why the crystal structure is not different compared to $Ni_{2.18}Mn_{0.82}Ga$ with no B. We can recognize that the B element on the boundary improves the brittleness marvelously.

The difference between free energy of tetragonal structure and that of orthorhombic one is presumably so small that the small amount of B on the boundary changes the balance of mass fractions of two structures.

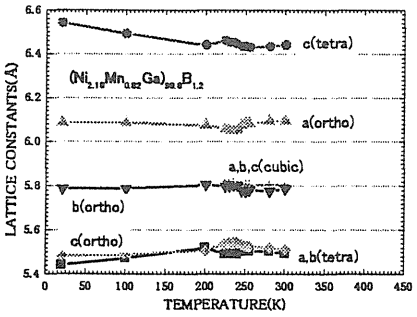


Figure 1: Each lattice constant of tetragonal, orthorhombic and cubic structures obtained with increasing temperature.

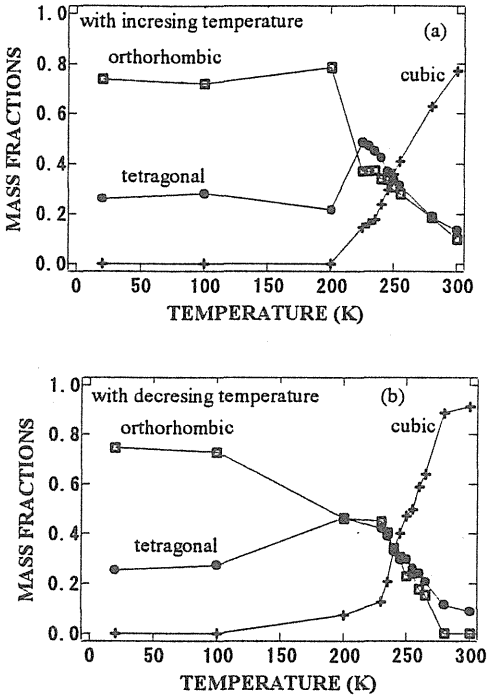


Figure 2: Mass fractions of each structure in the martensitic phase of $(Ni_{2.18}Mn_{0.82}Ga)_{98.8}B_{1.2}$, (a) with increasing temperature and (b) with decreasing temperature.

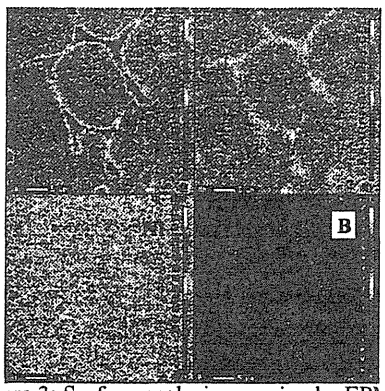


Figure 3: Surface analysis mapping by EPMA.

References

[1] K. Inoue et al., J. Phys. Soc. Jpn. 69 (2000) 3485.
[2] K. Inoue et al., *Proc. Forth Pacific Rim Int. conf. on Advanced Materials and Processing*, (The Japan Institute of Metals,2001) Vol.II (2001) 1689.
[3] K. Inoue et al., Activity Report on Neutron Scattrering Research, 9 (2002) 64.
[4] P. J. Brown et al., J. Phys: Condens. Matter 14 (2002)10159.

研究テーマ： 多層膜スピンスプリッターを用いたPd中吸蔵水素量の精密測定
表題： 中性子スピン干渉法を用いた水素吸蔵金属中の水素量精密測定の予備的結果

Preliminary report on precise hydrogen content in hydrogen absorbing materials using neutron spin interferometry

1-1-7

S. Tasaki[1], T.Ebisawa[2], D.Yamazaki[2], M. Hino[3], Y.Kawabata[3]

[1] *Dept. of Eng. Kyoto Univ. Yoshida-honmachi, Sakyou-ku Kyoto, 606-8501*
[2] *Japan Atomic Energy Research Institute, Tokai Ibaraki Pref. 319-1195*
[3] *Res.React. Inst. Kyoto Univ. Kumatori Osaka, 590-0494*

Hydrogen absorbing materials are old and new topics. Pd or Ti are well-known hydrogen absorber and have been investigated their absorbing properties in detail.

In our group, hydrogen content was measured in very thin Pd film (~300nm) using neutron micro-interferometer.[1] In this experiments, Pd film is sandwiched with Ni/Ti multilayer half mirrors, so that the reflection beams from the top and the bottom of Pd film interfere each other. The hydrogen content in the Pd film was detected due to the shift of the interference fringes when hydrogen was absorbed. The precision of hydrogen content was 5% in this experiments mainly because number of interference fringes referred to in the analysis was small.

Recently, we have developed neutron spin interference technique, which enables us to perform more precise measurement of hydrogen content in absorbing film.

In addition, for the practical use as 'New energy source', hydrogen absorbing materials has been much developed.

The aim of this research is to study the mechanism of hydrogen absorption to the new hydrogen absorbing materials usin neutron reflectometry and spin interferometry.

In the present study, we have tested the thin film quality of a hydrogen absorbing material LaNiAl alloy, supplied by Mr.T.Ebisawa (Nippon Seiko). LaNiAl was heated by electron beam and vacuum evaporated on Si wafers.

The neutron reflectivity is measured with the neutron reflectometer installed at C3-1-2-2 port of JRR-3M Reactor in Japan Atomic Energy Research Insitute. In Fig.1 the reflectivity is presented. Interference fringes characteristic for the reflectivity of a thin film are clearly shown.

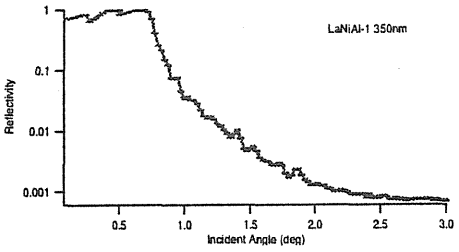


Fig. 1. Neutron reflectivity of a thin film of LaNiAl hydrogen absorbing material.

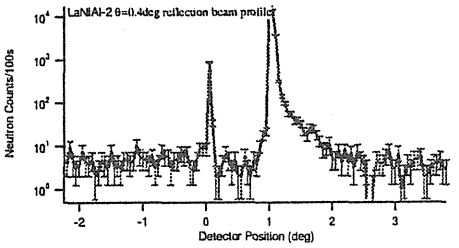


Fig. 2. Profile of the reflected beam from LaNiAl thin film at the incident angle of 0.4deg. ??

In addition to the reflectivity, we measured the reflected beam profile from the same sample at the incident angle of 0.4 deg.

From these data, the surface and thickness homogeneity are sufficient.

In the next steps, we will perform 1. reflectivity measurement of the above sample after hydrogen is absorbed, 2. spin interference measurement using multilayer spin splitters in which the gap layer is made of LaNiAl.

References

[1] S.Tasaki, T.Kawai, T.Ebisawa, J. Appl. Phys. 78(1995) 2398-402.

使用施設：JRR-3　装置： C3-1-2-2 (MINE)，分野： 1.Structures & Excitations.

研究テーマ：ヌクレオチド水和物結晶における水素結合網の動的挙動の解析
表題：イノシン5'-リン酸二ナトリウム水和物（中湿度領域安定相）における水素結合網の中性子回折法による解析

Neutron Diffraction Analysis of Hydrogen Bonding Networks of the Inosine 5'-Monophosphate Hydrate Stable in Medium Humidity Range

1-1-8

Y. Sugawara, S. Yamamura, H. Osamura, H. Kimura*, and Y. Noda*

*School of Science, Kitasato University, 1-15-1 Kitasato, Sagamihara, Kanagawa 228-8555, Japan; *Institute of Multidisciplinary Research for Advanced Materials, Tohoku University, 2-1-1 Katahira, Aoba-ku, Sendai 980-8577, Japan*

Hydrogen-bonding scheme and dynamics of crystal water molecules is of interest from the viewpoint of structural biology and crystal engineering of soft materials. We have been carrying out the crystallographic, spectroscopic and theoretical investigation of the humidity-induced phase transition of nucleosides and nucleotides. Increase or decrease of the number of crystal water molecules causes the phase transition coupled with re-construction of hydrogen-bond networks. [1]

The hydration number of disodium inosine 5'-monophosphate (Na_2IMP) changes from zero to ten in the relative humidity range 0 to 90% at room temperature. [2] Neutron diffraction analysis of $Na_2IMP.7H_2O$, which is stable in the relative humidity region 40 - 60% was carried out to determine hydrogen positions. Besides the hydrogen bond network was confirmed, the elongated nuclear distribution of several oxygen and hydrogen atoms was found, and it would be attributed to dynamic disorder of crystal water molecules.

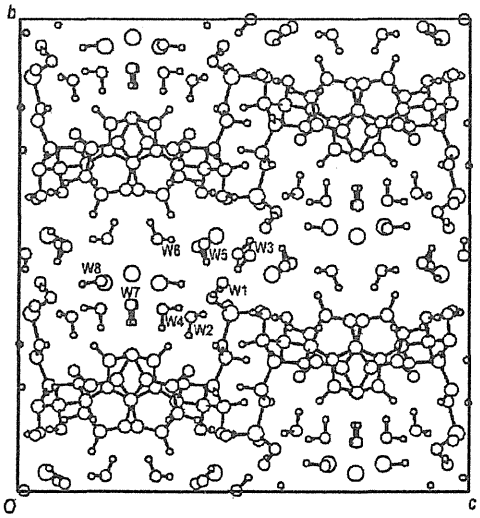


Figure 1: Crystal structure of Na_2IMP viewed along the *a* axis. Large isolated circles are Na^+ sites.

Table 1: Crystal data

Chemical formula	$Na_2C_{10}H_{11}N_4O_8P.7H_2O$
Crystal system	orthorhombic
Space group	$C222_1$
a/Å	8.697(5)
b/Å	23.208(8)
c/Å	21.975(9)
Z	8

The compound was purchased from Kohjin Co. Ltd., and crystallized from an aqueous solution. A crystal with approximate dimensions 7.6 x 3.5 x 1.5 mm^3 was sealed in a capillary tube with a saturated solution of NaBr to control the relative humidity at 58%, and the sample was used for data collection. Using a four-circle diffractometer, FONDER, at T2-2 of JRR3M in JAERI (Tokai), 1880 neutron intensity data were measured at room temperature. Crystal data are shown in Table 1. The neutron wavelength is 1.24 Å, and a resolution is up to 0.88 Å. Initial difference Fourier maps were calculated based on non-hydrogen atoms of the IMP molecule determined by X-ray analysis. In a series of full-matrix least squares refinement cycles followed by difference

使用施設：JRR-3　装置：FONDER(T2-2)，分野：Structure & Excitations

Fourier syntheses, Na^+ and O and H atom sites of crystal water molecules were assigned and refined. All hydrogen atoms of the IMP molecule and 13 hydrogen sites of eight crystal water sites were determined (Fig. 1). The sites of oxygen atoms and sodium ions are essentially the same as those determined by X-ray analysis. The final R factor is 0.077 for 1194 observed reflections ($|F_o|>4\sigma(F_o)$).

A layered structure of IMP molecules is formed perpendicular to the *b* axis. Intermolecular hydrogen bonds between a phosphate and a hydroxyl group of a ribose along the *a* axis and those between a phosphate and an amino group of a base moiety along the *c* axis are confirmed.

Out of eight water sites determined, four sites are disordered and two are partially occupied. The nuclear distribution of disordered water molecules is classified into three types. Those belonging to the first type (W3, W5) form two hydrogen bonds as hydrogen donors to two phosphate groups. The position of the oxygen atom is split into two sites, e. g. in the case of W3 each site is a coordination site to a sodium ion. On the other hand, the negative nuclear distribution due to each hydrogen atom is rather compact and spherical (Fig. 2). The water molecule belonging to the second type (W4) forms only one hydrogen bond as a proton donor (H4W). The other hydrogen atom (H4W') does not form a hydrogen bond, and the nuclear distribution of O4W and H4W' is elongated (Fig. 3). The nuclear distribution of the third type (W6) is channel-like and surrounded by multiple interaction sites.

It is rather an unexpected result that the nuclear distribution of an oxygen atom is larger than that of a hydrogen atom. The nuclear distribution seems to reflect several types of librational motions of crystal water molecules.

References

[1] Y. Sugawara et al., J. Chem. Phys. **106** (2002) 10363.

[2] N. Nagashima, Doctoral Dissertaion, University of Tokyo, Tokyo, Japan (1985).

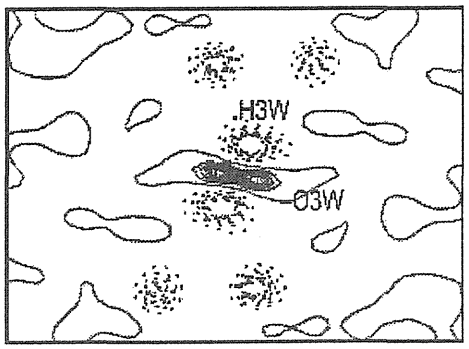


Figure 2: Nuclear distribution of Na_2IMP around W3 calculated by the maximum entropy method. The plane perpendicular to the *a* axis is shown.

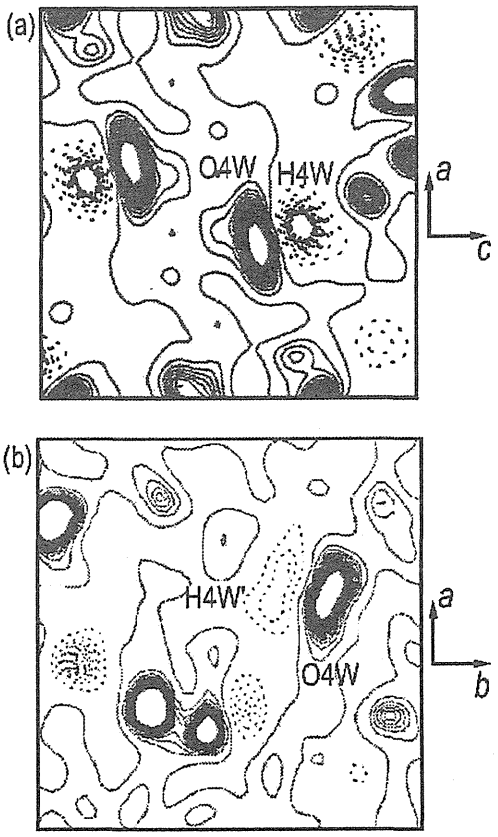


Figure 3: Nuclear distribution of Na_2IMP around W4 calculated by the maximum entropy method. The plane perpendicular to the *b* axis (a) and that perpendicular to the *c* axis (b).

研究テーマ：超イオン導電体における乱れ
表　題：Geにおける散漫散乱の温度依存性

1-1-9

Temperature dependence of diffuse scattering from crystalline Ge

M. ARAI, A. THAZIN, Y. FUJISHIMA, T. SAKUMA, H. TAKAHASHI[1] and Y. ISHII[2]

Faculty of Science, Ibaraki University, Mito, Ibaraki 310-8512
[1]Faculty of Engineering, Ibaraki University, Hitachi, Ibaraki 316-8511
[2]Advanced Science Research Center, JAERI, Tokai, Ibaraki 319-1195

Correlation effects between the thermal displacements of atoms play an important role in the superionic conductors. In addition to superionic conductors an oscillatory diffuse scattering was observed in semiconductor GaAs[1)]. In order to investigate the detailed thermal correlation among atoms at distances above second nearest neighboring atoms, diffuse neutron background intensity of Ge has been measured from 6 K to 673 K using a neutron diffractometer HRPD installed at JRR-3 in JAERI. A powder sample of Ge in a vanadium container with 10 mm in diameter was used. The incident neutron wave length of 1.83 Å was used. Neutron diffraction data were collected for 1 d over the 2θ range of 20° to 115°. Figure 1 shows the results of the measurement of Ge at 6, 290 and 673 K. Several sharp Bragg lines and a large diffuse scattering were observed except at 6 K. The oscillatory diffuse scattering from Ge crystals was confirmed by the measurement at high temperatures. The maximum intensity of the Bragg line is about 60,000. The first and second peak of the oscillatory diffuse scattering appear at 2θ~55° and 110° in Fig. 1, respectively. It is also found that small peaks of the oscillatory diffuse scattering appear at 2θ~30°, 60° and 90° at 673 K.

Numerical calculations of the diffuse background have been made based on diamond type structure including the correlation between the thermal displacements of atoms[2)]. The positions of the first and second peak in diffuse scattering of Ge in Fig. 1 at 673 K are related to the reciprocal of the distance between first nearest neighboring atoms; the distance in Ge is about 2.46 Å. The diffuse scattering intensity changes as $\sin(Qr)/Qr$. The main contribution to the oscillatory diffuse scattering was from the correlation among the displacements of first nearest neighboring atoms. The value of the thermal correlation between these Ge atoms is about 0.7.

Expected contributions from second nearest neighboring atoms in crystalline Ge to the diffuse scattering were calculated. The observed oscillatory diffuse scattering at 2θ~30°, 60° and 90° corresponded to the contribution from the correlation between the thermal displacements of the second nearest neighboring atoms. The value of the thermal correlation between these Ge atoms is less than that between first nearest neighboring atoms.

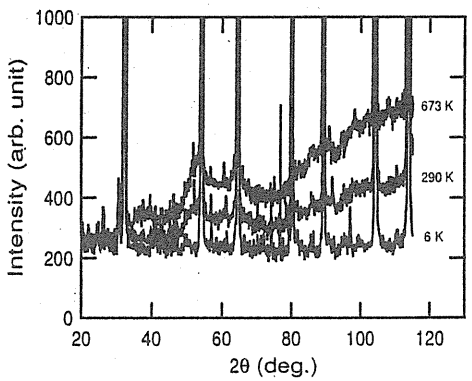


Figure 1: Observed neutron powder diffraction intensity for Ge at 6, 290 and 673 K.

References

1) M. Arai, K. Ohki, M. Mutou, T. Sakuma, H. Takahashi and Y. Ishii: J. Phys. Soc. Jpn. **70** (2001) 250.
2) T. Sakuma: J. Phys. Soc. Jpn. **42** (1993) 4150.

原子炉：JRR-3　　装置：HRPD(1G)　　分野：中性子散乱（構造）

研究テーマ：プロトンとデューテロンの波動関数
表題：(NH4)2SnCl6 と(ND4)2SnCl6 におけるプロトンとデューテロンのゼロ点分布の単結晶中性子回折による研究

Zero Point Distribution of Protons and Deuterons in $(NH_4)_2SnCl_6$ and $(ND_4)_2SnCl_6$ by Single Crystal Neutron Diffraction

1-1-10

T. Matsuo[1], N. Onoda-Yamamuro[2], O. Yamamuro[1], A. Inaba[1], R. Kiyanagi[3], H. Kimura[3] and Y. Noda[3]

1) Department of Chemistry, Graduate School of Science, Osaka University, Toyonaka, Osaka

2) Department of Natural Sciences, College of Science and Engineering, Tokyo Denki University, Saitama

3) Institute of Multidisciplinary Research for Advanced Materials, Tohoku University, Katahira, Sendai

Some of the deuterated ammonium hexachloro-metallates undergo phase transitions at low temperature which the corresponding normal ammonium compounds do not [1]. This occurs for M=Pt, Te, Pd and Pb. The transition entropy depends on M, but it is invariably larger than R (= 8.3145J/(K mol)), suggesting an interesting possibility that each of the protons belonging to the ammonium ions are distributed over a set of positions dictated by the cubic symmetry. For deuterated ammonium ions the multiple positions are a consequence of classical orientational disorder. For the hydrogenous ammonium compounds, the crystal symmetry is cubic even at the lowest temperature. Therefore, a multi-maximum proton distribution, if actually found, should be a property of the crystal in the ground state. As this is a hitherto unknown aspect of the crystal structure, we regard the possibility worth pursuing by neutron diffraction. In a previous report we described our experiment on $(NH_4)_2PtCl_6$ showing a novel structure of the ammonium ion in which each of the proton is distributed on a torus. For M=Sn, the hydrogenous and deuterated ammonium compounds are both cubic down to the lowest temperature. This gives us an opportunity to examine how the deuteron is distributed in the same cubic environment. We performed a low temperature neutron diffraction on ammonium and deuterated ammonium hexachlorostannate single crystals, $(NH_4)_2SnCl_6$ and $(ND_4)_2SnCl_6$ using the diffractometer FONDER at JRR-3M in JAERI (Tokai).

Experiment

The sample ($(NH_4)_2SnCl_6$) was prepared from acidified aqueous solution of ammonium chloride and tin tetrachloride $(ND_4)_2SnCl_6$ was prepared by recrystallization of $(NH_4)_2SnCl_6$ from deuterium oxide acidified with DCl. The recrystallization was repeated three times. Single crystals of an appropriate size (ca. 2 mm) were chosen and fixed to the cold finger of a closed-cycle refrigerator mounted on the diffractometer. Diffraction data were collected at T = 8 K and 300 K. The neutron wavelength was 1.5729 Å. In total 73 and72 (*hkl*) peak intensities were determined for $(NH_4)_2SnCl_6$ at 8 K and 300 K, respectively, and 78 intensities for $(ND_4)_2SnCl_6$ at both temperatures. Because of the high symmetry of the crystal, several equivalent Bragg peaks occurred within the available ranges (2θ<=150 deg.) of the diffraction angle for many of the indices. The above mentioned numbers of intensities are those of the independent peaks. All the peak intensities were collected, equivalent ones compared to

使用施設：JRR-3　装置：FONDER　分野：Structure and Excitations

check the consistency and then averaged.

Results

All the peaks observed were consistent with the *Fm*3m symmetry. The basic structure of the crystals has been established: the antifluorite K_2PtCl_6 structure. The known atomic positions were used as the initial values for the least squares analysis. All the atoms other than hydrogen (deuterium) are ordered. The hydrogen atoms were placed off the body diagonal axis but still on the mirror plane. There are three equivalent positions for a hydrogen atom. The number of variables in the least squares fitting was 13. The fitting converged satisfactorily. A different model with hydrogen atoms in the ordered positions on the triad axis gave a poorer fitting. A more general model placing 1/6 of a hydrogen atom in a general position did not give a better result than the 3-position model.

A result (for $(NH_4)_2SnCl_6$ at 8 K) is given below

	x	*y*	*z*
N	0.25	0.25	0.25
H	0.3168(25)	0.3168	0.2840(23)
Sn	0	0	0
Cl	0.2440(3)	0	0

	*U*11	*U*22	*U*33
N	0.007(4)	0.007	0.007
H	0.026(7)	0.026	0.042(12)
Sn	0.003(2)	0.003	0.003
Cl	0.001(1)	0.003(2)	0.003

	*U*12	*U*13	*U*23
N	0	0	0
H	-0.020(6)	0.000(15)	0.000
Sn	0	0	0
Cl	0	0	0

The position parameters agree well with literature values. An interesting point about the thermal parameters is that the components *Uij* of hydrogen are an order of magnitude larger than those of the other atoms. This result was obtained at 8 K where the crystal was essentially in its ground state. The difference between the *Uij* values of the hydrogen and heavy atoms was smaller at 300 K: *Uij*(H)'s was about only twice as large as *Uij*(Sn). The same trend was found for $(ND_4)_2SnCl_6$.

Having found that the hydrogen atom is delocalized in (at least) three positions at 8 K, we applied the Maximum Entropy transformation to the diffraction data to reconstruct the most likely distribution of the atoms in the unit cell. Without describing the detail of the analysis we present the result for the neutron scatterer density corresponding to ND_4 in $(ND_4)_2SnCl_6$ at 8 K. For $(NH_4)_2SnCl_6$ the MEM result was essentially the same, but with the protons even more delocalized. The depleted density at the center of the triangular torus is evidence for rotational tunneling of the ND_4 ion. We may describe the deuteron in $(ND_4)_2SnCl_6$ as a deuteron cloud, in analogy with the proton cloud for the proton in NH_4 in $(NH_4)_2PtCl_6$ reported previously.

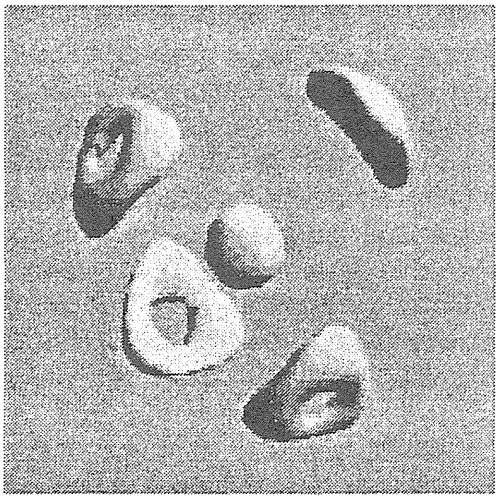


Fig. 1 MEM reconstruction of the neutron scatterer density for ND_4 in $(ND_4)_2SnCl_6$ at 8K.

研究テーマ：超イオン導電体における乱れ
表　題：AgClにおける原子の熱相関

1-1-11

Correlation among thermal displacements of atoms in crystalline AgCl

M. ARAI, A. THAZIN, Y. FUJISHIMA, T. SAKUMA, H. TAKAHASHI[1] and Y. ISHII[2]

Faculty of Science, Ibaraki University, Mito, Ibaraki 310-8512
[1]Faculty of Engineering, Ibaraki University, Hitachi, Ibaraki 316-8511
[2]Advanced Science Research Center, JAERI, Tokai, Ibaraki 319-1195

The diffuse scattering in solid electrolytes has been investigated by X-ray and neutron diffraction measurement[1, 2]. In case of the large thermal atomic vibration, the diffuse scattering intensities become large and show oscillatory form. The oscillatory diffuse scattering is explained by correlation effects between the thermal displacements of atoms.

Neutron scattering measurements were carried out for a powder AgCl from 10 K to 260 K in a cryostat using HRPD at JRR-3 in JAERI. The powder sample was contained in a vanadium container with 10 mm in diameter. The incident neutron wave length of 1.823 Å was used. Neutron diffraction data were collected for 1 d at 0.05° intervals over the 2θ range of 20° to 150°. Several sharp Bragg lines and a large oscillatory diffuse scattering were observed at 260 K. However the oscillatory characteristic in the diffuse scattering at 10 K is not clear. The values of thermal parameter at 260 K are larger than those at 6 K. The diffuse scattering intensity depends on thermal vibration parameter.

The observed powder diffraction intensities of AgCl at 260K are shown by broken line in Fig. 1. Solid line shows the calculated diffuse scattering intensities. Observed diffuse scattering has an oscillatory form and the peaks appear in the position of $2\theta \sim 35$, 60 and 100°. Diffuse scattering intensities calculated by the correlation effect between the thermal displacements of atoms showed similar oscillatory form, and the peaks appeared in the same positions as those of observed data.

The peaks of $2\theta \sim 60$ and 100° are based on thermal correlation between the first nearest neighboring atoms (Ag-Cl). The main contribution to the oscillatory diffuse scattering is from the correlation among the displacements of first nearest neighboring atoms. The peak of $2\theta \sim 35°$ is the influence of the correlation effect between the second nearest neighboring atoms (Ag-Ag, Cl-Cl). The value of correlation between the first nearest neighboring atoms is about 0.8 and the correlation between the second nearest neighboring atoms about 0.5. If the interatomic distances become greater than that of the third nearest neighboring atom, the values of correlation become less than 0.1, and most influences on diffuse scattering are not observed. The value of thermal correlation decreases rapidly with the interatomic distance.

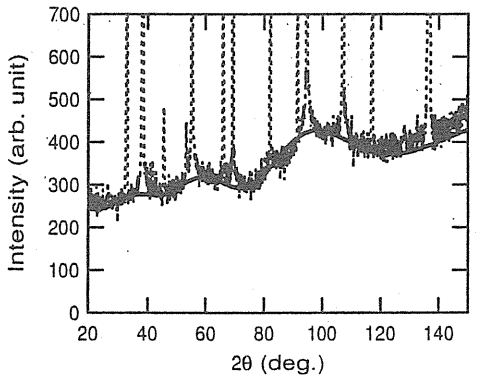


Figure 1: Observed neutron powder diffraction intensity (broken line) and calculated diffuse scattering intensity (solid line) for AgCl at 260 K.

References

1) T. Sakuma: J. Phys. Soc. Jpn. **42** (1993) 4150.
2) T. Sakuma, Y. Nakamura, M. Hirota, M. Arai and Y. Ishii: J. Phys. Chem. Solids **60** (1999) 1503.

原子炉：JRR-3　　装置：HRPD(1G)　　分野：中性子散乱（構造）

研究テーマ：有機結晶中における水素移動反応の機構の解明
表題：キラルチオラクタム形成における中性子回折による重水素移動機構の解明

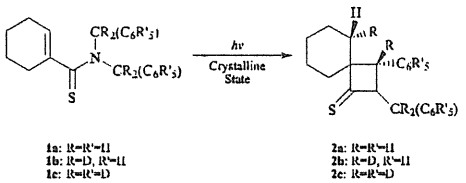
Analysis of Deuterium Migration Process in Chiral Thiolactam Formation by Neutron Diffraction

1-1-12

Takaaki Hosoya, Hidehiro Uekusa, Yuji Ohashi, Takashi Ohhara,* Hiroyuki Kimura,† and Yukio Noda†

Dept. of Chem. Mat. Sci., Tokyo Inst. Tech., Ookayama 2-12-1, Meguro, 152-8551
**Inst. of Mat. Struct. Sci., High Energy Accelerator Res. Org., Oho, Tsukuba 305-0801*
†Inst. of Multidisl. Res. Adv. Mat., Tohoku Univ., Katahira, Aoba-ku, 980-8577

The molecule of *N,N*-dibenzyl-1-cyclohexene-carbothioamide, **1a**, was photo isomerized to 1-benzyl-4-phenyl-2-thioxo-azetidine-3-spirocyclohexane, **2a**, in high optical yield.[1] From the crystal structure analyses of the reactant and product crystals by X-rays, the mechanism of the asymmetric induction was proposed.[1]



1a: R=R'=H
1b: R=D, R'=H
1c: R=R'=D

2a: R=R'=H
2b: R=D, R'=H
2c: R=R'=D

Recently we succeeded in isomerizing **1a** to **2a** with retention of the single crystal form after many trials.[2] A crystal was irradiated with a xenon lamp for 330 h and then the structure analyzed by X-rays indicated 65.7% of **1a** was converted to **2a** within the crystal. This disordered structure made clear how the benzyl carbon of **1a** makes a bond with the α carbon of the cyclohexene ring and why only one enantiomer of **2a** is produced from the chiral crystal. However, the question whether the β carbon of the cyclohexene ring abstracts the hydrogen atom within a molecule or from the neighboring molecule has not been made clear.

To analyze the hydrogen migration mechanism in the crystal, four hydrogen atoms of the two benzyl groups of compound **1a**, were replaced with the deuterium atoms, **1b**. If the crystal was irradiated with a xenon lamp, the photo isomerization occurred with retention of the single crystal form to produce **2b**. This work reports the deuterium-migration mechanism in the photo isomerization by neutron diffraction technique.

A large crystal of **1b**, 4.5 × 1.5 × 1.0 mm^3, before irradiation, was mounted on the T2-2 FONDER offset 4-circle diffractometer set up at the JRR-3M reactor in JAERI,[3] and the neutron diffraction data were collected.[4] The structure is in good agreement with that obtained by X-ray analysis except the deuterium atoms of the two benzyl groups. The C2...C8 distance is 2.87(9) Å and C3...D8A is 2.5(1) Å.

All other hydrogen atoms of two benzyl groups were replaced with the deuterium atoms, **1c**, in order to reduce the background intensity caused by incoherent scattering and the large neutron absorption by hydrogen atoms. A large crystal of **1c**, 10.0 × 2.2 × 0.8 mm^3, was divided into two, and both of them were irradiated for 20 days at 263 K with a xenon lamp through a filter, Y-44 filter (HOYA Y-44 sharp-cut). Two small crystals were quarried out from the surface and the center of one of the crystals. The sizes of them were 0.3 × 0.3 × 0.1 and 0.3 × 0.3 × 0.15 mm^3, respectively. From their crystal structure analyses by X-rays, approximately 20 and 15% of **1c** were photo isomerized to **2c**, respectively. Another large crystal was irradiated with the xenon lamp under the same conditions as those for the first one, assuming that about 20% would be isomerised to **2c**.

The neutron intensity data of the second crystal of **1c** after irradiation, 4.0 × 2.2 × 0.8 mm^3 were also collected using FONDER under the same conditions as before.[4] The difference Fourier map

使用施設：JRR-3 ，装置：FONDER(T2-2)，分野 Structure & Excitation

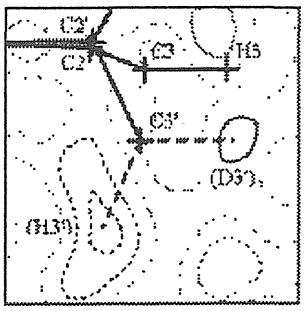


Figure 1. Difference Fourier map projected on the plane composed of H3-C3-C3'. All the atoms except H3' and D3' were included in the Fc calculation.[6] Solid and dotted/dashed contours indicate positive and negative ones, respectively.

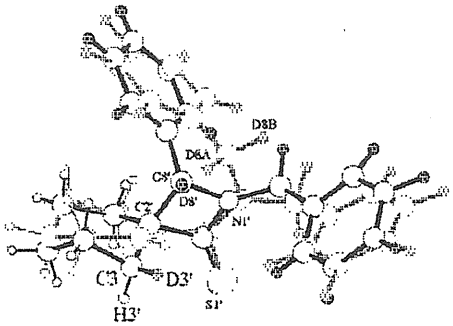


Figure 2. Molecular structure of **1c**: the deuterium atom bonded to C3' was occupied to equatorial site of cyclohexane ring moiety.

around C3 is shown in Fig. 1. The positive peak at H3 indicates that a part of the H3 atom is moved to the negative peak at H3'. The positive peak at D3' can be assigned to the position of the transferred deuterium atom. This indicates that the positions of deuterium and hydrogen atoms are equatorial and axial, respectively, shown in Fig. 2.

This result clearly suggests that the photoreaction proceeds via the intra-molecular deuterium migration as shown in Fig. 3. The β carbon of the cyclohexene, C3, abstracts an intra-molecular deuterium atom, D8A, involving homolytic bond cleavage. If the deuterium atom comes from the neighbouring molecule, the transferred deuterium, D8A', should occupy the axial position. The benzyl carbon radical would be generated after the deuterium abstraction. Then, the produced benzyl carbon radical

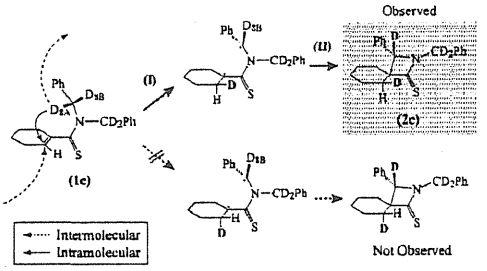


Figure 3. Reaction mechanism of **1c**: The first (I) and second (II) reaction steps indicate the intra- or intermolecular deuterium migration leaving a benzyl radical and the benzyl carbon radical makes the thiolactam ring, respectively.

moves to form the β-thiolactam ring with keeping its conformation, considering from the observation by X-rays.[2]

References and Notes

1 M. Sakamoto, M. Takahashi, W. Arai, T. Mino, K. Yamaguchi, S. Watanabe, and T. Fujita, Tetrahedron, **56**, 6795 (2000).

2 T. Hosoya, T. Ohhara, H. Uekusa, and Y. Ohashi, *Bull. Chem. Soc. Jpn.*, **75**, 2147 (2002).

3 Y. Noda, H. Kimura, R. Kiyanagi, A. Kojima, Y. Morii, N. Minakawa, and N. Takesue, *J. Phys. Soc. Jpn.* **70**, *Suppl.* A, 456 (2001).

4 Crystallographic details: all structures were refined by *SHELXL*-97,[5] and the surface indices for absorption correction were determined using Bruker Smart CCD diffractometer, initial structure was fixed by X-ray structure.[5] **(1b)** $C_{21}H_{19}D_4NS$, *monoclinic*, $P2_1$, a = 8.679(6), b = 10.202(8), c = 10.083(6) Å, β = 99.059(5)°, V = 881.7(11) Å^3, Z = 2, D_{calc} = 1.226 g/cm^3, R_1 (276 with $F^2 > 2\sigma(F^2)$) = 0.1486, $_wR_2$ = 0.2800, R_1 (all unique 672 data) = 0.3494, $_wR_2$ = 0.3492, R_{int} = 0.1041, GoF = 1.657 for 180 parameters refined on F^2 **(1c)** $C_{21}H_9D_{14}NS$, *monoclinic*, $P2_1$, a = 8.675(4), b = 10.25(2), c = 10.062(6) Å, β = 99.54(5)°, V = 883(2) Å^3, Z = 2, D_{calc} = 1.262 g/cm^3, R_1 (953 with $F^2 > 2\sigma(F^2)$) = 0.2067, $_wR_2$ = 0.4611, R_1 (all unique 1136 data) = 0.2380, $_wR_2$ = 0.4878, R_{int} = 0.0847, GoF = 2.077 for 35 parameters refined on F^2 (the molecule geometry was refined as a rigid body and the thermal parameters of non-hydrogen atoms and H3' and D3 were also refined).

5 M. G. Sheldrick, *SHELXL-97*, Program for the refinement of crystal structures, University of Göttingen, Germany (1997).

6 The X-ray analysis of 2a indicates that the positions of H3' and D3' are almost on the plane of H3-C3-C3'.

研究テーマ：ランタノイド-白金族元素を含む関連酸化物の磁気構造
表　題：三元系イリジウム酸化物 Pr_3IrO_7 における構造相転移

1-1-13

Structural Phase Transition for Ternary Iridium Oxide Pr_3IrO_7

H. Nishimine, M. Wakeshima, Y. Hinatsu, Y. Ishii[1]

Division of Chemistry, Graduate School of Science, Hokkaido University, Sapporo 060-0810
[1]Japan Atomic Energy Research Institute, Tokai-mura, Ibaraki 319-1195

Figure 1 shows the temperature dependence of specific heats for a ternary iridium oxide Pr_3IrO_7. A first order phase transition is observed at around 260 K in the $C-T$ curve. We have considered that this anomalies was due to a strucural phase transition. The crystal structure of the high-temperature phase was determined to be an orthorhombic La_3NbO_7-type structure with space group *Cmcm* through powder X-ray diffraction measurement at room temperature.

In order to elucidate the crystal structure of the low-temperature phase, powder neutron diffraction patterns for Pr_3IrO_7 were collected at 250 K and room temperature (RT) using a High Resolution Powder Diffractometer (HRPD) in the JRR - 3M reactor with a neutron wave length (λ = 1.82268 Å). The refinements for diffraction patterns were performed by the Rietveld method.

Both of the neutron diffraction patterns were refined with space group *Cmcm*. Figure 2 shows the diffraction patterns at RT. The refinement for RT data is successful and the lattice constants and the atomic positions are in good agreement with those for XRD data (R_{wp} = 6.66 %, R_I = 2.74 %, a = 10.9782(13) Å, b = 7.4389(9) Å, c = 7.5361(9) Å). The refined structral parameters are listed in Table 1. In the diffraction pattern at 250K, however, some additional Bragg reflections which could not be fitted with *Cmcm* appear. The results for neurton diffraction measurements provide the evidence that the structural phase transition occurs at the temperature that the thermal anomaly is observed. We tried to determine the structure of the low-temperature phase. Unfortunately, we could not obtain the valuable information on its structure because the number of extra reflections is limited and their intensity is very weak as well as XRD data.

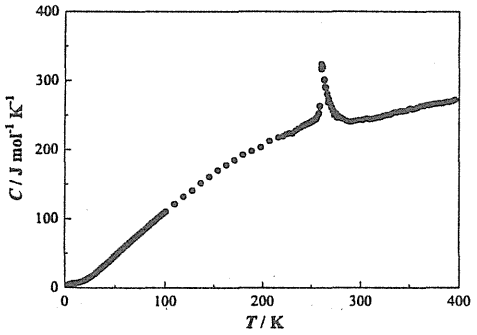


Figure 1: Temperature dependence of specific heats for Pr_3IrO_7.

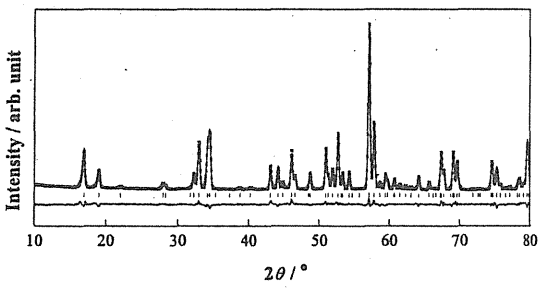


Figure 2: Powder neutron diffraction profiles for Pr_3IrO_7 at room temperature.

Table 1 Positional parameters for Pr_3IrO_7 at room temperature.

Atom	x	y	z	B(Å^2)
Pr(1)	0	0	0	0.93(8)
Pr(2)	0.2222(2)	0.3083(3)	0	0.66(6)
Ir	0	1/2	0	0.47(4)
O(1)	0.1256(1)	0.3171(2)	0.9582(2)	1.08(4)
O(2)	0.1308(2)	0.0289(3)	1/4	0.56(5)
O(3)	0	0.4098(4)	1/4	0.41(6)

原子炉：JRR-3　　装置：HRPD(1G)　　分野：中性子散乱（構造）

研究テーマ：Co 系熱電材料中の低エネルギー励起
表題：充填スクッテルダイト $Ba_{0.1}CoSb_3$ 中のフォノン状態密度の測定と計算

1-1-14

Observation and Calculation for Phonon Density of States in the Filled Skutterudite, $Ba_{0.1}CoSb_3$

T.Kajitani, Y.Ono, Y.Miyazaki, T.Goto[1], M.Sluiter[1] and Y.Kawazoe[1]

Department of Applied Physics, Graduate School of Engineering, and IMR[1], Tohoku University
Aoba05, Aoba-ku, Sendai 980-8579, Japan

Phonon density of states is one of the important physical quantity connected with the specific heat, Debye temperature, thermal conductivity, electric conductivity and structural stability, etc. Present authors observed phonon DOS curves of the filled and unfilled skutterudites , $Ba_{0.1}CoSb_3$ and $CoSb_3$, using JRR3M-AGNES at room temperature[1]. Powder samples were prepared by the co-melting procedure. Skutterudites are narrow gap semiconductors ($E_g \leqq 1.0$eV) and very promising Seebeck materials suitable for the thermo-electric conversion devices in the temperature range higher than 400K(lower than 1000K because of their melting points). The highest conversion efficiecy is recorded at about 12% (ZT>1.2), for the $Ce_{0.9}Fe_3CoSb_{12}$. Theoretical calculations using the computer codes,VASP (GGA + Molecular dynamics) and Wien2k(GGA-FLAPW), are carried out to obtain relaxed crystal structure , phonon density of states , elastic constants and band structure of the Ba filled skutterudite , $CoSb_3$.

Relaxed crystal structure of the $Ba_{0.5}CoSb_3$ is obtained from VASP calculation in Table I.

Table I : Optimized crystal structure of $Ba_{0.5}CoSb_3$,a=9.049Å (given) , Space group Pm-3(No.200)

Atom	site x y z
Ba	1b (1/2 1/2 1/2)
Co	8i (xxx),with x=0.2506
Sb_1	12j (0yz) with y=0.3334, z=0.1587
Sb_2	12k (1/2yz) with y=0.1605, z=0.3358

Main difference between the undoped one is in their space group, Im-3(No.204) for the $CoSb_3$, and inter-atomic distances between the Co and Sb, being 2.523 and 2.529Å in the doped one but 2.527Å in the $CoSb_3$, respectively. The elastic constants are calculated from the Born-Huang theory of long-wavelength limit as, C_{11}=174GPa, C_{12}=23GPa, C_{44}=52Gpa and B=73Pa ,respectively.

Figure 1 shows the observed and calculated phonon density(Ba vibration only) of states. There are 4-DOS peaks at about 5,13, 15 and 18 meV, in the Ba0.1 sample. Calculated DOS of the phonon modes at the Ba-site shown in the lower panel has similar peaks in the range from 9meV to 22 meV but 5meV mode is not obtained. 5meV peak are similarly observed in the Tl-filled $CoSb_3$ by Feldman et al.[2] Since calculated potential energy curve in the vicinity of Ba-site is nearly harmonic, 5meV mode could be due to the local vibration at the Sb-sites adjacent to the filler Ba.

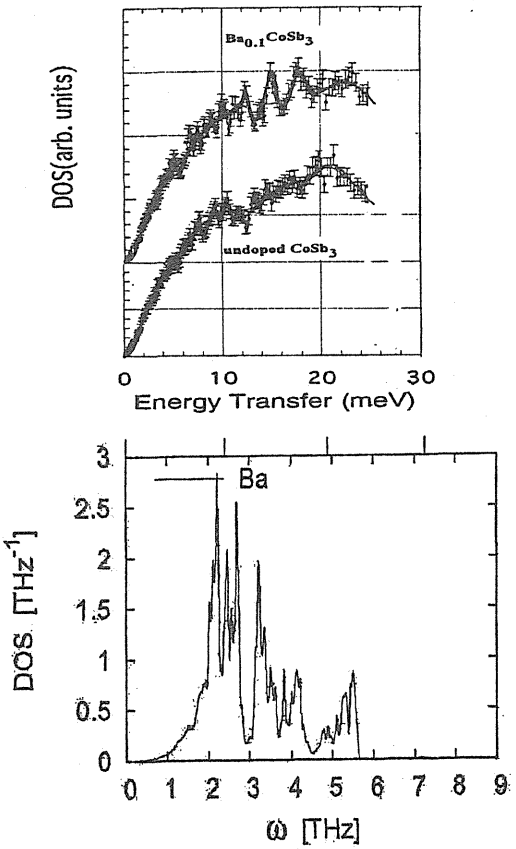


Fig.1:Observed DOS of $Ba_{0.1}CoSb_3$ (upper panel) and calculated one at Ba-site in $Ba_{0.5}COSb_3$ (lower panel).

References:

[1] T.Kajitani et al:Act.Rep. Neutron Scattering Res.,ISSP, Univ. Tokyo, 9(2002)61

[2] J.L.Feldman et al.:PRB 61(2000) R9209.

使用施設：JRR-3 ， 装置：AGNES (C3-1-1)、分野 Structures & Excitations

研究テーマ：ランタノイド-白金族元素を含む関連酸化物の磁気構造
表　題：擬一次元イリジウム酸化物 $Ca_5Ir_3O_{12}$ の構造と物性

1-1-15

Crystal Structure and Physical Properties of Pseudo-One-Dimensional Calcium Iridate $Ca_5Ir_3O_{12}$

M. Wakeshima, Y. Hinatsu, Y. Ishii[1]

Division of Chemistry, Graduate School of Science, Hokkaido University, Sapporo 060-0810
[1]Japan Atomic Energy Research Institute, Tokai-mura, Ibaraki 319-1195

The crystal structure of ternary oxide $Ca_5Ir_3O_{12}$ consists of infinite one-dimensional chains of the edge-sharing IrO_6 octahedra as shown in Fig. 1. This compound showed a weak ferromagnetic transition at 7.5 K through the magnetic susceptibility and specific heat measurements. Figure 2 shows the temperature dependence of the specific heats of $Ca_5Ir_3O_{12}$. In addition to the anomaly due to the magnetic ordering at 7.5 K, another λ-type anomaly which is not due to the magnetic ordering is observed at 105 K.

In order to elucidate the anomaly at 105 K, powder neutron diffraction patterns for $Ca_5Ir_3O_{12}$ were collected at 90 and 120 K using a High Resolution Powder Diffractometer (HRPD) in the JRR - 3M reactor with a neutron wave length (λ = 1.82268 Å). The refinements for diffraction patterns were performed by the Rietveld method.

The neutron diffraction profiles of $Ca_5Ir_3O_{12}$ at 90 and 120 K could be indexed in a hexagonal unit cell with space group of $P\bar{6}2m$. No difference between two diffraction profiles was observed and the Rietveld analyses of these diffraction data were performed by applying the same space group (a = 9.3472(5)Å, c = 3.1710(1)Å at 90 K, a = 9.3490(5)Å, c = 3.1713(1)Å at 120 K). The refined crystallographic parameters are listed in Table 1. The positional parameters, calculated bond lengths and bond angles at 90 and 120 K agree within the experimental error. If the anomaly at 105 K is due to only the local translation without transformations of the unit cell, such as a rotation of the IrO_6 octahedron, it is difficult to detect such as a change in the crystal structure by the powder diffraction technique because of the overlap of the reflection intensities.

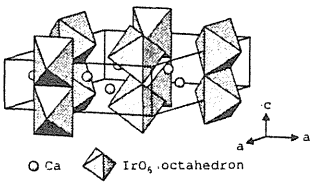


Figure 1: Schematic crystal structure of $Ca_5Ir_3O_{12}$.

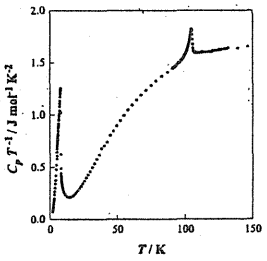


Figure 2: Temperature dependence of specific heats for $Ca_5Ir_3O_{12}$.

Table 1 Positional parameters for $Ca_5Ir_3O_{12}$ at 90 and 120 K.

Atom	x	y	z	B(Å^2)
90 K				
Ca(1)	1/3	2/3	1/2	0.18(17)
Ca(2)	0.7127(8)	0	1/2	0.18
Ir	0.3330(3)	0	0	0.43(8)
O(1)	0.2006(6)	0	1/2	0.59(8)
O(2)	0.4617(7)	0	1/2	0.59
O(3)	0.4460(5)	0.2407(4)	0	0.59
120 K				
Ca(1)	1/3	2/3	1/2	0.20(17)
Ca(2)	0.7131(9)	0	1/2	0.20
Ir	0.3334(3)	0	0	0.35(8)
O(1)	0.2008(6)	0	1/2	0.74(8)
O(2)	0.4620(6)	0	1/2	0.74
O(3)	0.4459(5)	0.2407(4)	0	0.74

原子炉：JRR-3　　装置：HRPD(1G)　　分野：中性子散乱（構造）

研究テーマ: $KRbSeO_4$のΣ_2フォノン分枝の振舞い
表題: $KRbSeO_4$のΣ_2-Σ_3フォノン分枝の振舞い

1-1-16 Behavior of Σ_2-Σ_3 Phonon Branches of $KRbSeO_4$

H. Shigematsu and T. Matsui*

Department of Physics, Faculty of Education, Shimane University, Matsue 690-8504, Japan
**Department of Quantum Engineering, Nagoya University, Nagoya 464-8603, Japan*

Rubidium Selenate Rb_2SeO_4 and Potassium Selenate K_2SeO_4 belong to a family of A_2BO_4-type crystals with β-K_2SO_4 type structure (space group *Pnam*). Among the A_2BO_4-type ferroelectrics, the low-temperature incommensurate phase was only in K_2SeO_4. However, in the case of Rb_2SeO_4, the calculated dispersion curves included an unstable Σ_2 phonon branch with qualitative and quantitative features similar to those obtained for the prototype incommensurate materials K_2SeO_4. Indeed the frequency excitations which soften slightly have been observed by inelastic neutron scattering technique below 100 K, but the results of both thermal analysis and neutron elastic scattering showed no phase transition.

We have studied in order to clarify the mechanism of low-temperature incommensurate phase transition and hypothetical one in A_2BO_4-type crystals. In order to obtain an additional information, the behavior of the low-energy Σ_2- Σ_3 phonon branches in $KRbSeO_4$, we performed inelastic neutron scattering experiments by using the triple-axis spectrometers (4G and T1-1) at JRR-3M in JAERI (Tokai). Energy scans were done with fixed incident neutron momentum k_i = 2.67 $Å^{-1}$.

Figure 1 shows the neutron scattering spectra at Q = (1 0 4) at 300 K. Two excitation peaks can be seen at about 4.5 and 7 meV. These modes, which anticrossed each other at around ξ = 0.7, were observed.

Figure 2 shows the phonon dispersion curves along the (ξ 0 0) line at 300, 200, 100 and 50 K. No phase transition could be found between room temperature and 8 K.

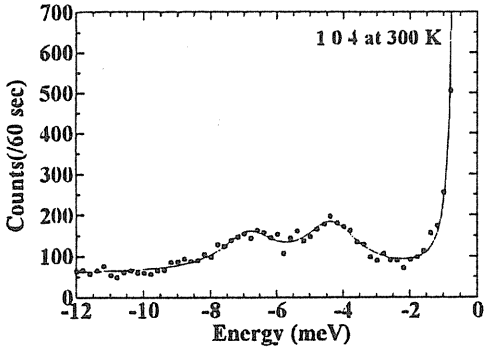


Fig. 1 Neutron scattering spectrum at Q = (1 0 4) at 300 K

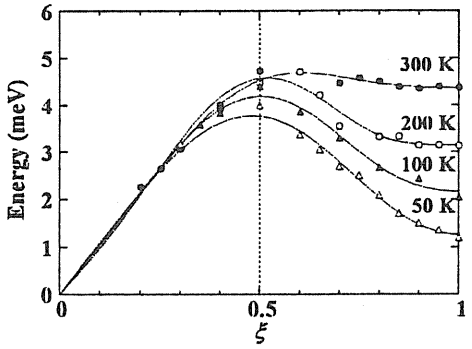


Fig. 2 Phonon dispersion curves in an extended-zone scheme on the (ξ 0 0)

Although the results of the Σ_2- Σ_3 phonon branches showed a clear softening around Γ point, no softening around ξ = 2/3 was recognized in contrast to the case of K_2SeO_4. The result indicates a close relation between the substitution of two kinds of A^+ ions and the increase of the effective interaction between an acoustic and an optical branch.

使用施設: JRR-3 , 装置: GPTAS(4G) and HQR(T1-1), 分野 Structure&Excitations

研究テーマ：ランタノイドと白金族元素を含むペロブスカイト関連酸化物の磁気構造
表　題：$Ba_3Tb_2WO_9$ の結晶構造

1-1-17

Crystal Structure of Perovskite $Ba_3Tb_2WO_9$

S. OYAMA, Y. DOI, Y. HINATSU and Y. ISHII[1]

Division of Chemistry, Graduate School of Science, Hokkaido University, Sapporo 060-0810
[1]Advanced Science Research Center, JAERI, Tokai, Ibaraki 319-1195

Quaternary oxides $Ba_3Ln_2WO_9$ (Ln = lanthanides) have a perovskite-type (ABO_3) structure. The Ln and W ions adopt a disordered arrangement in the B sites. The lattice parameters increase monotonically with the Ln^{3+} ionic radius. However, lattice parameters for $Ba_3Tb_2WO_9$ deviate greatly from this tendency. In addition, only this compound shows a reflection at $2\theta \sim 18°$ in the x-ray diffraction pattern, which indicates the B-site ordering.

In order to determine the detailed crystal structure for $Ba_3Tb_2WO_9$, powder neutron diffraction pattern was measured at room temperature using a High Resolution Powder Diffractometer (HRPD) at the JRR-3M reactor with a neutron incident wave length (λ = 1.82301 Å).

Figure 1 shows the observed and calculated diffraction patterns. The crystal structure was refined by applying the space group $P2_1/n$ (a =6.0059(4) Å, b = 6.0134(3) Å, c = 8.4931(7) Å, and β = 90.173(9)°). The structural parameters are listed in Table 1. The result of Rietveld analysis indicates that $Ba_3Tb_2WO_9$ is a 1:1 ordered compound, i.e., one of the B sites is fully occupied by Tb, whereas the other contains 2/3W and 1/3Tb with a random distribution. The crystal structure of $Ba_3Tb_2WO_9$ is illustrated in Fig.2. The Tb and W ions are alternatively arranged between Tb and (1/3Tb + 2/3W), and that this has a rock salt sublattice. Therefore, this compound should be described as $Ba_2Tb(Tb_{1/3}WO_{2/3})O_6$.

Table 1: Structural parameters for $Ba_3Tb_2WO_9$.

Atom	Site	g	x	y	z
Ba	4e	1.0	0.520	0.503	0.247
Tb(1)	2d	1.0	0	1/2	0
Tb(2)	2c	0.333	1/2	0	0
W	2c	0.667	1/2	0	0
O(1)	4e	1.0	0.235	0.233	-0.022
O(2)	4e	1.0	0.241	0.777	-0.018
O(3)	4e	1.0	0.479	-0.004	0.231

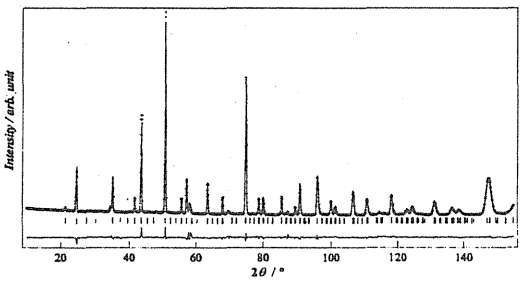


Figure 1: Powder neutron diffraction pattern of $Ba_3Tb_2WO_9$ at room temperature.

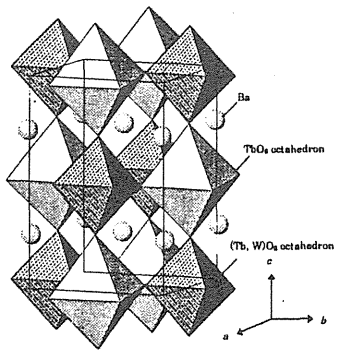


Figure 2: The crystal structure of $Ba_3Tb_2WO_9$.

原子炉：JRR-3　　装置：HRPD(1G)　　分野：中性子散乱（構造）

研究テーマ：亜硝酸ナトリウムの核座標，電荷密度，電気分極と格子振動
表題：$NaNO_2$の原子密度と分極

1-1-18

Atomic Density and Polarization of $NaNO_2$

H. Mashiyama, T. Asahi, H. Kasano, Y. Noda* and H. Kimura*

*Faculty of Science, Yamaguchi University, Yamaguchi 753-8512, Japan; *Institute of Multidisciplinary Research for Advanced Materials, Tohoku University, Sendai 980-8577, Japan*

Sodium nitrite ($NaNO_2$) is one of a typical ferroelectric crystal. In paraelectric phase, a nitrite molecule takes an up-and- down position, while it is ordered in ferroelectric phase. If fully ionic charge is assigned (Na^+, N^{3+} and O^{2-}), the spontaneous polarization is estimated as 78μC/cm^2 by using atomic coordinates determined from X-ray analysis; which is larger than the experimentally established value of 12μC/cm^2. The discrepancy may be explained by covalency of N-O bond. Indeed maximum entropy method (MEM) applied to X-ray data demonstrated broad charge distribution between the N and O (Fig. 1).[1]

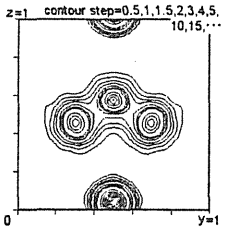


Figure 1: Electron density contour map of $NaNO_2$. X-ray diffraction intensity was analyzed by MEM.

Since the polarization stems from the difference between negative and positive charges, nuclear positions are desired to discuss the spontaneous polarization. Neutron diffraction intensity was collected by the use of four-circle diffractometer, FONDER, installed by Tohoku University at a beam line T2-2, JRR3M in JAERI (Tokai). The sample was mounted in a furnace. The incident wavelength was 1.541A; the measured range was 2θ<155deg. Intensity was measured at nine temperatures between 420K and 500K during a week.

Figure 2 displays nuclear density images at 402, 431 and 460K. Since atoms vibrate thermally, the nuclear bubbles are obtained by MEM. In ferroelectric phase below 436.5K, nitrite molecules are aligned with shifting sodium ions inducing the polarization. At 431K, near the transition temperature, the counterpart alignment takes place partially and decreases polarization. At 460K (paraelectric phase), nitrite and sodium are fully disordered. In principle there should be no density between N and O, however, additional nuclear density appears because of poor resolution.

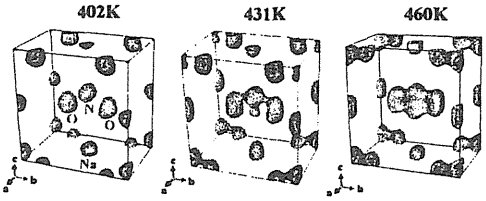


Figure 2: Nuclear density image of $NaNO_2$. Neutron diffraction intensity was analyzed by MEM.

The center of atom can be decided by least-square calculations. Both X-ray and neutron data give almost the same positions. This means the core electrons are just around each nuclear and does not contribute to the polarization. The net charge of ions and the covalent electrons will account the polarization. If we assign $+e$ to a sodium ion, which is consistent with the MEM result for X-ray data, then $-e/2$ at each oxygen position is enough for explaining the saturation polarization.

References

[1] Y. Kawamura *et al.*, Ferroelectrics **269** (2002) 321.

使用施設：JRR-3 ，装置：FONDER(T2-2)，分野：Structures & Excitations

研究テーマ：$PbTiO_3$ のフォノン
表　題：正方晶 $PbTiO_3$ のフォノン

1-1-19

Lattice dynamics of tetragonal $PbTiO_3$

I. TOMENO, Y. ISHII[1] and Y. TSUNODA[2]

Faculty of Education and Human Studies, Akita University, Akita 010-8502
[1]Neutron Science Research Center, JAERI, Tokai, Ibaraki 319-1195
[2]School of Science and Engineering, Waseda University, Shinjuku-ku, Tokyo 169-8555

$PbTiO_3$ undergoes only a single phase transition from a cubic paraelectric to tetragonal ferroelectric phase at T_C=763 K. The donation of 10 % Ti atoms to $Pb(Zn_{1/3}Nb_{2/3})O_3$ gives rise to a huge piezoelectric effect. Thus $PbTiO_3$ is the mother material of the relaxor $Pb(Zn_{1/3}Nb_{2/3})O_3$.

Figure 1 depicts the phonon dispersion relations along the [110] direction at room temperature. The bars refer to the FWHM obtained from Gaussian fits to the constant-Q or constant-E scans. The dashed lines are sound velocities determined by Brillouin scattering measurements. [1] The slope for each TA phonon branch around the Γ point is in good agreement with the sound velocity data. [1] The high-frequency phonon at Γ correspond to the A_1 TO mode, and the low-frequency phonon corresponds to the E TO mode. These results are consistent with the dielectric constant relation $\epsilon_{11} > \epsilon_{33}$ at room temperature, [1] in view of the Lyddane-Sacks-Teller relation. The zone-center TO phonon frequencies are in good agreement with the data determined by Raman scattering experiments. [2] The FWHM for the Σ_1 TO phonon around the zone center is extremely broader than that for the Σ_2 TO phonon. Similar tendency has been pointed out by the Raman scattering measurements. [2] The A_1 TO phonon behaves as the well-defined soft mode near T_C. [3] The origin of the broad width for the A_1 TO mode is still controversial. [4] We are planning an inelastic-neutron-scattering study at high temperatures.

References

1) Z. Li, M.Grimsditch, C.M.Foster and S.-K. Chan : Ferroelectrics **141** (1992) 313.
2) C.M.Foster, Z. Li, M.Grimsditch, S.-K. Chan and D.J. Lam : Phys.Rev. B **48** (1993) 10160.
3) G. Shirane, J. D. Axe, J. Harada and J. P. Remeika : Phys. Rev. B **2** (1970) 155.
4) S. M. Cho, H. M. Jang and T.-Y. Kim : Phys. Rev. B **64** (2001) 014103.

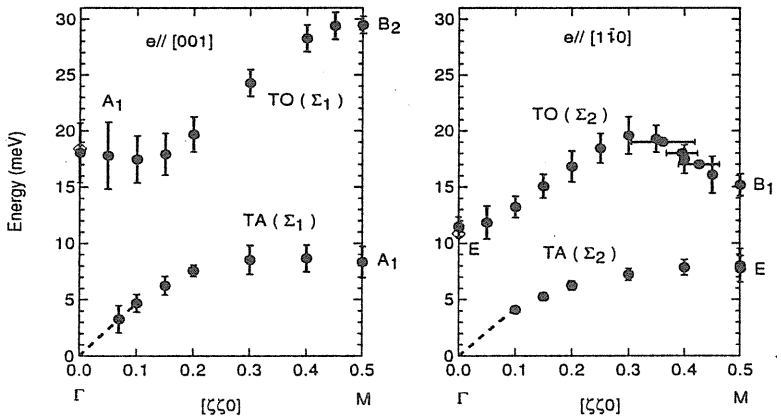


Figure 1: Phonon dispersion relations for $PbTiO_3$.

原子炉：JRR-3　　装置：TAS-1(2G)　　分野：中性子散乱（構造）

研究テーマ：擬一次元磁性鎖をもつ Pyroxene の磁性
表題： 結晶構造解析によるパイロキシン化合物の格子二量体化の検証

1-1-20

Crystalline Structural Analysis of the lattice dimerization in pyroxene compounds

E. Ninomiya[1], M. Isobe[2], Y. Ueda[2], M. Nishi[3], K. Ohoyama[4]

[1]*Graduate School of Science and Technology, Chiba University, Chiba 263-8522, Japan*

[2]*Material Design and Character. Lab., ISSP, University of Tokyo, Kashiwa 277-8581, Japan*

[3]*Neutron Science Laboratory, ISSP, University of Tokyo, Tokai 319-1106, Japan*

[4]*Institute for Materials Research, Tohoku University, Sendai 980-8577, Japan*

In the present work we investigate the lattice dimerization within the chain in the alkali metal pyroxene compounds, $NaTiSi_2O_6$ and $LiTiSi_2O_6$. The structure includes isolated zigzag chains made up of edge-sharing TiO_6 octahedra. Since the crystallographic Ti^{3+}-cation site is unique in the structure, the chains can be regarded as uniform linear chains at RT. A polycrystalline sample was prepared by a conventional solid-state reaction. We performed neutron powder diffraction experiments on the Kinken powder diffractometer for high efficiency and high resolution measurements, HERMES, of Institute for Materials Research (IMR), Tohoku University, installed at the JRR-3M reactor in JAERI, Tokai [1]. The diffraction data integrated for 6.5 hours were collected in the range between 10 and 300K. The diffraction patterns with a triclinic symmetry were analyzed using the RIETAN-2000 program [2]. There exist two crystallographically independent sites for Ti atom in the structure of the low temperature phase. The alternation of Ti-Ti distance within the chain was found from the analysis of the diffraction data in the low-temperature phase. Fig. 1 shows the temperature dependence of the Ti-Ti atomic distance along chains in $NaTiSi_2O_6$ (a) and $LiTiSi_2O_6$ (b). In the case of $NaTiSi_2O_6$, the alternation of Ti-Ti distances increases monotonously with decreasing temperature [3], but that of $LiTiSi_2O_6$ seems to disappear below 125 K [4]. However, the angles of Ti-O-Ti of $LiTiSi_2O_6$ change from 98 degree to 95 and 100 degree below 125 K. This result means the alternation of exchange interaction between Ti atoms to be kept along the chain. The lattice dimerization of both compounds $NaTiSi_2O_6$ and $LiTiSi_2O_6$ was analyzed from neutron powder diffraction data. This reveals the direct evidence for the formation of Ti^{3+}- Ti^{3+} singlet pairs.

References

[1] K. Ohoyama *et al.*, Jpn. J. Appl. Phys., **37** (1998) 3319.

[2] F. Izumi and T. Ikeda, J. Crystallogr. Soc. Jpn., **42** (2000) 516.

[3] E. Ninomiya *et al.*, Physica B in press.

[4] E. Ninomiya, Dissertation in Chiba University.

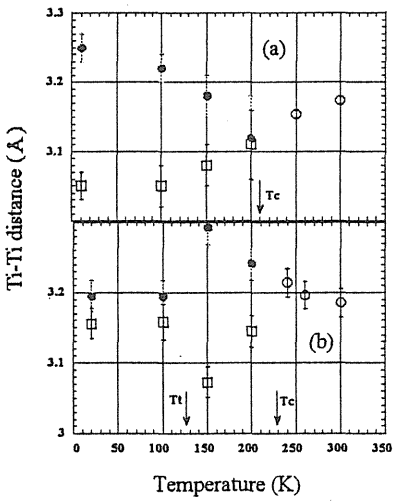


Fig. 1. Temperature dependence of the Ti-Ti atomic distance along chains in $NaTiSi_2O_6$ (a) and $LiTiSi_2O_6$ (b).

使用施設：JRR-3 ，装置：HERMES (T1-3), 分野：1. Structures & Excitations

研究テーマ：中性子回折を用いたハイシリカＭＦＩゼオライトの格子欠陥解析
表　題：中性子回折を用いたシリカライト欠陥の構造解析

1-1-21

Crystal Structure Study on Defective Silicalite by Neutron Diffraction

T. Suzuki, M. Inui, K. Sugita and Y. Ishii[1]

Basic Chemicals Research Lab., Sumitomo Chemical Co., Ltd., Sobiraki, Niihama, 792-5821
[1]ASRC, Japan Atomic Energy Research Institute, Tokai, Ibaraki 319-1195

Zeolites are used in the industry as catalysts. Performance of catalysts is strongly related to the crystal structure and the concentration of point defects in the zeolite crystal, because the point defects in the crystal often behave as active sites for reaction. Artioli *et al.*[1)] determined the crystal structure of silicalite by neutron diffraction experiments. However, information for concentration of the defect is insufficient. Therefore we study the crystal structure and defect concentration of silicalite with neutron diffraction measurements.

Silicalite powder samples were stirred in D_2O water at 353 K for H-D exchange. IR measurement of this sample was carried out for checking the H-D exchange. After this checking the fully deuterated sample was dehydrated at 673 K under He-gas flow. The sample was sealed in a special vanadium tube without air exposure. The neutron powder diffraction pattern of the deuterated silicalite sample was observed with the High-Resolution Powder Diffractometer (HRPD) installed at the JRR-3 in JAERI.

Measurements were carried out at low temperature of 3.5 K in order to minimize the diffraction effect due to thermal vibration of atoms. Data were collected between 5° and 155° in diffraction angle with an equal step of 0.05°. The diffraction data were refined by Rietveld method using the RIETAN-2000 software program.

Rietveld refinement of deuterated silicalite is shown in Fig.1. Lattice parameters were refined to be a=19.8342(8)Å, b=20.1031(8)Å, c=13.3658(5)Å and β = 90.952(2)°. The determination of Si T-site occupancy was very difficult because monoclinic phase has too many parameters.

References

1) G. Artioli, C. Lamberti and G. L. Marra: Acta Cryst. **B56** (2000) 2-10.

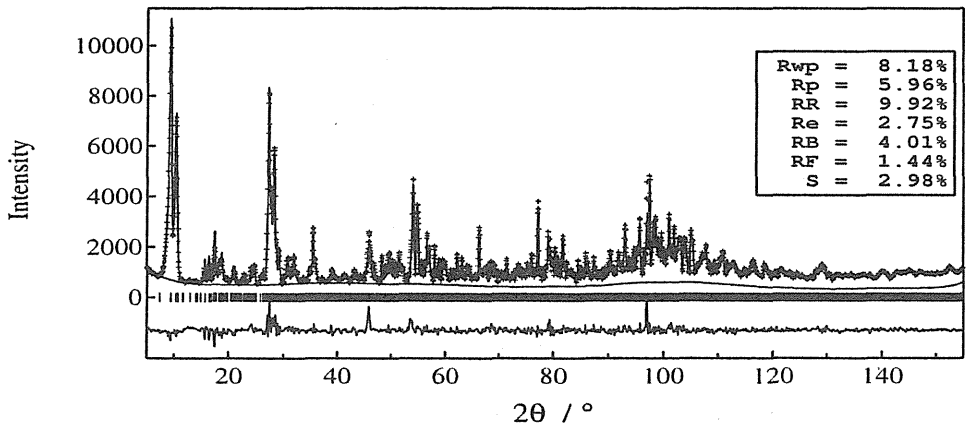


Figure 1: After refinements of deuterated silicalite measured at 3.5 K.

原子炉：JRR-3　　装置：HRPD(1G)　　分野：中性子散乱（構造）

研究テーマ：リチウム二次電池正極材料 $LiMn_{2-x}M_xO_{4-\delta}$の充放電に伴う結晶構造および熱力学安定性の変化と電池特性
表題：4V級リチウム二次電池正極材料 $LiMn_{2-x}M_xO_4$ (M=Co, Ni, Zn) の結晶構造，熱力学安定性，電子構造と電極特性の関係

1-1-22

Relation between Crystal Structure, Thermodynamic Stability, Electronic Structures and Electrode Characteristics of $LiMn_{2-x}M_xO_4$ (M = Co, Ni, Zn) as a Cathode Active Material for the 4V Class Lithium Secondary Battery

Y. Idemoto, Y. Ito, Y. Tsunoda and N. Koura

Faculty of Science and Technology, Tokyo University of Science,

2641 Yamazaki, Noda-shi, Chiba 278-8510, Japan

1. Crystal structure, thermodynamic stability and electrode characteristics of $LiMn_{2-x}M_xO_4$ (M=Co, Ni, Zn) as a cathode active material for Li secondary battery

We investigated the relation between the properties, cathode performance, and the thermodynamic stability of the spinel, $Li_yMn_{2-x}M_xO_4$ (M=Co, Ni, Zn).

First, the samples that substitution spinel to partially replace Mn by Co, Ni and Zn; $LiMn_{2-x}M_xO_4$ (M=Co, Ni, Zn) were synthesized. $Li_yMn_{2-x}M_xO_4$ ($0 < y < 1$) was prepared as follows: $LiMn_{2-x}M_xO_4$ spinel was put into a HCl or H_2SO_4-H_2O solution and washed by distilled water, then dried. The powder X-ray diffraction profiles of all the samples were identified as a single-phase cubic spinel with a space group Fd3m. The lattice parameter a decreased with increasing Mn valence. The metal compositions of these samples, were determined by ICP. Mn valence was determined by chemical analysis. Mn valence increased with increasing x or decreasing y. The standard enthalpy of formation, $\Delta_f H^0$, the enthalpy change of reaction, ΔH, and the enthalpy change per mole of atoms for the formation reaction, ΔH_R, were calculated form the heat of dissolution. Thermodynamic stability was examined by these parameters. Furthermore, the cathode performance of $LiMn_{2-x}M_xO_4$ was investigated. When ΔH and ΔH_R decreased, it brought to a good cycle performance. Accordingly, it was suggested that the stability of the host structure brought to improvement for cycle performance.

The crystal structure analysis by powder neutron diffraction was examined for $LiMn_{2-x}M_xO_4$ (M=Co, x=0.2, 0.5; Ni, x= 0.1, 0.3; Zn, x=0.05, 0.1) and $Li_yMn_{2-x}M_xO_4$. The bond length of (Mn, M)-O of $LiMn_{2-x}M_xO_4$ decreases and phase transition was suppressed at 200K by substitution of M. On the other hand, there were two spinel phases, which have different lattice parameter a regarding several samples of $Li_yMn_{2-x}M_xO_4$. The calculation of Madelung energy was carried out from the results of Rietveld analysis. The Madelung energy decreases with increasing content x, and it was associated with the thermodynamic data.

We investigated the electron density distribution using by Maximum Entropy Method (MEM) in order to make clear the bonding state. From the results, covalent bond of the (Mn, M)-O bond was shown to be stronger than the Li-O bond.

Consequently, thermodynamically stable sample has more a stable crystal structure and this leads to a good cycle performance.

2. Relation between crystal structure, electronic structures and electrode performances of $LiMn_{2-x}Zn_xO_4$(x=0.05, 0.1) as a cathode active material for Li secondary battery

We have been studied the relation between crystal structures, electronic

使用施設:JRR-3　装置:HERMES(T1-3), 分野 Structure & Excitations

structures, thermodynamic stability and cycle performances of $LiMn_{2-x}Zn_xO_4$(x=0.05, 0.1) as cathode active materials for 4V class Li secondary battery. The crystal structures are Fd-3m and the bond lengths of (Mn, Zn) -O of $LiMn_{1.9}Zn_{0.1}O_4$ decrease in comparison with that of $LiMn_2O_4$. The cycle performance improves on increasing Zn content. The heat of dissolution of the samples was measured. These samples are more stable thermodynamically with increasing Zn content. Moreover, we calculated the net charge of each atom, the bond overlap population of Li-O, Mn-O, Zn-O, the density of states, and the electron density of $LiMn_{1.75}M_{0.25}O_4$ (M= Mn, Zn) using first principles calculation by DV-Xα method. Li ionicity always keeps high and the covalent bonding of Mn-O in the octahedron of $LiMn_{1.75}Zn_{0.25}O_4$ is stronger than that of $LiMn_2O_4$.[1]

References

[1] Y. Ito et al., Electrochemistry, in printing.

研究テーマ：アミド類からラクタム環の形成における水素移動反応の機構解明
表　題：中性子回折によるキラルチオラクタム形成における水素移動機構の解明

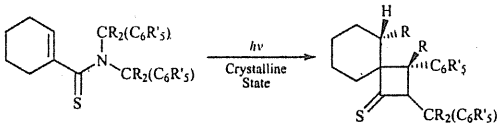
1-1-23

Deuterium Migration Mechanism in Chiral Thiolactam Formation by Neutron Diffraction Analysis

T. HOSOYA, H. UEKUSA, Y. OHASHI, T. OHHARA,[1] I. TANAKA[2] and N. NIIMURA[2]

Department of Chemistry and Materials Science, Tokyo Institute of Tech., Tokyo 152-8550
[1]Institute of Materials Structure Science, HEARO (KEK), Tsukuba, Ibaraki 305-0801
[2]Advanced Science Research Center, JAERI, Tokai, Ibaraki 319-1195

The molecule of *N,N*-dibenzyl-1-cyclohexenecarbothioamide, **1a**, was photoisomerized to 1-benzyl-4-phenyl-2-thioxoazetidine-3-spirocyclohexane, **2a**, in high optical yield.[1)] From the crystal structure analyses of the reactant and product crystals by X-rays, the mechanism of the asymmetric induction was proposed.



1a: R=R'=H
1b: R=D, R'=H
1c: R=R'=D

2a: R=R'=H
2b: R=D, R'=H
2c: R=R'=D

Recently we succeeded in isomerizing **1a** to **2a** with retention of the single crystal form after many trials.[2)] A crystal was irradiated with a xenon lamp for 330 h and then the structure analyzed by X-rays indicated 65.7 % of **1a** was converted to **2a** within the crystal. This disordered structure made clear how the benzyl carbon of **1a** makes a bond with the a carbon of the cyclohexene ring and why only one enantiomer of **2a** is produced from the chiral crystal. However, the question whether the β-carbon of the cyclohexene ring abstracts the hydrogen atom within a molecule or from the neighboring molecule has not been made clear.

To analyze the hydrogen migration mechanism in the crystal, four α-hydrogen atoms of the two benzyl groups of compound **1a**, were replaced with the deuterium atoms, **1b**. If the crystal was irradiated with a xenon lamp, the photo isomerization occurred with retention of the single crystal form to produce **1b**. This work reports the deuterium-migration mechanism in the photo isomerization by neutron diffraction technique.

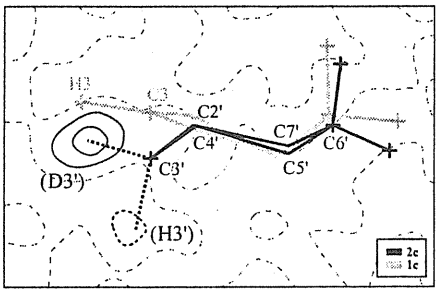


Figure 1: Difference Fourier map projected on the plane composed of H3-C3-C3'. All the atoms except H3' and D3' were included in the F_c calculation.[4)] Solid and dotted/dashed contours indicate positive and negative ones, respectively.

In this study, other hydrogen atoms of these two benzyl groups of **1b** was replaced with deuterium atoms, **1c**, in order to reduce the background intensity caused by incoherent scattering and the large neutron absorption by hydrogen atoms. A large crystal of **1c** was divied to some pieces, and these were irradiated for 20 days at 263 K with a xenon lamp through a Y-44 sharp-cut filter (HOYA).[3)] A small crystal was quarried out from the center of one of the crystals. From its crystal structure analysis by X-rays, approximately 28 % of **1c** were photoisomerized to **2c**, and absolute configuration of a chiral methine carbone was determined.

Another crystal of **1c** after irradiation, 4.5× 1.5 × 1.4 mm^3 was mounted on the BIX-III (1G) neutron imaging plate diffractometer set up at the JRR-3M reactor in JAERI. The neutron diffraction data were collected for 4 days at 290 K, and peak integration by *MAC*

原子炉：JRR-3　　装置：BIX-3 (1G)　　分野：中性子散乱（構造）

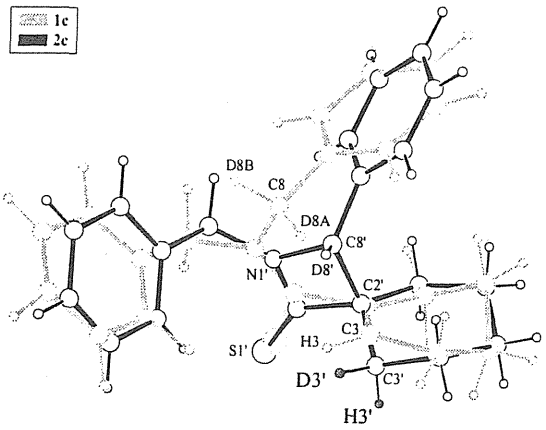


Figure 2: Molecular structure of **1c** & **2c** (disordered). The deuterium atom bonded to C3' was occupied to equatorial site of cyclohexane ring moiety.

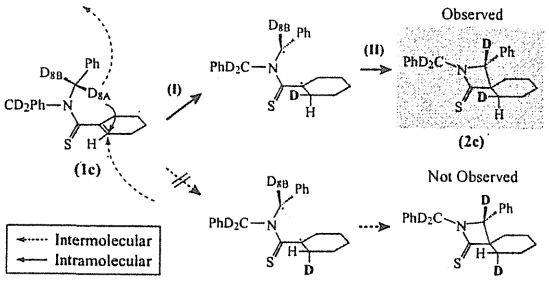


Figure 3: Reaction mechanism of **1c**: The first (I) and second (II) reaction steps indicate the intra- or intermolecular deuterium migration leaving a benzyl radical and the benzyl carbon radical makes the thiolactam ring, respectively.

DENZO created a *SHELX*-format *hkl* file. The crystallographic data and experimental details are summarized in Table 1.

The difference Fourier map around C3 is shown in Fig. 1. The positive peak at H3 indicates that a part of the H3 atom is moved to the negative peak at H3'. The positive peak at D3' can be assigned to the position of the transferred deuterium atom. This indicates that the positions of deuterium and hydrogen atoms are equatorial and axial, respectively, shown in Fig. 2. This result clearly suggests that the photoreaction proceeds via the intramolecular deuterium migration as shown in Fig. 3. The β-carbon of the cyclohexene, C3, abstracts an intra-molecular deuterium atom, D8A, involving homolytic bond cleavage. If

Table 1: Crystal data and experimental details.

[Crystal Data]	
Empirical formula	$C_{21}H_9D_{14}NS$
Temperature /K	290
Wavelength /Å	1.51
Crystal system, space group	Monoclinic, $P2_1$
a /Å	8.911(1)
b /Å	10.472(2)
c /Å	10.335(1)
β /°	102.526(6)
V /Å^3	941.5(2)
Z	2
Calculated density /Mg m^{-3}	1.183
Diffractometer	BIX-III
Crystal size /mm	4.50×1.50×1.40
[Data Collection]	
θ range / °	14.63–57.48
Limiting indices	$0 \le h \le 9$
	$0 \le k \le 11$
	$-11 \le l \le 11$
Reflections collected / unique	1270 / 1270
Completeness to θ /%	87.0
[Refinement]	
Refinement on	F^2
Data / restraints / parameters	1270 / 15 / 356
Goodness-of-fit on F^2	1.709
R_1 ($F^2 > 2\sigma(F^2)$), wR_2	0.1316, 0.3247
R_1 (all data), wR_2	0.1358, 0.3289
$\Delta\rho_{max}$, $\Delta\rho_{min}$ /eÅ^{-3}	0.073, -0.066

the deuterium atom comes from the neighbouring molecule, the transferred deuterium, D8A'(=D3'), should occupy the axial position. The benzyl carbon radical would be generated after the deuterium abstraction. Then, the produced benzyl carbon radical moves to form the β-thiolactam ring with keeping its conformation, considering from the observation by X-rays.

References

1) M. Sakamoto, M. Takahashi, K. Kamiya, K. Yamaguchi, T. Fujita, and S. Watanabe: *J. Am. Chem. Soc.*, **118**, 10664 (1996).
2) T. Hosoya, T. Ohhara, H. Uekusa, and Y. Ohashi: *Bull. Chem. Soc. Jpn.*, **75**, 2147 (2002).
3) This Y-44 filter shuts out the light whose wavelength is shorter than 440 nm.
4) The X-ray analysis of **2a** indicates that the positions of H3' and D3' are almost on the plane of H3-C3-C3'.

研究テーマ： 圧力誘起強磁性体 $Sr_3Ru_2O_7$ の一軸圧力下での４軸回折計による中性子構造解析
表題： $Sr_3Ru_2O_7$ の常圧室温構造解析

Structure Analysis of $Sr_3Ru_2O_7$ under the Ambient Pressure at Room Temperature

1-1-24

R. Kiyanagi, N. Aso[1], H. Kimura, Y. Noda, S. Ikeda[2], Y. Yoshida[2] and M. Uwatoko[3]

Institute of Multidisciplinary Research for Advanced Materials, Tohoku University, 2-1-1 Katahira, Aoba-ku, Sendai 980-8577

[1]*NSL, Institute for Solid State Physics, The University of Tokyo, 106-1 Shirakata, Tokai, 319-1106*

[2] *National Institute of Advanced Industrial Science and Technology, 1-1-1 Umezono, Tsukuba 305-8568*

[3]*Institute for Solid State Physics, The University of Tokyo, 5-1-5 kashiwanoha, kashiwa 277-8511*

$Sr_{n+1}Ru_nO_{3n+1}$ exhibits various physical properties, on changing n value. $Sr_3Ru_2O_7$(n=2) is paramagnetic down to 4K under the ambient stress. Recently, it was reported that $Sr_3Ru_2O_7$ undergoes the ferromagnetic phase transition at 70K under the uniaxial stress along the c-axis. So far only a neutron powder diffraction experiment has been performed [1]. The most reliable space group was *Bbcb* orthorhombic, among more than 10 candidates of space groups, while the lattice parameter was $a = b$. This time, we performed a neutron structure analysis of $Sr_3Ru_2O_7$ with a single crystal.

The four circle neutron diffractometer FONDER installed at T2-2 beam port in JRR-3M in JAERI(Tokai) was utilized for the present study. The obtained lattice parameters were a = 5.4979(4)Å, b = 5.5008(10)Å, c = 20.7327(19)Å, α = 90.00(1), β = 90.00(1), γ = 89.99(1) at room temperature. The following points were found, concerning the lattice parameters and the observed reflections. 1)According to the lattice parameters and the Laue symmetry, the Bravais lattice seemed to be a tetragonal. 2)Superlattice reflections on the basic bct-phase were observed at X-point of the bct lattice, but not at Z-point. 3)Few reflections corresponding to the extinction rules of the glide and screw symmetries were observed.

Recently, the space group of $Sr_3Ru_2O_7$ at room temperature was pin down to be *Bbcb* by means of the convergent beam electron diffraction [2]. And it was also found that the crystal contains twin components (about few hundred Å size along the c-axis). Taking these conditions into account, the least-square fitting of the structure analysis was performed. The obtained final reliable factor was 4.63%. The comparison of the $|F_O|$ and $|F_C|$ is shown in Fig. 1. It was found that $Sr_3Ru_2O_7$ has the distorted octahedron structure. In other words, the each octahedron connecting with each other rotates toward the opposite direction around the c-axis. This result agrees with the previous report [1]. We will perform the similar experiment and analysis under the uniaxial stress at the next stage.

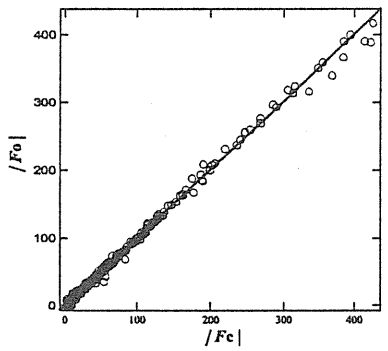


Fig. 1. The $|F_O|$ plotted against the $|F_C|$ after the least-square fitting.

References

[1] H. Shaked, J. D. Jorgensen, O. Chmaissem. S. Ikeda and Y. Maeno ; J. Solid State Chem. ; **154**, 361-367(2000).

[2] K. Tsuda, M. Tanaka, Y. Noda, N. Aso, S. Ikeda, Y. Yoshida and M. Uwatoko ; Meetings of Phys. Soc. Jpn ; **58**, No. 1 555(2003).

使用施設：JRR-3　装置： T2-2 (FONDER)，分野： 1. Structures & Excitations

研究テーマ：$Sr_3Ru_2O_7$ のナノスケール構造歪みとメタ磁性転移の関係
表　題：$Sr_3Ru_2O_7$ のナノスケール構造歪みとメタ磁性転移の関係

1-1-25

Structure refinements for single crystalline $Sr_3Ru_2O_7$ under magnetic field

Y. YOSHIDA[1,2], S. KATANO[3] , N. ASO[4], S.I. IKEDA[1], N. SHIRAKAWA[1] , M. NISHI[4], and Y. UWATOKO[4]

[1]NeRI, AIST, Tsukuba, Ibaraki 305-8568, Japan
[2]JSPS, Chiyoda, Tokyo 102-8471, Japan
[3]JAERI, Tokai, Ibaraki 319-1195, Japan
[4]ISSP, University of Tokyo, Kashiwa, Chiba 277-8581, Japan

Relation between magnetism and structural distortions due to oxygen displacements in transition metal oxides is a crucial issue to understand such materials microscopically. High critical- temperature cuprate superconductors, for instance, have been investigated based on such a perspective. Recently, strontium ruthenates with the layered perovskite crystal structure were found intriguing. Single layered Sr_2RuO_4 (tetragonal structure with the $I4/mmm$ symmetry) shows spin-triplet superconductivity [1] and double layered $Sr_3Ru_2O_7$ reveals magnetic field induced quantum criticality at around metamagnetic field of 7 tesla [2]. Particular instability of the crystal structure with rotations of RuO_6 octahedra along the c-axis (normal to the RuO_2 plane) subsists in $Sr_3Ru_2O_7$ (nearly tetragonal : orthorhombic with the *Bbcb* symmetry) [3,4]. Indeed, from the results of magnetization measurements under hydrostatic and uniaxial pressure, it is suggested that uniaxial pressure along the c-axis, normal to the two-dimensional RuO_2 plane, causes an outstanding transition from the enhanced-paramagnetic to ferromagnetic phase [5–7]. Although neutron scattering study for structural refinements under uniaxial pressure is under progress, it is appropriate to assume that the structural instability of the RuO_6 octahedron plays an important role in magnetic property of $Sr_3Ru_2O_7$.

In order to clarify whether the crystal structure changes at the metamagnetic field, we have tried to refine its structure for single crystalline $Sr_3Ru_2O_7$ under magnetic field at TAS-2 in JRR-3, JAERI. Single crystalline samples of $Sr_3Ru_2O_7$ were grown by a self-flux floating-zone technique using an image furnace. The dimension of the samples is 5 $\sim$ 6 mm in diameter and 10 $\sim$ 15mm in length.

According to Shaked *et al.*, superlattice reflections corresponding to the rotation of the RuO_6 octahedron are observed [8].As the first step, we tried a structural analysis under a zero field at several temperatures. In this study, we employed the [HHL] zone, and tried to find out some intensity changes of reflections in this plane with decreasing temperature . There we could not observe clear evidence of the expected intensity change associated with the greater rotation angle which was already reported on powder samples [3]. To investigate the superlattice reflections described above directly, we are now performing four-circle neutron diffraction experiments on single crystalline $Sr_3Ru_2O_7$ at FONDER to check whether the superlattice reflections are strong enough to be observed at the JRR-3 neutron source. After that, the measurements under magnetic fields will be examined.

References

1) Y.Maeno, T.M. Rice and M. Sigrist, Physics Today **54** (2001) 42.
2) S.A. Grigera *et al.*, Science **294**(2001) 329 .
3) H. Shaked *et al.*, Phys. Rev. B **62** (2000) 8725.
4) Q. Huang *et al.*, Phys. Rev. B **58** (1998) 8515 .
5) S.I. Ikeda *et al.*, Phys. Rev. B **62** (2000) R6089 .
6) S.I. Ikeda *et al.*, Physica C **364-365** (2001) 376 .
7) S.I. Ikeda *et al.*, preprint.
8) H. Shaked *et al.*,J. Solid State Chem. **154** (2000) 361.

原子炉：JRR-3　　装置：TAS-2(T2-4)　　分野：中性子散乱（構造）

研究テーマ：高温超伝導体$La_{2-x}Sr_xCuO_4$;x=0.17の低温構造特性
表題：高温超伝導体$La_{2-x}Sr_xCuO_4$;x=0.17の構造相転移

1-1-26 Structural phase transition of superconductor $La_{2-x}Sr_xCuO_4$;x=0.17

M.Hidaka[1], N.Tokiwa[1],S.Takahashi[1], T.Matsumoto[1] and K.Oda[2]
1.Department of Physics, Faculty of Science, Kyushu University, Fukuoka 812-0053,Japan
2. Department of Physics, Faculty of Science, Hokkaido University, Hokkaido060-0810, Japan

$La_{2-x}Sr_xCuO_4$ is well known to be a superconductor in a region from about 0.06 to 0.25 of substituting Sr ions (x) below about 30~35K(Tsc). However, it is still interested whether the structural phase transition in $La_{2-x}Sr_xCuO_4$ is a precursory modulation to the superconductive transition, as like that in Nb_3Sn. A parent compound La_2CuO_4 has an ideal tetragonal K_2NiF_4-type structure and shows a structural phase transition at Tc=530K. The structural phase transition from a tetragonal to orthorhombic-like symmetry results from tilts around primitive axes of CuO_6 octahedra. Thus, we deduced that such tilts are affected by substitution of La^{3+} with Sr^{2+}. In order to study a correlation between the structural modulation and the superconductivity in $La_{2-x}Sr_xCuO_4$, we carried out measurements of peak profiles and intensities of fundamental reflections and superlattice reflections by using a neutron diffractometer, FONDER. At the present investigations, the single crystal showed Tsc = 37K by means of SQUID method.

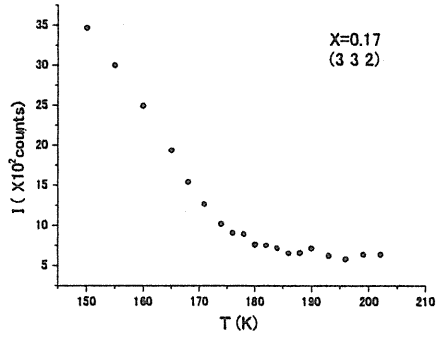


Fig.1. Temperature dependence of the integrated intensity of the (332) superlattice reflection.

Fig.1 shows integrated intensity of the (332) superlattice reflection as heating. The reflection is indexed with a unit cell A x B x C ; A=2ap, B= 2bp, C=cp, where the suffix p means a pseudo K_2NiF_4-type structure. From the figure, we confirmed the structural phase transition occurring at about 180K to be of second order. Thus, the substitution of Sr^{2+} ions decreases largely Tc with about ΔT=350Kto La_2CuO_4. Such a decreasing is mainly related to a difference of ionic size between La^{3+} (1.05Å) and Sr^{2+} ions (1.13 Å). Thus, Sr^{2+} ions interrupt cooperative shifts of nearest-neighbor apical oxygen ions of CuO_6 octahedra in (001) plane. It is well known that the substitution of Sr^{2+} systematically changes Tc. Multi-domains appear even in a single crystal below Tc, since the tetragonal axes are ambiguously transformed to one of orthorhombic-like axis A or B. Such domains modify a peak profile of reflection below Tc.

Fig,2 shows a (400) fundamental reflection as a function of temperature. The peak profiles are taken with ω-scan at the respective temperature.

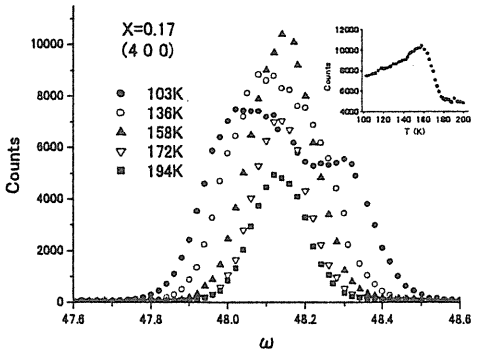


Fig.2.Peak profiles of the (400) fundamental reflection taken at several temperature below 200K.

A large split of the profiles result from the appearance of domains. The inserted figure is temperature dependence of maximum peak height

使用施設：JRR-3　装置：FONDER(T2-2)、分野：1.Structures & excitations

of the observed profiles, that is a light peak to the split reflections in Fig.2. Thus, the inset figure suggests that the peak split disappear below about 160K and the tetragonal to orthorhombic-like transition occurs at about 180K. Fig.3 shows an integrated intensity of the total peak profile of (400) reflection as a function of temperature.

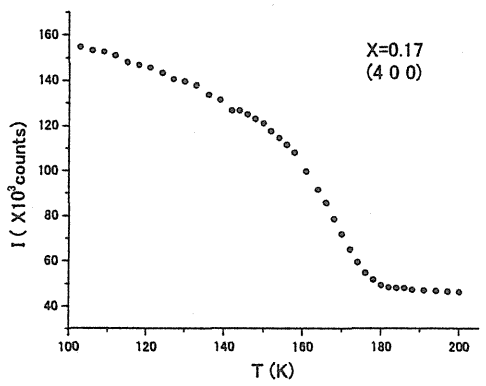


Fig.3. Temperature dependence of the intensity of the (400) fundamental reflection..

Fig.4 shows a peak profile of (840) fundamental reflection, taken at several temperatures, as like those of (400) reflection. The profile at 100K was approximately analyzed by three kinds of

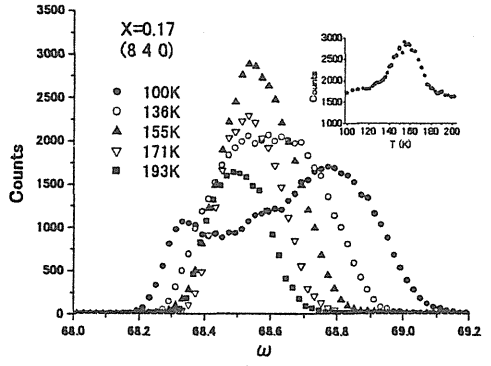


Fig.4. Peak profiles of the (840) fundamental reflection taken at several temperature below 200K.

Gaussian curves. The inset figure also shows temperature dependence of the peak height. As the split profiles, the maximum peak counts were drawn in the inset curve. We found the disappearance of the peak split at about 160K, in addition to the phase transition at about 180K. Fig.5 shows an integrated intensity of the total peak profile of (840) reflection as a function of temperature, that is a (I-T) curve.

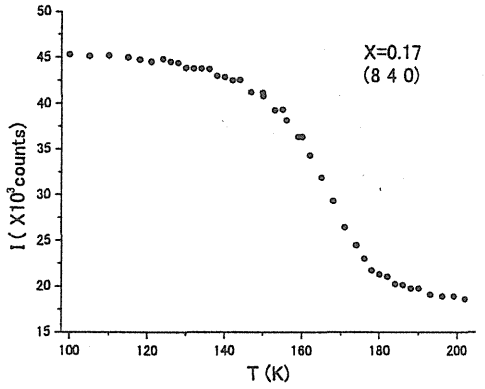


Fig.5 Temperature dependence of the intensity of the (840) fundamental reflection..

Thus, it was considered from Figs.2 and 4 that an angle γ between [100] and [010] axes is 90 degrees in a region from 180K to 160K, and not 90 degrees below 160K, though the symmetry is orthorhombic-like below 180K. An extrapolation of the (I-T) curves in Figs.3 and 4 give a transition point at about 155K.

We are now in progress to study the structural properties in $La_{2-x}Sr_xCuO_4$; x=0.17, especially for the intermediate region between about 160K and 180K. We considered that the substitution effect of Sr^{2+} ions is a local distortion in (La,Sr)O planes, where the planes are intercalated between superconductive CuO_2 planes.

研究テーマ：半磁性電気伝導体の磁性と化学構造
表　題：複合結晶 $(Ca_{0.80}Y_{0.20})_{0.82}CuO_2$ の変調構造

1-1-27

Modulated Structure of the Composite Crystal $(Ca_{0.80}Y_{0.20})_{0.82}CuO_2$

Y. MIYAZAKI, Y. ISHII[1], Y. MORII[1] and T. KAJITANI

Department of Applied Physics, Tohoku University, Sendai 980-8579
[1]Advanced Science Research Center, JAERI, Tokai, Ibaraki 319-1195

Quasi one-dimensional (1D) cuprate $(Ca_{1-x}Y_x)_{0.82}CuO_2$ [1,2] has recently attracted much attention owing to its unique magnetic properties. The crystal structure, on the other hand, has not yet been satisfactorily determined except for the terminal compounds. In this report, we present the crystal structure of the compound with $x = 0.20$ on the basis of a four-dimensional superspace group approach using powder neutron diffraction data.

Neutron powder diffraction (ND) data were collected at 293 K by means of HRPD diffractometer installed at the JRR-3M reactor in JAERI. The ND data were analyzed using a Rietveld refinement program PREMOS 91 [3] designed for modulated structure analyses. The superspace group of $F2/m(1+\alpha\ 0\ \gamma)0s$ was adopted.

Figure 1 shows the observed, calculated and difference profiles for the ND data. Short vertical lines below the patterns indicate the peak positions of main (upper) and satellite (lower) reflections for the two subsystems. A satisfactorily good fit was achieved and the final R_{WP} factor was 12.8 %.

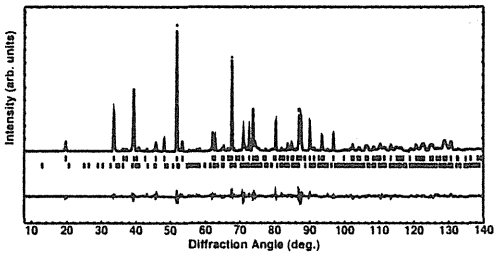


Figure 1: Observed, calculated and difference patterns of the powder neutron diffraction data for $(Ca_{0.80}Y_{0.20})_{0.82}CuO_2$ measured at 293 K.

Figure 2 shows the refined modulated structure viewed in perspective from the a-axis. The compound consists of mutually interpenetrating $[Ca_{0.80}Y_{0.20}]$ subsystem and edge-shared 1D $[CuO_2]$ chains, being incommensurate parallel to the a-axis. Lattice parameters were refined to be $a_1 = 2.8165(2)$ Å, $b = 6.2595(2)$ Å, $c = 10.5603(5)$ Å and $\beta = 90.06(1)°$. One can recognize markedly waved rows of the CuO_2 ribbons. The Cu atom sites are found to fluctuate larger than that of $x = 0.435$ sample but much smaller than that of $x = 0$ sample.

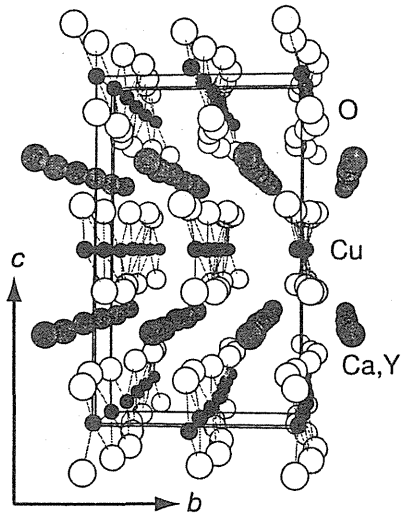


Figure 2: The refined fundamental structure of $(Ca_{0.80}Y_{0.20})_{0.82}CuO_2$ projected in perspective from the a-axis.

References

1) A. Hayashi *et al.*: Phys. Rev. B **58** (1998) 2678.
2) Y. Miyazaki *et al.*: Chem. Eur. J. **5** (1999) 2265.
3) A. Yamamoto: Acta Crystallogr. A **49** (1993) 831.

原子炉：JRR-3　　装置：HRPD(1G)　　分野：中性子散乱（構造）

研究テーマ　酸化ビスマスの構造変化とディスオーダー
表題　高温中性子粉末回折による δ-Bi_2O_3 の結晶構造とディスオーダーの研究

1-1-28

High-temperature neutron powder diffraction study of crystal structure and disorder of δ-Bi_2O_3

Daiju Ishimura, Masatomo Yashima, Atsushi Sakai , Mizuki Mori
Kenjiro Oh-uchi, Kenji Ohoyama[1] and Yasuo Yamaguchi[1]

Department of Materials Science and Engineering Interdisciplinary Graduate School and Engineering, Tokyo Institute of Technology, 4259 Nagatsuta-cho, Midori, Yokohama, 226-8502, JAPAN
[1]Institute for Materials Research, Tohoku University, Katahira, Aoba, Sendai, 980-8577, JAPAN

The bismuth oxide Bi_2O_3 transforms to the high-temperature δ-phase from low-temperature α-phase around 729°C. The δ-Bi_2O_3 is well known as the highest oxide-ion conductor. One of the reasons is the defect fluorite-type structure of δ-Bi_2O_3. The crystal structure of δ-Bi_2O_3 has been studied by many researchers [1-3]. But the accurate disorder of oxide ions has not been determined yet. The purpose of this work is to investigate the accurate disorder of oxide ions in δ-Bi_2O_3.

The neutron-diffraction measurements were performed in air with a 150-detector system, HERMES installed at the JRR-3M reactor in JAERI [4]. Diffraction data were collected in the 2θ range from 20° to 148° in step interval of 0.1° at 778 °C. A furnace with $MoSi_2$ heaters was placed on the sample table [5], and used for neutron-diffraction measurements at high temperatures. The temperature was kept constant within ±1.5°C during each data collection. The neutron-diffraction data were analyzed by the combination technique of Rietveld analysis using a computer program *RIETAN*-2000 [6] and the maximum-entropy method (MEM)-based pattern fitting.

Firstly Rietveld analysis of δ-Bi_2O_3 obtained at 778°C was done using three structural models shown in Figs. 1a, b and c. The Battle model (Fig. 1c) gave the best fit to the observed neutron-diffraction data, comparing with other models. The calculated profile with Battle model agreed well with the observed one (Fig.2).

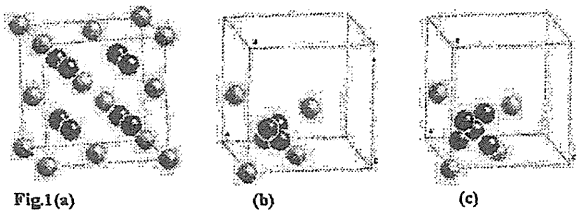


Fig. 1 Structural model of δ-Bi_2O_3 (a) Gattow model: Average distribution of six oxygen atoms at the site (8*c*) of *Fm*-3*m* (*xxx*, *x*=1/4), (b) Harwig model: Average distribution of six oxygen atoms at the site (32*f*) of *Fm*-3*m* (*xxx*, *x*=1/4+δ) (c) Battle model: Six oxygen atoms are distributed at the site (8*c* and 32*f*) of *Fm*-3*m*.

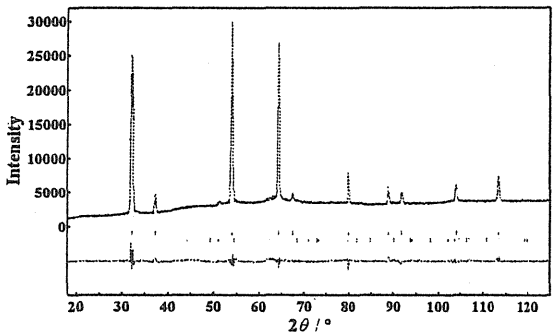


Fig. 2 Rietveld fitting pattern of δ-Bi_2O_3 measured at 778 °C. In this analysis Battle model was assumed.

Secondly, the MEM analysis was done using the structural factors obtained by the Rietveld analysis with the Battle model. MEM calculation was done using a computer program *PRIMA* [7]. To reduce the

使用施設: JRR-3.　装置: HERMES (T1-3),　分野：Structure and excitation

bias imposed by the simple structural model, an iterative procedure named by *REMEDY* cycle [8] was employed after the MEM analysis. After the 4th *REMEDY* cycle, the *R* factor based on the Bragg intensities, R_I was improved from 3.56% to 1.91%. The nuclear distribution for oxygen atoms changed from (a) to (b) in Fig.3 by the *REMEDY* cycles. The MEM map obtained after the 4th *REMEDY* cycle provided much information on the complicated disorder of oxide ions (Fig.3). To visualize the structural disorder at 778°C, the MEM density distribution map on the (110) plane is shown in Fig.4. The oxide ions have a complicated disorder and spread over a wide area. Two maxima of the nuclear density are seen at the 32*f* sites near an ideal 8*c* position of the oxide ion on the (110) plane. In this work we have successfully obtained the accurate disorder of oxide ions in δ-Bi_2O_3 by means of the MEM-based pattern fitting of neutron powder-diffraction data.

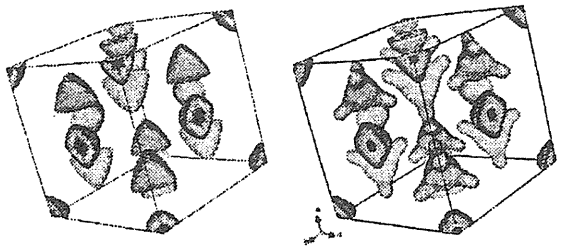


Fig.3(a) (b)

Fig. 3 Scattering amplitude distribution of δ-Bi_2O_3 at 778℃ with equicontour surface at 1.0 fm/Å^3. Distributions obtained by the MEM analyses (a) after the Rietveld analysis and (b) after the 4th *REMEDY* cycle.

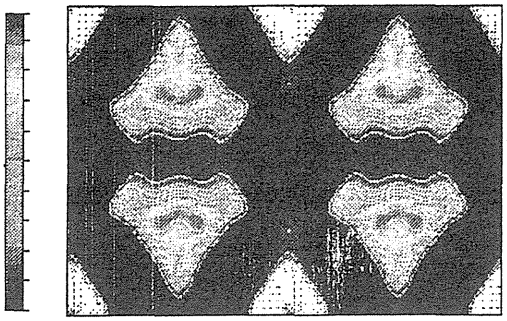


Fig. 4 Scattering amplitude distribution on (110) plane of δ-Bi_2O_3 at 778℃ with white contours in the range from at 0.3 to 20.0 fm/Å^3 (0.3 fm/Å^3)

Reference

[1] G Gattow and H. Schroder, Z. Alorg. Allg. Chem 318, 176-189 (1962).

[2] H. A Harwig, Z. Alorg. Allg. Chem 444, 151-166 (1978).

[3] P. D. Battle, R. A. Catlow, J. Drennan & A. D. Murray, J. Phys. C: Solid State Phys., 16, L561-L566 (1983).

[4] K. Ohoyama, T. Kanouchi, K. Nemoto, M, Ohashi, T.Kajitani, Y. Yamaguchi, Jpn. J. Appl. Phys, 37, 3319-3326 (1998).

[5] M. Yashima, J. Cryst. Soc. Jpn., 44, 121-126, 2002

[6] F. Izumi, T. Ikeda, Materia. Sci. Forum, 321-324, 198-204, (2000).

[7] Izumi, F., J. Crystllogr. Soc. Jpn. 44, 380-288 (2002).

[8] F. Izumi, S. Kumazawa, T. Ikeda, W.-Z. Hu, A. Yamamoto & K. Oikawa, Mater. Sci. Forum 378-381, 59-64 (2001).

研究テーマ：半磁性電気伝導体の磁性と化学構造
表　題：複合結晶 $[Ca_2(Co_{0.65}Cu_{0.35})_2O_4]_{0.63}CoO_2$ の変調構造

1-1-29

Modulated Structure of the Composite Crystal $[Ca_2(Co_{0.65}Cu_{0.35})_2O_4]_{0.63}CoO_2$

Y. MIYAZAKI, Y. MIURA, M. ONODA[1], Y. ISHII[2], Y. ONO, Y. MORII[2] and T. KAJITANI

Department of Applied Physics, Tohoku University, Sendai 980-8579
[1]Advanced Materials Laboratory, NIMS, Tsukuba, Ibaraki 305-0044
[2]Advanced Science Research Center, JAERI, Tokai, Ibaraki 319-1195

Misfit-layered cobalt oxides have recently attracted much attention as potential candidates for thermoelectric (TE) materials. We have discovered a new layered compound in the Ca-Co-Cu-O system and the compound also exhibits excellent TE properties. In this report, we present the structure analysis of the compound on the basis of a four-dimensional superspace group approach using powder neutron diffraction data.

Neutron powder diffraction (ND) data were collected at 293 K by means of HRPD diffractometer installed at the JRR-3M reactor in JAERI. The ND data were analyzed using a Rietveld refinement program PREMOS 91 [1] designed for modulated structure analyses. The superspace group of $C2/m(1\ p\ 0)s0$ was adopted on the basis of the observed systematic absences.

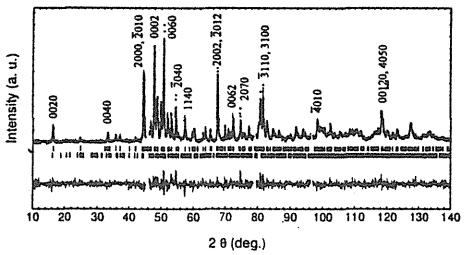


Figure 1: Observed, calculated and difference patterns of the powder neutron diffraction data for $[Ca_2(Co_{0.65}Cu_{0.35})_2O_4]_{0.63}CoO_2$ measured at 293 K.

Figure 1 shows the observed, calculated and difference profiles for the ND data. Short vertical lines below the patterns indicate the peak positions of main (upper) and satellite (lower) reflections for the two subsystems. A satisfactorily good fit was achieved and the final R_{WP} factor was 8.1 %. The structure formula was expressed as $[Ca_2(Co_{0.65}Cu_{0.35})_2O_4]_{0.63}CoO_2$.

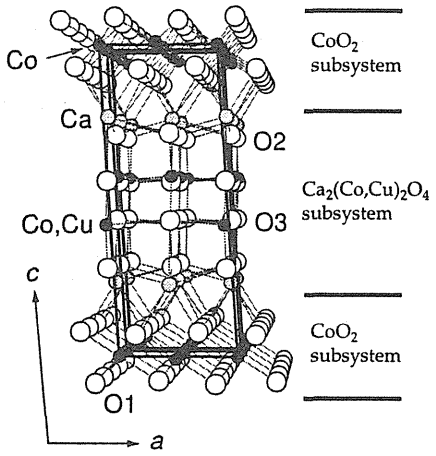


Figure 2: The refined fundamental structure of $[Ca_2(Co_{0.65}Cu_{0.35})_2O_4]_{0.63}CoO_2$ projected in perspective from the b-axis.

Figure 2 shows the fundamental structure viewed in perspective from the b-axis. The structure consists of a CoO_2 sheet (subsystem 1) and an ordered four-layered NaCl-type $Ca_2(Co_{0.65}Cu_{0.35})_2O_4$ block (subsystem 2), stacked parallel to the c-axis. The CoO_2 sheet is composed of edge-shared CoO_6 octahedra forming a triangular lattice as seen in the CdI_2-type structure. Lattice parameters were refined to be $a = 4.8212(4)$ Å, $b_1 = 2.8103(3)$ Å, $b_2 = 4.4915(3)$ Å, $c = 12.7671(8)$ Å and $\beta = 93.93(1)°$. The Cu^{2+} ions appear to play an important role to stabilize such a four-atom thick subsystem in this compound.

References

1) A. Yamamoto: Acta Crystallogr. A **49** (1993) 831.

原子炉：JRR-3　　装置：HRPD(1G)　　分野：中性子散乱（構造）

研究テーマ:ペロブスカイト型ジルコン酸塩の構造変化
表題:ジルコン酸ストロンチウムの構造変化の高温中性子粉末回折による研究

1-1-30 High-temperature Neutron Powder Diffraction Study of Structural Changes in Strontium Zirconate

K. Oh-uchi, M. Yashima, M. Mori, A. Sakai, D. Ishimura, K. Ohoyama*, and Y. Yamaguchi*

Department of Materials Science and Engineering, Interdisciplinary Graduate School of Science and Engineering, Tokyo Institute of Technology, 4259 Nagatsuta-cho, Midori-ku, Yokohama, 226-8502, Japan
**Institute for Materials Research, Tohoku University, Katahira, Aoba, Sendai, 980-8577, Japan*

Perovskite structured oxides have received recent attention as high-temperature proton conductors with potential applications as fuel cells and hydrogen sensors. Some doped zirconates (e.g. Yb-doped $SrZrO_3$) possess appreciable levels of proton conductivity. In order to understand the electrical properties of these materials, it is necessary to investigate the precise crystal structure of $SrZrO_3$. According to the literature, pure $SrZrO_3$ undergoes a sequence of phase transitions as follows: *Pnma* → *Imma* → *I4/mcm* → *Pm*-3*m* [1]. In this study, we have used neutron powder diffraction technique to investigate the structural changes and the nature of phase transitions of $SrZrO_3$.

The neutron-diffraction measurements were performed in air with a 150-detector system, HERMES, installed at the JRR-3M reactor in JAERI [2]. The neutron wave length was 1.8207Å and the diffraction data were collected in the 2θ range from 20° to 150° in step interval of 0.1°, in the temperature range from 25°C to 1203°C. A furnace with $MoSi_2$ heaters was placed on the sample table [3], and used for neutron-diffraction measurements at high temperatures. The temperature was kept constant within ± 1.5°C during each data collection. The neutron-diffraction data were analyzed using the Rietveld program RIETAN-2000 [4].

Figure 1 shows the temperature dependence of neutron-diffraction patterns for $SrZrO_3$. Since the diagnostic superlattice reflections disappeared with increasing temperature, it was confirmed at least two phase transitions of *Pnma* → *Imma* and *I4/mcm* → *Pm*-3*m*.

Figure 2 shows the temperature dependence of the tilt angle of the ZO_6 octahedron. In the tetragonal phase with a single tilt system, the angle of rotation of the oxygen octahedron can be taken as the order parameter. The tilt angle decreases as the temperature approaches the phase transition point. The variation of the tilt angle φ with temperature was well described by $\varphi = A(T_c - T)^{\beta}$, where T_c is the transition temperature. The critical exponent β thus obtained was approximately 0.25 that is the typical value of a tricritical phase transition.

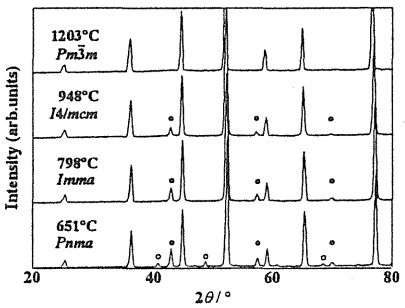


Figure 1: Parts of the observed diffraction patterns of $SrZrO_3$ recorded at 651, 798, 948 and 1203°C.

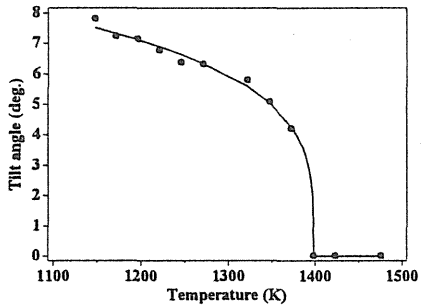


Figure 2: Temperature dependence of the tilt angle of the ZrO_6 octahedron. The fitted line is given by $\varphi = A(T_c - T)^{\beta}$, with $A \approx 1.8$, $T_c \approx 1400$K and $\beta \approx 0.25$.

References

[1] C. J. Howard *et al.*, J. Phys.: Condens. Matter **12** (2000) L677-L683.
[2] K. Ohoyama *et al.*, Jpn. J. Appl. Phys. **37** (1998) 3319-3326.
[3] M. Yashima, J. Cryst. Soc. Jpn. **44** (2002) 121-126.
[4] F. Izumi and T. Ikeda, Materia. Sci. Forum. **321-324** (2000) 198-204.

使用施設:JRR-3　装置:HERMES(T1-3), 分野:1. Structures & Excitations

研究テーマ：自己集合性錯体内における水クラスター $(H_2O)_{10}$ の構造決定
表　題：かご型分子内に形成される分子状" 氷" の構造決定

1-1-31

Determination of the Structure of a Molecular Ice that Forms within a Molecular Cage

M. YOSHIZAWA, T. KUSUKAWA, M. KAWANO, M. FUJITA, T. OHHARA[1], I. TANAKA[1], K. KURIHARA[1] and N. NIIMURA[1]

Dept. of Applied Chemistry, The University of Tokyo and CREST, JST, Tokyo 113-8656
[1]Advanced Science Research Center, JAERI, Tokai, Ibaraki 319-1195

Self-assembly of molecules is an essential feature of natural process controlled by weak interactions between molecules, and recently becomes an important synthetic methodology in organic and inorganic chemistry.[1)2)] In nature, one of the simplest but indispensable self-assemblies can be found in water clusters that form by hydrogen bonding interactions.[2)] Though there have been extensive studies on bulk water by experimental and theoretical approaches, the microscopic phenomena of small water clusters ($(H_2O)_n$, $n =\sim 10$) remain poorly understood because of their dynamic nature and low stability.[3)4)] Among them, we are interested in the character of water that is its preferential orientation in the hydration shell of non-polar solutes by hydrophobic interactions. We expect that if an isolated hydrophobic cavity is provided in an aqueous medium, the formation of discrete water networks can be found in the cavity. Accordingly, we have recently found the formation of a cluster of ten water molecules, $(H_2O)_{10}$, in a hydrophobic cavity of the self-assembled coordination cage (**1**).[5)] In the crystal structure of **1** with the $(H_2O)_{10}$ cluster, water oxygens can be located displaying adamantanoid framework (a static fundamental unit of ice Ic; **2**) but water hydrogen's are missing. The determination of hydrogen positions are, however, particularly important to understand how the cavity recognizes the cluster. Thus, in the present study, we examine neutron diffraction analysis for the complex to clarify the structure of the water cluster and the host-guest interaction.

A single crystal neutron diffraction measurement of the cage complex **1** with H_2O molecules was examined by BIX-4 diffractometer sited on the JRR-3 reactor at JAERI. The crystal size was 3.5x3.5x2.0 mm^3. 325 oscillation images ($\Delta\omega = 0.6°$) were obtained by 13 days measurement. As a result of data processing, the cell parameters were $a = 30.884(3), b = 30.884(3), c = 29.831(4)$, the space group was $P4_32_12$, and the number of unique reflections was 2456. The structure analysis is now progress.

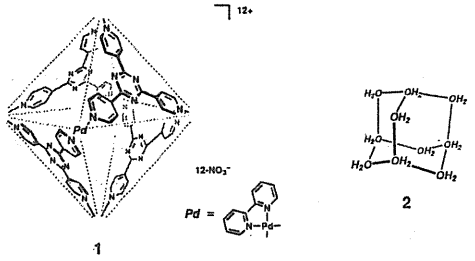


Figure 1: The self assembled coordination cage with water cluster.

References

1) Lehn J. -M. *Supramolecular Chemistry: Concept and Perspectives* (VCH, Weinheim, 1995).
2) Ball P. *H_2O: A Biography of Water* (Weidenfeld Nicolson, London 1999).
3) Ludwig R. *Angew. Chem. Int. Ed.* **40,** 1808-1827 (2001).
4) (a) Barhour L. J., Orr G. W. Atwood J. L. *Nature* **393,** 671-673 (1998). (b) Muller A., Fedin V. P., Kuhlmann C., Bogge H. Schmidtmann M. A. *Chem. Commun.* 927-928 (1999). (c) Wyndham B. B., Scott W., Gordon-Wylie George R. C., Kenneth D. J., John T. W., Urs. G., Terrence, J. C. *J. Am. Chem. Soc.* **121,** 3551-3552 (1999).
5) Fujita, M., Oguro, D., Miyazawa, M., Oka, H., Yamaguchi, K. Ogura, K. *Nature* **378,** 469-471 (1995).

原子炉：JRR-3　　装置：BIX-3M(1GB)　　分野：中性子散乱（構造）

研究テーマ：
同位元素置換して強誘電相転移する $SrTiO_3$ のソフトフォノンの観測と低温構造の決定
表題：同位元素置換された $SrTi^{18}O_3$ の強誘電低温相の構造とソフトフォノン

1-1-32 Study of Structure and Soft Phonon Mode of $SrTi^{18}O_3$ on the Ferroelectric Phase Transition at 23K

Y. Noda, K. Mochizuki, H. Kimura, T. Kyomen[1] and M. Itoh[1]
Institute of Multidisciplinary Research for Advanced Materials, Tohoku University, 2-1-1 Katahira, Aoba-ku, Sendai 980-8577
[1] *Materials and Structures Laboratory, Tokyo Institute of Technology, 4259 Nagatsuta, Midori, Yokohama 226-8503*

$SrTiO_3$ is well known to transform at 110K in terms of the phonon condensation of R_{25} mode at R-point (1/2 1/2 1/2)[1]. Simultaneously, TO phonon mode at Γ point (0 0 0) shows softening[2]. However, because of the quantum fluctuation, the phase transition to a ferroelectric phase at very low temperature is suppressed. This state is called 'quantum paraelectrics'. Recently, Itoh *et al.*[3] discovered that $SrTiO_3$ with isotope ^{18}O (STO18) shows anomaly at about 23K (T_c) on dielectric constant. It is expected that below T_c a ferroelectric phase takes place as a static long-range order.

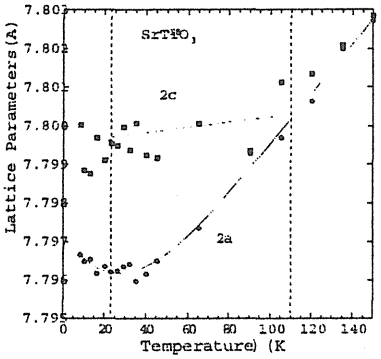


Fig. 1. Obtained lattice parameters based on a tetragonal unit cell.

We studied the phase transition phenomena with focusing on the structural change of STO18 using the four circle neutron diffractmeter FONDER installed at T2-2 beam port in JRR-3M. The lattice parameters are obtained as shown in Fig.1, where we assumed the tetragonal unit cell through the all temperature region since the data scattered very much when we calculated them without any restricted condition. It seems that small anomaly is seen below 23K, but probably the accuracy of the data is still poor. We need much higher-resolution experiment such like synchrotron radiation.

We also performed structural analyses at several temperatures. First we assumed the well-established space group I4/mcm below 110K. Structural analyses were well done, and the obtained rotational angle of TiO_6 octahedron is shown in Fig.2.

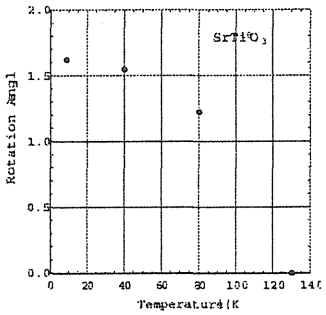


Fig. 2. Obtained rotational angle of TiO_6.

We have performed structural analysis at 8K (below T_c) based on several space groups in order to study the nature of the phase transition at 23K. Space group, R-factor and number of parameters are given in Table 1. Character of each phase is also shown. R-factor shown in parenthesis is taken with an isotropic thermal factor. We consider that almost no difference is found on these space groups. Therefore, at the moment the nature of the phase transition of STO18 at 23K is still open to future.

We have observed soft phonon mode of STO18 at 4G-GPTAS. E_i=14.7meV and 30.4meV are used with PG002 monochromator and analyzer, and collimators 40-40-40-40 minutes or 20-40-40-20 minutes are used depending on the condition. Energy resolution is about

使用施設：JRR-3　装置：T2-2 (FONDER),4G(GPTAS)，分野：1. Structures & Excitations

Table 1. Summary of structure analysis at 8K.

1)	I4/mcm	$R = 4.35\%$	(4.99%)
	non-polar	2+1+9	(3+4)
2)	I4cm	$R = 4.03\%$	(4.47%)
	$P_s//[001]_t$	2+4+11	(6+4)
3)	Iba2	$R = 3.86\%$	(4.43%)
	$P_s//[001]_t$	2+5+18	(7+4)
4)	I2cm	$R = 4.06\%$	(4.46%)
	$P_s//a$	2+7+20	(9+5)

1meV. The STO18 sample for phonon measurements is prepared by assembling 59 single crystal plates having a (110) plane with 10 x 4 x 0.35 mm^3 size. Another plate is used for dielectric measurements to check the transition temperature. Rocking curve of the assembled sample is shown in Fig. 3, and the mosaicness is about 1°.

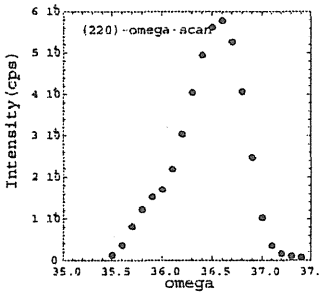


Fig. 3. Rocking curve of (2 2 0) Bragg reflection under the condition E_i=30.4meV and collimators 40-40-40-40 minutes.

The polar TO phonon mode whose symmetry is F_{1u} in the cubic phase shows remarkable softening. We successfully observed the soft phonon mode as shown in Fig. 4, but the softening is incomplete in terms of the phase transition at 23K. Moreover the behavior is essentially the same with that of STO16[2]. Both phonon frequencies are pointing to zero at about 27K, but softening is suppressed around 40K . This implies that the TO soft phonon mode is not responsible directly to the precursor effect of the ferroelectric phase transition at 23K.

We have also observed soft R_{25} mode, and the results are summarized in Fig. 5. Here the square of frequency is shown. Simultaneously, square of the TO phonon frequency is also shown. The complicated behavior below 110K

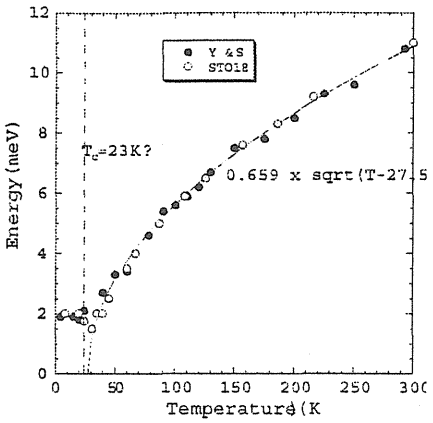


Fig. 4. Observed TO phonon mode at q=0.

is due to the cubic-to-tetragonal phase transition with cell doubling, and the degenerated mode splits and also an R-point becomes a Γ-point. Almost of the frequency observed here is consistent with the reported neutron[1, 2], Raman and hyper Raman scattering experiments.

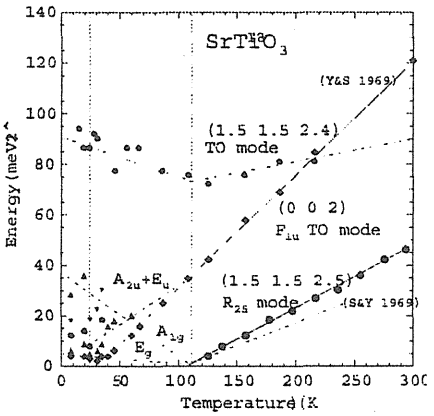


Fig. 5. Square of the phonon energy of R_{25} and TO phonon modes.

References

[1] G. Shirane and Y. Yamada ; Phys. Rev. B **177**, 858(1969).

[2] Y. Yamada and G. Shirane; J. Phys. Soc. Jpn. **26**, 555(2003).

[3] M, Itoh, R. Wang, Y. Inaguma, T. Yamaguchi, Y-J. Shan and T. Nakamura; Phys. Rev. Lett. ; **82**, 3540(1999).

研究テーマ：半磁性電気伝導体の磁性と化学構造 II
表　題：γ-Na_xCoO_2 (x=0.67,0.71,0.73 and 0.75) の結晶構造
1-1-33

Crystal structures of γ-Na_xCoO_2 (x=0.67, 0.71, 0.73 and 0.75)

Y. ONO, N.KATO, Y.ISHII[1], Y.MIYAZAKI and T.KAJITANI

Department of Applied Physics, Tohoku University, Sendai 980-8579
[1]Advanced Science Research Center, JAERI, Tokai, Ibaraki 319-1195

Recent discovery of potential oxide thermoelectric (TE) materials has attracted much attention for their high performance and chemical stability at high temperatures[1-4]. The layered cobaltite, γ-Na_xCoO_2($0.60 \leq x \leq 0.75$), is the most promising p-type TE-materials with dimensionless figure of merit, $ZT = S^2T/\rho\kappa = 1.2$ at T=800 K[5], where S, ρ and κ are Seebeck coefficient, electric resistivity and thermal conductivity, respectively. This ZT value sutisfies the criterion for practical applications. In this study, structure parameters of four samples with different x are refined by Rietveld analysis of powder neutron diffraction data.

Polycrystalline samples of γ-Na_xCoO_2 (x=0.67, 0.71, 0.73 and 0.75) were prepared by a solid state reaction. The mixture of Na_2CO_3 (99.5%) and Co_3O_4(99.9%) powders was pressed into pellets and calcined in air at 1073 K and sintered at 1123 K for 12 h in air with an intermediate grinding. Na and Co contents in the samples were determined by inductively coupled plasma (ICP) analysis. Neutron diffraction measurements were carried out at room temperature using HRPD (λ =1.82318 Å). The measured intensities were analyzed by a program RIETAN2000[6], assuming the space symmetry $P6_3/mmc$ (No.194). Total Na content was constrained to be equal to the ICP results during the analysis.

Figure 1 shows observed, calculated and difference neutron diffraction profiles of γ-$Na_{0.67}CoO_2$. There is good agreement between the observed and calculated intensities in all data sets (R_{wp}=4.5-7.4% and R_I=2.6-2.8%). Little changes are noticed in the crystal structure, except for Na contents at Na1 and Na2 sites[7]. As shown in Fig.2, the Na ions are unequally distributed at Na1 and Na2 sites despite of similar oxygen coordination to both sites. This discrepancy is possibly ascribed to the different coordinations of Co ions to the Na sites.

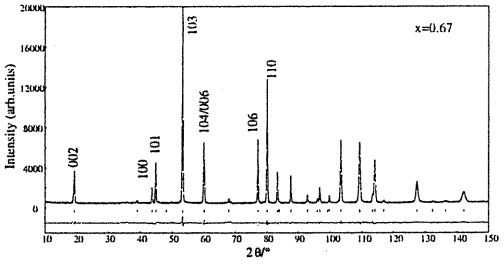


Figure 1: Observed, calculated and difference neutron diffraction profiles of γ-$Na_{0.67}CoO_2$.

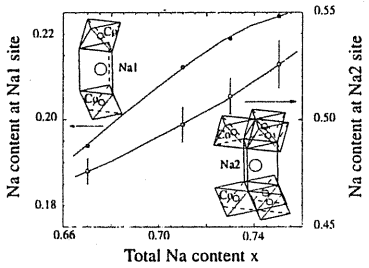


Figure 2: Na contents at Na1 and Na2 sites.

References

1) I. Terasaki *et al.*: Phys. Rev. **B56** (1997) R12685.
2) M. Yasukawa and N. Murayama : Mater. Sci. Eng. **B54** (1998) 64.
3) R. Funahashi *et al.*: Jpn. J. Appl. Phys. **39** (2000) 1127.
4) Y. Miyazaki *et al.*: Jpn. J. Appl. Phys. **40** (2001) L531.
5) K. Fujita: Jpn. J. Appl. Phys. **40** (2001) 4644.
6) F. Izumi and T. Ikeda: J. Crystllogr. Soc. Jpn. **42** (2000) 516.
7) Y.Ono *et al.*: J. Jpn. Soc. Powder and Powder Metallurgy. **50** (2003) 469.

原子炉：JRR-3　　装置：HRPD(1G)　　分野：中性子散乱（構造）

研究テーマ： リラクサ-PZN-8%PTの高電場下における静的・動的応答の研究 II
表題： 中性子回折法によるリラクサー強誘電体PZN-8%PTの電場中冷却効果の研究

Neutron Diffraction Study of Field Cooling Effects on Relaxor Ferroelectrics $Pb[(Zn_{1/3}Nb_{2/3})_{0.92}Ti_{0.08}]O_3$ [1]

1-1-34

K. Ohwada[1], K. Hirota[2], P. W. Rehrig[3], Y. Fujii[2], G. Shirane[4], H. Kimura[5] and Y. Noda[5]

[1] *Japan Atomic Energy Research Institute (SPring-8), 1-1-1 Kohto, Mikazuki, 679-5148*
[2] *Institute for Solid State Physics, The University of Tokyo, 106-1 Shirakata, Tokai, 319-1106*
[3] *TRS Ceramics, Inc., 2820 East College Ave. State College, PA 16801, U.S.A.*
[4] *Department of Physics, Brookhaven National Laboratory, Upton, NY 11973-5000, U.S.A.*
[5] *Institute for Materials Research, Tohoku University, Sendai 980-8577*

Solid solutions of $Pb(Zn_{1/3}Nb_{2/3})O_3$ and $PbTiO_3$ (PZN-xPT) are relaxor ferroelectrics with extremely high piezoelectric responses [2, 3], which are an order of magnitude larger than those of conventional piezoelectric ceramics such as $Pb(Zr_xTi_{1-x})O_3$ (PZT) [4, 5]. PZN-xPT has a cubic (C) perovskite-type structure at high temperatures, and undergoes a diffuse ferroelectric phase transition at low temperatures. It has been reported that the ferroelectric region is separated into rhombohedral (R) and tetragonal (T) symmetries by a morphotropic phase boundary (MPB), a nearly vertical line between the two phases, at $x \sim 10\%$. PZN-8%PT shows a complicated field-induced phase transitions: R $\rightarrow$ M_A [6] $\rightarrow$ M_C [6] $\rightarrow$ T on increasing field and T $\rightarrow$ M_C on decreasing field [7, 8]. To clarify the origin of the exceptional piezoelectric character of this system, it is necessary to resolve the complexities of the transformation sequences in more detail. In the present study, we have carried out high q-resolution neutron diffraction experiments of PZN-8%PT single crystal in the temperature and electric-field ranges $300 \leq T \leq 550$ K and $0 \leq E \leq 15$ kV/cm, which are significantly extended than those of the previous work. We have particularly focused upon how phase transitions depend on preceding thermal and electrical sequences.

The neutron diffraction experiments were carried out on the Tohoku University triple-axis spectrometer TOPAN (6G). Most of the experiments were performed using the tight horizontal beam collimation 15′-10′-S-10′-B (S = Sample, B = Blank). The incident neutron energy (E_i) was tuned to 14.7 meV ($\lambda = 2.36$ Å). Gold electric wires insulated with alumina tubes were carefully connected to the sample which was mounted on the cold head of a high-temperature closed cycle refrigerator (HT-CTI, $15 \leq T \leq 600$ K). The sample was wrapped with the glass wool for electric insulation, and fixed softly to a specially designed copper sample holder with care not to give unnecessary stress. The crystal was oriented to give the (H0L) scattering plane and the electrodes were attached to the (001) surfaces. Thus electric field was applied along the pseudo-cubic [001] direction in the present study. The lattice constant of PZN-8%PT in the cubic phase at $T = 540$ K, $E = 0$ kV/cm is $a = 4.04$ Å, thus the 1 r.l.u. corresponds to $a^*(= b^*) = 2\pi/a = 1.555$ Å^{-1}. We fixed the a^* $(= b^*)$ value at 1.555 Å^{-1} all the time for reciprocal lattice scanning. Scans ware carried out immediately after changing the sample condition.

We made comprehensive neutron-diffraction studies on high-temperature and high-electric-field effects on $Pb[(Zn_{1/3}Nb_{2/3})_{0.92}Ti_{0.08}]O_3$ (PZN-8%PT) in the ranges $300 \leq T \leq 550$ K and $0 \leq E \leq 15$ kV/cm. These results are summarized in Fig 1. In the field cooling process (FC, $E \geq 0.5$ kV/cm), a successive cubic (C) $\rightarrow$ tetragonal (T) $\rightarrow$ monoclinic (M_C) transition was observed. In the zero field cooling process (ZFC), however, we have found that the system does *not* transform to the rhombohedral (R) phase as widely believed, but to a new, unidentified phase, which we call X. X gives a Bragg peak profile similar to that expected for R,

使用施設：JRR-3　装置： 6G, T2-2 , 分野： 1. Structures & Excitations

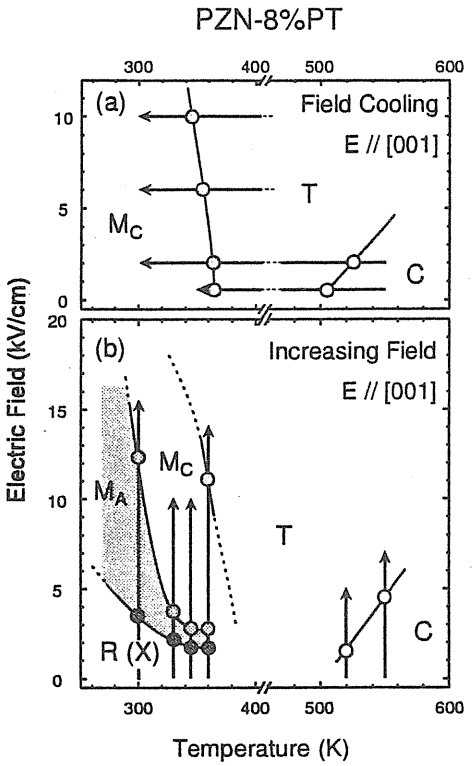


Fig. 1. *E-T* phase diagram of PZN-8%PT. (a) is obtained from structural measurements in the FC process. (b) is obtained from the increasing electric field process after ZFC (and ZFH for the X phase). Arrows indicate the scanning directions and ranges of the corresponding measurement sequences. Circles represent the transition temperatures and fields determined from each sequence.

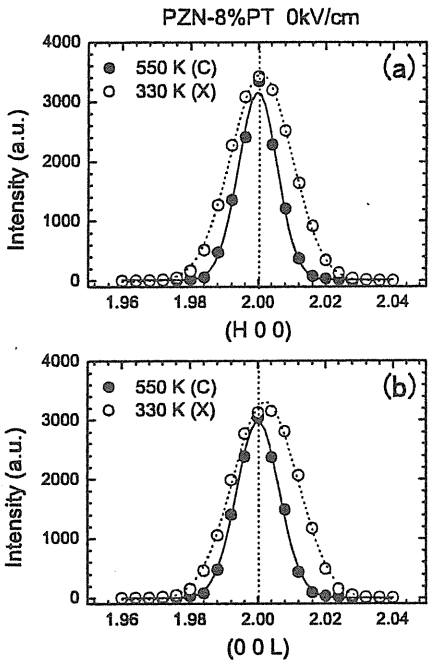


Fig. 2. The (H00) and (00L) peak profiles of the C phase and X phase respectively. Solid and dotted lines drawn through the data points are for guides to the eyes.

but the *c*-axis is always slightly shorter than the *a*-axis as shown in Fig 2. We expect that the discovery of the novel X phase as a ground state of PZN-8%PT urges revisions of theoretical frameworks of relaxors. It transforms into the M_C phase via another monoclinic phase (M_A) as expected from a previous report [8]. At a higher electric field, we confirmed the field-induced M_C $\rightarrow$ T transition, which shows a gradual *c*-axis jump contrary to a sharp *c*-axis jump observed by strain and x-ray diffraction measurements. Our precise *E-T* phase diagram will provide a fundamental aspect for future studies of relaxors. Our next goal is to clarify a true character of the X phase.

To study the average structure of the X phase, we collected some nuclear Bragg reflections (80 points) by the four-circle diffractometer FONDER (T2-2) at room temperature. Detailed analysis is now in progress.

After this work was completed, we have learned that a novel phase, which is similar to the X phase of PZN-8%PT, was found in PZN at room temperature by high energy x-ray diffraction [9].

References

[1] K. Ohwada *et al.*, Phys. Rev. B **67**, 094111 (2003).
[2] S-E. Park *et al.*, J. Appl. Phys. **82**,1804 (1997).
[3] S.F. Liu *et al.*, J. Appl. Phys. **85**, 2810 (1999).
[4] J. Kuwata *et al.*, Ferroelectrics, **37**, 579 (1981).
[5] J. Kuwata *et al.*, Jpn. J. Appl. Phys. **21**, 1298 (1982).
[6] The polarization vectors lie in the pseudo-cubic $\{1\bar{1}0\}$ ({100}, {010}) plane in monoclinic M_A (M_B, M_C). This notation is proposed by Vanderbilt and Cohen (Phys. Rev. B **63**, 094108 (2001)).
[7] B. Noheda *et al.*, Phys. Rev. Lett. **86**, 3891 (2001).
[8] B. Noheda *et al.*, Phys. Rev. B **65**, 224101 (2002).
[9] G. Xu *et al.*, Phys. Rev. B **67**, 104102 (2003).

研究テーマ：積層コーティング膜の内部応力測定
表　題：複合および膜材料の中性子応力測定

1-1-35

Neutron Stress Measurement of Composite and Film Materials

T. HANABUSA, K. KUSAKA, M. NISHIDA[1], N. MINAKAWA[2] and A. MORIAI[2]

Department of Mechanical Engineering, Tokushima University, Tokushima 770-8506
[1]Kobe City College of Technology, Gakuenhigashi-machi, Nishi-ku, Kobe 651-2194
[2]JAERI, Tokai, Ibaraki 319-1195

1 Internal Stress Measurement in Tungsten Fiber Reinforced Copper Composite

1.1 Introduction

Since there is commonly a large difference in the coefficient of thermal expansion between a matrix and a fiber, a microscopic stress state develops in a composite material. In this study, thermal residual stresses and thermal stresses in sub-zero temperature region in the tungsten fibers and in the copper matrix were measured by the neutron diffraction method.

1.2 Experimental procedure

The specimen used in this investigation is a tungsten-fiber (100 μm in diameter) reinforced copper composite. Tungsten fibers had a 110 texture along their longitudinal direction. A cross section of the specimen is shown in Fig.1. The volume fraction of the tungsten fiber is about 10 %. This specimen was annealed at 973 K for 2 hours before stress measurement. The wave length of a neutron beam was 0.20978 nm. The stress-free lattice spacings of each $\{hkl\}$ were measured from a bundle of tungsten-fibers annealed at 973 K, set up on a rotating sample attachment.

In this study, the ordinary triaxial measurement method by using Hooke's equation and the $\sin^2\psi$ were employed for stress evaluation.

1.3 Results of neutron stress measurement

The results of the stress measurement are shown in Table 1. The stress for 200 and 211 diffractions could not be evaluated by the triaxial measurement method because the diffraction peak from the tungsten fiber did not appear at $\psi = 0^\circ$. On the other hand, the $\sin^2\psi$ method could be adopted for each plane of 110, 200 and 211. The residual stresses in the tungsten fibers were compressive in three orthogonal directions. The residual stress evaluated from the $\sin^2\psi$ method using neutron diffraction is the difference of two principal stresses, $\sigma_{11} - \sigma_{33}$. It seems from the results that there is a small difference between the stresses in the interior and those in the surface.

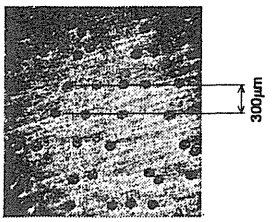


Figure 1: A cross section of W-fiber reinforced Cu composite.

A thermal stress was tried to measure in a temperature region below the room temperature to 50 K. The stress free lattice spacing is necessary for evaluating the triaxial stress state. The 110 diffraction of the tungsten fiber and the 111 diffraction of the copper were used for the thermal stress measurement. The thermal stresses both in the fiber and the matrix behaved non-linearly against the temperature. Since there is no systematic change in the thermal stress behavior, it is considered that the interface between the fiber and the matrix slipped each other in a sub-zero temperature region.

原子炉：JRR-3　　装置：RESA(T2-1)　　分野：中性子散乱（構造）

Table 1: Results of neutron stress measurement.

Triaxial measurement method (MPa)				$\sin^2\psi$ method (MPa)
hkl	σ_{11}	σ_{22}	σ_{33}	$\sigma_{11}-\sigma_{33}$
100	-467	-219	-150	-268
200	-	-	-	-215
211	-	-	-	-209

2 Residual Stresses Measurement in CrN and Cr Films

2.1 Introduction

CrN films are considered to be useful for a piston ring and a connecting rod in engines because of very hard and durable properties. A thick film over than 10 μm is needed for utilizing it in the automobile industry. Residual stresses always develop in the films, because the film and the substrate differ in an atomic distance, thermal expansion coefficients.

In this study, an arc-ion plating (AIP) system was employed to prepare films. Residual stresses in these films were investigated by neutron and X-ray diffraction.

2.2 Experimental procedure

CrN and Cr films and CrN films with Cr interlayer were deposited on a SUS304 substrate by arc-ion plating under the conditions shown in Table 2. The residual stresses in the CrN and Cr films and CrN film with Cr interlayer were measured by neutron diffraction at RESA in JAERI. The wavelength was 0.2098 nm and the incident slit size was 10 mm in width and 15 mm in height. The CrN film and the Cr film had a random orientation and 100 texture, respectively. Therefore, the residual stress in the CrN film was measured by $\sin^2\psi$ method with 220 diffraction, and that in Cr film was measured by two-tilt method with 200 diffraction. The residual stresses in these films were also measured by X-ray diffraction. The characteristic X-rays were CrKα (λ =0.2098 nm) and the incident slit size was 2×4 mm^2.

2.3 Results and discussion

Table 3 shows the results of residual stress measurement in the Cr and CrN film and CrN film with Cr interlayer. A large compressive stress was observed in all films. In the case of thick single-layered CrN film, compressive stress measured by neutron diffraction was smaller than that by X-ray diffraction. In the case of single-layered Cr thin film, compressive stress was almost equal to that by X-ray diffraction. In the case of CrN film with Cr interlayer, compressive stress measured by neutron diffraction was different from that by X-ray diffraction. The reason of the different results between neutron and X-ray diffractions is not clear. One reason would come from the different measurement conditions such as irradiated area size and used diffraction.

Table 2: Conditions of film preparation.

Film	CrN		Cr		CrN/Cr	
I_A (A)	100	200	100	200	100	200
V_B (V)	-300		-300		-300	
Ts (K)	573		573		573	
t ,(μm)	9-10	18-20	4	8	7	

Table 3: Results of residual stress measurement.

Method		Neutron		X-ray	
Film	I_A (A)	σ_N (GPa)		σ_X (GPa)	
CrN	100	-2.2		-2.7	
	200	-1.3		-1.5	
Cr	100	-1.3		-1.3	
	200	-1.6		-1.4	
CrN/Cr	100	CrN	-2.5	CrN	-3.0
		Cr	-0.7	Cr	-1.4
	200	CrN	-3.4	CrN	-1.9
		Cr	-4.8	Cr	-

研究テーマ：$LaGaO_3$系ペロブスカイト型酸化物イオン導電体の高温中性子回折
表題：高酸化物イオン導電体$(La_{0.8}Sr_{0.2})(Ga_{0.8}Mg_{0.15}Co_{0.05})O_{3-\delta}$の高温中性子回折

High-temperature Neutron Diffraction Study on Fast Oxide Ion Conductor $(La_{0.8}Sr_{0.2})(Ga_{0.8}Mg_{0.15}Co_{0.05})O_{3-\delta}$

1-1-36

K. Nomura, H. Kageyama, Y. Miyazaki, M. Yashima [1], N. Chitose [2] and K. Hoshino [2]

Special Division of Green Life Technology, National Institute of Advanced Industrial Science and Technology – Kansai, 1-8-31 Ikeda, Osaka 563-8577, Japan
[1]Department of Materials Science and Engineering, Interdisciplinary Graduate School of Science and Engineering, Tokyo Institute of Technology, 4259 Nagatsuta-cho, Midori, Yokohama, Kanagawa, 226-8502, Japan
[2]Central Research Institute Naka Research Center, Mitsubishi Materials Corporation, 1002-14 Mukohyama, Naka-machi, Naka-gun, Ibaraki, 311-0102, Japan

Recently, $LaGaO_3$-based perovskites have been investigated as new electrolyte materials for solid oxide fuel cells (SOFCs) operated at intermediate temperatures (600 -800°C). Of $LaGaO_3$-based perovskites, Sr-, Mg- and Co-doped one, $(La_{0.8}Sr_{0.2})$-$(Ga_{0.8}Mg_{0.15}Co_{0.05})O_{3-\delta}$ (LSGMC) is one of the best oxide ion conductors [1]. In this study, we have carried out high temperature neutron diffraction measurements for LSGMC, to investigate the change of the crystal structure, and the conduction path of oxide ion at elevated temperatures.

High purity LSGMC compound was prepared by using a solid state reaction method from La_2O_3 (4N), $SrCO_3$ (3N), Ga_2O_3 (4N), MgO (4N) and CoO (99.5%).

Neutron diffraction data were collected in the temperature range from 26 to 1391°C in air, using an electric furnace with $MoSi_2$ heaters [2] and a diffractometer HERMES installed at JRR-3M in JAERI (Tokai) [3]. The diffraction data obtained were analyzed using a Riedveld analysis program RIETAN-2000 [4].

Figure 1 shows the diffraction patterns of LSGMC from 26 to 1391°C. Between 26 and 992°C, broad super lattice peaks (which cannot be indexed as a cubic phase *Pm*-3*m*) were observed at around 2θ = 46, 61, 88, 100, 113, and 128°. The intensity of these peaks decreased with an increase in temperature, and the peaks disappeared at above 992°C. All the diffraction peaks of LSGMC could be indexed as rhombohedral symmetry (*R*-3*c*) between 26 and 992°C, and cubic one (*Pm*-3*m*) at 1193 and 1391°C. In the high temperature phase (*Pm*-3*m*), the atomic displacement parameters of oxygen were large and anisotropic ($U_{22} = U_{33} > U_{11}$, displacements perpendicular to (Ga, Mg, Co)-O bonds were large), which suggests that oxide ion is easy to move along the edges of (Ga, Mg, Co)O_6 octahedra. This feature agreed with the result obtained by a MD calculation [5]. At $T \leq 992$°C, the tilting angle of (Ga, Mg, Co)O_6 octahedra increased with decreasing temperature, which corresponds to an increase in the apparent activation energy for oxide ion conduction with decreasing temperature [1].

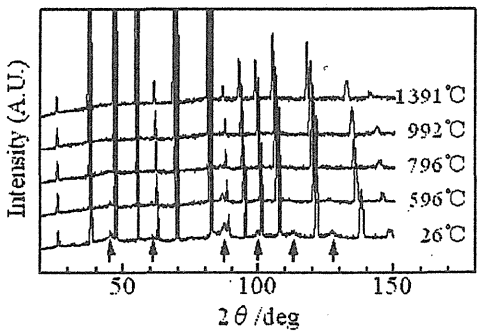


Fig. 1 Neutron diffraction patterns of LSGMC from 26 to 1391°C (arrows show the positions of super lattice peaks).

References

[1] T. Ishihara, T. Akbay, H. Furutani and Y. Takita, *Solid State Ionics*, **113-115**, 585 (1998).
[2] T. Yashima, *J. Am. Ceram. Soc.*, **85**, 2925 (2002).
[3] K. Ohoyama, T. Kanouchi, K. Nemoto, M. Ohashi, T. Kanitani and Y. Yamaguchi, *Jpn. J. Appl. Phys.*, **37**, 3319 (1998).
[4] F. Izumi and T. Ikeda, *Mater. Sci. Forum*, **321-324**, 198 (2000).
[5] M.S. Islam, *J. Mater. Chem.*, **10**, 1027 (2000).

使用施設：JRR-3　　装置：HERMES(T1-3)，分野 Structure & Excitations

研究テーマ：中性子回折による焼入れ材・傾斜機能材の熱応力解析評価
表　題：高周波焼入れしたS45C丸棒における残留応力

1-1-37

Residual Stress in the Induction Hardened S45C Round Bar

K. INOUE, M. SUGIMOTO, H. MAEDA, T. HORIKAWA, T. TSUJIKAMI,
N. MINAKAWA[1], A. MORIAI[1] and F. IKUTA[2]

Faculty of Science and Technology, Ryukoku University, Seta, Otsu 520-2194
[1]Advanced Science Research Center, JAERI, Tokai, Ibaraki 319-1195
[2]Heating Machine Division, Neturen Co., Tanuma, Hiratsuka 254-0013

The residual stress of an induction hardened S45C round bar was estimated from the resitual strain measured by neutron diffraction experiment with RESA at JRR-3. The obtained stress was compared with the results calculated by the finite element method, FEM.

The diameter of the round bar was 20 mm and the length was 60 mm. The surface of the bar was treated by induction heating of 50kHz for 8.5 s. The temperature of the surface was increased up to 950 °C and was cooled down to 26.9 °C with the water. It is expected that the martensitic phase occurs near the surface, whereas the inner region is not hardened and is in the coexistent state of ferrite and pearlite.

We prepared the sliced specimen cut from the round bar along the direction of the hight including the center of the bar. It was etched with 5% nital for 10s, after mirror finishing by buffing. The photograph of the hardened sliced specimen is swown in Fig.1. In Fig.1 we are able to distinguish the martensitic region near the surface from the coexitent region of pearlite and ferrite. The SEM images at each positon on the radius of central sectional plane, which was observed using this sliced specimen, are shown in Fig.2 for hardened bar and in Fig.3 for non-hardened bar. In Fig.2, we see that the fraction of the martensitic phase increases as we get near the surface.

The stress free lattice spacing, d_0, Young's modulus and Poisson ratio at each position are necessary to estimate the stress at each position of the sample. We have measured the (110) latttice spacing at each position of the surface of the sliced sample to obtain d_0. The diffraction was observed for the virtical

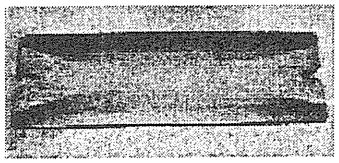


Figure 1: Photograph of the sliced specimen cut from the hardened round bar.

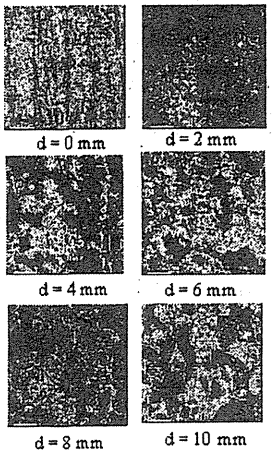


Figure 2: SEM images of the induction hardened S45C round bar at each positionon on the radius of central sectional plane. The letter, d, means the distance from the surface.

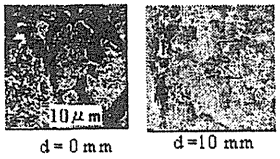


Figure 3: SEM images of the non heat treated S45C round bar at the surface and the center on the radius of central sectional plane. The letter, d, means the distance from the surface.

原子炉：JRR-3　　装置：RESA(T2-1)　　分野：中性子散乱（構造）

direction of the surface, because the stress is released in the virtical direction at the surface. The peak position of the 110 reflection was different due to each position of the specimen. The stress free lattice spacing, d_0, at each position was estimated and are shown in Fig. 4.

Young's modulous and Poisson ratio of the martensite single phase and of the pearlite single phase were estimated from the 110 reflection of each single state test piece under tensile condition. The experimantal results are shown in the previous report.[1] Young's modulous and Poisson ratio at each posion where the martensite and ferrite are coexistent were determined by averaging the experimentally obtained two values over the volume fraction of each phase. The volume fraction of the martensite at each position of the bar was estimated by simulation.[2]

As a result, the residual stress for three directions at each position on the radius of the central sectional plane of inducton hardened bar is shown in Fig.5. The residual stress calculated by FEM is shown in Fig.6. We see that coincidence between the stress obtained by neutron diffraction and that estimated by FEM is extremely good. They are also coincident with the stress measured by X-ray at the surface, as shown in Fig.6 where the measured values are also plotted.

We conlude that this success in determing the residual stress when the martensite and the ferrite are coexistent is owing to the precise determination of the stress free lattice spacing, d_0, for coexitent situation of two phase.

References

1) K. Inoue, T. Horikawa, N.Minakawa, A. Moriai *et al* : JAERI-Review 2003-019 (2003) 336.
2) F. Ikuta and T. Horino: Netsu-Syori **42** (2002) 359. (in Japanese)

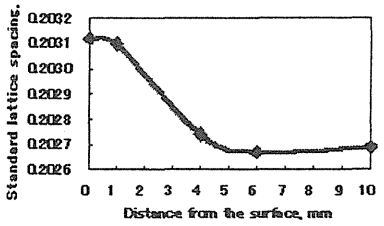


Figure 4: Stress free lattice spacing, d_0, at each position on the radius of the central sectional plane.

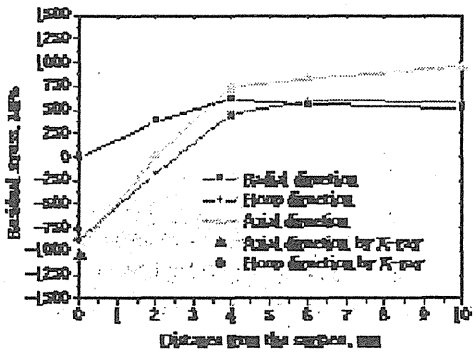


Figure 5: Residual stress at each position on the radius of central sectional plane of inductioned hardened round S45C bar, obtained by RESA.

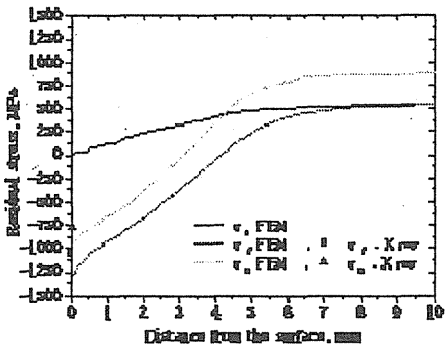


Figure 6: Residual stress at each position on the radius of central sectional plane of onduction hardened bar, calculated by FEM. At the surface measured values by X-ray are also plotted.

研究テーマ:ソフト化学により合成した d0 遷移金属を含む機能性材料の構造決定
表題:ナノサイズ $KNbO_3$ の中性子回折研究

1-1-38 Neutron Diffraction Study on Nano-size Perovskite $KNbO_3$

K. Toda, S. Tokuoka, M. Kawakami, K. Uematsu*, and M. Sato*

*Graduate School of Science and Technology, Niigata University, 8050 Ikarashi, Niigata 950-2181, Japan; *Faculty of Engineering, Niigata University, 8050 Ikarashi, Niigata 950-2181, Japan*

Lead-free ferroelectric materials have been extensively investigated for application in the piezoelectrics and memory devices. Perovskite-type potassium niobate ($KNbO_3$) is the most promising candidate for many lead-free piezoelectric devices because of its large electro-mechanical coupling factor [1]. However, sintered ceramic sample is unavailable due to its poor sinterability [2].

Recently, we demonstrate a new soft-solution synthetic method for well-crystallized $KNbO_3$ fine powders [3]. In this method, rock-salt-type KF blocks in a layered perovskite, K_2NbO_3F was selectively dissolved in water to produce perovskite nanosheets at room temperature. The self-assembly between the perovskite nanosheets in the colloidal solution could yield well -crystallized submicron (100 – 300 nm) $KNbO_3$ powders at room temperature.

The nano-sized $KNbO_3$ was prepared by the colloidal method [3]. We performed neutron powder diffraction experiments on the HERMES installed at the JRR-3M reactor. An incident neutron wavelength λ was 0.18207(7) nm. The fine powder sample was enclosed in a cylindrical vanadium vessel. The data were collected on thoroughly ground powders by a multi-scanning mode in the 2θ range from 3° to 153° with a step width of 0.1°.

In previous study, we indexed their powder XRD pattern based on a cubic (Pm3-m) or tetragonal (P4mm) unit cell [3, 4]. First, the cubic and tetragonal models were checked. However, the both refinements gave rather poor R-factors. All of the reflections could be assigned as an orthorhombic and not tetragonal symmetry. Possible space groups were orthorhombic Amm2 (No. 38). The positional parameters and temperature factors are listed in Table 1. The Rietveld refinement results showed that the crystal structure of the nano-sized soft chemical sample essentially maintained in the orthorhombic form which is the same as that of $KNbO_3$ prepared by a high-temperature solid state reaction [1, 2]. However, the soft chemical synthesis at room temperature relaxed the orthorhombic distortion of $KNbO_3$ product considerably. This effect is tentatively ascribed to a particle size effect on the microscopic cooperative phenomenon [5].

Table 1. Structural parameters and reliable factors of nano-sized soft chemical $KNbO_3$.

Atom	x	y	z	B($x10^{-2}nm^2$)
K - 2a	0.5	0	0.486(7)	0.9(1)
Nb - 2b	0	0	0	0.5(1)
O1 - 2a	0.5	0	0.962(2)	0.4(2)
O2 - 4e	0	0.254(1)	0.732(3)	0.9(1)

Lattice parameters (nm)
: a = 0.39906(6), b = 0.5688(1), c = 0.5698(1)

Reliable factors
: R_{wp} = 3.65 %, R_p = 2.84 %, R_I = 3.57 %, R_F = 1.39 %

References

[1] K. Yamanouchi et al., Elec. Lett. **33** (1997) 193.
[2] U. Fluckinger et al., J. Am. Ceram. Soc. **56** (1977) 575.
[3] K. Toda et al., Key Eng. Mater. **214-215** (2002) 67.
[4] K. Toda et al., Solid State Ionics **154-155** (2002) 393.
[5] K. Uchino et al., J. Am. Ceram. Soc. **72** (1989) 1555.

使用施設:JRR-3　装置:HERMES(T1-3), 分野 Structure & Excitations

研究テーマ：先端偏極中性子散乱によるスピン-格子物性の研究
表　題：FeCo-Zr-O 磁気フィルムの構造解析

1-1-39

HRPD study on FeCo-Zr-O soft magnetic films

M. OHNUMA, J. SUZUKI[1] and Y. ISHII[1]

National Institute for Metals, Tsukuba, Ibaraki 305-0047
[1]Advanced Science Research Center, JAERI, Tokai, Ibaraki 319-1195

Magnetic materials for application in recording heads are required to have a high saturation magnetization, high magnetic permeability at high frequencies and low coercivity. Xiong et al.[1)] reported that $(Fe_{0.65}Co_{0.35})_{99}99O_1$ sputtered film shows high saturation magnetic induction (B_s=2.45 T) and low coercivity (H_c=400 A/m) after annealing at 470 °C for 1 hour, while the as deposited films show large coercivity over than 8000 A/m. The peak width in profiles corresponding to bcc-Fe(Co) phase becomes sharp by annealing indicating the internal stress are released by annealing. Although the stress relief can decrease the coercivity, the obtained coercivity value is still smaller than the one for bcc-FeCo phase. One possibility which can explain the decreasing coarcivity is the existence of ordered FeCo phase whose anisotropy constant is known to be small. Neutron diffraction is the only technique that can detect ordered FeCo phase because scattering length of Fe and Co is almost same for XRD but they are different for ND. For clarifying the existence of ordered FeCo phase, we measured neutron diffraction patterns of sputtered $(Fe_{0.65}Co_{0.35})_{99}99O_1$ film. The samples are made by sputtering on polyimide films with 8 micron thick. The films with 100 mg (total weight with polyimide films) for as deposited and 50 mg for annealed samples are put into V holder. Figure 1 shows a profiles for as Deposited films. a simulated profile for CsCl type ordered FeCo phase are also shown in the lower part. Although the (100) peak is not visible because of low S/N, a peak corresponding to (111) peak appears at 66 degree indicating the existence of ordered phase even in as deposited film. The (111) peak become relatively clearer after annealing suggesting small increment of volume fraction of ordered phase. A series of fundamental peaks become sharp by annealing, which is same with the result of XRD measurements, indicating the stress relief. Therefore, we can conclude that decreasing of coacivity is due to both the stress relief and increment of volume fraction of ordered phase. The former is seems to be dominant because the ordered phase is already formed in as-deposited condition. As a summary we confirm the existence of ordered FeCo phase which can explain the low coercivity of $(Fe_{0.65}Co_{0.35})_{99}99O_1$ film.

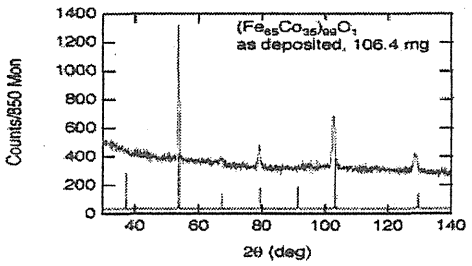


Figure 1: Neutron Diffraction pattern of as-deposited film.

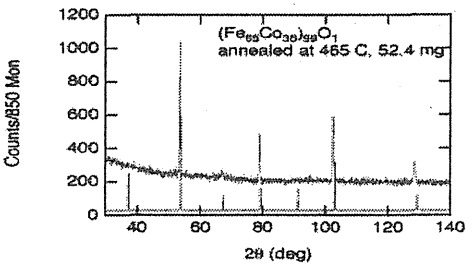


Figure 2: Neutron Diffraction pattern of annealed film.

References

1) X.Y. Xiong, M. Ohnuma, T. Ohkubo, D.H. Ping, K. Hono, S. Ohnuma, H. Fujimori, and T. Masumoto: J. Magn. Magn. Mat., in print.

原子炉：JRR-3　　装置：HRPD(1G)　　分野：中性子散乱（構造）

研究テーマ： $(La_{2/3-x}{}^{7}Li_{3x})_{1-y}Sr_yTiO_3$ の構造とフォノン分散

表題： $(La_{0.55}{}^{7}Li_{0.35})_{0.95}Sr_{0.05}TiO_3$ の結晶構造

1-1-40 Crystal Structure in $(La_{0.55}{}^{7}Li_{0.35})_{0.95}Sr_{0.05}TiO_3$

H. Shigematsu, S. Shioya[1], A. Tobo[2] and T. Matsui[1]

Department of Physics, Faculty of Education, Shimane University, Matsue 690-8504, Japan
[1]Department of Quantum Engineering, Nagoya University, Nagoya 464-8603, Japan
[2]Institute for Materials Research, Tohoku University, Sendai 980-8577, Japan

Recently, a wide variety of solid electrolytes with high ionic conductivity have been prepared with potential application as solid electrolytes in high energy batteries and other electrochemical devices. The fastest lithium-ion-conducting oxide electrolytes are the perovskite-type lanthanum lithium titanates $La_{2/3-x}Li_{3x}TiO_3$ and their variants. In the structure of these materials, there are a substantial number of A-site vacancies through which lithium can transport. It has been also reported that the substitution of large Sr^{2+} for La^{3+} can increase the ionic conductivity slightly at low substitution because of expanding the bottleneck sizes and $(La_{0.55}Li_{0.35})_{0.95}Sr_{0.05}TiO_3$ sample shows the highest ionic conductivity in $La_{2/3-x}Li_{3x}TiO_3$ system. In the system, the space group is considered to be *P4/mmm* or *Cmmm*.

Furthermore, we recently obtained the results of the Li isotope effect in the ionic conductivity: the lithium ionic conductivities of $(La_{0.55}Li_{0.35})_{0.95}Sr_{0.05}TiO_3$ with different lithium isotopic composition were measured by impedance spectroscopy and the ionic conductivity increased with ^{6}Li content.

In order to clarify the structure in $(La_{0.55}{}^{7}Li_{0.35})_{0.95}Sr_{0.05}TiO_3$, we performed neutron powder diffraction experiments using the Kinken power diffractometer for high efficiency and high resolution measurements, HERMES, of Institute for Materials Research (IMR), Tohoku University, installed at JRR-3M in JAERI (Tokai).

Figure 1 shows neutron powder diffraction patterns for $(La_{0.55}{}^{7}Li_{0.35})_{0.95}Sr_{0.05}TiO_3$ below 500 K. The lattice parameters are a = 7.7450(7), b = 7.75165 (6) and c = 7.7570 (9) Å for the $2a_p \times 2a_p \times 2a_p$ superlattice unit cell at room temperature. The space group is not *P4/mmm* but *Cmmm*, and $(La_{0.55}{}^{7}Li_{0.35})_{0.95}Sr_{0.05}TiO_3$ retains this structure down to 8 K. The observed superstructure peaks could be considered due to the ordering of La^{3+} irrespective of La^{3+} and vacancy and La and Li^{1+}. The diffuse scattering was observed around 13° because of partial disordering of oxygen atoms, which is now under analysis by Peverse Monte Calro method.

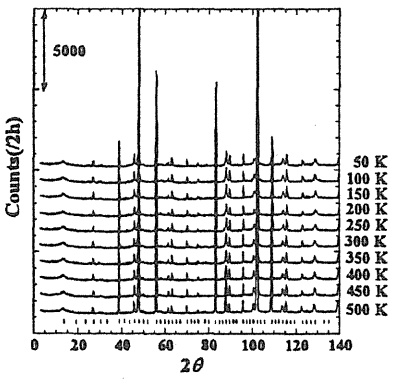


Fig. 1 Neutron powder diffraction pattern of $(La_{0.55}{}^{7}Li_{0.35})_{0.95}Sr_{0.05}TiO_3$ below 500 K.

使用施設： JRR-3 ， 装置： HERMES(T1-3) and HER(C1-1) ， 分野 Structure&Excitations

研究テーマ：ペロブスカイトPrAlO3の協同的ヤーン・テラー構造相転移
表題：PrAlO3 の協同的ヤーン・テラー構造相転移

1-1-41 Cooperative Jahn-Teller structural Phase transitions of $PrAlO_3$

M.Hidaka[1], S.Takahashi[1], and S.Watanabe[1,2]
1.Department of Physics, Faculty of Science, Kyushu University, Fukuoka 812-0053,Japan
2.Neutron scattering Laboratory, ISSP., University of Tokyo, Tokai, Ibaraki319-1106, Japan

Perovskite-type compound $PrAlO_3$ shows structural phase transitions at about 120K, 150K, 210K, and 1320K. An ideal cubic symmetry phase (Phase 1) is above 1320K. Multi-domains are usually made even in a single crystal below 1320K. Several structural determinations had been studying by X-ray and neutron diffraction. However, such multi-domains give an ambiguity of structural analysis in the phases, except Phase1.

The structural properties give information to study a mechanism of successive phase transitions, especially local structural modulation. It is known that the phase transitions occurring at 150K, 210K, and 1320K result from a condensation of soft phonons, R^x_{25}, R^x_{25}+R^y_{25}, and R^x_{25}+R^y_{25} +R^z_{25}, respectively. Such an interpretation is based on an appearance of superlattice reflections only at a R-type zone boundary point, but not M and X points in a cubic reciprocal lattice space. Thus, the phase transitions induce a systematic tilting of AlO_6 octahedra around <111>, <110> and <100>, as cooling down.

However, such interpretation does not describe about a correlation between an electronic state of Pr^{3+} ions and the micro-structural modulation in $PrAlO_3$. A $4f^2$-orbital of Pr^{3+} ions shows a Jahn-Teller effect in a crystal filed made by surrounding anions, O^{2-} Oxygen ions. The effect strongly correlates soft phonon modes of three-degenerated R_{25} (R^x_{25}+ R^y_{25} +R^z_{25}) mode. Usually, in the successive structural phase transitions, perovskite-type compounds show a condensation process of soft modes, for example from R^x_{25} to R^y_{25} or from M^z_3 to R^x_{25}+ R^y_{25}, while $PrAlO_3$ implies a release of the condensed soft modes; R^z_{25} at 210K, R^y_{25} at 150K, after R_{25} (R^x_{25}+ R^y_{25} +R^z_{25}) soft mode condensed at 1320K. Furthermore, the phase transition at 120K cannot be related to any kind of tilting scheme for AlO_6 octahedra. Therefore, it is considered that the cooperative Jahn–Teller distortion around Pr^{3+} ions should contribute the phase transitions in $PrAlO_3$.

In order to re-study a mechanism of the successive phase transitions, we carried out measurements of diffraction patterns by using a 4-circle neutron diffractometer, FONDER. Fig.1 shows peak profiles of a (400) fundamental reflection taken at 175K and 300K with ω-scan.

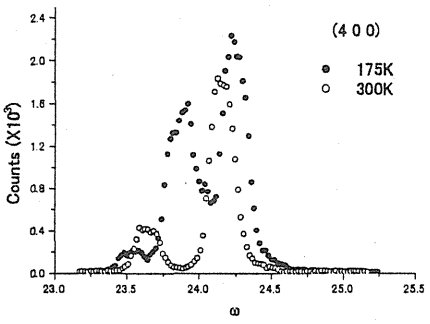


Fig.1.Peak profiles of (400) reflection taken at 175K and 300K.

The reflection is indexed with a unit cell of 2ap x 2bp x 2cp, where a suffix "p" means a pseudo-perovskite cell. It was from the figure that multi-domains are in a single crystal of about 3x3x3mm^3. The phase transition at 210K gives a large structural modulation. Fig.2 also shows peak profiles of a (040) fundamental reflection taken at 175K and 300K. The (400) and (040) reflections were simultaneously at same temperature to find a spatial distribution of the domains in the single crystal. From

使用施設：JRR-3　装置：FONDER(T2-2)、分野：1.Structures & excitations

Figs.1 and 2, it was found that, at

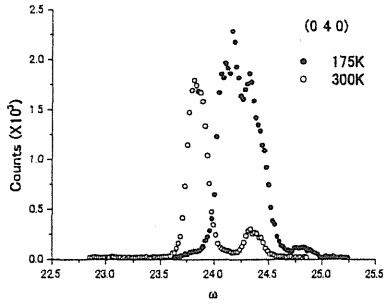


Fig.2. Peak profiles of the (040) reflection simultaneously taken with the (400) reflection in Fig. 1.

300K, there are mainly two kinds of domains and one of them is dominant to other. If needed, we can use such population-ratio of the domains as a refined parameter, when doing a structure determination. On the other hand, the peak profiles of the (400) and (040) reflections taken at 175K suggest that the spatial distribution of the domains is largely changed by passing through the phase transition at 210K. The fact implies that the phase transition from Phase 2 to Phase 3 is strongly elastic.

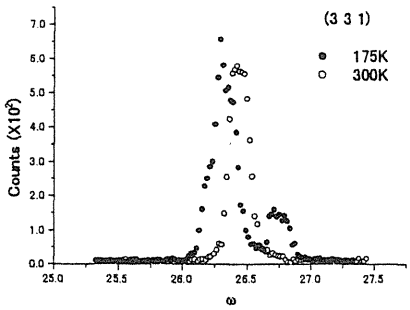


Fig.3. Peak profiles of (331) superlattice reflection taken at 175K and 300K.

In fact, we observed an interesting shift of domain walls in vicinity of its transition temperature by means of a polarized microscope view. It was also found with ω- and ω-2θ scan that lattice parameters (a, b, c and α, β, γ) are largely changed, and that a rhombic symmetry in Phase 2 is transformed to an orthorhombic-like symmetry in Phase 3, as reported. Thus, we consider a contribution of the Jahn-Teller effect of Pr^{3+} ions to the phase transition in $PrAlO_3$.

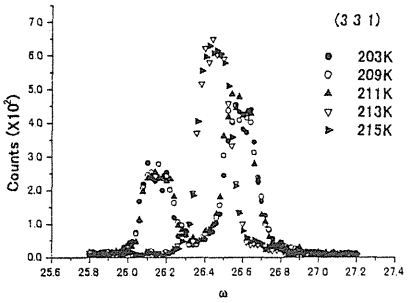


Fig.4.Peak profiles of (331) superlattice reflection as a function of temperature.

At the present investigations, superlattice reflections were observed only at R points in the cubic reciprocal lattice space of Pm3m below Phase 2. The results are shown in Fig.2. The peak profiles of (331) reflection are also simultaneously taken at the same temperature with the (400) and (040) reflections. Therefore, it was found from the peak-width that one of the (331) reflections is forbidden at 300K (Phase 2). Fig.3 shows temperature dependence of peak profiles of the (331) reflections. The phase transition to be of fist –order occurs at about 212K. If a tilt-angle of AlO_6 octahedron is same around a pseudo perovskite axes of [100] and [010], that is $\varphi_x = \varphi_y$, the (331) reflection shows the forbidden rule even at Phase 3. "$\varphi_x = \varphi_y$" indicates the condensation of degenerated soft mode (R^x_{25}+ R^y_{25}). Thus, we considered that the phase transitions occurring below room temperature are affected by the localized Jahn-Teller distortion around Pr^{3+} ions.

We are in progress to study the correlation between instability of (R^x_{25}, R^y_{25}, R^z_{25}) soft phonons and the cooperative Jahn-Teller effect in $PrAlO_3$ by using a neutron diffractometer, FONDER.

This is a blank page.

1. 中性子散乱 2) 磁　性

1. Neutron Scattering　2) Magnetism

This is a blank page.

研究テーマ：アクチノイド及び関連イオン性化合物の構造・物性研究
表　　題：$L_{0.5}A_{0.5}MnO_3$の磁気的性質（L=Eu, Gd, Tb 及び Dy, A=Ca 及び Sr）
1-2-1

MAGNETIC PROPERTIES OF PEROVSKITE MANGANITES $L_{0.5}A_{0.5}MnO_3$ (L=Eu, Gd, Tb AND Dy, A=Ca AND Sr)

K. YOSHII, Y.HIRAMITSU, Y. NISHIHATA, J. MIZUKI, A. NAKAMURA[1], Y. SHIMOJO[1], Y. ISHII[1], Y. MORII[1], H. ABE[2], K. NISHIDA[2]

Synchrotron Radiation Research Center, Japan Atomic Energy Research Institute (JAERI), Mikazuki, Sayo-gun, Hyogo, 679-5148

[1]*Advanced Science Research Center, JAERI, Tokai, Ibaraki, 319-1195*

[2]*National Institute for Materials Science, Tsukuba, Ibaraki 304-0047*

Rare-earth perovskite manganites have attracted considerable renewed attention in this decade, because of their intriguing properties such as colossal magnetoresistance. Among these oxides, $L_{0.5}A_{0.5}MnO_3$ (L=rare earth metal, A=alkaline-earth metal) is known to exhibit a wide variety of physical properties.[1,2] In this work, magnetic properties were studied for the system containing the small rare earths of L^{3+}=Eu^{3+}, Gd^{3+}, Tb^{3+} and Dy^{3+}.

Magnetization measurements (Quantum Design MPMS) showed a spin-glass-like transition around 40-50 K for $L_{0.5}Sr_{0.5}MnO_3$, while a charge-ordering was suggested for $L_{0.5}Ca_{0.5}MnO_3$ around room temperature.

Figure 1 shows the neutron diffraction pattern for $Tb_{0.5}Sr_{0.5}MnO_3$ at 9 K, taken at the high-resolution powder diffractomter of the JRR-3 reactor. The experimental pattern at room temperature could be fitted to an orthorhombic *Pnma* structure by the Rietveld analysis (RIETAN-2000). It was found that the weak magnetic peaks in the pattern at 9 K (inset) were appreciably wider than the nuclear Bragg peaks, indicating an existence of short-range magnetic order such as a spin-glass. The patterns of the isostructural $Tb_{0.5}Ca_{0.5}MnO_3$ could be fitted assuming a charge-ordering state of the Mn ions. The different behavior between the Sr- and Ca-systems may be explained in connection with the difference of the ionic radii of L^{3+} and A^{2+}. [2]

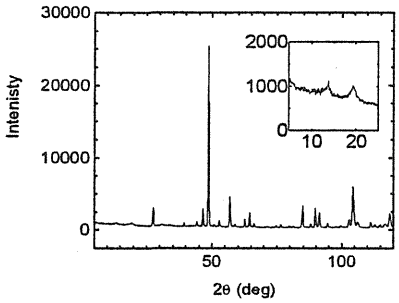


Fig. 1 Neutron powder diffraction patterns of $Tb_{0.5}Sr_{0.5}MnO_3$ at 9 K. The inset shows magnetic Bragg peaks.

References

1) P. M. Woodward *et al.*, Chem. Mater. 10 (1998) pp. 3652-3665.
2) T. Terai *et al.*, Phys. Rev. B61 (2000) pp. 3488-3493.

原子炉：JRR-3　　装　置：HRPD　　分　野：中性子散乱（磁性）

研究テーマ：GHz 帯電磁波吸収材料–六方晶 Co_2Z 型フェライト–の磁気構造の研究
表題：粉末中性子回折による Co_2Z 型六方晶フェライトの磁気構造の評価

Estimation of Magnetic Structure of Co_2Z-type Hexaferrite by Powder Neutron Diffraction

1-2-2

Y. Takada, T. Nakagawa, T. Tachibana, T. Ino, T. A. Yamamoto and *S. Kawano

*Depertment of Nuclear Engineering, Osaka University, 2-1 Yamadaoka, Suita, Osaka 565-0871, Japan; *Kyoto University Research Reactor Institute, Noda, Kumatori-cho, Sennan-gun, Osaka 590-0494, Japan*

In recent years, rapid progress in information society has been promoting minituarization and densification of various electric devices and processing signals with higher frequency, namely from MHz to GHz. However, electromagnetic noises radiated from these recent devices must be in GHz region, and have serious obstruction and/or interference in normal operation and severe influence on communication society. Therefore, electromagnetic noise absorbent materials effective even in GHz region have been required to shield crucial devices from higher frequency noises.

Co_2Z-type hexagonal barium ferrite $Ba_3Co_2Fe_{24}O_{41}$ is a promising candidate material in the range of GHz because of its high permeability even in the GHz region. We investigated the correlation of permeability with oxygen partial pressure P_{O2} in sintering process, and found that the permeability of Z-type hexaferrite sintered at P_{O2} = 101.3 kPa was about 18, and, on the other hand, that sintered at P_{O2} = 21.3 kPa was about 14. The relation of permeability of Z-type hexaferrite is as follows;

$$\mu_r = I_S/3H_p$$

where μ_r is permeability, I_S saturation magnetization, and H_p anisotropic field in the direction parallel to c-plane. We examined that the difference of oxygen partial pressure in preparing Z-type samples gives them different magnetic structure, especially the site distribution of magnetic cation Fe^{3+} and Co^{2+} and the orientation of magnetic moment. However, we can hardly find the data about crystal and magnetic structure of Co_2Z-type hexaferrites in detail[1]. To obtain a prospect of material design for better devices, it is necessary to understand dependence of magnetic properties on oxygen partial pressure in sintering process.

We reported on our results of neutron diffraction studies on Z-type hexagonal barium ferrite materials. And we performed the Rietveld analysis for their neutron diffraction patterns in order to determine the site occupied preferentially by iron and cobalt ions and the orientation of their magnetic moments.

The powder sample of $Ba_3Co_2Fe_{24}O_{41}$ was prepared by conventional solid-state reaction method. Stoichiometric amounts of $BaCO_3$ (99.7 %), Co_3O_4 (99.7 %) and Fe_2O_3 (99.7 %) powders were mixed in a ball-mill with distilled water for 20 hours, dried and calcined at 1273 K. They were then crushed and shaped into green pellets. The pellets were sintered at 1573 K for 16 hours under an oxygen partial pressure of 21.3 or 101.3 kPa which was controlled by adding Ar gas.

For the Rietveld analyses for neutron diffraction patterns[1], We performed neutron diffraction experiments on the Kinken powder diffractometer for high efficiency and high resolution measurements, HERMES(T1-3), of Institute for Materials Research (IMR), Tohoku University, installed at the JRR-3M reactor in Japan Atomic Energy Research Institute (JAERI), Tokai. Neutrons with a

使用施設：JRR-3　　装置：HERMES(T1-3)，分野 Magnetism

wavelength 1.8207 Å were obtained by the 331 reflection of the Ge monochrometer and 12'-blank-sample-22' collimation. The powder samples were sealed in a vanadium cylinder of 10 mm diameter. The diffraction angle 2θ was swept in a range 3 - 153° at intervals of 0.1°.

Figure 1 shows the result of the Rietveld refinement for the neutron diffraction pattern of $Ba_3Co_2Fe_{24}O_{41}$ sintered under P_{O2} = 101.3 kPa. Table 1 tabulates fractional occupation ratio g of iron and cobalt for sites of Me1 – 10 of $Ba_3Co_2Fe_{24}O_{41}$ of P_{O2} = 21.3 and 101.3 kPa. At the bottom of the table, there are tabulated spontaneous magnetization calculated on the basis of the distribution of iron and cobalt over these sites, and the optimized magnetic moment angle ϕ with *c*-axis. These results indicate that cobalt ions are located only on 5 sites; Me1, Me4, Me5, Me8 and Me10 and that the magnitude of magnetic moment angles with *c*-axis of these sample of P_{O2} = 21.3 or 101.3 kPa are 78.8° and 84.8°, respectively. From these results, we found that the difference of oxygen partial pressure in sintering process mainly influenced on magnetic moment angle ϕ with *c*-axis. Moreover, we indicate that, from the equation mentioned above, permeabilities of these samples mainly depend on their magnetic moment angle because their spontaneous magnetizations are almost the same. The permeability of P_{O2} = 101.3 kPa is larger than that of P_{O2} = 21.3 kPa because the magnetic moments of the sample of P_{O2} = 101.3 kPa are more in the basal planes than that of P_{O2} = 21.3 kPa, which indicates that H_p of P_{O2} = 101.3 kPa is smaller than that of P_{O2} = 21.3 kPa.

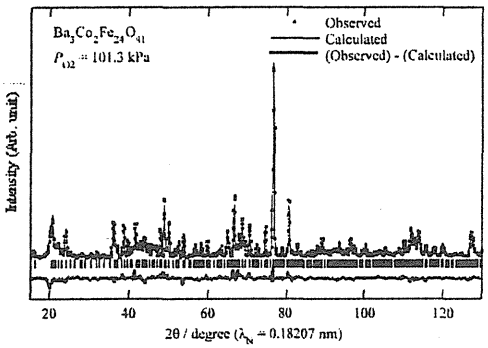


Figure 1. Result of the Rietveld refinements for neutron diffraction patterns of $Ba_3Co_2Fe_{24}O_{41}$ of P_{O2} = 101.3 kPa

Table 1. Site distribution of iron and cobalt determined by the Rietveld refinements of neutron diffraction patterns of $Ba_3Co_2Fe_{24}O_{41}$ of P_{O2} = 101.3 or 21.3 kPa

Label Spin Dir.	Wyckoff Letter Blocks	Fractional Occupation Ratio *g*			
		101.3 kPa		21.3 kPa	
		Fe	Co	Fe	Co
Me1-B↑	2*a*-T	0.67	0.33	0.69	0.31
Me2-A↓	4*f*-T	1	–	1	–
Me3-B↓	4*e*-T	1	–	1	–
Me4-B↑	12*k*-b_1	0.82	0.18	0.84	0.16
Me5-A↓	4*e*-S	0.91	0.09	0.88	0.12
Me6-B↑	4*f*-S	1	–	1	–
Me7-A↓	4*f*-S	1	–	1	–
Me8-B↑	12*k*-b_2	0.96	0.04	0.95	0.05
Me9-B↓	4*f*-R	1	–	1	–
Me10-5↑	2*d*-R	0.82	0.18	0.78	0.22
Spontaneous Magnetization / μ_B		26.7		26.9	
Magnetic Moment Angle ϕ with c-axis		84.8°		78.8°	

References

[1] T. Tachibana et al., J. Magn. Magn. Mater. **262** (2003) 248-257

研究テーマ： 非クラマース系 TmM_2Si_2 （M: 遷移金属）の低温磁性
表題：非クラマース系 TmM_2Si_2 （M: 遷移金属）の低温磁性

1-2-3

Low-Temperature Magnetic Properties in the Non-Kramers System TmM_2Si_2 (M: Transition Metals)

H. Amitsuka, M. Yokoyama, J. Nozaki, T. Sakakibara[1], A. Tobo[2], and K. Ohoyama[2]

Graduate School of Science, Hokkaido University, Sapporo 060-0810, Japan
[1]*Institute for Solid State Physics, The University of Tokyo, Kashiwa 277-8581, Japan*
[2]*Institute for Materials Research, Tohoku University, Sendai 980-8577, Japan*

One of the most interesting features of magnetism in f-electron systems will be the correlation between local f multipoles, which result from strong spin-orbit interaction. It is reported in the previous investigation that $TmCo_2Si_2$ (I4/mmm $ThCr_2Si_2$ type) shows antiferromagnetic (AF) order at T_N ~ 3 K with the Tm magnetic moment of ~ 6.2 μ_B lying in the tetragonal basal plane [1]. However, we found from magnetization (M) and specific heat (C) measurements on a single-crystalline sample that T_N increases with magnetic field applied along the a axis, indicating that the system is not a simple antiferromagnet. Correspondingly, the in-plane dc magnetization turns upward at T_N with decreasing temperature. In addition, for fields higher than ~ 3 T, both M and C show large irreversibility between the zero-field-cooled and the field-cooled measurements. To test the reported magnetic order, we reperformed the neutron diffraction (ND) measurements using HERMES installed in JRR-3M in JAERI (Tokai). The results are basically consistent with the previous report, and thus the ground state of this system is antiferromagnetic (Fig. 1 (a)). We consider that the observed unusual behavior in magnetic fields can be ascribed to the competition between the AF and the antifferro-quadrupole (AFQ) interactions in a pseudo-triplet crystalline-electric-field (CEF) lowest state.

Regarding the isostructural compound $TmAu_2Si_2$, so far no investigation has been made. We have studied C, M and ND for polycrystalline samples, and found that the system shows two successive phase transitions at T_1 = 2.1 K and T_2 = 5.5 K. From the ND results (Fig. 1 (b)), the phase transitions at T_1 is found to be an AF order with double-q structure specified by q_1 = (0, 0, 1) and q_2 = (0.37, 0, 0). On the other hand, there is no indication of magnetic order and structural deformation at T_2. The $C(T)$ data show that the entropy of only Rln2 takes part in the two transitions, and thus the AF-AFQ competition in the Γ_5 type CEF state can be expected in this system.

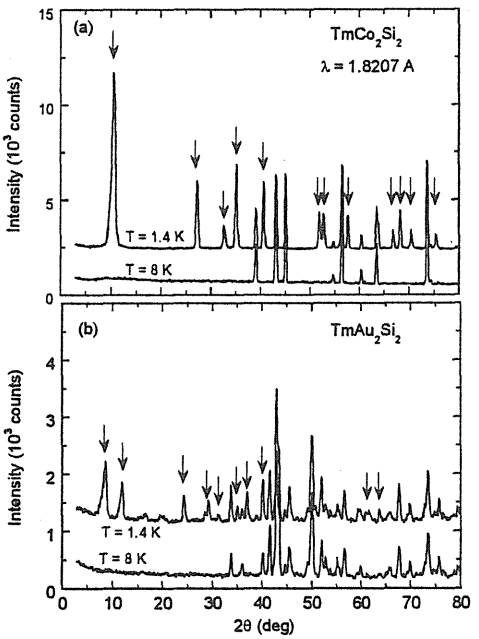


Fig. 1. Neutron powder diffraction patterns of (a) TmCo2Si2 and (b) TmAu2Si2 obtained on HERMES at 1.4 K and 8 K. Arrows indicate the magnetic Bragg reflections.

References

[1] J. Leciejewica and A. Szytula, Solid State Commun. 48 (1983) 55.

使用施設：JRR-3 ， 装置：HERMES (T1-3)， 分野 2. Magnetism

研究テーマ:$Ce(Ni_{0.90}Pd_{0.10})_2Ge_2$の弱い反強磁性の磁気構造
表題:$Ce(Ni_{1-x}Pd_x)_2Ge_2$の反強磁性整列

1-2-4

Antiferromagnetic ordering of $Ce(Ni_{1-x}Pd_x)_2Ge_2$

T. Fukuhara, and H. Kadowaki *

*Department of Liberal Arts and Sciences, Toyama Prefectural University, Kosugi, Toyama 939-0398, Japan; * Department of Physics, Tokyo Metroporitan University, Hachioji-shi, Tokyo 192-0397, Japan*

The pseudo-binary $Ce(Ni_{1-x}Pd_x)_2Ge_2$ indicates an antiferromagnetic instability at x_c that is expected to be ~0.06. For the alloy of x=0.35 showing T_N~3.8K, the incommensurate propagation vecter: q=(1/2 1/2 δ), δ~0.16 has been observed in the ordered state where ordered moments lie in the c-plane [1,2] On the other hand, the paramagnetic heavy-fermion compound $CeNi_2Ge_2$ indicates the dominant low-energy spin-fluctuation with q=(1/2 1/2 0), which governs the Non-Fermi-liquid behaviors shown in the compound. [3] The aim of this work is to investigate the antiferromagnetic ordering near the magnetic instability.

The single crystal of the alloy of x~0.13 ($Ce(Ni_{0.87}Pd_{0.13})_2Ge_2$) was prepared by the pulling-up method by the tetra-arc furnace. The composition of the crystal has been determined by the EDX analysis. Neutron scattering experiments were carried out on the triple axis spectrometer installed at the reactor hall beam line 4G for JRR3M in JAERI (Tokai).

The development of the complex antiferromagnetic ordering was observed by the temperature dependence of the scans along (1/2 1/2 L) line (Fig. 1). With decreasing temperature, a magnetic reflection appears around (1/2 1/2 1) below about T_{N1}~2K, and other magnetic reflections successively occur around (1/2 1/2 1±δ), δ~0.11 below about T_{N2}~1.0K. These magnetic reflections are respectively characterized by the propagation vectors q_1=(1/2 1/2 0) and q_2=(1/2 1/2 δ), δ~0.11. At 0.4K, no visible magnetic reflections were observed around (1/2 1/2 0) and (1/2 1/2 ±δ) within an experimental error, suggesting that the ordered moments almost lie in the c-plane. The temperature dependence of the peak intensity of the magnetic reflection at (1/2 1/2 1) was measured much precisely especially around T_{N2}, and no significant change of the peak intensity was observed.

At present, it is not conclusive whether these complex magnetic reflections arise from a homogeneous phase, because the crystal possesses inhomogeneity resulting from the atomic substitution. Since the magnetic properties are sensitive for control parameters at the critical region, such an inhomogeneity might yield two segregated magnetic phases having a different propagation vector.

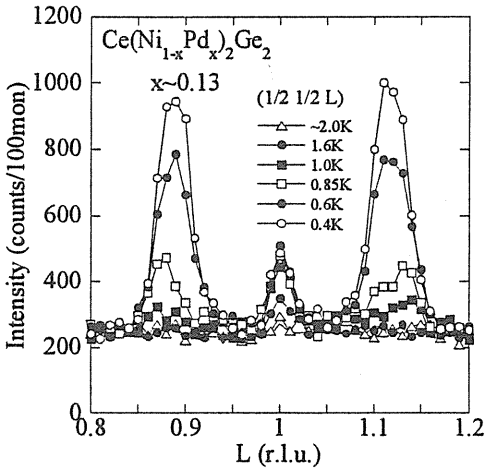


Figure 1: Temperature dependence of scans along (1/2 1/2 L) line. In the figure, the solid curves are guide to the eyes.

References

[1] B, Fåk et al., Solid State Comm. 115 (2000) 407.
[2] T. Fukuhara et al., J. P. S. Jpn. 71 (2002) 1360.
[3] H. Kadowaki et al, submitted to Phys. Rev. Lett .

使用施設:JRR-3 ,装置:GPTAS(4G), 分野 Magnetism

研究テーマ:$PrCu_2Ge_2$の不可逆磁化過程と磁気転移
表題: $PrCu_2Ge_2$の不可逆磁化過程と磁気転移

Irreversible Magnetization Process and Magnetic Transitions of $PrCu_2Ge_2$. 1-2-5

T. Shigeoka, K. Ohishi, M. Nishi[1] and Y. Uwatoko[1]

Faculty of Science, Yamaguchi University, Yamaguchi, 753-8512, Japan
[1]Institute for Solid State Physics, University of Tokyo, Chiba, 277-8581, Japan

The tetragonal ternary $PrCu_2Ge_2$ single crystal compound shows very peculiar magnetic behaviors [1, 2]. It orders antiferromagnetically below T_N=14.4 K. The magnetization curve along the c-axis is irreversible in low temperature; the virgin ascending process shows a four-step metamagnetic process while the magnetization in the descending process decreases to a value smaller than that of the virgin curve through a single-step transition. The magnetic susceptibility along the c-axis in the virgin state is enhanced below about Tt = 4 K while one experienced a saturation state becomes very small in the low temperature, indicating a magnetic transition.

In order to elucidate these magnetic behaviors, neutron diffraction study under non-magnetic and magnetic fields on a $PrCu_2Ge_2$ single crystal compound has been carried out. The experiments have been performed on the triple-axis spectrometer PONTA installed at JRR-3M in JAERI, Tokai. The single crystal was mounted in a cryomagnetic system so that the c-axis was horizontally oriented to make scan in the a*-c* reciprocal plane. Magnetic fields were applied up to 1.8 T along the c-axis and temperature was down to 1.6 K.

At low temperatures and non-magnetic field, antiferromagnetic reflections associated with propagation vector k=(0, 0, 1) were observed except for (0 0 L) (L=odd) reflections, confirming that the magnetic structure is simple AF-type I as reported previously [3]; the structure consists of ferromagnetic c-plane coupled antiferromagnetically with the + - + - sequence and magnetic moments along the c-axis. The intensity of antiferromagnetic reflections decreases rapidly around Tt with increasing temperature. As an example, the temperature dependence of (1 0 0) peak intensity is shown in Fig.1. The large hysteresis with width of 3 K appears around Tt, indicating a first-order transition. The antiferromagnetic peak disappears above T_N. For the intermediate temperature region Tt<T<T_N, a new antiferromagnetic peak which is associated with the propagation vector k'=(0.035, 0, 0) appears. The intensity is very weak; the order is 10^{-3} of the main (1 0 0) intensity. The magnetic structure can't be determined yet because the date on the new antiferromagnetic reflection is insufficient. Further experiment should be need.

Under magnetic fields, no significant change of antiferromagnetic reflections could be detected. No available information on the four-step metamagnetic process and irreversible magnetization process could be obtained. Further search of antiferromagnetic reflections will be planning.

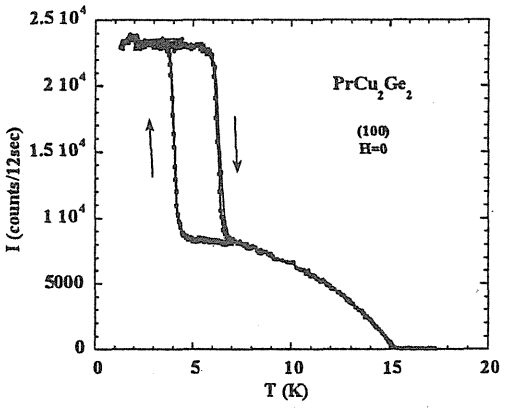


Fig. 1 The temperature dependence of antiferromagnetic (1 0 0) peak intensity in H=0 on a $PrCu_2Ge_2$ single crystal.

References

[1] T. Shigeoka et al., Act. Phys. Pol. B, in press.
[2] T. Shigeoka et al., Physica B, in press.
[3] V. Ivanov et al., J. Alloys and Comp., 234 (1996) L4.

JRR-3 , PONTA (5G), 2. Magnetism

研究テーマ：YbPtGe,YbPdGe 化合物の磁気構造
表題：YbPdGe 化合物の中性子回折

1-2-6

Neutron Diffraction Study on YbPdGe

M. Kurisu[1], G Nakamoto[1], Y. Andoh[2], T. Tsutaoka[3], and S. Kawano[4]
[1]*Japan Advanced Institute of Science and Technology, Ishikawa 923-1292, Japan*
[2]*Department of Environmental Sciences, Tottori University, Tottori 680-8551, Japan*
[3]*Graduate School of Education, Hiroshima University, Hiroshima 739-8524, Japan*
[4]*Research Reactor Institute, Kyoto University, Osaka 590-0494, Japan*

Among the many Ytterbium compounds, only YbNiSn is known to be ferromagnetic. Recently, Nikiforov *et al.* have suggested that YbPdGe compound is one candidate exhibiting ferromagnetism at low temperature [1]. They have also suggested the difficulty in preparing the sample with single phase.

In the present study, we report the results of the bulk magnetic measurements and the powder neutron diffraction experiment on the single phase sample of YbPdGe. We have prepared the YbPdGe ingot with the TiNiSi type orthorhombic symmetry by arc-melting the constituent metal elements in a tetra-arc furnace under purified Ar atmosphere. The neutron diffraction measurement was carried out by using the HQR spectrometer of JRR-3M of JAERI at Tokai in the temperature range from 1.5 K to 20 K.

The magnetic susceptibility follows the Curie-Weiss law above 150 K; $\theta_p = -26.7$ K and $\mu_{eff} = 4.52\ \mu_B$. The two anomalies are observed in the magnetic susceptibility at $T_C = 11.9$ K and $T_1 = 8.3$ K (Fig.1). The magnetization curve below T_1 is metamagnetic at low field, suggesting an antiferromagnetic spin configuration in the low temperature phase. The saturation magnetization reaches 1.4 μ_B at 70 kOe and 1.8 K.

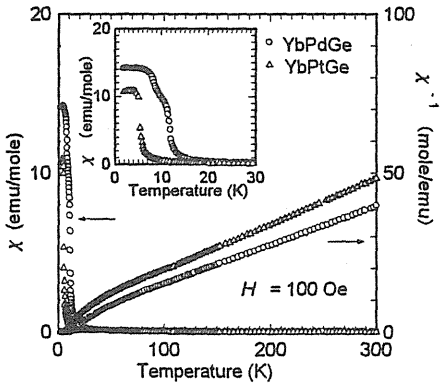


Fig.1. Temperature dependence of magnetic susceptibility of YbPdGe and YbPtGe.

The powder diffraction pattern for YbPdGe at 1.5 K and 20 K are shown in Fig.2. It is noted that the reflections in the magnetically ordered state appear at nuclear position with smaller intensity. An exception is the (002) reflection that indicates appreciable increase in intensity as the temperature lowers. This may suggest the evolution of ferromagnetic alignment of spins. A more detailed diffraction work is needed to determine the magnetic structure of the compound.

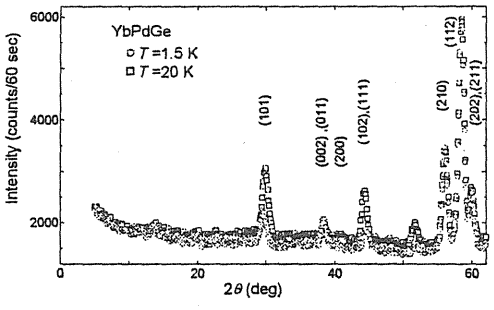


Fig.2. Powder neutron diffraction pattern of YbPdGe at 1.5 K and 20 K.

References

[1] V.N.Nikiforov *et al.*, Phys. Solid State **36** (1994) 259.

使用施設：JRR-3 、装置：HQR (T1-1)，分野：Magnetism

研究テーマ：R_7Rh_3 (R = Tb, Ho, Er)の磁気構造
表題：Tb_7Rh_3単結晶の中性子回折

1-2-7 Neutron Diffraction Studies on Tb_7Rh_3 Single Crystals

T. Tsutaoka, T. Tokunaga, Y. Andoh[1], and S. Kawano[2], G Nakamoto[3], and M. Kurisu[3]

Graduate School of Education, Hiroshima University, Higashi-Hiroshima, 739-8524, Japan
[1]Faculty of Education and Regional Sciences, Tottori University, Tottori, 680-8551, Japan
[2]Research Reactor Institute, Kyoto University, Osaka 590-0494, Japan
[3]Japan Advanced Institute of Science and Technology, Ishikawa, 923-1292, Japan

The rare earth compound Tb_7Rh_3 crystallizes in the hexagonal Th_7Fe_3 type structure. From the magnetic measurements, three magnetically ordered states (antiferromagnetic below T_N = 91 K, ferromagnetic below T_C = 73 K and another antiferromagnetic below T_t = 27 K) was found [1]. In the ferrimagnetic phase, the *c*-axis ferromagnetic component exists. We have reported that the propagation vector is Q = (0 0 1/3) at 1.5 K; the Q_z value does not change up to T_N [2]. In this work, we have performed more detailed studies on single crystalline Tb_7Rh_3. The neutron diffraction measurement was made in the a^* - c^* reciprocal plane using the HQR spectrometer of JRR-3M of JAERI at Tokai in the temperature range from 10 K to 120 K.

Figure 1 shows the magnetic and nuclear reflections in the a^* - c^* reciprocal plane at 10 K. The magnetic reflections appear at

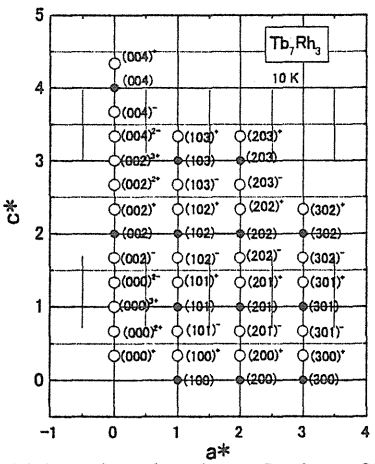


Fig.1 Magnetic and nuclear reflections of Tb_7Rh_3 in the a^* - c^* reciprocal plane.

the positions indexed by the propagation vector Q = (0 0 0.33). Thus a helical magnetic structure is most probable [1].

Figure 2 shows the temperature variation of the peak intensity for $(000)^+$, $(000)^{2+}$, and

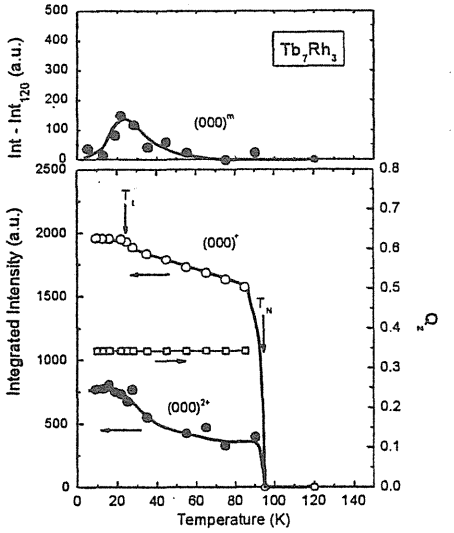


Fig.2 Temperature variation of the peak intensity of $(000)^+$, $(000)^{2+}$, $(300)^m$ reflections, and propagation vector Q_z.

$(300)^m$ reflections and Q_z component. The peak intensity of $(300)^m$ indicates the increase near T_t and an maximum at about 25 K. This behavior is satisfactorily explained by the bulk magnetic measurement results [1]. Therefore, a conical magnetic structure is concluded in ferrimagnetic phase between T_t and T_C.

References

[1] Y. Nakamori et al., Physica B **304** (2001) 1.
[2] T. Tsutaoka et al., J. Phys. Soc. Jpn. **70** (2001) Suppl. A 212.

使用施設：JRR-3　　装置：HQR(T1-1)，分野 Magnetism

研究テーマ：RPdSn (R=Tb, Ho, Er)化合物の磁気構造
表題：HoPdSn の磁気構造

1-2-8 Magnetic structure of HoPdSn

Y. Andoh, G. Nakamoto[1], M. Kurisu[1], T. Tsutaoka[2] and S. Kawano[3],

Faculty of Education and Regional Sciences, Tottori University, Tottori 680-8551, Japan
[1]*Japan Advanced Institute of Science and Technology, Ishikawa 923-1292, Japan*
[2] *Graduate School of Education, Hiroshima University, Higashi-Hiroshima 739-8524, Japan*
[3]*Reearch Reactor Institute, Kyoto University, Osaka 590-0494, Japan*

The ternary equiatomic rare-earth compound HoPdSn crystallizes in the orthorhombic (*Pnma*) TiNiSi-type structure. From the magnetic measurements, two magnetically ordered states have been found below T_1 = 2.7 K and T_N =3.6 K. We report the neutron-diffraction study on HoPdSn to reveal the magnetic structure.

Single crystals were grown with the Czochralski method using a tri-arc furnace. Neutron-diffraction measurements were made by using the HQR spectrometer of JRR-3M of JAERI at Tokai in the temperature range from 1.5 K to 5 K.

Figure 1 shows the positions of the nuclear and magnetic reflections in the a^*-c^* reciprocal plane at 1.8 K. The nuclear reflections appear at the Bragg positions (h 0 l) for $h = 2n$ and $l = 2n$. Two kinds of magnetic reflections, Q_1= (1, 0, 0.38) and Q_2= (0.33, 0, 0.93), appear.

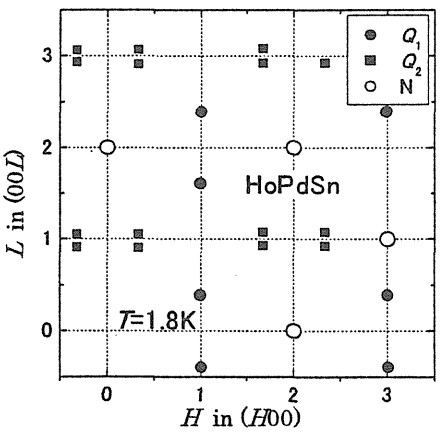


Fig.1 Neutron-diffraction data for HoPdSn single crystal at 1.8 K.

The existence of the magnetic reflections in the a^*-c^* reciprocal plane indicates that the Ho moment is nearly parallel to the b-axis. No higher order satellites have been observed. The peak intensity Q_1 decreases with increasing temperature and vanishes at 3.8 K and the z-component of Q_1 changes abruptly from 0.38 to 0.35 at T_t. On the other hand, the peak intensity Q_2 is decreasing and the reflections disappear at T_N with increasing temperature. There is no anomaly at T_t.

Figure 2 shows the powder diffraction pattern at 1.5 K. Using a description with two kinds of propagation vectors, we have indexed the magnetic reflections. The obtained propagation vectors Q_1 = (1.015, 0, 0.375) and Q_2 = (0.340, 0, 0.914) are in good agreement with

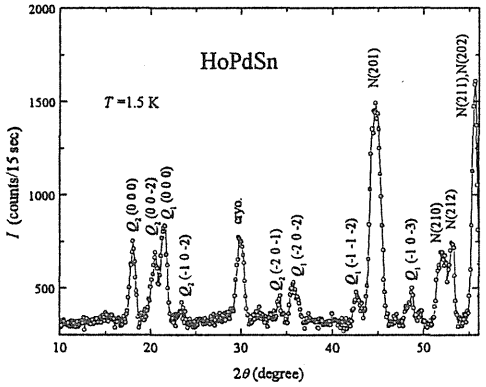


Fig.2 Powder neutron-diffraction data for HoPdSn at 1.5 K.

those determined in the single-crystal measurements.

In conclusion, the magnetic structure of HoPdSn consists of a modulated structure with two propagation vectors. The magnetic moments are aligned nearly parallel to the b-axis. A magnetic phase transition occurs at T_t with a change of the z-component of the Q_1.

使用施設：JRR-3I　装置：HQR(T1-1)，分野 Magnetism

研究テーマ：$Pt_{37}Fe_{33}$の磁気構造
表題：$Pt_{67}Fe_{33}$の磁気構造

1-2-9

The magnetic structure of $Pt_{67}Fe_{33}$

Y.Higashiyama and Y.Tsunoda
School of science and engineering, Waseda University, Okubo 3-4-1, Shinjuku-ku, Tokyo 169-8555, Japan

$Pt_{1-x}Fe_x$ alloys with Fe concentration of 30 at.% shows ferromagnetic-antiferromagnetic transition below Curie temperature(Tc~200K). In neutron scattering measurements, 1 0 0 & 1 1 0 magnetic peaks appear below Tc and increase the intensities with decreasing temperature. However below 120K, new peak appears at 1/2 0 0 at the sacrifice of the 1 0 0 & 1 1 0 magnetic peak intensities. Vinokurova *et. al* first observed this fact and explained using the spin flip transition as in the case of Pt_3Fe alloy. We grew a $Pt_{67}Fe_{33}$ alloy single crystal as one of $Pt_{1-x}Fe_x$ alloy series and studied magnetism using susceptibility and neutron scattering. Neutron scattering data for the sample are given in Fig.1. The 1 0 0 & 1 1 0 magnetic peak intensity starts decreasing at around 110K with decreasing temperature, qualitatively consistent with previous authors. However, careful data analysis shows that the line width of 1/2 0 0 Bragg peak dramatically increases when the intensity is decreasing. Furthermore at the tail of the Bragg peak, background counts increase with decreasing temperature. Results are given in Fig.2. In order to explain the experimental data, we propose a two phase model. At Tc, a part of the specimen shows ferromagnetic order. However, the rest of the specimen starts antiferromagnetic order at around 120K. Then, the ferromagnetic regions are exposed under the random field, resulting in a subdivision of the ferromagnetic regions. Thus, our model is an inhomogeneous model and well explains the susceptibility data which shows behavior of re-entrant spin-glass system.

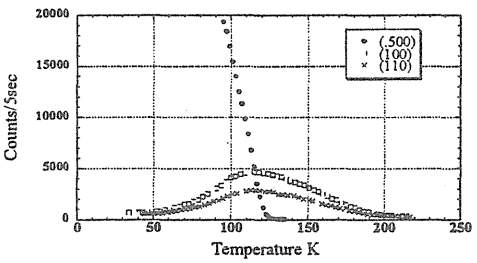


Fig.1 Temperature variations of magnetic peak intensities at 1/2 0 0, 1 0 0 and 1 1 0

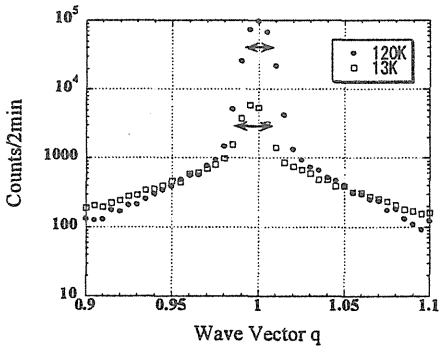


Fig.2 Line profile of 1 0 0 magnetic peak at 120K & 13K

使用施設：JRR-3，使用装置：HQR（T1-1），分野：magnetism

研究テーマ：PtFe 合金のマグノン
表題：PtFe 合金のマグノン
1-2-10

Magnons in Ordered PtFe Alloy

Hiroyuki Kobayashi and Yorihiko Tsunoda
School of Science and Engineering, Waseda University, 3-4-1, Ohkubo, Shinnjuku, Tokyo 169-8555

An $L1_0$(CuAu)-type PtFe alloy shows ferromagnetism with rather high Curie temperature (Tc~750K). Both of Fe and Pt atoms are considered to carry magnetic moments of 3.01 μ_B and 0.38 μ_B, respectively. Since the PtFe ordered alloy has a large magnetic anisotropy energy (MAE) (7×10^7 erg/cm^3) and saturation magnetization (1130 emu/cm^3), the alloy is considered to be an excellent candidate of the high density perpendicular magnetic recording media. However, microscopic magnetic data are still lacking. Thus, we tried to study the magnon dispersion relation curve in PtFe alloy and determine the exchange constants between spins.

Neutron inelastic scattering measurements were performed at 5G triple axis spectrometer installed in a reactor room of JRR-3M, Tokai. All of data were taken at room temperature.

Typical line profiles obtained by the constant-E mode and by scanning along the scattering vector (longitudinal scan) around the 1 0 0 RLP are given in Fig. 1. As known from the figure, the magnon dispersion curve originates at the 0 0 1 RLP, not at the 1 0 0. Similar measurements were also performed to the direction perpendicular to the scattering vector (transverse scan). The dispersion relations determined from the present data are given in Fig. 2. The slope of the dispersion curve for the [1 0 0] direction is steeper than that for the [0 0 1] direction. The quantitative data analysis using exchange couplings is now on progress.

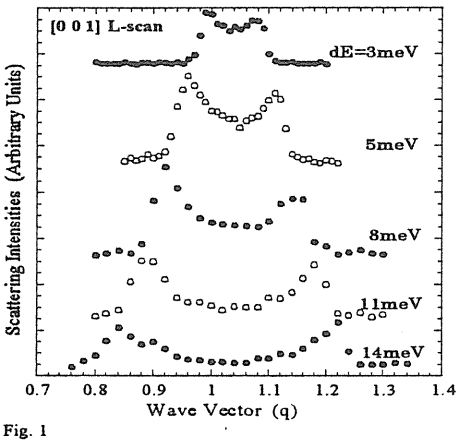


Fig. 1

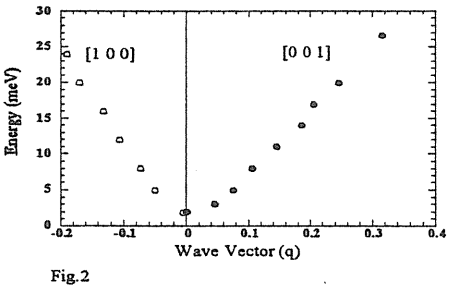


Fig.2

使用施設：JRR-3　　装置：PONTA（5G）、分野：2．Magnetism

研究テーマ：PtMn の磁気構造
表題：PtMn の磁気構造

1-2-11

Magnetic structure of MnPt Alloy

H.Hama, T.Ikeda and Y.Tsunoda
School of science and engineering, Waseda University, Okubo 3-4-1, Shinjuku-ku, Tokyo 169-8555, Japan

PtMn alloy slows an anti-ferromagnetism with a high Neel temperature and is an important material in the application to the GMR device.

This alloy has a tetragonal structure of the CuAu-I type in which Pt and Mn layers pile up alternately. From magnetic susceptibility measurement, the Neel temperature is reported as 913K and a magnetic phase transition takes place at 753K below the Neel temperature. However, magnetic structure in both low and high temperature phase reported by previous authors are still contradictory.

We succeeded to grow a single-crystal specimen of PtMn alloys with a single magnetic domain. To investigate the magnetic structure of this alloy, neutron scattering measurement was performed by using this specimen at the T1-1 (HQR) triple axis spectrometer installed at a thermal guide of JRR-3M, JAERI, Tokai.

In the PtMn alloy, magnetic Bragg peaks are observed at the 100 and 101 reciprocal lattice points. Figure 1 shows the temperature dependences of these magnetic Bragg peaks. From figure 1, the anomaly of the magnetic Bragg peak intensities was observed at 753K, indicating that the magnetic transition takes place at this temperature. From the comparison with intensities of a magnetic Bragg peaks at 100 and 101 RLPs, the magnetic structure in the each phase was determined, as illustrated in Figure 2. In the low temperature phase (T<753K), the magnetic moments of Mn atoms are parallel to the c axis of the crystal. At the magnetic phase transition at Tt=753K,it is considered that the spin flip takes place. In the high temperature phase (753K<T<913K), the magnetic moments of Mn lie on the (001) plane pointing to the [010] direction

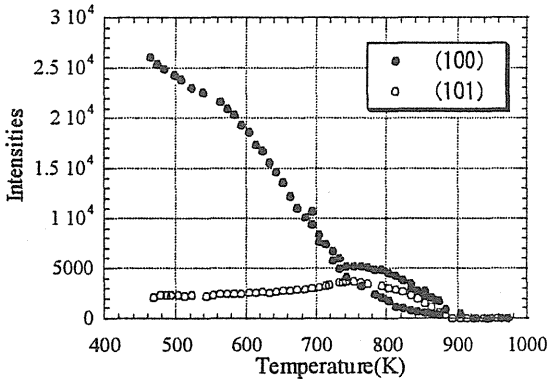
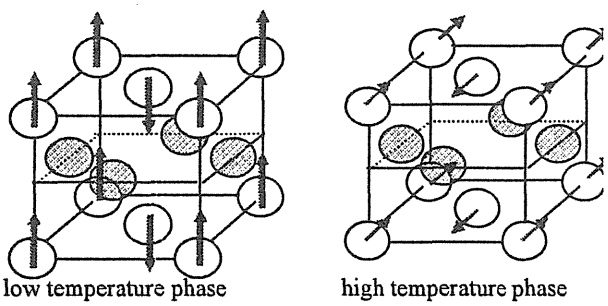


Figure 1, Temperature dependence of (100) and (101) magnetic bragg intensities



low temperature phase (T<753K)　　high temperature phase (753K<T<913K)

Figure 2, Magnetic Structure of PtMn alloy

使用施設：JRR-3　装置：T1-1(HQR)　分野：Magnetism

研究テーマ： 白金を多量に含むPt–Cr合金の原子配列と磁気相関
表題： Pt高濃度Pt–Mn合金の磁気構造

1-2-12 Magnetic Structure in Pt–rich Pt–Mn Alloys

M. Takahashi[1], K. Ohshima[1], T. Shishido[2] and Y. Noda[3]
[1] *Institute of Materials Science, University of Tsukuba, Tsukuba 305–8573*
[2] *Institute for Materials Research, Tohoku University, Sendai 980–8577*
[3] *Institute of Multidisciplinary Research for Advanced Materials, Tohoku University, Sendai 980–8577*

The atomic phase diagram of Pt–rich Pt–Mn alloys shows quite unique ordered states of two ordered phases at around 12-15 at.% Mn: a Cu_3Au type ordered state below the order–disorder transition temperature and an ABC_6 type ordered state below the lower transition temperature [1, 2]. The magnetic structures in Pt–rich Pt–Mn alloys with the ABC_6 type ordered structure were studied on samples of 12.5, 14.4 and 15.9 at.% Mn by using a four–circle diffractometer FONDER, installed at the T2–2 beam port of the thermal guide at the JRR3M in JAERI (Tokai). In the magnetic scattering, two characteristic kinds of magnetic structure were found in samples, both of which are characterized by a propagation vector $1/2, 0, 0$, however, in the plane vertical to the vector, one has incommensurate modulation parallel to the diagonal directions of the cubic axis, and the other has commensurate modulation parallel to the cubic axis.

The line profiles of magnetic peaks around $0, 1, 1/2$ in Pt–12.5 at.% Mn are plotted in Figs. 1(a) and (b). Two incommensurate peaks are observed at $\pm 0.06, 1 \pm 0.06, 1/2$ in Fig. 1(a), and two commensurate peaks are observed at $-1/4, 1, 1/2$ and $0, 5/4, 1/2$ with a quite anisotropic intensity distribution in Fig. 1(b). In Pt–14.4 at.% Mn, the incommensurate peaks completely disappear and the commensurate peaks grow up to be sharp superlattice reflections, which become only very weak diffuse scattering in Pt–15.9 at.% Mn. It is regarded that the incommensurate peaks are due to the interaction between the distant localized spins through the SDW in the conduction–electron gas, while the commensurate peaks are due to that between the near–neighbor localized Mn spins, and is more dominant in the ABC_6 type ordered structure. With the development of the Cu_3Au type order and higher Mn concentration, the dominant interaction changes to a ferromagnetic one on the structure. The variation in the magnetic structure is closely related to the characteristic atomic order in the alloys, showing a strong coupling between the magnetic and atomic structure.

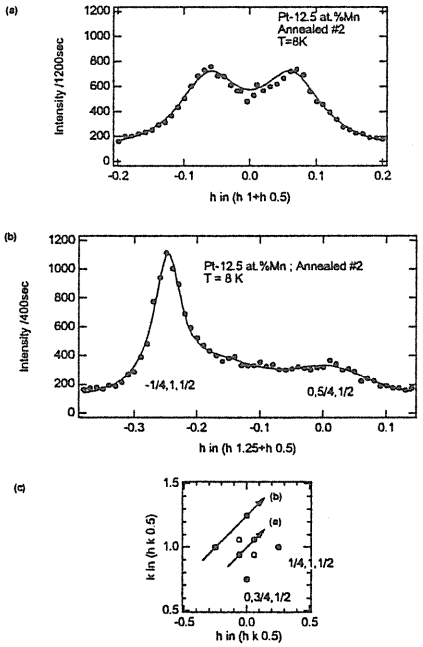


Fig. 1. Diffraction line profile parallel to [110] through (a)$0, 1, 1/2$ and (b)$-1/4, 1, 1/2$ and $0, 5/4, 1/2$ at 8 K measured in Pt– 12.5 at.% Mn at FONDER. (c)The diagram for scans (a) and (b).

References

[1] M. Takahashi *et al.*: J. Phys. Soc. Jpn. **71**, 681 (2002).
[2] T. Sembiring *et al.*: J. Phys. Soc. Jpn. **71**, 2459 (2002).

使用施設：JRR-3 ，装置： FONDER(T2-2) ，分野： 2.Magnetism

研究テーマ： 規則合金 $Pt_{1-c}Mn_c$ の動的磁気構造
表題： 規則合金 Pt–14.4 at.% Mn における磁気ゆらぎ

1-2-13 Magnetic Fluctuation in Ordered Pt–14.4 at.% Mn

M. Takahashi[1], K. Ohshima[1], T. Shishido[2] and K. Hirota[3]
[1] *Institute of Materials Science, University of Tsukuba, Tsukuba 305–8573*
[2] *Institute for Materials Research, Tohoku University, Sendai 980–8577*
[3] *Institute for Solid State Physics, The University of Tokyo, 106-1 Shirakata, Tokai, 319-1106*

Pt–rich Pt–Mn alloys show a double-step phase transition of the disordered state → Cu_3Au type → ABC_6 type in a narrow concentration region of 12-15 at.% Mn [1]. The magnetic structure around the concentration changes drastically with the atomic arrangement and Mn concentration, reflecting the unique atomic orders. In the ABC_6 type–ordered Pt–14.4 at.% Mn, magnetic superlattice reflections appear at $1/2, \pm 1/4, 0$ and $1/2, 0, \pm 1/4$ below T_N =20 K. They are regarded to be formed through an antiferromagnetic interactions between the near–neighbor localized spins on the ABC_6 type atomic order. However, the magnetic susceptibility show the same characteristics of the spin–glass like behavior as have been observed in disordered alloys, indicating the existence of a common fluctuation in both ordered and disordered alloys. In order to understand the relation between the magnetic structure and the spin–glass like behavior, inelastic neutron scattering measurements were performed on the ordered Pt–14.4 at.% Mn with using TOPAN(6G) in JRR3M at JAERI(Tokai).

In Fig. 1, the inelastic scattering pattern on the (hk0)–scattering plane around $1/2, 1/2, 0$ at 40 K is shown. Anisotropic diffuse rods are observed along [100] and [010] with their maxima being at around $1/2, 1/2 \pm 1/4, 0$ and $1/2 \pm 1/4, 1/2, 0$. The temperature dependence of the line profile along [010] at 1.5 meV is shown in Fig. 2. Their intensities increase with increasing temperature and show a maximum at 40 K ($2T_N$). These results indicate that the magnetic structure is not completely stable. Considering that the calculated Fermi–surface of the Pt_7Mn with ABC_6 type structure shows a set of parallel Fermi–surfaces as in host Pt metal, it seems that the SDW fluctuation still survives dynamically and causes spin–glass like behavior in the ABC_6 type ordered alloy.

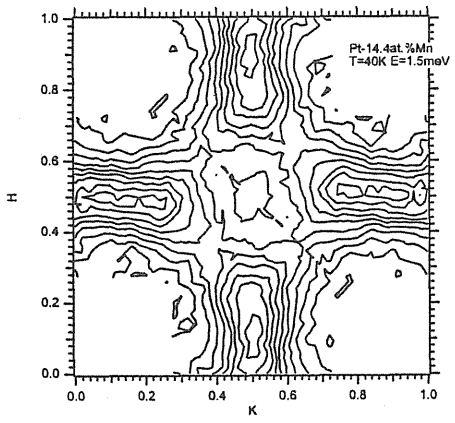


Fig. 1. Inelastic scattering pattern on the (hk0) plane at 40 K.

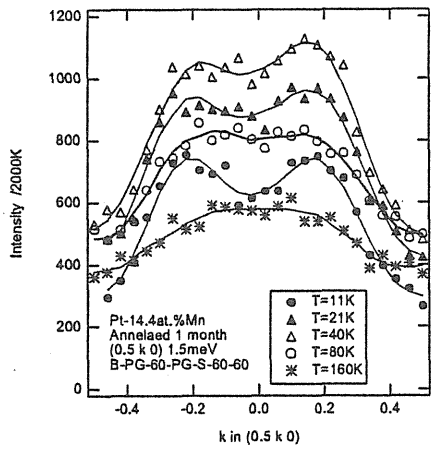


Fig. 2. Temperature dependence of the lin profile along [010] at 1.5 meV.

References

[1] M. Takahashi *et al.*: J. Phys. Soc. Jpn. **71**, 681 (2002).

使用施設：JRR-3 ， 装置： TOPAN(6G) ， 分野： 2.Magnetism

研究テーマ:周期的単原子非磁性層挿入による Cr 薄膜のスピン構造制御
表題:エピタキシャル Cr/Sn 人工格子における Cr のスピン構造の結晶成長方位依存性

Growth-Orientation Dependence of Spin Structures of Epitaxial Cr/Sn Multilayers with Monatomic Sn Layers

1-2-14

K. Mibu, N. Jiko, J. Suzuki, and M. Takeda

[1]Research Center for Low Temperature and Materials Sciences, Kyoto University, Uji, Kyoto 611-0011, Japan; [2]Institute for Chemical Research, Kyoto University, Uji, Kyoto 611-0011, Japan; [3]Advanced Science Research Center, JAERI, Tokai, Ibaraki 319-1195, Japan

Magnetic structures of epitaxial Cr/Sn multilayers, where monatomic Sn layers are periodically embedded in a Cr(001) or Cr(011) film, were studied by neutron diffraction measurements. The scans were carried out around the Cr(001) and Cr(010) reciprocal points using a triple-axis spectrometer, TOPAN, at JRR-3M. Nuclear reflections are forbidden around these reciprocal points, so that only magnetic peaks due to antiferromagnetic structures are expected to appear.

For Cr(001)/Sn multilayers, it was found that spin-density-wave (SDW) antiferromagnetic structures with the modulation along the perpendicular direction to the film plane are stabilized at low temperatures when the Cr layer thickness is larger than 8 nm. The wavelength of the SDW discretely changes as a function of the superlattice period. From ^{119}Sn Mössbauer spectroscopic studies, it was concluded that the magnetic moment of Cr at the Cr/Sn interfaces is somewhat enhanced. The enhanced magnetic moments of Cr are thought to pin the antinode of the SDW modulation at the interface, resulting in the SDW with the modulation harmonic to the superlattice period [1-4].

Neutron diffraction measurements ware also performed for a [Cr(8.0 nm)/Sn(0.2 nm)] multilayer with the (011) growth orientation. The contour map of the neutron diffraction intensities was measured around the Cr(010) reciprocal point in the *HK* plane, where the *H* and *K* axes are defined as being parallel to the Cr[011] and Cr[011] directions, respectively (Fig. 1(a)). The

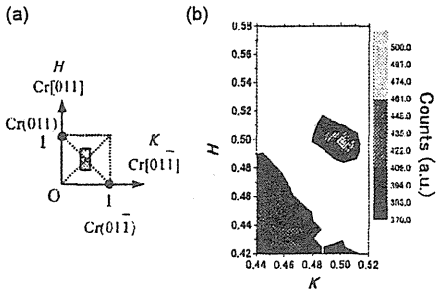


Figure 1: (a) Configuration of neutron diffraction measurements for a Cr(011)/Sn multilayer. The mesh-scans were performed in the shaded area. (b) Contour map of neutron diffraction intensity around Cr(010) at 7 K for a Cr(011)/Sn multilayer with t_{Cr}= 8.0 nm.

obtained contour map at 7 K is shown in Fig. 1(b). A single magnetic peak was observed at the (0.5, 0.5) point, which correspond to the Cr(010) reciprocal point, and no satellite peak appeared around it. This result suggests that the Cr in the Cr(011)/Sn multilayer, when t_{Cr} is 8.0 nm, does not form an incommensurate SDW structure but a commensurate antiferromagnetic structure. This behaviour is in contrast with that of the Cr(001)/Sn multilayer with the same Cr layer thickness, where an incommensurate SDW structure is stabilized at low temperatures.

References

[1] M. Takeda *et al.*, J. Phys. Soc. Jpn. **69** (2000) 1590.
[2] M. Takeda *et al.*, Appl. Phys. A **74** [Suppl.] (2002) S1554.
[3] K. Mibu *et al.*, J. Phys. D: Appl. Phys. **35** (2002) 2359.
[4] K. Mibu *et al.*, Phys. Rev. Lett. **89** (2002) 287202.

使用施設:JRR-3　装置:TOPAN(6G), 分野 Magnetism

研究テーマ:日米協力、反強磁性 Cr の磁気励起
表題:Cr のスピン密度波状態における新しい磁気励起

1-2-15 New Magnetic Excitations in the Spin-Density Wave of Cr

H. Hiraka, Y. Endoh, M. Fujita *, K. Yamada *, and G. Shirane **

Institute for Materials Research, Tohoku University, Katahira, Aoba-ku, Sendai 980-8577
** Institute for Chemical Research, Kyoto University, Gokasyo, Uji 611-0011*
*** Physics Department, Brookhaven National Laboratory, Upton, New York 11973*

The spin-density wave (SDW) in Cr is one of the most fascinating subjects in condensed matter physics. Cr sets in the antiferromagnetically ordered state below the Neel temperature (311 K) with the ordering wave-vector $Q_{\pm} = (0,0,1\pm\delta)$ where $\delta \sim 0.05$. The transversely polarized SDW (T-SDW) suddenly changes into the longitudinal one (L-SDW) below 121 K. As for the magnetic cross-section, an interesting behavior (the so-called Fincher-Burke mode) was reported near the antiferromagnetic zone-center (0,0,1) [1, 2], apart from the major incommensurate excitations rising steeply from the $Q_{\pm}$ positions as shown in Fig. 1 (a). Although many interesting results were presented through neutron scattering, no simple and conclusive explanation was obtained for the novel dynamical susceptibility.

Recently, we reinvestigated the low-energy excitations around (0,0,1) with unpolarized neutron using a single-$Q_{\pm}$ crystal. Inelastic neutron scattering experiments were conducted on the triple-axis spectrometer TOPAN. A single crystal with a volume of about 4 cc and η~35' was set up in the $(h,0,l)$ scattering plane. The population of a single-$Q_{\pm}$ domain was estimated to be more than 99%. The final energy of TOPAN was fixed at 14.7 meV, and two types of horizontal-collimation sequence were utilized giving the energy resolution of 1.4 and 0.8 meV.

Figure 1 (b) summarizes current data obtained in the T-SDW phase. We newly found a perpendicular mode which extends more than 2δ with a weak dispersion. In contrast to the parallel branch, or the Fincher-Burke mode, it shows a gap of about 4.5 meV at q =0 and the intensity drastically decreases with q. The characteristic response completely disappears in the L-SDW state, suggesting an intimate connection with the ordering of the spin-density wave. Further investigation

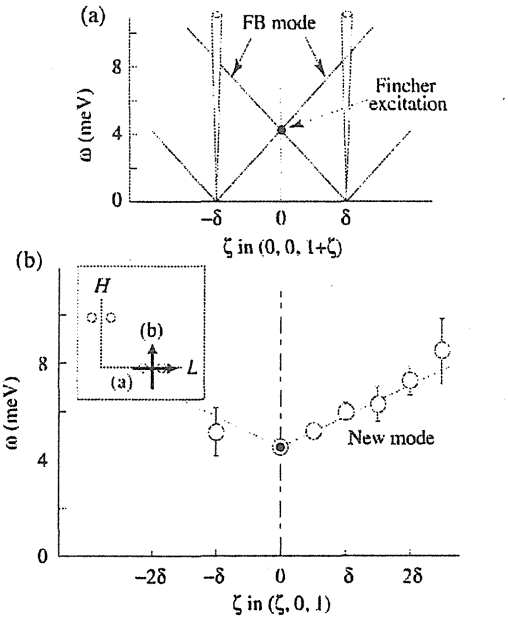


Fig. 1. Energy dependence of magnetic excitations in the single-$Q_{\pm}$ T-SDW phase of Cr. (a) High-velocity spin excitations (cones) and the Fincher-Burke mode (lines) parallel to $Q_{\pm}$. (b) Newly found data transverse to $Q_{\pm}$ with a gap of ~ 4.5 meV.

on the thermal evolution is now in progress.

References

[1] C. R. Fincher *et al.*, Phys. Rev. Lett. **43**, 1441 (1979).

[2] S. K. Burke *et al.*, Phys. Rev. Lett. **51**, 494 (1983).

使用施設:JRR-3 in JAERI (Tokai), 装置:TOPAN(6G), 分野 Magnetism

研究テーマ：Fe 置換 Z 型フェライト($Ba_3Co_{2-x}Fe_{24+x}O_{41}$)配向試料の中性子回折による磁気構造解析

表題：磁場配向させた $Ba_3Co_2Fe_{24}O_{41}$ の中性子回折による構造解析

Structural Analysis of Magnetically Oriented Samples of $Ba_3Co_2Fe_{24}O_{41}$ by Neutron Diffraction

1-2-16

Y. Takada, T. Nakagawa, T. Tachibana, T. Ino, T. A. Yamamoto and *S. Kawano

*Depertment of Nuclear Engineering, Osaka University, 2-1 Yamadaoka, Suita, Osaka 565-0871, Japan; *Kyoto University Research Reactor Institute, Noda, Kumatori-cho, Sennan-gun, Osaka 590-0494, Japan*

Co_2Z-type hexaferrite $Ba_3Co_2Fe_{24}O_{41}$ is a candidate material for noise absorbent devices in the range of GHz frequency because of its high permeability even at the high-frequency region. Permeability of Co_2Z-type hexaferrite $Ba_3Co_2Fe_{24}O_{41}$ depends on the magnitude of anisotropic field in the direction parallel to *c*-plane. And this magnitude is significantly related to the angle of magnetic moment with *c*-axis. To confirm this, we prepared the magnetically oriented sample of Co_2Z-type ferrite.

The powder sample of Co_2Z-type was prepared by conventional ceramics method as already reported[1]. The sample powder was mixed with deionized water, a bit of PVA and dispersant. The slurry was cast in a cylindrical stainless die. Then the die was mechanically rotated in a minute around its axis perpendicular to a static magnetic field of 0.8 MA/m. This magnetically oriented slurry was dehydrated, under the static magnetic field of 0.8 MA/m, by pressing under the pressure of 25.48 MPa in the direction of its axis. The pellet was sintered again at 1573 K for 16 hours under P_{O2} = 101.3 kPa. The resultant pellet was expected to have the *c*-axis preferentially oriented to the pellet axis, when the easy axis of the present samples is in the basal plane of the hexagonal structure.

Neutron diffraction pattern of the magnetically oriented sample was obtained by use of the Kinken single-crystal diffractometer, KSD (T1-2), of Institue for Materials Research (Tohoku University) installed at the JRR-3M in JAERI(Tokai). Neutrons with a wavelength 1.527 Å were obtained by the 311 reflection of the Ge monochrometer. The diffraction angle 2θ was swept in a range 5 - 75° at intervals of 0.1°.

Figure 1 shows the neutron diffraction pattern of the sample in the direction perpendicular to the rotating magnetic field. This pattern shows that peaks due to (00*l*) planes are reinforced, and that this sample is magnetically and structurally oriented. This indicates that permeability of the Co_2Z-type ferrite in the direction parallel to the rotating field would be enhanced by magnetic orientation.

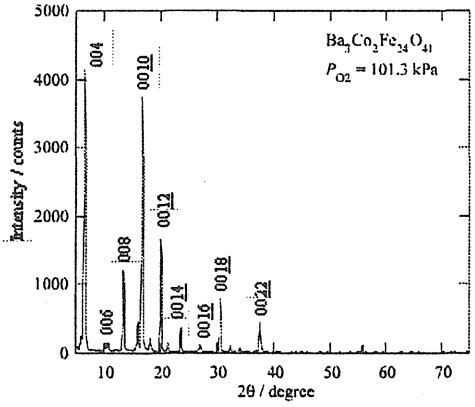


Figure 1. Neutron diffraction patterns of magnetically oriented sample of $Ba_3Co_2Fe_{24}O_{41}$ of P_{O2} = 101.3 kPa in the direction drawn in this figure.

Reference

[1] T. Tachibana et al., J. Magn. Magn. Mater. **262**(2003) 248-257

使用施設：JRR-3　　装置：KSD(T1-2)，分野 Magnetism

研究テーマ：鉄を含むカルコゲナイド $BaLn_2FeX_5$ (Ln = La-Nd, X = S, Se) の磁性
表題：$BaNd_2FeS_5$ の結晶構造と磁気構造

1-2-17 Crystal and Magnetic Structures of $BaNd_2FeS_5$

M. Wakeshima[1], Y. Hinatsu[1], A. Tobo[2], K. Ohoyama[2], and Y. Yamaguchi[2]
[1] *Division of Chemistry, Graduate School of Science, Hokkaido University, Sapporo 060-0810*
[2] *Institute for Materials Research, Tohoku University, Sendai 980-8577*

Quaternary iron sulfide $BaNd_2FeS_5$ have a tetragonal structure with space group $I4/mcm$. Its magnetic susceptibility and specific heat measurements showed that the Fe^{2+} ions were in the antiferromagnetic states below 44 K. In this compound, the Nd^{3+} ions also show an antiferromagnetic transition at 6 K. Through the previous powder neutron diffraction measurements, we have determined the aintiferromagnetic structure of Fe^{2+} which has dimensions $\sqrt{2}a \times \sqrt{2}a \times c$ in terms of the tetragonal chemical cell as shown in Fig. 1. In addition to these magnetic orderings, another anomaly is found at around 160 K in the temperature dependence of the electrical conductivities and specific heats (see Fig. 2).

In order to elucidate this anomaly, the powder neutron diffraction measurements were preformed above 100 K using the high efficiency and resolution powder diffractometer, HERMES, of Institute for Materials Research, Tohoku University, installed at the JRR-3M (Tokai) with a neutron incident wave length (λ = 1.8207 Å). The crystal structures were determined by the Rietveld technique.

The patterns calculated using the crystal structure with the space group of $I4/mcm$ between 100 and 250 K are in good agreement with the observed ones and which indicates that no structural transition occurs at around 160 K. Figure 3 shows the temperature dependence of the refined lattice parameters, a and c. The a and c values change discontinuosly at 160 K, and the variation of the c values is larger than that of the a value. This result suggests that the FeS_4 tetrahedra are distorted below 160 K. Through the ^{57}Fe Mössbauer spectrum measurements of $BaNd_2FeS_5$, we observed the increase in the quadrupole splittings due to the distortion of the FeS_4 tetrahedra below 160 K, and which is consistent with the result of the neutron diffraction measurements.

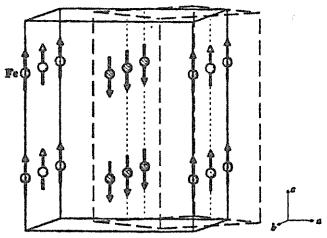


Fig. 1. Magnetic structure of Fe^{3+} ion in $BaNd_2FeS_5$.

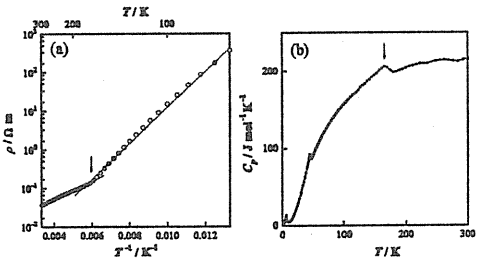


Fig. 2. Temperature dependence of electrical conductivities(a) and specific heats(b) of $BaNd_2FeS_5$.

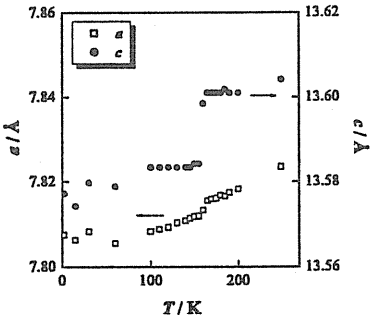


Fig. 3. Temperature dependence of lattice parameters, a and c of $BaNd_2FeS_5$.

使用施設：JRR-3　装置：T1-3 (HERMES)，分野：6. Magnetism

研究テーマ：$Tb_{1-x}Ca_xMnO_3$の磁気構造の電子濃度依存性
表題：電子濃度に依存した$Tb_{1-x}Ca_xMnO_3$の磁気構造
1-2-18

Doping-Dependent Magnetic Structure of $Tb_{1-x}Ca_xMnO_3$

A. Machida[1], Y. Moritomo[2], and K. Ohoyama[3]
[1]*Department of Crystalline Materials Science, Nagoya University, Nagoya 464-8603, Japan*
[2]*Department of Applied Physics, Nagoya University, Nagoya 464-8601, Japan*
[3]*Institute for Materials Research, Tohoku University, Sendai 980-8577, Japan*

In perovskite-type doped manganites, modulated structures are often observed along the crystallographic b-axis in the MnO_2-plane at low temperatures. The periodicity of the modulation increase as the electron density n (=1-x) increase. We have investigated the magnetic structure of $Tb_{1-x}Ca_xMnO_3$ ($0.5 < x < 0.8$) by means of neutron powder diffraction experiments at 10 K. We observed a series of magnetic Bragg reflections which can be indexed as (1/2 m/n 1) where m, n= integer. We found that the patterns of the magnetic Bragg reflections change discontinuously with increase of hole concentration x. We interpreted these magnetic Bragg reflections in terms of the lattice modulations due to the charge-/orbital-ordering.

The polycrystalline samples were synthesized by solid state reaction in air. A stoichiometric mixture of commercial Tb_4O_7, $CaCO_3$, and Mn_3O_4 powders was well ground and calcined twice at 1250-1300C for 24h.Then, the resulting powder was pressed into a disk and sintered at 1300-1350C for 30h. Densities of the obtained ceramics samples are 80-90% of the ideal value. We have performed neutron powder diffraction measurements, using the Kinken powder diffractometer for high efficiency and high resolution measurements (HERMES), of Institute for Materials Research, Tohoku University, installed at the JRR-3M reactor at the Japan Atomic Energy Research Institute, Tokai, Japan.

Figure shows variation of the neutron powder patterns in the low-2Θ region for $Tb_{1-x}Ca_xMnO_3$ against x. At x=0.5, the CE-type magnetic Bragg reflections due to the charge-/orbital-ordering are observed at 17 degree and 20 degree. With this spin-ordering, magnetic Bragg reflections are expected at (h/2 m/2 l), where h and l are odd integers and m is an integer, reflecting the two-fold periodicity along the [010] direction Actually, the observed reflections can be indexed as (1/2 m/2 1) with m= 0 and 1. The magnetic reflections are pinned at the same scattering angle in the concentration range $0.5 < x < 0.6$, indicating that the CE-type structure maintains in this x-range. At x=0.65, extra magnetic Bragg reflections appear at 18 degree and 21 degree.. These reflections can be indexed as (1/2 1/3 1) and (1/2 2/3 1), suggesting that the magnetic structure changes into a three-fold-type. The magnetic reflections are pinned again in the concentration range $0.65 < x < 0.67$.At x=0.72, the magnetic structure changes into a four-fold-type.

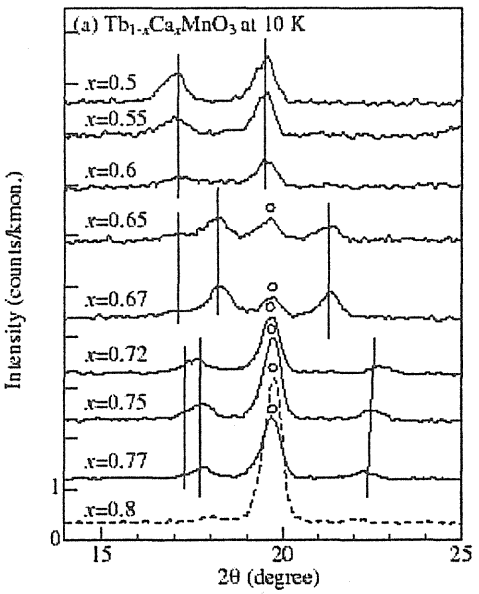


Fig.1: Neutron diffraction patterns of $Tb_{1-x}Ca_xMnO_3$ ($0.5 < x < 0.8$) at 10 K. Open circles indicate the magnetic Bragg reflections due to the C-type spin-ordering.

使用施設：JRR-3　装置：HERMES、分野：1 Structure&Excitation、2 Magnetism

研究テーマ：マンガン酸化物の電荷整列相に及ぼすBサイト置換効果
表題：$Nd_{1/2}Ca_{1/2}(Mn_{1-y}M_y)O_3$の磁気相図

1-2-19

Magnetic Phase Diagrams of $Nd_{1/2}Ca_{1/2}(Mn_{1-y}M_y)O_3$ (M = Ru, Cr and Sc).

Sh. Xu[1], A. Machida[1], Y. Moritomo[2] and K. Ohoyama[3]

[1]*Department of Crystalline Materials Science, Nagoya University, Nagoya 464-8603, Japan*

[2]*Department of Applied Physics, Nagoya University, Nagoya 464-8601, Japan*

[3]*Institute for Materials Research, Tohoku University, Sendai 980-8577, Japan*

We have derived a magnetic phase diagrams of $Nd_{1/2}Ca_{1/2}(Mn_{1-y}M_y)O_3$ (M = Ru, Cr and Sc).based on the neutron powder diffraction measurements. For all the compounds, we observed a two-phase state, i.e., the ferromagnetic long-c and the antiferromagnetic short-c phases at low temperatures in a limited y-range. In the heavily-doped region ($y < 0.05$), however, the system becomes a structurally single-phase. We found that the Cr-doping induces the antiferromagnetic-to-ferromagnetic transition at y = 0.01 - 0.02, while the Sc-doing doesn't induce the transition up to y = 0.10.

Ceramic compounds, $Nd_{1/2}Ca_{1/2}(Mn_{1-y}M_y)O_3$ (M = Ru, Cr and Sc)., were synthesized by a solid-state reaction in air. A stoichiometric mixture of commercial Nd_2O_3, $CaCO_2$, Mn_3O_4, Cr_2O_3, RuO_2 and Sc_2O_3 powders were well ground and calcined twice at 1300 C for 24h. Then, the resulting powders were pressed into a disk and were sintered at 1350 C for 24h. Neutron powder diffraction measurements were performed using the Kinken powder diffractometer for high efficiency and high resolution measurements (HERMES) of Institute for Materials Research, Tohoku University, installed at the JRR-3M reactor at the Japan Atomic Energy Research Institute, Tokai, Japan. The sample pellet was crushed into fine powder and sealed in a vanadium capsule with helium gas, and mounted at the cold head of a closed-cycle He-gas refrigerator. The diffraction data were accumulated for 1 h. We have analyzed thus obtained powder patterns with the RIETAN2000 program.

We show in Figure the magnetic phase diagram for (A) the Ru-doped system, (B) the Cr-doped system and (C) the Sc-doped system against the dopant concentration y. The blue, red, and hatched areas indicate the antiferromagnetic, ferromagnetic and structurally two-phase state regions, respectively. In the Ru-doped system, the ferromagnetic single phase dominates the large-y region (T_C = 280 K). The ferromagnetic phase, however, is much suppressed in the Cr-doped system. The ferromagnetic phase completely disappears, and is replaced by the paramagnetic single phase, in the Sc-doped system. These dopant dependence of the B-site substitution effects can be ascribed to widened one-electron bandwidth of the e_g band.

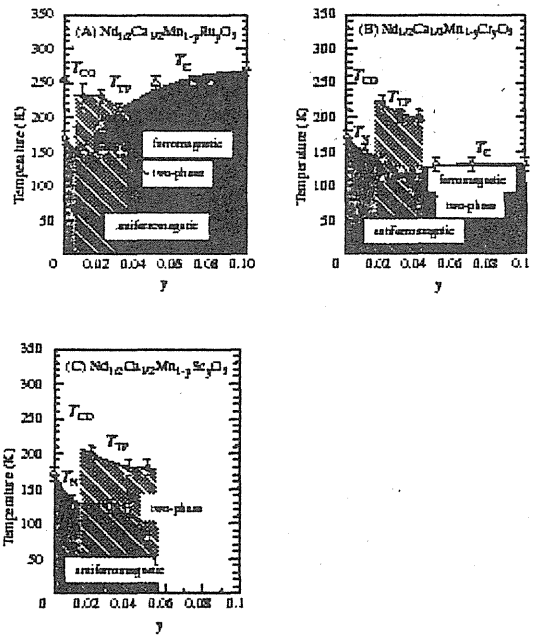


Fig.1: Phase diagrams for (A) $Nd_{1/2}Ca_{1/2}(Mn_{1-y}Ru_y)O_3$, (B) $Nd_{1/2}Ca_{1/2}(Mn_{1-y}Cr_y)O_3$ and (C) $Nd_{1/2}Ca_{1/2}(Mn_{1-y}Sc_y)O_3$ against y determined by neutron powder diffraction. The blue, red, and hatched areas indicate the antiferromagnetic, ferromagnetic and structurally two-phase state regions, respectively. T_N and T_C represent the Neel and Curie temperatures, respectively. T_{TP} represents the crossover temperature into the structurally two-phase state.

使用施設：JRR-3　装置：HERMES、分野：1 Structure&Excitation、2 magnetism

研究テーマ：アクチノイド及び関連イオン性化合物の構造・物性研究
表　題：$L_{0.5}A_{0.5}MnO_3$ の磁性（L=Eu, Gd, Tb 及び Dy, A=Ca 及び Sr）

1-2-20

Magnetic properties of perovskite manganites $L_{0.5}A_{0.5}MnO_3$ (L=Eu, Gd, Tb and Dy, A=Ca and Sr)

K. YOSHII, Y. HIRAMITSU, Y. NISHIHATA, J. MIZUKI, A. NAKAMURA[1], Y. SHIMOJO[1], Y. ISHII[1], Y. MORII[1], H. ABE[2], K. NISHIDA[2]

Synchrotron Radiation Research Center, Japan Atomic Energy Research Institute (JAERI), Mikazuki, Sayo-gun. Hyogo, 679-5148
[1]Advanced Science Research Center, JAERI, Tokai, Ibaraki, 319-1195
[2]National Institute for Materials Science, Tsukuba, Ibaraki 304-0047

Rare earth manganites with a perovskite structure have attracted considerable renewed attention in this decade, because of their intriguing properties such as colossal magnetoresistance, real-space charge-order and metal-insulator traisition. Among these oxides, $L_{0.5}A_{0.5}MnO_3$ (L=rare earth metal, A=alkaline-earth metal) is known to exhibit a wide variety of physical properties, which strongly depend on the ionic radii of the L^{3+} and A^{2+} ions.[1, 2, 3] In this work, magnetic properties were studied for this system containing the small rare earth ions of L^{3+}=Eu^{3+}, Gd^{3+}, Tb^{3+} and Dy^{3+} by means of magnetization and neutron diffraction measurements.

The samples were prepared by a solid-state reaction in air. Magnetization measurements were performed by use of a SQUID magnetometer (Quantum Design MPMS) between 4.5 and 400 K. Neutron diffraction experiments were conducted below 400 K with a high resolution powder diffractometer (HRPD) at the JRR-3 reactor to determine magnetic structures.

The magnetization measurements showed a spin-glass-like trantion around 40-50 K for $L_{0.5}Sr_{0.5}MnO_3$, while a charge-ordering transition was suggested for $L_{0.5}Ca_{0.5}MnO_3$ around room temperature. Figure 1 shows the neutron diffraction pattern for $Tb_{0.5}Sr_{0.5}MnO_3$ at 9 K. The experimental pattern at room temperature could be fitted to an orthorhombic *Pnma* structure by the Rietveld analysis (RIETAN-2000). The lattice paremeters were a=0.54191(3), b=0.76396(4), and c=0.54109(2) nm. The pattern at 9 K showed a few magnetic peaks at the low angle region, which is seen in the inset. It was found that these peaks were appreciably wider than the nuclear Bragg peaks. This result suggests that an origin of the peaks is short-range magnetic order such as either a spin-glass or a cluster-glass state, which is in accord with the result obtained from the magnetization measurements. The patterns of the isostructural $Tb_{0.5}Ca_{0.5}MnO_3$ below room temperatures could be fitted assuming a charge-ordering state of the Mn ions. The different behavior between the Sr- and Ca-systems may be explained in connenction with the randomness of magnetic interactions owing to the difference of the ionic radii of L^{3+} and A^{2+}.[2]

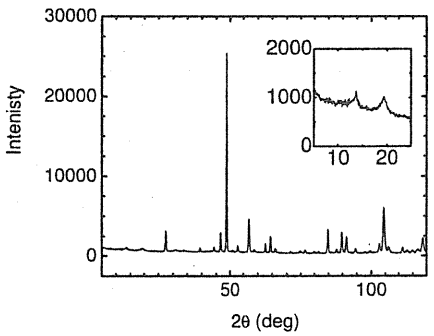


Figure 1: Neutron powder diffraction patterns of $Tb_{0.5}Sr_{0.5}MnO_3$ at 9 K. The inset shows magnetic Bragg peaks.

References

1) P. M. Woodward *et al.*: Chem. Mater. **10** (1998) 3652.
2) T. Terai *et al.*: Phys. Rev. **B61** (2000) 3488.
3) J. López *et al.*: Phys. Rev. **B66** (2002) 214402.

原子炉：JRR-3　　装置：HRPD(1G)　　分野：中性子散乱（磁性）

研究テーマ：$(V_{1-x}Ti_x)_2O_3$ の金属相は不均一系か？
表題：金属相 $(V_{1-x}Ti_x)_2O_3$ の磁気構造と磁気励起

1-2-21 Magnetic Structure and Excitations of Metallic $(V_{1-x}Ti_x)_2O_3$

J. Kikuchi, K. Motoya, and S. Tabaru
Department of Physics, Faculty of Science and Technology, Tokyo University of Science, 2641 Yamazaki, Noda, Chiba 278-8510

Ground-state properties of the anomalous metallic phase of V_2O_3 which exhibits a famous metal-insulator transition (MIT) around 170 K have long been studied over the last three decades. While stoichiometric V_2O_3 remains paramagnetic when applying pressure to stabilize the metallic phase over the low-temperature antiferromagnetic insulating phase, V-deficient and Ti-doped derivatives with the metallic ground state, $V_{2-y}O_3$ and $(V_{1-x}Ti_x)_2O_3$, respectively, were recently found to show an incommensurate spin-density-wave (SDW) order near the phase boundary of the MIT ($y \approx 0.02$ and $x \approx 0.05$) [1, 2, 3]. The SDW propagates along the hexagonal c axis and is characterized by a small ordered moment with a large fluctuating component, and the absence of ordinary spin-wave excitations. Although the SDW order in the vicinity of the MIT boundary has been well-characterized [1, 2, 3], development of the SDW phase upon formal doping of carriers are not yet known in detail. This is because in $V_{2-y}O_3$ a single phase is limited up to $y \approx 0.05$ [4], and in $(V_{1-x}Ti_x)_2O_3$ which forms a continuous solid solution for $0 \leq x \leq 1$, single crystals suitable for microscopic measurements such as NMR and neutron scattering were unavailable. In this study, we have grown single crystals of $(V_{1-x}Ti_x)_2O_3$ and have performed neutron scattering experiments to elucidate the evolution of the SDW phase and of magnetic excitations on carrier doping.

Single crystals of $(V_{1-x}Ti_x)_2O_3$ with $x =$ 0.1, 0.15, 0.2, 0.3, 0.4 were grown by a floating-zone method. Typical dimensions of the crystals are 6 mm in diameter and 15-20 mm in length. Neutron scattering experiments were carried out on the triple-axis spectrometers GPTAS(4G) and HQR (T1-1) installed at JRR-3M, JAERI, Tokai.

Incommensurate antiferromagnetic order has been found for all the samples investigated via an appearance of magnetic Bragg peaks characterized by a propagation vector $\boldsymbol{q} \propto \boldsymbol{c}^*$ as in $x = 0.05$ [3]. For $x = 0.1$, there is a region of temperatures $T_N' \leq T \leq T_N$ where the magnetic Bragg peak is absent along the (00ζ) reciprocal line. The order in that region is therefore a longitudinal SDW (the ordered moments parallel to the c axis). Below T_N' (T_N for $x \geq 0.15$) the magnetic Bragg peaks appear also along (00ζ), suggesting that the direction of the SDW moments deviates from the c axis in the ground state. Intensities of the observed magnetic Bragg peaks can well be reproduced by assuming the SDW structure propagating along the c axis, with the ordered moments making an angle θ to the c axis. In Table 1 we summarized parameters characterizing the SDW order determined from the present intensity analysis.

The gradual increase of $q = |\boldsymbol{q}|$ with x may support the nesting scenario of the SDW order in the doped V_2O_3 systems [5] because an increase in magnitude of the nesting vector is naively expected when hole carriers are increased by Ti doping. q was also found to increase on warming by a few percent of the low-temperature value. The amplitude of the SDW remains small compared with the fully-polarized values, suggesting the ex-

Table 1. Néel Temperatures, propagation vectors q, the SDW amplitude μ_0 in μ_B and the angle θ in the SDW phase of $(V_{1-x}Ti_x)_2O_3$. q, μ_0 and θ are values at 10 K.

x	T_N (K)	T_N' (K)	q/c^*	μ_0	θ/°
0.05†	19	16	1.78(1)	0.31(4)	43(5)
0.10	23	21	1.82(1)	0.32(5)	50(5)
0.20	39	-	1.95(1)	0.31(4)	63(5)
0.30	~ 80	-	2.23(1)	0.45(6)	75(7)
0.40	~ 90	-	2.47(1)	0.65(8)	85(8)

†Reanalysis from ref.[3].

使用施設：JRR-3　装置：4G (GPTAS), T1-1 (HQR)，分野：2. Magnetism

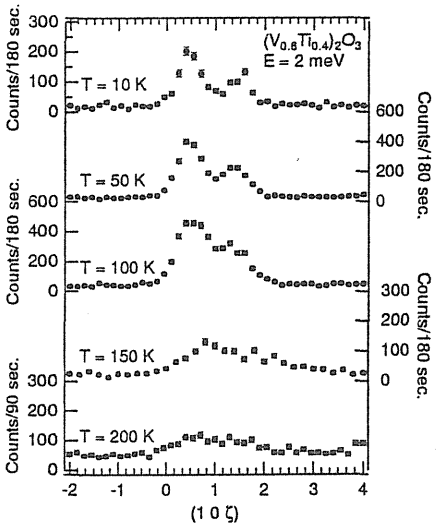


Fig. 1. Scattering profiles of constant-energy scans with the energy transfer of 2 meV along the (10ζ) line from $(V_{0.4}Ti_{0.6})_2O_3$ at various temperatures. The peaks are around (1 0 0.47) and (1 0 1.53) magnetic Bragg positions.

istence of large fluctuating components even for $x = 0.4$. The result of θ clearly shows that the SDW becomes transverse as x increases.

Typical examples of the inelastic neutron scattering profiles of $(V_{1-x}Ti_x)_2O_3$ are shown in Fig. 1. Qualitatively, the profiles do not change so much upon doping. Irrespective of the energy transfers (at least up to 16 meV), inelastic peaks appear at the wave vectors where the magnetic Bragg peaks appear. The width of the peaks becomes broader as the energy transfer and/or temperature increases. There is no anomaly on crossing T_N and the peaks remains observed around the magnetic Bragg positions even far above T_N. These characteristics are quite similar to those observed in $V_{2-y}O_3$ [1, 2]. Even quantitatively, an analysis based on the self-consistent renormalization theory for itinerant antiferromagnets [6] showed that the energy scale of spin fluctuations does not change appreciably on increasing x, in spite of the fact that T_N rises by a factor of $\sim$5 on going from $x = 0.05$ to 0.4. This means that T_N is not determined by the energy scale of the magnetic interaction, which may put the metallic phase of pure and doped V_2O_3 close to the quantum critical point [2].

In summary, we have found that in metallic $(V_{1-x}Ti_x)_2O_3$ the SDW ground state persists at least up to $x = 0.4$. The magnetic excitations are centered near each magnetic Bragg point and extend to the energies much higher than k_BT_N, suggesting critical nature of the metallic state of pure and doped V_2O_3.

References

[1] W. Bao, C. Broholm, S.A. Carter, T.F. Rosenbaum, G. Aeppli, S.F. Trevino, P. Metcalf, J.M. Honig, and J. Spalek, Phys. Rev. Lett. **71** (1993) 766.

[2] W. Bao, C. Broholm, G. Aeppli, S.A. Carter, P. Dai, T.F. Rosenbaum, J.M. Honig, P. Metcalf, and S.F. Trevino, Phys. Rev. B **58** (1998) 12727.

[3] K. Motoya, K. Nakaguchi, A. Nakaju, K. Ishiguchi, T. Kawasaki, M. Itoh, Y. Ueda, and S. Shin, J. Mag. Mag. Mat. **177-181** (1998) 593.

[4] Y. Ueda, K. Kosuge, and S. Kachi, J. Solid State Chem. **31** (1978) 171.

[5] T. Wolenski, M. Grodzicki, and J. Appel, Phys. Rev. B **58** (1998) 303.

[6] K. Nakayama, and T. Moriya, J. Phys. Soc. Jpn. **56** (1987) 2918.

研究テーマ：先端偏極中性子散乱によるスピン-格子物性の研究
表　題：Mgドープされたスピンギャップ系 $Tl(Cu_{1-x}Mg_x)Cl_3$ の不純物誘起反強磁性秩序相における磁気構造

1-2-22

Spin Structure of the Impurity-induced Antiferromagnetic Ordered Phase in the Doped Spin Gap System $Tl(Cu_{1-x}Mg_x)Cl_3$

A. OOSAWA, M. FUJISAWA[1], K. KAKURAI and H. TANAKA[2]

Advanced Science Research Center, JAERI, Tokai, Ibaraki 319-1195
[1]Dep. of Phys., Tokyo Inst. of Tech., Oh-okayama, Meguro-ku, Tokyo 152-8551
[2]Res.Cent.for Low Temp.Phys.,Tokyo Inst. of Tech.,Oh-okayama,Meguro-ku,Tokyo 152-8551

The spin gap in quantum spin systems is the macroscopic quantum phenomenon and has been attracting considerable attention theoretically and experimentally [1]. When nonmagnetic ions are substituted for magnetic ions in a spin gap system, the singlet ground state is disturbed so that staggered moments are induced around the impurities. If the induced moments interact through effective exchange interactions, which are mediated by intermediate singlet spins, three-dimensional (3D) long-range order can arise Such impurity-induced antiferromagnetic ordering was first observed in the well-known inorganic spin-Peierls system $CuGeO_3$ [2]. More recently, we performed the magnetization measurements in the Mg-doped spin gap system $Tl(Cu_{1-x}Mg_x)Cl_3$, and observed the novel ordering [3]. In order to investigate the spin structure of the impurity-induced antiferromagnetic ordered phase in the doped spin gap system $Tl(Cu_{1-x}Mg_x)Cl_3$, we carried out the neutron elastic scattering measurements in $Tl(Cu_{0.97}Mg_{0.03})Cl_3$.

The parent compound $TlCuCl_3$ has the monoclinic structure (space group $P2_1/c$). The crystal structure is composed of planar dimers of Cu_2Cl_6, in which Cu^{2+} ions have spin-$\frac{1}{2}$. The dimers are stacked on top of one another to form infinite double chains parallel to the a-axis. These double chains are located at the corners and center of the unit cell in the $b-c$ plane, and are separated by Tl^+ ions. The magnetic ground state of $TlCuCl_3$ is the spin singlet with the excitation gap $\Delta = 7.7$ K [4]. From the results of analyses of the dispersion relations obtained by neutron inelastic scattering, it was found that $TlCuCl_3$ can be characterized as the 3D strongly coupled antiferromagnetic dimer system [5].

The preparation of the single crystal of $Tl(Cu_{1-x}Mg_x)Cl_3$ has been reported in ref. 3. Neutron elastic scattering measurements were performed using the JAERI-TAS1. The constant-$\boldsymbol{k}_i$ mode was taken with a fixed incident neutron energy E_i of 14.7 meV and collimations were set as open-40'-80'-80'. A PG filter was placed to suppress the higher order contaminations. We used a sample with a volume of approximately 1 cm^3. The sample was mounted in an ILL-type orange cryostat with its a^*- and c^*-axes in the scattering plane.

The inset of Fig. 1 shows the $\theta-2\theta$ scans for $\boldsymbol{Q} = (1, 0, -3)$ reflection measured at $T = 1.4$ and 4.2 K in $Tl(Cu_{0.97}Mg_{0.03})Cl_3$. The resolution limited additional intensity at $T = 1.4$ K can be clearly seen. Figure 1 shows the temperature dependence of the peak intensity at $\boldsymbol{Q} = (1, 0, -3)$. The rapid increase of the intensity below $T_N = 3.45$ K is observed. This transition temperature is in agreement with the phase diagram of this doped sample obtained from the magnetization measurements [3]. We thus infer that the additional intensity at low T is of magnetic origin. In order to determine the spin structure of the impurity-induced antiferromagnetic ordered phase in $Tl(Cu_{0.97}Mg_{0.03})Cl_3$, we measured the integrated intensities of nine magnetic Bragg reflections at $\boldsymbol{Q} = (h, 0, l)$ with integer h and odd l. The results are summalized in Table 1. The intensities of nuclear Bragg reflections were also measured at $\boldsymbol{Q} = (h, 0, l)$ with even l in order to estimate the magnitude of the effective magnetic moment averaged per site. To refine the magnetic structure, we

原子炉：JRR-3　　装置：TAS-1(2G)　　分野：中性子散乱（磁性）

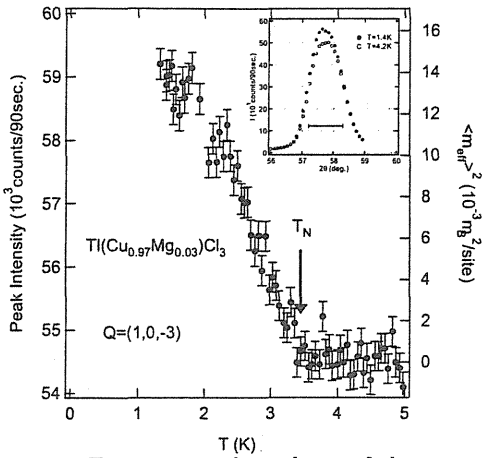


Figure 1: Temperature dependence of the magnetic Bragg peak intensity for $\boldsymbol{Q} = (1, 0, -3)$ reflection in $Tl(Cu_{0.97}Mg_{0.03})Cl_3$. The square of the effective magnetic moment averaged per site $\langle m_{\rm eff}\rangle^2$ is shown on the right abscissa. The inset shows the $\theta - 2\theta$ scans for $\boldsymbol{Q} = (1, 0, -3)$ reflection measured at $T = 1.4$ and 4.2 K in $Tl(Cu_{0.97}Mg_{0.03})Cl_3$. The horizontal bar indicates the calculated instrumental resolution widths.

Table 1: Integrated Intensities of the magnetic Bragg reflections at $T = 1.4$ K in $Tl(Cu_{0.97}Mg_{0.03})Cl_3$. The intensities are normalized to the $(0, 0, 1)_M$ reflection. R is the reliability factor given by $R = \sum_{h,k,l} |I_{\rm cal} - I_{\rm obs}| / \sum_{h,k,l} I_{\rm obs}$.

(h, k, l)	$I_{\rm obs}$	$I_{\rm cal}$
$(0, 0, 1)_M$	1 ± 0.021	1
$(0, 0, 3)_M$	0.006 ± 0.001	0.014
$(0, 0, 5)_M$	0.058 ± 0.010	0.106
$(1, 0, 1)_M$	0.039 ± 0.011	0.002
$(1, 0, -1)_M$	0.059 ± 0.002	0.100
$(1, 0, 3)_M$	0.024 ± 0.007	0.033
$(1, 0, -3)_M$	0.352 ± 0.006	0.332
$(2, 0, 1)_M$	0.017 ± 0.005	0.007
$(2, 0, -1)_M$	0.065 ± 0.013	0.075
R	0.11	

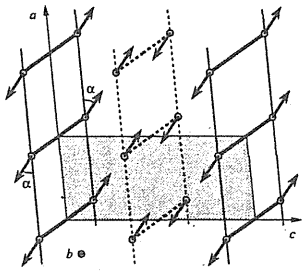


Figure 2: The spin structure observed in the impurity-induced ordered phase of $Tl(Cu_{0.97}Mg_{0.03})Cl_3$. The double chains located at the corner and the center of the chemical unit cell in the $b-c$ plane are represented by solid and dashed lines, respectively. The shaded area is the chemical unit cell in the $a-c$ plane. The angle α between the spins and the a-axis in the ordered phase is expressed in the text.

used the atomic coordinates of $TlCuCl_3$ [6] and the nuclear scattering lengths $b_{\rm Tl} = 0.878$, $b_{\rm Cu} = 0.772$ and $b_{\rm Cl} = 0.958$ in the unit of 10^{-12} cm. The magnetic form factors of Cu^{2+} were taken from ref. 7. The extinction effect was evaluated by comparing observed and calculated intensities for various nuclear Bragg reflections.

As a result, the spin structure, as shown in Fig. 2, with $\alpha = 34.4° \pm 4.4°$ were obtained. Although scans in the reciprocal plane including the b^*-axis were not performed, the spin structure shown in Fig. 2 is uniquely determined within the present measurements. The obtained angle α is consistent with the magnetization measurements of $Tl(Cu_{1-x}Mg_x)Cl_3$ [3], and is the same as that in the spin structure of the field-induced ordered phase of $TlCuCl_3$ in error bars [6]. Hence we conclude that the spin structure of the impurity-induced antiferromagnetic ordered phase on average in $Tl(Cu_{0.97}Mg_{0.03})Cl_3$ is the same as that of the field-induced magnetic ordered phase for $\boldsymbol{H} \parallel b$ in the parent compound $TlCuCl_3$ ("on average" means that the magnitude of the ordered moments in the impurity-induced antiferromagnetic ordered phase may be not uniform.). The magnitude of the effective magnetic moment averaged per site at $T = 1.4$ K was evaluated as $\langle m_{\rm eff}\rangle = g\mu_{\rm B}\langle S_{\rm eff}\rangle = 0.12(1)$ $\mu_{\rm B}$. This value is much smaller than 1 $\mu_{\rm B}$, which is the full moment of Cu^{2+}.

References

1) E. Dagotto *et al.*: Science **271** (1996) 618.
2) T. Masuda *et al.*: Phys. Rev. Lett. **80** (1998) 4566.
3) A. Oosawa *et al.*: Phys. Rev. B **66** (2002) 020405(R).
4) A. Oosawa *et al.*: J. Phys. : Condens. Matter **11** (1999) 265.
5) A. Oosawa *et al.*: Phys. Rev. B **65** (2002) 094426.
6) H. Tanaka *et al.*: J. Phys. Soc. Jpn. **70** (2001) 939.
7) P. J. Brown: *International Tables for Crystallography*, vol. C, ed. A. J. C. Wilson (Kluwer, Dordrecht, 1992) p. 391.

研究テーマ：RB_6の磁気構造の研究
表題：中性子回折によるTbB_6の磁気構造

1-2-23

Magnetic Structure of TbB_6

Yasuo YAMAGUCHI[1], Kenji OHOYAMA[1] and Satoshi KUNII[2]

[1]*Institutefor Materials Research, Tohoku Univ., Sendai 980-8577*
[2]*Department of Physics, Tohoku Univ., Sendai 980-8577*

Magnetic structures of RB_6 (R=rare earth) are very interesting. For example, complex magnetic structure of CeB_6 is thought to come from quadrupolar and octapolar interactions besides ordinary magnetic dipole interaction[1]. For light rare earth compounds, there are many data on the magnetic structure of RB_6, but progress is very slow for heavy rare earth compounds because of hardness of the sample preparation. Recently the magnetic structures of DyB_6[2] and GdB_6[3] have been studied using neutron diffraction, and concluded that both take collinear antiferromagnetic structure with the propagation vector of k=(1/4,1/4,1/2). Kuramoto et al have proposed a model of generalized RKKY interaction to explain these magnetic structures of RB_6 series[4].

In the present report we show the results of neutron diffraction study on TbB_6. We used high purity sample confirmed by X-ray diffraction. Small change of the preparation condition introduces impurity phases as reported before [5], therefore we used confirmed samples using natural boron which is heavy neutron absorber. In order to avoid neutron absorption, powder samples were thinly pasted using epoxy resin around vanadium cylinder of 10mm diameter. Amount of the sample was about 100mg which is about 1/200 of usual sample weight. High efficiency of the HERMES diffractometer made this experiment being possible.

We observed that TbB6 keeps cubic symmetry down to 2.2K, and antiferromagnetic ordering appears at T_N=19.5K with the propagation vector k=(d,d',1/2), where d=0.245 and d'=0.225. This structure resembles to that of the intermediate phase of PrB_6[6].

References

[1] H.Kusunose and Y.Kuramoto; J. Phys. Soc. Jpn., 70(2001)1751. [2] K.Takahashi; Dr. Thesis (Tohoku Univ., 2002). [3]K.Kuwahara et al.; App!. Phys. A [4] Y.Kuramotoand K.Kubo; Proc. of LT23(Hiroshima, 2002) (to be published) [5] A.Donni et al.; J. Phys. Soc. Jpn., 70(2001) Suppl. A p448. [6] C.M.McCarthy et al.; Solid State Commun.,36(1980)861.

使用施設：JRR-3　装置：HERMES（T1-3），分野：Magnetism

研究テーマ：先端偏極中性子散乱によるスピン-格子物性の研究
表　題：Mg ドープされたスピンギャップ系 $Tl(Cu_{1-x}Mg_x)Cl_3$ の不純物誘起反強磁性秩序相における磁気励起

1-2-24

Magnetic Excitations in the Impurity-induced Antiferromagnetic Ordered Phase of the Doped Spin Gap System $Tl(Cu_{1-x}Mg_x)Cl_3$

A. OOSAWA, M. FUJISAWA[1], K. KAKURAI and H. TANAKA[2]

Advanced Science Research Center, JAERI, Tokai, Ibaraki 319-1195
[1]Dep. of Phys., Tokyo Inst. of Tech., Oh-okayama, Meguro-ku, Tokyo 152-8551
[2]Res.Cent.for Low Temp.Phys.,Tokyo Inst. of Tech.,Oh-okayama,Meguro-ku,Tokyo 152-8551

The magnetic excitations in the spin gap systems are new subject in magnetism, and the information on the magnetic excitation is necessary to elucidate the microscopic mechanism leading to the novel impurity-induced antiferromagnetic ordering in the spin gap systems. In order to investigate the magnetic excitations in the impurity-induced antiferromagnetic ordered phase of the doped spin gap system $Tl(Cu_{1-x}Mg_x)Cl_3$, we performed neutron inelastic scattering measurements in $Tl(Cu_{0.97}Mg_{0.03})Cl_3$.

The parent compound $TlCuCl_3$ has the monoclinic structure (space group $P2_1/c$). The crystal structure is composed of planar dimers of Cu_2Cl_6, in which Cu^{2+} ions have spin-$\frac{1}{2}$. The dimers are stacked on top of one another to form infinite double chains parallel to the a-axis. These double chains are located at the corners and center of the unit cell in the $b-c$ plane, and are separated by Tl^+ ions. The magnetic ground state of $TlCuCl_3$ is the spin singlet with the excitation gap $\Delta = 7.7$ K [1]. From the results of analyses of the dispersion relations obtained by neutron inelastic scattering, it was found that the origin of the spin gap in $TlCuCl_3$ is the strong antiferromagnetic interaction in the chemical dimer Cu_2Cl_6, and that the neighboring dimers couple via the strong three-dimensional interdimer interactions along the double chain and in the $(1.0, -2)$ plane, in which the hole orbitals of Cu^{2+} spread [2]. Using the cluster series expansion, the intradimer and the important individual interdimer exchange interactions were obtained [2]. The notation of the exchange interactions is given in Fig. 1. The main intradimer interaction is denoted as J, and then the exchange interaction per bond between spins in dimers separated by a lattice vector $\boldsymbol{la}+\boldsymbol{mb}+\boldsymbol{nc}$ is denoted as the exchange energy J_{lmn} for pairs of spins at equivalent positions in their respective dimer and as J'_{lmn} for spins at inequivalent positions.

The preparation of the single crystal of $Tl(Cu_{1-x}Mg_x)Cl_3$ has been reported in ref. 3. Neutron inelastic scattering measurements were performed using the JAERI-TAS1. The constant-$\boldsymbol{k}_f$ mode was taken with a fixed final neutron energy E_f of 14.7 meV and collimations were set as open-80'-80'-80'. A PG filter was placed to suppress the higher order contaminations. We used a sample with a volume of approximately 1 cm^3. The sample was mounted in an ILL-type orange cryostat with its a^*- and c^*-axes in the scattering plane.

Constant-$\boldsymbol{Q}$ energy scan profiles were measured along $(h, 0, 1)$, $(0, 0, l)$, $(h, 0, 2h+1)$ and $(h, 0, -2h+1.4)$ with $0 \leq h \leq 0.5$ and $1 \leq l \leq 2$ at $T = 1.5$ K, which is lower than $T_N = 3.45$ K in $Tl(Cu_{0.97}Mg_{0.03})Cl_3$. Figure 2 (a) shows the representative scan profiles for $\boldsymbol{Q} = (h, 0, 2h+1)$, in which the magnetic excitation is most dispersive. A well-defined single excitation can be observed in almost all scans. The scan profiles were fitted with a Gaussian function to evaluate the excitation energy, as shown by the solid lines in Fig. 2 (a). The obtained scan profiles in $Tl(Cu_{0.97}Mg_{0.03})Cl_3$ were almost the same as those obtained in the parent compound $TlCuCl_3$ [2], and we confirmed that the origin of the observed excitation is magnetic from the temperature dependence. Hence we can expect that the observed excitation is the triplet magnetic excitation in the impurity-induced ordered state. The

原子炉：JRR-3　　装置：TAS-1(2G)　　分野：中性子散乱（磁性）

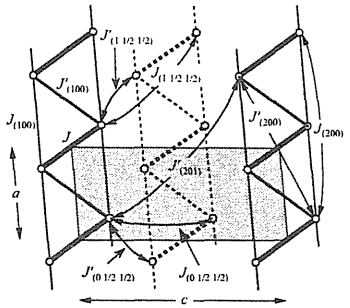


Figure 1: The exchange interactions of $Tl(Cu_{0.97}Mg_{0.03})Cl_3$. The double chains located at the corner and the center of chemical unit cell in the b-c plane are represented by solid and dashed lines, respectively. The shaded area is chemical unit cell in the a-c plane.

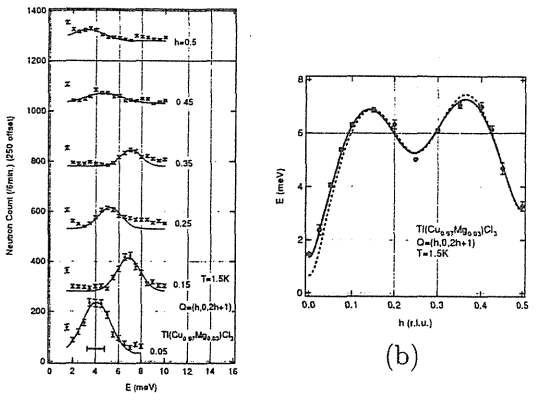


Figure 2: (a) Profiles of the constant-Q energy scans and (b) dispersion relation in $Tl(Cu_{0.97}Mg_{0.03})Cl_3$ for Q along $(h, 0, 2h+1)$ with $0 \leq h \leq 0.5$ at $T = 1.5$ K. The solid lines in (a) are fits using a Gaussian function. The horizontal bar in (a) indicates the calculated instrumental resolution width. Solid line in (b) is the dispersion curve calculated by RPA approximation using eq. (1). Dashed line in (b) is the dispersion curve of the triplet excitation in $TlCuCl_3$ [2].

dispersion relation $\omega(Q)$ of the excitation for $Q = (h, 0, 2h+1)$ at $T = 1.5$ K is shown in Fig. 2 (b). The dispersion curve of the triplet excitation in $TlCuCl_3$ [2] is also depicted in Fig. 2 (b) by the dashed line. As shown in Fig. 2 (b), there is not much difference between the dispersion relations of $Tl(Cu_{0.97}Mg_{0.03})Cl_3$ and those of $TlCuCl_3$, except in the vicinity of the lowest excitation at $Q = (0, 0, 1)$ corresponding to the spin gap.

We fit the obtained dispersion relations by the following equation obtained from the RPA approximation, which is applied to $TlCuCl_3$ [2]

$$\omega_{\pm}(Q) = \sqrt{J^2 + 2J\delta\omega_{\pm}(Q)}\ , \qquad (1)$$

where

$$\begin{aligned}\delta\omega_{\pm}(Q) &= [J^{\rm eff}_{(100)}\cos(2\pi h) + J^{\rm eff}_{(200)}\cos(4\pi h) \\ &+ J^{\rm eff}_{(201)}\cos\{2\pi(2h+l)\}] \pm 2[J^{\rm eff}_{(1\frac{1}{2}\frac{1}{2})}\cos\{\pi \\ &(2h+l)\}\cos(\pi k) + J^{\rm eff}_{(0\frac{1}{2}\frac{1}{2})}\cos(\pi k)\cos(\pi l)]. \quad (2)\end{aligned}$$

In the equations, J denotes the main intradimer exchange interaction, and $J^{\rm eff}_{(lmn)}$ denote the effective interactions between dimers separated by a lattice vector $la + mb + nc$ and are expressed as

$$\begin{aligned}&J^{\rm eff}_{(100)} = \frac{1}{2}(2J_{(100)} - J'_{(100)})\ , \qquad J^{\rm eff}_{(200)} = \frac{1}{2}(2J_{(200)} - J'_{(200)}) \\ &J^{\rm eff}_{(1\frac{1}{2}\frac{1}{2})} = \frac{1}{2}(J_{(1\frac{1}{2}\frac{1}{2})} - J'_{(1\frac{1}{2}\frac{1}{2})})\ , \quad J^{\rm eff}_{(0\frac{1}{2}\frac{1}{2})} = \frac{1}{2}(J_{(0\frac{1}{2}\frac{1}{2})} - J'_{(0\frac{1}{2}\frac{1}{2})})\ , \\ &J^{\rm eff}_{(201)} = -\frac{1}{2}J'_{(201)}\ , \qquad (3)\end{aligned}$$

where J_{lmn} and J'_{lmn} are shown in Fig. 1. Under the present experimental condition, *i.e.*, Q in the a^*-c^* plane, the $\omega_+(Q)$ branch gives the only nonvanishing contribution. The solid line in Fig. 2 (b) indicates the calculated results with the exchange parameters, as shown in Table 1. The experimental dispersion curves can be reproduced well by the fitting. Compared to the parent compound $TlCuCl_3$, the magnitude of the intradimer interaction J becomes slightly larger, while that of the important effective interdimer interactions $J^{\rm eff}_{(100)}$, $J^{\rm eff}_{(1\frac{1}{2}\frac{1}{2})}$ and $J^{\rm eff}_{(201)}$ become slightly smaller.

Table 1: The intradimer interaction J and the effective interdimer interactions $J^{\rm eff}_{(lmn)}$ in $TlCuCl_3$ [2] and $Tl(Cu_{0.97}Mg_{0.03})Cl_3$. All energies are in units of meV.

	$TlCuCl_3$ [2]	$Tl(Cu_{0.97}Mg_{0.03})Cl_3$
J	5.68	5.74
$J^{\rm eff}_{(100)}$	−0.46	−0.41
$J^{\rm eff}_{(200)}$	0.05	−0.03
$J^{\rm eff}_{(1\frac{1}{2}\frac{1}{2})}$	0.49	0.46
$J^{\rm eff}_{(0\frac{1}{2}\frac{1}{2})}$	−0.06	−0.03
$J^{\rm eff}_{(201)}$	−1.53	−1.41

No antiferromagnetic spin-wave excitation could be observed. This may be due to the large incoherent scattering by chlorines near the zone center $Q = (0, 0, 1)$ and the rapid broadening of spectra far from $Q = (0, 0, 1)$.

References

1) A. Oosawa *et al.*:J. Phys.:Cond. Mat. **11**(1999)265.
2) A. Oosawa *et al.*: Phys. Rev. B **65** (2002) 094426.
3) A. Oosawa *et al.*: Phys. Rev. B **66** (2002) 020405(R).

研究テーマ:$PrFe_4P_{12}$における低温秩序相の磁気特性と電子状態
表題:$PrFe_4P_{12}$におけるPrイオン4f電子状態の四重極秩序

1-2-25 Antiferro-quadrupolar ordering of Pr-ion 4f-electron state in $PrFe_4P_{12}$

K. Iwasa, L. Hao, M. Nakajima, M. Kohgi, H. Sugawara, Y. Aoki, T. D. Matsuda[1] and H. Sato

Department of Physics, Tokyo Metropolitan University, Hachioji, Tokyo 192-0397, Japan
[1] Advanced Science Research Center, Japan Atomic Energy Research Institute, Tokai, Ibaraki 319-1195, Japan

Among recent topics of strongly correlated electro systems, rare-earth filled skutterudites crystallizing in a cubic structure with Im $\bar{3}$ have been attractive for their various physical properties. $PrFe_4P_{12}$ exhibits heavy-electron phenomena novel for Pr-base compounds and an unusual phase transition at T_A = 6.5 K [1, 2]. No magnetic reflection was seen in neutron powder diffraction below T_A [3], in spite of a cusp of magnetic susceptibility at T_A like an antiferromagnetic (AF) ordering and a clear specific-heat jump [2]. This low-temperature phase is suppressed by external magnetic field and disappears above around H = 5 T. In the disordered phase, heavy-electron phenomena of electrical resistivity following $-\log T$ behavior [1], a large Sommerfeld coefficient of 1.4 J/mol/K^2 [2] and electron effective mass of $81m_0$ [4] were observed. X-ray diffraction experiments revealed a crystal-lattice modulation characterized by the wave vector q = {1, 0, 0} with a dominant Fe-ion longitudinal displacement in the low-temperature phase [5]. The superlattice formation is consistent with the Fermi-surface nesting predicted in the band structure study [6]. Inelastic neutron scattering experiment for a polycrystalline sample was carried out [7]. The spectrum above T_A is composed of a broad peak centered at energy transfer E = 0. It is similar to those of the typical heavy-electron Ce-based systems [8]. Below T_A, sharp peaks appear at 1.4 and 3.0 meV which are expected to originate from a localize nature of Pr-ion 4f electrons. In order to investigate a role of Pr-ion 4f electrons in the phase transition, we measured neutron diffraction from a single-crystal sample under magnetic field.

The measurements with neutron wavelength of 2.35 Å were performed by a spectrometer PONTA (5G) at JRR-3M, JAERI (Tokai). Sample temperature was controlled down to T = 1.5 K and magnetic field was applied up to H = 5.8 T along the [0, 0, 1] and [0, 1, -1] directions.

Figure 1 depicts longitudinal profiles thorough the reciprocal-lattice points Q = (1, 0, 0), (3, 0, 0) and (2, 1, 0). Superlattice reflections at Q = (h, k, l) with odd numbers of $h + k + l$ were detected below T_A at H = 0 as the (3, 0, 0) reflection, in contrast to those at (1, 0, 0) and (2, 1, 0) are not clear at zero field. The reflections at H = 0 are ascribed to the crystal-lattice modulation as observed by the previous X-ray diffraction. Applying external magnetic fields below T_A, not only ferromagnetic intensities at Q = (h, k, l) with $h + k + l$ = even but also the superlattice-reflection intensities increase with increasing magnetic field as shown in Fig. 1. At the phase boundary at H = 4 T and T = 1.6 K, these intensities suddenly disappear.

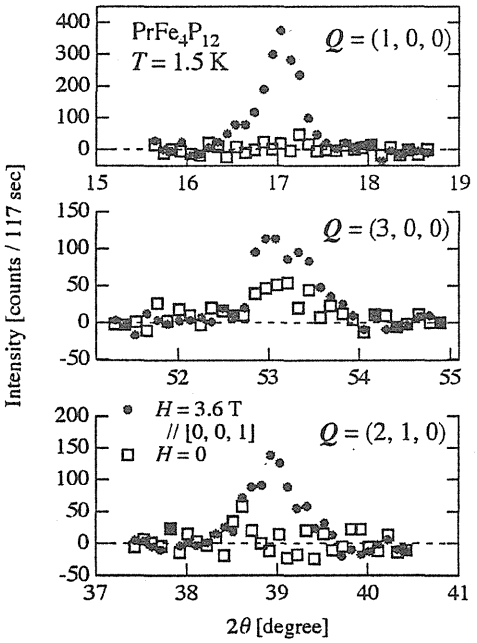


Figure 1. Neutron diffraction profiles at Q = (1, 0, 0), (3, 0, 0) and (2, 1, 0) at 1.6 K and 3.6 T along the [0, 0, 1] axis (solid circles) and at zero field (open squares). Background intensities measured at 10 K and at zero field were subtracted.

研究テーマ:$PrFe_4P_{12}$における低温秩序相の磁気特性と電子状態
表題:$PrFe_4P_{12}$におけるPrイオン4f電子状態の四重極秩序

The result was analyzed by taking into account the crystal-lattice modulation and a field-induced AF structure of the Pr ions. The lattice-modulation model represented by the Fe-ion displacement δ for fractional coordinate of $(1/4 + \delta, 1/4 + \delta, 1/4 - 2\delta)$ is adopted as in the previous X-ray study [5, 9]. We assumed two different magnetic moments μ_1 and μ_2 induced along the [0, 0, 1] at the corner and body-centered Pr-ion sites in the unit cell. Calculated superlattice intensities with δ, μ_1 and μ_2 determined by a least-squares fitting procedure reproduce the magnetic-field-dependent intensity pattern. The obtained value of $\delta \cong 0.27 \times 10^{-3}$ at zero field is very close to the X-ray diffraction result. The evaluated magnetic-field dependences of AF amplitude $(\mu_1 - \mu_2)/2$ shown in Fig. 2 increases up to $0.1\mu_B$/Pr just below the critical magnetic field of 4 T. This value is larger than $0.06\mu_B$/Pr at 5 T under magnetic field along the [0, -1, 1] direction [10].

The theoretical work on the phase transition of $PrFe_4P_{12}$ suggested a split of a non-magnetic doublet crystal-field state Γ_{23} in terms of T_h space group for the skutterudites due to coupling between the Pr-ion state and the tetragonal or orthogonal Fe-ion lattice distortion [9, 11]. The ground state Γ_{23} is also pointed out from the ultrasonic measurement [12]. Because the Fe-ion arrangements around the corner and body-center Pr-ion sites are different, the two Pr-ion states align on these sites with the wave vector $\boldsymbol{q}$ = (1, 0, 0), and the different size of magnetic moments are induced on these sites. Therefore, we conclude that $PrFe_4P_{12}$ exhibits antiferro-quadrupolar (AFQ) ordering of Pr-ion 4f-electron states below T_A. The observed AF components under the different fields are key to determine the order parameter.

It is novel that the low-temperature phase of $PrFe_4P_{12}$ is produced by a coupling between the AFQ ordering of 4f-electron states and the gap formation by Fermi-surface nesting with the crystal-lattice modulation by the wave vector $2k_F \cong (1, 0, 0)$.

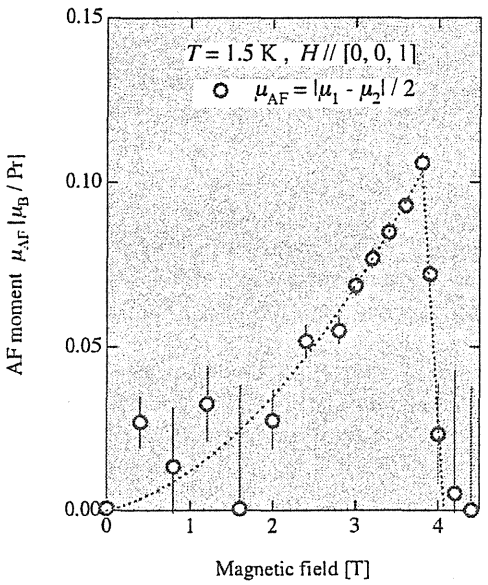


Figure 2. Magnetic-field dependences of the antiferromagnetic amplitude $(\mu_1 - \mu_2)/2$ at 1.5 K under the magnetic field along the [0, 0, 1] axis.

References
1) M. S. Torikachvili *et al.*: Phys. Rev. B **36**, 8660 (1987), H. Sato *et al.*: Phys. Rev. B **62**, 15125 (2000).
2) Y. Aoki *et al.*: Phys. Rev. B **65** 064446 (2002).
3) L. Keller *et al.*: J. Alloys and Compounds **323-324**, 516 (2001).
4) H. Sugawara *et al.*: Phys. Rev. B **66** 134411 (2002).
5) K. Iwasa *et al.*: Physica B **312-313**, 834 (2002).
6) H. Sugawara *et al.*: J. Phys. Soc. Jpn. **69**, 2938 (2000), H. Harima, K. Takegahara, Physica B **312-313**, 843 (2002).
7) K. Iwasa *et al.*: Acta Phys. Polonica B **34**, 1117 (2003).
8) E. Holland-Moritz and G. H. Lander, Handbook on the Physics and Chemistry of the Rare Earths Vol. 19, Elsevier Science B. V., Amsterdam 1994, p.1.
9) S. H. Curnoe *et al.*: Physica B **312-313**, 837 (2002).
10) L. Hao *et al.*: Acta Phys. Polonica B **34**, 1113 (2003).
11) K. Takegahara *et al.*: J. Phys. Soc. Jpn **70**, 1190 (2001).
12) Y. Nakanishi *et al.*: Phys. Rev. B **63**, 184429 (2001).

研究テーマ：先端偏極中性子散乱によるスピン-格子物性の研究
表　題：Mg ドープされたスピンギャップ系 $Tl(Cu_{1-x}Mg_x)Cl_3$ の不純物誘起反強磁性秩序相におけるスピンギャップと磁気秩序の共存

1-2-26

Coexistence of the Spin Gap and the Magnetic Ordering in the Impurity-induced Antiferromagnetic Ordered Phase of the Doped Spin Gap System $Tl(Cu_{1-x}Mg_x)Cl_3$

A. OOSAWA, M. FUJISAWA[1], K. KAKURAI and H. TANAKA[2]

Advanced Science Research Center, JAERI, Tokai, Ibaraki 319-1195
[1]Dep. of Phys., Tokyo Inst. of Tech., Oh-okayama, Meguro-ku, Tokyo 152-8551
[2]Res.Cent.for Low Temp.Phys.,Tokyo Inst. of Tech.,Oh-okayama,Meguro-ku,Tokyo 152-8551

The impurity-induced antiferromagnetic ordering in spin gap systems is the novel quantum phenomenon and attracted much interest and thus led to a large number of vivid experimental and theoretical investigations. Especially, the coexistence of the spin gap and the magnetic ordering in the impurity-induced antiferromagnetic ordered phase has been observed by neutron scattering experiments in $(Cu_{1-x}Zn_x)GeO_3$ and $Cu(Ge_{1-x}Si_x)O_3$ with low x [1,2], and the coexistence of the mutually exclusive phenomena at first glance is still argued vigorously by many theorists and experimenters. In order to investigate whether the coexistence occurs in the impurity-induced antiferromagnetic ordered phase of the doped spin gap system $Tl(Cu_{1-x}Mg_x)Cl_3$, we performed neutron scattering measurements in $Tl(Cu_{0.97}Mg_{0.03})Cl_3$.

The parent compound $TlCuCl_3$ has the monoclinic structure (space group $P2_1/c$). The crystal structure is composed of planar dimers of Cu_2Cl_6, in which Cu^{2+} ions have spin-$\frac{1}{2}$. The dimers are stacked on top of one another to form infinite double chains parallel to the crystallographic a-axis. These double chains are located at the corners and center of the unit cell in the $b-c$ plane, and are separated by Tl^+ ions. The magnetic ground state of $TlCuCl_3$ is the spin singlet with the excitation gap $\Delta = 7.7$ K [3]. From the results of analyses of the dispersion relations obtained by neutron inelastic scattering, it was found that the origin of the spin gap in $TlCuCl_3$ is the strong antiferromagnetic interaction in the chemical dimer Cu_2Cl_6, and that the neighboring dimers couple via the strong three-dimensional interdimer interactions along the double chain and in the $(1,0,-2)$ plane, in which the hole orbitals of Cu^{2+} spread [4, 5, 6].

The preparation of the single crystal of $Tl(Cu_{1-x}Mg_x)Cl_3$ has been reported in ref. 7. Neutron inelastic scattering measurements were performed using the JAERI-LTAS. The constant-$\boldsymbol{k}_f$ mode was taken with a fixed final neutron energy E_f of 5.0 meV and collimations were set as 24'-80'-80'-80'. We used a sample with a volume of approximately 1 cm^3. The sample was mounted in an ILL-type orange cryostat with its a^*- and c^*-axes in the scattering plane.

Figure 1 shows the constant-$\boldsymbol{Q}$ energy scan profiles in $Tl(Cu_{0.97}Mg_{0.03})Cl_3$ for $\boldsymbol{Q} = (0,0,1)$, where the lowest triplet excitation corresponding to the spin gap occurs in the parent compound $TlCuCl_3$, at various temperatures. A well-defined single excitation can be seen at all temperatures. Hence it is confirmed that the spin gap remains even in the impurity-induced ordered phase. Because the excitation was also observed at $T = 5.2$ K, which is higher than $T_N = 3.45$ K, the excitation is not spin-wave excitation by the antiferromagnetic ordering, but the triplet excitation from the ground state. The horizontal bar in Fig. 1 denotes the calculated instrumental resolution width. The broadening of the spectra can be seen. The solid lines in Fig. 1 are fits to the dispersion relations convoluted with the instrumental resolution. A Lorentzian function for the magnetic excitation is used. The free parameters are I, Γ and $E_{(0,0,1)}$, which are the integrated intensity, the Lorentzian width and the spin gap, respec-

原子炉：JRR-3　　装置：LTAS(C2-1)　　分野：中性子散乱（磁性）

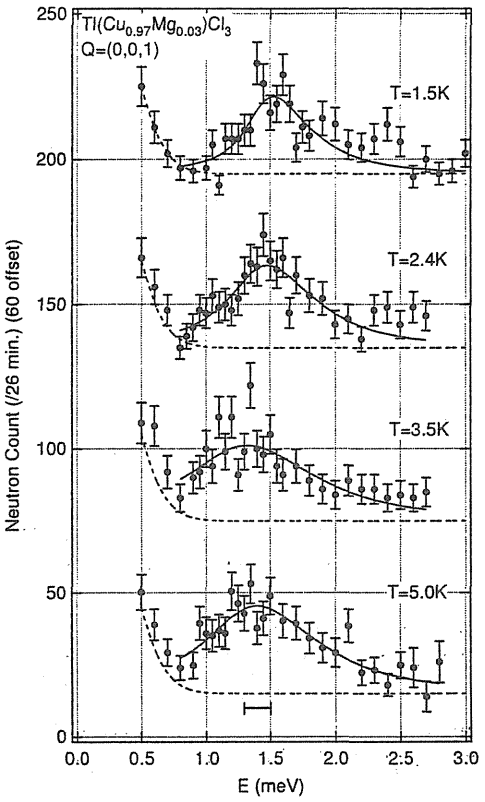


Figure 1: Constant-Q energy scan profiles in $Tl(Cu_{0.97}Mg_{0.03})Cl_3$ at $Q = (0, 0, 1)$ for various temperatures. The solid lines are fits to the dispersion relations convoluted with the instrumental resolution. The horizontal error bar indicates the calculated instrumental resolution widths. Dashed lines denote the background with the Bragg reflection at $Q = (0, 0, 1)$.

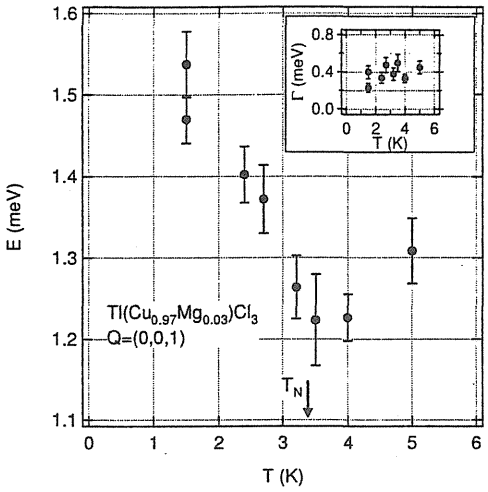


Figure 2: Temperature dependence of the energy of the magnetic excitation at $Q = (0; 0, 1)$. The inset shows the temperature dependence of the Lorentzian width Γ.

tively. The shape of the dispersion relation in the vicinity of Q=(0, 0, 1) was fixed to that obtained from the RPA approximation. The temperature dependence of the energy of the triplet excitation at $Q = (0, 0, 1)$ is shown in Fig. 2. The rapid increase of the excitation energy can be clearly seen below $T_N = 3.45$ K. The triplet excitation depends on temperature due to the temperature dependence of the occupation difference between the singlet and triplet states [8]. However, the increase of temperature causes to flatten the dispersion relation due to the suppression of the interdimer correlations by the decrease of the occupation difference, namely the energy of the lowest excitation corresponding to the spin gap should rather decrease upon decreasing temperature. Hence, we can expect that the rapid increase of the spin gap is caused by the impurity-induced antiferromagnetic ordering and can conclude that the impurity-induced antiferromagnetic ordering coexists with the spin gap in $Tl(Cu_{0.97}Mg_{0.03})Cl_3$. The energy of the lowest excitation is $E = 1.3$ meV at $T = 5.2$ K, which is higher than T_N, and is a little larger than that of $0.65 \sim 0.8$ meV estimated for the pure $TlCuCl_3$ [4, 5, 6]. This indicates that the spin gap is also enhanced by the Mg doping, irrespective of the ordering. The temperature dependence of Γ is also shown in inset of Fig. 2. No significant variation of Γ can be seen.

References

1) M. C. Martin *et al.*: Phys. Rev. B **56** (1997) 3173.
2) L. P. Regnault *et al.*: Europhys. Lett. **32** (1995) 579.
3) A. Oosawa *et al.*: J. Phys.: Condens. Matter **11** (1999) 265.
4) A. Oosawa *et al.*: Phys. Rev. B **65** (2002) 094426.
5) A. Oosawa *et al.*: J. Phys. Soc. Jpn. Suppl. A **70** (2001) 166.
6) N. Cavadini *et al.*: Phys. Rev. B **63** (2001) 172414.
7) A. Oosawa *et al.*: Phys. Rev. B **66** (2002) 020405(R).
8) N. Cavadini *et al.*: Eur. Phys. J. B **18** (2000) 565.

研究テーマ： 強磁性超伝導体と自発的渦糸構造について
表題： $ErNi_2B_2C$ における磁束格子の観測

1-2-27 Neutron scattering studies of the flux line lattice in $ErNi_2B_2C$

T. Nagata[1], F. Yano[2], E. Habuta[2], H. Kawano-Furukawa[1], M. Nagao[3], H. Yoshizawa[3]
N. Furukawa[4], H. Takeya[5], and K. Kadowaki[6]

[1] *Department of Physics, Ochanomizu Univ. Tokyo 112-8610*
[2] *Graduate School of Humanities and Sciences, Ochanomizu Univ., Tokyo 112-8610*
[3] *Neutron Scattering Laboratory, I.S.S.P., Tokyo Univ., Ibaraki 319-1106*
[4] *Department of Physics, Aoyama Gakuin Univ., Kanagawa 229-8551*
[5] *National Institute for Materials Science, Ibaraki 305-0047*
[6] *Institute of Materials Science, Univ. of Tsukuba, Ibaraki 305-0006*

A coexistence state between ferromagnetism and superconductivity has been theoretically considered [1]. In addition, if an internal magnetic field (H_{int}) mediated by ferromagnetism is larger than a lower critical magnetic field of H_{c1} but is smaller than an upper critical field of H_{c2}, then a realization of a spontaneous vortex phase established by the H_{int} is predicted [2, 3, 4]. But there has been no experimental report on the spontaneous vortex phase so far.

$ErNi_2B_2C$ ($T_c \sim 10.5$ K) is an attractive material to verify the spontaneous vortex phase, because (a) it is the first material in which the microscopic coexistence of weak ferromagnetism (WFM) and superconductivity was directly confirmed by a neutron scattering measurements in zero field below $T_{WFM} \sim 2.75$ K [5], and (b) H_{c1} and H_{int} at 1.8 K determined by magnetization curves were about 450 and 500 Oe, respectively, then the system satisfies the condition of the spontaneous vortex phase described above [6, 7]. To examine the influence of the WFM to the flux line lattice (FLL) and the possibility of spontaneous vortex phase, we observed temperature (T) and external magnetic field (H_{ext}) dependence of the FLL by a small angle neutron scattering (SANS) technique.

In this study, we used single crystals of $ErNi_2^{11}B_2C$ ($T_c \sim 8.6$ K) grown by a floating zone method [5]. The SANS experiments, performed with the SANS-U spectrometer at JRR-3M, JAERI, Japan, employed H_{ext} applied parallel to both the orthorhombic b axis and the incident neutron beam. Incident neutrons with wavelength $\lambda_n = 11$ Å were selected by a velocity selector, and an area detector at the end of a 16 m long evacuated chamber counted neutrons scattered by the FLL. A beam stopper was set at center position to eliminate a direct beam, which result in masking a Bragg reflection at (0 0 0) position.

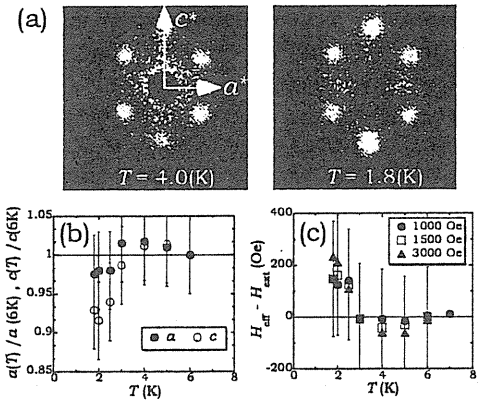


Fig. 1. (a) Typical FLL diffraction patterns observed at 4.0 and 1.8 K under $H_{ext} = 1500$ Oe after field cooled process. (b) T dependence of the FLL lattice constant under $H_{ext} = 1500$ Oe. (C) T dependence of H_{eff}-H_{ext}.

Figure 1(a) shows typical FLL diffraction patterns observed at 4.0 and 1.8 K under $H_{ext} = 1500$ Oe after a field cooled (FC) process. In all T region, rhombic FLL was observed. Nearest neighbor distances between the vortexes along the a and the c axis (lattice constant a and c) were determined to be 1280, 1860 Å at 6 K and 1250, 1730 Å at 1.8 K, respectively.

Figure 1(b) shows T dependence of FLL lattice constant a and c normalized by that at 6 K. The lattice constants started to decrease

使用施設： JRR-3 ， 装置： C1-2 (SANS-U) ， 分野： 2. Magnetism

below $\sim$ 3 K, and the change in $c(T)/c(6$ K) was larger than that in $a(T)/a(6$ K). A decrease of the lattice parameters indicates an increase of effective magnetic field (H_{eff}). H_{eff} were calculated from the lattice constant by assuming that each magnetic flux is quantized as Φ_0 ($\Phi_0 = 2.07 \times 10^{-15}$ Wb).

Figure 1(c) shows T dependence of H_{eff}, where each applied H_{ext} are already subtracted. At 1.8 K, H_{eff} increased by 200 Oe. Here, we interpret that the increase of H_{eff} below $\sim$ 3 K was caused by H_{int} made by the WFM order. However, the observed value of 200 Oe is smaller than H_{int} estimated by the observed WFM component of 0.34 μ_B/Er (cf. 500 Oe). The reason of the discrepancy is investigated at present.

With decreasing H_{ext} after FC process under H_{ext} = 3000 Oe, H_{eff} at 4 K monotonically decreased with H_{ext}, but that at 1.8 K deviated from H_{ext} below 1000 Oe and a finite H_{eff} ($\sim$ 1800 Oe) was observed at H_{ext} = 0 Oe (not shown) [8]. At this stage, we can not conclude that the remained FLL is spontaneous vortex or not, because the H_{eff} is larger than H_{int}. To obtain a final conclusion, we should clear whether the vortexes which have been made by H_{ext} is pinned or not below T_{WFM}. If the pinning force is weak enough, the remained FLL should be spontaneous vortex phase.

In conclusion, the SANS data clearly manifests that the WFM order gives raise of 200 Oe in H_{eff}. The present result strongly indicates that the spontaneous vortex phase would be realized in $ErNi_2B_2C$ if the H_{ext} could be removed smoothly.

We are grateful to Dr. M. Yethiraj for fruitful discussions and to Prof. Kohgi for giving us a chance to use their maxi orange cryostat.

References

[1] For a review, see O. Fischer, Ferromagnetic Materials (Vol. **5**, Eds. K. H. J. Buschow and E. P. Wohlfarth, Holland, Amsterdam, 1990)

[2] E. I. Blount *et al.*, Phys. Rev. Lett. **42**, 1079 (1979)

[3] M. Tachiki *et al.*, Solid State Commun. **31**, 927 (1979); ibid. **34**, 19 (1980)

[4] H. S. Greenside *et al.*, Phys. Rev. Lett. **46**, 49 (1981)

[5] H. Kawano *et al.*, J. Phys. Chem. Solids **60**, 1053 (1999)

[6] T. K. Ng *et al.*, Phys. Rev. Lett. **78**, 330 (1997)

[7] H. Kawano-Furukawa *et al.*, in *Rare Earth Transition Metal Borocarbides (Nitrides): Superconducting, Magnetic and Normal State Properties*, Vol. 14 of *NATO advanced Study Institute*, Series II, edited by K. H. Muller and V. Narozhnyi (Kluwer Academic, Dordrecht, 2001), p. 223.

[8] be in preparation.

研究テーマ：先端偏極中性子散乱によるスピン-格子物性の研究
表　題：スピンギャップ系 $TlCuCl_3$ の圧力誘起磁気秩序相における磁気構造
1-2-28

Spin Structure of the Pressure-induced Magnetic Ordered Phase in the Spin Gap System $TlCuCl_3$

A. OOSAWA, M. FUJISAWA[1], T. OSAKABE, K. KAKURAI and H. TANAKA[2]

Advanced Science Research Center, JAERI, Tokai, Ibaraki 319-1195
[1]Dep. of Phys., Tokyo Inst. of Tech., Oh-okayama, Meguro-ku, Tokyo 152-8551
[2]Res.Cent.for Low Temp.Phys.,Tokyo Inst. of Tech.,Oh-okayama,Meguro-ku,Tokyo 152-8551

Recently, the novel magnetic orderings induced by the magnetic field, the impurity ions and the pressure in spin gap systems have been energetically investigated. Quite recently, magnetization measurements were performed under hydrostatic pressures in the spin gap system $TlCuCl_3$, and the antiferromagnetic ordering was observed at zero field [1]. In order to investigate the spin structure of the pressure-induced magnetic ordered phase and the mechanism leading to the ordering, we performed neutron elastic scattering experiments under a high hydrostatic pressure.

The magnetic ground state of $TlCuCl_3$ is the spin singlet with the excitation gap $\Delta = 7.7$ K [2] and this system can be characterized as the three-dimensional strongly coupled antiferromagnetic dimer system [3].

The preparation of the single crystal of $TlCuCl_3$ has been reported in ref. 2. The sample with 0.2 cm^3 was set in the McWhan-type high-pressure cell (HPCNS-MCW®, Oval Co., Ltd.) [4]. As the pressure transmitting medium, a mixture of Fluorinert FC70 and FC77 was used. The applied hydrostatic pressure of $P = 1.48$ GPa at low temperature was determined from the pressure dependence of the lattice constants of a NaCl crystal in the sample space. Neutron elastic scattering measurements were performed using the JAERI-TAS1. The constant-$\boldsymbol{k}_i$ mode was taken with a fixed incident neutron energy E_i of 14.7 meV. Because the size of the sample has to be small due to the small sample space, collimations were set as open-80'-80'-80' in order to gain intensity. Sapphire and PG filters were placed to suppress the background by high energy neutrons, and higher order contaminations, respectively. The sample was mounted in the cryostat with its a^*- and c^*-axes in the scattering plane. The crystallographic parameters were determined as $a^* = 1.6402$ Å^{-1}, $c^* = 0.72843$ Å^{-1} and $\cos\beta^* = 0.0861$ at helium temperatures and $P = 1.48$ GPa. The lattice constants a and c become shorter by 1.5% and the angle β becomes closer to 90° than those at ambient pressure [3].

The inset of Fig. 1 shows the $\theta - 2\theta$ scans for the $\boldsymbol{Q} = (1, 0, -3)$ reflection measured at $T = 4.0$, 12.2 and 28.2 K for $P = 1.48$ GPa in $TlCuCl_3$. With decreasing temperature, the increase in the intensity of the reflection with a resolution limited width can be clearly seen. Figure 1 shows the temperature dependence of the Bragg peak intensity at the $\boldsymbol{Q} = (1, 0, -3)$ reflection for $P = 1.48$ GPa in $TlCuCl_3$. The rapid increase in the intensity with no pronounced diffuse scattering is observed below $T_N = 16.9$ K. Because it has already been observed that the pressure-induced magnetic ordering occurs at $T_N \approx 11$ K for $P \approx 0.8$ GPa in $TlCuCl_3$ [1], we can conclude that the $\boldsymbol{Q} = (1, 0, -3)$ reflection is the magnetic Bragg reflection indicative of the pressure-induced magnetic ordering. The magnetic Bragg reflections were observed at $\boldsymbol{Q} = (h, 0, l)$ with integer h and odd l. These reciprocal points are equivalent to those with the lowest magnetic excitation energy at ambient pressure [3]. This indicates that the spin gap corresponding to the lowest magnetic excitation energy closes under an applied pressure.

In order to determine the spin structure of the pressure-induced magnetic ordered phase in $TlCuCl_3$, we measured the integrated in-

原子炉：JRR-3　　装置：TAS-1(2G)　　分野：中性子散乱（磁性）

Table 1: Observed and calculated magnetic Bragg peak intensities at $T = 12.2$ and 4.0 K for $P = 1.48$ GPa in $TlCuCl_3$. The intensities are normalized to the $(0, 0, 1)_M$ reflection. R is the reliability factor given by $R = \sum_{h,k,l} |I_{cal} - I_{obs}| / \sum_{h,k,l} I_{obs}$.

	$T = 12.2$ K		$T = 4.0$ K	
(h, k, l)	I_{obs}	I_{cal}	I_{obs}	I_{cal}
$(0, 0, 1)_M$	1 ± 0.051	1	1 ± 0.051	1
$(0, 0, 3)_M$	0.018 ± 0.004	0.014	0.007 ± 0.003	0.014
$(0, 0, 5)_M$	0.085 ± 0.007	0.103	0.075 ± 0.006	0.103
$(1, 0, 1)_M$	0.014 ± 0.006	0.021	0.104 ± 0.009	0.113
$(1, 0, -1)_M$	0.127 ± 0.014	0.153	0.135 ± 0.016	0.165
$(1, 0, 3)_M$	0.037 ± 0.009	0.014	0.083 ± 0.004	0.085
$(1, 0, -3)_M$	0.448 ± 0.009	0.413	0.371 ± 0.007	0.375
$(2, 0, 1)_M$	0.006 ± 0.003	0.021	0.057 ± 0.005	0.051
$(2, 0, -1)_M$	0.114 ± 0.007	0.127	0.191 ± 0.008	0.157
R		0.08		0.06

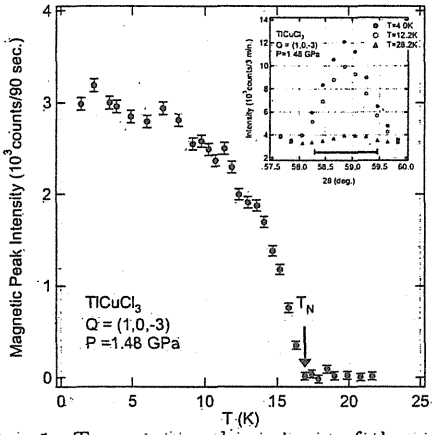


Figure 1: Temperature dependence of the magnetic Bragg peak intensity for $Q = (1, 0, -3)$ reflection measured at $P = 1.48$ GPa in $TlCuCl_3$. The inset shows $\theta - 2\theta$ scans for $Q = (1, 0, -3)$ reflection measured at $T = 4.0$, 12.2 and 28.2 K at $P = 1.48$ GPa in $TlCuCl_3$. The horizontal bar in the inset denotes the calculated instrumental resolution width.

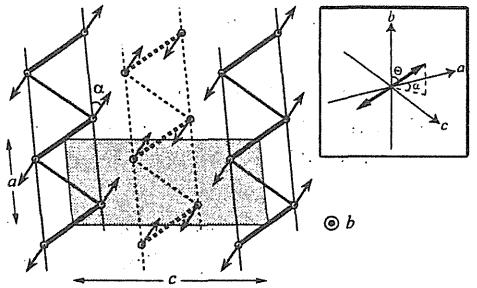


Figure 2: Projection of the spin structure observed in the pressure-induced magnetic ordered phase for $P = 1.48$ GPa in $TlCuCl_3$ onto the $a - c$ plane. The double chains located at the corner and the center of the chemical unit cell in the $b - c$ plane are represented by solid and dashed lines, respectively. The shaded area is the chemical unit cell in the $a - c$ plane. The inset shows the inclination of the ordered spin toward the b-axis. The angle α denotes the angle between the a-axis and the spin component projected onto the $a - c$ plane. The angle Θ is the angle between the spin and the b-axis.

tensities of nine Bragg reflections at $T = 4.0$, 12.2 and 28.2 K. The results are summarized in Table 1 together with the calculated intensities. To refine the magnetic structure, we carried out the same analyses as those of the field-induced magnetic ordered phase in $TlCuCl_3$ [5]. As a result, the spin structure shown in Fig. 2 with $\alpha = 42.6° \pm 1.4°$ and $\Theta = 90.0° \pm 9.0°$ for $T = 12.2$ K, and that with $\alpha = 49.5° \pm 2.4°$ and $\Theta = 58.0° \pm 3.4°$ for $T = 4.0$ K were obtained. This result means that the ordered moments lie in the $a - c$ plane just below T_N, and that they incline toward the b-axis with decreasing temperature. In the temperature dependence of the magnetic Bragg peak intensity shown in Fig. 1, there is no apparent anomaly indicative of an additional phase transition, at which the ordered moments start to incline toward the b-axis.

Comparing magnetic Bragg intensities with those of nuclear reflections, the magnitude of the ordered moment was evaluated as $\langle m \rangle = g\mu_B \langle S \rangle = 0.64(4)\ \mu_B$ at $T = 4.0$ K and $\langle m \rangle = 0.51(3)\ \mu_B$ at $T = 12.2$ K.

References

1) H. Tanaka *et al.*: Physica B (2003) in press.
2) A. Oosawa *et al.*:J.Phys.: Cond. Mat. **11**(1999)265.
3) A. Oosawa *et al.*: Phys. Rev. B **65** (2002) 094426.
4) D. B. McWhan *et al.*:Phys.Rev.B **20** (1979) 4612.
5) H. Tanaka *et al.*: J.Phys.Soc.Jpn. **70** (2001) 939.

研究テーマ：$Cr_{1-x}Te$系および関連物質系の磁気構造
表　題：$TbBaCo_2O_{5.5}$の逐次相転移
1-2-29

Successive Phase Transitions of $TbBaCo_2O_{5.5}$

M. Soda, Y. Yasui, T. Fujita, T. Miyashita, M. Ito, S. Iikubo, M. Sato and K. Kakurai[1]

Department of Physics, Nagoya University, Chikusa-ku, Nagoya 464-8602
[1]Advanced Science Research Center, JAERI, Tokai, Ibaraki 319-1195

Co^{3+} ions in Co-oxides often exhibit the spin state changes. They have the low spin (LS: S=0) ground state and the state changes to the intermediate spin (IS: S=1) state or the high spin (HS: S=2) state with increasing temperature T. This indicates that the energy difference δE between the spin states is small. Because the energy splitting between the t_{2g} and e_g orbital energies due to the crystal field generally increases with decreasing volume of the CoO_6 octahedra, δE can be controlled by the volume change of the octahedra and therefore we can seek a variety of physical behavior in the system related to the spin state change.

The perovskite oxides $R_{1-x}A_xCoO_{3-\delta}$ obtained by the substitution of R with divalent atoms A=Sr, Ba and Ca often exhibit ferromagnetic and metallic properties for small δ with increasing doping concentration x due to the double exchange interaction.[1)] When Ba and relatively small trivalent elements are chosen as A and R, respectively, the system forms the oxygen-deficient perovskite structure, in which the oxygen vacancies are ordered.[2-4)] Among such oxides, $RBaCo_2O_5$ ($\delta \sim 0.5$) exhibits transitions to the antiferromagnetic ordering and then, to the charge ordered state of Co^{2+} and Co^{3+}. $RBaCo_2O_{5.5}$ ($\delta \sim 0.25$) also exhibits several transitions. However, only restricted information is available on both the structural and the magnetic properties.

In the present work, neutron scattering studies have been carried out on a single crystal of $TbBaCo_2O_{5.5}$ to collect basic information on the spin state of Co ions and the magnetic structures. The oxygen-deficient perovskite structure of this system is formed by the linkage of alternating CoO_6 octahedra and CoO_5 pyramids along the b-axis. It has been reported that it has the orthorhombic unit cell, where Ba and Tb atoms are in different c-planes. The unit cell volume is described by $\sim a_p \times 2a_p \times 2a_p$, a_p being the lattice parameter of the cubic perovskite cell. With decreasing T, the metal-insulator (MI) transition takes place at $T_{MI} \sim 340$ K, the ferromagnetic transition occurs at $T_C \sim 280$ K, and then ferromagnetic phase suddenly changes to antiferromagnetic one at $T_N \sim 260$ K. Although transitions have been found at lower temperatures, too, in the present neutron diffraction studies, we mainly report here results of studies on the magnetic structures at 270 K and 250 K, where the spin states of Co ions within the CoO_6 octahedra and the CoO_5 pyramids are basically clarified.

Neutron measurements were carried out by using the triple axis spectrometer TAS-2 at JRR-3M. The single crystal of $TbBaCo_2O_{5.5}$ was oriented with the [100] (or [010]) axis vertical, where both $(0,k,l)$ and $(h,0,l)$ points in the reciprocal space could be observed due to the coexistence of the $\boldsymbol{a}^*$- and $\boldsymbol{b}^*$-domains. Several $0kl$ reflections can be distinguished from $h0l$ reflections by the difference between the lattice parameter a and $b/2$ (The parameter a is slightly smaller than $b/2$.).

The intensities of neutron Bragg reflections of $TbBaCo_2O_{5.5}$ have been measured in the temperature range of 7-370 K. In addition to the fundamental Bragg reflections for the unit cell with the size of $\sim a_p \times 2a_p \times 2a_p$, several superlattice reflections have been found. The points at which the reflections were observed at 7 K in the reciprocal space are shown in Fig. 1(a). ($\boldsymbol{Q}$=$(0,k,l)$ may be $(k/2,0,l)$.) The temperature dependence of the peak intensities of the typical fundamental and superlattice reflections are shown in Figs. 1(b) and 1(c), respectively. With decreasing T from

原子炉：JRR-3　　装置：TAS-2(T2-4)　　分野：中性子散乱（磁性）

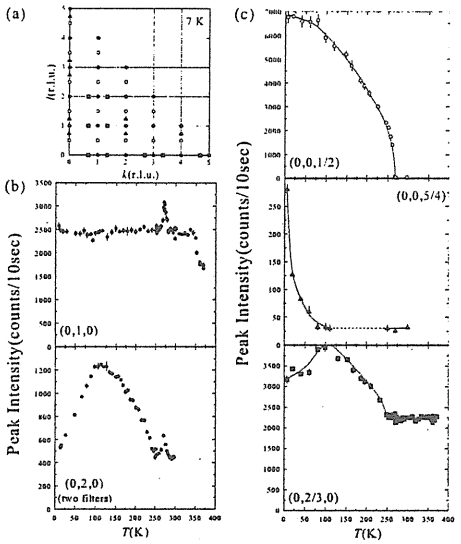


Figure 1: (a) Fundamental or superlattice points of the unit cell with the size of $\sim a_p \times 2a_p \times 2a_p$ in the reciprocal space at 7 K. (b) and (c) The peak intensities of several reflections are shown against T.

the temperature above 350 K, the intensities of several nuclear Bragg reflections change at $T_{MI} \sim 340$ K, and at $T_C \sim 280$ K additional reflections appear at several nuclear Bragg points. The additional reflections are considered to be magnetic, as is confirmed later by detailed analyses and corresponds to the appearance of the ferromagnetic moment. With further decreasing T, the additional component suddenly disappears at $T_N \sim 260$ K and the superlattice peaks corresponding to the period of $2c$ ($\sim 4a_p$) along the c-axis appear [$\boldsymbol{Q}$=(0,k,1/2), (0,k,3/2), etc.]. At $T \sim 100$ K, superlattice peaks corresponding to the period of $4c$ along the c-axis appear [$\boldsymbol{Q}$=(0,0,1±1/4), (0,0,3±1/4), (0,2,1±1/4), etc.] with decreasing T. The former group of the superlattice reflections may be magnetic, while we cannot distinguish if the latter superlattice reflections are magnetic or not. It should be also noted that the superlattice reflections corresponding to the modulation vector $\boldsymbol{q}=\boldsymbol{a}^*/3$ (the period of $\sim 3a_p$ in the real space) are observed even at temperatures higher than T_{MI}. We have not clarified detailed pattern of the modulation in

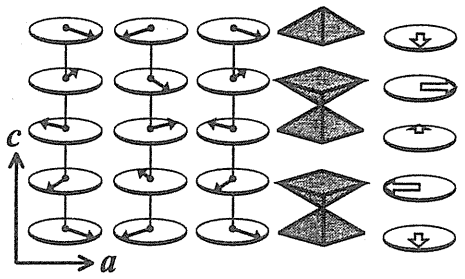


Figure 2: Schematic magnetic structure of only CoO_5 pyramids of $TbBaCo_2O_{5.5}$ at 250 K(in the antiferromagnetic phase). The open arrows drawn in the right side of the figure show the direction of the net moment of the CoO_2 layer. All Co^{3+} ions of CoO_6 octahedra are in the low spin state.

the present study. Furthermore the data of Fig. 1(b) suggest the existence of structurural transitions in the present system at three temperatures, T_{MI}, ~250 K and ~100 K

The magnetic structures have been determined at T=270 K (ferromagnetic phase) and T=250 K (antiferromagnetic one). We found that Co^{3+} ions of CoO_6 octahedra are in the low spin state (S=0) at both temperatures. Co^{3+} ions of CoO_5 pyramids are in the intermediate spin state (S=1) and their moments have the coplanar structure. At T=270 K, the Co^{3+} moments of CoO_5 pyramids have the canted structure, where the direction of the ferromagnetic moments is along the a-axis. At T=250 K, the structure changes to the helical one, where the modulation vector is along the c-axis and the net moment of each CoO_2 layer has nonzero value. This magnetic structure at T=250 K is shown in Fig. 2. We stress that the determination of the spin states of Co^{3+} within the CoO_6 octahedra and the CoO_5 pyramids has been first carried out in the present study.

References

1) H. Masuda *et al.*: J. Phys. Soc. Jpn. **72** (2003) 873.
2) A. Maignan *et al.*: J. Solid State Chem. **142** (1999) 247.
3) D. Akahoshi *et al.*: J. Solid State Chem. **156** (2001) 355.
4) H. Kusuya *et al.*: J. Phys. Soc. Jpn. **70** (2001) 3577.

研究テーマ： $Ho_{1-x}Tb_xB_2C_2$ での長周期磁気秩序相
表題： $Ho_{1-x}Tb_xB_2C_2$ での長周期磁気秩序相

1-2-30 Long Periodic Magnetic Phase of $Ho_{1-x}Tb_xB_2C_2$

K. Ido[1], A. Tobo[1], K. Ohoyama[1], H. Onodera[1] and Y. Yamaguchi[1]
[1] *Institute for Materials Research, Tohoku University, Sendai, Miyagi, 980-8577*

HoB_2C_2 undergoes an antiferromagnetic (AFM) ordering at T_N = 5.9 K and an antiferroquadrupolar (AFQ) ordering at T_Q = 4.5 K.[1] The magnetic structure in the AFM phase is a long periodic one described as a propagation vector k=[1+δ δ δ'] ($\delta \sim 0.1$, $\delta' \sim 0.04$), and magnetic diffuse components around k are observed.[2] TbB_2C_2 undergoes only an AFM ordering at T_N = 21.7 K.[3] An AFQ ordering transition is induced by external magnetic fields. The propagation vectors in the main AFM component are described as k_0=[0 1 1/2], k_2=[0 0 1/2] and k_3=[1+δ δ 0] (δ = 0.13).[3] Diffuse components are also observed around k_3 satellite peaks like the AFM phase in HoB_2C_2.

Anomalous magnetic properties in the AFM phase of HoB_2C_2 and TbB_2C_2 are quite similar in the long-periodic magnetic structure and diffuse component. These magnetic anomalies are possibly due to influence of quadrupolar interactions. Specific heat measurements for $Ho_{1-x}Tb_xB_2C_2$ shows that T_Q is hardly dependent on the concentration from x = 0.0 to 0.6 while peak height of specific heat at T_Q gradually decreases.[4] The results indicates that the Tb^{3+} ions seems to be cooperative to the AFQ ordering. Then we performed powder neutron diffraction on $Ho_{1-x}Tb_x^{11}B_2C_2$ to study the effect of Tb^{3+} substitution on the AFQ+AFM ordering phase in HoB_2C_2.

Figure 1 shows powder neutron diffraction patterns performed at 2.2 K using HERMES (T1-3) at JRR3M in JAERI(Tokai). The diffraction pattern of x = 0.2 is nearly the same with that of the AFQ+AFM phase of HoB_2C_2 which is described as the four propagation vectors [1 0 0], [1 0 1/2], [0 0 1/2] and [0 0 0]. However, the satellite peaks described as k=[1+δ δ δ'] emerge in x = 0.2. As x increases, the intensities of the satellite peaks become larger, while the original Bragg peaks described as k=[1 0 0] almost disappears for x = 0.6. For x = 0.8, however, all satellite peaks become small. The powder pattern of x = 0.2 is nearly same with that of the AFM phase in TbB_2C_2.

Specific heat measurements clarified that the ground state is the AFQ+AFM phase for x = 0.0 to 0.6. However the AFQ+AFM phase for x = 0.2 to 0.6 are long periodic ones. The competition between HoB_2C_2 and TbB_2C_2 magnetic interactions seems to increase the long periodic components.

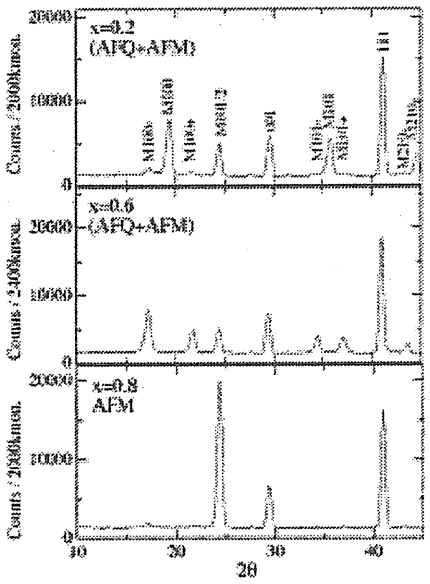


Fig. 1. Powder neutron diffraction patterns of $Ho_{1-x}Tb_x^{11}B_2C_2$.

References

[1] H. Onodera *et al.*: J. Phys. Soc. Jpn. **68** (1999) 2526.
[2] K. Ohoyama *et al.*:J. Phys. Soc. Jpn. **69** (2000) 3401.
[3] K. Kanako *et al.*: J. Phys. Soc. Jpn. **70** (2001) 3112.
[4] K. Ido *et al.*:J. Phys. Soc. Jpn. **71** (2002) 83.

使用施設：JRR-3' 装置： HERMES(T1-3)， 分野： 2. Magnetism

研究テーマ：先端偏極中性子散乱によるスピン-格子物性の研究
表　題：$La_2CuO_{4+\delta}$ における静的磁気相関

1-2-31

Static Spin Correlations in Lightly-Doped $La_2CuO_{4+\delta}$

M. MATSUDA, M. FUJITA[1] and K. YAMADA[1]

Advanced Science Research Center, JAERI, Tokai, Ibaraki 319-1195
[1]Institute for Chemical Research, Kyoto University, Gokasho, Uji 610-0011

In lightly-doped $La_{2-x}Sr_xCuO_4$ ($0< x <0.02$), which shows coexistence of a three-dimensional antiferromagnetic (AF) long-range ordered phase and a spin-glass (SG) phase at low temperatures, it was reported that the SG phase in the coexistence region shows a diagonal spin modulation [1] as in the pure spin-glass phase in $La_{2-x}Sr_xCuO_4$ ($0.02\leq x \leq 0.055$). Most interestingly, electronic phase separation of the doped holes occurs so that some regions with hole concentration $c_h \sim 0.02$ and the rest with $c_h \sim 0$ are formed, which is predicted for a doped antiferromagnet theoretically. [2] Some clusters with $c_h \sim 0.02$ exhibit diagonal stripe correlations while the rest of the crystal with $c_h \sim 0$ shows 3D AF order.

As the next step, we performed neutron scattering experiments in lightly-doped $La_2CuO_{4+\delta}$. Since the hole concentration can be controlled in a very lightly-doped region in this system, it is possible to check whether the phase separation into the AF and SG phases are observable in this region. Another interesting thing is whether the hole doping by Sr substitution is equivalent to that by excess oxygen. It can be checked by measuring the properties of the diagonal spin modulation, that is, incommensurability and peak width.

The single crystal of $La_2CuO_{4+\delta}$ was grown by the traveling solvent floating zone (TSFZ) method. The dimensions of the rod shaped crystal were $\sim 5\Phi \times 30$ mm^3. The crystal has two twins, which are estimated to be equally distributed based on the ratio of the nuclear Bragg peak intensities from both twins. The crystal was first annealed in 1 bar Ar atmosphere at 900 °C for 24 h. This sample is considered to be almost stoichiometric ($\delta \sim 0$) and shows a sharp AF transition at 320 K. The crystal was also annealed in 1 bar oxygen atmosphere at 900 °C for 72 h. This sample is considered to have excess oxygen $\delta \sim 0.015$, which is estimated in the analogy of the result in Ref. [3], and shows a sharp AF transition at 270 K. This sample also shows minor superconducting phase with $T_c \sim 35$ K.

The neutron scattering experiments were carried out on the cold neutron three-axis spectrometers LTAS and the thermal neutron three-axis spectrometer TAS2.

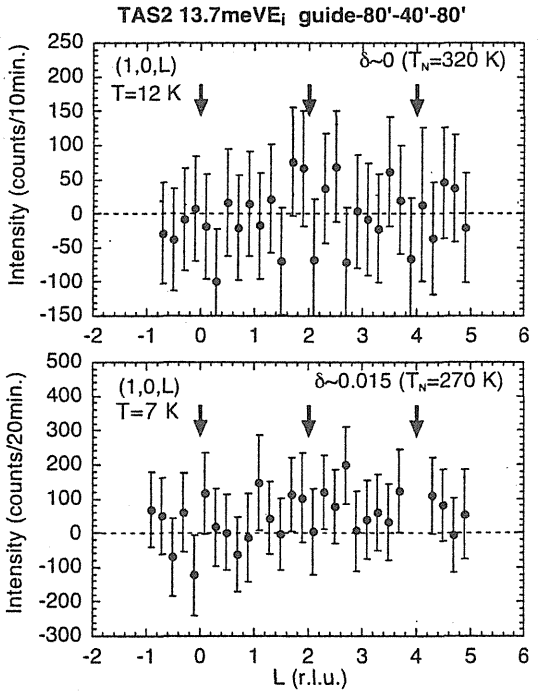


Figure 1: Elastic scans along $(1,0,L)$ at T=12 and 7 K in La_2CuO_4 and $La_2CuO_{4+\delta}$, respectively. Background intensities measured at T=50 K have been subtracted. The arrows show the positions where broad magnetic peaks originating from the SG phase are expected.

原子炉：JRR-3　　装置：TAS-2(T2-4), LTAS(C2-1)　　分野：中性子散乱（磁性）

Figure 1 shows elastic scans along $(1,0,L)$ perpendicular to the CuO_2 planes in La_2CuO_4 and $La_2CuO_{4+\delta}$. As shown in Ref. [1], if the SG phase appears at low temperatures, broad magnetic peak should be observed at (1,0,even). Magnetic signal is not appreciable in both samples, indicating that the volume fraction of the SG phase is negligibly small even in the sample with $La_2CuO_{4+\delta}$.

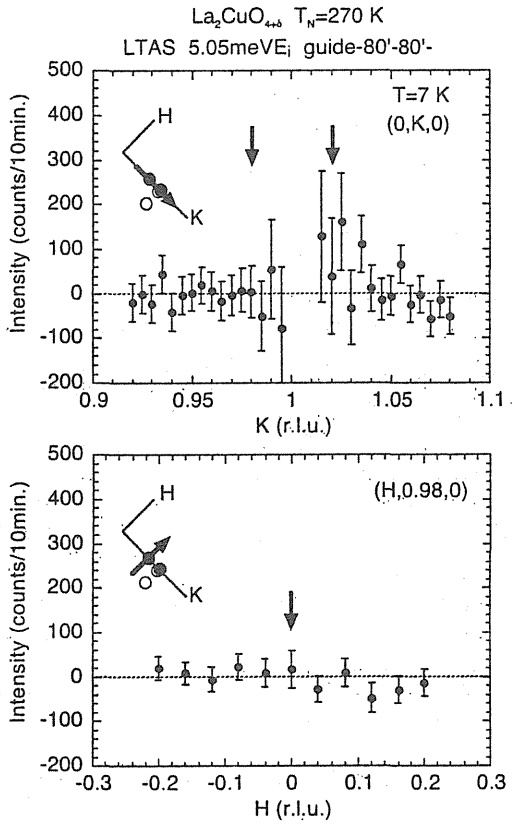


Figure 2: Elastic scans along $(0,K,0)$ and $(H,0.98,0)$ at T=7 K in $La_2CuO_{4+\delta}$ (T_N=270 K). The data measured at T=50 K are subtracted as background intensities. The arrows show the positions where broad magnetic peaks originating from the SG phase are expected.

In order to confirm absence of the magnetic signal originating from the SG phase, we also performed neutron scattering experiments in the $(HK0)$ scattering zone. Figure 2 shows elastic scans along $(0,K,0)$ and $(H,0.98,0)$ in $La_2CuO_{4+\delta}$. The error bar is large around (0,1.01,0) because a tail of the intense magnetic Bragg peak exists at this position. The magnetic peak originating from the SG phase is expected around (0,0.98,0) and (0,1.02,0). As in the results in the $(H0L)$ scattering zone, there is no sign of magnetic peaks originating from the SG phase.

Since $La_{1.99}Sr_{0.01}CuO_4$ shows a Néel temperature of 240 K, [1] the effective hole concentration in $La_2CuO_{4+\delta}$ (T_N=270 K) is estimated to be ~0.005, which is just between La_2CuO_4 and $La_{1.99}Sr_{0.01}CuO_4$. If the volume fraction of the SG phase is proportional to the hole concentration, ~25% of the total volume should be in the SG phase in $La_2CuO_{4+\delta}$ at low temperatures. From the data shown above, an upper limit for the volume fraction of the SG phase is estimated to be ~1%, suggesting that there may exist a threshold to realize the phase separation into the AF and SG phases.

In $La_2CuO_{4+\delta}$ system with $0.01 < \delta < 0.055$, the samples phase separates into hole-poor phase (0.01) and hole-rich phase (0.055) [4] so that samples with the hole concentration range cannot be available at low temperatures. Therefore, it is not possible to check whether the hole doping by Sr substitution is equivalent to that by excess oxygen. $La_{2-x}Bi_xCuO_{4+\delta}$ system, which does not show macroscopic phase separation and hole concentration at low temperatures gradually changes, [3] is appropriate to study the magnetic properties in the hole concentration range. We plan to perform neutron scattering experiments in the system in future.

References

1) M. Matsuda, M. Fujita, K. Yamada, R. J. Birgeneau, Y. Endoh andG. Shirane: Phys. Rev. B **65** (2002) 134515.
2) S. A. Kivelson and V. J. Emery: *Proceedings of the Los Alamos Symposium – 1993 : Strongly Correlated Electronic Materials*, ed K. S. Bedell *et al.* (Addison-Wele 1994), p. 619.
3) S. Wakimoto, C.-H. Lee, K. Yamada, Y. Endoh and S. Hosoya: J. Phys. Soc. Jpn. **65** (1996) 581.
4) B. O. Wells, Y. S. Lee, M. A. Kastner, R. J. Christianson R. J. Birgeneau, K. Yamada, Y. Endoh and G. Shirane: Science **277** (1997) 1067.

研究テーマ： TbB_2C_2 における散漫散乱の３次元構造の精密測定
表題： 正方晶 TbB_2C_2 における特異な磁気散漫散乱

1-2-32 Unusual Magnetic Diffuse Scattering in the Tetragonal TbB_2C_2

K. Kaneko[1], K. Ohoyama[2], R. Kiyanagi[3], H. Kimura[3], Y. Noda[3], H. Onodera[2] and Y. Yamaguchi[2]
[1] *Advanced Science Research Center, Japan Atomic Energy Research Institute, Tokai, Naka, Ibaraki 319-1195*
[2] *Institute for Materials Research, Tohoku University, Sendai 980-8577*
[3] *Institute of Multidisciplinary Research for Advanced Materials, Tohoku University, 980-8577*

The existence of the strong antiferro-quadrupolar (AFQ) interaction is characteristic to the tetragonal RB_2C_2 (R=rare earth) compounds. TbB_2C_2, where the effect of AFQ interaction is prominent under magnetic fields, shows an antiferromagnetic (AFM) order at T_N=21.7 K at H=0[1, 2]. Note that the unconventional magnetic diffuse scattering was observed in the AFM state, which is common to the AFM ordered state in HoB_2C_2[3, 4]. The diffuse scattering has an flat intensity surrounded by the satellite peaks which is represented by the incommensurate component $\boldsymbol{k}_L$=(1±δ, ±δ,0), where δ=0.13. In the present work, we provide the detailed diffuse scattering profile in three dimension studied on the 4-circle neutron diffractometer.

For sample preparation, the stoichiometric amounts of constituents, Tb, ^{11}B and C were synthesized through the argon arc melting. Single-crystalline sample of $Tb^{11}B_2C_2$ was grown by the Czochralski pulling method using a tetra-arc furnace. Neutron scattering experiments were carried out on the 4-circle diffractometer, FONDER installed at JRR-3 in Japan Atomic Energy Research Institute, Tokai[5].

Figure 1 shows the line scan along the (h 0 0) direction through (0 1 + δ, l) (l=0, 0.7, 0.12) measured at 8 K. At l=0 the diffuse scattering between h=-0.14~0.14, together with the sharp intense satellite peaks at h = ±0.13, was clearly observed. The sharp peak at h=0 is due to the multiple scattering. In higher l, the diffuse scattering component remains even at l=0.07, while the satellite peak disappears rapidly . Note that the diffuse scattering profile is characteristic; almost flat intensity was obtained between h = −0.14~0.14. The intensity of this uniform scattering reaches the background level at l=0.12.

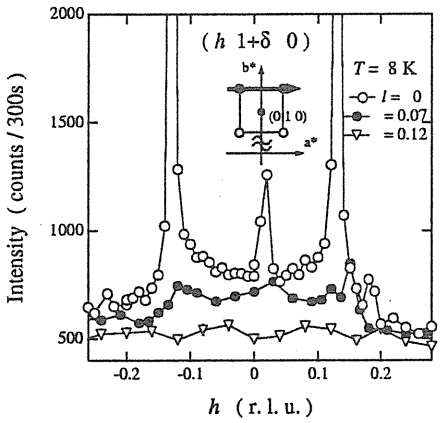


Fig. 1. The line scan along the (h 0 0) direction through (0 1 + δ l) with l=0, 0.07 and 0.12 measured at 8 K. The schematic scan trajectory is given as an inset.

The present experiments clarify that the diffuse scattering around (0 1 0) expands along the c direction as well as the (h k 0) plane. The diffuse scattering has an almost flat intensity between l = ±0.9 and h, k = ±0.14, indicating the diffuse scattering intensity centered at (0 1 0) forms an cubic in reciprocal space though the crystal symmetry of TbB_2C_2 is tetragonal. Further analysis is now in progress.

References

[1] K. Kaneko *et al.*: J. Phys. Soc. Jpn. **70** (2001) 3112.
[2] K. Kaneko *et al.*: Phys. Rev. B **68** (2003) in press.
[3] K. Kaneko *et al.*: J. Phys. Soc. Jpn. **71** (2002) 3024.
[4] A. Tobo *et al.*: Physica B **312-313** (2002) 853.
[5] Y. Noda *et al.*: J. Phys. Soc. Jpn. **70** (2001) Suppl. 456.

使用施設：JRR-3　装置： T2-2 (FONDER)， 分野： 2. Magnetism

研究テーマ：多重極限環境下における中性子散乱実験法の研究
表　題：$CeAgSb_2$ の磁性の研究
1-2-33

Magnetic and Crystal Structure of $CeAgSb_2$

S. ARAKI[1], N. METOKI[1,2] A. THAMIZHAVEL[3] and Y. ŌNUKI[1,3]

[1]Advanced Science Research Center, JAERI, Tokai, Ibaraki 319-1195
[2]Department of Physics, Tohoku University, Aoba, Sendai 980-8578
[3]Graduate School of Science, Osaka University, Toyonaka, Osaka 560-0043

$CeAgSb_2$ with tetragonal crystal structure orders at $T_c = 9.6$ K with a small net ferromagnetic component of $0.33\mu_B$/Ce parallel to the c-axis [1]. The in-plain magnetization below T_c increases linearly with magnetic field and reached about $1.2\mu_B$ at 3 T [2]. This induced moment is much larger than the spontaneous moment along the c-axis. Therefore, the antiferromagnetic (AFM) and/or complex magnetic structure was suggested to be the origin of the unusual magnetic properties. However, no AFM peak has been reported from neutron diffraction experiment [1]. The purpose of this study is to clarify the crystal and magnetic structure in $CeAgSb_2$.

The neutron diffraction experiments were carried out using TAS-1 and HRPD. A large amount of polycrystalline sample, 30 g, and single crystal with 0.85 g were used.

$CeAgSb_2$ crystallizes in the tetragonal structure with space group P4/nmm. Two controversial models have been proposed so far for the crystal structure of $CeAgSb_2$. Sologub *et al.* [3] and Brylak *et al.* [4] reported that $CeAgSb_2$ has the $ZrCuSi_2$-type structure, where Ce, Ag and Sb atoms occupy the crystallographical 2c (Ce), 2b (Ag), 2a (Sb1), and 2c (Sb2) sites. On the other hand, André *et al.* [1] attributed their neutron powder diffraction data to the same type of structure, but assumed different site occupations, namely, 2a (Ag) and 2b (Sb1) sites. This controversy is due to the weak contrast between Ag and Sb atoms both for X-rays and neutrons. Figure 1 shows the high-resolution neutron powder diffraction data of $CeAgSb_2$ measured at room temperature in the paramagnetic state. This powder diffraction data can be explained by both Sologub- and André-type structures, although reliable parameters for Sologub's model are slightly better than the ones for André's model. In order to clarify the crystal structure of $CeAgSb_2$, the weak (001), (002), (003), and (005) reflections from a large polycrystalline sample (30 g) and a high-quality single-crystalline sample were measured with very good statistics on the TAS-1 spectrometer. The observed integrated intensities are plotted in the inset of Fig. 1. The agreement of the experimental data with the calculated intensity for Sologub's model (solid line) is clearly better than that of André's model denoted by the dashed line. Therefore we conclude that Sologub's model describes the crystal structure of $CeAgSb_2$. The high-resolution neutron powder diffraction pattern in Fig. 1 was analyzed by means of Rietveld refinement with RIETAN-2000 [5] assuming Sologub's model. The fit of the data is satisfactory. The obtained structural parameters are listed in Ta-

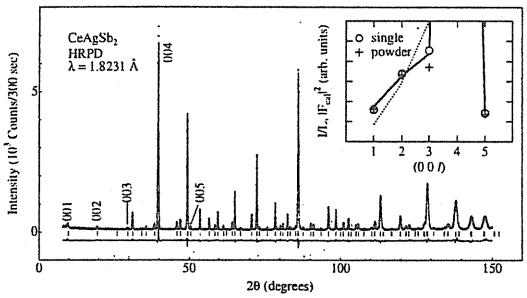


Figure 1: Neutron powder diffraction pattern at room temperature in $CeAgSb_2$. The inset shows the integrated intensities of the (00l) reflections at 12 K. The bold line and dashed line denote the square of the structure factor calculated based on the Sologub-type structure and André-type structure, respectively.

原子炉：JRR-3　　装置：TAS-1(2G)　　分野：中性子散乱（磁性）

ble 1.

Figure 2 shows the neutron powder diffraction pattern at $T = 4$ K and 12 K, which are below and above the Curie temperature $T_c = 9.6$ K, respectively. The low-temperature data after subtracting the high-temperature data are also plotted in Fig. 2. The clear ferromagnetic scattering from Ce moments were superposed on the (101) and (110) nuclear peaks. The ferromagnetic scattering on the (103) and (112) may also be observed, however, which are masked by the large nuclear scattering. Some small cusp-like structure, e.g., 2θ=36°, seen in Fig. 2 were investigated again with higher statics, however, these peak structures were not reproducible. Therefore, we conclude that no antiferromagnetic scattering was observed in our neutron powder diffraction experiment. The inset of Fig. 2 shows the integrated intensity divided by the Lorentz factor. The observed data can be explained by the ferromagnetic component of $0.41(3)\mu_B$ parallel to the c-axis. This is consistent with previous neutron scattering and magnetization studies. [1, 2] Although the statistical error of our neutron powder diffraction data is much smaller than that in the previous study [1], we could observe no trace of antiferromagnetic or incommensurate magnetic satellite peaks within the accuracy range of the order of $0.09\mu_B$/Ce. This value is much smaller than the in-plane antiferromagnetic component on the order of $1\mu_B$ expected from the magnetization measurements. An antiferromagnetic peak was also searched for in

Table 1: Crystallographic data in $CeAgSb_2$ obtained by Rietveld refinement of neutron powder diffraction data in Fig. 1.

a=4.3675(4) Å, c=10.708(1) Å				
Atom	site	x	y	z
Ce	2c	1/4	1/4	0.2388(2)
Ag	2b	3/4	1/4	1/2
Sb1	2a	3/4	1/4	0
Sb2	2c	1/4	1/4	0.6734(3)

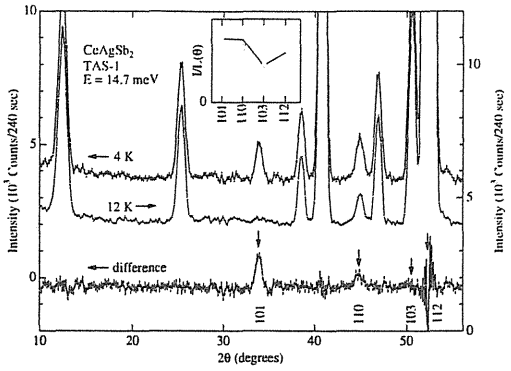


Figure 2: Neutron powder diffraction patterns below (4 K) and above (12 K) $T_c = 9.6$ K in $CeAgSb_2$. The magnetic diffraction pattern, which is obtained as the difference of patterns between 4 K and 12 K, is also plotted. The inset shows the integrated intensity of the magnetic scattering.

the case of the single-crystalline sample. Although the diffraction experiments with a single crystal presents a much higher sensitivity with low background, no trace of the antiferromagnetic peak was observed in the accuracy range of 3×10^{-3} of the (101) ferromagnetic peak along some high symmetry axes on the (hhl), $(h0l)$, and $(hk0)$ scattering planes. We also performed a mesh scan on the $(h0l)$ scattering plane. However no antiferromagnetic or SDW peak was detected.

We conclude that $CeAgSb_2$ has a simple ferromagnetic ground state with the ordered moment of $0.41\mu_B$ along the c-axis.

References

1) G. André, F. Bourée, M. Kolenda, B. Leśniewska, A. Oleś and A. Szytuła: Physica B **292** (2000) 176.
2) K.D. Myers, S.L. Bud'ko, I.R. Fisher, Z. Islam, H. Kleinke, A.H. Lacerda and P.C. Canfield: J. Magn. Magn. Mater. **205** (1999) 27.
3) O. Sologub, H. Noël, A. Leithe-Jasper, P. Rogl and O.I. Bodak, J. Solid State Chem. **115** (1995) 441.
4) M. Brylak, M. H. Möller and W. Jeitschko, J. Solid State Chem. **115** (1995) 305.
5) F. Izumi and T. Ikeda, Mater. Sci. Forum, **321-324** (2000) 198.

研究テーマ：熱中性子三軸スピンエコー実験方法の開発
表題：熱中性子スピンエコー法による $LuFe_2O_4$ の磁気散漫散乱の研究

Thermal neutron spin echo study on the magnetic diffuse scattering in $LuFe_2O_4$

K. Kakurai, M. Nishi[1], K. Nakajima, Y. Ishii, S. Nagai[1], N. Ikeda[2], H. Kito[3] and Y. Yamada[4]

1-2-34 *ASRC, JAERI, Tokai, 319-1195;[1]NSL, ISSP, University of Tokyo, Tokai, 319-1106,*

[2]JASRI, HYOGO Japan, 679-5198, [3]NRIM, Tsukuba, 305-0047, [4]ARCSE, Waseda Univ., Tokyo, 169-0072

$LuFe_2O_4$ belongs to a class of materials expressed by RFe_2O_4, R being rare-earth metals[1]. The crystals of these materials belong to the rhombohedral system. The Fe ions are arranged to form the hexagonal double layers and stack in the sequence of (AB), (CA), (BC),... along the rhombohedral unique axis. The average valence of the Fe ions is expected to be $Fe^{+2.5}$ in these materials and hence a mixed valence state of Fe^{2+} and Fe^{3+} ions occupying the equivalent Fe sites on the hexagonal plane with equal probability is expected. Recently Y. Yamada et al.[2] reported the sequential charge ordering in $LuFe_2O_4$ observed by means of X-ray scattering characterized by an 3-D incommensurate charge-density wave state in the lowest temperature phase for T<320K.

The preliminary neutron scattering study on this same sample indicated the existence of considerable magnetic correlation with rather strong diffuse scattering at the lowest temperature. The triangular arrangements of the magnetic Fe-ions may suggest the possible dynamical nature of the diffuse scattering due to the frustration. We thus performed thermal neutron spin echo experiment on the PONTA spectrometer installed at the 5G port of JRR-3M to investigate the nature of the magnetic diffuse scattering.

Figure 1 shows the non spin flip (NSF) scattering along Q=(1/3,1/3,l) at RT and T=7.2K. In the spin echo configuration the guide field at the sample is in the scattering plane perpendicular to the scattering vector. At low T one can clearly recognize a peak structure with diffuse component. In fig. 2 the T-dependence of the relaxation rates as determined by the spin echo experiment at some typical Q-points is summarized. The broken line indicates the experimental energy resolution of ~1μeV. One can conclude that the diffuse scattering observed at low T is of static nature at least within the time constant of this experiment. The magnetic components at different wave vectors seem to freeze differently over a rather broad temperature range of 250 to 200K.

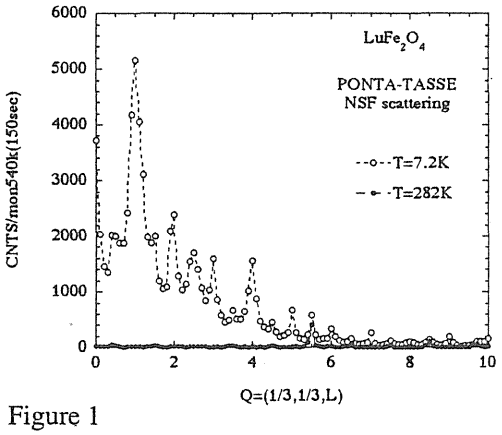


Figure 1

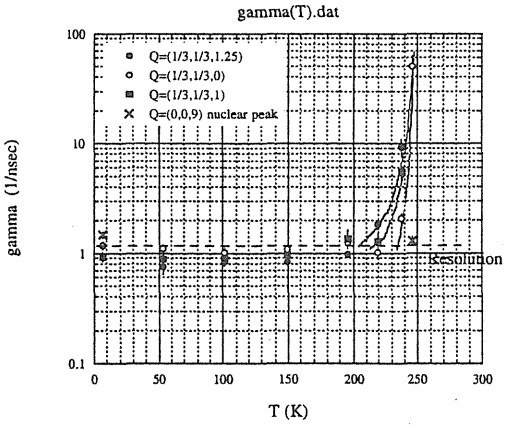


Figure 2

References

[1]N. Kamizuka, E. Muromachi and K. Shiratori, in Handbook on the Physics and Chmistry of Rare Earths, ed. by K.A. Gschneidner, Jr. and L. Eyring(Elsevier, Amsterdam, 1990), Vol.13,p.283ff.

[2]Y. Yamada et al., Phys. Rev. B62 (2000) 12167.

使用施設：JRR-3　　装置： PONTA(5G), 分野 Magnetism

研究テーマ：多重極限環境下における中性子散乱実験法の研究
表　題：$CeAgSb_2$ の磁性の研究

1-2-35

Magnetic Excitations in $CeAgSb_2$

S. ARAKI[1], N. METOKI[1,2] A. THAMIZHAVEL[3] and Y. ŌNUKI[1,3]

[1]Advanced Science Research Center, JAERI, Tokai, Ibaraki 319-1195
[2]Department of Physics, Tohoku University, Aoba, Sendai 980-8578
[3]Graduate School of Science, Osaka University, Toyonaka, Osaka 560-0043

$CeAgSb_2$ with tetragonal crystal structure orders at $T_c = 9.6$ K with a small net ferromagnetic component of $0.33\mu_B$/Ce parallel to the c-axis [1]. The in-plain magnetization below T_c increases linearly with magnetic field and reached about $1.2\mu_B$ at 3 T [2]. This induced moment is much larger than the spontaneous moment along the c-axis. Therefore, the antiferromagnetic (AFM) and/or complex magnetic structure was suggested to be the origin of the unusual magnetic properties. However, no AFM peak has been reported from neutron diffraction experiment [1]. Our recent experiment also revealed that $CeAgSb_2$ has a simple ferromagnetic ground state [4]. The purpose of this neutron scattering study is to reveal the origin of the unusual magnetization curve.

The neutron scattering experiments were carried out using TAS-1 at $E_f = 14.7$ meV and LTAS at $E_f = 4.0$ meV. A large amount of polycrystalline sample, 30 g, and single crystal with 0.85 g were used. The neutron diffraction experiment under magnetic fields was performed using TAS-2 and 5 T horizontal superconducting magnet.

Figure 1 shows the neutron inelastic scattering spectra on the polycrystalline sample of $CeAgSb_2$. At $T = 4$ K, we observed conspicuous excitation peaks at $\Delta E = 1.9$ and 5.9 meV, respectively. The q dependence of the intensity of these peaks is consistent with the square of the $4f$ magnetic form factor in the Ce^{3+} ion. This means that these inelastic peaks are due to magnetic excitations. On elevating the sample temperature to $T = 12$ K, just above $T_c = 9.6$ K, the excitation peak at 1.9 meV disappeared. This means that this peak is due to the spin wave excitation.

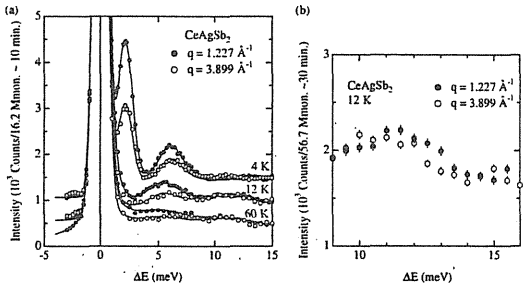


Figure 1: Inelastic neutron scattering spectra measured for a polycrystalline sample of $CeAgSb_2$.

The 5.2 meV peak, which corresponds to the 5.9 meV excitation at 4 K, survived in the paramagnetic state, although the peak became weak and broad. At a much higher temperature, $T = 60$ K, the excitation peak spread out in a wide energy range. From the q and temperature dependence, we concluded that the 5.2 meV peak is due to crystalline electric field (CEF) excitation. In addition to these clear excitation peaks, a very weak CEF excitation at $\Delta E = 12.5$ meV was also observed at 12 K, as shown in Fig. 1 (b). Recently, these two CEF excitations were also observed by Adroja *et al.* on a HET spectrometer at ISIS, independent of our work [3]. In CEF with tetragonal symmetry, the J multiplet of the Ce^{3+} ion splits into three doublets. Therefore the observation of two CEF excitation peaks is reasonably understood in terms of the excitation between the ground state and the two excited levels. We concluded that the ground state is $|\pm\frac{1}{2}\rangle$, the first and the second level are dominated by $|\pm\frac{3}{2}\rangle$ and $|\pm\frac{5}{2}\rangle$, respectively. The magnetic moment of the ground state, $g_J\mu_B J_z = 0.428\mu_B$, is in good agreement

原子炉：JRR-3　　装置：TAS-1(2G)　　分野：中性子散乱（磁性）

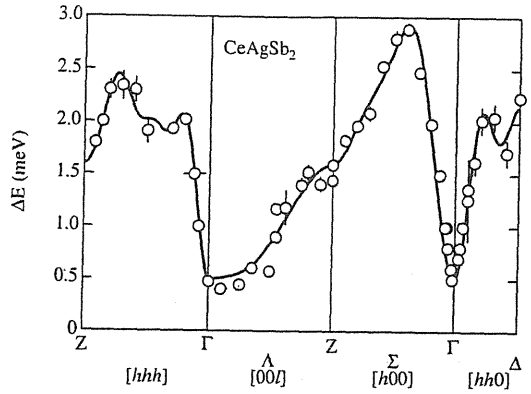


Figure 2: Spin wave dispersion in $CeAgSb_2$.

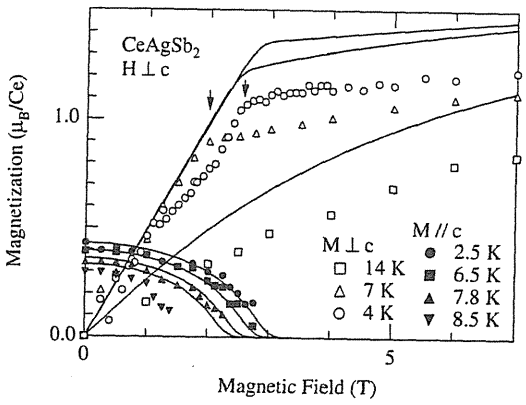


Figure 3: In-plane magnetization ($M \perp c$, open marks) and the ferromagnetic moment ($M \parallel c$, solid marks) are plotted as a function of magnetic field perpendicular to [001].

with the observed ferromagnetic moment of $0.41\mu_B$ [4]. The CEF level scheme determined by the present neutron scattering study is very similar to the result of the recent thermal expansion study by Takeuchi *et al.* [5]

The dispersion of the spin wave excitation has been measured with the use of a single-crystalline sample. Figure 2 is the dispersion relation of the spin wave excitation.The anisotropic exchange interaction between $4f$-moments in the $|\pm\frac{1}{2}\rangle$ ground state for the ferromagnet is introduced to account for the dispersion [4]. The solid line in Fig. 2 is the result of the calculated dispersion relation.The obtained interaction coefficient for the z component of J is about 10 times larger than that for the in-plane component of J, indicating the existence of ising like exchange interaction.

The CEF splitting and ising-like interaction, determined in this study, well account for the 'unusual' magnetic properties. The open marks in Fig. 3 show the in-plane magnetization measured from the neutron diffraction. The kink, denoted by arrows, appears below T_c. On the other hand, the closed marks in Fig. 3 show the ferromagnetic moment along the c-axis with the magnetic field parallel to [110] measured from the neutron diffraction intensity at the (110) peak position. With this configuration, the in-plane magnetization does not contribute to any magnetic scattering, because the induced in-plane magnetic moment is parallel to the scattering vector q. Therefore only the ferromagnetic component along [001] was observed. The ferromagnetic component along [001] exhibits a gradual decrease with increasing in-plane magnetic field, and disappears at the critical field H_c where the in-plane magnetic moment shows a kink behavior. Our data indicate that H_c is the field where the ferromagnetic moment switches its direction from parallel to perpendicular relative to [001]. This feature is well reproduced by the calculation based on the CEF and ising like exchange interaction, as shown in Fig. 3.

References

1) G. André, F. Bourée, M. Kolenda, B. Leśniewska, A. Oleś and A. Szytuła: Physica B **292** (2000) 176.
2) K.D. Myers, S.L. Bud'ko, I.R. Fisher, Z. Islam, H. Kleinke, A.H. Lacerda and P.C. Canfield: J. Magn. Magn. Mater. **205** (1999) 27.
3) D.T. Adroja, P.C. Riedi, J.G.M. Armitage and D. Fort Acta Phys. Pol. B **34** (2003) 945.
4) S. Araki, N. Metoki, A. Galatanu, E. Yamamoto, A. Thamizhavel and Y. Ōnuki: Phys. Rev. B, to be published.
5) T. Takeuchi, A. Thamizhavel, T. Okubo, M. Yamada, N. Nakamura, T. Yamamoto, Y. Inada, K. Sugiyama, A. Galatanu, E. Yamamoto, K. Kindo, T. Ebihara and Y. Ōnuki, Phys. Rev. B **67** (2003) 064403.

研究テーマ： 三角格子反強磁性体 $CuFeO_2$ の擬 Ising 性と磁気励起
表題： 三角格子反強磁性体 $CuFeO_2$ における異常磁気励起

Anomalous Magnetic Excitation on a Triangular Lattice Antiferromagnet $CuFeO_2$

1-2-36

N. Terada[1] and S. Mitsuda[1]

[1]*Department of Physics, Faculty of science, Tokyo University of Science, 1-3 kagurazaka, shinjuku-ku, Tokyo, 162-0825*

Delaffossite compound $CuFeO_2$ has been extensively investigate as one of ABO_2-type materials for triangular lattice antiferromagnet. In spite of the Heisenberg spin of orbital singlet Fe^{3+} (S=$\frac{5}{2}$, L=0) magnetic ions, *quasi-Ising character* is stabilized with delicate balance of competing exchange interactions[1]. In fact, as reported in our recent study[2, 3], by substitution of a small amount of non-magnetic Al^{3+} impurity, the quasi-Ising character disappears and the Heisenberg spin character is retrieved in $CuFe_{0.98}Al_{0.02}O_2$. This time, in order to investigate how such dramatic changing from quasi-Ising to Heisenberg spin character found in magnetic structural analysis[1, 2] is reflected in the magnetic excitation spectrum, inelastic neutron scattering experiments have been performed on $CuFeO_2$ and $CuFe_{0.98}Al_{0.02}O_2$ with HER.

As shown in Fig. 1(a), in the thermally induced state of both $CuFeO_2$ and $CuFe_{0.98}Al_{0.02}O_2$, diffusive magnetic excitation spectrum was observed, suggesting strong spin fluctuations in those thermally induced sate.

For the low temperature ground states, on the other hand, the magnetic excitation spectrum is entirely different between them. For the LT state of $CuFe_{0.98}Al_{0.02}O_2$, the normal acoustic spin-wave branches starting from the magnetic Bragg points, (q q $\frac{3}{2}$) and ($\frac{1}{2}$-q $\frac{1}{2}$-q $\frac{3}{2}$) with q~0.21, were observed as shown by closed symbols in Fig. 1(b), suggesting strongly that the Heisenberg spin character of orbital singlet Fe^{3+} is retrieved by substitution of a small amount of non-magnetic Al^{3+} impurity.

For the 4-sublattice ground state of $CuFeO_2$, as shown by open symbols in Fig. 1(d), the anomalous spin-wave dispersion curve along the (h h $\frac{3}{2}$) direction with energy gap was obtained. As seen in Fig. 1(b), the two bottom positions of the dispersion curve indicated by single arrows correspond not to the commensurate magnetic Bragg point of ($\frac{1}{4}$ $\frac{1}{4}$ $\frac{3}{2}$) for the 4-sublattice ground state indicated by double arrow, but to the incommensurate magnetic Bragg points, (q q $\frac{3}{2}$) and ($\frac{1}{2}$-q $\frac{1}{2}$-q $\frac{3}{2}$) with q~0.21 indicated by broken lines, for the LT ground state of $CuFe_{0.98}Al_{0.02}O_2$. These experimental findings suggest that $CuFeO_2$ does not show Heisenber spin character of orbital singlet Fe^{3+} in its magnetic structure[1, 2], but the spin-wave dispersion relation of $CuFeO_2$ knows the Heisenberg spin character which is retrieved in $CuFe_{0.98}Al_{0.02}O_2$.

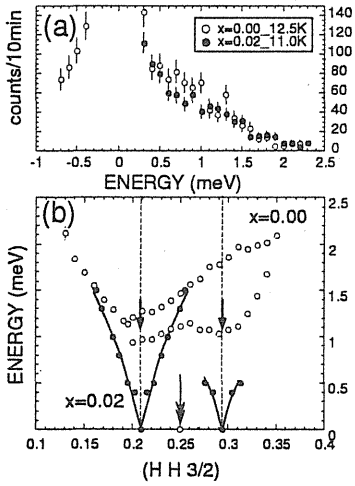


Fig. 1. (a)Typical E-scan profiles on (0.15 0.15 $\frac{3}{2}$) in the PD(T~12.5K) and the IM state(T~11K). (b)Spin-wave dispersion curves along (H H $\frac{3}{2}$) at T~4K in $CuFeO_2$ (open symbols) and $CuFe_{0.98}Al_{0.02}O_2$ (closed symbols).

References

[1] S. Mitsuda et al, J. Phys. Soc. Jpn. 67, 4026 (1998).
[2] S. Mitsuda et al, submitted to J. Phys. Soc. Jpn.
[3] N. Terada et al, submitted to Phs. Rev. B.

使用施設：JRR-3 ， 装置： HER(C1-1) ， 分野： 2. Magnetism

研究テーマ：先端偏極中性子散乱によるスピン-格子物性の研究
表　題：$Ca_2Y_2Cu_5O_{10}$ の CuO_2 鎖における偏極中性子散乱研究
1-2-37

Polarized Neutron Scattering Study of the Edge-Sharing CuO_2 Chains in $Ca_2Y_2Cu_5O_{10}$

M. MATSUDA, M. NAKAMURA, M. TAKEDA, K. KAKURAI, H. YAMAGUCHI[1], T. ITO[1] and K. OKA[1]

Advanced Science Research Center, JAERI, Tokai, Ibaraki 319-1195
[1]National Institute of Advanced Industrial Science and Technology, Tsukuba, Ibaraki 305-8568

In the edge-sharing CuO_2 chain in which the Cu ions are coupled by the nearly 90° Cu-O-Cu bond, large magnetic moments can be induced at oxygen sites because of the strong hybridization between Cu d and O p orbitals. An existence of the magnetic moments in the CuO_2 chains is predicted theoretically in Li_2CuO_2. [1)] and observed experimentally in $La_9Ca_5Cu_{24}O_{41}$ [2)] and in Li_2CuO_2 [3)].

$Ca_2Y_2Cu_5O_{10}$ is a quasi-one-dimensional magnet, which consists of the edge-sharing CuO_2 chains. This compound shows an antiferromagnetic long-range ordering below T_N=29.5 K with ferromagnetic coupling along the chain [4, 5)]. It is worth while studying the magnetic moment at the oxygen sites in this compound in order to check whether the phenomenon is universal. Previous magnetic structural analysis using unpolarized neutrons suggests that the magnetic moments are not localized at the Cu sites but some of the moments also exist at the oxygen sites [4, 6)]. However, without considering the oxygen moments, there is a slight possibility that the Cu moments are just tilted from the b axis perpendicular to the CuO_2 plane. This study using polarized neutrons confirms that the magnetic moments point along the b axis, strongly supporting the existence of the moments at the oxygen sites.

The neutron scattering experiments were carried out on the 3-axis spectrometer TAS-1. Heusler alloy (111) was used as monochromator and analyzer. A flipping ratio of ~20 was measured on some nuclear Bragg peaks. The horizontal collimator sequence was open-80'-S-80'-open. The incident neutron energy was fixed at E_i=32.4 meV. The single crystal of $Ca_2Y_2Cu_5O_{10}$ was grown using a traveling solvent floating zone method in air [7)]. The crystal structure is orthorhombic and the lattice constants are a=2.810 Å (chain direction), b=6.190 Å, and c=10.613 Å at room temperature. The crystal, which is oriented in the (hhl) scattering plane, was mounted in a closed cycle refrigerator. The $(00L)$ and $(11L)$ (L: integer) magnetic Bragg reflections were measured.

Figure 1 shows the typical data obtained from the polarized neutron measurements in the vertical field. The non-spin-flip (NSF) and spin-flip (SF) mode experiments give magnetic scattering caused by spin component parallel to the field direction [1,-1,0] and perpendicular to it, respectively. A correction originating from imperfect polarization of the neutron beam was made. The tail of the Bragg peaks probably comes from the poor mosaicity of the crystal and/or the the Heusler monochromator and analyzer. The $(00L)$ intensities originate from the spin component perpendicular to the c axis. From the ratio of the NSF and SF reflection in the $(00L)$ reflections ~5, as shown in Figs. 1(a) and 1(b), the angle between the field and the spin directions projected in the ab plane is estimated to be ~25°. This direction almost corresponds to the b axis. From the $(11L)$ intensities the spin component along the c axis can be estimated. Since the SF $(11L)$ intensities are weak, as shown in Figs. 1(c) and 1(d), the c component should be very small even if it exists. The broken lines in Fig. 1 represent the estimated values with the spin structure model in which the moments point along the b axis. [6)] The estimated intensities reproduce

原子炉：JRR-3　　装置：TAS-1(2G)　　分野：中性子散乱（磁性）

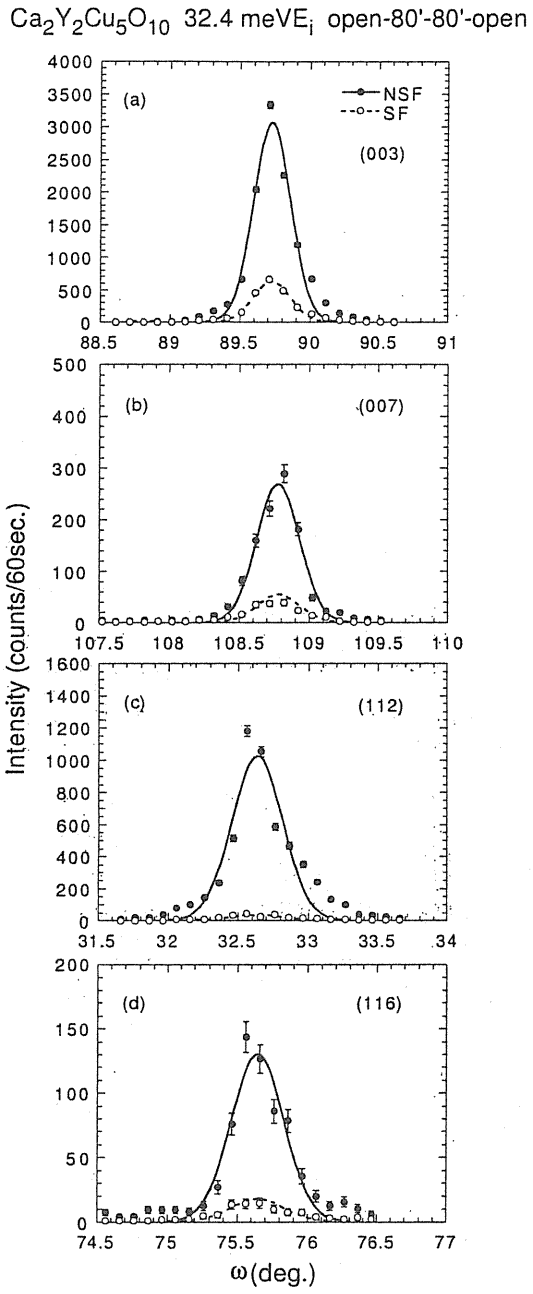


Figure 1: $Ca_2Y_2Cu_5O_{10}$ at (0,0,3), (0,0,7), (1,1,2), and (1,1,6) measured at T=15 K with polarized neutrons in the vertical field spin-flip (SF) and non-spin-flip (NSF) mode. A correction originating from imperfect polarization of the neutron beam was made. The solid lines represent the results of fits to a Gaussian. The broken lines show the intensities estimated for the SF mode.

the observed ones reasonably well. From these results, it can be concluded that the moments point along the b axis.

The previous neutron scattering measurements using unpolarized neutrons shows that a simple model that assumes magnetic moments only at the Cu sites does not describe the magnetic Bragg intensities, especially those of the $(11L)$ reflections [6]. Then, assuming that the moments point along the b axis, it is suggested that the magnetic moments are not localized at the Cu sites but extend to the oxygen sites. Since the present study confirms that the moments point along the b axis, it is clearly concluded that some fraction of the magnetic moments in the CuO_2 unit (~22%) exists at the oxygen sites.

References

1) R. Weht and W. E. Pickett: Phys. Rev. Lett. **81** (1998) 2502.
2) M. Matsuda, K. M. Kojima, Y. J. Uemura, J. L. Zarestky, K. Nakajima, K. Kakurai, T. Yokoo, S. M. Shapiro and G. Shirane: Phys. Rev. B **57** (1998) 11467.
3) U. Staub, B. Roessli and A. Amato: Physica B **289-290** (2000) 299.
4) M. Matsuda, K. Ohoyama and M. Ohashi: J. Phys. Soc. Jpn. **68** (1999) 269.
5) H. F. Fong, B. Keimer, J. W. Lynn, A. Hayashi and R. J. Cava: Phys. Rev. B **59** (1999) 6873.
6) M. Matsuda, K. Kakurai, H. Yamaguchi, T. Ito, C. H. Lee and K. Oka, Appl. Phys. A **74** (2002) 637.
7) H. Yamaguchi, K. Oka and T. Ito: Physica C **320** (1999) 167.

研究テーマ： 擬2次元S=1/2量子スピン系 Cs_2CuBr_4 の磁気励起
表題： 擬2次元 $S = 1/2$ 量子スピン系 Cs_2CuBr_4 のスピン構造と磁気励起

Magnetic excitation of $S = 1/2$ quasi two dimensional quantum spin system

1-2-38 Cs_2CuBr_4

T. Ono[1], H. Tanaka[2], A. Oosawa[3], Y. Koike[3], K. Kakurai[3] and K. Nakajima[4]

[1] *Department of Physics, Tokyo Institute of Technology, Meguro, 152-8551 Tokyo*
[2] *Low Temperature Center, Tokyo Institute of Technology, Meguro, 152-8551 Tokyo*
[3] *Advanced Scientific Research Institute, Japan Atomic Research Institute, Tokai, 319-1195*
[4] *Institute for Solid State Physics, The University of Tokyo, Tokai, 319-1106*

Cs_2CuBr_4 has the orthorhombic crystal structure with the space group *Pnma*, and magnetic Cu^{2+}-ions make a distorted triangular lattice within the *bc*-plane. This compound undergoes magnetic phase transition at Néel temperature $T_N = 1.4$ K. In the temperature region below T_N, a magnetization plateau appears at 1/3 of the saturation magnetization [1]. On the last annual report, we reported the experimental resuts of the magnetic excitation in the temperature region slightly above T_N ($T \geq 1.5$ K). In this report, we report the results of the elastic and inelastic neutron scattering below T_N.

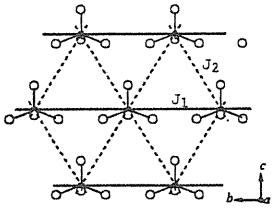


Fig. 1. Arrangement of the magnetic Cu^{2+}-ions and antiferromagnetic interactions J_1 and J_2 within the *bc*-plane.

Measurements were performed at HER triple axis spectrometer installed at JRR-3M, Tokai. Asingle crystal with 3 cm^3 in volume was mounted on the sample stage of the dilution refrigerator. Measurements were perfomed for the (a, b) scattering plane. Incident neutron wave length was $\lambda = 4.312\AA$, and the second, the third and the forth collimations were chosen as open - 80' - 80'.

Figure 2 shows the typical scattering profile scanned along the b^*-direction measured at $T = 100$ mK. Magnetic Bragg reflection appears at $Q = (0, 0.575, 0)$. This result indicates the magnetic structure is incommensurate with the lattice along the *b*-axis. This incommensuration originates from the frustration among the antiferromagnetic interactions J_1 and J_2 within the *bc*-plane (see Fig. 1). For isostructural Cs_2CuCl_4, magnetic Bragg reflection appears at $Q = (0, 0.528, 0)$[2]. Since the ordering vector is given by the ratio of J_1 and J_2 as $\cos(\pi Q_0) = -J_2/2J_1$ in view of classical spin model, we can obtain $J_2/J_1 = 0.467$ for Cs_2CuBr_4 and 0.175 for Cs_2CuCl_4. This result implies that Cs_2CuBr_4 is more frustrated than Cs_2CuCl_4.

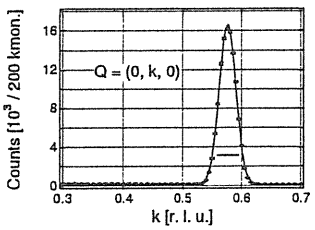


Fig. 2. A typical scattering profile scaned along the b^*-direction measured around $T = 100$ mK. Solid straight line below the magnetic Bragg peak indicates the instrumental resolution.

In the measurements of the inelastic neutron scattering, we confirmed that the dispersion relation shows the one-dimensional antiferromagnetic behavior also in the ordered phase. Although, we could not find a significant improvement from the previous experiment reported on the annual report 2001, due to the insufficiency of the scattering intensity. Precise measurements of the inelastic scattering are in progress in order to determin the detailed disperrsion relation.

References

[1] Ono *et al.*: Phys. Rev. B **67** (2003) 104431.
[2] Coldea *et al.*: J. Phys.: Condens. Matter **8** (1996) 7473.

使用施設：JRR-3' 装置： C1-1 (HER)， 分野： 2. Magnetism

研究テーマ：Ce化合物強相関伝導系における特異な磁気相
表　題：CePの圧力下における強磁性

1-2-39

Ferromagnetism in CeP under High Pressure

D. Kawana, T. Osakabe[1], A. Hannan, M. Kohgi

Department of Physics, Tokyo Metropolitan University, Hachioji, Tokyo 192-0397
[1]Advanced Science Research Center, JAERI, Tokai, Ibaraki 319-1195

CeP, with the simple NaCl-type crystal structure, shows dense-Kondo-like behavior in the transport properties in spite that its carrier number is very low (0.01/f.u.).[1)] It shows also unusual magnetic properties especially under high pressures, where double layers of ferromagnetic Ce(001)-plane with a large moment value of $\sim 2\mu_B$ appear periodically among the type-I antiferromagnetic structure of Γ_7 Ce ions. The period of the structure decreases one by one from 9 to 4 with increasing pressure up to 1.7GPa. It is remarkable that some of the magnetic structures around 2 GPa are similar to ones of CeSb and CeBi at ambient pressure.[2)] We have systematically investigated the magnetic strctures and complex phase diagram of this compound by neutron scattering.

Our previous work shows that, in the pressure range between 2.5 and 2.8GPa, a ferromagnetic phase appears at low temperatures below around 30 K. Above this temperature another phase 3* (↑↑○↓↓○; the arrow and circle represent ferromagnetic and paramagnetic Ce(001)-planes, respectively) appears. Interpolating phase boundaries, we expect that only ferromagnetic phase exists at the pressure above about 3.1GPa.[3)] In order to confirm this point, we performed an experiment at the triple-axis-spectrometer TAS-1(2G) installed at JRR-3 reactor, JAERI. To apply a pressure on the sample, we used a sapphire anvil cell. The sample of $0.3 \times 0.2 \times 0.15$ mm^3 was set in a hole of phosphorous bronze gasket, with a little ruby powder for pressure calibration and Daphne7373 as pressure transmitting medium. We achieved a pressure value of 3.2GPa.

Figure 1 shows the temperature dependences of peak intensities at (2 0 0) and (2 −1/3 0). With decreasing temperature, the former begins to increase at 41 K, but the latter does not show any clear change below 50 K. The experimental result clearly indicates that there is only one ordered-state, which is ferromagnetic, at 3.2GPa.

From the measurement of electric resistance, the critical temperature T_c of the ferromagnetic phase will decrease with increasing pressure and disappear at about 6 GPa.[4)] The process is quite interesting because a drastic change of $4f$-electron state of Ce atom is brought about by applying pressure. The present work is a part of the study of this phenomenon.

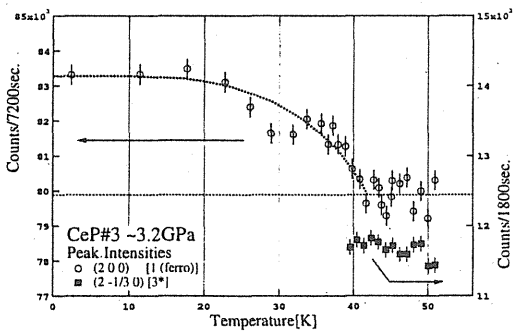


Figure 1: Temperature dependencies of peak intensities at (2 0 0) and (2 -1/3 0) on CeP in 3.2GPa.

References

1) T. Suzuki: Physica B, **186-188** (1993) 347.
2) M. Kohgi *et al.*: Physica B, **281-282** (2000) 417.
3) A. Hannan *et al.*: Applied Phys A, **74** (2002) S565.
4) N. Môri *et al.*: *Physcal Properties of Actinde and Rare Earth Compounds* JJAP Series **8** (1993) 182.

原子炉：JRR-3　　装置：TAS-1(2G)　　分野：中性子散乱（磁性）

研究テーマ： 誘電・磁性複合系 $RbCoBr_3$ の横成分磁気秩序
表題： 歪んだ三角格子イジング型反強磁性体 $RbCoBr_3$ の中性子散乱による研究

Neutron Diffraction Study of Distorted-Triangular-Lattice Ising-like Antiferromagnet $RbCoBr_3$

1-2-40

T. Kato[1], Y. Nishiwaki[2], K. Iio[2] and Y.Oohara[3]

[1] *Faculty of Education, Chiba University, 1-33 Yayoi-cho, Inage-ku, Chiba 273-8522*
[2] *Department of Physics (Cond.Mat.Phys.), Graduate School of Science and Engineering, Tokyo Institute of Technology, 2-12-1 Oh-okayama, Meguro-ku, Tokyo 152-8551*
[3] *Neutron Scattering Laboratory, Institute for Solid State Physics, University of Tokyo, Shirakata 106-1, Tokai, Ibaraki 319-1106*

$RbCoBr_3$ is a triangular lattice antiferromagnet with the Ising spins. $RbCoBr_3$ has a complex character of structural and magnetic frustrated system. This crystal crystallizes with the $CsNiCl_3$ structure (space group symmetry $P6_3/mmc$) and undergoes the successive structural phase transition at $T_{st1} = 90$K and $T_{st2} = 37$K. It is notable that $RbCoBr_3$ exhibits the onset of antiferromagnetic order just at the structural phase transition temperature at T_{N1}=T_{st2}. Below this temperature, a weak ferromagnetic moment perpendicular to the c axis appears, of which the orientation changes in the ab plane at lower temperatures $T < 28$K).

We performed single-crystal neutron diffraction measurements of $RbCoBr_3$ at HQR(T1-1), JRR-3M, Tokai. The peak intensity of the (1/3,1/3,2) Bragg reflection was measured as a function of temperature, as shown in Fig.1. The unit cell is enlarged from (a, a, c) to $(\sqrt{3}a, \sqrt{3}a, c)$ at T_{st1}. Below T_{st2}=T_{N1}, the peaks with odd l appeared. Figure 2 shows the temperature dependence of (1/3,1/3,1), (2/3,2/3,1) and (1,1,1) Bragg peak heights. Here, the peak of the (1,1,1) reflection increases just below T_{N1}. This is contrasted with the (1,1,1) intensities of the intermediate PD phase ($T_{N2} < T < T_{N1}$) of typical Ising triangular antiferromagnets $CsCoBr_3$ and $CsCoCl_3$.[1, 2] The present results revealed that Ferri phase ($T < T_{N2}$ for $CsCoBr_3$ and $CsCoCl_3$)[1, 2] appeared directly at T_{N1}. This may be because the exchange interactions are inequivalent due to the structural phase transitions.

The theoretical calculation for suitable spin models are in progress. Additional experiments to identify the crystal structure below T_{st1} and T_{st2} and to detect the transverse ordering of Ising-like spins are required for regorous treatments.

References

[1] M.Mekata and K.Adachi :J. Phys. Soc. Jpn. **42** (1978)806
[2] W.B.Yelon et al. :Phys. Rev. **B12** (1975)5007

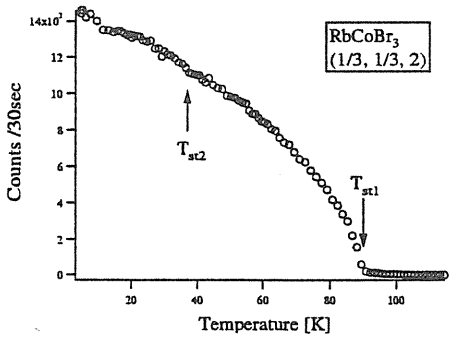


Fig. 1. The temperature dependence of the peak heights for Q=(1/3,1/3,2)

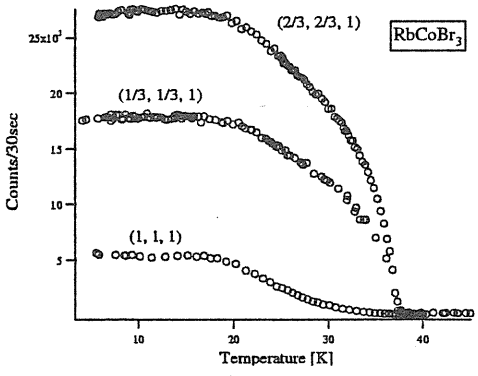


Fig. 2. Temperature dependence of the peak heights for Q= (1/3, 1/3, 1), (2/3,2/3,1) and (1,1,1).

使用施設：JRR-3`。装置： HQR(T1-1)，分野： 2. Magnetism

研究テーマ：先端偏極中性子散乱によるスピン-格子物性の研究
表　題：スピンギャップ系 $TlCuCl_3$ の圧力誘起磁気秩序相における新奇な相転移：偏極中性子散乱を用いて

1-2-41

Anomalous Phase Transition in the Pressure-induced Magnetic Ordered Phase of the Spin Gap System $TlCuCl_3$: Polarized Neutron Scattering Study

A.OOSAWA, K.KAKURAI, T.OSAKABE, M.NAKAMURA, M.TAKEDA and H.TANAKA[1]

Advanced Science Research Center, JAERI, Tokai, Ibaraki 319-1195
[1]Res.Cent.for Low Temp.Phys.,Tokyo Inst. of Tech.,Oh-okayama,Meguro-ku,Tokyo 152-8551

Recently, unpolarized neutron diffraction experiments under the hydrostatic pressure of $P = 1.48$ GPa were carried out in the spin gap system $TlCuCl_3$ and the pressure-induced magnetic order below $T_N = 16.9$ K has been confirmed [1]. Just below T_N the spin structure was determined as shown in Fig. 1, and the ordered moments lie in the $a-c$ plane. Upon lowering temperature, the magnetic diffraction intensities indicated the inclination of these moments toward the b-axis. Such a inclination can be directly observed using the polarized neutron scattering technique because the spin components in and out of scattering plane can be independently observed looking at a single diffraction peak. We thus performed a polarized neutron scattering experiment under the applied pressure in $TlCuCl_3$.

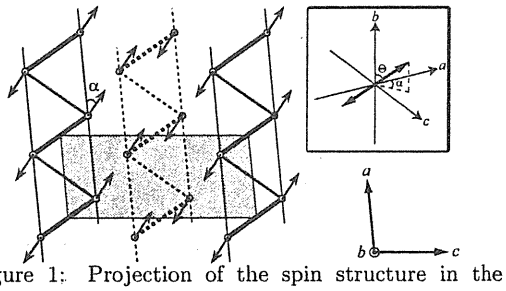


Figure 1: Projection of the spin structure in the pressure-induced magnetic ordered phase for $P = 1.48$ GPa in $TlCuCl_3$ onto the $a-c$ plane determined in the previous unpolarized measurements [1]. The inset shows the inclination of the ordered spin toward the b-axis. The angle α denotes the angle between the a-axis and the spin component projected onto the $a-c$ plane. The angle Θ is the angle between the spin and the b-axis.

The preparation of the single crystal of $TlCuCl_3$ has been reported in ref. 2. We used again the sample in the McWhan-type high-pressure cell [2] used in the previous unpolarized measurements [1] Uniaxial polarized neutron elastic scattering measurements [3] were performed using the JAERI-TAS1. Heusler(111)-Heusler(111) monochromator-analyser configuration was used. The sample was mounted in the cryostat with its a^*- and c^*-axes in the scattering plane. The guide field was applied perpendicular to the scattering $a-c$ plane ($\boldsymbol{Q} \perp \boldsymbol{P}$). The polarization was measured on the nuclear Bragg reflection and was determined to be around 71 %. This value is considerably worse than the polarization realized in the normal polarization analysis set-up, which is almost 90 %, and is due to the ferromagnetic components of the high-pressure cell. We checked that the polarization is independent of the sample temperature, *i.e.* high-pressure cell temperature. Other instrumental conditions were the same as those in the previous unpolarized measurements [1].

The inset of Fig. 2 shows the $\theta-2\theta$ scans for the Spin-Flip (SF) scattering at $\boldsymbol{Q} = (0,0,1)$ measured at $T = 3.5$, 10.0 and 29.5 K for $P = 1.48$ GPa in $TlCuCl_3$. For $T = 3.5$ and 10.0 K, which are lower than T_N, the increase of the intensity attributed to the magnetic Bragg reflection can be clearly seen. However, we can see that the magnetic Bragg intensity at $T = 10.0$ K is larger than that at $T = 3.5$ K. This means that the additional changes occur at low temperature in the ordered phase. It is noted that the Bragg reflection retains resolution limited width between the temperatures, as shown in the inset of Fig. 2. Figure 2 shows the temperature dependence of the peak intensities of the SF

原子炉：JRR-3　　装置：TAS-1(2G)　　分野：中性子散乱（磁性）

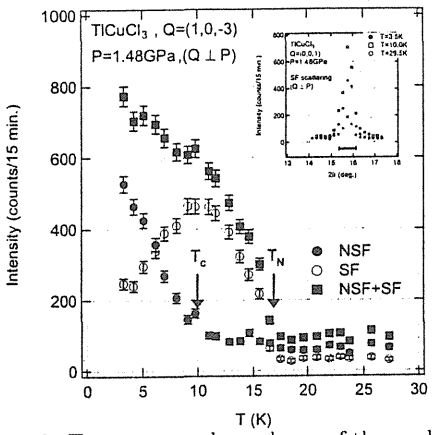


Figure 2: Temperature dependence of the peak intensities of the SF scattering, of the NSF scattering, and of the total peak intensity of the both scatterings for $Q = (1, 0, -3)$ reflection measured at $P = 1.48$ GPa in $TlCuCl_3$. The inset shows $\theta - 2\theta$ scans for the SF scattering at $Q = (0, 0, 1)$ measured at $T = 3.5$, 10.0 and 29.5 K for $P = 1.48$ GPa in $TlCuCl_3$. The horizontal bar in the inset denotes the calculated instrumental resolution width.

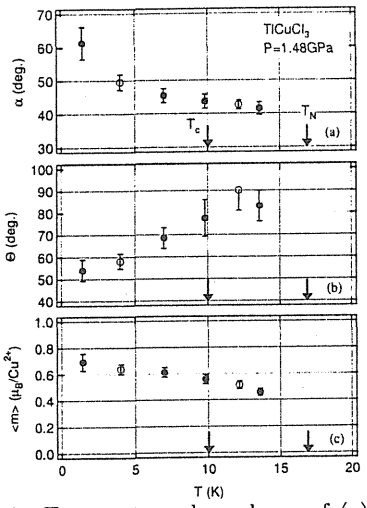


Figure 3: Temperature dependence of (a) α, (b) θ and (c) the ordered moment m at $P = 1.48$ GPa in $TlCuCl_3$. The open circles denote the values estimated in the previous measurements [1].

scattering, of the Non-Spin-Flip (NSF) scattering, and of the total intensity of the both scatterings for $Q = (1, 0, -3)$ reflection measured at $P = 1.48$ GPa in $TlCuCl_3$. As shown in Fig. 2, the peak intensity of the SF scattering increases, while that of the NSF scattering retains the background level just below T_N upon decreasing temperature. However, just at $T_c = 10.0$ K, the peak intensity of the SF scattering has a maximum, and then decreases below T_c. While the peak intensity of the NSF scattering begins to increase below T_c. Because all the observed intensity at $Q = (1, 0, -3)$ below T_N can be safely assumed to be of the magnetic origin, the intensity of the SF and NSF scattering in the present experiment are proportional to the square of the spin component perpendicular to the scattering vector Q in the scattering $a - c$ plane and parallel to the b-axis, respectively. We thus conclude that the ordered moments lie in the $a - c$ plane just below T_N, and then begin to incline toward the b-axis below T_c.

In order to investigate the temperature dependence of the angles α and Θ which are defined in Fig. 1, and of the ordered moment $\langle m \rangle$, we performed additional *un*polarized neutron scattering measurements. The obtained results are shown in Fig. 3. As shown in Fig. 3, the angles α and Θ retain about 40° and 90° just below T_N, and begin to increase and decrease below T_c, respectively, upon decreasing temperature. While, the temperature dependence of the ordered moment $\langle m \rangle$ shows no anomaly at T_c and increases monotonically with decreasing temperature.

From the SF and NSF scattering intensities the inclination angle Θ at the lowest temperature is estimated to be 35(1)°. The discrepancy to the value estimated from the unpolarized neutron experiment may be due to the magnetized components of the high-pressure cell causing an addtional field, so that the guide field at the sample position is not exactly perpendicular to the scattering plane. In order to perform polarized neutron scattering experiments with better polarization and more accurate guide field direction, a non-magnetic high-pressure cell is in preparation.

References

1) A. Oosawa *et al.*:J.Phys.Soc.Jpn. **72** (2003) 1026.
2) D. B. McWhan *et al.*:Phys.Rev.B **20** (1979) 4612.
3) R. M. Moon *et al.*: Phys. Rev. **181** (1969) 920.

研究テーマ:ハロゲン架橋型ニッケル錯体[NiBr(chxn)$_2$]Br$_2$の磁気励起
表題:ハロゲン架橋型ニッケル錯体の磁気励起

1-2-42 Magnetic excitations in halogen-bridged nickel complex

S. Itoh, S. Takaishi[1],R. Ikeda[1] and K. Nakajima[2]

Neutron Science Laboratory, High Energy Accelerator Research Organization, Tsukuba, 305-0801; [1]Department of Chemistry, University of Tsukuba, Tsukuba, 305-0006; [2]Neutron Science Research Center, Japan Atomic Research Institute, Tokai, 319-1195

Halogen-bridged metal complexes with a one-dimensional (1D) mixed-valence -X-M^{2+}-X-M^{4+}-X- structure have been studied as a Peierls distorted chain system with a strong electron-lattice interaction resulting from the off-centered position of halogen between neighboring metal atoms. Recently, a new complex, [NiBr(chxn)$_2$]Br$_2$ (chxn:1R, 2R-cyclohexanediamine), having the non-distorted 1D structure expressed as -Br-Ni^{3+}-Br-Ni^{3+}-Br-, has been synthesized [1,2]. This spin structure implies the formation of antiferromagnetically coupled S = 1/2 Heisenberg chains. Magnetic susceptibility measurements up to the room temperature suggested a large exchange constant of J ~ 0.3 eV [2]. Optical studies have been revealed that this system exhibits a 1D charge transfer insulator [3]. The observed optical properties can be explained by a 1D extended Hubbard model [4], and it suggested J ~ 0.4 eV, which is consistent with the result on the susceptibility.

In order to detect magnetic interactions in [NiBr(chxn)$_2$]Br$_2$ directly, we performed inelastic neutron scattering experiments on the triple axis spectrometers, HER (C1-1) and PONTA (5G) at JRR3M in JAERI (Tokai), by using 20 g of a single-crystal sample. We measured excitations at the magnetic zone center, at E (energy transfers) = 0.4 ~ 1.5 meV at T = 1.4 K on HER, and at E = 5 meV and 18 meV at T = 208 K (unfortunately, the sample was not cooled) on PONTA. However, we could not detect meaningful magnetic excitations at the point in the Qω space where we expected the detection. We tried to measure excitations on the chopper spectrometer, INC, at KENS. The incident neutron energy was chosen to be 27 meV. We observed a peak at around E = 6 meV at the magnetic zone center in the background subtracted spectrum as shown in Fig.1. When the sample crystal was rotated by 90°, the peak disappeared. Therefore, the peak is located only at the magnetic zone center. Also, the peak was observed to become broader as T increases. Thus, the peak is of magnetic origin. This experiment indicates that a chopper spectrometer covering the Qω space continuously is indispensable for detecting tiny magnetic excitations on large nonmagnetic background.

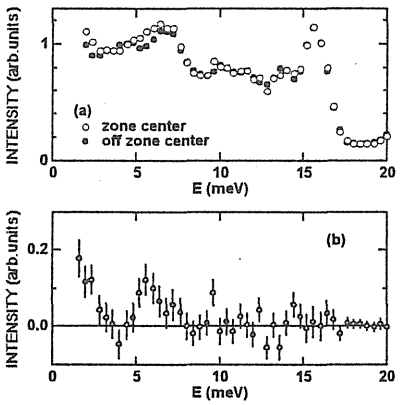


Figure 1: Inelastic spectrum measured on INC at KENS at T = 5 K, (a) at and off the magnetic zone center, (b) background-subtracted spectrum. The spectrum off the zone center was assumed to be the background.

References

[1] K. Toriumi et al., J. Am. Chem. Soc. 111 (1989) 2341.
[2] H. Okamoto et al., Phys. Rev. B 42 (1990) 10381.
[3] H. Okamoto et al., Phys. Rev. B 54 (1996) 8438.
[4] N. Tomita and K. Nasu, Phys. Rev. B 56 (1997) 3779.

使用施設:JRR-3M ,装置:HER(C1-1), PONTA(5G), 分野 Magnetism

研究テーマ：3次元スピンフラストレーション系 $CdFe_2O_4$ の高圧下におけるスピン相関
表　題：3次元スピンフラストレーション系 $CdFe_2O_4$ の高圧下におけるスピン相関

1-2-43

Diffuse Scattering of $ZnFe_2O_4$ Under High Pressure

Y. Tsunoda, K. Kamazawa and S. Katano[1]

School of Science and Engineering, Waseda University, Shinjuku, Tokyo 169-8555
[1] Advanced Science Research Center, JAERI, Tokai, Ibaraki 319-1195

As pointed out by P. W. Anderson, [1)] if only the B-site of normal spinel structure has magnetic moment and the nearest neighbor spin coupling is anti-parallel, there is no definite magnetic ground state. This is a so-called 3-D geometrical spin frustration. In $ZnFe_2O_4$ and $CdFe_2O_4$, since Zn and Cd ions occupy the A-site and both ions have no magnetic moments but all of magnetic ions Fe^{3+} occupy the B-site, these systems satisfy Anderson ' s condition. Actually, in recent neutron scattering measurements using $ZnFe_2O_4$ and $CdFe_2O_4$ single crystal specimens,[2, 3)] only strong diffuse scattering was observed without magnetic Bragg peaks at low temperature, indicating that both $ZnFe_2O_4$ and $CdFe_2O_4$ are the 3-D geometrical spin frustration systems. However, the locations of the diffuse peak positions in the reciprocal lattice space (RLS) for these systems are completely different; for the $ZnFe_2O_4$, the diffuse peak intensities are located slightly inside of the 1-st Brillouin zone boundary (BZB) of the fcc structure and for the $CdFe_2O_4$, slightly outside of the 2-nd BZB of the RLS, suggesting that the spin couplings for these substances are different although the atomic configurations of magnetic ions (Fe^{3+}) are the same for both systems. Only the difference between them is the atomic volumes of Zn^{2+} and Cd^{2+} ions. The Cd^{2+} has a larger volume than the Zn^{2+}. Then, due to the large volume of the A-site atom in $CdFe_2O_4$, the tetrahedron configuration of the B-site is slightly deformed and the angle of super-exchange coupling between Fe^{3+} spins deviates from the right angle, resulting in a big change of the spin coupling. Thus, if we apply the high pressure to $ZnFe_2O_4$ and deform the tetrahedron configuration of Fe^{3+} ions, then, the situations similar to the $CdFe_2O_4$ is expected to occur for $ZnFe_2O_4$ and the diffuse scattering peak position for the $ZnFe_2O_4$ would shift towards those for the $CdFe_2O_4$. This is a motivation of the present investigations.

Using a $ZnFe_2O_4$ single crystal specimen, measurements were performed at the TAS-1 spectrometer installed in JRR-3, Tokai, under the pressure of 1.8 GPa at 15 K and the data were compared with those under the atmospheric condition. A CuBe pressure cell was used for the present measurements.

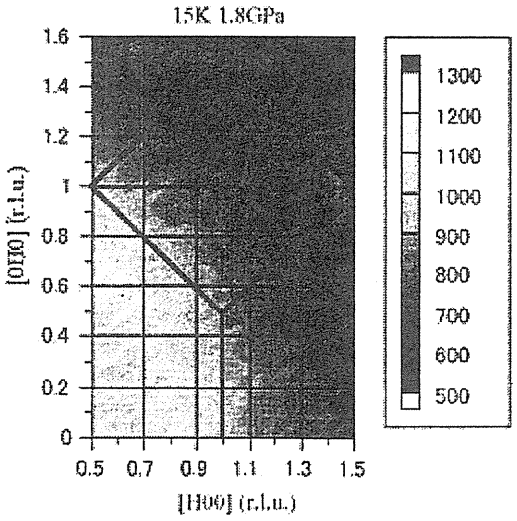


Figure 1: The elastic diffuse scattering intensity contour map studied at 15K under the pressure of 1.8Gpa. The solid lines indicate the Brillouin zone boundaries of the fcc structure.

In order to study the distribution of diffuse scattering extending in a wide area of the RLS, scattering intensity contour map was measured in the (0 0 1) scattering plane. Scattering intensity contour map obtained at 15

原子炉：JRR-3　　装置：TAS-1(2G)　　分野：中性子散乱（磁性）

K under the pressure of 1.8GPa is given in Fig. 1. In this figure, heavy lines indicate the Brillouin zone boundary of fcc structure. Strong intensities distributing slightly inside of the 1-st Brillouin zone boundary are diffuse scattering due to the spin correlations in $ZnFe_2O_4$. Broad circle along the 2-nd zone boundary is a diffraction line from the pressure transmitting medium 3M Fluorinert. At the first glance, the intensity contour map obtained under the 1.8GPa looked no difference from that obtained at the atmospheric condition. However, if we take the difference of the intensities between both maps, the effects of high pressure become appreciable. The subtracted data I(1.8GPa)- I(0GPa) are mapped in Fig. 2.

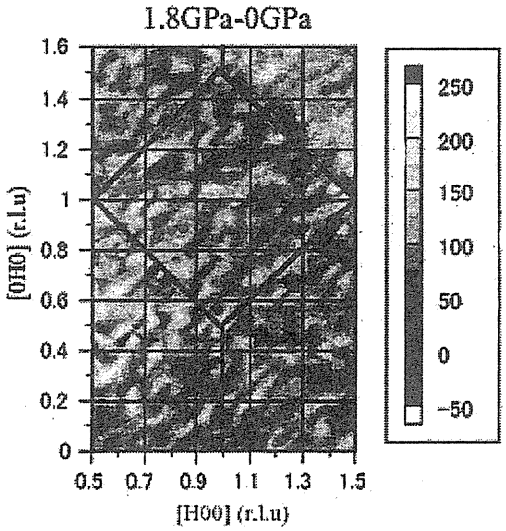


Figure 2: The subtracted intensity contour map I(1.8GPa)- I(0GPa) studied at 3.5K. The solid lines indicate the Brillouin zone boundaries of the fcc structure.

We can observe strong intensities slightly outside of the 2-nd zone boundary and weak intensities inside of the 1-st zone boundary. Since for the $CdFe_2O_4$, diffuse scattering appears slightly outside of the 2-nd zone boundary, experimental data indicate that the $ZnFe_2O_4$-type spin correlations were suppressed and the $CdFe_2O_4$-type spin correlations increased by applied high pressure. This is consistent with our first expectation. However, in order to obtain the persuasive results, further experiments for the data with better statistics are required.

References

1) P. W. Anderson: Phys. Rev. **102** (1956) 1008.
2) K. Kamazawa *et. al.*, *to be appeared in* Phys Rev. B.
3) K. Kamazawa *et. al.*, submitted to the Phys. Rev. Letters.

研究テーマ： 三角格子バナジウム硫化物 $BaVS_3$ 単結晶の磁気励起
表題： $BaVS_3$ 配向単結晶の中性子回折

1-2-44 Neutron diffraction of $BaVS_3$ oriented single crystals

H. Nakamura[1,*], K. Matsui[1], M. Shiga[1], T. Yamasaki[2], M. Nishi[3] and K. Kakurai[4]

[1] *Department of Materials Science and Engineering, Kyoto University, Kyoto 606-8501*
[2] *Graduate School of Human and Environmental Studies, Kyoto University, Kyoto, 606-8501*
[3] *Institute for Solid State Physics, The University of Tokyo, Tokai, Ibaraki 319-1106*
[4] *Advanced Research Center, Japan Atomic Energy Research Institute, Tokai, Ibaraki 319-1195*

Neutron diffraction experiments were performed for single crystals of $BaVS_3$ to determine the precise spin and charge structures below $T_X \simeq 30$ K. About 2000 pieces of needle-like shaped single crystals (total mass 1.00 g) were bundled to orient their c axes. In this condition, only c axes are fixed to a single direction but a axes distribute at random, enabling us to obtain only 2D information in the reciprocal lattice. Experiments were performed by triple axis spectrometers ISSP-HER and PONTA.

As an example of experimental results the a^*-c^* reciprocal plane is shown in Fig. 1 together with magnetic Bragg points (solid circles) observed by HER (wave length $\lambda = 4.05$ Å) at 7 K. Experimental results are summarized as follows: (1) Magnetic Bragg points were observed at the same h (= 0.394, 0.682 and 1.088) on $l = 0$ and 2 lines in the a^*-c^* plane but not on $l = 1$, indicating that the correlation along c is not antiferromagnetic but ferromagnetic (Note that the unit cell has 2 V atoms along c). (2) Each magnetic Bragg peak splits slightly along c^*. The split $\Delta l = 0.015$ indicates presence of a long-period magnetic modulation of about $67c \simeq 370$ Å. The magnetic propagation vector is refined as $(0.226\ 0.226\ 0.015)_{hex}$. The spin structure is interpreted as a helically modulated one derived from the 120° structure. (3) Expecting a spin density modulation corresponding to the crystal superlattice [2], we tried to observe reflections on $l = \frac{1}{2}$. However, magnetic scattering was not observable within the present experimental accuracy.

The spin structure together with the crystal superlattice structure [2], particularly a reduction of averaged spin to about half of $S = \frac{1}{2}$ [1] and a formation of the 4V atomic period below the metal-insulator transition at $T_{MI} \simeq 70$ K [2], suggest that Peierls- and Mott-type instabilities, due to a one-dimensional 1/4-filled d_{z^2} band and strongly-correlated and orbitally-degenerate d_{xy} bands, respectively, work cooperatively to form a set of 2 different molecular orbitals spreading over V–V pairs, each of which shares an unpaired d electron.

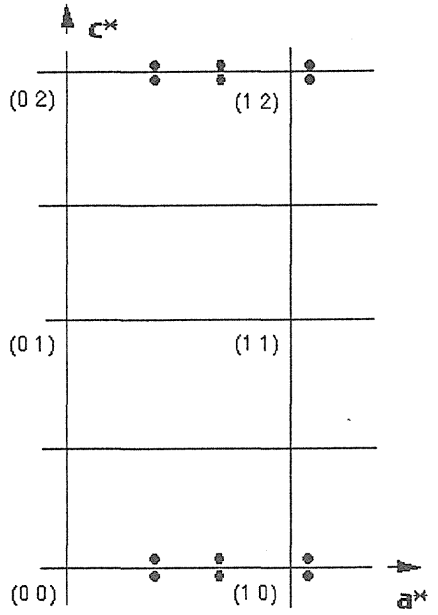


Fig. 1. The reciprocal lattice of $BaVS_3$ (a^*-c^* plane). Close circles represent magnetic Bragg points.

*present address: Graduate School of Science, Himeji Institute of Technology, Kamigori, Ako-gun, Hyogo 678-1297

References

[1] T. Inami *et al.*: Phys. Rev. B **66** (2002) 073108.
[2] H. Nakamura *et al.*: J. Phys. Soc. Jpn. **69** (2000) 2763.

使用施設： JRR-3 ， 装置： C1-1 (HER), 5G (PONTA) ， 分野： 2. Magnetism

研究テーマ：先端偏極中性子散乱によるスピン-格子物性の研究
表　題：一軸圧下中性子回折実験による UGa_3 の磁気秩序の研究

1-2-45

Magnetic order of UGa_3 investigated by neutron scattering under uniaxial pressure

M. NAKAMURA[1], T. D. MATSUDA[1], K. KAKURAI[1], G. H. LANDER[1,2], S. KAWARAZAKI[3] and Y. ŌNUKI[1,3]

[1]Advanced Science Research Center, JAERI, Tokai, Ibaraki 319-1195, Japan
[2]European Commission, JRC, Institute for Transuranium Elements, Postfach 2340, D-76125 Karlsruhe, Germany
[3]Graduate School of Science, Osaka University, Toyonaka, Osaka 560-0043

The uranium intermetallic compounds UX_3 demonstrate a wide variety of magnetic properties[1]. Among the UX_3 compounds, special attention was paid to UGa_3 because experiments and band structure calculations strongly suggested an itinerant nature for the magnetism of UGa_3. UGa_3 orders below $T_N = 67$ K with a type-II antiferromagnetic structure in which alternate (111) ferromagnetic planes of U moments are coupled antiferromagnetically[2,3]. The ordered moment is $\sim 0.6\ \mu_B$ per U atom. UX_3 systems crystallize in high symmetric structure, that is cubic $AuCu_3$ type. Therefore, the neutron diffraction measurement usually gives no conclusive information on the total magnetic moment orientation for UX_3 compounds because of their multidomain structures. In this study, we apply the weak uniaxial pressure to single crystalline UGa_3 so as to induce the anisotropic domain structure, which should bring a clue to the magnetic moment orientation of UGa_3. We demonstrate that the combination of uniaxial pressure and polarization analysis enables us to quantitatively estimate the domain population.

Experiments were carried out on triple axis spectrometer TAS-1 installed at the research reactor JRR-3M in JAERI. The scans were performed in (h, l, l) plane and the uniaxial pressure was applied along the $[01\bar{1}]$ axis up to 2 kbar, which is perpendicular to the scattering plane. Both polarized and unpolarized beam experiments were performed with an incident energy $E_i = 14.7$ meV. For polarized beam experiment, the incident neutron beam polarization was perpendicular to the scattering plane, that is vertical field geometry (VF). In this configuration all the magnetic components in the scattering plane (hereafter referred to as in-plane components) are detected in spin-flip (SF) channel and the magnetic components perpendicular to the scattering plane (out-of-plane components) are probed

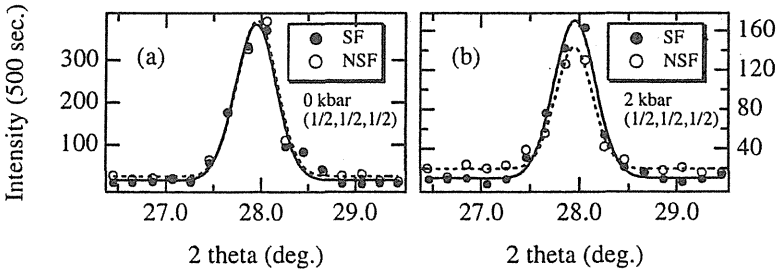


Figure 1: Polarization analysis of the (1/2, 1/2, 1/2) magnetic reflection at (a) 0 kbar and (b) 2 kbar. Measurements were performed at 8 K.

原子炉：JRR-3　　装置：TAS-1(2G)　　分野：中性子散乱（磁性）

in the non-spin-flip (NSF) channel.

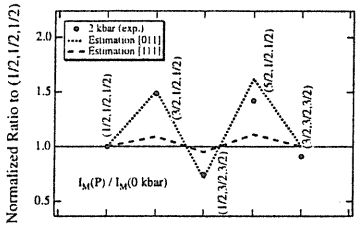


Figure 2: The ratio of intensities at 2 kbar to those at 0 kbar obtained by unpolarized measurements at 8 K. The estimated angle factors are also plotted for $\mu \parallel [011]$ (dotted line) and $\mu \parallel [111]$ (dashed line) All of the data are normalized to the intensity at (1/2,1/2,1/2).

Uniaxial pressure dependences of the polarization analysis for (1/2,1/2,1/2) magnetic reflection are shown in Fig.1. At 0 kbar the NSF intensity is almost equal to the SF intensity. At ambient pressure the ratio of in-plane and out-of-plane component is expected to be unity due to the isotropic domain distribution. On the other hand, the difference of the integrated intensities between NSF and SF becomes obvious at 2 kbar. The intensity ratio NSF/SF is estimated to be 0.61±0.07 and indicates the deviation from the isotropic distribution.

We now show, that the determination of the in-plane and out-of-plane component by means of polarized neutrons as described above, can be used to actually determine the domain population. Previously, we reported a method of estimating the magnetic moment orientation of UGa_3 from the pressure dependent behaviors of several magnetic reflections[4]. The same method is also applied to the magnetic intensities measured by unpolarized experiments under the 2 kbar uniaxial pressure as plotted in Fig.2. The y-axis represents the normalized *angle factors* to the value of (1/2,1/2,1/2). The angle factor is related to an angle between the magnetic moment vector and scattering vector. If the multidomain structure remains under uniaxial pressure, the values for each magnetic reflection must be unity in this figure. Therefore, the non-flat behavior in Fig. 2 confirms the induction of anisotropic domain structure by uniaxial pressure. In addition, this behavior tells us that an easy axis of ordered magnetic moment in UGa_3 is by no means along the [100] axis, because the calculated results for [100] axis[4] show opposite behaviors to the results for the present experiment.

We discuss the possibility that the total magnetic moment of UGa_3 is along the [011] or [111] axis. From the ratio of NSF/SF, we can analytically determine the domain population for both cases. The normalized angle factors calculated from domain populations are also plotted in Fig.2. The results of [011] direction successfully reproduce the experimental result. The domain population under 2 kbar uniaxial pressure is quantitatively solved, [011] direction occupies 25/42(∼ 60%) and $[01\bar{1}]$ direction 5/42 (∼ 12%). The other equivalent axes along $[1\bar{1}0]$,[101] ,$[10\bar{1}]$,$[1\bar{1}0]$ occupy 3/42 (∼ 7%). The finding of the [011] direction is consistent with that reported under hydrostatic pressure[4].

In summary, we have succeeded in determining the magnetic moment orientation of UGa_3 by polarized and unpolarized neutron beam experiments under uniaxial pressure. We found that the magnetic moment of UGa_3 is parallel to [011]. We consider that the determination of domain population by VF polarized beam experiments should serve us to obtain the *correct* form factor under hydrostatic pressure which includes the information on the orbital moment quenching[5], because the hydrostatic pressure contains the residual uniaxial component and may develop the anisotropic domain structure[4].

References

1) D. D. Koelling *et al.* : Phys. Rev. B **31** (1985) 4966.
2) A. Murasik *et al.* : Phys. Stat. Sol. A **23** (1974) K147.
3) P. Dervenagas *et al.* : Physica B **269** (1999) 368.
4) M. Nakamura *et al.* : J. Phys. Chem. Solids **63** (2002) 1193.
5) A. Hiess *et al.* : Europhys. Lett. **55** (2001) 267.

研究テーマ:Mn_3Pt 合金のスピンゆらぎ
表題:Mn_3Pt 合金について部分的なフラストレーション系

1-2-46 Partial Frustration System in the Ordered Mn_3Pt Alloy

T. Ikeda and Y. Tsunoda
School of science and engineering, Waseda University, Okubo 3-4-1, Shinjuku-ku, Tokyo 169-8555, Japan

The ordered Mn_3Pt alloy has a crystal structure of Cu_3Au type and is an antiferromagnet with a Néel temperature of T_N=475K. Below the Néel temperature, the first order AF-AF transition takes place at a transition temperature T_t. (The low and high temperature magnetic phases are named as the D-phase and the F-phase, respectively.) H.Yasui *et al.* carefully studied the transition temperature T_t, using the samples with less than 1% deviations from the stoichiometry is composition and determined T_t as 400K .

In the D-phase, all of the Mn sites have magnetic moments, which lie on the (111) plane and point to the <211> direction. In the F-phase, however, the magnetic moments are parallel to the crystal axis, that is to say, the collinear structure. In particular, one third of Mn atoms have no magnetic moments. It is characteristic of the ordered Mn_3Pt alloys to exist the collinear spin structure with the special Mn sites. At the phase transition T_t the magnetic moment changes from 2.2 (D-phase) to 3.3 (F-phase) μ_B per Mn atom with the unit cell volume expansion of 2.25 %. In the F-phase, careful examination using X-ray diffraction shows that the cubic lattice slightly distorts to the tetragonal structure with the tetragonality c/a=0.997.

In order to investigate the dynamics at the special Mn spins in the F-phase, we performed neutron inelastic scattering measurement at the T1-1 (HQR) triple axis spectrometer installed at a thermal guide of JRR-3M, JAERI, Tokai.

The intensity contour map on the (001) scattering plane measured by the constant-E mode of ΔE=6meV at T/T_N=0.940 (F-phase) is given in Fig.1. In this figure, solid lines indicate the Brillouin zone boundary of fcc structure. The inelastic diffuse scattering extends along the first zone boundary of the fcc structure. From the existence of the magnetic elastic Bragg peak at 1 0.5 0 RLP in this temperature, two third of Mn spins still show the magnetic long-range order.. Thus, magnetic long-range order and inelastic diffuse scattering coexist in the F-phase. In the F-phase, one third of Mn spins have ever been considered to be no moments, where the molecular field is cancelled. Resulting in the inelastic diffuse scattering observed along the first zone boundary of fcc structure, these Mn spins is not paramagnetic, but fluctuating with strong spin correlation, Tetragonal lattice distortion supports the suppression of the octahedral frustration and determine which Mn spins has to be non-magnetic. The F-phase is stabilized by suppressing the inconsistency of the triangle antiferromagnetic coupling through the dynamical motion of one third of Mn spins.

This is a characteristic of the octahedral spin frustration system.

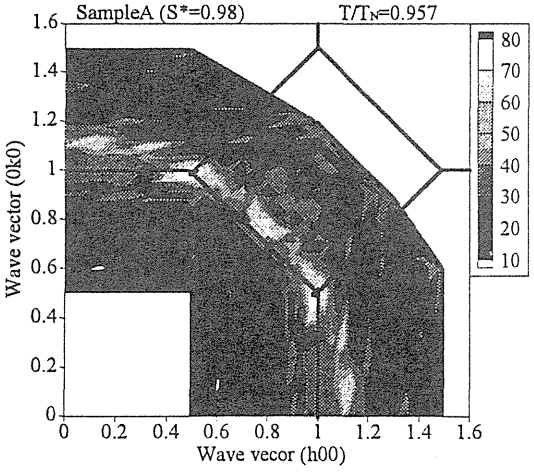


Fig.1. The scattering intensity contour map on the (001) scattering plane obtained at an energy transfer of ΔE=6meV at T/T_N=0.940. Solid lines represent the fcc zone-boundary

使用施設:JRR-3 ., 装置:T1-1(HQR), 分野:2.Magnetism

研究テーマ：擬2次元 $S = 1/2$ 量子スピン系 Cs_2CuBr_4 の磁気励起
表　題：$S = 1/2$ 擬2次元三角格子反強磁性体 Cs_2CuBr_4 の磁気構造と磁気励起
1-2-47

Spin Structure and Magnetic Excitation of $S = 1/2$ Quasi Two-dimensional Triangular Antiferromagnet Cs_2CuBr_4

T. ONO, H. TANAKA[1], A. OOSAWA[2], Y. KOIKE[2] and K. KAKURAI[2]

Department of Physics, Tokyo Institute of Technology, Tokyo 152-8551
[1]Low Temperature Center, Tokyo Institute of Technology, Tokyo 152-8551
[2]Advanced Science Research Center, JAERI, Tokai, Naka, Ibaraki 319-1195

Cs_2CuBr_4 has the orthorhombic crystal structure with the space group *Pnma*, and magnetic Cu^{2+}-ions form a distorted triangular lattice within the *bc*-plane. For the

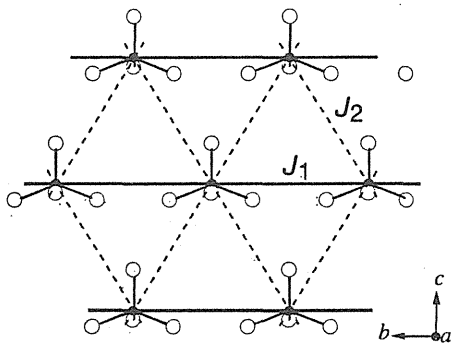


Figure 1: Arrangement of the magnetic Cu^{2+}-ions and the antiferromagnetic interactions J_1 and J_2 within the *bc*-plane.

isostructural compound Cs_2CuCl_4, the magnetic properties were well investigated by the neutron scattering experiments [1,2]. The magnetic properties of Cs_2CuCl_4 is well described by the quasi two dimensional antiferromagnetic model which has two different exchange coupling shown in Fig. 1 with weak Dzyaloshinskii-Moriya terms. Since Cs_2CuBr_4 has the same crystal structure, it is expected that the magnetic behavior of Cs_2CuBr_4 should be qualitatively described by the same hamiltonian which was determined for Cs_2CuCl_4 [2]. Although, the difference of the quantitative ratio between the exchange interactions J_1 and J_2 should give rise to the striking changes of the spin ordering in the magnetic field, since this system is fully frustrated.

This compound undergoes magnetic phase transition at Néel temperature $T_N = 1.4$ K. In the temperature region below T_N, a magnetization plateau appears at 1/3 of the saturation magnetization [3] for the field within the *bc*-plane.

In this report, we report the preliminary results of the inelastic neutron scattering experiments.

Measurements were performed at LTAS triple axis spectrometer installed at JRR-3M, JAERI Tokai. A single crystal with 3 cm^3 in volume was mounted on the sample stage of the dilution refrigerator. Measurements were performed for the *bc* scattering plane. Reflected neutron wave length was fixed at $\lambda_f = 4.045$ Å, and the collimation sequence was chosen as monochromator-80'-sample-80'-analyser-80'-detector. Figure 2 shows the typical scan of the magnetic Bragg peak along the b^*-axis at $T = 50$ mK. Magnetic Bragg reflec-

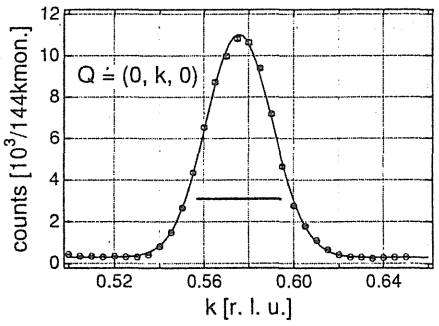


Figure 2: A typical scattering profile scanned along the b^*-direction measured around $T = 100$ mK. Solid straight line below the magnetic Bragg peak indicates the instrumental resolution.

原子炉：JRR-3　　装置：LTAS(C2-1)　　分野：中性子散乱（磁性）

tion appears at $Q_0 = (0, 0.576, 0)$. This result indicates the magnetic structure is incommensurate with the lattice along the b-axis. This incommensuration originates from the frustration among the antiferromagnetic interactions J_1 and J_2 within the bc-plane. For isostructural Cs_2CuCl_4, magnetic Bragg reflection appears at $Q = (0, 0.528, 0)$ [1]. Since the ordering vector is given by the ratio of J_1 and J_2 as $\cos(\pi Q_0) = -J_2/2J_1$ in view of classical spin model, we can obtain $J_2/J_1 = 0.467$ for Cs_2CuBr_4 and 0.175 for Cs_2CuCl_4. This result implies that Cs_2CuBr_4 is more frustrated than Cs_2CuCl_4.

In order to determine the magnitude of the exchange interactions experimentally, we have studied the magnetic excitation along the primary b-axis. Figure 3 shows the energy scan profiles along the b^*-axis. Solid lines are the fit

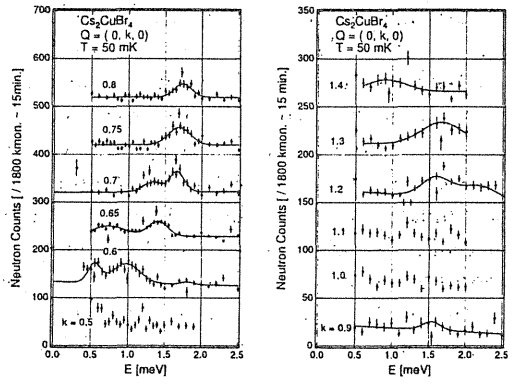


Figure 3: Energy scan profiles along the b^*-axis measured at 50 mK. Solid lines indicate the Gaussian fits to the experimental data.

to the Gaussian function(s). The energy scan profiles show the several excitation peaks at the energy indicated by the arrows. The observed peaks are summarized in Fig. 4. In this plot, the length of the vertical error bar are determined only from the fitting error. The solid line indicates the spin-wave mode [4]

$$\omega(k) = \sqrt{(J_k - J_{Q_0})\left[(J_{k+Q_0} + J_{k-Q_0})/2 - J_{Q_0}\right]}$$

of the Hamiltonian

$$\mathcal{H} = J_1 \sum_{\langle i,i' \rangle} S_i \cdot S_{i'} + J_2 \sum_{\langle i,j \rangle} S_i \cdot S_j$$

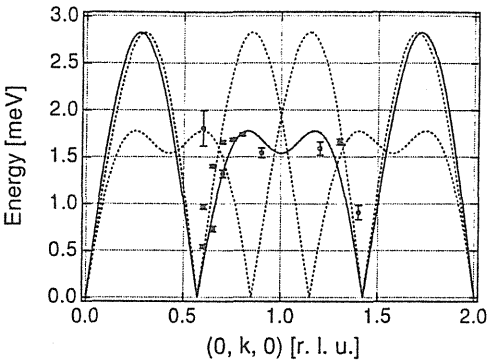


Figure 4: Plot of the dispersion of the magnetic excitations along the b^*-direction. The solid line indicates the linear spin wave dispersion described in the text.

, where J_k denotes the Fourier transformation of the exchange interaction $J_k = J_1 \cos(2\pi k) + 2J_2 \cos(\pi k) \cos(\pi \ell)$. The mode of the solid line indicates the spin wave which polarize out of the spin plane (bc-plane). In Fig. 4, the coupling constant J_2 is fixed as $J_2 = -2J_1 \cos(\pi Q_0)$, and the primary interaction J_1 is scaled as $J_1 = 2.15$ meV. The dashed lines indicate the secondary spin waves $\omega^{\pm}(k) = \omega(k \pm Q_0)$ which polarize within the spin plane [4]. In this model, Dzyaloshinskii-Moriya interactions and the inter-plane interactions are neglected. It is not clear whether this model corresponds to the experimental results because of the insufficiency of the data points. Precise measurements of the inelastic scattering are in progress in order to determine the detailed dispersion relation.

References

1) R. Coldea *et al.*: J. Phys.: Condens. Matter 8 (1996) 7473.
2) R. Coldea *et al.*: Phys. Rev. Lett. **88** (2002) 137203.
3) T. Ono *et al.*: Phys. Rev. B **67** (2003) 104431.
4) R. Coldea *et al.*: Phys. Rev. Lett. **86** (2001) 1335.

研究テーマ:軌道揺らぎが引き起こす磁性異常
表題:強磁性モット絶縁体 $Lu_2Cr_2O_7$ の3*d*軌道配列

1-2-48 3*d* Orbital Configuration in Ferromagnetic Mott Insulator $Lu_2Cr_2O_7$

S. Shamoto, S. Takeda, T. Kajitani, M. Azuma*, and M. Takano *

*Department of Applied Physics, Faculty of Engineering, Tohoku University, Sendai, 980-8579, Japan, * Institute for Chemical Research, Kyoto University, Uji, 601-0011, Japan*

Antiferromagnetic spin frustration in pyrochlore lattice has been studied by many researchers, while the orbital state has not been studied. Recently, we have pointed out the possible orbital frustration in ferromagnetic pyrchlore compounds [1]. However, the ferromagnetic pylochlore compound $Lu_2V_2O_7$ with T_c~73 K formed 109 degrees orbital structure to accommodate the frustration, according to our combined study of *ab initio* cluster calculation and crystal structure study [1].

Here we have synthesized adjacent ferromagnetic compound $Lu_2Cr_2O_7$ with T_c~170 K under high pressure, as the next possible compound with orbital frustration. However, the compound cannot be prepared as a single phase even under high pressure such as 7 GPa. Nevertheless, because of the known impurity phase $LuCrO_3$, we have successfully determined the crystal structure from 1.2 g sample by using neutron powder diffraction data (Fig. 1) at HERMES and Rietveld refinement program 'Rietan' [2] as shown in Table I.. It should be noted that aluminum foil was used for mounting the small amount of sample in the center of neutron beam.

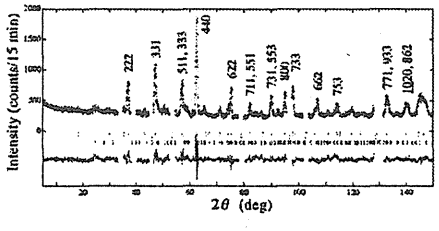


Figure 1: Observed, calculated, and difference patterns of neutron diffraction data. Indices are for $Lu_2Cr_2O_7$. Aluminum peaks are removed.

Table I.
Structural parameters of $Lu_2Cr_2O_7$ at room temperature.
Fd-3m (#227-2); *a*=9.8737(9) Å

Atom	Site	*x*	*y*	*z*	B_{eq} (Å^2)
Lu	16*c*	0	0	0	0.29(18)
Cr	16*d*	0.5	0.5	0.5	0.05(27)
O	8*a*	0.125	0.125	0.125	0.13(30)
O	48*f*	0.4222(4)	0.125	0.125	0.04 (15)

R_I=7.5%, R_p=7.1%, R_{wp}=9.3%, R_e=5.4%

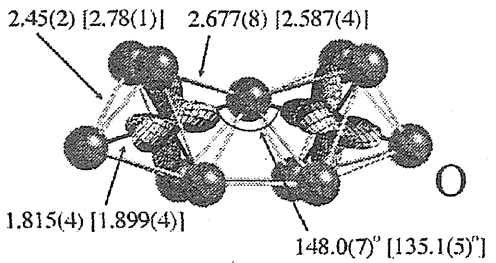


Figure 2: Configuration of e_g orbitals for two Cr atoms sitting in the center of CrO_6 octahedra. Spheres are oxygen atoms. Bond lengths (Å) and angles for $Lu_2Cr_2O_7$ [$Lu_2V_2O_7$] are shown.

Based on the crystal structure parameters, the energy levels of a CrO_6 (d^2) cluster was calculated by *ab initio* cluster calculation program 'SCAT' with DV-Xα method [3]. The results showed that e_g state had the lowest energy among the original t_{2g} orbitals in a cubic crystal field, which corresponded to Jahn-Teller distortion (Fig. 2). However, the high Curie temperature cannot be explained by our simple perturbation expansion up to the second order [1]. Since the energy levels of oxygen 2*p* orbital are close to Cr 3*d* orbital, the 2*p* orbital should play an important role in this compound.

References

[1] S. Shamoto *et al.*, J. Phys. Chem. Solids **63** (2002) 1047.
[2] Y.-I. Kim, F. Izumi, J. Ceram. Soc. Jpn. **102** (1994) 401.
[3] H. Adachi, *et al.*, J. Phys. Soc. Jpn. **45** (1978) 875.

使用施設：JRR-3 ，装置：HERMES(T1-3),AGNES(C3-1-1),KSD(T1-2),PONTA(5G)，分野 Magnetism

研究テーマ：先端偏極中性子散乱によるスピン-格子物性の研究
表　題：電荷秩序した$LuFe_2O_4$における磁気秩序形成の研究
1-2-49

Magnetic ordering process in the charge ordered $LuFe_2O_4$

S. NAGAI*, M. MATSUDA, Y. ISHII, K. KAKURAI, H. KITO[1], N. IKEDA[2] and Y. YAMADA[3]

ASRC, JAERI, Tokai, 319-1195
[1]NRIM, Tsukuba, 305-0047
[2]JASRI, Hyogo, 679-5198
[3]ARCSE, Waseda Univ., Tokyo, 169-0072
*Present address: NSL, ISSP, Univ. of Tokyo, Tokai, 319-1106

$LuFe_2O_4$ belongs to a class of materials expressed by RFe_2O_4, R being rare-earth metals.[1)] The crystals of these materials belong to the rhombohedral system. The Fe ions are arranged to form the hexagonal double layers and stack in the sequence of (AB), (CA), (BC),... along the rhombohedral unique axis. The average valence of the Fe ions is expected to be $Fe^{+2.5}$ in these materials and hence a mixed valence state of Fe^{2+} and Fe^{3+} ions occupying the equivalent Fe sites on the hexagonal plane with equal probability is expected. An earlier neutron scattering experiment on this compound by J. Iida *et al.* [2)] reports the observation of 2-D magnetic correlation even at lowest temperature (T=10K) in their single crystal sample. From their high temperature data (at RT) one can also deduce that there is no well developed 3-D charge ordering in their sample. Recently Y. Yamada *et al.*[3)] reported the sequential charge ordering observed by means of X-ray scattering in a $LuFe_2O_4$ single crystal grown by H. Kito. The charge ordering is characterized by an 3-D incommensurate charge-density wave state in the lowest temperature phase for T≤320K. It is of great interest to study the low temperature magnetic behavior in this charge ordered sample of $LuFe_2O_4$ to look for a correlation between the charge and spin ordering. We thus performed neutron scattering experiments on TAS-1 and TAS-2 in the temperature range of RT to 7K.

Figure 1 shows the purely magnetic scattering along (1/3, 1/3, L) at 270K and 7K measured by polarization analysis. At 270K 2-D scattering along c*-direction can be clearly seen and at T=7K 3-D like ordering can be observed. The insets indicate the temperature dependence of the peak intensities at Q=(1/3, 1/3, 1) and (1/3, 1/3, 2). One can clearly recognize the onset of the 3-D magnetic ordering at T_N=242K, but at the same time the temperature dependence of (1/3, 1/3, 1) and (1/3, 1/3, 2) indicates the existence of the second characteristic temperature T_f=177K. The hysteresis associated with T_f is remarkable. Figure 2 shows the detailed spectra at around this characteristic temperature along (1/3, 1/3, L) taken with better resolution (17'-20'-10'-20' collimations were used). The existence of both resolution limited peaks and broad peaks at 186K can be seen, while be-

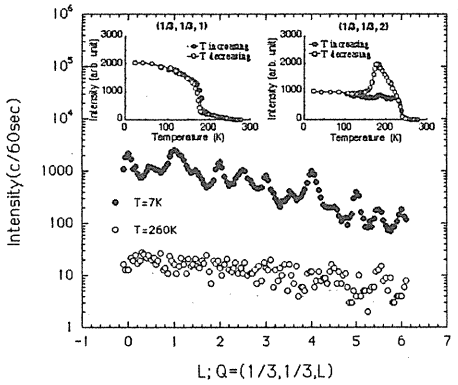


Figure 1: Purely magnetic intensity along Q=(1/3, 1/3, L) as obtained from the polarization analysis experiment at T=260K and 7K. Inset: T-dependence of the peak intensities at Q=(1/3, 1/3, 1) and (1/3, 1/3, 2).

原子炉：JRR-3　　装置：TAS-1(2G), TAS-2(T2-4)　　分野：中性子散乱（磁性）

low the characteristic temperature at T=161K the broad peaks considerably gain in intensities and at the same time the resolution limited peaks acquire finite widths resulting into the apparent diffuse contribution observed at lowest temperature. Figure 3 depicts the ferrimagnetic component showing up at Q=(1, 0, L), L=-6.5, -3.5, -0.5, 2.5. They also show the strong hysteretic behaviour as the (1/3, 1/3, 2) antiferromagnetic peak, as indicated in the inset.

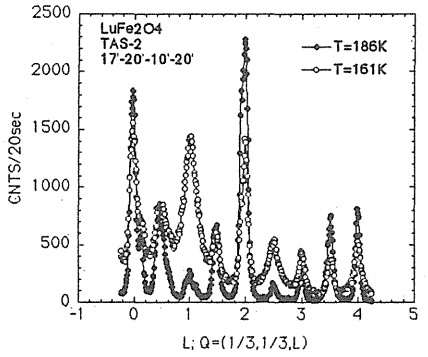


Figure 2: Magnetic scattering above and below T_f along Q=(1/3, 1/3, L) measured with tight collimations.

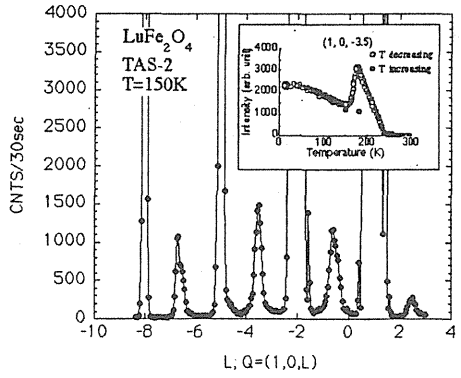


Figure 3: Scan along Q=(1, 0, L) at T=150K probing the ferrimagnetic component at L=-6.5, -3.5, -0.5 and 2.5. Inset: T-dependence of the peak intensity at Q=(1, 0, -3.5).

To summarize the following extraordinary magnetic ordering characteristics in $LuFe_2O_4$ were observed.

1) In contrast to the non-charge ordered sample a clear sign of 3-D magnetic ordering at T_N=242K is observed. Despite the triangular configuration a strong 2-D antiferromagnetic correlation with ferrimagnetic component in the double layer in the hexagonal plane develops to a 3-D order along the c-axis at this temperature.

2) At around 177K there is another characteristic temperature T_f, where new type of broad magnetic peaks start to grow and at the same time the magnetic peaks developing below T_N also acquire finite line width, including the peaks due to the ferrimagnetic component.

3) There is a strong hysteresis observed at T_f.

4) Due to the second 'transition' at T_f the low temperature magnetic peaks have a finite width along the c* direction causing the broad diffuse-like intensity distribution. The high energy resolution experiment using thermal neutron spin echo (see Activity Report on Neutron Scattering Research 2003 of NSL, ISSP) demonstrated that these diffuse intensities are of static nature within the resolution of 1μeV.

The surprisingly different charge and magnetic behaviour in the new sample may be explained by the difference in the oxygen stoichiometry, as has been already pointed out for YFe_2O_4 sample.[4] These results anyhow indicate that the charge ordering process strongly influences the low temperature magnetic ordering and that the subtle balance between charge frustration and spin frustration may cause the peculiar short range freezing of the spins in the ground state.

References

1) N. Kimizuka, E. Muromachi and K. Shiratori in *Handbook on the Physics and Chmistry of Rare Earths*, ed K.A. Gschneidner, Jr. and L. Eyring (Elsevier, Amsterdam, 1990) **Vol.13** p.283ff.
2) J. Iida *et al.* : J. Phys. Soc. Jpn. **62** (1993) 1723.
3) Y. Yamada *et al.* : Phys. Rev. B**62** (2000) 12167.
4) S. Funahashi *et al.* : J. Phys. Soc. Jpn. **53** (1984) 2688.

研究テーマ：γ-Mn 合金および β-Mn 合金の磁気構造
表　題：β-MnCoZn 合金に関する中性子回折研究
1-2-50

Neutron Diffraction Study on β-MnCoZn Alloys

T. HORI, H. SHIRAISHI and Y. ISHII[1]

Shibaura Institute of Technology, Saitama-city 337-8570
[1]Advanced Science Research Center, JAERI, Tokai, Ibaraki 319-1195

Pure β-Mn has a complicated cubic structure, so-called β-Mn structure, which contains 20 atoms distributed between two nonequivalents 8c and 12d sites.[1)] It is considered that this metal remains in paramagnetic state down to 1.4 K.[2)] β-Mn alloys containing some impurities show an antiferromagnetic behavior at low temperature. Two decades ago, we have made magnetization measurements and neutron diffraction experiments at KUR for β-Mn alloys containing Cobalt. The susceptibility for alloys with around 40 at. % Co has a maximum value at 80 K which must be the antiferromagnetic Néel temperature.[3)] However, this alloy has no applicable long range magnetic order structure.[3)]

On the other hand, β-CoZn alloy has a also β-Mn structure, and shows a typical ferromagnetism with the Curie temperature T_C = 460K.

We have found that wide solid solution from pure β-Mn to β-CoZn exist in ternary Mn–Co–Zn alloy system, so we have made X-ray and neutron diffraction experiments and magnetization measurements for ternary β-MnCoZn alloys.

Figure 1 shows magnetization in a field of 8.0 kOe versus temperature curves for β-CoZn alloy which shows a typical ferromagnetism with the Curie β-$Mn_{0.24}Co_{0.36}Zn_{0.40}$ alloys and show a temperature T_C = 460 K. Another alloy, β-$Mn_{0.24}Co_{0.36}Zn_{0.40}$, shows also a ferromagnetism with T_C = 200 K. However, more Mn rich alloy, β-$Mn_{0.42}Co_{0.28}Zn_{0.30}$, shows an antiferromagnetic behavior below around 70 K as shown in Fig. 1.

We have made neutron diffraction experiments for β-CoZn, β-$Mn_{0.24}Co_{0.36}Zn_{0.40}$ and β-$Mn_{0.42}Co_{0.28}Zn_{0.30}$ using HRPD.

Figure 2 shows observed and calculated neutron diffraction patterns for β-CoZn alloy at 7 K. The alloy shows a typical β-Mn structure with a = 4.000 Å. The site occupation and magnetic moment μ are as follows: Co on 8c, residual Co and Zn on 12d and $\mu = 1.3\mu_B$/Co atom. The detailed analysis for other alloys is now in progress.

References

1) P. Villars and L. D. Calvet: *Pearson Handbook of Crystallographic Datafor Intermetallic Phases.* **Vol. 4** (1999) 4321.
2) T. Kohara and K. Asayama: J. Phys. Soc jpn. **37** (1974) 401.
3) T. Hori: J. Phys. Soc. jpn. **38** (1975) 1738.

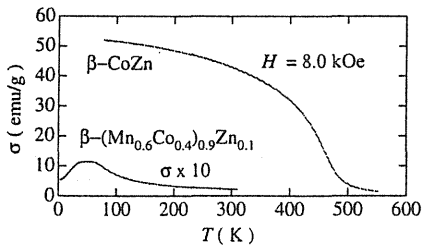


Figure 1: agnetization in a field versus temperature curves for β-CoZn and β-$Mn_{0.42}Co_{0.28}Zn_{0.30}$ alloys.

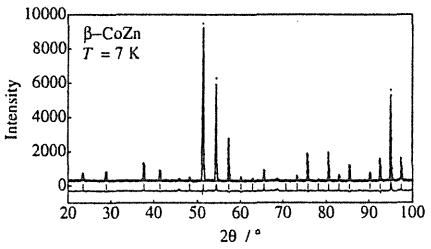


Figure 2: Observed (+) and calculated (a line) neutron diffraction patterns for β-CoZn alloy at 7 K. The difference between the observed and calculated intensities is shown by the lower curve.

原子炉：JRR-3　　装置：HRPD(1G)　　分野：中性子散乱（磁性）

研究テーマ：パイロクロア型化合物単結晶の静的・動的磁気相関
表題：パイロクロア型化合物 $Yb_2Ti_2O_7$ の中性子散乱

1-2-51 Neutron Scattering Study of Pyrochlore Compound $Yb_2Ti_2O_7$

Y. Yasui[1], M. Soda[1], S. Iikubo[1], M. Ito[1], M. Sato[1], N. Hamaguchi[1], T. Matsushita[1], N. Wada[1], N. Aso[2] and K. Kakurai[3]

[1]*Department of Physics, Nagoya University, Furo-cho, Chikusa-ku, Nagoya 464-8602*
[2]*Advanced Science Research Center, JAERI, Tokai, Ibaraki 319-1195*
[3]*Neutron Scattering Laboratory, ISSP, The University of Tokyo, Tokai, Ibaraki 319-1106*

Pyrochlore compounds $R_2Ti_2O_7$ (R=Y and various rare earth elements) have a cubic structure and consist of two kinds of three-dimensional networks individually formed by the corner-sharing R_4- and Ti_4-tetrahedra, respectively. Due to this structural characteristics, magnetic moments at the R sites are expected to be frustrated, if their nearest neighbor interaction is antiferromagnetic. For R=Tb, the Weiss temperature is -19K, indicating the interaction between the Tb^{3+} moments is antiferromagnetic. We have investigated the dynamical and static magnetic properties of $Tb_2Ti_2O_7$ by means of neutron scattering on a single crystal. The results have been reported in refs. 1 and 2. The frustration is also expected even for the moment system with the ferromagnetic nearest neighbor interaction, if the moments have strong uniaxial anisotropy. Such the situation can be found in $R_2Ti_2O_7$ with R=Dy[3] and Ho.[4] The low temperature magnetic behavior of $R_2Ti_2O_7$ depends on the electronic levels of R^{3+} ions in the crystal field and the interactions among the moments.

For $Yb_2Ti_2O_7$, the Weiss temperature is equal to be ~0.53K, indicating the interaction between the Yb^{3+} moments is ferromagnetic. The electronic ground state of Yb^{3+} ion was reported to be Kramers doublet with relatively small planar anisotropy, $g_\perp / g_{//}$ ~2.5, where $g_\perp$ and $g_{//}$ are the g-values perpendicular to and along the principal axis, respectively.[5] A sharp peak of the specific heat – temperature (T) curve was reported at 0.24K, indicating the existence of the phase transition.[6] However, Hodges *et al* [7] reported that there was no long range magnetic order below 0.24K .

In order to determine the low temperature magnetic state, we have carried out neutron diffraction study at HQR(T1-1) installed at the thermal guide of JRR-3M of JAERI in Tokai, where double axis condition was adopted. We have also carried out magnetic measurements on single crystals of $Yb_2Ti_2O_7$.

Temperature dependence of the real part of ac-susceptibility, χ' of $Yb_2Ti_2O_7$ is shown in Fig. 1, where a clear anomaly has been observed in T-dependence at 0.24K. The value of χ' at 0.24K is almost consistent in that of $1/4\pi N$, where N is the demagnetization coefficient of the used sample. This result indicates that the system exhibits a ferromagnetic transition at 0.24K. The value of saturation magnetization estimated from the M-H curve at 5K is ~1.8μ_B/Yb.

At T=0.03K, neutron scattering intensity

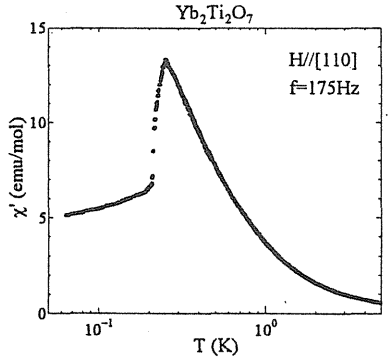


Fig. 1. Temperature dependence of the real part of the ac magnetic susceptibility, χ' of $Yb_2Ti_2O_7$.

使用施設：JRR-3 ，装置：HQR(T1-1)，分野：2. Magnetism

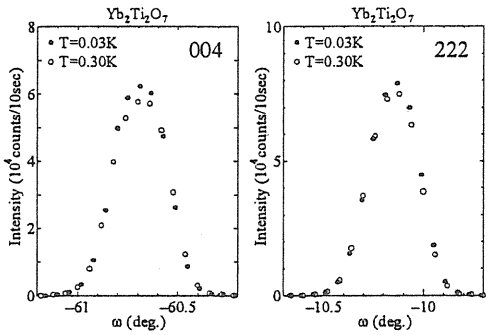


Fig. 2. Profiles of the ω-scans for 004 and 222 reflections taken at 0.03 K and 0.3 K.

has been measured at various Q-points in the (*hhl*) scattering plane. No reflection has been detected at Q-points except the nuclear Bragg points. The magnetic scattering intensities are observed at several nuclear Bragg points. Examples of the observed profiles are shown in Fig. 2. The profile widths of these magnetic reflections are equal to those of the instrumental resolution within the experimental error bars.

The T-dependences of the 004 and 111 reflection intensity are shown in Figs. 3 and 4, respectively, where the magnetic reflections are found to appear below ~0.24K. The intensity distribution at 0.03K is found to be explained by the simple collinear structure (see inset of Fig. 3). The value of the ordered moment of Yb^{3+} moments is estimated, by comparing the magnetic scattering intensities with the nuclear ones, to be $1.1\pm0.1\mu_B$, which is smaller than value of the saturation magnetization.

Hysteresis of the intensity-temperature curve has been observed, when the temperature is changed up and down, as shown in Fig. 4. The time dependence of the scattering intensity has also been observed at 0.03K after cooling to the temperature, as shown in the inset of the Fig. 4, where the typical time scale of the intensity change is of the order of hours. These results indicate that the motion of the moment system becomes slow with decreasing T, and the saturation moment of the ferromagnetic state does not correspond to the full moment of Yb^{3+}.

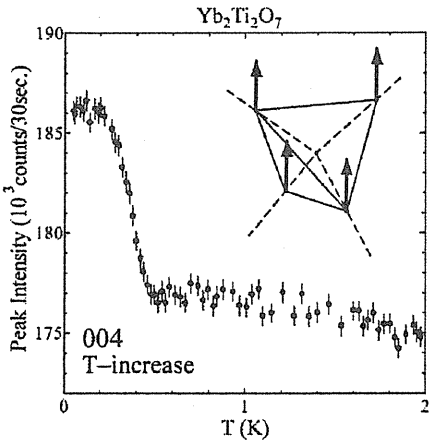
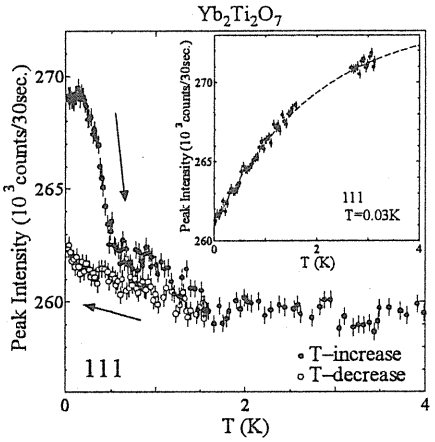


Fig. 3. Temperature dependence of the peak intensity of the 004 reflection. The inset shows the magnetic ordering pattern which can reproduce the observed magnetic scattering intensities taken at T=0.03K



.Fig. 4. Temperature dependence of the peak intensity of the 111 reflection. The inset shows the scattering intensity after cooling down to 0.03K as a function of the elapsed time.

References

[1] Y. Yasui *et al.*:J. Phys. Chem. Solids **62** (2001) 343.
[2] M. J. Harris *et al.*:Phys. Rev. Lett. **79**(1997)2554.
[3] S. Iikubo *et al.*:J. Phys. Soc. Jpn. **70** (2001) 212.
[4] M. Kanada *et al.*:J. Phys. Soc. Jpn. **71**(2002)313.
[5] J.A. Hodges *et al.*:J. Phys.: Condens. Matter **13** (2001) 9301.
[6] H.W.J.Blote *et al.*:Physica **43** (1969) 549.
[7] J.A. Hodges *et al.*: Phys. Rev. Lett. **88** (2002) 077204

研究テーマ：先端偏極中性子散乱によるスピン-格子物性の研究
表　題：四面体クラスタ化合物 GeV_4S_8 の磁気構造

1-2-52

Magnetic structure of GeV_4S_8 with V_4 tetrahedral clusters

H. NAKAMURA, H. CHUDO[1], Y. SHIMOJO[2], Y. ISHII[2] and K. KAKURAI[2]

Graduate School of Science, Himeji Institute of Technology, Kamigori, Ako-gun, Hyogo 678-1297
[1]Department of Chemistry, Kyoto University, Kyoto 606-8502
[2]Advanced Science Research Center, JAERI, Tokai, Ibaraki 319-1195

Critical phenomena of tetrahedral lattices such as Pyrochlore lattice attracts much attention recently. We are investigating compounds with tetrahedral clusters, which have (molecular-orbital like) direct mixing among d electrons, (1) in order to distinguish anomalies of an infinite lattice and an isolated tetrahedron, and (2) as miniatures of the itinerant-electron frustrated system. Johrendt [1] first synthesized GeV_4S_8 and reported its basic magnetic and transport properties. The crystal structure is characterized as $(V_4S_4)^{4+}$ cubane-type clusters are implanted in a cubic lattice, where V atoms form tetrahedral clusters. It is expected that a V_4 tetrahedron has 2 unpaired d electrons ($S = 1$ per V_4). So far, we determined an antiferromagnetic-like transition at $T_N = 18$ K, being consistent with [1], and also a small structural deformation from cubic to monoclinic at $T_S = 33$ K [2]. NMR measurements revealed that there exists 3 different internal field at V sites in the ground state; absolute values of the internal fields are 1.9, 4.9 and 5.9 T [2].

In order to determine the magnetic structure at low temperature and to know the reason why there exist 3 internal fields, we performed powder neutron diffraction experiments with use of HRPD at JAERI (wave length $\lambda = 1.823$ Å). Figure 1 shows the difference profile between 4 K and 25 K (i.e., magnetic scattering). Magnetic Bragg reflections are explained assuming a propagation vector $\mathbf{Q} = [\frac{1}{2}\frac{1}{2}0]$, suggesting that the compound has a relatively simple spin structure. Intensity analyses indicate that moments are parallel or antiparallel to $[1\bar{1}0]$, and that the magnitude is unique of 0.5 μ_B per V atom. The spin arrangement in the cluster is of interest, which is ferrimagnetic-like as $\uparrow\uparrow\uparrow\downarrow$, and the antiferromagnetism is satisfied as a whole magnetic unit cell. It should be noted that the moment magnitude is unique, indicating that the considerably different internal fields at V sites can not be attributed to simple separation of moment values but due to unconventional hyperfine coupling inherent to the tetrahedral cluster. On the basis of the proposed spin structure and assuming a large anisotropy in the hyperfine field and a large transferred field from neighboring V atoms within the cluster, we expect 3 different magnetic sites of V, which is in good accordance with the NMR observation. Hence we suggest that the internal field in this compound is dominated by the direction of moments rather than the magnitude of moments.

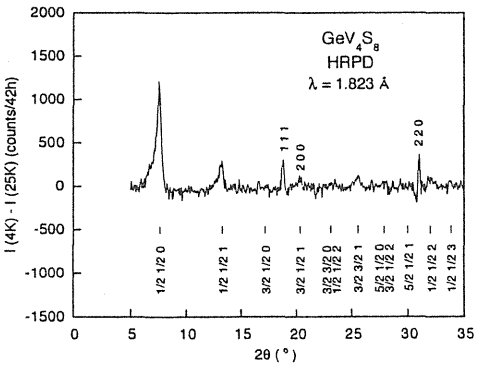


Figure 1: Magnetic scattering of GeV_4S_8.

References

1) D. Johrendt: Z. Anorg. Alleg. Chem. **642** (1998) 952.
2) H. Nakamura and H. Chudo: unpublished.

原子炉：JRR-3　　装置：HRPD(1G)　　分野：中性子散乱（磁性）

研究テーマ：パイロクロアおよびスピネル型化合物の non-trivial な磁気構造と特異な異常ホール効果
表題：パイロクロア型化合物 $Nd_2Mo_2O_7$ の異常ホール効果と磁気構造

Detailed Studies on the Anomalous Hall Effects and Magnetic Structure of $Nd_2Mo_2O_7$

1-2-53

Y. Yasui[1], T. Kageyama[1], S. Iikubo[1], M. Ito[1], M. Sato[1] and K. Kakurai[2]

[1]*Department of Physics, Nagoya University, Furo-cho, Chikusa-ku, Nagoya 464-8602*
[2]*Advanced Science Research Center, Japan Atomic Energy Research Institute, Tokai-mura, Naka-gun, Ibaraki 319-1195*

$Nd_2Mo_2O_7$ consists of individual networks of corner-sharing Mo_4- and Nd_4-tetrahedra and exhibits a ferromagnetic transition at temperature $T = T_C$=93K, where the Mo-moments primarily order. The ordering of the Nd-moments becomes significant below ~30K. The low temperature magnetic structure is non-collinear for both the Mo- and Nd-moments.[1)] Unusual behavior of the Hall resistivity ρ_H of $Nd_2Mo_2O_7$ has been reported by the authors' group:[2,3)] The magnetic field (H)- and T- dependences of ρ_H cannot be understood by the relation $\rho_H = R_0H + 4\pi R_sM$ usually used for ordinary ferromagnets, where M is the uniform magnetization, and R_0 and R_s are the ordinary and the anomalous Hall coefficients, respectively. Instead, the behavior can be described by $\rho_H = R_0H + 4\pi R_sM_{Mo} + 4\pi R_s'M_{Nd}$, where the anomalous Hall coefficients R_s and R_s' and the magnetizations M_{Mo} and M_{Nd} correspond to the Mo and Nd contributions, respectively. The existence of these two components is supported by the studies of doping effects on the behavior of ρ_H.[4)] Although many theoretical works have been reported on the anomalous Hall effect, any of classical theories cannot describe the whole behavior of ρ_H of $Nd_2Mo_2O_7$ consistently. A new proposal has been made that the ordering of spin chirality χ locally defined as $\chi \equiv S_1 \cdot (S_2 \times S_3)$ for three spins S_1, S_2 and S_3 contributes to the Hall resistivity.[5)]

Neutron diffraction studies in applied magnetic field (H//[0$\bar{1}$1]) up to 5.7 T have been carried out at HQR(T1-1) at JRR-3M of JAERI in Tokai to clarify the relationship between the order of the chirality χ and the behavior of ρ_H.[6)] The double axis condition was adopted.

In zero magnetic field, the Mo-moments align along the direction nearly parallel to [001] or other equivalent axes. They tilt by the angle α=4(±4)° at 1.6K towards the local principal axes (parallel to the lines connecting the center of gravity with their sites). The Nd-moments are along their principal axes with their net magnetization being antiparallel to that of the Mo-moments. The results indicate that there exists the relatively strong axial anisotropy at the Nd sites.

We have determined the magnetic structure at 1.6 K as a function of H, where the Mo-Mo and Mo-Nd exchange fields and the single ion anisotropies of the Mo- and

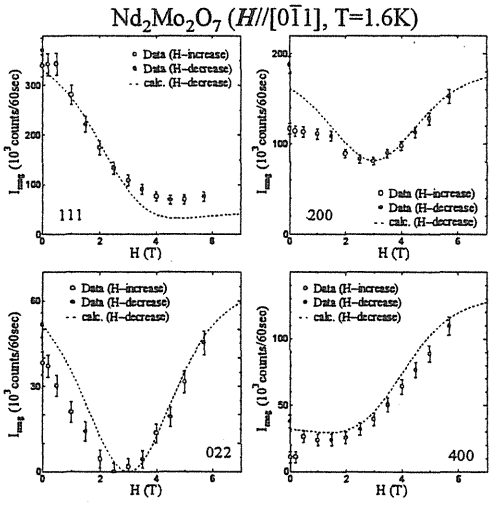


Fig. 1: Intensities of several magnetic reflections at 1.6K are plotted against H, applied along [011].

使用施設：JRR-3　装置：HQR(T1-1)，分野：2. Magnetism

Nd-moments are considered as the parameters. (From the results of the neutron inelastic scattering and the specific heat measurements, the interaction among the Nd-moments is found to be relatively small and can be neglected.) They are chosen to reproduce the H-dependence of the observed magnetic scattering intensities. The examples of the calculated results are shown in Fig. 1 by the dotted lines together with the observed ones. The Mo-moments align along the direction nearly parallel to H (//[0$\bar{1}$1]) and they are tilted from the direction by the single ion anisotropy and the Mo-Nd exchange interaction. For the two Nd sites with the principal axes perpendicular to H, the magnitudes and directions of the Nd- moments hardly change, because the anisotropy is very large. For the other Nd-sites, the population of the moments with the component anti-parallel to H decreases with keeping directional vectors along the principal axes and the average magnitude of the moments also changes. We have also determined the magnetic structures under the conditions H//[001] and [111] by using the same parameters as used for H//[0$\bar{1}$1].

In the chiral order mechanism of ρ_H, χ acts as the fictitious magnetic flux (Φ).

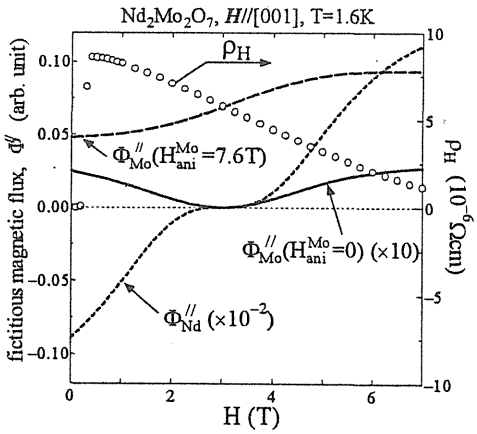


Fig. 2. Fictitious magnetic flux of the Mo- and Nd-moments along H (//[001]), $\Phi^{//}_{Mo}$ and $\Phi^{//}_{Nd}$, respectively, is shown at 1.6K against H. ρ_H is shown by the open circles.

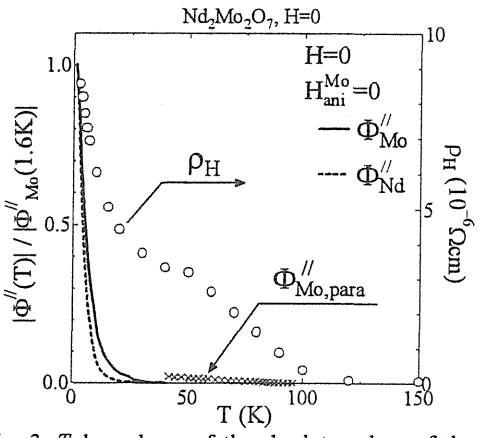


Fig. 3: T-dependence of the absolute values of the fictitious magnetic flux of the Mo- and Nd-moments, $\Phi^{//}_{Mo}$ and $\Phi^{//}_{Nd}$, respectively, is shown at H=0. The values are scaled by the data at 1.6K. The observed ρ_H is shown by the open circles.

Their components parallel to H, $\Phi^{//}$ is as functions of H and T by using the obtained magnetic structure. The H- dependences of $\Phi^{//}_{Mo}$ and $\Phi^{//}_{Nd}$ are shown in Fig. 2 for H//[001] for two effective magnetic field values, H_{Mo}^{ani} =7.6T and 0 introduced to consider the single ion anisotropy of the Mo-moments. The T- dependence of $\Phi^{//}_{Mo}$ and $\Phi^{//}_{Nd}$ at H=0 is shown in Fig. 3. The curves of $\Phi^{//}_{Mo}$ and $\Phi^{//}_{Nd}$ shown in Figs. 2 and 3 do not agree with the experimentally observed ρ_H (open circles). When the Mo-moments ferromagnetically order, the randomly oriented (along the principal axes) Nd- moments can induce the fictitious flux $\Phi^{//}_{Mo,para}$. However, as shown in Fig. 3, the $\Phi^{//}_{Mo,para}$ is much smaller than the observed ρ_H. Thus, the behavior of ρ_H cannot consistently be understood only by the chiral order mechanism. The essence of the present results is unchanged by this secondary effect.

References

[1] Y. Yasui *et al.*:J. Phys. Soc. Jpn. **70** (2001) 284.
[2] S. Yoshii *et al.*:J. Phys. Soc. Jpn. **69** (2000) 3777.
[3] S. Iikubo *et al.*:J. Phys. Soc. Jpn. **70** (2001) 212.
[4] T. Kageyama *et al.*:J. Phys. Soc. Jpn. **70** (2001) 3006.
[5] K. Ohgushi *et al.*:Phys. Rev. B62 (2000) R6065.
[6] Y. Yasui *et al.*:J. Phys. Soc. Jpn. **72** (2003) 865.

研究テーマ：先端偏極中性子散乱によるスピン-格子物性の研究
表　題：磁性薄膜・人工格子の特異な磁気構造の研究

1-2-54

Spin Orientation of Exotic Spin-Density Waves in Cr(001)/Sn Epitaxial films

M. TAKEDA[1,2], K. MIBU[3], J. SUZUKI[1], M. NAKAMURA[1], M. MATSUDA[1], K. KAKURAI[1] and Y. ENDOH[4]

[1]Advanced Science Research Center, JAERI, Tokai, Ibaraki 319-1195
[2]Physics Department, Graduate School of Science, Tohoku University, Sendai 980-8578
[3]Research Center for Low Temperature and Materials Sciences, Kyoto University, Uji, Kyoto 611-0011, Japan
[4]Institute for Material Research, Tohoku University, Katahira Sendai 980-8577

A variety of mysterious phenomena observed in metal Chromium (Cr) have attracted a lot of researchers for a long time. Among them most famous one is the spin-density wave (SDW) formed in bulk Cr below the Néel temperature of 311 K [1]. The SDW itself is now well known to condensed matter physicists, however, it is hard to say that the nesting model of Fermi surface can completely explain all magnetic behaviors of Cr. The SDW strongly depends on circumstances like impurities, temperature, internal stress and so on which affects the Fermi surface. The Fermi surface in Cr multilayers is expected to be effectively modified by the interfaces. By changing the counterpart of Cr multilayers we can have a variety of Fermi surface of Cr. This is a useful approach to elucidate all the details of the mechanism of the SDW which is governed by the nature of Fermi surface.

Recently we synthesized epitaxial Cr(001) / Sn multilayers in which monatomic Sn layers are periodically inserted in the Cr(001) epitaxial films and investigated the magnetic structures by complementary use of neutron and Mössbauer spectroscopies[2–5]. We have found that in the multilayers SDWs with complicated waveform were stabilized at low temperatures. The most exotic feature of the SDWs is that the artificial periodicity, Λ introduced by the embedded Sn monatomic layers, governs the wavelength of the SDWs, which is believed to be defined by the nesting vector in pure bulk Cr. In this brief report we focus on the Λ dependence of spin orientation: another prominent influence of the embedded Sn monatomic layers on the SDW state.

In the multilayers stacked bilayers of [Cr(t_{Cr})/Sn(0.2 nm)] (t_{Cr} = 4.0, 8.0, 10, 12 and 16 nm) were epitaxially deposited on MgO(001) substrates with a 5-nm-thick Cr buffer. The MgO[001] and bct Cr[001] directions are normal to the sample plane, and MgO[110] and Cr[010] are parallel each other. The stacking number of the bilayer in each sample, M, was determined to make the accumulated thickness of Cr 240 nm ($t_{Cr} \times M = 240$ nm). According to the t_{Cr}, the samples are called as CS4, CS8, CS10, CS12, CS14 and CS16, respectively. In X-ray diffraction profiles, the satellite peaks stemming from Λ were clearly observed up to the 4th order in all these samples, which indicated that the multilayer structures were well established.

Figure 1 shows the Λ dependence of in-plane and out-of-plane lattice parameters measured by TAS-1, TAS-2 and a conventional X-ray diffractometer at ambient temperatures where all of the sample have a commensurate antiferromagnetic structure [5]. Both in-plane (010) and out-of-plane (001) lattice constants were expanded in comparison with bulk Cr, however, they gradually approached the bulk value with increasing Λ. The in-plane lattice constants were larger than the out-of-plane one. The Λ dependence and the anisotropy leads to different internal stress in each sample. We performed scans along [001] and [010] through the (010) and (001) reciprocal points of the bct structure at 290 K. Single magnetic peaks at (010) and (001)

原子炉：JRR-3　　装置：TAS-1(2G), TAS-2(T2-4)　　分野：中性子散乱（磁性）

Table 1: The designed artificial period, Λ, the volume fraction of each S (spin direction) domains in the case of multi-S domain state, the easy axis of Cr moments in the case of single domain state and the magnitude of Cr magnetic moments at 300 K. The magnitude is common in both domain states.

	multi-S domain		single domain	
	in-plane	out-of-plane		
Λ (nm)	components (%)	component (%)	easy axis	M(300K) (μ_B)
4.2	37	63	[112]	0.57 ± 0.19
8.2	51	49	[223]	0.44 ± 0.10
10.2	68	32	[111]	0.38 ± 0.08
12.2	32	68	[112]	0.43 ± 0.16
14.2	32	68	[112]	0.44 ± 0.08
16.2	47	53	[223]	0.39 ± 0.10

appeared in the scan profiles of all samples, which indicates that the commensurate antiferromagnetic structure forms in the multilayers. Integrated intensities of those peaks were normalized by the intensity of Cr(020) and (002) nuclear peaks. The integrated intensities of the (001) and (010) are not identical even after the normalization. The degree of the unbalance indicates the direction of averaged Cr magnetic moments and the directions are consistent with the previous report on polarized neutron experiments [6].

If the sample is a single magnetic domain, the intensity of (010) peak is proportional to the summation of squared in-plane [010] and out-of-plane [001] components of Cr spins, and that of (001) to the summation of two squared in-plane components. In the case of multi-S domain state, in which domains with the easy axis of Cr moments being either [100] ([010]) or [001] coexist, the (010) intensity is proportional to sum of the volume of in-plane [100] and out-of-plane [001] S domains, and the (001) to that of two in-plane S domains.

When the single domain is assumed, the intensity ratio gives the spin orientation. Possible easy axes deduced from the intensity ratios are summarized in Table 1. This table also shows the volume fraction of each S domains in case of multi-S domain and the magnitude of averaged Cr magnetic moments. It is known that the easy axes of the SDW in bulk Cr are bcc principle axes. The hard axis of bulk Cr like [111] is unlikely to be the easy axes of these multilayers. At the moment we can not conclude either of domains is realized in each multilayers. CRYOPAD, which is now developed by our group, is going to give clear conclusion on this ambiguity [7].

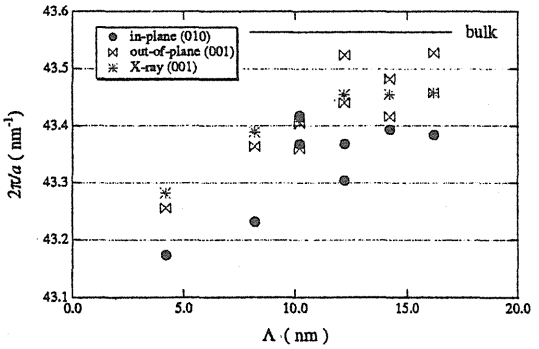


Figure 1: The artificial periodicity, Λ, dependence of in-plane and out-of plane lattice parameters of Cr/Sn(001) multilayers.

References

1) E. Fawcett, Rev. Mod. Phys. **60**, 209 (1988).
2) K. Mibu, S. Tanaka and T. Shinjo, J. Phys. Soc. Jpn. **67**, 2633 (1998).
3) M. Takeda, K. Mibu, K. Takanashi, K. Himi, Y. Endoh, T. Shinjo and H. Fujimori, J. Phys. Soc. Jpn. **69**, (2000) 1590.
4) K. Mibu, M. Takeda, J. Suzuki, A. Nakanishi, T. Kobayashi, Y. Endoh and T. Shinjo, Phys. Rev. Lett. **89** (2002) 287202.
5) M. Takeda, K. Mibu, T. Shinjo, J. Suzuki and Y. Endoh, App. Phys. **74** (2002) s1554.
6) M. Takeda, K. Mibu, J. Suzuki, M. Nakamura, M. Matsuda, K. Kakurai and Y. Endoh, JAERI-Review. **2002-028** (2002) 51.
7) M. Nakamura, M. Takeda, Y. Shimojo and K. Kakurai, see in this review.

研究テーマ:パイロクロア及びスピネル型化合物の non-trivial な磁気構造と特異な異常ホール効果
表題:$Cu_{0.3}Zn_{0.7}Cr_2Se_4$ の磁気構造

1-2-55

Magnetic Structure of $Cu_{0.3}Zn_{0.7}Cr_2Se_4$

S. Iikubo[1], Y. Yasui[1], Y. Kobayashi[1], Y. Ohno[1], M. Ito[1], M. Soda[1], M. Sato[1] and K. Kakurai[2]

[1]*Department of Physics, Division of Material Science, Nagoya University, Furo-cho, Chikusa-ku, Nagoya 464-8602*

[2]*Advanced Science Reserch Center, JAERI, Tokai, Ibaraki*

The problem of the Hall resistivity ρ_H of the ferromagnetic metals has been a long standing subject and discussed by many authors. However, the behavior observed for various systems has not yet been fully understood. Especially, unusual behaviors of the anomalous Hall resistivity have often been observed in systems with non-trivial magnetic structure.[1-4]

The spinel compound $Cu_{1-x}Zn_xCr_2Se_4$ is one of such systems. At x=0, it is a collinear ferromagnet with Curie temperature T_C ~450 K, and at x=1 it has a helical structure with the Neel temperature T_N=20 K. In the intermediate region of x, the structure seems to be conical[4,5]. The anomalous Hall coefficient R_s observed in this intermediate region changes its sign at around the temperature T_m~100 K, where magnetic superlattice peaks become appreciable and their intensities gradually grow with decreasing T, indicating the growth of the conical magnetic order[5]. The behavior of the Hall resistivity ρ_H of this system has been discussed in relation to the order of the spin chirality χ, which is locally defined as $\chi \equiv S_1 \cdot (S_2 \times S_3)$ for three spins S_1, S_2 and S_3 [5,6].

In order to accumulate further information on the relationship between the magnetic structure and the behavior of ρ_H, neutron diffraction studies have been carried out on single crystals of $Cu_{0.3}Zn_{0.7}Cr_2Se_4$ and detailed magnetic structure is clarified, where results of NMR measurements have also been considered.

Neutron measurements were carried out on the triple axis spectrometer at HQR (T1-1) at JRR-3M of JAERI in Tokai. The double axis configuration was utilized. The effective collimations were 17'-40'-60'. The Curie temperature T_C of the single crystal is ~350 K. Data of the integrated intensities of the nuclear reflections were collected at 450 K. Intensity data of the magnetic reflections at $(0,0,Q_0)$ (see fig.1), $(1,1,1-Q_0)$ and $(1,1,1+Q_0)$, for example, in the reciprocal space, were collected at 3.5 K and used in the present analyses, where Q_0 has the incommensurate(IC) value of ~0.4282 in the reciprocal lattice unit. The intensity of the 111 magnetic reflection at 3.5 K, estimated by subtracting the weak nuclear intensity at 450 K has also been used.

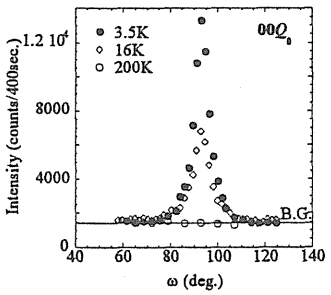


Fig.1. Intensity of the $00Q_0$ neutron reflection taken for the single crystal of $Cu_{0.3}Zn_{0.7}Cr_2Se_4$. The horizontal line indicates the background level.

Before going to the analyses of neutron data, a few remarks should be made concerning the results of NMR studies. In our recent NMR study, details of which are described elsewhere[7], following things are found on its magnetic features. First, the conical angle θ determined by using the

使用施設:JRR-3　装置:HER(T1-1), 分野:2. Magnetizm

NMR spectra is ~50° at 4.2K. Second, the static moment of Cr is nearly independent of x in the whole temperature region. The ferromagnetic component of the Cr moment, $\mu_f \equiv \mu_{Cr} \times \cos\theta$ can be estimated to be ~1.76 μ_B from the ratio of the intensity of the 111 magnetic reflection to those of the nuclear reflections and $\mu_{Cr}(\cong 1.76\mu_B/\cos 50°) \cong 2.74$ μ_B is also obtained. The value of μ_{Cr} is in rather good agreement with that (~2.85 μ_B) expected from the valence analysis.

We adopt the conical spin structure with the tilting angle θ (conical angle) from the conical axis and the difference $\delta\phi$ of the azimuthal angles between the neighboring planes perpendicular to the propagation vector Q_0(All spins within a plane perpendicular to Q_0 are assumed to be parallel. Note that Q_0 is not necessarily parallel, as shown later, but can be perpendicular to the conical axis.).

In the estimation of the intensities of the IC reflections, we have to consider that there exist two kinds of conical structures with the same propagation vector Q_0 and equal values of θ and $\delta\phi$, but different directions of the conical axes: For one of them, the conical axis is parallel to Q_0 and for another, it is perpendicular to Q_0. Assuming the equal distribution of these structures, the intensities, which are proportional to the square of $\mu_\perp \equiv \mu_{Cr} \times \sin\theta$ are deduced and from these ratios to the intensities of the nuclear reflections, $\mu_\perp$ is obtained to be ~1.43 μ_B, which should be compared with the value 2.74 μ_B $\times \sin 50° = 2.1$ μ_B expected from the values of μ_{Cr} and θ. Before discussing this discrepancy, we plot the observed and calculated magnetic structure factors F_{exp} and F_{cal}, respectively, in the form of $|F_{exp.}|^2$ -$|F_{cal.}|^2$, where F_{cal} are obtained for $\mu_\perp$ =1.43 μ_B. The points for the IC reflections are roughly on the straight line, indicating that the conical model adopted here is appropriate.

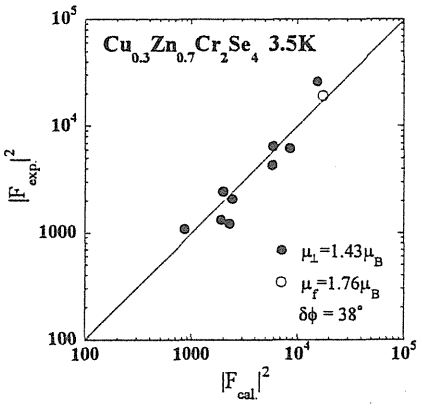


Fig. 2 $|F_{exp.}|^2$ of the IC reflections (solid circles) obtained from the integrated intensities are plotted against $|F_{cal.}|^2$ calculated by the conical model with the parameters $\mu_\perp$ =1.43 μ_B. The value of $\delta\phi$ =38°, respectively.

As the origin of the discrepancy between values of $\mu_\perp$ independently estimated by two different data, the random distribution of $\delta\phi$ around 38° is plausible, because the distribution with very small width (of the order 3) is enough to bring about the observed reduction of the intensities of the IC reflections.

Detailed magnetic structure of $Cu_{0.3}Zn_{0.7}Cr_2Se_4$ has been presented. We hope that results of these studies give a clue to understand the relationship between the non-trivial magnetic structure and the unusual behavior of the Hall resistivity.

References

1) S. Yoshii, S. Iikubo, T. Kageyama, K. Oda, Y. Kondo, K. Murata and M. Sato: J. Phys. Soc. Jpn. 69 (2000) 3777.
2) S. Iikubo, S. Yoshii, T. Kageyama, K. Oda, Y. Kondo, K. Murata and M. Sato: J. Phys. Soc. Jpn. 70 (2001) 212.
3) Y. Taguchi, Y. Oohara, H. Yoshizawa, N. Nagaosa and Y. Tokura: Science 291 (2001) 2573.
4) K. Oda, S. Yoshii, Y. Yasui, M. Ito, T. Ido, Y. Ohno, Y. Kobayashi and M. Sato: J. Phys. Soc. Jpn. 70 (2001) 2999.
5) S. Iikubo, Y.Yasui, K. Oda, Y. Ohno, Y. Kobayashi, M. Sato and K. Kakurai: J. Phys. Soc. Jpn. 71 (2002) 599.
6) K. Ohgushi, S. Murakami and N. Nagaosa: Phys. Rev. B 62 (2000) R6065.
7) S. Iikubo, Y.Yasui, Y. Kobayashi,Y. Ohno. M.Ito, M. Soda, M. Sato and K. Kakurai: submitted to J. Magn. Magn. Mat.

研究テーマ：多重極限環境下における中性子散乱実験法の研究
表　題：希土類反強磁性化合物 $ErAg_2$ の結晶場励起の観察
1-2-56

Crystal Field Excitation in rare earth Er-based antiferromagnet $ErAg_2$

I. Umehara[1], K. Sato[2], N. Metoki[3,4]

[1] Department of Physics, Faculty of Engineering, Yokohama National University, Tokiwadai, Yokohama 240-8501
[2] Department of Physics, Faculty of Science, Toyama University, Toyama 930-8555
[3]Advanced Science Research Center, JAERI, Tokai, Naka, Ibaraki 319-1195
[4] Department of Physics, Tohoku University, Aoba, Sendai, 980-8578

$ErAg_2$ is a rare earth compound with a body centered tetragonal $MoSi_2$-type (space group: I4/mmm) structure.[1-3] It has been reported that the magnetic moments on Er atoms order antiferromagnetically below the Néel temperature T_N = 5.2 K, and exhibit a magnetic structural change at T = 3.5 K. A previous neutron powder diffraction study[1] revealed a complicated incommensurate sinusoidal moduration at high temperature phase, while a commensurate antiferromagnetic ordering was observed below T = 3.5 K. On the other hand, our specific heat measurement on a single crystalline sample of $ErAg_2$ reported a new transition at T = 4.0 K[4]. Furthermore multi-step magnetization process has been observed in this compound, indicating the existence of a complicated magnetic H-T phase diagram. Recently the pressure effect of these transtions were also studied. In order to understand the origin of the successive magnetic transitions and the metamagnetic transitions, we tried to measure the crystal field excitation of $ErAg_2$.

The inelastic scattering profile was measured using triple-axis spectrometer TAS-2 with fixed E_f at 14.7 meV. The collimation was 40'-40'-80'. A polycrystalline sample was cooled by using a close cicle refregerator down to 10 K.

Figure 1 summarizes the result of the inelastic scattering profile of $ErAg_2$. We observed a clear excitation around 5.5 meV and 8.5 meV at T = 10 K. The intensity of these peaks decreased with elevating temperature at T = 100 K. Therefore we concluded that these peak were crystal field excitations. The excitation energy of these peaks were more or less consistent with CEF level scheme which explains susceptibility data, where the excitation energy would be 34 K, 77 K, and 85 K for the first, second, and third excitation level, respectively. On the other hand, the excitation observed below 3 meV at 100 K is considered as phonon.

References

1) M. Atoji: J. Chem. Phys. **57** (1972) 851.
2) S. Miura, T. Kaneko and M. Ohashi: J. Phys. Soc. Japan **37** (1974) 1464.
3) M. Ohasi, T. Kaneko and S. Miura: J. Phys. Soc. Japan **37** (1975) 588.
4) I. Umehara, Y. Takamo, M. Endo, F. Ishikawa, M. Yamaguchi and K. Sato: Physica **B281&282** (2000) 169.

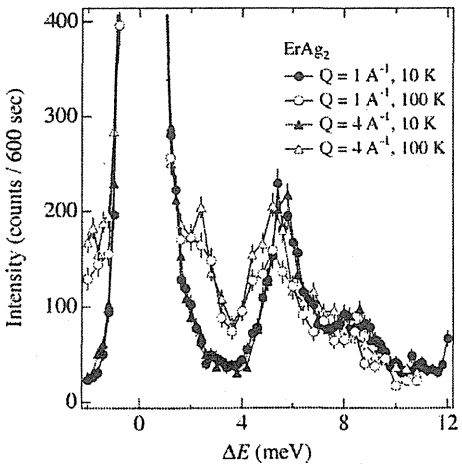


Figure 1: The inelastic scattering profile of $ErAg_2$.

原子炉：JRR-3　　装置：TAS-2(T2-4)　　分野：中性子散乱（磁性）

研究テーマ:$CoCr_2O_4$のスピン構造とスピンダイナミクス
表題:$CoCr_2O_4$の磁気構造と磁気短距離秩序

1-2-57 Magnetic structure and Magnetic short range order in $CoCr_2O_4$

K. Tomiyasu J. Fukunaga and Y. Tsunoda

School of science and engineering, Waseda University, 3-4-1, Ohkubo, Shinjuku-ku, Tokyo, 169-8555, Japan

$CoCr_2O_4$ has a crystal structure of a cubic normal spinel, that is, Co^{2+} ions occupy A-sites and Cr^{3+} ions occupy B-sites. The magnetic structure was first investigated by Menyuk, Dwight and Wold. They performed the neutron-scattering using a powder sample and concluded that the magnetic structure of $CoCr_2O_4$ is a long-range order (LRO) of a ferrimagnetic spiral one below T_S = 27 K. Figure 1 shows the magnetic structure below T_S. The propagation vector **q** of the spiral order is (0.62,0.62,0) and the spiral order is an incommensurate. Another magnetic structure is reported by Plumier from his neutron powder diffraction experiments under zero and nonzero magnetic field. His magnetic structure is different from the Menyuk et al's one at the two points; first, the spiral order and the ferrimagnetic order are a short-range order (SRO), and second, the both **q** is (2/3,2/3,0) and the spiral order is a commensurate one.

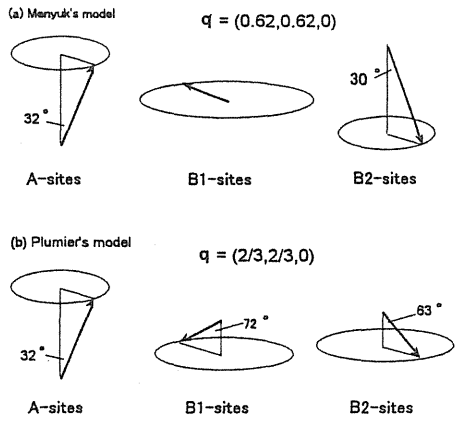


Fig.1 The magnetic structures reported by Menyuk et al (a) and Plumier (b).

All the experiments were performed at the triple axis spectrometer HQR(T1-1) installed at JRR-3M in JAERI (Tokai), using a single crystal. In this paper, we report the magnetic structure of $CoCr_2O_4$, and report to find that only the spiral order is a SRO, which is described a Lorentzian, and the ferrimagnetic order is a LRO.

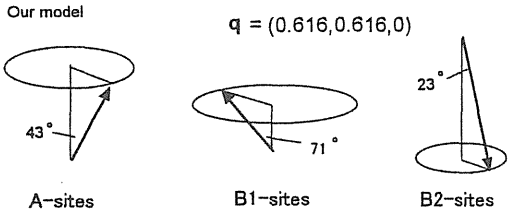


Fig.2 Our magnetic structure obtained from the scattering intensities of the satellite peaks.

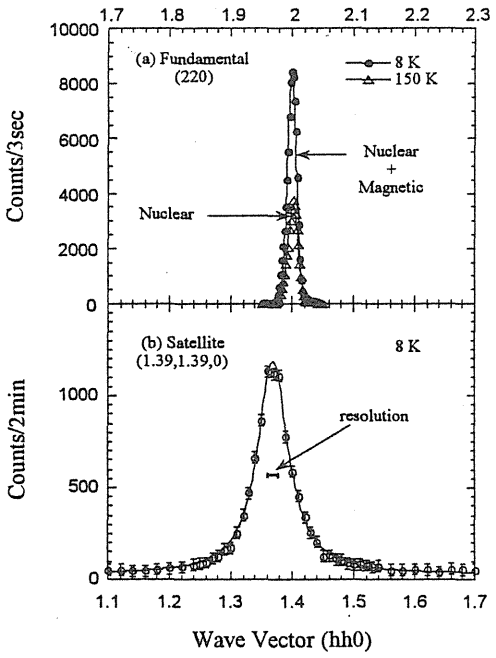


Fig.3 (a) Temperature dependence of 220 peak and (b) line profile of the satellite peak.

使用施設:JRR-3 in JAERI (Tokai), 装置:HQR(T1-1), 分野 Magnetism

研究テーマ：多重極限環境下における中性子散乱実験法の研究
表　題：遍歴5f反強磁性体 $UTGa_5$ (T: Ni, Pd, Pt) の中性子回折による構造研究

1-2-58

Structural study of itinerant 5f antiferromagnet $UTGa_5$ (T: Ni, Pd, Pt) by neutron diffraction

K. KANEKO[1], N. METOKI[1,2], N. BERNHOEFT[3], G. H. LANDER[1,4], Y. ISHII[1], Y. TOKIWA[1], S. IKEDA[1], Y. HAGA[1] and Y. ŌNUKI[1,5]

[1]Advanced Science Research Center, JAERI, Tokai, Ibaraki 319-1195
[2]Department of Physics, Tohoku University, Aoba, Sendai 980-8578
[3]DRFMC-CEA, 38054 Grenoble, France
[4]EC-JRC, Institute for Transuranium Elements, Postfach 2340, D-76125 Karlsruhe, Germany
[5]Graduate School of Science, Osaka University, Toyonaka, Osaka 560-0043

$UTGa_5$ with T=Ni, Pd and Pt exhibit itinerant antiferromagnetic ordering below the Néel temperature, T_N=86, 30 and 26K.[1-3] Our recent neutron scattering study revealed that the magnetic structures are different significantly between the iso-electronic compounds $UNiGa_5$ and $UPtGa_5$ [4]. It has been suggested that the orbital degree of freedom may play an important role on the stability of the magnetic structure. To address this issue, we studied crystal structure and its thermal evolution together with the magneto-striction.

The neutron powder diffraction data were measured on HRPD installed at JRR-3 in JAERI. The obtained diffraction patterns were analysed by the Rietveld method using RIETAN-2000[5]. The details of sample preparation were published elsewhere [2,3].

The structural and reliable parameters obtained in this work are summarized in Table I. The crystal structure of $UTGa_5$ consists of a UGa_3 block and an intercalating transition metal sheet stacking along the c axis, as shown in Fig. 1. The value of a, c and z_{Ga} gives the information on the tetragonality of the local UGa_3 block, $t = 1 - (2cz_{Ga}/a)$, where t =1 corresponds to the cubic UGa_3 with $AuCu_3$ type structure. We find that the tetragonality t of UGa_3 block in $UTGa_5$ increases markedly with changing the transition element. At room temperature, the local UGa_3 block with t=1.55% in $UNiGa_5$ is very close to cubic UGa_3, whereas t=7.02% in $UPtGa_5$ indicates the uniaxially compressed UGa_3 block along the c-axis.

Figure 2 shows the lattice constants a and c in $UTGa_5$ as a function of temperature. It is clear that there is magneto-striction in the $UTGa_5$ compounds. At base temperature, $UNiGa_5$ exhibits a relative increase in a of about 0.1% and decrease in c about 0.04% compared with their respective values at T_N. The lattice parameter a in $UPdGa_5$ exhibits a quasi-invar like plateau below T_N, indicating that a magneto-elastic interaction essentially compensates the paramagnetic thermal contraction in the basal plane, whereas the c-axis exhibits a monotonous decrease with decreasing temperature. The lattice constants in $UPtGa_5$ increase by $\sim$ 0.013 % at base temperature relative to their value at T_N in both a- and c-directions. The lattice contraction of a in $UPtGa_5$ was opposite from the lattice expansion in $UNiGa_5$, whilst the intermediate

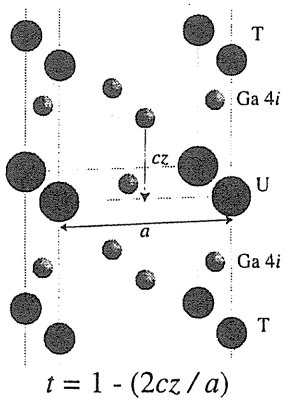


Figure 1: Crystal structure of $UTGa_5$.

原子炉：JRR-3　　装置：HRPD(1G)　　分野：中性子散乱（磁性）

Table 1: Structural parameters and conventional reliability factors obtained for $UTGa_5$ (T: Ni, Pd, Pt).

	T (K)	a (Å)	c(Å)	z_{Ga}	t (%)	R_{wp}	S	R_B
$UNiGa_5$	300	4.2380(1)	6.7864(1)	0.3074(1)	1.55	9.65	1.33	3.56
$UPdGa_5$	300	4.3218(1)	6.8637(1)	0.2987(1)	5.12	7.32	1.79	2.13
$UPtGa_5$	300	4.3386(1)	6.8054(1)	0.2964(1)	7.02	5.61	1.16	2.15

behavior was found in $UPdGa_5$.

The change in the sign of the basal plane contribution to the thermal expansion between $UNiGa_5$ and $UPtGa_5$ may reflect the different basal plane coupling: antiferromagnetic in $UNiGa_5$ whereas ferromagnetic in $UPtGa_5$.[4] This situation suggests the presence of a critical separation ε_0, where the effective U-U basal plane interaction changes its sign. On the other hand, the antiferromagnetic coupling as well as the negative thermal expansion for c-axis is common to $UNiGa_5$ and $UPtGa_5$. After subtracting the thermal contraction, a in $UPdGa_5$ also exhibit the lattice expansion due to the magnetic ordering. This fact suggests that the magnetic structure of $UPdGa_5$ may be the same as in $UPtGa_5$.

One possibility for the sign change of the nearest neighbor interaction is that a concurrent orbital ordering takes place in $UTGa_5$ and affects on the change of basal plane magnetic configuration. The present study clarifies the difference in the tetragonality of local UGa_3 block and the relevant lattice distortion corresponding to the different magnetic structure between $UNiGa_5$ and $UPtGa_5$. It is noteworthy that recent NMR [6] and resonant x-ray scattering [7] work on UGa_3 do suggest strong $5f$-$4p$ hybridisation and the possibility of some form of orbital ordering. Resonant x-ray scattering experiment on $UTGa_5$ is now in progress.

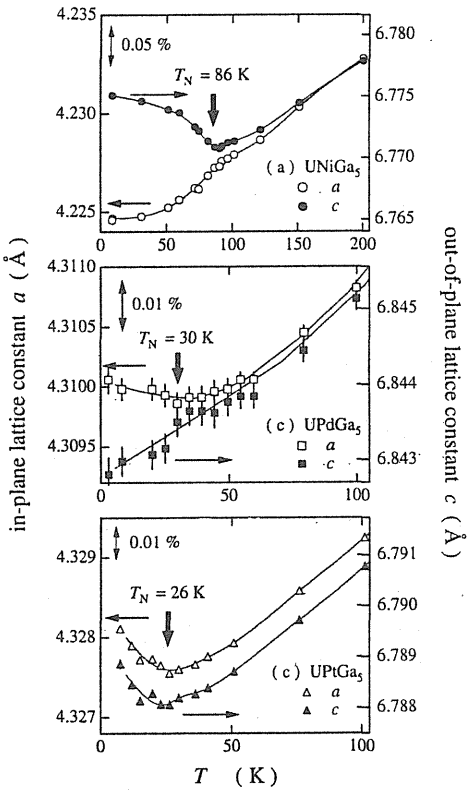


Figure 2: Temperature dependence of lattice constants, a(open circle) and c(closed circle) in $UTGa_5$.

References

1) Yu. N. Grin, P. Rogl, K. Hiebl, J. Less-Common Met. **121** (1986) 497.
2) Y. Tokiwa, Y. Haga, E. Yamamoto, D. Aoki, N. Watanabe, R. Settai, T. Inoue, K. Kindo, H. Harima, Y. Ōnuki, J. Phys. Soc. Jpn. **70** (2001) 1744.
3) Y. Tokiwa, S. Ikeda, Y. Haga, T. Okubo, T. Iizuka, K. Sugiyama, A. Nakamura, Y. Ōnuki, J. Phys. Soc. Jpn. **71** (2002) 845.
4) Y. Tokiwa, Y. Haga, N. Metoki, Y. Ishii, Y. Ōnuki, J. Phys. Soc. Jpn. **71** (2002) 725.
5) F. Izumi and T. Ikeda, Mater. Sci. Forum **321-324** (2001) 538.
6) S. Kambe, H. Kato, H. Sakai, R. E. Walstedt, D. Aoki, Y. Haga and Y. Ōnuki, Phys. Rev. B **66** (2002) 220403.
7) D. Mannix, A. Stunault, N. Bernhoeft, L. Paolasini, G. H. Lander, C. Vettier, F. de Bergevin, D. Kaczorowski and A. Czopnik, Phys. Rev. Lett. **86** (2001) 4128.

研究テーマ：$ZnCr_2O_4$の中性子散乱
表題：$ZnCr_2O_4$の磁気散乱における磁場冷却効果

1-2-59 Field Cooling Effect in Magnetic Neutron Scattering of $ZnCr_2O_4$ Crystal

I. Kagomiya[1], M. Toki[2], Y. Hata[3], K. Kohn[1], K. Nakajima[4], E. Kita[5], K. Kakurai[3] and K. Siratori

[1]*Department of Physics, Waseda University, 3 Okubo Shinjyuku-ku, Tokyo 169-8555, Japan*
[2]*KEK, 1-1 Oho, Tsukuba, Ibaraki 305-0801 Japan*
[3]*Advanced Science Research Center Japan Atomic Energy Institute, Ibaraki, 319-1195 Japan,*
[4]*Institute for Solid State Physics, University of Tokyo, Kashiwa, Chiba 277-8581, Japan*
[5]*Institute of Applied Physics, University of Tsukuba, Tsukuba, Ibaraki 305-8573, Japan*

A normal spinel $ZnCr_2O_4$ has increased interest as a typical example of a geometrically frustrated system. In this oxide, magnetic Cr^{3+} ions occupy the octahedral B sites, which form a three-dimensional network of tetrahedra sharing common corners. Consequently the magnetic moments of Cr^{3+} ions are frustrated with respect to the antiferromagnetic interaction between nearest neighbors. In fact, this crystal transforms into a magnetically-ordered phase at the first-order transition temperature T_N = 12 (±1) K.[1] Our previous powder diffraction experiment[2] has revealed the following extinction rules of the magnetic Bragg reflections that appear below T_N; (1) the (h, k, l/2) reflections are present only when $h + k = 2n$ +1, (2) the (h/2, k/2, l/2) and (h, k, l) reflections are absent. (3) No particular condition was noticed as for the (h, k/2, l/2) reflections. These rules seem to indicate that the magnetic unit cell is composed of four ($2a$×$2a$×$2a$) chemical cells with the lattice parameter a. In addition the lattice has the base-center translation within a plane normal to the c-direction from the rule (1).

With the studies, the magnetic structure of the ordered-phase, the most fundamental property of the system, is not yet known at present. The presence of antiferromagnetic domains makes the determination of the structure difficult. We face a psychological frustration that we need some knowledge of domain structure of the crystal to solve the magnetic structure, but it is difficult to estimate the domain structure before we determine the spin structure. One realistic way to resolve this is to study the effect of magnetic and possibly magnetoelectric field cooling in neutron diffraction, because we can rearrange the domain structure by these treatments. This is our strategy in the spin structure study of $ZnCr_2O_4$. In the previous study, we reported the effect of magnetic-field-cooling (MFC) along the [1 $\bar{1}$ 1]. The purpose of the present study is to obtain more detailed information of the cooling effect on the intensity of magnetic Bragg reflections of a single crystal sample. We used a single crystal grown with a Bi_2O_3 flux, whose dimension is approximately 4×4×4 mm^3.[3] Diffraction data at 2.5 K were collected with the PONTA diffractometer installed at JRR-3M in JAERI with the incident wavelength of 1.637 Å. Measurements were performed in two different geometries, where the magnetic Bragg reflections within the (001) (A) and (1 $\bar{1}$ 2) (B) reciprocal planes were recorded. The sample was at first set as the [1 $\bar{1}$ 1] axis was vertical for the MFC. Then it was put into the position corresponding to

使用施設：JRR-3　　装置：PONTA(5G)，分野 Magnetism

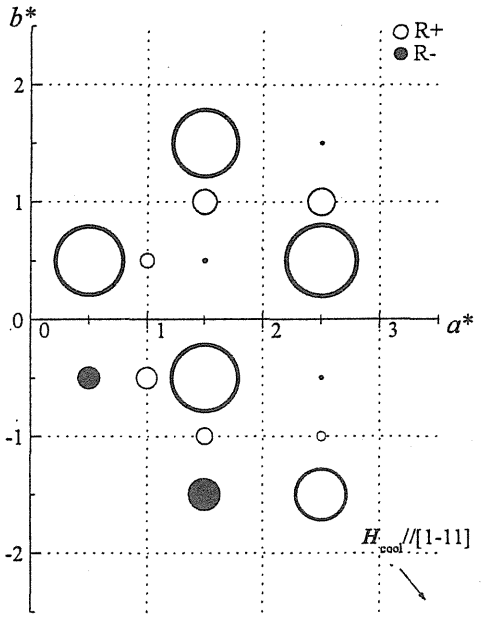


Fig.1: Magnetic field cooling effect of magnetic reflections on the (001) reciprocal plane. Effects of magnetic field cooling are expressed by R+ (open circles) and R-(solid circles) that mean increase and decrease in the diffraction intensity after field cooling, respectively.

the A or B geometry. After each experimental run, the sample was warmed up above 100 K, and then subjected to another cooling treatment in order to compare the results after MFC and zero-field-cooling (ZFC).

The effect of MFC is expressed for each reflection observed by the percent ratio

$$R=(I_{MFC} - I_{ZFC})/ I_{ZFC} \times 100,$$

where I_{MFC} and I_{ZFC} are the integrated after MFC and ZFC, respectively. The results in the case of configuration (A) are shown in Fig. 1, where the observed reflections are marked on the corresponding reciprocal planes. The effect of MFC on an individual reflection is qualitatively expressed by the relative size of the mark.

Several systematic rules were deduced from the results shown in Fig. 1 and were summarized as follows:

(1) The effect of MFC of the (h/2, k/2, l) type diffraction is generally larger than that of the (h/2, k, l) type.

(2) Symbols of the (h/2, k/2, l) type reflections on the fourth quadrant are opposite to them on the first quadrant. Besides, reflections of the (h/2, k, l) type are same symbols on the reciprocal plane.

(3) In the case of (h/2, k/2, l) type, the symbols of reflections of $h+k$=4m are opposite to that of $h+k\neq$4m.(m:integer)

From both the results and extinction rules obtained by the powder neutron diffraction, we consider a possible translation symmetry of the magnetic structure whose unit cell is 2×2×2 of the chemical unit cell. However, at this moment, it is difficult to determine the magnetic structure of $ZnCr_2O_4$ because of the complex domain structure. In order to make the magnetic structure clear, a diffraction study with more simplified domain state is necessary.

References

[1] For example, Y. Kino and B. Lüthi: Solid State Commun.: 9 (1971) 805.
[2] D. Eto, K. Siratori, Y. Hata, E. Kita, I. Kagomiya, K. Kohn, K. Ohyama and Y. Yamaguchi: unpublished .
[3] T. Tsushima: *Proc. Int. Conf. Mag. and Cryst.*, J. Phys. Soc. Jpn. **17** (1962) Suppl. B-I, p. 189.

研究テーマ：多重極限環境下における中性子散乱実験法の研究
表　題：TbB_2C_2 における反強四極子相互作用と特異な反強磁性
1-2-60

Unusual antiferromagnetic properties affected by antiferroquadrupolar interaction in TbB_2C_2

K. KANEKO[1], N. METOKI[1,2], K. OHOYAMA[3], H. ONODERA[3] and Y. YAMAGUCHI[3]

[1]Advanced Science Research Center, JAERI, Tokai, Ibaraki 319-1195
[2]Department of Physics, Tohoku University, Aoba, Sendai 980-8578
[3]Institute for Materials Research, Tohoku University, Sendai 980-8577

In f-electron systems, there is an upsurge of interest on the role of orbital degree of freedom , i.e., quadrupolar interactions in their magnetic properties. The existence of the strong antiferroquadrupolar (AFQ) interaction is a characteristic feature in the tetragonal RB_2C_2 (R=rare earth) compounds. DyB_2C_2 shows an AFQ ordering at T_Q = 24.7 K above an antiferromagnetic (AFM) transition at T_N = 15.3 K [1]. An AFQ order in HoB_2C_2 coexists with an AFM order below T_Q=4.5 K [2]. The present report focus on another isostructural compound TbB_2C_2, which shows an AFM order at T_N=21.7 K under H=0. [3] In TbB_2C_2 the effect of AFQ interaction becomes prominent by applying external magnetic fields. Magnetic fields stabilize a characteristic commensurate magnetic structure involving a slight distortion which are basically the same as those of the AFQ+AFM ordered phase in DyB_2C_2 and HoB_2C_2 [4].

Under H=0, the magnetic structure in the AFM ordered state of TbB_2C_2 has an incommensurate component of $\boldsymbol{k}_L$=(1±δ, ±δ,0) (δ=0.13) in addition to the dominant $\boldsymbol{k}_2$=(1 0 1/2) and $\boldsymbol{k}_4$=(0 0 1/2) components. Furthermore, the magnetic diffuse scattering exists around the satellite peak corresponding to $\boldsymbol{k}_L$. It should be pointed out that the existence of the diffuse scattering around satellites is common to the AFM ordered state in HoB_2C_2 [5,6]. In the present work, we provide details of the satellite and diffuse scattering in TbB_2C_2 studied by neutron scattering under high energy resolution, which reveal the unusual antiferromagnetic ordering in TbB_2C_2.

For sample preparation, the stoichiometric amounts of constituents, Tb, ^{11}B and C were synthesized through the argon arc melting. Single-crystalline sample of $Tb^{11}B_2C_2$ was grown by the Czochralski pulling method using a tetra-arc furnace. Neutron scattering experiments were carried out on the cold neutron triple-axis spectrometer, LTAS, installed at JRR-3M in Japan Atomic Energy Research Institute, Tokai. Pyrolytic graphite (PG) monochromator and analyser crystals were used with a Be filter to reduce the higher order contamination. The horizontal collimation of 80'-sample-80'-80' giving energy resolution of less than 0.15 meV was employed.

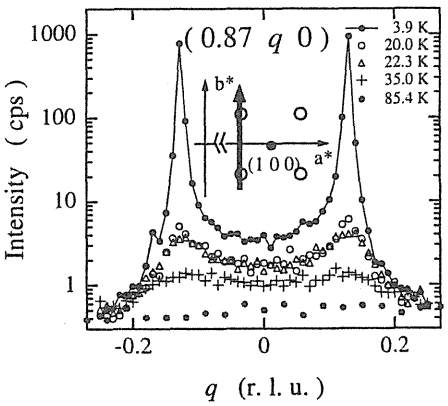


Figure 1: Line scan along (1-δ q 0) measured at various temperatures. Note that the vertical axis is displayed in the logarithmic scale. The schematic scan trajectory in the reciprocal space around (1 0 0) is given in the inset where the open circles correspond to the positions of the satellite peaks.

Figure 1 shows the line scan along (1−δ q 0) obtained at various temperature. The inset gives the schematic scan trajectory around the (1 0 0) reciprocal lattice point. Note that the vertical scale is displayed in the logarithmic

原子炉：JRR-3　　装置：LTAS(C2-1)　　分野：中性子散乱（磁性）

scale. At 3.9 K, the sharp and intense satellite peaks were observed at $q = \pm 0.13$. In addition, there exists the peculiar shape of weak and broad diffuse scattering between the satellites as well. The energy width of both the satellite and diffuse scattering corresponds to resolution limit at least in 3.9 K.

With increasing temperature, we observed the unusual temperature dependence in the scattering intensity. It is notable that only the sharp satellite peaks disappeared clearly below T_N of 20 K, whereas the broad diffuse scattering exists even above T_N. The diffuse scattering intensity decreases unevenly in q-space with increasing temperature and becomes almost flat between $q = \pm 0.15$ at 35.0 K. No trace of diffuse scattering can be seen at 85.4 K.

Figure 2 shows the detailed temperature dependence of the relative magnetic peak intensity of all components, 1 0 1/2 (·), 0 0 1/2(○), satellite at (1-δ δ 0)(+), and diffuse scattering at (1 0 0)(▲). The temperature dependence of these peak intensities is quite diversified. In particular, the satellite peaks exhibit unusual behavior among them. It becomes clear that the intensity of satellite peak disappears far below T_N of ~13 K, in other words, the incommensurate structure is not realized at T_N. On the other hand, the diffuse scattering, having almost the same q as satellites, shows no anomaly in its intensity around 13 K where satellites vanished. The intensity of diffuse scattering forms a small peak at T_N. The diffuse scattering survives even above T_N and exhibits monotonous decrease with increasing temperature. Finally around 60 K(~$3T_N$), the intensity reaches almost the background level. These behavior makes clear contrast to the 0 0 1/2 and intense 1 0 1/2 reflections, disappearing just at T_N.

It is quite interesting that no anomaly was observed in the specific heat, magnetic susceptibility and electrical resistivity around 13 K where the satellite peak disappeared. Furthermore, the present disappearance temperature of 13 K is different from the previous one of 18 K obtained under lower energy resolution of

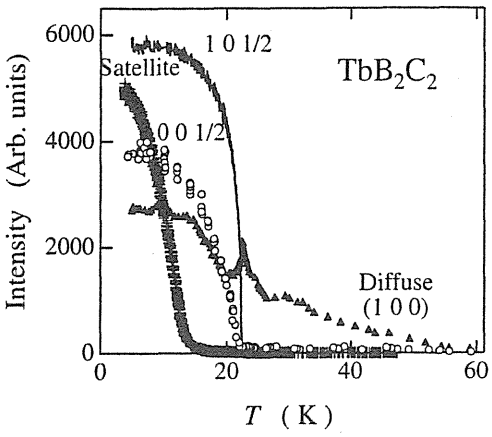


Figure 2: Peak intensities of the antiferromagnetic reflections 1 0 1/2(·), 0 0 1/2(○), satellite at (1-δ δ 0)(+), and diffuse scattering at (1 0 0)(▲) as a function of temperature.

0.9 meV, whereas the diffuse scattering as well as the $\boldsymbol{k}_2$=(1 0 1/2) and $\boldsymbol{k}_4$=(0 0 1/2) components exhibits the almost same temperature dependence in both experiments. This energy resolution dependence suggests the existence of dynamical effect on the development of incommensurate structure.

Unfortunately, we have no clear explanation for these unusual behavior of satellite and diffuse scattering at present. In order to clarify the origin of the diffuse scattering and incommensurate structure,further neutron scattering experiments are in progress.

References

1) H. Yamauchi, H. Onodera, K. Ohoyama, T. Onimaru, M. Kosaka, M. Ohashi and Y. Yamaguchi, J. Phys. Soc. Jpn. **68** (1999) 2057.
2) H. Onodera, H. Yamauchi and Y. Yamaguchi, J. Phys. Soc. Jpn. **68** (1999) 2526.
3) K. Kaneko, H. Onodera, H. Yamauchi, K. Ohoyama, A. Tobo and Y. Yamaguchi, J. Phys. Soc. Jpn. **70** (2001) 3112.
4) K. Kaneko, S. Katano, M. Matsuda, K. Ohoyama, H. Onodera and Y. Yamaguchi, Appl. Phys. A**74** (2002) S1749.
5) A. Tobo, T. Ohmori, T. Matsumura, K. Hirota, N. Oumi, H. Yamauchi, K. Ohoyama H. Onodera and Y. Yamaguchi, Physica B **312-313** (2002) 853.
6) K. Kaneko, K. Ohoyama, S. Katano, M. Matsuda, H. Onodera and Y. Yamaguchi, J. Phys. Soc. Jpn. **71** (2002) 3024.

研究テーマ: 量子スピンをもつフラストレーション系の研究
表題: スピネル化合物 ZnV_2O_4 の結晶構造転移および磁気相転移

1-2-61 Structural and Magnetic Transitions of Spinel Oxide ZnV_2O_4

M. Isobe[1], M. Nishi[2], Y. Ueda[1] and T. Ohyama[3]

[1]*Materials Design and Characterization Laboratory, ISSP, The University of Tokyo, Kashiwa, Chiba 277-8581, Japan;*
[2]*Neutron Science Laboratory, ISSP, The University of Tokyo, Tokai 319-1106, Japan;*
[3]*Institute for Materials Research, Tohoku University, Sendai 980-8577, Japan*

In the spinel compounds AB_2O_4, B atoms constitute a pyrochlore lattice, which is a typical one of the geometrically frustrated three-dimensional lattice. In ZnV_2O_4, the two transitions were observed at T_{C1} = 50K and T_{C2} = 40K [1,2]. The transition at T_{C1} is a structural transition from cubic to tetragonal phase [1]. Concerning with the transition at T_{C2}, there is only one short report of the powder neutron diffraction in 1973 [2]. In order to verify the magnetic transition at T_{C2}, we performed neutron diffraction measurements using the Kinken powder diffractometer, HERMES.

The results are shown in Fig. 1. We observed the two transitions; one is structure transition at T_{C1}, and the other is magnetic transition at T_{C2}. The transition at T_{C1} agrees with the previous report of powder X-ray diffraction [1]. Below T_{C1}, some reflections from lattice origin split, indicating the structural change. For example, the (008) reflection clearly splits into two peaks below 50K.

Below 40K, additional reflections appear, which indicates an antiferromagnetic ordering with (110) and (201) reflections in the elementary spinel cell. The antiferromagnetic order occurs along the direction [110] and [1-10] and the spin direction is parallel to the [001] axis.

According to the scenario proposed theoretically for the two transitions [3], an orbital order is concerned in the transition at T_{C1}, which is supported by Jahn-Teller lattice transition observed. The second transition, that is the magnetic order, at T_{C2} occurs as a result of the releases of the geometrical frustration caused by the structural transition at T_{C1}. In order to clarify this scenario, it should be needed to investigate the crystal and magnetic structures in detail by using single crystal.

References

[1] Y. Ueda *et al.*, J. Phys. Soc. Jpn **66** (1997) 778.
[2] S. Niziol, Phys. Status. Solidi A 18 (1973) K11.
[3] H. Tsunetsugu *et al.*, cond-mat/0305269v1.

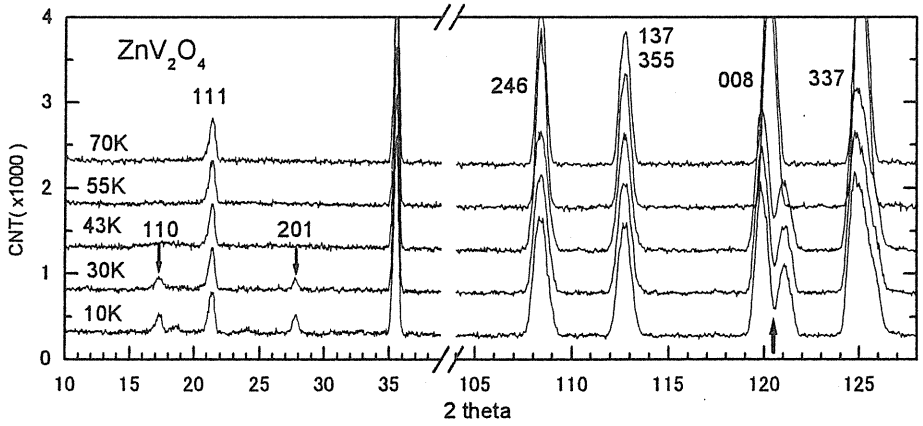


Figure 1: Neutron diffraction patterns of ZnV_2O_4at various temperature.

使用施設:JRR-3 装置:HERMES(T1-3), 分野:2. Magnetism

研究テーマ：先端偏極中性子散乱によるスピン-格子物性の研究
表　題：遍歴電子系 MnSi の中性子小角散乱測定
1-2-62

The neutron small-angle diffraction study of an itinerant electron metamagnet MnSi

M. Yamada, T. Goto, J. Suzuki[1], M. Takeda[1] and K. Kakurai[1]

ISSP, University of Tokyo, 5-1-5 Kashiwanoha, Kashiwa 277-8581
[1]Advanced Science Research Center, JAERI, Tokai, Ibaraki 319-1195

The intermetallic MnSi compound has the cubic B20-type crystal structure and exhibits a helical magnetic ordering with a long wavelength of λ = 180 Å in the [111] direction [1]. The helical ordering originates from the Dzyaloshinsky-Moriya interaction. By applying magnetic fields, the magnetic state changes from the helical state to a conical one and then into a forced ferromagnetic one at about B_f = 0.6 T. When the pressure is applied, the magnetic order vanishes at P_c = 1.5 GPa [2,3]. The magnetic transition at T_C is of second-order at $0 < P < P_t$, but becomes first-order transition at $P_t < P < P_c$, where P_t = 1.2 GPa. From AC susceptibility measurements, a broad maximum of the susceptibility is observed at $P > P_t$ [2]. These results are typical characteristics of the Itinerant Electron Metamagnet (IEM). From DC magnetization measurements, a hysteresis of the metamagnetic transition is observed above P_t [4]. We have revealed the metamagnetic properties of MnSi and determined the phase diagram. The obtained diagram corresponds to the theoretical one [5] very well. It is very interesting to investigate the metamagnetic transition by the neutron diffractions under the multiple extreme conditions, high fields, low temperatures and high pressures. In this report, the obtained results under ambient pressure measurements are shown.

A single crystal was prepared by Czochralski method. The cylindrical crystal 60 mm in diameter and 60mm in length with [001] long axis was used in this experiment. We have carried out a neutron small-angle diffraction study at JAERI (SANS-J). All reflections around the (000) reciprocal point in the (110) reciprocal plane were measured simul-

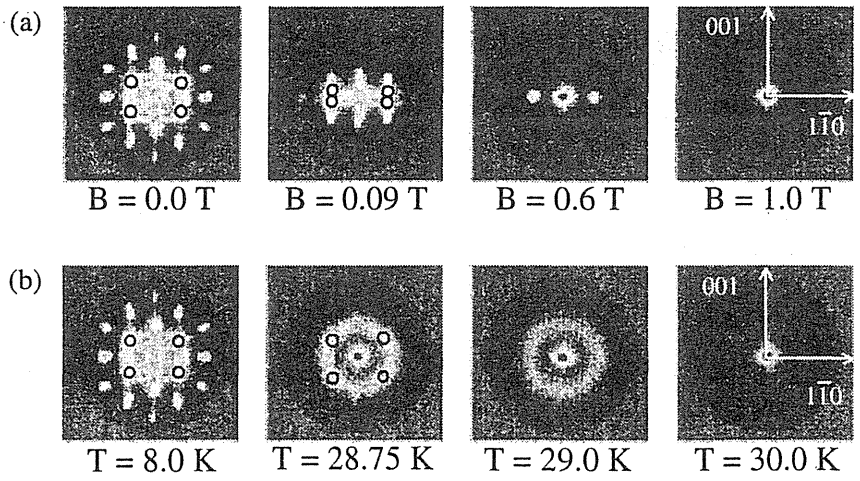


Figure 1: (a) The field and (b) temperature dependence of the satellite spots. The ⟨111⟩ satellites are emphasized by open circles at B = 0 T.

原子炉：JRR-3　　装置：SANS-J(C3-2)　　分野：中性子散乱（磁性）

taneously with the two dimensional multi-counters. For ambient pressure, the neutron diffraction study was carried out at 8 K $< T <$ 30 K without pressure cell. Magnetic field B is applied in the [1$\bar{1}$0] direction.

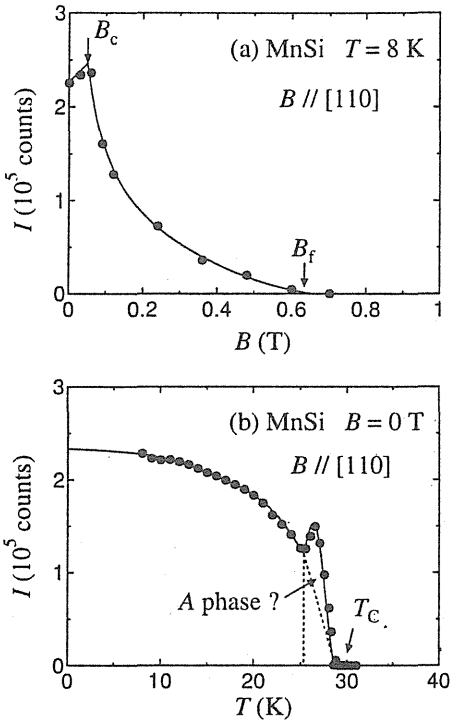


Figure 2: (a) The field dependence of the integrated intensity I of [111] satellites at T = 8 K. (b) The temperature dependence of I at B = 0 T.

Figure 1 (a) shows the magnetic field dependence of satellites spots at T = 8 K, observed by the neuton diffraction measurements. At B = 0 T, the main four satellite appears in the ⟨111⟩ direction. At $B >$ 0.06 T, the satellites begin to rotate from [111] to [1$\bar{1}$0] direction. From magnetization measurements [4], the spin structure changes from helical to conical one at B_c = 0.04 T. It has been confirmed that the helical state changes into conical one at $B = B_c$ by the present neutron diffraction measurements. With increasing field, these satellite spots are gathered along [1$\bar{1}$0] direction. Finally, $B > B_f \sim$ 0.6 T, no spots are observed, as the forced ferromagnetic state is stabilized. These results are consistent with the magnetization measurements [4]. On the other hand, these [111] satellites change with increasing temperature as shown in Fig. 1 (b) at zero field. The intensity of the [111] satellites decreases with increasing temperature. At just T_C = 29 K, the four spots vanish completely, while a ring, which comes from fluctuation of magnetic moments, is observed. Since this ring is symmetric, spin fluctuations will be isotropic.

Figure 2 (a) and (b) show the integrated intensities I of [111] satellites with increasing field and temperature, respectively. At $B < B_c$ (the helical state), the intensity of [111] satellites increases with increasing field. In this region, the magnetic field enhances the spin diffraction along [110]. On the other hand, at $B_c < B < B_f$ (the conical state), the intensity is suppressed by increasing field. In conical region, a cone axis turns to [110] direction and the spin diffraction is suppressed. With increasing temperature it decreases monotonically up to T = 25 K. We have observed the additional peak around T = 26.5 K. This intensity peak may be connected to the anomaly of AC susceptibility near T_C [3], which is so-called "A-phase".

The present obtained results are consistent with the previous report [1]. Never the less, MnSi should be measured under high pressure up to P = 1.7 GPa where the metamagnetic transition disappears. This is very interesting study as collapse of Mn moment by the pressure will be directly observed by the neutron small-angle diffraction measurements.

References

1) Y. Ishikawa, K. Tajima, D. Bloch and M. Roth, Solid State Commum. 19 (1976) 525.
2) C. Pfleiderer, G. J. McMullan, S. R. Julian and G. G. Lonzarich, Phy. Rev. B 55 (1997) 8330.
3) C. Thessieu, C. Pfleiderer, A. N. Stepanov and J. Flouquet, J. Phys.: Condens. Matter 9 (1997) 6677.
4) M. Yamada, T. Goto and T. Kanomata, J. Alloys and Compounds (2003). *in press.*
5) T. Goto, K. Fukamichi and H. Yamada, Physca B 300 (2001) 167.

研究テーマ：スピネル型 $CoFe_2O_4$ 関連物質の磁気・格子構造
表題：Mn_3O_4 の磁気散漫散乱

1-2-63

Diffuse scattering due to Geometrical Frustration in Mn_3O_4

A. Kuriki:[1], Y. Moritomo[2], and K. Ohoyama[3]
[1]*Department of Crystalline Materials Science, Nagoya University, Nagoya 464-8603, Japan*
[2]*Department of Applied Physics, Nagoya University, Nagoya 464-8601, Japan*
[3]*Institute for Materials Research, Tohoku University, Sendai 980-8577, Japan*

The tetrahedral geometry in the spinel B site forms the pyrochlore network, which consists of corner-linked arrays of tetrahedral plaquettes. If the B - B exchange coupling is antiferromagetic and the spin direction is collinear, the pyrochlore lattice leads to intense frustration of the magnetic bonds. Among the transition metal spinel, Mn_3O_4 has a tetragonal structure due to the Jahn-Teller instability of M^{3+} at the B site (octahedral site). Such a lattice distortion is advantageous for a collinear spin arrangement of the spinel B lattice. This compound shows a magnetic transition into the spin ordered phase at T_c = 41 K. The B - B antiferromagnetic exchange coupling is considered to be stronger than the A - B exchange coupling, since the M^{2+} at the A-site is electronically stable. Then, the B-site pyrocholre lattice is amenable to the geometrical frustration in the paramagnetic phase (> T_c) where the long-range spin order disappears.

Neutron powder diffraction measurements were performed using the Kinken powder diffractometer for high efficiency and high resolution measurements (HERMES) of Institute for Materials Research, Tohoku University, installed at the JRR-3M reactor at the Japan Atomic Energy Research Institute, Tokai, Japan. Powders of Mn_3O_4 were sealed in a vanadium capsule with helium gas, and mounted at the cold head of a closed-cycle He-gas refrigerator.

Figure shows temperature variation of neutron powder patterns in the small-2Θ region. At the lowest temperature (7 K << T_c), intense (101) magnetic Bragg reflection (indicated by a downward arrow) is observed at 21degree. The (101) reflection in the tetragonal setting corresponds to the (111) reflection in the cubic spinel. With increase of temperature, a broad diffuse scattering (hatched region) appears at 20 degree. Trace of the scattering is detectable even at 300 K (>> T_c = 41.9 K). This diffuse scattering can be ascribed to the short-range spin correlation on the B-site pyrochlore lattice, because the scattering extends around the (101) magnetic Bragg reflection. Existence of the short-range correlation of the B-spins is also supported by the specific heat measurements. We measured specific heat of a melt-grown Mn_3O crystal with use of Quantum Design PPMS machine. We observed λ-type anomaly at T_c (not shown), and estimated the spin entropy change is 2.2 k_B/ Mn_3O_4. This value is much smaller than the ideal value (2ln5+ln6 = 5.0 k_B/ Mn_3O_4), and is rather close to the A-spin contribution to the entropy change (ln6 = 1.8 k_B/ Mn_3O_4.

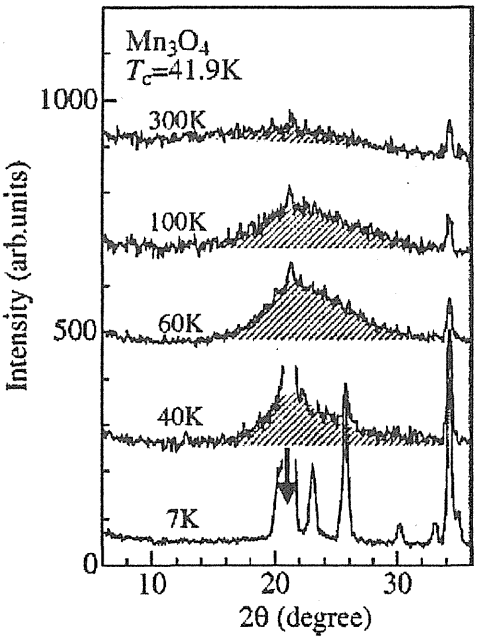


Fig.1: Temperature variation of neutron powder pattern of Mn_3O_4 in the small-2Θregion. T_c was determined by specific heat measurement.A downward arrow is (101) magnetic Bragg reflection..

使用施設：JRR-3　装置：HERMES、分野：1 Structure&Excitation、2 Magnetism

研究テーマ：多重極限環境下における中性子散乱実験法の研究
表　題：遍歴 $5f$ 反強磁性体 $UTGa_5$(T: Ni, Pt) における磁気形状因子

1-2-64

Magnetic form factors of $5f$ itinerant antiferromagnetic compound $UTGa_5$ (T: Ni, Pt)

K. KANEKO[1], N. METOKI[1,2], N. BERNHOEFT[3], G. H. LANDER[1,4], Y. ISHII[1], Y. TOKIWA[1], S. IKEDA[1], Y. HAGA[1] and Y. ŌNUKI[1,5]

[1]Advanced Science Research Center, JAERI, Tokai, Ibaraki 319-1195
[2]Department of Physics, Tohoku University, Aoba, Sendai 980-8578
[3]DRFMC-CEA, 38054 Grenoble, France
[4]EC-JRC, Institute for Transuranium Elements, Postfach 2340, D-76125 Karlsruhe, Germany
[5]Graduate School of Science, Osaka University, Toyonaka, Osaka 560-0043

The f electron systems attract much interest because of the unconventional superconductivity and the coexistence with the magnetic ordering around the quantum critical point. Recent studies reported a new series of heavy fermion superconductor $CeTIn_5$ (T:Rh, Co, Ir)[1-3], which is followed by the discovery of high-T_C heavy fermion superconductor $PuCoGa_5$ and $PuRhGa_5$[4,5]. On the other hand, the iso-structural compounds $UT'Ga_5$ exhibit strong itinerant character of $5f$ electrons. $UT'Ga_5$ with T'=Ni, Pd and Pt exhibit antiferromagnetic ordering at T_N=86, 31 and 26 K, respectively[6]. Our recent neutron scattering study revealed the significant difference in the magnetic structures between the iso-electronic compound $UNiGa_5$ and $UPtGa_5$; the nearest neighbor interaction is antiferromagnetic in $UNiGa_5$ whereas ferromagnetic in $UPtGa_5$[7]. The difference in the magnetic structure of these iso-electronic compounds were discussed in terms of the orbital ordering. In the present study we report on the magnetic form factor in $UNiGa_5$ and $UPtGa_5$ to shed light on the nature of the itinerant antiferromagnetism with uranium $5f$ electrons[8].

The magnetic form factors were measured on single crystals by the triple-axis spectrometers TAS-1 and TAS-2, installed at research reactor JRR-3 in JAERI. All collimation, except that in front of the monochromator, was removed and the background scattering from the sample cell and the cryostat was eliminated by a pair of beam slits. The magnetic contribution was extracted by subtracting the harmonic contaminations, measured at $T > T_N$, where T_N is the Néel temperature, and put on an absolute scale by calibration against selected nuclear peaks. The details of sample preparation were published

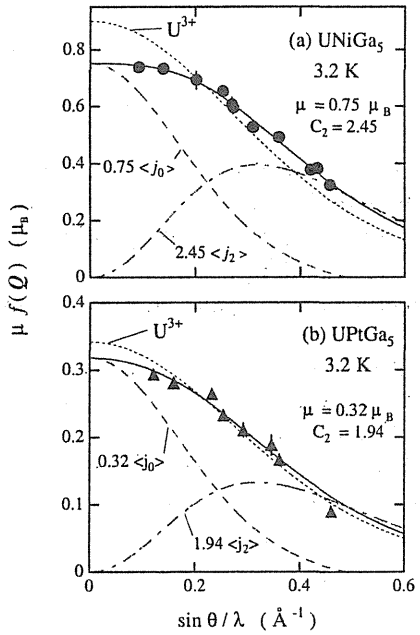


Figure 1: The experimentally obtained magnetic form factors for (a) $UNiGa_5$ and (b) $UPtGa_5$ denoted by circles and triangles, respectively. The solid lines are the best fit of the calculated form factors using Eq. (1) with μ and C_2 as fitting parameters. The dotted line indicates the magnetic form factor for U^{3+} free ion. The dashed line and dash-dot line show the calculated curves for $\langle j_0 \rangle$ and $\langle j_2 \rangle$ terms, respectively.

原子炉：JRR-3　　装置：TAS-1(2G)　　分野：中性子散乱（磁性）

elsewhere[9,10].

Figure 1 shows the magnetic form factor observed in (a) $UNiGa_5$ and (b) $UPtGa_5$. Within the dipole approximation, $\mu f(\boldsymbol{Q})$ can be described by the sum of Bessel's function,

$$\begin{aligned} \mu f(Q) &= \mu(\langle j_0\rangle + C_2\langle j_2\rangle) \qquad (1)\\ \text{where } C_2 &= \mu_L/\mu \\ \mu_L/\mu_S &= C_2/(1-C_2) \end{aligned}$$

where μ is the total magnetic moment and $\boldsymbol{Q}$ is the momentum transfer. The experimental form factors, given in Fig. 1, have been decomposed using Eq. (1). The result of a least square fitting to the moment μ and C_2 coefficient is denoted by the solid curves and values of μ, μ_L, μ_S and C_2 for $UNiGa_5$ and $UPtGa_5$ are listed in Table 1.

The most remarkable thing is the large orbital contribution, which is characteristic to the uranium intermetallic compounds based on itinerant $5f$ electrons. However, we found that the contribution of the orbital moments μ_L/μ_S is strongly suppressed in $UTGa_5$ from the value for U^{3+} free ion. For comparison the values of C_2 and μ_L/μ_S for U^{3+} with f^3 configuration are also described in Table 1. The $|\mu_L/\mu_S| = 1.68$ for $UNiGa_5$ is much smaller than the value of U^{3+} free ion, $|\mu_L/\mu_S| = 2.56$. The $|\mu_L/\mu_S| = 2.10$ for $UPtGa_5$ is smaller than that of U^{3+} free ion as well. The suppression of μ_L can be recognized in the large contribution of $\langle j_2\rangle$ term denoted by dash-dot lines in Fig. 1. The dotted lines in Fig. 1 is the magnetic form factor for U^{3+} free ion, which is obviously deviates from the experimental data, especially for $UNiGa_5$.

Large orbital contribution and the suppression of the magnetic orbital moment has been reported in UGa_3[11]. The results of UGa_3 are summarized in Table 1 for comparison. Note that the C_2 as well as μ_L/μ_S in $UNiGa_5$ are very similar to those for UGa_3. Besides, $UNiGa_5$ and UGa_3 show a very flat magnetic susceptibility for T> T_N, while a weak Curie-Weiss behavior with a small effective moment μ_{eff}=1.8 μ_B was observed in $UPtGa_5$. It roughly means that the strength of the hybridization in $UNiGa_5$ might be comparable with UGa_3 but stronger than that in $UPtGa_5$. Therefore, we conclude that the quenching of the orbital moment is correlated with the itinerancy of $5f$ electrons.

Table 1: Fitting results of total magnetic moment μ, orbital and spin magnetic moment μ_L and μ_S, $|\mu_L/\mu_S|$ and C_2 for U^{3+}, $UPtGa_5$, $UNiGa_5$, and UGa_3[11].

	μ (μ_B)	μ_L (μ_B)	μ_S (μ_B)	$\lvert\mu_L/\mu_S\rvert$	C_2
U^{3+}				2.56	1.64
$UPtGa_5$	0.32(5)	0.62(7)	-0.30(7)	2.10(20)	1.94(17)
$UNiGa_5$	0.75(5)	1.84(7)	-1.09(7)	1.68(4)	2.45(7)
UGa_3[11]	0.63(5)	1.5(1)	-0.9(1)	1.66(5)	2.52(5)

References

1) R. Movshovich, M. Jaime, J. D. Thompson, C. Petrovic, Z. Fisk, P. G. Pagliuso, and J. L. Sarrao, Phys. Rev. Lett. **86** (2001) 5152.
2) H. Hegger, C. Petrovic, E. G. Moshopoulou, M. F. Hundley, J. L. Sarrao, Z. Fisk and J. D. Thompson, Phys. Rev. Lett. **84** (2000) 4986.
3) C. Petrovic, R. Movshovich, M. Jaime, P. G. Pagliuso, M. F. Hundley, J. L. Sarrao, Z. Fisk and J. D. Thompson, Europhys. Lett. **53** (2001) 354.
4) J. L. Sarrao, L. A. Morales, J. D. Thompson, B. L. Scott, G. R. Stewart, F. Wastin, J. Rebizant, P. Boulet, E. Colineau and G. H. Lander, Nature **420** (2002) 297.
5) F. Wastin, P. Boulet, J. Rebizant, E. Colineau and G. H. Lander, J. Phys.: Condens. Matter **15** (2003) S2279 .
6) Yu. N. Grin, P. Rogl, K. Hiebl, J. Less-Common Met. **121** (1986) 497.
7) Y. Tokiwa, Y. Haga, N. Metoki, Y. Ishii, Y. Ōnuki, J. Phys. Soc. Jpn. **71** (2002) 725.
8) K. Kaneko, N. Metoki, N. Bernhoeft, G. H. Lander, Y. Ishii, Y. Tokiwa, S. Ikeda, Y. Haga anad Y. Ōnuki, submitted to Phys. Rev. B.
9) Y. Tokiwa, Y. Haga, E. Yamamoto, D. Aoki, N. Watanabe, R. Settai, T. Inoue, K. Kindo, H. Harima, Y. Ōnuki, J. Phys. Soc. Jpn. **70** (2001) 1744.
10) Y. Tokiwa, S. Ikeda, Y. Haga, T. Okubo, T. Iizuka, K. Sugiyama, A. Nakamura, Y. Ōnuki, J. Phys. Soc. Jpn. **71** (2002) 845.
11) A. Hiess, F. Boudarot, S. Coad, P. J. Brown, P. Burlet, G. H. Lander, M. S. S. Brooks, D. Kaczorowski, A. Czopnik, R. Troc, Europhys. Lett. **55** (2001) 267.

研究テーマ：3次元スピンフラストレーション系 $^{110}CdFe_2O_4$ のスピン相関
表題：HQR装置によるフラストレーション系 $^{110}CdFe_2O_4$ の磁気散漫散乱の温度依存性

High-Q-Resolution Neutron Scattering Study on Temperature Dependence of Magnetic diffuse scattering in a Frustrated $^{110}CdFe_2O_4$

1-2-65

K. Kamazawa, S. Park *, T. J. Sato *, S.-H. Lee *, and Y. Tsunoda

Dept. of Appl. Phys., School of Science and Enginnering, Waseda Univ., 3-4-1 Ohkubo, Shinjuku-ku, Tokyo 169-8555, Japan

**NIST Center for Neutron Research, 100 Bureau Drive, Stop 8562 Gaithersburg, MD 20899-8562*

$^{110}CdFe_2O_4$ has a normal spinel structure, and the magnetic ions construct the corner sharing tetrahedra. This structure is the same as pyrochlore and C15 inter-metalic Laves Phase compound. Since $^{110}CdFe_2O_4$ is studied with NIST group [1], here we focus on the temperature dependences of the accurate diffuse scattering position using High-Q-Resolution triple axis spectrometer at JRR-3M without the horizontally focusing analyzer. Although the pattern of the magnetic diffuse scattering is the same as $ZnCr_2O_4$ and $Y(Sc)Mn_2$, there is also the diffuse scattering pattern corresponding to $ZnFe_2O_4$ [2]. Fig.1 shows the temperature dependences of the diffuse scattering profiles along the [HH2] direction for $^{110}CdFe_2O_4$.

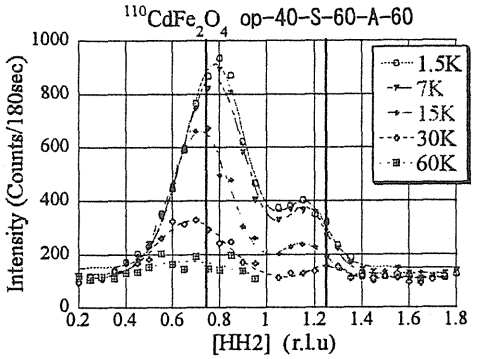


Figure 1: Temperature dependences of the magnetic diffuse scattering profiles for $^{110}CdFe_2O_4$.

The diffuse scattering position gradually shifts to the inner side of the Brillouin zone boundary with increasing temperature. Base on the Ref. [3], the data indicates that the antiferromagnetic nearest neighbor

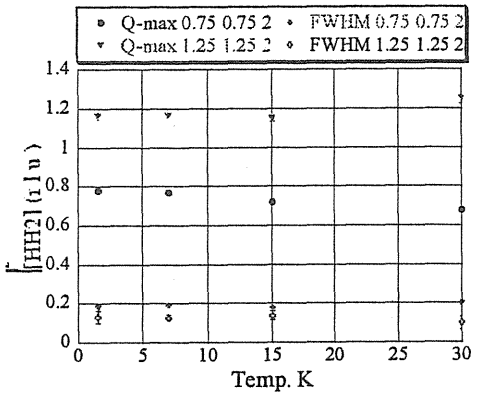


Figure 2: The diffuse scattering position and FWHM corresponding to each temperature in Figure 1.

interaction depends on the temperature and the third neighbor interaction also depends on the temperature. On the other hand, full width at the half maximum (FWHM) does not depend on the temperature. In addition, ratio of the intensities at (0.75, 0.75, 2) and (1.25, 1.25, 2) doesn't change by the temperature. Since super-lattice reflections were observed around nuclear Bragg peaks, we have to investigate the temperature dependences of the interaction in consideration of relations between the temperature dependences of the lattice constant and local lattice distortion carefully.

Acknowledgement

K. K. would like to thank Prof. K. Kohn for his advice in the single crystal growth.

References

[1] K. Kamazawa et. al., unpublished
[2] K. Kamazawa et. al., to be published.
[3] Y. Yamada et. al., Phys. Rev. B **66** 064401 (2002).

使用施設：JRR-3 ，装置：HQR(T1-1)，分野 Magnetism

研究テーマ：正方晶化合物 RB_2C_2 における反強四極子秩序の研究
表　題　：DyB_2C_2 における反強四極子秩序の磁場中中性子回折研究
1-2-66

Neutron Diffraction Study on the Antiferroquadrupolar Order of DyB_2C_2 under the Magnetic Field

H. Yamauchi, S. Katano[1], M. Matsuda[1], K. Ohoyama, K. Indoh, H. Onodera and Y. Yamaguchi

Institute for Materials Research, Tohoku University, Sendai, Miyagi 980-8577
[1]Advanced Science Research Center, Japan Atomic Energy Research Institute, Tokai, Ibaraki 319-1195

Generally speaking, a rare earth ion has an incomplete 4f shell, and an atomic magnetic moment and a quadrupolar moment arises from the 4f electrons. The quadrupolar moment is associated asphericity of the 4f electron distribution as same as the orbital magnetic moment, and strongly couples with the spin moment by strong LS interaction.

There are two kinds of couplings between quadrupolar moments. These are ferroquadrupolar(FQ) and antiferroquadrupolar(AFQ) coupling. FQ coupling is a parallel coupling of the electron distribution, and there is no discrepancy with the magnetic interaction. In the other hand AFQ coupling means rectangular configuration of the electron distribution, and it is completely inconsistent with any magnetic interaction. Therefore we can expect novel phenomena in the situation coexisting AFQ and magnetic interactions.

Tetragonal RB_2C_2 compounds are known as in which AFQ interaction is very strong. For example, AFQ ordering temperature of DyB_2C_2 is 24.7K about one order higher than other type of AFQ ordering compounds [1]. The magnetic unit cell below the Neel temperature, 15.3K, is two times large compared with the chemical one along the c-axis, and two rare earth layers are in it perpendicular to the c-axis. The magnetic moments lie in the c-plane, and the direction oscillates as 0-70-0-70 degrees along the c-axis. This structure is considered to come from competing of AFQ and antiferromagnetic(AFM) interactions.

In the present report we mention about the observation of AFQ ordering by neutron diffraction, and we pick up the phase change depending on the temperature and magnetic field applied

---

原子炉：JRR－3　装置：TAS-2 (T2-4)　分野：中性子散乱(磁性)

parallel to [110] direction of DyB_2C_2 crystal.

Magnetic phase diagram of DyB_2C_2 is shown [1] with the magnetic field applied parallel to [110]. This phase diagram was obtained by magnetization and specific heat measurements using stationary and pulsed high magnetic field. There are four phases in the diagram. The phase I is paramagnetic and paraquadrupolar state, and the phase III is AFM and AFQ ordered state concluded from the unique magnetic structure. The phase II is thought to be AFQ ordered state, and we have examined it by observing induced magnetic moments using neutron diffraction.

Temperature dependence of integrated intensity of (0,0,1/2) reflection under magnetic field of 4 and 8T is shown in Fig.1. Result under 8T is a simple curve showing a second order transition at T_Q. On the other hand, result under 4T is somewhat complex, and it is thought to show a new phase transition in the phase II which has been suggested by Dr. Indoh [2]. The change of the intensity is consistent to the magnetic structure model obtained by the magnetization measurements.

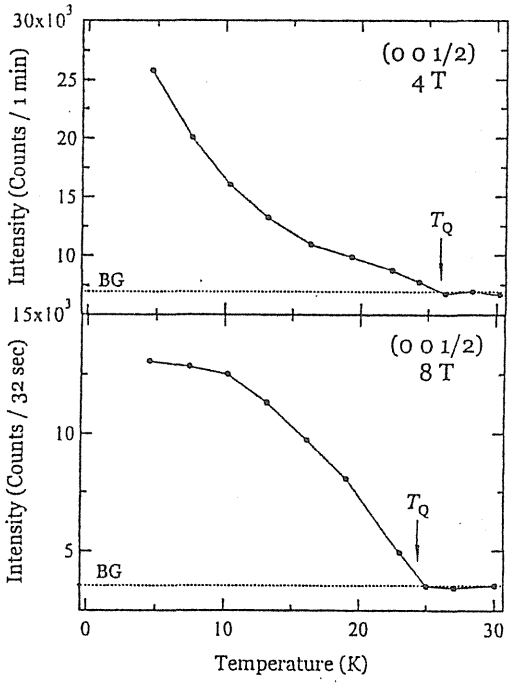


Figure 1. Temperature dependence of integrated intensity of (0,0,1/2) reflection under magnetic field of 4T (upper) and 8T (lower).

References

[1] H. Yamauchi *et al.*: J. Phys. Soc. Jpn. **68** (1999) 2057.

[2] K. Indoh, Doctor Thesis (Tohoku Univ., 2003)

研究テーマ:高分解能中性子散乱装置(T1-1)
表題:$ZnFe_2O_4$ 単結晶の高磁場下の磁化率と中性子散乱

High magnetic field susceptibility and neutron scattering measurements for $ZnFe_2O_4$ single crystal

1-2-67

K. Kamazawa, K. Nakajima[a], K. Kohn[b], and Y. Tsunoda

Dept. of Appl. Phys., School of Science and Enginnering, Waseda Univ., 3-4-1 Ohkubo, Shinjuku-ku, Tokyo 169-8555, Japan
[a]Institute for Solid State Physics, University of Tokyo, 106-1 Shirakata, Tokai 319-1106, Japan
[b]Dept. of Phys., School of Science and Enginnering, Waseda Univ., 3-4-1 Ohkubo, Shinjuku-ku, Tokyo 169-8555, Japan

$ZnFe_2O_4$ has a normal spinel structure. The magnetic Fe^{3+} ions in the B-sites form the network of corner sharing tetrahedra. The spins on this network are frustrated when the interactions of the nearest-neighbor spins are antiferromagnetic [1]. Although the magnetic susceptibility shows a peak which is similar to the Néel temperature, no magnetic long-range-order was observed in previous neutron scattering measurements [2]. Similar peak is observed in every normal spinel and its origin is explained by several models such as Néel temperature [3], spin glass transition [4], lattice distortion [5], and Schottky anomaly [6]. Nevertheless the details of the peak origin are still unclear because the essence is hidden by various phenomena related to this peak. To clarify this issue we studied field dependences of magnetic susceptibility and neutron scattering measurements for $ZnFe_2O_4$.

Fig. 1 shows the field dependences of field–cool and zero-field-cool magnetic susceptibility versus temperature for $ZnFe_2O_4$ and $^{110}CdFe_2O_4$. The magnetic field was applied along the [001] axis. The field–cool and zero-field-cool curves for both ferrites trace the same path over the whole temperature range.

The differences between $ZnFe_2O_4$ and $^{110}CdFe_2O_4$ are clear. The peak position for $ZnFe_2O_4$ moves toward the high temperature and converges on 28K with 4T (Tesla) (see Fig. 2). The peak position for

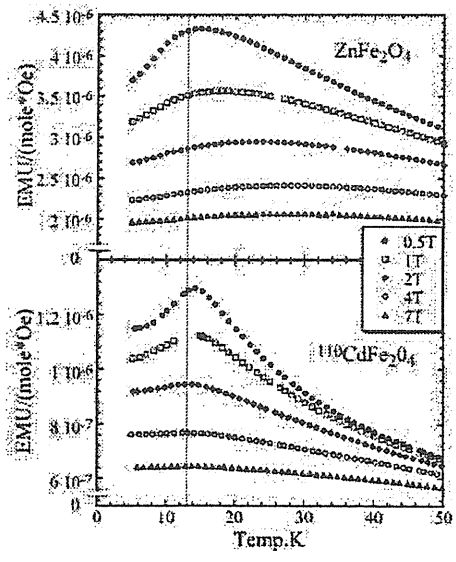


Figure 1: Magnetic field dependences of field–cool and zero-field-cool magnetic susceptibility versus temperature for $ZnFe_2O_4$ (upper) and $^{110}CdFe_2O_4$ (lower).

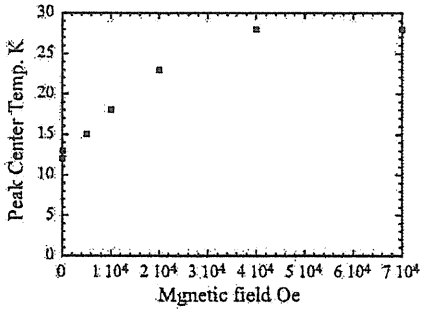


Figure 2: Temperature corresponding to the position of the peak center in Fig.1 for $ZnFe_2O_4$ versus magnetic field.

使用施設:JRR-3　装置:HQR(T1-1), 分野 Magnetism

$^{110}CdFe_2O_4$ does not change and only its intensity decreases.

Fig. 3 shows the neutron scattering data for $ZnFe_2O_4$ under the magnetic fields. The data were obtained with the high-Q-resolution (HQR) triple-axis spectrometer installed at the T1 thermal guide of JAERI. Under the magnetic field of 3T, the magnetic diffuse scattering intensity originating from the third neighbor antiferromagnetic interaction such as around (010), (030) and (050) increase, while the magnetic diffuse scattering intensity originating from the nearest-neighbor ferromagnetic interaction such as around (040) fades away. When the results obtained for the magnetic susceptibility are taken into consideration, it is reasonable to think that the spin correlations do not become ferromagnetic long-range-order. In fact, the ferromagnetic Bragg peak was not observed at the nuclear Bragg peak position. There is a relation between the disappearance of ferromagnetic diffuse scattering in the neutron scattering measurements and the peak shift in the magnetic susceptibility.

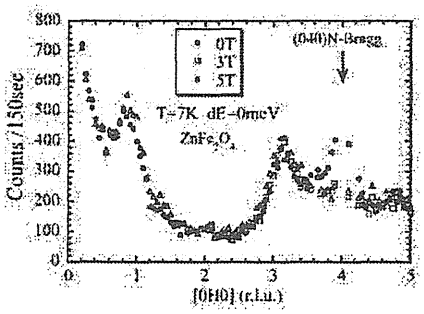


Figure 3: Field dependences of neutron scattering data along the [010] axis for $ZnFe_2O_4$.

As reported in Ref. [2], $ZnFe_2O_4$ is neither a spin glass system nor showing any magnetic long-range-order. We also investigated the temperature dependences of Bragg peak positions and intensities for $ZnFe_2O_4$ single crystal and signals of lattice distortion around 13K have not been observed. Therefore it is difficult to think that the susceptibility peak comes from the lattice distortion as well. When above results are taken into consideration, the 13K peak in the magnetic susceptibility is thought to be a certain change of spin order such as a formation of stable spin cluster, as it was suggested in Ref. [7]. The nearest-neighbor interaction is very weak [8] and spins are sensitive to the influence of the magnetic field, therefore spin arrangement varies according to the magnetic field, and it influences the temperature in which spin clusters form. Since $^{110}CdFe_2O_4$ does not have ferromagnetic diffuse scattering [9], one can not expect the similar behavior and we have not performed the neutron scattering measurements under the magnetic fields.

We conclude that antiferromagnetic long-range-order, lattice distortion, and spin glass transition are not necessary related with the peak. The unique feature of $ZnFe_2O_4$ observed in the neutron scattering measurements is the sensitivity of the magnetic diffuse scattering to the magnetic field.

References

[1] P. W. Anderson, Phys. Rev. 102 (1956) 1008.
[2] K. Kamazawa, et al., Phys. Rev. B (to be published).
[3] G. Blasse, et al., Philips Res. Repts. 18 (1963) 393.
[4] G. M. Kalvius, et al., Physica B 326 (2003) 490.
[5] S. -H. Lee, et al., Phys. Rev. Lett. 86 (2001) 5554.
[6] Steven T. Bramwell, et al., Science 294 (2001) 1495.
[7] S. -H. Lee, et al., Nature 418 (2002) 856.
[8] Y. Yamada, et al., Phys. Rev. B 66 (2002) 064401.
[9] K. Kamazawa, et al., (unpublished).

研究テーマ： $Ba_3LnM_2O_9$(Ln=La-Lu,Y;M=Ru,Ir) の磁気構造
表題： $SrNdFeO_4$ におけるスピン再配列

1-2-68 Spin Reorientation in $SrNdFeO_4$

S. Oyama[1], M. Wakeshima[1], Y. Hinatsu[1], A. Tobo[2], K. Ohoyama[2], and Y. Yamaguchi[2]
[1] *Division of Chemistry, Graduate School of Science, Hokkaido University, Sapporo 060-0810*
[2] *Institute for Materials Research, Tohoku University, Sendai 980-8577*

The layered perovskite type oxide $SrNdFeO_4$ is crystallized in an ideal tetragonal K_2NiF_4 type structure with space group $I4/mmm$. For this compound, an antiferromagnetic transition of Fe^{3+} occur at 270 K [1]. Through our magnetic susceptibility and specific heat measurements, two magnetic anomalies were found at around 15 and 36 K. The ^{57}Fe Mössbauer spectra suggest that the anomalies at 15 and 36 K correspond to an antiferromagnetic ordering of the Nd^{3+} ions and a change in the direction of magnetic moment of the Fe^{3+} ion, respectively.

In order to elucidate these magnetic anomalies for $SrNdFeO_4$, the powder neutron diffraction measurements were preformed using the high efficiency and resolution powder diffractometer, HERMES, of Institute for Materials Research, Tohoku University, installed at the JRR-3M(Tokai) with a neutron incident wave length (λ = 1.8207 Å). The magnetic structures were determined by the Rietveld technique.

In all the diffraction profiles below room temperature, magnetic Bragg reflections of the type $(h/2, k/2, l)$ with h, k = odd appeared. This result indicates that the magnetic moments of the Fe^{3+} ions in $SrNdFeO_4$ has a long-range magnetic ordering and that its magnetic structure has dimensions $\sqrt{2}a \times \sqrt{2}a \times c$ in terms of the tetragonal chemical cell below room temperature. Figure 1 shows the temperature dependence of the integrated intensities of some magnetic Bragg reflections. At around 36 K, the intensities are changed discontinuously. The diffraction profiles below 36 K were analyzed in consideration of the contribution of the Nd^{3+} magnetic moments. The results of the Rietveld analysis indicate that the ordered magnetic moments of Fe^{3+} are almost constant (~4.2 μ_B) below 40 K, but that the Fe^{3+} moments, which lie in the ab plane above 36 K, turn to the c direction below 36 K. Figure 2 represents the two magnetic structure modles above and below 36 K.

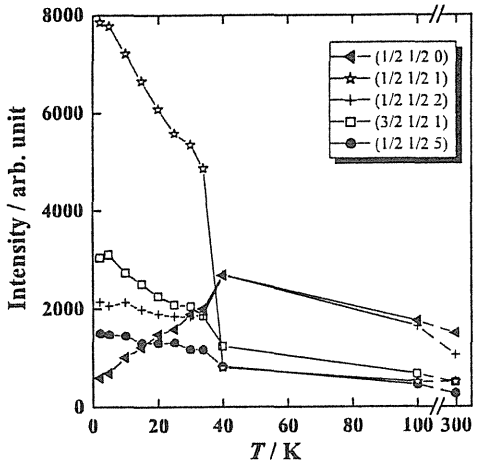


Fig. 1. Temperature dependence of the integrated intensities of the magnetic Bragg reflections for $SrNdFeO_4$.

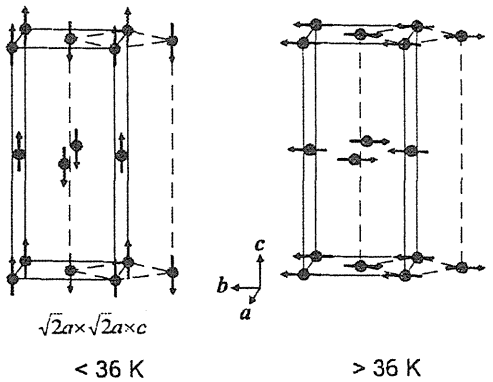


Fig. 2. Magnetic structure models of Fe^{3+} ion above and below 36 K.

References

[1] M. Shimada and M. Koizumi: *Mater. Res. Bull.*, **11** (1976) 1237.

使用施設：JRR-3` 装置： T1-3 (HERMES)， 分野： 6. Magnetism

This is a blank page.

1. 中性子散乱 3) 超伝導現象

1. Neutron Scattering 3) Superconductivity

This is a blank page.

研究テーマ： $La_{1-x}Sr_xMnO_3$ の軌道整列の観測
表題： $Nd_2Mo_2O_7$ の磁気形状因子の観測

1-3-1 Observation of magnetic form factor in $Nd_2Mo_2O_7$

L. Kano[1], M. Saitoh[1], M. Togasaki[1], T. Sasaki[1], T. Matsumura[2], M. Fujita[3], H. Hiraka[4], K. Nakajima[5], K. Hirota[5] and J. Akimitsu[1]

[1]Department of Physics, Aoyama-Gakuin University, 5-10-1 Fuchinobe, Sagamihara, 229-8558
[2]Department of Physics, Tohoku University, Sendai, 980-8578
[3]Institute of Chemical Research, Kyoto University, Gokasyo, Uji, 611-0011
[4]Institute for Materials Research, Tohoku University, Sendai, 980-8577
[5] Institute for Solid State Physics, The University of Tokyo, 106-1 Shirakata, Tokai, 319-1106

Pyrochlore molybdate $Nd_2Mo_2O_7$ is a ferromagnetic metal containing two magnetic ions Nd^{+3} and Mo^{+4}, and its electronic configurations are $(4f)^3$ and $(4d)^2$, respectively. Nd and Mo ions individually form the three-dimensional networks of corner sharing tetrahedra. This compound exhibits a ferromagnetic transition temperature with $T_C \approx 93$ K. The ordering is primarily associated with the Mo-moments, while the ordering of the Nd-moments become significant below $T^* \approx 30$ K. The net magnetization of the Nd-moments is antiparallel to that of the Mo-moments. Because of the strong single ion anisotropy directing along the center of gravity in a tetrahedron, Nd-moments configurate"two spin in, two spin out"structure. Oxygen has an octahedral coodination around Mo ions and has the three-fold distortion, therefore the ligand field of Mo^{4+}becomes trigonal.

In this study, we carried out the polarized neutron diffraction measurement to observe the magnetic form factor and to determine the wave functions in Nd and Mo ions [1].

Single crystal was grown by the floating zone method. The polarized neutron diffraction measurements were performed at JRR-3M reactor at Tokai JAERI. The energy of the incident neutrons is 80 meV. The data was taken at 50 and 2.5K under an applied magnetic field of 5T in parallel to the $< 1\bar{1}0 >$-axis of single crystal specimen. The procedures for correcting the incomplete polarization (neutron polarization $P_n = 95.17\%$), statistical uncertainty and extinction correction will be published elsewhere. The magnetic form factor of Mo ions is calculated and the result can be optimized after various wave functions($|\varphi_1\rangle$, $|\varphi_2\rangle$) in cubic field and trigonal field has been assumed. Consequently, the calculated values assuming the trigonal field mostly reproduce the observed ones. The final wave functions are

$$|\varphi_1\rangle = |\varphi_0\rangle = \frac{1}{\sqrt{3}}\left(|\varphi_{yz}\rangle + |\varphi_{zx}\rangle + |\varphi_{xy}\rangle\right) \quad (1)$$

$$|\varphi_2\rangle = \frac{1}{\sqrt{2}}(|\varphi_+\rangle - |\varphi_-\rangle)$$
$$= \frac{1}{\sqrt{6}}(|\varphi_{yz}\rangle + |\varphi_{zx}\rangle - 2|\varphi_{xy}\rangle) \quad (2)$$

, respectively, and probability coefficient of the electrons with wave function $|\varphi_1\rangle$ is 0.42, and the magnetic moment is determined to be $0.75\mu_B$ for this system.

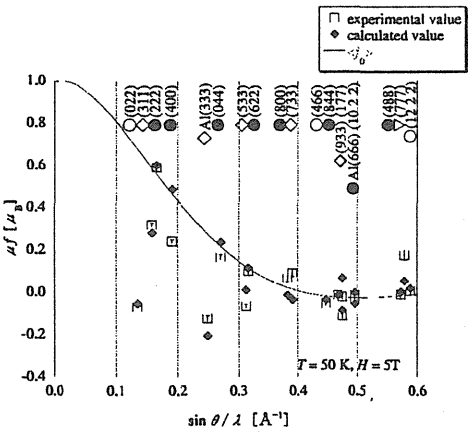


Fig. 1. Comparison between the observed(square with bar) and calculated (diamond) magnetic form factors at 50K.

References

[1] Y. Yasui et al.: J. Phys. Soc. Jpn. 70 (2001) 284.

使用施設：JRR-3 装置： TOPAN(6G) , 分野： Strongly Correlated Electron System

研究テーマ： NdB_6 及び CeB_2C_2 におけるスピン密度分布の観測
表題： PrB_6 及び NdB_6 におけるスピン密度分布の観測

1-3-2 Observation of the spin density distributions in PrB_6 and NdB_6

Y. Kousaka[1], M. Saitoh[1], M. Togasaki[1], Y. Kawaguchi[1], M. Sera [2], M. Nishi[3] and J. Akimitsu[1]
[1] *Department of Physics, Aoyama-Gakuin University, 5-10-1 Sagamihara, Kanagawa 229-8558*
[1] *Department of Quantum Matter, ADSM, Hiroshima University, Higashi-Hiroshima 739-8526*
[3] *Institute for Solid State Physics, The University of Tokyo, 106-1 Shirakata, Tokai, 319-1106*

Recently, we reported the spin density distribution of CeB_6 by using the polarized neutron diffraction technique and found that the magnetic moment exists not only on the Ce site, but also inbetween the B sites [1]. In order to clarify whether this phenomenon can apply to the other B_6 system, we measured the spin density distributions of PrB_6 and NdB_6 through the polarized neutron diffraction experiment.

PrB_6 and NdB_6 have a cubic CsCl-type structure with the space group of $Pm\bar{3}m$. The electronic configuration of Pr is $(4f)^2$ and that of Nd is $(4f)^3$. PrB_6 undergoes to incommensurate antiferromagnetic phase at 7.0 K with wave vector $\mathrm{k}_1^{IC} = (\delta\ \varepsilon\ 1/2)$ and $\mathrm{k}_2^{IC} = (\delta\ -\varepsilon\ 1/2)$ (δ and ε are very close to 1/4), and to commensurate antiferromagnetic phase at 4.2 K with wave vector $\mathrm{k}_1 = (1/4\ 1/4\ 1/2)$, $\mathrm{k}_2 = (1/4\ -1/4\ 1/2)$. NdB_6 undergoes to antiferromagnetic phase at 8.0 K with wave vector (0 0 1/2).

The single crystals of PrB_6 and NdB_6 were grown by the floating zone method using enriched ^{11}B to avoid the large neutron absorption due to ^{10}B.

The polarized neutron diffraction experiment was taken at PONTA (5G), JRR-3M reactor in JAERI (Tokai). The wavelength of the incident neutron beam was 1.55 Å for PrB_6, and in order to check the simultaneous reflection and extinction effect, 1.55 Å and 2.33 Å were used for NdB_6. The measurement was taken at 8.0 K (paramagnetic phase) for PrB_6 and 10.9 K (paramagnetic phase) for NdB_6 under an applied magnetic field of 5.9 T parallel to the ⟨110⟩-axis. The neutron polarization (P_n) was 94.5 % for PrB_6, 93.5 % for 1.55 Å of NdB_6 and 94.5 % for 2.33 Å of NdB_6. The incomplete polarization, the second order wavelength contamination and the statistical uncertainty estimation were taken into account.

The result of the magnetic form factor of NdB_6 is shown in Fig. 1. The bars indicate the statistical uncertainties. If the magnetic moment exists only on rare earth sites, the magnetic form factor mainly reflects the factor of $\langle j_0 \rangle$. However, the observed magnetic form factors of NdB_6 and PrB_6 were significantly scattered around $\langle j_0 \rangle$. This fact suggests that the magnetic moments are not localized only at the rare earth sites but also inbetween the B sites. However, as the observed magnetic form factor of NdB_6 strongly depends on the wavelength, these reflections are distorted by the extinction effect. Therefore after correcting the extinction effect, we can get the spin density distribution of these compounds through the maximum entropy method.

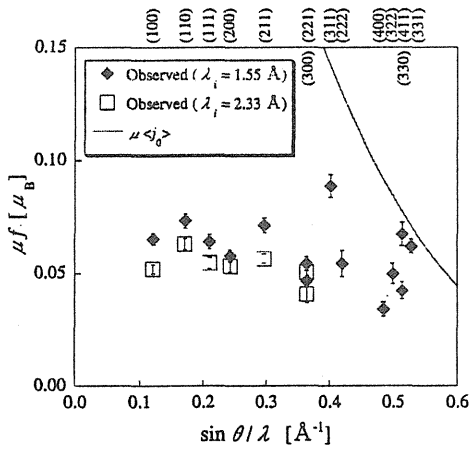


Fig. 1. Magnetic form factor of NdB_6. Diamond is $\lambda_i = 15.5$ Å and square is $\lambda_i = 2.33$ Å

References

[1] M. Saitoh *et al.*: J. Phys. Soc. Jpn. **71** (2002) 2369.

使用施設：JRR-3　装置： 5G (PONTA)，分野： 3. Strongly Correlated Electron Systems

研究テーマ： 4G IMT
表題： β-$Na_{0.33}V_2O_5$ の研究 (I)；金属絶縁体転移における格子の不安定性

1-3-3 Study of β-$Na_{0.33}V_2O_5$(I); Lattice instability at MI transition

S. Nagai[1,2], J. Muraoka[1], M. Nishi[1], Y. Fujii[1], Y. Oohara[1], H. Yoshizawa[1], K. Kakurai[2]
T. Yamauchi[3], J. Yamaura[3], M. Isobe[3], Y. Ueda[3]

[1] *Neutron Scattering Laboratory, ISSP, The Univ. of Tokyo, 106-1, Shirakata, Tokai, Ibaraki, 319-1106*
[2] *Advanced Science Research Center, JAERI, 2-4, Shirane, Shirakata, Tokai, Ibaraki, 319-1195*
[3] *Materials Design and Characterization Laboratories, ISSP, The Univ. of Tokyo, 5-1-5, Kashiwanoha, Kashiwa, Chiba, 277-8581*

β-$Na_{0.33}V_2O_5$ is one of the well known vanadium oxides, called vanadium oxide bronze. Very recently, a superconducting phase was discovered under high pressure [1]. We are interested in studying this material to examine it's unique properties.

One important property already revealed and having close relationship to this superconductivity is the metal-insulator(MI) transition seen at 136 K under ambient pressure. The metallic conductivity is realized only along **b** axis, which is naturally understood with its highly anisotropic one dimensional crystal structure. Therefore, the MI transition will be characterized with one dimensional electron-lattice model. The aim of present study is to get information of the atomic shifts developing below the MI transition temperature, which is complementary to the X-ray diffraction method.

The experiment was performed with general purpose triple axis spectrometer ISSP GPTAS (4G), installed at the JRR-3M reactor. The collimation were chosen to be $40' - 80' - 40' - 80'$. Two PG filters were inserted to eliminate higher order contamination. The wave number of incident neuron ($\mathbf{k_i}$) was chosen to be 3.826 ($\AA^{-1}$) (30.5 meV in energy). The size of the single crystal was about $8 \times 5 \times 3\,mm^3$.

In Fig.1, the peak top intensities of superlattice peaks at Q = (2,2/3,0), (6,1/6,0) and (2,5/3,0) are plotted against temperature. The lattice instability results in appearance of superstructure with the period of 2b along the **b** axis at 250 K, which changes from 2b to 6b at 136 K. This finding allows us to assume that one dimensional electron-lattice model can properly describe these two phase transitions.

The integrated intensities of superlattice peaks in these different phases are collected at 30 K, well below the MI transition temperature, at 150 K, and at room temperature. The detailed analysis is now under way.

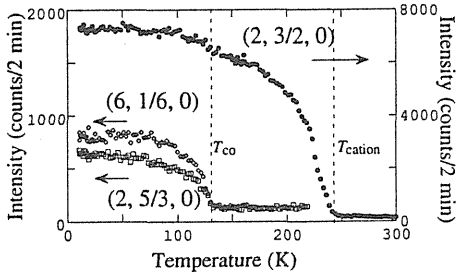


Fig. 1. Temperature dependence of superlattice peak intensities at typical Q. T_{co} and T_{cation} in the figure correspond to two structural phase transition temperatures, 136 K and 250 K, respectively.

References

[1] T. Yamauchi *et al.*: Phys. Rev. Lett. **89** (2002) 057002-1.

使用施設：JRR-3，装置： 4G (GPTAS)，分野： 3. Strongly Correlated Electron Systems

研究テーマ： β-$Na_{0.33}V_2O_5$ の電荷秩序
表題： β-$Na_{0.33}V_2O_5$ の研究 (II)；常磁性状態において磁場誘起される強磁性成分の検出

1-3-4

Study of β-$Na_{0.33}V_2O_5$(II); Detection of field-induced ferromagnetic component in the paramagnetic phase

S. Nagai[1], M. Nishi[1], Y. Fujii[1], K. Nakajima[1], K. Kakurai[2]
T. Yamauchi[3], J. Yamaura[3], M. Isobe[3], Y. Ueda[3]

[1] *Neutron Scattering Lab., ISSP, The Univ. of Tokyo, 106-1, Shirakata, Tokai, Ibaraki, 319-1106*
[2] *Advanced Science Research Center, JAERI, 2-4, Shirane, Shirakata, Tokai, Ibaraki, 319-1195*
[3] *Materials Design and Characterization Laboratories, ISSP, The Univ. of Tokyo, 5-1-5, Kashiwanoha, Kashiwa, Chiba, 277-8581*

β-$Na_{0.33}V_2O_5$ is a vanadium oxide, having quasi one dimensional conductivity along b axis, and metal-insulator(MI) transition was found at 136 K. The aim of this study is to understand this MI transition from microscopic point of view. In the view point of spin freedom, the paramagnetic moment corresponding to V^{4+} (S = 1/2) has been identified by magnetic susceptibility measurement. Our attention is mainly focused on identifying the atomic sites where the magnetic moments are located in the insulating phase.

In Fig. 1, two candidates of spin distribution models are shown. One is a "rectangle type" model, and the other is "homogeneously distributed" model. The former is consistent with the analysis of the atomic displacements based on X-ray diffraction measurement[1]. The latter has been proposed based on the results of the observed static magnetic correlation below T_N ($\simeq$ 24 K), using neutron diffraction measurement.

The idea of present experiment is to measure the induced magnetic moments, which brings information of the spatial correlation of the V^{4+} ions. The use of vertical field cryomagnet up to 6 T and the operation of polarization analysis mode of the triple axis spectrometer ISSP PONTA (5G), installted at the JRR-3M reactor, enabled the measurement of nuclear-magnetic interference term.

The experimental conditions are as follows: Incident neutron wave number ki was 6.19 Å, and collimations were open-80'-80'-open. Flipping ratio of the incident beam was about 24. Measurement was carried out at 30 K under vertical field of 6 T.

In Fig. 2, the observed magnetic structure factor is compared with the expected structure factors from these two models. This result shows that the "homogeneously distributed" model qualitatively explains the observed data. Now it will be important to understand its relationship with the insulating behavior.

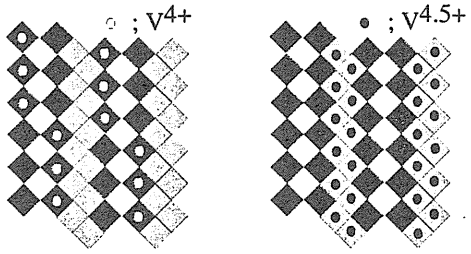


Fig. 1. Two charge distribution models, "rectangle type" model for left figure, "homogeneously distributed" model for right figure.

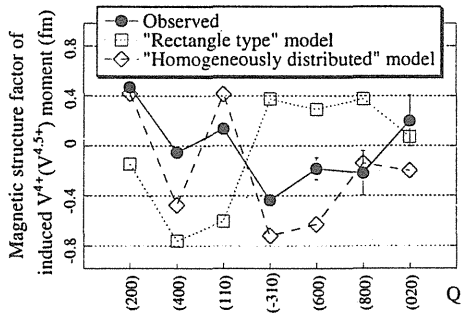


Fig. 2. Comparison of the observed magnetic structure factor with the expected structure factors of the two model described in Fig.1.

References

[1] J. Yamaura *et al.*: J. Phys. Chem. Solids **63** 957 (2002).

使用施設：JRR-3　装置： 5G (PONTA)，分野： 3. Strongly Correlated Electron Systems

研究テーマ：Aサイトが規則配列したLBaMn$_2$O$_6$(L=Y,Tb,Dy,Ho)の構造及び電荷・軌道秩序
表題：Aサイトが規則配列したペロブスカイトMn酸化物 RBaMn$_2$O$_6$

1-3-5 A-site Ordered Manganese Perovskites RBaMn$_2$O$_6$

T. Nakajima[1], H. Kageyama[2], M. Ichihara[1], H. Yoshizawa[1], K. Ohoyama[3] and Y. Ueda[1]
[1] *Institute for Solid State Physics, The University of Tokyo, Kashiwa, 277-8581*
[2] *Dept. of Chemistry, Graduate School of Science, Kyoto University, Kyoto, 606-8502*
[3] *Institute for Materials Research, Tohoku University, Sendai, 980-8577*

The A-site ordered manganese perovskites RBaMn$_2$O$_6$ (R = Y and rare earth elements) have successfully synthesized and investigated in the structures and electromagnetic properties [1, 2]. The structures and magnetic properties were studied by neutron powder diffraction using HERMES installed at T1-3 port of JRR-3M in JAERI (Tokai). The most significant structural feature of RBaMn$_2$O$_6$ is that the MnO$_2$ square sublattice is sandwiched by two types of rock-salt layers, RO and BaO, with much different sizes. The results of electromagnetic properties are summarized in Fig. 1, as an electronic phase diagram. Comparing with the A-site disordered $R_{0.5}A_{0.5}$MnO$_3$ (A = Sr, Ca), RBaMn$_2$O$_6$ displays significant features: (1) the charge/orbital order (CO) transition at T_{CO} far above 300 K, (2) a new stacking variation of the CE-type CO (COI(CE)) with a 4-fold periodicity along the c-axis (4CE-CO) [3], (3) the presence of structural transition (PM-to-PM') possibly accompanied by $d_{x^2-y^2}$ orbital order at T_t above T_{CO}, and (4) the electronic phase segregation. The high T_{CO} and the absence of critical region can be understood as the effect of the absence of A-site randomness. The 4CE-CO could originate from the layer-type order of A-site cations. The structural transition at T_t is the most remarkable feature in RBaMn$_2$O$_6$.

The large mismatch between RO and BaO lattices introduces a strong frustration to the MnO$_2$ sheet and must give a new perturbation to the competition of multi-degrees of freedom among charge, orbital, spin and lattice. The last feature, that is the coexistence of ferromagnetic metal (FM) and antiferromagnetic CE-CO (AFI(CE)) phases as the ground state in LaBaMn$_2$O$_6$ far from CO state, might be explained as the effect of the elongation of Mn-O distance (reduction of bandwidth). Such effect has never been seen in ordinary $R^{3+}_{1-x}A^{2+}_x$MnO$_3$. We have also synthesized the A-site disordered $R_{0.5}$Ba$_{0.5}$MnO$_3$. The A-site disorder suppresses both FM and CO transitions, and leads to magnetic glassy states. We have observed ultrasharp and stepwise changes of magnetization and resistivity in Pr$_{0.5}$Ba$_{0.5}$MnO$_3$. The detailed structures and magnetic properties of A-site disordered $R_{0.5}$Ba$_{0.5}$MnO$_3$ will be reported in the near future.

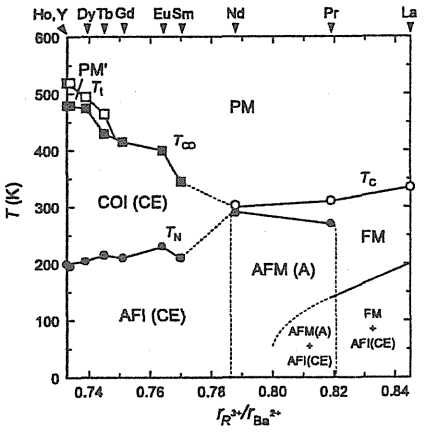


Fig. 1. Electronic phase diagram for RBaMn$_2$O$_6$, expressed as a function of the ratio of ionic radius (R^{3+}/Ba^{2+}). PM (PM'): paramagnetic metal, FM: ferromagnetic metal, AFM(A): A-type antiferromagnetic metal, COI(CE): CE-type charge/orbital ordered insulator, AFI(CE): CE-type antiferromagnetic insulator

References

[1] T. Nakajima *et al.*: J. Phys. Chem. Solids **63** (2002) 913.
[2] T. Nakajima *et al.*: J. Phys. Soc. Jpn. **71** (2002) 2483.
[3] H. Kageyama *et al.*: J. Phys. Soc. Jpn. **72** (2003) 241.

使用施設：JRR-3　装置：T1-3 (HERMES)，分野：3. Strongly Correlated Electron Systems

研究テーマ：ペロブスカイト型Mn酸化物における一次元軌道秩序
表題：$Nd_{1-x}Sr_xMnO_3$のC型反強磁性相におけるスピン波

1-3-6 Spin Wave in the C-type Antiferromagnetic Phase of $Nd_{1-x}Sr_xMnO_3$

R. Kajimoto[1], H. Yoshizawa[2], R. Kawasaki[3], K. Noda[3], and H. Kuwahara[3,4]
[1] *Dept. of Physics, Ochanomizu University, 2-1-1 Otsuka, Bunkyo-ku, Tokyo 112-8610*
[2] *NSL, ISSP, University of Tokyo, 106-1 Shirakata, Tokai, Ibaraki 319-1106*
[3] *Dept. of Physics, Sophia University, Chiyoda-ku, Tokyo 102-8554*
[4] *PRESTO, JST, Chiyoda-ku, Tokyo 102-0074*

The richness of the phase diagram of hole doped perovskite manganites is connected with variation of the orbital structure of manganese ions [1, 2]. A one-dimensional ordering of $d_{3z^2-r^2}$ orbitals along the ferromagnetic (FM) chain direction is expected to cause a chain-type (C-type) antiferromagnetic (AFM) phase at the highly doped region ($0.6 < x < 0.9$). This orbital ordering will induce an anisotropy in the spin exchange interactions, and an observation of such an anisotropy should be strong evidence of the orbital ordering in the C-type AFM phase. Accordingly, we performed a neutron scattering study of the spin dynamics in the C-type antiferromagnet $Nd_{0.25}Sr_{0.75}MnO_3$.

$Nd_{0.25}Sr_{0.75}MnO_3$ is an insulator and shows the C-type antiferromagnetism below $T_N = 295$ K. The crystal structure is tetragonal $I4/mcm$, and the FM chains in the C-type AFM structure run parallel to the c axis. The neutron scattering experiments were performed using the triple axis spectrometer GPTAS at the JRR-3M research reactor in JAERI, Tokai. The collimation was 40′-40′-40′-80′ and the final neutron energy was fixed at $E_f = 30.3$ meV.

Figure 1 shows the dispersion relation of the spin wave. The dispersion shows a noticeable anisotropy with a gap of 9 meV at $q = 0$. To parameterize the spin exchange interactions, we fit the observed dispersion to the Heisenberg model with exchange integrals between the nearest Mn sites J_c ($\parallel c$), J_{ab} ($\perp c$), and a uniaxial anisotropy H_A. The fit yields $4J_cS = 25.8(4)$ meV, $8J_{ab}S = -26.9(3)$ meV, and $g\mu_B H_A = 1.3(1)$ meV. The strong anisotropy $|J_c/J_{ab}| = 1.9$ should evidence the $d_{3z^2-r^2}$ orbital ordering along the c axis. The observed J_c is fairly large and is as large as the value of the FM metallic phase at $x = 0.3$ ($4JS = 22.1$ meV [3, 4]), where the magnetic coupling is governed by the double exchange interactions mediated by the hopping of holes. This fact implies that there is a substantial hopping probability of charges, at least locally, along the c direction.

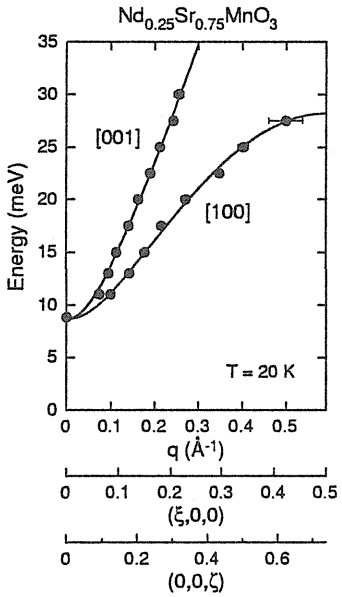


Fig. 1. Spin wave dispersion relations along the [100] and [001] directions at 20 K. Solid lines are fits to the Heisenberg model with nearest neighbor couplings.

References

[1] H. Kuwahara *et al.*, Mat. Res. Soc. Symp. Proc. **494** (1998) 83; T. Okuda *et al.*, Mater. Sci. Eng. B **B63** (1999) 163.
[2] R. Kajimoto *et al.*, Phys. Rev. B **60** (1999) 9506.
[3] J.A. Fernandez-Baca *et al.*, Phys. Rev. Lett. **80** (1998) 4012.
[4] This value is derived from the spin stiffness $D = 165$ meVÅ^2 in Ref. [3] by $D = 2JSa_c^2$ and $a_c = 3.86$ Å.

使用施設：JRR-3　装置：GPTAS(4G)，分野：3. Strongly Correlated Electron Systems

研究テーマ： 汎用3軸型中性子分光器 (TAS-4G)
表題： $Pr_{1-x}Ca_xMnO_3$ の強磁性絶縁体相

1-3-7 Ferromagnetic Insulating Phase in $Pr_{1-x}Ca_xMnO_3$

R. Kajimoto[1], H. Mochizuki[2], and H. Yoshizawa[2]
[1] *Dept. of Physics, Ochanomizu University, 2-1-1 Otsuka, Bunkyo-ku, Tokyo 112-8610*
[2] *NSL, ISSP, University of Tokyo, 106-1 Shirakata, Tokai, Ibaraki 319-1106*

$Pr_{1-x}Ca_xMnO_3$ exhibits a ferromagnetic insulating (FM-I) state for $0.15 < x < 0.3$ [1]. The FM-I state can not be explained only by the double exchange interactions, which induces ferromagnetic metallic (FM-M) state. The coexistence of the FM-M phase and the charge ordered insulating phase seems to be plausible. On the other hand, a recent resonant x-ray scattering (RXS) study suggested that the $LaMnO_3$-type orbital ordering (OO), where $d_{3x^2-r^2}$ and $d_{3y^2-r^2}$ orbitals are alternately aligned on all Mn sites, develops below about 500 K in $Pr_{0.75}Ca_{0.25}MnO_3$ [2]. To reveal the true origin of the FM-I state in $Pr_{1-x}Ca_xMnO_3$, we have performed a neutron scattering study on a single crystal of $Pr_{0.75}Ca_{0.25}MnO_3$ ($T_C = 130$ K).

The crystal structure is orthorhombic *Pbnm* with pseudo cubic lattice constants $a \sim b \sim c/\sqrt{2}$. The neutron scattering experiments were performed using triple axis spectrometers GP-TAS and HQR at the JRR-3M in JAERI, Tokai with neutron wave lengths $k_f = 3.81$ Å^{-1} (GP-TAS) and $k_i = 2.57$ Å^{-1} (HQR).

First, we tried to find signals from charge ordering (CO), but we found only a tiny fraction (~0.1%) of the CE-type charge ordered phase. Therefore, we conclude that the insulating behavior of $Pr_{0.75}Ca_{0.25}MnO_3$ does not come from the CO, but it is intrinsic to the FM state. Next, we examined the orbital state by measuring the anisotropies in the crystal structure as well as in spin fluctuations induced by an OO. Figure 1(a) shows a profile of the 220/004 doublet along the [110] direction at $T = 8$ K. The profile consists of two peaks by the Jahn-Teller distortions. The magnitude of the splitting is, however, quite small compared with $PrMnO_3$ (Fig. 1(b)), the latter is expected to have the $LaMnO_3$-type OO. Figure 1(c) shows the spin wave dispersion relations along the in-plane direction [110] and the out-of-plane direction [001] at $T = 8$ K. Two dispersion curves

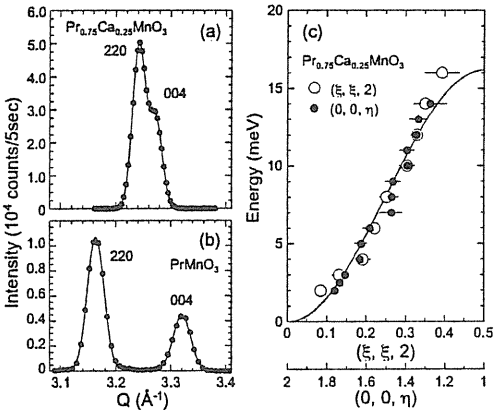


Fig. 1. (a) Profiles of the 220/004 doublets along the [110] direction for $Pr_{0.75}Ca_{0.25}MnO_3$ and (b) for $PrMnO_3$. (c) Spin wave dispersion relations in $Pr_{0.75}Ca_{0.25}MnO_3$ along the [110] and [001] directions.

well coincide, indicating that the spin exchange is isotropic ($J_{ab} \sim J_c$) against the expectation from the possible $LaMnO_3$-type OO. The observed anisotropy in the crystal structure means that there may exist a $LaMnO_3$-like OO, but its smallness and the isotropy in J suggest that there is substantial electron density along the z direction. Such an OO is recently proposed for the insulating phase of $La_{0.88}Sr_{0.12}MnO_3$ [3]. It is expressed as $(|d_{3z^2-r^2}\rangle \pm |d_{x^2-y^2}\rangle)/\sqrt{2}$, and it is compatible with the observation by the RXS study [2]. The FM-I state should be ascribed to this OO rather than any COs.

References

[1] Y. Tomioka *et al.*, Phys. Rev. B **53** (1996) R1689.
[2] M. v. Zimmermann *et al.*, Phys. Rev. B **64** (2001) 195133.
[3] Y. Endoh *et al.*, Phys. Rev. Lett. **82** (1999) 4328.

使用施設：JRR-3　装置： 4G,T1-1 , 分野： 3. Strongly Correlated Electron Systems

研究テーマ：$Sr_{1-x}La_xRuO_3$ の La 置換効果と磁気構造
表題：Sr1-xLaxRuO3(0.0≦x≦0.5)の強磁性抑制の証拠

The evidence of the suppression of ferromagnetic state in $Sr_{1-x}La_xRuO_3$ (0.0≦x≦0.5)

1-3-8

H. Nakatsugawa and Y. Oohara*

Division of Materials Science and Engineering, Graduate School of Engineering, Yokohama National University, Tokiwadai, Hodogaya-Ku, Yokohama 240-8501 Japan; Institute for Solid State Physics, The University of Tokyo, 106-1 Shirakata, Tokai 319-1106, Japan*

Because of the discovery of superconductivity at about 1K in Sr_2RuO_4, the properties of isostructural perovskitelike $SrRuO_3$, $CaRuO_3$, and $Sr_{1-x}Ca_xRuO_3$ (space group: *Pnma* (No.62), *Z=4*) have attracted significant interest. It is well established that the isostructural $SrRuO_3$ is a ferromagnetic (FM) metal with a Curie temperature T_C=165K. Recently, we have also reported the suppression of FM interactions in a series of $Sr_{1-x}La_xRuO_3$.[1] There is, however, a great lack of direct experimental evidence for the suppression of FM state. From these points of view, the magnetic properties, the parameters of the crystal structure, and the charge density distributions visualized by a combination of the maximum entropy method and the Rietveld refinement have been investigated in the present study.

Samples were characterised by the powder x-ray diffraction (XRD) and the powder neutron diffraction (ND) measurements. The ND measurements were carried out at 10K using the HERMES powder neutron diffractometer installed on T1-3 port of JRR-3M reactor in the Japan Atomic Energy Research Institute (JAERI), Tokai Establishment. An incident neutron wavelength λ =1.8207 Å was obtained from a Ge(311) monochromater. The ND data were collected on thoroughly ground powders by a multi-scanning mode in the 2 θ range from 20(deg.) to 153(deg.) with a step width of 0.05(deg.). A Rietveld structure refinement was analyzed using a Rietveld analysis program, RIETAN-2000.

The powder ND data showed that the sample of x=0.5 had also the $GdFeO_3$ type orthorhombic structure which was assigned to *Pnma* (No.62) at 10K. In Fig.1, the results of the Rietveld refinement are shown for these samples. The weighted profile reliability factors of the Rietveld refinement, R_{wp}, was 7.87% and the reliability factors based on the integrated intensities, R_I, was 3.16%.

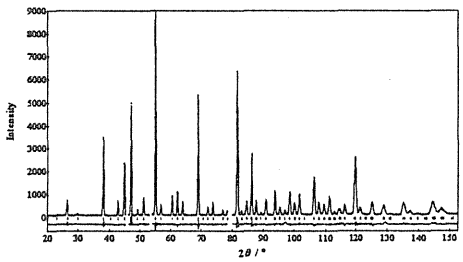


Fig.1 Rietveld fitting of powder ND data for x=0.5 at 10K.

The Ru-O(2)-Ru bond angle was approximately 8(deg.) larger than the Ru-O(1)-Ru bond angle below x=0.3, but both angles were equivalent for the sample of x=0.5. Furthermore, there found to be a little overlapping of the charge density between $Sr_{0.9}La_{0.1}$ and O(1), but no significant overlapping of the charge density between $Sr_{0.5}La_{0.5}$ and O(1). This is the clear evidence of the decrease of the Sr-O hybridization with increasing *x*, which acts as a trigger of the change in the local magnetic environment around Ru and the local charge state of Ru. As a result, the ferromagnetic states are suppressed even at small *x*.

Reference

[1] H.Nakatsugawa *et al.*, J.Phys.: Condens. Matter 14 (2002) 415.

使用施設：JRR-3 ，装置：HERMES(T1-3)，分野 Strongly Correlated Electron Systems

研究テーマ： NdB_6 及び CeB_2C_2 におけるスピン密度分布の観測
表題： CuO 単結晶における電荷整列に伴う磁気秩序の観測

Observation of magnetic order associated with charge order in single crystal CuO

1-3-9

X. G. Zheng[1], M. Togasaki[2], M. Saitoh[2], T. Sasaki[2], M. Nishi[3] and J. Akimitsu[2]

[1] *Department of Physics, Saga University, 1 Honjou-machi, Saga 840-8502*

[2] *Department of Physics, Aoyama-Gakuin University, 5-10-1 Sagamihara-Si, Kanagawa 229-8558*

[3] *Institute for Solid State Physics, The University of Tokyo, 106-1 Shirakata, Tokai, 319-1106*

One of the important questions on the high-T_c superconductivity is whether static or dynamic charge stripes are a key factor to the superconductivity. The charge stripes seem to be common characteristics of the antiferromagnetic(AFM) transition metal oxides. One of the authors (X. G. Z) reported the existence of the charge stripes in cupric oxide by using the electron microscopy [1].

Although CuO has the simplest composition among the copper oxides, its magnetic structure is rather complicated. CuO undergoes AFM transition at T_{N1}=230K followed by an incommensurate to commensurate transition with spin reorientation at T_{N2}, and behaviors suggesting strong short-range AFM interaction above T_N are observed in the magnetic susceptibility. The magnetic structure can be viewed as consisting of ferromagnetic(FM) chains aligned along [101] and AFM chains along [10$\bar{1}$]. On electron microcopy, charge stripes were observed with superlattice reflections at (0 $2n/3$ $m/3$), and the single crystal was separated into two domains of the charge-ordered one and the normal lattice. According to the ratio of Cu^{3+}/Cu^{2+} observed from the superlattice period and the relative area of the charge ordered domains, the crystal of CuO was estimated to contain an excess oxygen of 0.7%. Whether the charge order has an associated magnetic order is of strong interest.

We obtained large single crystals with dimensions up to $2 \times 35 \times 35mm^2$ by a chemical vapor transport technique. Neutron scattering measurement was carried out on the PONTA(5G) triple axis spectrometer. Neutron beam of energy $E = 14.7$meV was used with a pyrolitic graphite filter to eliminate the higher order contaminations. The sample was mounted with the $(0KL)$ reciprocal space parallel to the scattering plane.

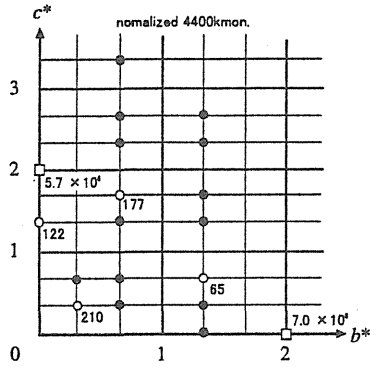


Fig. 1. Intensity of the diffraction peaks on the b*-c* plane. □ : Bragg peaks, ○ : superlattice peaks (normalized by 4400kmon), ● : the superlattice peaks observed by electron microscopy but not observed in the present experiment.

Figure 1 shows the diffraction intensities on the *bc* reciprocal plane. Contribution from the effect of the $\lambda/3$ was noted and carefully checked. However, the ratio of the intensities of the additional peaks to their Bragg peaks differed from each other, and the observed intensity values could not be reproduced by simply assuming a contribution due to the effect of the $\lambda/3$. Therefore, it is reasonable to conclude that these additional peaks reflect the superlattice. The superlattice reflections can be divided into two groups; the (0 $2n/3$ $m/3$) peaks exactly corresponding to the charge ordering, and the new (0 $n/3$ $m/3$) reflections only found with the present neutron diffraction. The latter ones are ascribed by the magnetic scattering associated to the charge order. The present research shows that the magnetic order associated to the charge order really exists in CuO.

References

[1] X. G. Zheng *et al.*: Phys. Rev. Lett. **85** (2000) 5170.

使用施設：JRR-3M　装置： 5G (PONTA)，分野： 3. Strongly Correlated Electron Systems

研究テーマ：$(La,Nd)_{2-x}Sr_xCuO_4$の磁気励起とフォノン
表題：$La_{1.48}Nd_{0.4}Sr_{0.12}CuO_4$の磁気励起スペクトル

1-3-10 Studies on the Magnetic Excitation Spectra of $La_{1.48}Nd_{0.4}Sr_{0.12}CuO_4$

M. Ito[1], Y. Yasui[1], S. Iikubo[1], M. Soda[1], M. Sato[1], K. Kakurai[2] and M. Nishi[3]

[1]*Department of Physics, Nagoya University, Furo-cho, Chikusa-ku, Nagoya 464-8602*
[2]*Advanced Science Research Center, JAERI, Tokai, Ibaraki 319-1199*
[3]*Institute for Solid State Physics, The University of Tokyo, 106-1 Shirakata, Tokai, 319-1106*

In the study of high-T_c cuprates, it is important to collect information on the magnetic excitation spectra $\chi''(q, \omega)$, q and ω being the wave vector and the energy of the excitation, respectively, because superconductivity itself is considered to be originated by the magnetic interaction of the electrons. As one of various specific studies, we have measured $\chi''(q, \omega)$ of $YBa_2Cu_3O_y$ ($YBCO_y$ or YBCO) system to get information on what roles the fluctuating "stripes" (dynamical "stripes") play in realizing the superconductivity.

The observed spectra have been fitted by numerical calculations,[1,2,3] where an expression $\chi(q, \omega) = \chi^0(q, \omega) / \{1+J(q) \chi^0(q, \omega)\}$ is used for the dynamical susceptibility with the exchange coupling $J(q)(=J(\cos q_x a+\cos q_y b))$ and the Lindhard function $\chi^0(q, \omega)$ of the electron system. The effective band parameters t_0, t_1 and t_2, which can reproduce the Fermi surface shape are used. The d-wave form of the energy gap $\Delta_s(k)= (\Delta_0/2)(\cos k_x a-\cos k_y a)$ is also used. Other details can be found in refs. 1-3. Figure 1 shows the ω- dependence of the q-dependent part of $\chi''(q, \omega)$ of $YBCO_{6.5}$ at (1/2,1/2) in the reciprocal space at 7 K and 147 K, together with the data measured by Bourges *et al.*[4] For this system with $_y$=6.5, $|\Delta_0|$ is assumed to be temperature(T)-independent, by considering the persistence of the pseudo gap up to rather high temperature. What we just want to emphasize here is that consideration of the experimentally observed quasi particle broadening Γ, which is as large as ~50 meV (full width at half maximum) for $YBCO_{6.5}$ is important to suppress the antiferromagnetic ordering and to reproduce the (q, ω)- and T-dependence of the spectra. We find that the magnetic excitation spectra of $YBCO_y$ ($y\geq6.5$) can be well understood without effects of dynamical "stripes".

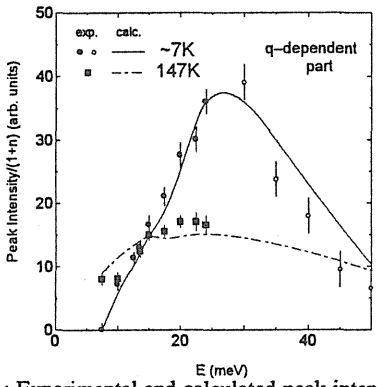


Fig 1: Experimental and calculated peak intensities of the magnetic scattering for $YBa_2Cu_3O_{6.5}$ at q=(1/2,1/2) in the two dimensional reciprocal space are shown, where the q-independent part of the intensities are removed. The data shown by open circles are obtained by Bourges *et al.*[4]

The above results suggest that effects of the dynamical "stripes" may not be important for the occurrence of the high-T_c superconductivity. To clarify this point, we have also studied effects of "stripes" on $\chi''(q, \omega)$ in La214 systems such as $La_{2-x}Ba_xCuO_4$, $La_{2-y-x}Nd_ySr_xCuO_4$, and other related systems with x~1/8. In $La_{1.48}Nd_{0.4}Sr_{0.12}CuO_4$, a first order structural transition takes place at ~69 K(=T_s), and below T_s, the superlattice reflections related to the charge ordering and magnetic one begin to grow from zero continuously with decreasing T.

The data of $\chi''(q, \omega)$ taken with the triple axis spectrometer ISSP-PONTA installed at JRR-3M of JAERI in Tokai have also been analyzed by the similar way used in the

使用施設：JRR-3　装置：PONTA(5G)，分野：3. Strongly Correlated Electron Systems

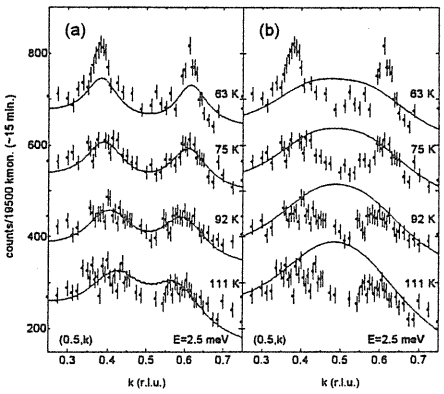


Fig 2: Observed profiles $\chi''(q,\omega)$ of $La_{1.48}Nd_{0.4}Sr_{0.12}CuO_4$ at ω=2.5 meV are shown together with the fitted curves for $\Gamma_0=\Gamma_h$=2 meV (a) and for $\Gamma_0=\Gamma_h$=50 meV (b)

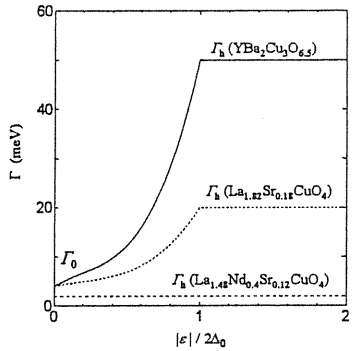


Fig 3: The values of Γ used for the calculations of the magnetic excitation spectra of $YBa_2Cu_3O_{6.5}$, $La_{1.82}Sr_{0.18}CuO_4$ and $La_{1.48}Nd_{0.4}Sr_{0.12}CuO_4$ at low temperatures are shown.

analyses of YBCO. For this system, the ratios, t_0:t_1:t_2 of the effective band parameters 1:-1/6:-1/15 are found to be the best within the restriction that the parameters can reproduce the shape of the Fermi surface of this system. The value of J has been so chosen that the systems do not exhibit antiferromagnetic ordering at finite temperature.

Figures 2(a) and 2(b) show the obtained $S(q,\omega)(\equiv(n+1)\,\chi''(q,\omega))$ of $La_{1.48}Nd_{0.4}Sr_{0.12}CuO_4$ together with the fitted curves, where n is the Bose factor. Fitted curves in the figures are obtained by using the quasi particle broadening Γ_h=2 meV and Γ_h=50 meV, respectively. We have to choose very small value of Γ to obtain the reasonable fittings. We note here that even in Fig. 2(a), the widths of the calculated peaks are broader than that of the observed peaks.

Figure 3 shows the value of Γ for YBCO and $La_{1.48}Nd_{0.4}Sr_{0.12}CuO_4$ obtained by the above fittings at low temperatures. The value of Γ for $La_{1.82}Sr_{0.18}CuO_4$ obtained by the similar fittings is also shown. We can see the value of Γ_h is smaller for La214 system than that of YBCO. On the other hand, the broadenings of the La214 systems are expected to be as large as that of YBCO from optical and transport studies. The suppression of Γ in La214 seems to be a main difference in the analyses of $\chi''(q,\omega)$ between YBCO and La214 systems. These results can be understood by considering the existence of the dynamical "stripe" correlation of the electron system, which induces the spatial variation of the hole density. Because the magnetic excitations are mainly determined by the spins in the hole poor regions, the width of the incommensurate peaks is sharper than the value expected in the state without the "stripe" correlation. The "stripe" correlation itself may contribute to the suppression of Γ, too.[5] These results indicate that effects of the dynamical "stripes" are significant only in La214 systems and that they are not, at least, appreciable in YBCO.

References

[1] M. Sato, M. Ito, H. Harashina, M. Kanada, Y. Yasui, A. Kobayashi and K. Kakurai : J. Phys, Soc. Jpn 70 (2001) 1342.

[2] M. Ito, H. Harashina, Y. Yasui, M. Kanada, S. Iikubo, M. Sato, A. Kobayashi and K. Kakurai : J. Phys, Soc. Jpn 71 (2002) 265.

[3] M. Sato, M. Ito, H. Harashina, Y. Yasui, M. Kanada, S. Iikubo, A. Kobayashi and K. Kakurai : Physica B (2003) No.4 (in press)

[4] *The gap Symmetry and Fluctuations in High Temperature Superconductors* Edited by J. Bok, G deutscher, D. Pavuna and S.A. Wolf. (Plenum Press, 1998). 349-371 (Vol. 371 in NATO ASI series, Physics).

[5] M. Ito, Y. Yasui, S. Iikubo, M. Soda, M. Sato, A. Kobayashi and K. Kakurai : J. Phys, Soc. Jpn 72 (2001) No.7 (in press)

研究テーマ： $La_{2-x}Sr_xCuO_4$ のオーバードープ超伝導相における低エネルギースピン揺動
表題： 中性子散乱による $La_{2-x}Sr_xCuO_4$ の擬スピンギャップの研究

1-3-11 Spin Pseudo Gap in $La_{2-x}Sr_xCuO_4$ Studied by Neutron Scattering

C. H. Lee[1], K. Yamada[2], H. Hiraka[3], C. R. Venkateswara Rao[3] and Y. Endoh[3]

[1] *National Institute of Advanced Industrial Science and Technology, 1-1-1 Umezono, Tsukuba, Ibaraki 305-8568, Japan*

[2] *Institute for Chemical Research, Kyoto University, Uji 611-0011, Japan*

[3] *Institute for Materials Research, Tohoku University, Sendai 980-8577, Japan*

Investigation of spin dynamics of high-T_c cuprates is important to understand their unusual magnetic as well as transport properties. One of their remarkable phenomena is the opening of a pseudo gap above the superconducting transition temperature (T_c). Since the origin of the gap is still controversial, more systematic experimental studies are highly required. In general, neutron scattering is a very useful method to study the energy spectrum of magnetic excitation and its q-dependence. Nevertheless, only a preliminary signature for the pseudo spin-gap in $La_{2-x}Sr_xCuO_4$ system has been reported from neutron study[1]. Thus, we started systematic study on the spin fluctuations of $La_{2-x}Sr_xCuO_4$ (x = 0.15, 0.18, 0.20) in the energy range 3 meV $\leq \omega \leq$ 12 meV and in the temperature range 8 K $\leq T \leq$ 150 K.

We observed a clear energy gap spectrum of the q-integrated dynamical spin susceptibility $\chi''(\omega)$ well below T_c. The $\chi''(\omega)$ has a peak around ω = 6 meV and vanishes into the background below $\omega \sim$ 4.5 meV. An enhancement of $\chi''(\omega)$ at 6 meV is accompanied with incommensurate peak - width broadening. The gap - like - structure and the enhancement of $\chi''(\omega)$ at 6 meV has also been observed at T = 45 K, a temperature higher than T_c (= 36.5 K), which suggests the existence of a so called spin pseudo gap. Upon heating of the sample to T = 150 K, $\chi''(\omega)$ becomes nearly temperature independent and the gap-like structure disappears.

Figure 1 shows the energy dependences of $\chi''(\omega)$ for the x = 0.15 (T_c = 37.5 K), 0.18 (T_c = 36.5 K) and 0.20 (T_c = 30 K) samples at $T = T_c$ [1, 2]. Among them, a gap-like structure of $\chi''(\omega)$ remains only for the x = 0.18 sample. For the x = 0.15 and 0.20 samples, $\chi''(\omega)$ decreases linearly with decreasing energy below $\omega \sim$ 5 meV, approaching zero only as $\omega \to 0$. It seems that the spin pseudogap depends strongly on Sr concentration. The fact that the spin pseudogap presents in single layer compounds $La_{2-x}Sr_xCuO_4$ as in the bilayer $YBa_2Cu_3O_{7-y}$ suggests that the spin pseudogap is a universal phenomenon in high-T_c materials. To understand the origin of the pseudo gap and the mechanism behind Cooper pair formation, further studies are required.

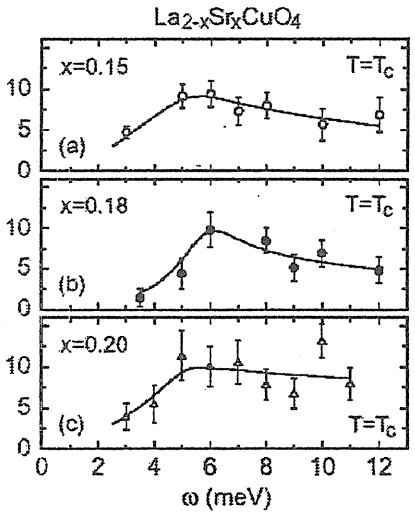


Fig. 1. Energy dependence of $\chi''(\omega)$ for the (a) x = 0.15, (b) 0.18 and (c) 0.20 samples at $T = T_c$. Among them, only the x = 0.18 sample shows a gap-like energy spectrum. Solid lines provide guides to the eyes.

References

[1] C. H. Lee *et al.* : J. Phys. Soc. Jpn. **69** (2000) 1170.

[2] C. H. Lee *et al.* : Phys. Rev. B **67** (2003) 134521.

使用施設：JRR-3　装置： TOPAN (6G)，分野： 3. Strongly Correlated Electron Systems

研究テーマ： 磁性・非磁性不純物置換 $La_{2-x}Sr_xCuO_4$ における低エネルギー磁気励起・静的磁気相関の研究
表題： Zn ドープ $La_{1.85}Sr_{0.15}CuO_4$ における低エネルギー磁気励起の磁場効果

Magnetic field effect on low-energy spin excitations in Zn-doped $La_{1.85}Sr_{0.15}CuO_4$

1-3-12

H. Kimura[1], M. Kofu[2], K. Hirota[3], and K. Nakajima[4]

[1] *Institute of Multidisciplinary Research for Advanced Materials, Tohoku University, Sendai 980-8577*

[2] *Department of Physics, Tohoku University, Sendai 980-8578*

[3] *Institute for Solid State Physics, The University of Tokyo, 106-1 Shirakata, Tokai, 319-1106*

[4] *Japan Atomic Energy Research Institute, Tokai, Ibaraki 319-1195, Japan*

Discovery of field-induced incommensurate spin excitations in $La_{1.837}Sr_{0.163}CuO_4$ have revealed that the inside of the vortices in the superconducting state is antiferromagnetic[1]. However, the relationship between the vortex state and the spin excitations has been poorly understood. It is well known that a small amount of Zn impurities significantly change the H-T phase diagram of the vortex state on high-T_c superconductors. Therefore, Zn-doping is one of the most suitable probe to explore how the spin excitations are affected by the change of vortex states. Thus in the present study, we have performed inelastic neutron scattering experiments under the magnetic field for systematically Zn-doped $La_{1.85}Sr_{0.15}CuO_4$.

Neutron scattering experiments were carried out with the TOPAN spectrometer installed at the 6G beam port. Detailed experimental conditions are denoted in Fig ??. Magnetic field up to 6 Tesla was applied perpendicular to the CuO_2 plane, namely, parallel to the c-axis using the *ENDOH magnet*. Single crystals of Zn-free $La_{1.85}Sr_{0.15}CuO_4$ ($y = 0$) and 0.4 % Zn-doped one ($y = 0.004$) were prepared for the present study. Note that both the samples show a well defined spin gap state below T_c[2].

Field dependence of spin excitations at $\omega = 3$ meV for $y = 0$ and $y = 0.004$ are summarized in Fig. 1(a) and (b), respectively. The data was taken at $T = 2$ K. At zero field, no excitation is observed in both $y = 0$ and $y = 0.004$, indicating the opening of the spin gap. At $H = 6$ T, a field-induced excitation is clearly seen at the incommensurate position in $y = 0$, while there is no excitation in $y = 0.004$. The result of $y = 0$ is qualitatively consistent with that of $La_{1.837}Sr_{0.163}CuO_4$[1]. At the same time, a well defined vortex lattice was recently observed in $La_{1.83}Sr_{0.17}CuO_4$[3]. These facts indicate that the field-induced spin excitation is closely connected with the formation of vortex lattice.

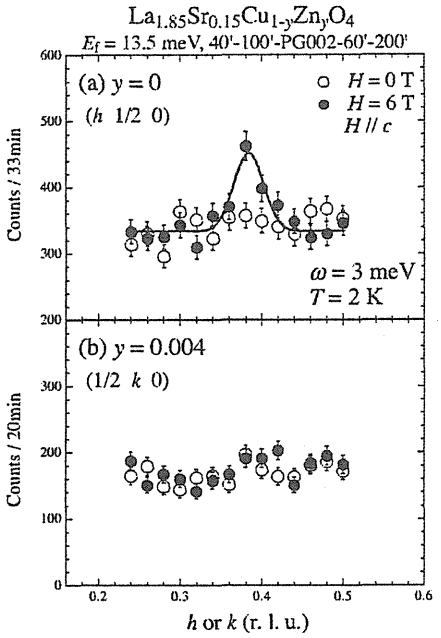


Fig. 1. q-profiles of spin excitations at $\omega = 3$ meV under the magnetic fields of 0 T (open circles) and 6 T (closed circles) for (a); $y = 0$ and (b); $y = 0.004$. The data was taken at $T = 2$ K.

The vortex state of Zn-doped system will be systematically studied in near future to elucidate the relevance between the spin excitations and the vortex state.

References

[1] B. Lake *et al.*: Science **291**, 1759 (2001).
[2] H. Kimura *et al.*: cond-mat/0209428.
[3] R. Gilardi *et al.*: Phys. Rev. Lett. **88**, 217003 (2002).

使用施設：JRR-3　装置： 6G, C1-1, T1-2 , 分野： 3. Strongly Correlated Electron Systems

研究テーマ： 高温超伝導体 (La,Ba,Sr)2CuO4 におけるストライプ秩序と超伝導の相関
表題： 高温超伝導体 $La_{1.875}Ba_{0.125}CuO_4$ におけるストライプ揺らぎの研究

1-3-13 Study of stripe fluctuation in high- T_c cuprate $La_{1.875}Ba_{0.125}CuO_4$

M. Fujita[1], H. Goka[2], and K. Yamada[3]
[1] *Institute for chemical research, Kyoto University, Uji, Gokasyo, 611-0011*
[2] *Department of Physics, Kyoto University, Kyoto 606-8502*
[3] *Institute of material research, Tohoku University, Sendai, 985-8577*

For the last couple of years, our neutron scattering studies on $La_{1.875}Ba_{0.125-x}Sr_xCuO_4$ revealed that both charge and spin stripe orders appear in the low temperature tetragonal (LTT) structure while the stability of charge order competes with superconductivity[1].

In the 1/8-doped La-214 system, the four-fold incommensurate (IC) magnetic superlattice peaks appear around (π, π) in the reciprocal lattice space where the magnetic inelastic signal is observed commonly in the hole-doped high-T_c cuprates. One of the motivations of research on the stripe correlation arises from the superconductivity which could be mediated by dynamical stripe fluctuations. Therefore, the main purpose of this study is to investigate the spin excitation in a system that shows the spin and charge stripe orders at the ground state. For the experiment, we prepared $La_{1.875}Ba_{0.125}CuO_4$ single crystal in which the superconductivity is strongly suppressed[2].

All neutron scattering experiments were performed by thermal and cold neutron triple-axis and double-axis spectrometers. We used TOPAN and KSD spectrometers installed at the 6G thermal beam hole and the T1-2 thermal beam guide. For low energy studies, we used the HER spectrometer installed at the C1-1 cold beam guide. In a single crystal of $La_{1.875}Ba_{0.125}CuO_4$ grown by a traveling solvent floating zone method, fractional superconductivity set in at T_c of $\leq$ 5 K, and the LTO-LTT structural transition occurs at T_{d2} ~60 K upon cooling.

As seen in the ordered state, the low energy spin excitation was found to strongly couple with the LTT structure. Upon heating the sample, the incommensurability δ decreases and the peak width increases at T_{d2}. The figure shows the imaginary part of dynamical magnetic susceptibility $\chi''(\omega)$ in the energy range of 0meV $\leq \omega \leq$ 12meV. Below the T_{d2}, $\chi''(\omega)$ clearly changes under ~10 meV. This energy dependence indicates that the typical energy of enhanced stripe fluctuation in the LTT phase is less than 10 meV similar to the energy scale of the stripe fluctuations in $La_{1.725}Sr_{0.275}NiO_4$[3].

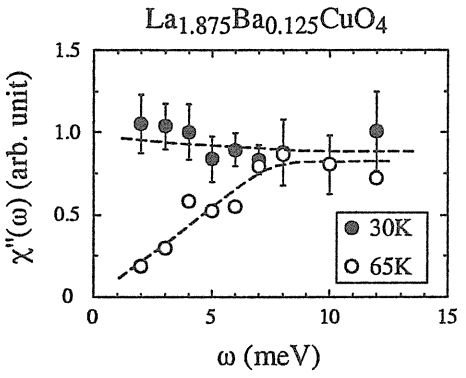


Fig. 1. The energy dependence of $\chi''(\omega)$ at several temperatures.

References

[1] M. Fujita, H. Goka, K. Yamada and M. Matsuda, Phys. Rev. Lett. 88 167008 (2002).
[2] A. R. Moodenbaugh, Y. Xu, M. Suenaga, T. J. Folkerts and R. N. Shelton, Phys. Rev. B 38 4596 (1988).
[3] S.-H. Lee, J. M. Tranquada, K. Yamada, D. J. Buttrey, Q. Li, and S.-W. Cheong, Phys. Rev. Lett. 88 126401 (2002).

使用施設：JRR-3　装置：TOPAN(6G),HER(C1-1),KSD(T1-2)　分野：Strongly Correlated Electrons Systems

研究テーマ： La系高温超伝導体における電荷・スピン秩序
表題： $La_{2-x}Ba_xCuO_4$ におけるストライプ秩序と超伝導の競合的関係

Competitive relation between stripe order and superconductivity in $La_{2-x}Ba_xCuO_4$

1-3-14

H. Goka[1], M. Fujita[2], T. Adachi[3], N. Kitajima[3], Y. Koike[3] and K. Yamada[4]

[1] *Department of Physics, Kyoto University, Kyoto 606-8502*

[2] *Institute for chemical research, Kyoto University, Gokasyo, Uji, 611-0011*

[3] *Department of Applied Physics, Graduate School of Engineering, Tohoku University, Aoba-yama 05, Aoba-ku, Sendai 980-8579*

[4] *Institute for Materials Research, Tohoku University, Katahira 2-1-1, Aoba-ku, Sendai 980-8577*

The systematic neutron-scattering studies on high-T_C cuprates $La_{1.875}Ba_{0.125-x}Sr_xCuO_4$[1] have recently revealed the appearance of charge and spin stripe orders at $\frac{1}{8}$ hole concentration ($\frac{1}{8}$-doping/Cu-ion) in the low temperature tetragonal (LTT) structure.

In $La_{2-x}Ba_xCuO_4$ (LBCO), the superconducting transition temperature T_C is remarkably suppressed to much lower than 10 K in $x = \frac{1}{8}$ sample, and the superconductivity recovers as x deviates from $\frac{1}{8}$. For example, T_C is 20 K for $x = 0.10$ sample even in the LTT structure. Thus x-dependence on the charge/spin stripe orders would provide crucial information regarding to the mechanism of the suppression of superconductivity.

In order to address this issue, we performed elastic neutron-scattering measurements on the LBCO single crystals with x=0.08 and 0.10. We used triple-axis spectrometers TOPAN(6G beam hole), HER(C1-1 cold guide) and double-axis spectrometer KSD(T1-2 thermal guide). Two single crystals were grown by a traveling solvent floating zone method. The T_C's are 21.7 K for x=0.10 and 24.2 K for x=0.08.

In x=0.08, a structural superlattice peak of (1 0 0) in LTT structure appears with intensity much weaker than that of $x=\frac{1}{8}$, and no evidence of charge/spin stripe peak was observed. These results are consistent with the previous conclusion that the charge stripe order strongly couples with the LTT structure.

On the other hand, in x=0.10, a structural superlattice peak of (1 0 0) in LTT appears at 50 K, and incommensurate peaks of charge/spin stripes appear at 40 K, as shown in Fig. 1(d). At 4.5 K, the intensity ratio between the structural superlattice peak and the incommensurate magnetic peaks is comparable with that in $x=\frac{1}{8}$. However, the incommensurate peaks of charge stripe order has much lower intensity than that in $x=\frac{1}{8}$. Therefore we summarize, (i) Even in the LTT structure, superconductivity is not severely suppressed when charge stripe order is not stabilized, which indicates it is the charge stripe order to suppress superconductivity directly. (ii) Even in the LTT structure, the charge stripe order becomes unstable when x deviates from $\frac{1}{8}$, that indicates the hole concentration of $\frac{1}{8}$ is important for the stability of the charge stripe order.

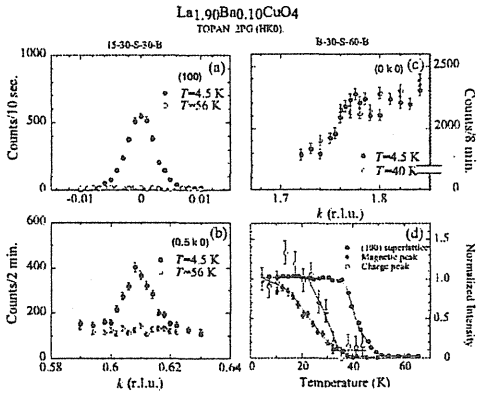


Fig. 1. Superlattice peaks in $La_{1.90}Ba_{0.10}CuO_4$. (a) a structural superlattice peak in LTT structure. (b) a magnetic incommensurate peak. (c) q-scans around the charge stripe peak expected from the position of magnetic incommensurate peak. (d) temperature dependences of these three peaks.

References

[1] M. Fujita et al., Phys. Rev. Lett. 88 167008 (2002).

使用施設：JRR-3　装置：TOPAN(6G),HER(C1-1),KSD(T1-2)　分野：Strongly Correlated Electrons Systems

研究テーマ： $PrPd_2Al_3$ おける磁気励起子の研究
表題： 基底一重項磁性 $PrPd_2Al_3$ の磁気励起

1-3-15 Magnetic Excitations in a Singlet-Ground-State Magnet $PrPd_2Al_3$

N. Aso[1], G. Motoyama[2], N.K. Sato[3] and H. Kadowaki[4]

[1] *Institute for Solid State Physics, The University of Tokyo, Tokai, Ibaraki 319-1106*
[2] *Graduate School and Fac. of Science, Himeji Institute of Technology, Kamigori, Hyogo 678-1297*
[3] *Department of Physics, Graduate School of Science, Nagoya University, Nagoya, 464-8602*
[4] *Graduate School and Fac. of Science, Tokyo Metropolitan Univ., Hachioji, 192-0397*

UPd_2Al_3 is famous for a heavy fermion superconductor coexisting antiferromagnetism. Recently it was argued that magnetic excitons mediate superconducting pairing interaction in UPd_2Al_3. [1] In general the magnetic exciton is a kind of spin waves propagating in a cryatal with a crystal-electric-field (CEF) singlet groud state. For UPd_2Al_3, the number of 5f electrons is nearly three; one of them is assumed to be delocalized to form heavy quasiparticles and carry superconducting currents, and the other two are well localized on each uranium ion site and are responsible for the localized magnetic moment. The even number of localized electrons makes it possible to assume the singlet ground state. This unusual nature of 5f electrons, motivates us to investigate the CEF state of the rare earth counterpart $PrPd_2Al_3$ that has two 4f localized electrons.

Dönni *et al.* [2] found CEF excitations of $PrPd_2Al_3$ by inelastic neutron scattering experiment for a powdered sample and obtained the CEF parameters, which lead to the Γ_1 singlet ground state, the first excited state of Γ_5 doublet with the energy separation from the groud state of $\Delta = 5.17$ meV, and the second excited state of $\Gamma_{6(1)}$ doublet with $\Delta = 16.82$ meV.

Recently, Motoyama *et al.*[3] succeeded in growing single crystals of $PrPd_2Al_3$. They confirmed the CEF model proposed Dönni by measuring temperature dependence of magnetic susceptibility and magnetization curves at several temperatures. Nonetheless, there still remains small deviation between experimental data and calculationa from the Dönni model, implying the existance of the magnetic exition. To reveal the nature of the magnetic exciton in $PrPd_2Al_3$, we performed the cold neutron inelastic scatteirng experiments on single crystals of $PrPd_2Al_3$ by using a 3-axis spectrometer HER (C1-1).

Figure 1 shows the contour plot of the excitation energy of the CEF transition $\Gamma_1 \rightarrow \Gamma_5$ centered around 5 meV. As one can see in the figure, there is the distinct dispersion relations indicating the existance of the magnetic exciton. Furthermore, there is the minimum zone along (0.5,0,L) line at about 5.1 meV, which is completely different with the case in UPd_2Al_3, where the minimum energy can be obtained at the (0,0,0.5) position. These difference can be possibly explained by the difference of the ground state between two compounds.

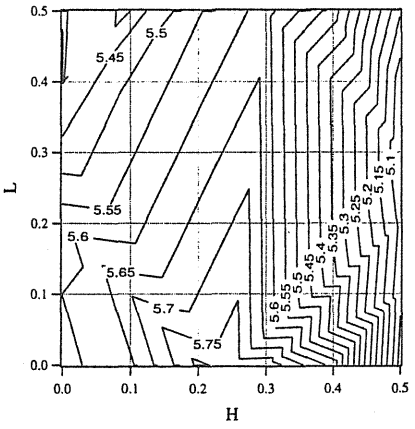


Fig. 1. Contour plot of dispersion relations in $PrPd_2Al_3$ at $T = 1.5$ K.

References

[1] N.K. Sato *et al.*: Nature (London) **410** (2001) 340.
[2] A. Dönni *et al.*: J. Phys.: Condens. Matt. 9 (1997) 5921.
[3] G. Motoyama *et al.*: J. Phys. Soc. Jpn **71** (2002) 1609.

使用施設：JRR-3　装置： C1-1 (HER)，分野： 3. Strongly Correlated Electron Systems

研究テーマ：反強磁性-非磁性境界付近の重い電子系化合物における反強磁性相関
表題：重い電子系 $CeNi_2Ge_2$ における低エネルギーのスピン揺動：非フェルミ液体的振舞の起源

Low-energy spin fluctuations of $CeNi_2Ge_2$: origin of non-Fermi liquid behavior

1-3-16

H. Kadowaki[1], T. Fukuhara[2], and K. Maezawa[2]

[1] *Department of Physics, Tokyo Metropolitan University, Hachioji-shi, Tokyo 192-0397*
[2] *Department of Liberal Arts and Science, Toyama Prefectural University, Kosugi, Toyama 939-039*

Non-Fermi-liquid (NFL) behavior has been investigated in a number of f-electron systems in recent years [1]. In heavy-fermion systems, large mass enhancements are brought about by fluctuations of the spin degrees of freedom participating in quasiparticles. When certain spin fluctuations are slowed down, the Fermi liquid (FL) description breaks down and NFL behaviors appear. For many NFL compounds, the slowing down is related to proximity to magnetic phases or quantum critical points (QCP), which requires tuning by chemical substitutions or static pressures.

An NFL compound $CeCu_{5.9}Au_{0.1}$ has been intensively studied experimentally [2]. The criticality of this system was discussed theoretically, posing an important question: Is the singularity described by the standard spin fluctuation theory of an itinerant character [3] or by a fixed point with a localized spin character [4]? Unfortunately, inevitable disorder effects on QCP by chemical tuning give some difficulty in its interpretation. Among many NFL compounds a few examples, such as $CeNi_2Ge_2$ and $YbRh_2Si_2$, are stoichiometric and provide opportunities of studying NFL behaviors or QCP in clean limits. The compound $CeNi_2Ge_2$ belongs to paramagnetic heavy-Fermion compounds with enhanced $C/T \simeq 350$ mJ/K^{2}mole and $T_K \simeq 30$ K [5]. However precise measurements at low temperatures, for example $C/T \propto \ln(T_0/T)$, revealed that $CeNi_2Ge_2$ shows NFL behaviors with an energy scale much smaller than T_K. In this study, we directly measured magnetic excitations of $CeNi_2Ge_2$ using neutron scattering and have found low-energy spin fluctuations relevant to the NFL behaviors [7].

A single-crystalline sample of 2.2 cm^3 in volume was grown using the isotope ^{58}Ni to avoid the large incoherent elastic scattering of natural Ni nuclei. Neutron scattering experiments were performed on the triple-axis spectrometer HER at JRR-3M JAERI. The typical energy resolution using a fixed $E_f = 3.1$ meV condition was 0.1 meV (FWHM) at the elastic position.

It has been found that a pronounced spin fluctuation grows around a wave vector $\mathbf{Q} = (\frac{1}{2}\frac{1}{2}1)$. Constant-$Q$ scans at this wave vector in the temperature range $1.5 < T < 20$ K are shown in Fig. 1(a), together with those at $\mathbf{Q} = (\frac{1}{2}\frac{1}{2}\frac{1}{2})$. At 20 K the both data are well described by the Lorentzian form $\mathrm{Im}\chi_L(\mathbf{Q},E) = \chi_L(\mathbf{Q})E\Gamma_\mathbf{Q}/(E^2+\Gamma_\mathbf{Q}^2)$ with $\Gamma_\mathbf{Q} \simeq 4$ meV $= 44$ K in agreement with the previous neutron scattering experiments [5,6]. The spin fluctuation of this energy scale is antiferromagnetic with a characteristic wave vector $\mathbf{k}_1 = (0.23, 0.23, \frac{1}{2})$ [6]. The same spectral shape persists down to 1.5 K for $\mathbf{Q} = (\frac{1}{2}\frac{1}{2}\frac{1}{2})$. On the other hand at $\mathbf{Q} = (\frac{1}{2}\frac{1}{2}1)$, the spectral weight in a low energy range increases below 10 K. Since the NFL behaviors of $CeNi_2Ge_2$ show salient features in this T range, we can conclude that this low-energy spin fluctuation is relevant to NFL. It should be noted that its characteristic wave vector $\mathbf{k}_2 = (\frac{1}{2}\frac{1}{2}0)$ is near the antiferromagnetic wave vector of $Ce(Ni_{1-x}Pd_x)_2Ge_2$, indicating the proximity to an antiferromagnetic phase. Since the observed spectral shapes in Fig. 1(a) show an additional peak structure below 1.5 meV, we tried to parameterize the data by adding either another Lorentzian or a Gaussian term to $\mathrm{Im}\chi_L$. Only the latter form

$$\mathrm{Im}\chi(\mathbf{Q},E) = \mathrm{Im}\chi_L + \delta\chi(\mathbf{Q})\frac{\sqrt{\pi}E}{\gamma_\mathbf{Q}}e^{-(E/\gamma_\mathbf{Q})^2}, \quad (1)$$

provides reasonable fits. The energy width of the Gaussian is 0.6 meV (HWHM) at $T = 1.5$ K.

使用施設：JRR-3　装置：HER(C1-1)，分野：3. Strongly Correlated Electron Systems

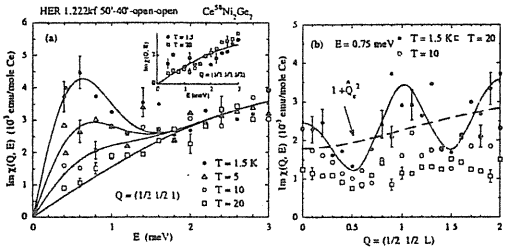


Fig. 1. (a) Constant-Q scans at $\mathbf{Q} = (\frac{1}{2}\frac{1}{2}1)$. Solid lines are fits to Lorentzian for data at $T = 20$ K and the function of Eq. (1) with an additional Gaussian for data below 10 K. The inset shows constant-Q scans at $\mathbf{Q} = (\frac{1}{2}\frac{1}{2}\frac{1}{2})$. (b) Constant-$E$ scans along a line $\mathbf{Q} = (\frac{1}{2}\frac{1}{2}L)$ taken with $E = 0.75$ meV. Solid and dashed lines are a guide to the eye and an orientation factor of spin fluctuations in the ab-plane, respectively.

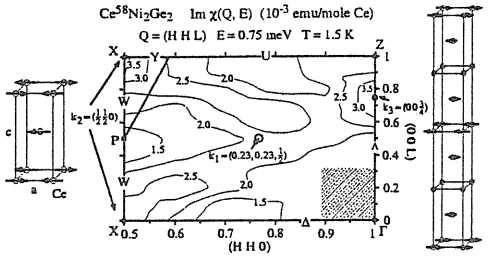


Fig. 2. A contour map of constant-E scans in the (HHL) scattering plane at $T = 1.5$ K. Antiferromagnetic spin configurations, depicted in left and right sides, illustrate low-energy spin fluctuations with wave vectors $\mathrm{k_2} = (\frac{1}{2}\frac{1}{2}0)$ (X point) and $\mathrm{k_3} = (00\frac{3}{4})$, respectively, assuming spins along the a-axis.

Fig. 1(b) shows constant-E scans taken with $E = 0.75$ meV along a line $\mathbf{Q} = (\frac{1}{2}\frac{1}{2}L)$ below and above 10 K. A modulation peaked at integral L implies that an antiferromagnetic correlation with $\mathrm{k_2}$ is formed only at low temperatures. Second information extracted from these data is an anisotropy of the spin fluctuation. The slow Q variation of the intensity is brought about by an orientation factor $(1+\hat{Q}_c^2)$ of the spin fluctuation in the ab-plane as shown by the dashed curve in Fig. 1(b).

A number of constant-E scans were carried out at 1.5 K in a wider Q range, to check the interesting possibility of two-dimensional (2D) spin fluctuations inferred from the resistivity exponent and to find out other spin fluctuations. A result is shown in Fig. 2 as a contour map of intensities with $E = 0.75$ meV in the (HHL) scattering plane. In this figure $\mathrm{k_2}$ corresponds the two X points $(\frac{1}{2}\frac{1}{2}0)$ and $(\frac{1}{2}\frac{1}{2}1)$. A simple rod-type scattering along $(\frac{1}{2}\frac{1}{2}L)$ of the 2D fluctuation has not been observed. There is, instead of this, another peak structure at a reduced wave vector $\mathrm{k_3} = (00\frac{3}{4})$, which also grows only at low temperatures. Constant-Q scans at $\mathrm{k_3}$ show similar spectra to those of $\mathrm{k_2}$ with a slightly larger energy width of the Gaussian term of 0.9 meV (HWHM), which suggests secondary importance of $\mathrm{k_3}$ to NFL.

It has been elucidated that a basic characteristic of $CeNi_2Ge_2$ is the existence of the low and high energy scales of the spin fluctuations with different Q dependences. In stark contrast with this, spin fluctuations of standard heavy-Fermion compounds, such as $CeRu_2Si_2$ and $CeCu_6$, possess continuous energy scales $\Gamma_\mathbf{Q}$ of the Lorentzian $\mathrm{Im}\chi_\mathrm{L}$, which are modulated by RKKY interactions. For NFL $CeCu_{5.9}Au_{0.1}$ chemical tuning reduces $\Gamma_\mathbf{Q}$ further to zero at the antiferromagnetic wave vector. On the other hand, the NFL behavior in $CeNi_2Ge_2$ is caused by the formation of the second low-energy spin-fluctuations, which is the Gaussian term of Eq. (1). Although the reason why this second spin fluctuation appear is not clear, at present, we may speculate that certain fine structures of quasiparticle bands formed well below T_K lead to the low-energy spin fluctuations.

[1] G. R. Stewart, Rev. Mod. Phys. **73**, 797 (2001). [2] A. Schröder *et al.*, Nature (London) **407**, 351 (2000). [3] T. Moriya, T. Takimoto, J. Phys. Soc. Jpn. **64**, 960 (1995). [4] P. Coleman *et al.*, J. Phys. Condens. Matter **13**, R723 (2001). [5] G. Knopp *et al.*, J. Magn. Magn. Mater. **74**, 341 (1988). [6] B. Fåk *et al.*, J. Phys. Condens. Matter **12**, 5423 (2000). [7] H. Kadowaki, T. Fukuhara, K. Maezawa, Acta Phys. Pol. B **34**, 375 (2003).

研究テーマ：T^*系高温超伝導体の磁気励起スペクトル
表　題：$La_{1.48}Nd_{0.4}Sr_{0.12}CuO_4$の面内縦波格子振動の研究

1-3-17

Studies on the In Plane Phonons of $YBa_2Cu_3O_y$ and $La_{1.48}Nd_{0.4}Sr_{0.12}CuO_4$

M. Ito[1], Y. Yasui[1], S. Iikubo[1], M. Soda[1], M. Sato[1] and K. Kakurai[2]

[1]Department of Physics, Nagoya University, Furo-cho, Chikusa-ku, Nagoya 464-8602
[2]Advanced Science Research Center, JAERI, Tokai, Ibaraki 319-1195

In-plane longitudinal phonons of high-T_c cuprates have been studied mainly to extract detailed information of "stripes". The suppression of the superconductivity by the "stripe" formation is known as the 1/8 anomaly in La214 systems such as $La_{2-x}Ba_xCuO_4$ and $La_{2-x-y}Nd_ySr_xCuO_4$. For these systems, even the fluctuations of the ordering or the dynamical "stripes", may have significant effects on the superconductivity. To study whether such dynamical "stripes" can play, under certain conditions, an important role on the occurrence of high-T_c superconductivity or not, we have performed the phonon measurements and tried to clarify effects of "stripes" in one of the La214 systems and in $YBa_2Cu_3O_y$ ($YBCO_y$ or YBCO).

If the ordering (or its fluctuation) of holes along the Cu-O-Cu direction exists, in-plane phonon modes are considered to be somewhat modified. Here, we have studied one of the longitudinal bond stretching branches on single crystal samples of $YBCO_y$ with several y values and on a single crystal of $La_{1.48}Nd_{0.4}Sr_{0.12}CuO_4$. Mook *et al.* [1] measured an in-plane phonon branch with the energy of ~(43~52) meV on a crystal of YBCO and reported anomalous wave vector(q) dependence of the phonon energy and the anomalous broadening of the observed profiles of the phonon vibrating perpendicular to the chain direction ($//b$) at around q=(2δ,0,0), where δ is the incommensurability of the magnetic excitation spectra. They suggested that these anomalies were due to effects of the dynamical "stripes". But recent research carried out by Pintschovius *et al.* [2] has shown that there is no anomaly in the peak width and the dispersion curve of the phonon branch.

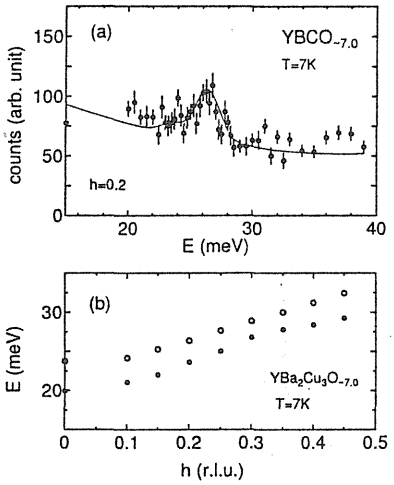


Figure 1: (a) Energy-scan profiles obtained for $YBa_2Cu_3O_{\sim 7}$ at Q=(3+h,0,0) are shown (h=0.2). Solid lines show the results of the fitting with two Gaussian lines. (b) The phonon energies of the $\langle B_{2u}/B_{3u}\rangle$ modes obtained by the fittings at T=7 K for $YBa_2Cu_3O_{\sim 7}$ are plotted against h.

In our previous study, we have measured similar in-plane phonons of $YBCO_y$ (y=6.5, 6.7 and ~7) with the energy of ~(18~34) meV which are assigned as B_{2u}/B_{3u} modes at Γ point. [3] Hereafter, we just call these branches B_{2u}/B_{3u} modes. The B_{2u} and B_{3u} modes vibrate along and perpendicular to the chain direction ($//b$), respectively, the B_{3u} mode has the significant amplitude of the chain oxygen motion. Figure 1(a) shows the phonon profile taken at T=7 K for the crystal with y ~7. We can see sharp and broad peaks in this figure. We have assigned a broad peak as B_{3u} mode. The broadening is considered to be the effect of the chain oxygen deficiency, because the broadening does not have significant temperature(T)-, Q- and y-dependences. As

原子炉：JRR-3　　装置：TAS-1(2G)　　分野：中性子散乱（超伝導）

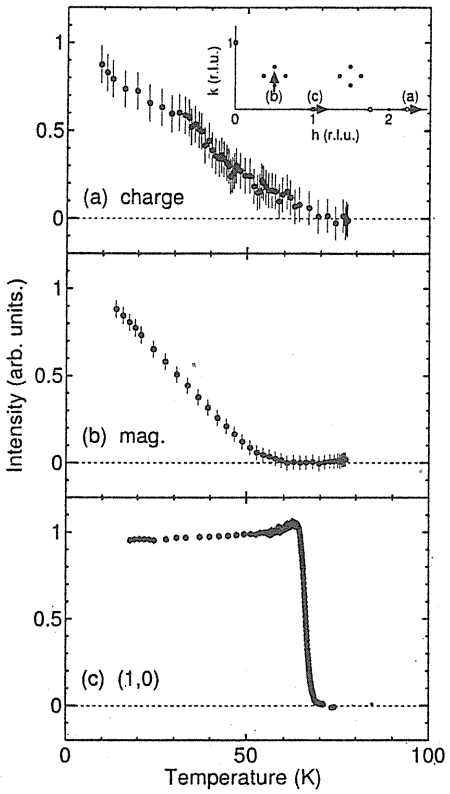


Figure 2: Temperature dependence of the peak intensities of the superlattice reflections. The data points (a) and (b) correspond to the reflections originating from the charge and magnetic ordering, respectively. The data (c) represent the reflections originating from the LTO1-LTO2 transition. In the inset of (a), the 2D reciprocal space is shown.

for the dispersion, smooth Q-dependence has been observed for all samples in the whole T-region studied here. These results are in a clear contrast to the results of Mook *et al.* [1)]

We have also adopted the $La_{1.48}Nd_{0.4}Sr_{0.12}CuO_4$ system. In Fig. 2, the T dependences of the superlattice reflection intensities originating from the structural transition and the "stripe" orderings are shown. Peaks are measured along the lines shown by arrows in the inset of Fig. 2(a). We can see that the superlattice peaks corresponding to the static "stripe" ordering begin to grow at ~69 K with decreasing T. The profiles of the bond stretching phonon,

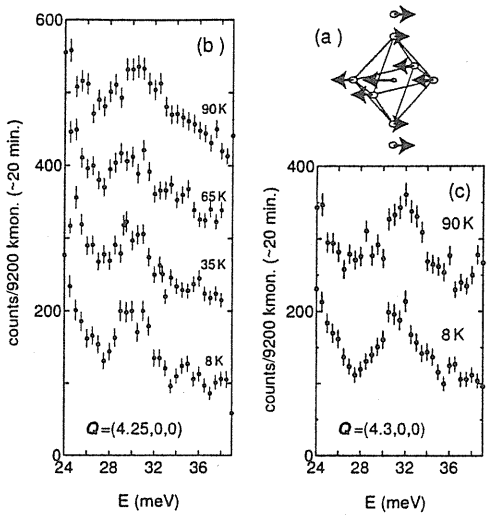


Figure 3: (a) The vibration pattern of the in-plane phonon for $La_{1.48}Nd_{0.4}Sr_{0.12}CuO_4$ at Γ point. Figures (b) and (c) show the energy-scan profiles obtained at h=0.25 and h=0.3, respectively.

whose vibration pattern at Γ point is shown in Fig. 3(a), were taken by using the triple axis spectrometer TAS-1 installed at JRR-3M of JAERI in Tokai.

The temperature dependence of the phonon profiles taken at Q=(4+h,0,0) with h=0.25 (~2δ) and 0.3 are shown in Figs. 3(b) and 3(c), respectively. We have not observed anomalous q-dependence of the peak width in the whole temperature range studied ($T \leq 90$ K). The dispersions were found to be smooth.

We have not found anomalous T-dependence of the widths of the phonon profiles at q=(0.25,0,0) and (0.3,0,0), either, on both systems of $YBCO_y$ and $La_{1.48}Nd_{0.4}Sr_{0.12}CuO_4$.

References

1) H. A. Mook and F. Dogan : Nature **401** (1999) 145.
2) L. Pintschovius, W. Reichardt, M. Klaser, T. Wolf, and H. v. Lohneysen : Phys. Rev. Lett. **89** (2002) 037001.
3) M. Ito, H. Harashina, Y. Yasui, M. Sato and K. Kakurai : Physica C **388-389** (2003) 363.

研究テーマ： 重い電子系の圧力誘起量子現象の研究
表題： 近藤格子系における磁気秩序の不安定性: 擬二元合金 $Ce(Ru_{0.90}Rh_{0.10})_2(Si_{1-y}Ge_y)_2$ の中性子回折実験

Instability of magnetic order in Kondo-lattice system: neutron diffraction study of the pseude-binary alloy system $Ce(Ru_{0.90}Rh_{0.10})_2(Si_{1-y}Ge_y)_2$

1-3-18

S. Kawarazaki[1], K. Watanabe[1], Y. Tabata[1], Y. Okita[1], H. Kadowaki[2] and Y. Uwatoko[3]
[1] *Graduate School of Science, Osaka University, Toyonaka, Osaka 560-0043*
[2] *Department of Physics, Tokyo Metroporitan University, Hachioji, Tokyo 192-0397*
[3] *Institute for Solid State Physics, The University of Tokyo, Kashiwa-shi, Chiba 277-8581*

The long-range magnetic order in the Kondo-lattice systems can be categorized into two regimes: the RKKY-regime and the quasi-particle band regime. In the RKKY-regime, the magnetic order is formed by reduced localized spins through the RKKY interaction, whereas, in the quasi-particle band regime, the spin density wave(SDW) is formed by nesting of the coherent quasi-particel bands. In order to serach for an evidence of an alternation between two regimes, we performed neutron diffraction experiments to the pseudo-binary alloy system $Ce(Ru_{0.90}Rh_{0.10})_2(Si_{1-y}Ge_y)_2$ in chemical and hydrostatic pressure[1]. The substitution of Ge for Si mainly plays a role of 'negative' pressure for the system. The experiments were carried out using the triple-axis spectrometer GPTAS at the JRR-3M reactor of the JAERI.

It is already known that the base material $Ce(Ru_{0.90}Rh_{0.10})_2Si_2$ undergoes a SDW transition at 4.8 K with the magnetic modulation vector $\boldsymbol{q} = (0\ 0\ q)$[2]. By substitution of Ge for Si, the transition temperature T_N and the amplitude of the magnetic modulation μ increase, as shown in Fig. 1. Especially, μ is enhanced almost twice when y is changed from 0 to 0.20. The manners of the y-dependence of T_N and μ change around $y = 0.08$, that is, T_N and μ increases rapidly with increasing y up to 0.08, while rather moderately for y greater than 0.08. The size of μ for $y = 0.2$ is about 1.6 μ_B, which is compatible with the full size of the moment of the ground doublet, that is 1.83 μ_B, deduced by Laceruda *et al* for $CeRu_2Si_2$[3]. Thus the magnetic order of the $y = 0.20$ compound will be in the RKKY-regime.

Fig. 2 shows the magnitude of the wave number q in $(0\ 0\ q)$ of the magnetic modulation for $y = 0$, 0.20 and 0.25 as functions of the hydrostatic pressure P. The most remarkable feature of this figure is that the q of the $y = 0$ compound is entirely unresponsive to P until the magnetic ordered state is collapsed at $P_C \approx 0.8$ GPa. The sensitivity of q to P is also very weak in the $y = 0.25$ compound. In contrast, the q for $y = 0.20$ increases with increasing P.

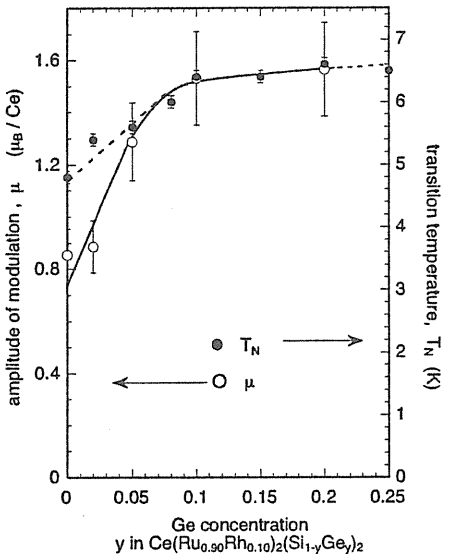


Fig. 1. The magnetic transition temperature and the amplitude of the magnetic modulation of the $Ce(Ru_{0.90}Rh_{0.10})_2(Si_{1-y}Ge_y)_2$ pseude-binary system. The solid and broken lines are guides to the eye.

The manners of pressure-dependence of the q for $y = 0$, 0.20 and 0.25 shown in Fig. 2 can be interpleted as follows. The wave vector of the magnetic modulation is determinded by the shapes and the nesting vector of the Fermi surfaces. The $y = 0$ compound belongs to the quasi-particle band regime. In

使用施設： JRR-3I　装置： 4G (GPTAS)， 分野： 3. Strongly Correlated Electron Systems

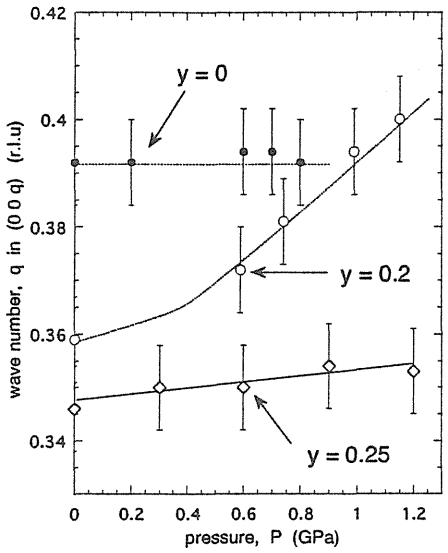


Fig. 2. Pressure dependence of the wave number, q, of the magnetic modulation in the $Ce(Ru_{0.90}Rh_{0.10})_2(Si_{1-y}Ge_y)_2$ systems for $y = 0$, 0.2 and 0.25.

this regime, the cf-coherence must have already grown up and be saturated, and hence the configuration of the Fermi surfaces are not changed by applying pressure. Therefore the magnetic wave vector never, or hardly, depends on the pressure in the quasi-paticle band regime. On the other hand, the $y = 0.25$ compound is considered to belong to the RKKY-regime. In this case, the wave vector of the magnetic modulation is determind by the static non-local susceptibility, $\chi_c(q)$, of the "bare" conduction electrons. When the compound has a strong localized f-electron nature, the pressure will give no significant growth of the cf-coherence and hence no significant change of the magnetic wave vector.

As a consequence of the above argument, we consider that the strong P-dependence of the q for $y = 0.20$ results from the change of the configuration of the Fermi surfaces due to the evolution of the cf-coherence. In Fig. 2, loosely speaking, the q of the $y = 0.20$ compound changes from that for $y = 0.25$ to that for $y = 0$ as increasing pressure. As a conclusion, we regard that we have observed the alternation of the scheme of the magnetic order between the RKKY-regime of the localized electrons and the quasi-particle band regime by applying pressure.

References

[1] K. Watanabe *et al.*: J. Phys. Soc. Jpn. in press
[2] Y. Miyako *et al.*: Physica B **230-232** 1011.
[3] A. Laceruda *etal.*: Phys. Rev. B **40** (1989) 295.

研究テーマ：多重極限環境下における中性子散乱実験法の研究
表　題：重い電子超伝導体 $PrOs_4Sb_{12}$ における磁場誘起四重極秩序

1-3-19

Magnetic-Field-Induced Quadrupolar Ordering in the Heavy-Fermion Superconductor $PrOs_4Sb_{12}$

M. KOHGI, K. IWASA, M. NAKAJIMA, N. METOKI[1], S. ARAKI[1], N. BERNHOEFT[2], H. SATO, Y. AOKI and H. SUGAWARA

Department of Physics, Tokyo Metropolitan University, Tokyo 192-0397
[1]Advanced Science Research Center, Japan Atomic Energy Research Institute, Ibaraki 319-1195
[2]DRFMC, SPSMS, CEA-Grenoble, 38054 Grenoble, France

$PrOs_4Sb_{12}$ is a filled-Skutterudite compound. It belongs to the space group $Im\bar{3}$ (T_h^5, #204). Maple et al. [1)] and Bauer et al. [2)] reported that the compound shows superconductivity below T_C = 1.85 K and electrons with a large effective mass of about 50 m_0 are responsible for the superconductivity from the value of specific heat jump at T_C. They suggested that the interaction of the quadrupole moments of Pr ions with conduction electrons is responsible for the heavy-fermion superconducting state in the material. Another interesting experimental fact is the appearance of a new phase found by specific heat and resistivity measurements under a magnetic field above approximately 5 T at low temperatures. [3)]

In order to clarify the nature of ordering in this field-induced ordered phase (FIOP), a neutron diffraction experiment on a single-crystal sample of this material was performed. A single-crystal sample of about 4 g was used in the experiment. It is actually an aggregate of smaller cubes of about 1 mm average size with sharing (100) crystal planes. The half-height width of rocking curves of the sample was about 1.1 degrees in the experimental condition described below. The neutron diffraction experiment was carried out on the cold neutron triple axes spectrometer LTAS at JAERI. A pyrolytic graphite (002) monochromator and analyzer were used with a neutron wave-vector of k = 1.5Å^{-1}. The collimation of the neutron beam was open-80'-80' in the beam paths between monochromator and sample, sample and analyzer, and analyzer and detector. A cooled Be filter was inserted before the sample to eliminate higher order contaminations from the monochromator. The sample was set in a dilution refrigerator, which is inserted into the center bore of the Helmholtz-type superconducting magnet, with its [001] direction vertical.

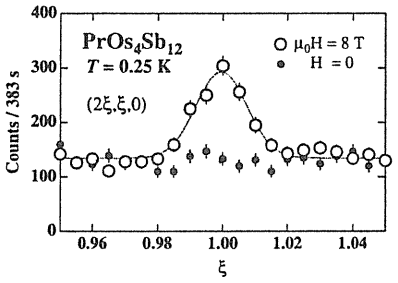


Figure 1: Scattering patterns of 210 superlattice reflection at 0.25 K with (8 T) and without magnetic field.

Scans in the reciprocal lattice plane (h,k,0) revealed resolution-limited peaks at superlattice positions characterized by the wave vectors q = [1, 0, 0] and [0,1,0] in the FIOP. Figure 1, for example, shows the observed 210 superlattice reflection at 0.25 K and 8 T together with the data at zero magnetic field. Figure 2 shows the magnetic field dependence of the peak intensity of the 210 superlattice reflection as well as that of 110 Bragg reflection where field-induced ferromagnetic Bragg scattering is superimposed. The 210 reflection starts to develop at about 5 T in accordance with the start of the FIOP at low tem-

原子炉：JRR-3　　装置：LTAS(C2-1)　　分野：中性子散乱（超伝導）

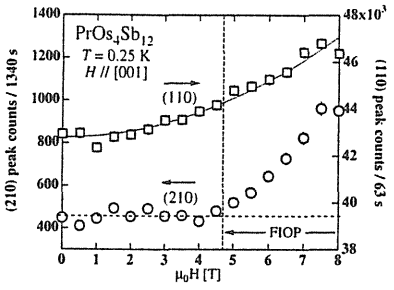


Figure 2: Magnetic field dependence of the peak intensities of the 210 and 110 reflections.

peratures. On the other hand, the intensity of the 110 reflection increases gradually with increasing field, indicating that the induced ferromagnetic moment is approximately proportional to the applied field. The superlattice peak intensities at 6 and 8 T decrease with increasing temperature, and disappear at the background level at about 0.8 and 1 K, respectively. These temperatures are also in accordance with the reported boundaries of the FIOP. Several superlattice reflections at 0.25 K and 8 T were measured in the (h,k,0) plane in order to see their origin. It was found that the integrated intensities of the observed peaks after correction of the dependence of magnetic form factor of Pr^{3+} are highly proportional to $\sin^2\alpha$ within experimental error where α is the angle between the scattering vector and the direction of the [010] axis. This fact clearly indicates that the observed superlattice reflections are due to magnetic Bragg scattering originating from antiferromagnetic moments on Pr ions parallel to the [010] direction. From the data, we can estimate the value of the antiferromagnetic moment μ_{AF} by comparing it with the integrated intensity of the 110 nuclear Bragg reflection measured at a zero magnetic field. The value of the induced ferromagnetic moment μ_F is also estimated from the integrated intensity of the field-induced component of 110 Bragg reflection. They are $\mu_{AF} = 0.025 \pm 0.006\mu_B$ and $\mu_F = 0.354 \pm 0.006\mu_B$, respectively, per Pr ion at 0.25 K and at 8 T. The antiferromagnetic component is only 8% of the induced ferromagnetic moment.

The present experimental result is reasonably explained by a model that the observed antiferromagnetic moment is due to the ordering of 4-f electron orbit such that the the magnetic field applied along the [001] direction (z-direction) gives rise to the induced magnetic moment whose component along the [010] direction (y-direction) changes sign from the corner site to the body center site of the *bcc* lattice. This type of ordering is actually realized by the ordering of the O_{yz}-type quadrupolar moment. This model is supported by the molecular field calculation based on the crystal field level scheme in which the ground state is the singlet Γ_1 and triplet $\Gamma_4^{(1)}$ is the first excited state at about 8 K [4]. The quadrupolar ordering is induced by the applied magnetic field due to formation of a pseudo-doublet by the Zeeman effect.

The present experiment revealed that there exists rather strong quadrupolar interaction than the magnetic interaction in $PrOs_4Sb_{12}$. This fact suggests that the unusual superconductivity in the compound may be mediated by the degrees of freedom of the quadrupolar moment in the system. A report of the present work has been published elsewhere [4].

References

1) M. B. Maple, P.-C. Ho, V. S. Zapf, N. A. Frederick, E. D. Bauer, W. M. Yuhasz, F. M. Woodward and J. W. Lynn: J. Phys. Soc. Jpn. **71** (2002) Suppl., 23.
2) E. D. Bauer, N. A. Frederick, P.-C. Ho, V. S. Zapf and M. B. Maple: Phys. Rev. B **65** (2002) 100506(R).
3) Y. Aoki, T. Namiki, S. Ohsaki, S.R. Saha, H. Sugawara and H. Sato: J. Phys. Soc. Jpn. **71** (2002) 2098.
4) M. Kohgi, K. Iwasa, M. Nakajima, N. Metoki[1], S. Araki[1], N. Bernhoeft[2],J.-M. Mignot., A. Gukasov, H. Sato, Y. Aoki and H. Sugawara: J. Phys. Soc. Jpn. **72** (2003) 1002.

研究テーマ： 重い電子系強磁性超伝導体 UGe_2 の 5f 電子状態
表題： UGe_2 のフォノンの分散関係

1-3-20 Phonon dispersion relations of UGe_2

H. Sagayama[1], K. Kuwahara[1], K. Iwasa[1], M. Kohgi[1],
T. D. Matsuda[2], E. Yamamoto[2], Y. Haga[2], Y. Ōnuki[2,3]

[1]*Department of physics, Tokyo Metropolitan University, Hachioji, Tokyo 192-0297, Japan*
[2]*Advanced Science Rserarch Center, Japan Atomic Energy Reseaech Institute, Tokai, Ibaraki, 319-1195, Japan*
[3]*Graduate School of Science Osaka University, Toyonaka, Osaka, 560-0043,Japan*

UGe_2 is the anisotropic ferromagnetic compound (T_{Curie} = 52 K at 0 GPa)[1]. This compound crystallizes in the base-centered orthorhombic structure (Cmmm)[2]. T_{Curie} decrease with applying pressure, and vanishes at ~1.6 GPa. Superconductivity appears below ~1 K in the pressure range 1~ 1.5 GPa where the ferromagnetic coexists[3].

The existence of an additional anomaly in several measurements such as the resistivity measurement in the ferromagnetic phase was seen at charactristic temperature called T* (30 K at 0 Gpa)[4]. The anomaly at T* is thought to be closely connected with the appearance of the superconductivity. A possible origin is proposed as a formation of a charge density wave (CDW)[5]. However, no direct evidence was found.

To clarify the origin of anomaly at T*, we have performed inelastic neutron scattering experiments and obtained the phonon dispersion relations in all three principal direction. The experiment has been done with the triple-axis spectrometer GPTAS (4G) installed at JRR-3M reactor, JAERI.

Representative phonon groups well below T* (~4K), near T* (~30K) and above T* (~ 60K) are illustrated in figure 1. In all energy loss scans measured, any notable temperature dependence is not seen except peak intensity decrease which is interpreted by Bose statistic. Figure 2 shows the obtained phonon dispersion relations along c* at 30 K. Any indication of a structural phase transition at T* is not found in the deta within the experimental precision.

References

[1] Y. Ōnuki*et al.*:J. Phys. Soc. Jpn. **61** (1992) 293-299.
[2] K. Oikawa*et al.*:J. Phys. Soc. Jpn. **65** (1996) 3229.
[3] S. S. Saxena*et al.*:Nature **406** (2000) 587.
[4] N. Tateiwa*et al.*:J. Phys.: Condens. Matter. **13** (2001) L17-L23.
[5] S. Watanabe*et al.*:J. Phys. Soc. Jpn. **71** (2002) 2489-2499.

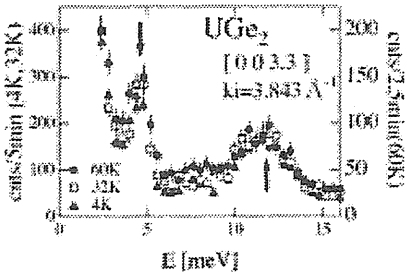


Fig. 1. Phonon groups observed below T* (~4K), near T* (~30K) and above T* (~ 60K) at Q = [0, 0, 3.3].

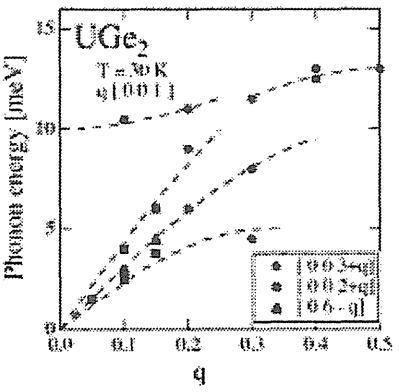


Fig. 2. Phonon dispersion relations along c* at ~30 K.

使用施設：JRR-3J　装置： GPTAS (4G)， 分野： 3. Strongly Correlated Electrons Systems

研究テーマ：MgB_2 中性子検出器の基礎実験と応用可能性の検討
表　題：MgB_2 中性子検出器の基礎実験と応用可能性の検討

1-3-21

Development of Neutron Detector by Using a Novel Metallic High-T_c Superconductor MgB_2

T. ISHIDA, K. TAKAHASHI, T. YOTSUYA[1], K. SATOH[1], A. SAITO[2], A. KAWAKAMI[2], H. SHIMAKAGE[2], Z. WANG[2], S. OKAYASU[3], K. HOJYOU[3], M. KATAGIRI[3], Y. MORII[3], AND N. NIIMURA[3]

Department of Physics and Electronics, Osaka Prefecture University, Sakai, Osaka, 599-8531
[1] Technology Research Institute of Osaka Prefecture 2-7-1 Ayumino, Izumi, Osaka 594-1157
[2] Kansai Advanced Research Center, Communications Research Laboratory, 588-2, Iwaoka-cho, Nishi-ku, Kobe, Hyogo 651-2429
[3] Japan Atomic Energy Research Institute, Tokai, Naka, Ibaraki 319-1195

[Introduction]

It is difficult to detect neutrons compared to charged particles. Neutrons are useful to investigate properties of the various substances. For example, the protein structure has been successfully determined by the diffraction experiment by using an imaging plate[2]. A BF_3 counter is widely used to detect neutrons. However, this counter requires a high voltage of 2000 V and is large in size to achieve a reasonable detection efficiency.

A novel metallic superconductor MgB_2 has a high-T_c of 40 K[1]. The ^{10}B has a huge cross section for the nuclear reaction of $^{10}B(n,\alpha)^7Li$. It reaches 3800 barns for thermal neutrons. We propose to develop a MgB_2 thin film detector with the aid of the nanofabrication technique of the electron beam lithography.

[Experiments and Results]

The MgB_2 thin films were prepared on an Al_2O_3 substrate (R-plane) by a multiple-target sputtering method[3]. This process is advantageous to make high quality devices because it requires neither a post-annealing process nor a high substrate temperature T_s. We fabricated six meandering pattern units on this film by using an electron beam lithograpy. Figure 1 is the drawing and the microscope photograph of the patterning. Since the range of α particles in the MgB_2 is on the order of 1μm, we chose the line width as 1μm. The nuclear reaction $^{10}B(n,\alpha)^7Li$ rate R_a of this MgB_2 film with neutrons is estimated as

$$R_a = \sigma I n dx, \qquad (1)$$

where σ is the cross section, $I \simeq 1 \times 10^7$ cm^{-2}s^{-1} is the beam intensity, $n = 1.38 \times 10^{22}$ cm^{-3} is the number of ^{10}B nuclides per volume, and $dx = 200$ nm is the thickness of the MgB_2 film. The cross section σ of our experiment is estimated 1.3×10^4 barns for the wave length of 6 Å. The neutrons intensity I of JRR−3M is about 1×10^7 cm^{-2}s^{-1}. We estimated R_a is 3.5×10^4 cm^{-2}s^{-1}. The total surface area of the one meandering patterns is $\sim 4.7 \times 10^{-3}$cm^2. Finally, we estimate that the nuclear reaction $^{10}B(n,\alpha)^7Li$ rate is 167 events per second.

Figure 2 is the $R-T$ curves of the two meandering patterns. The #1 patterning unit shows that $T_c^{onset} \simeq 14.8$K and $\Delta T = 0.6$K. The electric resistance in normal state is almost consistent with the value estimated from Ref. 3. We set a sample temperature in the transition regime.

Figure 3 is the schematic diagram of our detection system. The photographs in the left side are a sample holder of a 4-K refrigerator and a MgB_2 thin film. When neutrons react with ^{10}B in MgB_2, the reaction energy causes a partial destruction of superconductivity and a change in the resistivity. The slight variation of the voltage is amplified by a preamplifer and a linear amplifer. We searched a pulse signal caused by the nuclear reaction by a fast digital oscilloscope. The photographs in the

原子炉：JRR-3　　装置：LTAS(C2-1)　　分野：中性子散乱（超伝導）

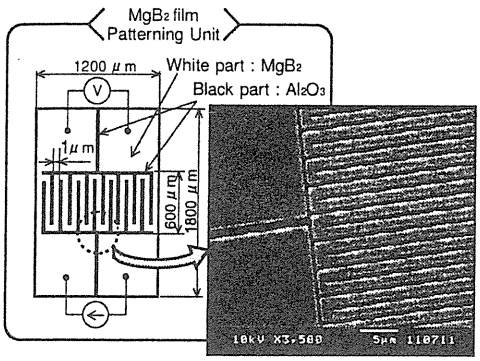


Figure 1: The shematic drawing (the MgB_2 films is the white part while substrate (Al_2O_3) is the black part) and the photograph of MgB_2 patterning unit. We measured electric resistance of meandering pattern by using the four terminal method.

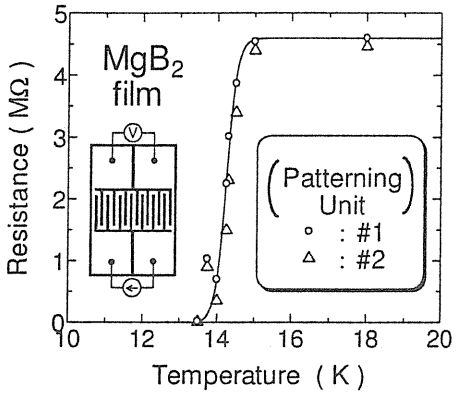


Figure 2: The $R-T$ curve of MgB_2 patterning unit. We can find T_c^{onset} is 14.8K. We performed the neutron irradiation experiment by maintaining the temperature at the trasition edge of the $R-T$ curve.

right side of Figure 3 show the examples of such pulse signals. However, we are not sure whether this comes from the nuclear reaction or from external noise signals.

[Conclusion]

We succeeded in fabricating the 1μm meandering patterns on MgB_2 thin film. This patterns showed a sharp resistive transition, which is suitable for neutrons detector. It is inclusive that the pulse signal observed by the digital oscilloscope is from the ^{10}B nuclear reactions. Further studies are necessary to complete the development of a novel neutron detector as one of the nanotechnology virtual laboratories of the JST-CREST projects.

The present work is partially supported by the REIMEI Research Resources of Japan Atomic Energy Research Institute.

References

1) J. Nagamatsu *et al.*, Nature **410** (2001) 63.
2) N. Niimura *et al.*, Nature Structural Biology, **4** (1997) 909-914.
3) A. Saito *et al.*, Supercond. Sci. Technol. **15** (2002) 1-5.

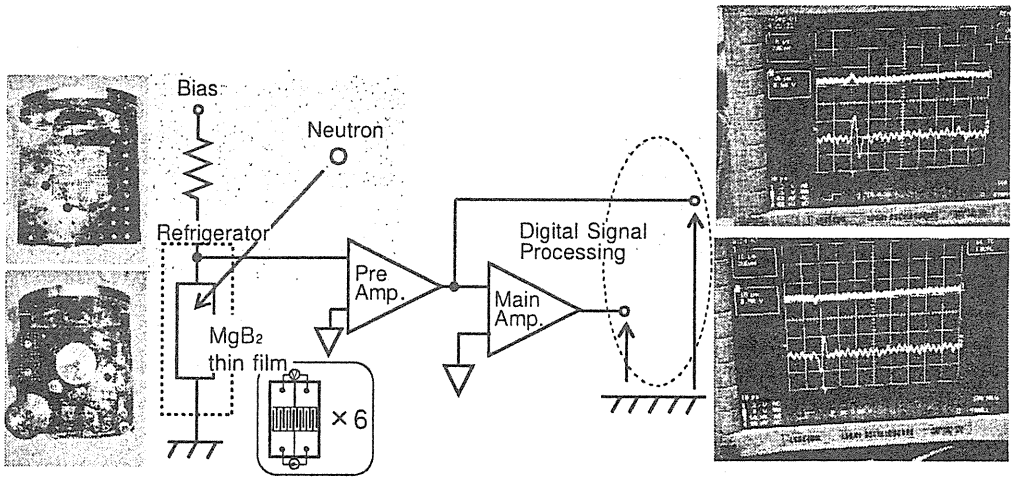


Figure 3: The schematic diagram of our neutron detection system. The left photographs are for the sample holder in 4K-refrigerator. A slight change in voltage due to the nuclear reaction of $^{10}B(n,\alpha)^7Li$ is amplified by a preamplifier and a linear amplifier. This signal is analyzed by a digital signal oscilloscope.

研究テーマ： 重い電子系強磁性超伝導体 UGe_2 の 5f 電子状態
表題： UGe_2 の異方的な格子歪み

1-3-22 Anisotropic lattice distortion of UGe_2

H. Sagayama[1], K. Kuwahara[1], K. Iwasa[1], M. Kohgi[1],
T. Osakabe[2], T. D. Matsuda[2], E. Yamamoto[2], Y. Haga[2], Y. Ōnuki[2,3]

[1]*Department of physics, Tokyo Metropolitan University, Hachioji, Tokyo 192-0297, Japan*
[2]*Advanced Science Rserarch Center, Japan Atomic Energy Reseaech Institute, Tokai, Ibaraki, 319-1195, Japan*
[3]*Graduate School of Science Osaka University, Toyonaka, Osaka, 560-0043,Japan*

UGe_2 is an anisotropic ferromagnetic compound (T_{Curie} = 52 K at 0 GPa). The easy axis is the a-axis in the base-centered orthorhombic structure (Cmmm)[1, 2]. T_{Curie} decreases with applying pressure, and vanishes at ∼1.6 GPa. Superconductivity appears below ∼1 K in the pressure range 1∼ 1.5 GPa in the ferromagnetic phase[3].

The existence of an additional anomaly in several measurements such as the resistivity measurement in the ferromagnetic phase was seen at charactristic temperature called T* (30 K at 0 Gpa)[4]. The anomaly is week at 0 GPa and becomes sharp under pressure down to about 1 GPa. The anomaly at T* is thought to be closely connected with the appearance of the superconductivity although the origin of anomalies at T* is not clear yet.

We have mesured the temperature dependence of lattice constants and spontaneous magnetic moment simultaneously at 0, 0.5, 0.8 and 1.2 GPa. The experiment has been done with the triple-axis spectrometer HQR(T1-1) installed at JRR-3M reactor, JAERI.

Figure 1 shows the relative temperature dependence of lattice constants along b-axis (db/b) and c-axis (dc/c) at 0, 0.5, 0.8 and 1.2 GPa. The db/b and dc/c are normalized at T_C. It is seen that the difference between db/b and dc/c becomes large suddenly at a temperature which is close to T*. The anisotropic lattice distotion and the enhancement of the magnetization occur almost simultaneously under high pressure. It is remarkable that this anisotropic lattice distotion is clearly seen ever at ambient pressure. This result reveals that a distinct transition occurs at T* in UGe_2.

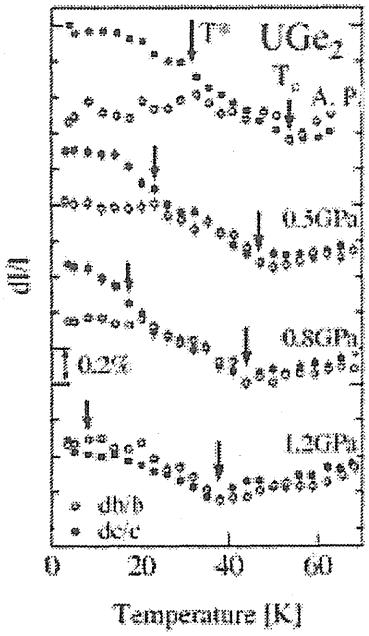


Fig. 1. Relative temperature dependence of lattice constants along b-axis (db/b) and c-axis (dc/c) at 0, 0.5, 0.8 and 1.2 GPa. db/b and dc/c are normalized at T_C.

References

[1] Y. Ōnuki *et al.* :J. Phys. Soc. Jpn. **61** (1992) 293-299.
[2] K. Oikawa *et al.* :J. Phys. Soc. Jpn. **65** (1996) 3229.
[3] S. S. Saxena *et al.* :Nature **406** (2000) 587.
[4] N. Tateiwa *et al.* :J. Phys.: Condens. Matter. **13** (2001) L17-L23.

使用施設：JRR-3　装置： HQR (T1-1)，分野： 3. Strongly Correlated Electrons Systems

研究テーマ：Ni置換した銅酸化物超伝導体LSCOにおける磁気励起の研究
表　題：Ni置換した$La_{2-x}Sr_xCuO_4$における磁気励起

1-3-23

Magnetic excitations in Ni-substituted $La_{2-x}Sr_xCuO_4$

H. HIRAKA, T. CHUREI[1], Y. ENDOH, K. YAMADA[1] and M. MATSUDA[2]

Institute for Materials Research, Tohoku University, Sendai 980-8577
[1]Institute for Chemical Research, Kyoto University, Uji 611-0011
[2]Advanced Science Research Center, JAERI, Tokai, Ibaraki 319-1195

Impurity doping of 3*d*-metal Zn or Ni upon high-T_c superconductors gives an invaluable information how magnetic spins concern the novel high-T_c superconductivity, because non-magnetic Zn^{2+} ($S = 0$) or magnetic Ni^{2+} ($S = 1$) directly substitutes for Cu^{2+} ($S = 1/2$) in CuO_2 planes. Although effects of Zn doping are intensively studied from experimental and theoretical aspects, there are few studies for Ni impurity, particularly through neutron scattering. Recently, Kimura *et al.* performed a systematic study on spin dynamics for Zn-substituted $La_{1.85}Sr_{0.15}CuO_4$. [1] They insist that Zn substitution induces an in-gap state and fills the spin gap structure of impurity-free system. [2] Therefore, it is also interesting to investigate how Ni impurity modifies the spin gap excitations.

We have grown a single crystal of $La_{1.85}Sr_{0.15}Cu_{0.98}Ni_{0.02}O_4$ by means of TSFZ techniques. After an annealing process under oxygen-gas flow, the onset T_c was determined to be 28 K with a somewhat broad transition. The neutron scattering experiments were carried out on thermal-neutron triple-axis spectrometers TAS-1 and TAS-2, and a cold-neutron triple-axis spectrometer HER at JRR-3M. The incident or final energy of thermal (cold) neutrons was fixed at 14.7 or 13.5 meV (5.0 meV). The sample with a total volume $v \simeq 1.7$ cc and an effective mosaic $\eta \simeq 40'$, was set in the tetragonal (h, k, 0) scattering plane.

In contrast to pure $La_{1.85}Sr_{0.15}CuO_4$, magnetic scattering below 3 meV is clearly observable in the Ni-doped compound even at well below T_c. Furthermore, Fig. 1 demonstrates that $\chi''(q_{IC}, \omega)$ strikingly increases at about 1 meV, associated with a sharpening of peak width as seen in κ in the inset. Substitution on Ni smears and fills the spin-gap structure like Zn does. However, judging from the less clear static component in the Ni-substituted system compared to Zn, [3] spin fluctuations are considered to slow down gradually around Ni in the wide space but never quench. This behavior seems to be consistent with the broad superconducting transition appeared in the shielding effect, if both T_c and spin-fluctuation energy vary locally in space with an intimate relation. The magnetic-impurity effects should be qualitatively different from non-magnetic Zn.

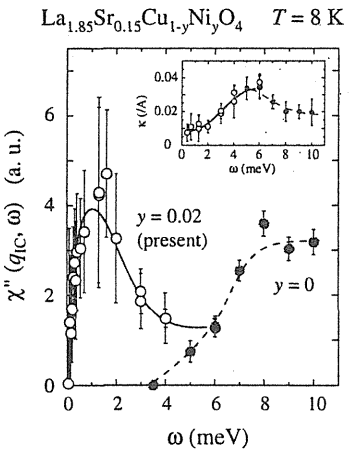


Figure 1: The dynamical susceptibility $\chi''(q_{IC}, \omega)$ and the inverse coherent length κ (inset) at 8 K. The open and solid circles represent data from Ni 2%-doped and Ni-free $La_{1.85}Sr_{0.15}CuO_4$ ($T_c = 38$ K) [2], respectively. The lines are drawn as a guide to the eyes.

References

1) H. Kimura *et al.*: cond-mat/0209428.
2) K. Yamada *et al.*: Phys. Rev. Lett. **75** (1995) 1626.
3) T. Churei *et al.*: submitted to Physica C (2003).

原子炉：JRR-3　　装置：TAS-1(2G), TAS-2(T2-4)　　分野：中性子散乱（超伝導）

研究テーマ： 重い電子系強磁性超伝導体 UGe_2 の 5f 電子状態
表題： UGe_2 のスピン揺らぎ

1-3-24 Spin fluctuations in UGe_2

H. Sagayama[1], K. Kuwahara[1], K. Iwasa[1], M. Kohgi[1], M. Nishi[2],
K. Nakajima[3], T. D. Matsuda[3], E. Yamamoto[3], Y. Haga[3], Y. Ōnuki[3,4]

[1]*Department of physics, Tokyo Metropolitan University, Hachioji, Tokyo 192-0297, Japan*
[2]*Insitute for Solid State Physics, University of Tokyo, Tokai, Ibaraki 319-1195, Japan*
[3]*Advanced Science Rserarch Center, Japan Atomic Energy Reseaech Institute, Tokai, Ibaraki, 319-1195, Japan*
[4]*Graduate School of Science Osaka University, Toyonaka, Osaka, 560-0043,Japan*

UGe_2 is the anisotropic ferromagnetic compound (T_{Curie} = 52 K at 0 GPa). The easy axis is the a-axis in the base-centered orthorhombic structure (Cmmm)[1, 2]. T_{Curie} decreases with applying pressure, and vanishes at ~1.6 GPa. Superconductivity appears below ~1 K in the pressure range 1~ 1.5 GPa in the ferromagnetic phase[3].

An unusual peak is seen in the temperature derivative of the resistivity curve at a charactristic temperature called T* (~30 K at 0 Gpa) in the ferromagnetic phase[4]. T* decrease with applying pressure, and vanishes at the critical pressure P* of about 1.2 GPa where the superconductiing temperature is highest[4]. Therefore the anomaly at T* is thought to be closely connected with the appearance of the superconductivity in UGe_2. The origin of anomaly at T* is not clear yet.

In our previous inelastic neutron scattering experiments with powder and single crystal samples, no well defined magnetic excitation such as spin wave or crystal field excitation was seen in the energy spectra in low temperatures. On the other hand, critical scattering like responses have been detected in a wide temperature range around T_C. To investigate this magnetic response in UGe_2, an inelastic neutron scattering experiment was performed with a sigle clystal sample.

The experiment has been done with the triple-axis spectrometer PONTA (5G) installed at JRR-3M reactor, JAERI. An incident neutron beam with ki = 2.67$Å^{-1}$ produced by the PG monochromater was used in the experiment.

Figure 1 shows the temperature variation of scattering intensities observed at fixed transfer energy (E = 2 meV) with different scattering vector Q parallel to c*. Bose factor is already corrected in the figure. The data show that spin fluctuations grow rapidly with increasing temperature above T*. This result suggests that the strong spin fluctuations observed in the temperature range between T* and T_{Curie} is closely connected with the appearance of the superconductivity in UGe_2.

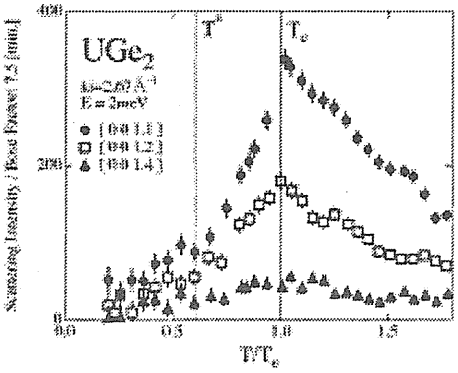


Fig. 1. Temperature evolusion of scattering intensities at 2 meV and difference Q potisions. Bose factor is already corrected in the figure.

References

[1] Y. Ōnuki*et al.* :J. Phys. Soc. Jpn. **61** (1992) 293-299.
[2] K. Oikawa*et al.* :J. Phys. Soc. Jpn. **65** (1996) 3229.
[3] S. S. Saxena*et al.* :Nature **406** (2000) 587.
[4] N. Tateiwa*et al.*:J. Phys.: Condens. Matter. **13** (2001) L17-L23.

使用施設：JRR-3　装置： PONTA (5G)，分野： 3. Strongly Correlated Electrons Systems

研究テーマ：電子ドープ型高温超伝導体 $Pr_{1-x}LaCe_xCuO_{4+y}$ のスピン揺動と超伝導の相関
表　題：電子ドープ型高温超伝導体 $Pr_{1-x}LaCe_xCuO_{4+y}$ のスピン相関に関する中性子散乱研究

1-3-25

Neutron scattering study of spin correlations in electron-doped $Pr_{0.89}LaCe_{0.11}CuO_{4+\delta}$ single crystals

M.FUJITA[1], S.KUROSHIMA[1], T.UEFUJI, M.MATSUDA[2], K.KAKURAI[2] and K.YAMADA[1]

[1]Institute for Chemical Research, Kyoto university, Uji 611-0011
[2]Advanced Science Research Center, JAERI, Tokai, Ibaraki 319-1195

Mechanism of high-T_c superconductivity mediated by spin fluctuations is one of the central topics in highly correlated electron systems. Studies of spin correlations in the hole-doped high-T_c cuprates such as $La_{2-x}Sr_xCuO_4$ (LSCO) have intensively been carried out by neutron scattering experiments, and show an intimate relation between incommensurate spin correlations and superconductivity.[1)] However, comprehensive study on the electron-doped system is lacking due to the difficulties in growing single crystal and post-anneal treatment for inducing superconductivity.

Quite recently, neutron-scattering study on the electron-doped $Nd_{1.85}Ce_{0.15}CuO_4$ (NCCO) first revealed that *commensurate* spin fluctuations exist in the superconducting (SC) phase as seen in the antiferromagnetic (AF) phase.[2)] This is crucial result for understanding the common role of the spin correlations for the mechanism of high-T_c superconductivity irrespective of carrier type. However, to investigate the universal nature in the electron-doped system further study using other electron-doped cuprates is important. Especially sample with negligible effects from large rare-earth moment is highly required since such as Nd^{3+} moment would impede the detailed study of inherent nature of Cu^{2+} spins that will play important role for superconductivity.

We therefore performed systematic susceptibility and neutron scattering measurements on the $Pr_{0.89}LaCe_{0.11}CuO_{4+\delta}$ (PLCCO) system in which the effect of rare-earth moment is much reduced compared with that in NCCO.[3)] By controlling the relative oxygen contents per unit formula δ during the annealed procedure, we study the change in the static and dynamical spin correlations and in the superconducting property in the PLCCO system. Note that as-grown sample is assumed to be stoichiometric (δ=0) and the values for annealed sample were determined by measuring the weight loss of the sample after the heat treatment. Neutron-scattering measurements were carried out at thermal neutron triple-axis spectrometers, TAS-1 and TAS-2.

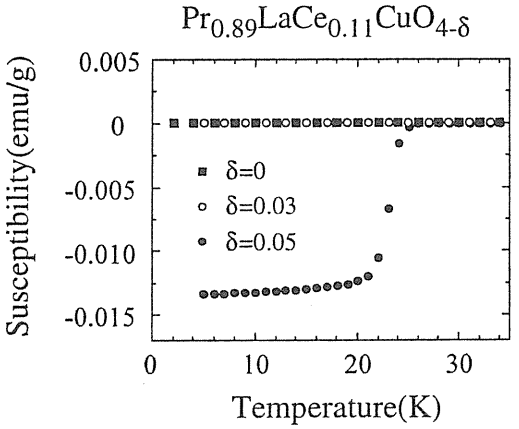


Figure 1: Magnetic susceptibility measured at 10 Oe for single crystal samples of $Pr_{0.89}LaCe_{0.11}CuO_{4+\delta}$ with (a) δ=0, (b) 0.03 and (c) 0.05 after the zero-field-cooling process.

Figure 1 shows magnetic susceptibility for x=0.11 samples with different δ. The as-grown (δ=0) and slightly oxygen-reduced (δ=0.03) samples do not show the superconductivity. However, in the sample with δ=0.05, bulk superconductivity appears at the onset temperature of 25.5 K. These results clearly demonstrate that there exists a critical value of oxygen loss, δ_c, for the appearance of

原子炉：JRR-3　　装置：TAS-1(2G), TAS-2(T2-4)　　分野：中性子散乱（超伝導）

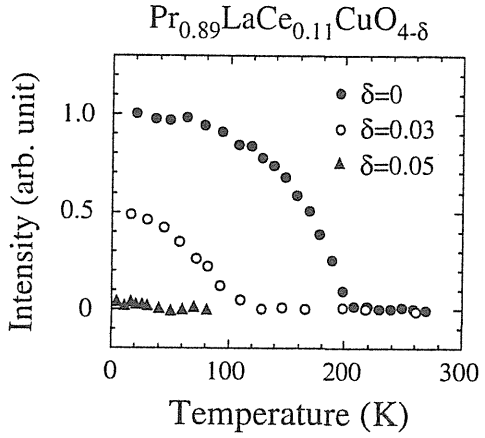


Figure 2: Temperature dependence of volume corrected peak intensity of (1 2 0) magnetic Bragg position measured for $Pr_{0.89}LaCe_{0.11}CuO_{4+\delta}$ with δ=0, 0.03 and 0.05.

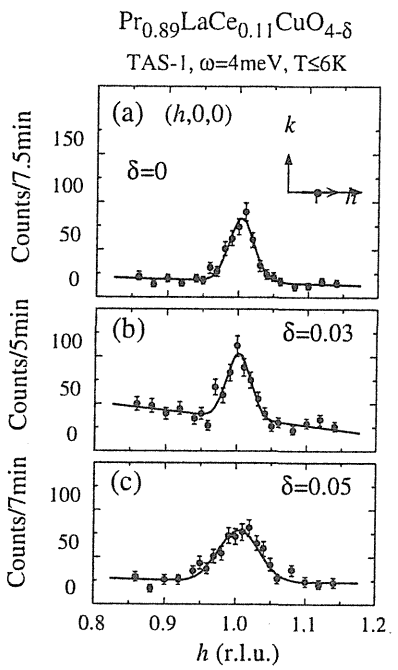


Figure 3: Constant-energy profiles at ω=4meV though (1 0 0) AF zone center for $Pr_{0.89}LaCe_{0.11}CuO_{4+\delta}$ with (a) δ=0, (b) 0.03 and (c) 0.05. Scan trajectory is shown in the upper panel. Solid lines are results fitted with a single Gaussian function by convoluting the experimental resolution.

superconductivity in the sample with a given Ce concentration.

We next investigated the magnetic properties in these samples. Temperature dependence of magnetic peak intensity at orthorhombic (1 2 0) reciprocal position are shown in Fig. 2. Intensities for three samples are measured under the identical experimental setups and normalized by the effective sample volume after subtracting the background. Comparing to the results for δ=0 and 0.03, it is obvious that both peak-intensity and T_N decreases with increasing δ. No clear evidence of magnetic order was observed in the superconducting sample with δ=0.05. Therefore, the AF order is degraded by the oxygen-reduction with decreasing ordered moment and/or region and T_N with increasing δ. Upon further oxygen-reduction, SC phase concomitantly appears with the disappearance of AF phase, suggesting the competitive relation between superconductivity and magnetic order.

On the other hand, spin fluctuations were observed even in the SC sample. Therefore, well-correlated spin fluctuations exist in the SC phase irrespective of the types of doped carrier, supporting a common role of the spin fluctuations for the high-T_c superconductivity. However, commensurate spin fluctuations observed in both AF and SC phases are contrastive to the incommensurate ones in the hole-doped LSCO system in which the spin density modulation changes from being diagonal to parallel to the Cu-O bond direction on crossing the insulator-superconductor phase boundary.[4)]

These similarities and differences in the spin correlation between the electron- and hole-doped system would provide important clues for understanding common mechanism of the high-T_c superconductivity.

References

1) K. Yamada *et al.* : Phys. Rev. B. **57** (1998) 6165.
2) K. Yamada *et al.* : Phys. Rev. Lett. **90** (2003) 137004.
3) M. Fujita *et al.* : Phys. Rev. B. **67** (2003) 014514.
4) M. Fujita *et al.* : Phys. Rev. B. **65** (2002) 064505.

研究テーマ： 重い電子系化合物 URu_2Si_2 の磁気形状因子
表題： 重い電子系化合物 URu_2Si_2 の磁気形状因子

1-3-26 Magnetic Form Factor in the Heavy-Electron System URu_2Si_2

K. Kuwahara[1], H. Sagayama[1], M. Kohgi[1], M. Nishi[2], K. Nakajima[2] and H. Amitsuka[3]
[1] *Department of Physics, Tokyo Metropolitan University, Tokyo 192-0397*
[2] *Institute for Solid State Physics, The University of Tokyo, 106-1 Shirakata, Tokai, 319-1106*
[3] *Graduate School of Science, Hokkaido University, Sapporo 090-0810*

The tetragonal heavy-electron compound URu_2Si_2 undergoes two successive phase transitions; a puzzling phase transition at $T_o = 17.5$ K and a superconducting transition at $T_C = \sim 1$ K. To study the electronic state of 5f electrons of this compound, we have measured the magnetic form factor of the induced moment in the paramagnetic state with polarized neutrons.

A single crystal of URu_2Si_2 was grown in a tetra-arc furnace using the Czochralski pulling method. It was cut into rectangular parallelepiped with the longest axis oriented to the c-axis ($1.0 \times \sim 3.0 \times 7.5$ mm^3). The polarized neutron experiment has been done using the triple axis spectrometer PONTA (5G) installed in the research reactor JRR-3M, Tokai. The sample was set inside a superconducting magnet with the c-axis vertical to the $(hk0)$ scattering plane. Polarized neutrons of wavelength $\lambda = 1.01$Å were produced by a Heusler alloy monochromator and a set of collimator OPEN-80'-80'-OPEN (2-axis mode) was used. Form factor measurements were performed in the paramagnetic state at $T = 60$ K in an applied magnetic field of 6 T along the c-axis.

Figure 1 shows the magnetic amplitudes μf of URu_2Si_2 as a function of $\sin\theta/\lambda$, where μ is the magnetic moment of 5f electrons and f is the 5f form factor. The results are analyzed by the following formula,

$$\mu f(Q) = \mu\left[\langle j_0\rangle + C_2\langle j_2\rangle\right], \qquad (1)$$

where C_2 is constant and $\langle j_n\rangle$ are averages of spherical Bessel functions over the uranium ion spin density. In this so-called dipole approximation, the values of C_2 are 1.75 and 1.50 for free U^{3+} and U^{4+} ions, respectively. We have fit the magnetic amplitudes μf calculated by Eq. (1) to the observed μf, where μ and C_2 are the fitting parameters. The solid and dashed lines in Fig. 1 are the theoretical fits for U^{3+} and U^{4+} ions respectively. The obtained fitting parameters are given in Table 1. The observed magnetic form factor is close to the free ion value as other U-based intermetallic compounds. On the other hand, it should be noted that the obtained magnetic moment μ is smaller than the value of the bulk magnetization ($1.0\mu_B$/U). This may be due to the extinction effect. To check this extinction effect, neutron experiments using smaller sample are planned.

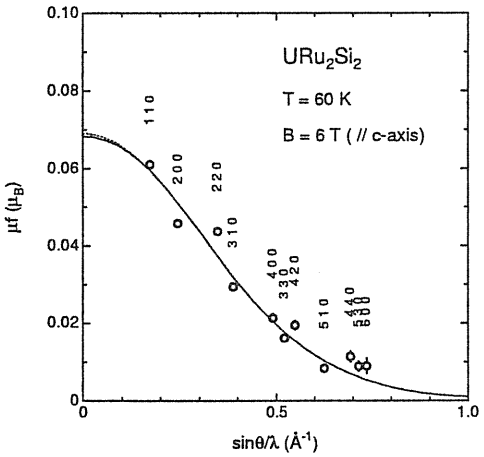


Fig. 1. The magnetic amplitudes μf as a function of $\frac{\sin\theta}{\lambda}$ for URu_2Si_2 at $T = 60$ K and $B = 6$ T ($\parallel$ c-axis). The solid and dashed lines are the theoretical fits for U^{3+} and U^{4+} ions respectively.

Table 1. The magnetic moments μ and the coefficients C_2 of Eq. (1) determined by the fitting in Fig. 1.

configuration	μ (μ_B)	C_2
U^{3+} ($5f^3$)	0.068 ± 0.001	1.90 ± 0.06
U^{4+} ($5f^2$)	0.069 ± 0.001	1.71 ± 0.05

使用施設：JRR-3 装置： PONTA(5G)， 分野： 3. Strongly Correlated Electron Systems

研究テーマ：単層 BISCO におけるスピン相関
表　題：単層ビスマス系銅酸化物における磁気揺動の探索

1-3-27

Search for Antiferromagnetic Fluctuations in Bismuth-Based Superconductors

N. Kaneko, M. Matsuda[1], K. Kakurai[1], and M. Greven

Laboratory for Advanced Materials, Stanford University, Stanford CA 94305, USA
[1]Advanced Science Research Center, JAERI, Tokai, Ibaraki 319-1195, Japan

It is widely believed that antiferromagnetic fluctuations play an important role in the physics of high-temperature superconductivity. The undoped parent compounds, such as La_2CuO_4, are antiferromagnetic insulators. Upon doping the CuO_2 sheets with a few percent of holes, these materials become metallic and superconducting, with "strange" metallic behavior in the normal state. Neutron scattering studies have demonstrated that dynamic antiferromagnetic correlations are a robust feature of both superconducting and normal states[1-6].

$La_{2-x}Sr_xCuO_4$ (LSCO) has been the only single-layer hole-doped high-temperature superconductor that has been studied systematically via neutron scattering, since it is relatively straightforward to grow the required large single crystals. Detailed studies have revealed many interesting properties, such as an incommensurate magnetic response[1,2,7,8]. The only other high-Tc family of materials for which sizeable crystals over a wide range of hole-doping have been available for neutron scattering studies is the structurally more complicated bi-layer system $YBa_2Cu_3O_{6+\delta}$ (YBCO)[3-6,9] The magnetic response of YBCO appears to be rather different from that of LSCO. In particular, it was found that the magnetic response is gapped and incommensurate only at high energies, and that there exists a magnetic resonance (at 41meV for optimally doped YBCO) in the superconducting state.

To better understand the connection between antiferromagnetic correlations and high-temperature superconductivity, it will be necessary to study additional materials. Neutron scattering experiments require sizeable samples, a fact that has presented a significant obstacle toward this end. We have succeeded with the growth of sizeable crystals of the single-layer and double-layer Bi-based superconductor $Bi_{2-y}Pb_ySr_{2-x}La_xCuO_{6+\delta}$ (Bi2201). The sample shown in Fig. 1 consists of 6 co-aligned single crystals with total volume of 1.1 cm^3. Initial crystal checks demonstrated the single-grain nature of the individual crystals. Small pieces from these crystals show excellent superconducting properties, with an onset of $T_c \sim 36$ K, which compares well with the highest values achieved in LSCO.

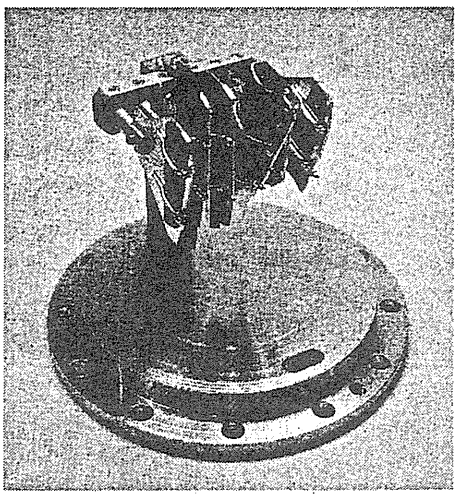


Figure 1: A set of $Bi_{1.7}Pb_{0.3}Sr_{1.6}La_{0.4}CuO_{6+\delta}$ crystals mounted on a sample holder in the (H0L) zone.

In light of the differences observed for LSCO and YBCO, a study of the magnetic response of Bi2201 should yield valuable new information about the connection between superconductivity and antiferromagnetic order and fluctuations. We have continued to pursue neutron scattering measurements to search

原子炉：JRR-3　　装置：TAS-1(2G), TAS-2(T2-4)　　分野：中性子散乱（超伝導）

for antiferromagnetic fluctuations in Bi2201. Specifically, we carried out inelastic neutron scattering measurements on the TAS-1 and TAS-2 triple-axis instruments at the JAERI JRR-3M research reactor. Previously we had conducted measurements in the (HK0) scattering plane in the range 3-12 meV. Our most recent measurements extended the search of inelastic magnetic features to the (H0L) zone and examined energy transfers up to 30 meV. Consistent with our previous results, these measurements reveal no obvious features. A possible (incommensurate) low-energy magnetic response may be harder to discern, perhaps because it is intrinsically broader than in LSCO. We note, that the experiment is made difficult by the fact that the scattering in Bi2201 results in a very high "background," in large part due to significant low-energy phonon scattering, a result of the complex crystal structure of Bi2201.

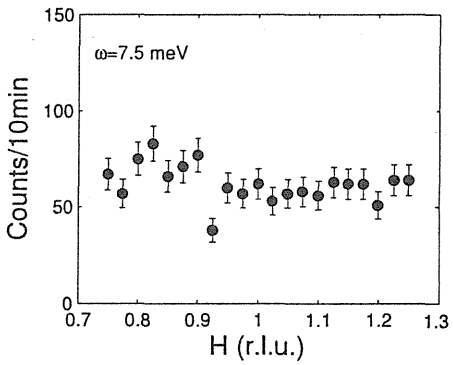


Figure 2: Data taken around (1,0,3.5) for Bi-2201 at an energy transfer of 7.5 meV just above the superconducting transition at T=40 K. The spectrometer configuration is Open-Sapphire-80-S-PG-80-80, E_f=14.7 meV.

In optimizing the crystal growth, it was very helpful to aim for a sample composition that resulted in the highest possible superconducting transition temperature and in very sharp transition widths. On the other hand, underdoped Bi2201 should exhibit more prominent antiferromagnetic fluctuations. While it has not been possible so far to obtain single crystals at half-filling (i.e., undoped CuO_2 sheets), we have managed to grow samples that are very underdoped and non-superconducting. Our goal for the near future is to continue our search for antiferromagnetic correlations in underdoped Bi2201.

References

1) M.A. Kastner, R.J. Birgeneau, G. Shirane and Y. Endoh, Rev. Mod. Phys. **70**, 897 (1998).
2) G. Aeppli *et al.*, Physica C **318**, 9 (1999).
3) H.F. Fong *et al.*, Phys. Rev. Lett. **78**,713 (1997).
4) H.F. Fong *et al.*, Phys. Rev. B **61**, 14773 (2000).
5) M. Arai *et al.*, Phys. Rev. B **83**, 608 (1999).
6) Y. Sidis *et al.*, Science **288**, 1234 (2000).
7) H. Kimura *et al.*, Phys. Rev. B **59**, 6517 (1999).
8) M. Matsuda *et al.*, Phys. Rev. B **65**, 134515 (2002).
9) P. Dai *et al.*, Phys. Rev. B **63**, 054525 (2001).

研究テーマ： URu_2Si_2における隠れた秩序と反強磁性の競合状態
表題：URu_2Si_2における隠れた秩序と反強磁性の競合状態

1-3-28 Competition between Hidden Order and Antiferromagnetism in URu_2Si_2

H. Amitsuka, M. Yokoyama, S. Itoh, S. Kawarazaki[1], and H. Yoshizawa[2]

Graduate School of Science, Hokkaido University, Sapporo 060-0810, Japan
[1]Graduate School of Science, Osaka University, Toyonaka 560-0043, Japan
[2]Institute for Solid State Physics, The University of Tokyo, Tokai 319-1106, Japan

Since the discovery of the coexistence between weak antiferromagnetism (WAF) and non-BCS-type superconductivity in UPt_3 and URu_2Si_2, the nature of small moments and their role playing in the normal and superconducting properties of heavy-electron systems have been intensively investigated. Our recent microscopic studies performed under hydrostatic pressure (P), however, strongly suggest that the WAF of URu_2Si_2 is not ascribed to the small moments but results from inhomogeneous antiferromagnetic (AF) order. First, neutron scattering (NS) measurements revealed that the AF Bragg-scattering intensity I_{AF} is enlarged with P by hundred times, which corresponds to an increase of the staggered moment μ_{ord} from ~ 0.02 μ_B/U (P ~ 0) to ~ 0.25 μ_B/U (P ~ 1 GPa) if the order is assumed to be uniform [1]. In parallel, ^{29}Si-NMR measurements showed that the central (paramagnetic) line is 'partially' split into two symmetrically located lines below the transition temperature T_o = 17.5 K, where the P-variable quantity was found not to be the resonant frequency but to be the intensity of the satellite lines [2]. The P evolution of I_{AF} is thus ascribed to an unusual P variation of the AF volume fraction $v_{AF}(P)$. Simple extrapolation using previous NS data may give the estimation, v_{AF} (P = 0) = $(\mu_{ord}/\mu_{AF})^2$ ~ 0.5 - 2.5 %, where the 'true' size of the staggered moment μ_{AF} is chosen as ~ 0.25 μ_B/U.

To understand the nature of this unusual two-phase competition, we studied the effects of uniaxial stress (σ) on the AF phase by performing NS measurements on the triple axis spectrometer GPTAS (4G) installed in JRR-3M in JAERI (Tokai) [3]. We observed that the AF phase is strongly induced by applying σ along the tetragonal basal plane. In the basal plane, on the other hand, there is no significant anisotropy. These experimental facts imply that the symmetry invariant strains are relevant to the AF evolution. From the detailed analyses based on the elastic response of this system, we found that the v_{AF} data obtained for the different types of stress are scaled not by the crystal volume but by the c/a ratio (Fig. 1). This strongly suggests that the axial type of magneto-elastic coupling plays an essential role in the first order phase transition between the hidden order and the AF state.

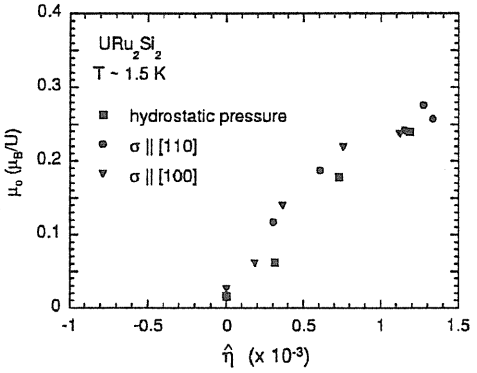


Fig. 1. The spatially averaged AF moment of URu_2Si_2 plotted as a function of the axial component of lattice distortion (c/a).

References

[1] H. Amitsuka et al., Phys. Rev. Lett. 83 (1999) 5114; J. Phys. Soc. Jpn. 69 (2000) suppl. A. 5.
[2] K. Matsuda et al., Phys. Rev. Lett. 87 (2001) 87203; Physica B 312-313 (2002) 504.
[3] M. Yokoyama et al., J. Phys. Soc. Jpn. 71 (2002) Suppl. 264; Ph.D. Thesis, Hokkaido Univ., 2003.

使用施設：JRR-3　装置：GPTAS(4G)，分野 3. Strongly Correlated Electron Systems

1. 中性子散乱 4)非晶質・液体

1. Neutron Scattering 4) Amorphous・Liquid

This is a blank page.

研究テーマ： 液体ヒ素-テルル混合系のネットワーク構造変化
表題： 液体 As-Te 混合系の半導体－金属転移点近傍における構造変化

Structural Changes in Liquid As-Te Mixtures around Semiconductor-Metal Transition

1-4-1

K. Maruyama[1], and T. Shibuya[2]
[1] *Faculty of Science, Niigata University, Niigata 950-2181*
[2] *Graduate School of Science and Technology, Niigata University, Niigata 950-2181*

Liquid As-Te mixtures show the semiconductor to metal transition with increasing temperature. Recent EXAFS[1] and neutron diffraction[2] studies reveals that the network structure of threefold coordinated As and twofold coordinated Te atoms is transformed into the twofold chain structure in the high temperature (metallic) region. In this region, the two structural configurations with different inter-chain distance coexist[3] and the occurrence of the fluctuation of the interchain correlation is expected. Hence the structural investigation over the scale of ten ångstroms is important. In order to study this structural change, we have performed the neutron scattering measurements for liquid $As_{40}Te_{60}$ by using HERMES spectrometer equipped at JRR-3M in JAERI Tokai.

The measurements have been performed with the usual procedure. The scattering intensity was accumulated for about ten hours for each sample and each temperature. After the correction of absorption, scattering from the silica cell and multiple scattering and after the normalization of the efficient of detectors, the structure factor $S(Q)$ for liquid As–Te mixtures was derived as shown in Fig. 1 with previous data. The obtained $S(Q)$ has enough accuracy for investigation especially in low Q region ($Q < 4\text{Å}^{-1}$).

It is notable that a small but clear prepeak at about Q =1.5Å^{-1} appears in the $S(Q)$ at melting point. The peak strength decreases with increasing temperature. With increasing As concentration, the position of the prepeak shifts toward low Q area. The appearance of the prepeak and its behavior is consistent with the model of structure change[1].

It is notable that at higher temperature another prepeak appears in very low Q region ($Q \sim 0.5\text{Å}^{-1}$), which suggests the creation of the large scale fluctuation caused by the structural transition. As the result, the HERMES spectrometer is very useful for the structural study of the liquid having intermediate range correlation.

In order to investigate the relation between the metal-non metal transition and the structural change, the analysis of $g(r)$ by using computer modeling is planned.

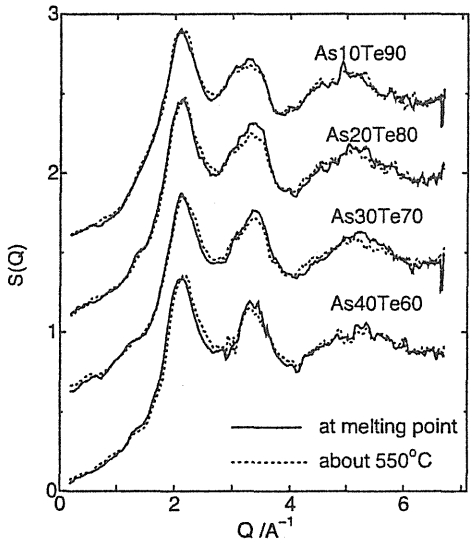


Fig. 1. The structure factor $S(Q)$ for liquid $As_{10}Te_{90}$, $As_{20}Te_{80}$, $As_{30}Te_{70}$ and $As_{40}Te_{60}$ at just above the melting point (solid lines) and at about 550 °C (dotted lines).

References

[1] H. Endo.*et al.*: J. Phys.: Condens. Matter **12** (2000)6077.
[2] K. Maruyama*et al.*:J. Non-Cryst. Solids **312-314** (2002)356.
[3] H. Endo*et al.*: Z. Phys. Chem. (2003) in print.

使用施設：JRR-3　装置： T1-3 (HERMES)，分野： 4. Glasses & Liquids

研究テーマ： 上部及び下部臨界温度を持つ混合液体の動的構造
表題： 閉環2相領域を持つ混合液体の準弾性散乱

Quasi Elastic Neutron Scattering Measurements on the Liquid Mixture Having Closed Two Phase Region

1-4-2

K. Maruyama[1], and S. Kawase[2]
[1] *Faculty of Science, Niigata University, Niigata 950-2181*
[2] *Faculty of Medicine, Niigata University, Niigata 951-8518, Japan*

The mixture of glycerol and guaiacol (*o*-methoxy phenol $C_6H_4OHOCH_3$) has a closed two phase region in its concentration-temperature phase diagram and has lower and higher critical points at 45°C and about 35 mol % guaiacol, and at 81°C and about 40 mol % guaiacol, respectively. The existence of the lower critical point is peculiar phenomenon according to the usual thermodynamic rules.

Recently we have measured the thermodynamic quantities, such as the Gibbs free energy of mixing, by using Rayleigh-Brillouin scattering measurements. Those studies shown the very small entropy of mixing compared to the ideal mixing in lower temperature region, which suggests the formation of clusters of glycerol or guaiacol molecules.

In order to confirm the existence of the clusters, we have performed quasi elastic neutron scattering measurements of the glycerol-guaiacol mixtures by using AGNES spectrometer equipped at JRR-3M in JAERI Tokai. Our previous data shows that the difusion constant is reduced for the mixtures of phase-separating composition. This result supports the existense of the clusters. In order to separate the motion of two constituents, we have measured the inelastic neutron scttering of glycerol-d8 and guaiacol mixtures. The measurements were carried out in the higher and lower one phase region, at 30 °C and 85°C, respectively, for samples with the composition of 35, 45 and 65 mol% guaiacol. The used sample cell was an aluminum double cylindrical cell with 0.5mm spacing to avoid multiple scattering by hydrogen atoms.

Figure 1 shows the obtained quasielastic scattering intensity as a function of the energy transfer. The width of the quasi elastic peak at higher temperature is wider than that at lower temperature, which means slower motion of molecules in lower temperature region. From the Q dependence of peak width, the diffusion constant d was derived. For the samples with the phase separation compositions, the d has low value compared to other samples. These results are consistent with the cluster formation.

We are now analysing the molecular motion separately for each constituent with previous data.

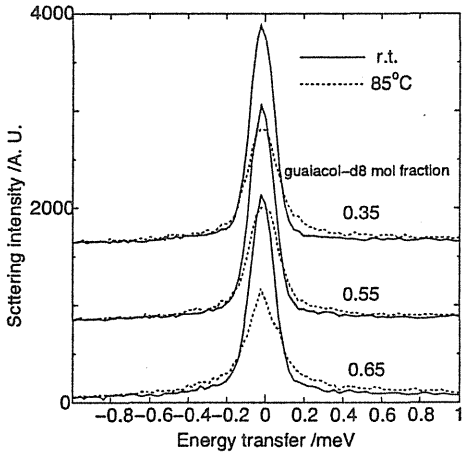


Fig. 1. The obtained quasielastic scattering intensity for glycerol-d8 and guaiacol mixtures as a function of the energy transfer.

使用施設：JRR-3　装置： C3-1-1 (AGNES)，分野： 4. Glasses & Liquids

研究テーマ:水-プロパノール系における分子相関
表題:水-プロパノール溶液の分子レベル構造

1-4-3 Molecular-level structure of 1-propanol aqueous solution

T. Sato and M. Misawa

Department of Chemistry, Faculty of Science, Niigata University, Niigata 950-2182, Japan

Water molecules play an important role in mesoscale pattern-formation in complex aqueous solutions. We have examined some details of the mesoscale structure formed in 1-propanol aqueous solution by means of small angle neutron scattering measurements combined with a large-scale reverse Monte Carlo (RMC) analysis[1]. It was found that the mesoscale structure was characterized by fractal with a fractal dimension of about 1.85 for 1/5 (a ratio of 1-propanol/water in mole) solution and most water molecules were located on the interface between water-cluster and propanol-cluster.

In the present study we measure the structure factor S(Q) in the ordinary Q region by using HERMES(T1-3) instrument, JRR3M in JAERI (Tokai) for the 1-propanol aqueous solution in order to clarify the molecular-level structure and the role of water molecules in the structure formation. The composition of 1-propanol aqueous solution studied is the same as that measured by SANS experiment (that is, 1/5 solution). Seven samples have been measured, each of which has different H/D isotope substitution. They are

(a) C_3D_7OD - 5 D_2O,
(b) C_3H_7OD - 5 D_2O,
(c) C_3D_7OH - 5 H_2O,
(d) C_3H_7OH - 5 H_2O,
(e) $C_3(D/H)_7OH$ - 5 D_2O ,
(f) $C_3D_7O(D/H)$ - 5 $(D/H)_2O$,
(g) $C_3(D/H)_7O(D/H)$ - 5 $(D/H)_2O$,

where (D/H) means a null composition.

Figures 1 and 2 compare the intensity I(Q)'s scattered from samples (a) to (g).

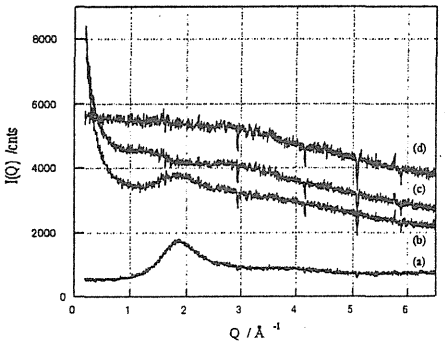


Figure 1: S(Q)'s measured for 1-propanol aqueous solution. See text for (a) to (d).

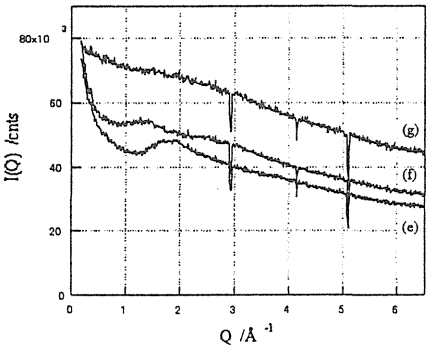


Figure 2: S(Q)'s measured for 1-propanol aqueous solution. See text for (e) to (g).

The I(Q) depends strongly on H/D substitution. Small angle scattering is clearly seen for the samples (b), (c), (e) and (g), which is in good agreement with the previous SANS result both in intensity and profile. Some downward sharp-peaks are due to the Bragg peaks of a vanadium rod used for intensity normalization. These seven S(Q)'s allow us to resolve the molecular level structure of the current solution. Such analysis is under way.

References

[1] M. Misawa, J. Chem. Phys., **116** (2002) 8463.

使用施設:JRR-3' 装置:HERMES(T1-3), 分野 Glasses & Liquids

研究テーマ：アミノ酸分子の疎水基周囲における水分子間水素結合
表題：グリシン分子のメチレン水素原子周囲の水和構造

Hydration Structure around the Methylene-Hydrogen Atom of Glycine Molecule

1-4-4

Y. Kameda, M. Sasaki, M. Yaegashi, K. Tsuji, S. Ohmori, and T. Usuki

Department of Material and Biological Chemistry, Faculty of Science, Yamagata University, Yamagata 990-8560, Japan

Structural information on hydrated water molecules around the amino acid molecule is indispensable for understanding the mechanism of chemical reactions occurring in the biological system. In the present study, we carried out neutron diffraction measurements on H/D isotopically substituted aqueous 4 mol% glycine solutions in order to obtain information on the hydration shell around the hydrophobic methylene group of the glycine molecule in the partial structure function level.

Neutron diffraction measurements for sample solutions, I $(ND_2CD_2COOD)_{0.04}(D_2O)_{0.96}$, II $(ND_2CH_2COOD)_{0.04}(D_2O)_{0.96}$, III $(N^0H_2CD_2COO^0H)_{0.04}(^0H_2O)_{0.96}$, and IV $(N^0H_2CH_2COO^0H)_{0.04}(^0H_2O)_{0.96}$, (^{0}H: H/D = 64/36, b_H = 0), were performed at 25°C using the ISSP 4G(GPTAS) diffractometer installed at JRR-3M research reactor in Japan Atomic Energy Research Institute (JAERI), Tokai, Japan. The incident neutron wavelength, λ = 1.104 ± 0.005 Å, was employed. Scattered neutrons were collected over the angular range of $3 \le 2\theta \le 115°$, corresponding to $0.3 \le Q \le 9.60$ Å^{-1} ($Q = 4\pi\sin\theta/\lambda$). Measurements of scattering intensities were made in advance for a vanadium rod, an empty cell, and a background. After corrections for absorption and multiple scattering, the observed count rates were converted to the normalized scattering cross section.

The first-order difference function, [1] $\Delta_H(Q)$, between corrected scattering cross sections for the sample solutions with the same isotopic ratio for the exchangeable hydrogen atoms, H_{ex}, but different one for the methylene-hydrogen atoms within the glycine molecule, H_M, can be written as follows,

$$\begin{aligned}\Delta_H(Q) = {} & A[a_{H_MO}(Q)-1] \\ & + B[a_{H_MH_{ex}}(Q)-1] \\ & + C[a_{H_MC}(Q)-1] \\ & + D[a_{H_MN}(Q)-1] \\ & + E[a_{H_MH_M}(Q)-1], \end{aligned} \quad (1)$$

where

$A = 4x(1+x)b_O\Delta b_{H_M}$,
$B = 4x(2+x)b_{H_{ex}}\Delta b_{H_M}$,
$C = 8x^2b_C\Delta b_{H_M}$,
$D = 4x^2b_N\Delta b_{H_M}$,
$E = 4x^2(b_{H_M}^2 - b_{H_M}'^2)$.

x is the mole fraction of glycine molecule in the solution. The difference in the coherent scattering length of the methyl-hydrogen atom is denoted by Δb_{H_M}. Numerical values of the coefficients A - E in Eq. 1 are listed in Table 1. Since magnitude of coefficients A and B are much larger than those of C - E in the present experimental condition, the observed $\Delta_H(Q)$ is dominated by the correlation between the methyl-hydrogen atom and water molecule. Particularly, the contribution from the $a_{H_MO}(Q)$ comprises 86 % of the observed $^0\Delta_H(Q)$ function. The present $^0\Delta_H(Q)$ can be well approximated to the H_M-O partial structure factor.

The Fourier transform of $\Delta_H(Q)$ gives

Table 1 Values of coefficients A - E in Eq. 1 (in mbarn)

	A	B	C	D	E
$^D\Delta_H(Q)$	98.56	221.88	8.68	6.11	1.78
$^0\Delta_H(Q)$	98.56	0.0	8.68	6.11	1.78

使用施設：JRR-3　装置：GPTAS(4G)，分野：Glasses & Liquids

the distribution function, $G_H(r)$, around the methyl-hydrogen atom,

$$G_H(r) = 1 + (2\pi^2\rho r)^{-1}(A+B+C+D+E)^{-1} \times \int_0^{Q_{max}} Q\Delta_H(Q)\sin(Qr)\,dQ. \quad (2)$$

The intramolecular $H_M\cdots\alpha$ contribution within the glycine molecule was calculated employing structural parameters reported for the crystalline [2,3] and gaseous [4] states, and then subtracted from the total $\Delta_H(Q)$ to obtain the intermolecular difference function, $\Delta_H^{inter}(Q)$. The partial structure factor, $a_{H_MH_{ex}}(Q)$, was derived from the second-order difference between $^D\Delta_H^{inter}(Q)$ and $^0H\Delta_H^{inter}(Q)$.

In order to obtain structural parameters concerning the nearest neighbor $H_M\cdots H_W$ and $H_M\cdots O_W$ interactions, the least squares fitting procedure has been adopted to the observed $a_{H_MH_{ex}}(Q)$ and $a_{H_MX}(Q)$ (= $^0H\Delta_H^{inter}(Q)/(A+B+C+D+E) + 1$), which are shown in Figs. 1a and 1c, respectively. The corresponding distribution functions, $g_{H_MH_{ex}}(r)$ and $g_{H_MX}(r)$, are represented in Figs. 2a and 2b, respectively. The nearest neighbor $H_M\cdots O_W$ and $H_M\cdots H_W$ distances was obtained to be 2.64(1) and 2.87(1) Å, respectively. The present results indicate that the water molecules in the first hydration shell of the methylene-hydrogen atom take some preferred orientation. The nearest neighbor $H_M\cdots O_W$ coordination number was determined to be 0.86(3), which implies that ca. 2 water molecules are involved in the first hydration shell of the methylene group of a glycine molecule in the aqueous solution.

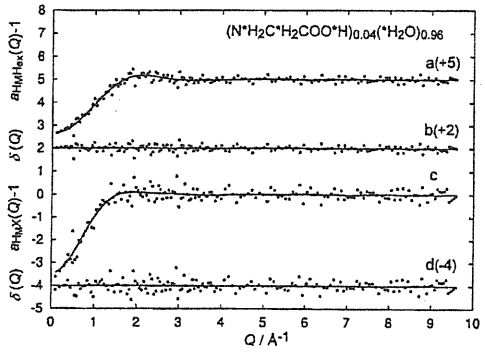


Figure 1: Partial structure factors, a) $a_{H_MH_{ex}}(Q)$ and c) $a_{H_MX}(Q)$ (dots) observed for aqueous 4 mol% glycine solutions. Solid lines indicate the best fit of the calculated structure factors. The residual functions, $\delta(Q)$, are shown below (b and d).

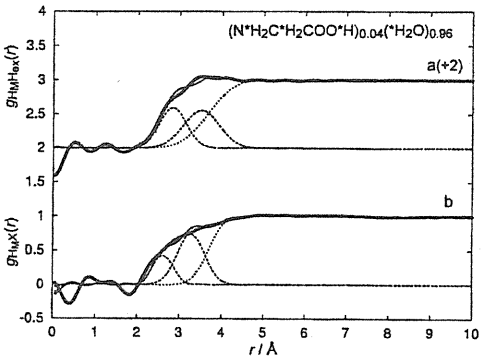


Figure 2: Partial distribution functions, a) $g_{H_MH_{ex}}(r)$ and b) $g_{H_MX}(r)$, around the methylene-hydrogen atoms of the glycine molecule (solid lines). Fourier transform of the calculated structure factor is indicated by broken line. The short- and long-range contributions are denoted by dotted lines.

References

[1] J. E. Enderby and G. W. Neilson, "*Water, A Comprehensive Treatise*", Plenum Press, (1979), vol. 6, p. 1.

[2] P-G Jönsson and Å. Kvick, *Acta. Cryst.*, **B28** (1972) 1827.

[3] J. Almlöf, Å. Kvick, and J. O. Thomas, *J. Chem. Phys.*, **59** (1973) 3901.

[4] K. Iijima, K. Tanaka, and S. Onuma, *J. Mol. Struct.*, **246** (1991) 257.

研究テーマ：アルコール水溶液の構造とダイナミクス

表題：ブトキシエタノール一水混合系の濃度ゆらぎとスローダイナミクス

Concentration Fluctuations and Slow Dynamics of 2-Butoxyethanol-water Mixtures

1-4-5

K. Yoshida and T. Yamaguchi

Department of Chemistry, Faculty of Science, Fukuoka University, Fukuoka 814-0180, Japan

Introduction

The formation of molecular aggregates or microinhomogeneities in alcohol-water mixtures has been observed by large-angle X-ray and neutron scattering. All results have been discussed in connection with the anomalies in various physico-chemical properties of the alcohol-water mixtures in a water-rich region. The most direct way of obtaining information on the microinhomogeneities in alcohol-water mixtures is small-angle X-ray and neutron scattering (SAXS and SANS, respectively).

Another interest in the molecular agregates is cluster dynamics which is the collective motion of the molecular aggregates. A unique way of observing the cluster dynamics is the neutron spin echo (NSE) technique that is easy to investigate the dynamics of system in time scale of 0.1 – 100 ns in mesoscopic spatial structure of $10 - 10^3$ Å.

In this study, we measured 2-butoexyethanol(BE)-water mixture by SANS and NSE. The BE has a long hydrophobic part, and its aqueous solution undergoes phase separation at a lower critical solution temperature (LCST) of 49°C.[1] SANS experiment of the mixture has revealed concentration fluctuations at temperatures even below the LCST, suggesting that the microinhomogeneities precede the macroscopic separation.[2] We investigate the correlation length by SANS and the cluster dynamics of molecular aggregation by NSE to reveal whether or not such an aggregation is stable like micelles or transit structure with a short lifetime.

Experimental

Since in BE-D_2O mixtures the BE hydroxyl hydrogen and deuterons of D_2O may exchange, we used deuterated BE ($C_4H_9OC_2H_5OD$, over 98 atom% D).

SANS measurements were made at two different facilities. The first run was made on neutron small-angle scattering spectrometer SWAN at the pulsed neutron facility (KENS) of the National Laboratory for High Energy Accelerator Research Organization (KEK). The scattering vector range 0.01 - 2 $Å^{-1}$. The second measurements were made on the small-angle spectrometer SANS-U ($C_{1\text{-}2}$) at the reactor JRR-3M in the Japan Atomic Energy Research Institute (JAERI). The distances between sample and detector were 2 and 8 m. The SANS data of the sample solutions and an empty cell were corrected for absorption by using the transmission data measured, and then the empty cell data were subtracted as background. Correction for the detector efficiency and data normalization were made by using data of Lupolen for the SANS-U data. To conbine two scattering data obtained with two spectrometers, the scattering intensity for the SWAN is normalized experimentally with SANS-U data in an overlapping Q-range.

The NSE spectrometer is equipped at $C_{2\text{-}2}$ cold neutron guide port of JRR-3M, JAERI. The scattering vector Q covered was 0.01 – 0.1 $Å^{-1}$. The Fourier time was varied from 0.15 to 15 ns. A plate of Grafoil was measured for resolution correction.

Results and Discussion

Figure 1 shows the SANS intensities of the BE-water mixtures after correction for incoherent scattering. The scattering

使用施設：JRR-3 ，装置：SANS-U(C1-2), NSE(C2-2)，分野 Glass and Liquid

Table 1. The scattering intensities at Q = 0 Å^{-1} and the correlation lengths of the BE-water mixtures at various BE concentrations and temperatures

	15°C	25°C	34°C
		x_{BE} = 0.040	
I_0 / cm^{-1}	33.7	93.8	651
ξ / Å	12.6	24.6	68.5
		x_{BE} = 0.065	
I_0 / cm^{-1}	52.0	156	1840
ξ / Å	11.3	26.6	99.3
		x_{BE} = 0.090	
I_0 / cm^{-1}	39.7	104	457
ξ / Å	7.17	19.5	47.9

intensities increase significantly with increasing temperature. It should been noted that the intensities at a large Q region (Q > 0.1 Å^{-1}) do not depend on temperature. In order to estimate the concentration fluctuations in the BE-water mixtures, the Ornstein-Zernike plots were made according to

$$I(Q)^{-1} = I(0)^{-1}\left(1+\xi^2 Q^2\right) \quad (1)$$

where ξ is the Ornstein-Zernike correlation length and $I(0)$ is the intensity for Q = 0 Å^{-1} that reflects the concentration fluctuations. Both values obtained from a least-squares fitting procedure are collected in Table 1.

The NSE method measures the energy transfer of neutrons at an extremely high energy resolution. Figure 2 shows the Q dependence of the relaxation rate $\Gamma(Q)$ on spin echo signals. The diffusion coefficient D was obtained from the following equation.

$$\Gamma = DQ^2 \quad (2)$$

The values of D at various temperatures are summarized in Table 2. According to the Stokes-Einstein model where a stable cluster forms, an increase in the cluster size makes the translational motion of the cluster slow. However, the values of D obtained from the present NSE measurements increase with increasing temperature in spite of an increase in the correlation length obtained from the SANS. Hence, these results indicate that a stable cluster does not exist in the mixtures.

Table 2. The diffusion constants of alcohol cluster in the BE-water mixtures at various temperatures by NSE

x_{BE}	11°C	25°C	37°C
0.040	4.7±0.3	8.3±0.4	12.2±0.5
0.065	4.0±0.3	6.5±0.3	9.1±0.3
0.090	3.8±0.4	6.6±0.3	8.5±0.3

A model supported from the present results is that the aggregation is preserved only for short time characterized by the relaxation time, the reciprocal of Γ (Q) , of the NSE (nanoseconds).

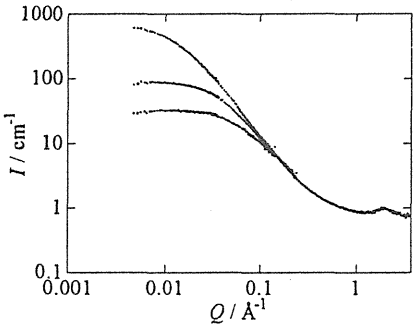


Figure 1: Small-angle neutron scattering profiles of the BE-water mixture at 9.0 mole fraction of BE.

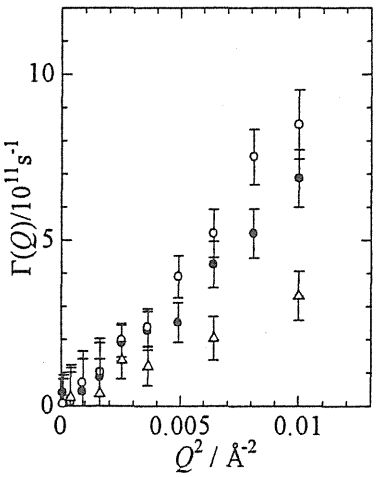


Figure 2: Q dependence of the relaxation rates $\Gamma(Q)$ in the BE-water mixture at 9.0 of mole fraction of BE. Open and filled circles, and triangles indicate the results at 11, 25, and 37°C, respectively.

References

[1] N. Ito, et al., Bull. Chem. Soc. Jpn. **56** (1983) 379.

[2] G. D'Ariggo et al., J. Chem. Soc. Faraday Trans. **86** (1990) 1503.

研究テーマ：水素結合性超臨界-アルコール２成分流体の小角散乱
表題：水素結合性超臨界-アルコール２成分流体の小角散乱

Small-angle neutron scattering of supercritical water-alcohol binary fluids

1-4-6

Makoto Shimohira[1], Koji Yoshida[1], Michihiro Nagao[2], Toshio Yamaguchi[1]
[1]*Department of Chemistry, Faculty of Science, Fukuoka University, Fukuoka 814-0180, Japan*
[2]*Insitute for Solid State Physics, University of Tokyo, Tokai 319-1106, Japan*

Introduction

Supercritical water has novel properties not available under ambient conditions and is used as medium in solvent extraction and chemical reactions. In recent years, supercritical water has been proved to decompose hazardous compounds, such as PCB, dioxin, etc. into environmentally friendly carbon dioxide, mineral acid, and water. It has also been found that addition of alcohols moderates experimental conditions of supercritical water reactions, the so-called co-solvent effect, and that the poorer the co-solvent effect the longer the hydrophobic group of the alcohols. In order to understand the co-solvent effect and further develop the supercritical water technology, it is essential to investigate the structure of supercritical alcohols–water mixtures from the microscopic to mesoscopic scale.

So far, we have elucidated the microscopic structural information, such as interatomic distance, coordination number, a change in the hydrogen bond, etc. of moderate-density water [1], methanol [2], and methanol-water [3] mixtures in subcritical and supercritical region by X-ray diffraction, neutron diffraction with isotopic substitution, and Raman scattering methods. It has been found from these studies that chemical reactions in supercritical water take place very effectively near the critical point. It will thus be of interest to investigate density fluctuations of supercritical alcohols-water mixtures around the critical point and relate them to various properties and chemical reactions in supercritical water.

In this work, we have measured small-angle neutron scattering of supercritical methanol and methanol-water mixtures and obtained the mesoscopic structure information, such as density and concentration fluctuations, as a function of temperature and pressure (density).

Experiment

Small-angle neutron scattering (SANS) measurements were performed on the SANS-U spectrometer of the Institute for Solid State Physics, the University of Tokyo, installed at the beamline of a cold source in JRR-3M. We used a high-temperature high-pressure SANS cell (Toyo Koatsu). The high-temperature high-pressure system is shown in Fig. 1. A sample solution was injected into a cell with a syringe *in vacuo*. The pressure was controlled with a high-pressure pump using water as a pressure medium in a high-pressure pump to a separator. The sample to detector distance was 2 m, where the Q-range obtained was from 0.008 to 0.15 $Å^{-1}$. The measurement times of background, Luporen used for normalization, an empty cell, and samples were 1, 0.5, 1, and 0.5 h, respectively.

We measured two samples: pure methanol (CD_3OD) and methanol-water (CD_3OD-D_2O) mixtures at methanol mole fraction x_M=0.3. In the present study, we did not degas the samples. The reduced pressure range (P_c = 159.6 bar) was 1.0 to 2.0 at the reduced temperatures T_R=1.03, 1.05, and 1.07 (T_c = 592.7 K). For lack of the critical parameters of the D-substituted solvents, the critical parameters of the samples were estimated from those of normal methanol.

使用施設：JRR-3　装置：SUNS-U(C1-2), 分野：4. Amorphous & Liquid

Results and Discussion

To estimate density fluctuations of the samples, we made the Ornstein-Zernike plot given by

$$\frac{1}{I(Q)} = \frac{\xi^2}{I(0)} \cdot Q^2 + \frac{1}{I(0)} \qquad (1)$$

where $I(Q)$ and $I(0)$ are the scattering intensities of the samples at Q and $Q = 0$, respectively. Q is the scattering vector ($= 4\pi/\lambda\sin\theta$, λ the wavelength, θ the Bragg angle), and ξ is the correlation length.

Fig. 2 shows pressure dependence of the correlation length obtained at the various temperatures. The correlation lengths of methanol and methanol-water mixture gradually decrease as increasing reduced temperatures as expected. It should be noted that the correlation lengths of supercritical methanol are slightly larger than those of the supercritical methanol-water mixtures at the same reduced temperatures.

A detailed study of the clusters is in progress.

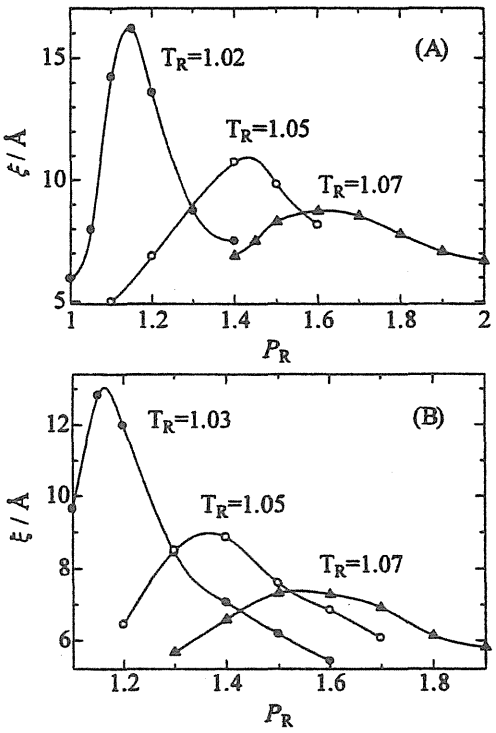


Fig. 2. Pressure dependence of the correlation length of methanol (A) and the methanol-water mixture (B) at x_M=0.3 at the various supercritical temperatures.

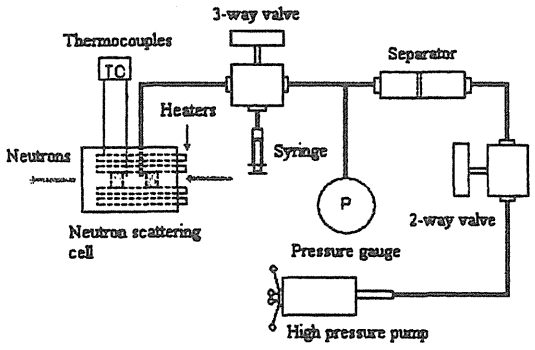


Fig. 1. The high-temperature and high-pressure system for neutron scattering.

References

[1] T. Yamaguchi, *J. mol. Liq.*, 78, 43 (1998).

[2] T. Yamaguchi, C. J. Benmore, A. K. Soper, *J. Chem. Phys.*, 112, 8976 (2000).

[3] M. Shimohira, T. Umeki, K. Yoshida, K. Ujimoto, T. Yamaguchi, Abstracts, the 67th Annual meeting of SCEJ, Fukuoka, March, 2002.

使用施設：JRR-3 ，装置：SUNS-U(C1-2), 分野：4. Amorphous & Liquid

研究テーマ：ハロゲン化有機溶媒－水混合溶液中のクラスター形成の研究
表題：中性子小角散乱法による TFE－水混合溶液のクラスター形成の研究

Small-Angle Neutron Scattering Study on Cluster Formation in TFE-Water Mixtures

1-4-7

T. Takamuku,[a] T. Kumai,[a] K. Yoshida,[b] T. Yamaguchi,[b] and M. Nagao[c]

[a]Department of Chemistry and Applied Chemistry, Faculty of Science and Engineering, Saga University, Honjo-machi, Saga, 840-8502, Japan; [b]Advanced Materials Institute and Department of Chemistry, Faculty of Science, Fukuoka University, Nanakuma, Jonan-ku, Fukuoka 814-0180, Japan; [c]Institute for Solid State Physics, The University of Tokyo, 106-1 Shirakata, Tokai 319-1106, Japan

2,2,2-trifluoroethanol (TFE) and 1,1,1,3,3,3-hexafluoro-2-propanol (HFIP) promote the α-helix structure of proteins in their aqueous solutions more strongly than ethanol and propanol [1]. It has often been discussed that alcohol clusters formed in aqueous solutions play an important role in the mechanism of the protein folding; i.e. the interactions between alcohol clusters and protein molecule would be essential for alcohol-induced folding of proteins. However, cluster formation in TFE-water mixtures has not been clarified at the mesoscopic level by using a small-angle neutron scattering (SANS) technique.

In the present investigation, small-angle neutron scattering (SANS) experiments with H/D substitution have been performed on TFE-water mixtures at various TFE mole fractions x_{TFE}. Two systems of CF_3CH_2OD (TFE-d_1)-D_2O and CF_3CD_2OH (TFE-d_2)-H_2O mixtures were prepared as sample solutions. Since H and D atoms have different scattering lengths of -3.74 and 6.67 fm, respectively, the former will mainly give us information on D_2O clusters, while the latter will provide that of TFE clusters.

SANS measurements on the TFE-d_1-D_2O and TFE-d_2-H_2O mixtures at 298 K were made on SANS-U at a reactor JRR-3M in JAERI, Tokai. The momentum transfer Q (= $4\pi\lambda^{-1}\sin\theta$; λ the wavelength, 2θ the scattering angle) range covered was 0.02–0.15 Å [2]. The SANS intensities on SAUS-U were corrected for background, absorption, and cell scattering and normalized by using the scattering of lupolen [3].

In Figure 1, the SANS spectra for the TFE-d_1-D_2O mixtures are depicted at various x_{TFE}. As shown in Figure 1, the SANS intensities

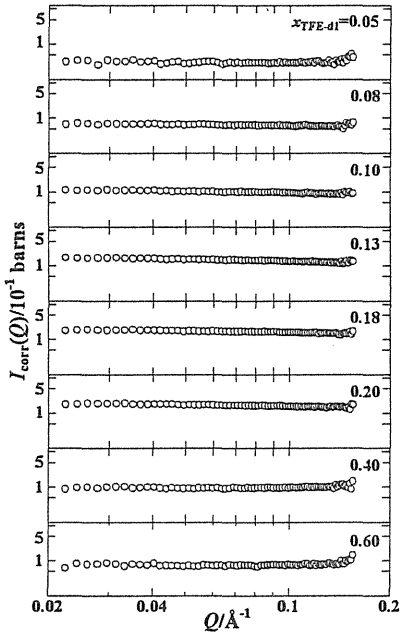


Figure 1: SANS spectra for TFE-d_1-D_2O mixtures at various x_{TFE}.

gradually increase when the x_{TFE} increases from 0.05 and are most strengthened at x_{TFE} = 0.13. With further increasing x_{TFE}, the intensities decrease again. Therefore, the concentration fluctuation for TFE-d_1-D_2O mixtures is most enhanced at x_{TFE} = 0.13. The SANS intensities for the TFE-d_2-H_2O mixtures change with increasing x_{TFE} in the same manner.

In order to quantitatively clarify D_2O and TFE clusters from the SANS intensities for the TFE-d_1-D_2O and TFE-d_2-H_2O mixtures, respectively, the SANS intensities $I_{corr}(Q)$ were plotted against Q^2 and fitted by the Debye equation:

JRR-3 SANS-U(C1-2), Glasses & Liquids

$$I_{corr}(Q) = I_0\left(1 - \frac{L_D^{\,2}}{6}Q^2\right), \qquad (1)$$

where I_0 is the scattering intensity at Q = 0 Å^{-1} and L_D is the Debye correlation length [4]. Figure 2 shows the plots of $I_{corr}(Q)$ for the TFE-d_1-D_2O mixtures as a function of Q^2. The theoretical values (solid lines) from a least-squares fitting procedure with eq. (1) reproduce the experimental ones (circles) well.

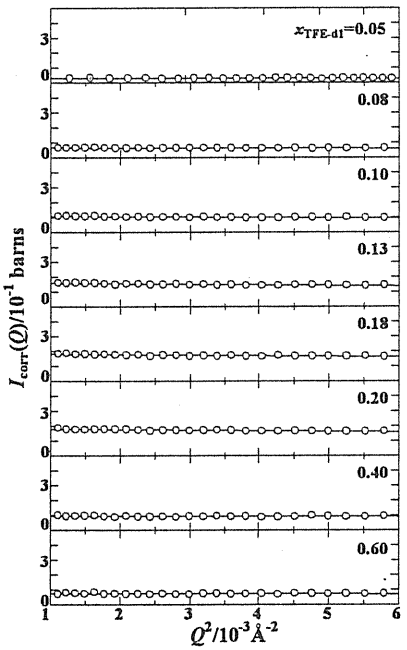


Figure 2: $I_{corr}(Q)$ against Q^2 values for TFE-d_1-D_2O mixtures. The observed values (circles) and least-squares fitted ones (solid lines) calculated through eq. (1).

Figure 3 (a) and (b) show the mole fraction dependence of L_D values for the TFE-d_1-D_2O and TFE-d_2-H_2O mixtures, respectively. The L_D values for both mixtures increase as the x_{TFE} increases from 0.05 and reach a maximum at x_{TFE} = 0.15 and 0.20, respectively. Then, the values decrease with further increasing x_{TFE}. Thus, the present results indicate that TFE and water molecules most heterogeneously mixed in the narrow range of x_{TFE} = 0.15-0.20, i.e. both TFE and water clusters are formed in the mixtures.

Interestingly, this mole fraction range is in good agreement with the specific mole fraction where folding of several proteins begins by addition of TFE into their aqueous solutions. Therefore, the formation of TFE and water clusters may be an important key of folding of proteins.

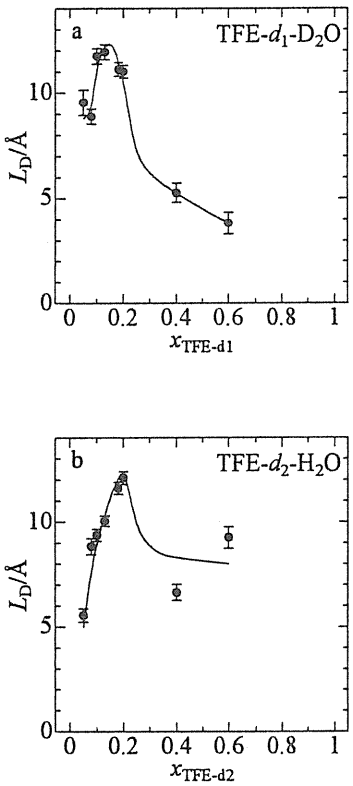


Figure 3: L_D values with the standard deviation σ values as error bars for (a) TFE-d_1-D_2O and (b) TFE-d_2-H_2O mixtures as a function of x_{TFE}.

References

[1] D-Y. Hong, M. Hoshino, R. Kuboi, and Y. Goto, *J. Am. Chem. Soc.*, **121**, 8427 (1999).
[2] Y. Ito, M. Imai, and S. Takahashi, *Physica B*, **889**, 213 (1995).
[3] G. D. Wignall and F. S. Bates, *J. Appl. Cryst.*, **20**, 28 (1987).
[4] P. Debye, *J. Chem. Phys.*, **31**, 680 (1959).

研究テーマ：塩化アルカリ塩誘起によるアセトニトリル－水混合溶液の相分離メカニズムの解明
表題：中性子小角散乱法による塩化アルカリ塩誘起のアセトニトリル－水混合溶液の相分離に関する研究

1-4-8 Alkali Chlorides-Induced Phase Separation of Acetonitrile-Water Mixtures Studied by Small-Angle Neutron Scattering Technique

T. Takamuku,[a] Y. Noguchi,[a] E. Yoshikawa,[a] T. Kumai,[a] and M. Nagao[b]

[a]Department of Chemistry and Applied Chemistry, Faculty of Science and Engineering, Saga University, Honjo-machi, Saga, 840-8502, Japan; [b]Institute for Solid State Physics, The University of Tokyo, 106-1 Shirakata, Tokai 319-1106, Japan

At 298 K acetonitrile (AN) can be mixed with water at any ratio. However, phase separation of acetonitrile-water mixtures occurs when suitable salt, such as NaCl and $CaCl_2$, is added into the mixtures. We have investigated NaCl-induced phase separation of acetonitrile-water mixtures at the molecular level by using large-angle X-ray scattering (LAXS) and small-angle neutron scattering (SANS) techniques [1,2]. On the basis of these results, we concluded that the NaCl-induced phase separation occurs by the following manner; (1) acetonitrile and water molecules are heterogeneously mixed each other even in pure mixtures, i.e. microheterogeneity occurs, (2) when NaCl is added into the mixtures, Na^+ and Cl^- are preferentially solvated by water molecules, (3) thus, the microheterogeneity is progressed with increasing NaCl concentration, (4) finally, acetonitrile-water mixtures are separated to acetonitrile-rich and water-rich phases. Thus, LiCl and KCl-induced phase separation behaviors are very important to more clarify the salt-induced phase separation of acetonitrile-water mixtures.

In the present investigation, SANS experiments at 298 K by using the SANS-U spectrometer at a reactor JRR-3M in JAERI, Tokai, have been made on MCl-acetonitrile-water (M^+ = Li, Na, and K) mixtures at various MCl concentrations. Two systems of MCl-CH_3CN-D_2O and MCl-CD_3CN-H_2O mixtures were prepared as sample solutions. The former will provide mainly information on D_2O clusters, while the latter will give us that on acetonitrile clusters, because of different scattering lengths of -3.74 and 6.67 fm for H and D atoms, respectively. The momentum transfer Q ($= 4\pi\lambda^{-1}\sin\theta$; λ the wavelength, 2θ the scattering angle) range covered was 0.02–0.15 Å [3]. The SANS intensities on SAUS-U were corrected for background, absorption, and cell scattering and normalized by using the scattering of lupolen [4].

Before the SANS experiments, phase diagrams of MCl-acetonitrile-water mixtures at 298 K were prepared. The phase diagrams showed that phase separation occurs at lower total MCl concentration $[MCl]_{tot}$ in the sequence of NaCl < KCl < LiCl, though the cation is more strongly hydrated in the sequence $Li^+ > Na^+ > K^+$.

Figure 1 shows the SANS spectra for NaCl-CH_3CN-D_2O mixtures as a function of $[NaCl]_{tot}$. As seen in this figure, the SANS intensities gradually increase with increasing $[NaCl]_{tot}$, suggesting that D_2O clusters are enhanced in the mixtures.

To qualitatively analyze the SANS intensities, Ornstein-Zernike [5] plots were made with:

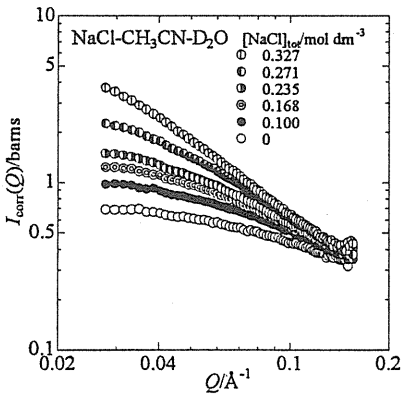


Figure 1: SANS spectra for NaCl-CH_3CN-D_2O mixtures at various $[NaCl]_{tot}$.

JRR-3 SANS-U(C1-2), Glasses & Liquids

$$I_{corr}(Q)^{-1} = I_0^{-1}\left(1+\xi^2 Q^2\right), \quad (1)$$

where ξ represents the correlation length and I_0 is the scattering intensity at Q = 0 Å^{-1}. The correlation lengths were estimated from a least-squares fitting procedure by using eq. (1). Figure 2 shows the plots of $I_{corr}(Q)$ for the NaCl-CH_3CN-D_2O mixtures as a function of Q^2. The theoretical values (solid lines) obtained from a least-squares fitting procedure with eq. (1) reproduce well the experimental ones (circles).

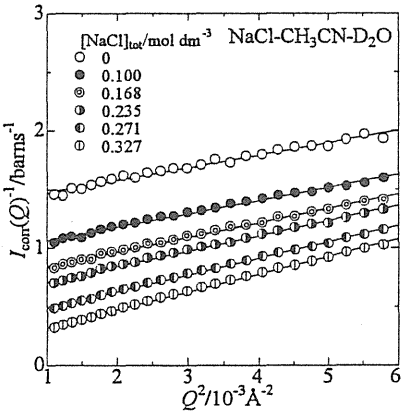


Figure 2: Ornstein-Zernike plots for NaCl-CH_3CN-D_2O mixtures. The observed values (circles) and least-squares fitted ones (solid lines) calculated through eq. (1).

In Figure 3 (a) and (b), the correlation lengths for the MCl-CH_3CN-D_2O and MCl-CD_3CN-H_2O mixtures are depicted as a function of $[MCl]_{tot}$, respectively. Figure 3 (a) reveals that D_2O clusters in the mixtures are more rapidly enhanced with increasing $[MCl]_{tot}$ in the sequence NaCl > KCl > LiCl. Figure 3 (b) shows that CD_3CN clusters are also more quickly evolved in the same sequence. These results agree well with the fact that the phase separation occurs at lower $[MCl]_{tot}$ in the sequence of NaCl < KCl < LiCl. Thus, the present results support the mechanism of phase separation proposed, i.e. water clusters are evolved around M^+ and Cl^- hydration shells, and acetonitrile clusters are simultaneously enhanced in the mixtures with increasing $[MCl]_{tot}$. When water and acetonitrile clusters are apart from each other, finally, the phase separation takes place. The plausible reason for the difficulty of LiCl-induced phase separation is that very strongly hydrated Li^+ is less suitable to evolve the water clusters around Li^+ than Na^+ and K^+.

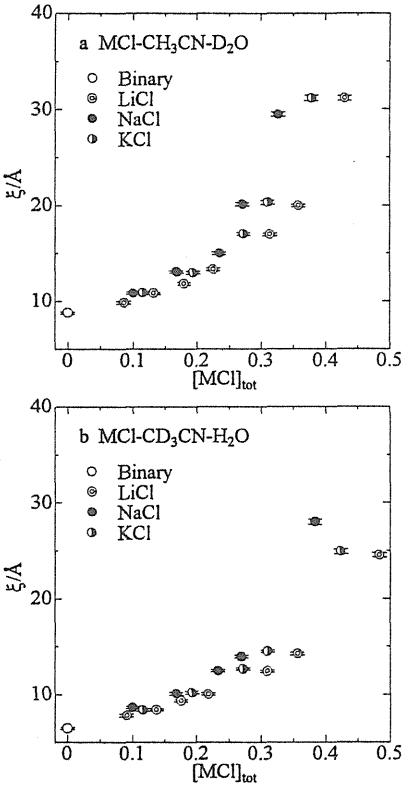


Figure 3: The correlation lengths with the standard deviation σ values as error bars for (a) MCl-CH_3CN-D_2O and (b) MCl-CD_3CN-H_2O mixtures as a function of $[MCl]_{tot}$.

References

[1] T. Takamuku *et al.*, *J. Phys. Chem. B*, **105**, 6236-6245 (2001).
[2] T. Takamuku *et al.*, *Chem. Lett.*, **2000**, 878-879.
[3] Y. Ito, M. Imai, and S. Takahashi, *Physica B*, **889**, 213 (1995).
[4] G. D. Wignall and F. S. Bates, *J. Appl. Cryst.*, **20**, 28 (1987).
[5] H. E. Stanley, *Introduction to Phase Transitions and Critical Phenomena*, (Clarendon Press, Oxford, 1971).

研究テーマ：制限空間内における水分子のダイナミクス
表題： MCM-41 メソ孔内の水分子のダイナミクスへの表面状態の影響

Effects of Surface State on Dynamics of Water Molecules in Mesopores of MCM-41

1-4-9

S. Kittaka, S. Takahara, Y. Kuroda,* T. Mori,* and T. Yamaguchi**

*Department of Chemistry, Faculty of Science, Okayama University of Science, 1-1 Ridaicho, Okayama 700-0005, Japan; *Department of Chemistry, Faculty of Science, Okayama University, Tsushima, Okayama 700-8530, Japan; **Advanced Materials Institute and Department of Chemistry, Faculty of Science, Fukuoka University, Nanakuma, Jyonan-ku, Fukuoka 814-0180, Japan*

We have investigated the dynamics of water molecules confined in mesopores of MCM-41 samples with different pore sizes by using quasi-elastic neutron scattering (QENS) technique.[1] It is expected that the dynamics of the confined water molecules depends not only on pore size, but also on the state of pore surface, for example, the amount of surface hydroxyl groups. In the present study, we have elucidated the effect of surface state on dynamics of water molecules in MCM-41 based on QENS measurements.

According to a similar method reported by several authors,[2,3] two kind of MCM-41 samples having different amount of the hydroxyl groups was synthesized; Sample A : 0.7 OH's/nm^2; Sample B : 2.6 OH's/nm^2. [4] Both the samples had the same pore sizes (pore diameter: 33.6 Å). The water adsorbed MCM-41 samples were prepared by the following procedure: the MCM-41 samples were evacuated for 72 h at room temperature and exposed to water vapor (relative pressure $p/p_0 = 0.7$) for 72 h at 298 K to achieve capillary condensation of water. QENS measurements were carried out by using a time-of-flight type spectrometer AGNES (C3-1-1) installed at JRR3M in JAERI (Tokai).

Concerning the line shapes of QENS spectra, the Samples A and B gave almost the same results (not shown). This indicates that the self-diffusion of the confined water molecules is not affected by the amount of the hydroxyl groups. On the other hand, for the Q-dependence of intensity of spectra, difference between the Samples A and B was detected. Figure 1 shows the temperature dependence of the mean-square vibrational amplitude $\langle u^2 \rangle$ of the water molecules. As shown in Figure 1, $\langle u^2 \rangle$ of the Sample A is smaller than that of the Sample B. This result is explained as follows. The water molecules in the Sample A form stable clusters in which the hydrogen-bond network among water molecules grows well. On the other hand, the stable clusters are not able to be formed in the sample B because the water molecules near the pore walls are fixed on the surface hydroxyl groups that exist in a large amount. These interpretations are consistent with the heats of adsorption of water in MCM-41.[4] More quantitative data analysis is now in progress.

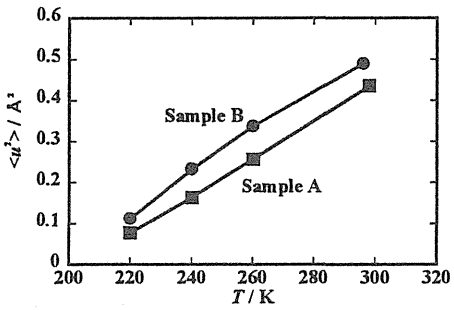


Figure 1. Temperature dependence of $\langle u^2 \rangle$ of the water molecules in the MCM-41 samples.

References

(1) Takahara, S. et al.; *J. Phys. Chem. B*, **1999**, *103*, 581.
(2) Beck, J., et al., *J. Am. Chem. Soc.* **1992**, *114*, 10834.
(3) Cheng, C. –F., et al., *J. Chem. Soc., Faraday Trans.* **1997**, *93*, 193
(4) Mori, T., et al., *Langmuire*, **2002**, *18*, 1595.

使用施設：JRR-3　　装置：AGNES,　分野：Glasses & Liquids

研究テーマ：超イオン導電体における乱れ
表　題：超イオン電導ガラスの中性子小角散乱

1-4-10

Small Angle Neutron Scattering from Superionic Conducting Glasses

H. TAKAHASHI, T. OGIHARA, T. SAKUMA[1], Y. ISHII[2] and J. SUZUKI[2]

Faculty of Engineering, Ibaraki University, Hitachi 316-8511
[1]Faculty of Science, Ibaraki University, Mito, 310-8512
[2]Advanced Science Research Center, JAERI, Tokai, Ibaraki 319-1195

In the previous study, new FSDP was observed in $10AgI\text{-}3Ag_2O\text{-}2V_2O_5$ glass from the elastic neutron scattering experiment[1)]. The medium range structure for superionic conducting glasses is of interest in connection with the origin of the FSDP in low-Q region.

Small-angle neutron scattering experiments were performed by the SANS-J at JRR-3. The incident neutron wavelength of 0.650 nm is employed. The scattering data was recorded in the range $0.04 \leq Q \leq 0.3$ nm^{-1} at room temperature. Obtained data was corrected from the background and then normalized using standard sample.

Figure 1 shows the SANS profiles for $nAgI\text{-}Ag_2O\text{-}V_2O_5$ glasses (hereafter referred to as n-3-2, n=0, 2, 5, 12 and 15). It is observed by X-ray diffraction that 15-3-2 glass include precipitated β-AgI crystal. SANS profile for 15-3-2 is clearly different from those for samples within glass forming region. Sub-figure (a) indicates the composition dependence of relative intensity at q=0.1 nm^{-1}. The intensity decreases with AgI concentration within glass forming region and then increases at AgI-precipitated composition. It is well known that the host glass network has the density fluctuation. The density fluctuation occurs from the interstitial void, which is built up by cross-linked or folded VO_4 polymeric chains. Doped-AgI is incorporated into the interstitial void. As a result, apparent density fluctuation is considered to reduce with AgI content. It is considered that the reduction of density fluctuation with AgI concentration leads to the decrease of SANS intensity. On the other hand, the increase of SANS intensity beyond the glass forming range would result from the formation of the crystalline phase. The normalized intensity divided by the SANS intensity for AgI-free glass is shown in the sub-figure (b). The normalized intensity for 15-3-2 glass increases above 0.1 nm^{-1}. It is natural to connect this behavior with crystallization process. Similar trend, however, seems to appear at 5-3-2 glass. In order to clarify the medium range order accompanied by crystallization, it is necessary to investigate the SANS study for the composition at around glass forming limit in the higher q range.

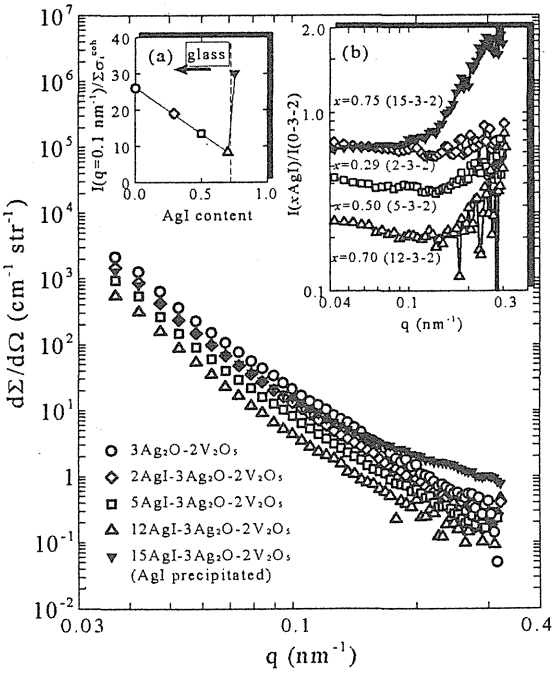


Figure 1: SANS profiles for several AgI concentration of silver vanadate glasses.

References

1) H. Takahashi, N. Rikitake, T. Sakuma and Y. Ishii : J. Non-Cryst. Solids, to be published.

原子炉：JRR-3　　装置：SANS-J(C3-2)　　分野：中性子散乱（液体・不規則物質）

研究テーマ:クラスレート水溶液のダイナミクス
表題:中性子準弾性散乱によるクラスレート水溶液中の水分子の拡散運動の研究

Quasielastic Neutron Scattering Study on Diffusive Motions of Water Molecules in Some Clathrate Aqueous Solutions

1-4-11

O. Yamamuro, N. Tanaka, T. Matsuo, and N. Onoda-Yamamuro *

*Department of Chemistry, Graduate School of Science, Osaka University, Toyonaka, Osaka 560-0043, Japan; *College of Science and Technology, Tokyo Denki University, Hatoyama-cho, Hiki-gun, Saitama 350-0394, Japan*

Clathrate hydrate [1] is a type of inclusion compound in which various guest molecules are accommodated inside the cage-like structure formed by water molecules. Methane hydrate, which is deposited on seabed near Japan, is expected to be utilized as energy resource in future. Furthermore, clathrate hydrates give many useful applications, *e.g.*, transport of natural gas, fixation of CO_2 on deep seabed, heat reservoir for air conditioners, *etc*. For these applications, the most important knowledge is the microscopic mechanism of the dissociation/formation process of the clathrate hydrates. Recently, we are investigating the diffusive motions of the water molecules in some aqueous solutions of guest molecules, which is called "clathrate aqueous solutions" in this report.

The neutron scattering experiments were performed using a direct geometry chopper-type TOF spectrometer AGNES [2] installed at the cold neutron guide (C3-1) of JRR-3M (Tokai, Japan). The elastic energy resolution was ca. 0.1 meV and the energy window was $-3 < E < 20$ meV. In this experiment, 122 ^{3}He tube counters were installed at $2\theta = 9$—$130°$ at steps of 1°, covering the scattering vector Q region of 0.23—2.70 Å^{-1}. The liquid sample was confined in a concentric double-cylinder aluminum can. The thickness of the sample was 0.3 mm corresponding to the transmission of neutron beam of 87 %. The data were collected at several temperatures in the range -4—60°C using a thermostat designed for liquid samples.

We examined the clathrate aqueous solutions of tetrahydrofuran (THF), acetone (Ac), and 1,4-dioxane (DXN). Their molecular structures and average van der Waals diameters are shown in Fig. 1. These guest molecules were fully deuterated to investigate preferentially the motion of water molecules.

Figure 2 shows the quasielastic spectra of deuterated THF aqueous solution and pure water. The solid curve in the figure is the result of the fitting to the model function, the convolution of the translational (Lorentzian) and rotational (Bessel function) diffusive motions of water

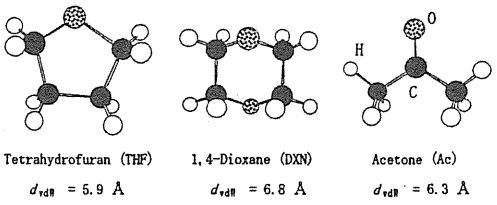


Figure 1: Structures and van der Waals diameters of the guest molecules examined in this study.

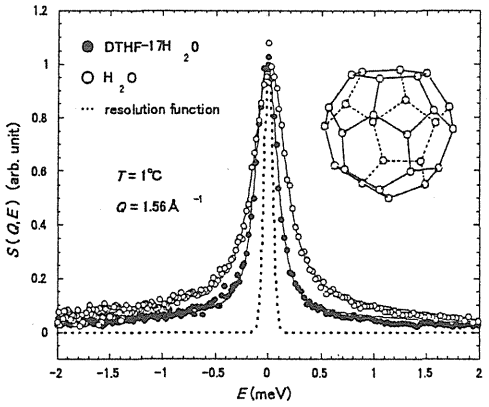


Figure 2: Quasielastic spectra of the deuterated THF

使用施設:JRR-3　装置:AGNES(C3-1-1), 分野 Glasses and Liquids

aqueous solution and pure water.

molecules. This analysis is based on the established method by Teixeira et al. [3]. The fittings were satisfactory and the determined parameters showed that the motions of water molecules in clathrate aqueous solutions are clearly slower than those in pure water. Quasielastic spectra such as Fig. 2 were measures at various Q values, at various temperatures, and for the three guest molecules.

Figure 3 shows the HWHM (Γ) of the Lorentzian component as a function of Q^2 values for pure water and the three clathrate aqueous solutions at T = 0°C. These data were fitted to the jump-diffusion model

$$\Gamma = DQ^2/(1+DQ^2\tau_0) \qquad (1)$$

where D is the diffusion coefficient and τ_0 the residence time between two successive jumps. The fitting was satisfactory for every sample. The D values thus determined are plotted as a function of inverse temperature in Fig. 4. The data of each sample were fitted well by a straight line and the activation energy ΔE_a was obtained by

$$D = D_0\exp(-\Delta E_a/RT). \qquad (2)$$

The determined ΔE_a values (kJ mol^{-1}) were as follows. THF-17H_2O: 20.9, Ac-17H_2O: 19.5, DXN-17H_2O: 17.7.

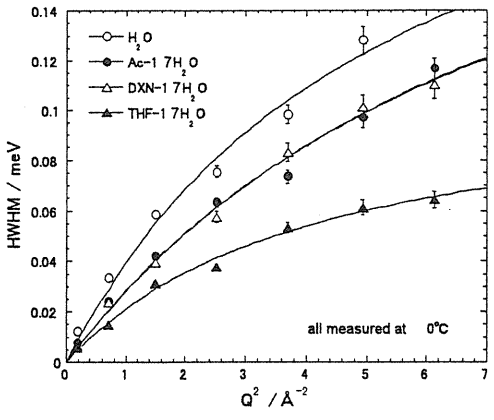


Figure 3: Q dependence of the HWHM (Γ) of the Lorentzian component as a function of Q^2 values for the three clathrate solutions at 0°C.

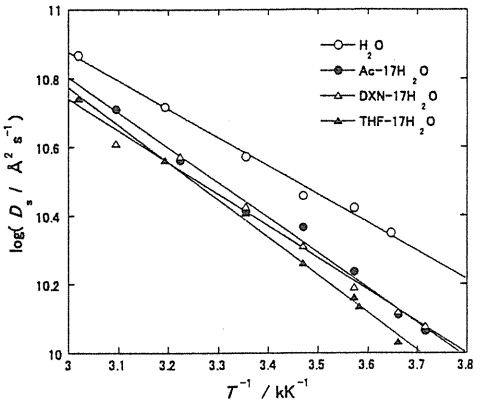


Figure 4: Arrhenius plot for the diffusion coefficient of water molecules in pure water and the clathrate aqueous solutions.

It is of interest that the diffusion of water molecules became remarkably slower by adding only 1/17 mole fraction of the guest molecules. This result suggests that the clathrate aqueous solution has some local cage-like structure (such as in Fig. 2) due to hydrophobic interaction as in clathrate hydrate crystals. There may be a systematic relation between the activation energy and the van der Waals diameter; *i.e.*, the smaller the guest molecule is, the larger the activation energy becomes. For further discussion, it is desirable to measure clathrtae aqueous solutions with smaller guest molecules (*e.g.*, trimethylene oxide, ethylene oxide, *etc.*). We are also planning the neutron diffraction measurement of clathrate aqueous solutions. Thus, the present work has shown that the QENS study of clathrate aqueous solution can provide important information on the formation/dissociation process of clathrate hydrate crystals.

References

[1] D.W. Davidson, in "Water: A Comprehensive Treatise", ed. F. Franks, Plenum Press, New York (1973), Vol. 2, Chap. 3.; O. Yamamuro and H. Suga, J. Therm. Anal. **35**, 2025 (1989).

[2] T. Kajitani et al., Physica B **213&214** (1995) 872.

[3] J. Teixeira et al., Phys. Rev. A **31** (1985) 1913.

This is a blank page.

1. 中性子散乱 5) 高分子

1. Neutron Scattering 5) Polymer

This is a blank page.

研究テーマ： 中性子非干渉性非弾性散乱による配向有限鎖ポリメチレンダイナミックスの固相ー液相変化

表題： 中性子非干渉性非弾性散乱による奇数鎖ヘプタデカン ' 回転相 ' でのダイナミックス

Neutron Qausielastic Scattering Study on 'Rotator' Phase of Heptadecane

1-5-1

N. Achiwa, K. Kumagai

Department of Physics, Kyushu University, 6-10-1 Hakozaki, Higashi-Ku, Fukuoka, 812-6561
present adress:Graduate School of Science, Osaka University, Toyonaka, 560-0043, Japan

Odd-numbered paraffin heptadecane, $C_{17}H_{36}$ is known to have 'Rotator' phase below liquid phase between 284C and 295K, in which the crystal shows space group of Ccmm[1]. Below the 'Rotator' phase it shows crystal phase of Pcam[1]. The lowest accordion mode of Raman scattering spectra of heptadecane at 140cm^{-1} shows clear intensity difference in the crystal, 'Rotator' and liquid phases[2]. We have carried out neutron incoherent quasielastic scattering experiment using TOF spectrometer AGNES with an incident neutron energy 4.59meV at JRR3. Figure 1 shows a temperature dependence of diffusion constant at various temperatures in crytal, rotator, liquid phases of heptadecane determined by the data of qusielastic scattering. The diffusion constants were determined by the linear coefficient of Lorentzian width as a function of Q^2.

For a molecular motion in the 'Rotator' phase, a plausible model is the hindered rotation of the entire alkane chain about its long axis and a translational motion along the chain axis. The former is rapid and frequent than the latter. We will follow Barnes[3] circular rasndom walk(CRW) model for rotational diffusion of a single axis rotator. A hydrogen is located at the i-th site of a circle on whose circumference there are N sites. The calculated incoherent scattering cross-section following.

$$S_{inc}(Q,\omega) = A_N(Q)\delta(\omega) + \pi^{-1}\sum_{l=1}^{N-1} A_l(Q)\frac{\tau_l}{1+(\omega\tau_l)^2} \quad (1)$$

Of course, convolution product with Debye-Waller factor must be carried out.

But the experimental quasielastic scattering is most well fitted with a linear Q^2 dependence of τ of a simple Lorentian curve. Then, CRW model can be reduced to a simple diffusion model with with effective diffusion constant, D_{eff} for the limit of N and d large values.

$$S_{inc}(Q,\omega) = \frac{1}{\pi}\frac{D_{eff}Q^2}{\omega^2 + (D_{eff}Q^2)^2} \quad (2)$$

Figure 1 shows the logarithmic value of D_{eff} plotted against temperature. Compared with the crystal phase at 265 K, the diffusion constal in the rotational phase is large enough comparable with that in liquid phase.

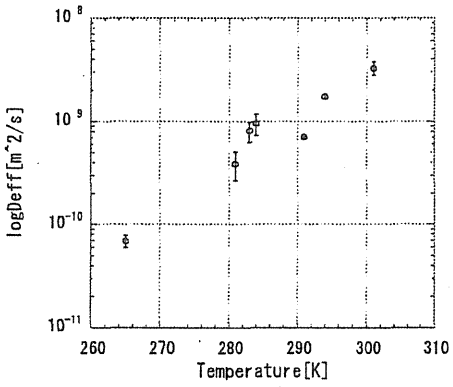


Fig. 1. Temperature dependence of effective diffusion constant D_{eff} at various temperatures in crytal, rotator, liquid phases obtained from the data of qusielastic scattering. The diffusion constants were obtained by the linear coefficient of Lorentzian width as a function of Q^2.

References

[1] J. Doucet *et al.*: J. Chem. Phys. **75** (1981)1523.
[2] N. Achiwa *et al.*: to be published
[3] J. D. Barnes: J. Chem. Phys. **58** (1973) 5193.

使用施設：JRR-3　装置： C3-1-1 (AGNES)，分野： 6. Softmatters

研究テーマ：磁性流体マグネタイト微粒子ブラッグ反射によるドップラーシフト中性子スピンエコー
表題： 磁性流体マグネタイト微粒子ブラッグ反射によるドップラーシフト中性子スピンエコー

Doppler Shift Neutron Spin Echo at Bragg Reflection of Magnetite Particle in Ferrofluid

1-5-2

N. Achiwa[1], H. Nishioka[1], T. Ebisawa[2], M. NIshi[3], K. Nakajima[3], and K. R. Maruyama[4]

[1] *Department of Physics, Kyushu University, Higashi-Ku, Fukuoka, 812-8581*
Present aderess: Graduate School of Science, Osaka University, Toyonaka 560-0043, Japan
[2] *Japan Atomic Energy Research Institute, Tokai, Ibaraki, 319-1195, Japan*
[3] *Institute for Solid State Physics, The University of Tokyo, Shirakata, Tokai, 319-1106, Japan*
[4] *Advanced Science Research Center, JAERI, Tokai, Ibataki, 319-1195, Japan*

Velocities of magnetite particle crystals in heavy water based ferrofluid have been studied by neutron spin echo PONTA in JRR-3M at the Bragg positions, following the previous report[1][2]. Moving and rotating magnetite particle crystals in ferrofluid bring Doppler shift of neutron velocity at Bragg reflection though the scattering is elastic. This change of velocity is firstly measured by neutron spin echo (NSE) spectrometer as the function of Larmor precessions. Since the structure factor of (311) Bragg reflection is mainly nuclear scattering, the decay of NSE signal is interpreted as Doppler velocity shift due to Brownian motion of magnetite crystals, such as translational and rotational motions. The spin echo signals of (311) Bragg reflection show rather simple decay up to the number of Larmor precession, 967 turns. The estimated velocity distributions from equation (1) are 1.5 ± 0.2 m/s and 1.2 ± 0.1 m/s at 295 K and 317 K, respectively.

$$P_{NSE} = P_0 cos(\delta N) =< cos(N_0 \frac{\delta v}{v_0}) > . \quad (1)$$

Usually NSE signal is plotted against spin echo Fourier time for inelastic scattering, while for Doppler shift scattering, against number of Larmor precession it should be plotted[2].

The spin echo signals of magnetic (111) reflection show spin flip scattering of which visibility should be below 1/2. The experiment of small angle scattering on the ferrofluid with weight % of magnetite from 1.3% to 40.5% concludes that the particle radius is 4.2 ± 0.2 nm, the cluster radius is 17.8 ± 0.2 nm and the neighboring average distance is around 11.3 ± 1.1 nm at 298 K.

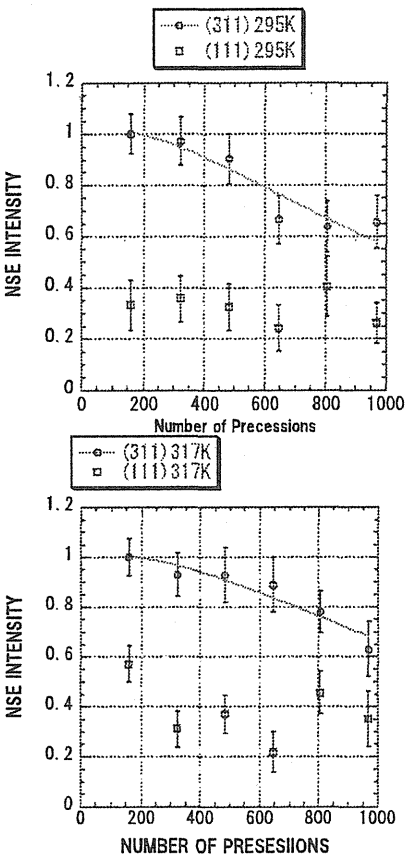


Fig. 1. (a),(b): NSE signals for a nuclear (311) and a magnetic(111) Bragg reflections of magnetite particles in the ferrofluid of 40.5 wt% at temperatures 295 K(1a) and 317 K(1b), which are normalized by NSE signal of Al(111) Bragg reflection. Theoretical curves are fitted with a simple exponential decay function.

References

[1] N. Achiwa *et al.*: Activity Rep. on Neutron Scattering Research **9** (2002) 195.

[2] N. Achiwa *et al.*: Physica **335/1-4** (2003)104.

使用施設：JRR-3　　装置： G5 (PONTA)，分野： 6, Softmatters

研究テーマ：複合膜の静的および動的構造
表題：界面活性剤／水系の秩序構造に及ぼすゲスト疎水性分子の影響

1-5-3 Effects of Guest Hydrophobic Molecule on Stability of Ordered Meso Structure of a Surfactant/Water System

M. Imai, I. Takahashi and K. Nakaya

Department of Physics, Ochanomizu University, Otsuka, Bunkyo, Tokyo 112-8910, Japan

Block copolymers and surfactant/water systems show various ordered meso-phases. These structures are stabilized by the balance of the interfacial energy and conformational entropy of molecular chains. Addition of guest molecules to the ordered meso phases affects the conformations of the molecular chains in the microstructure and brings a unique order-order transition. The purpose of this study is to elucidate the guest molecule induced order-order transition in the surfactant/water/ hydrophobic guest molecule system.

Addition of the hydrophobic guest molecule ($C_{12}H_{26}$) into the 55 wt% $C_{16}E_7/D_2O$ system modifies the phase behavior. We will examine the distribution of the added guest molecule in the lamellar layer and the interfacial structure using a small angle neutron scattering (SANS) technique. The system can be described by a three layer model consisting of water layer, hydrophilic interfacial layer and hydrophobic layer (hydrophobic group of the surfactant and hydrophobic guest molecule). In order to extract the structural parameters, the scattering profiles for the system at 57.5。C were fitted by the model scattering function for the lamellar structure proposed by Nallet et al.

Figure 1(a) shows the variation of the hydrophobic layer thickness d as a function of ϕ_{C12H26} and a solid line is the expected dependence of the hydrophobic layer thickness assuming that the added guest molecules are completely segregated in the center of bilayer. The hydrophobic layer width d increases linearly as ϕ_{C12H26} (ϕ_{C12H26}: volume fraction of dodecane) increases, although the values are somewhat smaller than the expected values assuming completely segregation. Thus the $C_{12}H_{26}$ molecule is mostly segregated from the hydrophobic part of surfactant molecules, but partially penetrates into the hydrophobic part. The partially penetrated molecules increase the surface area per surfactant molecule, which brings the decrease of thickness of the hydrophilic part due to the connectivity. The ratio σ/d of the interfacial thickness to the lamellar spacing decreases with the addition of hydrophobic guest molecules as shown in Fig. 1(b). Thus the addition of the hydrophobic guest molecules into the surfactant/water system brings sharp boundary of the surfactant bilayer, which causes the order-order transition as predicted by the numerical calculation by Teramoto et al.

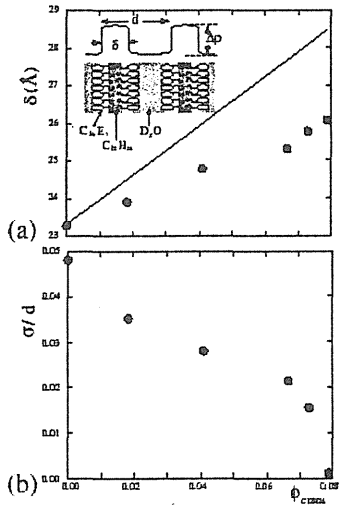


FIG. 1: (a) Dependence of hydrophobic width on added C12H26 volume fraction and schematic illustration of a three layer model. (b) Dependence of interfacial thickness on added $C_{12}H_{26}$ volume fraction.

使用施設：JRR-3.　装置：SANS-U(C1-2)，分野 Softmatter

研究テーマ：非イオン界面活性剤が作るラメラ相の構造に対するずり流動場効果と膜のダイナミックス

表題：ずり流動場による非イオン界面活性剤/水系のラメラ面間隔の変化

Change in Lamellar Spacing in Nonionic Surfactant/Water System by Shear Flow

1-5-4

T. Kato, K. Minewaki, K. Miyazaki, Y. Kawabata, and M. Imai*

Department of Chemistry, Tokyo Metropolitan University, Hachioji, Tokyo 192-0397, Japan
** Department of Physics, Ochanomizu University, Bunkyo, Tokyo 112-0012, Japan*

In recent years, much attention has been paid to the effects of shear flow on the structure of a lamellar phase by using microscopy and various scattering techniques. In the previous studies [1], we have measured small-angle neutron scattering (SANS) on a 55wt% lamellar phase of nonionic surfactant $C_{16}H_{33}(OC_2H_4)_7OH$ ($C_{16}E_7$) in D_2O at 55 and 70°C under shear flow for the shear rates 10^{-3} – 10^2 s^{-1} much lower than those for other studies reported so far. It has been shown that both the position and the intensity of the first reflection changes abruptly in the range 0.3 – 1 s^{-1}. In the present study, measurements have been made for the sample containing 40 and 48 wt% of $C_{16}E_7$ at 70°C. We have found that the repeat distance decreases significantly by shear flow, suggesting local phase separation.

Measurements of SANS were carried out at the instrument SANS-U of Institute for Solid State Physics of University of Tokyo in JRR-3M at Tokai with a Couette shear cell [2].

Figure 1 shows examples of the observed diffraction patterns for different shear rates. In the range 0 – 0.3 s^{-1}, the diffraction intensity decreases with increasing shear rate while the repeat distance (d) does not change very much. At 1 s^{-1}, d is reduced suddenly from 7.2 nm to about 5 nm. With the further increase in the shear rate, d increases slightly. So d takes a minimum value (referred to as d^* hereafter). Such a specific shear rate dependence of d has been obtained for three different orientations of lamellae, i.e., perpendicular, parallel, and transverse orientations.

From the results obtained for the samples containing 40, 48, and 50wt% of $C_{16}E_7$, it has been found that d^* depends on concentration only slightly in spite of the variation of the repeat distances at rest (d_0). Moreover, d^* is nearly equal to the total film thickness, i.e., the sum of the thicknesses of the hydrophobic and hydrophilic layers at rest obtained from analyses of peak position and line shape of small angle X-ray scattering reported before [3]. These results suggest that the water layer between the films is excluded and local phase separation is induced by shear flow.

References

[1] K. Minewaki et al. J. Thermal Analysis Calorimetry **57** (1999) 753, Studies in Surface Science and Catalysis **132** (2001) 185.
[2] Y. Takahashi et al., J. Soc. Rheol. Jpn. **28** (2000) 187.
[3] K. Minewaki et al. Langmuir **17** (2001) 1864.

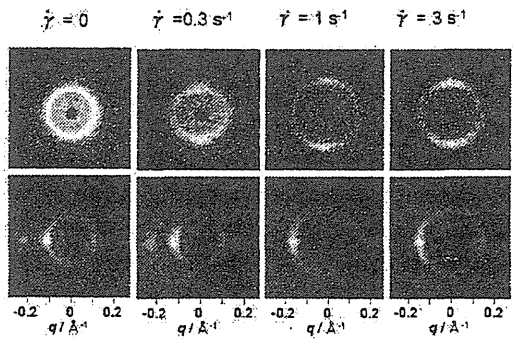


Fig. 1 Examples of the observed diffraction patterns for radial (top) and tangential (bottom) configurations for different shear rates at 48 wt% and 70°C.

使用施設：JRR-3　装置：SANS-U(C1-2)，分野 Softmatter

研究テーマ：界面膜ダイナミクスのdroplet濃度依存性
表題：AOT系マイクロエマルションにおける準希薄droplet相でのダイナミクス

A Dynamic Behavior of a Semi-Dilute Droplet Phase in a Ternary Microemulsion Consisting of AOT

1-5-5

M. Nagao[1], H. Seto[2], N. L. Yamada[3], and M. Shibayama[1]
[1] *Institute for Solid State Physics, The University of Tokyo, Tokai, 319-1106*
[2] *Faculty of Science, Kyoto University, Kyoto, 606-8502*
[3] *Grad. School of BioSphere Sci., Hiroshima Univ., Higashihiroshima, 739-8521*

A mixture of AOT (Aerosol-OT; dioctyl sulfosuccinate sodium salt), D_2O, and oil forms stable water-in-oil droplet microemulsion in the vicinity of room temperature. The static and the dynamic structures of this system have been well investigated by means of small-angle x-ray and neutron scattering (SAXS and SANS), dynamic light scattering (DLS), and neutron spin echo (NSE).[1, 2, 3, 4] By using these scattering methods, it is expected to be observed a form factor of the spherical droplet at the low droplet density, ϕ, region. On the other hand; at the high ϕ region, contributions of both the form factor and a structure factor are expected and the coupling of these essential scattering makes the data analysis being difficult even for SANS or SAXS.

Recently, we performed a contrast variation SANS experiment at the SANS-U spectrometer with varying ϕ. We introduced a relative form factor in order to analyze the SANS profiles.[5] Because it is able to be assumed that the structure factor is the same when only the scattering contrast of samples is changed with the same composition of ingredients, the division of the scattering intensities from the different contrast samples shows a ratio of each form factor. Therefore, this method allows one to estimate a form factor without the influence of the structure factor, and a model independent structure factor is also obtained. The results showed that the radius of droplets did not change, while the polydispersity decreased with increasing ϕ below $\phi \sim 0.6$. Above $\phi \sim 0.6$, the radius of droplets decreased and the polydispersity increased. This shows that the deformation of the water droplets occur at high ϕ. The obtained structure factor shows an existence of attractive interactions among the water droplets at low ϕ, while that repulsive interactions among the droplets determines the packing properties of the droplets at high ϕ.

Considering the dynamic properties of the droplet microemulsions at low ϕ region, a translational diffusion and a deformation of the droplets are the mainly observable modes in the dynamic range of the NSE spectroscopy.[6] At the concentrated droplet regions, an additional dynamic mode due to the fluctuations of the structure factor is expected. Therefore, in order to understand the dynamical properties of the microemulsion systems, it is necessary to discuss the fluctuations of the form factor and the structure factor separately.

For the first step, we performed a NSE experiment on AOT/water/*n*-decane microemulsion system at ISSP-NSE installed at C2-2 port of JRR3M in JAERI, Tokai. In order to discuss the dynamic mode as well as the static structure, the molar ratio of water to AOT was selected to be 38.2, so that the droplet size was expected to be the same as the previous SANS measurement.[5] ϕ was selected to be 0.3 and the measurement was done for two contrast samples; one is the bulk contrast ($AOT/D_2O/C_{10}H_{22}$) and the other is the film contrast ($AOT/D_2O/C_{10}D_{22}$). At the concentration, results of a DLS measurement performed by Sheu *et al.*[2] showed a non-single exponential decay curve and it was explained by the stretched exponential form with the stretched exponent β of about 0.8. This discrepancy of the value of β from unity is considered as the packing properties of the water droplets.

In Fig. 1, the obtained intermediate correlation functions, $I(q,t)$, for the bulk contrast sample are shown. It is difficult to conclude

使用施設：JRR-3, 装置：C2-2 (NSE), 分野：6. Softmatter

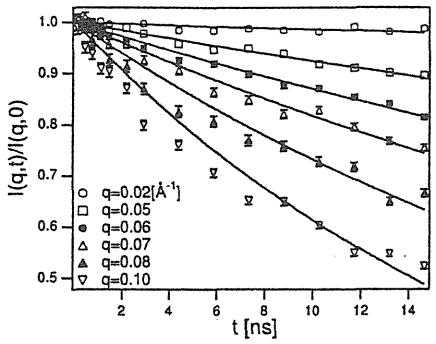


Fig. 1. The observed intermediate correlation function from the bulk contrast sample. The solid lines indicate results of fitting according to eq. (1).

that these decay curves follow the single exponential functions or the stretched exponential functions. As a preliminary data analysis, it is assumed that the main contribution to $I(q,t)$ comes from the shape fluctuations, and we used a model proposed by Milner and Safran[7] in order to compare results from the bulk with that from the film contrast. The fitting function is as follows;

$$I(q,t)/I(q,0) = \exp(-\Gamma t), \qquad (1)$$

$$\Gamma = D_{\rm eff} q^2, \qquad (2)$$

where, Γ and $D_{\rm eff}$ are the decay rate and the effective diffusion coefficient of water droplets, respectively. $D_{\rm eff}$ is expressed as,

$$D_{\rm eff}(q) = D_{\rm tr} + D_{\rm def}(q). \qquad (3)$$

$D_{\rm tr}$, which does not depend on q, is the translational diffusion coefficient of water droplets and $D_{\rm def}(q)$ the diffusion coefficient due to the deformation of water droplets.

Figure 2 shows the SANS profile and the q dependence of $D_{\rm eff}$ from the bulk contrast (Fig. 2(a)) and from the film contrast (Fig. 2(b)). In Fig. 2(a), $I(q)$ shows a slight peak due to packing of the water droplets at $q \sim 0.035$Å^{-1}. At almost the same q, a dip was obtained from $D_{\rm eff}$. This indicates that the elastic component mainly contributes to the scattering at $q \sim 0.04$Å^{-1}. In Fig. 2(b), $I(q)$ shows a dip at $q \sim 0.05$Å^{-1} and $D_{\rm eff}$ has a peak at the same q. The peak of $D_{\rm eff}$ in Fig. 2(b) indicates that the inelastic component is

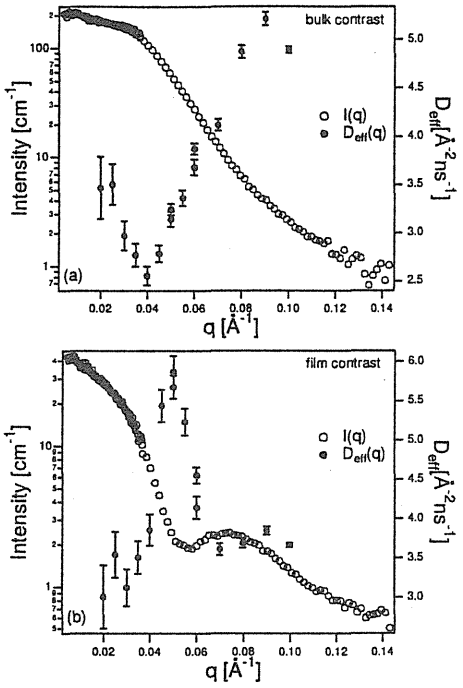


Fig. 2. The comparisons of the SANS profile and the effective diffusion coefficient obtained by NSE (a) for the bulk contrast and (b) for the film contrast.

relatively larger than the other q scale. This length scale is the same as the radius of the water droplets. Therefore, the deformation motion of the water droplets appears at this q range.

References

[1] M. Kotlarchyk *et al.*: Phys. Rev. A **29** (1983) 2054.

[2] E.Y. Sheu *et al.*: Phys. Rev. A **39** (1989) 5867.

[3] H. Seto *et al.*: J. Chem. Phys. **115** (2001) 9496.

[4] M. Nagao *et al.*: J. Chem. Phys. **115** (2001) 10036.

[5] M. Nagao *et al.*: J. Appl. Cryst. **36** (2003) 602.

[6] J.S. Huang *et al.*: Phys. Rev. Lett. **59** (1987) 2600.

[7] S.T. Milner and S.A. Safran: Phys. Rev. A **36** (1987) 4371.

研究テーマ： 非イオン性界面活性剤系マイクロエマルションの静的、動的構造に及ぼす圧力効果

表題： 非イオン性界面活性剤、水、油マイクロエマルションの圧力誘起構造相転移

Pressure-Induced Phase Transition in a Microemulsion Composed of Non-ionic Surfactant, Water, and Oil

1-5-6

M. Nagao[1], D. Ihara[2], H. Seto[3], and T. Takeda[2]

[1] *Institute for Solid State Physics, The University of Tokyo, Tokai, 319-1106*

[2] *Fac. of Int. Arts and Sciences, Hiroshima Univ., Higashihiroshima, 739-8521*

[3] *Faculty of Science, Kyoto University, Kyoto, 606-8502*

Recently, self-assemble mechanisms in microemulsion systems are widely investigated. We have demonstrated the pressure dependences of the static and the dynamic structures in microemulsion consisting of AOT (dioctyl sulfossucinate sodium salt), water and *n*-decane.[1, 2] In the system, increasing temperature and increasing pressure shows almost the same phase behavior. On the other hand; the dynamic structure is quite different. This experimental result was interpreted as follows; a counter-ion dissociation from the head group of AOT molecules occurs and repulsive interaction between the head groups increased with increasing temperature, while attractive interaction among the tail groups of AOT molecules increased with increasing pressure.

In this case, the counter-ions affect the physical properties of the surfactant monolayers. In order to understand the characteristic and/or the universal features of surfactant monolayers, pressure effects on the dynamical behavior on a different type of the surfactant monolayers should be clarified. A non-ionic surfactant $C_{12}E_5$ is a typical surfactant to form a microemulsion, and the static and the dynamic structures have been well investigated by many researchers. However, only a few experiments with the variation of pressure have been done so far.[3]

A small-angle neutron scattering (SANS) experiment was performed at the SANS-U spectrometer installed at C1-2 port of JRR3M in JAERI, Tokai. The covered momentum transfer, q, was ranged over $0.008 \leq q \leq 0.3\text{Å}^{-1}$. Both the bulk and the film contrast samples were measured, and two compositions of samples were prepared; the ratio of the volume fraction of oil and that of surfactant was kept to be 1.37:1, and the volume fraction of water, Φ_w, was selected to be 0.62 and 0.37. $C_{12}E_5$ and C_8H_{18} were purchased from Tokyo Kasei Co., D_2O from CDN Isotopes, and C_8D_{18} from Aldrich Chemical Co., respectively. These materials were mixed in weight without any further purification.

Figure 1 shows the obtained temperature-pressure phase diagram from the film contrast sample of $\Phi_w = 0.62$. The phase diagram obtained from the bulk contrast sample was almost the same. At lower temperature region, a pressure-induced phase transition from the lamellar, L_α, to the droplet, L_1, phase with the coexisting region in between was observed. At high temperature region, another pressure-induced phase transition from the bicontinuous microemulsion, L_3, to L_α was observed. The phase boundaries show the positive slope ($\frac{dT}{dP} > 0$), and it indicates that increasing pressure gives the same effects as the lowering temperature.

Figure 2 shows the pressure dependence of the SANS profiles from the film contrast sample at $T = 310$K for $\Phi_w = 0.62$. The scattering intensity of the correlation peak

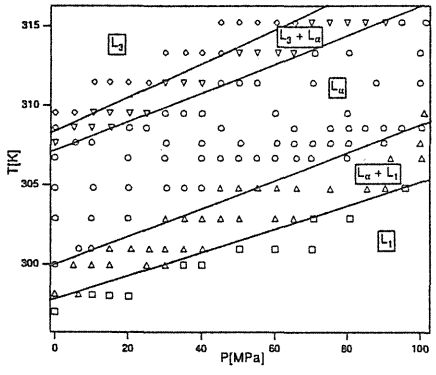


Fig. 1. Obtained phase diagram of $C_{12}E_5$, D_2O, and $C_{10}D_{22}$ for $\Phi_w = 0.62$ of the film contrast sample.

使用施設：JRR-3　装置： C1-2 (SANS-U)，分野： 6. Softmatter

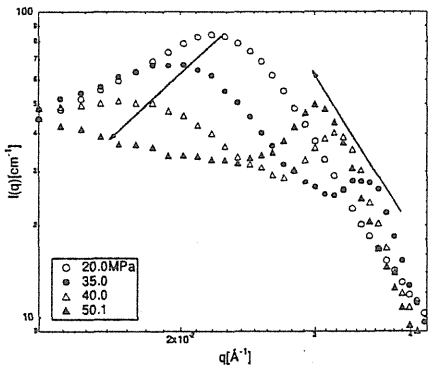


Fig. 2. The observed pressure dependence of the SANS profiles from the film contrast sample for $\Phi_w = 0.62$ at $T = 310$K.

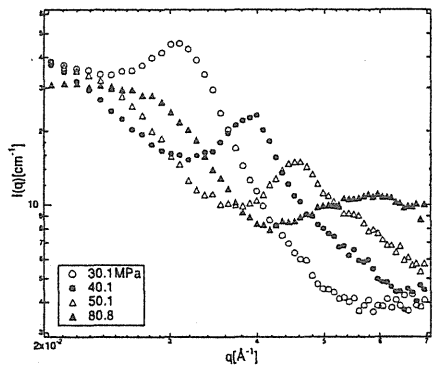


Fig. 3. The observed pressure dependence of the SANS profiles from the film contrast sample for $\Phi_w = 0.62$ at $T = 300$K.

from L_3, appeared at lower q, decreased with increasing pressure with the peak position shifting to the lower q. On the other hand; the scattering intensity of the peak from L_α, appeared at higher q, increased with increasing pressure.

In Fig. 3, a pressure dependence of SANS profiles from the film contrast sample at $T =$ 300K for $\Phi_w = 0.62$ is shown. In this case, a peak position of L_α was shifted to higher q with increasing pressure, and a scattering profile from L_1 was observed at high pressure.

For $\Phi_w = 0.37$ another scattering profile was observed at low temperature and high pressure region as shown in Fig. 4. The multi-peak profile shows a ratio of $1{:}\sqrt{3}{:}\sqrt{7}$ for the peak position. The bcc or the hexag-

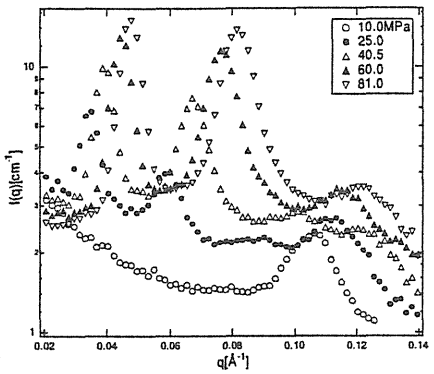


Fig. 4. The observed pressure dependence of the SANS profiles from the film contrast sample for $\Phi_w = 0.37$ at T =300K.

onal structure can have this peak assignment. Leaver *et al.*[5] showed an existence of the hexagonal structure at low temperature in $C_{12}E_5$/water/n-decane system. At $T = 292$K and $P = 0.1$MPa, we observed almost the same SANS profile with the high pressure multi-peak profile. Therefore, the multi-peak profile shows the hexagonal structure as it is observed at low temperature.

The present SANS results indicate that increasing pressure plays the same role as decreasing temperature in $C_{12}E_5$/water/n-octane system. In order to understand the effects of pressure on this system, however, the elastic properties of surfactant monolayers should be discussed. In the present system, mobility of surfactant tails mainly affects to the elastic properties of the monolayers. Therefore, not only the phase behavior and the static structural parameters but also the bending modulus of the monolayers should be elucidated in future.

References

[1] M. Nagao *et al.*: J. Chem. Phys. **115** (2001) 10035.

[2] Y. Kawabata *et al.*: Appl. Phys. A **74** (2002) s534.

[3] J. Eastoe *et al.*: J. Phys. Soc. Faraday Trans. **90** (1994) 3121.

[4] S. Ferdinand *et al.*: Langmuir **16** (2000) 10106.

[5] M.S. Leaver *et al.*: J. Chem. Soc. Faraday Trans. **91** (1995) 4269.

研究テーマ：界面活性剤／水系ラメラ相で観測される揺らぎと秩序-秩序転移の関係
表題：界面活性剤／水系ラメラ相における最小安定揺らぎモードのダイナミクス

1-5-7 Dynamical Nature of Least Stable Fluctuation Modes of Lamellar Structure Observed in a Nonionic Surfactant/Water System

M. Imai, K. Nakaya, T. Kawakatsu[1] and H. Seto[2]

Department of Physics, Ochanomizu University, Otsuka, Bunkyo, Tokyo 112-8910, Japan
[1]Department of Physics, Tohoku University, Aoba, Sendai 980-8578, Japan
[2]Department of Physics, Kyoto University, Sakyo, Kyot606-8502, Japan

An interesting feature of the ordered mesophases observed in surfactant/water systems is the appearance of the double-gyroid (DG) phase that has a three dimensional periodic constant mean curvature (CMC) surface.

From the phase transition kinetics point of view, a characteristic rhombohedral (R) network structure is observed on the kinetic pathway from lamellar (L) phase to DG phase experimentally. The intermediate structure is a metastable state and transforms to the most stable DG phase spontaneously. Furthermore, a modulation fluctuation layer (MFL) structure appears prior to the L to R transition. A small angle x-ray scattering study reveals that the MFL is the least stable fluctuation modes (LSFMs) of the lamellar structure predicted by Qi and Wang. In this study we investigate the dynamic nature of the MFL using a neutron spin echo (NSE) technique.

The intermediate scattering functions of the undulation fluctuation layer structure (UFL) at 51 °C and the MFL structure at 36°C are shown in Figure 1. Here we assume that the $S(Q,t)$ profile consists of two components, the undulation fluctuation mode and the modulation fluctuation mode. Then, the obtained intermediate scattering functions were fitted by a double-exponential function

$$S(Q,t) = a(Q)\exp(-\omega_1(Q)t) + (1-a(Q))\exp(-\omega_2(Q)t) \quad (1)$$

where ω_1 and ω_2 are relaxation rates.

In Figure 2 we show temperature dependence of the relaxation rate ω_1 and ω_2 at Q=0.075 Å^{-1}. Decreasing the temperature from the L phase to the R phase, the ω_1 does not show significant temperature dependence. On the other hand, the ω_2 decreases linearly with decreasing the temperature and then reaches an equilibrium value just before T_{LR}=34°C (T_{LR}: L to R transition temperature). At T_{LR} the ω_2 jumps suddenly, indicating transition to the R phase. This ω_2 behavior agrees well with the temperature dependence of the diffuse scattering intensity at Q=0.075 Å^{-1} observed in the SAXS measurements as shown in Figure 2. Thus the behavior of ω_2 mode is governed by the diffuse scattering of the MFL structure, or the LSFMs of L structure.

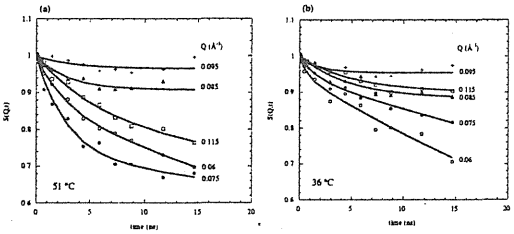


Figure 1. Typical NSE relaxation profiles for (a) the UFL structure at 51°C and (b) the MFL structure at 36°C.

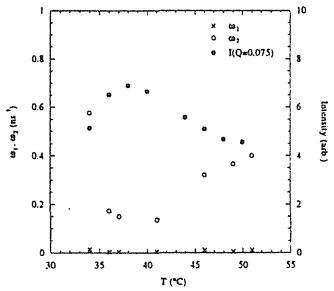


Figure 2. Temperature dependence of the relaxation rate ω_1 and ω_2 at Q=0.075 Å^{-1} with that of the diffuse scattering intensity at Q=0.075 Å^{-1}.

使用施設：JRR-3　装置：SANS-U(C1-2), NSE(C2-2) 分野 Softmatter

研究テーマ： 非イオン性界面活性剤系マイクロエマルションの静的、動的構造に及ぼす圧力効果

表題： 三元系マイクロエマルションのラメラ構造における動的振る舞いへの圧力効果

1-5-8 Pressure Effects on the Dynamical Properties of the Lamellar Structure in a Ternary Microemulsion

M. Nagao[1], D. Ihara[2], H. Seto[3], and T. Takeda[2]

[1] *Institute for Solid State Physics, The University of Tokyo, Tokai, 319-1106*

[2] *Fac. of Int. Arts and Sciences, Hiroshima Univ., Higashihiroshima, 739-8521*

[3] *Faculty of Science, Kyoto University, Kyoto, 606-8502*

As described in another report in this issue, increasing pressure and decreasing temperature play the same role in the phase behavior in $C_{12}E_5$, water, and octane system.[1] In order to understand the effects of pressure on this system, the elastic properties of surfactant monolayers were investigated by means of neutron spin echo spectroscopy (NSE). The measurement was done at the ISSP-NSE installed at C2-2 port of JRR3M in JAERI, Tokai. The composition of the sample was the same as $\Phi_w = 0.37$ measured by SANS, and the film contrast was used. In this experiment, temperature was kept to be 305K and pressure was set at 0.1, 41.5, and 80.4MPa. At these conditions the lamellar structure is formed as shown in Fig. 1.

In Fig. 2, the observed intermediate correlation function, $I(q,t)$, at $T = 305$K and $P = 80.4$MPa is shown. The solid lines in the figure are the fitting results according to the stretched exponential function, $I(q,t)/I(q,0) = \exp[-(\Gamma t)^{2/3}]$, where Γ is the decay rate and t the time.

In Fig. 3, the obtained q dependence of Γ is shown. In this result, no typical pressure dependence of the dynamical structure was observed. However, it is the possibility that the slight increase of Γ at $P = 80.4$MPa is observed because the condition is close to the phase boundary between the lamellar and the hexagonal.

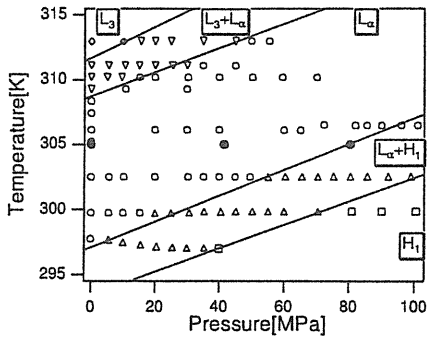


Fig. 1. The observed temperature-pressure phase diagram. Open marks were measured points by SANS and full circles by NSE.

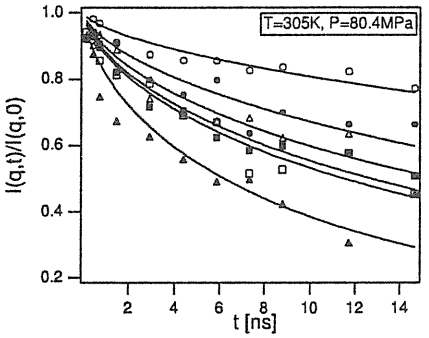


Fig. 2. Obtained intermediate correlation functions, $I(q,t)$, in $C_{12}E_5$, D_2O, and $C_{10}D_{22}$ for $\Phi_w = 0.37$ at various q.

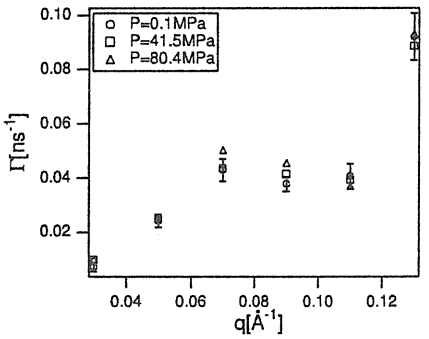


Fig. 3. The observed pressure dependence of Γ. No typical pressure dependence was observed.

References

[1] M. Nagao *et al.*: NSL-ISSP Activity Report (in this issue) **10** (2003).

使用施設：JRR-3' 装置： C2-2 (NSE)， 分野： 6. Softmatter

研究テーマ： リン脂質膜の圧力誘起 interdigitated 構造
表題： DPPC/水/エタノール系の interdigitated 相近傍における膨潤ゲル相

A swollen gel phase neighboring the interdigitated phase observed in aqueous solution of DPPC with or without ethanol.

1-5-9

H. Seto[1], N. L. Yamada[2], H. Nobutou[2], M. Nagao[3] and T. Takeda[2]
[1] *Department of Physics, Kyoto University, Sakyo, Kyoto 606-8502*
[2] *Faculty of Integrated Arts and Sciences, Hiroshima University, Higashihiroshima 739-8521*
[3] *Institute for Solid State Physics, The University of Tokyo, Tokai 319-1106*

An aqueous dispersion of dipalmitoyl-sn-glycero-3-phosphatidylcholine (DPPC) exhibits a rich structural polymorphism depending on their environmental conditions such as temperature and pressure. A fluid lamellar phase (L_α) is characterized by ordered stacking of lipid bilayers at about 60 Å. Two thermotropic lamellar phase transitions have been observed below the fluid lamellar phase; a gel-to-gel (L'_β / P'_β) pretransition and a gel-to-liquid crystalline (P'_β /L_α) main transition. The P'_β phase is characterized not only by the regular stacking of bilayers, whose characteristic repeat distance is about 60 Å, but also by the intrabilayer ripple structure, whose repeat distance is 160 Å. However, this structure does not immediately formed when temperature is decreased crossing the main transition temperature. The system stays at a metastable phase, $P'_{\beta(\mathrm{mst})}$, in which the ripple bilayers do not stack regularly. By applying pressure up to about 150 MPa, it transforms to a different gel phase called the interdigitated phase ($L_{\beta I}$). This structure is the same as the one induced by adding ethanol, [?] however, the microscopic origins of these transitions must not be the same and the difference between the pressure and the ethanol effects on structural formation should be clarified. [?]

Recently, the authors have found a new phase in the region at $45 \leq T \leq 55$°C and $15 \leq P \leq 60$MPa, where among L_α, P'_β, and $L_{\beta I}$ phases, in an aqueous solution of DPPC with small amount of ethanol (0.7 M and 0.8 M). [?] In this phase, a characteristic repeat distance was a little larger than that of the other phases, for example, $d = 81.2$Åat $T = 48$°C and $P = 40$MPa for 0.8M ethanol; a thickness of the lipid bilayer was 47.5 Å, which is almost the same as the gel phases, and only a thickness of water between bilayers was larger than the other phases. Thus the authors named this phase as a "swollen gel phase"; only the amount of water between bilayers increases, and the structure of the phospholipid bilayer is the same as that of the ripple-gel phase.

The purpose of the present small-angle neutron scattering study was to confirm the existence of the swollen gel phase and characterize its detailed behaviors. The experiments were performed at SANS-U, and a new high-pressure cell developed by Teramex Co. was used to apply pressure up to 200 MPa. 15 wt% of DPPC was dissolved in mixtures of D_2O and ethanol, whose ethanol contents were 0, 0.3, 0.5, 0.7, 0.8 and 1.2M.

For all the samples measured, the swollen gel phase was observed between the liquid crystalline (L_α) phase and the interdigitated

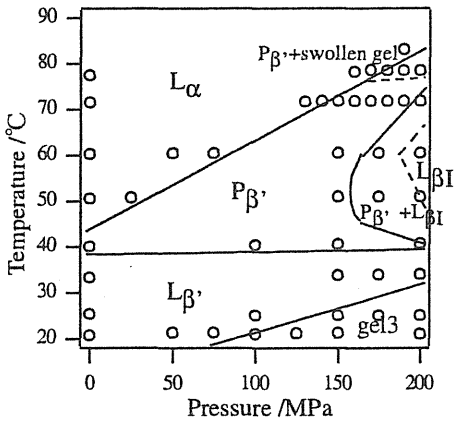


Fig. 1. Obtained phase diagram of DPPC and D_2O without adding ethanol. It has been confirmed that the appearance of the swollen gel phase is not the effect of ethanol. The open circles indicate points measured by SANS.

使用施設：JRR-3I　装置： C1-2 (SANS-U)，分野： 6. Softmatter

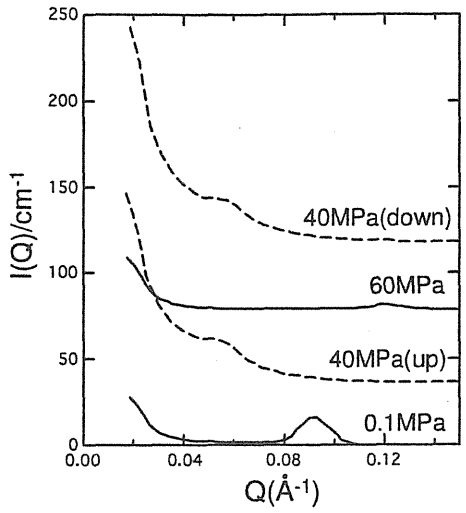


Fig. 2. Pressure dependence of SANS profile at 45 °C for DPPC/D_2O/ethanol(0.8M). Pressure was increased from ambient pressure (P = 0.1MPa) to 60 MPa, and decreased to 40 MPa. The swollen gel phase (dashed line) was observed both when increased pressure from L_α phase and when decreased pressure from $L_{\beta I}$ phase.

($L_{\beta I}$) phase. A position of this phase in the $P-T$ phase diagram depended on the ethanol concentration; both temperature and pressure decreased with increasing ethanol. This phase was observed even in the binary mixture of DPPC and D_2O. (See Fig. 1.) Thus adding ethanol is not essential to have the swollen gel phase. In Fig. 2, typical pressure dependence of the SANS profile for DPPC/D_2O/ethanol(0.8M) at T = 45°C is shown. The result indicates that the swollen gel phase appeared both with increasing and decreasing pressure. This structure could be characterized as an intermediate phase, which could be a precursor to the interdigitated phase.

The structural formations with increasing temperature from the P'_β phase and decreasing temperature from the L_α phase were also compared. Unlike the case of pressure, the swollen gel phase was observed only when the temperature decreased from the L_α phase. These result suggested that the swollen gel is a metastable phase similar to the $P'_{\beta(\mathrm{mst})}$ phase.

References

[1] T. Adachi *et al.*: Biophys. J., **68** (1995) 1850.
[2] R. Winter and W. C Pilgrim: Ber. Bunsenges. Phys. Chem., **93** (1989) 708.
[3] H. Seto *et al.*: J. Appl. Cryst.

研究課題:両親媒子系複雑液体のスローダイナミックス
表題:中性子スピンエコー法による DPPC/D_2O/$CaCl_2$ 系における脂質二重層膜のスローダイナミクスの研究

1-5-10

Neutron Spin Echo Study on Slow Dynamics of Lipid Bilayers in the DPPC/D_2O/$CaCl_2$ System

T. Takeda[A], N. L. Yamada[B], Y. Kawabata[C], H. Seto[D] and M. Nagao[E]

[A] *Faculty of Integrated Arts and Sciences, Hiroshima University, Higashi-Hiroshima 739-8521, Japan*
[B] *Graduate School of Bio-Sphere Science, Hiroshima University, Higashi-Hiroshima 739-8521, Japan*
[C] *Graduate School of Science, Tokyo Metropolitan University, Hachioji 192-0397, Japan*
[D] *Graduate School of Science, Kyoto University, Kyoto 606-8502, Japan*
[E] *NSL, ISSP, University of Tokyo, Tokai, Naka, Ibaraki 319-1106, Japan*

In order to study the dynamics in undulation of lipid bilayers, NSE experiments were carried out on the dilute lamellar phase of the dipalmitoylphosphatidylcholine (=DPPC)/D_2O /$CaCl_2$ system with the lamellar repeat distance d_l longer than 500 Å in order to avoid the effect on the single membrane dynamics from neighbouring sheets of membranes.

Small angle neutron scattering (SANS) experiments were carried out again in order to examine the dependence of SANS profiles on the sample preparations using SANS-U at C1-2 port of JRR-3M in JAERI(Tokai). In SANS experiments, we observed the peaks corresponding to d_l for lipid samples in which DPPC dispersed in D_2O solutions with 7mM $CaCl_2$. On the other hand, we did not observed such peaks for the samples with d_l larger than 280Å in small angle X-ray scattering (SAXS) experiments using BL15A at PF in KEK and BL40B2 at SPring8. In the SAXS experiments, we observed the scattering corresponding to the correlation between the polar head parts of a lipid bilayer instead of the lamellar peaks. The disapprearance of diffraction peaks in SAXS reflects the X-ray form factor of a lipid bilayer for the lamellar peaks which approaches to zero because the undulation of the bilayer increases with increasing d_l. The values of d_l obtained from the SANS experiments are roughly in inverse proportion to the DPPC concentration C in the dilute lamellar region as shown in Fig. 1.

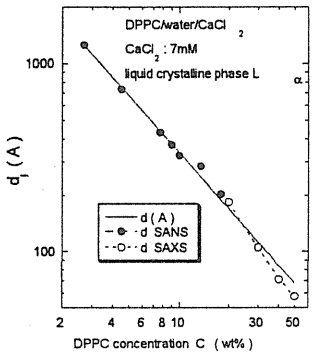


Fig. 1. DPPC cencentration C dependence of the lamellar repeat distance d_l. The solid line indicate C^{-1} proportionality.

The neutron spin echo (NSE) experiments were performed using ISSP-NSE at C2-2 port of JRR-3M in JAERI(Tokai). The scattering vector Q and time t dependent intermediate functions $I(Q,t)$ obtained from the NSE experiments using ISSP-NSE were well fitted to the following equation,

$$I(Q,t) = I(Q,0) \exp[-(\Gamma t)^{2/3}] \quad . \quad (1)$$

The relaxation Γ obtained from the fitting to Eq.(1) increased as Q^3 over the range of Q from 0.05 $Å^{-1}$ to 0.14 $Å^{-1}$. So with the case of the non-ionic surfactant n-dodecyl pentaoxyl-ethylene glycol ether ($C_{12}E_5$)/n-octane/ D_2O system[1], these NSE

使用施設:JRR-3　　装置:NSE(C2-2), SANS-U(C1-2), 分野:6. Softmatter

results supported the theory presented by Zilman and Granek[2]. They considered an ensemble of membrane plaquettes at random orientations and used the Helfrich bending free energy to describe membrane undulations in sponge and lamellar phases and predicted a stretched exponential relaxation of $I(Q,t)$ as follows Eq.(1) where Γ is given by

$$\Gamma = 0.025\gamma(k_B T/\kappa)^{1/2}(k_B T/\eta)Q^3 \quad , \qquad (2)$$

where κ is the bending modulus of the membrane and η the viscosity of the surrounding medium. The bending modulus of the membrane κ was estimated using their theory. The values of κ estimated from the results of the NSE experiments decrease monotonically with increasing temperature and with increasing d_l as shown in Fig.2. They seem to depend strongly on d_l though d_l is longer than 300Å.

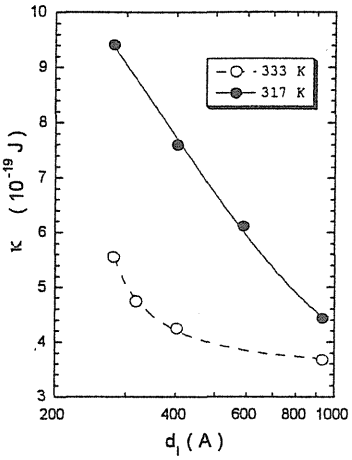


Fig. 2. The dependence of the reduced bending modulus κ of the membrane on the lamellar repeat distance d_l obtained from NSE experiments for the lipid sample in which DPPC was dispersed in D_2O solutions with 7 mM $CaCl_2$.

References

[1] T. Takeda et al: J. Phys. Soc. Jpn. **70** (2001) Suppl. A 323.

[2] A. G. Zilman and R. Granek: Phys. Rev. Letters 77 (1996) 4788.

研究テーマ： リン脂質膜のラメラ構造の形成要因
表題： 中性子小角散乱による DPPC/D_2O/$CaCl_2$ 系における圧力効果の観測

1-5-11 Study of Pressure Effect with Small-Angle Neutron Scattering in DPPC/D_2O/$CaCl_2$ System

N.L. Yamada[1], T. Takeda[2], H. Seto[3], M. Nagao[4]

[1] *Graduate School of Bio-Sphere Science, Hiroshima University, Hiroshima, 739-8521, Japan*
[2] *Facility of Integrated Arts and Sciences, Hiroshima University, Hiroshima, 739-8521, Japan*
[3] *Department of Physics, Kyoto University, Kyoto 606-8502, Japan*
[4] *Institute for Solid State Physics, The University of Tokyo, Tokai 319-1106*

Biomembranes are composed of phospholipids, proteins, glycolipids, cholesterol, and so on. In particular, phospholipids are basic molecules of the biomembranes and well studied as model systems and DPPC is one of the most studied lipid. In excess water, DPPC self-assembles bilayers which displays gel phase (L_{β}'), ripple gel phase (P_{β}'), and liquid crystalline phase (L_{α}) with increasing temperature and an interdigitated gel phase($L_{\beta I}$) appears by applying pressure.(Fig.1) The bilayers conform a lamellar structure, whose inter-bilayer distance is determined by the equiliburium condition of the interactions; van der Waals force, hydration force, and Helfrich repulsion. Inoko et al. reported that the inter-bilayer distance also varies by adding $CaCl_2$ to the DPPC/water system with SAXS experiments though the hydrophilic head of a DPPC molecule is electrically neutral.[2] This phenomenon is caused by the electrostatic force of the Ca^{2+} ions binding to the heads of DPPC molecules.

Pressure is one of the most important thermodynamic parameters to investigate structural formation. In the aqueous solution of DPPC, pressure tends to suppress the temperature-induced transition, and induces the interdigitated gel phase above 150MPa. However, no study has done on the effect of $CaCl_2$ to the mechanism of the structural formation under high pressure. We expect that the change of the interaction by adding $CaCl_2$ affects the structure of the bilayer. From these viewpoints, we performed a small-angle neutron scattering(SANS) experiment at high pressure on DPPC/D_2O/$CaCl_2$ system.

DPPC was purchesed from Sigma Chemical Inc. Deuterated water of 99.9% purity was purchased from Isotec Inc. and $CaCl_2$ was purchesed from Kishida Chemical Inc. The materials were used without further purification. The sample was mixed with DPPC of 12wt.% and D_2O with 7mM of $CaCl_2$. SANS experiments were performed at the SANS-U installed at C1-2 port of JRR3M in JAERI, Tokai. The wavelength was 7Å and both the sample-detector distance and the collimation were 8m. The expriment was carried out at 35°C $\leq T \leq$ 50°C and 0.1MPa $\leq P \leq$ 100MPa.

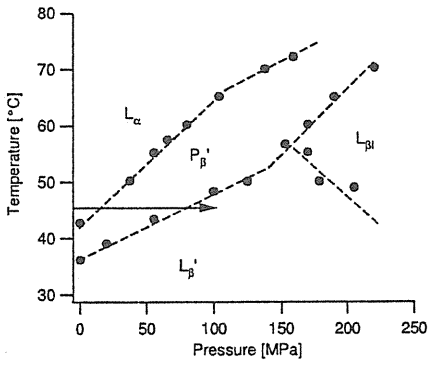


Fig. 1. The pressure-temperature phase diagram of DPPC/D_2O system, which is the result of Kaneshina.[1]

Figure2 shows the pressure dependence of the SANS profiles at T=46°C. (The arrow in Fig.1 corresponds to this condition) The profile at P=0.1MPa indicates L_{α} and 10MPa $\leq P \leq$ 70MPa indicates P_{β}'. The Bragg peaks in these profile correspond to the regular stacking of bilayers of the lamellar structure. However, the Bragg peak in the profile at P=80MPa became broad, and the peaks at P=90,100MPa disappeared. This transi-

使用施設：JRR-3 ， 装置： C1-2 (SANS-U) ， 分野： 6. Softmatter

tion is considered to be different from the P_{β}'/L_{β}' transition in the DPPC/D_2O system shown in Fig.1, since the lamellar structure in L_{β}' is generally more ordered than in P_{β}'.

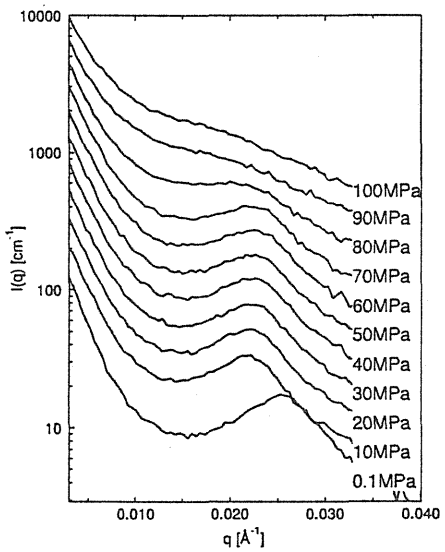


Fig. 2. The SANS profiles at T=46°C with changing pressure.

This result indicates that $CaCl_2$ may affect the mechanism of the structural formation. However, details have not been clarified only by this experiment. The new high-pressure cell of SANS-U can apply higher pressure (over 200MPa) and the experiment with this cell can be expected to revail the more details of this effect.

References

[1] S. Kaneshina *et al.*: *Chem. Lett.*, (1992) 1963.

[2] Y. Inoko *et al.*: *Biochim. Biophys. Acta*, **413**, (1975) 24.

研究テーマ：cis－不飽和鎖脂肪酸を含むトリアシルグリセロールにおけるアシル酸の運動性
表題：cis－不飽和鎖脂肪酸を含むトリアシルグリセロールにおけるアシル酸の運動性

1-5-12

Dynamical Analysis of Triacylglycerol with *cis* Unsaturated Acyl Chain

Akita Chikayo, Kawaguchi Tatsuya and Kaneko Fumitoshi
Graduate School of Science, Osaka University, 1-1 Machikaneyama, Toyanaka 560 – 0043, Japan

The major part of the natural Triacylglycerols (TAGs) contain *cis*-unsaturated fatty acids. It is well known that the large steric hindrance arising from *cis*-unsaturated bond disturbs the closed packing of hydrocarbon segments and brings about the high mobility. In previous studies, we clarified that in solidstate of *cis* unsaturated TAGs, the lateral packing of acyl chains was different from that of saturated TAGs. In this study, we investigated how the difference of the lateral packing affected the dynamical properties of acyl chain by neutron quasi elastic scattering using selectively duetrated specimens triolein (OOO) [*cis*-$C_3D_5(O_2C(CH_2)_7CH=\ 6CH(CH_2)_7CH_3)_3$] and tristearin (SSS) [$C_3D_5(O_2C(CH_2)_{16}CH_3)_3$].

Fig.1 shows the Q dependence of the elastic scattering intensity (I_{el}) measured with AGNES of JRR3M in JAERI. Using the Debye - Waller formula: $I_{el}(Q) = I_{el}(0) \exp(-1/3\langle U^2\rangle Q^2)$, the mean square displacement $\langle U^2\rangle$ in each crystalline phase was obtained from the slope. The results were summarized in Table 1, together with the data about the cross section of acyl chain. As to OOO at 193K, the α phase having a looser lateral packing exhibits a rather large value for $\langle U^2\rangle$ compared with the β phase. SSS also shows the same tendency as OOO. The value of $\langle U^2\rangle$ increases as the cross section becomes large in the following order; β, β' and α. Comparing SSS, OOO with *cis* double bond shows large displacement. Even the β phase of OOO having an ordered lateral packing shows the larger $\langle U^2\rangle$ than the α of SSS. It can be pointed out that *cis* unsaturation surely increases the mobility of acyl chains. We suppose that the measurements at higher temperature would reveal the dynamical properties characteristic of each crystalline phase of *cis* unsaturated TAG. In case of $\langle U^2\rangle$ of the α phase of SSS, differences among β, β' and α phase are obvious at 293 K. However, the α phase of OOO is very difficult to measure at higher temperature because this phase transformers to the β phase soon above 193 K. As a future prospect, we are now contemplating the experiment using the Trierucin whose α phase is stable elevated temperatures.

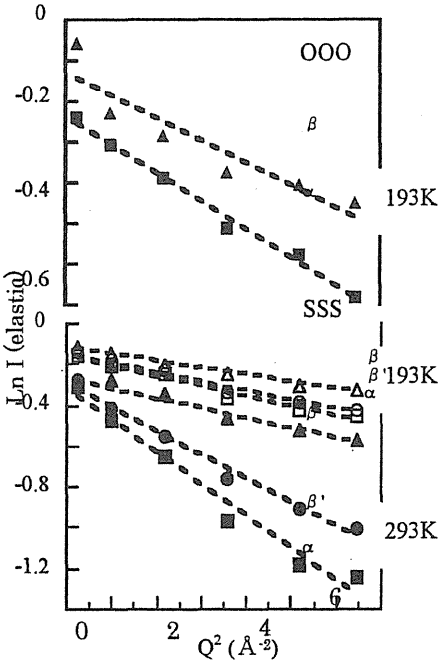


Fig. 1 The Q dependence of the elastic scattering intensity

Table 1 Cross section and Mean square displacement

			α	β'	β
Cross section (Å²)	OOO	193K	20.6	—	18.9
	SSS	193K	18.9	18.4	18.2
		293K	19.7	18.7	18.5
Mean square displacement $\langle U^2\rangle$ (Å²)	OOO	193K	0.17	—	0.21
	SSS	293K	0.47	0.35	0.15
		193K	0.15	0.13	0.10

使用施設：JRR-3　装置：AGNES(C3-1-1)　分野：Softmatter

研究テーマ：トリアシルグリセロールの準安定相におけるアシル鎖の充填構造の秩序性関する研究
表題：トリアシルグリセロールの準安定相におけるアシル鎖の充填構造の秩序性関する研究

1-5-13

Structural Analysis of Metastable Phase of Triacylglycerols; the Order of the Acyl Chain packing

Akita Chikayo, Kawaguchi Tatsuya and Kaneko Fumitoshi

Graduate School of Science, Osaka University, 1-1 Machikaneyama, Toyanaka 563 – 0046, Japan

Triacylglycerols (TAGs) are main components of natural fats and oil and widely used as raw materials for industrial products.

TAGs crystallize into various solid modifications depending on crystallization conditions. The α phase having the lowest melting point is obtained by cooling a melt rapidly, so that the acyl chains form relatively loose hexagonal (H) subcell. In previous studies using IR and Raman spectroscopy and X-ray diffraction, it was clarified that the H subcell of the α phase gradually transformed to the O⊥ like subcell (pseudohexagonal; p-H) due to the sub α phase by cooling. In this study, we investigated how the new domain of the p-H subcell appeared and grew in the matrix of the H subcell by neutron coherent elastic scattering using fully duetrated specimens tristearin (SSS) $[C_3D_5(O_2C(CD_2)_{16}CD_3)_3]$, which removed a strong background due to incoherent scattering of hydrogen atoms and enabled line shape analysis for higher order reflections.

Fig.1 shows the temperature change of the powder diffraction diagram of the α phase measured with HERMES of JRR3M in JAERI. In the region of about 0.24 $Å^{-1}$ (=2sinθ/λ), the α phase exhibited an intense reflection due to the (100) plane of the H subcell and two very weak reflections due to the (110) and (200) plane of the p-H subcell at 295K. Unlike X-ray diffraction, the second order reflection could be observed around 0.46 $Å^{-1}$ because the scattering length does not depend on the scattering angle. Comparing the first order reflection, the second order reflections showed a significantly broadened profile. The increase in integral breadths of the reflection with successive order (h) suggests a loss of the long-range order in subcell. The profiles at 0.24 $Å^{-1}$ and 0.46 $Å^{-1}$ regions were decomposed into the first and second order reflections due to the H and p-H subcells. Using the paracrystal theory of Hosemann, the integral breadth (δb) of each reflection was plotted versus the square of its order (h^2), so that we could get the relative statistical deviation g and the average number N of netplane spacing. The results for each temperature in Table 1 suggested the following picture about the subcell structure change on the α phase -> sub α phase transition. At 295K, the H subcell occupying most part formed large sized domains. On cooling, however, this domain gradually became small with increasing statistical deviation. On the other hand, the p-H subcell was generated among the area of the H subcell and its domain size became large. Especially, the growth toward the direction normal to the (110) plane was remarkable. In 200K, this transition almost ceased and the domain size and the long-range order remained constant during the further cooling.

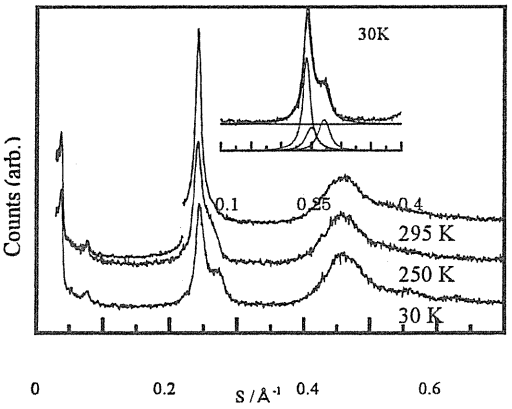


Fig. 1 the temperature change of the powder deflection diagram

Table 1 the relative statistical deviation g, the relative intensity and the average number N of netplane spacing

	N / The relative intensity (%)			g (%)		
	200	100	110	200	100	110
295K	13/15	912/74	15/11	8.7	8.1	8.7
250K	12/17	82/40	43/43	8.7	11.8	8.4
30K	15/26	18/21	60/53	8.4	10.3	8.4

使用施設：JRR-3　　装置：HERMES(T1-3)　分野：Softmatter

研究テーマ:両親媒性ブロックコポリマーの自己組織化機構の研究
表題:疎水性低分子の可溶化が引き起こす両親媒性ブロックコポリマーミセルの構造転移

Structure Transition of Amphiphilic Block Copolymer Micelles Induced by Solubilization of Hydrophobic Small Molecules

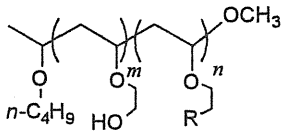
1-5-14

K. Matsumoto, H. Mazaki, T. Ishizuka, S. Maeda, P, Kaeusaiha, and H. Matsuoka

Department of Polymer Chemistry, Yoshida, Sakyo-ku, Kyoto, 606-8501, Japan

Among many interesting properties of amphiphilic block copolymers, solubilization of small hydrophobic molecules into water could be the most attracting properties from both academic and industrial point of view. Here, we examined the effect of solubilization of hydrophobic dyes on the block copolymer micelle structure.

Fluorine-containing block copolymers F0, F3, F5, and F6 shown in Figure 1 were used as amphiphilic block copolymers and decafluorobiphenyl (DFB) and dimethylnaphthalene (DMN) were used as hydrophobic dyes.



F3: R = OCH_2CF_3 $m = 78, n = 23$
F7: R = $OCH_2CF_2CF_2CF_3$ $m = 79, n = 19$
F0: R = CH_2CH_3 $m = 70, n = 22$

Figure 1. Chemical structure of block copolymers

To examine the micelle structure, small-angle neutron (SANS), small-angle X-ray (SAXS), and dynamic light scattering (DLS) measurements of the block copolymer aqueous solutions in the absence and presence of hydrophobic dyes were carried out.

The SANS profiles in the absence of dyes are shown in Figure 2. The SANS data were analyzed by model fitting using core-shell sphere and core-shell rod coexistence model. The fitting parameters were listed in Table 1. We could also reproduce SAXS data by using the same fitting parameters, indicating the high accuracy of the parameters. DLS data also supported the coexistence of spherical and rod-like micelles.

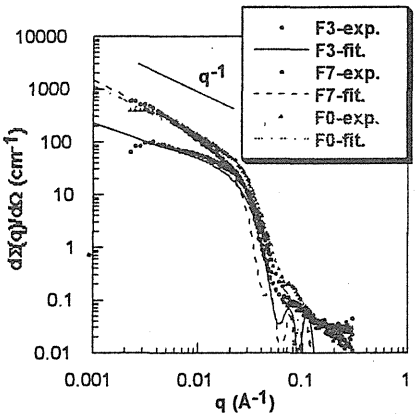


Figure 2. SANS profiles of block copolymer micelles in the absence of hydrophobic dyes

Table 1. Fitting Parameters for Block Copolymer Micelles in the Absence of Hydrophobic Dyes

copolymer	ϕ_{rod}	R_c [Å]	R_s [Å]
F3	0.1	55	110
F5	0.7	53	110
F0	0.4	55	120

ϕ_{rod}: volume fraction of the rod-like micelle
R_c: sectional radius of the micelle core
R_s: sectional radius of the overall micelle

使用施設:JRR-3 装置:SANS-U(C1-2), 分野 Soft matters

SANS profiles in the presence of DFB were given in Figure 3. Although difference of scattering length density in the micelle core by solubilization of DFB was negligible, the intensity of neutron scattering decreased practically by the solubilization in all SANS measurements. The first slope of the SAXS profiles in the small angle region became gentler and the second maximum caused by micelle internal structure shifted to a larger angle region after adding DFB in all cases. These observations indicated that the micelles became smaller by solubilization. Interestingly, the SANS profiles of F7 and F0 still showed the q^{-1} dependence in the medium angle region, while that of F3 showed a scattering pattern typical to a spherical micelle.

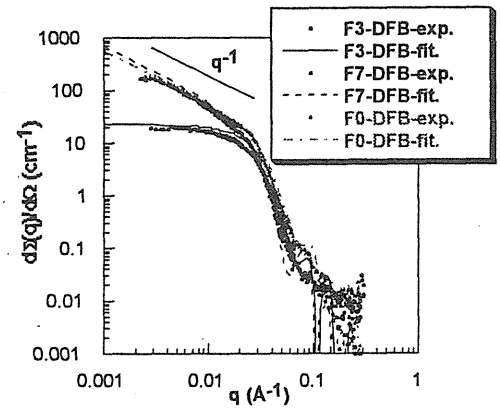


Figure 3. SANS profiles of block copolymer micelles in the presence of DFB

We again analyzed the SANS data by using the core-shell sphere and core-shell rod-like micelle model. SANS data could be moderately reproduced by the fitting parameters shown in Table 2. SAXS data in the presence of DFB were also reproduced by the same parameters. Using DMN instead of DFB as a solubilizate, we examined SANS and SAXS of the block copolymer solutions. SANS and SAXS profiles of the block copolymer micelles solubilizing DMN gave almost same scattering curves as in the cases of DFB.

Table 2. Fitting Parameters for Block Copolymer Micelles in the Presence of DFB

copolymer	ϕ_{rod}	R_c [Å]	R_s [Å]
F3	0	43	94
F7	1	35	95
F0	0.5	35	84

ϕ_{rod}: volume fraction of the rod-like micelle
R_c: sectional radius of the micelle core
R_s: sectional radius of the overall micelle

DLS results also indicated that F3 formed small spherical micelle, F7 formed large rod-like micelle, and F0 formed both small spherical and large rod-like micelles. SANS, SAXS, and DLS analysis suggested that after solubilization of hydrophobic compounds the F3 formed spherical micelles and F7 formed rod-like micelles reducing the micelle radius, while F0 formed both spherical and rod-like micelles also reducing the micelle radius. Solubilization of a hydrophobic compound is usually thought to cause an increase of the micelle size. However, the solubilization significantly reduced the micelle size in our case. The reason for this unusual phenomenon is unknown, but there may be a possibility that the copolymer micelle structure before solubilization was not thermodynamically stable and the solubilization accelerated the transformation to a more stable structure. Investigation on the time evolution of the micelle structure is now in progress.

研究テーマ:高分子薄膜のガラス転移
表題:中性子反射率によるポリスチレン薄膜の厚さに対するアニーリング効果

Annealing Effects on Thickness of Polystyrene Thin Films As Studied by Neutron Reflectivity

1-5-15

T. Kanaya[a], T. Miyazaki[a,b], H. Watanabe[a], K. Nishida[a], H. Yamano[a], S. Tasaki[c], D. B. Bucknall[d]

[a] *Institute for Chemical Research, Kyoto University, Uji, Kyoto-fu 611-0011, Japan*
[b] *Nitto Denko Corporation, 1-1-2 Shimohozumi, Ibaraki, Osaka-fu 567-8680, Japan*
[c] *Research Reactor Institute, Kyoto University, Kumatori, Osaka-fu 590-0494, Japan*
[d] *Department of Materials, Oxford University, Parks Road, Oxford, OXON, OX1 3PH, UK*

We have performed neutron reflectivity measurements on deuterated polystyrene thin films supported on silicon substrate as a function of temperature. In order to see effects of annealing on the thickness the films were annealed at 80 °C for 12 h and 135 °C for 12 h, termed *weakly* and *strongly annealed* films, respectively. One of the main purposes of this study is to see if the negative expansivity reported for very thin films reported by Orts et al. [1] is caused by unrelaxed structure due to lack of annealing.

Neutron reflectivity (NR) measurements were performed using MINE spectrometer in JRR-3M reactor, and CRISP spectrometer in ISIS.

Figure 1(a) shows the temperature dependence of the thickness for the *weakly annealed* film with initial thickness d_0 = 91 Å. The negative thermal expansivity is clearly observed. For this film, we cannot estimate the glass transition temperature T_g because no clear reflection point is observed. The negative expansivity is much clearly observed for the thinner films. The results agree with those reported by Orts et al. [6]. On the other hand, the *well annealed* film with initial thickness d_0 = 89 Å shows positive expansivity as shown in Figure 1(b) and the expansivities in the glassy and molten states agree with those expected from those of bulk. This suggests that the negative expansivity observed in the *weakly annealed* films is partly caused by unrelaxed structure due to lack of annealing. It is interesting to point

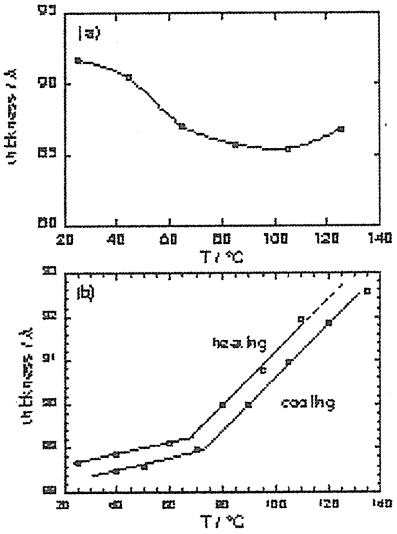


Figure 1. (a): Temperature dependence of thickness of weakly annealed film. (b): temperature dependence of well annealed film in heating and cooling processes.

out that the film thickness in the cooling process is lower than that in the heating process, implying that the film thickness decreases very slowly after annealing at 135 K for 12 h. This decrease must be caused by a slow motion of polymers. One of the candidates of this slow motion is "sliding motion" proposed de Gennes [2].

This work wlll soon appear in *Polymer*.

References

[1] W. J. Orts, et al., Phys Rev Lett; **71**, 867 (1993).
[2] P. G. de Gennes, Eur. Phys. J., **E2**, 201 (2000).

使用施設:JRR-3 装置:MINE(C3-1-2-2), 分野 Softmatter

研究テーマ:中性子反射率測定による高分子二層膜界面での分子鎖拡散挙動の評価
表題:中性子反射率測定によるバルクガラス転移温度以下での高分子二層膜界面厚の時間発展

Time Evolution of Interfacial Thickness in Polymer Bilayers below Its Bulk Glass Transition Temperature by Neutron Reflectivity

1-5-16

K. Tanaka, D. Kawaguchi, S. Tasaki*[1], A. Takahara*[2] and T. Kajiyama

Graduate School of Engineering, Kyushu University, Fukuoka 812-8581, Japan
*[1]*Research Reactor Institute, Kyoto University, Osaka 590-0494, Japan*
*[2]*Institute for Materials Chemistry and Engineering, Kyushu University, Fukuoka 812-8581, Japan*

Surface mobility in polystyrene (hPS) films was studied by neutron reflectivity (NR) using (hPS/deuterated PS) bilayer films. When the bilayer was annealed at a temperature above bulk glass transition temperature, T_g^b, the interfacial thickening was well expressed by Fickian diffusion. On the other hand, at a temperature above surface glass transition temperature, T_g^s, and below T_g^b, the interface monotonically thickened with the time at first, and then, turned to be independent. This means that chains went across the "*mobile*" interface and then reached the "*dead*" bulk region in which the diffusivity should be frozen.

Bilayers composed of hPS and dPS with the number-average molecular weight, M_n, of 190k were used. NR measurements were made using MINE. The incident neutrons have the wavelength of 1.26 nm and the resolution of 3.5 %. Figure 1 shows the NR curves for the bilayer film annealed at 365 K for various times. The solid lines denote the best-fit calculated reflectivity to the experimental one based on model scattering length density, (b/V), profiles normal to the surface shown in Figure 2. Since the calculated curves are in good agreement with the experimental data, it can be claimed that the model (b/V) profiles correspond well to the composition profiles in the bilayer film along the direction perpendicular to the surface. For the hPS and the dPS, the (b/V) values of 1.41 x 10^{-4} and 6.46 x 10^{-4} nm^{-2} were used, respectively. When the annealing time increased, the bilayer interface broadened out, resulting in gradual loss of the sharpness for higher order fringes on the reflectivity curves. The interfacial thickness monotonically increased with the annealing, and then, reached a constant value of 4.7 nm at 5.5 x 10^5 s. Using the bulk diffusion coefficient being under the same condition, temperature and M_n, after 5.5 x 10^5 s, the interfacial broadening was predicted by open reverse triangles in Figure 2. This exhibits visibly how the surface layer is mobile in comparison with the bulk.

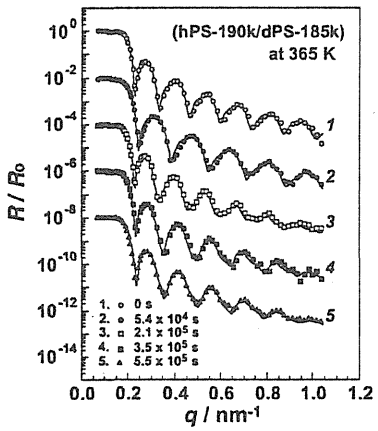


Figure 1 NR curves of the as-prepared (hPS-190k/dPS-185k) bilayer and annealed ones at 365 K for various times.

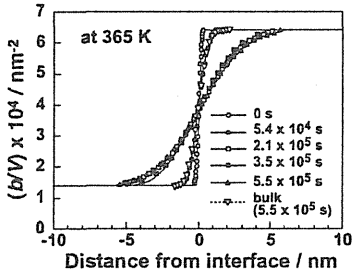


Figure 2 Scattering length density profiles at the as-prepared (hPS-190k/dPS-185k) interface and annealed ones at 365 K for various times.

使用施設:JRR-3 装置:MINE2 (C3-1-2--2), 分野 Soft Matter

研究テーマ:中性子反射率測定に基づく高分子薄膜中での分子鎖末端基の空間分布評価
表題:中性子反射率測定による(ポリスチレン/ポリビニルメチルエーテル)ブレンド膜の界面組成

Neutron Reflectivity Studies on Interfacial Composition in Blend Films of Polystyrene and Poly(vinyl methyl ether)

1-5-17

A. Takahara, D. Kawaguchi*[1], K. Tanaka*[1], S. Tasaki*[2] and T. Kajiyama*[1]

Institute for Materials Chemistry and Engineering, Kyushu University, Fukuoka 812-8581, Japan
*[1]*Graduate School of Engineering, Kyushu University, Fukuoka 812-8581, Japan*
*[2]*Research Reactor Institute, Kyoto University, Osaka 590-0494, Japan*

Surface and interfacial chemical compositions in miscible blends of monodisperse deuterated polystyrene (dPS) and poly(vinyl methyl ether) (PVME) were studied by neutron reflectivity (NR). In the case of symmetric blends in terms of degree of polymerization, N, PVME and dPS were preferentially segregated at the film surface and the interface with a silicon wafer, respectively, to minimize free energy of the system. The concentration profile near the surface obtained by experiments was consistent with a mean-field prediction.

A concentration profile normal to the surface in the blend films can be directly examined by NR measurement. NR measurements were made using MINE. The incident neutrons have the wavelength of 0.88 nm and the resolution of 5.1 %. Figure 1 shows the scattering vector, q [=$(4\pi/\lambda)\sin\theta$], dependence of neutron reflectivity for the dPS/PVME blend films. Each film thickness was fixed to be about 110 nm. The solid curves denote the best-fit calculated reflectivity to the experimental data based on the model scattering length density, (b/V), profiles, as shown in the inset of Figure 2. Since the calculated curves are in good agreement with the experimental data, it can be claimed that the model (b/V) profiles well reflect to the compositional changes in the blend films along normal to the surface. For dPS and PVME, the (b/V) values of 6.46×10^{-4} and 3.40×10^{-5} nm^{-2} were used, respectively. The PVME fraction exponentially decayed with increasing depth in the surface region and eventually

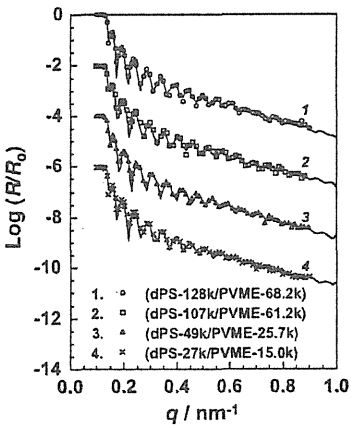


Figure 1 NR profiles for symmetric dPS/PVME blend films with different M_n pairs. Experimental data sets are shown by symbols. Solid curves depict the best-fit ones calculated from model scattering length density profiles, which are shown in Figure 2.

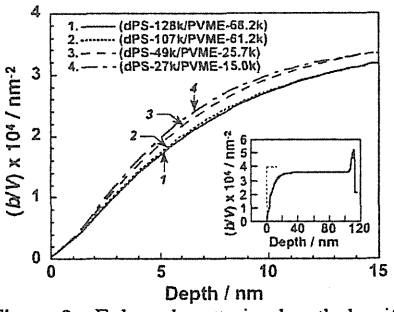


Figure 2 Enlarged scattering length density profiles near the surface region for symmetric dPS/PVME blend films. The inset figure shows the whole profile of dPS-128k/PVME-68.2k blend film as a

reached the bulk value, whereas dPS was enriched at the polymer/substrate interface. This result can be simply explained in terms of minimization of free energy at the both of surface and interface.

使用施設:JRR-3 ,装置:MINE2 (C3-1-2--2), 分野 Soft Matter

研究テーマ:ポリオレフィン混合系の流動誘起構造変化
表題:中性子小角散乱による定常流動下における非相溶ポリオレフィン混合系の構造

Structure of Immiscible Polyolefin Blends under Steady Shear Flow Studied by Small Angle neutron Scattering

1-5-18

Yoshiaki Takahashi, Yoshiaki Ukai[#], Motohiro Seki[#] and Yushu Matsushita[#]

Department of Molecular & Materials Sciences Kyushu University, Fukuoka, 812-8581 Japan,
[#]Department of Applied Chemistry, Nagoya University, Nagoya 464-8603 Japan

It is well known that immiscible polyolefin blends show a wide variety of flow induced structure due to the difference in processing condition. Since the basic chemical unit of polyolefin is $-(CH_2)-$, there is no apparent difference in reflective index and electron density among different polyolefins in the melt states. In such a case, SANS measurements under the flow is most powerful experimental technique to study their structure under the flow. In this work, we report preliminary results of such study.

The samples used were isotactic polypropylene (i-PP) and ethylene-octene random copolymer (EOR). Weight averaged molecular weights of normal i-PP, deutrated I-PP and EOR determined by GPC-MALLS measurements were 4.6×10^4, $5.1\times10^4$and 8.4×10^4, respectively. Octene content of EOR was 15.2mol%. Detailed characterizations of I-PP samples are reported elsewhere [1]. Blend ratio of ipp:EOR was 3:7 by weight.

Viscoelastic properties of components and blends under oscillatory and steady shear flow were measured with a Rheometrics RMS-800.

Flow-SANS was measured by SANS Shear Cell [2] attached to SANS-U spectrometer of NSL, ISSP, The University of Tokyo, at JAERI (C1-2 at JRR3M) Tokai, Japan. The wavelength was 0.7 nm while the sample to detector distance was changed between 2- to12 m. Tme measureing temperature was 150 °C.

At low shear rate, anisotropy of intensity, i.e, higher intensity in the perpendicular direction, was observed in through view measurements (incident beam perpendicular to the flow). In edge view measurements (incident beam parallel to the flow), no anisotropy was observed. At higher shear rates (>50 sec^{-1}), anisotropy became very weak but intensity itself became rather strong.

A simple explanation of these observations may be given by assuming existence of string like domain at low shear rates and there burst at high shear rates. This may be supported from the low interfacial tension between polyolefins.

Refferences

1. M. Seki, H. Uchida, Y. Maeda, S. Yamauchi, K. Takagi, Y. Ukai and Y. Matsushita, Macromolecules, **33**, 9712 (2000).
2. Y. Takahashi, M. Noda, M. Naruse, T. Kanaya, H. Watanabe, T. Kato, M. Imai, Y. Matsushita, Nihon Reoroji Gakkaishi (J. Soc. Rheol. Japan), **28**, 187 (2000).

使用施設:JRR-3　装置:SANS-U(C1-2), 分野 Softmatter

研究テーマ： ポリプロピレン系結晶材料と同系非結晶材料の相互作用解析
表題： ポリプロピレン系結晶材料と同系非結晶材料の相互作用解析

Molecular Interaction Analysis on Crystalline-Amorphous Polypropylene Blends

1-5-19

K. Abe[1], S. Okabe[2], M. Shibayama[2]

[1]*Oita Research Lab., SunAllomer Co., Ltd., 2 Nakanosu, Oita 870-0189*

[2]*Institute for Solid State Physics, The University of Tokyo, 106-1 Shirakata, Tokai, 319-1106*

Perdeuterated isotactic-polypropylene (d-PP; MW = 6.78×10^4) and ordinary hydrogenated isotactic polypropylene (h-PP; MW = 8.41×10^4) were synthesized with metallocene catalyst. Some portion of d-PP was chemically bonded with anionically-polymerized alternative poly(ethylene-*alt*-propylene) copolymer (EPR) (d-PP95-*b*-EPR5), where the numbers indicate the weight fractions. Blend samples were also prepared by mixing d-PP and h-PP with the compositions of 50/50 (d-PP/h-PP= 50/50), and 95/5 (d-PP/h-PP= 95/5) as reference samples. Blending was made by dissolving the component samples in hot xylene, precipitation in methanol, followed by hot pressing with a mold. Thus, disk-shape samples of ca. 2 mm thick and of 2 cm diameter were prepared. Here, pressing was carried out under low pressure in order to remove residual solvent and voids.

SANS experiments were carried out at SANS-U, the University of Tokyo. The incident neutron beam was monochromatized to 7.0 Åwith a velocity selector. The sample-to-detector distance was 2.0 and 8.0 m. The samples were installed in a heat chamber and the chamber was evacuated in order to avoid oxidation of the samples. The temperature range was covered up to 252 °C.

Figure 1 shows the SANS function for the h/d-50/50 blend at 158.1 °C and the curve-fit with the so-called RPA (random phase approximation) equation derived by de Gennes for molten polymer blends.[1] According to the analysis, it was found that the radius of gyration and the Flory interaction parameter were 90 Åand less than 1.0×10^{-4}, respectively.

Figure 2 shows the variation of SANS intensity function of d-PP95-*b*-EPR5 at various temperatures. The scattering maximum indicates the presence of lamellar structure

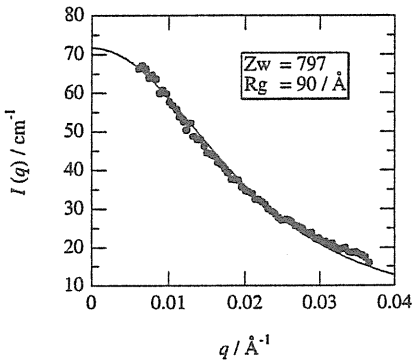


Fig. 1. SANS function of d-PP/h-PP= 50/50 at 158.1 °C and the curve-fit with the RPA equation.

at temperatures below 150 °C. Above 160 °C, the system becomes a molten state and $I(q)$ decreases with increasing temperature, indicating that the d-PP95-*b*-EPR5 is an LCST system. The details of the analyses will be reported in the near future.

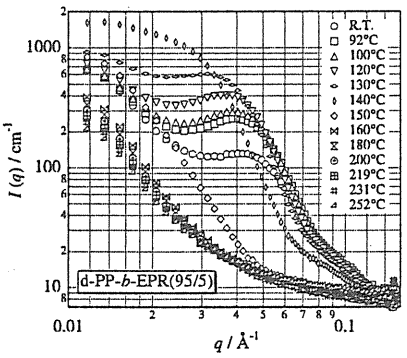


Fig. 2. SANS intensity function of d-PP95-*b*-EPR5 block copolymers at various temperatures.

References

[1] P. G. de Gennes: *Scaling Concepts in Polymer Physics*, Cornell U. Press (1979).

使用施設：JRR-3 装置： C1-2 (SANS-U)， 分野： 6. Softmatter

研究テーマ:流動場における高分子の結晶化
表題:ポリエチレンのシシカバブ構造
1-5-20

Shish-Kebab Structure of Polyethylene

T. Kanaya, Y. Ogino, H. Fukushima, N. Takahashi, K. Nishida

Institute for Chemical Research, Kyoto University, Uji, Kyoto-fu 611-0011, Japan

Extensive studies have been carried out on crystallization of polymer melts under flow because in most polymer processing operations such as extrusion, injection molding and fiber spinning, the molten polymers are exposed to various flows such as elongational, shear and mixed flows. Polymer chains are oriented in the melts under flow and crystallize with morphologies different from those under quiescent condition: shish-kebab or row-nucleated structure. In such structure, extended chains in the direction of the applied flow act as row-nuclei and chain folded lamellae grow in a direction perpendicular to the extension axis.

In some experiments it was reported [1] that kebab structure is observed but shish structure is not. This result was sometimes interpreted that the shish structure is not developed under some crystallization condition. However, it is considered that we cannot observe the shish structure if the number of shish structures is very little and the scattering contrast of shish is not high. In this work, we performed small angle neutron scattering (SANS) experiments to see small number of shish structures using deuterium labeling method.

The sample used in this study was deuterated polyethylene (PE) with molecular weight M_w = 200,000. In order to give a high scattering contrast we mixed 2.8 wt % protonated PE with ultrahigh molecular weight M_w = 2,000,000. These two polyethylenes were mixed in a xylene solution. The mixed polyethylene was crystallized under one dimensional elongation at about 127 °C.

SANS measurements were carried out with SNAS-U spectrometer installed at a cold neutron guide (C1-2) in JRR-3M reactor.

In SANS measurements on this mixed polyethylene, shish structure is clearly observed as a streak in the direction normal to the elongation direction and kebab structure is also observed as a two-spot long period along the direction parallel to the elongation direction (Figure 1). We also performed small angle X-ray scattering (SAXS) measurement on the same sample in SPring-8 facility. It was found that kebab structure is observed as a two-spot long period along the elongation direction as in SANS measurements but shish structure is not. It suggests that the shish structure consists of high molecular weight protonated polyethylene. Because the scattering contrast of protonated polyethylene in SANS is much higher than in SAXS we observed both of shish and kebab structures in SANS measurements.

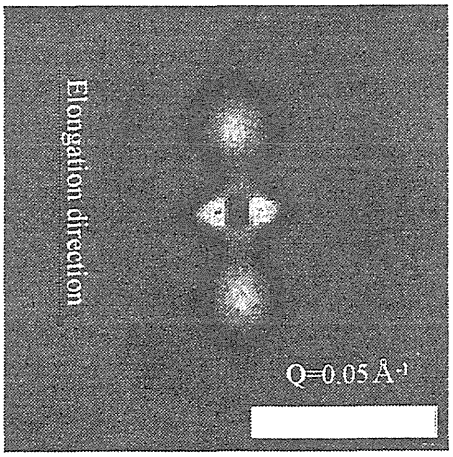


Figure 1. Two dimensional SANS pattern of crystallized mixture of protonated PE with Mw = 2,000,000 and deterated PE with Mw = 200,000. Concentration of protonated PE is 2.8 wt %. Crystallized at 127 °C under one dimensional elongation.

References

[1] R. H. Somani, et al., Macromolecules, **33**, 9385 (2000).

使用施設:JRR-3, 装置:SANS-U(C1-2), 分野 Softmatter

研究テーマ： 溶媒分子を含むシンジオタクチックポリスチレンのδ型結晶の精密構造解析
表題： シンジオタクチックポリスチレン/トルエンδ型結晶の構造解析

Structural Analysis of the clathrate δ form syndiotactic polystyrene containing toluene

1-5-21

T. Kawaguchi, Y. Uda, and F. Kaneko
Graduate School of Science, Osaka University, 1-1 Machikaneyama, Toyonaka, 560-0043

Syndiotactic polystyrene (sPS) posesses a very complex polymorphic behaviour. Four distinct crystalline forms have been described. One of interesting crystalline phases is characterized by the clathrate formation with various organic molecules, so called δ-form crystal. The clathrate δ form can be prepared by exposing a solid polymer sample to solvent liquid or solvent vapors which results in producing solid samples. In other cases, compounds are prepared from homogeneous solutions obtained at high temperatures and cooled to lower temperatures.

The crystal structures of δ-form including molecules of toluene and iodine have been reported by Chatani *et al.*[1] Chatani *et al.* have shown that δ-forms containing similar organic compounds, e.g., toluene, benzene, *p*-xylene, are isomorphous.

The δ-form can be transformed to the mesophase without change of the packing by releasing the guest molecules according to suitable annealing and/or solvent extraction. This mesophase has the molecular cavity and the capability of the shape and size-selection on the absorption of solvent mixtures.

The deutrated sPS was synthesized in our laboratories. The δ-form of sPS samples were obtained by exposing amorphous sPS samples, which were previously prepared by quenching the melt in ice-water, to deuterated toluene vapor at 320K for 20h.

We performed neutron powder diffraction experiments on the Kinken powder diffractometer for high efficiency and high resolution measurements, HERMES[1], of Institute for Materials Research(IMR), Tohoku University, installed at the JRR-3M reactor in Japan Atomic Energy Research Institute(JAERI), Tokai.

Neutron diffraction has several advantages compared with X-ray diffraction; the scattering length does not change with scattering angle, the cross section of deuterium atom is close to that of carbon atom, and it is easy to measure at low temperature. Figure 1 shows the X-ray diffraction pattern and Neutron diffraction pattern of δ-form of deuterated sPS containing deuterated toluene. The each position of reflection shows good agreement between X-ray diffraction pattern and Neutron diffraction pattern. Unfortunately, broad and intense background, amorphous halo makes it difficult to proceed the structure analysis. However, it is notable that even in a high angle region, reflection peaks of neutron diffraction remain their keen shape. This future was what we expected and it would be of benefit to further analysis. We have been trying to analyse with X-ray diffraction data and planing to measure an amorphous profile.

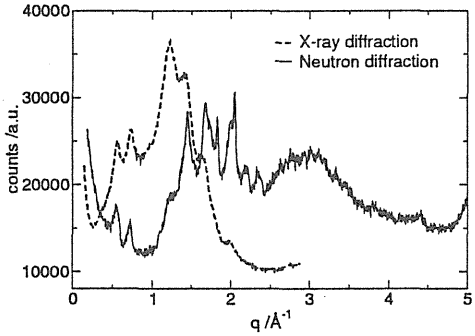


Fig. 1. Powder diffraction pattern of clathrate δ-form of syndiotactic polystyrene containing toluene. Neutron diffraction pattern was measured at 30K while X-ray diffraction was measured at room temperature. Hydrogens of both compounds were fully subssubstituted by deuteriums.

References

[1] Y. Chatani*et al.*: Polymer **34** (1993)1620.

使用施設：JRR-3 ， 装置： T1-3 (HERMES) ， 分野： 6. Softmatter

研究テーマ:ABCトリブロックコポリマーの複雑相転移に関する研究
表題:ABCトリブロック共重合体の複雑相転移

1-5-22 Complex Microphase Transitions in an ABC Triblock Terpolymer

K. Yamauchi, H. Hasegawa, T. Hashimoto and M. Nagao

Department of Polymer Chemistry, Graduated School of Engineering, Kyoto University, Sakyo-ku, Kyoto, 606-8501 Japan

Introduction

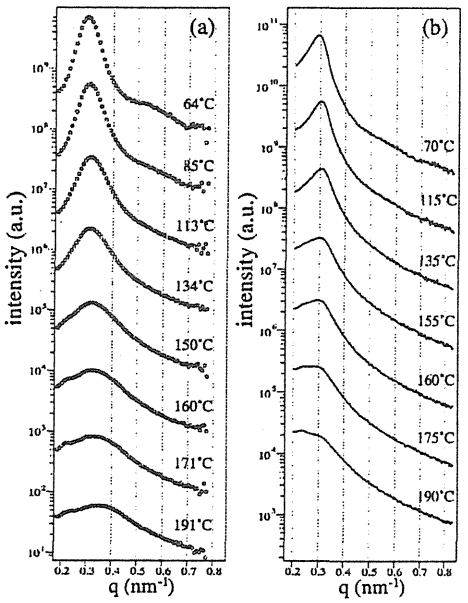
Microphase separation (MS) of a polyisoprene-*block*-poly(D$_8$-styrene)-*block*-poly(vinyl methyl ether) triblock terpolymer were investigated by small-angle neutron scattering and small-angle X-ray scattering. At low temperature, DPS and PVME are miscible but PI is immiscible with both DPS and PVME so that the terpolymer is separated into two microphases, i.e., the PI phase and the phase of DPS and PVME which are moleculary mixed. In the temperature range covered in this experiment, the segregation power between PI and DPS decreases with increasing temperature but that between DPS and PVME increases, while PVME remains immiscible with PI. The competing short-range interactions with the opposite temperature dependences result in a complex but novel MS behavior and a change of the microdomain-structure with temperature as discussed in the text.

Experiment

PI-DPS-PVME (M_n = 4.1 x10^3, 2.1x10^4 and 3.4x10^3 for each block, respectively) triblock terpolymer sample cast from toluene solution. SANS-U (λ=7.0 Å, SDD=4.0m) equipped with a heating stage controlled by TEMCON was used. The SAXS data were obtained for a heating and a cooling cycle by 5°C step for each between room temperature and 214°C. The SAXS measurement was performed for the heating cycle from 27 to 220°C.

Results

Figure 1 shows the SANS (a) and the SAXS (b) profiles from PI-DPS-PVME



obtained at various temperatures during the heating process. Logarithm of the SANS and the SAXS intensity is plotted

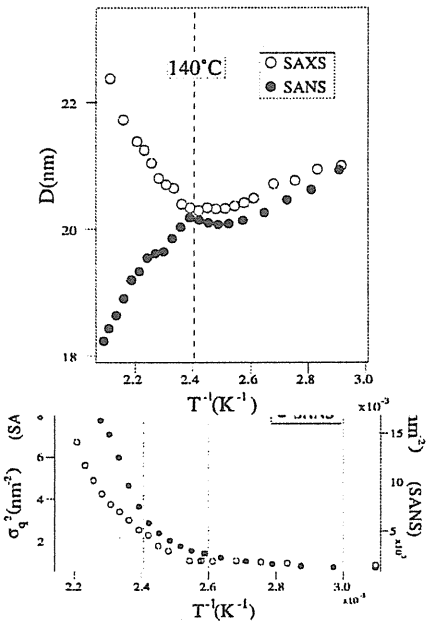
Figure 1 SANS (a) and SAXS (b) profiles for PI-DPS-PVME. The intensity (in arb. unit) is shown in logarithmic scale. The profiles have been shifted vertically for clarity.

against q. The profiles are vertically shifted to avoid overlapping. At room temperature, only a single scattering peak is seen for both the SANS and the SAXS profiles and it was sharp enough to suggest a microphase-separated state though long range order is not well developed. Since PI component is only 15% by volume, and since DPS and PVME components having a LCST-type phase diagram are reported to be miscible at room temperature, the morphology is expected to be the spherical microdomains consisting of PI block chains

使用施設:JRR-3 装置:SANS-U(C1-2), 分野 Softmatter

irregularly packed in the matrix of DPS/PVME mixed phase. As temperature increased from room temperature, the

Figure 2. σ_q^2 (square of the half-width at half-maximum of the peak) plotted as a function of T^{-1} (inverse of absolute temperature). (filled circles:



SANS, unfilled circles: SAXS).

Figure3. Temperature dependence of Bragg spacing D. (filled circles: SANS, unfilled circles: SAXS)

SANS and the SAXS scattering peak decreased in its intensity and became broad. However, a discontinuous change in the scattering profiles with temperature indicative of MS transition was not clearly discerned in either the SANS or the SAXS measurement. To characterize the change in the SANS and the SAXS profiles with T, square of the half-width at half-maximum (σ_q^2) of the scattering peak and the characteristic length D ($D=2\pi/q_m$ where q_m is the q at the maximum scattering intensity) were plotted as a function of reciprocal absolute temperature (T^{-1}) in Figures 2 and 3, respectively. σ_q^2 for the SANS and the SAXS peaks indicated the similar temperature dependence, i.e., both continuously decrease with increasing T^{-1} as shown in Figure 2. However, we note clearly a quantitative difference of the two values at temperature above 140°C ($T^{-1}<2.4\times10^{-3}$ K^{-1}). Temperature dependence of the D values as observed by the SANS and the SAXS showed an intriguing difference above T>140°C.

At temperatures below 140°C, as shown in Figure 3, the D values for SANS and SAXS, defined hereafter as D(SANS) and D(SAXS), respectively, show the similar behavior. D(SANS) reflects the average distance between the PI spherical microdomains, because the contrast between the PI phase and the mixed phase of DPS and PVME is high enough. Similarly, D (SAXS) reflects the average distance between the PI microdomains because the contrast for X-rays between the PI phase and the others is high enough. Since there is no difference in the spatial distribution of the scattering contrast for this structure between SANS and SAXS, D showed the similar behavior below 140°C.

At temperatures above 140°C, as shown in Figure 6, D(SANS) decreases sharply with increasing temperature, while D(SAXS) increases. This surprising difference may be the results of MS between DPS and PVME. D(SANS) corresponds to the average intersphere distance between PI-PI, PI-PVME and PVME-PVME spherical microdomains. On the other hand, the PVME spheres cannot be observed by SAXS, because the electron density of DPS and that of PVME are almost the same. Consequently, D(SAXS) should reflect the intersphere distance between the PI microdomains and show the different behavior from D(SANS). Therefore, the difference between D(SAN-S) and D(SAXS) implies the existence of both PI and PVME microdomains.

研究テーマ： 構造不均一性を考慮した高分子網目の構造の特性化に関する研究
表題： ガンマ線架橋高分子ゲルの構造不均一性の特性化

1-5-23 Characterization of Structure Inhomogeneities in Polymer Gels

M. Shibayama[1], T. Norisuye[2], N. Masui[1], and S. Okabe[1]
[1] *Institute for Solid State Physics, The University of Tokyo, 106-1 Shirakata, Tokai, 319-1106*
[2] *Dept. of Polym, Sci. and Eng., Kyoto Inst. of Tech., Matsugasaki, 606-8585*

The degree of built-in inhomogeneities and dynamics fluctuations of γ-ray irradiated poly(N-isopropylacrylamide)(PNIPA) gels were evaluated as a function of the cross-linking degree and the gel preparation temperature by intensity decomposition methods for both types of gels. It is concluded from the small angle neutron scattering (SANS) and static/dynamic light scattering (SLS/DLS). results that the monomer cross-linked gels have extra built-in inhomogeneities due to the spatial distribution of cross-links in addition to the frozen concentration fluctuations inherent in polymer gels. Here, we briefly report some results obtained by SANS experiments.

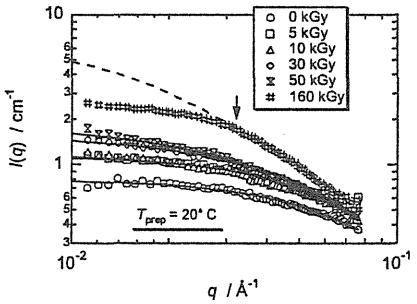


Fig. 1. The neutron scattering intensity functions for the γ-ray gels prepared with different irradiation doses and at 20°C. The experimental curves level off at a wave vector, indicated by solid arrows. The scattering functions are well reproduced by the theory (solid line) except for the case of high irradiation doses (dashed lines).

The scattering functions for the γ-ray gels having different irradiation dose prepared at 20 °C were shown as a function of the wave vector in Fig. 1. The scattering intensity, $I(q)$, for the PNIPA solutions indicated by open circles is described by a Lorentz function. On the other hand, those for gels deviate from Lorentz behavior for lower intensity as shown by the dashed lines. The intensity increased with the irradiation dose, indicating the larger contribution from frozen inhomogeneities. Contrary to the low q behavior, $I(q)$s marge at high q region irrespective of the irradiation dose except that for 200kGy. As reported in our previous paper,[1] the scattering function for PNIPA gels can be well described by the Panykov-Rabin theory, which takes into account both conditions at observation and the preparation. The solid lines indicated in the figures are the results of fitting by the PR theory[2]. The following facts were disclosed. The PR theory allowed us to make a concrete discussion about inhomogeneous network structure and to reproduce our experimental results for the SANS functions of the PNIPA gels prepared by conventional radial polymerization of monomers as reported before.[3] However, the theory was not applicable for the γ-ray gels when the gel was prepared at higher irradiation dose or even high preparation temperature. In addition, the scaling approach ensures the suppression of apparent inhomogeneities by strong thermal fluctuations, rather succeeded in reproduction of our data. The details of the discussion are reported elsewhere.[4]

References

[1] T. Norisuye, *et al.*: Polymer, **43** (2002)5289.
[2] S. Panyukov, Y. Rabin: Physics Report **269** (1996)1.
[3] S. Takata, T. Norisuye, M. Shibayama: Macromolecules **35** (2002)4779.
[4] T. Norisuye, *et al.*: Macromolecules, in press.

使用施設；JRR-3 装置： C1-2 (SANS-U)， 分野： 6. Softmatter

研究テーマ:2527 2.026 カルボン酸間の水素結合により不均一性ドメインを形成する弱荷電性高分子ゲルの研究
表題:混合溶媒中で局所的な疎水性ミクロ凝集を有する弱荷電高分子ゲルの構造解析

Microstructure of Poly(12-acryloyloxydodecanoic acid-co-acrylic acid) Gels in Ethanol/Water System.

1-5-24

F. IKKAI[1], N. MASUI[2], T. KARINO[3], S. NAITO[1], K. KURITA[4], M. SHIBAYAMA[5]

[1] *L'ORÉAL Tsukuba Center, L'ORÉAL Recherche, 5-5 Tokodai, Ibaraki 300-2635, Japan;*
[2] *Dept. of Polym. Sci. & Eng., Kyoto Inst. of Tech., Matsugasaki, Sakyo-ku, Kyoto 606-8585, Japan;*
[3] *Dept. of Mat. Struc. Sci., Grad. Univ. for Adv. Studies, 1-1 Oho, Tsukuba, Ibaraki 305-0801, Japan;*
[4] *College of Sci. & Tech., Nihon Univ., Kandasurugadai, Chiyoda-ku, Tokyo 101-8308, Japan;*
[5] *Neutron Science Laboratory, ISSP, The Univ. of Tokyo, Tokai, Naka-gun, Ibaraki 319-1106, Japan*

INTRODUCTION

Copolymers of 12-acryloyloxydodecanoic acid (ADA) and acrylic acid (AA) have hydrophobic and ionizable groups and groups capable of hydrogen bonding (See. Fig. 1). Regarding this copolymer as a model of protein molecule, we have prepared gels consisting of those polymers and investigated the gel microstructure change depending on the surrounding solvent composition.

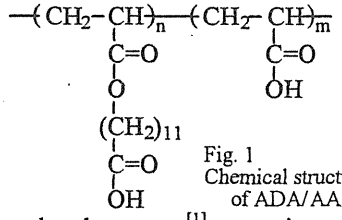


Fig. 1
Chemical structure of ADA/AA copolymer

In the last year[1], we investigated the microstructure of ADA/AA gels in two kinds of solvent, 1-propanol/water (PrOH/W) and propionic acid/water (PAc/W) mixed solvents, which have almost the same hydrophobicity. The small-angle neutron scattering (SANS) results proved that the slight difference of the solvent acidity resulted in a significant difference in forming high order structure of the gels. In the current year, we have investigated the ethanol/water solvent composition (x) dependence of static structure and dynamics of the ADA/AA gels, as well as the comparison between the macro- and microscopic structural changes of the gels by x changes.

EXPERIMENTAL

JRR-3 , SANS-U, 6. Polymer

The ADA/AA gels were prepared by heat-induced radical polymerization in ethanol at 60 °C using 0.5 M of ADA monomer and 4.5 M of AA monomer. After washing and drying, those gels were swollen by mixed solvents having a given ratio (x) of EtOH/W. The SANS measurement (with SANS-U, C1-2, JRR3M in ISSP, Tokai, Univ. of Tokyo) was carried out with wavelength of 7 Å at room temperature for 1.0 and 1.5 h for 1 and 4 m sample-to-detector distance conditions. The solvents for SANS were replaced by deuterated ones, i.e., combinations of D_2O and deuterated ethanol (d-EtOH).

RESULTS AND DISCUSSION

Fig. 2 shows x dependence of the SANS profiles ($I(q)$) for ADA/AA gels. For $x \leq$ 25 vol%, the $I(q)$s had a long spacing correlation peak at q = ca. 0.1 Å^{-1}. This peak is probably ascribed to microphase separation between the hydrophobically aggregated part and the hydrophilically swelling part. To clear the fluctuation size,

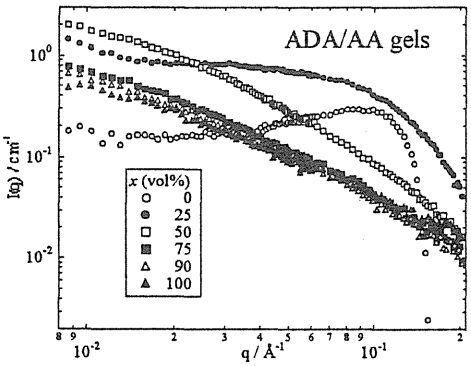


Fig. 2 SANS profiles for ADA/AA gels

we evaluated static correlation functions from the $I(q)$s by the following function:

$$G(r)=\frac{\int_0^\infty I(q)\frac{\sin(qr)}{qr}4\pi q^2 dq}{\lim_{r\to 0}\int_0^\infty I(q)\frac{\sin(qr)}{qr}4\pi q^2 dq}=\frac{\frac{1}{r}\int_0^\infty I(q)\sin(qr)q dq}{\int_0^\infty I(q)q^2 dq} \quad (1)$$

The static correlation function ($G(r)$) is shown in Fig. 3. The $G(r)$s at x = 0 and 25 vol% oscillated and the peak positions indicated that the fluctuation size was 46 Å.

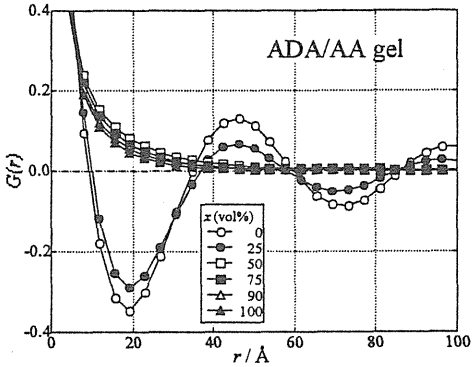


Fig. 3 Spatial correlation function, $G(r)$, for ADA/AA gels

The other $G(r)$s are monotonically decreasing functions of r, indicating the absence of any aggregated inhomogeneities. Hence, we estimated a static correlation length (Ξ_{OZ}), corresponding to the averaged gel network size by a fitting analysis with a sum of the Ornstein-Zernike scattering function, valid for polymer solutions in semi-dilute regime, and an excess scattering function characteristic of gels[2];

$$I(q)=\frac{I_{OZ}(0)}{1+\Xi_{OZ}^2 q^2}+I_{excess}(q) \quad (2)$$

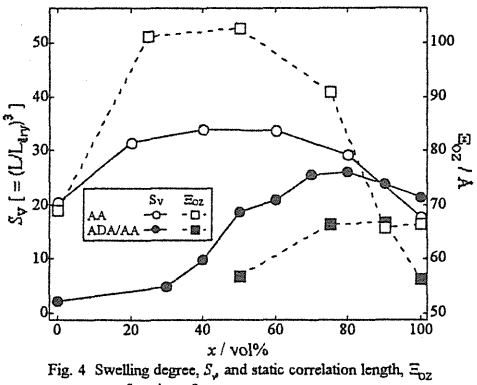


Fig. 4 Swelling degree, S_v, and static correlation length, Ξ_{OZ} as a function of x

Fig. 4 shows the variation of Ξ_{OZ} as a function of x while comparing with swelling degree (S_v) of the gels. The figure indicated an analogy between the macroscopic swelling behavior and microscopic correlation length. Next, we evaluated cooperative diffusion coefficient (D_{SANS}) of the gel network, corresponding to the dynamics of polymer chains, from the $G(r)$ on the basis of the mode-mode coupling theory. D_{SANS} is defined by[3]

$$D_{SANS}=\frac{\int_0^\infty 4\pi r^2 G(r)\frac{kT}{6\pi\eta r}dr}{\int_0^\infty 4\pi r^2 G(r)dr} \quad (3)$$

Fig. 5 shows the x dependence of D_{SANS}, which was a concave function of x, as opposed to the x dependence of S_v and Ξ_{OZ}.

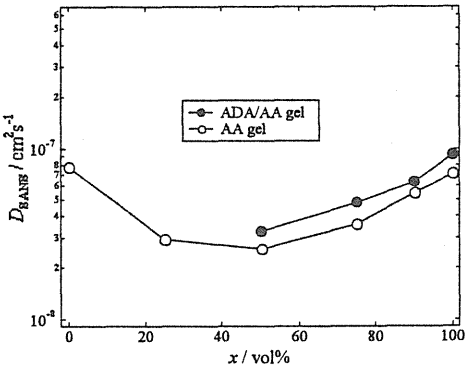


Fig. 5 Variation of D_{SANS} as a function of x

For $x \geq 50$ vol%, D_{SANS} increases with x, indicating that the system recovered the original structure as has been prepared in ethanol. This phenomenon was also verified by dynamic light scattering. As a summary, this study demonstrated the close relationship among the macroscopic swelling behavior, local structure, and local chain dynamics of heteropolymer. This result and discussion have already published in the full paper[4].

REFERENCES

[1] N. Masui et al., *Langmuir* **18**, 5092-5098 (2002).
[2] M. Shibayama, *Macromol. Chem. Phys.* **199**, 1 (1998).
[3] P. G. de Gennes, *Scaling Concepts in Polymer Physics*; Cornell Univ.: Ithaca, NY (1979).
[4] F. Ikkai et al., *Langmuir* **19**, 2568-2574 (2003).

研究テーマ：反応系ブロックコポリマーに関する研究
表　題：動的に非対称な混合系の核生成・成長における粘弾性効果

1-5-25

Viscoelastic effects on the nucleation and growth in dynamically asymmetric mixtures

M. TAKENAKA[1], N. IWASE[1] and T. HASHIMOTO[1] and S. KOIZUMI[2]

[1]Department of Polymer Chemistry, Graduate School of Engineering, Kyoto University, Kyoto 606-8501
[2]Advanced Science Research Center, JAERI, Tokai, Ibaraki 319-1195

Recently, it has been found that the dynamical asymmetry between constituent components in a mixture causes the coupling between stress and diffusion during phase separation processes of the mixture due to the asymmetric stress division. This coupling is called "viscoelastic effects" and has been found to causes shear-induced phase separation in polymer solutions and non exponential decay in dynamic scattering near equilibrium. We aim to explore how the viscoelasticity affects the nucleation and growth processes in dynamically asymmetric semi-dilute polymer solutions. The strength of the effects of the viscoelastic effects is characterized by the viscoelastic length ξ_{ve} defined by

$$\xi_{ve} = \left(\frac{4D\eta_0}{3K_{OS}}\right)^{0.5},$$

where D, η_0, and K_{OS} are, respectively, the inter-diffusion coefficient, the zero-shear viscocity, and the osmotc compressibility. In order to estimate the ξ_{ve}, we need to obtain the the value of K_{OS}. Thus in this study we measured the scattering function of the solution and estimated K_{OS}. The sample used here was deutarated polystyrene (dPS, weight average molecular weight = 5.0×10^6)/Ddiethyl Moronate (DEM) =96/4 (wt.wt.). A SANS experiment of dPS/DEM was done using SANS-J. Fig.1 shows the temperature dependence of the scattered intensity S(q) of dPS/DEM. S(q) increases with decreasing temperature since dPS/DEM becomes close to the spinodal point with decreasing temperature. S(q) in the measured temperature region can be fitted with the following Ornstein-Zernike form:

$$S(q) = \frac{S(0)}{1+q^2\xi^2},$$

where ξ is the thermal correlation length. We obtained ξ and S(0) from fitting. From S(0) we estimated K_{OS}. The osmotic compressibility increases with temperature, indicating that the system has the UCST type phase diagram. We will estimate ξ_{ve} by combining the results of the dynamic light scattering experiment for the solution.

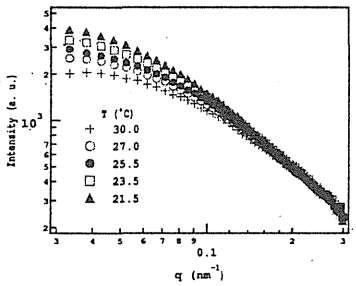


Figure 1: Fig.1 T-dependence of S(q) for dPS/DEM.

原子炉：JRR-3　　装置：SANS-J(C3-2)　　分野：中性子散乱（高分子）

研究テーマ: PVA ゲルの階層構造
表題:化学架橋 PVA ゲルの動的ゆらぎ

1-5-26 Dynamic Fluctuations in Chemically Cross-liked PVA Gels

N. Takahashi, K. Nishida, T. Kanaya, M. Nagao[1], H. Seto[2] and T. Takeda[3]

Institute for Chemical Research, Kyoto University
Institute for Solid State Physics, University of Tokyo[1]
Department of Physics, Kyoto University[2]
Faculty of Integrated Arts and Science, Hiroshima University[3]

In previous works, we have studied dynamic and static fluctuations in two kinds of poly(vinyl alcohol) (PVA) gels using small angle neutron scattering (SANS) and neutron spin echo (NSE) techniques. One is PVA gels fromed in mixtures of dimethyl sulfoxide (DMSO) and water, and the other is PVA gels in aqueous borax solutions. In this work, we have extended similar measurements to chemically cross-linked PVA gels.

NSE measurements were performed on NSE spectrometer installed at the C2-2 cold neutron guide in JRR-3M reactor, Tokai.

PVA was cross-linked using glutaraldehyde (GA) and the degree of cross-linking (CR) was controlled by changing the concentration of GA. Measurements were done on the chemically cross-linked PVA gels as a function of Q and as a function of CR.

Figure 1shows normalized intermediate scattering function I(Q,t)/I(Q,0) of the PVA gels for various degree of cross-linking, including PVA solution (CR=0). I(Q,t)/I(Q,0) decays the fastest for the solution and it becomes slower as CR increases. The solution data was fitted to the theoretical Zimm function $I(Q,t)_{Zimm}$ and the agreement is good as shown in Figure 1 by a solid curve. It was found that I(Q,t)/I(Q,0) of the gels can be well described by sum of the Zimm function $I(Q,t)_{Zimm}$ and a non-decaying component, and the fraction of the non-decaying component increases with CR, suggesting that the static fluctuations increases with CR. It is natural to consider that the static fluctuations arise from the frozen structure of the cross-linking points.

Figure 2 shows I(Q,t)/I(Q,0) of the gels with CR=3 for various Q values after the

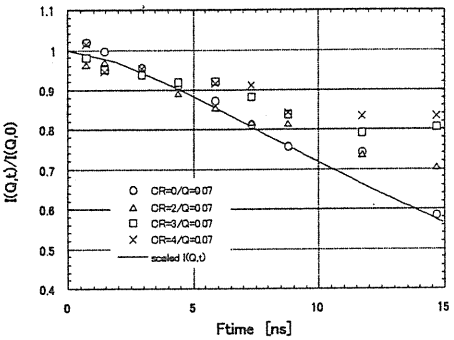


Figure 1. I(Q,t)/I(Q,0) of PVA gels with various CR=0. Solid curve is the Zimm function.

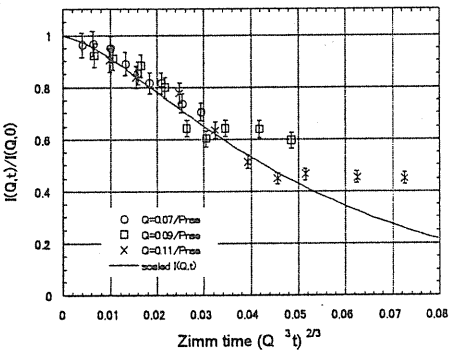


Figure 2. Zimm scaled I(Q,t)/I(Q,0) of PVA gels for various Q. Solid curve is the Zimm function.

Zimm scaling. In a short time region, the Zimm scaling works well while in a long time region it deviates from the Zimm scaling. These results indicate that the polymer chains in the gels behave like in a solution in the short time region, while in the long time region they feel the restriction due to the cross-linking and the motion slows down. Then, the static fluctuations increase with CR.

使用施設:JRR-3 ,装置:NSE(C2-2), 分野 Softmatter

研究テーマ：自己組織化を活用したブロック共重合体のラジカル重合の制御
表　題：中性子小角散乱法によるラジカル重合のその場観察

1-5-27

Small-angle Neutron Scattering Study on in-situ observation of NIPA-*block*-PEG qiasi-living polymerization

Ryuhei Motokawa, Masahiko Annaka, Takayuki Nakahira, and Satoshi Koizumi[1]

Department of Materials Technology, Chiba University, Inage-ku, Chiba 263-8522, Japan
[1]Advanced Science Research Center, Japan Atomic Energy Research Institute, Tokai-mura, Ibaraki 319-1195, Japan

The thermal sensitive diblock copolymer which is composed of poly(N-isopropylacrylamide) (NIPA) and monomethoxy-poly(ethylene glycohl) (PEG) shows immensely unique phase behavior in water. NIPA polymer is a well-known thermal sensitive polymer. It is soluble in water at room temperature but undergoes a phase separation at temperatures higher than its lower critical solution temperature (LCST) at around 32°C. An aqueous solution of NIPA-*block*-PEG indicates three distinct macroscopic phases reversibly, on varying temperature; sol, gel, and phase-separated phase, where the driving force is the coil-grobule transition due to hydrophobic interaction with NIPA block chains.

NIPA-*block*-PEG was prepared for radical polymerization by using ceric ammonium nitrate (IV) as a redox initiator in aqueous solution. A ceric ion redox system was applied for the formation of radical at the terminal carbon of PEG (-CH_2-OH). These PEG termination radicals are used for the polymerization of NIPA monomer. The polymerization method can yield the diblock copolymer with comparatively narrow molecular weight distribution ($M_w/M_n \sim$ 1.25). The cause is supeculated as follows. Performing this polymerization in water above the LCST for NIPA polymer, NIPA chains happen to aggregate with propagating reaction. Therefore, it seems that micelle like structure is organized itself, NIPA-core and PEG-corona, propagation step proceeds within the core of the micelles. Namely, the self-organized structure, which is induced by the polymerization process, has NIPA monomers consume effectively like an emulsion polymerization. We carried out in-situ observation for NIPA-*block*-PEG polymerization process using the time sliced SANS measurement in order to investigate the structure formation and the effect of the micro-structure on polymerization products in non-equilibrium condition.

The neutron scattering experiment was employed Pinhole type Small Angle Neutron Scattering with spectrometer SANS-J at JRR-3M research reactor of Japan Atomic Energy Research Institute (JAERI), Tokai, Ibaraki, Japan. In SANS, the incident neutron beam was collimated into 0.65 nm with $\Delta\lambda/\lambda = 14\%$. The scattered neutrons detected on the 2-dimensional position sensitive detector with a diameter of 0.58 m. The beam stopper size has 40 mm diameter. NIPA-d_7 substituted by isopropyl hydrogen -$CD(CD_3)_2$ was prepared ourselves, and conducted polymerization in H_2O at 32°C on account of obtaining for good contrast between NIPA and PEG-H_2O. Sample in quartz cell of 2 mm thickness was irradiated by neutron beam. The observation time slice scale was carried out 10 min in order to get sufficient statistics of scattering intensity. The sample to detector distance was 6 m ($0.06 < q = 4\pi sin\theta/\lambda < 0.5nm^{-1}$).

Figure 1 shows SANS profiles. The rise in scattering intensity was observed with proceeding polymerization. The results indicate that two effects of propagation reaction and growth of aggregation structure were reflected simultaneously. The power law behaviors of q^{-2} and q^{-4} in Figure 1 maybe make it follow that mass distribution of micelle structure and NIPA strongly aggregated domain forming a clearly sharp interface into PEG-H_2O matrix respectively. We are investigating more detail due to reveal the correlation between polymerization reaction and self-organized structure.

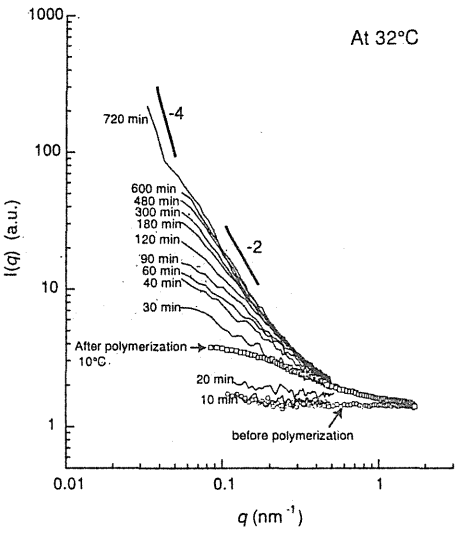


Figure 1: SANS profiles were obtaned for in-situ observation of NIPA($-d_7$)-*block*-PEG polymerization process at 32°C (solid lines), before (open circles) and after (open squares) polymerization.

原子炉：JRR-3　　装置：SANS-J(C3-2)　　分野：中性子散乱（高分子）

研究テーマ：トポロジカルゲルのゾルーゲル転移と不均一性解析
表題：トポロジカルゲルのゾルーゲル転移と不均一性解析

1-5-28 Inhomogeneities and Sol-gel Transition of Topological Gels

M. Shibayama[1], S. Okabe[1], T. Karino[1],Y. Okumura[2], Y. Domon[2], and K. Ito[2]
[1] *Institute for Solid State Physics, The University of Tokyo, 106-1 Shirakata, Tokai, 319-1106*
[2] *Graduate School of Frontier Sciences, The University of Tokyo, Kashiwa, Chiba, 277-8561*

Polymer gels inherently possess inhomogeneities due to non-randam distribution of cross-links. These inhomogeneities usually increase upon a change of their environment, such as swelling or deformation, because the cross-links are permanently fixed on the polymer chains in topological point of view and the gel cannot adjust its cross-link distribution upon the change of envrironment.[1]

Okumura and Ito recently succeeded in preparation of the so-called "topological gel", in which 8-of-letter shape cross-links were introduced.[2] It is expected that the topological gels have a capability of minimizing the sum of strain energy on the network by sliding cross-links along the polymer chain, irrespective of a change of environment. In order to verify this hypothesis, we carried out small-angle neutron scattering (SANS) studies on topological gels at SANS-U. The topological gels were prepared by coupling α-cyclodextrins on different polyrotaxane chains consisting of poly(ethylene glycol) (PEG) and α-cyclodextrin (CD) in deuterated dimethylsulfoxide (DMSO-d6). The molecular weigh of PEG was 1.00×10^5, the CD concentration was 17 %, and the gel concentration was 10%. The wavelength was 7 Å.

As shown in Fig. 1, the two-dimensional SANS intensity pattern for $DR = 1.0$ was isotropic. However, by uniaxially stretching the gel up to $DR = 1.5$, the topological gels exhibited so-called normal-butterfly patterns, which means a prolate isointensity pattern in the direction perpendicular to the stretching direction. Here, the stretching direction was horizontal. Abnormal-butterfly patterns, i.e., prolate patterns parallel to the stretching direction, have been usually observed in conventional chemical gels,[3] and those SANS patterns were qualitatively explained by the the theory of Onuki.[4] Therefore, the SANS behavior of the topological gels is opposite to those of conventional gels and quite unique. The origin of the difference in deformation mechanism between the two types of gels as well as the cross-link density dependence of the inhomogeneities will be discussed by focusing on the unique architecture of the topological gels.

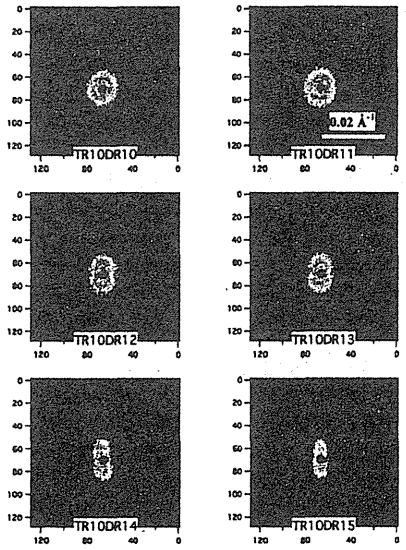


Fig. 1. Two-dimensional SANS patters for uniaxially stretched topological gel. The draw ratios, λ, are indicated with the numbers following DR, and are from λ =1.0 to 1.5. The stretching direction is horizontal.

References

[1] M. Shibayama: Macromol. Chem. Phys. **199** (1998)1.
[2] Y. Okumura, K Ito: Adv. Mater. **13** (2001)485.
[3] C. Rouf, *et al.*: Phys. Rev. Lett. **73** (1994)830.
[4] A. Onuki: J. Phys. II France **2** (1992)45.

使用施設：JRR-3　装置： C1-2 (SANS-U)，分野： 6. Softmatter

研究テーマ：中性子イメージングプレートを利用した合成高分子の精密結晶構造解析への初挑戦
表　題：合成高分子結晶構造解析における水素原子の直接抽出

1-5-29

Direct Extraction of Hydrogen Atoms in the Crystal Structure Analysis of Synthetic Polymers by Utilizing 2-Dimensional Neutron Imaging Plate System

K.TASHIRO, N.NIIMURA[1,2], I.TANAKA[1] and S.FUJIWARA[1]

Graduate School of Science, Osaka University, Osaka 560-0043
[1]Advanced Science Research Center, JAERI, Tokai, Ibaraki 319-1195
[2]Faculty of Engineering, Ibaraki University, Hitachi, Ibaraki 316-8511

In order to clarify the relation between structure and mechanical property of polymer crystals in a quantitative manner, we need to know the exact atomic positions in the crystal lattices, in particular the positions of hydrogen atoms. Unfortunately, however, there had been almost no trial to reveal the hydrogen atom positions as exactly as possible for the synthetic polymer materials because of poor x-ray diffraction data in general compared with the cases of low-molecular-weight compounds. In the previous paper[1)] we succeeded in extract the hydrogen atoms by calculating the Fo-Fc Fourier map based on the X-ray imaging-plate system. But we may expect to obtain the hydrogen atom positions in more exact and direct manner by taking the 2-dimensional neutron diffraction patterns of the deuterated polymer materials through the neutron imaging plate system.[2)] This is a report about the first success of direct extraction of hydrogen atoms of synthetic polymer crystals by measuring the 2-dimensional neutron fiber diagrams.

Figure1 shows the 2-dimensional neutron fiber diagrams taken for the uniaxially-oriented samples of fully-deuterated (D) and totally-hydrogeneous (H) polyethylenes, which were measured by using a JAERI BIX-3 system. In this figure are also shown the neutron fiber diagrams predicted for D and H polyethylene crystals (see Fig. 2), which give good correspondence with the actually observed patterns. By evaluating the inte-

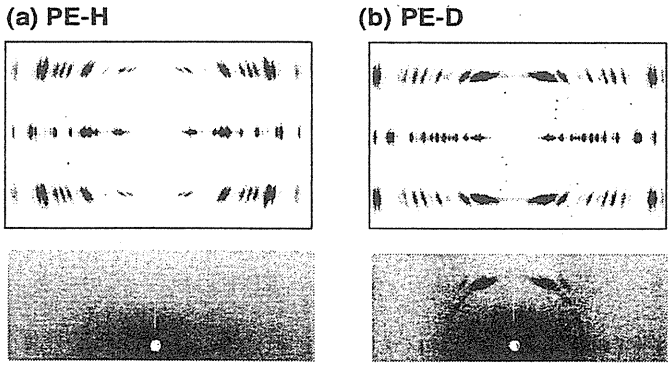


Figure 1: Neutron fiber diagrams of uniaxially-oriented (a) H and (b) D polyethylene samples.

原子炉：JRR-3　　装置：BIX-3(1GA)　　分野：中性子散乱（高分子）

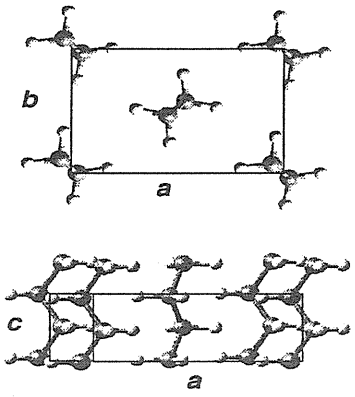


Figure 2: Crystal structure of orthorhombic polyethylene.

grated intensities of the observed reflections, the Fourier map was calculated for the D sample. Different from the X-ray structure analysis, where only the carbon atoms were found as shown in Fig. 3 (b), the neutron fiber diagram of the D sample allowed us to extract the hydrogen atoms quite clearly and directly as seen in Fig. 3 (a). We are now refining the crystal structure by using the thus extracted hydrogen (and carbon) atom positions.

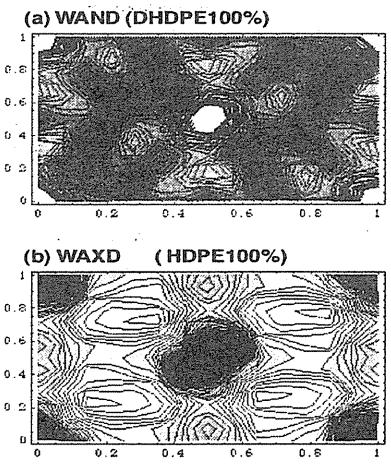


Figure 3: Fourier maps calculated from (a) WAND data of deuterated polyethylene and (b) WAXD data of normal polyethylene. Refer to Fig. 2.

Figure 4 shows the neutron equatorial diffraction patterns measured for a series of random copolymers between D and H ethylene monomeric units. With a change in the relative content of the deuterated component, the diffraction pattern changed systematically. This systematic change can be reproduced reasonably and quantitatively by assuming statistically random arrangement of the D and H units in the crystal lattice. This is consistent with the infrared spectral data showing a systematic change in the band splitting width due to the vibrational correlation between the adjacent chain stems.[3)]

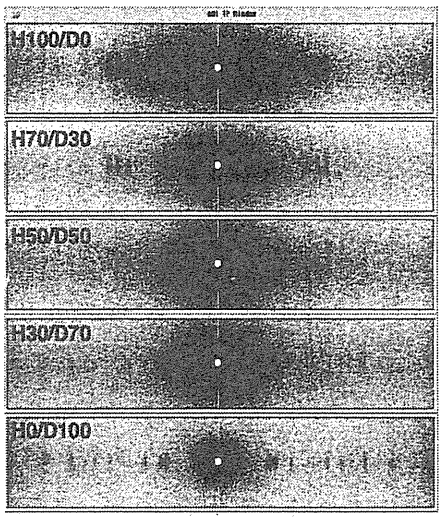


Figure 4: Neutron fiber diagrams (equatorial line) measured for a series of uniaxially-oriented D/H random ethylene copolymers .

References

1) K. Tashiro, H. Asanaga, K. Ishino, R. Tazaki, and M. Kobayashi, J. Polym. Sci.: Part B: Polym. Phys. **35** (1997) 1667.
2) N. Niimura, Y. Karasawa, I. Tanaka, J. Miyahara, K. Takahashi, H. Saito, S. Koizumi, and M. Hidaka, Nucl. Instrum. Meth. Phys. Res. A. **349** (1994) 521.
3) K. Tashiro, M. Sato, Y. Cho and M. Kobayashi, Polym. Prepr. Jpn. **48** (1999) 3574.

表題:高分子鎖を閉じ込めた球状膜の構造転移

1-5-30

Morphological Transition Induced by Confinement the Polymer Chains in a Dilute Microemulsion Droplet System

K. Nakaya and M. Imai

Ochanomizu University, 2-1-1 Otsuka, Bunkyo-ku, Tokyo 112-0012, Japan

Microemulsion is the unique system in which water and oil coexist stably through a surfactant monolayer. It shows some different topologies in membrane structure, such as globular (droplet), layered (lamellar) or structure of network state (bicontinous) dependent on compositions or external fields. We noticed the droplet structure, which gives the isolated meso-scale space. In previous paper [1], we investigated the static behavior of the droplet structure confining a single polymer chain in a dilute microemulsion system. It was proved that the balance of membrane elastic energy and entropy loss due to the polymer confinement governs the droplet size. In this study we reported the morphological change of the spherical membrane induced by very strong confine-ment of polymer chains.

The system studied was water-in-oil microemulsion droplets, which consisted of AOT, iso-octane, and water. As a confined polymer it was adopted the water-soluble polymer, gelatin. The radius of the droplet (R) was controlled by changing the water to surfactant ratio (ω_0) in the vicinity of the radius of gyration (R_g) of gelatin, R_g=81Å. The volume fraction of the dispersed phase which consists of water and AOT (and polymer) was fixed to 0.07. The static structure of the membrane was investigated by small angle neutron scattering (SANS) technique. The SANS measurements were performed using JRR3M SANS-U(C1-2) in JAERI (Tokai). All samples were prepared with the film contrast condition.

Figure 1 shows the SANS scattering profiles for water-in-oil microemulsion droplet (ω_0=57.6) with and without polymer. By confining the polymer chains strongly, the peak observed in the droplet without the polymers shifted to the high q side, and the scattering intensity increased in low q region. The scattering spectra of droplet are described by form factor P(q) and structure factor S(q). We fitted the experimental profiles with the spherical shell model [2] as P(q) and Percus-Yevic model as S(q). Then the profile of droplet without the polymers was fitted very well, and we got the results of R=78Å. On the other hand, in the case of the polymer confinement system, the spherical model could not fit the observed profile well. Then we adopted the rotational ellipsoidal model as P$_r$(q), which is approximated to rod (or sphero-cylinder) model. For simplicity, it was assumed S (q)=1 because it was difficult to estimate structure factor of semi-dilute rod solution. The scattering curve with polymer could be described well with the rotational ellipsoidal model. This result suggests the morphological transition of a membrane from sphere to rod by strong confinement of the polymer chains. It was found that the radii of the minor axis and the major axis are about 58.5 and 350 Å, respectively. Using these parameters the number of the polymer chains was calculated to about 4.5 chains per ellipsoid.

In order to elucidate this morphological change, we must estimate the geometrical effect of the confinement on the total energy of the system.

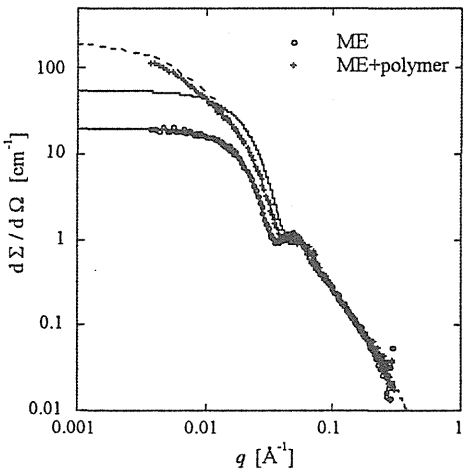


Fig.1 SANS profiles for the system of AOT-isooctane-water microemulsion droplet of ω_0=57.6 without (opened circle) and with (cross) gelatin at 30°C. The solid lines are curves fitted with the sphere model and dashed line is with the rotational ellipsoidal model.

References

[1] K.Nakaya et al., J.Phys.Soc.of Japan, 70 Suppl.A (2001) 338.

[2]M.Grazielski et al., Phys.Rev.E 53 (1996) 3900.

使用施設:JRR-3. ,装置:SANS-U(C1-2), 分野 Softmatter

研究テーマ：相溶性高分子混合系における動的不均一と濃度揺らぎの関係2
表題：ポリスチレン/ポリビニルメチルエーテル混合系の非干渉性弾性散乱研究

1-5-31

Elastic incoherent scattering studies of poly(styrene) and poly(vinyl methyl ether) mixtures

H. Takeno and S. Koizumi[1]

Department of Biological and Chemical Engineering, Faculty of Engineering, Gunma University, Gunma 376-8515
[1]Japan Atomic Energy Research Institute, Tokai, Ibaraki 319-1195

In the past few decades, numerous studies have been performed on the miscibility of polymer blends. It is strongly affected by local packing of molecules such as free volume. Such local packing may affect scales of local motions such as mean square displacement of the system. We studied elastic incoherent scattering of polystyrene (PS) and poly(vinyl methyl ether) (PVME) blends with a low energy triple axis spectrometer (LTAS). Since incoherent scattering cross section of hydrogen is much larger than those of other atoms, we can obtain information about geometry of molecular motions through incoherent scattering due to hydrogen. In order to pursue the effect of the motion of each component on blending, we used two kinds of blends, deuterated PS(dPS) /PVME and protonated PS (hPS) /PVME blends (since synthesis of deuterated PVME is technically very difficult, we cannot use it), and those of pure protonated components for comparison. When the motion of the system is vibrational, the elastic incoherent scattering behavior can be described by Debye-Waller factor $I(q,\omega=0) = I_0\exp(-<u^2>q^2)$, where $<u^2>$ is the mean square displacement and $q(=(4\pi/\lambda)\sin(\theta/2))$ is the scattering vector. In fact, the scattering intensity observed for all samples had a small coherent scattering peak. Therefore, in order to eliminate the coherent effects,[1] we divided the scattering intensity at a given temperature by that at lowest temperature (ca. $T_{\rm min}$ = 10K). Though plot of the logarithm of the divided intensity $\ln[I_T(q,\omega=0)/I_{T_{min}}(q,\omega=0)]$ against q^2 showed the linear behavior at lower temperature region than 90 or 120 K at least in the q-region covered in our measurements and it has a slight curvature at temperature region of or $T \geq 90$ or 120 K, i.e., it shows the non-Gaussian behavior. Therefore, in the latter region, we carried out the non-Gaussian analysis,

$$I(q,\omega=0) = I_0\left[\exp\left(-\alpha_T q^2 + (1/2)A_{0,T}\alpha_T^2 q^4\right)\right]$$

, where $\alpha_T = <u^2>/6$ and $A_{0,T}$ is a parameter, which characterizes non-Gaussian nature. $A_{0,T}$ may be related to dynamical heterogeneity due to different local environments. For hPS/PVME, both components involve hydrogen atoms, we analyzed it with double non-Gaussian equation, assuming additivity of non-Gaussian contribution for each component. In the fitting procedure with the double non-Gaussian equation, since we had too many adjustable parameters, we fixed the parameters for PVME by using the parameters obtained for dPS/PVME blends and obtained parameters them for hPS. The α_Ts and $A_{0,T}$s obtained thus for all the samples are shown in Figures 1 and 2, respectively. In comparison of dPS/PVME with PVME, although $A_{0,T}$ is almost the same for both samples, α_T for dPS/PVME is larger than that of PVME in the temperature region of $T \geq 120$K. The latter result indicates that spatial scale of motion of PVME in the blend is larger than that of pure components. On the other hand, as compared with the motions of PS, though α_T is hardly affected by blending, $A_{0,T}$ becomes remarkably larger relative to that of pure PS. Broadening of the distribution of local motions has been reported by Fisher et al. for a mixture of a low-molecular weight substance and polycarbonate with the same

原子炉：JRR-3　　装置：LTAS(C2-1)　　分野：中性子散乱（高分子）

benzene ring as PS.[2] Especially, we would like to note the behavior of α_T, which is related to the mean square displacement. By blending, the mean square displacement for PVME with small side groups became larger, while it for PS with bulky side groups did not. The result supports our "interstices model" proposed from phase diagram and glass transition temperature behavior of polymer blends, in which the small molecules go into interstices produced by another bulky molecules.[3]

References

1) T. Kanaya , T. Kawaguchi and K. Kaji: J. Chem. Phys. **104** (1996) 3841.

2) E. W. Fisher, G. P. Hellmann, H. W. Spiess, F. J. Horth, U. Ecarius and M. Wehrle: Macromol. Chem. Suppl. **12** (1985) 189.

3) M.Naoki and H. Takeno: to be submitted.

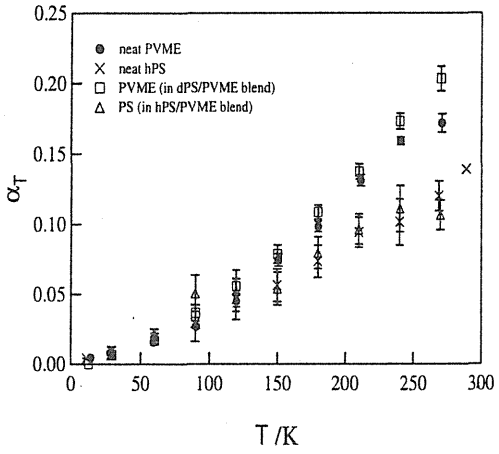


Figure 1: Temperature dependence of α_T for various samples.

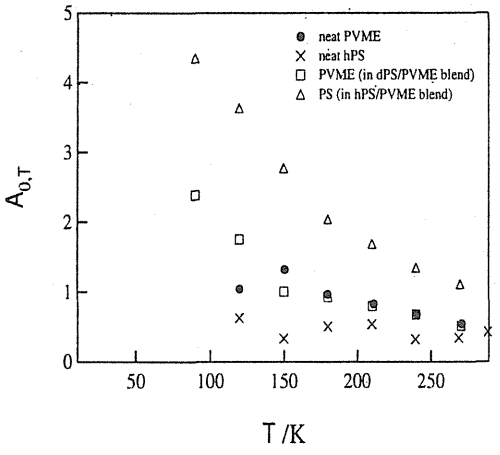


Figure 2: Temperature dependence of $A_{0,T}$ for various samples.

研究テーマ:動的に非対称な高分子混合系の相分離過程における応力と拡散のカップリングの効果に関する研究
表題:動的に非対称な高分子準希薄溶液の濃度揺らぎのダイナミックスにおける粘弾性効果

Viscoelastic effects on the dynamics of concentration fluctuations in dynamically asymmetric semi-dilute polymer solutions

1-5-32

Mikihito Takenaka, Koichiro Tada, Naoki Iwase, Taekji Hashimoto and Michio Nagao*

*Department of Polymer Chemistry, Graduate School of engineering, Kyoto University, Kyoto 606-8501, Japan; *Institute for Solid State Physics, The University of Tokyo, 106-1 Shirakata, Tokai 319-1106, Japan*

Recently, it has been found that the dynamical asymmetry between constituent components in a mixture causes the coupling between stress and diffusion during phase separation processes of the mixture due to the asymmetric stress division. This coupling is called "viscoelastic effects" and has been found to causes shear-induced phase separation in polymer solutions and non exponential decay in dynamic scattering near equilibrium. We aim to confirm the Doi-Onuki theory can well-describe the viscoelastic effects on the dynamics of the relaxation processes in dynamically asymmetric semi-dilute polymer solutions as well as to explore how the viscoelasticity affects the relaxation of the concentration fluctuations in dynamically asymmetric semi-dilute polymer solutions. The strength of the effects of the viscoelastic effects is characterized by the viscoelastic length ξ_{ve} defined by

$$\xi_{ve} = \left(\frac{4D\eta_0}{3K_{OS}}\right) \qquad (1)$$

where D, η_0, and K_{OS} are, respectively, the inter-diffusion coefficient, the zero-shear viscocity, and the osmotc compressibility. In order to estimate the ξ_{ve}, we need to obtain the the value of K_{OS}. Thus in this studt we measured the scattering function of the solution and estimated K_{OS}. The sample used here was deutarated polystyrene (dPS, weight average mo;ecu;ar weight = 2.0×10^6)/Dioctyl =96/4 (wt.wt.).

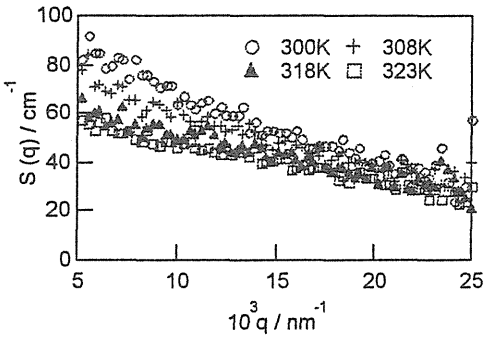


Figure 1: The change in he scattered intensity of dPS/DOP=(4wt%96wt%) with temperature.

A SANS experiment of dPS/DOP at 300K < T < 323K was done using SANS- U with 7Å of incident neutron beam. The covered q range was $0.005 \le q \le 0.15 Å^{-1}$. Fig.1 shows the temperature dependence of the scattered intensity $S(q)$ of dPS/DOP. $S(q)$ increases with decreasing temperature since dPS/DOP becomes close to the spinodal point with decreasing temperature. $S(q)$ in the measured temperature region can be fitted with the following Ornstein-Zernike form:

$$S(q) = \frac{S(0)}{1+q^2\xi^2} \qquad (2)$$

where ξ is the thermal correlation length. We obtained ξ and $S(0)$ from fitting. From $S(0)$ we estimated K_{OS}. The osmotic compressibility increases with temperature, indicating that the system has the UCST type phase diagram. We will estimate ξ_{ve} by combining the results of the dynamic light scattering experiment for the solution.

使用施設:JRR-3', 装置:SANS-U(C1-2), 分野 Soft matter

研究テーマ：中性子小角散乱法による高分子構造変形のその場観察
表　題：中性子小角散乱法による高分子鎖の変形のその場観察

1-5-33

Dynamical Asymmetry Effect of Long-Chain Branching in Polyethylene Blends

T. KASAHARA, S. UTSUMI, T. SAKURAI, N. YAMAGUCHI and S. KOIZUMI[1]

Petrochemicals Research Laboratory, Sumitomo Chemical Co., Ltd.,
2-1 Kitasode Sodegaura, Chiba 299-0295, Japan
[1]Advanced Science Research Center, JAERI, Tokai, Ibaraki 319-1195, Japan

The purpose of this work is to make clear the effect of dynamical asymmetry of long-chain branchings in polyethylene blends. Samples that were mixed two kinds of hydrogenous polyethylenes (H-PEs) with a deuterated high-density polyethylene (D-HDPE) were measured small-angle neutron scattering (SANS) under shear-flow. H-PEs are linear low-density polyethylene (LLDPE) and low-density polyethylene (LDPE). The LLDPE and the LDPE are evaluated as a linear polyethylene and as a long-chain blanched polyethylene, respectivery. The effect to dynamical asymmetry of a long-chain branched polyethylene under shear-flow was compared with it of a linear polyethylene by using two-dimensional SANS patterns.

Table 1: Characteristics of materials for blend samples.
*: The number of short-chain blanchings.
**: The number of CH_3s.

		LLDPE	LDPE	D-HDPE
MFR	g/10 min	2.1	2.0	-
SR	-	1.09	1.41	-
density	g/cm^3	0.912	0.923	-
$[\eta]$	dl/g	1.48	0.88	-
Mw	-	88000	61000	493000
Mn	-	44000	19000	76000
Mz	-	146000	134000	1894000
Mw/Mn	-	2.0	3.2	6.5
SCB*	/1000C	17.8	20.7**	-

Characteristics of the D-HDPE and H-PEs that were used in this study are shown in Table 1. The D-HDPE and H-PEs were mixed by using xylene. D/H composition of blend samples were 20/80 wt%. The LLDPE (EXACT 3030) that is ethylene-hexane copolymer was purchased from ExxonMobil Chemical Company. The LDPE (SUMIKATHENE F200-0) was supplied by Sumitomo Chemical Co., Ltd.

The SANS measurements were performed with a spectrometer SANS-J at research reactor JRR-3M of JAERI. Camera length was set 10 m and scattered neutrons were detected on the Two-dimensional ^{3}He position sensitive detector. A shear cell installed in the SANS-J was Linkam Cambridge Shearing System CSS 450. Its viewing area was converted into 5mmϕ. Blend samples were once melted completely at 200 ℃ before SANS measurements. The static experiment and the shear-inducing experiment were conducted at 160 ℃ . Shear mode and shear rate of shear-inducing experiments were steady mode and 1.0 s^{-1}, respectively.

Figure 1 and 2 show the two-dimensional SANS patterns of D-HDPE/LLDPE (20/80) blend (linear blend) of static and shear rate 1 s^{-1}, respectively. Although the SANS pattern of the linear blend was isotropic before shear-inducing (Fig. 1), The pattern of the blend under shear became elliptic shape whose major axis was perpendicular to flow direction (Fig. 2). This can be interpreted that the gaussian chains of polyethylenes were extended into the flow direction.

Figure 3 and 4 show the two-dimensional SANS patterns of D-HDPE/LDPE (20/80) blend (branching blend) of static and shear rate 1 s^{-1}, respectively. The SANS pattern of the branching blend was also isotropic before shear inducing (Fig. 3). The pattern of the branching blend under shear- flow became specific SANS pattern (Fig. 4). We can see

原子炉：JRR-3　　装置：SANS-J(C3-2)　　分野：中性子散乱（高分子）

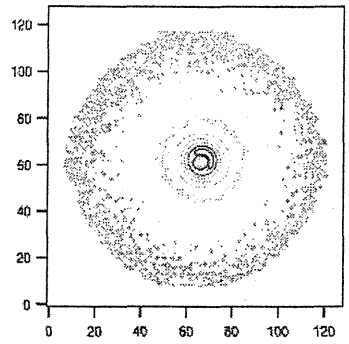


Figure 1: The two-dimensional SANS pattern of the D-HDPE/LLDPE (20/80) blend.
Befor shear-inducing.
The flow direction is the longitudinal direction.

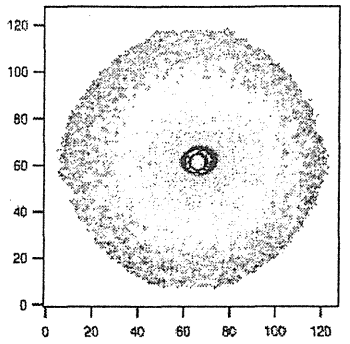


Figure 2: The two-dimensional SANS pattern of the D-HDPE/LLDPE (20/80) blend.
Shear rate is $1.0s^{-1}$.
The flow direction is the longitudinal direction.

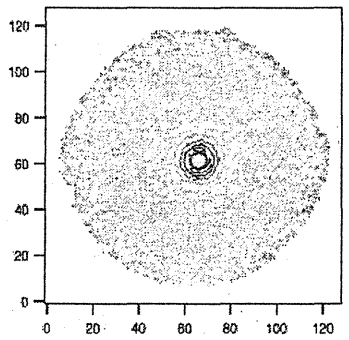


Figure 3: The two-dimensional SANS pattern of the D-HDPE/LDPE (20/80) blend.
Befor shear-inducing.
The flow direction is the longitudinal direction.

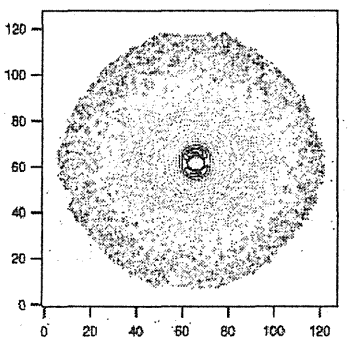


Figure 4: The two-dimensional SANS pattern of the D-HDPE/LDPE (20/80) blend.
Shear rate is $1.0s^{-1}$.
The flow direction is the longitudinal direction.

two phenomena from the specific SANS pattern. One is elliptic shape whose major axis was perpendicular to the flow direction similar to the linear blend. This showed that the gaussian chains of the blend were extended into the flow direction. The other is a abnormal butterfly pattern [1] was appeared in the parallel to the flow direction of lower q region.

Such a scattering pattern shows that phase-separation arises from different viscosity of blended polymers under shear-flow. We think that these phenomena are based on the effect of the dynamical asymmetry of long-chain blenchings in polymer melt.

References

1) Satoshi Koizumi : J. Appl. Cryst. **36** (2003) 381.

研究テーマ： 圧力誘起による高分子ゲルの相転移に関する研究
表題： 圧力誘起によるPNIPA溶液の相転移に関する研究

Pressure-induced Phase Separation of Poly(*N*-isopropylacrylamide) Aqueous Solutions

1-5-34

M. Shibayama, K. Isono, S. Okabe, S. Takata, M. Nagao
Institute for Solid State Physics, The University of Tokyo, 106-1 Shirakata, Tokai, 319-1106

Poly (N-isopropylacrylamide) (PNIPA) aqueous solutions are known to be environment-sensitive systems undergoing phase separation at *ca* 32 °C upon an increase of temperature.[1] The environment sensitivity is mainly ascribed to the strong hydrophobicity of the *N*-isopropyl group located on the side chain. Compared with temperature dependence,[2] pressure effects on phase behavior of (PNIPA) aqueous systems have been much less investigated. Here, we report preliminary results of pressure-dependent SANS on PNIPA solutions.

PNIPA aqueous solutions were prepared with 700 mM of recrystallized N-isopropylacrylamide monomer, 8.63 mM bisacrylamide, and 1.7 mM of ammonium persulfate, and 3.0 mM of *N,N,N'*,*N'*-tetramethylenediamine. A pregel solution was degassed and then polymerized in D_2O at 20 °C. Pressure-dependent small-angle neutron scattering (SANS) experiments were carried out at the SANS-U, the Univerist of Tokyo. The wavelength of the neutron was 7.0 Å.

Fig.1 shows temperature-pressure ($T-P$) phase diagram obtained by light-cloud point method, which is close to the binodal temperature (T_b) curve. The $T-P$ diagram was a convex-upward function of P, having the critical point at 33.6 °C at 51.7 MPa. Note that there exists a significant effect by cross-linking (gel). The scattering intensity, $I(q)$, increased with increasing P, and was nicely fitted with the so-called Ornstein-Zernike equation given by

$$I(q) = \frac{I(0)}{1+\xi^2 q^2} \qquad (1)$$

where q is the magnitude of the scattering vector and ξ is the correlation length.

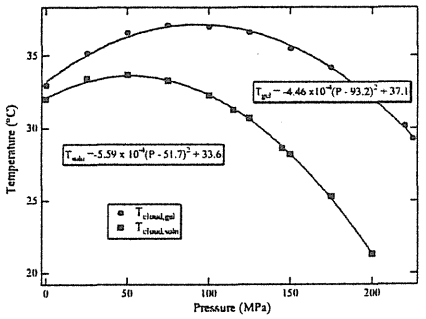


Fig. 1. $T-P$ phase diagram of PNIPA aqueous solutions and gels.

Fig. 2 shows the variation of $I(0)^{-1}$ and ξ as a function of P. Both $I(0)$ and ξ increased with increasing P and showed a tendency to diverge at T_{sp}. The critical exponents were

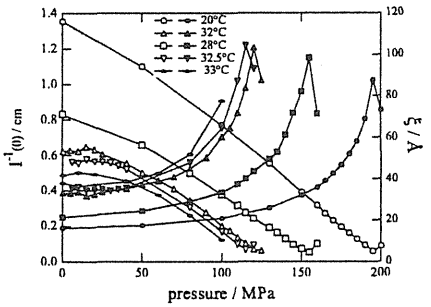


Fig. 2. Variation of $I(0)^{-1}$ and ξ as a function of P evaluated for PNIPA solutions at various Ts .

obtained to be $1.1 \leq \gamma \leq 1.23$ and $0.5 \leq \nu \leq 0.6$. The spinodal temperature, T_{sp} seems to merge at the critical point. These results will be compared with those of the polymer gels.

References

[1] M. Shibayama,*et al.*: J. Chem. Phys. **97** (1992)6829.
[2] M. Shibayama,*et al.*: Adv. Polym. Sci. **109** (1993)1.

使用施設：JRR-3　装置： C1-2 (SANS-U)， 分野： 6. Softmatter

研究テーマ：中性子散乱によるソフトマターの構造と機能
表　題：アニオン重合のその場観察

1-5-35

Small-Angle Neutron Scattering Study on Living Anionic Polymerization Process of Styrene

Kazuhiro Yamauchi, Hirokazu Hasegawa, Takeji Hashimoto and Satoshi Koizumi[1]

Graduate School of Engineering, Kyoto University, Kyoto 606-8501, Japan
[1]Advanced Science Research Center, JAERI, Tokai-mura, Ibaraki 319-1195, Japan

In addition polymerization of styrene monomers by an anionic process monomers are added to the living ends of polystyril anions and the polymer chains grow with time until all the monomer molecules are consumed. We planed the time-resolved SANS measurements of such polymerization processes. This is a report of our preliminary result.

SANS-J instrument at JAERI JRR-3M research reactor was used for this study with neutron wavelength of 0.7 nm. The polymerization of styrene monomer was performed with d_6-benzen as solvent and s-butyllithium as initiator at room temperature in a quartz cell with the sample thickness of 5 mm sealed with a 3-way cock under nitrogen gas atmosphere. Time-resolved SANS intensity profiles were obtained with 5 min interval after addition of initiator into the mixture of the monomer and the solvent. The final polymer concentration was 30% and the molecular weight of the resulting polystyrene was 5,000.

Figure 1a shows the time-resolved SANS intensity profiles. The scattering intensity increased after 5 min from the initiation. After 10 min the scattering intensity increased significantly, but it remained almost constant with time beyond this point implying that the polymerization was completed in 10 min. Figure 1b shows the change of scattering profile on addition of ethanol to kill the living anion ends of the polystyrene. It is intriguing that the scattering intensity once increased after addition of trace amount of ethanol (The orange color of living polystyrillithium disappeared and the solution underwent gelation.), but decreased again after addition of larger amount of ethanol. (The gel turned into solution.) The scattering intensity of the solution of the dead polymer is smaller than that of the living polymer suggesting the association of thechain ends for the living polymer.

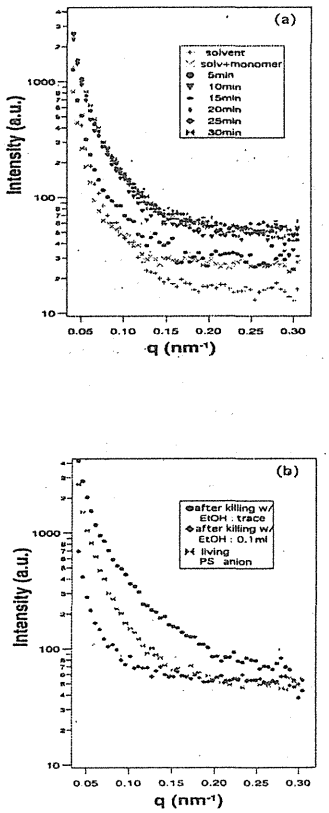


Figure 1: (a) Time dependence of SANS profiles in the anionic polymerization process of styrene in d_6-benzen. (b) Effect of adding ethanol to the solution of the living polystyril anions.

原子炉：JRR-3　　装置：SANS-J(C3-2)　　分野：中性子散乱（高分子）

研究テーマ： PVA のゲル化に及ぼすせん断流動効果

表題：中性子小角散乱によるせん断流動場下におけるポリビニルアルコールのゲル化

1-5-36 **Rheo-SANS Study on Gelation of Poly(vinyl alcohol)**

N. Takahashi, T. Kanaya, K. Nishida, and Y. Takahashi*

*Institute for Chemical Research, Kyoto University, Uji, Kyoto 611-0011, JAPAN; *Department of Molecular and Material Sciences, Interdisciplinary Graduate School of Engineering Sciences, Kyusyu University, Hakozaki, Fukuoka 812-8581, JAPAN*

The gelation of poly(vinyl alcohol) (PVA) under shear flow have been studied by Small-Angle Neutron Scattering (SANS) instruments. SANS measurements were carried out on SANS-U spectrometer at a beam port (C1-2) of JRR-3M reactor, in JAERI (Tokai). The steady and oscillatory shear flows were performed by using a couette type flow cell [1].

PVA solution with polymer concentration C_p = 5 g/dl in a mixture of deuterated dimethyl sulfoxide (DMSO-d_6) and D_2O with volume fraction of DMSO-d_6 ϕ_{DMSO} = 0.6 and 0.8 were used. The homogenized PVA solution at 100 °C was quenched to 25 °C and quickly filled into the rotation cell to gelation. The steady shear flow (shear rate $\dot{\gamma}$ range is between 1.0 and 100 sec^{-1}) and oscillatory shear flow (frequency f range is between 0.1 to 10 Hz, strain ε range is between 30 to 200 %) were respectively induced immediately and time resolved 2D-SANS measurements were performed in the scattering vector Q ranges between 5.8 x 10^{-3} and 6.3 x 10^{-2} $Å^{-1}$ with "through view".

Steady shear flow

All 2D-SANS profiles on PVA gelation under shear flow were azimuthally symmetric that the circular averaged scattering intensities were calculated. Figure 1 shows the time evolution of the circular averaged scattering intensities of PVA solution (ϕ_{DMSO} = 0.6) with steady shear flow ($\dot{\gamma}$ = 5 sec^{-1}). The solid and dotted lines indicate the Ornstein-Zernike (OZ) formula (eq.1)

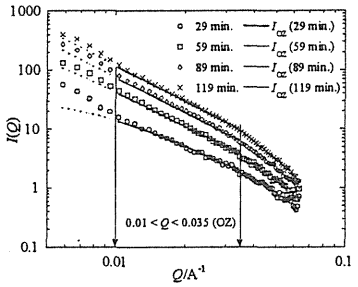


Figure 1: Time evolution of SANS profiles of PVA solution under shear flow ($\dot{\gamma}$ = 5 sec^{-1}) quenched from 100 °C to 25 °C. $I(Q)$s are well described by eq. 1 for 0.01 < Q < 0.035 $Å^{-1}$, which is indicated by solid and dashed lines.

$$I(Q) = \frac{I(0)}{1+\xi^2 Q^2} \qquad (1)$$

where ξ is a correlation length and $I(0)$ is the scattering intensity at Q = 0. The solid lines, which indicate the Q-range between 0.01 and 0.035 $Å^{-1}$, are well fitted to $I(Q)$s but dashed lines are not. $I(Q)$s turn up from OZ formula in the Q-range smaller than 0.01 $Å^{-1}$ due to the structural inhomogeneity becoming from phase separation. In order to leave off the

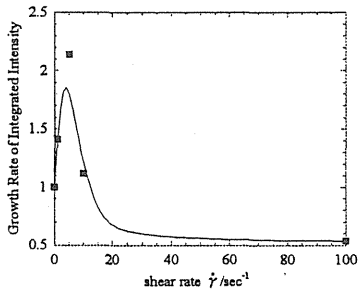


Figure 2: The growth rate of integrated intensity is plotted against shear rate $\dot{\gamma}$. ϕ_{DMSO} = 0.6

使用施設：JRR-3， 装置：SANS-U(C1-2)，分野 Softmatter

contribution of phase separation, we have calculated the integrated scattering intensity (*II*) in the *Q*-range larger than 0.01 Å^{-1} and the growth rate of them from the slope of the initial state of the plot, *II* against time. It was previously reported [2] that we can observe the evolution of concentration fluctuation in this *Q*-range, which indicates smaller than 600 Å in the real space so that the growth rate indicates the gelation rate (structure formation rate) without involving the effects of phase separation. Figure 2 shows the normalized growth rate of *II* against shear rate $\dot{\gamma}$. The growth rate, corresponding to gelation rate was accelerated by inducing steady shear flow, which shear rate $\dot{\gamma}$ is smaller than 5 sec^{-1} and bigger than that value the deceleration of it has overcame. At $\dot{\gamma}$ = 100 sec^{-1}, the gelation rate is smaller than one at quiescent state. In the case of ϕ_{DMSO} = 0.8, corresponding to the transparent gel forming condition, the effects on gelation under shear flow without considering about phase separation was clearly discussed. The growth rate of *II* was plotted against shear rate (data not shown). Gelation acceleration and deceleration was observed and gelation rate had a maximum value at $\dot{\gamma}$ = 5 sec^{-1}. These results supposed that crystal nuclei generation rate was accelerated due to polymer chain orientation under steady shear flow with slow shear rate and destruction of crystal nuclei was revealed under much faster shear flow.

Oscillatory shear flow

PVA gelation under oscillatory shear flow was also studied by SANS. All 2D-SANS profiles were azimuthally symmetric as same as them under steady shear flow that the circular averaged scattering intensities, the integrated scattering intensity (*II*) in the *Q*-range larger than 0.01 Å^{-1} and then the growth rate of them from the slope of the initial state of the plot, *II* against time were calculated. Figure 3 shows the normalized growth rate of *II* as a function of frequency *f* on PVA gelation with ϕ_{DMSO} = 0.6 under oscillatory shear flow (ε = 30 %). It was revealed that the gelation rate accelerates as well as steady shear flow and has a maximum at *f* = 1 Hz. The degree of gelation rate acceleration is more effective than steady shear by comparing the peak intensity of Figure 2 and 3. The dependences of strain ε was also studied (Figure 4). The most effective strain for accelerating gelation rate is 30 % in this measuring range.

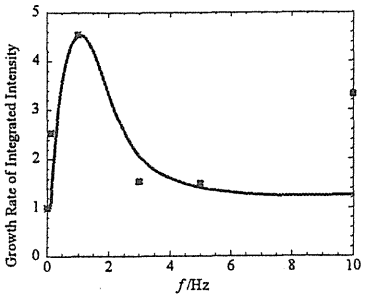


Figure 3: The growth rate of integrated intensity plotted against frequency *f* during gelation of PVA solution under oscillatory shear flow (ε = 30 %).

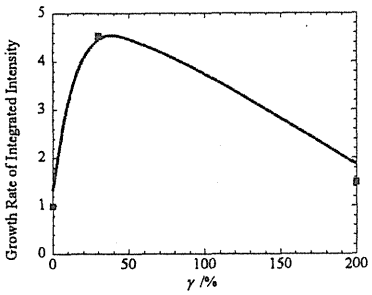


Figure 4: The growth rate of integrated intensity plotted against strain ε during gelation of PVA solution with frequency *f* = 1 Hz.

References

[1] Y. Takahashi et al., Nihon Reoroji Gakkaishi **28** (2000) 187.

[2] T. Kanaya et al., Macromolecules **28** (1995) 3168.

研究テーマ：中性子散乱によるソフトマターの構造と機能
表　題：動的非対称な高分子ブレンドの中性子小角散乱 I

1-5-37

Small-Angle Scattering on Polystyrene/Poly (vinyl methylether) mixture I -Anomalous Suppression of Small-Angle Scattering in Quiescent State-

S. KOIZUMI and H. TAKENO[1]

Advanced Science Research Center, JAERI, Tokai-mura, Ibaraki 319-1195, Japan
[1]Faculty of engineering, Gunma University

We performed SANS measurements on polystyrene (PS)/poly (vinyl methylether) (PVME) mixture. The details of sample specimens are described in ref.1. A temperature-range is wide in a single mixed phase from above $T_{g,PS}$ to $T_{g,mix}$, where $T_{g,mix}$ is the glass transition temperature of the mixture. We found that anomalous suppression of small-angle scattering at intermediate temperature between two T_g's. We finally attributed this finding to *dynamical asymmetry enhanced by temperature change.*[1)]

In the temperature region higher than $T_{g,PS}$, the q-behavior and temperature change of SANS profiles are well reproduced by a scattering function on a basis of a mean-field random phase approximation (RPA) with an interaction parameter χ ($\sim A + B/T$). As temperature decreases below $T_{g,PS}$, however, the scattering at lower q ($< 1/\xi$ where ξ is a correlation length) decreases more than that predicted from higher temperature [2)] Simultaneously, the q-positions q_c where we observe a deviation from q-profiles calculated by RPA, shift to higher q, which means correlation lengths also decrease more than expected [2)].

These anomalous behaviors are well recognized in the forward scattering intensity $S(q = 0)$, which was determined from a small q-region according to the Ornstein-Zernike formalism. Figure 1 shows the results for the mixture of the volume fraction of PS, $\phi_{PS} =$ 0.5 and 0.8 or (50/50) and (80/20). In the high temperature region, the inverse forward scattering intensity $S(q = 0)^{-1}$ changes according to $\sim T^{-1}$. However, below about $80°C$ for the mixture of (50/50), $S(q = 0)$ is anomalously suppressed more than expected from the high temperature region. This suppression behavior becomes more pronounced as temperature decreases. For the PS-rich mixture of (80/20), in which this anomalous suppression starts from a slightly higher temperature, these trends are more obvious. Finally, at $T_{g,mix}$, $S(q = 0)$ freezes and no longer shows temperature change.

It should be noted that this anomalous suppression is a characteristic behavior only for the mixture with largely different T_g's. In the case of mixtures with similar T_g's, *e.g.*, a polybutadiene/polyisoprene (PB/PI) mixture, the scattering intensity decreases normally according to $\sim T^{-1}$ and freezes at $T_{g,mix}$ [2)].

Figure 2 shows the phase diagram of the PS/PVME mixture, where a spinodal point T_s and a cloud point T_c determined by SANS measurements are indicated.[1)] The glass transition temperature for the mixture $T_{g,mix}$ was also determined by SANS, where small-angle scattering freezes. $T_{g,mix}$ is very close to the calorimetric glass transition temperature. In Figure 2, we also show the crossover temperature T_A of anomalous suppression. From SANS measurements, we determined T_A, at which $S(q = 0)^{-1}$ deviates from a linear decrease according to T^{-1} observed in the high temperature region. The temperature T_A increases slightly as ϕ_{PS} increases.

The local segmental dynamics in the miscible mixtures of polymers with largely different T_g's is believed to be heterogeneous. Here we refer to three experimental findings obtained by rheological, spectroscopic and calorimetric measurements: (1) breakage of time-temperature superposition principle, (2) spectrum broadening and (3) T_g broadening.

原子炉：JRR-3　　装置：SANS-J(C3-2)　　分野：中性子散乱（高分子）

These suggest heterogeneous local dynamics. The proposed interpretation is the heterogeneous cooperative motion within thermally enhanced concentration fluctuations (Kumar *et al.*,1994 & Zetsche and Fischer, 1994) or by chain connectivity (Chung *et al.*,1994, Arendt *et al.*, 1997 & Lodge and Mcleish, 2000). It is further reported that for the PS-rich mixture of $\phi_{PS} > 0.9$, PS and PVME chains move independently and the PVME chain becomes faster than pure PVME due to larger of free volume in PS-rich circumstance, which is called *"dynamical decoupling"* (Urakawa, private communication).

In the case of the PS/PVME mixture, in a temperature region above $T_{g,PS}$, PS and PVME chains are free from vitrification and there is smaller dynamical asymmetry between the two components. So far, many researchers have focused on this regime of smaller dynamical asymmetry , e.g., Schwahn et al. have shown a viscoelastic effect by determining the q-dependent Onsager coefficient $\Lambda(q)$, where the dynamical asymmetry is attributed to a large difference in molecular sizes. ($M_{w,DPS}/M_{w,PVME} \simeq 5.9$). However, as temperature decreases into an intermediate temperature region between $T_{g,PS}$ and $T_{g,mix}$, the dynamical asymmetry is enhanced by temperature. Although the concentration fluctuations become smaller at lower temperatures due to the LCST phase behavior, we expect that local contacts of PS segments in the PS-rich region tend to freeze and cause enhanced dynamical asymmetry.

References

1) S. Koizumi *J. Appl. Cryst.* **36** (2003) 381-388.
2) H. Takeno, S. Koizumi, H. Hasegawa and T. Hashimoto *Macromolecules* **29** (1996) 2440-2448.

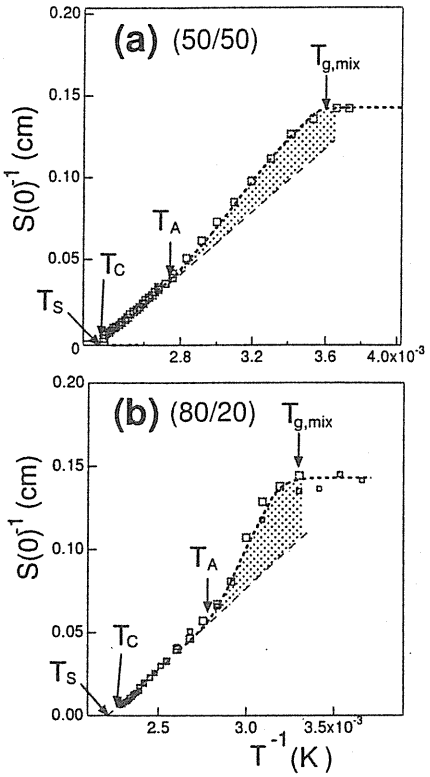


Figure 1: Forward scattering $S(q = 0)$ for d-PS/PVME (50/50) and (80/20) mixtures determined according to a Ornstein-Zernike formalism. Anomalous suppression is observed between T_A and $T_{g,mix}$.

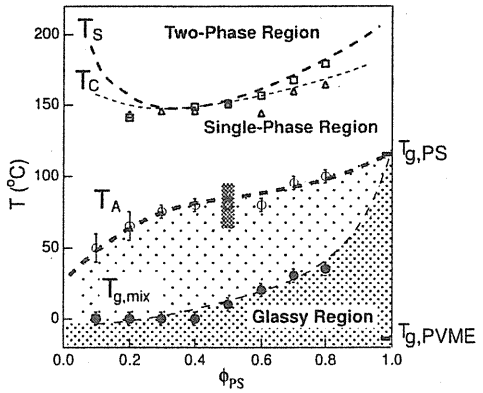


Figure 2: Phase diagram for the d-PS/PVME mixture, showing a spinodal line T_s, a binodal line T_C and glass transition temperature for the mixture T_g, mix. Crossover line for anomalous suppression is also included.

研究テーマ：環状ポリスチレンスルホン酸ナトリウムのコンフォーメーション
表題：中性子小角散乱による環状ポリスチレンの溶液中における拡がり

1-5-38 Chain Dimension of Ring-Shaped Polystyrene in Dilute Solution Investigated by Small-Angle Neutron Scattering

Atsushi TAKANO, Tomohiro NAKANO, and Yushu MATSUSHITA

Department of Applied Chemistry, Nagoya University
Furo-cho, Chikusa-ku, Nagoya, 464-8603 Japan

INTRODUCTION

Study on ring polymers has been a quite interesting subject in polymer science for many years, since they are expected to have quite different properties from those of the corresponding linear ones. Although a lot of reports exist for synthesis of ring polymers so far, purity of ring molecule in samples has not been investigated quantitatively in most cases. The authors of those reports actually just assumed that there exist considerable amount of ring molecules in the samples. In this study, we have synthsized ring polystyrene by end-to-end ring closure reaction, and the purity of the sample was quantitatively checked by end-group analysis. Furthermore chain dimension of the ring polymer with high purity was investigated by small-angle neutron scattering (SANS) in both good and theta solvents, and compared the results with that of the linear counterpart.

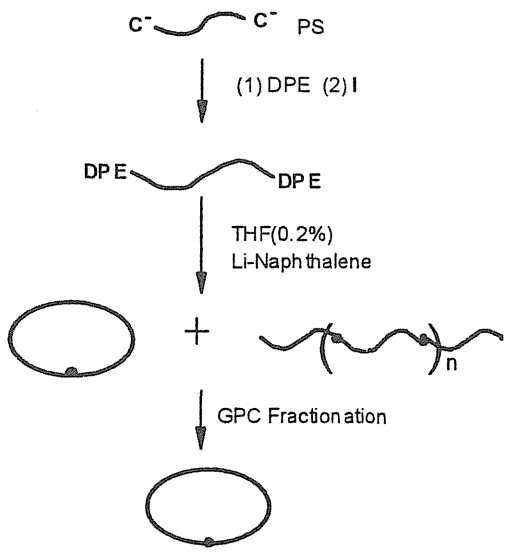


Figure 1 Synthetic scheme of Ring Polystyrene.

EXPERIMENTS

Synthesis and isolation of ring polystyrene was illustrated in Figure 1. All the operations were carried out under high vacuum by breakseal technique. In order to prepare a linear telechelic polystyrene, styrene was anionically polymerized with lithium naphthalenide as an initiator in THF at -78℃, and 1,1-diphenylethylene (DPE) was added for end-capping at the ratio of [DPE]/[Li]≒3/1, followed by termination with 1-[3-(3-chloropropyldimethylsilyl) phenyl]-1-phenylethylene (I) at the ratio of [I]/[Li]≒3/1 at room temperature. The polymer obtained was purified by precipitation in methanol to remove the residual DPE and I. The cyclization reaction in between two end-vinyl groups within a telechelic polymer was carrried out by adding lithium naphthalenide into the dilute THF solution of the telechelic polymer (c.a.0.2 w/v%) at the ratio of [DPE]/[Li]≒5 at 25℃, and stirred for 1 days.

Ring polymer was isolated by GPC fractionation to remove high molecular weight polycondensation products.

Number-average molecular weight, M_n, was measured by end-group analysis using ^{1}H NMR in $CDCl_3$. Apparent molecular weights and molecular weight hetrogeneities, M_w/M_n, were determined by GPC.

SANS measurements were performed by using SANS-U spectrometer (λ=0.70nm) equipped with a 2.0 mm thick quartz cell. Adopted measuring temperature for

使用施設：JRR-3　装置：SANS-U(C1-2), 分野 Softmatter

solutions of benzene-d_6 as a good solvent was 25℃, while those of cyclohexane-d_{12} as a theta solvent was 40.0℃ for a linear polymer, and 35.0℃ for a ring polymer.

RESULTS AND DISCUSSION

Molecular characteristics of linear and ring polymer were listed in Table 1. Absolute molecular weights (M_n) of both samples are almost equal, though apparent molecular weights by GPC are considerably different and molecular weight distributions are relatively narrow as shown in Figure 2. Furthermore, purity of ring molecule in fractionated sample determined by ^{1}H NMR was 96%.

Table 1 Molecular Characteristics of linear and Ring polymers.

Sample	$10^{-4}M_n$ [1]	$10^{-4}M_n$ [2]	M_w/M_n [2]	P [1,3]
Linear	2.3	1.9	1.05	—
Ring	2.4	1.3	1.01	0.96

[1] Determined by ^{1}H NMR

[2] Determined by GPC

[3] purity of Ring molecule

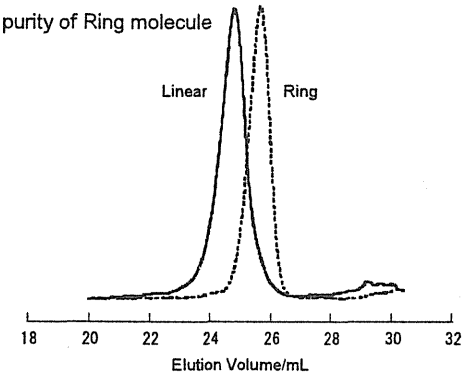


Figure 2 GPC Chromatograms of linear and Ring polystyrene

The apparent radii of gyration (R_g) of linear and ring polymer at several finite concentrations were evaluated by Guinier plots of the measured coherent intensities. A example of Guinier plot is shown in Figure 3. The R_gs of both sample were obtained by extrapolation of the apparent R_g value to infinite dilution and compared in Table 2 and 3, in theta and good solvent conditions, respectinely.

The ratio of the R_g for ring molecule to that for linear one, i.e. R_g(Ring) /R_g(Linear), has been theoretically predicted to be $1/\sqrt{2} \fallingdotseq 0.707$ for polymer solution in a theta solvent,[1] and also to be $\sqrt{0.516} \fallingdotseq 0.718$ in a good solvent by renormalized two-parameter theory.[2]

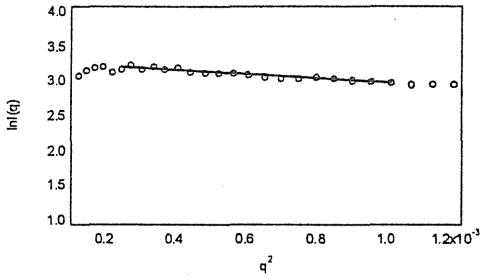


Figure 3 Guinier plot of Ring Polystyrene in Cyclohexane-d_{12} (C=1.2%).

Table 2 Radii of Gyration of Linear and Ring Polystyrenes.

Sample	$R_{g\theta}$/Å	R_g/ Å
Linear	39.7	42.1
Ring	28.5	28.0

Table 3 Comparison of Radii of Gyration of Linear and Ring Polystyrenes.

Sample	Theta condition	Good condition
R_g(ring)/R_g (linear)	0.71	0.68

From Table 3, one notices that the observed ratios 0.71 in cyclohexane and 0.68 in benzene agree with both almost same to the theoretically predicted values, 0.707 and 0.718, respectively.

References

1. Zimm, B.H.; Stockmayer, W.H., J.Chem. Phys. **1949**, *17*, 1301
2. Douglas, J.F.; Freed, K.F. Macromolecules **1984**, *17*, 2344

研究テーマ：中性子散乱によるソフトマターの構造と機能
表　題：動的非対称な高分子ブレンドの中性子小角散乱 II
1-5-39

Small-Angle Scattering on Polystyrene/Poly (vinyl methylether) mixture II -Competition between Rheological and Concentration Fluctuation Relaxations-

S. KOIZUMI

Advanced Science Research Center, JAERI, Tokai-mura, Ibaraki 319-1195, Japan

Generally for polymer mixtures, there are vicous and gel-like limits, determined by a balance between stress and fluctuation relaxations. In the viscous limit, the rheological relaxation is faster than the concentration fluctuation, while in the gel-like limit where the rheological relaxation is much slower than the concentration fluctuation.

With respect to a polymer mixture of DPS/PVME (50/50) , which was studied in Part I of this report, we performed a mechanical measurement of a shear modulus in order to confirm our situation (koizumi and Inoue in preparation). We determined the rheological relaxation time as the point where the storage modulus $G'(\omega)$ and the loss modulus $G''(\omega)$ merge. For higher temperatures in the range from 120 $°C$ to 80 $°C$, we could clearly recognize this point on the spectra, while for lower temperatures below 60 $°C$, it is out of the range of our mechanical spectrometer. Therefore, we estimated the rheological relaxation time by using a shift factor a_T, although the temperature-time superposition principle is not well established for the mixture with largely different T_g's.

In Fig. 1, we show the temperature dependence of rheological relaxation time for the DPS/PVME mixture of (50/50). Additionally, we plot a relaxation time of several 10 seconds for the concentration fluctuations ($\sim 1/R(q)$) of $0.01\mathring{A}^{-1}$, which was determined by time-resolved SANS measurements after a shallow quench into a meta-stable region. Due to the LCST phase behavior, this relaxational rate $1/R(q)$ might decrease as temperature decreases (broken line). However, near $T_{g,PS}$, the kinetic coefficient $\Lambda(q)$ might be affected by $T_{g,PS}$ and may become smaller. According to the "*fast mode*" ansatz (Kausch and Tirrell, 1989) , the faster moving component of PVME governs the temperature dependence of $\Lambda(q)$. Therefore, we expect that the temperature change of $\Lambda(q)$ might be as illustrated by the shadow region in Fig. 1. Thus at around 100 $°C$, there exists a crossover from a *viscous limit* at high temperature to a *gel-like limit* at intermediate temperature.

A stress-diffusion coupling has a variety of effects depending on vicous and gel-like limits. We stress that in the viscous limit of the high temperature region, the dynamical coupling effect between stress and diffusion appears as a *viscoelastic* effect. Schwahn et al. have shown this viscoelastic effect by determining the q-dependent Onsager coefficient $\Lambda(q)$ according to q^{-2} for $q\xi_{VE} > 1$ (Schwahn *et al.*, 1992). In this study, the dynamical asymmetry is attributed to the large difference in molecular sizes of the mixture constituents (Schwahn *et al.*, 1992).

In the gel-like limit, on the other hand, we support that a long-living shear modulus G_1 starts to appear in the osmotic compressibility as a coupling effect between stress and diffusion. In other words, we expect the following modified scattering function:

$$S'(q) = \frac{1}{r_0 + Cq^2 + \frac{4}{3}\alpha^2 G_1}. \qquad (1)$$

This modified scattering function has an additional term of $4/3\alpha^2 G_1$ which disappears for the dynamically symmetric mixture with $\alpha = 0$. Eq.(1) reproduces well our observations described in Part I of this report : the suppression of the forward scattering intensity $S(0)$ and decrease of the correlation length ξ. Our experimental findings that the suppression becomes more pronounced as temper-

原子炉：JRR-3　　装置：SANS-J(C3-2)　　分野：中性子散乱（高分子）

ature decreases suggests that the dynamical asymmetry or α is more enhanced by temperature decrease. At the same time, temperature decrease might induce a slowing down of local internal modes, and the number of local internal modes, which are responsible for the stress decaying more slowly than the concentration fluctuation, becomes larger. With a larger magnitude of G_1, the suppression becomes more pronounced. Irrespective of dynamical symmetry or asymmetry, crossover from viscous to gel-like limits generally occurs when the mixture approaches $T_{g,mix}$. In the case of a dynamically symmetric mixture, e.g., PB/PI, we could not observe any suppression of small-angle scattering. Thus, in order to observe the suppression of small-angle scattering, the dynamical asymmetry ($\alpha \neq 0$), in other words, a *one-sided stress division*, is needed. This is consistent with our hypothesis that for the PS/PVME mixture, the dynamical asymmetry is enhanced by temperature.

For elastic materials such as chemical polymer gels or metal alloys with modulus inhomogeneity, stress does not decay. For these materials, the modified structure factor $S'(q)$ can be obtained from an equilibrium argument considering free energy (Cahn, 1961, Tanaka *et al.*, 1973 & Onuki and Nishimori, 1991). In such a case, the non decaying modulus G shifts the critical point to a higher temperature. Therefore, $S(q = 0)$ is apparently suppressed more than expected in the case without non decaying G or α.

However, in the case of the PS/PVME mixture, a rheological relaxation occurs with a finite relaxational time τ_R ($=\tau_1$). Here we encounter a simple question: if we wait long enough as compared to the rheological relaxational time τ_R, can we observe small-angle scattering free of the rheological relaxation or $S_0(q)$ ($\sim 1/(r_0 + Cq^2)$)? Our measurement time under each condition is of the order about 1000 seconds after changing temperature. In order to confirm this point, we performed a time-resolved measurement at 60.0 $^\circ C$, monitoring the change of intensity over a period longer than τ_R. However, we could not observe any recovery of scattering intensity and the suppression remained. This observation leads us to believe that the suppression of small-angle scattering or the concentration fluctuation results from a competition between two kinetic processes, i.e., the thermally activated concentration fluctuation of a finite wave number q and the rheological relaxation. In the gel-like limit, a long-living stress field suppresses the fast decaying concentration fluctuation of the q fourier mode. When q becomes smaller, the relaxational rate $R(q)$ becomes smaller according to q^2. Therefore, at $q = 0$, τ_{CF} ($\sim 1/R(q)$) becomes infinite. In this limit, we expect to observe a viscous limit again. On the other hand, for a smaller length scale of $q\xi > 1$, corresponding to the power law regime of q^2, the small-angle scattering is not influenced by the osmotic compressibility itself (see Fig. 1 of Takeno *et al.*, 1996). Thus, this suppression behavior of small-angle scattering has upper and lower length scale limits, between which our SANS measurements were performed.

References

1) S. Koizumi *J. Appl. Cryst.* **36** (2003) 381-388.

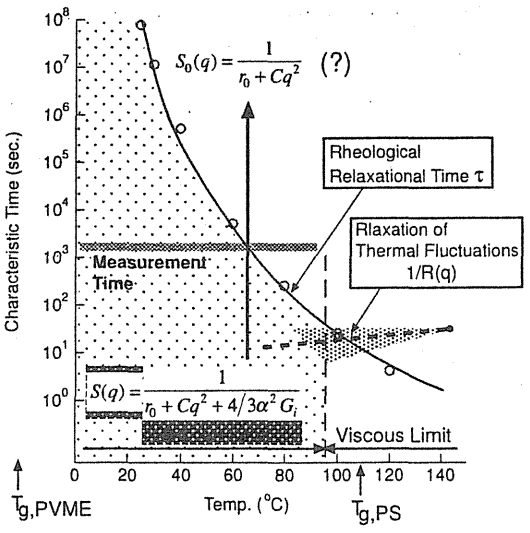


Figure 1: Schematic view for a crossover from a viscous to a gel-like limits, which happens as temperature decreases.

研究テーマ:リビング重合反応機構の解明
表題:リビング重合機構の中性子散乱による解明

1-5-40 Investigation of Living Polymerization Mechanism by Neutron Scattering

K. Matsumoto and H. Matsuoka

Department of Polymer Chemistry, Yoshida, Sakyo-ku, Kyoto, 606-8501, Japan

It is generally considered that in ionic polymerization some active end groups in the different polymer chains associate by coordination or ionic interactions. In fact, the association has been confirmed by nuclear magnetic resonance (NMR) analysis of propagating species or kinetic analysis of the polymerization. To clarify the association mechanism of propagating polymers, here we examined a styrene anion polymerization solution by small-angle neutron scattering (SANS).

A "living polystyrene" was prepared by polymerizing styrene with butyllithium initiator in benzene-d_6 at room temperature under argon atmosphere and transferring the solution into a quartz cell without terminating the polymerization. A "dead polystyrene" was prepared by synthesizing polystyrene under the same polymerization conditions as the "living polymer", terminating with methanol, purifying, and re-dissolving the polymer in benzene-d_6.

SANS profiles for the polymer solutions were given in Figure. In the case of the "dead polystyrene," the profile was reproduced well by Debye function describing a Gauss coil (R_g = 12 Å) of a single polystyrene molecule (broken line). On the other hand, in the case of "living polystyrene," the profile could not be reproduced by such a function. Strong scattering from much larger particles was clearly observed in the smaller angle region. By gel permeation chromatography (GPC) analysis of the samples, it was revealed that the "living polystyrene" had bimodal molecular weight distributions (higher M_n = 4800 and lower M_n = 2000), while the "dead polystyrene" had almost mono-disperse molecular weight distributions (M_n = 2100, M_w/M_n = 1.07). Here, M_n and M_w represent number-averaged molecular weight and weight-averaged molecular weight of the polymer, respectively. Proton NMR analysis of the "living polystyrene" suggested that the polymer had oxidized chain ends.

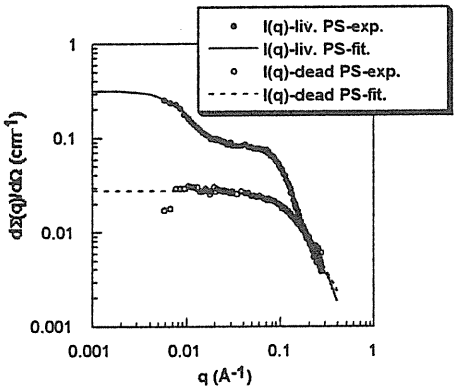


Figure. SANS profiles for 5.6wt% "living" and "dead" polystyrene benzene-d_6

Based on these observations, it was considered that the "living polystyrene" was not real "living" but a mixture of polymers with -OLi end and oxidatively coupled polymers. The SANS profile for the "living polystyrene" was reproduced well by a sum of three different scattering functions (solid line), which were functions for a Gauss coil (R_g = 11 Å), a small hard sphere (R_g = 15 Å), and a large hard sphere (R_g = 208 Å). They may be explained as scatterings from individual coupled polymer, aggregated O-Li site, and aggregated polystyrenes with O-Li groups.

Consequently, this study demonstrated that SANS is quite useful to examine the association behavior of living polymers.

使用施設:JRR-3　装置:SANS-U(C1-2), 分野 Soft matters

研究テーマ：中性子散乱によるソフトマターの構造と機能
表　題：動的非対称な高分子ブレンドの中性子小角散乱 III

1-5-41

Small-Angle Scattering on Polystyrene/Poly (vinyl methylether) mixture III -Shear-induced Phase Separation-

S. KOIZUMI

Advanced Science Research Center, JAERI, Tokai-mura, Ibaraki 319-1195, Japan

We performed SANS measurements on a shared specimen of polystyrene (PS)/Poly (vinyl methylether) (PVME) mixture at intermediate temperature between $T_{g,PS}$ and $T_{g,mix}$, where $T_{g,PS}$ or $T_{g,mix}$ is the glass transition temperature of PS or the mixture, respectively. If we apply a shear field to this mixture at at intermediate temperature around T_A (see PartI in this report), the mixture shows an abnormal butterfly pattern as a result of shear-induced phase separation.[1] Figure 1 shows a 2-dimensional SANS patterns of PS/PVME (50/50) sheared at 70.0 $°C$ and quenched below $T_{g,mix}$. The shear rate and deformation rate were $\dot{\gamma} = 0.5 rad/s.$ and $\lambda > 2.0$, respectively. Before shearing, small-angle scattering is isotropic for a single mixed state. However, after shearing, we clearly recognize an abnormal butterfly pattern, i.e., enhancement of scattering intensity along the shear direction with a clear scattering maximum at q_{max}. As q increases, the 2-dimensional pattern becomes more isotropic. The sample specimen sheared at 90.0$°C$ also shows an abnormal butterfly pattern which appears at lower q but less obviously.

As a control experiment, we performed SANS measurements on the sheared mixture of DPS/HPS (50/50). Here we chose identical chain lengths of $M_n \simeq 60K$ for DPS and HPS in order to avoid dynamical asymmetry due to a difference in molecular sizes. This mixture, sheared at 150.0 $°C$ and quenched, shows an elliptical 2-dimensional scattering pattern, elongated to the direction perpendicular to shear flow. In this control experiment, shear-induced phase separation does not occur but chain deformation occurs due to shearing.

The q-profiles, which are sector-averaged over an azimuthal angle of 30° along directions parallel and perpendicular to the shear direction.[1] show two q-regions of (I) and (II). In q-region (I) at low q, we observed a shear-induced phase separation showing stronger intensity than that for the perpendicular direction and with an obvious scattering maximum at around $q = 0.006 \AA^{-1}$. The q-profile parallel to shear flow decreases, according to the Porod law q^{-4}, indicating a sharp interface between PS-rich and PVME-rich domains. The scattering maxima are predominantly in the q-Fourier mode, grown up during shearing. In the q-region (II) at high q, we observed a crossover of the scattering intensity; scattering in the perpendicular direction exceeds that in the parallel direction. The asymptotic q-behaviors for both directions are closer to q^{-2}, which is attributed to chain deformation due to shearing.

For a mixing state of the sheared mixtures, we must consider the time evolution of the concentration fluctuations under shear. The total growth rate $\Gamma(q)$ for the concentration fluctuations under shear is given by the two terms of (1) thermodynamic force and (2) imbalanced stress under shear. The imbalanced stress term can have a negative contribution relative to the first thermodynamic term which stabilizes a single mixing state when $r_0 > 0$. If $\Gamma(q)$ becomes totally negative, the corresponding q-Fourier modes can grow up during shearing. For our argument, we consider a simple case of $q_x = q_y = q$. We stress that the imbalanced stress term disappears for a vorticity direction of $q = q_z$. In this limit, $\Gamma(q)$ is given as follows (Onuki, 1997);

$$\frac{\Gamma(q)}{q^2} = \Lambda(q)(r_0 + Cq^2) - \alpha(\frac{\partial G}{\partial \phi})\dot{\gamma}$$

原子炉：JRR-3　　装置：SANS-J(C3-2)　　分野：中性子散乱（高分子）

where Λ, α and G are an Onsager kinetic coefficient, a symmetric param ter and a shear modulus.

Figure 2(a) schematically shows the growth rate $\Gamma(q)/q^2$ where (1) the thermodynamic term and (2) the imbalanced stress term are separately drawn. The shaded region corresponds to the q-Fourier modes which give a negative relaxational rate $\Gamma(q)$. A larger contribution from the imbalanced stress is required to observe the butterfly scattering pattern by SANS, which generally covers a higher q-region of as compared to light scattering. Due to the LCST phase behavior, as temperature decreases, the thermodynamic contribution increases. As temperature decreases to intermediate temperature, the enhanced dynamical asymmetry is expected to give larger contribution of the imbalanced shear. Therefore, we successfully observed the butterfly scattering pattern by SANS at around T_A. With a higher shear rate, the shaded region expands to higher q so that the higher q-mode can respond as shear-induced phase separation. For the q-mode outside this shaded region, a shear effect appears as only chain deformation. In Fig. 2(b), we schematically draw $\Gamma(q)$, which might have a minimum at a certain q in the q-region of SANS. The dominant q-mode, which appears as a scattering maximum at q_{max}, corresponds to that where $\Gamma(a)$ is minimum. This argument is equivalent to the stability analysis for the early stage of spinodal decomposition in a quiescent state; shear rate $\dot{\gamma}$ is equivalent to a quench depth ΔT for spinodal decomposition. In this discussion, we neglected the effects of a convective flow and the first normal stress difference which are discussed in detail elsewhere (Saito *et al.*, 2001), as related to the experiment on the polystyrene solution in dioctyl phthalate (DOP).

References

1) S. Koizumi *J. Appl. Cryst.* **36** (2003) 381-388.

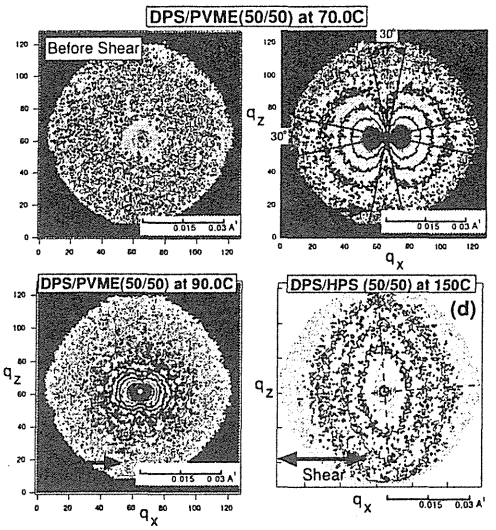


Figure 1: 2-dimensional SANS pattern for the sheared DPS/PVME mixture of (50/50), where a butterly pattern is clearly observed. As a control exeriment, the SANS pattern for DPS/HPS mixture of (50/50) shows an elliptical pattern which is elongated to a direction perpendicular to shear.

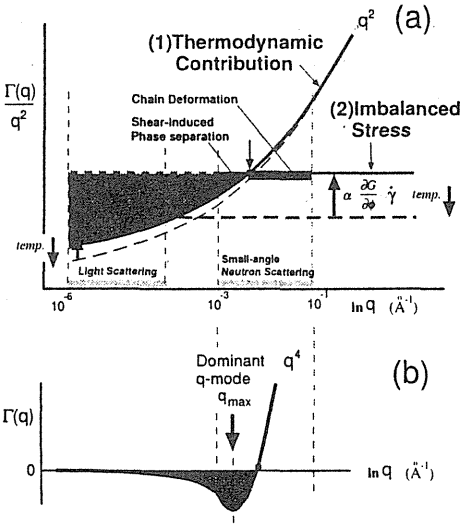


Figure 2: Schematic view for stability analysis under shear in a theoretical frame of stress-diffusion coupling.

研究テーマ：中性子散乱によるソフトマターの構造と機能
表　題：重合と微粒子形成過程のその場観察

1-5-42

Small-angle Neutron Scatttering on Polystyrene Microsphere Formation Induced by In-situ Radical Polymerization

S. KOIZUMI, R. MOTOKAWA and M. ANNAKA[1]

Advanced Science Research Center, Japan Atomic Energy Research Institute, Tokai-mura, Ibaraki 319-1195, Japan
[1]Department of Chemistry, Faculty of Science, Kyushu University, 33 Hakozaki, Higashi-ku, Fukuoka 812-8581, Japan

By using a pin-hole and a double crystal small-angle neutron scattering spectrometers (SANS-J and PNO at JAERI), we investigated radical polymerization of polystyrene (PS) and a followed microsphere formation process which occurs in a polymerization matrix of poly(vinyl methylether) (PVME) solution with mixed solvents of ethanol and n-hexane. The polymerization matrix, composed of PVME/ethanol/n-hexane, is crucial to avoid precipitate of PS from the solution. Especially the matrix polymer PVME plays a important role to stabilize a PS microsphere in size of sub-micrometer. It is because that the matrix posesses balanced solubility with PS chains; PVME and PS are soluble each other, due to a LCST type phase diagram with a phase boundary about 120 $°C$, while ethanol and n-hexane are poor solvents for PS. In this study, we report the results obtained with the polymerization matrix; mixed solvents of ethanol/n-hexane (80/20 wt/wt) and PVME content of 8.3 $wt\%$. This condition of ethanol/n-hexane (80/20) realizes the smallest size of microspheres about 0.5 mm, which was confirmed by scanning electron micrography (SEM).[1)]

In order to have a strong scattering contrast, we prepared a reaction solution with fully deuterated styrene (d8-St) solubilized in the protonated polymerization matrix of PVME/ethanol/n-hexane. The solution was filled in a quartz cell with 1mm thickness, whose temperature was controlled at 55.0 $°C$. Radical polymerization was initiated by *2,2'-Azobisisobutyronitrile* (AIBN). For ultra small-angle scattering by PNO, we terminated radical polymerization with *1,1-Diphenyl-2-picrylhydrazyl* (DPPH), in order to observe a time-evolution of scattering profiles during radical polymerization.

Figure 1 shows scattering profiles obtained by two spectrometers of SANS-J and PNO, covering a wide range of wave number $q(= 4\pi/\lambda sin(\theta))$ from 10^{-4} nm^{-1} to 1 nm^{-1}, where λ and θ are wave length and scattering angle.

Small-angle scattering region from 0.01 to 1 nm^{-1}: For the reaction solution before starting radical polymerization, we obtained only spin incoherent scattering, which appears at the intensity level of 1 cm^{-1}. At 20 *min.* after starting radical polymerization, we observed a strong upturn of small-angle scattering in the q-region around 0.1 nm^{-1}. As a reaction-time proceeds over 60 *min*, the upturn becomes an asymptotic q-behavior close to q^{-4}, which is a so-called Porod law originating from a interface of deuterated polystyrene (DPS) microspheres dispersed in the polymerization matrix. In case when the interface has a finite thickness of t_I, we obtain a following equation in the Porod q-region;

$$\frac{d\Sigma}{d\Omega}(q) \sim (2\pi)^{1/2}\Delta B^2[\frac{S(t)}{V_0}q^{-4}]exp[-\sigma(t)^2q^2] \quad (t_I = (2\pi)^2\sigma(t), S(t) = 4\pi R(t)^2 N_s) \quad (1)$$

where $\Delta B, S, V_0, R$ are difference of scattering length between PS and the matrix, a total surface of microspheres, a sample volume and a radius of microsphere. S/V_0 is a specific interface. N_s is a number-density of PS

原子炉：JRR-3　　装置：SANS-J(C3-2)　　分野：中性子散乱（高分子）

microspheres. By using Porod plot on a basis of eq() that is given by eq(), we analyzed time-evolution of surface structure of the PS microphere (see Fig. 2).

Figure 2 shows time-evolution of a characteristic thickness t_I and a spcific interface S/V_0 thus estimated. A specific interface S/V_0 contineuously increases, as reaction-time proceeds up to about 600 *min.* The total surface area S is given by a product surface area of a microsphere $4\pi R(t)^2$, and number density of microspheres N_s. If we assume that the number density N_s is time-independent, the increase of S/V_0 is attributed to growth of R. A characteristic interface t_I, on the other hand, is about 15 nm and seems to be time-independent.

Ultra small-angle scattering region from 10^{-4} to $10^{-2}nm^{-1}$: The ultra small-angle scattering spectrometer PNO is a Bonse-Hart type, where ultra small-angle scattering is detected by precisely rotating a channel-cut perfect crystal Si(110) with angular resolution of micro-radian order. Due to low luminecity of monochromatized incident neutron, it takes more than 10 hours in order to have a whole q-profile ranging from 10^{-4} to $10^{-2}nm^{-1}$. In order to detect time-evolution of q-profiles in ultra small-angle region, we need to terminate radical polymerization process with ***. We terminated radical reaction at different reaction-times of 60, 200, 300 and 400 *min.* and measured ultra small-angle scattering. In order to have q-profiles in a ultra small angle scattering region, we calibrated these intensities with a secondary standard of polymer films whose macrophase separated structure gives monotonous q-behavior of q^{-4} over a wide q-range from 10^{-4} to $10^{-2}nm^{-1}$ for both PNO and SANS-J spectrometers.

We plotted the q-profiles thus obtained in Fig. 1. At 60 *min.* we could not obtain enough signal to noise ratio (S/N); a noise level due to dark current and thermal diffuse scattering from a single crystals appears at about 10^4 cm^{-1} in absolute unit. For reaction-times shorter than 200 *min*, We drew speculated scattering curves as shown by broken lines. For longer reaction-times over 200 *min*, on the other hand, we obtained q-profiles which increase in its intensity as a reaction-time proceeds. The q-profiles at higher q around 0.01 nm^{-1} show the asymptotic q-behavior close to q^{-4} which would be reasonably connected to the q-profiles obtained by SANS-J at corresponding reaction-times (The broken straight lines in Figure 1 show a guide for eyes.)

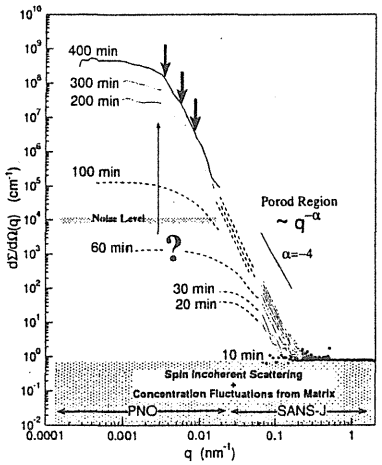


Figure 1: Time-evolving scattering profiles for microsphere formation during radical polymerization, obtained by pin-hole and double crystal small-angle neutron scattering spectrometers (SANS-J and PNO).

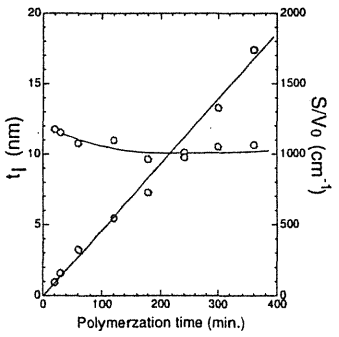


Figure 2: Time-evolution of Interfacial Structure.

References

1) Shigeki Chujo, Masayosi Rikukawa, Kohei Sanui, Noaya Ogata, Satoshi Koizumi and Takeji Hashimoto: *Polymer Journal* **Vol.33 No.1** (2001) 1-8.

This is a blank page.

1. 中性子散乱 6) 生物学

1. Neutron Scattering 6) Biology

This is a blank page.

研究テーマ:細胞における蛋白質の高次構造化不全と細胞の異常死に関する研究
表 題:遺伝子から合成されたケラチンタンパク質の自己集合に関する中性子散乱研究

1-6-1 Neutron scattering study on self-assembly of keratin molecules in water

S. NAITO, T.KARINO[1], M. FURUSAKA[1], S. FUJIWARA[2], and N. NIIMURA[2]

The Institute of Advanced Science Research, L'ORÉAL Tsukuba Center, Tsukuba, Ibaraki 300-2635
[1]High Energy Accelerator Research Organization, Tsukuba, Ibaraki 305-0801
[2] Japan Atomic Energy Research Institute, Ibaraki 319-1195

The aim of this study is to clarify structural changes of proteins in apoptosis. Once apoptotic trigger is pulled in a hair cell, the cell begins to produce enormous amount of keratin proteins. Then, SS cross-linking is induced between the molecules and keratin proteins are finally gelated [1]. Keratin is a major component of many tissues such as hair, nails, and quills. It consists of 2 types of keratin, *i.e.*, Type I 48kDa, acidic) and Type II (53kDa, basic). Wide-angle X-ray diffraction patterns of hair and other keratin fibers show an equatorial spacing of 9.8 Å, corresponding to the thickness of the α-helical coiled coil compound constructed of Type I and Type II keratins. Indeed, it is known that keratin assembles spontaneously multimer, and finally forms 10nm filaments. However, the organization process and structure of keratin in aqueous solution have not been well understood. We synthesized gene-expressed Type I and Type II keratins and the chemically modified the cysteine resides to the s-carboxymethyl alanyl disulfide (R-S-SCH_2COO^-, CMADK), and investigated the structure of keratin proteins in aqueous solution by small-angle neutron scattering (SANS). We confirmed the presence of keratin multimers in the buffer (10 mM Tris-HCl buffer solution, pH 7) containing a higher salt concentration, 50mM by SANS (SANS-J) measurement [2].

SANS was undertaken at SANS-J [neutron wavelength (λ = 7 Å) , sample distance (L=10m)] situated at the end of a cold-neutron guide tube from the JRR-3 reactor and at WINK [Pulsed Neutron Scattering Facility in KEK]. Figure 1 shows the scattering mixture in the buffer (10 mM Tris-HCl buffer, pH 6.2) by SANS measurements. CMADK formed the multimers without the higher concentration of salt when the pH of the solution approached to the isoelectric point (~pH 5). Double logarithmic SANS plot profiles of CMADKs in the buffer solution showed straight line which has a equimolar mixture in the buffer (10 mM Tris-HCl buffer, pH 6.2) by SANS measurements. CMADK formed the multimers without the higher concentration of salt when the pH of the solution approached to the isoelectric

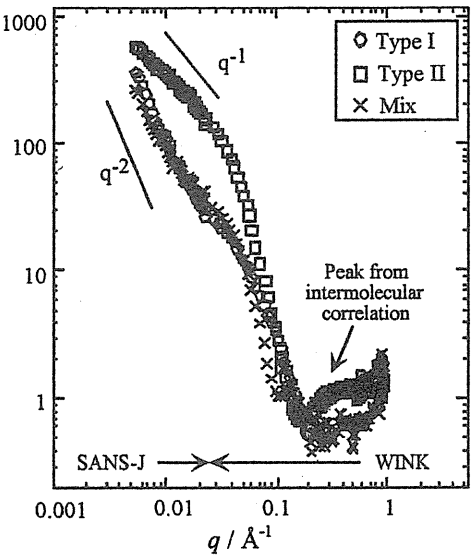


Figure 1 SANS profiles of CMADKs aq. soln. at pH 6.2.

point (~pH 5). Double logarithmic SANS plot profiles of CMADKs in the buffer solution showed straight line which has a slope of −1 (0.01<q<0.3), however, the slope increased in the lower q range. This suggests that CMADKs exist as bent rod-like molecules. The scattering function, which a cylindrical scattering function combined with Debye one was applied to fit the scattering curves from bent rod-like CMADKs. The scattering intensity $\langle I(q)\rangle$ for the bent rod-like cylindrical chain was given by the following equations.

$$I(q)=\frac{a}{V_{cyl}}\int_0^{\pi/2} f^2(q,\alpha)\sin\alpha d\alpha+\frac{b}{q^2} \quad (1)$$

$$f(q,\alpha)=2(\rho_{cyl}-\rho_{solv})V_{cyl}j_0(qH\cos\alpha)\frac{J_1(qr\sin\alpha)}{qr\sin\alpha} \quad (2)$$

$$V_{cyl}=\pi r^2 L \quad j_0=\frac{\sin(x)}{x}$$

where r is the radius of cylinder, $2H$ the height, ρ_{cyl} the scattering length of cylinder, ρ_{sol} the scattering length of solvent, a the volume ratio of particle

原子炉:JRR-3 装置:SANS-J (C3-2) 分野:生物

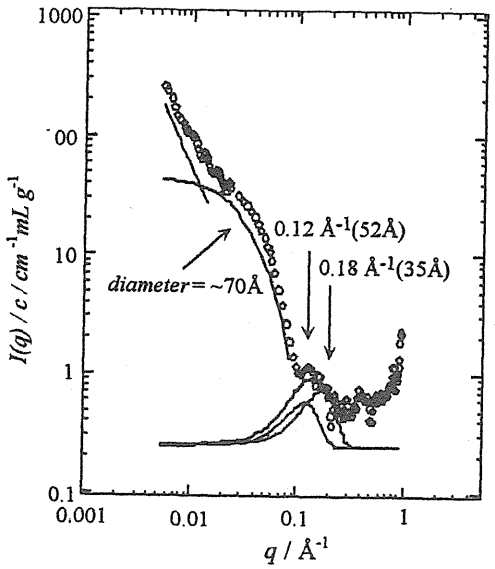


Figure 2 Modified cylindrical analysis and Gaussian fitting of SANS profiles of the eqimolar mixture consisting of Type I and Type II CMADK.

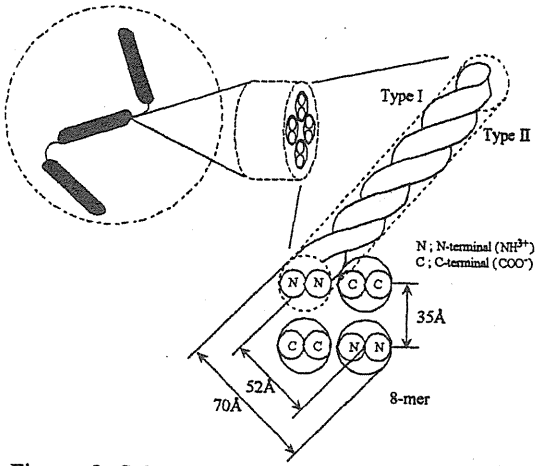


Figure 3 Schematic diagram of the assembled structure between Type I and Type II keratin in water or Type II.

and *b* the extent of bending. Gaussian fitting was performed to the scattering profiles observed in the higher *q* ranges to determine the intermolecular correlations. Figure 2 shows typical fitting curves for the scattering profile of the equimolar mixture consisting of Type I and Type II CMADK in the buffer (pH 6.2). The diameter of the cylindrical rod-like multimer was 70Å and 2 intermolecular correlation lengths were determined from Gaussian fitting, 52Å and 35Å. On the other hand, it was found Type I and Type II CMADK was self-assembled in the buffer (pH6.2) respectively. The diameter of Type I was 38Å (4-mer) and Type II 65Å (12-mer). The minimum correlation size was 15Å and common to both types. This length suggested corresponding to the correlation between each molecule of Type I or Type II. However, the scattering intensities of the peaks from intermolecular correlation were very weak compared with those of the equimolar mixture, meaning the same type of keratin is self-assembled by very weak mutual interactions.

On the basis of the results, the schematic diagram of the assembled structure between Type I and Type II keratin in water is shown in Fig. 3. When Type I keratin is mixed with Type II at the same morality, two molecules form 8-mer consisting of 4 pieces of coiled-coil dimmer as a basic unit. Type I or Type II form aggregates in water respectively, however, not coiled-coil form. The interaction between the same type of keratin is considered owing to the electrostatic interaction betweenα-amino terminal and β-carboxy one. This kind of interaction is generally very weak, so the antiparallel aggregation may occur randomly. Therefore, intermolecular correlation becomes ambiguous. Whereas, the different type of keratins curiously assemble forming stable coiled-coil structure, in which N-terminal or C-terminal faces each other, that is, in parallel. We consider that both of Type I and Type II have specific sites in variable region to recognize each type just like a relation between key and keyhole. The coiled -coil formation does not begin until the molecular recognition arises between Type I and Type II keratin. However, those critical recognition sites have not cleared. The 8-mers easily assemble in axial direction one after another by electrostatic interaction since the electrical distribution at the distal end of 8-mer is well-balanced. The linking part among rod-like 8-mer corresponds to the variable region of keratin molecules, so it suggests the flexible bent rod-like molecules.

Reference

1)F. Ikkai and S. Naito: *Biomacromolecules* **3** (2001) (3) 482-487.

2) S.Naito *et al.*: JAERI-Review **2002-028** (2002) 84.

研究テーマ：機能性生体物質の水和構造研究
表　題：DsrD 蛋白質の中性子回折実験

1-6-2

Neutron diffraction experiment of DsrD protein

T. CHATAKE, N. MIZUNO[1], G. VOORDOUW[2], Y. HIGUCHI[3], I. TANAKA and N. NIIMURA

Neutron Science Research Center, JAERI, Tokai, Ibaraki, 319-1195
[1]Division of Chemistry, Kyoto University, Sakyo, Kyoto 606-8502
[2]Department of Biological Sciences, the University of Calgary, Alberta, T2N 1N4
[3]Department of Life Science, Himeji Institute of Technology, Kamigori, Hyogo 678-1297

It is well known that hydrogen bond networks around DNA-binding protein play important roles in DNA recognition. The protein interacts with DNA molecules by direct hydrogen bonds and water-mediated hydrogen bonds, and achieves the specific and precise recognition. However, nobody knows the details of these networks. Dissimilatory sulfite reductase D (DsrD) from the sulfate-reducing bacterium *Desulfovibrio vulgaris* has DNA-binding motif.[1)] We are trying to determine hydrogen-bond networks of this protein including hydrogen atoms by neutron crystallographic analysis, for finding hints to the mechanism of DNA recognition.

In order to get large crystals for neutron experiment, we found a proper condition by two analyses, 'crystallization phase diagram' and 'crystal-quality'. According to the results of these analyses, a largest crystal of DsrD was obtained from D_2O solution by the macro-seeding technique.A largest crystal available to us (1.7 mm^3) was sealed into a NMR sample capillary with D_2O crystallization solution for neutron experiment. Neutron diffraction data was collected at room temperature using monochromatic neutron beam (λ = 2.88 Å) with the BIX-3 [2)] in a neutron reactor JRR-3M at JAERI. 254 still diffraction patterns were recorded on a neutron imaging plate. The total time for the measurement was 30 days. The diffraction patterns were processed with the programs DENZO and SCALEPACK,[3)] which were modified for neutron experiment.

The crystal of DsrD belongs to the space group of $P2_12_12_1$, with cell dimensions of a = 60.5 Å, b = 65.1 Å, c = 46.5 Å. The diffraction patterns were processed up to 2.4 Å. A total of 5,035 independent reflections were obtained from 8,585 observed reflections with an overall R_{merge} of 11.8 %. The completeness of the data was 66.2 %. Only one data set with one rotation axis could be obtained due to the insufficient time for data collection, so the completeness of the data set is not so high. The neutron experiment for collecting reflections missed by the 'blind region' is presently scheduled. Using the present incomplete data, we are trying to solve the neutron structure of DsrD. The initial phases were determined by the molecular replacement method with the program CNS.[4)] Before the refinement, deuterium atoms in the main polypeptide chain and hydrogen atoms, whose positions could be estimated stereochemically, were added into the model. After the first refinement, R-factor was 27.5 % (R_{free} = 31.0 %).This work was supported in part by an 'Organized Research Combination System' Grant from the Ministry of Education, Culture, Sports, Science and Technology, Japan.

References

1) N. Mizuno, D.S. Hittel, G. Voordouw and Y. Higuchi : Acta Cryst. **A58** supplement (2002) C304.
2) I. Tanaka, K. Kurihara, T. Chatake and N. Niimura, : J. Appl. Cryst. **35** (2002) 35.
3) Z. Otwinowski, and W. Minor : Methods Enzymol. **276** (1997) 307.
4) A.T. Brünger, P.D. Adams, G.M. Clore, W.L. DeLano, P. Gros, R.W. Grosse-Kunstleve, J.S. Jiang, J. Kuszewski, N. Nilges, N.S. Pannu, R.J. Read, L.M. Rice, T. Simonsonand G.L. Warren, G. L. : Acta Cryst. **D54** (1998) 905.

原子炉：JRR-3　　装置：BIX -1(1GA)　　分野：中性子散乱（生物）

研究テーマ：機能性生体物質の水和構造研究
表　題：　B型DNA十量体d(CCATTAATGG)の中性子結晶回折

1-6-3

Neutron crystallography of B-DNA decamer d(CCATTAATGG)

S. ARAI, T. CHATAKE, T. OHHARA, K. KURIHARA, I. TANAKA and N. NIIMURA

Research Group for Neutron Structural Biology, Neutron Science Research Center, JAERI, Tokai, Ibaraki, 319-1195

Water has long been recognized as an important determinant of nucleic acid structure; the stability, polymorphism and flexibility of the DNA double helix are all hydration-dependent. Moreover, specific hydration patterns play a role in nucleotide sequence recognition by proteins and drugs. [1] In those studies, the observed hydration structure was obtained from the network of only the oxygen atoms of water molecules since it is difficult in an X-ray crystallographic analysis to identify the hydrogen atoms. In order to more fully understand the role in nucleotide sequence recognition by proteins, the location of the hydrogen atoms in this network structure of water molecules is important.

The neutron diffraction is a very powerful method to determine the detailed structure of the biological materials including hydration and hydrogen positions. [2] We are trying to determine the structure of B-DNA duplex by using the neutron diffractmeter BIX-4 [3] with a large single crystal of B-DNA decamar d(CCATTAATGG).

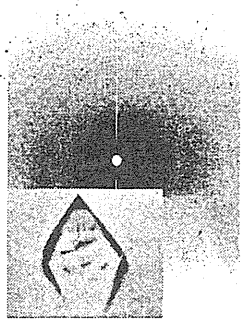


Figure 1: Neutron diffraction pattern of B-DNA decamer and the used crystal.

The DNA decamer was synthesized with a DNA synthesizer. The purity of DNA was analyzed with HPLC and the impurity arising from other macromolecule or species was less than 3.9 %. Salt impurities were removed by the reversed-phase cartridge refinement. A large single crystal was obtained by using the phase diagram information for $MgCl_2$-DNA systems [4] at 6 ℃ for 5 months, in which the size of obtained crystal was 2.8 mm^3. In a neutron diffraction experiment, in order to avoid the high background coming from the incoherent neutron scattering of hydrogen atoms, DNA crystal was grown in D_2O solution. Figure1 shows an example of the neutron diffraction pattern of DNA crystal. The exposure time of each frame was 3-6 hours

Table 1: Crystallographic and refinement statistics of B-DNA decamer d(CCATTAATGG). The values of R-factor, R-free and number of water molecules will be changed because we are refining the structure continuously.

Exposure time	3 - 6 hours /1 frame
Method	Step Scan ($\Delta\phi \sim 0.3°$)
Unit cell	a=b=32.6 Å, c=95.5 Å $\alpha = \beta = 90°$, $\gamma = 120°$
Space group	$P3_221$
Unique reflections	1422
Resolution Range	10-3.0 Å
Completeness (final shell)	63.1 % (64.7 %)
R-merge (final shell)	0.258 (0.240)
R-factor	0.271
R-free	0.359
No. of D_2O	43

原子炉：JRR-3　　装置：BIX -4(1GB)　　分野：中性子散乱（生物）

and the total time for data collection was 31 days. The wavelength of the incident neutron beam was 2.60 Å. Table 1 shows the crystallographic and refinement statistics of B-DNA decamer d(CCATTAATGG). In the previous study, the 2.3 ÅX-ray structure of this B-DNA duplex has been analyzed and the positions of O atoms of 44 water molecules have been determined. [5] However, the hydrogen positions have never been reported. By the neutron diffraction experiments, we have succeeded in observing many water molecules including the deuteium positions. Several hydrogen atoms, which covalently bound to C atoms, also have been identified.

Figure 2 and Fig. 3 show the $(2|Fo| - |Fc|$ neutron density map contoured at 2.0 σ.

Figure 2 shows an example of water molecules around the phosphate group. Many D atoms of D_2O molecules bound to O atoms of the phosphate group. Moreover, the hydrogen bonds are formed between D_2O molecules. Such as this example, the phosphate groups are surrounded by many water molecules.

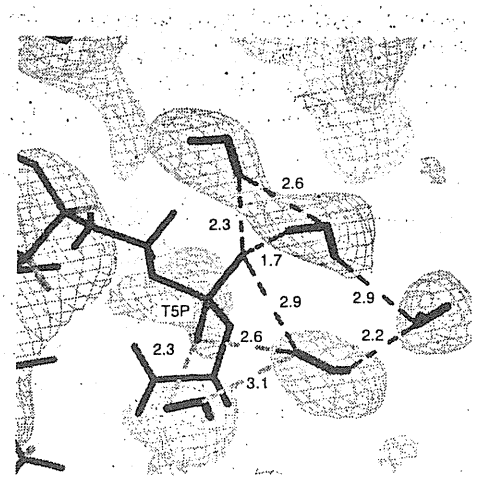


Figure 2: Water molecules near the phosphate group of THY5.

Figure 3 shows one region of the hydration structure in the minor groove. Water molecules form the network structure and connect ADE3 with GUA19. Such as this example, it can be presumed that there are several water molecules to connect the chain A with chain B.

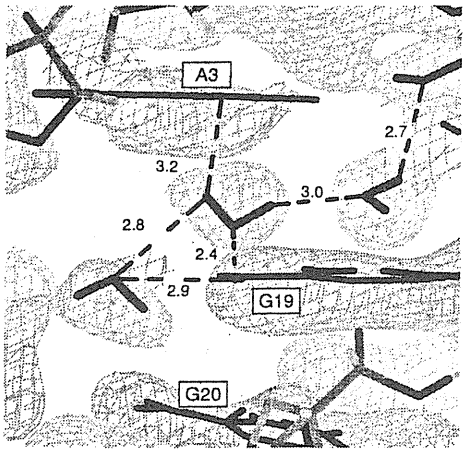


Figure 3: Network structure of the water molecules in the minor groove.

Now we are refining the structure of this DNA duplex including the locations of water molecules. This study is carried out as a part of "Development of New Structural Biology Including Hydrogen and Hydration" in ORCS promoted by Ministry of Education, Culture, Sports, Science and Technology of Japan.

References

1) Z. Owtinowski, R. W. Schevitz, R.-G. Zhang, C. L. Lawson, A. Joachimiak, R. Q. Marmorstein, B. F. Luisi, and P. B. Sigler : Nature **335** (1988) 321.
2) N. Niimura : Curr. Opin. Struct. Biol. **9** (1999) 602.
3) K. Kurihara, I. Tanaka, M. Refai Muslih, A. Ostermann, and N. Niimura : Journal of Synchrotron Radiation, in press.
4) S. Arai, T. Chatake, and N. Niimura : Acta. Cryst. D. **58** (2002) 151.
5) D.S.Goodsell, M. Kaczor-Grzeskowiak, and R.E. Dickerson : J. Mol. Biol. **239** (1994) 79.

研究テーマ：機能性生体物質の水和構造研究
表　題：立方晶インスリンの中性子回折実験

1-6-4

Neutron diffraction experiment of cubic insulin crystal

M. MAEDA[1], T. CHATAKE[1], I. TANAKA[1], A. OSTERMANN[2] and N. NIIMURA[1,3]

[1]Neutron Science Research Center, JAERI, Tokai, Ibaraki 319-1195
[2]Physik-Department E 17 der TUM, James Frank Str., 85747 Garching, Germany
[3]Faculty of Technology, Ibaragi University, Naka-Narusawa, 4-12-1,Hitach, Ibaragi 316-8511

Hydrogen atoms and hydration water molecules surrounding protein play important roles in many physiological functions. Neutron diffraction for protein crystallography using a neutron imaging plate system has become a powerful method for locating position of hydrogen (deuterium) atoms and bound waters of protein.[1)] The cubic insulin crystal (space group $I2_13$, a=b=c=78.9Å) contains a solvent volume of 65 % and has multiple hydration layers.[2)] The first neutron protein crystallography of 2Zn insulin has been reported at 2.2 Å resolution,[3)] however, the difinite structure of hydrogen and hydration could not be obtained. On the other hand, there is no report of the cubic insulin. To elucidate hydrogen and hydration in cubic insulin crystals, a large single crystal of cubic porcine insulin for neutron protein crystallography has been grown in D_2O by using a phase diagram technique. We have succeeded in growing a large single crystal (4.0 x 4.0 x 1.3 mm^3 in volume) of cubic porcine insulin using the technique.

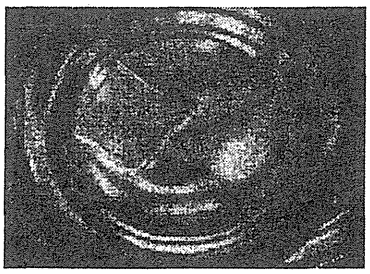


Figure 1: The photograh of cubic porcine insulin crystal grown in D_2O.

The neutron diffraction experiments were carried out with the neutron single crystal diffractometer BIX-3 installed at JRR-3 reactor in JAERI at room temperature. The crystal was sealed in quartz capillary for the measurement. The step scanning method was used for the data collection. The collection time per a frame was 55 minutes controlled by the monitor counts of direct beam in front of the crystal. The total number of 300 frames (which corresponds to 90 ° crystal rotation) was collected in the measurements.

One of the topical results is shown as follows. The protonation and deprotonation of two nitrogen atoms (Nπ, Nτ) in imidazole ring of histidine are very important information to discuss protein crystallography. This information can be given by neutron diffraction. In His 5 in B-chain, Nπ is protonated and Nτ is deprotonated. On the contrary, in His 10, both Nπ and Nτ are protonated. This means that His 5 is electrically neutral and His 10 is positively charged.

This study is supported by a grant from the Organized Research Combination System (ORCS).

References

1) N. Niimura, Y. Minezak, T. Nonaka, J-C Castanga, F. Cipriani, P. Hoghoj, M. S. Lehmann and Wilkinson: Nat Struct Biol. 4 (1997) 909.
2) J. Badger : Biophys. **61** (1993) 816.
3) A. Wlodawer, H. Savage and G. Dodson: Acta. Cryst. B. **45** (1988) 99.

原子炉：JRR-3　　装置：BIX -3(1GA)　　分野：中性子散乱（生物）

研究テーマ：高分子の結晶構造（セルロースの結晶構造））
表　題：高分子の結晶構造（セルロースの結晶構造）

1-6-5

Crystal Structure of Polymer (Cellulose)

Yasuhiro TAKAHASHI

Department of Macromolecular Science, Graduate School of Science, Osaka Univeristy
Toyonaka, Osaka 560-0043, Japan

Neutron diffraction has several advantages in comparison with X-ray diffraction for crystalline polymers.[1-7] New Information about crystal structure could be obtained differing from the X-ray work. The scattering length of an atom is independent of the atomic number. Accordingly, the hydrogen and deuterium atoms have different scattering lengths for neutron diffraction, although they have the same scattering length for X-ray diffraction. The scattering lengths of hydrogen (-3.74) and deuterium (6.67) located on the outer shell of the molecule are comparable to the scattering lengths of carbon (6.65) and oxygen (5.80). Therefore, the azimuthal angle of the molecule can be determined by neutron diffraction more accurately than by X-ray diffraction. Furthermore, the scattering lengths by neutron diffraction are independent of the scattering angle θ. The intensities of the refections with large θ values can be observed strongly and can be measured accurately. Accordingly, it can be said that neutron structure analysis gives more accurate crystal structure than X-ray structure analysis.

In the previous works, [1-7] neutron structure analyses of crystalline polymers were carried out on the equatorial reflections in the temperature range 10 -300K by using powder diffractometer. In the case of poly(vinyl alcohol),[3] the intramolecular hydrogen bond was found in the isotactic sequence of the atactic polymer. In the cases of deuterated polyethylene,[4] poly(p-phenylenebenzobisoxazole)(PBO),[5] and poly(p-phenylenebenzobisthiazole)(PBZT),[6] the more detailed structure than X-ray works could be obtained. In the case of poly(pyridobisimidazole)(PIPD),[7] the statistical structure was clarified by utilizing the difference in scattering lengths between nitrogen and carbon. However, only two-dimensional structure projected through the fiber axis can be obtained by using the powder diffractometer.

Therefore, in order to obtain the three-dimensional structure, the attempts to take the fiber diagram of crystalline polymers were made by using neutron imaging plate in the present study. Unfortunately, the fiber specimen of dueterated cellulose II was broken during the drying procedure. But the fiber diagrams of the several crystalline polymers could be taken. However, the number of observed reflections was not sufficient to analyse the crystal structure because the signal-to-noise ratio is not good. The development of the following procedure is now in progress. After summing the data of several imaging plates in order to improve the signal-to-noise ratio, the integrated intensities are estimated according to the procedures in X-ray diffraction.[8]

References

1) Y. Takahashi, "Neutron Structure Analyses of Crystalline Polymers", Recent Res. Devel. in Macromol. Res., **3** (1998) 265.
2) Y. Takahashi, "Neutron Diffraction by Crystalline Polymers", ACS Symposium Series 739, "Scattering from Polymers" edited by P. Cebe, B. S. Hsiao, and D. J. Lohse, Chapter 5 **74** (2000).
3) Y. Takahashi: J. Polymer Sci. **Part B** Polym. Phys., **35** (1997) 193.
4) Y. Takahashi: Macromolecules **31** (1998) 3868.
5) Y. Takahashi: Macromolecules **32** (1999) 4010.
6) Y. Takahashi: Macromolecules **34** (2001) 2012.
7) Y. Takahashi: Macromolecules **35** (2002) 3942.
8) Y. Takahashi and H. Sul, *to be published.*

原子炉：JRR-3　　装置：BIX -3 (1GA)　　分野：中性子散乱（生物）

研究テーマ：機能性生体物質の水和構造研究
表　題：様々な条件下におけるニワトリ卵白リゾチーム単結晶の中性子回折測定

1-6-6

Neutron Diffraction Measurements of Single Crystals of Hen Egg White Lysozyme under Various Conditions

S. FUJIWARA

Neutron Science Research Center, JAERI, Tokai, Ibaraki 319-1195

Hydrogen atoms play essential roles in various aspects of functions of proteins. Moreover, hydrogen bonds between the atoms in the protein as well as hydration are important in the stability of the protein. Locating the positions of hydrogens and hydrated water is therefore important in considering the molecular mechanism of the protein function and the stability of the proteins. Neutron crystallography, which can locate the hydrogens, is one of the important methods to investigate these problems. We have started projects of exploring various aspects of hydrogens and hydrogen bonds in a protein with neutron crystallography. We used hen egg white lysozyme (HEWL) as a model protein, and measured neutron diffraction of single crystals of this protein under various conditions. In order to obtain information of the protonation state of amino acid residues in the protein at various pH, since the charge distribution of the protein, we collected the neutron diffraction data of the single crystal of HEWL grown in pH 4.9[1)2)]. and 3.4[3)], and preliminary structure analysis[4)] of these data detected the hydrogen-bond networks including the hydrated water around the active site of this enzyme.

Another ongoing project has been related to the mechanism of enzyme activity of HEWL. HEWL is an enzyme that hydrolyses a polysaccharide. To gain insight into the mechanisms of enzyme activity such as lysozyme, we performed the measurements of neutron diffraction of single crystals of the complex of HEWL and substrate-analogue, NAG_3[5)]. A solution containing 30 mg/ml HEWL in 50 mM sodium acetate (pH 4.3) in D_2O was mixed with a solution containing NAG_3 and NaCl to make 1:1 complex of HEWL and NAG_3. Crystals were formed in about two weeks, and the crystals grew only to the size of about 3 mm^3. The space group of the crystals was $P4_32_12$, and the cell parameters were $a = b = 7.91nm$, $c = 3.66nm$. Neutron diffraction patterns of the crystal were measured with BIX-2[6)]. The oscillation method of 0.4 degrees has been employed. Exposure time per one frame has been 24 hours. In addition to the data taken during the last fiscal year, the data of 30 degrees of rotation range were collected, and the data reduction and structural analysis are currently underway.

We have also been measuring neutron diffraction patterns of single crystals of HEWL in H_2O to investigate a possibility of extracting hydrogen and water positions without interferences from other atoms by difference intensities between the diffraction from HEWL in D_2O and that in H_2O. We prepared single crystals of HEWL grown in H_2O for this purpose. Crystals were grown to the size of about 10 mm^3. Neutron diffraction measurements with BIX-2 yielded clear diffraction patterns even in the crystals in H_2O. The data reduction and structural analysis are now ongoing.

References

1) S. Fujiwara et al.: JAERI Review **99-003** (1999) 13.
2) S. Fujiwara et al.: JAERI Review **2000-005** (2000) 7.
3) S. Fujiwara et al.: JAERI Review **2002-006** (2002) 19.
4) M. Maeda et al.: J. Phys. Soc. Jpn. **70** (2001) Suppl. A 403.
5) S. Fujiwara et al.: JAERI Review **2002-028** (2002) 86.
6) S. Fujiwara et al.: Physica B **241-243** (1998) 207.

原子炉：JRR-3　　装置：BIX-2(T2-3)　　分野：中性子散乱（生物）

研究テーマ：機能性生体物質の水和構造研究
表　題：筋肉の細いフィラメントの中性子繊維回折
1-6-7

Neutron Fiber Diffraction of the Muscle Thin Filaments

S. FUJIWARA[1], F. MATSUMOTO[1,2], and S. DESHIMARU[1,2]

[1]Neutron Science Research Center, JAERI, Tokai, Ibaraki 319-1195
[2]Laboratory for Structural Biochemistry, RIKEN Harima Institute, Hyogo 679-5148

Muscles consist of the structural units called sarcomeres that consist of mainly two kinds of filamentous structures; actin-based "thin" filaments and myosin-based "thick" filaments. We have been studying the structures of muscle and muscle proteins using neutron diffraction and scattering[1-3]. In studying such filamentous structures, measurements of the oriented samples increase the structural information obtained. It is, however, difficult to orient large amount of the samples. In order to check feasibility of neutron fiber diffraction, we oriented the purified thin filaments in quartz capillaries and measure diffraction patterns of these samples.

We put the thin filament sols purified from bovine hearts into a quartz capillary with a diameter of 3 mm. The thin filaments were then oriented in magnetic field of 19 Tesla. Length of the oriented region in the capillary was about 3 mm. The sample containing the oriented region was put on a sample holder specifically made for the capillary samples, and the regions other than the oriented region were masked with Cd plates. The sample was then illuminated with neutrons. These neutron fiber diffraction measurements were done with the Small-Angle Neutron Scattering Instrument (SANS-J) at the guide hall of the reactor JRR-3M in Japan Atomic Energy Research Institute. Neutrons with the wavelength of 6.5 Å($\Delta\lambda/\lambda$=12.98%) were employed, and the sample-to-detector distance was 1.5 m.

Figure 1 shows an example of the neutron diffraction patterns of the oriented thin filaments. Exposure time of this pattern was 20 hours. A strong intensity on the equator, actin-based layer lines at 59 Åand 51 Å, and a weak cross-pattern across the equator due to tropomyosin were observed. Moreover, at least up to 3rd layer lines of the meridional reflections due to troponin were clearly observed. This suggests a possibility of extracting the layer-line reflections of each subunit within the troponin complex by combining neutron fiber diffraction measurements with selective deuteration and the contrast-matching technique. These projects are currently underway.

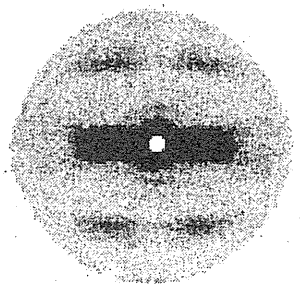


Figure 1: An example of neutron diffraction patterns of the oriented samples of the thin filaments.

Supported in part by Special Coordination Funds for Promoting Science and Technology from the Ministry of Education, Culture, Sports, Science and Technology, the Japanese Government.

References

1) S. Fujiwara *et al.*: J. Phys. Soc. Jpn. **70** (2001) Suppl. A 408.
2) S. Fujiwara *et al.*: JAERI Review **2002-028** (2002) 87.
3) F. Matsumoto *et al.*: JAERI Review **2002-028** (2002) 88.

原子炉：JRR-3　　装置：SANS-J(C3-2)　　分野：中性子散乱（生物）

研究テーマ：蛋白質表面の水和水の動力学特性の評価

表題：蛋白質表面に分布する水和水クラスターのダイナミクス

1-6-8 Dynamics of the hydration cluster distributed on the protein surface

Hiroshi Nakagawa[1], Hironari Kamikubo[1], Itaru Tukushi[2], Toshiji Kanaya[3] and Mikio Kataoka[1]

[1]Department of Materials Science, Nara Institute of Science and Technology; [2]Chiba Institute of Technology; [3]Institute for Chemical Research, Kyoto University

Water molecules on a protein surface interact strongly with the protein to form a hydration layer. Protein stability and function depend on the hydration water. It is well known that the physical properties of hydration water are distinct from the bulk water. For example, the relaxation time of water molecules in the hydration layer is 10^{-7} ~ 10^{-9}sec, while that of bulk water is 10^{-12}sec. It is also suggested that the protein dynamics is affected by hydration water. Water molecules in the hydration water are considered to form cluster through hydrogen bond network. Thus, a realistic picture of protein in a functional state is that the protein is trapped in a hydration cluster net. Therefore, the protein dynamics are closely related to the dynamics of hydration waters.

In the present study, incoherent elastic neutron scattering(IENS) is applied to reveal the dynamical properties of the hydration cluster on a protein surface. The used protein was hydrated Staphylococcal nuclease(SNase). IENS of SNase was measured under various temperatures with the use of the triple axis spectrometer, HER in JRR-3M at Tokai JAERI. The contribution of hydration cluster to EINS was estimated by subtraction of the IENS spectrum of dry SNase from that of hydrated SNase. The mean square displacement of hydration cluster thus obtained was plotted against temperature(Fig.1). It is clear that the dynamical transition of hydration cluster is observed around 200K. Below 200K, average mean square displacement would be below the measurement limitation, suggesting that the hydration water is immobile with this energy resolution. Above 200K, anharmonic motion is activated and the mean square displacement increases as temperature increases. The transition temperature of bulk water is known to be about135K. The difference in the transition temperature strongly indicates that the dynamical properties of the hydration clusters are distinct from the bulk water.

In the figure, the mean square displacements for both hydrated SNase and dried SNase are also plotted. Below 200K the behaviors are harmonic despite of hydration state, above 240K the deviation of the behavior of hydrated sample from that of the dried sample becomes remarkable, which is already reported in the previous study. The dynamical transition of protein occurs gradually in the temperature range between 200K and 240K. These regard as the general dynamical property of protein[1]. The dynamical transition of protein looks concomitant of the dynamical transition of hydration cluster. The present study demonstrates that the separation of the dynamics of hydration cluster from the dynamics of protein is important and essential to understand the protein dynamics. For the further sophistication, we are planning to prepare the hydrated SNase with heavy water and deuterated SNase.

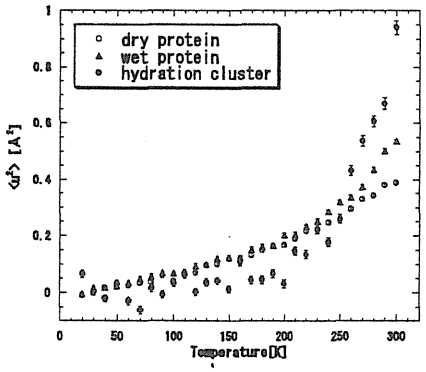


Figure1: Temperature dependent mean square displacement of the hydration cluster. The data of dry and wet Staphylococcal nuclease are also displayed.

References

[1] V. Reat, R. Dunn, M. Ferrand, J.L.Finney, R. M. Daniel and J.C. Smith. Proc. Natl. Acad. Sci. USA 97,9961-6(2000)

使用施設：JRR-3　装置：HER(C-1-1)，分野：5.Biology

研究テーマ：機能性生体物質の水和構造研究
表　題：細いフィラメント上のトロポニンCの中性子小角散乱測定

1-6-9

Small-Angle Neutron Scattering Measurements of TroponinC on the Thin Filament

F. MATSUMOTO[1,2], K. MAKINO[2], K. MAEDA[2], Y. MAEDA[2], and S. FUJIWARA[1]

[1]Neutron Science Research Center, JAERI, Tokai, Ibaraki 319-1195
[2]Laboratory for Structural Biochemistry, RIKEN Harima Institute, Hyogo 679-5148

Main components of muscles are two kinds of filaments, actin-based "thin" filaments and myosin-based "thick" filaments. Muscle contraction occurs via sliding of these filaments past each other. The molecular mechanism of the muscle contraction and its regulation is one of the most important problems in biophysics, as it is a typical example of energy transduction mechanisms of living organisms. In vertebrate skeletal and cardiac muscles, muscle contraction is regulated via the interactions between the thin filament proteins, troponin (Tn) C, TnI, TnT, tropomyosin, and actin. These interactions are triggered by binding of Ca^{2+} to TnC. We have been investigating the structure of TnC on the thin filament with and without Ca^{2+}, as a first step toward understanding the regulation mechanism of the muscle contraction.

Neutron scattering was employed to do this. Structural information of a selected component within a protein complex can be obtained with this method, when it is combined with the strategies of selective deuteration and contrast matching. We prepared the deuterated (d-) TnC by expressing the protein in *E. coli* in D_2O medium containing deuterated algal peptone. The purified d-TnC was exchanged into the native thin filaments by CDTA treatment. The native thin filaments containing d-TnC were then exposed to neutrons under the condition where the contrast of the other components of the thin filaments were matched out with 40% D_2O.

During the last fiscal year, we had measured small-angle neutron scattering patterns of these samples with and without 1.1 mM $CaCl_2$ with the Small-Angle Neutron Scattering Instrument (SANS-J) at the guide hall of the reactor JRR-3 in JAERI[1)]. Experimental setting had been as follows: neutrons with the wavelength of 6.5 Å($\Delta\lambda/\lambda$=12.98%) were employed, and the sample-to-detector distance was 4 m. This year we performed similar measurements with the sample-to-detector distance of 2 m, in order to obtain the scattering curves covering wider Q-range. Figure 1 shows the merged scattering curves of d-TnC on the thin filaments with and without Ca^{2+}. Excellent agreements in the overlap Q-range between the curves with different sample-to-detector distances were observed.

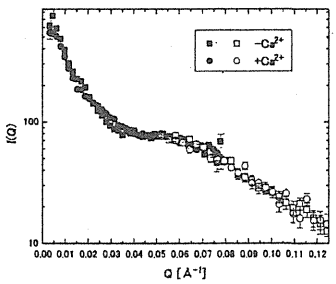


Figure 1: The merged neutron scattering curves of d-TnC on the thin filaments with and without Ca^{2+}.

Analysis of these scattering curves by model calculation is now underway. Supported by Special Coordination Funds for Promoting Science and Technology from the Ministry of Education, Culture, Sports, Science and Technology, the Japanese Government.

References

1) F. Matsumoto *et al.*: JAERI Review **2002-028** (2002) 88.

原子炉：JRR-3　　装置：SANS-J(C3-2)　　分野：中性子散乱（生物）

研究テーマ:ナノ構造解析によるモデル生体膜の糖脂質ラフトの機能構造とダイナミックスに関する研究
表題:Ganglioside/Cholestrol/DPPC 混合ベシクルの構造とダイナミックス

1-6-10 Strcutre and Dynamics of Ganglioside/Cholestrol/DPPC Mixed Vesicle

M. Hirai, T. Hayakawa, and K. Koisumi.

Department of Physics, Gunma University, Maebashi 371-8510, Japan.

1. Introduction Structure and function of mammalian cell membrane domains, so-called rafts, have been attracting a huge interest and are one of the current hot topics in cell biology since these domains are postulated to have a significant function as a molecular device for localization of specific proteins and to be involved in important membrane-associated events such as signal transmission, cell adhesion and lipid/protein sorting. A common feature of cell membrane domains is their peculiar lipid composition, being rich in glycosphingolipids (GSLs), sphingomyelin and cholesterol. Gangliosides are major components of GSLs. Gangliosides are mostly located on the cell surface membranes in central nervous system, and are rich in lipid microdomains with other particular lipids and proteins in neuronal cells. Functionality of the GSLs microdomains is assumed to be closely relate the peculiar features of ceramide and oligosaccharide portions. However, even structural information of model membrane vesicle containing gangliosides is rather limited. Thus, we have carried out small-angle neutron scattering (SANS) and neutron spin echo (NSE) measurements to characterize the structure and dynamics of monosialoganglioside (GM1)/ cholesterol/dipalmitoyl phosphatidylcholine (DPPC) mixed vesicle as a model raft system.

2. Experimental In SANS experiments we employed the inverse contrast variation as reported recently [1]. For this purpose, we dissolved the mixed vesicles in 99.9+ atom % D_2O solvent with 50 mM Hepes adjusted to pH 7. The contrast of the vesicle was varied by changing the molar ratio of DPPC/deuterated-DPPC (d-DPPC). Small uni-lamellar vesicles (SUV were prepared by ultrasonication. SANS and NSE experiments were carried out at C1-2 and C2-2 beam ports at JRR-3M, Tokai, Ibaraki, Japan.

3. Results and Discussion Fig.1A shows the SANS curves from the of the GM1/ cholesterol/DPPC=0.1/0.1/1 mixed SUVs. The variation of the SANS curves depending on the DPPC/d-DPPC ratio is attributed to the change of the contrast. Fig. 1B shows the Fourier time dependence of the NSE signal amplitude P_{NSE} of the same sample at 25 °C. From both SANS and NSE data we can understand dynamical structure of the model raft. The detailed analyses and results will be seen in elsewhere.

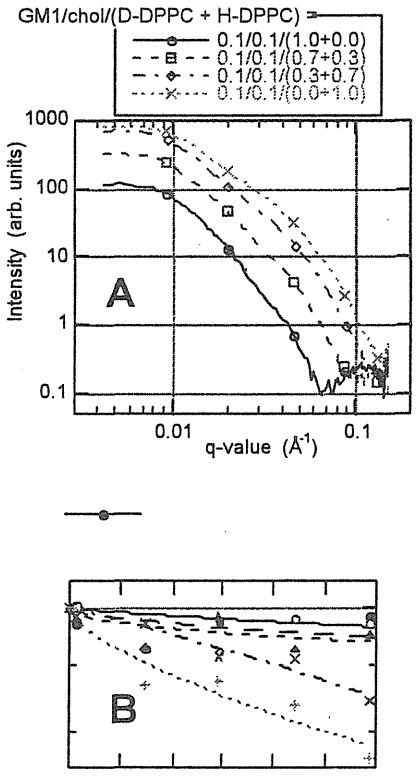


Fig. 1A. SANS curves of GM1/DPPC SUV samples with diffrent inverse contrasts at 25 °C. Fig. 1B. shows the ormalized NSE signal amplitude of the same SUV at 25 °C.

references

[1] M. Hirai et al., Biophysical J., 2003, in press.

JRR-3 SANS-U(C1-2), 5. Biology

研究テーマ：機能性生体物質の水和構造研究
表　題：時分割中性子散乱によるニワトリ卵白リゾチームアミロイドプロトフィラメントの会合過程の研究

1-6-11

Association of the Amyloid Protofilaments of Hen Egg White Lysozyme Studied by Time-Resolved Neutron Scattering

S. FUJIWARA[1], F. MATSUMOTO[1,2], and Y. YONEZAWA[3]

[1]Neutron Science Research Center, JAERI, Tokai, Ibaraki 319-1195
[2]Laboratory for Structural Biochemistry, RIKEN Harima Institute, Hyogo 679-5148
[3]Institute for Protein Research, Osaka University, Suita, Osaka 565-0871

Amyloid fibrils are filamentous protein aggregates found in a wide variety of proteins including the disease-related proteins. Understanding of the mechanism of the amyloid fibril formation is not only important for the development of therapeutic strategies against the amyloid diseases but also of considerable help to gain an insight into the generic properties of proteins related to the mechanisms of folding and stability. It was found recently that hen egg white lysozyme (HEWL) forms the amyloid fibrils in highly concentrated ethanol solution[1]. The HEWL-water-ethanol system is suitable to study the general mechanism of the amyloid fibril formation. We investigated structural states of HEWL in this model system with static small-angle X-ray and neutron scattering (SAXS and SANS) measurements[2] and proposed a pathway of the amyloid fibril formation of HEWL as the process consisting of three stages; the formation of the dimers, the formation of the protofilaments, and the formation of the amyloid fibrils *via* a lateral association of the protofilaments.

Here we performed time-resolved SANS measurements to monitor process of the formation of the amyloid fibrils[3] with SANS-J at the guide hall of the reactor JRR-3M in JAERI. The time-resolved measurements were done by successive collection of the data of 30 minutes exposure. Figure 1 shows the association process of the protofilaments of HEWL at 0.5 mM NaCl in 90% ethanol, in terms of the relative changes in the structural parameters estimated from the cross-sectional Guinier analysis of the scattering curve of each frame in the time-resolved measurements.

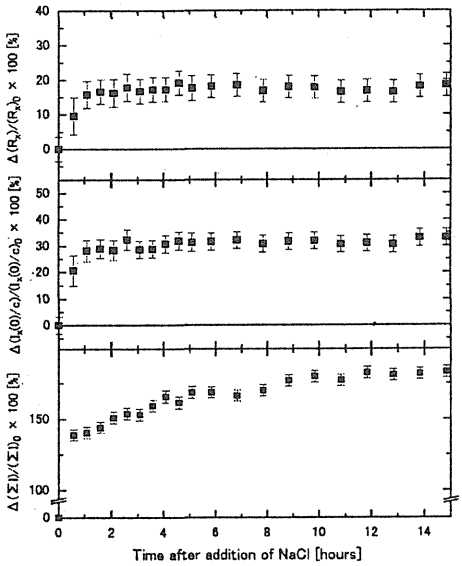


Figure 1: Time courses of the relative changes in the parameters (cross-sectional radius of gyration, $I_X(0)/c$, and integrated intensity) after addition of NaCl.

The manner in which these changes occur suggests that the association of the protofilaments of HEWL occurs *via* the lateral association of the protofilaments, followed by the cross-linking of the fibrils formed.

References

1) S. Goda et al.: Protein Sci. **9** (2000) 369.
2) Y. Yonezawa et al.: J. Mol. Biol. **323** (2002) 237.
3) S. Fujiwara et al.: J. Mol. Biol. **331** (2003) 21.

原子炉：JRR-3　　装置：SANS-J(C3-2)　　分野：中性子散乱（生物）

研究テーマ:コントラスト変調法によるミリストイル化タンパク質とカルモデュリン複合体の溶液構造解析
表題:カルモデュリン/ニューロン特異的タンパク質 NAP-22 複合体の溶液構造解析

1-6-12

Solution Structure of Ca^{2+}-saturated Calmodulin Complexed with N^{α}-myristoylated NAP-22

Y.Izumi, N.Hayashi[1], Y.Jinbo, T.Matsufuji, N.Matsushima[2]

Graduate School of Science and Engineering, Yamagata University, Yonezawa, Yamagata 992-8510, JAPAN;
[1]Fujita Health University, Toyoake, Aichi 470-1192 JAPAN;
[2]School of HealthScience, Sapporo Medical University, Sapporo

N^{α}-myristoylated NAP-22, a neuron-specific protein kinase C substrate, interacts with calmodulin (CaM) in the presence of Ca^{2+} ions. The myristoylated N-terminal nonapeptide of NAP-22 (mC/N9) also binds to Ca^{2+}-saturated CaM (Ca^{2+}/CaM). The binding of two moles of mC/N9 induced a drastic structural change in Ca^{2+}/CaM. The radius of gyration (Rg) for the Ca^{2+}/CaM-mC/N9 complex was 19.8 A [1]. The result indicates that the complex takes an intermediate structure between a dumbbell structure and a compact globular structure. It suggests that the Ca^{2+}/CaM complexed with N^{α}-myristoylated NAP-22 also takes an intermediate structure similar to the Ca^{2+}/CaM-mC/N9 complex [1].

In this report, small-angle neutron scattering (SANS) with contrast variation has been utilized to obtain the first low resolution structure of $4Ca^{2+}$/CaM complexed with N^{α}-myristoylated NAP-22. Deuterated CaM (DCaM) was used. The solutions with molar ratio of 1:2 were prepared at a DCaM concentration of 5.0mg/mL. The neutron scattering experiments were performed with SANS-U spectrometer [2].

Table 1 summarizes the radius of gyration Rg at various contrast points for the $4Ca^{2+}$/CaM cogplexed with N^{α}-myristoylated NAP-22. The Rg value near the matching point (30-40%D_2O) is about 18-19 A which is consistent with that (Rg=19.3A) obtained from SAXS for $4Ca^{2+}$/CaM/mC/N9 with the same molar ratio at the same concentration of CaM. The Stuhrman plot shows a negative slope, suggesting that DCaM is inside the complex. However, we cannot claim that these results are conclusive because of the scattering of our experimental data. It is necessary to improve the SANS optics as shown in Table 2, in which new optics gains 4 times in the intensity compared with the present optics.

Table 1: Radius of gyration Rg at various contrast points for the $4Ca^{2+}$/CaM complexed with N^{α}-myristoylated NAP-22.

% D_2O	Rg/A	S/N
0	57	bad
30	18	good
40	19	good
60	91	bad
80	105	bad

Table 2: SANS/U Optics Parameters.

Pinhole /mmϕ	sample /mmϕ	beam stop /mmϕ	q_{min} /A^{-1}	I(q)
7	9.0	36.0	0.0040	1.0
10	12.3	42.3	0.0047	2.0
15	17.6	52.6	0.0059	4.5

References

[1] N.Hayashi, Y.Izumi, K.Titani and N.Matsushima, Protein Sci. 9(2000)1905.
[2] Y.Izumi, N.Hayashi, Y.Jinbo and N.Matsushima, This report, 8(2001)232.

使用施設:JRR-3　装置:SANS-U(C1-2), 分野 Biology

1. 中性子散乱 7) 基礎物理学・中性子光学

1. Neutron Scattering 7) Fundamental Physics

Neutron Optics

This is a blank page.

研究テーマ：構造用材料の残留応力および負荷荷重下での材料特性評価
表　題：形状記憶合金の切欠き近傍における相変態の測定

1-7-1

Phase Transformation in Smooth Specimen and at Notch Root in Shape Memory Alloy TiNi

Y. AKINIWA, H. KIMURA, K. TANAKA, N. MINAKAWA[1] and Y. MORII[1]

Department of Mechanical Engineering, Nagoya University, Nagoya 464-8306
[1]Advanced Science Research Center, JAERI, Tokai, Ibaraki 319-1195

1. Intruduction

The equiatomic TiNi alloy is an intermetallic compound that shows not only excellent resistance against corrosion and wear but also shape memory effect with large recovery strain and superelasticity. Though TiNi has been used for pipe couplings and the frames of glasses utilizing the shape memory effect and superelastic property [1], the practical application is limited because the fatigue properties of TiNi has not been fully clarified. In addition to the conventional use, TiNi has attracted attention as an actuator of intelligent structure in recent years and the fatigue reliability over long-term use has been recognized as an important subject in the utilization [2]. In order to evaluate the fatigue properties, it is necessary to understand the martensitic transformation behavior under applied loads, especially at stress concentration area.

In this study, stress-induced martensitic transformation was investigated in shape memory TiNi, hereinafter denoted as FML4, and superelastic TiNi, FML6. The smooth specimen and notched specimen were utilized for the measurement by neutron diffraction patterns in order to clarify the overall martensitic transformation and the local transformation around the notch root.

2. Materials and measurement

Shape memory TiNi, FML4, was heated to 450 degrees Celsius in order to introduce shape memory effect at room temperature. Superelastic TiNi, FML6, was heated to 750 degrees Celsius to introduce superelastic property at room temperature. Because the martensitic transformation start temperature of FML4 is 21 degrees Celsius, it is composed of austenitic and martensitic phases at room temperature of approximately 20 degrees Celsius without loading. On the other hand, the martensitic transformation start temperature of FML6 is -60 degrees Celsius. Therefore, it is fully austenitic at the room temperature without loading.

Smooth specimens with the dimension of 10 x 70 x 2 mm^3 were prepared. Single-edge-notched specimens with the same dimension containing a notch of 1 mm at the center were also prepared. The specimens were shaped by electrical discharge machining followed by electrolytic polishing.

The neutron facility of JAERI (RESA) was used for the neutron diffraction measurement. The wave length of the beam was 0.21009 nm with the preset time of 1800 sec. The diffraction planes of (110) in austenite and (022) in martensite were employed for the measurement.

3. Martensitic Transformation in Smooth Specimen

The phase transition was investigated by neutron diffraction measurement under the applied stress of 5, 50, 100, 200, 350, 550MPa and 5 MPa during unloading in a smooth specimen. The results of the diffraction intensity from austenitic (110) and martensitic (022) phases in FML4 are presented in Fig.1 and Fig.2, respectively. Under the stress level of 100 MPa, only austenitic phase was observed. At the stress level of 100 MPa, the existence of both the austenitic and martensitic phases were confirmed. Above the stress level of 100 MPa, the austenitic phase disappeared and martensitic phase remained even after unloading.

原子炉：JRR-3　　装置：RESA(T2-1)　　分野：中性子散乱（基礎物理）

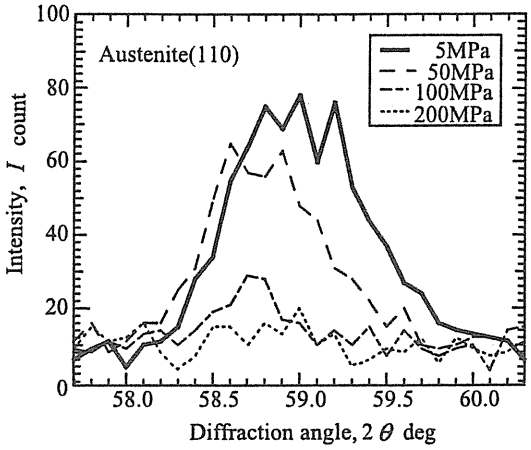


Figure 1: Results of neutron diffraction in FML4 (Austenite)

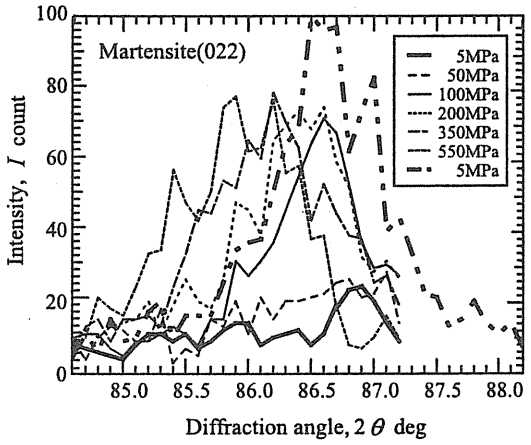


Figure 2: Results of neutron diffraction in FML4 (Martensite)

4. Martensitic Transformation at Notch Root

The distribution of martensitic phase at notch root was also investigated. Load of 33 N was applied on the specimen with the sectional dimension of 6 x 3 mm^2 under 4-point bending with the outer span of 60 and inner span of 20 mm. The width of the incident beam was 0.3 mm with the preset time of 1800 sec. The diffraction profiles at 14 measurement points marked by x in Fig.3 were obtained. The contour of the stress-induced martensitic phase was determined as depicted in the figure. The result shows that the stress-induced martensitic phase stretched about 0.5 mm from the notch root to the direction of the notch. It was found to stretch further in the perpendicular direction. Based on this result, the stress induced martensitic phase at a crack tip, which is indispensable to understand the fatigue crack propagation behavior in those materials, can also be expected to be measured in the same manner.

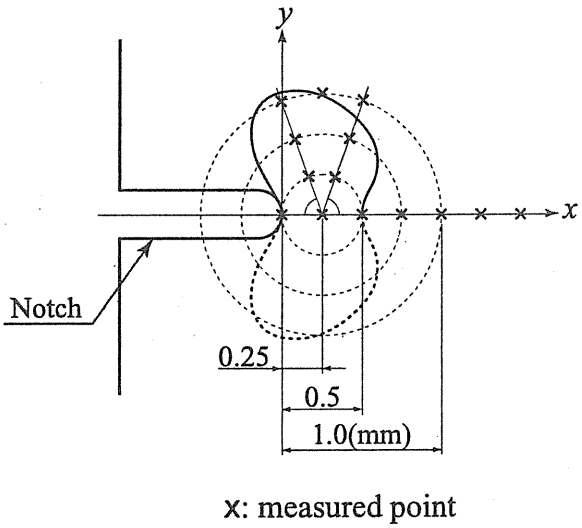


Figure 3: Martensitic phase at notch root

5. Conclusion

(1) The phase transition from austenite to martensite was observed at the stress level of 100 MPa. The existence of the residual martensitic phase was confirmed in the shape memory TiNi.

(2) The distribution of martensitic phase at notch root was measured. It was found to stretch further in the direction perpendicular to the notch. The measurement by neutron diffraction was found to be effective to determine the distribution of stress-induced martensitic phase at a crack tip by enabling the measurement at a small local area.

References

1) H.Sakamoto: Trans. Jpn. Inst. Met. **24** (1983) p. 665.
2) H. Tobushi: J. of JSTP **35-403** (1994) p. 910.

研究テーマ：複合磁気ミラーとフィゾー効果による横方向干渉性の測定
表題：5Qc スーパーミラー中性子反射鏡の開発

1-7-2 Development of a 5Qc Ni/Ti supermirror using ion beam sputter instrument

M. Hino, S.Tasaki *, H.Yoshino and Y.Kawabata

Research Reactor Institute, Kyoto University, Kumatori, Osaka 590-0494, Japan
**Department of Nuclear Engineering, Kyoto University, Sakyo, Kyoto 606-8501, Japan*

A Multilayer mirror is one of the most useful devices for slow neutron experiments. Multilayer mirrors and supermirrors are applied to neutron optical devices, such as neutron guide tube [1]. The multilayer mirror consists of alternating layers of two materials with different potential energies for the neutron. It has artificial lattice spacing(*d*-spacing) and gives one-dimensional optical potentials for a neutron beam. Supermirror is a stack of multilayers with gradually increasing value of the *d*-spacing. A multilayer with small *d*-spacing and supermirror with large-m is desirable to enlarge utilization efficiency for neutron scattering experiments.

Recently we succeeded in fabricating large-m Ni/Ti using ion beam sputtering technique. In this report, we show the performance of multilayer as a neutron mirror.

Multilayers were deposited on silicon wafer using ion beam sputtering instrument installed in the Kyoto University Research Reactor Institute (KURRI).The polished silicon wafer is 3 inches diameter and 3mm in thickness The measurement of reflectivity of multilayer mirrors was carried out at C3-1-2 port of the JRR-3M reactor in the Japan Atomic Energy Research Institute (JAERI). The incident wavelength is 0.88 nm and the resolution is 2.4 % in full width half maximum. The divergent angle is smaller than 2 mrad.

Figure 1 shows reflectivity of neutron with 5Qc Ni/Ti supermirror whose number of layers is 2820. The '5Qc' means that the critical angle of the supermirror is five times as large as a critical angle of nickel. Here the number of 'm' is a multiple of the unit of critical angle of nickel. The sequence of layers in the multilayer and supermirror is deigned using the method proposed by Ebisawa [2]. The reflectivity by this supermirror is above 0.6. The reflectivity decreases suddenly at the incident angle (m=1~2) which is just larger than the critical angle of nickel. The reason can be considered that grain size grows in nickel layer whose thickness is above about 10 nm and interface roughness reduces the reflectivity. Though there is still some points to improve, it is, in our knowledge, first 5Qc neutron supermirror with such a high reflectivity.

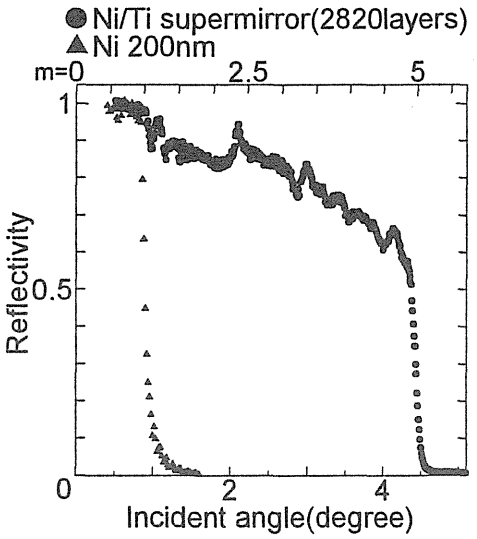


Figure 1: Reflectivity of neutrons with Ni/Ti supermirror (m=5) as a function of the incident angle of multilayer. The closed circle (●) and triangle (▲) show reflectivities of neutrons with the Ni/Ti supermirror and nickel layer whose thickness is 200 nm, respectively.

[1] F. Mezei, Comm. Phys.,1(1976)81.
[2] T.Ebisawa, N.Achiwa, S.Yamada, T.Akiyoshi and S.Okamoto, J.Nucl.Sci.Technol., 16 (1979) 647.

使用施設：JRR-3 MINE(C3-1-2), 8. Neutron Optics

研究テーマ：ITER真空容器の研究
表　題：ITER真空容器における部分溶け込み溶接の残留ひずみ測定
1-7-3

Neutron Diffraction Measurement of Residual Strain of Partial Penetration Welds for ITER Vacuum Vessel

M. NAKAHIRA, A. MORIAI[1] and N. MINAKAWA[1]

Department of ITER Project, JAERI, Naka, Ibaraki 311-0193
[1]Advanced Science Research Center, JAERI, Tokai, Ibaraki 319-1195

The vacuum vessel (VV) of ITER is a double-walled "doughnut" structure made of stainless steel SS316L with D-shaped cross section. The development of the partial penetration welding by through-wall electron beam welding (EBW) is carried out for the T joint of the outer shell (40-60mm plates) and the rib, because it has advantage from distortion and cost points of view. In this study, neutron diffraction measurement of residual strain of this new welding had been carried out in order to investigate an applicability of the welding to the VV. The configuration of weld and the measurement positions of residual strain are shown in Fig. 1. RESA (Neutron Diffractometer for REsidual Stress Analysis) in the JRR-3 is used for the measurement. The results in last year showed that the wider slit area was required to obtain sufficient neutron intensity within practical exposure time, because the test piece was thick. The slit of 2 × 15 mm was used this time (3 × 3 mm was used at last time). The neutron intensity was obtained in the toroidal direction. The test condition and results are shown in Table 1 and Fig. 2, respectively. D-space is the lattice length and the unit is Å. The exposure time of each step is 5 min. The result shows that the area of weld metal which leis in 3.5 to 8.5 mm from sample surface has larger lattice length. It can be considered that the tension stress remains in toroidal direction at weld metal. Other two directions are under measuring with more exposure time, because path length of neutron is much longer than the toroidal direction measurement. The result will be obtained in next fiscal year.

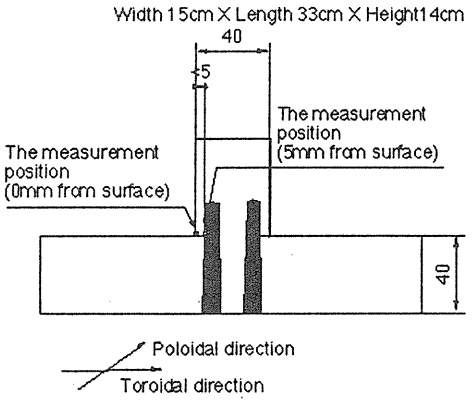


Figure 1: The configuration of weld specimens and the measurement positions.

Table 1: Test conditions

Structure	Wave length (Å)	Slit(mm)
FCC (220)	2.09632	2W × 15H

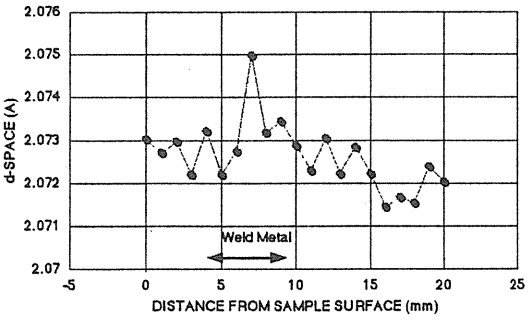


Figure 2: Obtained lattice length.

原子炉：JRR-3　　装置：RESA(T2-1)　　分野：中性子散乱（基礎物理）

研究テーマ： 多層膜冷中性子干渉計の改良 -干渉性の向上-
表題： 冷中性子ビーム横方向可干渉長の直接測定

Direct measurement of the transverse coherence length of cold neutron beam

1-7-4

M. Kitaguchi[1,3], H. Funahashi[1], T. Nakura[1], K. Taketani[1],
M. Hino[2], and H. M. Shimizu[3]

[1] *Department of Physics, Kyoto Univ. Kitashirakawa, Kyoto, 606-8502*
[2] *Research Reactor Institute, Kyoto Univ. Kumatori, Osaka, 590-0494*
[3] *RIKEN, 2-1 Hirosawa, Wako, Saitama, 351-0198*

We have measured the transverse coherence length of cold neutron beam directly. New cold-neutron interferometer of Jamin-type was developed and clear interference fringes with the contrast of 60% was observed.[1] The new interferometer contains a pair of beam splitting etalons (BSEs). An etalon is an optical device, mainly used in laser optics, which has two parallel planes. When neutron mirrors are deposited on the two planes of an etalon, the etalon divides incident neutrons into two parallel beams with large separation according to the gap of the etalon. After the reflection off the second etalon, the two beams are recombined and the optical path-difference is compensated (Fig.1). By twisting the optical system, the present interferometer can change the vertical dislocation between the superposed two waves continuously with no dispersion. The tilting angle of the second etalon of α makes the vertical dislocation of $2D\sin\alpha$, where D is a gap of the etalon (Fig.2). The vertical coherence length L_c which gives the contrast of $1/e$ of the maximum is related to vertical beam collimation. The relation is

$$\sigma_k L_c = \sqrt{2}, \qquad (1)$$

where σ_k is the standard deviations of vertical wavenumber for the beam having Gaussian vertical momentum distributions defined by the collimation.

The experiments were performed at cold neutron beam line MINE2 at the JRR-3M reactor in JAERI(Tokai). The beam had a wavelength of 8.8Å and a bandwidth of 2.4% in FWHM. The gap thickness of the etalons was 9.75μm. We observed the contrast of interference fringes decreased with the dislocation (Fig.3). The measured coherence lengths was 57±2 nm at $\sigma_k = 0.024\text{nm}^{-1}$ (solid line) and 127±10 nm at $\sigma_k = 0.011\text{nm}^{-1}$ (dashed line) respectively.

We have confirmed that the contrast varies according to the coherence function determined by the collimation of the beam line and that the measured coherence length is consistent with the estimate by Eq.(1). The achievement of precision manipulation for this interferometer system has been demonstrated by the clear understanding of the three-dimensional coherency depending on the wavelength dispersion and the beam collimation as shown in the ref.1 and the present study.

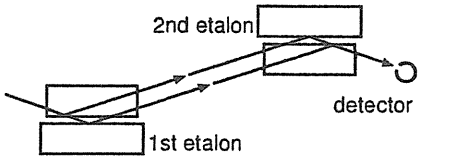


Fig. 1. Jamin-type interferometer using a pair of etalons. (Beam Splitting Etalons)

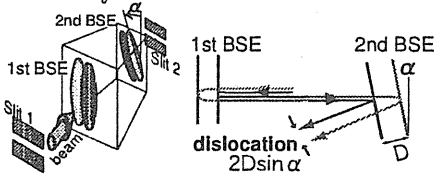


Fig. 2. Twisting the optical system.

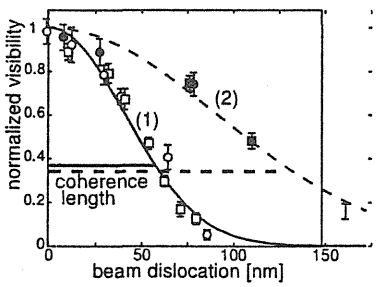


Fig. 3. Changes of the contrast of interference fringes with the dislocation caused by tilting angle.

References

[1] M. Kitaguchi *et al.*: Phys. Rev A **67** (2003) 033609.

使用施設：JRR-3　装置： C3-1-2-2 (MINE)，分野： 8. Fundamental Physics & Neutron Optics

研究テーマ:核破砕中性子源用長寿命ターゲットの開発研究
表　　題:中性子散乱法によるSS316鋼と鉛ビスマスの両立性研究

1-7-5

Compatibility study of SS316 with Pb-Bi by neutron diffraction method

K. Kikuchi, N. Minakawa, A. Moriai and Y. Morii

Advanced Science Research Center, Japan Atomic Energy Research Institute, Tokai, Ibaraki, 319-1195

Lead bismuth target has been studied as a spallation neutron source of accelerator-driven nuclear transmutation system, ADS. The ADS aims at managing long-lived high-level waste as minor actinides, MA, and long-lived FP in order to reduce the burden of waste disposal. Proton beams injected from accelerator react with spallation target produce neutrons and transmute the waste in the fuel. In this system lead bismuth is used as target material and reactor coolant. Advantage for usage of lead-bismuth is that a melting temperature of the lead-bismuth alloy is quite low, 125°C, in the ratio of 45 Pb/55 Bi (wt%) and small neutron absorption enables the lead-bismuth a candidate for coolant in sub-critical reactor. Material issue of the system is corrosion. In order to know corrosion of the material, flowing lead-bismuth experiment was done under the condition of 450°C maximum temperature and 50°C temperature difference during 3000 hrs. Figure 1 showed neutron radiography image (JRR-3) of tube cut from the circulating loop. After drain out Pb-Bi from the loop it still existed in the circulating tube. Figure 2 showed cross section of the tube. It showed that corrosion depth of SS316 was 0.1 mm. Tested tube was 12 mm in diameter and 2 mm in thickness. Our interest is to know the substantial depth of mass transfer by diffusion from flowing Pb-Bi to SS316 tube thickness. Figure 3 and 4 showed the result of neutron diffraction experiment of tube after and before flowing test. X-axis means the position from the outer surface of the tube. So x=2 indicates the inner surface of the tube. After the test Pb-Bi remained in the tube. Measured length is extended to 2.5mm. Bismuth and Pb oxides were formed in the adhered area. They consist of different type of oxides. We looked at only the 2-theta fitted assuming the Gaussian distribution and the peak area for SS316 (200). The results showed that SS316 (200) was disturbed by Pb-Bi in the range of x=1.5 to 2 mm roughly. So corrosion depth after 3000 hrs operations was 0.1 mm but the tube was affected by 0.5mm length in the lattice arrangement.

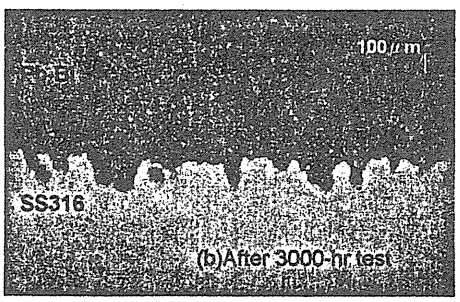


Figure 1: Cross-section of circulating lead bismuth loop.

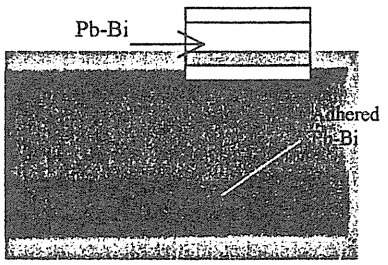


Figure 2: Neutron radiography image (JRR-3) of tube cut from the circulating loop.

原子炉：JRR-3　　装置：RESA(T2-1)　　分野：(基礎物理)

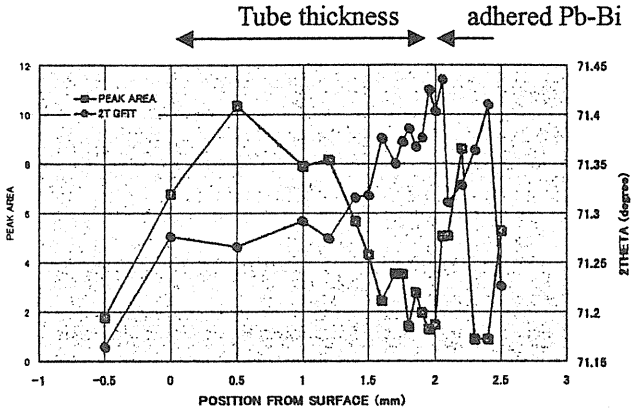


Figure 3: Two theta and peak area distribution of Pb-Bi adhered SS316 (200) after the flowing test.

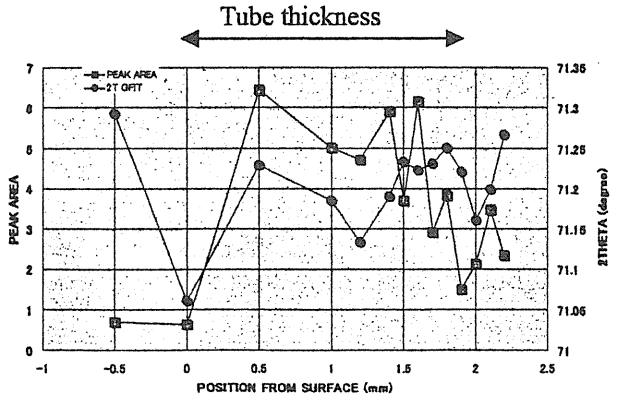


Figure 4: Two theta and peak area of SS316 (200) tube before the flowing test.

研究テーマ： 中性子時間エコー干渉計による多重ブラッグ反射、屈折率等による時間遅れ
表題： 中性子時間干渉計による Si 単結晶透過中性子の屈折率による微少時間遅れの測定

A Tiny Velocity Change of Neutrons through Si Crystal by Time Beat Neutron Interferometer due to Refractive Index

1-7-6

N. Achiwa[1], T. Ebisawa[2], M. Hino[3], D. Yamazaki[2], R. Maruyama[4], S. Tasaki[4]

[1] *Department of Physics, Kyushu University, Higashi-Ku, Fukuoka, 812-8581*
Present aderess: Graduate School of Science, Osaka University, Toyonaka 560-0043, Japan
[2] *Japan Atomic Energy Research Institute, Tokai, Ibaraki, 319-1195, Japan*
[3] *Research Reactor Institute Kyoto University, Kumatori, Osaka, 590-0494, Japan*
[4] *Department of Nuclear Engineering Kyoto University, Kyoto, 606-8501, Japan*

Using Larmor clock we have previously measured velocity change through Si crystals up to 80cm in applied magnetic field, following equation[1].

$$\Delta\phi = -\omega_L \frac{D}{v_0}(1-n) \qquad (1)$$

where $\omega_L = 2\mu B/\hbar$, D the thickness of of crystal, v_0 the velocity of neutron in vacuum. The obtained refractive index is $1 - (1.85 \pm 1.2) \times 10^{-5}$ for 0.57 nm which is 1.7 times larger than the theoretical value [1]. Now, figure 1 shows the arrangement to measure a delay of phase in time beat through a Si crystal by means of neutron spin interferometer using RF flippers which is similar to the MIEZE spectrometer which is installed in C3-1-2 cold neutron guide, MINE at JRR-3M[2][3]. Previously we have shown if we put in a sample after down stream of the analyser in the MIEZE-type neutron time interferometer, what we measure by a pase shift of time beat can be interpreted as the velocity shift through the sample[2]. By the velocity shift through the sample we can determine refractive index of the sample for neutron following equation (1), where ω_L is replaced by the frequency of time beat. For this purpose, frequency of the time beat is higher the better, the neutron wavelength is longer the better, as well as the sample length is longer the better. At present stage frequency of the time beat is 200kHz, the wavelength is 0.85 nm and the sample length is 80 cm. The estimated phase shift of the time beat is 5.2×10^{-2} radian. The estimated exprimental error is must be less than the estimated phase shift.

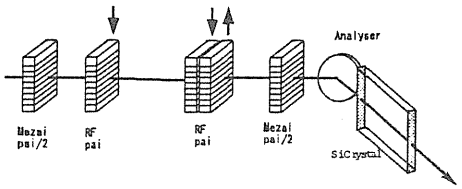


Fig. 1. Arrangement for time of flight measurement through Si crystal by a neutron time beat.

This is the first traial to measure velocity shift due to a change of refractive index through a material instead of through a vacuum by real time of flight.

The spatial non-homogeniety of neutron intensity was proofed by Yamazaki[4] who introduced a spin flip chopper after analyser. He observed a sinusoidal intensity modulation as the function of the beam cutting position. Detector must be located at echo position where wavelength dependent phase are cancelled out. Since for the present experiment one time beat corresponds to 2.3mm, detector thickness is choosed to be very thin ^{6}Li-glass scintillator below than 0.1mm. So the estimated error of the time beat is rather the same order of systematic errors.

References

[1] H. Hino *et al.*: Physica B **213-214** (1995) 842.
[2] N. Achiwa *et al*: J. Phys. Soc. Jpn. **70** (2001) Suppl.A 436.
[3] T. Kawai *et al*: In this report, Development of the modified neutron spin echo spectrometer 'MIEZE'.
[4] D. Yamazaki: Nucl. Instru. Method, A **488**(2002) 623.

使用施設：JRR-3　装置： C3-1-2 (MINE)，分野： 8, Fundamental Physics and Neutron Optics

1. 中性子散乱 8)装　置

1. Neutron Scattering　8) Instrument

This is a blank page.

研究テーマ：静電場試料浮遊加熱装置をもちいた極限環境における融液構造測定
表　題：高温液体の中性子散乱のための静電場試料浮遊加熱装置の開発

1-8-1

Development of an Electrostatic Levitation Furnace for Neutron Scattering Experiments of High Temperature Liquids

T. MASAKI, T. ISHIKAWA, P.-F. PARADIS, H. AOKI, T. AOYAMA, Y. ARAI, Y. ISHII[1] and S. YODA

National Space Development Agency of Japan, 2-1-1, Sengen, Tsukuba, Ibaraki 305-8505
[1] Advanced Science Research Center, JAERI, Tokai, Ibaraki 319-1195

In recent years, considerable attention has focused on the containerless techniques for the experimental research of high temperature melts or deeply undercooling liquids, especially for structure analysis by neutron or X-ray scattering.[1)] Recently, NASDA has developed an electrostatic levitation furnace for microgravity experiments in the international space station as well as for ground-based experiments. Since this technique is attractive for neutron scattering experiments, NASDA and JAERI have developed a dedicated electrostatic levitation furnace (ESL) for neutron scattering experiments of extremely high temperature melts and deeply undercooling liquids. Last year, the ESL was developed and its technical capability was investigated with the neutron scattering measurements of levitated sintered alumina at room temperature. The sample could be kept levitated continuously for more than 11 hours. In this "cold" experiment, the diffraction peaks of alumina were clearly observed without any other peaks coming from the background. The details are described in ref. 2.

This year, the verification of ESL operation with high temperature melts was performed. The facility configuration was identical as last year's except for sample heating. In order to heat the levitated sample, a CO_2 laser was added to the facility. The heating laser heated the sample the top of the vacuum chamber through a ZnSe optical window. Zirconium was selected as the test material for the "hot" experiment because its low vapour pressure makes it suitable for long duration experiments. The "hot" experiment was very successful, with the continuous levitation of a molten zirconium sample for eight hours. Fig. 1 shows the levitated liquid zirconium at 2500 K. It can be seen that the levitation method provides a nearly spherical sample for which the data correction, in particular the correction of absorption, could be easily performed on the diffraction data analysis. Since the sample size was rather small (ca. 2 mm diameter), the scattering intensity acquired from the levitated sample was not sufficient within the duration of levitation of this experiment. In the near future, experiments of much longer duration are planned to obtain the scattering data.

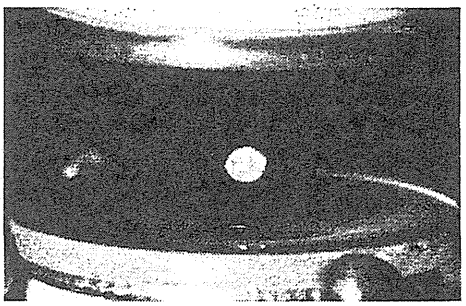


Figure 1: Levitated liquid Zr at 2500 K.
The bright sphere is the levitated sample. The upper and lower disks are electrodes for controlling electrostatic field.

References

1) T. Schenk, D. Holland-Moritz, V. Simonet, R. Bellissent, and D.M. Herlach : Phys. Rev. Lett. **89** (2002) 075507.
2) H.Aoki, P.-F. Paradis, T. Ishikawa, T. Aoyama, T. Masaki, S. Yoda, Y. Ishii, and T. Itami : Rev. Sci. Instr. **74** (2003) 1147.

原子炉：JRR-3　　装置：HRPD(1G)　　分野：中性子散乱（装置）

研究テーマ：中性子イメージング用輝尽性蛍光体の研究
表　題：輝尽性蛍光体 $SrBPO_5:Eu^{2+}$ の２次元特性

1-8-2

2-dimesional Characteristics of $SrBPO_5:Eu^{2+}$ Photostimulable Phosphor

K.SAKASAI, M.KATAGIRI, K.TOH, H.TAKAHASHI[1], M.NAKAZAWA[1], and Y.KONDO[2]

Neutron Science Research Center, JAERI, Tokai, Ibaraki 319-1195
[1]Dept. of Quantum Engineering and System Science, University of Tokyo, Tokyo, 113-8656
[2]Dept. of Applied Physics, Tohoku University, Sendai 980-8579

The neutron imaging plate (NIP) has made a great success in the field of neutron scattering study but the NIP is sensitive to not only neutron but also gamma ray. Therefore, it is difficult to discriminate neutron signal from gamma ray one when the NIP is read out. To overcome the problem, the authors have been studying a $SrBPO_5:Eu^{2+}$ material as a new neutron storage phosphor consisting of light materials.

The $SrBPO_5:Eu^{2+}$ powder sample was prepared by firing raw materials ($SrCO_3$, H_3BO_3, $(NH_4)_2HPO_3$, and $EuCl_3 \cdot 6H_2O$) in a muffle furnace in a nitrogen atmosphereat 600°C for 2 hours and at 800°C for 2 hours. A disk-like sample with a diameter of 12 mm and a thickness of 1mm was prepared for 2D image measurement. This sample was made by the Spark Plasma Sintering (SPS) method. In the SPS method, the $Sr^{10}BPO_5:Eu^{2+}$ (2%) powder was set in a carbon vessel and then fired for 10 minutes at 800°C. The powder sample was pressed with a stress of 5 kN in a vacuum atmosphere throughout the firing.

After the sample was irradiated with a collimated neutron beam with a diameter of 1.5 mm, its surface was scanned with focused laser light by using an X-Y stage controller. The neutron flux and neutron irradiation time were 3.1 x 10^4 n/cm^2/s and 30 minutes, respectively. The scanning was carried out every 0.25 mm on the sample surface. The results are shown in Fig.1. The beam intensity image can be clearly obtained. Fig.2 shows the edge spread function measured with the sample, where half of the surface (left side) was irradiated with neutrons. Although Lorentzian line spread function (LSF) is usually applied to photographic film, the imaging plate detector's LSF was reported to have a strong similarity to Gaussian[1)]. Therefore the authors fitted the data in Fig.2 by ESF of a Gaussian LSF and estimated the spatial resolution to be about 0.4 mm when FWHM of LSF is defined as the spatial resolution.

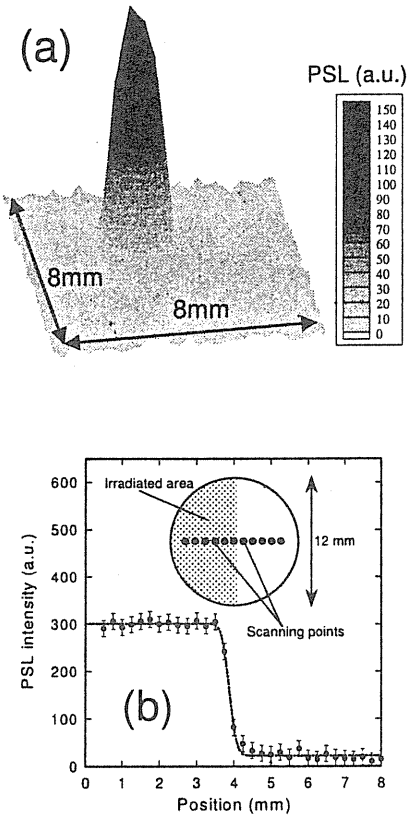


Figure 1: (a) A collimated neutron beam image obtained with the sample. The beam size was 1.5 mmϕ. (b)The measured the edge spread function.

References

1) Jens Hofmann and Christian Rausch : Nucl. Instrum. Methods **A355** (1995) 494.

原子炉：JRR-3　　装置：SANS-J(C3-2)　　分野：中性子散乱（装置）

研究テーマ：低エネルギー中性子による高コントラストイメージング取得法の開発
表題：低エネルギー中性子による高コントラストイメージング

1-8-3 High Contrast Neutron Imaging Using Low Energy Neutrons

Y.Kawabata, M.Hino, H.Sunohara*, S.Tasaki *, and T.Nakano *

Research Reactor Institute,Kyoto University, Kumatori, Osaka 590-0494, Japan;
**Faculty of Engineering, Kyoto University, Sakyo, Kyoto 606-8501, Japan*

Neutron radiography is a unique nondestructive research method as compared with X-ray radiography because of the difference of the transmission characteristics through materials. The research fields of the neutron radiography are wide, and the botany is one of the most promising ones because water plays an important role in the activity of plants.

As the neutron flux is high, the L/D of thermal neutron radiography can be better than cold or very cold neutron radiography. That makes the spatial resolution of thermal neutron imaging better. But it is not equivalent to show very small objects. The contrast of thermal neutron imaging is not good, because the attenuation factor is lower than cold or very cold neutrons. The only way for high contrast is to use very low energy neutrons because the absorption cross-section is inversely proportional to neutron velocity.

As cold neutron radiography has good sensitivity to estimate the water distribution, it is effective in the general plant research, especially the water distribution in thin leaves, flowers and stems. Though very cold neutron radiography in KUR has better contrast and is suitable to measure the slight change of water, it requires longer measuring time because of small neutron flux. So we use both cold neutrons to get images to have the flexibility for the measurement time because flowers change their condition easily in a short time.

A CCD neutron imaging system is installed. The converter is ^{6}LiF/ZnS(Ag) (Kasei Optonix Co.) and the CCD system is BS-30L(Bitran Co.). It is a cooled CCD and has 0.33 M pixcels. It is shown in Fig.1. This CCD system is mainly used for the long time observation of one sample. The image of needles (0.13, 0.26, 0.41 mm of inner diameters) of medical injection with water by this CCD system is shown in Fig.2. This CCD system is also used for CT imaging with a sample rotation system. An image of carnations by an imaging plate is shown Fig.3. They were scanned horizontally to get a larger image.

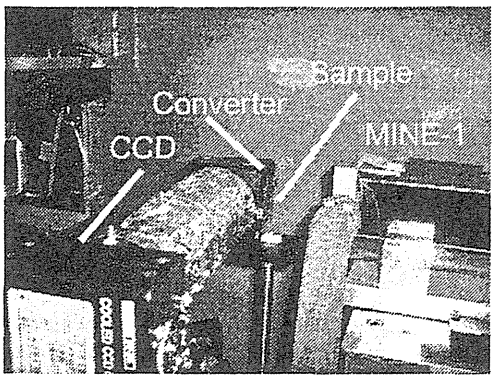


Figure 1: Experimental set up with CCD imaging system,

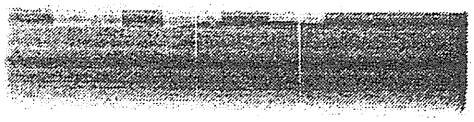


Figure 2: Images of needles of medical injection, inner diameters are0.13, 0.26, 0.41 mm,

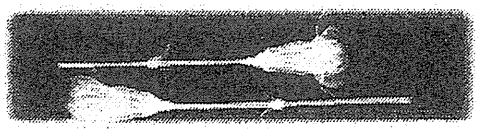


Figure 3: Images of carnations by an imaging plate,

使用施設：JRR-3 ，装置：C3-1-2，分野 Instrumentations

研究テーマ：機能性生体物質の水和構造研究
表　題：高度なビーム共有のための弾性湾曲Siモノクロメータと中性子透過率の湾曲度依存性
1-8-4

An Elastically Bent Si Monochromator to Share the Whole Beam Neutron Size Tandem Among Three Diffractometers

I. TANAKA[1], M. REFAI-MUSLIH[2],
K. KURIHARA[1] and N. NIIMURA[1,3]

[1]Neutron Science Research Center, JAERI, Tokai, Ibaraki 319-1195
[2]National Nuclear Energy Agency, BATAN, Indonesia
[3]Faculty of Engineering, Ibaraki Univ., Hitachi, Ibaraki 316-8511

Neutron is a very rare and powerful probe for structure determination and dynamics observation of materials in an atomic resolution. Because the number of relatively-higher-flux neutron sources and the beam ports are so limited compared to that of other probes, it is important to use them efficiently. From this standpoint, it is well known that beams with tall height cross-section at the guide halls have been shared by several instruments but each instrument is allocated a particular beam height width not to decrease the beam intensity in the spectrum which may be absorbed or scattered by upstream instruments. On the other hand, at 1G port in the reactor hall in JRR-3, there are three instruments. Two of them are diffractometers for biological macromolecules; BIX-4 [1], BIX-3 [2], and One of them is a high resolution powder diffractometer; HRPD (from upstream). They share whole height and width beam cross section by Elastically Bent Perfect Silicon (EBP-Si) monochromators [3] one another. EBP-Si is one of the most useful monochromators, which realizes higher transmission compared to PG in wider spectrum with focusing effect and so on.

When EPB-Si monochromators are set at the 1G beam port so that they cover the whole cross section; 45mm in width and 80mm in height at the BIX-3 monochromator position, not a small absorption was observed by HRPD monitor counter under various conditions of BIX-4 and BIX-3 monochromators (Fig.1). BIX-4 had Si(111) monochromator with 10mm in thickness, curvature R~4.1m (300 μ strain) and 49° in $2\theta_M$ (λ=2.60Å),

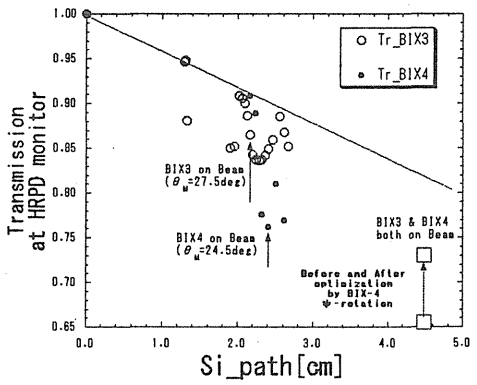


Figure 1: Neutron transmission of BIX-4 and BIX-3 at HRPD monitor count at 1G port at JRR-3. Horizontal is the total thickness of EBP-Si monochromators corresponding to ω angles. Vertical axis is normalized transmission. Open circle: BIX-3 monochromator ω-scan without BIX-4's (down). Closed circle: BIX-4 ω-scan without BIX-3's (down). Solid line are absorption curve when absorption coefficient μ is twice of the table value (0.02 cm^{-1}). Open square: Normal transmission with BIX-3 and BIX-4 are on beam.

BIX-3 had Si(111) with 10mm in thickness, R~3.4m (400 μ strain) and 55° in $2\theta_M$ (λ =2.90Å), and HRPD had hot-pressed Ge(331) with 89° in $2\theta_M$ (λ =1.82Å). The monochromator Si plates were cut from ingots, purchased from Shin-Etsu-Kagaku Co. Ltd., Japan, whose conductivities were not determined, and the surfaces were treated by chemical etch so that the larger surface was 250mm in width and 20 to 40mm in height. 4 plates of 2.5mm in thickness were stacked.

To measure the R dependence of EBP-Si monochromator, transmission/absorption of EBP-Si for certain neutron wavelength

原子炉：JRR-3　　装置：TAS-2(T2-4)　　分野：中性子散乱（装置）

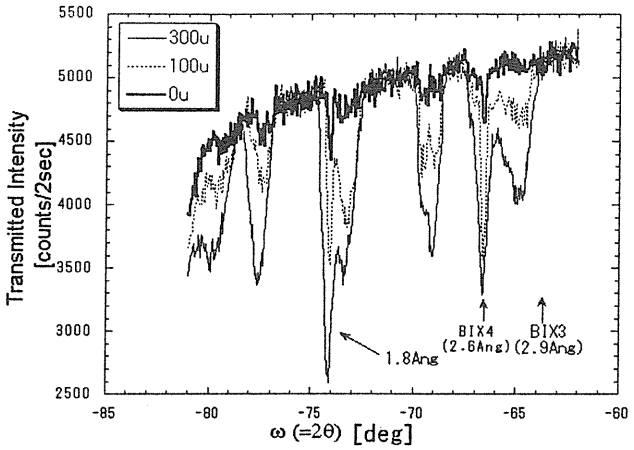


Figure 2: 1.82Å neutron transmission curvature dependence of EBP-Si(111) 10mm thickness at TAS-2. Horizontal axis is ω angle of EBP-Si sample. 0u, 100u and 300u corresponds to the curvature in strain gauge (μ strain); R$\sim\infty$, 12m, 4.1m, respectively. Arrows and numbers (wavelengths) correspond symmetric Bragg conditions of ω angle at TAS-2 for all instruments at the 1G port, respectively.

(1.82Å) for each R was examined (Fig.2). The EBP-Si(111) sample dimension was 250 x 40 x 10 (4 plates stacked in thickness) mm and Si(111) plane was 250 x 40mm^2. The stronger the curvature of EBP-Si became, the deeper the absorption dips became. It is thought that these absorption-dips were caused by asymmetric reflections of sample EBP-Si monochromator crystal. The absorption was at most 30% for all ω rotation of sample crystal except the exact symmetric Bragg condition of the sample. Then the EBP-Si sample was rotated and scanned around ψ axis (perpendicular to the plane of Si(111)) at the BIX-4 ω angle (Bragg condition). Significant difference of transmission was observed (Fig.3). This fact was quickly expected to improve the transmission at the 1G port.

When the BIX-4 monochromator was rotated around ψ axis by 1.5°, the transmission of 1.82Å neutrons of BIX-4 and BIX-3 was improved from 66% to 73% at HRPD monitor counter just like square plots in Fig. 1.

Computer simulation was also tried to explain and predict something valuable to design monochromators to share neutron beam at higher level.

In this way, with relatively minimum loss of neutrons in the downstream instrument(s), beam sharing with more instruments was established by EBP-Si monochromators. Though there are still some problems in shorter wavelengths, but this beam sharing procedure will stimulate the higher level utilization of neutron beam.

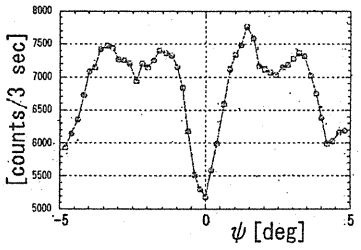


Figure 3: ψ-scan profile under BIX-4 monochromator Bragg condition at TAS-2.

References

1) K. Kurihara *et al.*: J. Synchrotron Rad. (2003) *submitted.*
2) I. Tanaka, K. Kurihara, T. Chatake and N. Niimura: J. Appl. Cryst. **35** (2002) 34.
3) I. Tanaka, N. Niimura and P. Mikula: J. Appl. Cryst. **32** (1999) 525.

研究テーマ： 多層膜スピンスプリッターを用いた中性子スピンエコー分光器の開発 III
表題： 真空蒸着法による残留磁気偏極ミラーの開発

Preliminary results on remanent neutron polarizer with vacuum evaporation

1-8-5

S. Tasaki[1], Y.Yoshimura[1], M. Hino[2], T.Ebisawa[3], R.Maruyama[1], Y.Kawabata[3]
[1] *Dept. of Eng. Kyoto Univ. Yoshida-honmachi, Sakyou-ku Kyoto, 606-8501*
[2] *Japan Atomic Energy Research Institute, Tokai Ibaraki Pref. 319-1195*
[3] *Res.React. Inst. Kyoto Univ. Kumatori Osaka, 590-0494*

Multilayer spin splitter (MSS) is a device which gives a phase difference between spin-states of a neutron in spin-superposing state. The function of MSS is equivalent to that of a static magnetic field for a spin-superposing neutron. The goal of our research is to replace huge precession magnets in neutron spin echo spectrometer with two pairs of MSS's in order to realize compact NSE spectrometer.

One of the requirements to develop MSS-NSE is polarizing supermirror. In our design, the gap layer thickness of MSS, which determines the magnitude of phase difference as well as neurton wavelength. As an NSE spectrometer, phase difference is reversely propotional to the energy resolution. Hence, it is prefarable to change the wavelength instead of gap layer thickness to change energy resolution. For this purpose, it is necessary to develop supermirror polarizing mirror which works under low magnetic field.

In the present research we have made some trials to fabricate a remanent polarizing mirrors. The requirements are as follows: 1. it should work under low magnetic field (~10 Oe). 2. The optical potential of the magnetic material and non-magnetic material should be very close.

For this purpose, we adopt FeCoV and V as magnetic and non-magnetic materials, respectively and vacuum evaporation as deposition method at Research Reactor Institute Kyoto University. The arrangement of the vacuum evaportation is shown in Fig.1. During the evaporation, the substrate is tilted. The tilt angle is 0, 30 and 60 degree. The spacing d=17nm, and number of layer is 40.

Polarizing reflectivity is measured at C3-1-2-2 beam port (MINE). An example of the reflectivity is shown in Fig.2 for 60-degree sample.

As shown clearly, contrast of the reflectivity for π-ON and OFF is very high. The reflectivity for other angles was not so good.

The problem of tilted evaporation is that the thickness distribution over the substrate is not uniform. The inhomogeniety should be compensated for the future.

Since the present study is preliminary, the polarizing mirror is a monochromator. In the next step, the mirror will be a supermirror.

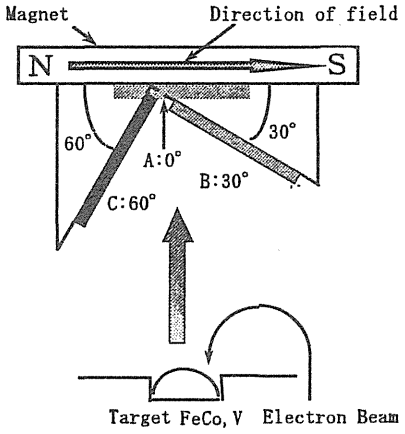


Fig. 1. Arrangement for evaporation of remanent polarizer on tilted substrate.

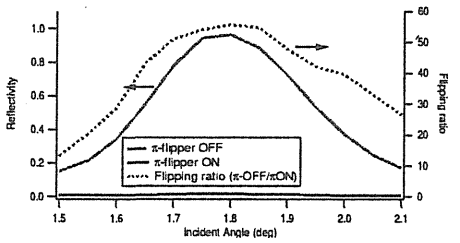


Fig. 2. Polarizing reflectivity of remanent monochromator evaporated on 60-degree tilted substrate.

使用施設：JRR-3! ， 装置： C3-1-2-2 (MINE)， 分野： 7.Instrumentations

研究テーマ：多重極限環境下における中性子散乱実験法の研究
表　　題：HOPG前置結晶による中性子ビームの増強

1-8-6

Neutron Beam Enhancement with a HOPG Pre-Crystal

H.TOMIMITSU, Y.HASEGAWA[1] and K.AIZAWA[2]

Advanced Science Research Center, JAERI, Tokai, Ibaraki 319-1195
[1]Atominstitut, Austria University, Wien, Austria A-1020
[2]Center for Proton Accelerator Facilities, JAERI, Tokai, Ibaraki 319-1195

In the research on the development and application of the neutron interferometry[1,2], we often feel the insufficiency of the neutron beam intensity. Therefore, we are trying to realize a convenient and practical method to enhance the neutron flux.

Neutron experiment was carried out at the PNO apparatus in the JRR-3 of JAERI. With the double monochromator system of the highly oriented pyrolytic graphite (HOPG) with the mosaic spread of 0.4 deg., the collimation being of 30min. We measured the intensity I_o diffracted by the Si plate with 220 reflection put directly in the incident beam without any pre-crystal, and the intensity I_p diffracted in the diffraction beam from the pre-crystal, and compared $I_p/\ I_o$ with unity. We also observed their FWHMs. In every case, with the original $10*10mm^2$ beam, the $3*3mm^2$ slit was used as the incidence slit for the following Si plate.

As the pre-crystal, we tryed the asymmetric reflection of a silicon perfect crystal, and also the asymmetric reflection of imperfect single crystals, such as Cu-based alloys, Ni-based super alloy, in addition to the HOPG.

After all, we found a simple but useful effect with a flat HOPG pre-crystal in the symmetric arrangement, beam enhancement by around 3 times with 2Åwavelength[3], Fig.1. We studied further on the nature of the effect, and got the results as follows.

(1) Both surfaces of a HOPG plate showed the similar result, by around 3-times enhancement and with improved FWHM by around one third with 2Åwavelength. These seem to suggest that the beam-enhancement is not due to the macroscopic deformation of the HOPG plate, such as concave.

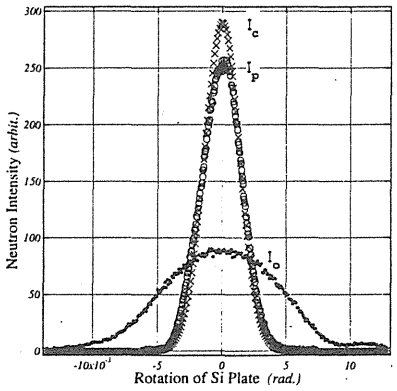


Figure 1: Comparison of the rocking curves of a Si 220 reflection without the pre-crystal (I_o, closed circle) and with a HOPG pre-crystal (I_p, open circle). I_c, crosses, represent the calculated curve, see Text.

(2) We tried, on the other hand, the double or triple thicknesses of the HOPG plate, namely, we measured on the attached two or three HOPG plates, observing the similar rocking curve with that by a single HOPG plate.

(3) In order to ensure the effects mentioned above, we tested on various HOPG plates with each thicknesses, as summarized in the Table 1. All of them were made by the same company as the best grade products, "ZYA" class with mosaicity of 0.4deg., but at the quite different time and with different sizes, especially the thicknesses is quite different. All the HOPGs tested, with the thickness ranging from 1.2 mm to 1.8 mm, showed the similar effect, suggesting that this beam-enhancement is not special nor accidental but general and due to intrinsic nature of the HOPG plates.

原子炉：JRR-3　　装置：PNO(3G)　　分野：中性子散乱（装置）

Table 1: Summary of results on the peak intensity ratio and on the FWHM ratio by various HOPGs, on both surface, with their thicknesses.

HOPG Pre-Crystal	thickness	Peak Ratio	FWHM ratio
(No pre-crystal)		1.00	1.00
M1-surface	1.8 *mm*	2.40	0.38
back face		2.45	0.33
M2-surface	1.8	1.84	0.35
back face		1.86	0.35
M3-surface	1.8	3.49	0.32
back face		2.96	0.35
T415-surface	1.6	3.43	0.34
back face		3.45	0.33
T4665-surface	1.6	3.22	0.35
back face		2.81	0.35
N1606-surface	1.2	3.21	0.31
back face		3.28	0.32

(4) For all cases above, the observed rocking curves were clearly fitted with the simple Gauss-functions. This strongly suggests that the pre-crystal make the incident-beam-divergence narrower at once with a single cause, rather than multiple causes.

(5) Once, we tested instantly this beam-enhancement effect on a LLL-type interferometer in order to ensure whether we can really utilize the effect or not. We could clearly recognize the beam intensity being kept more than twice, and furthermore the oscillation was clearly seen in the profile with pre-crystal.

(6) The phenomenon of the beam enhancement by a HOPG pre-crystal, mentioned above, seems that another factor in the HOPG reflection, *i.e.* the very sharp distribution of the lattice spacing deviation[4,5], condenses or focuses the original beam divergence into the main direction within around one third, and consequently enhances the peak value by around three times, as compared in Fig.1[6]. In the figure, I_c is the calculated curve with the assumption of the reflectivity of the HOPG equals to unity, I_p being around 85% of I_c with the actual reflectivity.

As the conclusion, a HOPG pre-crystal in symmetric arrangement enhance the neutron flux for the following Si reflection, more than 3 times with 2Åwavelength. This effect can be generally utilized in the so-called precise neutron optics, such as the double LL-type neutron interferometry, for example. The origin of this effect seemed to be explained phenomenologically with the idea of the very sharp distribution of the deviation of the lattice parameter in the HOPG itself.

We are studying this effect on the relation with the wavelengths and with the reflecting planes, and, especially, if the effect can be applied in the case of "imperfect" crystals.

References

1) H.Tomimitsu, Y.Hasegawa and K.Aizawa: *Proc. Int. Conf. Present Status and Future Aspects of Neutron Interferometry*, NSL News Letter 2002-1, ISSP, Univ. Tokyo, 2002, pp.3-6.
2) H.Tomimitsu, Y.Hasegawa and K.Aizawa: JAERI-Report **2002-028** (2002), 124.
3) H.Tomimitsu, Y.Hasegawa and K.Aizawa: Physics Letters **A274** (2000), 175.
4) A.W.Moore, M.Popovici, A.D.Stoica: Physica **B276-278** (2000), 858.
5) T.Keller, K.Habicht: Appl. Physics **A74** (2002), s127.
6) H.Tomimitsu, Y.Hasegawa and K.Aizawa: Physics Letters **A309** (2003), 175.

研究テーマ： Drabkin型中性子エネルギー・フィルターの開発
表題： Drabkin 型スピン・フリッパー試作器のスピン反転率測定

1-8-7 Measurement of spin-flip probabilities of N=10 Drabkin spin-flipper

S. Tasaki[1], D. Yamazaki[2], K. Soyama[2] and T. Ebisawa[2]
[1] *Department of Nuclear Engineering, Kyoto University, Kyoto, 606-8501*
[2] *Neutron Science Research Center, JAERI, Tokai-mura, Ibaraki 319-1195*

We have developed Drabkin spin flippers with alternating field of 10 periods, and carried out performance tests [1].

A Drabkin spin flipper, which gives rise to resonant spin-flip, is the main part of a Drabkin energy filter, which could be used for pulse shaping without loss of band-width and with small loss of peak-intensity [2].

The Drabkin spin flippers we have developed are composed of zig-zag folded pure-aluminum foil of 50 mm in width, the shape of which is fixed with 22 teflon spacers of 5.0 mm in thickness. Direct current in the pure-aluminum foil generates alternating magnetic field of 10 periods. A teflon spacer has a hole of 50 mm × 30 mm to let neutrons go through and ditches of 5 mm in width and 2 mm in depth to let air go through.

Performance tests of the Drabkin spin flippers were carried out on C3-1-2(MINE) in JAERI JRR-3M. Figure 1 shows field current versus spin-flip probability measured with monochromatic neutron of 8.8 Å. In this measurement, the ratio of a current for guide field B_z and that for alternating field B_x is fixed to 0.488, and both currents are varied. Threfore the field currents in Fig.1 correspond to total field strengths with a fixed direction. The figure shows that measured data are in good agreement with numerical calculation which is carried out by means of quantum mechanical manner.

Figure 2 shows neutron wavelength dependency of spin-flip probability measured with broad-band neutrons of 8.28 Å (FWHM 14.9 %). The continuous beam was chopped by a spin-flip chopper (SFC) which is composed of pulsed adiabatic spin-flipper and polarization analyzer. Again, measured data agree well with calculation.

The suppression of main peak is due to the wavelength resolution attributed to the opening time of the SFC. Subpeak on the right of the main peak is suppressed and that on the left is amplified because of non-homogeneity of guide field B_z.

In conclusion, it was confirmed that the N=10 Drabkin spin-flipper works in good agreement with calculation.

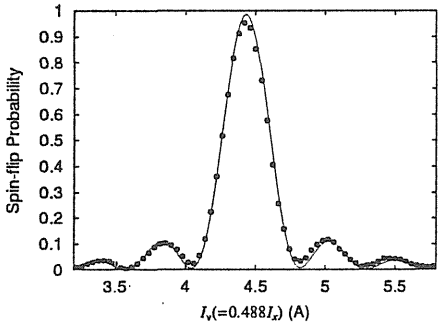


Fig. 1. Measured data plots and calculated curves of spin-flip probability as a function of field current.

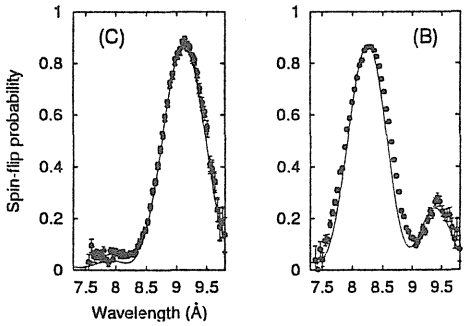


Fig. 2. Measured data plots and calculated curves of spin-flip probability as a function of neutron wavelength.

References

[1] D. Yamazaki *et al.*, Physica B, to be published.
[2] For example, A. Parizzi *et al.*, Proceedings of ICANS-XV, 2001, p572.

使用施設：JRR-3　装置： C3-1-2 (MINE)，分野： 7. Instrumentations

研究テーマ：先端偏極中性子散乱によるスピン-格子物性の研究
表　題：TAS-1 における更新された偏極解析オプションの性能

1-8-8

Performance of the renewed polarization analysis option on TAS-1

M. NAKAMURA, M. TAKEDA, Y. SHIMOJO and K. KAKURAI

Advanced Science Research Center, JAERI, Tokai, Ibaraki 319-1195, Japan

Our research group is currently making efforts to install the CRYOgenic Polarization Analysis Device (CRYOPAD) on thermal neutron triple axis spectrometer TAS-1 at JRR-3M reactor in collaboration with French neutron scattering scientists†. We will be able to carry out the zero-field spherical neutron polarimetry (SNP) by using the CRYOPAD[1].

However, a great improvement of the incident polarized neutron flux is indispensable for utilizing the advantage of SNP. We are currently upgrading the polarization analysis option on TAS-1 spectrometer. Recently, the installation of new Heusler monochromator was completed, and here we report the first neutron test of its performance. A new doubly focusing Heusler monochromator has 140 mm wide and 100 mm height with horizontal focussing mechanism. The vertical focussing is optimized and fixed at E_i=30.5 meV. When installing the new Heusler monochromator on TAS-1, we carefully covered all its non-crystal parts, especially the magnetic york, with B_4C rubber and Cd sheet in order to suppress the back ground.

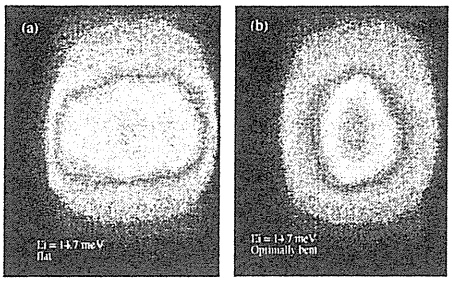


Figure 1: Polarized neutron beam distribution at sample position measured by neutron imaging plate; (a) horizontal bent is zero, that is "flat", and (b) horizontal bent is optimized. Incident neutron energy was 14.7 meV.

We measured the polarized neutron beam distribution at sample position using the neutron imaging plate as given in Fig. 1. It is confirmed that the beam focussing works well as we expected. Figure 2(a) gives the direct comparison of the intensity from the (113) nuclear Bragg peak of Al_2O_3 polycrystal between the old set-up and the new one. The comparison of magnetic scattering intensity is also given in Fig. 2(b), whose intensities are from the para-

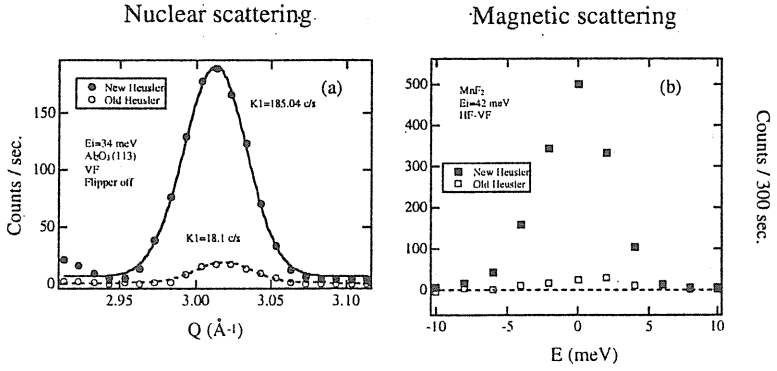


Figure 2: Comparison of the scattered intensity between old set-up and new set-up (a) for coherent nuclear scattering from Al_2O_3 and (b) for paramagnetic scattering from MnF_2.

原子炉：JRR-3　　装置：TAS-1(2G)　　分野：中性子散乱（装置）

magnetic scattering of MnF_2. The relation between neutron polarization $\vec{P}$ and scattering vector $\vec{\kappa}$ gives significant information for polarization analysis of magnetic scattering[2]. We refer the experimental geometry $\vec{P} \parallel \vec{\kappa}$ as HF geometry, and $\vec{P} \perp \vec{\kappa}$ as VF geometry. For the spin flip (SF) scattering only the nuclear spin scattering and paramagnetic scattering (NS) contribute. The experiment in HF geometry gives

$$\left(\frac{d\sigma}{d\Omega}\right)_{HF:SF} = \left(\frac{d\sigma}{d\Omega}\right)_{para} + \frac{2}{3}\left(\frac{d\sigma}{d\Omega}\right)_{NS} \quad (1)$$

whereas, in VF geometry

$$\left(\frac{d\sigma}{d\Omega}\right)_{VF:SF} = \frac{1}{2}\left(\frac{d\sigma}{d\Omega}\right)_{para} + \frac{2}{3}\left(\frac{d\sigma}{d\Omega}\right)_{NS} \quad (2)$$

Therefore, we can obtain the pure magnetic scattering by subtracting $I_{HF:SF} - I_{VF:SF}$, as shown in Fig. 2(b).

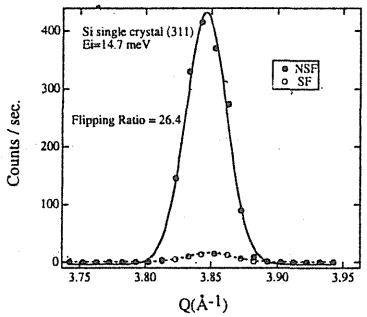


Figure 3: Polarization analysis of the coherent nuclear scattering from Si single crystal.

In addition, the polarization efficiency was estimated from the coherent nuclear scattering of Si single crystal as given in Fig. 3. We confirm that the flipping ratio is 26.4, which means that polarizing efficiency is more than 90%.

By installing the new Heusler monochromator, the data collection rate in the polarization analysis option of TAS-1 increases by a factor 5–15 without decreasing the polarization efficiency as compared to the old set-up as demonstrated in Fig. 4. We should

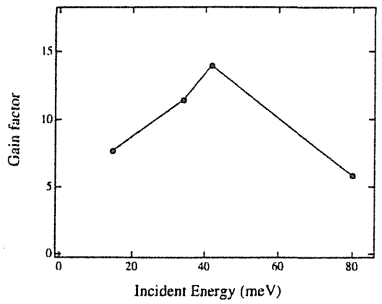


Figure 4: Estimated gain factors by installing the new Heusler monochromator.

note that the analyzer used in these measurements is unchanged, which will be upgraded in the coming fiscal year. New Heusler analyzer is expected to further increase the data collection rate by a factor 4. We have already started the polarization analysis experiments for quantum spin dimer systems, $TlCuCl_3$ and $SrCu_2(BO_3)_2$, using greatly improved polarized neutron beam flux.

References

1) F. Tasset *et al.* : Physica B **267-268** (1999) 69.

2) R. M. Moon *et al.* : Phys. Rev. **181** (1969) 920.

† Dr. F. Tasset (ILL), Dr. E. Leliévre-Berna (ILL) and Dr. L. P. Regnault (CEA-Grenoble)

研究テーマ：共鳴スピンフリッパーを用いたスピンエコー分光器の開発
表題：MIEZE 型スピンエコー分光器の開発
1-8-9

Development of the modified neutron spin echo spectrometer "MIEZE"

T. Kawai[1], R.Maruyama[2], T.Ebisawa[3].
[1] *Taktech Inc., 2-11-11 Yayoi-cho, Izumi, Osaka, 590-0061*
[2] *Dept. of Nucl. Eng., Kyoto Univ., Sakyo, Kyoto, 606-8501*
[3] *Japan Atomic Energy Research Institute, Tokai, Ibaraki, 319-1195*

We have installed MIEZE (Modulation of Intensity by Zero Effort) spectrometer[2, 3], which is a modified version of neutron resonance spin echo (NSE) spectrometer[1], but in contrast to NRSE, resonance spin flippers (RSF) are not needed downstream a sample and hence scattering with spin-flip process is measurable with Mieze. We measure the interference due to the energy difference between two spin states of a neutron as the modulation of neutron intensity.

The experiment is carried out using JRR-3M/C3-1-2-2(MINE1). Fig. 1 shows the experimental arrangement. The modulation

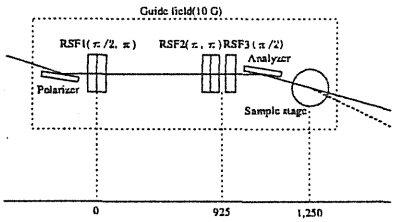


Fig. 1. The experimental arrangement of MIEZE spectrometer.

of neutron intensity in MIEZE method is understood by considering a neutron as a plane wave $\exp(ikx)\exp(i\omega t)$. The continuous neutron beam with wavelength longer than 0.80 nm is obtained as an incident beam at MINE1. The polarizer and the analyzer are FeCo/V magnetic mirrors, which are fabricated with the vacuum evaporation system in Research Reactor Institute, Kyoto University. The reflected beam from them is polarized into spin-up state and monochromatized with wavelength 0.80 nm and wavelength resolution 5∼10 %. The neutron energy transfer with spin-flip process in an RSF leads to the phase difference between two plane waves, which are split in energy and wavenumber space by the RSF1($\pi/2$). We used RSFs(π) to enlarge the phase difference, which leads to higher energy resolution. Two plane waves are superposed by RSF3($\pi/2$) and detected by the scintillation detector. RSFs and detector are placed as the phase difference in wavenumber space is completely cancelled at the detector. The interference due to the phase difference in energy space is observed as a spin echo signal.

The spin echo signal is observed for the direct beam from analyzer and shown in Fig. 2. Its frequency is 200 kHz, which is pro-

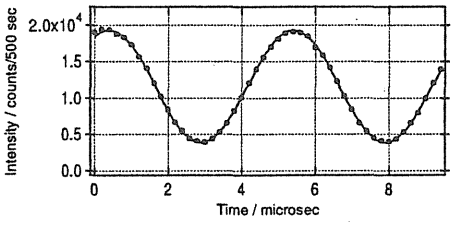


Fig. 2. The measured spin echo signal for the direct beam from analyzer.

portional to the frequency of the oscillating magnetic field applied to RSFs. The visibility of the spin echo signal is 0.67. The precise placement of every component such as an RSF and the detector is needed in MIEZE method since the spin echo signal is sensitive to flight path length of neutrons. Further beam studies must be performed before applications of this spectrometer.

References

[1] M. Köppe *et al.*, Physica B **266** (1999) 75.
[2] P. Hank *et al.*, Physica B **234-236** (1997) 1130.
[3] T. Ebisawa *et al.*, J. Soc. Jpn. **70** Suppl. A (2001) 442.

使用施設：JRR-3　　装置：MINE(C3-1-2-2)　分野：Instrumentation

研究テーマ：多重極限環境下における中性子散乱実験法の研究
表　題：低温、3 GPa以上での中性子磁気回折実験のための高圧装置
1-8-10

High-Pressure Apparatus for Magnetic Neutron Diffraction beyond 3 GPa at Low Temperature

T. OSAKABE, M. KOHGI[1], D. KAWANA[1], A. HANNAN[1], K. SOYAMA and H. KITAZAWA[2]

Advanced Science Research Center, JAERI, Tokai, Ibaraki 319-1195
[1]Department of Physics, Tokyo Metropolitan University, Hachioji, Tokyo 192-0397
[2]National Institute for Materials Science, Tsukuba, Ibaraki 305-0047

On the transport and magnetic properties of 3d, 4f, and 5f electron systems, interesting phenomena, such as the magnetic phase transition, insulator-metal transition, and superconductivity, appear by pressurization up to about 10 GPa. Therefore, if neutron scattering experiments can be performed at low temperature, putting pressure to the range of about 10 GPa, it can make a great contribution to the research of the magnetism of these systems. However, the highest attainment pressure in almost all magnetic neutron scattering experiments has stopped at about 3 GPa generated by piston-cylinder-type high-pressure cells. In this paper we report recent development of the high-pressure apparatus for magnetic neutron diffraction experiments beyond 3 GPa in JAERI.

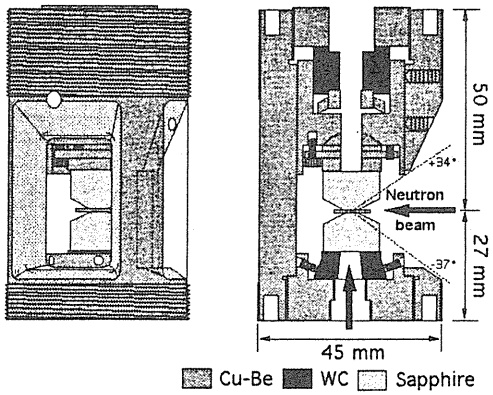


Figure 1: Schematic drawings of the sapphire-anvil high-pressure cell.

The most suitable method for generating pressure beyond 3 GPa is using anvil technique. Figure 1 shows the schematic drawing of the newly developed anvil-type high-pressure cell. The main parts of the cell are made of non-magnetic Cu-Be alloy. The cell is so compact that it is easily attached in a standard cryostat or superconducting magnet. The cell has three large windows for the neutrn beam, which have the horizontal and vertical opening angles of about 90 degrees and about 80 degrees. We adopted a pair of sapphire (single crystal of Al_2O_3) anvils because sapphire is a hard material (Knoop hardness: ~2000) and hardly absorbs neutrons. We also use the moissanite (single crystal of SiC) anvils [1)] or Ti-doped sapphire anvils, which are harder (Knoop hardness: ~3000) than the sapphire anvils. The mechanism for angular adjustment and centering of the anvils follows that of usual diamond anvil cells. A gasket sandwiched between the anvils is made of Cu-0.3% P alloy, aluminum alloy (7075T6) or Cu-Zn alloy. The thickness and diameter of the gasket is 0.3-0.4 mm and 5-6 mm. A hole with a diameter of 0.7mm is made in the center of the gasket. A single crystal sample and small splinterd rubys are put into the hole together with a pressure-transmitting medium. We usually use the 4:1 deuterated methanol-ethanol solution, some kinds of oil (Daphne oil 7373, Silicon oil KF96-50cs, Fomblin oil Y140/13) or Fluorinert FC70-77 mixture as the pressure-transmitting medium. The pressure is measured by the standard ruby-fluorescence method. The highest attainment pressure by the sapphire anvil cell (SAC, hereafter) depends on the combination of the anvil shape especially the smooth-

原子炉：JRR-3　　装置：TAS-1(2G)　　分野：中性子散乱（装置）

ness of the culet edge, the material of the gasket and the kind of pressure-transmitting medium. Maximum pressure generated by the SAC with 2.5 mm anvil tip and Cu-P gasket is about 6 GPa at present. Figure 2 shows the temperature dependence of (1,-2,0) and (1/2,-2,0) magnetic Bragg intensities of CeSb in the SAC at 4.6 GPa [2,3]. The peaks correspond to the type-I and type-IA antifferomagnetic orders of 2 μ_B magnetic moments of Ce ions. The sample size is about 0.5×0.4×0.1 mm^3. In spite of the tiny sample, the S/N ratio was nearly the same as that of the standard piston-cylinder cell. This was achieved both by covering almost all parts of the SAC with Cd sheets and by optimizing the condition of the spectrometer so as to increase the incident neutron flux. From this result, it is expected that, when magnetic moments are 1 μ_B or more, the magnetic signal is observed.

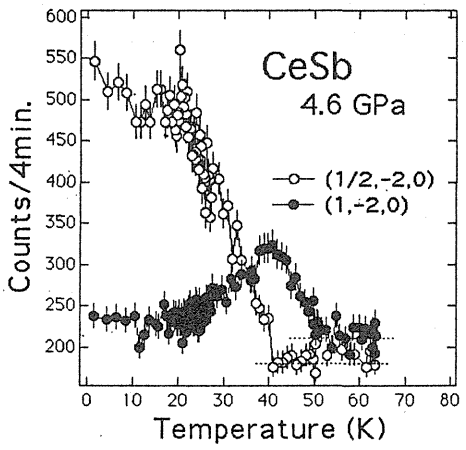


Figure 2: Temperature dependence of the magnetic Bragg intensities of CeSb in the SAC at 4.6 GPa.

The best method for compensating weak magnetic signals from a tiny sample in SAC is focusing the incident neutron beam on a sample position. The most likely successful method for the focusing is mirror reflection. We are now developing the focusing device with a lot of curved supermirrors according to the proposal of D.F.R.Mildner [4]. The inset of Fig. 3 shows the schematic drawing of the device. The shape of the cross section of each supermirror is a circle arc. The extension of the end of each mirror meets at a focal point (sample position). Neutrons are repeatedly reflected with the same angle by the inner side of the circle and arrive at the sample position. Figure 3 shows results of Monte Carlo ray-tracing simulation for a triple-axis neutron spectrometer TAS-1. The closed circles indicate the neutron intensity distribution at the sample position. This is the case of placing the device of 450 mm length that has 16 supermirrors with Q of 3.0 in the space of 600 mm between the 2nd collimator and the sample. Here, Q is the critical wave number of the total reflection of the mirror relative to that of natural nickel. The open circles indicate the distribution for the general experiment condition without the device. It is clear that the considerable gain of about 7 is obtained using the device. Therefore, it is expected that the device is very effective not only in the high-pressure experiments but also in the neutron inelastic scattering experiments with very weak signals.

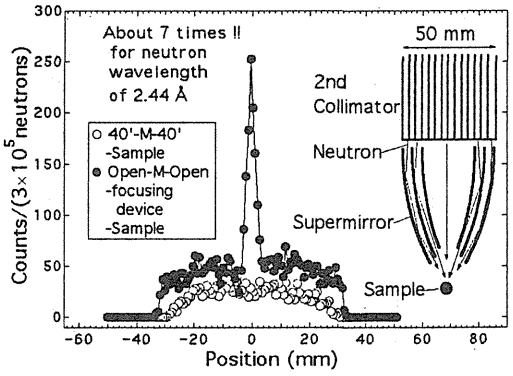


Figure 3: Calculated distribution of the neutron intensities.

References

1) Ji-an Xu, Ho-kwang Mao: SCIENCE, **290** (2000) 783.
2) T. Osakabe, A. Hannan, N. Tachi, M. Kohgi, H. Kitazawa: Appl. Phys. A**74** (2002) 799.
3) T. Osakabe, A. Hannan, D. Kawana, M. Kohgi, H. Kitazawa: Acta Physica Polonica B**34** (2003) 1469-1472.
4) D.F.R. Mildner: Nucl. Instr. And Meth. A**299** (1990) 416.

研究課題:両親媒子系複雑液体のスローダイナミックス
表題:TOF-NSE 分光器用の定常電流で働くスピンフリッパーの開発

1-8-11

Development of Spin Flippers with Steady Current for the TOF-NSE Spectrometer

Takayoshi Takeda[A], Norifumi L. Yamada[B], Hideki Seto[C] and Youhei Kawabata[D]

[A]*Faculty of Integrated Arts and Sciences, Hiroshima University, Higashi-Hiroshima 739-8521, Japan*
[B]*Graduate School of Bio-Sphere Science, Hiroshima University, Higashi-Hiroshima 739-8521, Japan*
[C]*Graduate School of Science, Kyoto University, Kyoto 606-8502, Japan*
[D]*Graduate School of Science, Tokyo Metropolitan University, Hachioji 192-0397, Japan*

We designed π and π/2 flippers for a time-of-flight neutron spin echo (TOF-NSE) spectrometer at a pulsed spallation neutron source. The flippers operate with steady current for a white neutron beam. The π flipper with the first modified current sheet which was made by winding Al-conductor wires operated well as a π flipper[1]. We present the results of performance tests of the new-type π and π/2 flippers with the second modified current sheet which was made of Al alloy plates[2].

The π flipper consists of a modified current sheet and Helmholtz coils. The modified current sheet produces magnetic fields B_s parallel to the sheet surface without magnetic fields perpendicular to the sheet surface at the surface of the sheet for a large neutron beam cross section. The correction field from Helmholtz coils B_c cancels out the perpendicular component of the magnetic field from the precession coils B_0 at the current sheet.

The new type of a π/2 flipper is similar to the above π flipper and consists of the above modified current sheet and Helmholtz coils. The correction field from Helmholtz coils B_c perpendicular to the sheet modifies the magnetic field from the precession coils B_0 so that $|B_0+B_c| = |B_s|$ at the current sheet.

Performance tests of the new-type flippers with the modified current sheet were carried out using ISSP-NSE at C2-2 port of JRR-3M in JAERI(Tokai). The neutron beam with the wavelength λ = 7.14 Å of its resolution $\Delta\lambda/\lambda$ = 18% (FWHM) and λ = 5.9 Å of $\Delta\lambda/\lambda$ = 15% (FWHM) was used. We replaced the Mezei-type π or π/2 flipper with the new-type one. We observed the NSE signal of neutrons scattered elastically from grafoil.

The flipping ratio (FR) experiments using the π flipper with the first modified current sheet were carried out using the neutron beam with λ = 7.14 Å and 5.9 Å by replacing only the monochromator, where any other conditions were the same for a given precession field. The flipping ratios for λ = 5.9 Å were nearly equal to those for λ = 7.14 Å. This indicates that the new π flipper operates well without tunning independently of the neutron wavelength.

Figure 1 shows the polarization P_{FR} obtained from the FR experiments using the π flipper with the second modified current sheet and the Mezei-type one at the scattering vector Q = 0, 0.05, 0.10 and 0.13 Å^{-1} for the beam cross section at the current sheet W_{CS} = 23^{w} x 40^{h} mm^2, the beam cross section at the analyzer W_A = 60^{w} x100^{h} mm^2 and λ = 7.14 Å. The abscissa is the current of the precession coils I_{pc}. The values of P from the new type flipper are larger than those from the Mezei-type one, especially at higher Q, though the tuning for the new type one was not fully optimized. This shows that the new π flipper operates well with a simple tuning.

The normalized NSE signal amplitude P_{NSE} is given as $P_{NSE} = |A_{NSE}/B|$ where A_{NSE} is the maximum amplitude of the NSE signal intensity and B the scattering intensity without spin echo, were obtained using a least-squares fit of the NSE signal intensity I_C to the following equation,

$$I_C = A_{NSE}\exp[-a(I_s - I_0)^2]\cos[b(I_s - I_0)] + B,$$

where I_s is the symmetry coil current and I_0, a and b fitting parameters. The values of P_{NSE}

使用施設:JRR-3　装置:NSE(C2-2)，分野:7. Instrumentations

obtained using the new-type π flipper at Q = 0, 0.05, 0.10 and 0.13 Å^{-1} for I_{pc} = 1 ∽ 100 A (Fourier time t = 0 ∽ 15 ns), W_{CS} = 23 ^{w} x 40 ^{h} mm^2 and I = 1.24 [A] were larger than one obtained using the Mezei type flipper. Figure 2(a) shows an example of the NSE signal profile observed at Q = 0.1 Å^{-1} using the new-type π flipper for I_{pc} = 1 A, W_{CS} = 23 ^{w} x 40 ^{h} mm^2, W_A = 60 ^{w} x100 ^{h} mm^2 and I = 0.57 [A], where P_{NSE} is 0.91 which is larger than 0.86 obtained using the Mezei type one.

Performance tests of the new-type π/2 flipper with the second modified current sheet were carried out by replacing the first Mezei-type π/2 flipper with the new-type one. Figure 2(b) shows an example of the NSE signal profile observed at Q = 0 using the new-type π/2 flipper for I_{pc} = 1 A, W_{CS} = 20 ^{w} x 50 ^{h} mm^2, W_A = 60 ^{w} x100 ^{h} mm^2 and I = 0.29 [A], where P_{NSE} is 0.88 which is nearly equal to that obtained using the Mezei type one. This shows that the new flipper operates well as a π/2 flipper.

In conclusion, the performance of the new type π and π/2 flipper operated well as the flippers. The new-type π flipper operated well without tuning independently of the neutron wavelength. The operation is very easy, that is, one has to tune only the correction field from Helmholtz coils B_c for a given precession field.

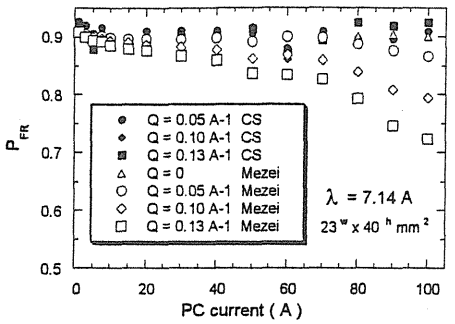


Fig. 1. Polarization P_{FR} = (I_{off} - I_{on}) /(I_{off}+ I_{on}) obtained from the flipping ratio experiments using the π flipper with the second modified current sheet and the Mezei-type one.

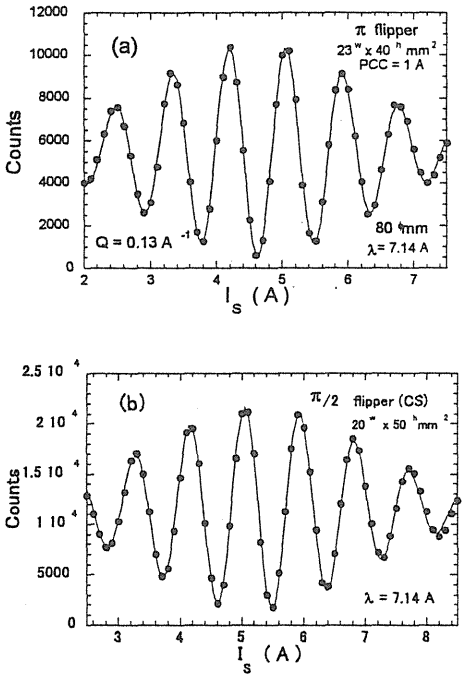


Fig. 2. Example of the NSE signal profile observed using the new type flipper.
(a): π flipper (b): π/2 flipper

References

[1] T. Takeda, H. Seto, Y. Kawabata; Appl. Phys. A 74 (2002) S177.
[2] T. Takeda, N. Yamada, H. Seto, Y. Kawabata; Physica B, in press.

1. 中性子散乱 9) その他

1. Neutron Scattering 9) Others

This is a blank page.

研究テーマ：中性子イメージングプレートを用いた中性子回折環全体を利用した残留応力測定法の開発
表　題：中性子イメージングプレートを用いた中性子回折環全体を利用した残留応力測定法の開発　1-9-1

Development of A Method for Determining Residual Stress Using Diffraction Ring Detected with Neutron Image Plate

T.SASAKI[1], N.MINAKAWA[2], Y.MORII[2], N.NIIMURA[2] and Y.HIROSE[1]

[1]Department of Materials Science and Engineering, Kanazawa University, Kanazawa, Ishikawa 920-1192
[2]Advanced Science Research Center, JAERI, Tokai, Ibaraki 319-1195

A neutron image plate (NIP) was used to determine tensile stress in a steel specimen. The thickness of the specimen was 5 mm. Debye-Scherrer rings of the 211 back-reflection neutron beams were obtained under the exposure time of 5 hours, and spatial resolution of 100μm. As the mean residual stress over the thickness of the sample must be zero, it can not give rise distinguished change in the behavior of the radius. From a numerical simulation on the formation of the composed neutron diffraction profiles under the same conditions as the experiment, it was found that the diffracted beams from inside the material can cause a change in the radius as seen in the experiment even if for stress free state. Namely, the diffraction radius can be changed due to both the stress state and the thickness (or geometry) of the material, whereas the thickness of the material has generally no effects on the diffraction profiles for X-ray image plate experiment without a steep stress gradient case and so on. The stress determination was then carried out to the NIP image data using the cosα method, which was developed by Tanaka *et al.* Figure1 shows the stresses obtained as a function of the applied stresses which were converted from strains detected with the strain gauges on the specimen.

The open circles in the figure indicate values obtained from the cosα method, which shows a proportional behavior as well almost constant intervals against the applied stresses. The closed circles indicate the result obtained from the correction, in which the original NIP data were subtracted by those at stress free state and then the cosα method was used. It can be seen in the figure that the corrected data agree with the applied stresses (solid line). This means that the cosα method, which is adequate only to the X-ray experiment, is also effective to the neutron experiment. The reason of the result can be explained that the behaivior of the angular peak in the composed neutron profile on the NIP is almost the same as that of the diffracted beam on the most surface of the sample, because such beams act as the cosα method as same as X-ray beams. However, it should be noted that the present result will be obtained only in the case of samples with no stress gradients. As examples of this type of use of a NIP for the stress measurement, a mean stress evaluation in a layer joined to the other materials such as the SHS method, or phase stresses in composite materials. But the goal of the authors' study is the development of a method for determining depth profiles of residual stresses in the materials over the thickness in a nondestructive way.

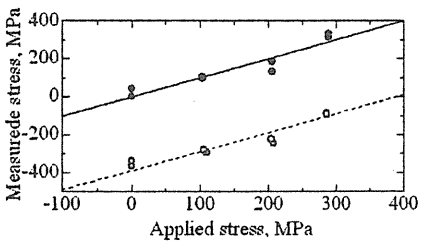


Figure 1: Stresses obtained from raw data (o) as well as from corrected data (•) using the cosα method as a function of applied stress.

原子炉：JRR-3　　装置：RESA(T2-1)　　分野：中性子散乱（その他）

研究テーマ：冷中性子屈折光学系と評価用検出器の基礎研究
表　題：冷中性子光学素子の開発
1-9-2

Development of optical devices for cold neutrons

H. M. Shimizu[1], T. Adachi[1], T. Oku[1], K. Ikeda[1], H. Sato[1], Y. Takizawa[1], K. Morimoto[1], S. Morita[1], H. Ohmori[1], K. Sakai[1,2], F. Tokanai[3], K. Sasaki[4], Y. Kiyanagi[4] and J. Suzuki[5]

[1]RIKEN, Wako, Saitama 351-0198
[2]Department of Physics, Tokyo Institute of Technology, Ohokayama, Meguro 152-8551
[3]Department of Physics, Yamagata University, Yamagata 990-8560
[4]Atomic Science and Nuclear Engineering, Hokkaido University, Sapporo, Hokkaido 060-8628
[5]Advanced Science Research Center, JAERI, Tokai, Ibaraki 319-1195

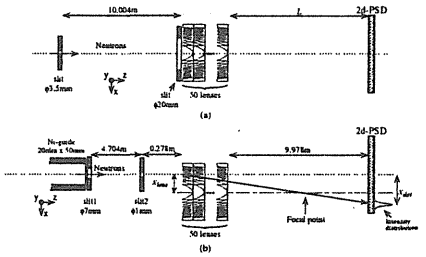


Figure 1: Experimental setups for lens characterization.

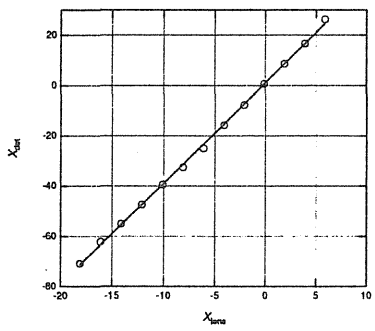


Figure 2: Measurement of the focal performance. The circles represent the observed data. The line is the result to fit with the observed data by least square method. The slope of this line is 4.0 at 1.6 nm. The focal length of 1.6 nm is 2.5 m.

We have developed more penetrative lens in large aperture (45 mm in diameter). Typical application of neutron focusing lens is Focusing geometry Small Angle Neutron Scattering (F-SANS) instruments [1)]. Neutron beam can penetrate all aperture area of Fresnel-type lens very well. Considerable gain will be expected compared to Pinhole geometry Small Angle Neutron Scattering (P-SANS).
We have fabricated lens elements made of MgF_2 single crystals which provide an effective scattering potential-energy difference of (131-0.00018i) neV with respect to vacuum. Each element was made from a 1 mm in thickness and 50 mm in diameter optically polished disk, ground to a Fresnel shape using the electrolytic inprocess dressing (ELID) grinding technique [2)]. The detailed design was described before [3)]. The root-mean-square roughness (in μm) of the two faces of a lens element is approximately 0.01 (polished side) and 0.2 (ground side). A set of lens elements is composed of 50 disks.
The microstructure in a MgF_2 single crystal was measured by small-angle neutron scattering using the SANS-J instrument at the JRR-3M reactor of JAERI. Little small-angle scattering and high transmission of 0.998 ± 0.001 for 0.8 nm neutrons were observed. The results were described elsewhere [4)].
The performance of the compound lens was investigated using a cold neutron beam from the SANS-J instrument at the JRR-3M reactor of JAERI. The experimental setup is shown schematically in Fig. 1. A collimated neutron beam entered the lens, and the transmitted and refracted intensities were measured by a two-dimensional position sensitive detector (PSD) located at 10 m downstream from the center of the lens. The PSD has 128 × 128 position channels over a 640-mm in diameter sensitive area. The position resolution of the PSD was specified to be 5 mm.
The transmission was measured with the setup in Fig. 1(a). The observed transmission of the lens is 0.829 for 1.14 nm neutrons. The expected transmission calculated from the measurement of a plate sample is 0.954 for 1.14 nm neutrons. The measured transmission is less than the expected.

原子炉：JRR-3　　装置：SANS-J(C3-2)　　分野：中性子散乱（その他）

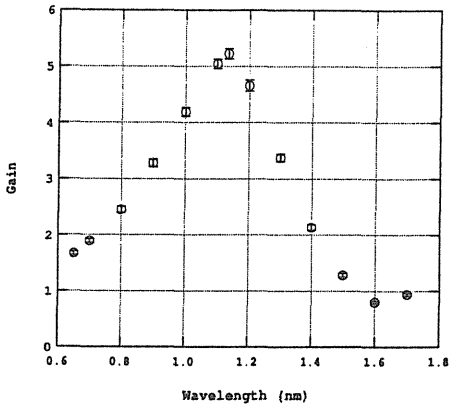


Figure 3: Ratio of peak intensity of focusing beam to plain beam at various wavelength on the 10 m distance (L) between lens and PSD. Experimental setup of measurement is as shown in Fig. 1(a). Neutron counts on the detector is integrated in the area same as the first pinhole which is 3.5 mm in diameter after fitted to two-dimensional Gaussian function. The gain becomes the maximum at 1.14 nm in L=10 m.

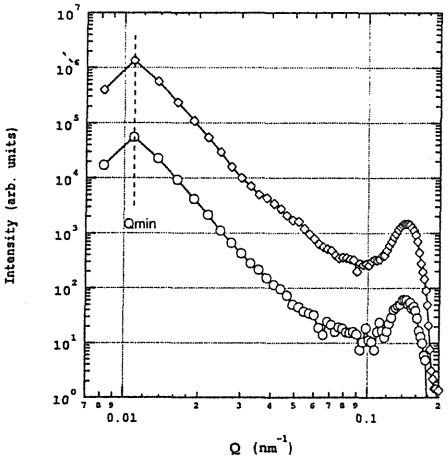


Figure 4: Typical measurement of small-angle scattering. The circles and the rhombuses represent the observed data of P-SANS and F-SANS, respectively. The intensity is relatively normalized. The factor between curves shows gain of the instrument configuration. The gain in the condition of this beam-line is more than ten times.

In order to investigate the lens characteristics carefully, a neutron beam collimated by a 1 mm in diameter pinhole was used. The setup of this experiment is shown in Fig. 1(b). The two-dimensional neutron images ware observed by PSD at 10 m downstream position from the lens. The peak of the distribution were determined to fit the Gaussian to the observed data. Figure 2 shows result of the measurement of the focal performance. The slope of this line indicates L/f, where L means distance between lens and PSD and f means focal length. The focal length of this lens is 2.5 m at 1.6 nm neutrons.

To measure the gain by focusing of the neutrons, a neutron beam collimated by a pinhole of 20 mm in diameter in front of the lens and a pinhole of 3.5 mm in diameter at 10 m upstream position of the lens were used. The setup of this experiment is shown in Fig. 1(a). Figure 3 shows the ratio of peak intensity of focusing beam to plain beam at various wavelength on the 10 m distance (L) between lens and PSD. The gain becomes the maximum at 1.14 nm in L=10 m.

We obtained considerable, more than 5 times, gain of beam intensity using focusing lens. However, the gain is too less than 33 times simply calculated by the ratio of the area because a divergence of the beam coming into the first pinhole is not enough large.

Typical small-angle scattering measurements were performed, and we compared focusing method, F-SANS, with conventional method, P-SANS. The condition of pinholes was selected as being able to measure same minimum momentum transfer. The intensity ratio F-SANS to P-SANS was more than ten. That value is the gain by beam focusing using lens. If a divergence of the beam coming into the first pinhole is enough large, more gain would be observed. In order to get better performance, we need investigate details of the noise from lens further.

References

1) S.-M. Choi, J. G. Barker, C. J. Glinka, Y. T. Cheng and P. L. Gammel, *J. Appl. Cryst.*, **33** (2000) 793.
2) H. Ohmori, *Int. J. Japan Soc. Prec. Eng.* **26** (1992) 273.
3) T. Oku, S. Morita, S. Moriyasu, Y. Yamagata, H. Ohmori, Y. Takizawa, H. M. Shimizu, T. Hirota, Y. Kiyanagi and J. Suzuki, *Nucl. Instrum. Methods A* **462** (2001) 435.
4) T. Adachi, T. Oku, S. Morita, H. Ohmori, Y. Takizawa, H. M. Shimizu, J. Suzuki, C.-K. Loong, K. C. Littrell and R. Goyette, *Appl. Phys. A* **74** (2002) S180.

研究テーマ：高温照射に関する先端的基礎研究
表　題：中性子散乱法による炭素複合材料の残留応力の研究

1-9-3

Study of Residual Stress for Carbon/Carbon Composite by Neutron Scattering

S. BABA, M. ISHIHARA, N. MINAKAWA[1] and J. SUZUKI[1]

Department of Advanced Nuclear Heat Technology, JAERI, Oarai, Ibaragi 311-1394
[1]Department of Advanced Science Research Center, JAERI, Tokai, Ibaragi 319-1195

1. INTRODUCTION

The carbon fiber reinforced carbon matrix composite (c/c composite) is thought to be one of advanced heat resistant material in the nuclear engineering field. However, a lot of cracks are observed in manufacturing process of the ring type c/c composite due to the delamination between the fiber and the matrix by the residual stress. This is because of the different shrinkage between the fiber and the matrix during carbonization and graphitization heat treatment. Therefore, we investigated the residual stress in the ring type c/c composite aiming at the improvement of the manufacturing process. In this study, we measured the distributed residual stress in the ring type specimen using the neutron scattering experimental facility in the Japan Research Reactor No.3 Modified (JRR-3M) of Japan Atomic Energy Research Institute (JAERI).

2. EXPERIMENTAL PROCEDURE

2.1. Specimen preparation

The c/c composite material, CX-270G (made by TOYO TANSO Co.Ltd.,) was prepared as following process. The 6K plane weaves, 6000 PAN-based fiber in a fiber bundle with phenol resin coating, were molded by a so-called the vacuum bag method. After that, performing the hardening by heat treatment, carbon fiber reinforced plastic (CFRP) was made. The CFRP was heat treated over 800 ℃ under inert gas atmosphere to achieve carbonization and then heat treated finally about 2800 ℃ under unoxidation atmosphere to achieve graphitization. To product cylindrical shaped c/c composite specimen, the cylindrical shaped prepreg made of flat cloths was heat treated and harden to get the CFRP. After this process, the same treatment as above was conducted. Two kinds of isotropic graphites (IG-110, ISO-88) were prepared so as to obtain basic data on the c/c composite. Figure 1 shows the ring type c/c composite with 100mm outer diameter and 5mm thickness.

2.2. Apparatus

(1) High Resolution Powder Diffractometer, HRPD

The HRPD is a device to analyze the crystal structures as well as magnetic structures of the powder sample and also polycrystalline sample. We measured the standard lattice parameter of strain-free materials using the HRPD. In the experiment, to secure high resolution in a wide range, we set small divergence angle in the horizontal direction of the first and third collimators, and set large scattering angle of the monochrometer. Furthermore, to achieve high efficiency of measurement, we used a quasicurve type monochrometer to converge the neutron in the vertical direction at the sample position, and also used 64 sets of neutron detectors at every 2.5 degree of the scattering angle.

(2) Diffractometer for the residual stress analysis, RESA

The single crystal for monochromization of RESA has achieved the wavelength of 0.13～0.3nm by adopting a level vertical lightgathering type silicon crystal, Si(311), and also vertical vent light-gathering type pyrolytic graphite crystal, PG(002). The goniometers can move in one direction Z, three directions X, Y,

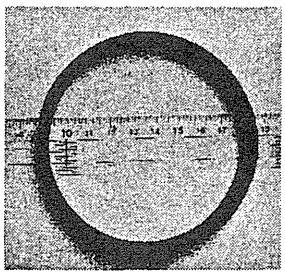


Figure 1: Ring type c/c composite specimen.

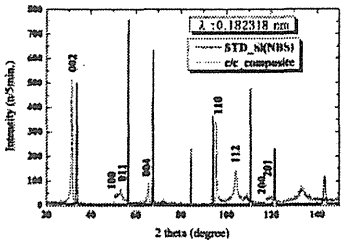


Figure 2: Powder diffraction patern of c/c composite and silicon(NBS).

原子炉：JRR-3　　装置：RESA(T2-1)　　分野：中性子散乱（その他）

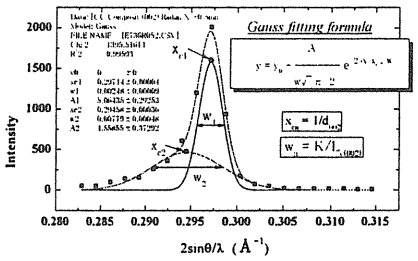


Figure 3: Gauss fitting formula of 002 layer spacing and crystallite, Lc for c/c composite.

Z, and five directions χ, ϕ, X, Y, Z. Furthermore, the diffraction angle can be measured under in-situ loading condition by the tension tester of the RESA apparatus.

3. RESULTS AND DISCUSSIONS

3.1. Measurement of layer spacing of strain-free sample

The powder sample of the c/c composite was prepared using an iron file. The calibration of incidence wave-length was carried out by a standard sample, silicon of National Bureau Standard, (silicon (NBS)). Measured in-tensity of the c/c composite powder and the silicon (NBS) samples is shown in Fig.2. From the measurement, we determined the wavelength of HRPD as λ =0.182318 nm. Then the strain-free diffracting plane, d002, is determined to be 0.33542 nm from 002 diffraction angle obtained by Gauss approximation of the measured diffraction peak for the powder sample of the c/c composite. To determine the d002, we used the diffraction neutron intensity vs. 2sinq/l plot corresponding to a reciprocal lattice layer spacing, 2sinq/l=1/d002. From the 1/d002 corresponding to a diffraction peak, we can determine the d002 value directly. The measured d002 diffraction intensity of the c/c composite sample showed the peak with the shoulder on the low angle side as shown in Fig.3. In the c/c composite, there are well-graphitized matrix part and not well-graphitized carbon fiber part just as a turbostratic structure.[1,2] The intensity peak in Fig.3 appears respectively at higher position with narrow width for well-graphitized parts and at lower position with wide width for not well-graphitized parts. This is thought to be a reason why the shoulder appeared. Average crystallite height in 002 plane, Lc, was determined by the half-width, Wn, as shown in Fig.3.

3.2. Residual stress in ring type c/c composite

The neutron radiation diffracts in accordance with the diffraction condition of Bragg's law as given in equation (1) like the X-ray diffraction fundamentally,

$$n \lambda = 2d\sin\theta \quad (1)$$

where, n is the dimensional number, λ neutron wave-length, d lattice distance and θ diffraction angle. As for the lattice distance of a crystal, a diffraction angle changes by the applied stress. By differentiation of the equation (1), we rewrite the strain as

$$\varepsilon = \Delta d/d = (d\text{-}d0)/d0 = -\cot\theta\ 0\ \Delta\theta, \quad (2)$$

where d0 is the layer spacing and θ 0 the diffraction angle of strain-free condition. Accordingly, the stress σ is estimated by equation (3) based on the Hooke's law, if E and ν are respectively the diffraction elastic constant and Poisson's ratio for the specific diffraction plane.

$$\sigma = E\ \varepsilon / \nu \quad (3)$$

The diffraction lines in the radius direction of the ring type c/c composite were measured of the interval of 0.5mm from outside to inside surface. The diffraction angle for 002 was measured for 4minutes at 0.2 degrees of stepping interval. As shown in Fig.4, the residual stress/strain decreased from inner to outer surface of the ring type c/c composite. Here, we should note that the obtained stress/strain within about 0.5mm from the inner surface express not true value, because in this region a part the neutron beam volume misses from the gauge volume.

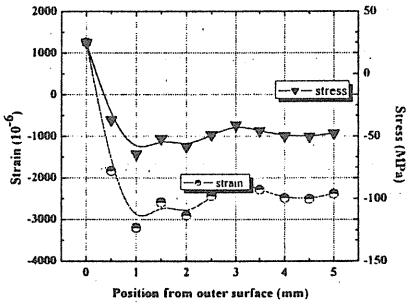


Figure 4: Residual stress and strain of ring type c/c composite.

4. CONCLUSIONS

The residual stress distribution in the c/c composite was studied aiming at the improvement of the manufacturing process using the neutron diffraction method. As a result of this study, it is the compressive stress, and that the macroscopic residual stress/strain is absorbed mainly microstructural change such as pore shape change.

References

1) T. Tamotsu, S. Baba and M. Eto, Changes of Tensile Property and X-Ray parameter for Carbon Fiber after
2) M. Eto and T. Oku : J. Nucl. Mater 54 (1974) 245-253.

研究テーマ：多重極限環境下における中性子散乱実験法の研究
表　　題：小ビームによる試料表面測定における回折角誤差の検討

1-9-4

Diffraction angle error investigation of the sample surface measurement by the small neutron beam

N. Minakawa, A. Moriai, Y. Morii

Advanced Science Research Center, JAERI, Tokai, Ibaraki 319-1195

In order that to evaluate the soundness of material or processed goods, safety, and a life, an internal spacing of lattice planes is measured from the material surface, and it determines for a strain and a stress distribution. Near the surface, it measures the spacing of lattice planes more than a forecast then. Therefore, using the carbon steel sample of the non-strain condition which heat-treated, we reproduced this phenomenon.

We used SM400 carbon steel with heat-treated suitable vertical 50 mm, a length 100 mm, and a thickness of 10mm for the measurement sample. By the beforehand neutron diffraction measurement, a crystal structure is BCC and it determined for a lattice constant being 0.28682nm. The slit of 1 mm width and 15 mm height was used for the measurement at the incidence and scattering side, using the neutron wavelength of 0.20963nm. Mostly, the diffraction angle used the 200 reflections, which is 90 degrees, and measured the measurement diffraction lattice planes by the reflection method and the transmission method. The measurement position was used as 0.5mm step near the surface, and the inside was measured at 1mm step. The distribution of a forecast intensity with a method of measurement is shown in Fig. 1.

The result, which measured by the reflection method and the transmission method, is shown in Fig. 2 and Fig. 3. The absorption coefficient of SM400 was μ = 1.17 as a result of measurement, and maximum diffraction intensity thickness t_{Imax} was 0.584mm from the next equation.

$$t_{Imax} = 1 / \mu \sec \theta$$

The maximum intensity position, which can be found from the integrated intensity distribution curve of Fig. 3, is equivalent to calculation value. Therefore, it can be said that a sample mount position is exact.

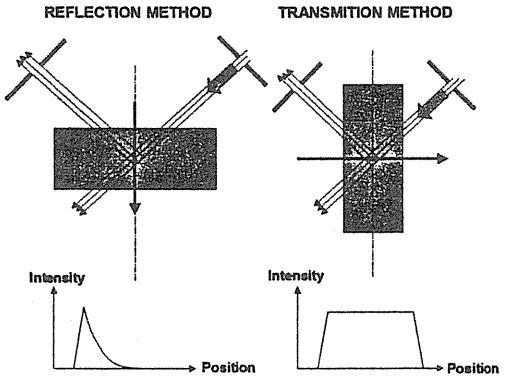


Figure 1: Measurement method of sample.

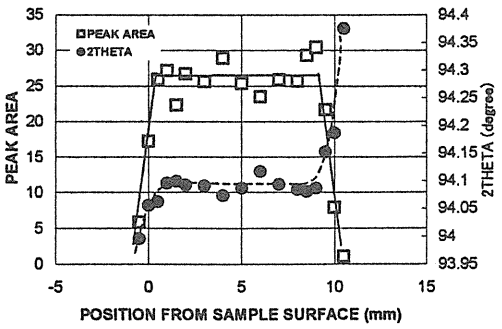


Figure 2: Distribution of 2Theta and intensity by the reflection method.

原子炉：JRR-3　　装置：RESA (T2-1)　分野：中性子散乱（その他）

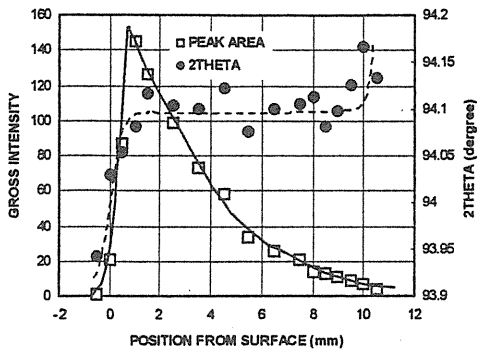


Figure 3: Distribution of 2Theta and intensity by the transmission method.

Originally, the diffraction angle distribution of Fig.2 and Fig. 3 has the desirable same angle from the surface of sample to back, but an angle becomes high exponentially also from this measurement result, or the diffraction angle near the surface becomes low, and the result as expected was obtained.

In order that the neutron guide tube is using super mirror of the 2Q, the divergence angle to a monochromator crystal is 0.36 degrees equivalent to a critical angle. The locking curve FWHM of the monochromator crystal was about 0.2 degrees, and in order that the bending stress was applied in the horizontal plane to the crystal, the divergence angle of a monochromatic neutron beam was 0.3 degrees as a result of measuring by the photograph method. The beam divergence angle by the diffraction is determined with the distance between sample and detector, and the size of collimator and slit. The position of a sample and the condition of the diffraction by the divergence angle are shown in Fig. 4.

An incidence beam passes the center of the sample table. The diffraction angle outputted to data is a true rotation angle of a sample table center. The neutron diffraction near the sample surface becomes strong the diffraction by the divergence angle. Therefore, we understood that it was different from the diffraction angle of an inside of sample part. Moreover, the bending stress is loaded to the monochromator crystal for the control of crystal mosaic spread. Therefore, when a crystal bends, it has a wavelength distribution in a horizontal plane. These conditions overlap near the surface, and in order that the diffraction is performed, the complicated correction method is needed and it is under investigation now.

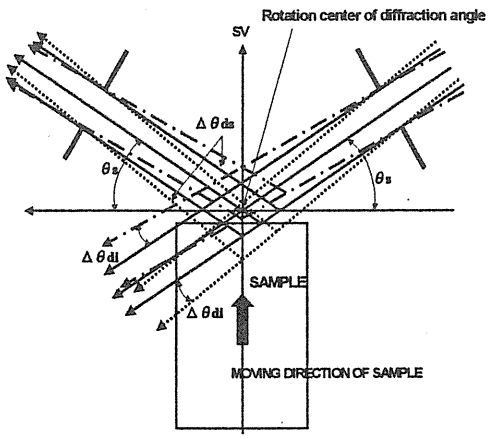


Figure 4: Neutron diffraction by the divergence beam.

研究テーマ：多重極限環境下における中性子散乱実験法の研究
表　　題：アルミエンジン切削ひずみの中性子回折法とひずみゲージ法による比較測定

1-9-5

The comparison measurement of the strain gauge method and the neutron diffraction methods by the automobile aluminum engine

N. Minakawa[1], A. Moriai[1], Y. Morii[1], K. Goto[2], S. Nishii[2],
S. Yamada[2], H. Hosoda[2], A. Nomura[2], and T. Hamamoto[2]

[1]Advanced Science Research Center, JAERI, Tokai,Ibaraki 319-1195
[2]The 4th Development Center, Toyota Motor Corp

The automobiles engine is loading continuously the thermal stress with severe repetition impact stress. Inside of automobile engine, the intensity that can bear the stress is maintained, safeness and soundness are guaranteed, and we utilize. When we imagine, in a future automotive society, it will become an important assignment to guarantee safeness scientifically. Therefore, becoming an important technique after this for the purpose of residual stress measurement at the inside of engine by the neutron diffraction method is expected.

Now, the stress measurement for the inside of engine has the cutting strain method by the strain gauge. Therefore, this fiscal year compared and measured the surface strain measurement by the strain gauge, and the neutron diffraction method. Measurement equipment used the neutron diffractometer for residual stress analysis (RESA) installed in the experimental hall of neutron guide tube in JRR-3. The rosette type strain gauge with a diameter of 5mm was used for the strain gauge method. The measurement sample cut from an aluminum engine and used a small block with 21.5 mm width, 15.7 mm height, and 11.5 mm depth. The strain gauge was affixed on the small block, and strain was measured by the strain gauge method and the neutron diffraction method. After that, moreover, sample was cut to a small block by the electrical discharge machining, and strain was measured by the both methods, and we searched for about change of strain value. The cut aluminum engine block is shown in Fig. 1.

The measurement method by the neutron

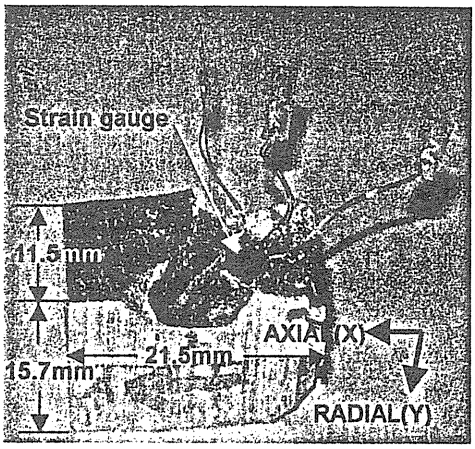


Figure 1: The cut aluminum engine block.

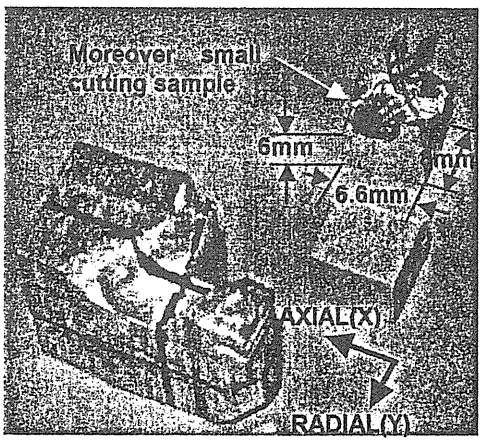
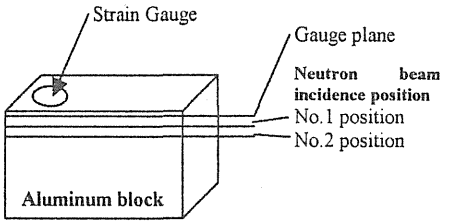


Figure 2: The engine block cut moreover smaller by the electrical discharge machining.

原子炉：JRR-3　　装置：RESA (T2-1)　　分野：中性子散乱（その他）

diffraction made a beam size 1 mm height, 2 mm width and measured that bottom of the gauge and downward direction at the 1 mm step. The measurement mirror index used (311), and neutron wavelength is 0.20891nm. The incidence neutron flux of a measurement beam size was 3.3 x 10^3 (n/2mm^2/30sec) = 1.1 x 10^3 (n/2mm^2/sec), measurement time was wanted. Therefore, 7.5 hours was used in order that to measure one diffraction (311) pattern. By electrical discharge machining, the engine block cut moreover small is shown in Fig. 2. A measurement sample position is shown in Fig. 3. and a measurement result is shown in Table 1.



An incident position is 1mm interval

Figure 3: Measurement sample position.

By the strain gauge method, it measures the surface strain of the affixed position. By the neutron diffraction method, it measures the average strain in a gauge volume. The figure of a gauge volume in this measurement with consideration to the divergence angle is shown in Fig. 4.

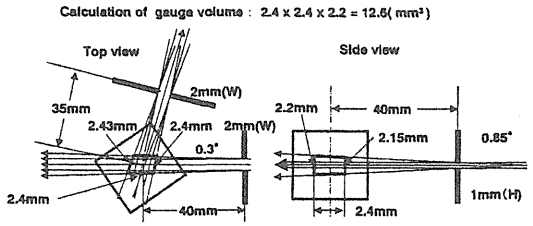


Figure 4: The gauge volume in this measurement with consideration to the divergence angle.

The difference before and behind cutting of the AXIAL direction by the strain gauge is 128 (micro strain), the RADIAL direction is 51 (micro strain) and these are very small strain change. That is, on the surface, it can be said that the strain is opened for the surface by cutting. At the result of the strain measurement by the neutron diffraction, it was 543 (micro strain) in the AXIAL (X) direction and 495 (micro strain) in the RADIAL (Y) direction. Although this result is not an extremely big strain, either, it can be said that it was about change by the open strain by cutting. Moreover, the AXIAL (X) direction was –1233 (micro strain) and the RADIAL (Y) direction was –276 (micro strain) of the strain of a gauge to 1mm lower part. By cutting a small block, the compression strain was generated. Even though it was the block smaller cut from this result, it understands that a residual strain cannot be opened perfect.

Table 1 : Measurement result of strain

DIRECTION	POSITION	BEFORE CUT	AFTER CUT	A-B *
AXIAL	strain gauge	-255	-127	128
AXIAL	No.1	265	760	495
AXIAL	No.2	1180	-53	-1233
RADIAL	strain gauge	-340	-289	51
RADIAL	No.1	652	1153	501
RADIAL	No.2	898	578	-319

* A : After cutting B : Before cutting

研究テーマ：中性子回折による構造物の残留応力測定
表　題：中性子回折法によるピーニング材の残留応力測定

1-9-6

Residual stress measurement of peened material by neutron diffraction method

S. OKIDO, T.MACHIDA[1], M. HAYASHI[2],
Y. MORII, N. MINAKAWA and A. MORIAI[3]

[1]Mechanical Engineering Research Laboratory, Hitachi, Ltd., Hitachi, Ibaraki 317-8511
[2]Power and Industrial Systems, Hitachi, Ltd., Hitachi Ibaraki 317-8511
[3]Advanced Science Research Center, JAERI, Tokai, Ibaraki 319-1195

Shot peening deforms and hardens a metal surface plastically with particles of metal or glass. As a result, compressive residual stress appears and the surface properties are improved. The region of compressive residual stress by shot peening is less than a few-mm depth. The neutron diffraction method is inferior to X-ray diffraction method when the residual stress near the surface is measured. So the accuracy of residual stress near surface of the peened materials measured by neutron diffraction was discussed comparing with that measured by X-ray diffraction.

The material used in this research wwa peened stainless steel Type-304. The lattice strain was measured by using RESA. The 111 diffraction of γ-Fe in type-304 steel was used in the measurement of strain. The wavelength, λ was 0.20995 nm. Cadmium masks were inserted in both the incoming beam and the diffracted beam to define a sampling volume of 0.3x0.3x8 mm^3.

The residual stress measurement at the surface make the peak angle of diffraction profile shift from veritable peak angle, causing a bias of neutron irradiation. So, peak angles obtained from diffraction profiles at surface of stress free specimen are shown in Fig.1. A peak shifts appeared at the surface less than 0.7 mm depth. This result shows that the peak angle correction is required measuring at the surface less than 0.7 mm depth.

The results of surface residual stress obtained from before and after peened specimen are shown in Fig. 2. The results of measured by x-ray diffraction method added to Fig.2 to discuss the accuracy of those of neutron diffraction method. These residual stresses measured by neutron diffraction method at the surface less than 0.7 mm depth is corrected with results of Fig.1. The peening effects produce a difference between before and after peening residual stress less than 0.5 mm depth. The residual stress over 0.5 mm depth was not affected by the shot peening. Moreover, the residual stresses as obtained by neutron diffraction almost agreed with those by x-ray diffraction. These results show that peak profile correction make the neutron diffraction method possible application of measuring the surface residual stress.

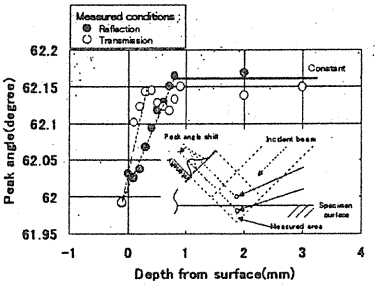


Figure 1: Change of diffraction profile obtained from stress free material surface.

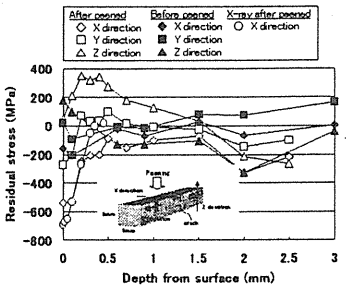


Figure 2: Residual stress distributions vicinity of crack before and after peening.

原子炉：JRR-3　　装置：RESA(T2-1)　　分野：中性子散乱（その他）

研究テーマ：構造用材料の残留応力および負荷荷重下での材料特性評価
表　　題：引張変形させたパーライト鋼の残留相応力の異方性

1-9-7

Anisotropy in Residual Phase Stresses in a Pearlitic Steel Subjected to Tensile Deformation

T. Suzuki, Y.Tomota[1], A. Moriai[2], N. Minakawa[2] and Y. Morii[2]

Research Center for Superplasticity, Faculty of Engineering, Ibaraki University, Hitachi, Ibaraki, 316-8511
1. Department of Materials Science, Faculty of Engineering, Ibaraki University, Hitachi, Ibaraki, 316-8511
2. Advanced Science Research Center, Japan Atomic Energy Research Institute, Tokai, Ibaraki, 319-1195

The strength of a drawn pearlite steel wire along the drawing direction is higher than that along the transverse one but the reason is unclear[1]. Two possible reasons, i.e., texture and residual phase stress, were examined in this study. Tensile deformation was employed because the drawing was complicated in plastic manner. The results obtained are compared with the results for the drawn wires obtained previously.

A hypereutectoid steel with the chemical compositions of 0.85C, 0.24Si, 0.82Mn, 0.011P, 0.01S, 0.02Al and 0.05Cr in mass% was hot-rolled and patented through an industrial process to produce fully pearlitic structure (specimen P1). They were drawn by 75% in area reduction (P2) and aged at 698 K for 0.6 ks (P4): Zn-plating simulated heat. The details in sample preparation were reported in ref. 2.

The texture of P1(ϕ 11mm) was evaluated by 110 pole figure obtained by X-ray diffraction with the Schulz reflection method using nickel-filtered Cu K_α radiation. Because the specimen diameter of P2 and P4 is small (ϕ 5 mm), their textures were measured by neutron diffraction. The measurements were conducted using the Neutron Diffractometer for Residual Stress Analysis (RESA) at Japan Atomic Energy Research Institute (JAERI).

Tensile tests were carried out at 300 K using a gear type tester with an initial strain rate of 6.7×10^{-4} s^{-1}. Figure 1 (a) shows shape and dimensions of tensile specimen. After the tensile tests, specimens for the measurement of residual strains were prepared by cutting from their parallel part; uniformly elongated part. The residual strain measurements were conducted by a conventional θ-2θ method with neutron diffraction by using RESA at JAERI. Lattice plane spacing of (110) ferrite was measured, where a specimen was rotated by 0, 22.5, 45, 67.5 and 90° with respect to the tensile direction as illustrated in Fig. 1 (b). Peak positions of the diffraction profiles were determined by curve fitting with a Gaussian function.

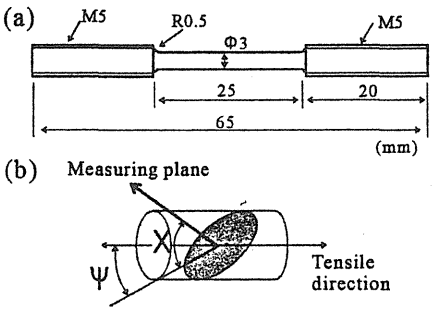


Figure 1: Shape and dimensions of a tensile specimen (a) and geometrical arrangements for texture and residual strain measurements (b).

The microstructure observations reveal that the pearlite colonies in P4 are elongated along the drawing direction and their lamellar spacing becomes smaller in comparison with P1. In a 110 pole figure of the ferrite matrix in P1 obtained by the X-ray diffraction, no areas of high pole density could be found, indicating very weak texture. The pole figure for P4 is shown in Fig. 2 which is quite similar for P2. As seen, a maximum intensity of

原子炉：ＪＲＲ－３　　装置：ＲＥＳＡ（Ｔ２－１）　　分野：（その他）

6.8 times of the average density exhibiting the 110 fiber texture. The texture was formed by the drawing process (P2) and was hardly affected by the annealing at 698 K (P4).

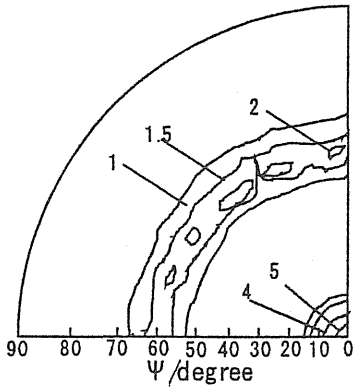


Figure 2: 110 pole figure obtained by neutron diffraction for P4.

Figure 3 shows lattice plane strains of P1 and P4 after tensile deformation. The residual strain of P1 simply increases from compression to tension with increasing of the measuring angle from 0 to 90° . This is quite acceptable from the view point of phase stress generation between hard and soft phase in a two-phase material. On the other hand, in the lattice plane strains of P4 (b), the overall trend is from compression to tension with increasing of the measuring angle, but the residual strain at 90° is lower than that at 67.5°. This is the same trend observed in the drawn wire that shows strength anisotropy. This unusual results stem from the texture.

Comparing the features of P1, P2 and P4 before testing, the texture is similar for P2 and P4 while the residual phase stress is similar for P1 and P4. When tensile deformation is applied to P1 and P4, different phase stresses are yielded. The stresses for P4 subjected to tensile deformation resemble that for P2. The strength anisotropy is found only in P2 not in P1 and P4[3]. Hence, it is concluded that the strength anisotropy stems from the features of residual phase stress not from the texture. It should, however, be noted the texture brings the different residual stress distribution after plastic deformation. This can be explained from the influence of texture on the plastic flow in individual grains. Such discussion will be given in ref. 3.

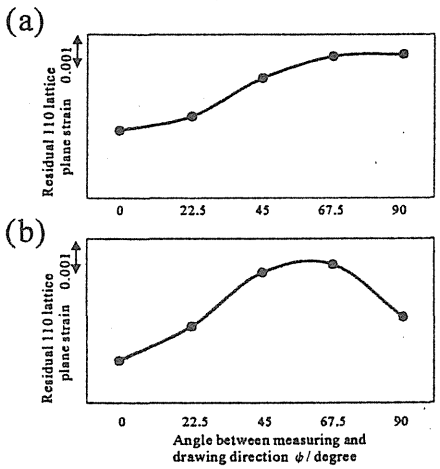


Figure 3: Residual elastic strains in the ferrite matrix of P1 (a) and P4 (b) after tensile tests.

REFERENCES

1. T. Fujita, Y. Yamada and T. Yamada: Tetsu-to-Hagane **59** (1973) S255.
2. Y. Tomota, P. Lukas, D. Neov, S. Harjo and Y. R. Abe: Acta mater. **51** (2003) p.805.
3. T. Suzuki, Y. Tomota, A. Moriai, N. Minakawa and Y. Morii, ATEM.03, Nagoya, (2003), Sept., JSME-MMD.

研究テーマ：構造用材料の残留応力および負荷荷重下での材料特性評価
表　　題：４GPaで引抜いたパーライト鋼ワイヤーの強度化機構の研究
1-9-8　-引張条件下その場中性子回折-

Strengthening Mechanism of a Heavily Drawn Pearlite Wire with 4 GPa - *In situ* Neutron Diffraction under Tensile Loading-

Y. Tomota, A. Kanie[1], Y. Shiota[1], T. Suzuki[2] , A. Moriai[3], N. Minakawa[3] and Y. Morii[3]

Department of Materials Science, Faculty of Engineering, Ibaraki University, Hitachi, Ibaraki, 316-8511
1. Graduate student of Ibaraki University, Hitachi, Ibaraki, 316-8511
2. Research Center for Superplasticity, Ibaraki University, Hitachi, Ibaraki, 316-8511
3. Advanced Science Research Center, Japan Atomic Energy Research Institute, Tokai, Ibaraki, 319-1195

Much attention has been paid on the micro structure of a heavily drawn pearlitte wire because it shows ultra high strength; the champion strength. The microstructure of pearlite consisting of ferrite and cementite changes drastically by sever plastic deformation; cementite plate in lamellae dissolved in to the ferrite matrix and hence strengthening mechanism to exhibit more than 4 GPa is unclear. Thus, many workers have been investigated the microstructural evolution during sever deformation by Mossbauer spectroscopy, AP-FIM, TEM etc. Although the structural feature has been revealed to some degree, but the strengthening mechanism is quite difficult to study. Neutron diffraction is a powerful tool to investigate the strength of such a wire. Thus, *in situ* neutron diffraction during tensile loading was performed.

The chemical compositions of a steel used are listed in Table 1. The hot-rolled bars were patented and then drawn through an industrial process at Sumitomo metal industry Ltd. They were drawn to wires with several diameters as shown in Table 2.

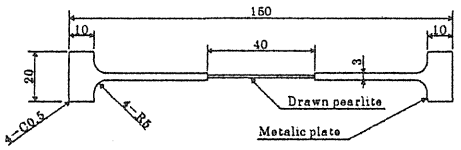


Figure 1: Shape and dimensions of specimen holder.

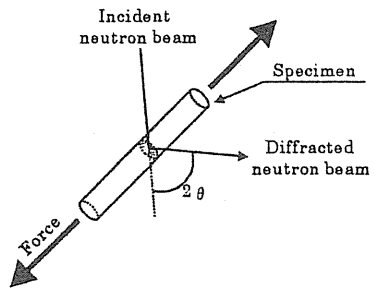


Figure 2: *In situ* neutron diffraction experiment for a wire under tensile loading.

To hold a wire, a special holding jig was prepared as shown in Fig. 1; a wire was bonded by two steel plates. Figure 2 shows the testing condition of *in situ* neutron diffraction. Even for a wire with 0.2 mm in diameter, it becomes possible to obtain a (110) diffraction profile with sufficient intensity to determine the center of the peak by

Table 1: Chemical compositions of a pearlitic steel

C	Si	Mn	P	S	Cr	Al	N
0.88	0.16	0.51	0.009	0.005	0.03	0.001	0.0029

Table 2: Specimens prepared by drawing

Diameter(mm)	φ1.5	φ0.72	φ0.43	φ0.27	φ0.20
Decrease rate of section(%)	0	77.0	91.8	96.8	98.2
Drawn strain	0	1.5	2.5	3.4	4.0

原子炉：ＪＲＲ－３　　装置：ＲＥＳＡ（Ｔ２－１）　　分野：（その他）

exactly adjusting the tensile direction because the strong 110 fiber texture was evolved in the wire. Even in such a condition, the gauge volume was so small for the 0.2 mm wire ($0.47mm^3$) that the measuring time of 5.4 ks was needed to obtain an individual diffraction profile. The peak positions were determined by Gaussian curve fitting.

Figure 3 shows the (110) lattice plane strain as a function of the tensile stress, in which the data previously obtained for a patented pearlite steel [1] were also plotted. As has been made clear in ref. 1, the high strength of a pearlite steel, presumably up to 2 GPa is attributed to the stress partitioning between ferrite and cementite; work hardening due to phase stress. The cementite plate is estimated to bear more than 5 GPa and then the steel can achieve 2 GPa. Hence, as can be seen in Fig. 3, the lattice plane strain in the ferrite matrix stops to increase at approximately 0.004. Here, the volume fraction of cementite is about 0.14. A heavily drawn pearlite exhibits more than 5 GPa and then a question has risen why so strong and what is the strengthening mechanism. Figure 3 answers that the ferrite matrix itself is strengthened. As seen in the figure, the lattice plane strain goes up to 0.018; the elastic strain of 1.8% is extremely large value for steel. The residual strains for (110) in the drawing direction was - 0.0034 in compression so that the net tensile strain for (110) spacing is about 0.015, still extremely large. Another point to be noted here is the curve observed in Fig. 3. The curve obtained deviates from the linear relation after the strain of 0.011 or the external load of 2.5GPa. Nonlinear elastic relation seemed to be verified at extremely high stress actually.

The strength of 3.4 GPa in Fig. 3 is achieved for the ferrite in which the cementite plates were dissolved. Because the maximum strength for pure or low carbon steel subjected to sever deformation is less than 2 GPa at the similar deformation and 3 GPa at true strain of 10 (extremely sever deforamtion)[2], the present high strength is attributed to carbon atoms. It is, however, the dissolution mechanism and the location of carbon atoms after the dissolution are not made clear.

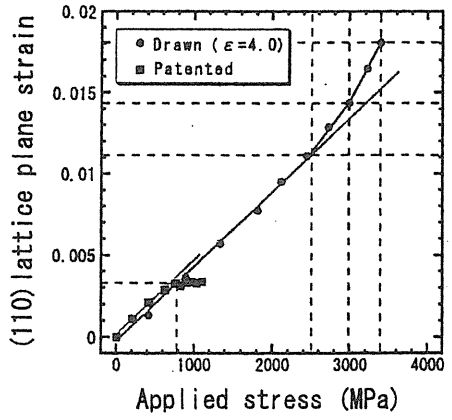


Figure 3: Lattice plane strain determined from (110) diffraction as a function of the external stress.

REFERENCES

1. Y. Tomota, P. Lukas, D. Neov, S. Harjo and Y. R. Abe: Acta mater. **51** (2003) 805.
2. H.Tashiro, Ph. D thesis, (1992) Tohoku Univesity.

研究テーマ：構造用材料の残留応力および負荷荷重下での材料特性評価
表　　題：引抜きフェライト鋼の残留粒界応力と超高強度の研究
1-9-9

Residual Grain Stress and Ultra-High Strength of a Heavily Drawn Ferrite Steel

Y. Tomota, M. Uno[1], T. Suzuki[2], A. Moriai[3], N. Minakawa[3] and Y. Morii[3]

Department of Materials Science, Faculty of Engineering, Ibaraki University, Hitachi, Ibaraki, 316-8511
1. Graduate student of Ibaraki University, Hitachi, Ibaraki, 316-8511
2. Research Center for Superplasticity, Ibaraki University, Hitachi, Ibaraki, 316-8511
3. Advanced Science Research Center, Japan Atomic Energy Research Institute, Tokai, Ibaraki, 319-1195

The utra-fine gained materials or nano crystals have recently been studied by many workers [1-3]. Some of them are made through very sever plastic deformation including ball milling, ECAP, ARB etc. The concept of continuous recrysatlization has been proposed. It is possible to give an extremely sever deformation to a mateiral by drawing, but little report has been made. The pearlite wire subjected to extremely sever deformation is another topic in hot discussion because the cementite dissolution takes place during deformation. The dissolution was first recognized in drawing and it is engineeringly important as a production of tire-code wire with higher than 4GPa. It is helpful to study ferrite wire and pearlite wire to compare their behavior under sever deformation and the mechanical properties of the deformed specimens. Therefore, the microstructural evolution and tensile behavior of drawn ferrte wires were studied.

The chemical compositions of a steel used are 0.008C, 0.01Si, 0.13Mn, 0.012P, 0.004S, 0.01Ni, 0.02Cr, 0.01Cu in mass%. The hot-rolled bars with 5.5 mm in diameter were drawn to several wires with diameters of 2.0, 0.73, 0.38 and 0.20 mm, true strains of 2.0, 4.0, 5.3, and 6.6, respectively, at the Kamaishi factory of Nippon Steel Co.

The Vickers hardness was plotted as a function of true strain in Fig. 1. The hardness increases with increasing of true strain. Stress-strain curves obtained by tensile test were

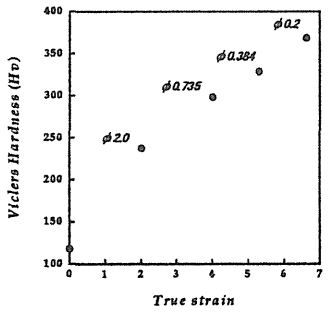


Figure 1: Hardness as a function of true strain given by the drawing.

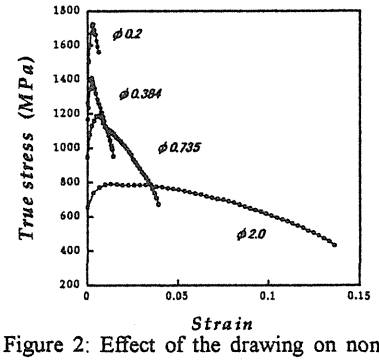


Figure 2: Effect of the drawing on nominal stress-strain curves of wires at room temperature.

shown in Fig. 2. As seen, strength increases but uniform elongation decreases with true strain. This is consistent with the stress-strain behavior observed in ultra-fine grained ferritic steels produced through mechanical milling and sintering, ECAP or ARB.

The lattice plane spacing was measured by neutron diffraction using RESA. Figure 3 shows

原子炉：ＪＲＲ－３　　装置：ＲＥＳＡ（Ｔ２－１）　　分野：（その他）

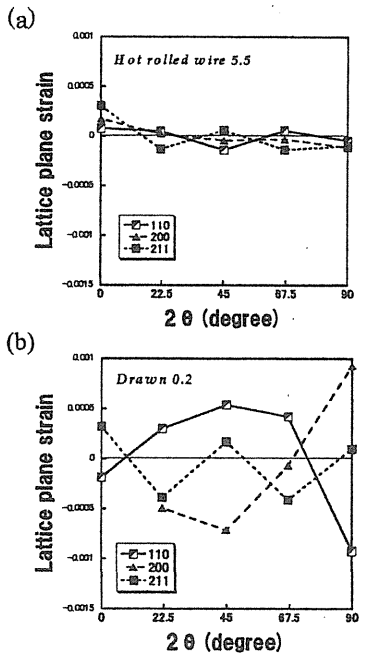


Figure 3: Residual lattice plane strains as a function of the angle with respect to the drawing direction.

the lattice plane strains of specimens measured in various directions for (110), (200) and (211). In hot-rolled samples (a), the dependence of the observing angle and (hkl) plane seems to be within an experimental error, i.e., no residual stress. However, the influence of the observing angle and (hkl) plane employed are obviously found in drawn wires with 0.2 mm in diameter (b). Such dependence is very similar to that found in a pearlite steel. It is hence made clear that the lattice plane strains, i.e., residual stresses, are remained after the drawing in a ferritic steel as well as a pealitic steel. This is a kind of classical concept of Heyn stress, that is, grain stress.

The residual stress was relieved by annealing. Figure 4 shows the influence of annealing temperature on lattice plane strain (annealing time: 3.6 ks). The residual stress was relaxed by recovery and/or recrystalization. Figure 5 shows the effect of annealing temperature on hardness. It is reported that only the grain growth occurs in an ultra-heavily deformed specimen because the continuous recrystallization took place during the deformation. The hardness behavior of the heavily drawn wires are similar to that of such grain growth.

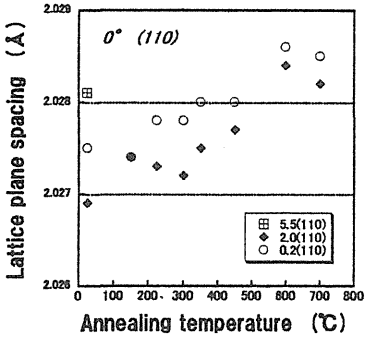


Figure 4: Stress relaxation behavior with annealing.

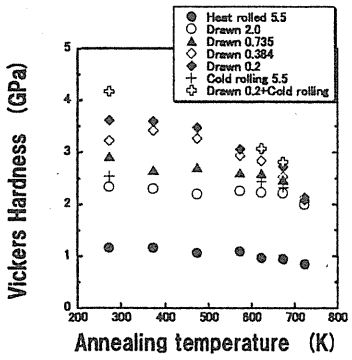


Figure 5: Influence of annealing on hardness.

The *in situ* neutron diffraction during tensile deformation was also performed using RESA. It is found the lattice plane stain of 0.007 was measured when 1.4 GPa was applied to a 0.2 mm wire. The present samples are therefore very suitable to study the ultra-fine grained specimens.

REFERENCES

1. K. S. Kumar, S. Suresh, M. F. Chisholm, J. A. Horton and P. Wang: Acta mater. **51** (2003) 387.
2. D. Jia, K. T. Ramesh and E. Ma: Acta mater. **51** (2003) 3495.
3. For example, S. Takaki: Materia (Japan) **41** (2002) 418.

研究テーマ：中性子回折法による焼入れ鋼の残留応力測定
表　題：中性子回折法による焼入れ鋼の内部残留応力測定
1-9-10

Inside Residual Stress Measurement of Quenched Steel by Neutron Diffraction Method

R.Mukai[1],D.Y.Ju[1],N.Minakawa[2],Y.Morii[2],and A.Moriai[2]

[1]Department of Material Science and Engineering, Saitama Institute of Tech, Okabe, Saitama 369-0293
[2]Advanced Science Research Center, JAERI, Tokai, Ibaraki 319-1195

The measurement of residual stress by the neutron diffraction method has difficulty in case of the material being thermochemical treated such as quenching, etc. As the factor, it is necessary to measure the non-distortion diffraction lattice spacing d_0[1]. Since the lattice spacing is variable depend on the composition and microstructure, d_0 is not uniform in the heat treated material in which various phase transformations were generated. In addition, since it changes also with fraction of the microstructure, the microstructure distribution must be sufficiently grasped in order to measure the residual stress with multiple microstructures.

This study measures residual stress in the cylinder steel with phase transformation after quenching using the equipment RESA (Residual Stress Analysis Equipment) installed at the JRR-3M of JAERI. Moreover, from metallo-thermo-mechanical theory, coupled simulation by finite element method is carried out, and the residual stress considering phase transformation is predicted. Then, the experiment results and calculated values are compared and examined.

The measurement principle is completely equal to diffraction method by the X-ray only one different point is it could get the internal distribution of three-dimensional stresses. By agreeing on the scattered neutron in striking the neutron on the material, the phase produces the resistant diffracted ray when next Bragg's the diffraction condition is satisfied.

$$\lambda = 2d \cdot sin\theta \qquad (1)$$

Here, λ is a neutron wavelength, d is the lattice spacing and θ is diffraction angle. Strain ε is required for by the following formula from lattice spacing d required from degree of angle of diffraction.

$$e = \frac{d - d_0}{d_0} = -cot\theta_0 \cdot \Delta\theta \qquad (2)$$

Here, d_0 and θ_0 are the lattice spacing and diffraction angle for non-distortion state. The peak position of the diffraction profile approximates the diffraction profile by Gaussian distribution, and it is determined by the center line.

In the neutron diffraction method, stress is required by the measurement of total strains in space, since the stress is not obtained only by measuring the uniaxial strain. For the analysis in cylinder coordinate system, from equation (2), the stress is required from the measured strains, when distortion ϵ_R of radius direction, distortion ϵ_H of hoop direction and distortion ϵ_A of axial direction were measured, in the following equations. Stress σ_R of radius direction is given by equations (3).

$$\sigma_R = \frac{E}{(1+\nu)(1-2\nu)}\{\epsilon_R(1-\nu) + \nu(\epsilon_H + \epsilon_A)\} \qquad (3)$$

Stress σ_H of hoop direction, stress σ_A of axial direction are also similar.

When calculating stress from the direction distortions using equation (3), Young's modular E and the Poisson's ratio ν are needed. There was the diffraction plane dependence in these, and in this study, the (110) plane was measured.

In residual stress measurement by the neutron diffraction method, it is necessary to measure d_0 lattice spacing of the non-distortion state. The material used ϕ 3 × 20mm cylinder of carbon steel S45C on the d_0 measurement test piece. And, in order to investigate the change of d_0 by quenching condition, four kinds of pieces of a quenching examination, normal, air-cooling, oil quenching, and water quenching, were used. In addition, the beam slit width is 20mm × 20mm.

The diffraction profile obtained in the measurement is shown in Fig.1. In the case of quenching, from this profile we could obviously see, the peak is shifting to low-angle side, and turns lower and wider simultaneously. This is regarded as the reason of the martensite phase transformation occurred by quenching. The measured results of θ_0 and d_0 for S45C in the neutron diffraction measurement is shown in Table.1. From these results, it is proven that considering the microstructure distribution is important for residual stress measurement in the quenching material.

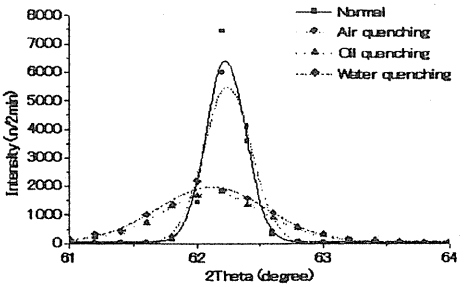


Figure 1: Diffraction profile.

原子炉：JRR-3　装置：RESA(T2-1)　分野：中性子散乱（その他）

Table 1: Physical properties value of (110) plane.

Measurement conditions and result Quenching condition	Wavelength λ (Å)	Non-distortion diffraction angle θ_0(deg)	Non-distortion diffraction lattice spacing d_0	Young's modular E(GPa)	Poisson's ratio ν
Normal	2.097210882	62.23787	2.028914	242.3	0.278
Air cooling	2.097210882	62.24275	2.028828	231.8	0.259
Oil quenching	2.096931247	62.12606	2.031986	222.6	0.236
Water quenching	2.097210882	62.10950	2.032745	217.8	0.221

The change of lattice spacing was measured by the neutron diffraction method, while tensile test was carried out. This time, a Young's modulus in the (110) direction is required, because to carry out the residual stress measurement of the cylinder was the (110) plane. And, Poisson's ratio was obtained from (110) and shrinkage percentage of the rectangular direction. Quenching condition and beam slit width of the measurement test piece are similar to the d_0 measurement. The measurement result is shown in Table.1. From the result, both Young's modulus and Poisson's ratio have lowered, as the cooling speed is rapider. The martensitic phase mainly produces this, and it is proven that the strength increases.

A cylinder test piece (Fig.2) was used as the specimen to the residual stress water quenching. Measurement points are the 6 points of 0,3,5,7,8.5,9.4mm from the center of the 30mm height. In addition, simulation using heat treatment analysis program COSMAP is also carried out in order to predict the microstructure distribution with the residual stress. Analytical model by the simulation used two-dimensional half model, which made central axis the symmetry. All node numbers are 2541, and all number of element are 2400. Condition of constraint fixed all nodes, which there was taking all nodes as X direction in central axis at the 30mm height in the Y direction. And, 3 edges except for the central axis were handled and were set as heat transfer boundary condition. Then, martensite distribution by simulation is Fig.3.

From the proportion of the martensite phase calculated by simulation analysis, d_0 E and ν were decided at the every measurement point. It is shown in residual stress measurement result Fig.4 of (110) direction by the neutron diffraction method of cylinder test piece. In the central part, from neutron diffraction measurement result, tensile stress is measured direction of 3 axes. However, with approaching on the surface, it becomes compressive stress in the axial direction. These are typical residual stress in the quenching material. From these results, it seems to improve the accuracy of residual stress measurement by the neutron diffraction method, if the distribution of the microstructure is grasped in detail.

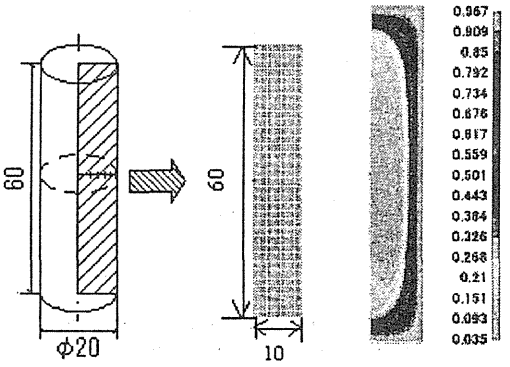


Figure 2: Measurement test piece and analysis model (unit mm).

Figure 3: Martensite distribution by simulation.

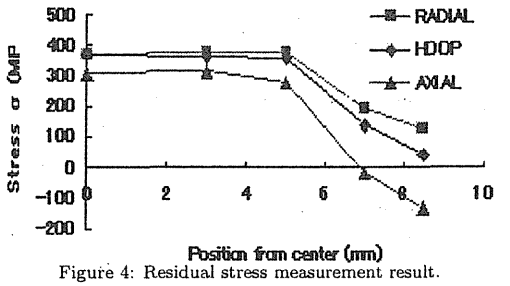


Figure 4: Residual stress measurement result.

In this study, d_0, E and ν by the difference between volume fraction of martensite phase were measured with the test piece after various quenching processes using neutron diffraction method. It was possible to clarify the relationship between microstructure and residual stress in the neutron diffraction method by introducing those values into residual stress measurement inside the material, and comparing with the simulation analysis result.

References

1) T. Saito, N. Minakawa, Y. Morii, T. Sasaki and Y. Hirose: J. Soc. Mat. Sci. Japan Vol. 50, No. 7, (2001) p.702

2. 中性子ラジオグラフィ

2. Neutron Radiography

This is a blank page.

研究テーマ：中性子ビーム利用技術の開発研究
表　　題：中性子ビーム利用技術の開発研究

2-1

中性子ビーム利用技術の開発研究

松林 政仁、片桐 政樹、[1]菊池 賢司、[2]柏木 美恵子
中性子利用研究センター,[1]大強度陽子加速器施設開発センター,[2]核融合工学部

1. シンチレーション検出器の開発

大強度陽子加速器施設の物質・生命科学実験施設に設置される中性子実験装置として提案するパルス中性子ラジオグラフィ装置では a)瞬間的な高強度中性子ビームを利用するストロボ高速度ラジオグラフィ及び b)中性子飛行時間(TOF)法を用いたエネルギー分析型中性子ラジオグラフィが可能となる。TOF エネルギー分析型中性子ラジオグラフィには高位置分解能を有した二次元シンチレーション検出器の開発が必要であり、特性の異なる二種類の波長変換ファイバーを互いに直交した X 及び Y 方向に配置してシンチレータからの発光位置を読み出す方式を提案し冷・熱中性子ラジオグラフィ装置のフィールドを使用してシステムの開発を行っている。信号処理系には光子計数法を採用しているが、位置分解能を向上させるためにさらに X,Y それぞれの方向で隣り合うファイバー同士でコインシデンスを取る方法を提案している。現状の方式での分解能は 0.5mm 程度が実験により確認された。シンチレータとしては ZnS:Ag、YSO をベースとして検討を進めているが、民生用の $Li_2B_4O_7$ 単結晶が輝度を除く発光特性に優れていることを実験的に確認できたため、中性子コンバータ材として ^{10}B を濃縮した $Li_2{}^{10}B_4O_7$ を製作し性能測定等の試験も開始した。

2. 鉛ビスマス循環ループ配管の非破壊検査

加速器駆動核変換システム ADS の核破砕中性子源として中性子収率の観点で優れさらに、未臨界炉における冷却材候補である鉛ビスマスターゲットが研究されている。材料の腐食を調べるために常温引き伸ばしシームレスタイプ SS316 配管が使用された鉛ビスマス循環ループが設置、運転されている。稼動時における鉛ビスマスは最高温度：450℃、温度差：50℃及び流速：約 1m/s となる。3,000 時間循環ループを稼動させた後、鉛ビスマスを貯蔵タンクへドレインし、ループから検査用サンプルを切り出した。熱中性子ラジオグラフィ装置を用いて透過画像撮影及び CT(computed tomography)撮影を行った結果、内部に残留した鉛ビスマスの様子を可視化することができた。実機の運転では鉛ビスマスにポロニウム等のような放射性物質が生成されることから取扱い上の重要な情報を与えるものである。

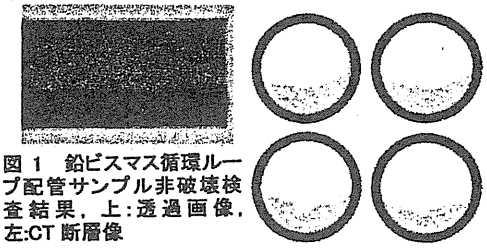


図 1　鉛ビスマス循環ループ配管サンプル非破壊検査結果，上：透過画像，左:CT 断層像

3. イオン源用電極の非破壊検査

検査を行った電極は厚メッキ法[注)]で製作された物で、ビーム加速実験の際にビームの一部が電極に当たり表面がスポット上に熔融したものから切り出した物である。表面が熔融していない個所について内部の健全性を確認するために中性子ラジオグラフィによる非破壊検査を行った。亀裂がある場合、発生個所として水冷溝、磁石溝に面する銅母材と厚メッキの接合面が考えられた。その際、亀裂の幅は数十ミクロン程度と予想された。冷・熱中性子ラジオグラフィを用いた透過画像撮影により、接合面での剥離が観察された。実機サイズの検査は撮影レイアウトの観点から困難と考えられるが、水冷溝、磁石溝に水を通すことで亀裂部にも水が浸透すると考えられることから、適切なコントラストエージェントが利用可能であれば実機サイズでも検査が可能であると考えられる。

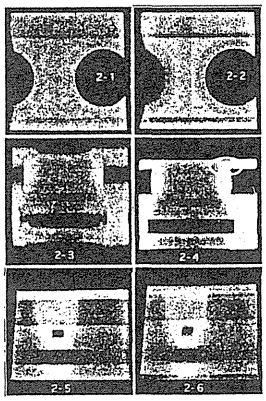


図 2 イオン源用電極サンプル非破壊検査結果，同一サンプルを方向を変えて撮影した。2-4 画像の楕円で囲まれた部分に剥離が確認できる。

注）銅溶剤の中に銅母材を入れ電界を制御することで銅を蒸着させる方法。水冷溝などを残したまま蒸着できるため、機械加工の必要が無いことが製作上の利点である

原子炉：JRR-3　　装置：TNRF, CNRF　分野：中性子ラジオグラフィ(熱水力)(その他)

研究テーマ：高時間分解能中性子ラジオグラフィ技術の開発と応用

表　　題：高時間分解能中性子ラジオグラフィ技術の開発と応用

2-2

高時間分解能中性子ラジオグラフィ技術の開発と応用

三島　嘉一郎、日引　俊、齊藤　泰司、松林　政仁[1]

京都大学原子炉実験所　原子力基礎工学研究部門

[1]日本原子力研究所　中性子利用研究センター

1. 緒言　現在、中性子ラジオグラフィは非破壊検査のみならず、様々な混相流計測に適用され、ボイド率や速度分布の計測に適用されている。一般には、時間平均ボイド率などの時間平均量の測定を目的としたものが多いが、近年、高速度撮像法の開発により、様々な熱流動現象が明らかにされつつある。しかし、これまでの、中性子ラジオグラフィ法の計測精度評価は、主として静止物体について行われており、高速で移動する物体についての計測精度評価はほとんどなされていない。このとき、計測精度評価には、撮像システムの残光特性を明らかにする必要がある。また、この残光特性は、パルス中性子源を用いたラジオグラフィの実現にとっても極めて重要な要素となっている。そこで、本研究では、撮像システムの残光特性の評価のために、1～10mm までの直径の穴を有した固体金属円板を中性子ラジオグラフィにより、可視化・計測し、撮像システムの残光特性が局所ボイド率測定誤差に与える影響を評価することにした。

2. 実験装置及び実験方法　**Fig.1** に試験部の概略を示す。試験部は SUS316 製回転円板（直径 100mm、厚さ 10mm）と直流モーター、ギヤボックスからなり、回転数は 0～350rpm まで変化させることができる。回転円板には、1～10mm までの直径の穴（穴の深さも変えた）をあけており、回転数及びシャッター速度を変化させて撮影を行った。撮影には高速度カメラを用い、撮像速度は 500fps とした。蛍光コンバータは、化成オプトニクス製 NR コンバータであり、現在開発中のNi含有量を変化させたコンバータも用いて実験を行った。

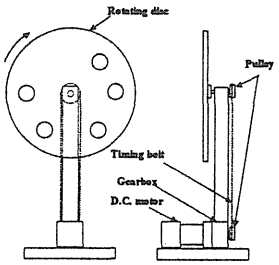


Fig. 1 Experimental Apparatus.

3. 結果 **Fig.2** に回転数 350rpm の場合の回転座標系における時間平均ボイド率分布を示す。図から、各模擬気泡の通過により、生じた残像が確認できる。さらに、**Fig.3** に周方向ボイド率分布を示す。図から、回転数の増加とともに残像の影響により、ボイド率分布が変化していることがわかる。このボイド率分布は、シャッター速度によっては、ほとんど影響を受けない。したがって、この残像は、蛍光コンバータによる残光特性によるものであることがわかる。このとき、局所ボイド率の測定誤差はピーク値の 20%に達し、中性子ラジオグラフィを高速現象に適用する場合には、コンバータの残光特性を考慮することが重要であることがわかる。

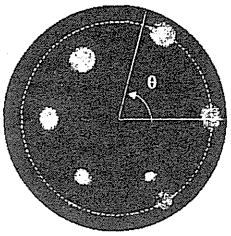


Fig.2　Time averaged void fraction profile. (rotatiing speed: 350rpm)

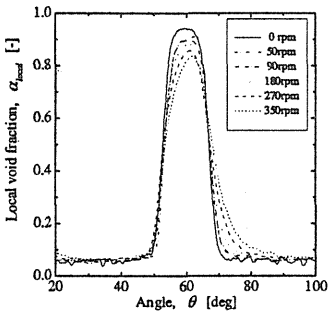


Fig.3 Tangential distribution of the time averaged void fraction.

4. 結言　1～10mm までの直径の穴を有した金属製回転円板を中性子ラジオグラフィを用いた可視化・計測を行い、回転座標系における時間平均ボイド率分布を求め、蛍光コンバータの残光特性による計測誤差を評価した。実験結果から、現在用いている撮像システムでは、蛍光コンバータの残光特性により残像が形成され、局所ボイド率の測定誤差は、20%にもなることがわかった。

原子炉：JRR-3　　装置：TNRF　　分野：中性子ラジオグラフィ（熱水力）

2-3 イオン伝導性固体材料中の水素ならびにリチウムの定量と拡散挙動の解明

Analysis of Hydrogen and Lithium in Ion Conducting Solid-State Materials

坂口裕樹[1)]，高井茂臣[1)]，松林政仁[2)]，江坂享男[1)*]

Hiroki Sakaguchi[1)], Shigeomi Takai[1)], Masahito Matsubayashi[2)], and Takao Esaka[1)*]

鳥取大学工学部物質工学科[1)]

日本原子力研究所[2)]

1．序論

これまでに，われわれは中性子ラジオグラフィー(NRG)を用いて，セラミックスや合金中のイオンの分布とその挙動を調べてきた．しかしながら，中性子ラジオグラフィーで得られるのはあくまで試料の投影像であるため，中性子線の照射方向に存在するすべての元素の減衰係数が画像の濃淡に寄与し，解析が複雑になるという問題があった．そのため，この手法に用いることのできる試料は，照射方向のリチウムイオン分布が均一である必要があり，照射方向に不均一であるような試料の精密な測定は不可能であった．そこで，本研究では中性子断層撮影法に注目した．断層撮影法（CT: Computed Tomography）は，観察対象の内部構造を非破壊で可視化する技術のひとつである．この方法を利用することによりイオン伝導性セラミックスあるいは水素吸蔵合金の断層像を得ることができ，その像に現れている元素の分布から，導電イオンあるいは吸蔵水素の挙動を解析することができる．

リチウムはその質量数が異なると，中性子減衰係数が大きく異なるという性質を持つ．^{7}Li はほとんど中性子を減衰しないが，^{6}Li は高い中性子減衰係数を持つ．したがって，^{6}Li のほかに中性子減衰係数の大きな元素を持たない試料に対して，中性子断層撮影法を用いて試料中のリチウムイオンの分布を観察することができる．そこで，リチウムイオン伝導性酸化物焼結体に対して，この手法の適用を試みた．

一方，われわれのグループはこれまでに，NRG を用いることで，水素吸蔵合金中の低濃度水素を，その存在を確認した(可視化)上で定量できることも示してきた．本研究ではこれをさらに発展させ，次世代の水素吸蔵合金として期待されている Mg-Ni 系合金(Mg_2Ni および Mg_3Ni)中への水素吸収の初期過程について調べた．さらに，これらの合金が水素化物を生成した際における両者の性状の違い(粒子サイズや相状態)を明らかにすることで，固溶状態から水素化物形成にいたるまでの一連の水素吸蔵過程を評価した．

2．実験

2．1　試料調製

2．1．1　リチウムイオン伝導体 $Li_{1.33}Ti_{1.67}O_4$

実験には，スピネル型構造を持つリチウムイオン伝導体 $Li_{1.33}Ti_{1.67}O_4$ を用いた．試料調製は通常の固相反応法を用いた．粉末状の Li_2CO_3，TiO_2 を化学量論比で混合し，円柱状のペレットに成形し，電気炉中で仮焼した．その後粉砕し，円柱状または円錐状に成型して焼成した．試料の底面を鏡面研磨し，片方の面にのみ金ペーストを薄く塗布し，600℃で 2 時間，空気中で焼き付けて電極とした．

^{6}Li のみを含む円柱状試料と ^{7}Li のみを含む円柱状試料を組み合わせた面接触電解試料，および，^{6}Li のみを含む円錐状試料と ^{7}Li のみを含む円柱状試料を組み合わせた点接触電解試料を用いて，^{7}Li のみを含む試料がカソード側になるように電気炉にセットし，電解を行った．電解は 5V の定電圧で行い，温度は 800℃，通電量は 200C で行った．

2．1．2　Mg-Ni 系水素吸蔵合金

測定にはアーク溶融法で合成した Mg_2Ni および Mg_3Ni (Mg_2Ni と Mg の共晶) を用いた．この合金を所定の大きさ（数ミリ角の長方体）に整形し，2.6M $NaBH_4$ 水溶液を用いて水素化処理を施した．合金中の水素の拡散挙動を調べるため，水素化処理時間を様々に変えた試料を用意した．

２．２　NRG 測定

電解後のカソード側の円柱状試料あるいは水素を吸蔵させた合金の長方体を中性子断層撮影に用いた．測定は日本原子力研究所の 3 号原子炉施設内の中性子断層撮影実験装置で行った．

３．結果と考察

３．１　リチウムイオン伝導性セラミック中のイオン分布

撮影された投影像の一例を図１に示す．この図は点接触電解試料のカソード側の像である．投影像では，画像は中性子線の減衰が大きいほど暗くなる．試料の上部に他の部分に比べて暗い部分が見られるのは，この部分に中性子を減衰する元素が存在する為である．これは，アノード側に存在していた ^6Li が，電解することによりカソード側に侵入したことを明らかに示している．

これらの投影像から再構成した点接触電解試料中央部の断層像を図２に示した．投影像とは逆に，断層像は中性子線の減衰が大きいほど明るくなる．したがって ^6Li の侵入した部分は他の部分に比べて明るくなるはずである．ややわかりにくいが，試料の内部では中心部分がやや外側よりも明るくなっているように見える．画像の濃淡差をよりはっきりさせるために，画像の濃度を数値化した結果を図３に示した．これは，試料の中心からの距離に対する画像の濃度のプロファイルである．白化度 (White level) で示した縦軸の値が大きいほど画像が明るい，すなわち ^6Li の濃度が高いことを示している．このプロファイルから，点接触電解試料では，試料の中心部分にのみ ^6Li が侵入していることがわかった．面接触電解した試料に関しては，図には示していないが，プロファイルは平坦で，試料全体にわたってリチウムが侵入していることがわかった．また，点接触電解試料中の，リチウムの山形の分布は，試料中に形成される電場が，通常の金属導体中の電場と同様に形成されることを示している．このように，中性子断層撮影法を用いることで，イオン伝導性酸化物焼結体中のリチウムイオンの分布を初めて可視化することができた．

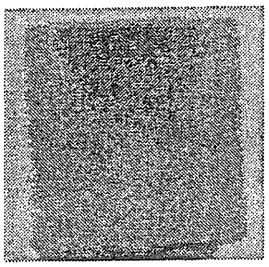


図１　点接触電解試料の投影像

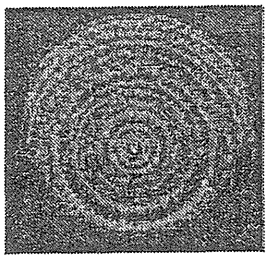


図２　点接触電解試料中央部の断層像

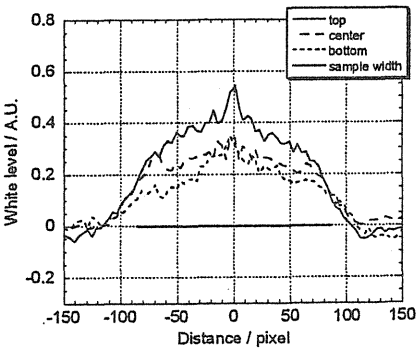


図３　点接触電解試料の断層像の濃度プロファイル

３．２　水素吸蔵合金中の水素分布

図４に水素化処理を施したMg_2Ni塊状試料に対す

るNRG測定の結果の一例を示す．上部の図がNRG像であり，白い部分は水素の存在していることを示している．また，像中の白線で示した部位について，像の濃淡の違いを数値化したもの（黒化度）を下部に示した．

様々な時間で水素処理を施した試料に対して，それぞれ水素浸入深さを見積もり，水素化時間を関数としてまとめたものが図５である．この図は，水素が金属平板へ吸収される場合を想定した拡散モデル（水素浸入深さ＝(拡散係数×時間)$^{1/2}$）に基づいて表したものである．多少ばらつきがあるが，これが直線関係であるとしてその傾きから導いた水素拡散係数(23℃)は，Mg_2NiおよびMg_3Niについて各々，1.6×10^{-7}および2.2×10^{-7} cm^2s^{-1}であった．両合金中の水素拡散係数はほぼ一致していることがわかった．このように，NRGを用いると，合金への水素の初期吸蔵過程における拡散挙動を定量的に評価できることが示された．

一方，水素浸入深さと水素吸収層の厚さの関係（水素吸収による合金の膨張率）をみてみると，図６に示すように，二つの合金の傾向は大きく異なっていた．すなわち，吸蔵水素濃度が低い時点においては，Mg 量の多い合金は大きく膨張しても破壊されにくいものであることがわかった．これは，Mg_3NiはMg_2Ni と Mg の共晶であることから，Mg 金属の存在が試料塊のじん性を高めていることに起因すると考えられる．

次に，水素化物を形成する際における両合金の性状の違いを，粒子サイズや相状態の観点から調べた．水素吸蔵-放出サイクル前後の粒子サイズの変化をみてみると，上述の水素化初期過程からの予想に反して，Mg量の多い合金の方が粒子径がより小さくなっていることが明らかになった．水素化された試料をX線回折で調べてみると，Mg_2Niの水素化物が形成されているだけでなく，Mgも水素化物となっていることが確認された．これらのことから，Mg量の多い合金の組織は，結晶粒の小さいMg_2NiをMg相がつなぎとめているものであると推測できる．水素化初期の段階ではまだMg相がつなぎとして働いているが，吸

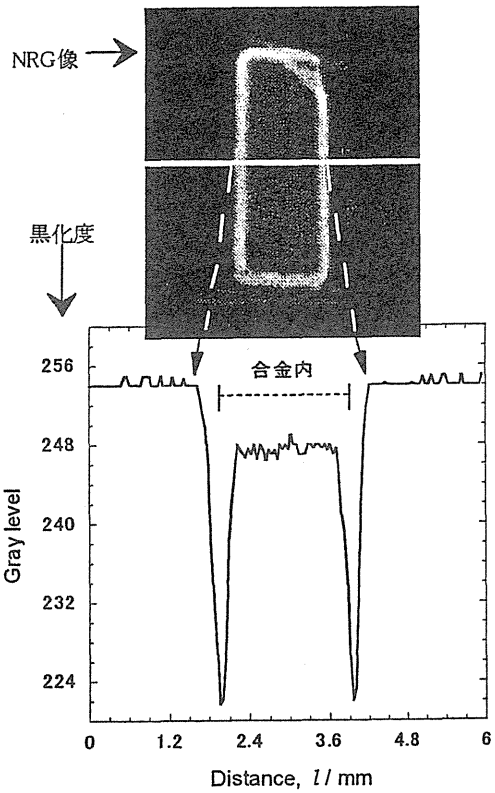


図４　水素化処理を施したMg2Niの
NRG像と黒化度
（像中の白い部分に水素が分布しており、
濃度が高いほど黒化度は低い）

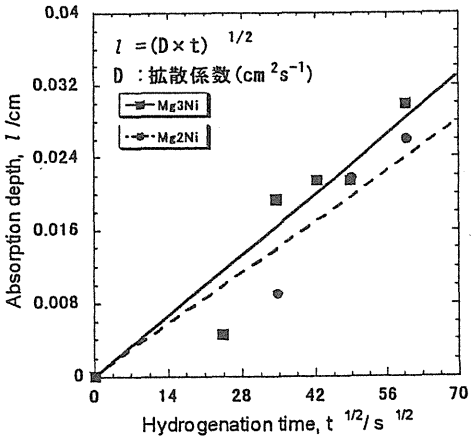


図５　水素化処理時間に対する
水素浸入深さの関係

蔵水素濃度が高くなるとMgが水素化物となるためつなぎの役割を果たせなくなり，一気に微粉化が進行したものと考えられる．

以上のように，従来の方法に加えて中性子ラジオグラフィーを用いると，固溶状態から水素化物形成にいたるまでの一連の水素吸蔵過程を評価できることがわかった．

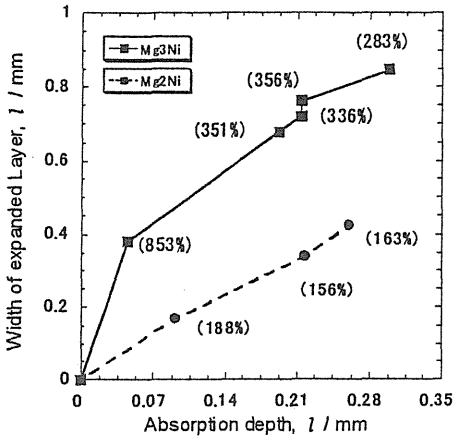


図６　水素侵入深さと
水素吸収層の厚さの関係

４．成果の公表

1) Analysis of Lithium Ion Distribution in Electrolyzed Li1.33Ti1.67O4 by Neutron Computed Tomography, T. Esaka, M. Hayashi, H. Sakaguchi, S. Takai, and M. Matsubayashi, *Solid State Ionics*, 147 (2002) 107-114.

2) Analysis of Hydrogen Distribution in Hydrogen Storage Alloy Using Neutron Radiography, H. Sakaguchi, Y. Satake, K. Hatakeyama, S. Fujine, K. Yoneda, M. Matsubayashi, and T. Esaka, *Journal of Alloys and Compounds*, 354 (2003) 208-215.

研究テーマ：中性子利用技術に関する開発研究
表題：中性子ラジオグラフィによる生体組織の画像解析

2-4

中性子ラジオグラフィによる生体組織の画像解析

武田 徹，土屋佳則[1]，松林政仁[2]，呉 勁，ティティルイン，米山明男[3]，板井悠二
筑波大学臨床医学系，[1]芝浦工業大学先端工学研究機構，
[2]日本原子力研究所中性子利用研究センター，[3]日立製作所基礎研究所

本研究では生体試料に対して中性子ラジオグラフィを適用し，X 線マモグラフィと比較することで，中性子によりどのような特異的な情報が得られるかを検証する．また，骨の中性子 CT 撮影により加齢による骨の変化の観察を試み，さらに造影物質を用いたイメージングの可能性を知るため，ガドリニウム造影剤を封入したファントムの中性子 CT 撮影によりその造影効果を検証し，これらの実験を通して中性子イメージングが医学目的に応用できる可能性を考察するとともに将来の新薬開発や医療診断，治療技術に対する基礎的な情報を得ることを目的とする．

生体組織としてホルマリン固定した癌組織（VX-2)を含むウサギ肝臓切片，ウサギ，8 週および 104 週齢のラット骨，また MRI 用 Gd 製剤封入ファントムの中性子ラジオグラフィ撮像を JRR-3M に設置の熱，冷中性子ラジオグラフィ装置 TNRF，CNRF にて実施した．中性子イメージングプレートを用いた中性子吸収像撮影の露光時間は熱，冷中性子でそれぞれ 2 秒と 2.4 秒，CT 撮影では熱中性子ラジオグラフィ装置で冷却 CCD カメラを使用し，試料を 1 度ステップで 180 度回転させ，1 ステップ 3 秒，180 プロジェクションの撮影とした．

厚さ約 2mm のウサギ肝臓切片の中性子ラジオグラフィ像では図 1 に示すようにX線マモグラフィよりも良好に正常，癌組織の弁別ができ，特に冷中性子ラジオグラフィでコントラストのよい画像が得られ，血管も 100 μm 程度の直径まで描出された[1,2]．骨の中性子 CT では，X 線イメージングでは観察不可能な内部の軟部組織が骨表面と明瞭に区別して観察でき，さらに加齢により骨の水分が減少することが示唆された．Gd 造影剤ファントムではその濃度による CT 値の変化が観測でき，蒸留水に比較しても十分なコントラストがつくことから水分を多く含む生体試料においても造影効果が期待できる結果が得られた．本研究により，小型の試料に対しては生体組織観察が可能であることが判明した．

参考文献

1) Y. Tsuchiya, M. Matsubayashi, T. Takeda, Thet Thet Lwin, Jin Wu, A. Yoneyama, A. Matumura, T. Hori, Y. Itai: Jpn. J. Appl. Phys., 42 (2003), 印刷中.
2) 土屋佳則，松林政仁，呉 勁，ティティルイン，米山明男，松村 明，堀 富栄，武田 徹: 断層映像研究会雑誌，投稿中.

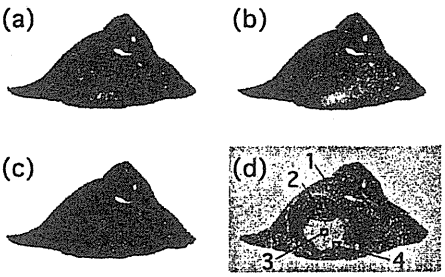


図 1. 厚さ約 2mm の癌組織を含むウサギ肝臓切片（横幅約 3cm)．(a)：熱中性子ラジオグラフィ，(b)：冷中性子ラジオグラフィ，(c)：X線マモグラフィ，(d)：切片写真（HE 染色）．1：正常組織，2：癌組織，3：硝子様変性，4：癌周辺組織．

原子炉：JRR-3　装置：TNRF，CNRF　分野：中性子ラジオグラフィ（医学）

2-5 中性子ラジオグラフィによる固気二相流の定量評価

Qualitative Measurements of Gas-solid Two-phase Flow by using Thermal Neutron Radiography

関西大学工学部 梅川尚嗣 小澤守 古井秀治 林幸一 大島圭裕 都築雅和

Hisashi UMEKAWA, Mamoru OZAWA, Shyuji FURUI, Kouichi Hayashi, Masakazu Tsuzuki and Yoshihiro Oshima, Kansai University.

研究背景

流動層は低品位炭，廃棄物，RDF などの燃焼が可能である上，Thermal-/Fuel-NOx, SOx などの排出抑制が比較的容易に行えるという利点を有している．特に，近年では今後のエネルギー供給事情から不可避である石炭利用技術の一つとして注目を集めている加圧流動層燃焼(PFBC)や石炭ガス化複合発電(IGCC)の関連技術として重要なものと認識されている．

この流動層は，粉体下部から気体を流すことで粉体を擬似流体状に保つ技術であり，固気相間の界面面積の多さ，粉体のもつ熱容量の大きさ，粉体の滞留時間の長さなどに起因して高い反応性と伝熱特性を有する．このため，流動層の伝熱・流動特性を把握するには層材挙動を把握することが重要となる．

充填された粉体層の内部状態を把握するためには，可視化技術が有用であり，これまでにもさまざまな手法がとられている.これらの可視化手法のなかで中性子線を用いた本研究と類似のものとしてはX線を使ったものがあげられる． しかし，X線ではその透過特性・装置特性に制限され十分な情報が得られているとは言えない．特にX線では原子番号に減衰係数が依存するため減衰係数の高い物質は必然的に質量が大きくなる．このため，質量差によりセグレゲーションが発生する流動層では，本研究で採用している層材へのトレーサー混入や層材のマーキングといった手法はX線では用いることができない．

以上のように，中性子線の特性を利用し他手法では得られなかった流動層内の層材特性を得ることが本研究の目的である．

研究内容

本報告書の対象期間では二成分系流動層で発生する偏析挙動の動的評価，CT 法によるバンドル型垂直流動層熱交換器周りの水平断面ボイド率分布特性，垂直型流動層熱交換器周りのボイド率分布，サブチャンネル流路での流動層層材混合特性などの検討をおこなったが，本報告では垂直型流動層熱交換器周りのボイド挙動特性を中心に述べる．

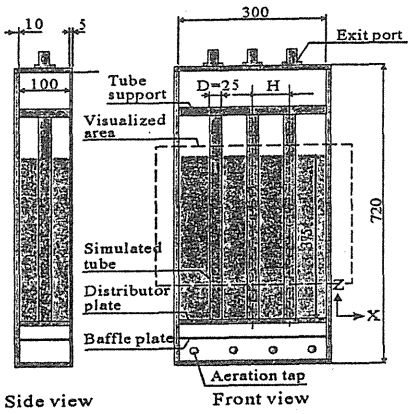
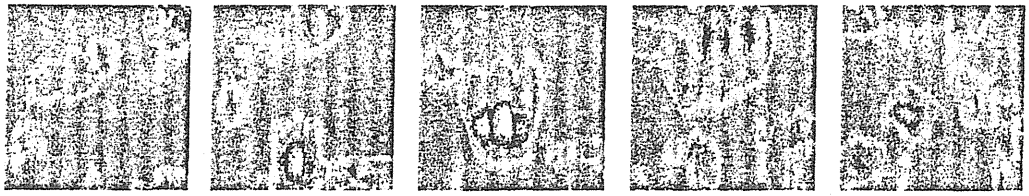


Fig.1 Test section

本実験では，図１に示す模擬伝熱管を流動層内に一列に配置したテストセクションを使用した.本装置は中性子に対して透過性の高いアルミニウムで作成されている．使用した流動層層材は SiO_2 を主成分とするけい砂であり Geldalt による分類ではＡ粒子とＢ粒子に分類される(それぞれ，平均粒子径 62, 218μm,粒子密度 2310, 2555kg/m^3).

実験ではこの流動層下部より，コンプレッサーからの空気を臨界ノズルにより所定の流量に調整して流入させる．こうして流動化させた状態を，中性子ラジオグラフィにより可視化する．可視化画像は SIT 管カメラにて撮影し，VTR に 30(フレーム/秒)で録画を行い，この画像に対して画像処理を施すことで種々の定量評価を行った．



1/30 sec　2/30 sec　3/30 sec　4/30 sec　5/30 sec

Fig.2 Flow pattern in B-particle bed (H/D=1.2, J_G=0.17 m/s)

実験結果ならびに成果の概要

図2は図1の装置を流動化状態に保って可視化・録画した結果を，画像処理によりボイド率分布に換算したものである．図中白い部分が気泡に相当する．ここでは詳細は割愛するが，本研究ではこれらの画像から求まる気泡の移動軌跡から従来報告例がなかった垂直管群周りでの気泡上昇特性を明らかにし，気泡挙動が管群の挿入により強く拘束されることを示した．

以上の他にこれらの画像をもちいて行った定量評価の例から，ボイド率，気泡上昇速度，気泡径に関する結果の一例を図3～6に示す．

図3は気泡径と流動化速度を整理したものであり，本研究の成果として提案した修正 Mori-Wen の計算値を併記している．修正式は H/D=3.0 で若干気泡径を大きめに予測するなどの傾向も見られるが，おおむね実験値とよい一致を示していることがわかる．

修正 Mori-Wen 式で計算された気泡径を用いて気泡上昇速度に対する整理式を求め，実験値との比較を行ったものが図4である．なおこの整理式は気液二相スラグ流における大気泡上昇速度を与える

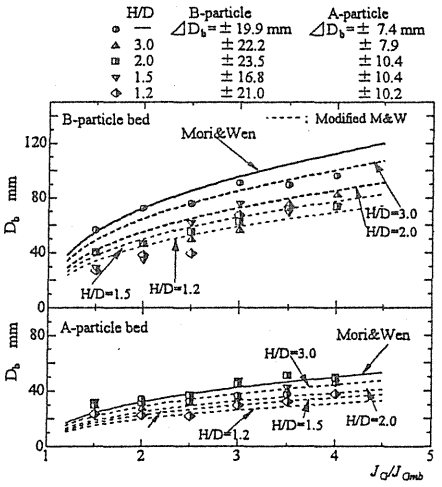


Fig.3 Equivalent bubble diameter

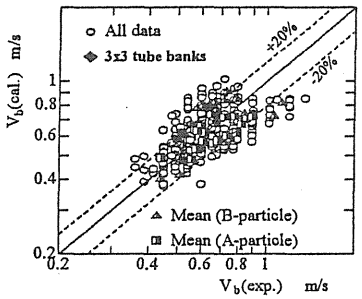


Fig.4 Correlation of equivalent bubble diameter

Nicklin の式にならって Davidoson らが行った気泡上昇速度に関する整理を踏襲して求めたものであるが，係数は本実験結果を元に求めなおしている．

次に,Zuber-Findlay によるドリフト-フラックスモデルを空隙率の推算に用いることを考える.まず，分布パラメータ，ドリフト速度を実験結果に基づいて決定するために図5を作成する．また，図ではドリフト速度を推算するために Ergan の流動化開始速度推算式を応用して求めた値を図中に破線で示している．本系では図中の線の勾配で求まる分布パラメータは流動層層材によらず 1.6 で整理された．また，層材により異なるドリフト速度は先の Ergan の式に基づく計算で概略求まることが判る．

図5で求まった各パラメータを用いて，ドリフトフラックスモデルに基づき計算したボイド率を実験値と比較したものが図6である.なお，ここで用いたドリフト速度は Ergan の式に基づいて計算で求

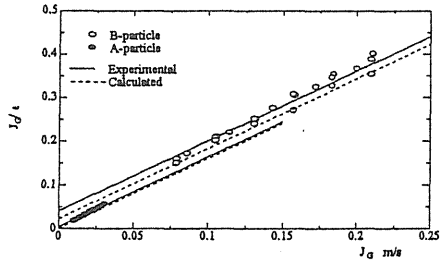


Fig.5 Weighted mean gas velocity

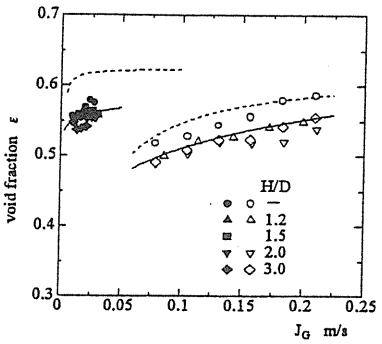


Fig.6 Void fraction by drift flux model

めた値を使用している．こうして求まった値が，図中破線で示されている．計算値は，実験値とは若干差があるものの，データの整理は十分可能でありドリフトフラックスモデルに基づく考え方が大筋で間違っていないことが判る．

総括

以上，今回の研究で示された結果の一部を報告した．なお，始めに述べたように流動層の可視化に関して中性子ラジオグラフィは他の手法にたいし大きな利点を有しており今後も成果が期待される．

成果の公表

1. 古井秀治,梅川尚嗣，林幸一，小澤守，流動層内の層材循環の可視化と画像計測，日本混相流学会年会講演会 2001 講演論文集(2001), 239-240.
2. H.Umekawa, M.Ozawa, S.Furui, K.Hayashi, Quantitative Measurement of Fluidized bed by using Neutron /X-ray Radiography, 3rd Int. Sympo. Measurement Techniques for Multiphase Flow, Fukui (2001), 121-128.
3. 古井秀治，梅川尚嗣，林幸一，小澤守，中性子ラジオグラフィによる流動層内セグレゲーション過程の可視化,第 7 回流動層シンポジウム(2001), 443-448.
4. 都築雅和，小澤守，梅川尚嗣，竹中信幸，古井秀治，大島圭裕，流動層内垂直管群周りの伝熱・流動特性，日本混相流学会年会講演会 2002 講演論文集(2002), 33-34
5. M.Ozawa, H.Umekawa, S.Furui, K.Hayashi and N.Takenaka, Bubble Behavior and Void Fraction Fluctuation in Vertical Tube Banks Immersed in a Gas-solid Fluidized-bed model, Experimental Thermal and Fluid Science, Vol.26 (2002), 643-652.
6. S.Furui, H.Umekawa, K.Hayashi, M.Ozawa and N.Takenak, Flow Visualization of Segregation Process in a Fluidized Bed by Neutron Radiography, 7th World Conf. on Neutron Radiography, Rome (2002), 154.
7. H.Umekawa, S.Furui, K.Hayashi, M.Ozawa and N.Takenaka, Void Fraction Characteristics in a Fluidized Bed with Vertical Tubes, 7th World Conf. on Neutron Radiography, Rome (2002), 122-123.
8. 梅川尚嗣，古井秀治，小澤守，垂直型流動層熱交換器内部の層材挙動の可視化，中性子ラジオグラフィ高度技術の開発と応用 KURI-KR-84 (2002), 21-30.
9. 都築雅和，大島圭裕，古井秀治，竹中信幸，梅川尚嗣，小澤守，流動層内垂直管郡周りの伝熱・流動特性，2002 年度熱工学講演会講演論文集(2002), 251-252
10. 梅川尚嗣，古井秀治，小澤守，中性子ラジオグラフィによる流動層熱交換器内ボイド率分布の三次元計測，関西大学工学会誌，Vol.12 No.4 (2002), 1-4.
11. 梅川尚嗣，古井秀治，小澤守，竹中信幸，中性子ラジオグラフィによる垂直形流動層熱交換器周りのボイド拡散挙動の可視化，日本中性子科学界第二回年会講演概要集 (2003), 79
12. 古井秀治，梅川尚嗣，小澤守，竹中信幸，中性子ラジオグラフィによる流動層内垂直管郡周りにおける気泡挙動，日本中性子科学会第二回年会講演概要集 (2002), 81.
13. 古井秀治，梅川尚嗣，林幸一，小澤守，竹中信幸，流動相熱交換器内に配置された伝熱管周りの気泡挙動，機論 B，Vol.68 No.676 (2002), 3432-3438.
14. 古井秀治，都築雅和，梅川尚嗣，小澤守，竹中信幸，垂直型流動層熱交換器周りの空隙率・熱伝達率分布特性，第 40 回伝熱シンポジウム講演論文集，Vol.2 (2003), 577-578.
15. 小澤守，流動層燃焼炉/反応炉における熱流動の数理モデル構築に関する研究(ホットモデルにおける実時間可視化画像計測と構成関係式の同定) 課題番号 11450091，平成 11 年度～平成 13 年度科学研究費補助金(基盤研究(B)(2)) 研究成果報告書，(2003)

研究テーマ：蛇行細管ヒートパイプの熱輸送性能と内部流動体挙動の相関にかかる実験的研究

表　　題：振動流型ヒートパイプの中性子ラジオグラフィによる可視化実験

2-6

振動流型ヒートパイプの中性子ラジオグラフィによる可視化実験

遠山　伸一、二俣亮介、永井大樹、松林　政仁[1]

宇宙航空研究開発機構

[1]日本原子力研究所東海研究所

1．目的および背景

将来の衛星や宇宙機では小型高性能化の要求が高まっており、バス系としての熱制御素子にはこれまで以上の高発熱機器の高密度実装化への対応が要求されることが予想される。振動流型ヒートパイプ（Oscillating Heat Pipe、以下 OHP と言う。）は民生分野では開発が進み有力な熱制御素子になりつつあり、現在は宇宙適用のための研究開発が進んでいる。[1)] 本可視化試験は、設計指針の確立の一環として、熱負荷量や加熱箇所による温度推移を測定しながら OHP 内部の作動流体の挙動や熱負荷との関係を明らかにすることが目的である。

2．OHP の特徴

OHP は内面にウィック加工を必要としない細管からなるもので、図１のように、熱輸送はヒートパイプと異なり冷媒の振動で行われる。そのため、非凝縮性ガスによる性能劣化の問題が少なく、構造が簡単なので高い生産性が期待できる。また熱輸送能力も高く、重量に関してもヒートパイプより数倍軽量である。平板などで構成されるため衛星の設計自由度の増大も期待できる。

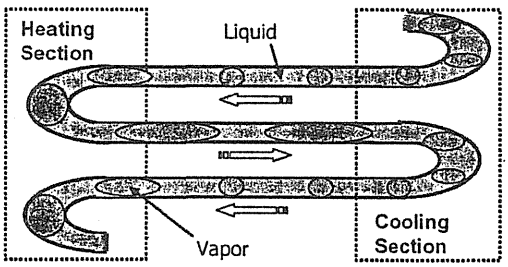


図１

しかしながら、OHP の開発実績は殆ど地上用途に限られており、その動作原理の明確化や熱輸送距離等の性能向上のための研究は今後の課題でもある。軌道上の試験としては、2002 年に NASDA の技術研究本部（現 JAXA 総合技術研究本部）が開発した小型衛星（μ-LabSat）にサブスケールモデルを搭載して軌道上評価実験を実施しており、現在データ解析が進行中である。[1)]

3．可視化実験

熱流体を利用した熱制御素子では、伝熱流動現象を理解するために内部流体の挙動を把握することが重要である。本研究では、研究用原子炉 JRR-3 の熱中性子ラジオグラフィ装置を用いて可視化実験を行った。供試体はビデオシステムの直前に設置しており、供試体内部に封入されている冷媒を構成する水素により中性子が散乱されることで、内部冷媒の挙動が画像化される。図３に供試体のセットアップ状態を示す。この図は、上部に加熱部を設けた場合であり、放熱は加熱部以外の自然冷却によっている。

今回使用した供試体をその断面とともに図３に示す。材質はアルミであり、供試体の厚みは 2mm と非常に薄いが、内部には 120 ターンの細管が一筆書きのように通っている。細管の直径は 1.5mm で間隔は 2mm おきに配置されている。ま

原子炉：JRR-3　　装置：TNRF　　分野：中性子ラジオグラフィ（航空・宇宙）

た冷媒としてHFC-134aが飽和状態で封入されている。

4．試験結果

試験結果の典型的な温度プロファイルを図4に示す。また、一例として可視化結果写真を図5に示す。試験条件は、上部加熱で熱負荷は60Wで行った。可視化結果では液相の速い振動と流路間隔一本ごとのゆっくりとした上昇が60Wまで確認された。下部加熱での可視化結果は上部加熱とほぼ同様であり、限界熱入力量の違い以外に差はあまり見られなかった。いずれの試験条件においても可視化結果では管路方向に気液の速い振動と10秒から40秒程度の周期の管路全体にわたる振動が見られる。この全体的振動は温度プロファイルに見られる周期的な温度変動にほぼ一致している。

今回の可視化写真では、典型的な流動パターンが確認されたが、不明瞭な点も残っている。これは気液の振動が速いことと流路が非常に小さいことに起因する。従って、ボイド率など定量的な判断を行うには実験手法および装置の改良が必要である。

5．まとめと今後の予定

今回の中性子ラジオグラフィ実験により、熱入力条件、設置条件などによって変化する典型的な流動パターンが複数確認できた。今後、温度挙動と流動との相関や設置形状による振動周期などの系統性からOHPの熱輸送性能についての定性的・定量的な検討を進める予定である。

参考文献

1）岡本　篤, 二俣亮介： 第47回宇宙科学技術連合講演会講演集,(2003),pp.894-896

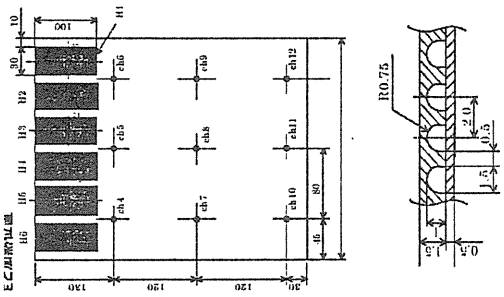


図3

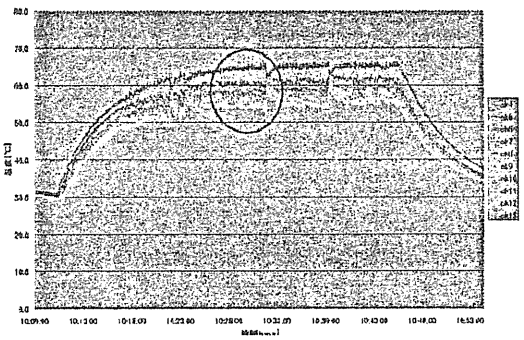


図4

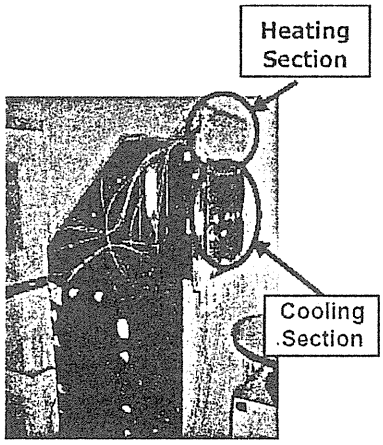


図2

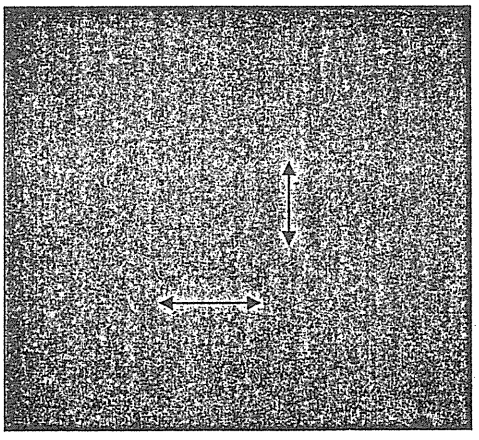


図5

2-7
中性子寿命の精密測定

Precision Measurement of the Neutron Lifetime

高エネルギー加速器研究機構	真木晶弘	Akihiro Maki, KEK
高エネルギー加速器研究機構	前澤秀樹	Hideki Maezawa, KEK
高エネルギー加速器研究機構	安見真次郎	Shinjiro Yasumi, KEK
立教大学 RCMAS	坂本泰伸	Yasunobu Sakamoto, Rikkyo Univ.
佐賀大学理工学部	小林茂治	Shigeharu Kobayashi, Saga Univ.
東京家政大学短期大学部	稲垣洋輔	Yosuke Inagaki, Tokyo Kasei Univ.
筑波大学物理工学系	森　茂樹	Shigeki Mori, Univ. of Tsukuba

はじめに

中性子は陽子、電子とともに、宇宙の全ての物質の構成要素であると言う意味において、最も基本となる粒子である。また、宇宙の創成期における、元素合成の過程にあって、その寿命は陽子との存在比を決定する重要なパラメーターである。すなわち、中性子の寿命を精度良く知ることは、宇宙創成期の元素合成のメカニズムの解明にとって、決定的な重要性を持つ。このことは、もう少し後の、恒星内における核融合反応の解明（重い元素の合成およびエネルギー放出）についても言える。

中性子の寿命は宇宙物理学のみではなく、素粒子物理学においても重要な役割を担う。原子核の崩壊の原因たる弱い相互作用の結合常数の決定についても重要な物理量である。中性子という最も単純な原子核を用いる事により、原子核効果からくる不確定性を最小に押さえる事が可能となる。

中性子寿命の測定は、近年、超冷中性子の発明などにより長足の進歩を遂げたが、物質との相互作用などに不確定性を残し、系統誤差の入りくむ余地を残している。現に、異なる測定間には 1%程度のばらつきが見られる。

この状況を改善するため、われわれはまったく新しい、単純な（従って系統誤差の可能性の少ない）測定方法を考案した。過去の中性子ビームを用いた測定では、中性子崩壊の頻度と中性子ビームの強度は独立に測定されていたため、それぞれに絶対測定を必要とした。特に、中性子の崩壊空間と測定効率の決定は困難であった。

新しい測定方法では、中性子の通過空間（崩壊が起こる空間）に少量の ^{3}He ガスを充たし、^{3}He(n,p)t 反応から来る陽子を、電子と同じ測定器で同時に捉える。これにより、空間的な測定効率は電子に対しても陽子に対しても完全に同一となり、崩壊空間と測定効率を決定する必要が全くなくなった。これにより系統誤差を最少にできると期待される。

新しい方法においても、充填した ^{3}He ガスの密度と ^{3}He(n,p)t 反応の断面積は絶対値が必要である。前者は付録 A に述べる方法を考案し、0.1%以下の精度で決定する事が可能になった。後者は過去に測定がなされており、その精度は 0.2%であることが分かっている。

測定原理

^{3}He(n,p)t の反応頻度は、ϕ_n を中性子の流束密度、σ_r を反応断面積, ρ_m を ^{3}He ガスの密度とすると、

$$\frac{dN_r}{dt} = \int \varepsilon_r \phi_n \left(1 - e^{-\sigma_r \rho_m dl}\right) dA$$
$$\approx \int \varepsilon_r \phi_n \sigma_r \rho_m dl dA$$
$$= \rho_m \sigma_0 v_0 \int \varepsilon_r \rho_n dl dA \qquad (1)$$

と書ける。上の式の２行目から３行目に移る際には断面積の 1/v 則($\sigma=\sigma_0 v_0/v$)を用いた。$\sigma_0 v_0$ は精度良く測られていて、速度 v_0=2200 m/s の中性子に対して、断面積σ_0は 5333±7 秒である。

一方、中性子の寿命は、崩壊生成粒子、この場合は電子の計数率を n_d、立体角を含む測定効率をε_dとすると、

$$\tau_n = \int \varepsilon_d \rho_n dV_d / n_d \qquad (2)$$

と表される。反応頻度 $dN_r/dt=n_r$ とおいて、先の式(1)を式(2)に代入すると、中性子寿命は

$$\tau_n = \frac{\int \varepsilon_d \rho_n dV_d}{\int \varepsilon_r \rho_n dV_d} \frac{n_r}{n_d} \frac{1}{\rho_m \sigma_0 v_0} \qquad (3)$$

となる。ここで、ε_d とε_r が完全に等しいと、中性子寿命の測定は

$$\tau_n = \frac{n_r}{n_d} \frac{1}{\rho_m \sigma_0 v_0} \qquad (4)$$

となって、反応頻度と崩壊頻度の比の測定に還元される。しかし、ε_d とε_r は立体角は完全に一致するものの、電子は数パーセントの確率で物質表面から反射される。これにより、電子が測定されない確率が生じるが、これは、測定のしきい値、測定器の配置等によるのでモンテカルロ法により評価する必要がある。

また、^{3}He(n,p)t 反応断面積の 1/v 則と、中性子の滞在時間（1/v に比例）が相殺することにより、中性子のエネルギースペクトルが関与しなくなる事も、本測定方法の優れた点である。

測定装置

図１に測定の全体配置を示す。(図は縦横比が大きく誇張されているので注意。)

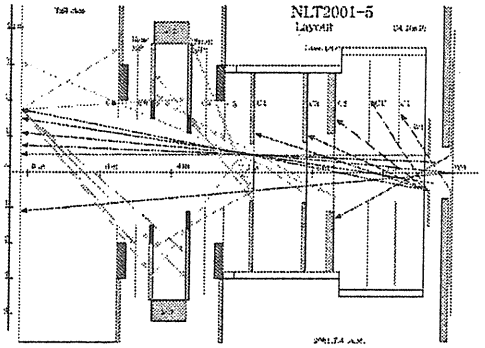


図１　中性子寿命測定実験配置。　M1, M3 はメインカウンター。その他は遮蔽物質で、LiF（赤）、鉛（灰色）、タングステン（茶色）

C1 から C4 は中性子ビームのコリメーションで、濃縮された ^{6}LiF 板である。C2 から C4 はガンマ線を止めるために鉛ブロックでバッキングされている。ビームサイズは基本的に真空パイプ直前に置かれた可動式コリメータと C4 によって決定されている。それらは中性子寿命測定時は 10mm x 10mm に設定されていた。その他 C5 から C6 および、測定器の前後に設置されたタングステン遮蔽の内面もおなじ ^{6}LiF 板で覆われた。中性子ビームは最終的に測定器の約２メートル下流に置かれた ^{6}LiF 板に吸収させた。

測定器は 1/4 インチ厚のプラスチックシンチレーター（BICRON 社製　BC-408）を４枚組み合わせ、内寸 70x70x500 mm^3 の中空四角柱をなし、それぞれ上下流端からライトガイドを介して光電子増倍管でシンチレーション光を検知する。またこの外側には内寸 150x150x600 mm^3 の中空四角柱に組まれた４枚のシンチレーションカウンターが配置され宇宙線、実験室内の放射線など外部からのノイズを遮断するように設計された。このヴィトカウンターも内部のメ

インカウンター同様上下流端から光電子増倍管で光が読み出される（図２）。

これら全てのカウンター、遮蔽物質はステンレル製の真空容器に納められた。ヴェトカウンターは個別に光遮蔽がなされたが、メインカウンターの中性子ビームに面した面には遮蔽物質はなく、プラスティックシンチレーターがむきだしになっている。従って、外部からの光は真空容器によって遮蔽されている。

全体の配置は、中性子ビームそのものはもちろん、中性子ビームがコリメーターなどの物質と相互作用した結果２次的に発生されるガンマ線、中性子なども直接カウンターに入らない設計となっている。

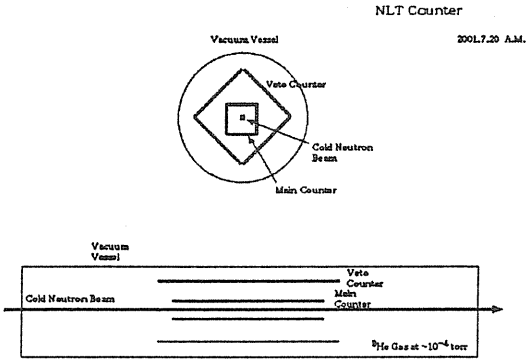


図２　カウンター断面図。上はビームに垂直な断面。下は側断面図。

冷中性子ビーム

冷中性子ビームはJRR-3M炉のC-2ビームを使用した。中性子ビームのエネルギー分布は中心エネルギーが波長で５オングストローム（3 meV, 800 m/s）であった。中性子ビーム強度は、原子炉20MW運転時、ガイドチューブ出口で $1x10^8$ n/cm^2/s と言われていたが、われわれの ^{3}He(n,p)t 反応を用いた測定では、ガイドチューブ出口から４メートル下流の測定器の位置で $1x10^7$ n/cm^2/s であった。この強度から期待される、中性子ベータ崩壊の電子がカウントされる頻度は約６カウント/s である。

本実験の初期にあっては、測定器上流の中性子ビームコリメーションの改良と、外部からのバックグラウンドに対する測定器の遮蔽に多くの勢力をさいた。

データ収集

データ収集は基本的にメインカウンターの８個の光電子増倍管とヴィトカウンターの８個の光電子増倍管の波高とタイミングを CAMAC　ADC と TDC で読み取る。メインカウンターの８個の光電子増倍管の、いずれか１個がしきい値以上の光を感知する事をトリーガーの条件とする。メインカウンターは内面の光遮蔽がないので、1 粒子が特定の１カウンターのみに入射した場合も、シンチレーション光は他のカウンターにも漏れ入るため、入射粒子のエネルギーは４つのカウンターの出力を足し合わせて初めてわかる。ただし、典型的な光の配分は粒子の入射したカウンターが 60%, 対向するカウンターが 20%, 両隣のカウンターがそれぞれ 10%ずつであり、入射カウンターの同定は可能である。

ADC, TDC のデータ以外に、データ収集系の効率に影響されないトリーガー頻度を、高速スケーラーでもってデータ収集ラン毎に記録した。実際にデータ収集系に記録されたイヴェント数とスケーラーで計数された頻度の比により、データ収集系の効率が評価された。

TDC の情報は、ビーム方向における粒子の入射位置の特定に使用された。同一カウンターの上下流端の光電子増倍管のタイミングの差から入射位置が判明する。ただし、上下流の TDC データを要求することは、結果的にデータ収集のしきい値を高くすることになり、最終的に電子の個数評価の際のゼロエネルギーへの外挿が長くなるので、TDC データはカウンターの性能確認のみに使用した。

収集したデータは基本的に以下の３種類である。

１）ビームシャッターを閉じた状態でのデータ（ビームなしデータ）。実験室内の環境バックグラウンドである。イヴェント頻度は 129.31/s、データ読み込み効率は 53.145%。総データ量は 1.79×10^7 イヴェントである。

２）高真空状態で ^{3}He ガスを充填せず、中性子ビームを通したデータ（ガスなしデータ）。１）に加えて崩壊電子とビームに起因するバックグラウンドが加わる。イヴェント頻度は 165.55/s、データ読み込み効率は 52.561%。総データ量は 1.41×10^7 イヴェントである。

３）容器を高真空に引いた後一定量の ^{3}He ガスを充填して中性子ビームを通したデータ（ガスありデータ）。２）に加えて ^{3}He(n,p)t 反応による陽子が加わる。イヴェント頻度は 236.69/s、データ読み込み効率は 45.151%。総データ量は 2.06×10^7 イヴェントである。

この他に補助的なデータとして、トリガーのタイミングを外したペデスタルデータと上下ヴェトーカウンターと上下メインカウンターをトリガーに組み込んだ宇宙線データを収集した。前者は、ゼロ入力に対する ADC の反応、すなわち ADC のゼロ点の決定のためであり、後者は、高エネルギー粒子の通過に対する上下メインカウンターの出力により、エネルギースケールを決定するためである。

データ解析

まず、ヴェトカウンターが何らかの信号を感知したイヴェントは、外部からのバックグラウンドとして、解析から除外した。

メインカウンターの８個の光電子増倍管のゲインは、事前に放射性同位元素や宇宙線を用いて調整されていたが、最終的には 3He(n,p)t 反応を用いて調整された。

ガスなしデータからビームなしデータを差し引き、これを中性子崩壊にともなう電子とした。この際ビーム以外から来るバックグラウンドは時間に比例するものと仮定して、データ収集時間とデータ収集系の効率の積をもって規格化した。結果を図３に示す。低エネルギーのバックグラウンドは存在するが電子の分布は明瞭に見える。バックグラウンドは、電子と思われる領域の上下で、２つの指数関数でフィットして評価した（赤い破線）。

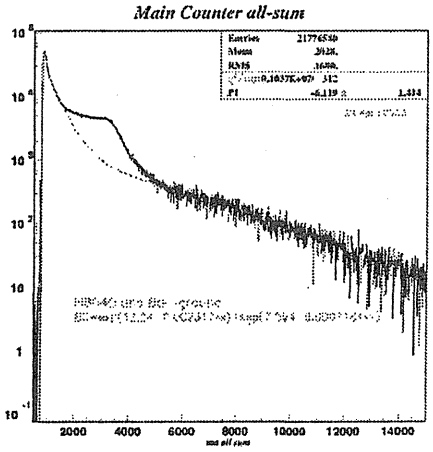


図３　電子スペクトラム。データセット２（ガスなし）からデータセット１（ビームなし）を差し引いたスペクトル。電子の他にビームから来るバックグラウンドが残っている。

図４ではガスありデータからビームなしデータを差し引いた。ここには図３に加えて、3He(n,p)t 反応による陽子のピークが見える。この陽子のエネルギーは 574 keV であるが、密度効果のため、プラスティックシンチレーターには 92.9 keV 電子相当の

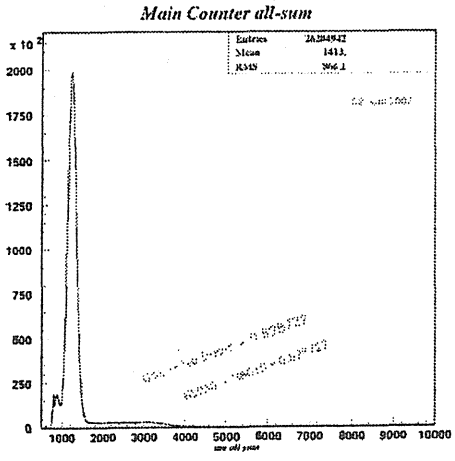


図４　電子と陽子のスペクトル。データセット３（ガスあり）からデータセット１（ビームなし）を差し引いた。

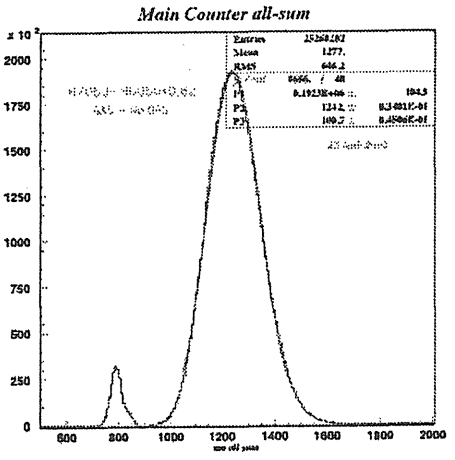


図５　陽子のスペクトル。データセット３（ガスあり）からデータセット２（ガスなし）を差し引いた。

信号を与える事がわかっている。同様にして、ガスありデータからガスなしデータを差し引くと陽子のみが残る（図５）。８００チャネルに見える小さなピークはADCのペデスタルである（８００チャネルがゼロエネルギーとなるように表示されている）。

図５の陽子ピークをガウス関数でフィットすると中心値１２４２チャネルが得られる。これから中性子ベータ崩壊のエンドポイント782 keVは４５２０チャネルと得られるが、図３とよく一致する。

次に、図３の電子スペクトラムを中性子のベータ崩壊の理論関数

$$P(E)dE = \frac{E^2(E_0 - E)^2}{1 - \exp\left(-2\pi\alpha / \sqrt{E^2 - m_e^2}\right)} dE$$

でフィットを試みたが、満足な一致が得られなかった。理由はいくつか考えられる。一つは理論関数のフェルミ関数部に非相対論近似を用いていること。もう一つは、電子のエネルギーがゼロから782 keVと、その質量511 keVの上下をカバーするため、測定器の反応が一様ではなく、電子のエネルギースペクトラムを歪めている可能性がある。現在この原因を調査中である。

これが原因で図４において、電子分布（ベータ崩壊関数）と陽子分布を同時にフィットして、電子と陽子の頻度比を求める本来の解析法が取れずにいる。

そこで、今回の測定自体に大きな誤りのないことを確認するために、図３から電子数、図５から陽子数を別個に求めて、中性子ビーム強度の時間変動が無いものとして、データ収集時間とその効率を使って規格化を行う方法で、中性子寿命の概算値を求めてみた。

図３において、２つの指数関数で近似されるバックグラウンドを差し引いて電子数をもとめる。同様に

図５では、陽子ピークをガウス関数でフィットすることにより陽子の数が求まる。２つのデータセットのデータ収集時間と効率を考慮して、電子(n_d)と陽子(n_r)の比は

$$\frac{n_d}{n_r} = \frac{N_d}{N_r}\frac{T_3\eta_3}{T_2\eta_2} = 0.0854787$$

と得られる。ただし、N は収集された電子または陽子数で、T,ηはそれぞれのデータセットの収集時間と収集系の効率である。

電子および陽子に対する測定効率ε_dとε_rはモンテカルロ法(Geant-4)を用いて評価したが、その比は、電子エネルギー50 keV で 99,00 %、750 keV で 99.99 %と小さく、現段階では等しいと見なせる。したがって、式（４）を使用して差し支えない。付録 A の方法で得られた ^{3}He ガス密度

ρ_n=1.2732x10^{13} cm^{-3}

を用いて、式（４）より、中性子寿命が

$$\tau_n = 783\ sec$$

と得られた。この値は、現在のワールドアベレジより約 10%小さいが、現段階では測定誤差の範囲内と考えられる。

結論

系統誤差の少ないと思われる、新しい測定方法を考案し、中性子寿命の測定を試みた。ビーム中性子の約１００万分の一以下の確率で生成される電子が明瞭に補足され、測定方法そのものの有効性が確認されたが、いくつかの課題も明らかになった。それらは

１）期待される崩壊イヴェント　６カウント／秒に対し、環境バックグラウンドが　１２９カウント／秒、ビーム起因のバックグラウンドが３０カウント／秒と圧倒的である。

２）30 - 782 keV という微妙なエネリギーの電子に対する測定器の反応を理解する必要がある。

今後の方向としては

１）遮蔽強化も含めて、より静かな実験室環境を確保すること。

２）中性子ビームのコリメーションを改良して、ビームに付随するバックグラウンドの軽減を図ること。

３）相対論から非相対論領域にまたがる電子に対する測定器の反応をより深く理解すること。

が必要である。

謝辞

本実験の過程では、多くの人が参加して実験に貢献した。それらの人は、久良木宏司（佐賀大)、岩見竜也（佐賀大)、大石竜雄（筑波大)、田村詔生（新潟大)，高橋真也（新潟大)、中村雅俊（新潟大）である。

実験の実施にあたっては、日本原子力研究所の大友昭敏、中村清、盛合敦の各氏、東京大学の澤幡浩行、川手稔の両氏にいろいろお世話になりました。ここに改めてお礼を申し上げます。

付録A ^{3}Heガス密度の測定

一般に真空状態におけるガス密度の精密測定は困難である。このためわれわれは特別な測定方法を考案した。

ガス注入系にバルブで仕切られた、大きさの異なるいくつかの空間を用意し、精度良い圧力測定が可能な、大気圧に近い圧力のガスを用いて各空間間の体積比を測定する。最初の小さな空間に注入された大気圧近いガス圧力を高精度圧力計（Druck 社製 DPI705R）で測定した上で、順次大容積空間に希釈する。体積比が測定されているので、測定器真空容器内のガス圧力、すなわち、ガス密度が精度よく求まる。

希釈時におけるガス温度の変化については、その緩和時間が評価され、本実験条件では1ミリ秒以下と、操作時間数分に比べて問題とならないことが確認されている。

ガス注入システム

実験に使用された測定系のガスシステムは FIG1 の通りである。

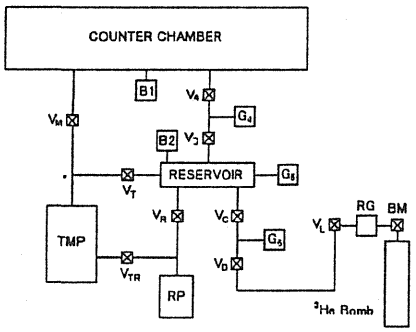


FIG.1

^{3}Heの導入系は、電子／陽子検出器本体を納める真空容器からリザーバーを経て ^{3}He ガスボンベに取り付けられた調圧弁(以下RG)まで、4つのバルブ V_A、V_B、V_C、V_Dで仕切られた4つの体積部分 S_M、S_{AB}、S_{BC}、S_{CD}からなる。このうち、S_Mは真空容器、S_{BC}はリザーバーに対応し、S_{AB}、S_{BC}、S_{CD}にそれぞれ圧力計G_4、G_5、G_6が取り付けられている。以下、S_M等の記号を各体積部分の呼称とその体積とに共用する。真空容器とリザーバーの真空度は 冷陰極真空計（以下 CCG）B1、B2 によってモニターされる。

体積比測定の原理

体積比測定の系をモデル化すると FIG 2 のようになる。

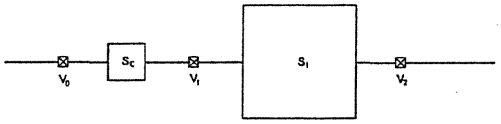


FIG.2

手順は次のようになる。はじめにV_0を閉じ、V_1、V_2を開いて、S_0、S_1部分を充分高真空にしてから、V_1、V_2を閉じる。このときのS_0、S_1部分の圧力をp_0とする。次にV_0を開いてS_0部分に大気を導入し、V_0を閉じる。このときのS_0部分の圧力をp_Aとする。次にV_1を開いてS_0部分の大気を(S_0+S_1)に膨張拡散させ、充分な時間経過の後、V_1を閉じる。このときの(S_0+S_1)部分の圧力をp_1とする。以下、この手順を繰り返す。もし測定中に大気圧の変動も零点の変動もなければ、

$$p_A S_0 + p_0 S_1 = p_1 (S_0 + S_1)$$
$$p_A S_0 + p_1 S_1 = p_2 (S_0 + S_1)$$
$$p_A S_0 + p_{n-1} S_1 = p_n (S_0 + S_1)$$

ここで$r = S_0 / S_1$（体積比の逆数）とおくと、

$$(p_A - p_n) r = p_n - p_{n-1}$$

今、$r \ll 1$ だから$p_n - p_{n-1} = dp_n / dn$とおいてよい。ここで$n$は上記操作の回数である。

$$rdn = \frac{dp_n}{p_A - p_n}$$

$$rn = \ln(\frac{p_A - p_0}{p_A - p_n})$$

p_0は大気圧p_Aに比べて７桁以上小さいので

$p_0 = 0$としてよい。よって

$$rn = \ln(\frac{p_A}{p_A - p_n})$$

こうして体積比の逆数rは函数$f_n = \ln(\frac{p_A}{p_A - p_n})$を回数$n$を引数としてプロットしたときの傾きとして得られる。

実際には測定中に大気圧の変動も零点の変動もあるが、１連の測定中、大気圧の変動は0.1％以下、また零点の変動は５桁の内の１桁程度なので、データの解析は上記の原理を採用してよい。但し注意すべき点は、p_nを測る圧力計とp_Aを測る圧力計とが同じ物でなければならないことである。

体積比測定例

以下に測定例を示す。FIG3に圧力計G5を用いて得られた一連の測定値（函数f_n）を、操作回数nに対してプロットする。

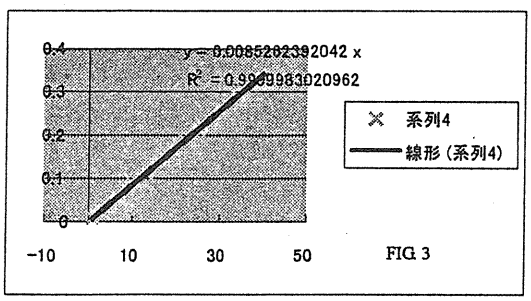


FIG. 3

FIG. 3において、f_nの値は、p_Aの１回目から４０回目までの値の平均値

$\bar{p}_A = 102.233375$[kPa]

を採って求めたものである。

これより

$$r_3 = \frac{S_{BC}}{S_M + S_{AB}}$$
$$= 0.0085262392042 \pm 0.0211319681\ \%$$

が得られる。

体積比と密度の希釈率

体積 S_{CD}を単位に採った各部体積を

$R_B = S_{BC} / S_{CD}$、 $R_A = S_{AB} / S_{CD}$、

$R_M = S_M / S_{CD}$ のように定義すると、

$$r_1 = \frac{S_{CD}}{S_{BC}} = \frac{1}{R_B}$$
$$= 0.006387946063 \pm 0.0569901\ \%$$

(1)

$$r_2 = \frac{S_{AB}}{S_{BC}} = \frac{R_A}{R_B}$$
$$= 0.011863421619 \pm 0.0191519\ \%$$

(2)

$$r_3 = \frac{S_{BC}}{S_M + S_{AB}} = \frac{R_B}{R_A + R_M}$$
$$= 0.0085262392042 \pm 0.0211319681\%$$

(3)

第１段階の希釈における密度の希釈率は

$$D_1 = \frac{S_{CD}}{S_{CD} + S_{BC}} = \frac{1}{1 + R_B} = \frac{r_1}{1 + r_1}$$

で与えられる。第２段階の希釈における密度の希釈率は、１回目の希釈では

$$D_{2,1} = \frac{S_{BC}}{S_{BC} + S_{AB}} \cdot \frac{S_{AB}}{S_{AB} + S_M}$$
$$= \frac{R_B}{R_A + R_B} \cdot \frac{R_A}{R_A + R_M}$$

n回目の希釈では、$S_M >> S_{AB}$ だから

$$D_{2,n} = (\frac{R_B}{R_A + R_B})^n \cdot \frac{R_A}{R_A + R_M}$$

で与えられる。従って第２段階の希釈をm回目からn回行ったときの真空容器の密度 N_{mn} は、最初に

S_{CD} 部に充填された ^{3}He の密度を N_0 とすると、

$$N_{mn} = N_0 D_1 \sum_{j=m}^{m+n-1} D_{2,j}$$

$$= N_0 D_1 \frac{R_A + R_B}{R_A + R_M} (\frac{R_B}{R_A + R_B})^m \{1 - (\frac{R_B}{R_A + R_B})^n\}$$

となる。式 (1), (2), (3) から

$$\frac{R_A + R_B}{R_A + R_M} = r_3(1 + r_2)$$

$$\frac{R_B}{R_A + R_B} = \frac{1}{1 + r_2}$$

だから、

$$N_{mn} = N_0 K_1 K_2^{m-1}(1 - K_2^n)$$

ここで、

$$K_1 = D_1 r_3 = \frac{r_1 r_3}{1 + r_1}$$

$$K_2 = \frac{1}{1 + r_2}$$

因子$(1 + r_1)$、$(1 + r_2)$の相対誤差は無視できるから、K_1の相対誤差はr_1、r_3のそれらで決まり、K_2の相対誤差は無視できる。但し、

$$1 - K_2^n = 1 - (\frac{1}{1 + r_2})^n \approx 1 - (1 - r_2)^n \approx n r_2$$

から因子$(1 - K_2^n)$の相対誤差は　r_2　のそれで決まる。N_0は最初にS_{CD}部に ^{3}He を充填したときの圧力計 G_6 の読みをP_0[kPa]、そのときのS_{CD}部の温度をT_0[°C]としたとき、

$N_A = 6.0221367 \cdot 10^{23}$[Mole^{-1}]を Avogadro 数として

$$N_0 = N_A \frac{273.15}{273.15 + T_0} \cdot \frac{1}{22414.1} \cdot \frac{P_0}{101.325} [\mathrm{cm}^{-3}]$$

従って最終的には

$$N_{mn} = \frac{p_0}{273.15 + T_0} A \cdot K_2^{m-1}(1 - K_2^n) [\mathrm{cm}^{-3}]$$

$$A = N_A \frac{273.15}{22414.1 \times 101.325} \cdot \frac{r_1 r_3}{1 + r_1}$$

$$= 3.919829920 \times 10^{15}$$

$$K_2 = 0.98827566908$$

ここで、　$\Delta\rho_1 \equiv \Delta r_1 / r_1$、　$\Delta\rho_2 \equiv \Delta r_2 / r_2$、

$\Delta\rho_3 \equiv \Delta r_3 / r_3$、　$\Delta\pi \equiv \Delta p_0 / p_0$、

$\Delta\tau \equiv \Delta T_0 / (273.15 + T_0)$　なる量を導入する。一般に積の相対誤差は各因子の相対誤差の和になる、即ち、

$$\ln\{(a + \Delta a)(b + \Delta b)\} \approx \ln(ab) + \frac{\Delta a}{a} + \frac{\Delta b}{b}$$

であるから、結局求める量N_{mn}の相対誤差ΔN_{mn}は

$$\Delta N_{mn}$$

$$= \sqrt{(\Delta\pi)^2 + (\Delta\tau)^2 + (\Delta\rho_1)^2 + (\Delta\rho_3)^2 + n(\Delta\rho_2)^2}$$

となる。

研究テーマ：中性子ラジオグラフィによる沸騰流のボイド率計測
表　題　　：中性子ラジオグラフィによる稠密７本バンドル流路内沸騰流のボイド率計測

2-8

中性子ラジオグラフィによる稠密７本バンドル流路内沸騰流のボイド率計測

呉田 昌俊、 秋本 肇
日本原子力研究所
エネルギーシステム研究部
熱流体研究グループ

中性子ラジオグラフィ（NRG）を用いた稠密バンドル内を流れる沸騰流の瞬間ボイド率計測技術[1]と、ボイド率の３次元分布計測技術[2]を開発した。平成14年度は、低減速軽水炉を模擬した７本バンドル試験体を用いて瞬時ボイド率の計測と３次元計測を実施し、可視化技術として高く評価された[3]。

実験は、JRR-3M 熱中性子ラジオグラフィ実験施設（TNRF-2）を利用した。ボイド率計測実験には、７本バンドル試験体（発熱棒間隙が1mm、棒径12mm、加熱長890mm）を用いた。図１に実験装置の概略図を示す。この試験体の中で発生する沸騰流を計測した。

図２に瞬時ボイド率を計測した一例を示す。図２は、約1000フレーム毎秒で記録したNRG画像を画像処理して得られたボイド率の分布を示しており、この結果を動画観察して現象を分析した[4]。本計測結果から、周辺部より中心部の方が流体の移動速度が高速であること等が分かった。NRG技術とCT技術を融合した独自の中性子トモグラフィ技術を開発し、３次元のボイド率分布を測定した結果を図３に示す。図３から、発熱棒間の狭間隙領域に水が溜まり易いこと等が分かった。

本研究により、稠密バンドル内沸騰流のボイド率を1/1000秒、また0.1mmの空間分解能で３次元計測できる技術を開発し、バンドル流路内沸騰流現象の解明に役立てた。また、得られたボイド率データからボイド率相関式を導出して設計に役立てたり[5]、３次元データは、詳細数値解析コードの検証に用いている。

参考文献
1) 可視化情報学会誌, Vol.23-89, (2003), pp.21-26.
2) 噴流工学, Vol.20-2, (2003), pp. 24-31.
3) 日経サイエンス、2004年１月号, Visual Science Festa 2003 特集.
4) Proc. ISFV-10, F0231, Kyoto (2003).
5)Proc. NURETH-10, B00205, Seoul (2003).

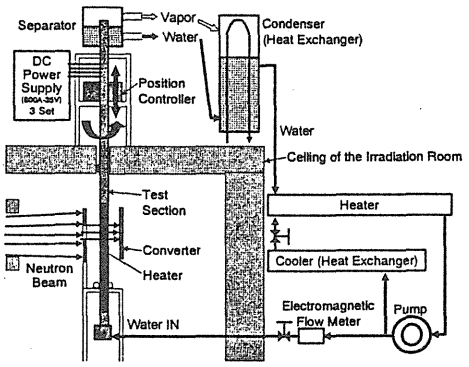


図１　ボイド率計測実験用装置の概略図

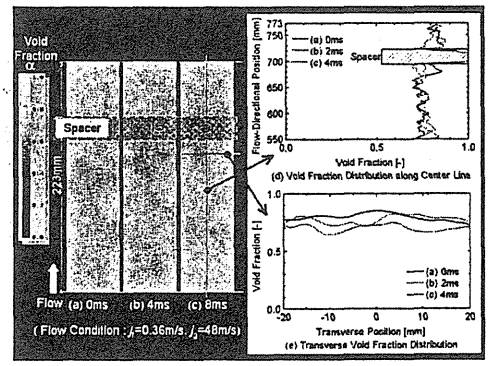


図２　瞬時ボイド率の計測

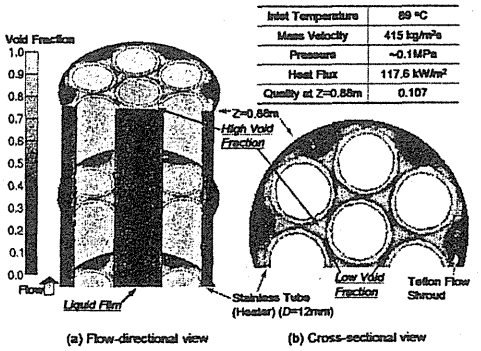


図３　ボイド率の３次元計測

原子炉：JRR-3　装置：熱中性子ラジオグラフィ施設　分野：中性子ラジオグラフィフィ（熱水力）

3. 放射化分析

3. Neutron Activition Analysis

This is a blank page.

3-1

ホタテガイのカドミウム結合分子の研究

Cadmium Binding Protein in Scallop *Mizuhopecten Yessoensis*

大西俊之[1)]、大西玄一[2)]、野矢洋一[1)]
Toshiyuki Ohnishi,Gen-ichi Ohnishi,Youichi Noya
1)北海道大学アイソトープ総合センター
Central Institute of Isotope Science,Hokkaido University
2)北海道大学歯学研究科
Graduate School of Dental Medicine,Hokkaido University

1．はじめに

ホタテガイは、北海道の代表的な産物の一つであり、その生産量も大きい。しかし、体内にカドミウムを濃縮することが知られており、その大部分は、中腸腺や腎臓内で蛋白質と結合して存在している[1),2),3)]。これらのカドミウム結合機構の詳細は、未だ解明されていない部分が多い[1)]。

今回、ホタテガイに含まれるカドミウム等の金属濃度を測定し、結合物質の分離等の実験により、カドミウム濃縮機構の検討を行ったので報告する。

2．方法

（１）試料

ホタテガイ(*Mizuhopecten yessoensis*)は、北海道岩内郡漁協で購入した３年貝を用いた。採取後、直ちに中腸腺、腎臓等の部位に分け、実験開始時まで冷凍保存した。

（２）ホタテガイの金属元素濃度の測定

ホタテガイの各部位は、硝酸－過塩素酸中で加熱分解を行った。これらの試料は石英管に封入し、日本原子力研究所（ＪＲＲ－４）で、中性子束密度３×１０^{13}n/cm^{2}sの条件で３０分間の中性子照射を行った。１～２週間の冷却後、ピュアゲルマ半導体検出装置により金属元素濃度の測定を行った。

（３）カドミウム結合蛋白の分離

腎臓に２倍量の５０ｍＭトリス塩酸緩衝液（ｐＨ8.6）を加え、ホモジナイザーでホモジナイズした後、10,000ｇで３０分間遠心分離した。その上清液を更に100,000ｇで２時間超遠心分離を行い、上清液と沈殿等に分画した。得られた100,000ｇ上清液を0.45μｍのメンブランフィルタでろ過した。

そのろ液の内、比較的低分子量蛋白（分画範囲70,000以下）をSephadex G-75を用いて、比較的高分子量蛋白（分画範囲30,000～600,000程度）をSephacryl S-300を用いて、それぞれゲルろ過を行った。得られた各フラクションは、280nmの吸光度を測定した後、原子吸光光度計で金属濃度を測定した。

10,000ｇと100,000ｇの沈殿は、硝酸－過塩素酸中で加熱分解を行った後、放射化分析法により金属濃度を測定した。

3．結果と考察

（１）ホタテガイの金属元素濃度

ホタテガイの部位別の主要金属濃度をTable１に示す。腎臓と中腸腺にカドミウムの特異的な濃縮があり、海水のカドミウム濃度と比較して、中腸腺は100万倍、腎臓では1000万倍の値を示していた。人体のカドミウム濃度は腎皮質において最高値を示すことが知られており、ホタテガイも同様の結果であった。また、カドミウムと同属の亜鉛が同程度の濃度を示しているのも興味深い。

（２）カドミウム結合蛋白の分離

JRR-4 Ｓ－パイプ　放射化分析（環境）

Table 1 Concentrations of Metals in Scallop (μg/g dry wt)

Metal	Adductor muscle	Gill	Mantle	Gonad	Kidney	Digestive gland	Rest
Cr	0.217	0.858	0.931	0.472	0.496	2.48	1.94
Fe	36.3	144	181	273	468	1004	865
Co	0.0612	0.992	0.610	0.270	3.84	0.901	0.654
Zn	96.3	522	491	148	450	119	289
Se	N.D	2.36	0.346	0.548	1.59	1.85	N.D
Cd	3.32	4.42	2.30	7.25	1290	136	53.2

Adductor muscle：貝柱、 Gill：エラ、 Mantle：外套膜、 Gonad：生殖腺
Kidney：腎臓、 Digestive gland：中腸腺、Rest：胃、心臓等、上記以外の部位

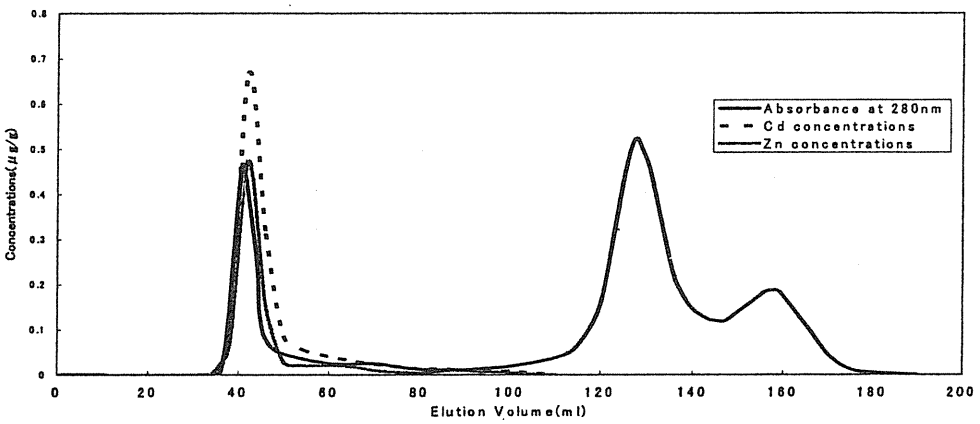


Fig.1 Elution Profiles of Sephadex G-75

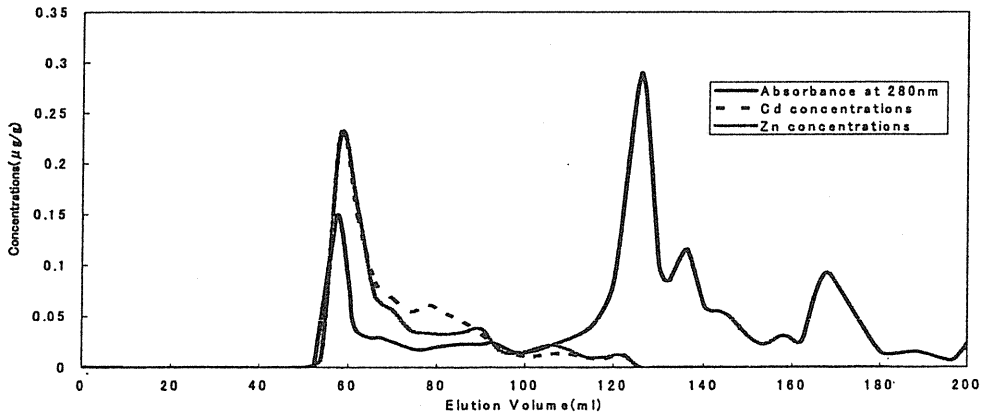


Fig.2 Elution Profiles of Sephacry S-300

Table 2に10,000ｇ及び100,000ｇ沈殿を不溶成分、100,000ｇ上清液を水溶性成分として、それぞれの元素濃度を示す。Ｃｒ，Ｆｅ，Ｓｅは不溶成分の方に多く存在していたが、カドミウムの約５２%、亜鉛の約４５%が水溶性成分に存在していた。これらの水溶性成分をSephadex G-75（低分子量）及びSephacryl S-300（高分子量）を用いて、それぞれゲルろ過を行った。

Table 2 Concentrations of Metals in kidney

Metal	Soluble(μg/g)	Insoluble(μg/g)
Ｃｒ	N.D.	0.19
Ｆｅ	7.8	24
Ｃｏ	0.25	0.34
Ｚｎ	38	48
Ｓｅ	0.49	1.2
Ｃｄ	93	88

Sephadex G-75によるゲルろ過の結果をFig.1に示す。カドミウム、亜鉛濃度及び280nmの吸光度は、ボイド体積（４０ｍｌ）に大きなピークが認められた。この部分には分子量70,000以上の物質が含まれており、腎臓のカドミウム及び亜鉛の大部分が高分子量物質と結合していることが分かった。このピークの後、カドミウム、亜鉛濃度ともに減少し、溶出量６０ｍｌ（分子量30,000程度）、９０ｍｌ（分子量10,000程度）付近に亜鉛の小さなピークが認められた後、溶出量１２０ｍｌ以降に遊離のアミノ酸によるものと思われるピークを示した。分子量１万の物質は、その分子量と280nmの吸光度を有しないことからメタロチオネイン様蛋白質と考えられた。メタロチオネインは、カドミウム、亜鉛等の重金属を結合するタンパク質として多くの生物に見出されているが[4]、ホタテガイ腎臓では亜鉛との結合のみを検出できた。

Sephacryl S-300によるゲルろ過の結果をFig.2に示す。カドミウム、亜鉛濃度及び280nmの吸光度ともにボイド体積（６０ｍｌ）に大きなピークが認められた後、溶出量８０ｍｌ（分子量200,000程度）にカドミウム、溶出量９０ｍｌ（分子量80,000程度）と、１１０ｍｌ（分子量30,000程度）に亜鉛のピークが認められた。

Fig.1及びFig.2のゲルろ過の結果により、ホタテガイ腎臓に含まれるカドミウムは、分子量２０万程度の物質と結合している以外、明確なピークを有していない。腎臓と同様にカドミウム濃度の高い中腸腺においては、カドミウムは少量のメタロチオネインの他に４万、９万、２０万程度の分子量をもつ物質と結合していた[5]。分子量４万、９万、２０万の物質は中腸腺内の糖タンパクであり、カドミウムの大部分はこれらの表面に吸着された状態で存在していると考えられている[6]。これに比して腎臓ではカドミウムとメタロチオネインとの結合が見られず、糖タンパクとの結合も明らかに異なっていた。一方、亜鉛のゲル濾過の結果は中腸腺のカドミウム分布と類似しており、メタロチオネインとの結合も認められた他、同程度の分子量を持つ糖タンパクと思われる物質との結合も見られた。

通常、細胞内に取り込まれた亜鉛、カドミウム等の重金属はメタロチオネインを誘導し、これと結合する。中腸腺内ではカドミウムの一部分が細胞内に入り込み、メタロチオネインと結合していた。一般にカドミウムとメタロチオネインの結合は亜鉛の結合よりも強く、亜鉛ーメタロチオネインはカドミウムによって速やかに置換されると考えられる。しかし、腎臓内では亜鉛によってメタロチオネインが誘導されているにもかかわらず、カドミウムーメタロチオネインがほとんど存在していないことが分かった。これは、細胞外における糖タンパクとカドミウムとの吸着性が極めて強いことが主要因であろうが、メタロチオネインとの結合において亜鉛からカドミウムへの置換反応が容易に起こらないこと、又は亜鉛元素の存在によってカドミウムの細胞内への進入が阻止されること等の要因も考えられる。

３万以上の分子量における亜鉛とカドミウム

の結合タンパクについても、両者のピークは異なっていた。亜鉛とカドミウムという類似の化学的性質を持つ元素でありながら、吸着されるタンパク質に大きな違いがある。これらは結合を行うタンパク表面の官能基の違い、元素の反応性等種々の要因が考えられ、今後の検討課題としたい。

４．成果の公表

大西俊之,大西玄一,野矢洋一,ホタテガイのカドミウム結合分子の研究,Proceedings of the Third Workshop on Environmental Radioactivity,159(2002)

参考文献

1)Ponzano,E.et al.,Polar Biol.,24,147 (2001)
2)中山憲司他,北海道立衛生研究所報,第４５集, 13(1995)
3) Evtushenko,Z.S.et al.,Mar.Biol.,104, 247(1990)
4)Kagi JHR.et al.,Metallothionein.Ⅲ. Birkhauser,Basel,29(1993)
5) 大西俊之他,Proceedings of the Third Workshop on Environmental Radioactivity, 159(2002)
6) 吉崎司郎他、第１１回廃棄物学会講演論文集,1196(2000)

3-2 痴呆疾患脳の組織中における微量元素の定量解析

Quantitative Analysis of Trace Elements in the brain tissue of patients with dementia

宮崎医科大学精神医学講座　植田　勇人、　宮崎医科大学化学　中島　暉

Yuto Ueda and Akira Nakajima

Department of Psychiatry, Department of Chemistry, Miyazaki Medical College

【目的と意義】

生体には自然界に存在する各種の元素と同様の元素が存在しており[1]、それらの微量元素はある濃度範囲内において平衡を保っている。生体内微量元素はそれぞれの元素が単独で生理的に作用するのみでなく、各種微量金属元素のバランスが相互に関連して作用していると考えられる。これら微量元素の欠乏や過剰状態はWilson 氏病に代表されるように代謝機構に障害をもたらす。したがって、変性疾患の病態解明に向けてのメタルバランスの解明は極めて重要な位置に占拠している。本稿では、変性型痴呆疾患として senile dementia of Alzheimer's type (SDAT), Pick 病, 運動ニューロン疾患を伴う痴呆(dementia with motor neuron disease; D+MND) と脳血管型痴呆(cerebrovascular dementia; CVD)および非痴呆患者として精神分裂病(schizophrenia; ^{1}Sc)の患者死後脳の大脳皮質中における微量元素、特にアルミニウムを、放射化分析を用いて定量解析を行い、疾患病態と微量元素の関わりについて考察した。

【実験方法】

剖検によってホルマリン固定された脳組織から大脳皮質を採取し凍結乾燥したものを試料として用いた。各疾患の試料数は Sc が 5 名、CVD が 8 名、MND+D が 3 名、SDAT が 5 名、Pick が 3 名である。ポリエチレン袋に三重にシーム封入した試料 10 - 100 mg を、JRR-4 炉気送管で 1 分間照射し、1 - 10 分間冷却後、Ge(Li) 検出器、多重波高分析器でγ線を計測し、金属量を求めた。使用した核種は、^{28}Al ($t_{1/2}$ = 2.31 min, 1778.9 KeV)), ^{47}Ca ($t_{1/2}$ = 8.75 min, 3083 KeV), 52V ($t_{1/2}$ = 3.75 min, 1434.4 KeV), ^{66}Cu ($t_{1/2}$ = 5.10 min, 1039.0 KeV), ^{64}Cu($t_{1/2}$ = 12.8 h, 1345.5 KeV) であった。

施設・装置：東海研究所、JRR-4 号炉気送管、　研究分野：微量元素の放射化分析

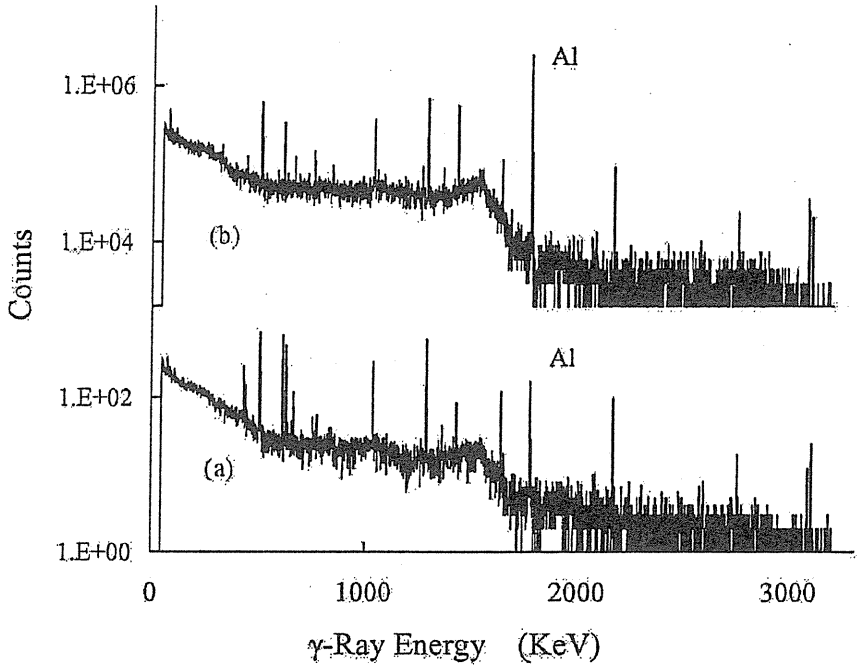


図１．大脳皮質のγ線スペクトル　(a) Sc　(b) SDAT

【結果・考察】

毛髪は生体内金属の排泄器官であることから、SDAT の毛髪中におけるアルミニウム(Al)の定量解析が盛んに行われ、高濃度の Al と SDAT の病態間の関わりが注目されている[3]。家兎にアルミニウムを投与し神経原線維変化を呈する実験に見られる[2] ように生体内微量金属と痴呆疾患の病態には何らかの因果関係があると推測される。本研究結果では非変性疾患である Sc と CVD 群と比べ、SDTA におけるアルミニウム含有量が有意に多く、他の研究者らの示した実験結果と一致する。さらに本研究では SDAT に限らず、変性型痴呆を示す Pick や MND+D におけるアルミニウム含有量も有意に高い値を示すことが本研究で新たに明らかとなった（図２参照）。この研究成果は、脳内アルミニウムなどの遷移金属がフリーラジカルの産生に関与し、SDAT に限らず、Pick や MND+D などの変性型痴呆疾患における病態形成に関与していることを示唆するものである。

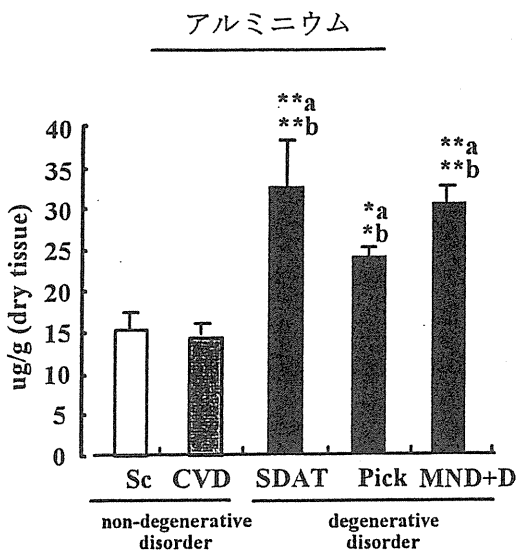


図2. 脳組織におけるアルミニウム含量

Sc, CVD と比較し変性痴呆疾患のアルミニウム含有量は有意に高い Students t-test。

**aP<0.01, *aP<0.05 vs. Sc; **bP<0.01, *bP<0.05 vs. CVD

【参考文献】

[1] Bowen, H.J.M., Trace elements in biochemistry, Academic Press, London, 1966.

[2] Klatzo, I., Winsniewski, H. and Streicher, E., Experimental production of neurofibrillary degeneration: I. Light microscopic observations, J. Neuropathol. Exp. Neurol., 24 (1965) 187-199.

[3] Ohmori, S., Ishii, T., Tsuda, K., Imai, S., Suzuki, Y., Takeuchi, T. and Nakano, H., Trace elemental concentration in hair of patients with Alzheimer type of dementia, Biomed. Res. Trace Elements, 2 (1991) 43-49.

3-3

蓄光性塗料の放射化分析（Ⅱ）

森脇一成[1]、萩原芳幸[2]、小幡　純[3]、古山俊介[4]

[1]日本大学歯学部 RI、[2]補綴学Ⅲ、[3]歯周病学、[4]松戸歯学部生理学

The activation analysis of phosphorescent phosphor (Ⅱ)

K. Moriwaki[1], Y. Hagiwara[2], J. Obata[3] and S. Furuyama[4]

[1]Division of RI Research, [2]Department of Crown and Bridge Prosthodontics ,
[3]Department of Periodontology, Nihon University School of Dentistry
[4]Department of Physiology, Nihon University School of Dentistry at Matsudo

Ⅰ　はじめに

我々が入手した Pinbadge に用いられていた蓄光性塗料を同定するため放射化分析を行ったところ、新しい Type の蓄光性塗料であることが判った。

我々は陶歯、陶材中に蛍光剤として添加されている Uranium を定量し、それによる口腔組織の被爆線量を算定して報告してきた[1)]。その報告で放射性蛍光剤すなわち Uranium の添加の中止とそれに替わる蛍光剤の開発を勧告してきたが、この蓄光性塗料は陶磁器や Ceramic にも応用できるとされている[2)]ので、陶歯、陶材の蛍光剤に利用できるものと考え、その可能性について検討した。

Ⅱ　方法

1　放射化分析：日本原子力研究所（JAERI）の 4 号炉（JRR-4）で 10 分間、熱中性子照射（flux:4.5×10^{13}n/cm^2・sec）を行った後、γ-Spectrometry を行った。（Genie-2000, CANBERRA series 35 plus）（図 1）

2　陶材粉末の焼成：金属焼付用陶材粉末、BIOBOND（Dentsply、USA）の構成粉末のうちウランが含まれていない E2 に長残光性蛍光体 LumiNova BG-300M（$Sr_4Al_{14}O_{25}$：Eu,Dy）を重量比で 5%加えて焼成した（焼成円盤）。

焼成法

①水で練和した試料粉末を直径 5mm に成型し断熱材上に移す。

研究施設	研究分野
JRR－4	放射化分析

②減圧（74mmHg）したポーセレン・ファーネス（DEKEMA-AUSTROMAT 3001）中で昇温速度 55℃/min、繋留温度 954℃-3min で焼成する。

③超音波洗浄した試料を開始温度 732℃、昇温速度 55℃/min、繋留温度 960℃-3min、待機温度 732℃で glazing を行う。

3　発光スペクトルの測定：天然歯、陶歯および焼成円盤のスペクトルを蛍光分光光度計（PERKIN-ELMER LS-5）で測定した。（図 2）

Ⅲ　結果と考察

蓄光性塗料の蓄光性とは、あたかも光を一時蓄えて発光するかのように見えるので蓄光という言葉が使われている。蓄光性を持つ物質が工業的に生産、使用されたのは 20 世紀になってからであり、ZnS:Cu や CaSrS:Bi などの硫化物蛍光体が用いられてきた。しかし、それらは発光時間が短かったり、弱かったため、これに放射性物質を加えて利用されていた。1996 年 Matsuzawa ら（根本特殊化学）が① $SrAl_2O_4:Eu,Dy$ ② $Sr_4Al_{14}O_{25}:Eu,Dy$ ③ $CaAl_2O_4:Eu,Nd$ これらのアルカリ土類アルミン酸塩を主成分とした蓄光性塗料を開発した[2]。

そこで、我々の入手した Pinbadge に使われている塗料がどの Type の蓄光性塗料であるかを確かめるため放射化分析を行った。その際、根本化学から提供された試料も同時に放射化してγ-Spectrometry を行った。この照射条件では Zn や Ca の Peak は認められず 1780keV に ^{28}Al の Photo Peak が認められたので、新しい Type の蓄光性塗料であることが判った。さらに、この蓄光性塗料は陶磁器や Ceramic にも応用できるとされているので陶歯、陶材の蛍光剤にも利用できるのではないかと考え、ウランの検出されなかった金属焼付用陶材粉末にこれを添加して焼成し、天然歯および陶歯の発光スペクトルと比較したところ、天然歯の発光ピークと反対の長波長側のほぼ等距離に長残光性蛍光体の発光ピークが認められた。すなわち、ウランと同様の効果が認められたので、この蓄光性塗料は陶歯の非放射性蛍光剤として有用であることが示唆された。

Ⅳ　おわりに

夜光塗料には自発光性と蓄光性とがあり、前者は放射性であるが故に用途に制限がある。後者は従来の硫化亜鉛 Type では残光時間や輝度に問題があったが、新しく開発されたアルミン酸塩タイプの蓄光性塗料はこれらの問題をクリアし、現在、時計や交通標識などに全世界的に使われ始めている。

我々は陶歯、陶材中に蛍光剤として添加されている Uranium を定量し、それによる口腔組織の被爆線量を算定して報告してきた。その報告で放射性蛍光剤すなわち Uranium の添加の中止とそれに替わる蛍光剤の開発を勧告してきたが、この蓄光性塗料は陶歯、陶材の蛍光剤にも利用できるものと考えている。

この研究の一部は原研施設利用総合共同研究により行った。

謝辞

蓄光性塗料を提供して頂いた根本特殊化学株式会社に感謝いたします。

研究成果

K. Moriwaki, J. Obata, T. Ezawa, O. Tuzukibashi, Y. Shimpuku, M. Makimura and F. Shiraishi: The activation analysis of the pinbadge paint that is doubted as a radioactive material. Radioisotopes 50,7, 308-312 (2001)

文献

1) E. Sairenji, K. Moriwaki, M. Shimizu, K. Noguchi, I. Anzai and N. Ikeda: Determination of uranium content in dental porcelains by means of the fission track method and estimation of radiation dose to oral mucosa by radioactive elements. Health Physics 38, 483-492 (1980)

2) T. Matsuzawa, Y. Aoki, N. Takeuti and Y. Murayama: A new long phosphorescent phosphor with high brightness, $SrAl_2O_4$: Eu^{2+}, Dy^{3+}. J.Electrochem.Soc. 143, 8, 2670-2673 (1996)

3) N. Yamagata : Radioactivity in daily goods. Bull.Inst.Publ.Health 26, 179-180 (1977)

4) H. Chisaka and Y. Igoshi : Mesurements of radioactive substance and surface dose rate in some wares for health improvements. Radioisotopes 27, 687-689 (1978)

5) P. Brunner, P. Schneider, H. Schneider and G. Seyoul : Tritium intake by exposure to plastic case watches. Health Physics 70, 484-487 (1996)

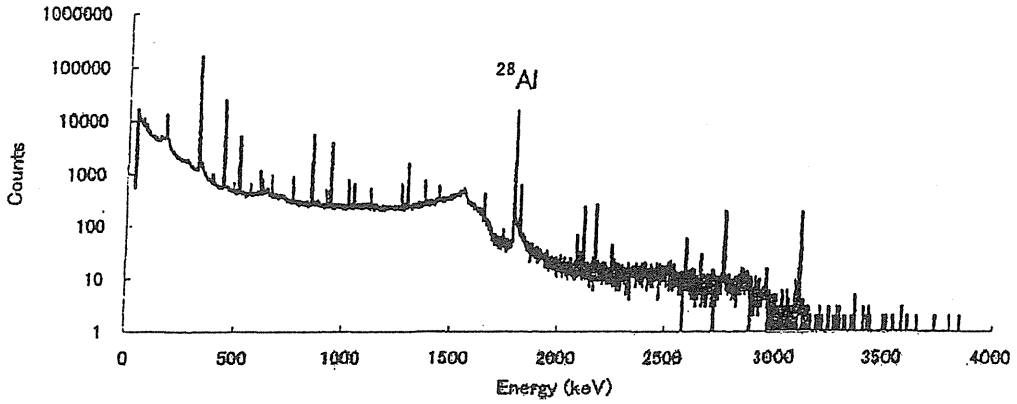


Fig.1 The badge surface paint samples were irradiated for 10 minutes with thermal neutron, which flux was 4.5 X 10^{13}n/cm^2·sec by JAR-4 that is installed at JAERI. After irradiation, the radioactivities of samples were measured by Ge detector (CANBERRA series 35 plus). A photo peak at 1780kev for ^{28}Al was detected.

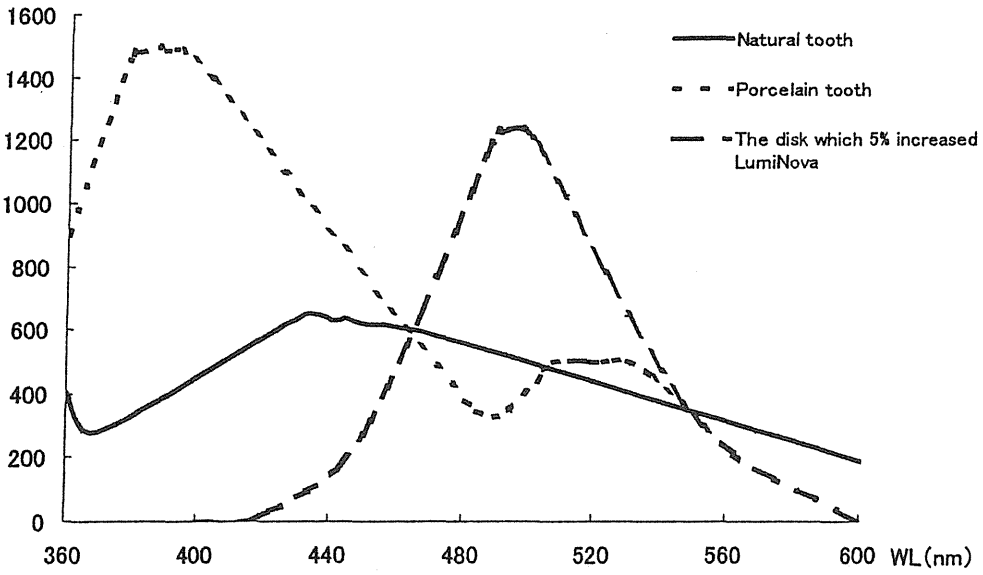


Fig.2 An emission spectrum of natural tooth, porcelain tooth and the disk which 5% increased LumiNova and burnt.

3-4 ko標準化法を用いた炭酸塩岩中の微量元素の中性子放射化分析

Neutron activation analysis of trace elements in carbonate rocks by using a ko standardization method

相沢省一（群馬大学工学部）、澤幡弘之、川手稔（東大原総センター）
S. Aizawa (Faculty of Engineering, Gunma Univ.)
H. Sawahata, M. Kawate (RCNST, The Univ. of Tokyo)

1. はじめに

ko 法は標準物質を必要としない機器中性子放射化分析による元素定量法である。この方法では、試料への中性子照射条件とガンマ線エネルギーの計測に関する様々なパラメータ（中性子照射場の中性子束密度、中性子のエネルギー分布、核種の生成反応断面積、ガンマ線放出率、測定器の検出効率など）をあらかじめ求めておけば、照射試料から放出されるガンマ線のエネルギーを計測するだけで、様々な元素の定量分析が可能である。近年、日本原子力研究所東海研究所の研究用原子炉 JRR-4 及び JRR-3 については種々のパラメータが求められ、ko 法による中性子放射化分析が可能になった。

本研究では炭酸塩岩標準試料 JLs-1（石灰岩）及び JDo-1（ドロマイト岩[$CaMg(CO_3)_2$]）を用いて ko 法で微量元素の定量分析を行ない、繰り返し分析の精度や、得られた定量値をすでに報告されている推奨値と比較して定量値の正確さについて検討し、炭酸塩岩試料への ko 法による放射化分析法の有用性を確かめた。

2. 実 験

試料への中性子照射及びガンマ線の測定は以下に示す条件で行なった。なおガンマ線スペクトルの解析及び元素濃度の計算には市販のソフト『SAMP090』及び『KAYZERO/SOLCOI』を使用した。

試料質量：約 0.2g/個
（ポリエチレンで三重にシール）

原子炉：原研 JRR-4
照射設備：気送管（短寿命核種）
Tパイプ（中寿命及び長寿命）
気送管照射：通常出力（3.5MW）
Tパイプ照射：通常出力（3.5MW）
照射時間： 30 秒（気送管）
15 分（Tパイプ）

	短寿命	中寿命	長寿命
冷却時間	5分	3～4日	38～40日
計測時間	600秒	7,200秒	10,000秒

3．結果及び考察

炭酸塩岩を構成する主成分元素は Ca、Mg、C 及び O である。これら 4 元素の内、C は定量を妨害するγ線を放出する核種が生成しない。他の 3 元素の核データを表 1 に示した。このデータから、O-19 は半減期が短く計測時に妨害しないが、Mg-27 はドロマイト岩では短寿命核種の計測で妨害する可能性があることが分かる。特に 844.0keV は近接する 846.9keV の Mn-56 の計測を妨害する恐れがある。コンプトン散乱によって、Ca-49 は短寿命核種の計測時にバックグラウンドを、Ca-47 及び Sc-47 は中寿命核種の計測時にバックグラウンドを高くする可能性のあることが分かる。

ちなみに、Ca-46 は天然の同位体存在比が小さく、放射化断面積も小さいため、Ca-47 の

JRR-4、 気送管、Tパイプ、 地球科学試料放射化分析

表１　炭酸塩岩を構成する主成分元素の核データ

元素	標的核種	同位体存在比(%)	生成核種	熱中性子放射化断面積(barn)	半減期	壊変様式	主なγ線エネルギー(keV)(相対強度)
O	^{18}O	0.2039	(n,γ)^{19}O	0.00021	29.1s	β^-	197.4(100)
Mg	^{26}Mg	11.17	(n,γ)^{27}Mg	0.027	9.51m	β^-	844.0(70), 1014.1(30)
Ca	^{46}Ca	0.0033	(n,γ)^{47}Ca	0.25	4.53d	β^-	160.0(100), 1296.9(90)
			(n,γ,β^-)^{47}Sc		3.43d	β^-	160.0(100)
	^{48}Ca	0.185	(n,γ)^{49}Ca	1.1	8.7m	β^-	3083(100)

表２　中寿命測定で得られたカルシウムの定量値

試料	Ca(wt.%)					平均値	R.S.D.	推奨値
	1	2	3	4	5		(%)	(wt.%)
JDo-1（ドロマイト岩）	22.76	21.97	24.79	25.31	24.77	23.92	6.12	24.27
JLs-1（石灰岩）	36.20	35.90	39.16	40.91	39.35	38.30	5.66	39.37

計測エネルギー：1296.9keV.

表３　短寿命計測で得られた結果（単位はμg/g）[1)]

	Na	Mg		Al	V	Mn			Sr	Ba
	1369	843.8	1014.4	1778.9	1434.1	846.8	1810.7	2113.1	388.5	165.9
JLs-1-1		5480	5320	120	4.6	22	19		370	410
JLs-1-2		5300	6050	120	4.1	21	20			470
JLs-1-3		5300	5790	120	3.9	21	22			470
JLs-1-4		5650	6290	120	3.8	22	23			410
JLs-1-5		5250	5470	120	4.3	20	22			330[2)]
平均値		5396	5784	120	4.1	21	21		370	440
R.S.D(%)		3.1	6.9	0.0	7.75	3.7	7.3			7.9
推奨値(μg/g)		3650	3650	110	3.6	16	16	16	295	476
JDo-1-1	140	137000	136000	110	4.3	540	61	54		
JDo-1-2	190	136000	138000	110	4.0	530	62	56		
JDo-1-3	140	131000	132000	110	4.2	540	56	57		
JDo-1-4	180	138000	137000	99	4.6	570	57	62		
JDo-1-5	170	129000	132000	100	4.2	530	59	55		
平均値	164	134200	135000	106	4.3	542	59	57		
R.S.D(%)	14	3.0	2.1	5.4	5.1	3.0	4.3	5.5		
推奨値(μg/g	96	112000	112000	92	3.1	51	51	51	116	6.1

1) 空欄は定量値が得られず.
2) この値は統計計算から除外.

表5　定量計算へのパラメータ値の影響（単位はμg/g）

JLs-1（石灰岩）

Run	V (1434.1 keV)		Mn (1810.7 keV)	
	方法1[1)]	方法2[2)]	方法1[1)]	方法2[2)]
JLs-1-1	4.6	4.6	19	19
JLs-1-2	4.1	4.0	20	20
JLs-1-3	3.9	3.9	22	21
JLs-1-4	3.8	3.5	23	22
JLs-1-5	4.3	4.2	22	21
平均値	4.1	4.0	21	21
標準偏差	0.32	0.40	1.5	1.0
推奨値	3.6	3.6	16	16

JDo-1（ドロマイト岩）

Run	V (1434.1 keV)		Mn (1810.7 keV)	
	方法1[1)]	方法2[2)]	方法1[1)]	方法2[2)]
JDo-1-1	4.3	4.1	61	57
JDo-1-2	4.0	3.6	62	55
JDo-1-3	4.2	3.7	56	50
JDo-1-4	4.6	4.0	57	50
JDo-1-5	4.2	4.1	59	57
平均値	4.3	3.9	59	54
標準偏差	0.22	0.23	2.5	3.6
推奨値	3.1	3.1	51	51

1) パラメータ値を試料毎に変えて出した定量値.
2) パラメータ値をJLs-1-1に固定して出した定量値.

1296.9keV のγ線エネルギーを計測することによってCaの定量が可能である。表2に中寿命計測で得られた定量結果を示した。同一試料5個の測定で幾分ばらつきが大きいものの、ほぼ推奨値と同じ値が得られた。本実験は微量元素の定量を目的としているが、主成分のCaの定量も可能である。

3.1 短寿命核種

表3に石灰岩標準試料(JLs-1)及びドロマイト岩標準試料(JDo-1)について、短寿命核種測定で得られた結果を同一試料5個のそれぞれの定量値とその算術平均値で示し、地質調査所の推奨値を下欄に示した。相対標準偏差はいずれもほぼ10%以下であり、再現性のある値が得られた。推奨値と比較すると、Al及びBaでよい一致が見られる。MgやV、Mn、Srでは推奨値に比較して幾分高い値が得られている。また予想通り、846.8keVでのMnの測定は、ドロマイト岩ではMg含量が多いためにその妨害で正確な定量ができないことが分かる。

JRR-4原子炉は通常出力運転時、時間経過とともに中性子束密度が変化することを考慮して、短寿命核種の定量では試料照射毎に金及びジルコニウムを同時に照射し、パラメータを計算してそれを定量計算に用いた。表3はそのような計算で得られた値である。ちなみに、表4は個々のパラメータを示し、表5はそれらのパラメータを用いて計算した値と、最初の照射(JLs-1-1)で得られたパラメータで計算して求めた値を併記したものである。これによると、再現性では両者に大きな違いは無いことが分かり、パラメータを固定して得られた定量値のほうがむしろ推奨値に近い。

表4 短寿命核種の定量に使用したパラメータ値

Sample	Parameter		
	α	f	Fc
JLs-1-1	-0.1542	125.536	101044.936
JLs-1-2	-0.1787	138.535	88204.919
JLs-1-3	-0.1753	144.389	87013.640
JLs-1-4	-0.1163	97.940	121147.246
JLs-1-5	-0.1397	118.592	102975.109
JDo-1-1	-0.1086	91.468	130496.062
JDo-1-2	-0.1022	88.796	126447.599
JDo-1-3	-0.1681	124.762	91457.267
JDo-1-4	-0.1579	117.170	95113.779
JDo-1-5	-0.1575	123.531	98818.492

3.2 中寿命核種

表6及び表7に、中寿命核種測定で得られた結果を示した。本来はその半減期から長寿命核種として計測すべき元素でも、中寿命核種の計測時に定量値が得られたものは表中に記載した。n.d.は定量値の得られなかったものである。

半減期1日ないし10日程度の中寿命核種の計測で定量値の得られた元素はSm、Ho、U、Yb、Ba、Br、As、W、Eu、Na、K、Laの12元素である。これらのうち、Sm、U、Yb、Ba、Eu、Laの6元素については推奨値と比較的よい一致を示している。Asは参考値であるが、それとよく一致している。Brについては参考値と比較して幾分小さい値が得られており、Hoについてはかなり小さい値となっている。Wについては報告値がないため、正確さの検討はできないが、ドロマイト岩及び石灰岩いずれも5個測定して得られた値は非常に精度がよく、ばらつきが小さい。

Naについては推奨値に比較して今回得られた値が非常に大きい。理由としては2つ考えられる。ひとつは、試料を封入したポリ袋のブランク値を求めなかったため、ポリ袋中のNaによる寄与である。二つ目は炭酸塩岩試料ではMgが相当量含まれており、特にドロマイト岩では主成分である。そのため、Mgの(n,p)反応で生成したNaによる寄与である。ただし、石灰岩とドロマイト岩ではMg含量が1桁異なる。今回の定量値を見ると、推奨値との差は石灰岩試料(JLs-1)で約120ppm、ドロマイト岩試料(JDo-1)で約160ppmである。これらの含量差分がすべてMgの(n,p)反応によるものとは考えにくい。100ないし120ppmはポリ袋からのNaで、ドロマイト岩の40ppm程度がMg

表６　石灰岩(JLs-1)について中寿命計測で得られた元素の定量値

元素	核種	半減期	keV	定量値 (μg/g)					平均値	R.S.D.	推奨値
				1	2	3	4	5		(%)	(μg/g)
Sm	Sm-153	47.1h	103.2	n.d.	0.097	n.d.	n.d.	n.d.	0.097		0.135
U	Np-239	2.35d	106.1	1.6	1.5	1.8	1.8	1.7	1.7	7.8	1.75
Ba	Ba131	11.5d	124.2	418	443	475	486	469	458	6.0	476
Mo	Mo-99	67.0h	140.5	2.8	2.5	2.7	2.8	3.0	2.8	6.6	
Ba	Ba-131	11.5d	496.3	388	416	451	474	476	441	8.7	476
Br	Br-82	35.9h	554.3	0.089	0.11	0.13	0.13	0.094	0.11	17	
As	As-76	26.4h	559.2	n.d.	0.15	0.15	0.15	0.16	0.15	3.3	0.145*
W	W-187	24.0h	685.7	0.13	0.13	0.14	0.16	0.14	0.14	8.7	
Sc	Sc-46	84.0d	889.4	n.d.	n.d.	n.d.	0.041	0.034	0.038		0.0307
Na	Na-23	15.0h	1368.4	121	153	156	140	130	140	11	19
K	K-42	12.5h	1524.7	41	46	42	54	49	46	11	25
La	La-140	40.3h	1595.4	0.088	0.11	0.11	0.12	0.10	0.11	11	0.153

*参考値

表７　ドロマイト岩(JDo-1)について中寿命計測で得られた元素の定量値

元素	核種	半減期	keV	定量値 (μg/g)					平均値	R.S.D.	推奨値
				1	2	3	4	5		(%)	(μg/g)
Sm	Sm-153	47.1h	69.7	0.72	0.67	0.72	0.77	0.75	0.73	5.2	0.788
Ho	Ho-166	26.9h	80.6	0.19	0.16	0.18	0.17	n.d.	0.18	7.4	0.42*
Sm	Sm-153	47.1h	103.2	0.68	0.66	0.73	0.74	0.74	0.71	5.3	0.788
U	Np-239	2.35d	106.1	0.63	0.60	0.65	0.72	0.71	0.66	7.8	0.858
Cr	Cr-51	27.8d	320.0	7.4	7.0	8.0	7.2	8.4	7.6	7.7	7.93
Eu	Eu-152	12.3y	344.2	0.20	0.16	0.18	0.17	n.d.	0.18	9.6	0.176
Yb	Yb-177	101h	396.1	0.34	0.30	0.31	0.31	0.33	0.32	5.2	0.323
Br	Br-82	35.87h	554.3	0.55	0.51	0.67	0.60	0.64	0.59	10.9	0.79*
As	As-76	26.4h	559.2	0.14	0.11	n.d.	n.d.	0.15	0.13		0.114
W	W-187	24.0h	685.7	0.23	0.24	0.27	0.29	0.25	0.26	9.4	
Eu	Eu-152m	9.3h	841.6	n.d.	0.14	0.17	n.d.	n.d.	0.15		0.176
Sc	Sc-46	84.0d	889.4	0.13	0.13	0.15	0.15	0.13	0.14	7.9	0.136
Zn	Zn-65	245d	1115.4	n.d.	38.2	n.d.	37.5	n.d.	38		35.4
Na	Na-23	15.0h	1368.4	242	250	265	289	276	264	7.2	96
La	La-140	40.27h	1595.4	8.1	7.8	8.7	8.8	8.7	8.4	5.3	7.83

表８　石灰岩(JLs-1)について長寿命計測で得られた元素の定量値

元素	核種	半減期	keV	定量値 (μg/g)					平均値	R.S.D.	推奨値
				1	2	3	4	5		(%)	(μg/g)
Ce	Ce-141	32.5d	145.4	0.82	0.75	0.71	1.12	n.d.	0.85	21.8	0.521
Cr	Cr-51	27.8d	320.0	3.5	3.6	3.7	3.9	4.0	3.7	5.5	3.37
Ba	Ba-131	11.5d	496.3	455	467	455	515	511	481	6.2	476
Sr	Sr-85	64d	514.0	n.d.	n.d.	313	n.d.	299	306		295
Sc	Sc-46	84.0d	889.4	0.028	0.024	0.030	0.029	0.028	0.028	8.2	0.0307
Fe	Fe-59	45.0d	1098.6	118	130	129	n.d.	n.d.	126	5.3	117
Zn	Zn-65	245d	1115.4	n.d.	3.8	3.4	3.8	3.7	3.7	5.2	3.19
Fe	Fe-59	45.0d	1291.5	121	131	104	n.d.	n.d.	119	11.5	117

表９　ドロマイト岩(JDo-1)について長寿命計測で得られた元素の定量値

元素	核種	半減期	keV	定量値 (μg/g)					平均値	R.S.D.	推奨値
				1	2	3	4	5		(%)	(μg/g)
Ce	Ce-141	32.5d	145.4	2.7	2.8	2.9	2.7	2.8	2.8	3.0	2.49
Yb	Yb-169	30.6d	197.8	0.25	0.23	0.23	0.26	0.27	0.25	7.2	0.323
Tb	Tb-160	73.0d	298.6	0.12	0.10	0.12	0.14	0.12	0.12	12	0.116
Cr	Cr-51	27.8d	320.0	7.7	7.7	9.0	8.5	8.7	8.3	7.1	7.93
Eu	Eu-152	12.3y	344.2	0.13	0.14	0.14	0.16	0.15	0.14	7.9	0.176
Sr	Sr-85	64d	514.0	n.d.	109	n.d.	n.d.	n.d.	109		116
Tb	Tb-169	73.0d	879.4	0.12	0.11	0.12	0.14	0.14	0.13	11	0.116
Sc	Sc-46	84.0d	889.4	0.15	0.15	0.17	0.16	0.16	0.16	5.3	0.136
Fe	Fe-59	45.0d	1098.6	164	154	179	168	151	163	6.9	139
Zn	Zn-65	245d	1115.4	37.9	35.4	41.8	42.9	41.5	40	7.9	35.4
Co	Co-60	5.26y	1173.1	0.20	0.18	0.19	0.22	0.20	0.20	7.5	0.168
Fe	Fe-59	45.0d	1291.5	134	146	154	169	170	155	9.9	139
Co	Co-60	5.26y	1332.4	0.18	0.22	0.24	0.22	0.23	0.22	10	0.168

の(n, p)反応による寄与かもしれない。K については石灰岩試料で推奨値に比較して今回幾分高い値が得られた。測定に用いた K-42 の半減期が 12.5h のため、今回の計測では冷却時間が長すぎ、しかも石灰岩中のカリウム含量が少ないために正確な定量が困難であった。

3.3 長寿命核種

表８及び表９に長寿命核種について得られた定量値を示した。定量値の得られた元素は Ce、Yb、Tb、Cr、Ba、Eu、Sr、Fe、Zn、Co の 10 元素である。ほとんどの元素で推奨値とよい一致を示しているが、石灰岩試料の Ce は推奨値に比較して幾分高い値が得られている。またドロマイト岩の Yb で推奨値に比較して低い値が得られている。ただし Yb は半減期 101h の Yb-177 での計測値が推奨値とよく一致している。

Sr はドロマイト岩及び石灰岩試料とも値の得られたものが少ない。これは 511keV の大きなアニヒレーションピークがすぐそばにあるため、ピークとして認識されなかったことによるためである。ただし、いくつかの得られた定量値は推奨値とよく一致している。

表10 ろ紙に保持した定量目的元素の定量値

元素	核種	半減期	計測エネルギー (keV)	添加量 (μg)	中寿命測定 定量値(μg)		長寿命測定 定量値(μg)	
					Run 1	Run 2	Run 1	Run 2
Sm	Sm-153	47.1h	69.7	0.050	0.058	0.054		
Ho	Ho-166	26.9h	80.6	1.0	1.2	1.2		
Tm	Tm-170	129d	84.4	2.0				
Nd	Nd-147	11.1d	91.4	3.0	3.1	3.0		
Sm	Sm-153	47.1h	103.2	0.050	0.050	0.050		
Se	Se-75	121d	136.0	1.0			1.3	1.3
Ce	Ce-141	32.5d	145.4	2.0	2.0	2.2	2.2	2.4
Yb	Yb-169	30.6d	197.8	0.25	0.21	0.23		0.20
Lu	Lu-177	6.75d	208.4	0.25				
Se	Se-75	121d	264.6	1.0			1.1	1.1
Tb	Tb-160	73.0d	298.6	0.10	0.096	0.088		0.098
Th	Pa-233	27.0d	311.8	0.10				
Cr	Cr-51	27.8d	320.0	5.0		5.3		5.8
Cd	Cd-115m	4.5h	336.6	20.2	21.6	22.8		
Eu	Eu-152	12.3y	344.2	0.10	0.16	0.10	0.089	0.090
Gd	Gd-159	18.0h	363.5	1.0				
Yb	Yb-177	101h	396.1	0.25	0.26	0.26		
Sr	Sr-85	64d	514.0	100			84.0	
Cd	Cd-115	2.3d	527.7	20.2	21.4	22.7		
Nd	Nd-147	11.1d	531.0	3.0	4.1	3.7		
As	As-76	26.4h	559.2	2.0	1.7	1.8		
Sb	Sb-122	2.75d	564.0	2.0	1.9	1.7		
Ag	Ag-110m	253d	657.8	1.0	0.87	0.98	1.1	1.1
Tb	Tb-169	73.0d	879.4	0.10	0.11	0.11		0.10
Sc	Sc-46	84.0d	889.4	0.10	0.11	0.11	0.12	0.12
Rb	Rb-86	18.7d	1076.6	100	108	111	116	118
Fe	Fe-59	45.0d	1098.6	500	533	534	564	565
Zn	Zn-65	245d	1115.4	100	104	105	110	113
Co	Co-60	5.26y	1173.1	1.0	1.2	1.2	1.2	1.2
Fe	Fe-59	45.0d	1291.5	500	542	539	576	550
Co	Co-60	5.26y	1332.4	1.0	1.1	1.2	1.2	1.2
Pr	Pr-142	19.2h	1575.2	2.0	1.9	2.3		
La	La-140	40.27h	1595.4	0.25	0.26	0.29		

3.4 ろ紙標準試料の分析

今回分析した炭酸塩岩標準試料（JLs-1 及び JDo-1）は不純物含量が非常に少ないため、定量できた元素の数が少ない。実際の炭酸塩岩はケイ酸塩鉱物や鉄の酸化物、あるいは硫化物などを数%以上含むものが多い。そこで、ろ紙に定量目的元素を一定量含ませた試料（本来、比較法で定量の基準になる試料）を作成し、ko 法で中寿命及び長寿命核種について定量を試みた。照射条件及び測定条件は炭酸塩岩標準試料の場合と全く同一である。結果を表 10 に示した。表によれば Ho をはじめ、Nd、Se、Cd、Sb、Ag、Rb、Fe、Pr の９元素が定量可能であることがわかった。

4. まとめ

ko 法による中性子放射化分析法で、不純物含量が非常に少ないドロマイト岩及び石灰岩標準試料中の微量元素を定量した結果、短寿命核種測定で２元素、中寿命核種測定で９元素、長寿命核種測定で 10 元素、推奨値とよい一致を示す定量値が得られた。

短寿命核種では正確な定量値の得られた元素数が少なかったが、これは通常出力での結果である。低出力条件下での照射などを行なうことによってその数を増やせると考えている。

定量値の得られた元素

試料	短寿命	中寿命	長寿命
JLs-1	Al, (Mn), (V) Ba, (Mg)	Sm, U, Ba, As, Sc, (La)	(Ce), Cr, Ba, Sr Sc, Fe, Zn
JDo-1	Al, Mn, (V) (Mg)	Sm, U, Cr, Eu, Yb, As, Sc, Zn, La	Ce, (Yb), Tb, Cr, Eu Sr, Sc, Fe, Zn, (Co)

（ ）推奨値との差が幾分大きい.

成果の公表

1）相沢省一、川手稔、澤幡弘之（2002）ko 法による炭酸塩岩標準試料中の微量元素の中性子放射化分析．第６回分析化学東京シンポジウム 2002 機器分析東京討論会発表，p. 150 （幕張メッセ、2002 年９月）．

3-5 k_0放射化分析システムの評価及びデータベース化

Evaluation and database of k_0-standardization neutron activation analysis system

伊藤泰男[1]、尾嵜大真[1]、澤幡浩之[1]、川手稔[1]、相沢省一[2]、福岡孝昭[3]、片山幸士[4]、松尾基之[5]、中西友子[6]、海老原充[7]
Y. Ito[1], H. Ozaki[1], H. Sawahata[1], M. Kawate[1], S. Aizawa[2], T. Fukuoka[3], Y. Katayama[4], M. Matsuo[5], T. Nakanishi[5], M. Ebihara[7]

[1]東京大学原子力研究総合センター、[2]群馬大学工学部、[3]立正大学地球環境科学部、[4]人間環境大学人間環境専攻、
[5]東京大学大学院総合文化研究科、[6]東京大学大学院農学生命科学研究科、[7]東京都立大学大学院
[1]Research Center of Nuclear Science and Tehnology, The Univ. of Tokyo, [2]Faculty of Engneering , Gunma Univ.,
[3]Faculty of Geo-Enviromental Science, Rissho Univ., [4]The Division of Human Enviroment , The Univ. of Human Enviroments
[5]Graduate School of Art and Sciences, The Univ. of Tokyo, [6]Graduate School of Agricultual and Life Sciences, The Univ. of Tokyo
[7]Graduate School of Science, Tokyo Metro. Univ.

1975 年、Simonits らによって単一標準放射化分析法が提案された。その後、いくつかの機関との共同作業により^{198}Auを指標核種としたk_0値と呼ばれる核種ごとの普遍的な複合核定数が実験的に求められ、k_0標準化中性子放射化分析法(以下、k_0法)として確立された。k_0法ではあらかじめ照射場の中性子および測定器の特性を求めておけば、彼らが求めたk_0値を用いることにより分析試料のγ線のスペクトル強度のみから元素濃度を得ることができる。測定器の特性は一度求めておけば大きくは変わらないものであるし、照射場の中性子特性は数個のモニターを分析試料とともに照射・測定するだけで求めることができる。k_0法は標準試料を必要とせず、分析試料のγ線スペクトル中に検出されるすべての核種についての定量が可能であり、非破壊中性子放射化分析(INAA)法の非破壊多元素同時分析法としての能力を最大限に引き出すものである。

大学開放研究室では DSM 社製の SAMPO、KAYZERO、SOLCOIという一連のソフトウェア群を利用したk_0法の導入および利用促進をすべく、以下のような課題について取り組んできた。

- ・分析結果の信頼性の実証
- ・利用の簡便化のための整備
- ・多くの試料に対する分析の実績の蓄積
- ・分析結果および実験条件のデータベース化

さらに研究を進めていく中で上記の一連のソフトウェア群にいくつかの不備があることがわかってきたため、独自のソフトウェアの開発も目的の一つとして加えられた。

k_0法を利用する上で照射場の中性子特性を正確に求めることは非常に重要である。1 サイクル 25 日間連続で運転される JRR-3 については原研利用課によって中性子の直接測定が行われ、非常によく安定していることが示されている。しかし、1 日 6 時間運転の繰り返しである JRR-4 の照射設備については安定性に関しての情報は示されていなかった。大学開放研究室ではk_0法の導入に先立ち、JRR-4 の照射場の中性子特性に関しての測定を行った。k_0法でパラメータ測定に用いられる Au、Zr および Al を照射し^{28}Al、^{198}Au、^{95}Zr、^{97}Zr の生成放射能を測定した結果、6 時間の運転時間内に出力調整のための制御棒の位置調整があった場合 10%を越える中性子束の変動が認められた(図 1、2)。3.5MW の定常出力運転時では6時間の間に 3～4 回の制御棒の位置調整があり(図 1)、100kW 運転時でも条件次第では必要となり(図 2)、中性子束の変動が認められる。したがって、JRR-3 のようにサイクルで一度原子炉パラメータを求めればよいという訳にはいかず、それぞれの照射ごとにモニターを用いた照射場パラメータの決定が必要となることがわかった。

測定器については検出効率、FWHM、PTT (peak to total ratio)およびエネルギーの校正が必要とされる。検出効率、FWHM、PTT については一般的に大きな変動のあるものではなく、現在大学開放研究室に設置されている測定器についてはすでに実施され、実際の分析にも利用している。エネルギーの校正は停電対策などのための電源断や測定目的に則した意図的な変更をすることもあり、変更するたびに校正が必要である。また、そのような変更がない場合も一ヶ月程度の期間で定期的に行っていく予定である。

研究施設・装置
JRR-4 気送管、T-パイプ

研究分野
放射化分析

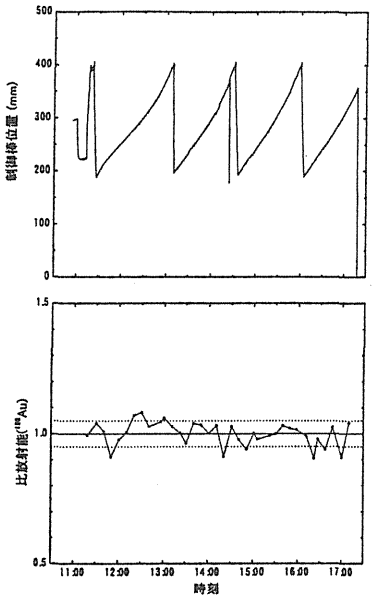


図1 JRR-4 3.5MW運転時の制御棒の位置とAuモニターの比放射能

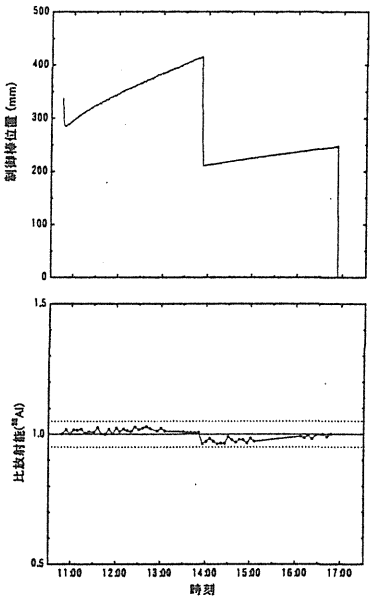


図2 JRR-4 100kW運転時の制御棒の位置とAlモニターの比放射能

実際のk_0法を用いた分析では標準試料として推奨値が示されている地質研究総合センター(旧地質調査所)より配布された標準岩石試料 10 種類(JA-1、JB-1、JB-1a、JG-1、JGb-1、JP-1、JR-1、JCh-1、JSl-1、JSd-1)および文献値の豊富なAllende 隕石を用いた。JB-1a については異なる出力でそれぞれ複数回の分析を行い、分析結果の繰り返し精度も求めた。

一連の実験における中性子照射および試料の測定のスケジュールを表1に示した。γ線スペクトルの解析、元素濃度の計算には SAMPO90、KAYZERO、SOLCOI を用いた。

表1 中性子照射および測定のスケジュール

		中性子照射			測定	
		100kW	350kW	3.5MW	冷却時間	測定時間
短半減期核種	気送管	2分間	30秒間	6秒間	10分	300秒
中半減期核種	Tパイプ	30分間	10分間	1分間	12～24時間	3600秒
長半減期核種	Tパイプ	6時間	2時間	10分間	7日	3600秒
					10日	10000秒
					14日	40000秒

本研究による分析結果を表 2、3、4 に示し、図 3、4 には分析値を文献値あるいは推奨値により規格化し、元素ごとにプロットした。図からも明らかなように多くの分析値が文献値と20%の範囲内で一致しており、20%以上のずれを示すものは検出下限に近いものがほとんどである。

得られた結果の中で Mg の分析値で推奨値や文献値より高くなる傾向が認められた。これは Al からの副反応の寄与によるものと考えられ、実際に同時に照射・測定した Al 標準試料中の Mg の生成量を用いて補正したところ(表中の corrected)、推奨値とほぼ一致した。図 3、4 には補正後の値を用いた。また表 2、3、4 には記載されてないが、いくつかの試料について Mo の分析値が得られたものの、明らかに文献値よりも高かった。図 5 に U 濃度と Mo 分析値の文献値に対する過剰分の相関図を示した。U 濃度と Mo 分析値の過剰分との間には正の相関関係が見られることから、Mo 分析値の過剰は中性子捕獲による U の核分裂片の影響と考えられる。これも Mg と同様に U の核分裂からの寄与を補正することにより正確な分析結果を得ることは可能であると思われる。Zn については JB-1a の

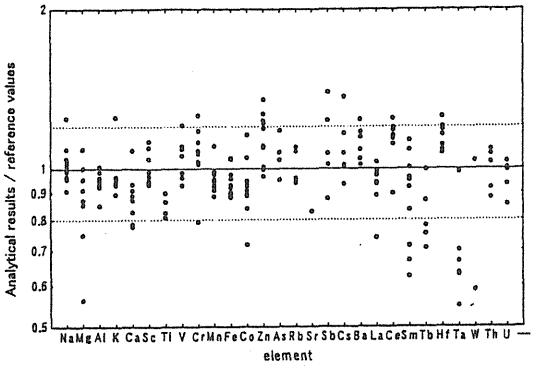


図3 k_0法による分析結果と文献値との比較

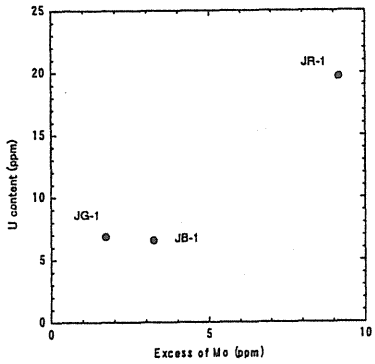


図4 Mo分析値の過剰分とU濃度の相関関係

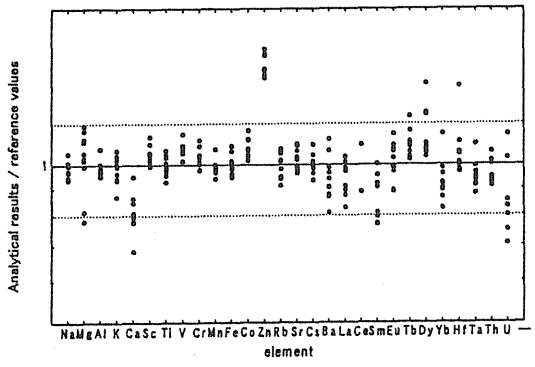


図5 JB-1aのk_0法による分析値の分散

すべての結果が推奨値に比べ50%程度大きい。これは従来の比較法でも大きくなることがあり、k_0法の計算法にではなく、他に原因があるものと考えられる。

Allende隕石のγ線スペクトル中には^{192}Irのピークが確認されたが、分析値が算出されなかった。これは^{192}Irのk_0値が求められていないためである。このようなk_0値のない核種は他にもいくつかあり、その影響はその核種に対する分析ができないことだけでない。これらの核種のγ線を他の核種のものと誤同定してしまい、間違った分析結果を生む可能性もある。今後k_0値が求められることが望まれる。

これらのDSM社製のSAMPO、KAYZERO、SOLCOIという一連のソフトウェア群による計算法における問題点を踏まえて、独自の解析ソフトウェアの開発も進めており、その骨格は完成しつつある。

さらに本研究では様々な試料の分析を行い、それらの結果や照射場のパラメータをデータベース化することも目的としている。これは必ずしも達成されたとは言い難いが、少なくとも評価のために行われた分析についてのデータは分析値、照射場パラメータ(表 5)ともに蓄積され、今後の分析にも生かされるはずである。

以上、計画のすべてを完遂した訳ではないが、申請した期間およびそれ以前からの成果により、大学開放研究室におけるk_0法の利用は実用の域に達し、実際にいくつかのグループでの利用もある。今後も新規利用者や完全な未知試料の分析などに利用を促していきたい。

参考文献

Imai et al. (1996a) *Geostandards Newsletter*, **19**, 135-213
Imai et al. (1996b) *Geostandards Newsletter*, **20**, 165-216
Jarosewich et al. (1987) *Smithsonian Contrib. Earth Sci.* **27**, 1-12.
Kallemeyn and Wasson (1981) *Geochim. Cosmochim. Acta* **45**, 1217-1230.
Kallemeyn et al. (1989) *Geochim. Cosmochim. Acta* **53**, 2747-2767.
Simonits et al. (1975) *J. Radioanl. Chem.*, **24**, 31-46.

成果の公表

尾嵜大真、澤幡浩之、川手稔、伊藤泰男 "宇宙・地球化学的試料に対するk_0標準化中性子放射化分析法の適用－標準試料を必要としない非破壊多元素同時分析法－", 2001年度日本地球化学会年会、2001年10月
H. Sawahata, M. Kawate, H. Ozaki, Y. Ito, "The k_0 standardization NAA on the low power operation at JRR-4", 2001 Asia-Pacific Symposium on Radiochemistry and the Annual Meeting of the Japan Society of Nuclear and Radiochemical Sciences, November, 2001
伊藤泰男、川手稔、澤幡浩之、尾嵜大真 "放射化分析解析プログラム Interactive NAA Windows の開発", 2002年度日本放射化学会年会、2002年9月

表2 標準岩石の分析結果

element		JA-1 this work	JA-1 literature[1]	JB-1 this work	JB-1 literature[1]	JG-1 this work	JG-1 literature[1]
Na	%	3.10 ± 0.13	2.85	2.10 ± 0.07	2.05	2.59 ± 0.10	2.51
Mg	%	2.28 ± 0.15	0.95	6.17 ± 0.014	4.65	1.96 ± 0.15	0.45
corrected		0.500		4.41		0.452	
Al	%	7.78 ± 0.36	8.06	7.69 ± 0.15	7.69	6.58 ± 1.10	7.54
Cl	ppm	<500	43	<300	176	<500	58.1
K	%	0.800 ± 0.153	0.64	1.11 ± 0.13	1.19	2.95 ± 0.12	3.3
Ca	%	3.70 ± 0.33	4.07	5.76 ± 0.31	6.61	1.30 ± 0.26	1.57
Sc	ppm	29.7 ± 0.7	28.5	27.1 ± 0.6	27.5	6.15 ± 0.15	6.53
Ti	%	<0.4	0.51	0.683 ± 0.048	0.79	<0.6	0.16
V	ppm	101 ± 14	105	233 ± 8	211	<100	25.2
Cr	ppm	9.23 ± 1.14	7.83	536 ± 20	425	57.5 ± 2.6	53.2
Mn	%	0.108 ± 0.001	0.122	0.130 ± 0.002	0.118	0.0462 ± 0.0005	0.049
Fe	%	4.82 ± 0.12	4.95	5.86 ± 0.13	6.29	1.35 ± 0.03	1.52
Co	ppm	11.0 ± 0.2	12.3	36.2 ± 0.7	38.2	3.41 ± 0.09	4.06
Zn	ppm	108 ± 4	90.9	104 ± 4	85.2	40.8 ± 1.8	41.1
As	ppm	3.28 ± 0.35	2.78	2.50 ± 0.33	2.33	<1.5	0.33
Br	ppm	<2		<2	0.58	<1.5	0.068
Rb	ppm	<15	12.3	45.3 ± 3.3	41.3	174 ± 6	182
Sr	ppm	<300	263	<300	444	<150	184
Sb	ppm	0.235 ± 0.050	0.22	0.346 ± 0.051	0.28	0.181 ± 0.034	0.13
Cs	ppm	<0.7	0.62	1.43 ± 0.11	1.23	10.2 ± 0.2	101
Ba	ppm	364 ± 40	311	535 ± 31	493	534 ± 23	466
La	ppm	5.20 ± 0.14	5.242	37.9 ± 0.8	38.6	16.6 ± 0.3	22.4
Ce	ppm	16.5 ± 1.5	13.3	80.1 ± 3.7	67.8	41.1 ± 2.0	45.8
Sm	ppm	3.39 ± 0.04	3.52	4.73 ± 0.07	5.13	3.30 ± 0.01	4.62
Tb	ppm	0.748 ± 0.074	0.75	0.616 ± 0.052	0.82	0.551 ± 0.036	0.78
Hf	ppm	3.03 ± 0.48	2.42	3.92 ± 0.66	3.31	4.12 ± 0.23	3.56
Ta	ppm	<0.3	0.13	1.86 ± 0.09	2.93	1.13 ± 0.07	1.79
W	ppm	<4	0.34	10.1 ± 0.5	17.1	<3	1.58
Th	ppm	0.891 ± 0.80	0.82	9.91 ± 0.25	9.3	11.6 ± 0.3	13.2
U	ppm	<0.4	0.34	1.72 ± 0.15	1.67	3.24 ± 0.21	3.47

表2 (続き)

element		JGb-1 this work	JGb-1 literature[1]	JP-1 this work	JP-1 literature[1]	JR-1 this work	JR-1 literature[1]
Na	%	0.929 ± 0.035	0.89	0.0249 ± 0.0006	0.02	2.97 ± 0.13	2.98
Mg	%	6.32 ± 0.27	4.73	26.0 ± 0.8	26.9	1.33 ± 0.08	0.07
corrected		4.29				<0	
Al	%	8.88 ± 0.19	9.262	<0.9	0.35	6.60 ± 0.07	6.79
Cl	ppm	<400	81	<200	97	804 ± 141	920
K	%	<0.4	0.2	<0.15	0.002	3.45 ± 0.29	3.66
Ca	%	7.56 ± 0.56	8.5	<0.15	0.39	<0.3	0.48
Sc	ppm	33.4 ± 1.1	35.8	6.86 ± 0.24	7.24	4.73 ± 0.17	5.07
Ti	%	0.791 ± 0.074	0.96	<0.5		<0.15	0.066
V	ppm	700 ± 16	635	<60	27.6	<15	7
Cr	ppm	61.7 ± 7.2	57..8	3150 ± 198	2807	<3	2.83
Mn	%	0.142 ± 0.009	0.146	0.0873 ± 0.0005	0.094	0.0700 ± 0.0004	0.077
Fe	%	9.69 ± 0.34	10.53	5.22 ± 0.20	5.85	0.547 ± 0.020	0.62
Co	ppm	56.0 ± 1.6	60.1	107 ± 4	116	0.595 ± 0.126	0.83
Zn	ppm	120 ± 7	109	51.5 ± 6.2	41.8	29.6 ± 1.8	30.6
As	ppm	<3	1.09	<1.5	0.34	15.5 ± 0.9	16.3
Br	ppm	<3		<1.5		2.50 ± 0.30	
Rb	ppm	<20	9.87	<15	0.8	241 ± 16	257
Sr	ppm	<300	327	<150	3.32	<150	29.1
Sb	ppm	<0.3	0.085	<0.15	0.034	1.04 ± 0.02	1.19
Cs	ppm	<0.6	0.26	<0.4	0.15	19.4 ± 1.0	20.8
Ba	ppm	<150	64.3	<100	19.5	156 ± 59	50.3
La	ppm	3.49 ± 0.10	3.6	<0.6	0.084	20.3 ± 0.7	19.7
Ce	ppm	9.67 ± 1.01	8.17	<3	0.19	56.4 ± 4.0	47.2
Sm	ppm	1.62 ± 0.10	1.49	<0.05	0.019	3.76 ± 0.19	6.03
Tb	ppm	<0.4	0.29	<0.3	0.003	0.787 ± 0.039	1.01
Hf	ppm	0.942 ± 0.083	0.88	<0.3	0.2	4.99 ± 0.26	4.51
Ta	ppm	<0.2	0.18	<0.2	0.02	1.24 ± 0.06	1.868
W	ppm	<5	0.81	<3	0.85	<4	1.59
Th	ppm	0.493 ± 0.095	0.48	<0.3	0.19	27.5 ± 0.8	26.7
U	ppm	<0.5	0.13	<0.5	0.036	9.16 ± 0.43	8.88

表2 (続き)

element		JCh-1 this work			JCh-1 literature[2]	JSd-1 this work			JSd-1 literature[2]	JSl-1 this work			JSl-1 literature[2]
Na	%	0.0205	±	0.00005	0.0226	1.96	±	0.08	2.02	1.64	±	0.06	1.62
Mg	%	0.125	±	0.025	0.0455	2.61	±	0.20	1.09	3.23	±	0.11	1.46
corrected		<0				0.783			1.09	1.21			1.42
Al	%	0.597	±	0.021	0.388	7.96	±	0.20	7.75	8.79	±	0.22	9.31
Cl	ppm	<100			14	<500			67.5	<500			21.5
K	%	<0.2			0.183	1.75	±	0.15	1.81	2.26	±	0.13	2.36
Ca	%	<0.05			0.0321	2.02	±	0.15	2.17	1.14	±	0.15	1.06
Sc	ppm	0.946	±	0.038	0.0979	10.3	±	0.3	10.9	15.8	±	0.6	16.7
Ti	%	<0.05			0.0189	0.311	±	0.060	0.39	0.39	±	0.06	0.43
V	ppm	9.66	±	1.48	10.4	91.7	±	9.0	76	143	±	9	131
Cr	ppm	5.58	±	0.41	7.04	22.2	±	3.0	21.5	62.1	±	5.1	60.9
Mn	%	0.0123	±	0.0003	0.0134	0.0703	±	0.0013	0.07156	0.0439	±	00012	0.04639
Fe	%	0.238	±	0.011	0.249	3.19	±	0.12	3.54	4.23	±	0.17	4.73
Co	ppm	14.1	±	0.7	15.5	9.94	±	0.34	11.2	13.8	±	0.4	151.5
Zn	ppm	8.68	±	1.64	7.93	97.2	±	7.0	96.5	109	±	6	108
As	ppm	<0.7			0.567	<3			2.42	15.5	±	1.1	14.9
Br	ppm	<0.5				2.22	±	0.36	1.65	<3			
Rb	ppm	9.27	±	0.90	8.61	64.6	±	5.1	67.4	111	±	4	117
Sr	ppm	<90			4.2	282	±	32	340	<200			193
Sb	ppm	80.9	±	10.8		<0.3				0.950	±	0.083	0.933
Cs	ppm	0.332	±	0.043	0.243	1.92	±	0.25	1.89	8.13	±	0.42	7.6
Ba	ppm	307	±	20	302	542	±	44	520	377	±	36	305
La	ppm	1.48	±	0.04	1.52	17	±	1	18.1	27.6	±	0.7	29.3
Ce	ppm	6.02	±	0.41	5.21	39.2	±	2.7	34.4	67.4	±	4.6	60.6
Sm	ppm	0.240	±	0.084	0.359	3.31	±	0.03	3.48	5.02	±	0.40	6.02
Tb	ppm	<0.06			0.0385	0.429	±	0.037	0.431	0.624	±	0.051	0.717
Hf	ppm	0.234	±	0.029	0.195	3.79	±	0.38	3.55	5.02	±	0.43	4.63
Ta	ppm	0.179	±	0.034	0.182	0.65	±	0.035	0.893	0.461	±	0.048	0.842
W	ppm	95.5	±	2.6	92.3	<4				<2			2.47
Th	ppm	0.675	±	0.067	0.735	4.57	±	0.17	4.44	10.3	±	0.4	9.97
U	ppm	0.629	±	0.084	0.736	0.994	±	0.092	1	2.64	±	0.19	2.63

literature : 1 Imai et al. (1996a); 2 Imai et al. (1996b)

表3 Allende 隕石の分析結果

element		this work			Smithsonian	UCLA
Na	%	0.325	±	0.009	0.34	0.329
Mg	%	15.2	±	0.3	14.78	14.8
corrected		14.8				
Al	%	1.70	±	0.03	1.74	1.76
Cl	ppm	316	±	14		
Ca	%	1.44	±	0.15	1.84	1.86
Sc	ppm	12.4	±	0.1	11	11.3
V	ppm	97.3	±	0.7	92	99
Cr	ppm	0.433	±	0.012	0.36	0.364
Mn	%	0.143	±	0.002	0.15	0.145
Fe	%	24.7	±	0.3	23.57	23.7
Co	ppm	694	±	7	600	662
Zn	ppm	148	±	6	110	117
As	ppm	1.68	±	0.35		1.57
Se	ppm	10.5	±	1.1		8.2
Br	ppm	1.83	±	0.41		1.6
La	ppm	0.492	±	0.061	0.52	0.495
Sm	ppm	0.342	±	0.036	0.34	0.302
Os	ppm	1.09	±	0.24		0.832
Au	ppm	0.130	±	0.008	0.15	0.145

Smithsonian : Jarosewich et al. (1987)
UCLA : Kallemeyn and Wasson (1981), Kallemeyn et al. (1989)

表4 標準岩石 JB-1a の分析結果

element		100kW 1	100kW 2	100kW 3	100kW 4	literature[1]
Na	%	1.90 ± 0.07	1.90 ± 0.05	1.96 ± 0.06	2.02 ± 0.05	2.03
Mg	%	7.08 ± 0.62	6.40 ± 0.25	6.46 ± 0.26	6.50 ± 0.27	4.72
corrected		5.48 ± 0.48	4.86 ± 0.19	3.83 ± 0.15	4.96 ± 0.21	
Al	%	7.50 ± 0.07	7.46 ± 0.12	7.52 ± 0.06	7.64 ± 0.02	7.65
K	%	1.01 ± 0.10	1.24 ± 0.11	1.17 ± 0.04	1.19 ± 0.10	1.16
Ca	%	4.54 ± 0.40	5.38 ± 0.27	5.27 ± 0.70	5.73 ± 0.15	6.65
Sc	ppm	28.3 ± 0.1	28.0 ± 0.1	28.8 ± 0.1	30.6 ± 0.6	27.9
Ti	%	0.820 ± 0.115	0.763 ± 0.078	0.734 ± 0.04	0.805 ± 0.009	0.77
V	ppm	217 ± 9	208 ± 7	220 ± 7	218 ± 4	205
Cr	ppm	398 ± 1	383 ± 2	393 ± 2	426 ± 40	392
Mn	%	0.108 ± 0.001	0.112 ± 0.001	0.114 ± 0.001	0.115 ± 0.001	0.115
Fe	%	6.09 ± 0.01	6.04 ± 0.01	6.27 ± 0.02	6.71 ± 0.18	6.33
Co	ppm	40.3 ± 0.0	40.4 ± 0.1	41.3 ± 0.1	43.2 ± 0.2	38.6
Zn	ppm	125 ± 1	123 ± 1	125 ± 1	137 ± 2	82.1
Rb	ppm	35.8 ± 1.3	37.2 ± 0.9	38.5 ± 0.6	41.5 ± 6.8	39.2
Sr	ppm	470 ± 13	431 ± 14	425 ± 1	481 ± 40	442
Cs	ppm	1.30 ± 0.05	1.32 ± 0.01	1.22 ± 0.04	1.31 ± 0.05	1.31
Ba	ppm	457 ± 18	455 ± 16	438 ± 13	564 ± 111	504
La	ppm	31.1 ± 0.5	36.6 ± 0.7	38.9 ± 0.6	34.2 ± 1.2	37.6
Ce	ppm	58.6 ± 5.2	72.0 ± 7.6	< 500	< 150	65.9
Sm	ppm	3.91 ± 0.20	4.59 ± 0.02	5.08 ± 0.08	3.32 ± 0.14	5.07
Eu	ppm	1.59 ± 0.21	1.55 ± 0.15	1.50 ± 0.05	1.67 ± 0.53	1.46
Tb	ppm	0.755 ± 0.055	0.746 ± 0.059	0.704 ± 0.032	0.763 ± 0.041	0.69
Dy	ppm	5.02 ± 0.43	4.31 ± 0.67	4.25 ± 0.74	4.38 ± 0.40	3.99
Yb	ppm	2.07 ± 0.16	2.40 ± 0.32	1.88 ± 0.05	1.82 ± 1.12	2.1
Hf	ppm	3.42 ± 0.10	3.40 ± 0.07	3.34 ± 0.03	4.83 ± 0.70	3.41
Ta	ppm	1.92 ± 0.15	1.80 ± 0.14	1.70 ± 0.12	1.84 ± 0.15	1.93
Th	ppm	8.38 ± 0.03	8.21 ± 0.04	8.34 ± 0.03	9.18 ± 0.50	9.03
U	ppm	1.30 ± 0.27	< 0.6 ±	1.11 ± 0.70	< 1 ±	1.57

表4 (続き)

element		350kW 1	350kW 2	350kW 3	350kW 4	literature[1]
Na	%	2.13 ± 0.08	2.05 ± 0.06	1.97 ± 0.05	1.97 ± 0.06	2.03
Mg	%	7.14 ± 0.22	6.91 ± 0.28	6.58 ± 0.27	6.92 ± 0.27	4.72
corrected		5.61 ± 0.18	5.23 ± 0.21	4.81 ± 0.20	5.28 ± 0.21	
Al	%	8.20 ± 0.03	7.66 ± 0.05	7.52 ± 0.02	7.45 ± 0.09	7.65
K	%	1.08 ± 0.04	1.15 ± 0.05	1.09 ± 0.04	1.21 ± 0.00	1.16
Ca	%	6.30 ± 0.25	5.62 ± 0.30	5.17 ± 0.28	5.30 ± 0.29	6.65
Sc	ppm	27.7 ± 2.4	28.7 ± 0.1	29.4 ± 0.2	28.4 ± 0.1	27.9
Ti	%	0.745 ± 0.004	0.776 ± 0.003	0.795 ± 0.13	0.754 ± 0.017	0.77
V	ppm	235 ± 1	223 ± 2	208 ± 6	222 ± 1	205
Cr	ppm	383 ± 75	398 ± 2	409 ± 1	404 ± 0	392
Mn	%	0.123 ± 0.01	0.115 ± 0.001	0.112 ± 0.001	0.113 ± 0.001	0.115
Fe	%	5.98 ± 0.47	6.20 ± 0.01	6.37 ± 0.01	6.22 ± 0.01	6.33
Co	ppm	39.3 ± 0.3	41.1 ± 0.1	43.1 ± 0.1	40.0 ± 0.1	38.6
Zn	ppm	121 ± 7	123 ± 10	133 ± 3	125 ± 1	82.1
Rb	ppm	36.8 ± 8.2	40.0 ± 1.6	41.2 ± 0.6	39.8 ± 0.6	39.2
Sr	ppm	430 ± 72	439 ± 15	457 ± 6	434 ± 15	442
Cs	ppm	1.29 ± 0.12	1.30 ± 0.10	1.37 ± 0.03	1.26 ± 0.08	1.31
Ba	ppm	442 ± 21	408 ± 36	473 ± 14	486 ± 18	504
La	ppm	32.8 ± 1.1	33.5 ± 1.0	37.0 ± 0.8	38.0 ± 0.4	37.6
Ce	ppm	58.4 ± 3.6	< 60	< 500	< 60	65.9
Sm	ppm	3.90 ± 0.23	4.11 ± 0.92	4.66 ± 0.14	5.09 ± 0.22	5.07
Eu	ppm	1.42 ± 0.16	1.30 ± 0.01	1.45 ± 0.15	1.57 ± 0.07	1.46
Tb	ppm	0.709 ± 0.075	0.715 ± 0.021	0.729 ± 0.029	0.705 ± 0.028	0.69
Dy	ppm	5.72 ± 0.52	4.99 ± 0.78	4.20 ± 0.82	4.14 ± 0.06	3.99
Yb	ppm	1.73 ± 0.17	1.89 ± 0.05	2.01 ± 0.07	1.90 ± 0.09	2.1
Hf	ppm	3.30 ± 0.81	3.44 ± 0.11	3.57 ± 0.07	3.44 ± 0.09	3.41
Ta	ppm	1.81 ± 0.13	1.82 ± 0.14	1.77 ± 0.12	1.76 ± 0.13	1.93
Th	ppm	8.32 ± 0.87	8.42 ± 0.03	8.55 ± 0.04	8.50 ± 0.04	9.03
U	ppm	1.79 ± 0.15	1.34 ± 0.11	< 1	1.62 ± 0.20	1.57

表4 (続き)

element		3.5MW 1			3.5MW 2			literature[1]
Na	%	1.97	±	0.07	1.92	±	0.07	2.03
Mg	%	6.77	±	0.26	6.25	±	0.24	4.72
corrected		3.68	±	0.14	4.68	±	0.18	
Al	%	7.28	±	0.08	7.27	±	0.00	7.65
K	%	1.12	±	0.01	1.20	±	0.08	1.16
Ca	%	5.33	±	0.28	5.15	±	0.15	6.65
Sc	ppm	29.3	±	0.2	31.6	±	0.1	27.9
Ti	%	0.746	±	0.024	0.713	±	0.031	0.77
V	ppm	216	±	11	217	±	0	205
Cr	ppm	407	±	1	437	±	2	392
Mn	%	0.112	±	0.001	0.111	±	0.001	0.115
Fe	%	6.43	±	0.12	6.88	±	0.01	6.33
Co	ppm	41.1	±	0.1	44.9	±	0.1	38.6
Zn	ppm	126	±	1	134	±	2	82.1
Rb	ppm	41.9	±	3.2	42.0	±	0.9	39.2
Sr	ppm	451	±	9	484	±	15	442
Cs	ppm	1.33	±	0.07	1.43	±	0.04	1.31
Ba	ppm	497	±	24	537	±	27	504
La	ppm	39.5	±	0.4	33.7	±	0.6	37.6
Ce	ppm	< 400			< 50			65.9
Sm	ppm	4.84	±	0.10	4.03	±	0.27	5.07
Eu	ppm	1.44	±	0.03	1.31	±	0.13	1.46
Tb	ppm	0.853	±	0.061	0.800	±	0.034	0.69
Dy	ppm	4.29	±	0.71	4.35	±	0.68	3.99
Yb	ppm	1.94	±	0.05	1.93	±	0.12	2.1
Hf	ppm	3.60	±	0.07	3.77	±	0.11	3.41
Ta	ppm	1.86	±	0.16	2.11	±	0.17	1.93
Th	ppm	9.04	±	0.11	9.55	±	0.04	9.03
U	ppm	1.18	±	0.80	1.26	±	0.27	1.57

literature : 1 Imai et al. (1996a)

表5 JRR-4における照射場のパラメータ

irradiation channel and time	α	f	Fc
100kW operation			
PN 2min	0.0406	22.935	12007.507
PN 2min	0.0330	23.569	11383.999
PN 2min	0.0371	24.566	10988.554
PN 2min	-0.0312	34.337	7553.582
PN 2min	0.0233	25.095	10568.914
PN 2min	0.0187	27.095	9892.782
PN 2min.	0.0317	27.080	11249.737
PN 2min	0.0367	23.946	11282.261
PN 2min	0.0166	26.413	10145.198
PN 2min	0.0409	22.674	11991.933
PN 2min	0.0391	22.797	11853.993
PN 2min	0.0315	23.973	11143.757
PN 2min	0.0058	26.650	9834.536
PN 2min	0.0123	26.033	10126.353
PN 2min	0.0100	25.791	10388.554
TA 30min	0.1226	18.669	24798.268
TA 30min	0.0531	22.672	19392.365
TA 30min	0.0219	30.029	15938.790
TA 30min	0.0309	28.079	16569.765
TB 6h	0.0139	40.998	8625.231
TB 6h	0.0408	35.116	9757.024
TB 6h	0.0529	31.668	12559.841
TB 6h	0.0616	31.451	10631.410

表5 続き

irradiation channel and time	α	f	Fc
350kW operation			
PN 30sec	0.0697	17.654	47607.103
PN 30sec	0.0418	22.349	40676.479
PN 30sec	0.0243	26.549	35004.474
PN 30sec	0.0181	27.272	34266.001
PN 30sec	0.0394	23.212	37801.383
PN 30sec	0.0374	23.097	38938.696
PN 30sec	0.0250	25.390	34909.679
PN 30sec	0.0300	24.707	37033.738
PN 30sec	0.0279	24.672	35465.805
PN 30sec	0.0229	25.277	36599.840
PN 30sec	0.0340	23.272	38793.954
PN 30sec	0.0308	24.422	36888.652
PN 30sec	0.0236	24.317	36720.929
PN 30sec	0.0192	24.860	37146.815
PN 30sec	0.0042	27.776	33140.307
TA 10min	0.0365	31.287	55155.794
TA 10min	-0.0038	45.959	42086.025
TA 10min	0.0126	28.809	58679.827
TA 10min	0.0401	38.693	28526.812
TB 2h	-0.0077	28.185	52944.265
TB 2h	0.0334	33.793	40635.250
TB 2h	0.0804	27.829	39722.190
TB 2h	0.0443	38.527	35722.995
3.5MW operation			
PN 6sec	0.0494	22.317	259132.959
PN 6sec	0.0701	17.729	303777.131
PN 6sec	0.0474	22.813	240087.530
PN 6sec	0.0453	22.316	250480.042
PN 6sec	0.0430	21.870	252074.514
PN 6sec	0.0463	21.943	263972.363
PN 6sec	0.0389	22.869	295792.108
TA 1min	-0.0203	43.770	384093.978
TA 1min	0.0472	24.377	556311.392
TB 10min	0.0293	41.007	301140.592
TB 10min	-0.0006	49.636	257226.015

3-6

炭素材料による環境モニターの開発と応用(2)

Application of Carbon Fiber for Environmental Monitor

九州大学大学院理学研究院　前田米蔵、杉原真司

Yonezo Maeda, Shinji Sugihara, Faculty of Sciences, Kyushu University

九州大学大学院理学府　亀田周二、川村一徳

Kameda Shuji, Kazunori Kawamura, Graduate School of Sciences, Kyushu University

１．はじめに

環境中に存在する有害元素、有害物質の分析定量を正確、迅速に行うことは現在重要な問題の一つである。環境中におけるこれらの有害元素はその多くが微量であるため、測定は困難な場合が多く、試料の採取時点或いは分析時点での測定値を得るためには多量の試料を利用するか、濃縮等の前処理が必要である。そこで、元素の濃縮法の一つとして、炭素材料の吸着、収着性を利用して、新しい環境指針として利用できる環境モニターの開発を目的としている。この環境モニターは、環境濃度の積算値又は平均値を求めることになり、瞬間の濃度は測定できないが、環境への影響を考える場合は、微量元素の定常時の変動を観測する必要があり、採取操作等が簡便であることも考慮しなければならない。

炭素繊維は、様々な用途に使用されている。材料としての利用が主な用途であるが、樹脂や金属などと混ぜ合わせて使用される複合材料である。これは炭素繊維が軽くて強度が大きいという点を活用したものである。一方、炭素繊維には微生物が大量に集まる現象があることがわかり、水質浄化、下水処理や、魚の藻場や漁礁、砂漠の緑化材等に利用されつつある。これは、炭素繊維の高い生物親和性を活用したものである。

炭素繊維のこの２番目の特性を利用して、環境水中に存在する微量有害元素の長期的モニターとしての開発の発展性を研究することを目的とした。環境モニターとしての応用のため、炭素材料への環境中の微量元素の吸着の様子や生物親和性による微生物の生育状況を探り、数種類の元素を溶かした実験水と実際の河川水につけた炭素繊維を試料として、吸着した元素を放射化分析で定量した。

２．実験

今実験で使用した炭素繊維は、トレカ T-300（東レ(株)）である。

a）炭素繊維を河川水に浸漬することによる、河川水中の各元素濃度の経時変化測定

河川水(30Ｌ)に、Cr を 2ppm となるように添加した水槽へ炭素繊維を浸け、その河川水を数日置きに 100ml ずつ採水し、河川水中の各元素(Na,Mg,Ca,Cr)濃度の経時変化を原子吸光法を用いて測定した。さらにそのときに浸けていた炭素繊維は、灰化炉で灰化し、硝酸抽出後、原子吸光法を用いて各元素（Na,Mg,Ca,Cr）の吸着量を測定した。

b）河川水中の元素濃度の変化による、炭素繊維への吸着量変化測定

河川水へ、Cr 濃度が 0.01,0.1,1ppm となるように添加した溶液(500ml)を調製した。この溶液に炭素繊維を３日間浸けた後、炭素繊維への Cr 吸着量を測定した。また、イオン交換水へ Cr 濃度が 0.05,0.1,0.2,0.5ppm となるように添加した溶液(500ml)を調製した。この溶液に、あらかじめ河川中に３日間浸けていた炭素繊維を３日間浸けた後、Cr 吸着量を測定した。

c）炭素繊維吸着元素の定性および定量分析

JRR-3,PN-3 JRR-4HR-1　環境試料放射化分析

環境モニターとしての指標となる元素を調べるため、河川水に浸けていない炭素繊維、採水した河川水へ3日間浸けていた炭素繊維、実際に河川中へ3日間浸けていた炭素繊維の3試料について、放射化分析法を用い吸着元素の定性および定量を行った。中性子照射は、JRR-3で10秒間照射、直後に100秒測定、JRR-4で3時間照射、照射後1週間冷却し、その後HPGe半導体検出器を用いて1000秒間γ線スペクトルの測定を行った。標準試料にはJB-1を用いた。

3．結果と考察

a）炭素繊維を浸漬することによる、河川水中の各元素濃度の経時変化測定

河川水中のNa,Mg,Ca濃度の経時変化をFig.1に、Cr濃度の経時変化をFig2.に示す。Na,Mg,Ca濃度については、炭素繊維を浸けることによる濃度の減少は見られなかったが、Crについては炭素繊維を浸けることにより顕著な濃度の減少が見られた。

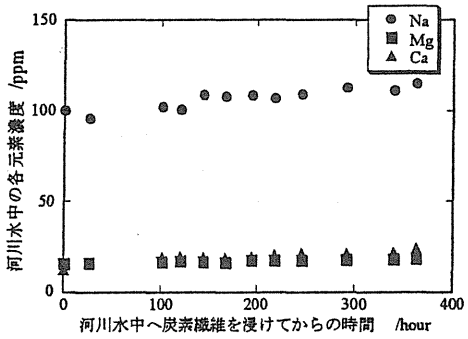


Fig.1 河川水中の各元素濃度の経時変化

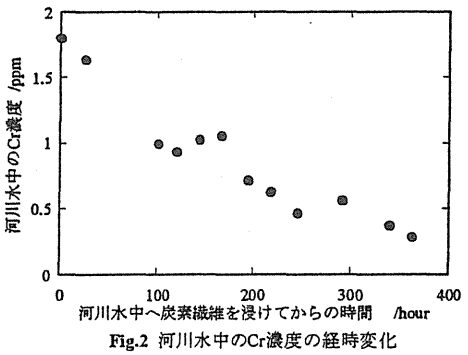


Fig.2 河川水中のCr濃度の経時変化

このときの各元素の炭素繊維への吸着量をTable 1に示す。河川水中のCr濃度はNa濃度の50分の1、Mg,Ca濃度の5分の1程度であるにもかかわらず、炭素繊維への吸着量はCrが最も高い値を示した。このことから、他の3元素に比べCrが炭素繊維に吸着しやすいことがわかった。また、溶液中に低濃度で存在するCrを濃縮していると言える。

Table1 炭素繊維への各元素吸着量(μg/炭素繊維g)

Na	Mg	Ca	Cr
48.9	4.85	N.D.	62.2

b）河川水中の元素濃度の変化による、炭素繊維への吸着量変化測定

結果をFig.3に示す。溶液中のCr濃度が増加するにつれ、炭素繊維へのCr吸着量も増加した。このことから、炭素繊維を用いて河川水中の元素濃度を、定量的に測定できる可能性が示唆される。しかし溶液中のCr濃度の増加の割合に対し、炭素繊維へのCr吸着量の増加の割合が小さいことから、予想していたような微生物膜による河川水中の微量元素の濃縮が、効果的になされていないと考えられる。また、あらかじめ河川中に浸けていた炭素繊維への、吸着量の変化の結果をFig.4に示す。Fig.3とは違い溶液中のCr濃度が増加するにつれ、炭素繊維へのCr吸着量の増加は見られなかった。これは、河川水に3日間浸けるという前処理によって、他元素の吸着が起こったり、Crの吸着が阻害されたためと考えられる。

c）炭素繊維吸着元素の定性および定量分析

結果をTable 2に示す。実験a）において測定した4種類の元素の他に、8種類の元素の吸着が見られた。このことから、多くの元素において炭素繊維への吸着が行われており、それらの元素について炭素繊維がモニターとして用いられる可能性が考えられる。またこの結果においても実験a）と同様に、Crについて多くの吸着が見られた。またこの実験において河川中にあらかじめ3日間浸けておいた炭

素繊維は、実験ｂ）において３日間浸けておいた炭素繊維とは異なる時期に浸けていたにもかかわらず、吸着量が 25.5μg/炭素繊維ｇと Fig.4 における結果と非常に近い値を示した。他元素の共存下での

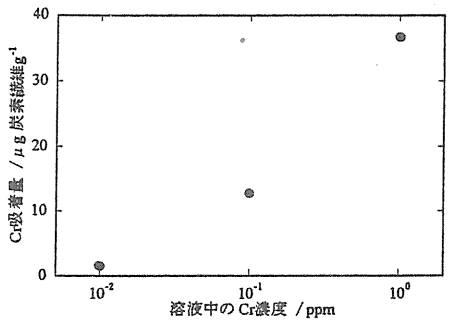


Fig.3 炭素繊維へのCrの吸着量変化

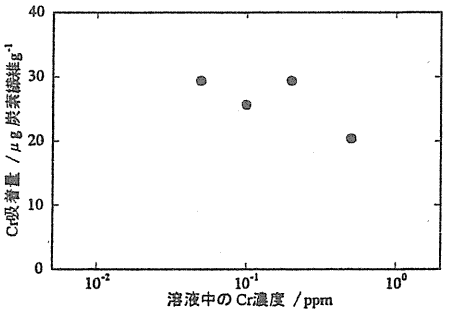


Fig.4 あらかじめ河川中に浸けておいた炭素繊維へのCrの吸着量変化

Cr の吸着量が一定であるかあるいは炭素繊維自体への特徴であるかは特定できていない。標準の関係で定量できなかったが、約３０元素のピークが検出できた。また、Cr のほかに Ce,Fe において顕著な吸着が見られていることから、これらの元素おいて特に炭素繊維が環境モニターとして用いられる可能性が高いと思われる。

４．結論

今回の実験では、予想していたほどの河川水中の物質の吸着が行われず、炭素菌の生育状況や生育環境等を調べることが出来なかった。これは河川水中では、炭素繊維に固着現象が見られた汚泥中と比べ炭素菌の量が少ないためであると考えられる。そのような河川水中においても、一定条件の下では溶液中の濃度の増加に伴い炭素繊維への吸着量にも増加が見られ、モニターとしての可能性が見られた。

今後は、各元素の存在形態の違いによる吸着量の差を調査したり、炭素繊維上の固着物が流水によって損失することがあるため固定の方法を更に考慮する必要がある。また、炭素繊維上への炭素菌の定量的な培養法について更に実験を行い、定量的評価を可能にする必要がある。

５．成果の公表

１）亀田周二、学士卒業論文（２００１）
「環境モニターとしての炭素繊維の利用」
２）亀田周二、Ｃ＆Ｃプロジェクト２００１報告書
「炭素繊維を用いた環境モニターの有効性の研究」

Table 2 炭素繊維への吸着元素と吸着量

	炭素繊維への各元素吸着量(μg/炭素繊維 g)								
	Ce	Co	Cr	Cs	*Fe	Th	Sb	Sc	Tb
B.G.	4.58	N.D.	N.D.	N.D.	N.D.	1.24	N.D.	0.0048	0.164
河川水中	16.1	3.60	3.19	0.501	3.86	2.02	0.099	0.391	0.257
河川中	11.0	4.22	25.5	0.950	8.62	2.28	0.160	3.09	0.293

(*x10^3)

3-7

放射化による金属フラーレンの研究(II)

Study of metallofullerenes with neutron activation (II)

末木啓介 *[1]、趙宇亮 *、秋山和彦 *[2]、佐藤渉 **、菊地耕一 *、片田元己 *

* 東京都立大学大学院理学研究科

** 理化学研究所

Keisuke SUEKI*, Yulang ZHAO*, Kazuhiko AKIYAMA*, Wataru SATO**, Koichi KIKUCHI*, Motomi KATADA*

* Graduate School of Science, Tokyo Metropolitan University

**The Institute of Physical and Chemical Research (RIKEN)

1 平成14年3月16日から筑波大学化学系

2 平成14年4月から日本原子力研究所博士研究員

研究の目的

金属フラーレンを中性子放射化することによって高感度で定量性が高い実験が行うことができる。ごく少量しか生成しない新規金属フラーレンに関する合成条件の改良の問題や、希土類元素内包金属フラーレンに関する系統的な研究を続けて行ってきた。

1. Hfフラーレンの合成条件の検討

Hfフラーレンとして$Hf_2@C_{80}$と$Hf@C_{84}$の存在を前回の課題中に明らかにした。Hfは中性子放射化で^{181}Hfを得ることができ^{181}Ta(<-^{181}Hf)はPAC核であることからTDPAC法などによる物性研究ができると期待される。しかし、その収率は希土類のとき得られた収率の1/10以下であり、このままでは物性研究をするために必要な量を得るにはかなりの努力が必要であることから、アーク放電法でより効率よく合成する条件についてHe雰囲気の圧力依存性とNi金属を混合したときの収率変化の効果とを調べた。これらの研究は、様々な金属フラーレンを合成するとき用いる金属元素の物性との関係を明らかにする上でも重要であると考えられる。

【実験】 直径6mmの炭素棒に内径4mmの穴をあけてその中にグラファイト粉末と目的の金属を含む粉末を適当な濃度になるように混合してつめた。Hfは炭化ハフニウムの粉末をNiは金属粉末を用いた。今回の実験ではHfとCの原子数比は約1:130となった。NiはHfに対して原子数比で0.1, 1, 2, 4となるように調整した。この調整した炭素棒を陽極にして小型のフラーレン合成槽内にHeガスを5kPaから70kPa詰めてアーク放電を行った。炭素棒を約50mm消費したところでアーク放電をやめススを回収した。ススは上蓋に付着した分を別に回収した。回収したススはo-ジクロロベンゼンを用いて還流によって抽出し、ろ過して抽出成分(crude)を得た。crudeはCS_2溶媒に溶解して5PBB固定相を用いてHPLC展開し$Hf_2@C_{80}$が含まれるところを分画した。それぞれ得られた試料をすべて中性子放射化分析でHf濃度を定量した。HPLC分画した試料は放射化後、Buckyprep固定相にトルエン溶媒下で打ち込み、^{181}Hfのラジオクロマトを確認した。

【結果と考察】 上蓋に付着したススの量は、Heの圧力が30kPaを超えるとほとんど一定となった。図1はHe圧と上蓋のスス中のHf濃度変化を示した。Hfを含む炭素棒から得られたススのHf濃度は10から30kPaで最大になる。ス ス、crudeと5PBBでの$Hf_2@C_{80}$分画でのHf濃度は相関関係があることが示された。今までアーク放電は50kPaで行っていたが、He圧を10-30kPaにすることで2から3倍収量が増加することが期待される。また、Niを Hfの原子数と同量加えてときのHeの圧力変化はNiを含まな

研究施設 JRR3 , JRR4

研究分野 放射化学

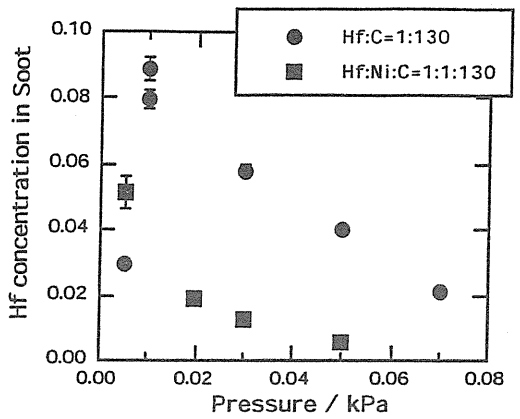


Fig.1 Pressure dependence of Hf concentration in Soot.

い条件から大きく変化し、より圧力が低いときに最大の収量が得られる傾向がある。50kPaでNi濃度を変化したとき、Ni濃度が高いほどス中のHfの濃度が減少しており、希土類で報告されている収量の増加とはまったく違う傾向であることが明らかとなった。以前の研究でHf, Taについてはアーク放電した後の陽極を観察した場合に残った部分の表面に金属光沢があり、混合した金属が析出していることが分かっており、実試料でも条件によっては蒸発したスにはHfがほとんど含まれない場合が存在していた。収量が増加するのは放電時の直流電流が大きく流れる条件を設定できる場合であることがわかった。この傾向とまったく逆なことがマルチトレーサーを用いた場合の融点が低い元素で見られた。アルカリ土類やEu, Ybはより緩やかな放電条件で収率が増加することが観察されている。

5PBBでC_{82}-C_{86}（含む$Hf_2@C_{80}$），C_{88}-C_{92}の分画した試料を放射化した後にBuckyprep固定相をもちいてトルエンで展開した。得られた分画試料についてオフラインでGe半導体検出器を用いて^{181}Hfのγ線測定を行いラジオクロマトグラフが得られた（図2、3）。図2は今までに明らかにした$Hf_2@C_{80}$が合成されそのHPLC挙動を再現した。図3でラジオクロマトから主に溶出時間83.5分と100.5分に^{181}Hfの放射能が観測されHfフラーレンの存在を強く示唆している。これらの分子種についてはこれから再度合成して単離を行い、質量分析などで分子種の決定をする予定である。

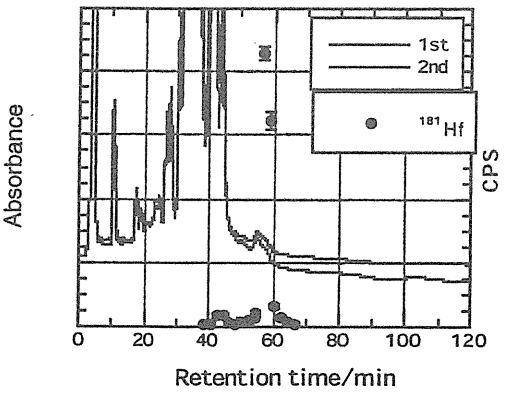


Fig.2 The elution curves of the radioactive Hf fullerene sample. The fraction sample collected within C_{82}-C_{86} from 5PBB column was injected into a Buckyprep column (4.6 mmf x 250mm, toluene eluent, flow rate of 0.75 mL/min). The solid lins monitored by UV detector. The circles were measured by HPGe detectors.

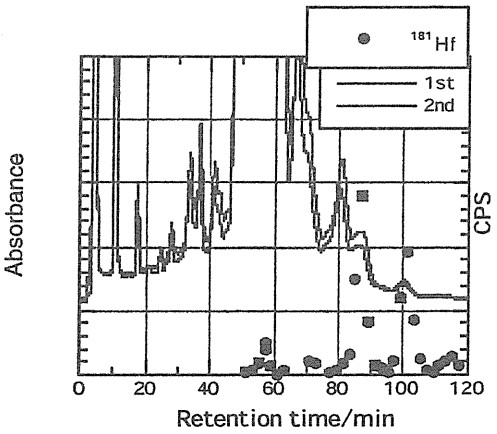


Fig.3 The elution curves of the radioactive Hf fullerene sample. The fraction sample collected within C_{88}-C_{92} from 5PBB column was injected into a Buckyprep column (4.6 mmf x 250mm, toluene eluent, flow rate of 0.75 mL/min). The solid lins monitored by UV detector. The circles were measured by HPGe detectors.

2. ランタノイド内包金属フラーレンの系統的研究

LaからLuまでのランタノイド元素はフラーレンに内包したときにSm, Eu, Tm, YbはLaなどと異なる挙動をすることが明らかになっている。しかし、他のLa, Ce, Pr, Nd, Gd, Tb, Dy, Ho, Er, Luにおいても生成分子種の種類や生成量の違いを明らかにしてきた。$M@C_{82}$と$M_2@C_{80}$を中心に生成量やそのHPLC挙動の詳細な違いについて検討してみた。

【実験】La, Ce, Pr, Nd, Gd, Tbの6種類の軽希土類を含む炭素棒を作製して、アーク放電法で金属フラーレンを合成した。この試料について5PBBとBuckyprepの2段階のHPLC分離を行った。Buckyprep展開した試料を1分毎に分取して放射化分析でそれぞれの元素についてのクロマトグラムを得た。$M@C_{82}$と$M_IM_{II}@C_{80}$については総量も求めた。

【結果と考察】 それまでに行っていたLa-Luまでの同時合成の実験とあわせて得られた結果をまとめた。図4aが$M@C_{82}$の生成量を$La@C_{82}$で規格化したものであり、図4bは$M_IM_{II}@C_{82}$で図4cは$M_IM_{II}@C_{80}$の場合で前者は$LuM_{II}@C_{82}$で後者は$LaM_{II}@C_{80}$の生成量で規格化してある。同じC_{82}のケージに原子が1個入りと2個入りの場合ではその生成量は明らかに

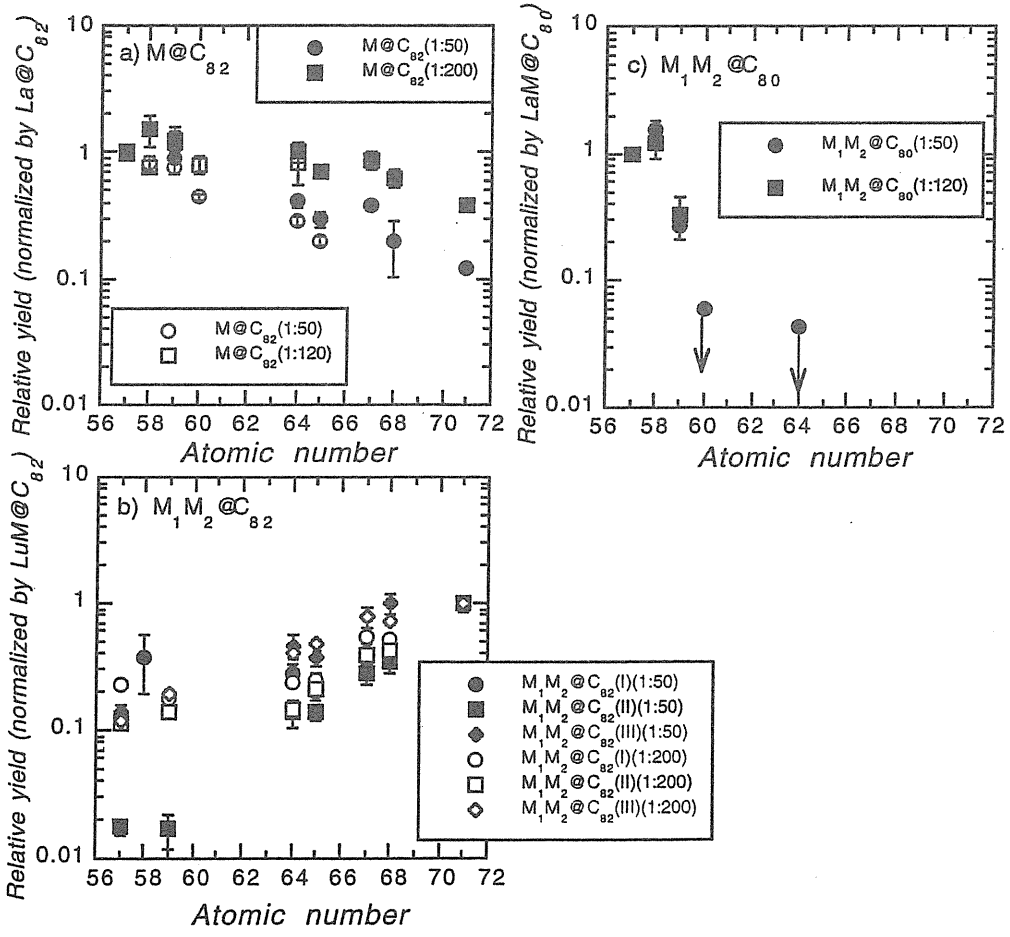


Fig.4 Relative production yields of lanthanoid metallofullerenes. (a) The relative productionn yields of $M@C_{82}$ normalized to the yield of $La@C_{82}$, (b) the relative production yields of $M_1M_2@C_{82}$ normalized to the yield of $LuM@C_{82}$, and (c) the relative production yields of $M_1M_2@C_{80}$ normalized to the yield of $LaM@C_{80}$.

逆相関を示している。また、C_{80}に2個原子が入る場合にはCeを中心に生成している傾向が観察された。C_{82}で2個入りの場合にイオン半径が小さなLuが内包されやすいことから、この生成量の変化にはランタノイド元素のイオン半径が関係しているのではないかと考えられる。C_{80}でCeが最も多い収量を持っていることからケージの大きさによっては内包する元素のイオン半径の選択性も存在することが推測される。

図5は$M@C_{82}$のBuckyprep固定相の溶出時間R_fを原子番号に対して図示した。LaからLuまで緩やかに増加する傾向が見られるが、Gd, Tbはその傾向からR_fが大きいほうに外れていることが分かった。この原因が分子の持つ双極子モーメントにかかわっているという報告もあるが、具体的にはまだ検討中である。

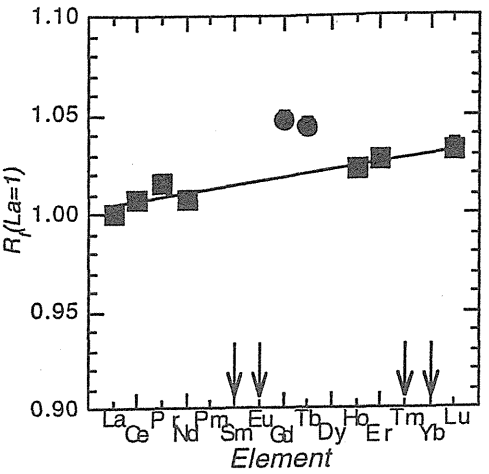


Fig. 5 Retention time of $M@C_{82}$ normalized to that of $La@C_{82}$ in toluene elution through the Buckyprep column. The retention time of $M@C_{82}$ encapsulating Sm, Eu, Tm, and Yb is shorter by about 80 % than that for $La@C_{82}$. The solid line is drawn by least square fits to the data for La, Ce, Pr, Nd, Ho, Er, and Lu.

3. 今後の計画

新規内包フラーレンに関する研究では、融点の高い金属元素を内包する条件としてより高温の温度条件を作る必要があることが明らかになり、Taなどの元素を内包することも可能になってきたと考えている。Hfフラーレンはその収率を2－3倍にすることで、物性研究の足がかりができたと考えていて、大量合成をしていくつかの分子種について研究を進めて行きたい。

Hfフラーレンの研究の一部は平成14年度筑波大学学内プロジェクトの助成を受けて行われた。

発表論文

1) Systematic study of lanthanoid endohedral metallofullerenes. K. Sueki, K. Akiyama, Y.L. Zhao, I. Ito, Y. Ohkubo, K. Kikuchi, M. Katada, H. Nakahara, *J. Radioanal. Nucl. Chem.*, 255 (2003) 159.

3-8

高純度鉄標準物質及び高純度金属中の微量元素分析法の開発

Development of neutron activation analysis for ultra-trace elements in high purity materials and metals

岡田往子、平井昭司 ： Yukiko Okada, Shoji Hirai

武蔵工業大学 工学部 :Faculty of Engineering, Musashi Institute of Technology

1. 緒言

近年、循環型を目指した社会の構築計画に伴い、年々増加する鉄鋼スクラップの利用拡大が進められている。鉄鋼スクラップのリサイクル化は、資源の有効活用であり、また、鉄鉱石還元に使用するエネルギーの三分の一で済むことなど地球環境保全にも貢献する。一方、鋼の高機能化によるめっき鋼材やグリット鋼の増加、電気製品の小型化による分別の困難さが鉄鋼スクラップ中の不純物元素の増大をもたらすことになる。そのため、不純物元素が鋼中に多量に存在すると製品の品質が劣化し、スクラップ前の加工性を維持することもできない。増大するスクラップをリサイクルし、かつ鉄鋼品質を維持するためには不純物を除去する技術の開発と不純物元素を分析する技術の開発が不可欠である。不純物の中でも特に分析方法が急がれている元素はトランプ元素（Zn, As, Sn, Sb, Pb, Bi）といわれる元素である。現在ＪＩＳ法で定められている分析方法として、Snは原子吸光法(JIS G1257-1994)、よう化物抽出分離フェニルフルオロン吸光光度(JIS G1226-1994)、Pbは原子吸光法(JIS G1257-1994)、鉄分離ジフェニルカルバゾン抽出吸光光度法(JIS G1229-1994)、Znは原子吸光法(JIS G1257-1994)、Asは原子吸光法(JIS G1257- 1994)と水酸化ベリリウム共沈・三水素化ひ素気化分離ジエチルチオカルバミン酸銀吸光光度法(JIS G1225-1992)、Sbは原子吸光法(JIS G1257-1994)と吸光光度法(JIS G1235-1991)、ブリリアングリーン- トルエン抽出吸光光度法(JIS G1235- 1991)、Biは原子吸光法(JIS G1257-1994)などある。しかしながら、これらの元素の定量範囲は0.1%から数10ppm程度と、数ppm以下を定量するには分析法の開発が望まれている。本研究では高感度分析法である機器中性子放射化分析法でトランプ元素の中で放射化しないPb及びBi以外の4元素（Zn、As、Sn、Sb）及び本法により鉄試料では高感度で定量できるCr, Co, Ni, Mo, Ta, Wを対象にNIST鉄標準物質の分析を行った。

2. 実験

分析試料はNIST1763,NIST1765、JSS168-7を用いた。分析に使用した試料量は40mgから130mgである。また、Table1に示す照射・測定条件を示す。中性子照射はJRR-4（最大熱中性子束密度：1.3×10^{13}n cm

$^{-2}sec^{-1}$) で出力 3.5MW と 100kW を用いて行った。出力 3.5MW では分析試料を石英管に封入し、アルミニウム製のカプセルに入れ、照射した。100kW ではポリエチレン袋に二重封入し、ポリエチレン製カプセルに詰め、照射した。照射終了後、試料を開封し、あたらしいポリエチレン袋に二重封入され、測定を行った。照射終了 2 日後に一回目のγ線測定、照射 7 日後に二回目のγ線測定、照射 36 日～72 日後に三回目のγ線測定を行った。γ線測定は高純度 Ge 検出器とマルチチャネル波高分析器で行った。収集したγ線スペクトルの解析は、武蔵工業大学で独自に開発した GAMA98 解析ソフトプログラムを用いて行った。

定量には比較法を用い、JSS168-7 を比較標準物質として用いた。

Table1 Irradiation and counting conditions and analyzed nuclide

Irradiation facility, Thermal neutron flux	Irradiation time	Cooling time	Counting time	Analyzed nuclide
JRR-4				
T-pipe 3.5MW	1h	12d	20min	^{76}As ^{122}Sb ^{99}Mo ^{187}W
		24d-25d	1hr-1.3hr	^{65}Zn ^{113}Sn ^{124}Sb ^{51}Cr ^{54}Mn ^{59}Fe ^{60}Co ^{58}Co ^{182}Ta
S-pipe 100kW	6h	5d	20min	^{76}As ^{122}Sb ^{99}Mo ^{187}W
		17d	1hr-2hr	^{65}Zn ^{113}Sn ^{124}Sb ^{51}Cr ^{54}Mn ^{59}Fe ^{60}Co ^{58}Co ^{182}Ta

出力 3.5MW では試料照射に石英管を用いるため、比較標準物質との照射位置の熱中性子束密度の差が生じる。今回の試料は高純度鉄標準物質であるので、熱中性子束密度補正には鉄の放射能を用いた。

Table2 にはトランプ元素の Zn、As、Sn、Sb、主成分の Fe 及び Cr, Co, Ni, Mo, Ta の中性子による原子核の主な核反応を示す。

中性子放射化分析による定量では、主に（n , γ）反応で生成する核種のγ線を測定する。鉄鋼試料ではマトリックスである Fe からは ^{51}Cr、^{54}Mn などの核種が生成する。今回分析した対象の Cr では ^{51}Cr の核種からのγ線を測定するため、Fe からの寄与分を差し引かなければならないが、本実験では行わなかった。

Table2 Nuclear data of Fe,Zn, As, Sn, Sb, Cr,Co, Ni, Mo, Ta, W used for analysis

elements	Target nuclide	Natural abundance (%)	Nuclear reaction	Activated Nuclide	Half-life
Fe	^{54}Fe	5.84	n , γ	^{55}Fe	2.6y
			n , p	^{54}Mn	313d
			n , α	^{51}Cr	27.8d
	^{56}Fe	91.68	n , γ	^{57}Fe	stable
			n , p	^{56}Mn	2.58h
	^{57}Fe	2.17	n , γ	^{58}Fe	stable
	^{58}Fe	0.31	n , γ	^{59}Fe	45.0d
Zn	^{64}Zn	48.99	n , γ	^{65}Zn	245d
As	^{75}As	100	n , γ	^{76}As	26.5h
Sn	^{112}Sn	0.96	n , γ	^{113}Sn	115d
Sb	^{121}Sb	57.25	n , γ	^{122}Sb	2.8d
	^{124}Sb	42.75	n , γ	^{124}Sb	60d
Cr	^{50}Cr	4.31	n , γ	^{51}Cr	27.8d
Co	^{59}Co	100	n , γ	^{60}Co	5.26yr
Ni	^{58}Ni	67.76	n , p	^{58}Co	71.3d
Mo	^{98}Mo	23.78	n , γ	^{99}Mo	2.8d
Ta	^{181}Ta	99.99	n , γ	^{182}Ta	115d
W	^{187}W	28.4	n , γ	^{187}W	24h

3. 結　果

3-1　熱中性子束密度

出力 3.5MW では試料照射に石英管を用いるため、比較標準物質との照射位置の熱中性子束密度の差が生じる可能性があると考え、試料中の Fe の値で検討したが、差は現われなかった。

3-2　照射条件の違いによる値の検討

Table3 に T-pipe 3.5MW1 時間と S-pipe 100kW 6 時間で照射して分析した NIST1763 及び 1765 の分析結果の比較を示す。

Cr, Mo, As, Co は照射条件で値の違いが

Table3 Comparison of Analytical values with Irradiation Conditions

NIST1763 (ppm)

Irradiation facility	S-pipe 100kW				T-pipe 3.5MW				
Irradiation time	6h				1h				
	A	B	C	Ave.	D	E	F	G	Ave.
Mo	4700	5000	5000	4900 ±170		4700	4900	5200	4900 ±250
Cr	4200	4900	5000	4700 ±440	4700	4600	4800	4900	4800 ±150
As	520	570	570	550 ±29		510	540	540	530 ±17
Sb	85	55	55	65 ±17	74	91	97	100	96 ±5
Co	910	930	940	930 ±15	900	892	950	960	930 ±37

NIST1765 (ppm)

Irradiation facility	S-pipe 100kW				T-pipe 3.5MW				
Irradiation time	6h				1h				
	H	I	J	Ave.	K	L	M	N	Ave.
Mo	51	53	48	51 ±2.5	42		46	46	46 ±0
Cr	480	500	500	490 ±12	470	470	490	500	490 ±15
As	12	11	11	11 ±0.58			12	11	12 ±0.7
Sb	9.7	5.4	5.5	6.9 ±2.5	8.7	8.8	10	10	9.6 ±0.7
Co	14	13	13	13 ±0.58	13	13	12	13	13 ±0.6

Table4 Concentration of elements in NIST1763,1765 high pure iron (ppm)

	NIST 1763		NIST 1765	
	This work	Certified	This work	Certified
B		54		9
C		2030		60
Mg				<1
Al		430		(60)
Si		6300		(40)
P		120		52
S		230		38
Ti		3100		55
V		3000		40
Cr	4700 ±300	5000	490 ±10	510
Mn		15800		1440
Co	930 ±30	950	13 ±1	12
Ni	*	5100	*	1540
Cu		430		13
Zn	<100		<60	
As	540 ±30	550	11 ±1	10
Zr		440		(2)
Nb		1000		4
Mo	4900 ±200	5000	48 ±4	
Sn	<400	110	<300	20
Sb	96 ±5	(110)	9.6 ±0.7	10
Ta	*		*	
W	*			
Pb				3
Bi				(<1)

なく、良い一致が見られた。

しかしながら、Sbの値でS-pipe 100kW 6時間照射分析で低めの値を示した。これは両試料とも同じ傾向を示した。NISTで示しているSb値はNIST1763で110ppm(参考値)、1765で10ppm（認証値）であることから、T-pipe 3.5MW 1時間で照射・分析した値が近いことが分かった。他の元素の値が両照射方法で違いがないことから、照射方法でなんらかの誤差を生じたとは考えにくい

Crの値はNIST1763及び1765とも良い一致があり、照射条件による違いは現れなかった。本来はFeから生成する^{51}Crの影響が考えられるが、本試料のように含有しているCrが比較的多い場合は寄与分の補正を行わなくても良いことが分かった。

3-3 分析値と認証値の比較

Table4にNIST1763、1765の分析結果と認証値を示す。Cr, Co, As, Mo, Sbともに認証値との良い一致があった。Znの定量下限値はTable3で記述したとおり、T-pipe 3.5MW 1時間で照射・分析した値を採用した。

表中に＊で示されている部分は検出されが、比較標準試料として用いたJSS168-7で検出されなかった元素であるため、定量ができなかった。また、ZnとSnについてはJSS168-7でも検出されず、NIST1763, 1765でも検出されなかったが、大まかな検出限界を立教大原子炉の中央実験管のデータから算出したものである。この結果から、今回の照射・測定条件ではZnの定量下限値は100ppm程度、Snは数100ppm程度であり、微量なZn及びSnの分析は出来ないことがわかった。＊で示した元素の値を立教大原子炉の中央実験管のデータから算出したところ、NIST1763でNiが数千ppmレベル，Taが数十ppmレベル，Wが十ppmレベルに含有していることがわかった。また、NIST1765ではNiが千数ppmレベル，Taが数十ppmレベルに含有していることがわかった。

Facilities and Instruments

JRR-3M(HR-1, 2)

Research field

Neutron activation analysis

3-9 生理活性物質中の微量元素に関する研究

Study on trace elements in physiologically active substances.

共立薬科大学 先端技術講座
森田裕子、村上 勲、飯島史朗
Laboratory for Advanced Science and Technology, Kyoritsu College of Pharmacy
Yuko Morita-Murase, Isao Murakami, Shiro Iijima

1. 研究目的と意義

生体中の微量元素の中には、ヘモグロビンやクロロフィルにおける鉄やマグネシウムのように、活性に極めて重要な役割を果たすものが存在する。

本研究室では、生体内の微量元素の役割を解明する研究の一環として、金属酵素、金属タンパク質など種々の生理活性物質中の微量元素を熱中性子放射化分析による定量を行った。

さらに生理活性物質の機能を理解するために、X線や放射光による立体構造解析を目的として、金属含有量の高い生理活性物質についてその結晶化を試みた。本研究により得られる知見は、生体内中の微量元素の役割を明らかにするための基礎データとして極めて重要と思われる。

2. 研究の方法

139種類の生理活性物質試料3～5 mgを秤量し；よく洗浄、乾燥したポリエチレン製の袋に二重に封入して照射試料とした。熱中性子照射は、日本原子力研究所東海研究所のJRR-4研究用原子炉の気送管照射設備を利用した。熱中性子束は最大で3.2×10^{17} ($m^{-2}\cdot sec^{-1}$)、照射時間は0.5～5分であった。照射終了後、3～10分冷却後および5～6時間冷却後にゲルマニウム半導体検出器を用いてγ線の測定を行った。測定時間は300秒または1000秒で、dead timeは10%以下であった。

得られたγ線スペクトルから、試料中に含まれる微量元素の同定を行った。さらに定量のための試料の精製、調製、照射を以下のように行った。

精製は遠心式濃縮器を用いて、5100 rpm、1時間で数回脱塩、濃縮を繰り返し、最後に精製した濃縮液を1400 rpm、2分間遠心分離を行い試料とした。

得られた液体試料はろ紙に滴下し、乾燥後ポリエチレン製の袋に封入した。金属元素量既知の標準試料を作製し、試料とともに2～3分の熱中性子照射を行った。3～5分冷却後に、試料については300秒間、標準試料は200秒間γ線スペクトルを測定した。さらに5～6時間冷却後に試料、標準とも1000秒間測定をし、これらのデータから相対法により、試料中の含有微量元素量の定量を行った。

照射の結果、金属含有量が高い試料については、放射光による構造解析を目的として結晶化を試みた。これらタンパク質の結晶化には蒸気拡散法を用いた。ハンギングドロップ蒸気拡散法は、密閉容器にタンパク質溶液と沈殿剤、さらにそれより濃い濃度の沈殿剤を入れておくことで、タンパク質溶液中の水を徐々に蒸発しゆっくりと結晶化が開始される。

結晶化のために、まず高分子結晶化試薬クリスタルスクリーニング・キットを用いて、pH、塩、沈殿剤等の結晶化条件の検索を行った。スクリーニングは、まず組織培養用プレートに緩衝溶液、塩、沈殿剤の組み合わせを変えた98種類のリザーバー溶液を入れた。次にタンパク

日本原子力研究所東海研究所、JRR-4 気送管、放射化分析

質溶液と各リザーバー溶液の混合液（1:1）をシリコン処理したカバーグラスの中央にのせてから、反転させてリザーバー溶液を入れたプレートの上に置いた。カバーグラスとプレート間は、シリコングリースでシールし密閉性を高め、数週間にわたって静置した。その間、実体顕微鏡で結晶化の進行状況の観察を続け、結晶化の最適条件を検索した。なおタンパク質濃度の測定は、280 nm の吸光度を分光光度計で測定することにより行った。

3. 結果とその評価

(1) 熱中性子放射化分析によるタンパク質中の微量金属定量結果

試料として用いたタンパク質の中に Ag, Ba, Ca, Co, Cu, Mg, Mn, S, Se, V, Zn などの元素がふくまれていることが明らかとなった。Al, Ar は全ての試料に検出されたが、これは気送管由来のものと考えられる。標準試料と同時照射する相対法によって得られた定量分析の結果、Co, Cu, Mg, Mn, Se, Zn については、試料 1 mg に対してそれぞれ、Co（10^{-4} ～10^{-7} mg），Cu（10^{-4} ～10^{-6} mg），Mg（10^{-3} ～10^{-5} mg），Mn（10^{-5} ～10^{-7} mg），Se（10^{-4} ～10^{-7} mg），Zn（10^{-3} ～10^{-5} mg）、含まれていることが明らかになった。

遠心式濃縮器による脱塩の操作により、Cl, Na の含有量は 10 分の 1 程度にまで減少し、その結果、^{38}Cl, ^{24}Na などによるコンプトンスペクトルの影響がかなり抑えられた。このことから試料と検出器との距離を近づけることが可能となり、結果として目的核種の光電ピークが高計数率で得られ、元素の定量が容易なものとなった。

(2) タンパク質試料の結晶化

照射を行ったタンパク質試料の中から、Protein Data Bank に解析の報告がなく、金属元素量として試料 1mg 中に 10^{-4}mg 以上の金属元素を含んでいるタンパク質（12 種類）を選び、蒸気拡散法による結晶化を試みた。（表 1）

ハンギングドロップ蒸気拡散法による 98 種類の沈殿剤、pH 等を検討した結果、現在までに 5 種類のタンパク質について微細な結晶が得られている。それぞれの条件（タンパク質濃度、緩衝剤、沈殿剤等）を表 2 に示す。

さらに、放射光による構造解析に用いるため、良質な結晶を得る試みを続けているが、現在までのところ、構造解析に必要な 0.1 mm 以上の大きさの結晶には到達していない。

原因としては、試料の精製が不十分であったこと、試料の初期濃度が不適当であったこと、さらに静置時の環境の変動等が考えられるので、現在、これらの点に留意し、再検討を行い、タンパク質の結晶化を試みている。また、継続して、さらに広範囲の金属含有タンパク質の探索を行っている。

4. 成果の公表

1) 大原久美子、森田裕子、村上 勲、本間義夫：SOD の酵素活性と含有金属量の相関について、原子力研究総合センターシンポジウム（1999 年 12 月）.
2) 大原久美子、森田裕子、村上 勲、本間義夫：金属含有タンパク質の結晶化とその構造解析－1、日本薬学会第 121 年会（2001 年 3 月）.
3) 大原久美子：酵素中の微量金属の定量と金属含有酵素の結晶化に関する研究、修士論文、共立薬科大学（2001）.

表１　結晶化の条件検索を行ったタンパク質と含有元素

タンパク質	含有元素	タンパク質	含有元素
A	Zn	G	Cu,Zn
B	Ba,Cu,Mg,Zn	H	Se,Zn
C	Zn	I	Co,Zn
D	Ca,Zn	J	Zn
E	Cu,Zn	K	Zn
F	Zn	L	Zn

表２　蒸気拡散法による結晶化の条件

タンパク質	結晶化条件
C	タンパク質濃度：3.275mg/mL 緩衝液：0.1M HEPES-Na（pH7.5） 沈殿剤：2%v/v Polyethylene Glycol 400, 2.0M Ammonium Sulfate
D	タンパク質濃度：1.38mg/mL 緩衝液：0.1M TRIS （pH8.5） 沈殿剤：3.4M 1,6Hexanediol 0.2M Magnesium Chloride hexahydrate
E	タンパク質濃度：2.02mg/mL 沈殿剤：0.4M Potassium Sodium Tartrate tetrahydrate
I	タンパク質濃度：2.67 mg/mL 緩衝液：0.1M Na Citrate（pH5.6） 沈殿剤：2.5M 1,6 Hexanediol
K	タンパク質濃度：1.01 mg/mL 緩衝液：0.1M Na Acetate（pH4.6） 沈殿剤：30% Polyethylene Glycol 400, 0.1M Cadmium chloride

3-10

セレン欠乏ラット生体内抗酸化ネットワークに関する遷移金属元素の挙動解析

遠藤和豊、松本謙一郎、宇井伊織、
昭和薬科大学

Dynamics of transition elements in antioxidant networks of selenium deficient rat

By Kazutoyo Endo, Iori Ui, and Matsumoto Ken-ichiro
Showa Pharmaceutical University

1．はじめに： Se 欠乏および VE 欠乏ラット体内で惹き起こされる酸化的ストレスと生体内に存在する必須微量元素の動態を解明する。Se は生体内ではグルタチオンペルオキシダーゼ(GSH-Px)の活性中心であり、過酸化水素の消去に深くかかわっている。生体内で Se が欠乏すると、GSH-P x が低下して肝臓は過酸化水素を介した酸化的ストレスに曝されると考えられている。GSH-Px は主に肝臓に多く存在しており、この酵素の活性が低下した状態では、肝臓は H_2O_2 を介した酸化的ストレスに暴露されると考えられる。ビタミン E (VE) は脂質ラジカルに水素を与えて安定化し、生体内における過酸化の連鎖反応を抑制して過酸化脂質の生成をふせぐ。Se 欠乏あるいは VE 欠乏ラット体内では活性酸素の消去が低下し、タンパクや核酸が酸化的障害を受ける。Se、Fe, Co、Zn、Mn などの金属イオンは酵素の活性中心として生体内の酸化還元反応を制御している。Se 欠乏と VE 欠乏ラットにより与えられる酸化的ストレスと生体内での必須元素の動態との関係を明らかにするために、これらのラット臓器を摘出し、凍結乾燥させ、その一定量のなかに含まれる Se、Fe、Co、Zn、Mn などの金属イオンを放射化分析法により定量した。 生体内酸化還元系で働くいくつかの酵素やビタミンには、その活性中心に金属イオンを含むものが多くある。Se は GSH-Px の活性中心である。Fe はキサンチンオキシダーゼ、シトクロム P−450、カタラーゼ等の活性中心であり、さまざまな酸化還元反応に関与している。Co はビタミン B_{12} (VB_{12}) の成分で、欠乏症には悪性貧血がある。Zn はスーパーオキシドジイスムターゼ (SOD) の構成成分であり、様々な Zn 含有酵素が知られており、その働きは多岐にわたっている。
酸化的ストレスの負荷により生体内の酸化還元反応のバランスが崩れると、これらの酵素の活性や、またこれらに伴う元素動態の変化が予想させる。

本研究では、Se 欠乏あるいは VE 欠乏により与えられる酸化的ストレスと生体内必須微量元素動態との関係を調べるために、正常ラット、Se 欠乏ラット、VE 欠乏ラットの各臓器に含まれる元素の量を中性子放射化分析法により測定し、相互比較をおこった。とくに Se 欠乏ラットの飼育期間の異なるいくつかの Se 欠乏ラット群を作成し、Se 欠乏の期間と体内元素分布、GSH-Px 活性に注目した。肝細胞の画分ごとの元素分布についても検討した。VE 欠乏ラットの結果については成果の公表の（2）にまとめてあるので本報告の結果の部分では Se 欠乏ラットの結果を要約する

JRR-4 D-パイプ、生体試料放射化分析

２．実験の部

２－１　実験動物

（株）日本医科学動物資材研究所ラットから購入した妊娠確定 15 日目の Wister 系ラットに、Se 欠乏餌（オリエンタル酵母株式会社、　東京）をあるいは VE 欠乏餌(オリエンタル酵母株式会社)をそれぞれ与えた。飲料水として両ラットともに超純粋を与えた。生まれた仔ラットの離乳（４週齢）までは、親ラットと同様の餌と水を与えた。これを SeD８群とした。

超純水にセレン酸ナトリウムを添加して Se 濃度として 0.01ppm に調整した。これを飲料水として SeD8 群と同様に飼育したものを SeC 群とした。７週齢、６週齢、５週齢、４週齢、３週齢の Wister 系雄性ラットを購入し、Se 欠乏餌と超純水を与えて、８週齢になるまで飼育し、実験に供した。これらを、それぞれ、SeD'7-8 群、SeD'6-8 群、SeD'5-8 群、SeD'4-8 群、SeD'3-8 群とした。また、８週齢の Wister 系雄性ラットを購入し、normal 群として使用した。

２－２　照射試料の作成

実験には各群4～５匹のラットを使用した。ラットをペントバルビタール(0.05mg/g)麻酔し、腹大動脈からの脱血により屠殺した。全身を氷冷した生理食塩水（0.09%NaCl）で十分潅流した後、肝臓、腎臓、脾臓を単離した。各群の臓器を週齢ごとにあわせ、超純水を加えてホモジナイズした後、凍結乾燥した。乾燥した各試料をメノウ乳鉢でよく磨り潰して粉末にした。粉末にした試料の約 100mg を精秤して石英管に減圧封入した。同様に Standard Reference Material 1577b bovine liver (National Bureau of Standards) 約 100mg を精秤して石英管に減圧封入し、標準試料とした。

２－３　中性子照射及びγ線測定

放射化分析法により肝臓、腎臓、脾臓中における Se, Fe, Zn, Co の濃度を測定した。試料は日本原子力研究所 JRR-4 原子炉 D パイプ（f = 4.3×10^{13}n・cm^2）で１時間中性子照射をおこなった。Ge 半導体検出器（Ortec EG&G 社）と 4096ch.波高分析器（Seiko EG & G (株)・松戸）によりγ線スペクトルを測定した。

３．結果と考察

３－１　飼育の餌：

我々が用いた Se 欠乏餌の Se 濃度は正常餌の約 1/50 であり、充分に低 Se 状態である。Fe 濃度は Se 欠乏餌でやや多いが有意差はみられない。Co 濃度は、Se 欠乏餌で有意に低く正常餌の約 30 分の１である。NRC によればラットのビタミン B_{12} の推奨値は 0.05mg/kg で、Co に換算すると 0.0022mg/kg となる。正常餌の分析値（カタログ記載値）は 0.034mg/kg であり、いずれの餌もビタミン B_{12} の濃度としては推奨値より若干低くなっている。これは餌原料に由来するビタミン B_{12} の自然混入を期待しているためと思われる。今回、Co 含量は、Se 欠乏餌及び正常餌でそれぞれ 0.029mg/kg, 0.9mg/kg であり、これらはビタミン B_{12} 中の Co 濃度に換算すると大きく上回っている。このことから、正常餌には何らかの餌原料に由来する無機 Co の混入があるのではないかと思われる。Se 欠乏餌および正常餌中の Zn 濃度は同程度であった。

３－２　臓器中の元素含量

Se 欠乏による Se 欠乏状態への移行は肝臓と腎臓でよく表れた。肝臓の Se 濃度は、Se 欠乏餌による飼育期間が長く成るほどひくくなり、SeD8 群、SeD'3-8 群、Se'4-8 群では検

出されなかった。腎臓においてもSe欠乏餌による飼育期間が長いほどSeの濃度は低くなったが、SeD'7-8群はSeD'5-8群、SeD'6-8群よりも低く、またSeC8群からは検出されなかった。肝臓については、Se濃度にバラツキがみられた。

低Se状態では、Seを活性中心にもつグルタチオンペルオキシダーゼ(GSH-Px)の活性が低下し、H_2O_2を介する酸化的ストレスに暴露されることになる。Se欠乏ラットでは、血小板機能が増加することや、大動脈血管内皮細胞のプロスタサイクリン活性が低下することが観察されている。これはGSH-Px活性の低下によって循環系に過酸化脂質が蓄積し、アラキドン酸代謝のバランスが崩れるためであろうと考えられている。血小板凝集能の増加や、プロスタサイクリン活性の低下はアテローム性動脈硬化などの欠陥障害の助長因子であり、Se欠乏が虚血性心疾患の誘因であると考えられている。

Fe濃度はSeD8群がSeC8群の肝臓及び腎臓で約2倍、脾臓においては約3.5倍ほど高かった。また、SeD8群は3つの臓器すべてにおいて正常群よりFe濃度は高くなっていた。その他の群は、脾臓ではSeD群とほぼ同程度の濃度を示した。腎臓ではSeD'7-8群を除きSeD群の約2倍であった。肝臓ではSeD'7-8群を除きSeC8群の約2倍であった。肝臓ではSeD'3-8群と正常群以外がSeC群の半分若しくは半分以下の濃度であった。

Se欠乏によるFeの蓄積は、飼育開始時期に影響されるものとおもわれる。Fe過剰症の実験的研究によると、組織に沈着したFeが生体内の配位子（アスコルビン酸、クエン酸など）と結合することにより生成した錯体がH_2O_2の存在かで・OHを産生し、これが細胞内の核酸、酵素タンパク、あるいは膜構造を破壊し組織障害を起こすものと考えられている。Se欠乏状態では、H_2O_2の増加とFeの蓄積によりFe錯体の関与するフェントン反応による・OH生成が促進されている可能性が高いと考えられる。鉄タンパク質としては、ヘモグロビン、ミオグロビン、シトクロムP450、ペルオキシダーゼ、カタラーゼ、亜硝酸還元酵素など、また非ヘムタンパク質してトランスフェリン、フェリチン、ヘモシデリンなどが挙げられる。しかしながら、ここで蓄積したFeがどのような形で体内にあるかはまだ明らかではない。

Co濃度は、どの臓器においても正常分だけがかなり高くなった。これは、SeC8群も低かったことから餌に含まれるCo濃度の違いによると思われる。Coは腸管からよく吸収される。メチルコバラミン（ビタミンB_{12}）は二酸化炭素から酢酸の生成、ホモシステインからのメチオニン生成、二酸化炭素からのメタン生成に共同因子として関与している。ビタミンB_{12}化合物以外のCo含有酵素としてはトランスカルボキシラーゼ、リボキシゲナーゼ、アミノペプチダーゼなどがあるが、酵素活性に必要であるのは他の金属であってCoは構造保持のために存在すると考えられている。Co^{2+}はCuタンパク質やZnタンパク質などの活性中心研究のプローブとして有用であり、多くのCo^{2+}置換体が作られている。

Zn濃度は、腎臓ではSeC8群が他の群の約2倍であり、SeD'7-8群については約5倍であった。肝臓では、SeC8群と正常群がほぼ同じであり、Se欠乏餌の飼育期間が長いSeD8群とSeS'3-8群ではSeC8群より高く、比較的飼育期間の短い他の群ではSeC8群の約半分の

濃度であった。脾臓では、どの群も同程度であり差は見られなかった。生体中のZn含量は遷移金属としてFeについで多いが、Znの過剰症は起りにくいようである。

今回の研究ではSe欠乏の影響としてFe濃度に比較的大きな変化が観測された。また、比較的長期間のSe欠乏がZn濃度に何らかの影響を示す可能性があることが示唆された。

3－3　肝細胞画分の元素動態：　とくにCu, Zn, Mn濃度に注目した．Cu, Znはともに SODの活性中心で正常ではCu/Zn－SODはおもに細胞質に存在することが知られている．Mnは Mn-SODとして主にミトコンドリアに存在することが知られている．Se欠乏により Seが活性中心となっているグルタチオンパーオキシダーゼ（GSH-Px）活性が低下するため、生体内過酸化水素による酸化的ストレスが増加してくることが予想される。SODはO_2^-をH_2O_2とO_2に不均化する働きをもつ。このため、Se欠乏の酸化的ストレス解消を SODのみに依存させるならばSOD活性はSe欠乏により減少することが期待される。また、Cu/Zn-SOD はH_2O_2により失活することが知られている。SOD活性の測定にはまだ誤差が大きく精度の良い測定法が望まれるが，現在のところでは正常群に比べて Se 欠乏群では増加する傾向にあることが明らかにした。

肝細胞画分の核、ミクロソーム、ミトコンドリア、可溶性画分のCu, Zn, Mnの定量を放射化分析法により行った。その結果、Se－欠乏ラットではミトコンドリア画分とミクロソーム画分で Cu 濃度は有意に大きな値を示した．核と可溶性画分ではCu濃度はほぼ同じレベルであった。今後、細胞画分ごとのSOD活性とCu, Zn, Mnの精度のよい定量を行うことにより詳しい情報が得られるものと期待される．今回のSOD活性測定は活性中心金属を分けて測定することまではできていない。また、細胞画分ごとのSOD活性の測定も終了していないので、今後これらの測定を行う必要がある．これまでの実験によりSe欠乏ラットの肝臓全体として Fe が多くなることは確かめられていたが、さらに細胞分画を行うことにより、ミクロソーム画分にはFeが正常群に比べて２倍以上の量になることがわかった．増加した Fe の化学形を検討する一つのアプローチとして、ミクロソーム画分の P-450 活性を測定した。その結果、Se－欠乏ラット（６週齢雄性）の方が正常群に比べて有意に高い値を得ることができた．

Fe を含む酵素してはH_2O_2を水と酸素に還元するカタラーゼ(CAT)がよく知られている。肝ホモジェネートの CAT 活性の測定をおこなったが、正常群とSe欠乏群との差は現在のところ、測定の誤差が大きく、明言はできないが、Se欠乏によるカタラーゼ活性の増加は少ないか、変わらないかのいずれかであろう。H_2O_2を消去するカタラーゼは細胞中ではペルオキシソームに存在しており、H_2O_2に対するK_mは非常に高いため、親和性が弱く実際に生体内での H_2O_2 の消去には主要な役割を果たしていないという報告に一致する。Se欠乏によりFeが含まれている酵素、あるいは非酵素について上述したように多数が知られており今後の更なる研究を期待しなければならない。今回の実験では，Se 欠乏の影響として，Fe の濃度に比較的大きな変化が観測された．また，比較的長期間の Se 欠乏が Zn 濃度にも何らかの影響を示す可能性も示唆されており、Se欠乏による酸化ストレスが及ぼす生体元素の体内動態をより詳しく研究するためには、

動物の性別、餌、飼育環境などの違いによる酸化ストレスの兼ね合いと金属が結合しているタンパクなど化学形を検討していくことが、大切である。

研究成果の公表

1）Matsumoto et al.,"Contents and uptake rates of Mn, Fe, Co, Zn, and Se in Se-deficient rat liver cell fractions", *Anal. Science*, 17, 587-591 (2001).

2）Matsumoto et al.,"Meaurement of Contents in organs of selenium- or Vitamin E deficient rat using instrumental neutron activation analysis", *Yakugaku Zasshi*, 122,(4) 283-290 (2002).

学会発表

1）セレン欠乏ラットおよびビタミンＥ欠乏ラット臓器中元素含量の変動と酸化的ストレスの関連；松本謙一郎、遠藤和豊 京都大学原子炉実験所専門研究会、(於；熊取、平成１３年１２月)

2）放射化分析法によるセレン欠乏ラットおよびビタミンＥ欠乏ラット臓器中元素含量の測定；松本健一郎、　山崎慈、佐藤和恵、牛尾房雄、遠藤和豊、日本薬学会第１２２年会（於；千葉、平成１４年３月）

3）生体への酸化的ストレス負荷による臓器中元素含量の変化；遠藤和豊、宇井伊織、松本謙一郎、山崎　慈、2002 日本放射化学会年会　(於；札幌、平成 14 年 9 月 23-25 日)

4）　放射化分析法によるセレン欠乏ラットにおける微量元素の定量；遠藤和豊、松本謙一郎、宇井伊織、有吉麻里恵、寺田幸代、岡城　彩、平成 14 年度　京都大学原子炉実験所専門研究会、(於；熊取　平成 14 年 11 月)

5）セレン欠乏期間がラット体内の微量元素動態に及ぼす影響、松本謙一郎、宇井伊織、岡城　彩、寺田幸代、有吉麻里恵、○遠藤和豊、日本薬学会第 123 年会（(於；長崎、平成 15 年 3 月）

3-11 中性子放射化分析法による生体中未同定有機態ヨウ素の検索

Detection of extractable organic iodine in biological samples using instrumental neutron activation analysis

鹿島勇治，青柳光洋*，堺 温哉，松井三明**，岡部とし子

(横浜市立大学医学部衛生学講座，*現所属：横浜国立大学環境情報学府，**現所属：国立国際医療センター国際医療協力局派遣協力課)

KASHIMA Yuji , AOYAGI Mitsuhiro*, SAKAI Haruya, MATSUI Mitsuaki** and OKABE Toshiko

Department of Hygiene, Yokohama City University School of Medicine

** Present address: Graduate School of Environmental Information & Sciences, Yokohama City University National University*

*** Present address: International Medical Center of Japan Bureau of International Cooperation*

【はじめに】

ダイオキシン類の主要な発生源である廃棄物焼却場から採取した焼却灰中に、ダイオキシン類と類似した物理化学性を有する有機態ヨウ素が存在することを、我々は中性子放射化法を用いて明らかにした(Kashima et al. 1999; Matsui et al. 2003)。この有機態ヨウ素は、一般廃棄物よりも医療廃棄物焼却灰で高く、病院で消毒・殺菌剤として使用された無機ヨウ素が焼却過程で有機化されたものと現在考えている。しかし、これらの有機態ヨウ素の化学構造、毒性等についてはまったく不明である。

一般に、有機態ヨウ素は、有機態塩素、有機態臭素に比較して、環境中では光分解しやすく、また脊椎動物では、有機態ヨウ素である甲状腺ホルモンの代謝機構として脱ヨウ素化機構を有していることから、生体内半減期も短いと考えられている。そのため、これまで、環境汚染物質としてあまり問題視されていないのが現状である。しかし、現在問題となっている内分泌攪乱化学物質には、生物蓄積性、環境残留性の低い化合物も多くあるため (EPA 1997)、有機塩素化合物と類似した化学構造を持つ有機ヨウ素化合物も、その存在量あるいは、生理作用によっては、生体影響を及ぼす可能性は否定できない。特に、野生生物において、ダイオキシン類や水酸化 PCBs による毒性影響が疑われる甲状腺ホルモン機能障害 (Brouwer et al. 1998, Rolland 2000, Fox 2001) が観察されており、これらの化合物と類似した性質を持つ有機ヨウ素化合物もまた甲状腺ホルモン攪乱を引き起こす可能性が考えられる。

そこで、本研究では、食品や野生生物に存在する甲状腺ホルモン以外の有機ヨウ素化合物、特に、ダイオキシン類や水酸化 PCBs と類似した化学構造を有する化合物を探索する目的で、以下の検討を行った。

1) 甲状腺ホルモン輸送蛋白質 (transthyretin、TTR) と thyroxine (T4) との結合に対する有機ヨウ素化合物の競争結合試験：

水酸化 PCBs や pentabromophenol などは、TTR との結合親和性が強く、T4 の輸送を阻害することが報告されている (Lans et al. 1993, Meerts et al. 2000)。そこで、工業材料や農薬として製造された有機ヨウ素化合物のうちベンゼン環を持つ化合物について、Lans et al. (1993)による in vitro の試験法を用いて甲状腺ホルモン攪乱作用についてスクリーニングした。

2) 食品および野生生物中有機態ヨウ素量の測定：

水酸化 PCBs あるいはダイオキシン類の分析法を用い

研究施設・装置：原子炉JRR-4 気送管 (東海)
研究分野：環境毒性学

て分画された有機溶媒抽出画分について、中性子放射化分析法(INAA)により有機態ヨウ素量を測定した。

3）甲状腺ホルモン（3,5,5'-triiod-L-thyronine, T3）様作用の検定：

2）で有機態ヨウ素が検出された一部の画分について、遺伝子操作された細胞を用いて、甲状腺ホルモンであるT3様作用について検定した。

【試料と方法】

1．TTRとT4との結合に対する競争結合試験

対象物質としてヨウ素化フェノール化合物4種、ヨウ素化ビフェニル化合物1種を選択し（Fig.1）、positive controlとしてL-thyroxin（$L\text{-}T_4$）を用いた。試験方法は、7段階の濃度の対象物質をLans et al.(1993)の方法に従い、55nM TTR及び30nM [^{125}I] $L\text{-}T_4$と共にインキュベートした後、Spin column P-6（Bio-Rad）で遊離[^{125}I] $L\text{-}T_4$とTTRを分画し、TTR画分の放射性強度（cpm）をγ-counter（Cobra 5003、Packard）で測定した。

2．有機態ヨウ素量の測定

1）試料

① 食品： 総ヨウ素含有量の高いことが知られている乾燥コンブ、サバの切り身、ウシ肝臓の3食品を市場で購入した。購入後、食品は、ホモジナイズし、一部は、総ヨウ素濃度を測定するため、乾燥後、乳鉢ですりつぶし、デシケータ内で保存した。ホモジナイズの残りは-20℃で有機溶媒抽出時まで保存した。

② 野生生物： ダイオキシン類測定用に調製されたカワウ肝臓の粗抽出液およびクリーンナップ行程で分画されたPCBs溶出画分、農薬溶出画分、ダイオキシン類溶出画分の各々の測定残液を横浜国立大学から提供頂き、それらの画分中有機態ヨウ素を測定した。

カワウは魚食性鳥類で、日本に生息する野生生物の中でもダイオキシン類やPCBsなどを高濃度に蓄積していることが報告されている（井関ら2000）。

2）有機態ヨウ素抽出法

① 食品： 奥村（2003）が開発した水酸化PCBs分析法に従い抽出した。-20℃で保存した食品試料にアセトニトリル30mLを加え、ポリトロンホモジナイザーあるいはソニケーターで抽出した。この操作を2回繰り返し、アセトニトリル抽出液を合わせ、脱脂のためヘキサンで2回洗浄した（1回目20mL、2回目10mL）。このヘキサン抽出画分には脂肪酸など脂溶性の高い物質が抽出される。この画分をFr.1とした。次に、アセトニトリル抽出液に5% Na_2SO_4水溶液を300mLを加え、ヘキサン50mLで2回抽出した。このヘキサン抽出画分には、水酸化PCBs、PCBsなどが抽出される。この画分をFr.2とした。Fr.1および2のヘキサン画分は、各々無水硫酸ナトリウムで脱水後、KD濃縮器で濃縮し、さらに、これらの濃縮液は、窒素気流下で適当量に少量濃縮し、EOXの測定および甲状腺ホルモン作用の検定に供した。

② 野生生物： 横浜国大より供与頂いたカワウ肝臓抽出液は、ジクロロメタンによるソックスレー抽出液をヘキサン転溶後に水洗処理した粗抽出液(Crude extract, Fig.1)、ダイオキシン類、コプラナーPCBsが分画されるダイオキシン類画分(Dioxin Fr., Fig.1)、コプラナーPCBs以外のPCBsが分画されるPCBs画分(PCBs Fr., Fig.1)、DDTs、HCHs等の農薬が分画される農薬画分(Pestcides Fr., Fig.1)の4種である。分析方法の詳細は、井関ら（2000）の方法を参考頂きたい。

3）照射および測定条件

デシケータで保存した乾燥試料あるいは有機溶媒抽出液、標準溶液を各々ポリエチレン管に添加・溶封後、蒸留水、アセトン、ヘキサンで順次洗浄後、ドライヤーで乾燥した後、ポリエチレン袋で2重にシームし、照射当日まで-20℃で保存した。INAAによる照射は、試料を入れたポリエチレン管1或いは2個と標準溶液を封入したポリエチレン管1個を照射用の標準キャプセル（ポリエチレン製）にドライアイスと共に装填し、

原子炉内で熱中性子を照射した。INAA の中性子源として、日本原子力研究所・研究用原子炉 JRR-4 を用い、単寿命核種照射装置に敷設されている気送管により熱中性子束下（JRR-4：3.2 x 10^{13}n/cm^2・sec）で乾燥試料については 15 秒間、有機溶媒抽出液については２分間の照射を行った。照射後、直ちに外側のポリエチレン袋を取り替えて、γ線スペクトロメーターを用いて、^{128}I（443 keV）、^{80}Br（617 keV）、^{38}Cl（1634 keV, 2168 keV）のγ線を測定した。

4）T3 作用の検定

甲状腺ホルモンレスポンスエレメント（DR4）を pGL2 promoter に挿入したレポータープラスミドを HeLaTR に導入した（HeLaTRDR4-luc）細胞（Sakai et al. 2003）を D-MEM（フェノールレッド不含、無血清）で 72 時間培養後、24 あるいは 48 well plate に継代し、D-MEM（フェノールレッド不含、5%活性炭処理済み FBS 添加）培地で 12 時間培養した。抽出液を単独あるいは T3 と同時に培地へ添加し、さらに 36 時間培養後、細胞を lysis buffer（Promega）で溶解した。溶解液を遠心分離後、細胞粗抽出液を作成し、抽出液中のルシフェラーゼ活性を luciferase assay system（Promega）を用いて測定した。また、蛋白質濃度は、BCA protein assay reagent（Pierce）を用いて測定した。

【結果と考察】

1. TTR 競争結合試験

競争結合試験結果から、TTR と[^{125}I] L-T_4 との結合を 50%阻害する対象物質の濃度（IC_{50}）を算出し、L-T_4（native）の IC_{50} を 1.0 とした時の各対象物質の Relative Potency（RP）を求めた（Table 1）。その結果、今回試験したフェノール系化合物については、全般的に TTR 結合能が強く、競争結合試験の結果では、2,4,6-triiodophenol（TIP）は L-T_4 の 58 倍の競争結合能を示し、また TIP の４位のヨウ素がニトロ基に置換された 2,6-diiodo-4-nitorophenol も L-T_4 の 7.5 倍の競争結合能を有していた。

ハロゲン化フェノール類は、一般に、生体内半減期が短く、急性毒性も低いため、ヒトや野生生物におけるこれらの汚染状況に関する報告は少ない（Hovander et al. 2002）。しかし、2, 4, 6 位全てにヨウ素、ニトロ基の何れかが置換したフェノール系化合物は、TTR との結合能が L-T_4 の同等以上であるため、甲状腺ホルモン機能を攪乱する可能性があり，これらの暴露量について調査が必要と思われる。

2. 有機態ヨウ素濃度

1）食品

有機態ヨウ素濃度は、総ヨウ素濃度の高い順位で高く、コンブで最も高濃度であった（総ヨウ素濃度は、乾燥重量当たりの濃度を水分含量から湿重量濃度に換算した、Table 2）。しかし、総ヨウ素濃度に占める有機態ヨウ素の割合は、コンブで最も低く、サバの切り身、ウシ肝臓では、有機態の占める割合が高かった。

Hou et al.（1997）は、コンブ中ヨウ素の約 10%が有機態ヨウ素であると報告しているが、今回の抽出法で抽出された有機態ヨウ素は、総ヨウ素濃度の 0.07%で非常に低い割合であった。この結果は、コンブ中に存在する有機態ヨウ素の大部分が、今回の方法では抽出できない水溶性の高い化合物であることを示唆する。TTR 競争結合試験で強い阻害能の認められたヨウ素化フェノール類も今回の抽出法では回収率が低い可能性があり、今後、フェノール類分析法により抽出される有機態ヨウ素濃度について確認が必要である。

ウシ肝臓およびサバ筋肉中の有機態ヨウ素については、比較できる報告はないが、総ヨウ素濃度に占める割合が高かったことから、その大部分が甲状腺ホルモンおよびその代謝産物と思われる。しかし、甲状腺ホルモン以外の有機態ヨウ素が存在する可能性も否定できないため、抽出液中の甲状腺ホルモン量を今後確認する必要がある。

2）カワウ肝臓抽出液

粗抽出液中有機態ヨウ素濃度は 0.04～0.42ng/g と非

常に低濃度であり(Table 3)、またダイオキシン類分析行程で分画された3画分中（Pesticides Fr., PCBs Fr., Dioxin Fr.）の有機態ヨウ素濃度はさらに低く、大部分の試料で検出限界以下であった。廃棄物焼却灰抽出液に検出されたダイオキシン類やPCBsと類似した物理化学的性質を有する有機態ヨウ素は、環境汚染物質を高濃度に蓄積しているカワウにおいても検出できなかった。しかし、ダイオキシン類分析法では、抽出効率や分析行程における光分解などにより回収率が低く検出できなかった可能性もある。またTTR競争結合試験結果で強い結合阻害能を示したヨウ素化フェノール類は、ダイオキシン類分析法では、クリーンナップ過程で多くが除去されると考えられるため、甲状腺ホルモンやヨウ素化フェノールを対象とした分析法による再検討が必要と考える。

3．T3様作用

コンブ抽出液のFr.1およびFr.2について、T3様作用について検定した結果、Fr.2にT3様作用が認められた（Fig.3）。特に、抽出液単独暴露によるT3様活性の増加は統計学的に有意な差として検出できなかったが、5nMのT3を抽出液と同時に暴露した場合には、5nMのT3単独暴露群に比較して、抽出液暴露群のT3様活性は暴露量依存的に有意な増加を示した（Fig.4）。Fig.3の高濃度暴露群における活性の低下は、死亡細胞の増加、蛋白質量の減少が確認されたことから、コンブ抽出液に含まれる何らかの成分による毒性が発現したものと推察される。

本結果からコンブの過剰摂取は、無機ヨウ素自体による甲状腺機能亢進に加えて、有機溶媒抽出成分によって、甲状腺機能がさらに亢進する可能性のあることを示唆する。現時点では、T3様作用を示した化合物が有機態ヨウ素やその他の有機ハロゲン化合物によるものかは特定できないが、多くの海藻類は、ハロゲン化酵素であるハロペルオキシダーゼを産生し、多様な有機ハロゲン化合物を含有することが知られており（大城・和泉1994）、また、ある種の紅藻類にはiodotyrosineや甲状腺ホルモンであるT3も検出されている（納谷1979）。コンブは褐藻類であり、甲状腺ホルモンの存在については、これまで報告されていないが、コンブ中にも、甲状腺ホルモンと類似構造を持つ有機ヨウ素化合物が存在する可能性がある。今後、Fr.2をさらにゲル濾過分画や化学処理することにより、甲状腺ホルモン活性を有する成分の絞り込みを行い、HPLCやLC-MSなどにより、甲状腺ホルモン作用を示す成分の同定を行いたいと考えている。

【おわりに】

必須元素であるヨウ素は、世界的には摂取不足による甲状腺機能障害が問題とされているが、日本では、海藻や魚介類摂取量が多く、ヨウ素の過剰摂取による甲状腺機能障害が問題になることが多い。海藻類や魚介類中には、生体内で生成された天然の有機ヨウ素化合物が多様に存在することは知られているが、それらの存在量や生理活性については多くが未解明である。本研究において、コンブ抽出液中には、甲状腺ホルモン機能を亢進する可能性のある物質が存在し、この抽出液には高濃度の有機ハロゲン化合物が存在することを示した。この結果は、コンブの過剰摂取は、無機ヨウ素の過剰摂取による甲状腺機能亢進に加えて、有機ハロゲン化合物を含む有機成分により、甲状腺機能亢進が増悪する可能性のあることを示唆している。

現在、有機ハロゲン化合物に関する研究の多くは、人為的な環境汚染物質による健康影響に注目が集まっているが、今後は汚染物質と同様に食品から摂取される天然の有機ハロゲン化合物による生体影響についても、栄養学・毒性学的見地から評価する必要があると考える。

【謝辞】

本研究の実施にあたり、中性子線の照射にご協力を頂いた澤幡浩之及び川手稔技官に感謝致します。

また、貴重な抽出液を提供頂いた横浜国立大学の井関直政博士（現所属：国立環境研究所環境ホルモン・ダイオキシン研究プロジェクト）に感謝致します。

【参考文献】

井関直政，羽山伸一，益永茂樹，中西準子（2000）カワウにおける PCDDs，PCDFs およびコプラナーPCBs の蓄積レベル，環境化学 10(4)：817-831

大城 隆，和泉好計（1994），海藻と微生物が生産するハロゲン化酵素，化学と生物，32：35-43

奥村為男（2003）水酸化ポリ塩化ビフェニル(PCB-OH)の分析について，第 12 回環境化学討論会（新潟，6 月）講演要旨集，pp. 212-213.

納谷洋子（1979），含ハロゲン成分の構造と起源・分布，海洋天然物化学（化学総説 No. 25），日本化学会編，学会出版センター，東京，pp. 87-110

Brouwer A, Morse DC, Lans MC, Schuur AG, Murk AJ, Klasson-Wehler E, Bergman A, Visser TJ.(1998) Interactions of persistent environmental organohalogens with the thyroid hormone system: mechanisms and possible consequences for animal and human health. Toxicol Ind Health. 14: 59-84

EPA (1997) Special report on environmental endocrine disruption: An effects assessment and analysis, risk assessment forum, U.S. Environmental Protection Agency, Washington DC, pp.111

Fox GA (2001) Wildlife as sentinels of human health effects in the Great Lakes--St. Lawrence basin. Environ Health Perspect. 109 (Suppl 6): 853-861.

Sakai H, Yamada-Okabe T, Kashima Y, Matsui M, Aono T, Aoyagi M, Hasegawa J (2003) Effects of brominated flame retardants on transcriptional activation mediated by thyroid hormone receptor, Organohalogen Compounds, 61: 215-218

Hou X, Chai C, Qian Q, Yan X, Fan X (1997) Determination of chemical species of iodine in some seaweeds (I). Sci. Total Environ. 204: 215-221

Hovander L, Malmberg T, Athanasiadou M, Athanassiadis I, Rahm S, Bergman A, Wehler EK.(2002) Identification of hydroxylated PCB metabolites and other phenolic halogenated pollutants in human blood plasma. Arch Environ Contam Toxicol. 42:105-17

Kashima Y, Matsui M, Kawano M, Ueda M, Tojo T, Takahashi G, Matsuda M, Anbe K, Doi R, Wakimoto T. (1999) Characteristics of extractable organic halogens in ash samples from medical solid waste incinerator, Organohalogen Compounds 41: 191-194

Lans MC, Klasson-Wehler E, Willemsen M, Meussen E, Safe S, Brouwer A.(1993) Structure-dependent, competitive interaction of hydroxy-polychlorobiphenyls, -dibenzo-p-dioxins and -dibenzofurans with human transthyretin. Chem Biol Interact. 88: 7-21

Matsui M, Kashima Y, Kawano M, Matsuda M, Ambe K, Wakimoto T, and Doi R (2003). Dioxin-like potency and extractable organic halogens (EOX) in medical, municipal and domestic waste incinerator ashes in Japan. Chemosphere. 53: 971-980.

Meerts IA, van Zanden JJ, Luijks EA, van Leeuwen-Bol I, Marsh G, Jakobsson E, Bergman A, Brouwer A. (2000) Potent competitive interactions of some brominated flame retardants and related compounds with human transthyretin in vitro. Toxicol Sci. 56: 95-104

Rolland RM. (2000) A review of chemically-induced alterations in thyroid and vitamin A status from field studies of wildlife and fish. J Wildl Dis. 36(4): 615-35.

【成果の公表】

(学会発表)

青柳光洋，鹿島勇治，長谷川 淳，堺 温哉，松井三明，岡部とし子，土井陸雄：トランスサイレチンに対する塩素化ジフェニールエーテル系化合物の競争結合作用，第４回日本内分泌撹乱化学物質学会，筑波，2001. 12

青柳光洋，鹿島勇治，長谷川 淳，堺 温哉，松井三明，岡部とし子，土井陸雄：Amyloid fibril 生成能を指標とした内分泌撹乱物質の Transthyretin 結合親和性試験，第 11 回環境化学討論会，箱根，2002. 6

Table 1. TTR binding potency of organoiodine compounds using competitive binding assay

Compounds	IC_{50} (nM)[a]	Relative Potency[b]
L-thyroxine	24	1.0
phenol compounds		
2,4,6-triiodophenol	0.41	58
2,6-Diiodo-4-nitrophenol	3.2	7.5
Ioxynil	5.3	4.5
Diiodotyrosine	3300	0.0072
bipheny compound		
4,4'-Diiodbiphenyl	ND	ND

ND: no displacement observed within tested range.
[a]Concentration of competitor at 50% competition.
[b]Calculated as ratio of $IC_{50}(T_4)/IC_{50}$(competitor).

Table 3. Extractable organic iodine concentration in liver of Common Cormorant

Sample No.	ng/g tissue Pest. Fr.	PCB Fr.	Dioxin Fr.	Crude
CC05	ND	ND	ND	-
CC06	ND	0.19	ND	-
CC07	ND	ND	ND	-
CC08	ND	ND	ND	-
CC09	0.12	ND	ND	-
CC10	-	-	-	0.42
CC11	-	-	-	0.17
CC12	-	-	-	0.04
CC13	-	-	-	0.30

Table 2. Total halogen and extractable organic halogen concentrations

		Bovine liver (n=1)		Mackerel muscle (n=1)		Konbu, dried (n=1)	
		μg/g wet	(%)	μg/g wet	(%)	μg/g dry	(%)
I	Total	0.126	(100)	0.086	(100)	1043	(100)
	Fr.1	0.004	(3)	0.017	(19)	0.61	(0.06)
	Fr.2	0.051	(41)	0.070	(82)	0.14	(0.01)
	Fr.1+Fr.2	0.055	(44)	0.087	(101)	0.75	(0.07)
Br	Total	18	(100)	2.7	(100)	561	(100)
	Fr.1	0.052	(0.30)	0.47	(17)	38	(6.8)
	Fr.2	0.020	(0.11)	0.36	(13)	1.0	(0.2)
	Fr.1+Fr.2	0.072	(0.41)	0.83	(31)	39	(7.0)
Cl	Total	3187	(100)	781	(100)	106541	(100)
	Fr.1	2.5	(0.08)	0.21	(0.03)	0.47	(0.0004)
	Fr.2	7.4	(0.23)	0.52	(0.07)	2.2	(0.0020)
	Fr.1+Fr.2	9.9	(0.31)	0.73	(0.09)	2.6	(0.0025)

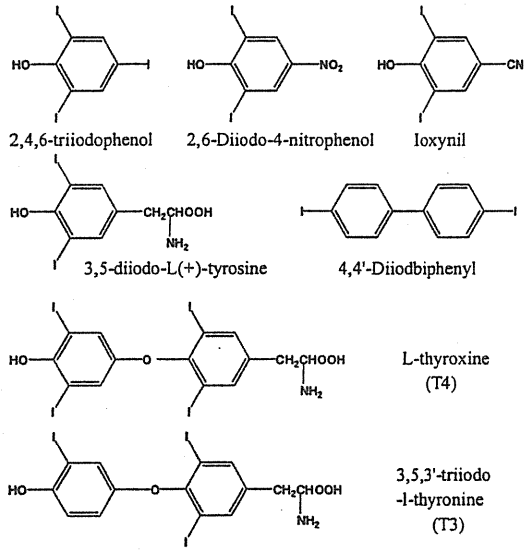


Fig. 1. Chemical structures of organic iodine compounds

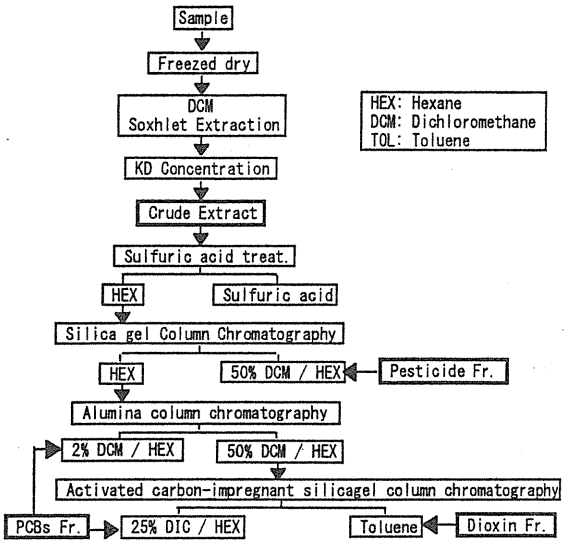


Fig. 2 Analytical procedure for liver of cormorant

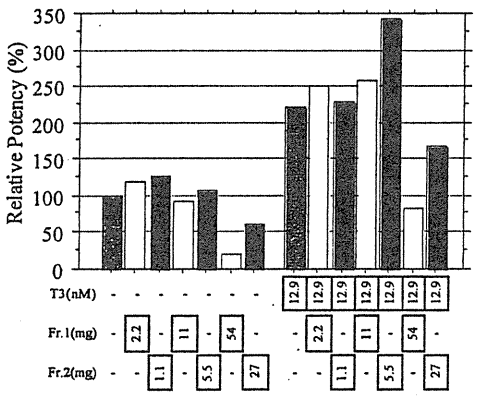


Fig.3. Relative potency of T3 like activity in Konbu extracts

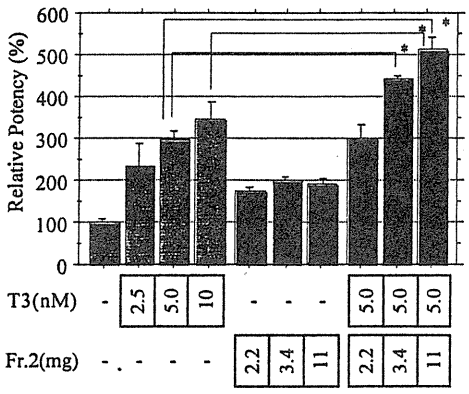


Fig.4. Relative potency of T3 like activity in Fr.2 of Konbu extract
(*: Significant difference with Scheffe, $p<0.05$)

3-12 サンゴ礁ボーリング試料の放射化分析

Instrumental Neutron Activation Analysis of Drill-core Samples in Coral Reefs

大出 茂[1]、M. M. M. Hossain[1]、尾嵜大真[2]

S. Ohde[1], M. M. M. Hossain[1], H. Ozaki[2]

[1]琉球大学理学部、[2]東京大学原子力総合センター

[1]Faculty of Science, University of the Ryukyus, [2]RCNST, The Univ. of Tokyo

1. はじめに

本研究は、平成 11 年度立教大学原子炉利用共同研究として始めた。しかし、立教炉は、11 年度をもって、25 年間の原子炉利用共同研究に幕をおろすこととなった。そこで、平成 12 年度から、原研炉（JRR-3M, JRR-4）を利用した本研究を再スタートさせた。

原子炉を利用した放射化分析によってサンゴ礁炭酸塩物質中に含まれるできるだけ多くの元素を定量することが本研究の目的である。

海洋生物の石灰質殻はアラゴナイトとカルサイトの同質異像の結晶から構成されている。さらに、炭酸塩殻中の微量成分含量から、その生物が生息していた環境水の化学組成が推定されている。また、生物の死後の化石化過程すなわち続成作用に関する情報を化石炭酸塩殻の化学分析から得ることが可能である。そこで、サンゴ礁ボーリング試料の放射化分析を行った。さらに、平成 14 年度には、即発ガンマ線分析を同じサンゴ試料に応用した。

2. サンゴ試料

サンゴ礁の形成に関する Charles Darwin の海洋底沈降説を証明するために、南大平洋エリス諸島フナフチ島において、1896 年に約 340m のサンゴ礁ボーリング調査が英国科学院によって行われた。大英博物館にそのボーリング試料が保存されており、我々は、31 試料のストロンチウム同位体年代、および、9 試料の放射性炭素年代測定を行った(Ohde et al. 2002)。地表から地下 25m の 9 試料は 3000 年から 8000 年前に生息したサンゴであった。その化石サンゴはアラゴナイト結晶のままほとんど変質していないことも明らかになった。したがって、今から 3000 年から 8000 年の間の南大平洋海水中の化学成分の変動および古環境についての情報を得るために、原子炉を利用した研究によって、化石サンゴ中のできるだけ多くの元素の定量を行った。

3. 放射化分析

化石サンゴは主成分が炭酸カルシウム(約 97%)であり、^{49}Ca および ^{47}Ca を内部標準としてして使用し、次の照射、測定条件によって非破壊放射化分析を行った。

(1) 気送管(JRR-4)15 秒照射：サンゴ試料（粉末またはブロック状）5-10mg をポリ袋に封入、照射キャプセルに 1 試料入れ、気送管で 15 秒

研究施設と装置

JRR-3(PN-3, PGA)

JRR-4(気送管、S パイプ)

研究分野

環境化学、地球化学

照射、3 分間の冷却時間をおきガンマ線スペクトロメーターを用いて 2 分間測定を行い、Al、Ca、Mg を定量した。さらに、30-90 分の冷却時間をおき、5 分間測定を行い、Na、Cl、Mn、Sr、I が分析可能であった。

(2) PN-3(JRR-3M):サンゴ中のフッソを定量するために、サンゴ試料（粉末またはブロック状）30-50mg をポリ袋に封入、高純度ポリエチレン照射用キャプセルに 1 試料入れ、PN-3 気送管で 15 秒照射、6 秒間の冷却時間をおき、キャプセルを開封しないで、ガンマ線スペクトロメーターを用いて 15 秒間測定を行い、F を定量した。標準はフッ化カルシウムを炭酸カルシウムに混合させて作成した。

(3) S パイプ(JRR-4)6 時間照射：サンゴ試料（粉末またはブロック状）100-200mg を石英管に封入、照射キャプセルに 3 試料入れ、S パイプで 6 時間照射、1 ヶ月間の冷却時間をおきガンマ線スペクトロメーターを用いて 10000 秒間測定を行い、Sc、 Ca、Co、Ba 、Eu 、Th 、Fe の定量が可能であった。

4、即発ガンマ線分析

サンゴ試料（粉末またはブロック状）約 50-150mg をポリ袋に封入後、テフロンシート (FEP) に再封入し、照射試料を作成した。ホウ素標準は、1000 および 2000ppm ホウ酸標準溶液を口紙上に 10 μl 塗布し、乾燥させ、テフロンシート中に封入して作成した。JRR-3M の冷中性子ビームおよび熱中性子ビームを使って、試料にそれぞれ、2000 秒および 6000 秒中性子照射し、即発ガンマ線を測定した。即発ガンマ線スペクトルを解析した結果、サンゴ試料中の B、 Ca、Na が定量可能であった(表 1) 。

5、結果と考察

すでに年代測定がおこなわれたフナフチ環礁サンゴ礁ボーリング試料（地表から地下 25m）を研究に用いた。試料の化石サンゴはアラゴナイト結晶のままほとんど変質していないことから、今から 3000 年から 8000 年の間の南大平洋海水中の化学成分の変動および古環境についての情報を得られることが期待される。本研究では、特に、サンゴ化石中のホウ素、フッソ含量から、サンゴが生息していた環境水の化学組成を推定することを試みた。海水からアラゴナイトへのフッ化物イオンの共沈は次のイオン交換反応式で起こることが知られている (Ichikuni 1979)。

$$CaCO_3(s) + 2F^-(aq) = CaF_2(s) + CO_3^{2-}(aq)$$

上式は、海水のフッ化物イオンと炭酸イオンの比が、炭酸塩に共沈するフッ化物イオン量をコントロールすることを示している。さらに、海水の炭酸イオンは、pH と関係する。したがって、同じ陰イオンであるホウ酸イオンでも同様に、海水の pH に関する情報が得られる可能性がある。そこで、サンゴ殻のホウ素の正確な定量がフッソと同様に重要である。

サンゴ試料のホウ素の即発ガンマ線分析条件等を表 1 に示す。478keV のホウ素の即発ガンマ線ピークを使ってサンゴ中のホウ素を定量した。472keV のナトリウムピークとホウ素のピークが重なるので、放射化分析で定量したナトリウムのデータと炭酸ナトリウム標準(10mg)を同様に即発ガンマ線分析したデータを比較することによって、ナトリウムピークの補正を行った。サンゴのナトリウム含量は約 5000ppm であった。サンゴはホウ素を約 50ppm 含んでいるが、約 1ppm のナトリウムの寄与によるマ

イナス補正が必要であった。本研究で用いた即発ガンマ線分析の正確さ（再現性）を確かめるために、標準試料の分析をくり返し行った（表2）。この分析データの再現性は2-3%である。

フナフチ環礁のボーリング試料のフッソとホウ素の分析結果を図1、図2に示す。試料は化石サンゴであり、その年代は3000年（0.3m）から8000年（24m）である。図に示すように、フッソとホウ素量のボーリングの深度にたいする変化は非常に似ている。サンゴが生息していた環境水の化学組成との関係を考察する予定である。

5、今後の方針

琉球大学に設置されているICP-MSを使って、放射化分析をおこなった同じサンゴ試料について、できるだけ多くの元素の定量を行う予定である。そして、データを比較検討する。

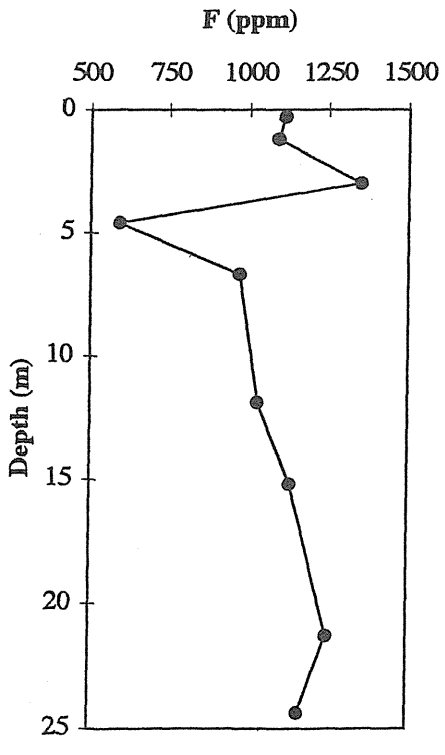


図1

6、引用文献

Ichikuni M. Chem. Geol. 27(1979)207.

Imai et al. Geostandard Newslett. 20(1996)165.

Ishikawa T., Nakamura E.EPSL 117(1993)567.

Ohde et al. Proc. R. Soc.A458(2002)2289.

Okai et al. Geostandard Newslett. 26(2001)95.

7、成果の公表

佐藤悠介、大出茂（2001）サンゴ骨格のSr/Ca温度計、地球化学、35、1-11

Hossain M. M. M., Ohde S. (2002) Uranium in pore water from coastal sediments determined by chemcal neutron activation analysis. J. Radioanal. Nucl. Chem 251, 333-336

Ohde S., Greaves M., Masuzawa T., Buckley H. A., Van Woesik R., Wilson P. A., Pirazzoli P. A., Elderfield H. (2002) The chronology of Funafuti Atoll: revisiting an old friend. Proc. R. Soc. Lond. A458, 2289-2306

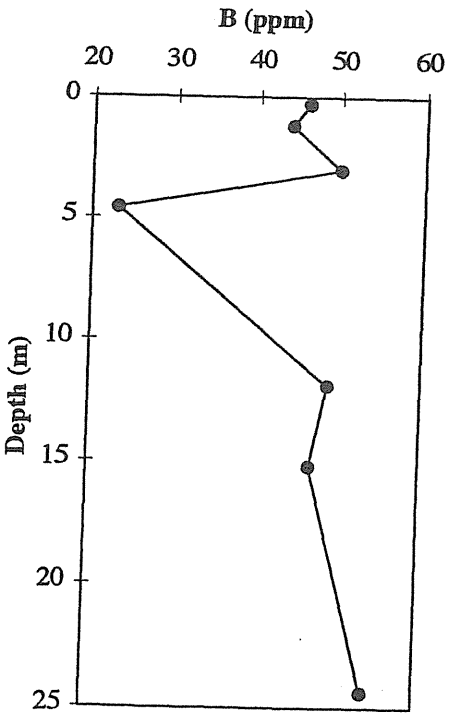


図2

表1 サンゴ骨格の即発ガンマ線分析の条件等

	Cold neutron beam	Thermal neutron beam
Neutron flux ($n \cdot cm^{-2} \cdot s^{-1}$)	1.4×10^8	2.4×10^7
Sample weight (mg)	50-100	100-150
Counting time (sec)	2000	6000
^{10}B (478 keV) (cps/mg)	1437 ± 9 1489 ± 13	356.7 ± 1.7
^{23}Na (472 keV) (cps/mg)	0.464 ± 0.004 0.463 ± 0.005	0.110 ± 0.001
Ca (1942 keV) (cps/mg)	0.0657 ± 0.0006 0.0643 ± 0.0006	0.0177 ± 0.0002

表2 サンゴおよび炭酸塩標準の即発ガンマ線分析

No.	Material	Ca (%)	Na (ppm)	Boron (ppm)	Average ± 1σ (ppm)	Literature value (ppm)
A2	Coral	37.84	4700	54.8 ± 0.6 53.1 ± 0.6 58.8 ± 0.7 55.7 ± 0.6 53.9 ± 0.7 54.8 ± 0.6 55.9 ± 0.7 56.7 ± 0.8	55.5 ± 1.8	-
JCp-1	Coral	38.25*	4350*	47.1 ± 0.3 47.9 ± 0.5 48.1 ± 0.5 47.7 ± 0.5 47.9 ± 0.5 49.4 ± 0.5 46.2 ± 0.7 46.7 ± 0.5 49.8 ± 0.6 47.8 ± 0.7 49.6 ± 0.6	48.0 ± 1.2	47.7 ± 1.2*
JLs-1	Limestone	39.37***	14.4***	0.353 ± 0.022 0.208 ± 0.045 0.252 ± 0.074	0.271 ± 0.074	0.29 ± 0.04** 0.45*** 0.17****
JDo-1	Dolomite	24.27***	95.7***	1.57 ± 0.08 1.69 ± 0.09	1.63	1.31 ± 0.05** 1.49***

*OKAI *et al.* (2001), **TERASHIMA *et al.* (1998), ***IMAI *et al.* (1996),
****ISHIKAWA and NAKAMURA (1993)

3-13 環境指標としての樹木年輪中の微量元素の定量

Determination of trace elements in tree rings as environmental monitors

人間環境大学人間環境学部　片山幸士、長井正博、
京都大学大学院農学研究科　岡田直紀、幸　進、
京都大学放射性同位元素総合センター　青木　達、
京都大学原子炉実験所　高田實彌、
東京農工大留学生センター　川端良子
Division of Human Environment, The Univ. of Human Environments
Yukio Katayama, Masahiro Nagai
Graduate School of Agriculture, Kyoto Univ. Naoki Okada, Susumu Ko
Radioisotope Research Center, Kyoto Univ. Toru Aoki
Research Reactor Institute, Kyoto Univ. Jitsuya Takada
Internat. Student Center, Tokyo Univ. of Agr. and Tech. Yoshiko Kawabata

緒言

樹木は、葉で数年、樹皮で数十年、木部は長いものでは数千年の寿命を持つ生物である。したがって、樹木の年輪中の微量元素や放射性核種を定量することによって、過去に遡って、その成育環境についての情報がえられる。

著者らは20年来植物試料を中心に環境試料を京大炉（KUR、出力５MW）や立教炉（TRIGA、出力100kW）で熱中性子放射化分析を行ってきた。すでに立教炉は平成12年３月に運転を終了し、京大炉は平成18年３月をもって運転の終了が予定されている。

原子力研究所４号炉（JRR-4、出力３MW）を初めて利用するに当たりこれまで蓄積してきた経験を活かし、データの継続性を確かめるため標準物質を照射し感度を比較するとともに精度を調べた。立教炉との比較を行うため出力100kWの低出力運転でも照射した。

実験

標準物質として、地質調査所の岩石標準試料JB1またはJB1aとJG1またはJG1a、およびNISTのApple leavesとPeach leavesを用いた。

JB1、JB1aとJG1、JG1aは約20mgをApple leavesとPeach leavesは約200mgを精秤し照射試料とした。

各試料を５個ずつポリエチレンフィルムで二重に封入し、日本原子力研究所４号炉（JRR-4、熱中性子束 4.0×10^{13} n·cm^{-2}·sec)の気送管で20秒間照射した。100kWの低出力運転時は気送管で300秒間照射した。いずれの照射も、カプセルに試料を２個ずつ入れた。

数分間冷却後、200～300秒間γ線を測定し、^{28}Al、^{27}Mg、^{49}Ca、^{56}Mnなどの短寿命核種の計数率を求めた。^{56}Mnなどの減衰を待って約５時間後再度測定し^{24}Naと^{42}Kの計数率を求めた。

結果と考察

表１に定格出力5MW運転で照射して得られた結果を表２に低出力100kW運転で照射した結果を示す。放射能強度は照射直後に減衰補正した各元素１μg当たりのcpsで表した。

表１から分かるように同一試料の変動係数は、岩石標準物質のClを除き、最大で10％程度であった。岩石標準物質中のClは濃度が低いため正確な値は求められなかった。JG1のcps値が高くなったが、与えられているMg濃度が低く見積もられているため、他の試料から得られた値と比べ高くなったと考えら

JRR-4 気送管　環境科学試料放射化分析

表１　ＪＲＲ－４（定格出力3MW運転）の気送管で放射化した標準物質の生成放射能（照射時間20秒、測定時間300秒、検出器から測定試料までの距離10cm（Na、Kは1cm））

単位は照射直後に補正したcps/μg

物質名		Al	Mg	Ca	Mn	Cl	Na	K
Apple leaves	No.1	12.0	0.029	0.0102	1.29	0.082	1.27	0.025
	No.2	12.0	0.027	0.0098	1.32	0.084	1.12	0.025
	No.3	12.2	0.028	0.0103	1.31	0.087	1.15	0.025
	No.4	11.7	0.027	0.0099	1.25	0.084	1.14	0.024
	No.5	12.3	0.030	0.0101	1.34	0.086	1.22	0.024
	average	12.0	0.028	0.0101	1.30	0.085	1.18	0.025
	STD	0.25	0.001	0.0002	0.04	0.002	0.06	0.001
	RSD	2.0	5.1	1.8	2.8	2.1	5.4	2.7
Peach leaves	No.1	12.2	0.028	0.0099	1.33	0.089	1.34	0.025
	No.2	11.7	0.026	0.0099	1.30	0.083	1.28	0.024
	No.3	11.5	0.027	0.0094	1.20	0.083	1.44	0.024
	No.4	11.9	0.028	0.0099	1.31	0.086	1.43	0.024
	No.5	12.3	0.028	0.0099	1.33	0.086	1.53	0.025
	average	11.9	0.027	0.0098	1.30	0.085	1.40	0.024
	STD	0.32	0.001	0.0002	0.06	0.003	0.10	0.001
	RSD	2.7	3.8	1.8	4.4	3.1	7.1	2.3
JB1	No.1	12.5	0.041	0.0107	1.41	0.105	1.21	0.030
	No.2	12.8	0.038	0.0104	1.41	-	1.18	0.027
	No.3	11.4	0.037	0.0102	1.25	0.048	1.05	0.025
	No.4	11.7	0.035	0.0094	1.27	0.096	1.06	0.023
	No.5	11.9	0.041	0.0099	1.30	0.081	1.08	0.026
	average	12.1	0.038	0.0101	1.33	0.083	1.12	0.026
	STD	0.55	0.003	0.0005	0.08	0.025	0.08	0.003
	RSD	4.6	6.9	1.8	5.9	30.6	6.7	10.1
JG1	No.1	11.8	0.128	0.0092	1.37	0.076	1.04	0.025
	No.2	12.0	0.115	0.0086	1.32	-	1.10	0.027
	No.3	12.0	0.126	0.0088	1.38	0.226	1.09	0.027
	No.4	12.3	0.144	0.0101	1.44	-	1.12	0.027
	No.5	12.5	0.124	0.0101	1.45	0.069	1.15	0.027
	average	12.1	0.128	0.0094	1.39	0.124	1.10	0.026
	STD	0.27	0.010	0.0007	0.05	0.088	0.04	0.001
	RSD	2.2	8.2	1.8	3.7	71.3	3.8	3.1

表２　ＪＲＲ－４（低出力100kW運転）の気送管で放射化した標準物質の生成放射能（照射時間300秒、測定時間200-300秒、検出器から測定試料までの距離10cm（Na、Kは1cm））

単位は照射直後に補正したcps/μg

物質名		Al	Mg	Ca	Mn	Cl	Na	K
Apple leaves	No.1	14.5	0.018	0.0066	0.730	0.049	0.65	0.013
	No.2	15.3	0.018	0.0067	0.728	0.053	0.71	0.014
	No.3	14.8	0.018	0.0066	0.722	0.049	0.66	0.013
	No.4	15.0	0.017	0.0068	0.730	0.053	0.69	0.013
	No.5	15.1	0.017	0.0065	0.746	0.051	0.72	0.013
	average	14.9	0.018	0.0066	0.731	0.051	0.69	0.013
	STD	0.31	0.001	0.0001	0.009	0.002	0.03	0.001
	RSD	2.1	3.3	1.8	1.2	3.8	4.5	3.8
Peach leaves	No.1	15.0	0.017	0.0065	0.696	0.075	0.71	0.013
	No.2	15.5	0.019	0.0068	0.757	0.075	0.89	0.014
	No.3	15.3	0.019	0.0067	0.740	0.079	0.79	0.013
	No.4	15.3	0.019	0.0066	0.727	0.076	0.76	0.014
	No.5	15.6	0.019	0.0065	0.761	0.082	0.80	0.014
	average	15.3	0.019	0.0066	0.736	0.078	0.79	0.013
	STD	0.22	0.001	0.0001	0.026	0.003	0.07	0.000
	RSD	1.4	5.2	1.8	3.6	4.2	8.4	3.4
JB1a	No.1	13.9	0.021	0.0056	0.650	-	0.63	0.014
	No.2	13.6	0.022	0.0054	0.654	-	0.60	0.014
	No.3	13.7	0.022	0.0058	0.650	-	0.58	0.014
	No.4	13.6	0.023	0.0063	0.646	-	0.59	0.014
	No.5	13.6	0.023	0.0061	0.658	-	0.59	0.014
	average	13.7	0.022	0.0059	0.652		0.60	0.014
	STD	0.14	0.001	0.0003	0.005		0.02	0.000
	RSD	1.0	4.1	1.8	0.7		3.4	1.8
JG1a	No.1	13.8	0.078	0.0058	0.653	-	0.60	0.014
	No.2	13.6	0.089	0.0063	0.664	-	0.59	0.014
	No.3	13.6	0.089	0.0064	0.685	-	0.60	0.013
	No.4	13.7	0.080	0.0059	0.737	-	0.57	0.013
	No.5	13.7	0.072	0.0052	0.709	-	0.58	0.014
	average	13.69	0.082	0.0059	0.690		0.59	0.014
	STD	0.09	0.007	0.0005	0.034		0.01	0.000
	RSD	0.7	8.9	1.8	4.9		2.0	3.4

表3 KUR（出力5MW運転）の気送管（Pn-3）で放射化した標準物質の生成放射能（照射時間30秒、測定時間200-300秒、検出器から測定試料までの距離10cm）

単位は照射直後に補正したcps/μg

物質名	照射日	Al	Mg	Ca	Mn	Na	K
Apple leaves	2000.9.7	14.5	0.031	0.0139	1.59	0.196	0.0029
	2000.9.8	16.2	0.033	0.0139	1.57	0.107	0.0028
	2001.7.11	13.1	0.029	0.0116	1.43	0.093	0.0024
	2001.7.12	14.0	0.028	0.0116	1.44	0.116	0.0025
	2002.1.24	15.1	0.0317	0.0126	1.56	-	-
	2002.1.25	14.7	0.0298	0.0125	1.54	-	-
Peach leaves	2000.9.7	14.0	0.034	0.0132	1.44	0.150	0.0029
	2000.9.8	16.3	0.033	0.0134	1.48	0.192	0.0029
	2001.7.11	13.0	0.027	0.0116	1.39	0.114	0.0024
	2001.7.12	14.3	0.028	0.0117	1.46	0.138	0.0024
	2002.1.24	13.4	0.030	0.0128	1.51	-	-
	2002.1.25	14.5	0.032	0.0129	1.49	-	-
JB1a	2000.9.7	13.0	0.039	0.0134	1.43	0.124	0.0039
	2000.9.8	14.6	0.038	0.0033	1.47	0.120	0.0037
	2001.7.11	12.2	0.033	0.0109	1.32	0.107	0.0042
	2001.7.12	12.5	0.032	0.0113	1.30	0.109	0.0029
	2002.1.24	12.5	0.033	0.0111	1.36	-	-
	2002.1.25	12.4	0.035	0.0121	1.43	-	-
JG1a	2000.9.7	13.3	0.140	0.0138	1.47	0.131	0.0030
	2000.9.8	15.9	0.111	0.0130	1.54	0.128	0.0030
	2001.7.11	13.0	0.130	0.0113	1.50	0.108	0.0032
	2001.7.12	13.5	0.099	0.0133	1.46	0.113	0.0025
	2002.1.24	-	-	-	-	-	-
	2002.1.25	14.3	0.108	0.0138	1.54	-	-

れる。100kWの低出力運転により得られた結果を表２に示した。５個の同一試料のバラツキは最大８％程度で表１と同様の傾向を示した。3MWの定格出力運転に比べ、100kWの低出力運転時の方が熱中性子束の変動が少なく、安定しているといわれる。しかし、表１の結果と表２の結果を比べると3MWの定格出力運転で照射してもほとんど差の無いことがわかる。

表３にKURの気送管（Pn-3、熱中性子束 2.34 $\times 10^{13}$ n·cm^{-2}·sec）照射で得られた標準物質の生成放射能を、JRR-4の結果と比較するため示した。照射日や検出器が異なるにもかかわらず両者の計数率は近い値となった。

以上の結果をまとめるとJRR-4の気送管を用いた熱中性子放射化分析で環境試料中の短寿命核種を生成する元素を定量できることが明らかになった。

3-14

胎児期および成長期における亜鉛欠乏がその後の発育に与える影響(II)

Effects of Zn deficiency during the pregnant and lactating period on growth of mice (II)

矢永誠人、菅沼英夫、野口基子、吉田　努、大山拓也、前津仁美、笈田多加史、
小木貴憲、川本有美、小池真理子、梶田良行、衣川信之　(静岡大学理学部)
Makoto YANAGA, Hideo SUGANUMA, Motoko NOGUCHI, Tsutomu YOSHIDA,
Takuya OHYAMA, Hitomi MAETSU, Takashi OIDA, Takanori OGI,
Yumi KAWAMOTO, Mariko KOIKE, Yoshiyuki KAJITA, Nobuyuki KINUGAWA
(Faculty of Science, Shizuoka University)

1．はじめに

生体微量元素の一つである亜鉛は、様々な酵素反応に関与しているため、この亜鉛が欠乏すると、成長障害、性腺機能低下、味覚・嗅覚障害、皮膚障害、脱毛、免疫不全、胎児への催奇性などが引き起こされることが知られている。

我々は、以前より、この亜鉛に注目し、その欠乏が他の微量元素の挙動に与える影響、すなわち、微量元素間の相互作用について検討してきている。亜鉛欠乏状態に陥る原因として、遺伝的要因と食生活が考えられるが、本研究では、食餌中の亜鉛不足に伴う亜鉛欠乏を対象としている。その手段として、これまでは、亜鉛欠乏餌および対照餌(亜鉛添加餌)で飼育したマウスの各臓器・組織そのものについて、機器中性子放射化分析法により種々の微量元素の定量・比較検討を行ってきた。

食餌中の亜鉛欠乏の影響および亜鉛投与による欠乏状態からの回復の様子は、亜鉛欠乏餌を摂取した期間やマウスの週齢(成長期にある場合と成獣の場合)によっても異なることが予想されるため、生後３日目、３週齢、４週齢、８週齢から食餌中の亜鉛を一定期間欠乏させた場合、あるいは、亜鉛を欠乏させた後に亜鉛を投与した場合等、様々な飼育条件下のマウスを分析対象としている。さらに、亜鉛の欠乏と生体内の金属挙動との関係をより詳細に検討するために、金属タンパク質の合成に深く関与している肝臓について、遠心分離法により分離した各細胞成分中の微量元素の分析も行っている。

本報告では、これらのうち、３週齢から３週間、また、８週齢から３週間にわたって亜鉛を欠乏させたマウス肝臓について、遠心分画法により分離した各細胞成分中の微量元素の分析結果を中心に述べることとする。

2．実験

2－1　供試動物および肝細胞の分画

３週齢および８週齢のＩＣＲ系のオスマウスを、それぞれ、亜鉛欠乏群と対照群の２群に分け、亜鉛欠乏群には亜鉛欠乏餌およびミリポア水を、また、対照群には対照餌(亜鉛欠乏餌に塩基性炭酸亜鉛を添加した飼料)およびミリポア水を与えて飼育した。なお、各飼料は、(株)日本クレアに調製を依頼したものを使用した。各々のマウスについて、３週間の飼育の後、エーテル麻酔下において、肝臓を摘出した。摘出した肝臓を HEPES 緩衝液中にてホモジナイズし、その後、３回の遠心操作(1,000×g　20 分、9,000×g 20 分、105,000×g 65 分)により核画分、ミトコンドリア画分、ミクロソーム画分および可溶性画分の４つの画分に分離した。分離した各画分は、秤量した後に凍結乾燥し、分析試料とした。

研究施設・装置
JRR-3 気送照射設備(PN-1, PN-3)
JRR-4 気送管およびＴパイプ

研究分野
生体試料の放射化分析

2－2　照射および測定

凍結乾燥した各画分をポリエチレンで二重封入または三重封入し、照射試料とした。標準試料には、NIST SRM 1577b Bovine Liver および原子吸光分析用 Mg 標準溶液の一定量をろ紙上に滴下し乾燥させたもののそれぞれを、ポリエチレンで二重封入または三重封入したものを用いた。

熱中性子照射は、JRR-3M または JRR-4 において、目的元素に応じて２種類の照射を行った。短寿命核種により定量する元素については、JRR-3M 放射化分析用照射設備(PN-3)または JRR-4 気送管にて 10 秒間の照射を行った。まず、Mg、Cl、Ca の定量を目的として、照射２～８分後に高純度 Ge 半導体検出器にて 120 ～ 250 秒間のγ線スペクトロメトリーを行い、次に、Na および Mn の定量のため、１回目の測定から 60 ～ 150 分後に、再度、200 ～ 500 秒間の測定を行った。

また、長寿命核種により定量する元素(Fe、Co、Zn、Se および Rb)の放射化のために、JRR-3M 気送照射設備(PN-1)にて 20 分間の照射または JRR-4 T-パイプにて 30 ～ 40 分間の照射を行い、８～ 50 日後に３～ 24 時間のγ線測定を行った。

３．結果および考察

３週齢から亜鉛欠乏餌を用いて飼育したマウスは、飼育開始から３週間経過した後においてもほとんど体重の増加が見られず、明らかな成長障害が認められていた。摘出時の肝臓の生重量も対照群が 2.27 ± 0.12 g (n = 16)であったのに対し、亜鉛欠乏群では、わずか 0.91 ± 0.19 g (n = 16)と著しく小さいものであった。一方、８週齢から飼育したマウスについては、亜鉛欠乏群と対照群の間には、体重については有意な差は認められなかった。また、摘出した肝臓の生重量についても、亜鉛欠乏群 2.09 ± 0.27 g (n = 14)、対照群 2.07 ± 0.38 g (n = 11)と、両群の間には有意な差は認められなかった。

本研究では、遠心分離法により分画した肝細胞成分中の Na、Ma、Cl、Co、Fe、Mn、Cu、Zn、Se、Rb の 10 元素について定量を行うことができた。これらのうち、Zn および Co についての分析結果を図１に示した。

図１には、標準偏差を示してはいないが、成長期、すなわち、３週齢から亜鉛を欠乏させたマウスの核画分中の亜鉛濃度は、対照マウスと比較して有意に低下していた。亜鉛は、DNA の合成やその構造の維持に必要とされるものであることから、成長期に亜鉛を欠乏させたマウスの肝細胞の核画分において亜鉛濃度が著しく低いことは、細胞分裂や細胞の成長が阻害され、結果として、成長障害となって現れてきていることを示しているのではないかと考えられる。一方、成獣、すなわち、８週齢から亜鉛を欠乏させたマウスの肝細胞の核画分については、こ

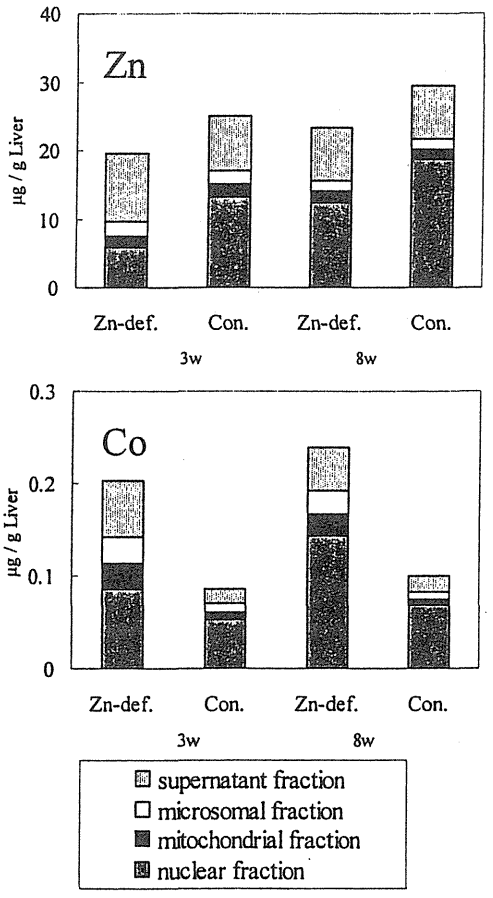


図１　マウス肝臓の各画分中の Zn と Co の濃度（3w、8w は、実験開始時の週齢）

のような傾向は認められていない。これは、以前にも報告したように、成獣の場合には、骨中に充分な量の亜鉛備蓄があり、食餌中の亜鉛が欠乏した場合においても、ある程度は、この骨中の亜鉛を消費することができることによるものと考えられる。[1-3]

一方、コバルト濃度は、成長期にあるマウスおよび成獣マウスのいずれの場合も、亜鉛欠乏群での濃度が高まっていた。亜鉛欠乏条件下では、全ての臓器・組織中のコバルト濃度が高まることは以前にも示したとおりである。[1-3] 本研究の結果では、亜鉛欠乏群では、分離した各肝細胞成分の全てについてコバルト濃度が増加しているようにも思われるが、今回の分離条件では核画分には未破壊の細胞も多数含まれること等を考慮すると、可溶性画分での増加が著しく、このことは、増加したコバルトは、遊離した状態か、あるいは、可溶性のタンパク質に結合した状態で存在しているものと考えられる。

3週齢から亜鉛を欠乏させたマウス肝臓中の微量金属では、亜鉛及びコバルト濃度のほか、鉄、マンガンおよび銅の濃度上昇も認められた。これらの濃度変化は、肝臓のマクロ的分析においても検知されていたことは以前にも示したとおりである。[3] 本研究で、各肝細胞成分に分離して分析したところ、鉄についてはミクロソーム画分で、また、マンガンおよび銅については可溶性画分で、それぞれ、濃度が有意に上昇していた。鉄の大幅な増加分がミクロソーム画分分で検出されたことは、この鉄がフェリチンといった貯蔵鉄タンパク質の形で存在していることを示しているものと思われるが、可溶性画分においてその増加が認められたマンガンおよび銅の存在状態については現時点では不明である。

一般的に授乳期あるいは離乳直後の成長期にある動物では、腸壁の発達が不完全であるためにマンガンの吸収を調整することができず、成獣に比べて過剰にマンガンを吸収することが知られている。[4] 本研究の場合におけるマンガンの増加は、亜鉛欠乏による生体内における金属元素間の相互作用によるものというよりは、3週齢から亜鉛を欠乏させたために腸壁が未発達であったためにマンガンの吸収を調整できなかったためであろうと考えている。銅についてもマンガンの場合と同様のことがいえるのかも知れないが、現時点では断定することはできない。いずれにしろ、可溶性画分中に過剰に存在しているマンガンおよび銅が、遊離した状態で存在しているのか、あるいは、特異的な可溶性タンパク質と結合しているのか、または、ある種の金属結合タンパク質の中心金属と置換してしまってるのかは興味あるところである。

4．まとめと今後の方針

本研究において、亜鉛欠乏マウスの臓器や組織そのものをそのまま分析するのみではなく、肝細胞について遠心分離法により各細胞成分に分画して分析を行ったところ、亜鉛、コバルト、鉄、マンガンおよび銅といった、主な生体必須微量元素についての興味ある知見を得ることができた。

現在、ここで記した分析のほか、肝細胞をさらに細分画した細胞成分についての分析や亜鉛が欠乏すると直ちに濃度低下が認められるすい臓についての同様な分析を行っている。今後は、これらの分析とともに、可溶性タンパク質に着目し、可溶性画分をさらに分離し、可溶性タンパク質とこれら金属との相互作用について分析・検討していく予定である。

参考文献

1 M. Yanaga, M. Iwama, K. Takiguchi, M. Noguchi and T. Omori, *J. Radioanal. Nucl. Chem.*, 231, 187(1998).

2 M. Yanaga, M. Iwama, K. Shinotsuka, K. Takiguchi, M. Noguchi and T. Omori, *J. Radioanal. Nucl. Chem.*, 243, 661(2000).

3 M. Yanaga, H. Wakasa, T. Yoshida, M. Iwama, K. Shinotsuka, M. Noguchi and T. Omori, *J. Radioanal. Nucl. Chem.*, 245, 255 (2000).

4 M. E. Le Feure and D. D. Joel, *Life Sci*, 21, 1403(1977).

成果の公表

学会発表

1 吉田 努、釜谷恵実、犬飼佳子、前津仁美、大山拓也、矢永誠人、野口基子、菅沼英夫、大森 巍、「授乳期の母マウスにおける亜鉛欠乏の影響」、2000 日本放射化学会年会・第 44 回放射化学討論会 (2000 年 9 月 神戸).

2 前津仁美、犬飼佳子、釜谷恵実、吉田 努、大山拓也、矢永誠人、野口基子、菅沼英夫、大森 巍、「亜鉛投与による亜鉛欠乏状態からの回復」、2000 日本放射化学会年会・第 44 回放射化学討論会 (2000 年 9 月 神戸).

3 H. Maetsu, T. Oida, Y. Ohashi, T. Yoshida, T. Ohyama, M. Noguchi, H. Suganuma, T. Omori and M. Yanaga, "Studies on zinc deficiency and recovery: changes in trace elements in organs and tissues of zinc-deficient mice", 2001 Asia-Pacific Symposium on Radiochemistry (APSORC 2001 and 45th SORC) (30th Oct. - 1st Nov., 2001, Fukuoka).

4 小池真理子、大山拓也、小木貴憲、川本有美、前津仁美、菅沼英夫、野口基子、 石川勝利、蛭沼利江子、榎本秀一、矢永誠人、「機器中性子放射化分析法による亜鉛欠乏マウス肝臓中の微量元素の定量」、 第 13 回日本微量元素学会 (2002 年 7 月 千葉).

5 大山拓也、小池真理子、小木貴憲、川本有美、前津仁美、菅沼英夫、野口基子、石川勝利、蛭沼利江子、榎本秀一、矢永誠人、「亜鉛欠乏マウス肝細胞の各画分における微量金属の分布」、2002日本放射化学会年会・第 46 回放射化学討論会 (2002 年 9 月 札幌).

6 小木貴憲、川本有美、前津仁美、小池真理子、大山拓也、野口基子、菅沼英夫、矢永誠人、「軽度の亜鉛欠乏が生体内微量元素濃度に及ぼす影響」、2002日本放射化学会年会・第 46 回放射化学討論会 (2002 年 9 月 札幌).

7 T. Ohyama, M. Koike, T. Ogi, Y. Kawamoto, H. Maetsu, H. Suganuma, M. Noguchi, K. Ishikawa, R. Hirunuma, S. Enomoto, and M. Yanaga, "Distribution of trace elements among subcellular fractions in livers of Zn-deficient mice", International Symposium on Bio-Trace Elements 2002 (Oct. 28 - Nov. 2, 2002, Saitama and Yamanashi, Japan).

8 T. Ogi, Y. Kawamoto, H. Maetsu, M. Koike, T. Ohyama, S. Enomoto, M. Noguchi, H. Suganuma and M. Yanaga, "Effects of zinc content in a diet on concentrations of trace elements in organs and tissues of mice", International Symposium on Bio-Trace Elements 2002 (Oct. 28 - Nov. 2, 2002, Saitama and Yamanashi, Japan).

Publications

1 小池真理子、大山拓也、小木貴憲、川本有美、前津仁美、菅沼英夫、野口基子、石川勝利、蛭沼利江子、榎本秀一、矢永誠人、「機器中性子放射化分析法による亜鉛欠乏マウス肝臓中の微量元素の定量」(M. Koike, T. Ohyama, T. Ogi, Y. Kawamoto, H. Maetsu, H. Suganuma, M. Noguchi, K. Ishikawa, R. Hirunuma, S. Enomoto, and M. Yanaga, "Concentrations of trace elements in liver subcellular fractions of Zn-deficient mouse"), *Biomed. Res. Trace Elements*, 13, 234 -235 (2002).

2 T. Ohyama, M. Koike, T. Ogi, Y. Kawamoto, H. Maetsu, H. Suganuma, M. Noguchi, K. Ishikawa, R. Hirunuma, S. Enomoto, and M. Yanaga, "Distribution of trace elements among subcellular fractions in livers of Zn-deficient mice", Proceedings of International Symposium on Bio-Trace Elements 2002, 80-82(2003).

3 T. Ogi, Y. Kawamoto, H. Maetsu, M. Koike, T. Ohyama, S. Enomoto, M. Noguchi, H. Suganuma and M. Yanaga, "Effects of zinc content in a diet on concentrations of trace elements in organs and tissues of mice", Proceedings of International Symposium on Bio-Trace Elements 2002, 83-85(2003).

3-15 カンボジア・プノンペン市の大気エアロゾル中元素濃度に関する研究

Study on element concentrations in aerosol in ambient air from Phnom Penh, Cambodia

鹿島勇治，堺 温哉，松井三明*

(横浜市立大学医学部衛生学講座，＊現所属：国立国際医療センター国際医療協力局派遣協力課)

KASHIMA Yuji, SAKAI Haruya, and MATSUI Mitsuaki*

Department of Hygiene, Yokohama City University School of Medicine

** Present address: International Medical Center of Japan Bureau of International Cooperation*

【はじめに】

我々は、1995 年から 2002 年２月まで、社会主義経済から資本主義経済への転換期にあるカンボジアの環境調査を実施した。カンボジアは現在も、環境基準、環境汚染物質測定施設など環境汚染監視システムが十分機能しておらず、経済成長に伴い、環境汚染が進行する恐れがある。これまでの調査結果より、砒素による環境汚染を除けば、農薬や重金属による環境汚染は非常に軽微であることがわかっている（高橋 2002）。しかし、1997 年より、我々が実施した首都プノンペン市沿道の大気汚染調査結果では、二酸化窒素、一酸化炭素は、日本の大都市と類似したレベルであり、また浮遊粒子状物質（SPM）については、日本の環境基準（日平均値 100 μg/m^3）の約５倍に達していることがわかった（鹿島・他 2001，高橋 2002）。近年、自動車排ガス中の SPM には、発ガン性や内分泌攪乱物質作用があることが報告されており（Tokiwa et al. 1998, Meek 1998, Taneda et al. 2002）、また、多くの疫学調査結果は SPM 濃度と呼吸器疾患、死亡率など健康影響との関連性を指摘しており（Dockery 2001, WHO 1999; 2000）、プノンペン市の沿道住民の健康影響が懸念される。そこで、プノンペン市の SPM の低減対策に必要とされる基礎情報を得る目的で、SPM 中に含まれる元素濃度を ICP 質量分析装置（ICP-MS）および中性子放射化分析法（INAA）により測定し、その起源について推定を試みた。

【試料と方法】

１．試料の採取

2001 年の 6、8、11 月および 2002 年の 2 月にプノンペン市内中心部の交差点沿道（1 地点、24 時間採取 11 試料、7～16 時間採取 14 試料）及び住宅地（2 地点、24 時間採取 13 試料、16 時間採取 1 試料）で SPM を採取した。SPM は分粒装置（10 μm 以上の粒子を 100%カット）を装着したハイボリュームエアサンプラー（HV1000F、柴田科学）を地上 8～9m の高さに設置し、混合セルロース製メンブレンフィルター（A100A、ｱﾄﾞﾊﾞﾝﾃｯｸ）あるいは石英フィルター（QR-100、柴田科学）を用い 1000L/min の吸引量で最大 24 時間連続採取した。メンブレンフィルターを用いた SPM の 24 時間採取は、SPM 量の多い交差点沿道では、吸引圧力損失を防ぐため、7～16 時間でフィルターを交換した。

SPM の起源を推定するために、2001 年 6 月に SPM 採取地点付近の路肩集積粉塵・土壌（2 地点、9 試料）を、また 11 月には自動車および発電機の排気筒に付着した煤（二輪車 11 試料、四輪車：ガソリン車７試料、ディーゼル車 10 試料、発電機 6 試料）を採取した。路肩集積粉塵・土壌は、0.5mm のステンレス製ふるいにかけた後、デシケーター内で十分に乾燥した。

研究施設・装置：原子炉JRR-4 気送管およびＴ－パイプ（東海）
研究分野：環境化学，環境衛生学

2．ICP-MSによる元素濃度の測定

SPMを捕集したメンブレンフィルター20cm²あるいは自動車・発電機排筒付着粒子、路肩集積粉塵・土壌を各々テフロン分解容器に入れ、硝酸1.0ml、過酸化水素2.0mlを加え、電子レンジで分解した。分解後、純水で50mlに希釈し、一晩静置し、上澄みをICP-MS（SPQ6100、ｾｲｺｰｲﾝｽﾂﾙﾒﾝﾂ製）により元素濃度を測定した。MnやHgなど一部の元素については、原子吸光光度法によっても測定した。標準試料（自動車排ガス微粒子NIES CRM No.8）を用いたICP-MS法による分析精度をTable 1-1に示す。

3．INAAによる元素濃度の測定

1）照射試料のシーム方法

① 短寿命核種測定用試料：SPMを捕集したメンブレンフィルター20cm²を200μLのイソプロピルアルコールで湿潤させた後、ポリエチレン袋で3重でシームし、-20℃で照射時まで保存した。また、自動車・発電機排気筒付着粒子および路肩集積粉塵・土壌については、試料をポリエチレン管に入れ、秤量後、溶封し、ポリエチレン袋で2重でシームした後、照射時まで-20℃で保存した。

② 中・長寿命核種測定用試料：SPMを捕集した石英フィルター20cm²をポリエチレン袋でシーム後、濾紙をはさみ、さらにポリプロピレン袋で2重にシームし、照射時まで-20℃で保存した。また、路肩集積粉塵・土壌は、ポリエチレン管に封入後、石英フィルターと同じ方法でシームした。

2）照射および測定条件

① 短寿命核種：ドライアイスと共に、試料1個と標準溶液を封入したポリエチレン管（あるいは袋）1個を照射用の標準キャプセル（ポリエチレン製）に装填し、原子炉内で熱中性子を照射した。中性子源として、日本原子力研究所・研究用原子炉JRR-4を用い、単寿命核種照射装置に敷設されている気送管により熱中性子束下（JRR-4：3.2×10^{13}n/cm²·sec）で15秒間照射後、外側のポリエチレン袋を取り替えて、γ線スペクトロメーターを用いて、短寿命核種（^{29}Al、^{38}Cl、^{52}V、^{56}Mnなど）について300～400秒間測定した。

② 中・長寿命核種：PEN製キャプセルに試料を5～10個、標準1個を入れ、水力照射設備（B系統）で40分間照射後、1から2日間冷却後、外側のポリエチレン袋を取り替えて、中寿命核種（^{24}Na、^{42}K、^{76}Asなど）のγ線を1000秒間測定した。さらに、同じ試料を20～30日間冷却後、長寿命核種（^{51}Cr、^{65}Zn、^{60}Co、^{59}Fe、^{124}Sbなど）について2000或いは4000秒間測定した。

自動車排ガス微粒子（NIES CRM No.8）および鉱石（CCRMP RTS-2）の標準試料を用いたINAAの分析精度をTable 1-2に示す。

4．統計解析

統計解析はStatView V.5.0.1（SAS Institute Inc.）で処理した。2群間の差の比較についてはMann-Whitney検定、多群間の差の比較についてはScheffe検定を用いた。因子分析は主因子法（固有値1.0以上）、バリマックス変換法を用いた。

【結果と考察】

1．大気中SPM濃度および元素濃度

SPM濃度は67～1000μg/m³（平均値410 μg/m³）であり、住宅地よりも沿道で高値を示した（Table 2）。またSPM濃度を反映して、毒性元素の濃度も、Cdを除き沿道で高値を示した。Pb濃度は平均で44ng/m³であり、WHOのガイドライン（年平均値500ng/m³, WHO 1999）の約1/10の濃度であった。

2．SPMおよび路肩集積粉塵・土壌の元素組成の比較

SPMおよび路肩集積粉塵・土壌中の元素組成は比較的類似していたが、Cr以外の元素濃度は、SPMで有意に高値を示した（Fig.1）。

3．SPMおよび自動車・発電機排気筒付着粒子の元素組成の比較

自動車・発電機排気筒付着粒子のCrおよびZn、Mo、Pb濃度は、SPMよりも高値を示し、これらの濃度は大きく変動した（Fig.2 a）。しかし、MnおよびCo、Ga、As、Se、Sb、Ba、Hg、Tl濃度は、SPMの方が有意に高値を示した（Fig.2 b）。

発生源別に自動車・発電機気筒付着粒子の元素濃度を比較すると、Ni、Cu、Ga、Pbの各元素がディーゼル車よりもガソリン車で有意に高値であった。またZn濃度は、自動車に比べて発電機で有意に高値を示した（Fig.3）。

4．SPM中元素の起源推定

Miller et al.（1972）は、SPM中の化学物質の起源を海洋性、土壌性、自動車排ガス、石油燃焼の4起源と仮定して、マスバランスを推定している。この報告によれば、SPM中のBaは土壌性起源の寄与が最も多く、Vは約90%が石油燃焼、Pbは100%近くが自動車排ガス起源であると推定している。

そこで、SPM中に検出された元素のうちBa、V、Pbを含む18元素を用いて因子分析を実施した結果、3つの因子が抽出された。この3つの因子でSPM中元素の全変動の89.3%（因子1：42.6%、因子2：39.4%、因子3：7.3%）が説明できると推定された（Table 3 a）。

因子1は、土壌起源と考えられるBaと正の相関関係にあり、その他にも土壌中に存在するGa、Cu、Mo、Co、Ge、Niなど多くの元素と正の相関関係にあった（Table 3 b,c,d）。また、自動車排ガスからの寄与が大きいとされるPbとは負の相関関係にあり、石油燃焼からの寄与が大きいとされるVとの相関関係は弱かったことから、因子1は土壌起源粒子と推察した。

因子2は、自動車排気ガス起源と考えられるPbと正相関し、その重みも大きかった（Table 3 b,c,d）。またTlとの間に正の相関関係が認められた（Table 3 b,c,d）。今回分析した自動車・発電機排気筒付着粒子中のTl濃度は、ディーゼル自動車あるいは発電機よりもガソリン自動車で高値を示したことから（Fig.3）、因子2は、自動車排ガス（主にガソリン自動車）起源と推察した。

因子3については、V、Mnなど石油燃焼起源と考えられる元素と正の相関関係があり、Vの重みが最も大きかった。しかしTlとの間に正相関は認められなかった（Table 3 b,c,d）。さらに、自動車・発電機排気筒付着粒子および路肩集積粉塵・土壌の各V濃度は、SPMよりも低濃度であったことから（Fig.1,2,3）、因子3をV濃度の高い重油（木村・他 1977）など化石燃料起源と推察した。プノンペン市近郊には2つの火力発電所があり、それらの煤煙がSPMに寄与している可能性が考えられた。

以上の結果より、プノンペン市内のSPMの主要な起源は、自動車排ガス粒子と土壌粒子であると推定されたが、推定に用いたデータ数が少ないため、推定の精度を高めるためにも、火力発電所などの煤煙やガソリン・軽油など燃料油自体の元素分析も今後必要と考える。

【おわりに】

WHO（1999）は近年欧米で実施されたSPMによる健康影響に関する疫学調査結果を踏まえて、SPMによるヒトへの健康影響には閾値がないと言う見地に立ちPM_{10}（10μm以下のSPM、10μmを50%カット）などのガイドラインの見直しを実施した。現在、WHOは環境基準値の代わりにSPM濃度と死亡率や呼吸器疾患等との一次回帰モデルを提示し（WHO1999）、例えば、平均50 $\mu g/m^3$ のPM_{10}に3日間暴露された場合には、10万人のうち4人が死亡する可能性があるとしている（WHO 2000）。このモデルはPM_{10}が200 $\mu g/m^3$を超える、あるいは20 $\mu g/m^3$以下の場合には、疫学データなどの不足により適用すべきではないとしている。プノンペン市内のSPM濃度（67～1000 $\mu g/m^3$、平均値410 $\mu g/m^3$）は、測定された最低濃度でも、10万人のうち5人が死亡する可能性のあるレベルにあり、プノンペン市内住民のSPMによる健康影響が憂慮される。近年、自動車保有台数は増加傾向にあり、早急に自動車排ガスを削

減するための対策を講じる必要があると思われる。

【謝辞】

本調査を実施するにあたりご協力頂いたカンボジア環境省及びシャンティ国際ボランティア会のスタッフ一同に感謝致します。また、中性子線照射にご協力を頂いた澤幡浩之及び川手稔技官に感謝致します。

【参考文献】

鹿島勇治，堺　温哉，松井三明，土井陸雄．カンボジア・プノンペン市内の二酸化窒素、二酸化硫黄、浮遊粒子状物質濃度．第 10 回環境化学討論会講演要旨集，松山，2001．5．(pp. 396-397)

木村正巳，小野哲，和田攻（監訳）．環境汚染物質の生体への影響２　クロム・バナジウム．東京化学同人，東京，1977

高橋敬雄（編）．メコン川流域各国の経済発展に伴う生態系への影響評価およびその保全に関する研究．2002 年度トヨタ財団研究助成報告書，新潟大学工学部高橋敬雄研究室，新潟，2002

Dockery DW. Epidemiologic evidence of cardiovascular effects of particulate air pollution. Environ Health Perspect. 109 Suppl 4: 483-486, 2001

Meek MD, Ah receptor and estrogen receptor-dependent modulation of gene expression by extracts of diesel exhaust particles. Environ Res. 79: 114-121, 1998

Miller MS, Friedlander SK, Hidy GM, Chemical element balance for the Pasadena aerisol. J Colloid Interface Sci. 39: 165-176, 1972

Taneda S, Hayashi H, Sakushima A, Seki K, Suzuki AK, Kamata K, Sakata M, Yoshino S, Sagai M, Mori Y. Estrogenic and anti-estrogenic activities of two types of diesel exhaust particles. Toxicology. 170:153-161, 2002

Tokiwa H, Nakanishi Y, Sera N, Hara N, Inuzuka S. Analysis of environmental carcinogens associated with the incidence of lung cancer. Toxicol Lett. 99: 33-41, 1998

WHO. Guidelines for Air Quality, World Health Organization, Geneva, 1999

WHO. Air Quality Guidelines for Europe, Second edition, 2000, WHO Regional Office for Europe, Copenhagen.

【成果の公表】

(学会発表)

鹿島勇治，堺　温哉，松井三明，土井陸雄．カンボジア・プノンペン市内で捕集された大気浮遊粒子状物質の元素組成．第 11 回環境化学討論会，箱根，2002．6．(pp. 328-329)

Table 1-1. Analytical accuracy and precision for certified reference material (NIES-CRM No.8*) using ICP-MS

Element	Certified values (μg/g) Mean ± SD	Isotope	n	Recovered values (μg/g) Mean ± SD	(%)
	Recommended values				
V	17 ± 2	^{51}V	3	16.3 ± 2.4	(96)
Cr	25.5 ± 1.5	^{52}Cr	3	19.8 ± 2.5	(78)
Co	3.3 ± 0.3	^{59}Co	3	3.3 ± 0.6	(100)
Ni	18.5 ± 1.5	^{60}Ni	3	18.9 ± 3.0	(102)
Cu	67 ± 3	^{63}Cu	3	64.7 ± 9.8	(97)
Zn	1040 ± 50	^{66}Zn	3	961 ± 243	(92)
As	2.6 ± 0.2	^{75}As	3	2.9 ± 0.4	(110)
Cd	1.1 ± 0.1	^{111}Cd	3	1.2 ± 0.2	(108)
Sb	6 ± 0.4	^{121}Sb	3	4.0 ± 0.7	(67)
Pb	219 ± 9	^{208}Pb	3	170 ± 20	(78)
	Informational values				
Se	1.3	^{77}Se	3	0.70 ± 0.08	(54)
Rb	4.6	^{85}Rb	3	2.92 ± 0.28	(63)
Mo	6.4	^{95}Mo	3	5.88 ± 0.51	(92)
Ag	0.2	^{107}Ag	3	0.18 ± 0.05	(91)
Cs	0.24	^{133}Cs	3	0.22 ± 0.01	(90)
La	1.2	^{139}La	3	0.99 ± 0.05	(82)
Ce	3.1	^{140}Ce	3	2.94 ± 0.23	(95)
Sm	0.2	^{147}Sm	3	0.18 ± 0.02	(89)
Lu	0.02	^{175}Lu	3	0.01 ± 0.00	(44)

*: vehicle exhaust particulates

Table 1-2. Analytical accuracy and precision for certified reference materials using INAA

Element	Certified values (μg/g) Mean ± SD	Radio Isotope	γ ray (keV)	n	Recovered values (μg/g) Mean ± SD	(%)
NIES-CRM No.8						
Cr	25.5 ± 1.5	^{51}Cr	320.1	4	28.0 ± 2.8	(91)
V	17 ± 2	^{52}V	1434.1	2	17.3 ± 1.2	(98)
Co	3.3 ± 0.3	^{60}Co	1332.5	4	3.5 ± 0.3	(94)
Zn	1040 ± 50	^{65}Zn	1115.5	4	1029 ± 104	(101)
As	2.6 ± 0.2	^{76}As	559.1	4	2.7 ± 0.5	(95)
CCRMP RTS-2 (sulphide ore mill tailings)						
Cr	125*	^{51}Cr	320.1	1	134	(107)
Mn	400*	^{56}Mn	846.8	1	366	(91)
Co	72 ± 7	^{60}Co	1332.5	1	72	(101)
Zn	117 ± 10	^{65}Zn	1115.5	1	143	(122)
As	6.3 ± 1.8	^{76}As	559.1	1	10	(151)

*: informational values

Table 2. SPM and element concentrations in ambient air

	Area	N	Mean ± SD	(Min - Max)	Geom. Mean
SPM	Total	13	419 ± 321	(67 - 1028)	308
(μg/m^3)	Residence	6	157 ± 60	(67 - 232)	145
	Roadside	7	644 ± 276	(306 - 1028)	587
V	Total	13	45 ± 43	(12 - 157)	31
(ng/m^3)	Residence	6	14 ± 2	(12 - 17)	14
	Roadside	7	71 ± 44	(26 - 157)	61
Cr	Total	11	26 ± 25	(ND - 75)	15
(ng/m^3)	Residence	4	5 ± 2	(ND - 8)	4
	Roadside	7	38 ± 25	(11 - 75)	30
Mn	Total	13	447 ± 497	(87 - 1842)	281
(ng/m^3)	Residence	6	125 ± 42	(87 - 205)	120
	Roadside	7	722 ± 548	(241 - 1842)	583
Co	Total	13	12 ± 13	(1 - 37)	6
(ng/m^3)	Residence	6	2 ± 1	(1 - 3)	2
	Roadside	7	21 ± 12	(8 - 37)	18
Ni	Total	13	14 ± 10	(2 - 33)	11
(ng/m^3)	Residence	6	6 ± 3	(2 - 9)	5
	Roadside	7	21 ± 8	(12 - 33)	20
As	Total	13	12 ± 11	(1 - 36)	7
(ng/m^3)	Residence	6	3 ± 2	(1 - 5)	2
	Roadside	7	20 ± 10	(10 - 36)	18
Cd	Total	13	0.5 ± 0.3	(0.1 - 1.1)	0.4
(ng/m^3)	Residence	6	0.5 ± 0.4	(0.1 - 1.1)	0.4
	Roadside	7	0.5 ± 0.1	(0.4 - 0.6)	0.5
Hg	Total	13	0.4 ± 0.2	(0.1 - 0.8)	0.4
(ng/m^3)	Residence	6	0.2 ± 0.1	(0.1 - 0.3)	0.2
	Roadside	7	0.6 ± 0.1	(0.4 - 0.8)	0.6
Pb	Total	13	44 ± 28	(6 - 100)	34
(ng/m^3)	Residence	6	38 ± 39	(6 - 100)	22
	Roadside	7	50 ± 14	(32 - 68)	48

Table 3. Results of factor analysis

a) Eigenvalues

	Magnitude	Variance Prop.
Value 1	7.674	0.426
Value 2	7.087	0.394
Value 3	1.316	0.073
Value 4	0.651	0.036
Value 5	0.365	0.020
Value 6	0.286	0.016
Value 7	0.264	0.015
Value 8	0.109	0.006
Value 9	0.093	0.005

b) Unrotated Factors

	Factor 1	Factor 2	Factor 3
Cl	-0.550	0.707	0.236
V	0.418	-0.644	0.490
Cr	0.881	-0.240	0.249
Mn	0.536	-0.596	0.420
Co	0.963	-0.124	0.077
Ni	0.602	0.712	-0.101
Cu	0.767	0.594	-0.062
Zn	0.093	0.952	-0.107
Ga	0.919	0.259	-0.084
Ge	0.967	-0.148	0.035
As	0.824	0.256	0.216
Se	-0.221	0.917	0.194
Mo	0.779	0.339	-0.160
Sb	-0.220	0.82	0.475
Ba	0.944	0.175	-0.068
Hg	0.264	0.831	-0.352
Tl	0.026	0.956	0.052
Pb	-0.347	0.750	0.524

c) Oblique solution primary pattern matrix

	Factor 1	Factor 2	Factor 3
Cl	-0.325	0.817	-0.065
V	0.151	0.068	0.929
Cr	0.739	-0.017	0.526
Mn	0.285	0.0003	0.838
Co	0.870	-0.150	0.275
Ni	0.803	0.252	-0.333
Cu	0.919	0.193	-0.214
Zn	0.394	0.483	-0.507
Ga	0.961	-0.076	-0.087
Ge	0.869	-0.214	0.234
As	0.842	0.278	0.277
Se	0.056	0.852	-0.159
Mo	0.861	-0.087	-0.232
Sb	0.001	1.107	0.231
Ba	0.958	-0.116	-0.029
Hg	0.542	0.099	-0.741
Tl	0.316	0.677	-0.318
Pb	-0.146	1.137	0.304

d) Oblique score weights

	Factor 1	Factor 2	Factor 3
Cl	-0.054	0.280	0.174
V	-0.012	0.353	0.509
Cr	0.081	0.173	0.265
Mn	0.010	0.295	0.442
Co	0.113	-0.034	-0.126
Ni	0.108	0.034	0.097
Cu	0.125	-0.014	-0.079
Zn	0.061	-0.007	-0.155
Ga	0.131	-0.068	-0.079
Ge	0.111	-0.004	0.059
As	0.098	0.192	0.205
Se	-0.001	0.255	0.128
Mo	0.123	-0.123	-0.158
Sb	-0.025	0.488	0.400
Ba	0.129	-0.062	-0.058
Hg	0.094	-0.232	-0.377
Tl	0.041	0.132	-0.005
Pb	-0.048	0.527	0.448

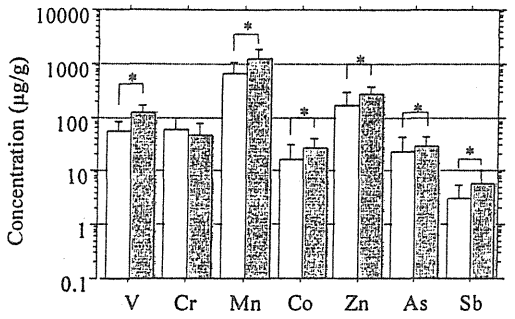


Fig.1. Element concentrations in SPM, roadside dust and soil (*: Significant difference with Mann-Whitney U, p<0.05) ☐ Roadside dust & soil ▨ SPM

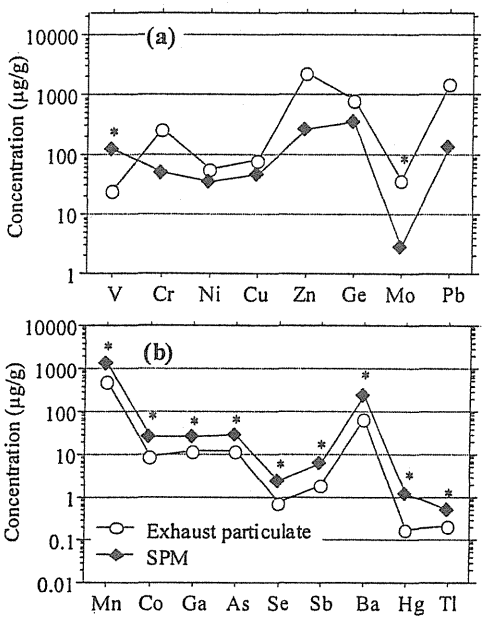


Fig.2. Element concentrations in SPM and exhaust particulates collected from vehicle and electric generator (*: Significant difference between SPM and exhaust particulates, Mann-Whitny U; p<0.05)

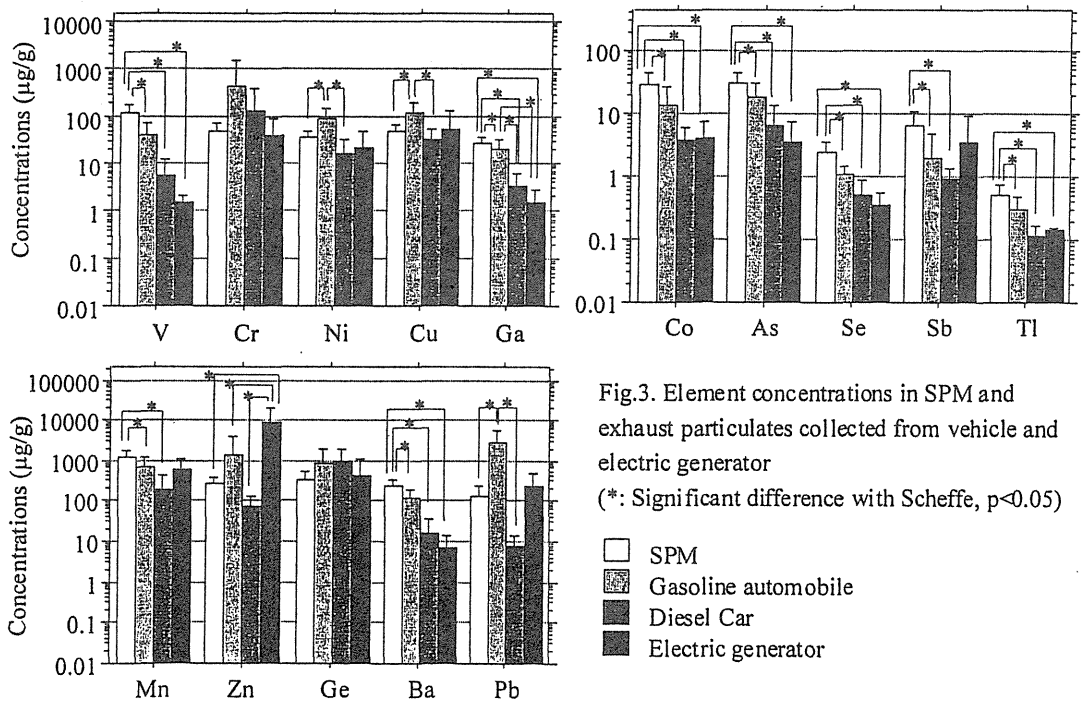


Fig.3. Element concentrations in SPM and exhaust particulates collected from vehicle and electric generator
(*: Significant difference with Scheffe, p<0.05)

☐ SPM
▨ Gasoline automobile
■ Diesel Car
■ Electric generator

研究テーマ：リアルタイム非破壊超微量分析法の開発
表　　題：多重ガンマ線放射化分析法による鉄鋼中の微量 As,Sb の定量

3-16

多重ガンマ線放射化分析法による鉄鋼中の微量 As,Sb の定量

木村 敦　藤 暢輔　初川 雄一　大島 真澄
日本原子力研究所　物質科学研究部　原子核科学研究グループ

1. 緒言　近年、環境意識の高まりとともに、鉄鋼スクラップの利用拡大が年々進められている。しかし、スクラップを鉄源として再溶解した場合、不純物元素が増大し材料の特性に大きな影響を与える可能性がある。そのため、増大するスクラップ鉄をリサイクルし、かつ鉄鋼製品の品質を維持するためには不純物を除去する技術及び分析・定量する技術の開発が急務である。我々のグループでは、物理学の実験で用いられる多重ガンマ線検出法と中性子放射化分析法を組み合わせた新しい元素定量法(多重ガンマ線放射化分析法)を用い、鉄鋼中の微量元素（As,Sb）の定量を行った。

2. 多重ガンマ線放射化分析法概要　多重ガンマ線検出法では多くの放射性核種が同時に複数のガンマ線を出すことに着目し、これらのガンマ線の同時測定を行う。こうして得られた測定結果は、ひとつのイベントに対して二つのエネルギー情報を持つので、これを２次元マトリックスで表記し解析することができる。これにより、従来の放射化分析では主要成分の妨害により観測できなかった極微量元素の分析が可能となり、82安定元素のうち49元素について、ppm~ppt の高感度、%オーダーの高精度で、化学分離なしに定量が可能となった。

3. 鉄鋼試料中の微量元素測定　現在我々のグループでは 16 台のアンチコンプトンガンマ線分析器からなる多重ガンマ線分析装置（GEMINI-II）を用いて測定を行っている。

Sb の定量については日本鉄鋼標準物 JSS001-5、JSS003-2,4 など 7 種類の試料各 100mg を JRR-3 水力照射管（熱中性子束$9.6\times10^{17}m^{-2}s^{-1}$）で 5 時間照射し、21 日間の冷却後 GEMINI-II で 24 時間測定を行った。

また、As については JSS001-5、JSS168-7 約 50mg を原研所有の JRR-3 気送管（熱中性子束$5.2\times10^{17}m^{-2}s^{-1}$）で 10 分間照射し、8 時間の冷却後 GEMINI-II で 12 時間測定を行った。

測定結果を表に示す。測定結果は認証値とよく一致しており、本分析法により、鉄鋼中の微量 As,Sb が定量できることが確認された。

4. 多重ガンマ線放射化分析法のばらつき　日本鉄鋼標準物 JSS001-5 約 50mg5 個を JRR-3 気送管で別々に 10 分間照射し、その後 GEMINI-II で 12 時間測定を行った。その結果、2.20±0.21、2.14±0.22、2.50±0.23、2.36±0.22、2.36±0.22、2.13±0.21(ppm)となり、測定結果のばらつきは 2.26±0.14(ppm)となった。これにより、多重ガンマ線分析法の測定ごとのばらつきは十分に小さく、定量手法として十分に有効であることが確認された。

5. 結言　鉄鋼に含まれる微量 As、Sb が多重ガンマ線放射化分析法を用いて高い精度で 0.01ppm まで定量できることが確認された。

参考文献

1) 平井昭司, 岡田往子, 鈴木章悟、材料とプロセス、VOL.10,NO.3 PAGE.693-696 1997

表　各標準物質中の Sb、As の定量結果及び認証値(文献値)

Sample	This Work (ppm)		Certified value (ppm)	
	Sb	As	Sb	As
JSS001-5	0.010±0.003	2.20±0.21	———	2.1±0.5
JSS003-2	0.051±0.005		0.039±0.006[1)]	
JSS003-4	0.033±0.004		0.029±0.002[1)]	
JSS175-7	210±7		200±7	
JSS168-7	1.22±0.04	111.0±1.1	———	120±10
NIST 1763	9.53±0.33		10	
NIST 1765	98.9±3.3		(110)	

原子炉：JRR-3　　装　置：気送管、水力照射管　　分　野：放射化分析(工業材料)

3-17 植物による大気中エアロゾルの補足能力と滞留時間

Capture Capability and Residence Time of Atmospheric Aerosols in the plant

九州大学アイソトープ総合センター　大崎　進

Susumu Osaki, Radioisotope Center, Kyushu University

九州大学大学院理学研究院　杉原真司、亀田周二

Shinji Sugihara, Syuji Kameda, Faculty of Sciences, Kyushu University

1．はじめに

大気中に放出された汚染物質や放射性物質は、その拡散過程において、エアロゾルに捕捉され、エアロゾルと伴に沈降・移動を行うため、エアロゾルは大気中での物質の移動媒体として大きな役割を持っている。近年は、酸性雨や地球温暖化などの環境変動の影響研究と関連して、エアロゾルの研究は行われているが、地域、気候により分布や移動の条件が異なり、種々の条件下におけるデータの蓄積が必要である。

植物は、陸上におけるエアロゾルの大きなリザーバと考えられる。植物葉は、その形態、形状、表面状態等によって、エアロゾルの捕捉能力が異なり、また保持能力も異なる。エアロゾルの捕捉に寄与する要因を探ることによって、環境汚染のモニターとして植物を選定する際の判断基準ともなる。

福岡は、大陸起源のエアロゾルの寄与が考えられる地点であり、植物へのアジア地区からの影響の程度も見積もることが可能であり、滞留時間を知ることができる。

また、エアロゾルは、種々の発生源を持ち、季節や気象条件によってその寄与の割合も異なると考えられ長期間に渡る観測が必要である。

エアロゾル粒子の地球の気候にもたらす影響メカニズムを理解することが目的であるが、本課題においては、捕捉媒体である植物に着目し、降下量、捕捉能力の違い、季節変動を測定した。植物自体の元素含有量とエアロゾルの季節変動を比較し、エアロゾルの挙動を考察した。

2．実験

（試料採取）

福岡市南部の背振山山頂部（標高約１ｋｍ）において、８種類の植物を採取した。採取地点は、人為的汚染の少ないバックグランウンド地点の代表とした。植物は、葉の形状・植生等が異なるものを選んだ。（１．Quercus acuta（アカガシ）、2. Petasites japonicus（フキ）、3. SasaVeitchii（クマササ）、4. Miscanthus sinensis（ススキ）、5. Bryum argentums,Hedw（コケ）、6. Ilex crenata（イヌツゲ）、7. Pinus thunbergii（クロマツ）、8. Lycopodium clavatum（ヒカゲノカズラ））　植物の葉だけを分別し、灰化後測定試料とした。植物葉の表面積を Table 1 に示す。

Table 1　Surface area of leaf

No	Sample Name	Surface Area(cm^2/g)
1	Quercus acuta	47
2	Petasites japonicus	80
3	Sasa veitchii	198
4	Miscanthus sinensis	121
5	Bryum argentum, Hedw	150
6	Ilex crenata	75
7	Pinus thunbergii	30
8	Lycopodium clavatum	120

（照射・測定）

照射は３時間照射と気送管による１０秒照射の２種類行った。それぞれ、約３０ー４０ｍｇを石英管とポリエチレン袋に封入して照射した。３時

JRR-3 JRR-4　HR-1,2,PN-3　　環境試料放射化分析

間照射分は、１０日程度冷却し、１０秒照射分は直後に原研の Ge 半導体検出器でガンマ線を測定した。測定時間は、各２０００秒及び１００秒である。標準としては、JB-1 を利用した。

（天然放射性核種の測定）

灰化試料は、そのままプラスチック容器にいれ、Ge 半導体検出器で測定した。対象核種は宇宙線生成核種である Be-7 と地殻起源の Pb-210 及び K-40 である。測定時間は約１日である。測定値は、採取時期に半減期補正した。

３．結果と考察

Figs.1-a,b に、植物葉中の Pb-210、Figs. 2-a,b に Be-7、 Figs. 3-a,b に K-40 の含有量を示す。Fif.1-b,Fig2-b では、Bryum argentums, Hedw だけが左の軸である。両核種において、エアロゾル降下物と同様に、春に高い傾向が見られた。しかし、

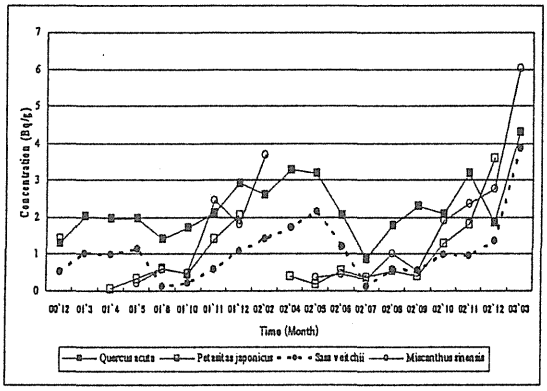


Fig.1-a Concentration of ^{210}Pb in ash sample

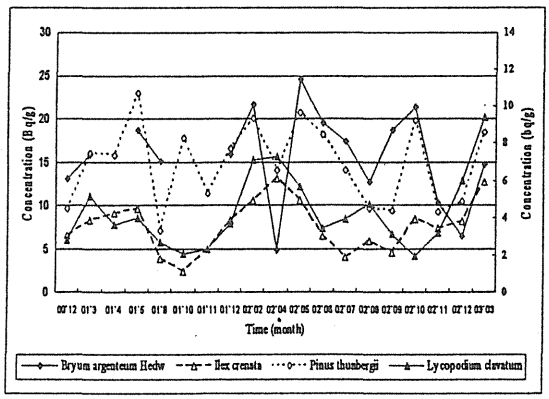


Fig.1-b Concentration of ^{210}Pb in ash sample

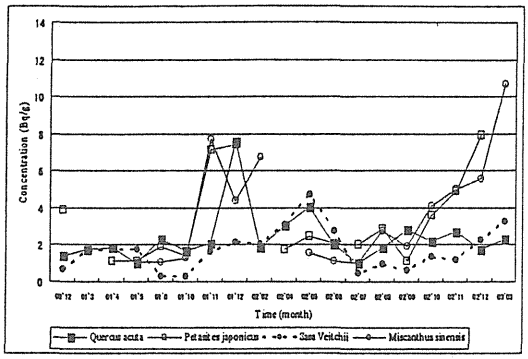


Fig.2-a Concentration of ^{7}Be in ash sample

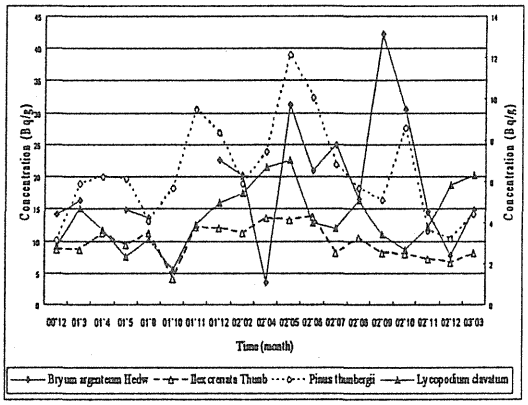


Fig.2-b Concentration of ^{7}Be in ash sample

そのピークに大きな時期的な差はない。Be-7、Pb-210 両核種とも、Bryum argentums, Hedw だけが高濃度であるが、これは植生の関係で付着している木の幹や岩との分離が試料調製の際に行われなかったことが一原因と考えられる。その他の種では、ほぼ同程度の濃度を示すが、Pinus thunbergii と Ilex crenata が若干高濃度を示し、前者は表面積が小さいため、捕捉効率が高いと考えられる。

一方、K-40 は、顕著に高濃度を示す種はなく、ほぼ一定であるが、一年で更新する Petasites japonicus と Miscanthus sinensis では、成長期に高く、徐々に減少しているパターンが見られた。

このように、植物の構成元素であるカリウムには変動がないことから、植物がエアロゾルを捕捉し、含有濃度に季節変動がみられることがわかる。また、その捕捉能力は、単純に表面積には関係していないことがわかる。

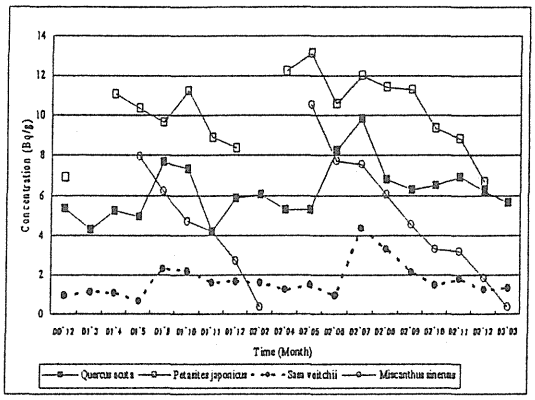


Fig.3-a Concentration of ^{40}K in ash sample

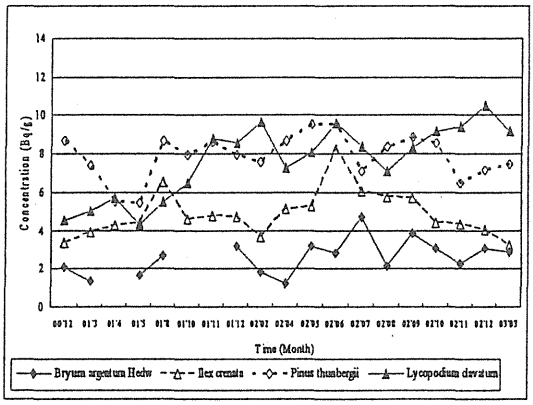


Fig.3-b Concentration of ^{40}K in ash sample

放射化分析によって定量できた元素の内、含有量が多く、すべての種で検出できた、Co、Cr、Feについて、Fig. 4に示す。これらの元素においては、季節変動を示さず、ほぼ一定であるが、夏季に若干上昇する傾向があった。すなわち、K-40 の変動と同様であり、主に径根吸収によってこれらの元素が移動していることがわかった。今回の採取地点は、人為的汚染の少ない地点であり、汚染されたエアロゾルが降下していないことが考えられるため、都市部において、同種の変動をみることにより、エアロゾルの寄与を見積もることが可能となる。

今回は、多くの測定点を実施することができなかたので、エアロゾルの影響が異なる地点での測定を行うと伴に、捕捉能力の評価には、さらに種の範囲を広げれば、環境モニターとして選択する場合の基準をつくることが可能であると考えられる。

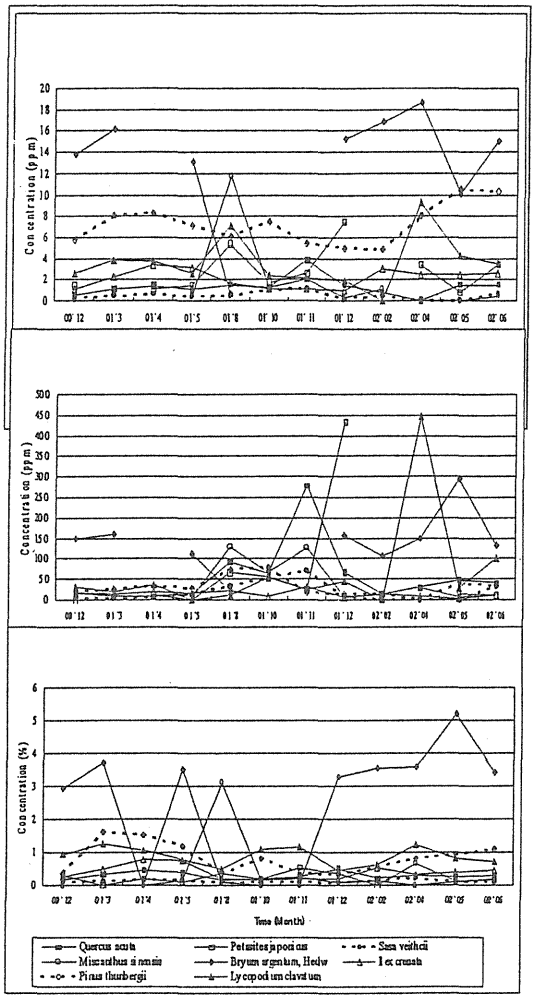


Fig.4 Concentration of element (Co, Cr, Fe)

4．成果の公表

1）エフリザル、杉原真司、大崎　進、前田米蔵：「Accumulation and Seasonal Variation of ^{210}Pb, ^{7}Be and Some Elements in Plants Leaf」

第 16 回日本化学会九州支部・韓国化学会釜山支部合同セミナー（２００３）

研究テーマ：中性子放射化分析法の環境影響元素・物質研究に対する新利用法と高度化技法の開発
表題：臭素同位体比(Br-81/Br-79 比)測定法の開発による土壌浸透水の野外・長期間追跡への利用

3-18 土壌水を追跡するための臭素同位体比測定法の野外適用

木方展治、藤原英司
農業環境技術研究所

1. はじめに

農耕林地での浸透水の動きを正確かつ精密に把握することは、水資源のかん養・保全、圃場での水管理技術の向上のみならず、これに溶存して移行する環境影響元素・物質の動態や影響評価を解析する上で極めて大切である。土壌浸透水のより改善された追跡手法として、自然存在比（^{81}Br と ^{79}Br）が大きく異なる臭素安定同位体試薬溶液をトレーサとして利用する方法を開発する。

本年度は前年度作成した土壌カラムを解体し、土壌内の残存臭素の垂直分布を見るとともに、裸地圃場に臭素安定同位体試薬を散布し、圃場における臭素の動態を追跡した。

2. 実験方法

1）カラム作成；農業環境技術研究所（農環研）で前作小麦を栽培していた圃場より、ハンマーによる打ち込み式採土器で、直径 5cm の塩化ビニル製容器に表層腐植質黒ボク土壌を充填し（充填時水分 35.7%）、長さ 29.5cm の土壌カラムを作成した。採取した雨水を土壌カラム上方から 3 日間で 130 mL 流した後、90atom%^{81}Br の 100mg/L 臭化アンモニウム溶液 10mL をカラムに添加した。試薬添加当日以降、1 日 30mL 雨水を添加し、土壌浸透水を採取した。浸透水採取終了後、２ヶ月経過して土壌カラムを 1cm の厚さに輪切りにし、土壌試料を採取した。

2）臭素同位体散布；カラムを採取したのと同一ほ場に 45cm×45cm の木製の枠を３区設置した。第１図に示すように同位体比を違えた３種の 100mg/L NH_4Br 試薬をそれぞれ各区に 810mL 添加した。添加は枠を９×９に分割し、各区画に試薬を 10ml づつマイクロピペットで注液する方法で行った。

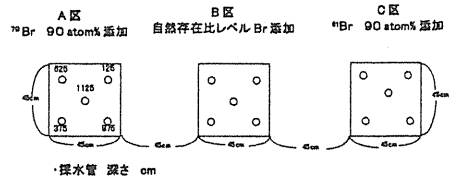
第１図に示す深さに採水管を埋設した。50mm の積算降雨を目安に降雨停止後、第 2b 図に示す真空ポンプで 45～50mm Hg の負圧を約２日間保つことにより、土壌水を採水管先端のポーラスセラミックカップを通過させ、第 2a 図に示す集液フラスコに採取した。

3）分析法；土壌浸透水および土壌水は、ろ紙に 100 μL 吸わせ、ポリエチレン製袋（以下ポリ袋と称す）に２重封入し、所定のカプセルに入れ、土壌浸透水は原研東海研の JRR-4 炉（水力Ｔパイプ）および JRR-3M 炉（気送管）（ともに熱中性子束、約 $5\times10^{17}m^{-2}s^{-1}$）で２分間および 10 分間照射し、外側の袋を包み替えて測定用試料とした。土壌は微粉砕の後 10mg を２重封入し、所定のカプセルに入れ、上記 JRR-4 炉で 20 分間照射し、外側の袋を包み替えて測定用試料とした。Ge 半導体検出器にマルチチャンネルアナライザを装着したγ線スペクトロメトリにより、実効測定時間(live time)500 秒以上で臭素の定量を行った。

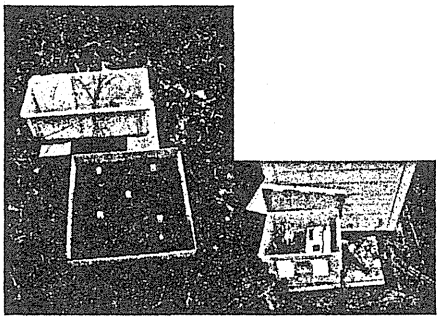
3. 結果および考察

(カラム試験)

第３図には 90atom% ^{81}Br を添加したカラムにおける浸透水中の臭素濃度変化を示した。放射化分析による ^{79}Br 濃度と ^{81}Br 濃度の合計（全臭素濃度）と、イオンクロマトグラフィーによる臭素濃度の分析値は良い一致を示した。全臭素濃度のピークと添加した ^{81}Br 濃度のピークは、試薬添加時のバイパス流による一気の浸透も含め同時期に現れた。これらのピーク時には ^{79}Br 存在比(=^{79}Br 濃度 /(^{79}Br 濃度+^{81}Br 濃度))は負のピークを示した。徐々に浸透するピストン流の ^{81}Br ピークの頂点と思われる時期に浸透水の添加を停止し、乾燥後カラムを解体した。第４図に解体したカラムから採取した土壌の臭素分析結果を示した。カラム最下部で ^{81}Br 濃度は高くなり、^{79}Br 存在比は低くなった。

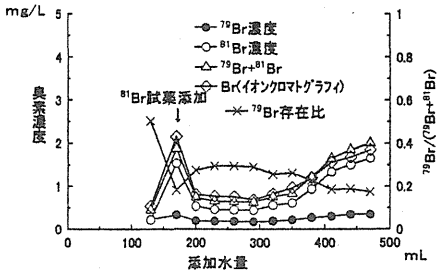


第１図 ほ場における試薬添加試験配置

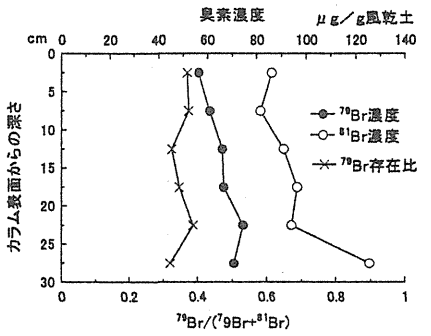


第 2a 図 試験枠と集液部　第 2b 図 減圧部
第２図　試験枠と減圧装置

原子炉：JRR-3　JRR-4　装置：気送管、水力Ｔパイプ　分野：放射化分析（環境、農・水産物）



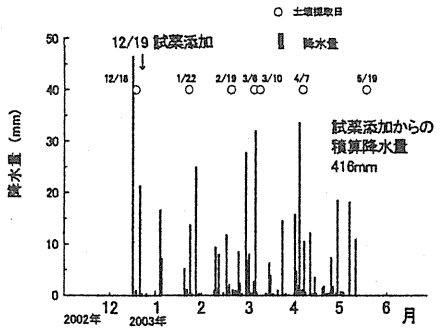
第３図 ^{81}Br 添加カラムの浸透水中臭素濃度変化



第４図 ^{81}Br 添加カラム土壌の臭素濃度分布

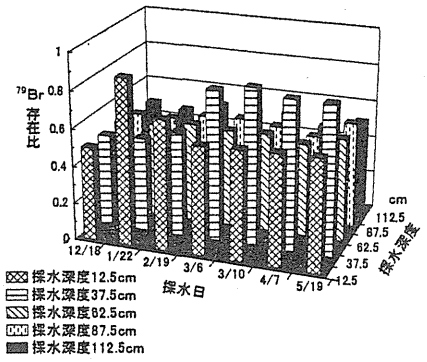
(ほ場試験)

90atom%^{79}Br 添加区では、試薬添加直後の 12/12 に採水深度 12.5cm で ^{79}Br 存在比が一気に上昇し、その後漸減する一方、採水深度 37.5cm では 3/5 に ^{79}Br 存在

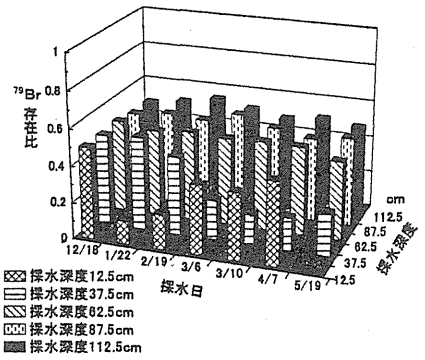


第５図 降水と土壌水採取日

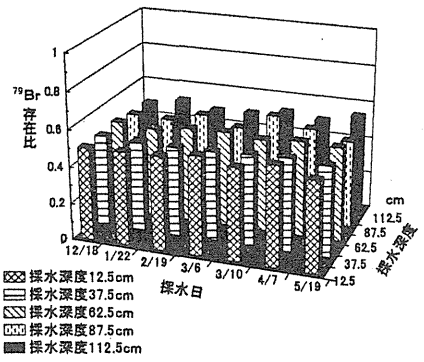
比の上昇が起こった（第６図）。90atom%^{81}Br 添加区では、試薬添加直後に採水深度 12.5cm で ^{79}Br 存在比が一気に低下し、その後漸増する一方、採水深度 37.5cm では 2/19 から ^{79}Br 存在比が高まっていくことが確認された。なお 5/19 の採水深度 12.5cm は土壌水が採取できず欠測値となっている（第７図）。自然存在比臭素添加区では、臭素濃度の増減はあったが、^{79}Br 存在比の変化は認められなかった（第８図）。



第６図 ^{79}Br 添加区における深度別土壌水の ^{79}Br 存在比変化



第７図 ^{81}Br 添加区における深度別土壌水の ^{79}Br 存在比変化



第８図 自然存在比臭素添加区における深度別土壌水の ^{79}Br 存在比変化

参考文献

第40回理工学における同位元素・放射線研究発表会要旨集(2003), p. 54

3-19 河川および干潟堆積物試料の放射化分析

Activation analysis of river and estuarine sediments

松尾基之・久野章仁・片岡正樹[1]・田中佑人・清宮貴美子[1]・高橋 統
M. Matsuo, A. Kuno, M. Kataoka[1], Y. Tanaka, K. Seimiya[1], O. Takahashi

東京大学大学院総合文化研究科広域科学専攻
[1]東京大学大学院理学系研究科化学専攻
Graduate School of Arts and Sciences, The University of Tokyo
[1]Graduate School of Science, The University of Tokyo

1．はじめに

近年、河口域や干潟の環境保全は人々の重大な関心事となっているが、これらの場所は、淡水と海水が混ざり合う複雑な系であり、そこにおける化学的環境や元素の挙動については、まだ詳しくは理解されていない。我々はこれまで ^{57}Fe メスバウアー分光法を用い、鉄の化学状態を指標として河川底質の化学的環境、特に酸化還元状態を推定してきた。これに対し、従来多くの研究により、試料中の微量元素の分布が化学的環境を反映することも知られている。本研究では、メスバウアー分光法により得られた鉄の化学状態と、出来るだけ多くの微量元素の分布との関連を調べ、比較検討するために多元素同時分析が可能な放射化分析を行った。このような観点から、次に掲げる試料について種々の環境化学的、地球化学的な検討を行ったので、それぞれの試料ごとに研究内容およびその結果を報告する。また、河川や干潟ではないが、同じ堆積物である遠洋深海性層状チャート中の元素の定量及び状態分析についても放射化分析法を適用して有用な知見を得ることができたので、併せて報告する。

2．谷津干潟底質中の元素及び化学状態の垂直分布

【序】 干潟は多くの生物の生活の場であると同時に環境浄化作用を持っており、周辺の水の汚れを除去し、綺麗な水を海へ流し出すことでも知られている。このような干潟の底質中で、どのような物質移動及び化学変化が起こっているかを明らかにすることは、環境評価の上で重要な情報を与える。本研究ではフィールドとしてラムサール条約登録地である谷津干潟を選び、機器中性子放射化分析(INAA)、及び中性子誘起即発γ線分析(PGA)を用い、30 数元素の定量を行った。また、底質中では嫌気性の微生物である硫酸還元菌が硫酸イオンを還元し、硫化水素を発生させていることが知られている。その際に底質中の鉄イオンと反応し、硫化鉄や Pyrite(FeS_2)が生成している。このことから、メスバウアー分光法で底質中の鉄の化学状態を測定することにより、これらの鉄の硫化物の分布を明らかにすることを試みた。

【実験】 試料は東京湾奥に位置する谷津干潟の底質を垂直方向に採取した。採取には内径 11cm の HR 型不撹乱柱状採泥器を用い、得られた約 50cm のコアを現地で 3cm ごとに分別し、N_2 中に封入した。得られた試料は N_2 を用いた加圧濾過により間隙水を取り除き、メスバウアー測定に用いた。またその後、風乾し、めのう乳鉢で粉砕し、INAA の測定に用いた。照射には、日本原子力研究所の JRR-4 を用いた。短寿命核種は 100kW の低出力運転時に気送管で 1 分間照射し、10 分間冷

研究施設と装置名
JRR-4、気送管、Tパイプ、γ線ｽﾍﾟｸﾄﾛﾒｰﾀｰ

研究分野
環境化学、地球化学、放射化分析

却後、γ線を測定した。中、長寿命核種については3.5MW定格出力時にTパイプで5分間照射し、中寿命核種は3日間冷却後、長寿命核種は約2週間冷却後、大学開放研のTD-ASCもしくはASCにてγ線の測定を行った。

【結果及び考察】 INAA, PGA法により、30数元素の垂直分布を得ることができた。谷津干潟底質中の重金属元素の多くは他の東京湾に流入する河川の底質に比べ濃度が低く、汚染が少ない場所であるということがわかった。得られた元素を垂直分布の特徴に従って、いくつかのグループに分けることができた。表層部から深層部に行くに従って減少する元素としてはNa, Ca等があった(図1)。

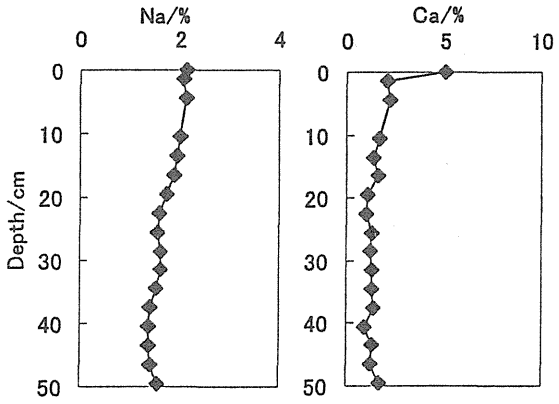


図1 谷津干潟底質中のNa, Caの垂直分布

Naは底質の母岩を構成する鉱物中に含まれており、深層部に行くほど溶脱が進んでいるものと解釈された。また、Sc, La等の微量金属の一部は深層部に行くに従って増加する傾向が見られた(図2)。底質深層部では粒径が細かく、底質の表面積が広くなっており、それらの元素の吸着がより多く起こっていると思われた。更に、これらの元素間の濃度に関して相関係数を計算することにより、類似の挙動をとる元素の分類を数値により明確に表すことを試みた。メスバウアー分光法を用いた鉄の状態分析の結果、Pyriteが20-35cmに多く存在する傾向が見られた。また、Pyriteの増加に伴いFe^{3+}が急激に減少していることがわかった。これは20cm付近を境にして底質中は著しく還元的になっており、主にFe^{3+}が硫酸還元菌によってPyriteになり底質中に固定されたものであると解釈された。このことから干潟底質中の鉄の化学状態を指標として底質中の酸化還元環境の変化を知ることができた。

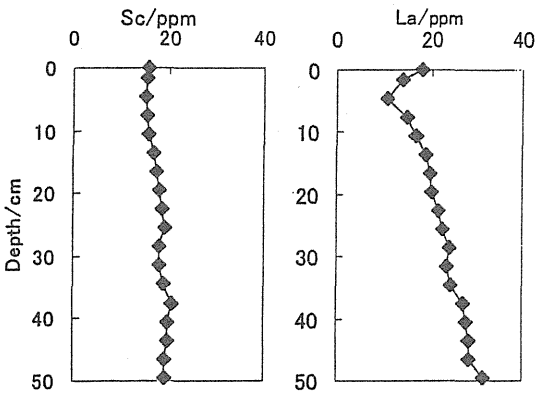


図2 谷津干潟底質中のSc, Laの垂直分布

3．荒川底質中の元素及び化学状態の垂直分布

【序】 荒川は東京湾にそそぎ込む一級河川であり、中・下流域では人口の集中している地域を横断している。このような都市の中を流れる河川は人間活動による汚染が起こっていると考えられ、河川底質にはその汚染が記録されていると考えられる。そこで本研究では、INAA及びPGAを用いて30数元素の定量を行い、それらの垂直分布を調べた。また、河口域底質中では海水起源の硫酸イオンが還元され、悪臭を持つ硫化水素が発生し問題となっている。そこで、底質中で硫化物を生成すると考えられるFe, Mnについてメスバウアー分光法、XAFS (X線吸収微細構造)法をそれぞれ用いて、深さごとに化学状態分析を行い、底質中での硫化物の分布を調べた。

【実験】 試料はアクリルパイプを用いて垂直方向に約50cmのコアとして採取した後、現地で3cmごとに切り分け、変質を防ぐために窒素ガス中に封入した。得られた試料は4気圧の窒素を用いて加圧濾過を行い、間隙水を取り除き、メスバウアー分光法を用いてFeの化学状態分析を、またXAFS法を用いてMnの化学状態分析を行った。試料はその後、風乾しINAA, PGA測定に用いた。

INAA, PGA 法は日本原子力研究所 JRR-4, JRR-3M でそれぞれ行った。また、XAFS 法の測定は高エネルギー加速器研究機構(KEK)の放射光実験施設において Lytle 型検出器を用いた蛍光法で行った。

【結果及び考察】 得られた底質は表層部では泥質であり粒径が細かく、中層から深層にかけては砂質であり、粒径が大きかった。我々はこれまでに東京湾内に位置する干潟や都市の内部河川底質について研究を行ってきたが、それらの地点では粒径が中層から深層部で細かくなる傾向があり、荒川の底質は粒径の分布が他の地点と大きく異なっていた。元素分析の結果、Al, Ti 等の垂直分布は他の地点と同様の傾向を示したが、希土類元素の一部は他の地点とは逆に、深くなるに従って減少する傾向が見られた。これらの元素は粒径が細かいほど表面積が大きくなることで吸着しやすくなり、粒径の分布と相関があるものと考えられた。また、Cr は汚染の少ない谷津干潟と比較すると高濃度で存在していた。メスバウアー分光法を用いた鉄の状態分析の結果、ここでも Pyrite は中層部に多く存在する傾向が見られた。このことから粒径や塩分濃度等の環境因子や人為的な負荷の影響によらず、Pyrite は中層部で極大をとる傾向が見られることがわかり、様々な環境の汽水域で鉄が底質中から発生した硫化水素をトラップしているということがわかった。また、XAFS 法を用いた Mn の状態分析から底質の表層部に MnS が多く含まれている傾向が見られた。

4．遠洋深海性層状チャート中の元素の定量及び状態分析

【序】 生物史上複数の大量絶滅が知られており、その原因の一つとして地球全体にわたる酸素欠乏事件が挙げられている。元素は各々の酸化還元電位によって化学状態を変化させるが遠洋深海で起こるこれらの反応は局所的な現象ではなく、全地球的な海洋環境を反映したものであると考えられる。従って遠洋深海で堆積した層状チャートの分析から年代を追って地球規模での酸化還元状態の変化を見ることが可能である。酸化還元環境の変動については多くの研究がなされているが、単一の指標のみでは変化の程度を明らかにすることは不十分である。そこで本研究ではMn、Fe、U 、Sを分析対象とした。最も酸化的な条件下ではMnとFeは沈殿し、UとSは溶解しているが、徐々に還元的になるにつれてMnの溶解、Feの溶解、Uの沈殿、Sの沈殿が順に起こると考えられる。このような複数の元素の酸化還元電位の差を利用して段階的な酸化還元状態の変化を推定した。

【実験】 美濃帯犬山地域で採取したジュラ紀及び三畳紀の遠洋深海性層状チャートを試料とし、年代順に重なる層毎にスタンプミル及びめのう乳鉢を用いて紛体にしたのち測定を行った。対象元素の定量分析のために日本原子力研究所JRR-4にてINAA法を、同 JRR-3MにてPGA法を用いた。さらにFeはメスバウアー分光法、Mnは高エネルギー加速器研究機構においてXAFS法を用いてLytle型検出器を使用した蛍光法で状態分析を行った。

【結果及び考察】 ここで便宜上、酸化還元状態を段階別に名称をつける。Mn^{4+}が沈殿している最も酸化的な状態を Level 1、次に酸化的な、Mn^{4+}は溶解し、Fe^{3+}が沈殿する状態を Level 2、Fe^{3+}が溶解し、Fe^{2+}/total Fe 比が増加する状態を Level 3 とする。三畳紀とジュラ紀の境界の前後では、メスバウアー分光法及び INAA 法より Level 2 であることがわかった。しかし境界付近において、前後の層に比べ Fe^{2+}/total Fe 比が約 2 倍、赤鉄鉱の比率が約 1/3 となり、より還元的な Level 3 と考えられる部位が見られた。この層より時代を遡った三畳紀側に隣接した層では Mn 含有量の一時的な増加が見られ(前後の層の含有量に比べ2～3 倍)、Mn の沈殿が起きた最も酸化的な状況であると考えられた。また XAFS 法の結果からこの層の Mn の化学形態は MnO_2 であることがわかり、酸化的条件での沈殿形態と一致した。従って Mn 含有量の増加は酸化還元状態の変化によるものと考えられた。これは Level 1 に相当する。ジュラ紀前期試料にて見られた Mn は $MnCO_3$ に近い化学形態であり、MnO_2 と区別ができた。以上の結果から三畳紀とジュラ紀の境界付近では Level 2 から Level 1、Level 3、Level 2 へと変遷していることがわかった。このように複数の元素の状態変化の情報を組み合わせる事で酸化還元状態の程度を評

価することができた。

５．成果の公表

学術誌

1. "A study of environmental analysis of urban river sediments using activation analysis", Y. Tanaka, A. Kuno and M. Matsuo, J. Radioanal. Nucl. Chem., Articles, 255(2), 239-243 (2003)
2. "A study on vertical distribution of elements and their chemical states in Yatsu Tideland sediments", M. Kataoka, A. Kuno and M. Matsuo, J. Radioanal. Nucl. Chem., Articles, 255(2), 283-286 (2003)
3. "Moessbauer spectroscopic study on characterization of iron in the Permian to Triassic deep-sea chert from Japan", M. Matsuo, K. Kubo and Y. Isozaki, Hyperfine Interact. (C), 5, 435-438 (2003)

学位論文

4. "干潟堆積物中に含まれる元素の化学状態と垂直分布"、片岡正樹、東京大学大学院理学系研究科化学専攻 修士論文 (2001年2月)
5. "河川底質中に含まれる多元素の定量データの多変量解析を用いた環境評価"、高橋統、東京大学教養学部広域科学科 卒業論文Ⅰ (2001年11月)
6. "底質中の元素とその化学状態に着目した都市河川環境分析"、田中佑人、東京大学大学院総合文化研究科広域科学専攻 修士論文 (2002年2月)
7. "遠洋深海性層状チャート中の元素の定量及び状態分析"、清宮貴美子、東京大学大学院理学系研究科化学専攻 修士論文 (2002年2月)

学会発表

8. "都市河川底質中の金属元素の化学状態に関する研究"、田中佑人・松尾基之・金井豊、日本地球化学会年会 (2000年9月)
9. "Moessbauer spectroscopic study on characterization of iron in the Permian to Triassic deep-sea chert from Japan", M. Matsuo, K. Kubo and Y. Isozaki, International Conference on the Applications of the Moessbauer Effect (ICAME 2001), (Sep. 2001)
10. "底質中元素とその化学状態に着目した都市河川及び干潟の環境分析"、松尾基之・田中佑人・片岡正樹・久野章仁、第5回分析化学東京シンポジウム (2001年9月)
11. "都市河川および干潟底質中の元素の分布と化学状態を用いた環境分析"、松尾基之・田中佑人・片岡正樹・久野章仁、日本化学会第80秋季年会 (2001年9月)
12. "遠洋深海性層状チャート中の微量元素の酸化還元状態による古環境の評価"、清宮貴美子・松尾基之・磯崎行雄、日本地球化学会年会 (2001年10月)
13. "A study of environmental analysis of urban river sediments using activation analysis", Y. Tanaka, A. Kuno and M. Matsuo, 2001 Asia-Pacific Symposium on Radiochemistry (APSORC 2001), (Oct. 2001)
14. "A study on vertical distribution of elements and their chemical states in Yatsu Tideland sediments", M. Kataoka, A. Kuno and M. Matsuo, 2001 Asia-Pacific Symposium on Radiochemistry (APSORC 2001), (Oct. 2001)
15. "谷津干潟底質中の元素の化学状態と硫酸還元菌の関係"、片岡正樹・松尾基之・杉森賢司、日本分析化学会第50年会 (2001年11月)
16. "遠洋深海性層状チャート中の元素の定量及び状態分析：古海洋の環境変動の推定"、清宮貴美子・松尾基之・磯崎行雄、日本分析化学会第50年会 (2001年11月)
17. "干潟および河口域底質中における重金属の化学状態に関する研究"、片岡正樹・田中佑人・久野章仁・松尾基之、日本分析化学会第51年会 (2002年9月)
18. "荒川底質中の元素及び化学状態の垂直分布"、片岡正樹・松尾基之、第46回放射化学討論会 (2002日本放射化学会年会) (2002年9月)
19. "底質中元素とその化学状態に着目した河口域及び干潟の環境分析"、松尾基之・片岡正樹・高橋統・久野章仁、東京コンファレンス (2003年9月)

研究テーマ：バイオマス燃焼による大気中微量ガスの発生量推定に関する研究
表題：中性子放射化分析による大気ー陸域系の微量元素動態に関する研究

3-20

バイオマス燃焼に関わる植物体に含まれるハロゲン元素量と燃焼により発生した揮発性ハロゲン化合物の比較評価

須藤重人
農業環境技術研究所地球環境部温室効果ガスチーム

１．はじめに

アジア域では、森林火災、野焼き、バイオマス燃料、農作物残さ焼却など、さまざまな形のバイオマス燃焼が人為的に起きている。これらの燃焼から発生するガス状成分は、人間への健康影響から、大気環境汚染まで様々な形で、地域および地球環境に影響を与えている。本研究では、これら燃焼起源のハロゲン化メチルの量的評価を行うため、燃焼（植生）形態別の野外燃焼実験をによる現地でのガスの採取とガス分析を行った。また、燃材中のハロゲン含有率を知るための手段として、中性子放射化分析による非破壊分析を活用した。

２．実験方法

二次林燃焼および泥炭火災については、インド国立物理学実験所、およびインドネシア・スマトラ島におけるボゴール農科大学との共同実験を実施し、また、農作物残さの焼却については、農業環境技術研究所の圃場および、群馬県内の農家の耕作地における模擬実験により結果を得た。放射化分析は日本原子力研究所東海研究所の JRR-3 および JRR-4 研究炉を使用した。

供試試料は、５０℃で２４時間乾燥後、タングステン材の粉砕器にて微粉砕し、秤量後ポリエチレン袋にて２重封入したのち、気送管キャプセルにて、放射化した。塩素および臭素の分析には、それぞれ 50mg で１分および 100mg で１０分の照射をし、放射能の計測には、３００秒および５００秒を１試料あたり要した。

また、燃焼実験は、インドネシアの泥炭、インドの二次林、日本の農地での残さ焼却を現地で実施し、テドラーバッグによりガスを採取したあと、全金属製の大気捕集容器に保存、日本への運搬の後、低温濃縮法による ECD, FID および RGD ガスクロマトグラフにより定量分析を行った。また、燃焼実験地で、ガス採取と同時に燃材となったバイオマスの採取も行った。

３．結果および考察

図１に、バイオマス燃焼を特徴づける植生別の平均濃度を示した。図中で"Secondary forest"は「二次林の火災」、"peat soil"は「泥炭地中火災」、"Crop"は「農作物残さ焼却」をそれぞれ代表するものとした。

これに対し、塩化メチル、臭化メチル濃度の二酸化炭素濃度に対するモル比、即ち、CO_2 ベースのハロゲン化メチルの発生量比(emission factor)は、図２のような結果となった。塩素と臭素の間の関係に関しては、CH_3Br/CH_3Cl モル比は、概ね、その含有量

原子炉：JRR-3　JRR-4　装置：気送管　分野：放射化分析（環境，農・水産物）

は、３種類植生別には、臭素／塩素含有量比と傾向が一致した。しかし、植生の異なるものについて、ハロゲン含有量とハロゲン化メチルの発生量比の間に明確な関係は見いだすことはできなかった。これは、燃焼形態が大きくことなる場合、ガス発生量が、燃焼形態（温度等）により、大きく支配されるためであると考えられる。今後、温度条件の詳細な制御を考慮にいれた実験を行い、当該ガス等の発生制御要因をさらに明らかにしていく予定である。

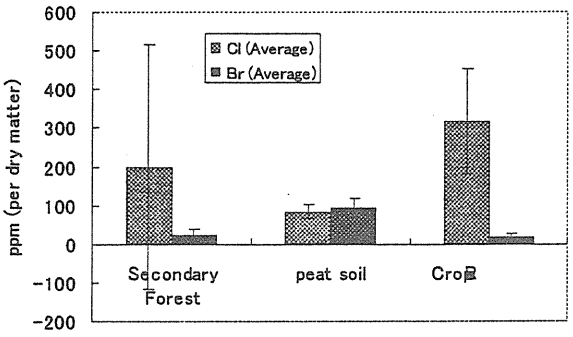


図１　植生別のハロゲン含有量比

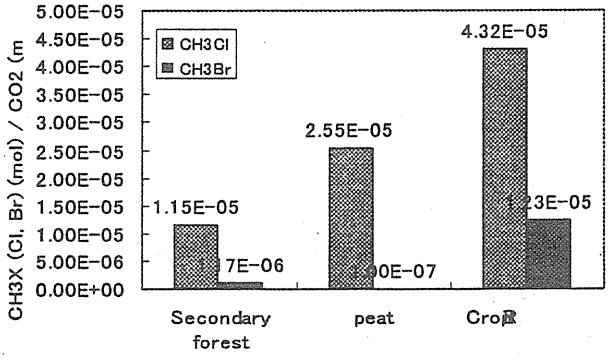


図２　植生別のバイオマス燃焼によるハロゲン化メチル発生量比

参考文献：
２００３年８月日本土壌肥料学会神奈川大会にて報告済み
演題名：「須藤重人，八木一之，米村正一郎，木方展治，藤原英，B.H.サハルジョ，スウィドリミン，早坂洋史，高橋英紀，インドネシア泥炭地火災による大気質の変調について，２００３年８月日本土壌肥料学会神奈川大会講演要旨集」

原子炉：JRR-3　JRR-4　装置：気送管　分野：放射化分析（環境，農・水産物）

3-21 海底熱水性沈殿物の放射化分析

Geochemical Studies on Submarine Hydrothermal Deposits by Neutron Activaton Analysis

佐藤千穂・中島和夫（山形大学理学部）
Chiho SATO and Kazuo NAKASHIMA

1．はじめに

大西洋中央海嶺(MAR)や東太平洋中央海嶺(EPR)をはじめとして、海底からの熱水噴出によって形成される海底熱水鉱床が世界各地から報告されている。沖縄本島の北西に位置する沖縄トラフからも伊是名海穴[1)]、伊平屋凹地[2)]、北部海丘[3)]、南庵西海丘[4)]から海底熱水活動域が発見されており、それぞれの熱水域ごとに異なった特徴があることが明らかとなっている。特に伊是名海穴では1989年に日本周辺から320℃の熱水を噴出するブラックスモーカーが初めて発見され[5)]、その構成鉱物から現世の"黒鉱鉱床"として注目された[6)]。

1988年に行われた日本、旧西ドイツ合同調査において、海洋調査船ゾンネ号によって伊是名海穴からチムニーやマウンド試料と思われる硫化物や火山岩などの試料がドレッジによって採取された。本研究ではこれらの熱水性沈殿物について、Ag、Auをターゲットとして中性子放射化分析を行い、これらの元素とAs、Sbなどの元素との関係について明らかにすることを目的とした。伊是名海穴は他の熱水域に比べAg、Au含有量が多いことが特徴であり、これらの微量元素がどのように挙動しているかを明らかにすることは、海底熱水系での鉱物沈殿作用を考える上で重要である。

2．研究手法

(1)分析試料

本研究では、伊是名海穴から採取された熱水性沈殿物の中から特徴的なものを8個選び、分析を行った。試料は蒸留水で数回洗浄し乾燥させ、海水中の塩分をできるだけ取り除いて分析に用いた。熱水性沈殿物は鉱物学的特徴から次の2つのグループに分類した。

・鉱石サンプル Ore sample (M27 34-5 、96)：黒色を呈し、堅いサンプル。主に閃亜鉛鉱、白鉄鉱(黄鉄鉱)からなり、微細なアイソキューバ鉱などを伴う。

・重晶石サンプル Barite sample (M10、M1-100、M2-100、25、96-M2)：ほとんどが重晶石からなり、もろいサンプル。硫化鉱物として少量の閃亜鉛鉱やフランボイダル黄鉄鉱を伴う。

(2)分析方法

放射化分析法(NAA : Neutron Activation Analysis)は、高感度、非破壊、同時多元素分析という大きな特徴を持っており、分析に必要な試料は極少量でよいため希少性の高い熱水性沈殿物の分析に適している。本研究では、日本原子力研究所東海研究所内、東京大学原子力研究総合センター全国共同利用部門大学開放研究室で分析を行った。

試料は蒸留水でよく洗い乾燥させた後、全岩をめのう乳鉢で粉末にしたものと、重晶石サンプルに分類されるM10、M1-100、25については外観の異なる部分をデンタルドリルで削り出した後、めのう乳鉢で粉末にものを使用した。試料重量は短時間照射用には20～30 mg、中時間照射用には10 mgとし、

研究施設、装置： JRR-3, JRR-4　　研究分野：金属鉱床学、地球化学

したマイクロ天秤で秤量した。試料重量による誤差を軽減するために、窒素ガス雰囲気の中でライトの光を当てて水分を蒸発させながら秤量し、薬包紙の代わりに小さく切ったアルミホイルを使用した。短時間照射用、中時間照射用ともに高純度ポリエチレンに粉末を入れ、ポリシーラーで封入し、さらにそれをポリエチレンで二重に封入した。短時間、中時間照射それぞれの条件と目的核種を以下に記す。

・短時間照射（照射時間：10秒）

原子炉：JRR-4　クーリング時間：約5分(サンプルごとに若干の差がある)

測定時間：300秒　　目的核種：Ag-108

・長時間照射（照射時間：40分）

原子炉：JRR-4　クーリング時間：24時間

測定時間：1000 秒　　目的核種：As-76、Sb-122、Au-198など

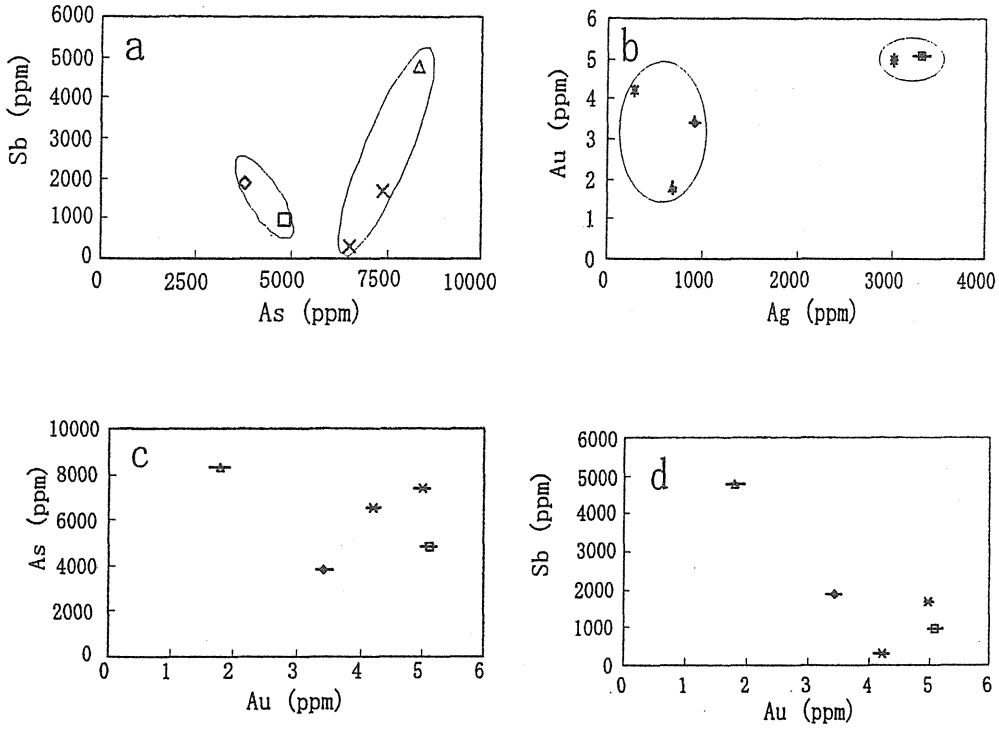
データの解析はk0(ケイゼロ)標準化法で行った。k0標準化法は、不正確なデータをk0因子という包括的な確定数で置き換えて濃度計算を行う。解析には、核種の同定、データの取り込みを行うSAMPOと濃度計算、半減期補正を行うKAYZEROの2種類のプログラムを使用した。

3．結果と考察

(1)本研究で用いた熱水性沈殿物について

放射化分析により得られた各試料の分析結果を表1に示す。分析をおこなった試料のうちM10-As（Asに富む部分）、M1-100B2（硫化鉱物に富む部分）、M2-100については短時間照射のみしか行っておらず、本来ならば中時間照射による分析が適しているZn、As、Sb、Auについても短時間照射による分析値であるため、それらの分析値は信頼性が低いと思われる。

今回の分析ではAg(283.6 ppm～0.44 %)、Au(0.12～5.09 ppm)という高い値が得られた。分析を行った試料のうち、AgとAuをともに含んでいるものについて各元素の相関関係をプロットした(図1)。なお、図1でM1-100としたものはM1-100の赤色部に相当し、M1-100Bは灰色部に相当する。Asについては鉱石サンプルより重晶石サンプル中の含有量が高くなっているが(図1a)、これは重晶石サンプル中には鉱石サンプルに比べて、As硫化鉱物やAs、Sbを含むPb硫化鉱物が多いためと考えられる。As鉱物は一般に熱水活動の後期に低温で晶出するとされていることから、As鉱物を多く含む重晶石サンプルのほうが鉱石サンプルに比べ低温で沈殿したと考えられる。AgとAuの関係をプロットしたグラフ(図1b)では鉱石サンプル、重晶石サンプルともにAu含有量は同一レンジに入るものの、同一試料であるM1-100とM1-100Bではag含有量に違いがある。これはM1-100灰色部では重晶石の間を埋めるように晶出しているAs鉱物にAgが多く含まれているというEPMAによる定量分析結果と調和的な結果となった。本研究では四面銅鉱などのAg硫化鉱物は確認されておらず、Agは主に方鉛鉱やFe水酸化物などに含まれていることから、AgはAsやSbといった硫塩鉱物をつくりやすい元素とは挙動を共にしていないと考えられる。しかし、M1-100についてはAs鉱物中にAg鉱物が見られることから、AsとAg挙動を共にしている可能性は否定できない。また、JADEサイトのチムニーサンプル中ではAs硫化鉱物とAuは密接な付随関係を持っており、Auの濃集機構としてAs硫化鉱物中への吸着が重要な役割を果たした可能性があるとされており[7]、本研究の試料中でも重晶石の間を多くのAs鉱物が埋めているM1-100はAuが高い値を示していることから、この可能性が考えられる。しかし、AuとAsの関係をプロットしたグラフ(図1c)では相関が見られず、As濃度が高い重晶石サンプル全てにおいてAuとAsが正の相関関係を持つとは言えない。さらに、重晶石をほとんど含まず鉱石サンプルに分類される96でも高いAu量を示すことに加え、エレクトラムは確認されていないなどAuの存在形態が未確認であることから、全てのサンプルにおいてAuとAs硫化鉱物が密接な付随関係を持つとは言えない。また、AuとSbの関係についても負の相関が見られることから(図1d)、本研究のサン



◇：M27 34-5　□：96　－：測定誤差
△：M10-B　×：M1-100　×：M1-100B

図1　各サンプル中の各元素の相関関係

プル中では Au は硫塩鉱物中に取り込まれている可能性は低いと考えられる。

(2)他の分析方法を用いた結果との比較

今回の分析では Ag(283.6 ppm～0.44 %)や Au(0.12～5.09 ppm)という高い値が得られたが、これらの値はこれまで伊是名海穴から得られた最高値(Ag：1.09 %、Au：24.4 ppm、ICP、AAS による分析値 7))よりは低い。本研究の分析結果と「しんかい 2000」によって伊是名海穴から採取された塊状硫化物についての中性子放射化分析と ICP による分析値とを比較した(図 2)。Ag については、本研究で用いた試料がドレッジされた場所に近い熱水域から採取されたチムニー試料の値(○、△でプロット)よりも本研究の分析値が高い。一方、Au 含有量は中間的な値となっているが、As や Sb についてはチムニーサンプルよりやや低い値となった。As については、本研究以外の分析に用いた試料には As 硫化鉱物に富むチムニー外縁部も含まれているため、相対的に本研究のサンプル中の As 含有量が低くなっていると考えられる。全体的に分析値がばらついてはいるが、本研究の分析値が極端に外れているといったことが見られないことから今回の分析結果が妥当なものだと判断される。

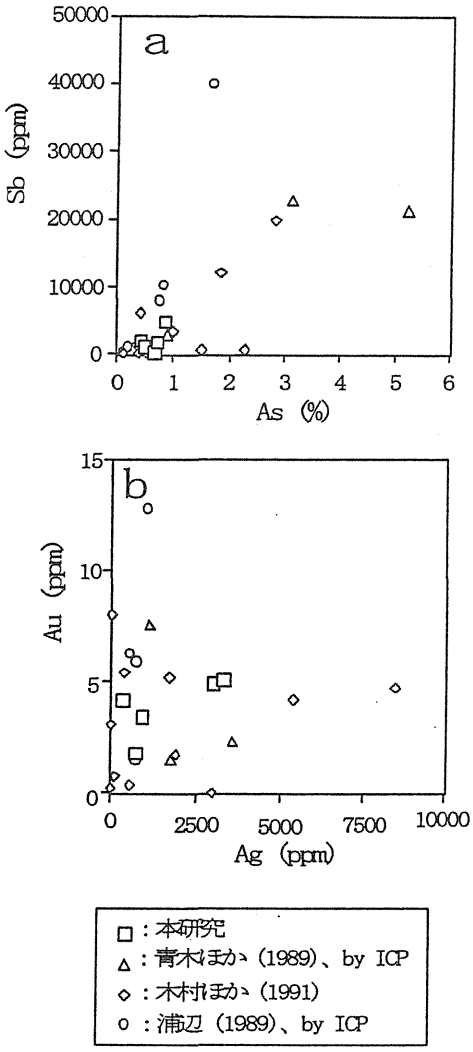


図 2　沖縄トラフ熱水沈殿物の化学組成の比較

4．問題点と今後の課題

放射化分析は同時に多元素を分析できるという利点があるが、半減期の違いやバックグランドの影響でピークが重なり、濃度計算が困難になる場合がある。本研究の分析では、As、Mn のピークが高すぎるため微量元素のピークを読みとれないということがあった。さらに、同一のサンプルを分析しているにも関わらず分析値が一定しないなど再現性にも問題がある。正確な分析値を得るために、ターゲットとする元素に最適な照射時間、クーリング時間などの条件を探る必要がある。また、試料の均一性を追求し、標準試料を作成することも必要である。

謝辞

本研究の中性子放射化分析を行う上で、実験計画や試料調整など多くの便宜をはかって頂きました澤幡浩之氏、川手 稔氏、尾嵜大真氏をはじめ大学開放研究室のスタッフの皆様に感謝いたします。

引用文献

1) Halbach, P., Nakamura, K. Washsner, M., Lange, ., Sakai, H., Kaselitz, L., Hansen, R. D., Yamano, M., Post, J., Prause, B., Seifert, R., Michaelis, W., Teichmann, F., Kinoshita, M., Marten, A., Ishibashi, J., Czerwinski, S. and Blum, N. (1989) ; Probable modern analogue of Kuroko-type massive sulphide deposits in the Okinawa Trough bach-arc basin. Nature, 388, 496-499.

2) 田中武男・満沢巨彦・堀田 宏(1989) ; 沖縄トラフ伊平屋小海嶺東部の 1988 年潜航調査について. 第 5 回「しんかい 2000」研究シンポジウム報告書, 267-279.

3) 根建心具・上野宏共・小坂丈予・上野健治・橘本惇・藤倉克則・三浦知之 (1992) ; 沖縄トラフ南奄西海丘の海底熱水鉱床 -特に構成鉱物について-. 第 8 回「しんかい 2000」研究シンポジウム報告書, 95-106.

4) 千葉 仁・石橋純一郎・上野宏共・大森 保・内山明・武田哲一・高峯朝一郎・李 受映・糸満彩子 (1996) ; 伊平屋海凹北部海丘の熱水活動. JAMSTEC 深海研究, 第 12 号, 211-219.

5) 中村光一・丸茂克美・青木正博(1990) ; 沖縄トラフ伊是名海穴海底熱水鉱床地帯におけるブラック・スモーカーと二酸化炭素に富む流体湧出変質帯(ポックマーク)の発見. 第 6 回「しんかい 2000」研究シンポジウム報告書, 33-50.

6) 中村光一・浦辺徹朗・丸茂克美・青木正博・金沢康夫・酒井 均・P. ハルバック (1988) ; 沖縄トラフ、伊是名海穴で発見された現世の"黒鉱"について. 三鉱学会講演要旨集, 127.

7) Halbach, P., Pracejus, B. and Marten, A. (1993) ; Geology and mineralogy of massive sulfide ores from the Central Okinawa Trough. Econ. Geol., 88, 2110-2225.

8) 青木正博・中村光一 (1989) ; 伊是名海穴、鉱床サイト 2 のチムニー群の産状、及び硫化物チムニーの組織と鉱物組成. 第 5 回「しんかい 2000」研究シンポジウム.

成果の公表

(1) 小笠原篤子・中島和夫・加藤和浩・藤岡換太郎 (1977) TAG 熱水マウンド(MAR)における熱水性沈殿物の鉱物学的特徴. 資源地質学会第 46 回年会講演会.

(2) 中島和夫・小笠原篤子・加藤和浩・藤岡換太郎・澤幡浩之(1999) 大西洋中央海嶺 TAG 熱水マウンドの化学的特徴. 資源地質学会第 48 回年会講演会.

(3) 佐藤千穂・中島和夫(2000) 沖縄トラフ伊平屋凹地 (クラムサイト) の硫酸塩・炭酸塩チムニー. 資源地質学会第 47 回年会講演会

(4) 佐藤千穂・中島和夫・村尾 智・澤幡浩之(2001) 沖縄トラフ JADE サイトの熱水性沈殿物の微細組織と化学組成. 日本岩鉱学会 2001 年度学術講演会, 245.

研究テーマ：中性子放射化分析法の環境影響元素・物質研究に対する新利用法と高度化技法の開発
表　　題：金属元素類（重金属元素等）の同位対比測定法の開発による土壌中の挙動解明

3-22

安定同位体による土壌有機物中重金属の標識化

櫻井泰弘、木方展治
農業環境技術研究所

環境中の無機元素（Cd, Se, Zn, Cu等）の動態解明や影響評価に資するために、野外での使用が可能である安定同位体(SI)による環境物質の標識化法と中性子放射化分析によるこれら安定同位体の高精度測定法を開発する。本年度はSIのセレンで標識化した土壌有機物（フルボ酸）を調製し、SI標識化土壌有機物の土壌中での結合の安定性を土壌カラム実験で検討する。

堆肥を連用した淡色黒ボク土壌から抽出したフルボ酸をアニオン交換樹脂(Amberlite CG 400)でイオン交換後、Se-74で標識化した。黒ボク土３種（茨城、秋田、新潟)、灰色低地土１種（兵庫）の風乾細土を供試し、クロマト管に各土壌（2.5g, 5.0 g）を充填し、SI標識化フルボ酸の水溶液(フルボ酸濃度 5000 mg/L)を10 mLづつ添加し、通過液中のフルボ酸をXAD-7樹脂に吸着、溶離し、中性子放射化分析によりSI濃度を定量した。

１）イオン交換水を土壌カラムに通液し、自然賦存するSe-74の溶出によるバックグラウンド値を測定した結果、放射化分析の検出限界以下であった。

２）Se-74標識化フルボ酸溶液中のSe-74濃度を土壌カラムの通過前後の溶液で測定した結果、土壌中での通過率は30～90％であり、吸着量は通過する土壌量にほぼ比例した。土壌種による吸着量の差は土壌の粒径組成、土壌pHなどの影響が推定される。

３）土壌カラム通過液と通過液をXAD-7樹脂で吸着・溶離した液中のSe-74濃度を比較し、土壌通過による標識化したSe-75のフルボ酸からの解離を測定した結果、Se-74標識化フルボ酸溶液は土壌カラムを通過後でもSe-74とフルボ酸との解離は約2～6％であり、XAD樹脂への吸着・溶離処理による損失量（10％以下）にほぼ相当し、土壌カラム通過による解離はほぼ無視できると考えられ、Se-74標識化フルボ酸はフルボ酸との錯体を形成したセレンの土壌中トレーサとしての利用が可能と考えられた（図１）。遊離のSe-74のXAD樹脂への吸着量は放射化分析の検出限界以下であった。

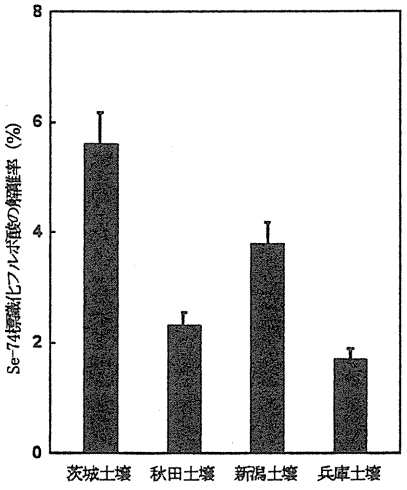


図1 土壌カラム通過による標識化フルボ酸のフルボ酸とSe-74の解離

原子炉：JRR-3　　装置：気送管　　分野：放射化分析（農・水産物）

海底堆積物コア試料における微量元素の分布と特徴

3-23

Distributions and characteristics of trace elements in marine sediment core samples

研究代表者：本多照幸（武蔵工業大学原子力研究所）
研究協力者：野崎徹也（武蔵工業大学原子力研究所）
木川田喜一（上智大学理工学部）
森本隆夫（(財) 日本分析センター）

Teruyuki HONDA, Tetsuya NOZAKI
(Atomic Energy Research Laboratory, Musashi Institute of Technology)
Yoshikazu KIKAWADA (Faculty of Science and Technology, Sophia University)
Takao MORIMOTO (Japan Chemical Analysis Center)

Ⅰ．はじめに

海底堆積物は、海洋底であれ、沿岸海底であれ、海洋環境ひいては地球環境全体の変化を過去から現在に至るまでシステマティックに留めている貴重な証“人”である。また、マンガン・ノジュールなど鉱物資源の探査ばかりでなく、地球科学の研究、さらには火山噴火など災害との関連においても重要な位置を占めているのは言を待たないところである。

本研究では、海底堆積物中に存在する微量元素並びに放射性核種の地球環境科学に焦点を絞り、大別して二つの試料について、分析・解析する。一つは、北海道(噴火湾)から九州(島原湾)までの日本沿岸部(内湾)15地点から得られたコア試料(13～31層／地点)で、水産庁中央水産研究所から提供された(1984～1991年)。もう一つは外洋のコア試料で、これは沿岸部堆積物試料との比較対象であり、国際原子力機関海洋環境研究所（IAEA-MEL）の主導する”Research on Worldwide Marine Radioactivity (MARAD)”計画により、北西太平洋から採取された（1997年10月～11月)。何れの試料も鉛直方向に何層にも正確に区分されている、貴重なものである。

本研究では、先ず、日本近海の沿岸部を中心に外洋（北西太平洋）の海底堆積物も含め、それらに存在するランタノイド($_{57}$La～$_{71}$Lu)やトリウム(Th)、ウラン（U）等の微量元素および酸化還元に敏感な元素（Fe、Mn、U、Ce等)、さらに鉛210（^{210}Pb)やセシウム137（^{137}Cs）等の放射性核種を分析し、各々の分布状況を把握する。得られた分析データから、酸化還元状態に敏感な元素の深度分布などを求め、堆積環境について考察し、ランタノイド元素パターン（始原的隕石名対する試料中の各ランタノイドの存在度の比を原子番号順にプロットしたパターン）やThとスカンジウム（Sc）の存在度比（Th/Sc比）等から各海域における堆積物の起源について検討する。ランタノイド元素はその化学的性質が互いに類似している(ほとんどがLn(Ⅲ))が、CeがCe(Ⅳ)、EuがEu(Ⅱ)をとりうることなどから、各海域の堆積環境を探る上でも重要な元素群である。

JRR-4　S-パイプ、D-パイプ、PN（気送管）
地球科学試料放射化分析

また、過剰 ^{210}Pb の放射能分析から、各地点・各層の時間高分解能な堆積速度が求められるので、ここ100年ほどの堆積環境や堆積メカニズムについて時間軸を与えることができる。従って、各元素の深度分布やランタノイド元素パターン、それにフォールアウト起源の ^{137}Cs が、いつ、どのように変化したかを把握し、その原因について考察し、新たな海洋環境科学的知見を見出すことを目的とする。

本研究により得られた成果を以下に要約する。

Ⅱ．成果の概要

1．鉛210堆積速度並びに堆積年代測定

①東京湾海底堆積物に広範囲エネルギー用 Ge 半導体検出器を用いることにより、^{210}Pb、^{214}Bi、^{137}Cs が同時に定量できた。

②過剰 ^{210}Pb 放射能濃度の深度分布の回帰直線から、平均堆積速度(平均重量堆積速度)は東京湾Ⅱ試料では 1.10cm/y(0.618g/cm^2/y)、東京湾Ⅳ試料では 0.823cm/y (0.468g/cm^2/y) と求まった。

③試料全体での混合が示唆された東京湾Ⅳ試料について、部分的な堆積速度を求めた結果、0.292cm/y～0.598cm/y (0.166g/cm^2/y～0.340g/cm^2/y)となった。このように混合が起きている試料については、部分的回帰直線から堆積速度を求める方法が適していると考えられる。

④東京湾Ⅱ試料について、^{137}Cs 法から求めた平均堆積速度は、1954 年を起点とすると 1.18cm/y (1.12～1.24cm/y)、1963 年を起点とすると 1.10～1.13cm/y となった。これらの値は ^{210}Pb 法による値(1.10cm/y)とよく一致した。このように、同時に測定した ^{137}Cs を用いた ^{137}Cs 法は、^{210}Pb 法による堆積速度の正確さを評価する一つの指標となることが判明した。

2．中性子放射化分析法

①日本沿岸部海底堆積物試料に前処理として超音波洗浄を加え、中性子放射化分析を適用したところ、Mn、Fe 等の主要元素、並びにランタノイド 11 元素（最大）、Sc および Th、U 等の微量元素が定量でき、分析法を確立することができた。

②前処理に化学処理（Al 共沈）を用いて得られた検出元素数は、ランタノイド元素で最大 10 元素にとどまり、超音波洗浄以上の妨害元素の除去効果は得られなかった。

3．堆積環境並びに堆積メカニズム

（1）東京湾海底堆積物中のランタノイド元素およびトリウム、ウラン

①ランタノイド元素パターンはいずれも陸上起源の岩石に似た負の傾きをもつが、その傾き（軽ランタノイドでの多寡）については試料が内湾部か湾口部かにより異なり、粒径が大きいと傾きが小さくなると考えられ、また湾口部の試料は、分別（細粒）試料でLa-Ce間において正のアノマリーを示すなど複雑な組成であることが明らかになった。

②フッ酸によって分解された試料は、陸上岩石とよく似たランタノイド元素パターンを示したが、フッ酸未分解試料のパターンは、試料中に含まれる生物起源などの有機物による影響の可能性を示した。

③ランタノイド元素の深度分布は、表層に近い 10cm 位のところまで濃度の変動があり、これは生物等による物理的撹乱や化学的相互作用の結果と考えられる。

④Th 並びに U の深度分布より、試料によっては、両元素とも数倍から１桁の違いがあった。また、表層近くで、Th と U では対称形に近い分布を示し、両元素の海底面における化学的振舞いが全く異なっていることを示唆した。

（2）日本沿岸部海底堆積物中のランタノイド元素およびトリウム、ウラン

①東京湾を除く、日本沿岸部１０箇所（噴火湾、陸奥湾、仙台湾、伊勢湾、紀伊水道、大阪湾、広島湾、土佐湾、鹿児島湾および島原湾）から採取された試料を用いて、分析を行った。その結果、噴火湾、陸奥湾および仙台湾の沿岸部海底堆積物試料は、他の地域の堆積物や河川堆積物と比べて、軽ランタノイドに濃縮している負の傾き（La/Lu 比）が明らかに小さかった。

②Ce/La 比が比較的低く、かつ La/Lu 比が比較的高い紀伊水道、土佐湾および島原湾堆積物では、河川

等からの陸起源物質の寄与が比較的大きく、それに対して、Ce/La 比が比較的高く、かつ La/Lu 比が比較的低い噴火湾および陸奥湾堆積物は生物起源物質の影響等、通常の陸起源物質とは異なった堆積物の起源が考えられる。

③一般に、Ce/U比並びに Th/U 比は、堆積深度とともにそれらの比が小さくなった。このことより、海水中は酸化環境であっても、堆積物中では還元環境に変化しているものと考えられる。

（3）東日本沿岸海底堆積物中の主要並びに微量元素

①東京湾(Ⅱ)(湾奥部)、東京湾(Ⅳ)(湾口部)、陸奥湾および噴火湾の東日本沿岸海底堆積物コア試料、およびそれらの比較対象として外洋の北西太平洋海底堆積物コア試料中の主要および微量元素延べ 14 元素を、超音波洗浄を加えた中性子放射化分析により定量した。

試料の採取データを Table 1 に、中性子の照射条件およびγ線の測定条件を Table 2 に示す。また、各採取海域の表層について得られた定量結果を Table 3 に記載する。

Fe および Mn の定量結果より、太平洋堆積物の Mn 濃度は沿岸堆積物に比べて数倍～1 桁ほど高く、噴火湾第 5 層(堆積深度 8～10 cm)以深では上層部に比べて、Fe および Mn 濃度が明瞭に高い値を示した。また、明らかに還元環境の特徴を示したのは、東京湾(Ⅱ)の Mn、東京湾(Ⅳ)の Mn および Fe(6～8 cm 以深)のみであった(Fig.1 参照)。

②ランタノイド元素パターンは全ての試料において負の傾きを持つことから、それら堆積物の起源は主に陸源物質であることが示唆された(Fig.2 参照)。また、コンドライトで規格化した La*/Lu*比および Ce*/La*比より、東京湾(Ⅱ)および陸奥湾堆積物は、La*/Lu*比が比較的高く、かつ、Ce*/La*比が 1 よりやや低く、河川等からの陸源物質の寄与を、より直接的に反映しているものと思われる(Fig.3 参照)。

さらに、Th/Sc 比より、沿岸堆積物は同比が 0.3 前後と比較的低いことから河川等を通じた島弧起源物質の寄与が大きく、一方、北西太平洋堆積物は同比が 0.6 前後と明らかに高く、風送による大陸起源物質の寄与が支配的であることが明かとなった(Fig.3 参照)。

③Ce/U 比－Th/U 比の相関において、全てのコア試料で相関係数が 0.920～0.991 と極めて高い相関を示した。また、東京湾(Ⅱ)および噴火湾では全コアを通じて還元環境にあり、一方、東京湾(Ⅳ)および

Table 1 Profiles of sediment core samples in this study.

Sample	Sampling location	Sampling date	Water depth (m)	Number of layers
Tokyo Bay (Ⅱ)	35° 34″ N, 139° 55″ E	1987/5/15	44	31
Tokyo Bay (Ⅳ)	35° 09″ N, 139° 45″ E	1987/5/15	455	20
Mutsu Bay	41° 04″ N, 141° 04″ E	1988/7/27	42	22
Funka Bay	42° 19″ N, 140° 35″ E	1986/7/15	95	13
Pacific (St.9)	22° 22″ N, 152° 41″ E	1997/11/16	5600	16

Table 2 Conditions for neutron irradiation (JRR-4) and γ-ray measurement.

Facility	Irradiation time	Cooling time	Measuring time (sec)	Target element	Sample weight (mg)
S or D	20min	1～4weeks	1500～5000	Sc,Fe,La,Ce, Sm,Eu,Tb,Yb, Lu,Th,U	30
S or D	20 or 15min	1～4weeks	1500～7000	La,Ce,Sm,Eu,Tb, Yb,Lu,Th,U	100
S or D	7min	1day	400～600	Ho	80
PN	15sec	2～3hours	400～600	Mn,Dy	30

Thermal neutron flux densities ($n \cdot cm^{-2} \cdot s^{-1}$) ; S (4.0×10^{13}) , D (4.3×10^{13}) and PN (3.2×10^{13})

Table 3 Analytical results (ppm) of Tokyo Bay (Ⅱ), Tokyo Bay(Ⅳ), Mutsu Bay, Funka Bay and Pacifc sediment surface samples by instrumental neutron activation analysis.

	Tokyo Bay (Ⅱ)	Tokyo Bay (Ⅳ)	Mutsu Bay	Funka Bay	Pacific
Sc	17.1 ± 0.3	ND	16.8 ± 0.3	14.1 ± 0.2	22.1 ± 0.1
*Mn (%)	0.130 ± 0.001	0.066 ± 0.001	0.0346 ± 0.0004	0.0430 ± 0.0005	0.457 ± 0.004
*Fe (%)	4.20 ± 0.08	5.26 ± 0.07	4.24 ± 0.08	3.66 ± 0.05	5.85 ± 0.07
La	13.4 ± 0.5	11.5 ± 0.4	21.8 ± 0.7	13.7 ± 0.5	50.1 ± 0.5
Ce	33 ± 4	28 ± 5	41 ± 5	38 ± 4	123 ± 9
Sm	2.5 ± 0.1	2.3 ± 0.1	3.4 ± 0.2	3.0 ± 0.2	9.5 ± 0.2
Eu	0.89 ± 0.08	1.2 ± 0.1	1.2 ± 0.2	0.92 ± 0.09	2.1 ± 0.2
Tb	0.47 ± 0.12	ND	ND	ND	1.5 ± 0.1
Dy	ND	4.3 ± 0.3	3.8 ± 0.1	ND	6.1 ± 1.3
Ho	ND	ND	ND	ND	ND
Yb	1.6 ± 0.2	2.6 ± 0.3	2.6 ± 0.3	3.2 ± 0.4	7.0 ± 0.4
Lu	0.21 ± 0.02	0.30 ± 0.03	0.42 ± 0.05	0.45 ± 0.02	0.78 ± 0.04
Th	5.3 ± 0.2	3.8 ± 0.2	5.7 ± 0.3	4.5 ± 0.3	12.8 ± 0.4
U	0.83 ± 0.08	2.5 ± 0.2	4.7 ± 0.4	1.6 ± 0.1	2.3 ± 0.1

±: γ-ray counting error (1σ) ND : not determined

(The contents of the elements with an asterisk are given in percentage (%).)

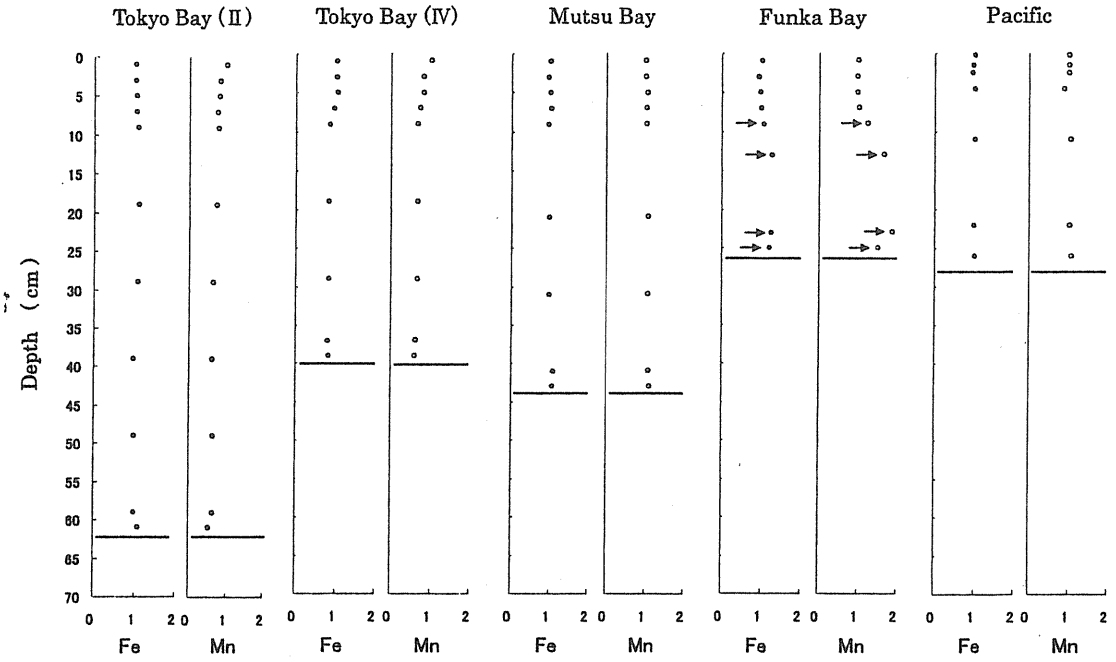


Fig.1 Ratios of Fe and Mn contents at each depth to those of surface ($(Fe)_i / (Fe)_{sur}$ and $(Mn)_i / (Mn)_{sur}$) in Tokyo Bay (Ⅱ), Tokyo Bay (Ⅳ), Mutsu Bay, Funka Bay and Pacific sediment core samples

陸奥湾では、少なくとも上層部で酸化的な環境にあることが示唆された。

ところで、Fe および Mn から得られた堆積環境と、Ce/U 比－Th/U 比から得られた堆積環境では、その傾向が必ずしも一致しなかった。本研究で新たに導入した Ce/U 比－Th/U 比を用いる方法は、堆積環境を知るうえで極めて有効と思われる。

④鉛 210 堆積速度および堆積年代より、沿岸部の堆積速度は太平洋堆積物に比べて 10^3～10^4 倍ほど速いことが確認された。また、同一湾内であっても、東京湾湾奥部(Ⅱ)は湾口部(Ⅳ)と比べて堆積速度が 2 倍ほど速く、堆積環境と同様、堆積メカニズムにおいても明らかな相違があることが判明した(Table 4 参照)。

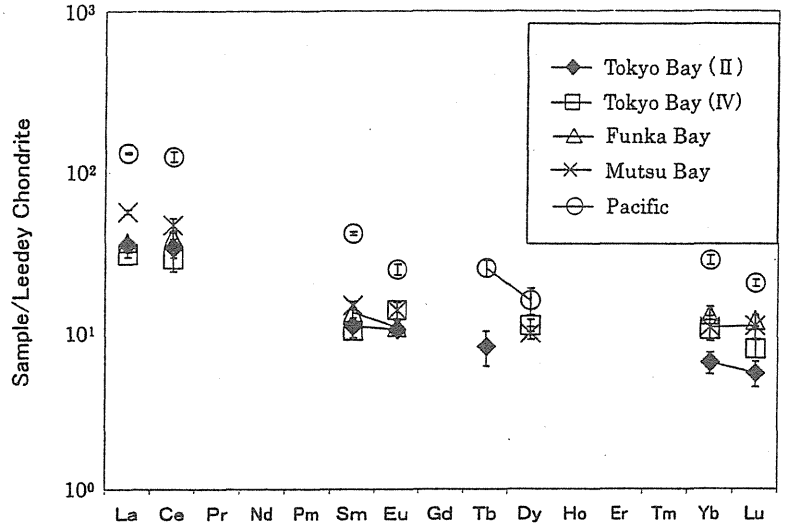


Fig.2 Lanthanoid abundance patterns of surface layer samples from Tokyo Bay (II), Tokyo Bay (IV), Funka Bay, Mutsu Bay and Pacific core sediments

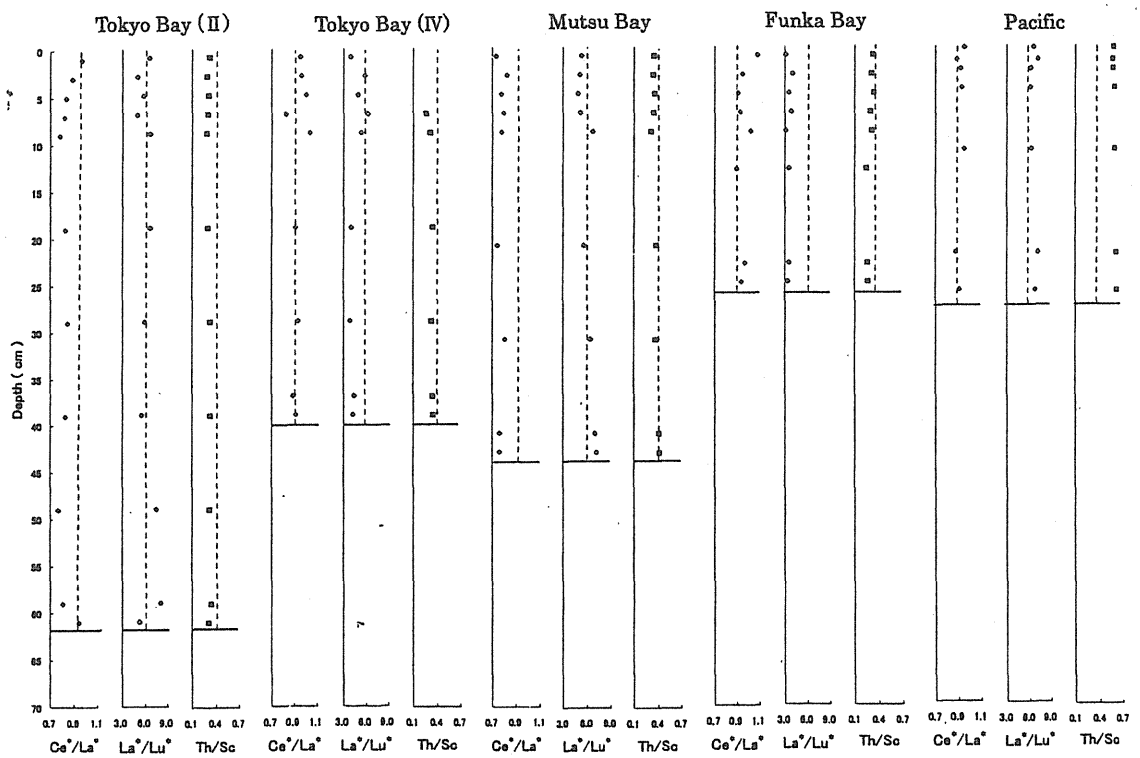


Fig.3 Ce*/La*, La*/Lu* and Th/Sc ratios in Tokyo Bay (II), Tokyo Bay (IV), Mutsu Bay, Funka Bay and Pacific sediment core samples

Table 4 Sedimentation rate in Tokyo Bay (II), Tokyo Bay (IV), Mutsu Bay and Funka Bay sediment cores.

Location	Sedimentation rate	
	($g/cm^2/y$)	(cm/y)
Tokyo Bay (II)	0.79	1.4
Tokyo Bay (IV)	0.45	0.68
Mutsu Bay	0.17	0.38
Funka Bay	0.083	0.22

さらに、Fe および Mn の濃度上昇が見られた噴火湾第 5 層の堆積年代はおよそ 1940～50 年と求められ(Fig.4 参照)、その年代は有珠火山の噴火により昭和新山が形成された 1943～45 年と一致した。このことより、噴火湾の第 5 層以深の鉄および Mn 濃度の上昇(Fig.1 参照)は、有珠火山の噴火の影響を反映している可能性がある。

Ⅲ. 今後の課題

以上のように、海底堆積物中の主要・微量元素の分析および放射能分析より、日本沿岸部を中心とした堆積環境並びに堆積メカニズムについて重要な知見を得ることができた。従って、本研究の所期の目的は十分達成することができた。しかしながら、海底堆積物の謎は深く、解明すべき点は依然として存在している。今後の主な課題を以下に要約する。

①本研究では、日本沿岸部試料として内湾 15 地点から採取された試料を分析、解析の対象としたが、そのうち東日本沿岸部の試料（特に東京湾、陸奥湾および噴火湾）については詳細に分析したものの、マシン・タイムの都合上、他の地点の試料については、表層、中層および最下層の 3 点のみの深度分布を得るに留まった。今後は、特に西日本の試料についても詳細な分析を行い、ほぼ日本全域をカバーする沿岸堆積物について、堆積環境並びに堆積メカニズムの視点から、より精度のよい解明が求められる。

②海底堆積物を含む海洋環境は、大気環境や陸上環境と密接な関係にあり、相互に連関していることは言を待たない。従って、今後、他の領域の環境動態を把握しつつ、海洋環境との関連性について詳細な研究が必須となろう。

[成果の公表]

Ⅰ. 著書

1. J. Gayol, T. Honda, P. P. Povinec, E. M. Scott et al., Global marine radioactivity (GLOMARD), International Atomic Energy Agency (IAEA), 2000, Vienna.

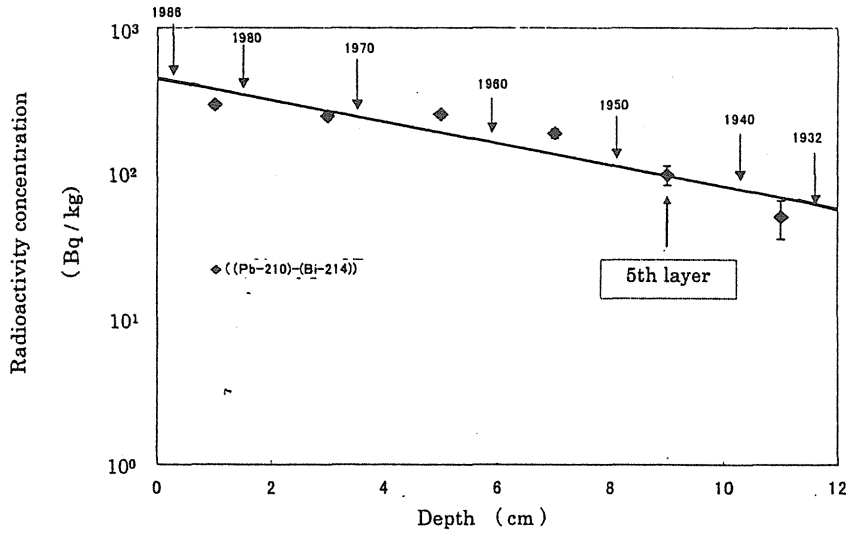


Fig.4 Vertical profiles of excess ^{210}Pb radioactivity concentrations and sedimentatoin ages in Funka Bay sediment core samples

Ⅱ．学術誌

1．本多照幸，木村賢一郎，東京湾，陸奥湾および噴火湾海底堆積物における微量元素の分布と挙動，日本海水学会誌，第57巻(第3号)，166-180(2003).

2．本多照幸，木村賢一郎，森本隆夫，鈴木顕介，噴火湾海底堆積物の鉛210堆積年代と昭和新山の形成，フィッション・トラック　ニュースレター，第16号，2003(印刷中).

3．本多照幸，木村賢一郎，森本隆夫，鈴木顕介，噴火湾海底堆積物のPb-210堆積速度とその特徴，フィッション・トラック　ニュースレター，第15号，40-42(2002).

4．市村哲成，木村賢一郎，森本隆夫，鈴木顕介，本多照幸，γ線スペクトロメトリを用いたPb-210法による東京湾海底堆積物の堆積速度，フィッション・トラック　ニュースレター，第14号，55-59(2001).

5．Y. Kikawada, T. Ossaka, T. Oi and T. Honda, Experimental studies on the mobility of lanthanides accompanying alteration of andesite by acidic hot spring water, Chemical Geology, vol.176, 137-149(2001).

6．本多照幸，海洋生物中の放射性核種，日本海水学会誌，第55巻(第1号)，11-20(2001).

7．本多照幸，海底堆積物中の放射性核種，日本海水学会誌，第54巻(第5号)，348-359(2000).

8．本多照幸，鈴木顕介，森本隆夫，過剰Pb-210法による海底堆積物の堆積年代について，フィッション・トラック　ニュースレター，第13号，39-41(2000).

9．本多照幸，海水中の天然放射性核種，日本海水学会誌，第54巻(第2号)，91-101(2000).

Ⅲ．学内紀要

1．本多照幸，海底堆積物中の人工放射性核種－その分布と挙動－，武蔵工業大学原子力研究所　研究所報，第28号，37-47(2002).

2．本多照幸，海底堆積物中の天然放射性核種，武蔵工業大学原子力研究所　研究所報，第27号，65-76，(2001).

3．本多照幸，海洋表層水中の人工放射性核種の分布と挙動，武蔵工業大学原子力研究所　研究所報，第26号，77-89(2000).

4．本多照幸，海洋における天然放射性核種の放射非平衡，武蔵工業大学原子力研究所　研究所報，第26号，90-98(2000).

Ⅳ．口頭発表

1．本多照幸，木村賢一郎，森本隆夫，鈴木顕介，噴火湾海底堆積物の鉛210堆積年代と昭和新山の形成，第27回フィッション・トラック研究会，2002.

2．本多照幸，柳下　智，五十嵐康人，青山道夫，廣瀬勝己，2000年長崎及びつくばにおける降下物のランタノイド元素パターン，日本地球化学会第49回年会講演要旨集p.52，2002.

3．五十嵐康人，本多照幸，柳下　智，廣瀬勝己，青山道夫，2000年長崎及びつくばにおける210Pb，7Be及びトリウム降下量，日本地球化学会第49回年会講演要旨集p.67，2002.

4．本多照幸，木村賢一郎，森本隆夫，鈴木顕介，噴火湾海底堆積物のPb-210堆積速度とその特徴，第26回フィッション・トラック研究会，2001.

5．本多照幸，柳下　智，鈴木健二，五十嵐康人，青山道夫，廣瀬勝己，降下物中Pb-210のγ線測定とその存在量，第26回フィッション・トラック研究会，2001.

6．市村哲成，木村賢一郎，森本隆夫，鈴木顕介，本多照幸，γ線スペクトロメトリを用いたPb-210法による東京湾海底堆積物の堆積速度，第25回フィッション・トラック研究会，2000.

7．本多照幸，海水中の人工並びに天然放射性核種の分布と挙動，日本原子力産業会議原子動力研究会(依頼講演)，2000.

研究テーマ：放射化分析による家畜・家禽における土壌摂取量の推定
表　　題：家畜・家禽の糞中の土壌特有元素の定量

3-24

家畜・家禽の糞中の土壌特有元素の定量

西村宏一、木方展治[1]、宮本　進
独立行政法人農業・生物系特定産業技術研究機構畜産草地研究所　茨城県つくば市池の台２
１：独立行政法人農業環境技術研究所　茨城県つくば市観音台３－１－３

豚および鶏の一般的な飼養法では家畜が土壌と隔離されている。この飼養法では、飼料から家畜体組織へ移行するダイオキシンの量が少ないことを確認している。最近増加してきた自然飼育法や有機農法では、豚や家禽が土壌と接触する機会が多く、土壌に含まれる有害な化学物質も家畜の体内へ取り込まれる恐れがある。これらの解明のために、家畜の土壌摂取量を調べる必要がある。土壌特有の元素であるスカンジウム（Sc）とユーロピウム（Eu）について家畜糞中のこれら元素の含量を、放射化分析で定量し、家畜における土壌摂取量を推定する。

鶏における土壌に摂取量を調べるため、鶏を用いて屋内・屋外飼養実験を行った。白色レグホーン系のデカルブ種の雛を、屋内、屋外飼養区とも 15 羽ずつ供試し、約６ヶ月間群飼で飼育した。屋内区は通常の鶏舎内に設けた。屋外飼養区は黒色土（園芸用庭土）を約 10cm の厚さに敷いた園芸用ネットハウス内に設けた。ハウスの広さは 5.4 × 5.4 mで、中に 0.9 × 1.8 mのプレハブハウスを庇陰小屋として設置した。両区とも飼料は飽食させ、供試鶏の体重と採食量を２週間毎に秤量するとともに、大雛期および産卵期に採糞した。屋内区および屋外区に分けて飼養した供試鶏から得られた糞を乾燥し、妨害元素（^{24}Na、^{56}Mn 等）の影響を避けるために１ヶ月以上クーリングを行った後に、試料中の Sc（^{46}Sc、0.889MeV 他）と Eu（^{152}Eu、0.122MeV 他）の測定を行った。

その結果、Sc と Eu の検量線（0.02 ～ 20 μｇ）は良好で、20 分間の照射で両元素とも、微量レベルで測定出来ることが明らかとなった（図１、図２）。屋内区および屋外区に分けて飼育した供試鶏から得られた糞中の Sc、Eu は、屋内区ではほとんど検出されなかった。一方、屋外区では、かなり高いレベルで検出され、屋外飼養の鶏はかなりの土壌を摂取していたことが示唆された。

現在、これらのデータから、供試鶏の土壌摂取量を計算しており、２回目の実験（平成 15 年度実施）の結果と合わせて検討する予定である。

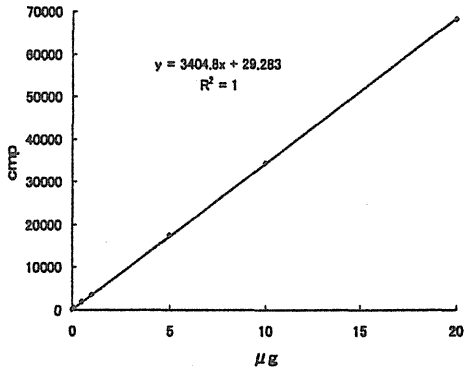


図１　Sc の検量線

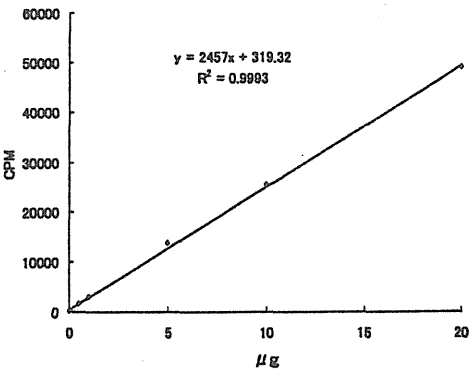


図２　Eu の検量線

原子炉：JRR-3　　装　置：気送管　　分　野：放射化分析（農・水産物）

3-25 地層中の年間線量評価のためのU,Thの放射化分析

Neutron activation analysis of U and Th for annual dose measurement

雁沢 好博*
Yoshihiro Ganzawa*

＊北海道教育大学函館校
*Hakodate School, Hokkaido University of Education

はじめに

ルミネセンス年代測定では鉱物に蓄積された線量を熱ルミネセンスや光ルミネセンスで評価する．一方，年間線量の測定には試料採取地点での直接測定やγスペクトロメトリーによる長期間の測定方法がとられている．筆者は少量の試料で効率よく，しかも精度の良い測定方法として放射化分析に注目し，2000年度から3年間にわたって東大原研施設総合共同研究を利用して，とくにUおよびThの定量を進めてきた．この間，計6回の照射を行い，標準試料を含めたデータの蓄積を行うことができた．以下，その概要を報告する．

施設の概要と実験方法

利用原子炉はJRR-4（中性子束：7.0×10^{13}n/cm^2・sec，Cd比＝4），照射設備はTパイプである．従来放射化分析で利用された立教炉Fリング（中性子束：1.4×10^{12}n/cm^2・sec，Cd比＝3）より中性子束は40倍程度高い．測定試料は火山灰，黄砂試料，更新世後期の海成堆積物などである．これらはいずれも年代測定の対象試料である．また，標準岩石試料としてJB3，JA3，JG1a，JG2，JG3，JR1，JR2の7種類を用いた．これらの試料のUとThの含有量はそれぞれ0.48～11.3ppmおよび1.27～31.2ppmの範囲にあり，一般的な火成岩の含有量の範囲に概ね一致している．

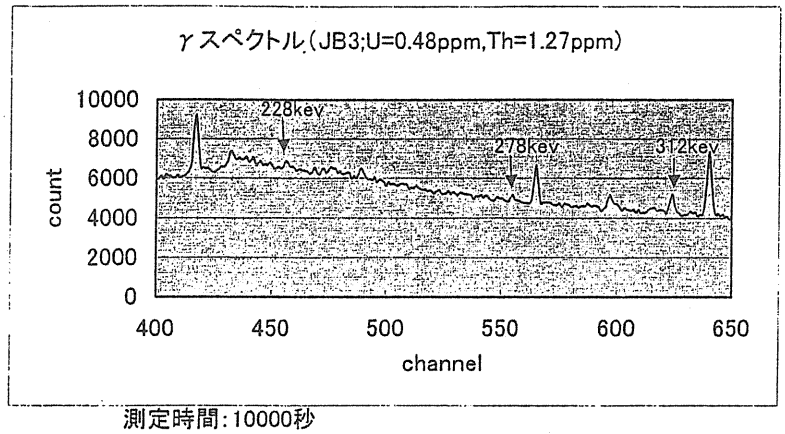
照射試料は1試料あたり約80mgをポリ袋に封入し，標準試料を含め計約20試料を1回の実験に供した．Tパイプでの照射時間は7分，冷却時間は約6日間，計数時間はライブタイムで1000～10000秒である．測定にはORTECのTD-ASCを利用した．また，波高解析にはSAMPOを用いた．測定エネルギーはUが228kevおよび278kev，Thが312kevである．同様の実験を1997年から1999年にかけて，立教炉にて行なった．

測定結果

a)立教炉照射での測定実験

1997年から1999年にかけて，立教炉にてUおよびTh濃度測定のための実験を行なった．全ての実験を通して，UおよびThの標準試料としてSPEXを，岩石試料としてJG1aを用いた．9回繰り返し行なった照射実験結果は平均値でU＝4.71±0.49

JRR-4　　地球科学試料放射化分析



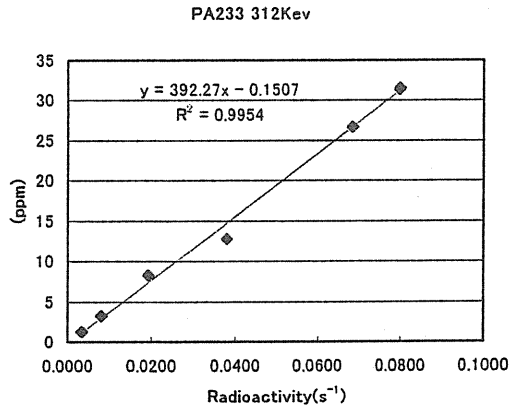
測定時間:10000秒

図-1 U,Th のスペクトルの 1 例(JB-3)

ppm, Th=11.83±1.15ppm で各測定値の集中度も良く，公表値と誤差内で極めてよく一致した．その後，立教炉の閉鎖や SPEX の入手の困難性から，新たに東海原研で標準岩石試料用いての精度の良い測定値の追求が課題となった．

b)標準岩石試料を用いた測定結果

実験当初，JB-3 や JA-3 の低濃度の U および Th 測定精度が著しく劣っていた．しかし，測定条件を上記に述べたように改善することにより，各濃度が 1ppm 以下であっても測定が可能なレベルまで到達した．図-1 に測定チャンネル実測図の例を示した．JB-3 ではカウントは少ないが，解析プログラム SAMPO を利用することで，ピークを確認しながらのエリアルカウントを解析することが効果的である．こうして改善された実験および解析方法から，1mg あたり U の放射能強度（228kev と 278kev）は JB3 (0.48ppm) で 0.007～0.0088 程度（測定誤差約 9%)，JG2 (11.3ppm) では 0.138 程度（測定誤差約 1%）が得られた．また，



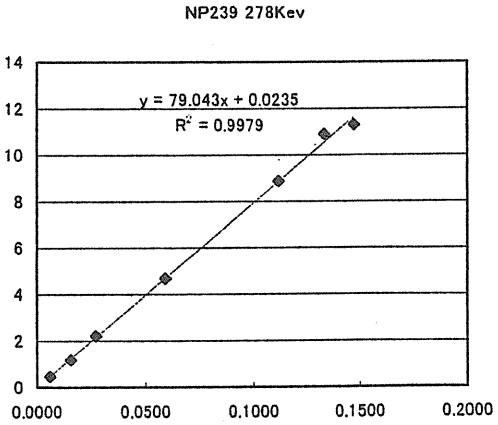


図-2 標準岩石試料の U,Th 公表値と放射能強度

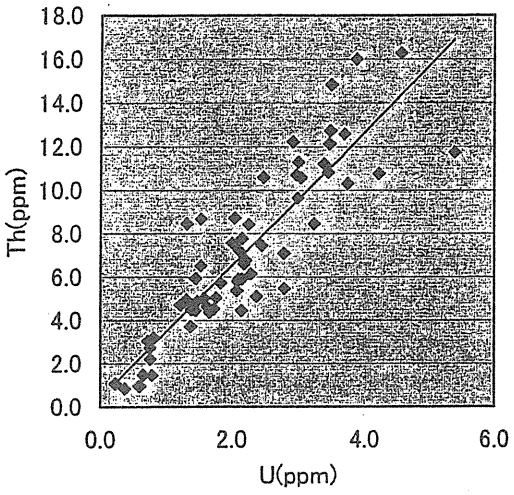


図-3 年代測定試料の U,Th 濃度の分布

Th (312Kev) では，それぞれ 0.0028 (測定誤差約 6%) および 0.00736 程度 (測定誤差約 0.6%) である．この値を標準岩石試料の U および Th の公表値と比較すると，U の放射能強度 (228kev と 278kev) においても Th (312Kev) においても，きわめて良好な相関関係 (R^2=0.99) が得られた．図-2 に実験例 (実験コード：TK021A) を示した．図中の検量線を用いて，未知試料の U と Th 値を決定した．

c)未知試料の U,Th 測定結果

ルミネセンス年代測定の対象試料として，これまで火山灰，黄砂，海成堆積物を選択してきた．これらには石英や長石類が普遍的に含まれている．現在中心的に進めている熱ルミネセンスでは特に石英が有効である．SiO2 に富む石英はとりわけ放射性元素が少ない傾向がある．したがって，正確な U，Th の測定手法の確立が正確な年間線量を測定する上で重要である．これまで測定した試料の U 濃度と Th 濃度の分布表を，図-3 に示した．対象とした試料は全て U 濃度は 5ppm 以下であった．また，Th 濃度は 16ppm 以下であった．

終わりに

以上のように，東海原研，JR-4 で U,Th 測定を始めて 3 年が経過して，ようやく実際の年間線量に利用できる精度の値が得られるようになった．今後は，本論で述べた手法に基づき未知試料の計画的な測定を開始する予定である．

成果の公表

雁沢好博，奥山尚登，佐野正樹 (2002)，ピリカ遺跡D地点ローム層のルミネセンス年代測定．今金町文化財報告書「ピリカ遺跡 II」89-92. Y. Ganzawa, M. Momoi (2002) Red TL dating of dune sand deposits from middle to late Pleistocene in Northern Honshu, Japan. 10th international conference on luminescence and ESR dating. 108

Y. Ganzawa, H. Furukawa (2001) Dating of Toya Caldera about 100ka volcanic activities.
ESR Applications, 17. 51.

雁沢好博，Naomi Porat，荒屋純一，椎名孝 (2001) 広域風成塵堆積物のルミネセンス年代測定．地質学雑誌, 107, 762-772

研究テーマ：広域環境モニタリング試料の微量元素分析
表　　題：広域環境モニタリング試料の微量元素分析

3-26　広域環境モニタリング試料の微量元素分析（3）

宮本 ユタカ，齋藤 陽子，間柄 正明，桜井 聡，臼田 重和
原研，環境科学研究部，環境技術開発グループ

はじめに

大気に放出された極微量の放射性核種や大気汚染物質の挙動，分布などを評価するために，これらの直接的な輸送媒体である大気浮遊塵の量や組成についてモニタリングすることは重要である。本研究では大気浮遊塵をエアーダストサンプラーによる方法に加え，松葉表面に付着したものを洗い落として捕集し，放射化分析法で元素分析を行っている。大気浮遊じんの物質輸送経路は大気の流れによって決まるが，輸送途中にさらされる環境条件，例えば降雨などによって大気浮遊じんの組成は異なってくるので，環境条件による影響を考慮することが必要である。ここでは気象条件などの違いが大気浮遊じんの組成にどのように影響を与えているのかをエアーダストサンプラーで捕集した大気浮遊じんの元素組成の変動から探ることを試みた。

実験方法

原研東海研 CLEAR 施設周辺にハイボリュームエアーダストサンプラー[平均流量：120 m^3/h]を設置し，大気浮遊塵を石英ガラス繊維製のフィルター上に捕集した。捕集は2001年5月14日から開始し，天候の変化に応じて2～6日ごとにフィルターを交換した。原研保健物理部環境放射線管理課の協力を得て，原研東海研敷地内（捕集場所から約400 m 北）の気象観測塔で連続観測されている湿度，風速，降水量などの1時間毎の平均値を入手し，それを捕集時の気象観測データとした。

捕集したフィルターから 15 mm×15 mm の試料を切り取り，ポリ袋に二重封入して照射試料とした。比較標準試料として日本地質調査所（現産業技術総合研究所）発行の4種類の標準岩石試料を用いた。これに加えて試薬から調製した溶液を石英フィルターに染み込ませたものも標準試料として使った。中性子照射は原研 JRR-3M の圧気輸送管 PN-3 あるいは PN-2 で行った。照射時間はそれぞれ10秒間と10分間であった。中性子照射後，適当な冷却時間をおいて高純度 Ge 半導体検出器でγ線スペクトロメトリーを行い標準試料との比較法で元素定量を行った。

結果と考察

この実験で捕集した大気浮遊じんでは，捕集場所が砂浜海岸から約800 m と近いことから海塩粒子と土壌粒子が主となり，それにばい煙などの人工汚染成分が加わったものになるであろうと予想される。そこで，捕集試料中に土壌成分と海塩成分が含まれる割合について検討するため，それぞれの成分に特徴的な元素について2次元の濃度分布図を作成して成分分析を行った。土壌成分を代表する元素として Sc，海塩成分については Cl を選び，この2つの元素濃度を土壌と海塩のどちらにも多く含まれる Na で規格化した元素濃度比の分布，すなわち Sc/Na－Cl/Na 濃度比の分布図で調べた。Fig. 1にその分布図を示す。捕集期間中に風速8 m/s 以上の強風が吹いた試料や黄砂の降下が観測されたもの，あるいはその両方が観測されたもの，台風が接近した時のものに対して記号の横にそれぞれ W，Y，WY，T の文字を添えてこれらの特徴を示した。また，これらの分布点を捕集期間中の相対湿度の平均値（以降，平均湿度と略する）の高さによって記号を変えて区別した（○：<65%，△：65%-80%，＊：>80%）。Fig. 1には捕集場所付近の砂地の定量値，海水の平均値[1]，地殻の平均値[1]，国立環境研究所が調製した黄土標準試料（CJ-1）の文献値[2]も示した。砂，地殻平均値，CJ-1 の Sc/Na 比は 7.8～9.4 であった。海水の平均値と耕作土および砂を結ぶ直線を図中に示した。捕集期間中に強風や黄砂の降下が観測された試料は分布点はこれらの直線上に並んでいた。これは海塩と耕作土あるいは砂（地殻成分）を端成分とする2つの混合物であるということを示している。つまり，強風によって耕作土や砂など土壌が再浮遊したもの，あるいは偏西風によって運ばれてきた黄砂と海塩粒子からの2成分が主成分であることを示している。一方，台風時に捕集した試料（矢印Tで指し示されている分布点）では8 m/s～10 m/s の強風が観測されていたにもかかわらず，これらの直線から低 Sc/Na 比側に外れた所に分布していた。降雨によって大気浮遊じんの特定成分が大気から除去されてしまい，その残存成分がフィルターに捕集されたのではないかと考えられる。平均湿度が高い（Fig. 1で＊印で示される）試料でも直線よりも低 Sc/Na 比側に集まる傾向があることから，低 Sc/Na 比側に集まるのは，台風時に捕集した試料と同様に大気浮遊じんの特定成分が大気から除去されたた

原子炉：JRR-3　　装置：照射設備（PN-2, PN-3）　利用分野：放射化分析（環境）

めではないかと考えられる。齋藤ら[3]はアンダーセンサンプラーで捕集した試料の元素組成分析から，粒径が細かくなるに従い，V/Sc 濃度比が高くなることを報告した。そこで，試料捕集時の平均湿度に対する V/Sc 濃度比の関係を調べた。Fig. 2 にその関係を示す。平均湿度が高くなるにつれて V/Sc 比が高くなる傾向があった。齋藤らの結果が捕集した試料についても当てはまるとするならば，平均湿度が高くなるにつれて，大気浮遊じんの粒径が細かくなると言える。つまり，平均湿度が高くなるにつれて，降雨や霧などによって粒径が粗い粒子ほど大気から除去されやすく，粒径の細かい粒子が大気に残存されやすいと言える。

参考文献

1) B.Mason, "Principles of Geochemistry", John Wiley & Sons, Inc., New York (1966).
2) 国立環境研究所，特別研究報告「大気エアロゾルの計測手法とその環境影響評価手法に関する研究」, SR-43-2001, pp.38 (2001).
3) Y.Saito, M,Miyamoto, M.Magara, S.Sakurai, S.Usuda, *J.Radioanal. Nucl. Chem.*, 255, 341 (2003).

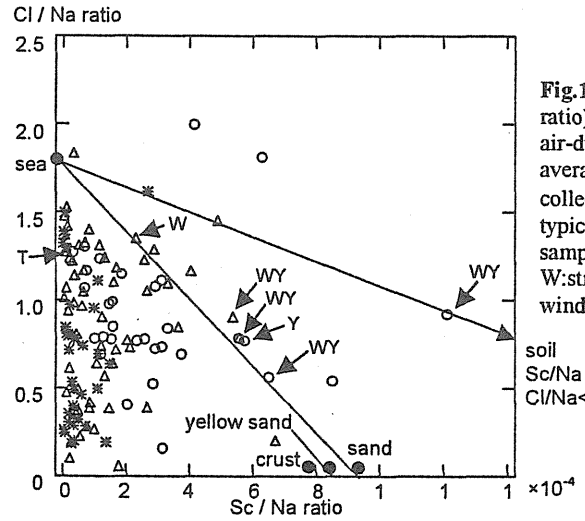


Fig.1 Elemental composition (Sc/Na ratio and Cl/Na ratio) of the airborne dust collected with a high-volume air-dust sampler. The symbols show the level of average relative humidity in a period of sample collection (○:<65%, △:65%-80%, ＊:>80%). The typical meteorological characteristics in a period of sample collection are shown in the figure as the letters; W:strong wind, Y:fall out of yellow-sand, WY:strong wind and fall out of yellow-sand, T:typhoon.

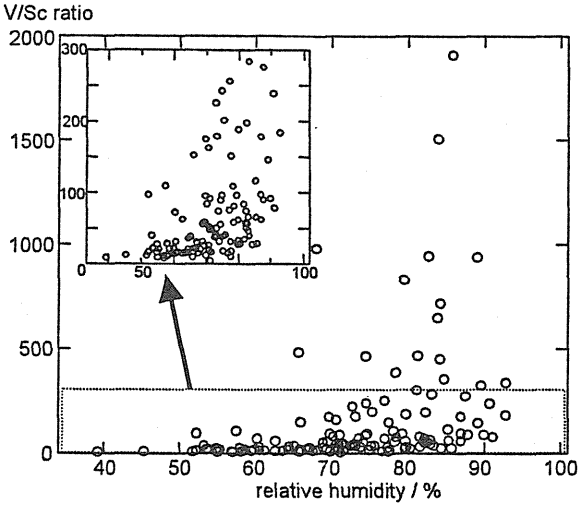


Fig.2 The correlation between V/Sc ratio of the airborne dust and average relative humidity in a period of sample collection.

研究テーマ：多重ガンマ線分析の分析化学への応用
標　　題：多重ガンマ線分析による高感度多元素同時定量

3-27

深海底土中のイリジウム分析

High sensitive iridium determination in deep sea sediment using multiparameter coincidence method

初川雄一、藤暢輔、木村敦、ホセイン　ガライ、大島真澄、野口高明[1)]、豊田和弘[2)]

物質科学研究部原子核科学研究グループ

1）茨城大学

2）北海道大学

イリジウムは地球科学的に地球外物質の影響を大きく受ける元素であり、その分析は多くの分野で興味がもたれている。特に隕石中に高く含まれているのでイリジウムの異常濃集は巨大隕石の飛来と関連付けられている。 イリジウムの分析は ^{191}Ir (37.3%) が 700 b という大きな中性子断面積を有しているために、これを利用して高感度での検出が可能である。 しかし一般にイリジウムの含有量は極微量でありｐｐｂ以下の分析が求められる。 特に地質学的試料の場合共存するクロム、スカンジウムから生成する ^{51}Cr や ^{46}Sc からのガンマ線による妨害が激しく中性子照射後の化学分離が必要となる。 このために多くの手間と時間が掛かりさらに測定の誤差を生じる事もある。 一方我々は最近ガンマ線の同時計測に基づいた多重ガンマ線分析法を開発し、これを中性子放射化分析と組み合わせることにより高感度の元素分析を行うことを可能にした。 この多重ガンマ線分析法を利用することによりバックグラウンドを大幅に低減することができるため主要元素からの妨害を受けることなく微量元素の分析を非破壊で行うことが可能となった。

この方法を用いて深海底土中のイリジウムの分析を行った。 サンプルは日本海洋科学技術センター（JAMSTEC）においてフィリピン沖採取したコアは全長１２６センチメートルで採取されたボーリングコアより作成した。(17 03.5’ N 130 15.0’ W)水深 5880m の海底であるがこのうちの１５、４１、６７，９３センチメートルの位置からそれぞれ約１００ミリグラムの試料を取った。 秤量した深海底土試料は石英管に封入し、また同時に隕石標準試料 Allende（10.9m g）および KT 境界の標準試料として Fish Cray（32.6m g）もそれぞれ秤量後、石英管に封入した。 イリジウムの標準としてイリジウム標準溶液から希釈した溶液を石英管中で風乾させた 6.9ng のイリジウム試料を用い、これらを同一条件で原子炉において照射を行った。 照射は原研研究炉 JRR-3M HR にて行い中性子束 9.8 x 10^{13}n/sec/cm^2 において４８時間行った。 約４０日の冷却後、原研タンデムに設置されている多重ガンマ線分析装置 GEMINI に於いてガンマ線分析を行った。 一試料につき約２４時間の測定を行い、イリジウムから発せられるガンマ線 316 keV-468 keV の同時測定を行い、標準試料との比較法により試料中のイリジウムの定量を行った。 表に本研究で得られた深海底土サンプル中のイリジウム濃度を示す。全体的に 130 から 250 ppt という高い Ir 濃度が観測された。 一般に深海底土の堆積速度は非常に遅く地球外物質の寄与が大きいことが期待されるが本研究によりそれが確認された。

表－１多重ガンマ線分析による深海底土中の Ir 濃度

Sampling core	Depth B.S.F	Ir (ppb)	Ref. Value
KR-98-01PC4	15 cm	0.18±0.03	
KR-98-01PC4	41 cm	0.25±0.03	
KR-98-01PC4	58 cm	0.13±0.03	
KR-98-01PC4	94 cm	0.19±0.02	
Fish Clay(32.6mg)		30.5±0.6	32±2
SARM-7(10.9mg)		927±16	743

原子炉：JRR-3

研究テーマ:ラジオアイソトープ技術者の養成
表　　題 :実習　放射化分析

3-28

貝殻中の銅・ﾅﾄﾘｳﾑの放射化分析

上沖　寛
国際原子力総合技術センター（東京研修センター）

本研究は、ＲＩ技術者の養成を目的とする研修コースの中で実習教科として行うものである。本報告では、平成14年度の研究炉をもちいた成果として、国内原子力技術および放射線利用に関係する人材養成を行った基礎課程における実習教科としての放射化分析について報告する。

原子力の基礎として中性子核反応の理論や応用を理解させることは重要である。放射化分析の実際を経験させることはこれらの知識の理解を深めるのに大変重要であり、結果としてガンマ線スペクトル解析による放射能測定法および非密封ＲＩの安全取扱法を習得させることになる。

平成１４年度は基礎課程で２回の放射化分析実習を行った。分析試料は海水産の大アサリであり、炭酸カルシウムをマトリックスにして微量元素を含有する。分析目的核種は、放射化生成核種のガンマ線スペクトルで主成分となるﾅﾄﾘｳﾑ24、放射化生成物が 陽電子壊変を伴い陽電子消滅ピークを主要放射線ピークとする銅64である。照射条件は研究炉の気送管で2～5分間照射とし、ナトリウムと銅の標準試料と共に大アサリ貝殻の照射を２回行った。

銅の分析：

銅64の陽電子消滅放射線は、他の放射化生成核種からの高エネルギーガンマ線や宇宙線が物質にもたらす電子対生成による放射線と同一放射線であるから、銅64の分析には化学分離を必要とした。簡単な銅の化学分離法として金属亜鉛により銅イオンを還元させて銅の沈殿分離を行った。この化学分離の操作は、30分間の所用時間で0.1ppm Cu 濃度に対して5%の精度で分析された。本実習は、生成核種を同定および定量することにより核反応の理解を深め、ＲＩ実験における放射線被ばくに対する工夫、除染、サーベイ等、一連の安全取扱いの基礎を習得させるものとして有効であった。

本実験による研修生の被ばく線量は、線源が10^6Bq位に対し最大1μSv程度であった。

原子炉：JRR－3　JRR－4　装置：気送管　分野：放射化分析（環境）

3-29 讃岐平野周辺の瀬戸内火山岩類の地球化学的研究

新正裕尚（東京経済大学経営学部）
角井朝昭（産業技術総合研究所・地球科学情報部門）

Geochemical study of the Setouchi Volcanic Rocks around the Sanuki Plain.

Hironao SHINJOE (Department of Business Administration, Tokyo Keizai University)
Tomoaki SUMII (Geological Survey of Japan, AIST)

1. はじめに

西南日本弧においては，第四紀の火山フロントより海溝寄りの地域に多様な中新世中期の火成岩類が分布する．その主な構成要素は、（1）西南日本弧の伸長方向に対してほぼ平行に走る中央構造線付近からその北側にかけて分布する瀬戸内火山岩類、（2）中央構造線より海溝寄りに分布し主に珪長質の貫入岩体からなる外帯花こう岩類、（3）海溝に最も近接して分布する、ソレアイト質玄武岩/はんれい岩、あるいはアルカリはんれい岩～花こう岩・閃緑岩からなる火成岩体（高橋，1986の「外縁帯」）である．これらの活動は日本海の拡大による西南日本弧の時計まわり回転，それに伴う熱い四国海盆の沈みこみと相前後して起こったものであり，これらの火成活動の成因はこの特殊なテクトニックな環境と結びつけて理解されるべきものである．

上記の３つの構成要素のうち．瀬戸内火山岩類についてはマントル由来のカルクアルカリ安山岩である高マグネシア安山岩の出現が注目され数多くの岩石学的，地球化学的研究が行われてきた(Tatsumi and Ishizaka, 1982; Shimoda et al., 1998)．しかしながら瀬戸内火山岩類には珪長質な火山岩も相当量含まれる．近年 Shimoda and Tatsumi (1999)により香川県小豆島の流紋岩～デイサイトについて地球化学的研究が行われ，これらの珪長質火成岩について沈み込むスラブ表面に存在する堆積岩類の融解したメルトにその起源をもとめる考えを提案した．さらにこのような珪長質メルトがマントルウェッジ内を上昇する際にかんらん岩との反応を行うことにより高マグネシア安山岩マグマが形成された可能性についても議論が行われている．このように瀬戸内火山岩類のなかでも珪長質なメンバーは，苦鉄質・中間質マグマの成因の鍵を握る．さらにスラブ融解というマグマ発生プロセスが正しければ，沈み込むフィリピン海プレートの当時の温度構造に対する制約を与え，地域のテクトニクスに対する拘束条件となり得る．

我々は西南日本弧の中新世中期火成岩について上記の３つの構成要素全てについて広域的に試料採取を行い，中性子放射化分析を含む地球化学的検討を行っている．ここではそれらの中から四国東部の讃岐平野周辺の瀬戸内火山岩類の珪長質火成岩について分析を行った例を紹介したい．そして瀬戸内火山岩の珪長質メンバーについてのスラブ融解によるマグマ成因について微量元素組成から若干の議論を加えたい．

JRR-4 T パイプ　地球科学試料放射化分析

2. 試料と実験方法

瀬戸内火山岩類の主な分布域は東から愛知県の設楽地域，大阪・奈良地域，香川県讃岐平野と周辺の島嶼，愛媛県高縄半島と周辺の島嶼，大分周辺である．今回，香川県の讃岐平野および小豆島に分布する瀬戸内火山岩から70個あまりの試料を採取し，粉末試料を作成して蛍光X線分析を行った．その中から5個の珪長質火成岩を選び出し，中性子放射化分析を行った．分析を行った試料は以下のとおりである．

(1) SNK80 ざくろ石黒雲母流紋岩，高松市二子山；(2) SNK82 紫蘇輝石黒雲母デイサイト，木田郡三木町白山；(3) SNK83 黒雲母デイサイト，木田郡三木町白山；(4) SNK86B 普通角閃石デイサイト，小豆郡内海町拇指岳；(5) SNK87 黒雲母普通角閃石デイサイト，小豆郡内海町権現崎．

それぞれおよそ200mgの粉末試料をポリエチレンバイアルに融封後，JRR4原子炉Tパイプで定格出力の下で20分間照射した．冷却後の試料について大学開放研究室のγ線検出器を用いてγ線測定を行った．

γ線の測定は照射後およそ1週間冷却した後4000秒，1カ月冷却した後約6時間と2回に分けて行った。分析は産業技術総合研究所の岩石標準試料JB-1，JR-2を同時に照射しこれらを標準試料として相対法により行った．分析の確度のチェックのため，産業技術総合研究所の他の岩石標準試料や米国地質調査所の標準試料などもしばしば同時に照射を行い定量した．

3. 結果と考察

代表的な3試料の中性子放射化分析結果を表1に示した．また，測定した5試料のコンドライトで規格化した希土類元素パターンを図2に示した．全ての試料は右下がりの希土類元素パターンを示す（La/Yb_N=8 - 48）．希土類元素パターンからは重希土元素の枯渇の程度が大きくEu負異常が見られないもの（SNK80, 86B, 87）および重希土元素の枯渇の程度が小さくEu負異常が見られるもの（SNK82, 83）の二つのタイプに大きく分けることができる．前者の3試料のような微量元素組成の特徴は，融解時の残渣にざくろ石が存在し斜長石

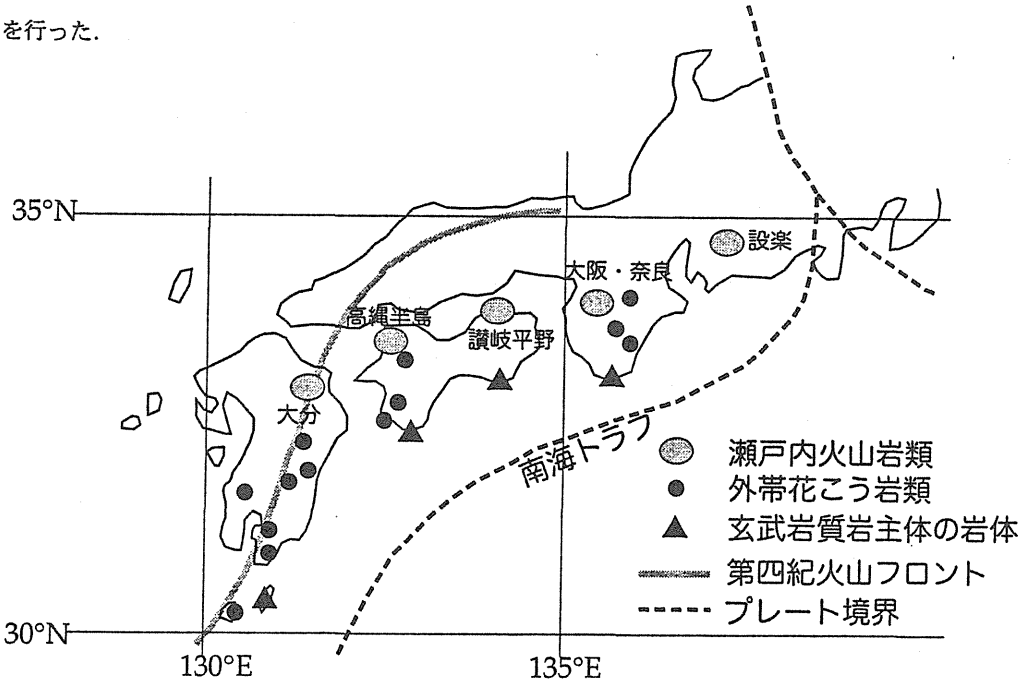


図1：西南日本弧の海溝より地域に分布する
中新世火成岩体

表１：代表的な試料の中性子放射化分析の結果

(ppm)	SNK80	SNK82	SNK87
Sc	2.2	10.7	6.8
Cr	1.8	7.5	25.4
Co	0.7	8.0	6.1
Hf	3.3	3.9	3.2
Ta	1.0	0.7	0.6
Rb	142.8	129.4	149.0
Cs	12.0	11.5	8.9
Th	11.4	10.6	8.7
U	3.0	3.7	3.1
La	21.3	18.1	14.2
Ce	46.4	45.5	33.7
Nd	15.7	19.2	13.9
Sm	2.4	4.1	2.4
Eu	0.56	0.96	0.78
Tb	0.17	0.58	0.37
Yb	0.30	1.53	0.97
Lu	0.05	0.24	0.17

を欠くような場合に期待され，いわゆるアダカイトと呼ばれるスラブ融解で生成されたことが主張されている岩石について見られるものである．またアダカイトの特徴として高いSr/Y比が掲げられるが，蛍光X線分析により求めたSr/Y比はこれら3試料は35-52と高い．しかしながら一般にアダカイトの成因として主張される沈み込むスラブを構成する玄武岩質岩の深部での融解をこれらの岩石に直接あてはめることはできない．まずこれらの岩石は比較的カリウム量にとむ流紋岩～デイサイトでありこのような主成分元素組成をMORB類似の玄武岩質岩の融解で作ることは容易でない，またShimoda and Tatsumi (1999)によるSr, Nd, Pb同位体組成はむしろ堆積岩に近い領域にある．従って堆積岩類の融解にこれらの岩石の成因を求めるほうが適切かもしれない．しかし堆積岩の部分融解を考えた場合，上記の微量元素組成に基づく制約，すなわち残渣にざくろ石が存在し斜長石を欠くという融解条件がどのような圧力（＝深度）で達成されるかは十分に拘束されておらず，今後適切な出発物質による高温・高圧実験で制約を与えて行く必要がある．

現在のところ瀬戸内火山岩類の珪長質火成岩類について今回見いだされた特徴は讃岐平野周辺以外では紀伊半島において確認している．今後より広域的に分析を進めたい．またスラブ融解一般についての理解を深めるためにピルバラクラトンの太古代TTGの中性子放射化分析も行った（下記成果欄参照）．このように西南日本弧の中新世火成岩の岩石成因を他地域と比較した研究を行うためにこのような分析も積極的に進めたい．

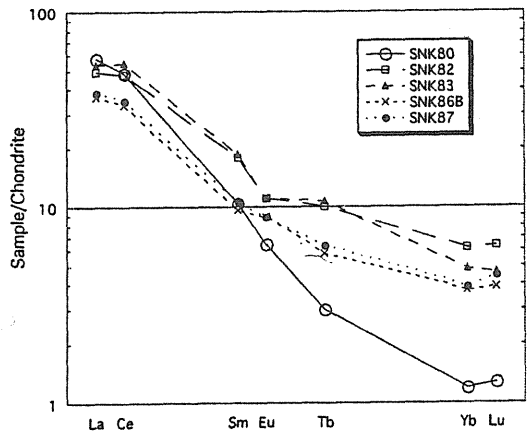


図２：讃岐平野周辺の珪長質な瀬戸内火山岩類のコンドライトで規格化した希土類元素パターン

4. 成果の公表

新正裕尚：愛媛県別子地域のS13試錐中で得られた流紋岩の全岩化学組成　東京経済大学人文自然科学論集114. 25-29. (2002).

新正裕尚：西オーストラリア，ピルバラクラトン東部のMuccan，Warrawagineバソリスの太古代花こう岩の中性子放射化分析　東京経済大学人文自然科学論集116.（2003印刷中）.

新正裕尚・折橋裕二・角井朝昭・岩野英樹・和田穣隆・檀原　徹：玉手山凝灰岩および室生火砕流堆積物の全岩化学組成：その給源への手掛り　日本火山学会秋季大会　2001年10月

新正裕尚・角井朝昭・折橋裕二・中井俊一：紀伊半島・讃岐平野に産する珪長質な瀬戸内火山岩類について　地球惑星科学関連学会2002年合同大会　2002年5月

研究テーマ：フィッショントラック法による環境試料中の核物質の検出
表　　題：フィッショントラック法を用いた微量核分裂性物質の分析

3-30

フィッショントラック法による天然ウラン含有粒子の検出（2）

江坂 木の実、江坂 文孝[1]、福山 裕康、小野寺 貴史、伊奈川 潤、井口 一成、李 致圭、
桜井 聡、臼田 重和、渡部 和男[1]

日本原子力研究所　環境科学研究部　環境技術開発グループ
[1]日本原子力研究所　環境科学研究部　分析科学研究グループ

国際原子力機関（IAEA）は保障措置強化策の一環として保障措置環境試料分析法を導入した。これは、原子力関連施設内で主に拭き取りにより採取した試料（スワイプ試料）中に含まれるウラン等の極微量核物質の同位体比を調べることにより、未申告の原子力活動がないことを検認するものである。現在、原研では環境試料に含まれる核物質の極微量分析技術の開発を進めており、すでに基本技術は確立され分析をはじめている[1)]。更なる分析の高度化の一環として、1μm以下の粒子のパーティクル分析を目的に、フィッショントラック法を用いた微小粒子の検出法を現在開発している。本報告では新たに開発した試料調製法[2,3)]と天然ウランを含む粒子を用いた実験の中からフィッショントラックによる粒子状態について述べる。

試料は原研施設内で採取したスワイプを用いた。ポリカーボネートメンブランフィルターおよびサポートスクリーンをプラスチックホルダー中に収納して粒子回収系（図1）を構成し、そのホルダーの一端を吸引ポンプに結合し、そのホルダーの他端の粒子吸引口をスワイプ試料にあてて吸引することにより、スワイプ試料中の粒子をメンブランフィルター上に捕集した。吸引処理後、粒子回収系のホルダーからポリカーボネートメンブランフィルターを取り出し、図2の手順で試料の調製を行った。まず、粒子が捕集されているフィルターを 1,2-ジクロロエタンおよびジクロロメタンの混合液で溶解した。この溶液をガラス板上に均一に延ばして乾燥させ、粒子をポリカーボネートに閉じ込めたフィルムを形成した。このポリカーボネートは固体飛跡検出器の役割を果たす。

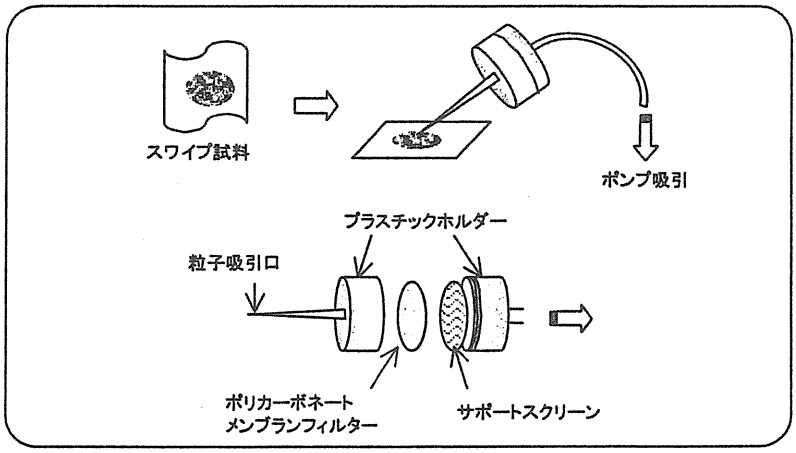


図1　粒子回収系

原子炉：JRR-4　　装　置：気送管　　分　野：放射化分析（環境科学）

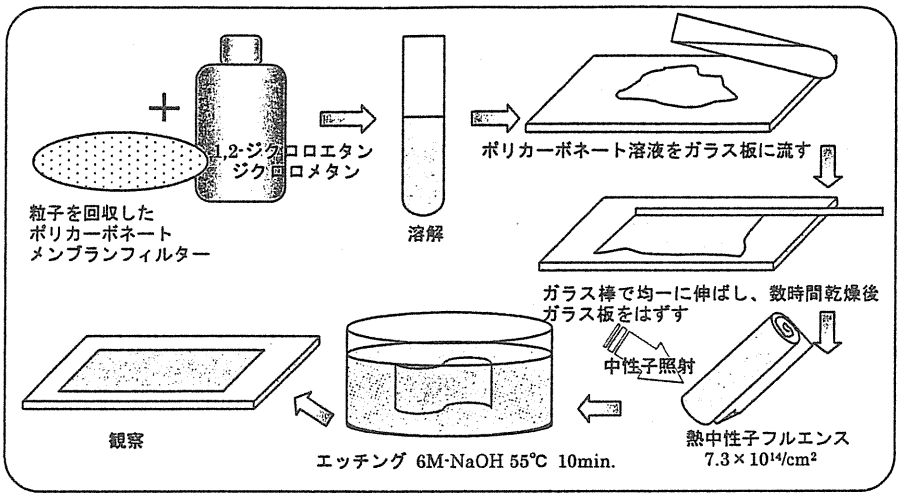


図2 フィッショントラック試料作製手順

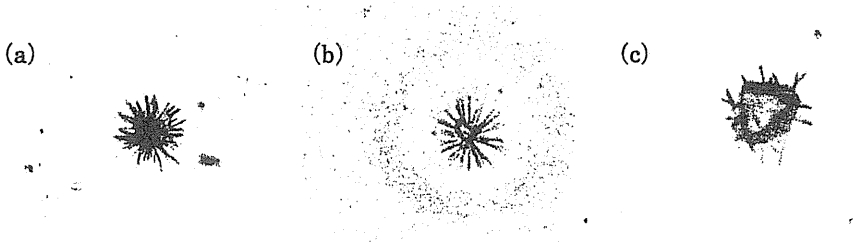


図3 フィッショントラック顕微鏡写真

フィルム試料はポリエチレン袋に封入し、熱中性子フルエンス 7.3×10^{14}/cm ^{2}で照射した。その結果、試料中の ^{235}U の誘導核分裂により、ポリカーボネート中に核分裂片による飛跡（フィッショントラック）が形成される。照射済試料の放射能が減衰した後、このフィッショントラックを明瞭にするため、55℃の 6N-NaOH 中で 10 分間エッチング処理した。試料は純水で十分に濯ぎ、乾燥させた後、顕微鏡観察した。

図 3 は、顕微鏡（400 倍）で観察した写真であり、フィッショントラックは 3 種類に分類することができた。(a) は粒子像が確認できないほど粒子全体からトラックが観察されていることから、ほぼウラン化合物で構成される粒子と考えられる。(b) は粒子像がはっきりと見え、右下奥を中心として後方に向かうトラックが観察される。非核分裂性物質でできた粒子の一部にウランが付着している粒子と考えられる。(c) はまばらなトラックが観察されることから、ウランが粒子中に低濃度に分散しており、天然起源と考えられる。従って（a）および（b）に含まれるウランは人工的に生成されたものである可能性があることから、保障措置を目的とする分析の対象となる。このように粒子とそこから生じるフィッショントラックの形状から、その粒子のウラン含有状態が推測でき、以後の分析に有用な情報を与える。今後は、本法を用いて検出した個々の粒子について、同位体比の正確な測定法の確立を目指す。

参考文献

1) S.Usuda et al. #192, Proc. INMM 44th Annual Meeting (2003)
2)発明考案「吸引回収された極微量核分裂性物質を含む粒子からフィッショントラック法の適用が可能なフィルム状の被検出試料を調製する方法」申請中.
3)江坂木の実 他 第 50 回応用物理学関係連合講演会予稿集, 28pYM-3 (2003), p135.

3-31 メスバウアー分光法による無機化合物の研究（IV）
Mössbauer Spectroscopic Studies on Inorganic Compounds IV

（東邦大学理学部）高橋 正，王 軍虎，西村 健，鈴木 勝也，北澤孝史，竹田満洲雄
Department of Chemistry, Toho University Masashi Takahashi, Jinhu Wang, Tatsuru Nishimura, Katsuya Suzuki, Takafumi Kitazawa, Masuo Takeda
（東京大学原子力研究総合センター）澤幡浩之，伊藤泰男
RCNST, The University of Tokyo Hiroyuki Sawahata, Yasuo Ito

メスバウアー効果は 45 元素，91 核種について観測されるが，鉄，スズおよびユウロピウム以外の元素については，市販の線源がないことや低温（通常液体窒素温度以下）での測定が必要なため，化学的には有益な情報を与えると期待されても，測定に用いられることが少ない．この研究は，そういった余りなじみのない元素のメスバウアー分光法を用いて，結合や構造に関する情報を得ることを目的としている．この 3 年間にわたる研究では，(a)新たに ^{161}Dy メスバウアー線源（^{161}Tb/GdF_3）を作成し，シアノ架橋高分子錯体の研究をおこなった，(b) ^{155}Gd メスバウアー分光法を用いて，ポリエチレングリコール錯体の結合に関する研究をおこなった，(c) ^{127}I メスバウアー分光を用いてヨードニウムイリドの結合について研究をおこなった．

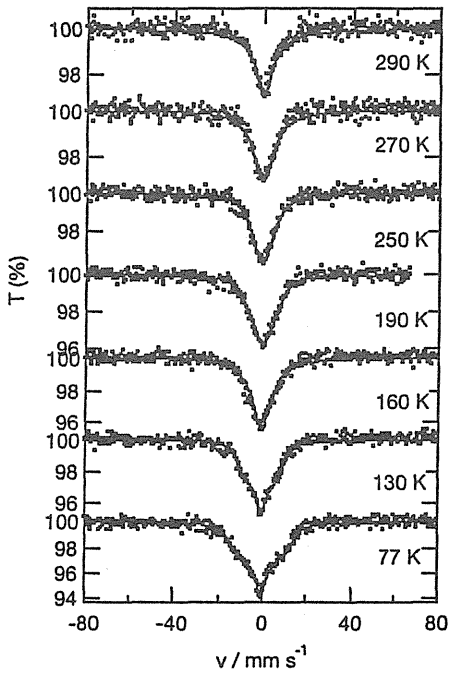


Fig. 1 ^{161}Dy Mössbauer spectra for $Dy[Fe(CN)_6]\cdot 4H_2O$ at various temperatures

I ^{161}Dy メスバウアー分光法

^{161}Dy はメスバウアー γ 線のエネルギーが低く室温でもスペクトルの観測が可能で，励起状態の寿命が比較的長いので線幅が狭く，かつ磁気モーメントが大きいという特色があり，数ある希土類元素のメスバウアー核種の中でも魅力的な核種である．われわれは最近希土類元素を含む超分子錯体の構造や磁性に興味を持ち，研究を行ってきた．^{161}Dy メスバウアー分光法はこのような研究に有用な研究手段であるので，本研究で取り組むことにした．

［実験］

線源の作成：$^{160}Gd_2O_3$ (98.2%) 90 mg とフッ化アンモニウム 173 mg を混合し，白金ボートに移してインコーネル管中，300°C で 12 時間反応させて $^{160}GdF_3$ 113 mg を得た．そのうちの 6 mg を φ3 mm のペレ

研究施設・装置：JRR-3 (BR-1, HR-2), JRR-4 (T-パイプ)，モニタリングケーブ，低温メスバウアー分光器
研究分野：メスバウアー分光法，錯体化学，有機金属化学，有機典型元素化学

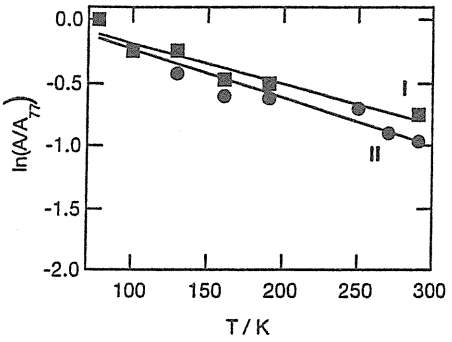


Fig. 2 Temperature dependence of the area (normalized to 78 K)

ットとしてから，低密度ポリエチレン（Aldrich 社，融点 90°C）の中に溶封した．これを JRR-3M HR-2 照射孔（ϕ = 1.4 x 10^{14} cm^{-2} s^{-1}）で 72 時間中性子照射を行い，$^{161}Tb/GdF_3$（242 MBq）を得た．線源は 3 週間程度測定に使用できた．

メスバウアースペクトルの測定：^{57}Fe と同じように線源を室温に保ち，30〜50 mgDy cm^{-2} の試料をガスフロー型クライオスタットの中に置いて，Wissel 社の駆動システム（DFG-1200, MDU-1200）を用いて測定した．線源の駆動速度は，レーザー干渉計（MVC-1200）を用いて測定した．

スペクトルの解析は I_g = 5/2−I_e = 5/2 の許容遷移に対して Sum-of-Lorentzian 近似で行った．異性体シフトの値は，線源を基準とした．

［研究成果］

シアン化物イオン CN^-は架橋配位子として，多様な 3 次元高分子錯体を構築することはよく知られている．特に$[Fe(CN)_6]^{n-}$ユニットを構成要素とするランタノイド錯体における d−f 相互作用が最近注目されている．我々はすでに Gd^{3+}と Fe^{2+}または Fe^{3+}を CN^-が架橋した錯体の研究を行っていたが，今回は $Dy[Fe(CN)_6]\cdot 4H_2O$ (I)，$KDy[Fe(CN)_6]\cdot 4H_2O$ (II)，$Dy[Co(CN)_6]$ (III)，$KDy[Ru(CN)_6]\cdot 4H_2O$ (IV)を取り上げることにした．Fe^{n+}は八面体構造で CN の C 末端が配位している．これに対して Dy^{3+}は正方ねじれプリズム型構造で，CN の N 末端六つと二つの配位水が Dy^{3+}に配位している．

Table 1 relaxation times and $M\Theta^2$ values for I — IV

comp	τ (77) (ns)	τ(290) (ps)	$M\Theta^2(^{161}Dy)$ (10^6 amu K^2)	$M\Theta^2(^{57}Fe)$ (10^6 amu K^2)
I	2	1	7.4	5.7
II	2	10	6.3	4.6
III	2	700		
IV	2	6		

図 1 に I の ^{161}Dy メスバウアースペクトルの温度変化を示す．室温ではほぼ Lorentzian の線形をしたシングレットの吸収であるが，温度が低くなるに従ってブロードとなって Lorentzaian からのずれが大きくなっていく．この線形の変化は常磁性緩和によるものである．そこで，Nowick-Wickman モデルにより緩和時間を求めたところ，77 K においては I〜IV とも 2 ns と見積もれらた．この値は低温で磁気分裂が観測される $DyCrO_3$ の同じ温度の値 50 ps よりも長くなっている．そこで II について 5 K でのスペクトルを測定したが，緩和時間はそれほど長くならず，磁気分裂は観測されなかった．

異性体シフト（線源基準）の値は，−0.32〜−0.59 mm s^{-1}であり，報告されている Dy^{3+}化合物（−0.07 mm s−1: Dy-EDTA, −0.46 mm s^{-1}: $Dy_2(SO_4)_3$）と大きな違いはなかった．

格子力学的な知見を求める目的で，I と II について面積強度の温度変化（図 2）をもとに，分子間力のパラメータ $M\Theta^2$ の値を求めた．結果を表 1 にまとめた．$M\Theta^2$ の値は I の方が若干大きい．これは IR スペクトルの CN^-の伸縮振動の波数が I の方が II よりも大きいことと一致しており，格子の固さを反

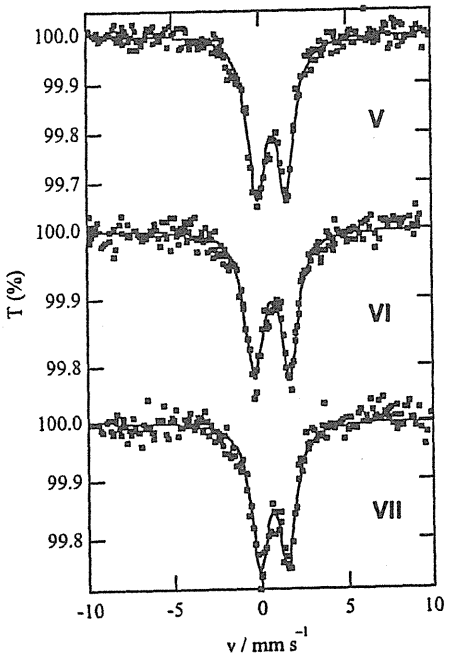


Fig.3 ^{155}Gd Mössbauer Spectra at 12 K for Gd(III)-PEG Complexes

映しているといえる．表には ^{57}Fe メスバウアースペクトルの温度変化を測定して求めた ^{57}Fe の $M\Theta^2$ の値も示した．二つの $M\Theta^2$ の値は一致してよいように思われるが，^{57}Fe の方の値が小さくなっている．おなじ傾向は同形の Eu 錯体についても報告されている．その原因としては，Dy^{3+}および Eu^{3+}は八位配位であるのに対して Fe^{n+}は 6 配位であるため，Ln^{3+}の方が結晶内でより強く束縛されているためと，今のところ考えている．

II ^{155}Gd メスバウアー分光法

^{155}Gd メスバウアースペクトルの特色は，異性体シフトと四極結合定数から，電荷分布や結合についての議論ができることにある．本研究では，ポリエチレングリコール（PEG）錯体の構造に関する研究を行った．PEG は抽出剤としての用途があり，アクチノイドとの錯体は放射性廃棄物の再処理との関連も考えられ興味深い．アクチノイド錯体の研究を始める前に，ランタノイド錯体について再検討することを目的に行った．

Table 2 ^{155}Gd Mössbauer parameters and calculated V_{zz}

comp	δ	e^2qQ	$V_{zz\,cal}$
	mm s^{-1}	mm s^{-1}	10^{20} V m^{-2}
V	0.68	3.53	1.64
VI	0.65	4.34	1.93
VII	0.67	3.37	0.327

［実験］

線源：前回報告した ^{155}Eu/$SmPd_3$ 線源（半減期 1.81 y）を引き続き測定に使用した．

［研究成果］

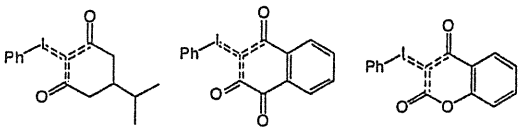
PEG として H $(OC_2H_4)_nOH$ (n = 3—5)および $Me(OC_2H_4)_mOMe$ (m = 2—4) の Gd(III) 錯体 $Gd(NO_3)_3L(H_2O)_x$, $[GdL(H_2O)_3](ClO_4)_3$ を合成し，結晶構造解析を行なった．これらの錯体において，PEG はすべての酸素原子が配位し，硝酸イオンの配位様式（単座もしくは二座配位）と配位水の数を調整することで，錯体は 10 配位構造をとっていた．結晶構造が明らかになった錯体のうち，メスバウアー測定に必要な量の試料を合成できた$[Gd(\eta^2\text{-}NO_3)_2(\eta^1\text{-}NO_3)(EO_4)]$ (V)，$[Gd(\eta^2\text{-}NO_3)_2(EO5)]NO_3$ (VI)，$[Gd(EO5)(H_2O)_3](ClO_4)_3$ (VII)（EO4 = $H(OC_2H_4)_4OH$, EO5 = $H(OC_2H_4)_5OH$）のメスバウアー測定を行なった．12 K でのスペクトルを図 3 に示した．いずれも四極相互作用によって，分裂したスペクトルを与えた．

今回の測定で得られた異性体シフトの値は 0.65 — 0.68 mm s^{-1} であり，これらの値はβ-ジケトナト錯体が示す値の範囲内に分布している．四極結合定数（e^2qQ）は，Gd 核位置での電場勾配の大きさを反映している．Gd^{3+}の電子配置は $4f^7$ なので，1 次

近似として 4f が電場勾配に寄与しないとすると，電場勾配の起源はいわゆる格子の寄与，すなわちイオン性の配位子や対イオンによるものと考えることができる．PEG は中性の配位子であるので，NO_3^- や ClO_4^-が電場勾配に寄与しているとして，点電荷モデルを用いて V_{zz} の値を計算してみると表 2 のようになった．V と VI の e^2qQ 関係は点電荷モデルの値とよく一致している．しかしながら VII は点電荷モデルによれば V や VI よりも一桁小さな e^2qQ の値を示すと予想されるが，実際は V と同程度の値であった．そこで PEG も分極していて酸素原子が負電荷を帯びているとして，点電荷モデルの計算を繰返してみたが，実測の関係を再現することはできなかった．これらのことは，おそらく 4f 軌道に電子が均等に分布しているという仮定が成立しないこと，すなわち 4f 電子も化学結合に関与して，ポピュレーションに差があることを示唆していると考えている．実際，化学結合に 4f 電子が寄与していると最近考えられるようになってきている．

III ^{127}I メスバウアー分光法

ヨウ素はハロゲンの中では高原子価の化合物を作りやすく，いろいろな高原子価ヨウ素化合物が知られている．ヨウ素と炭素原子間に二重結合を持つ構造が可能なヨードニウムイリド VIII–X におけるヨウ素の電子状態の研究を，^{127}I メスバウアー分光法を用いておこなった．



VIII　　IX　　X

［実験］

メスバウアー線源 ^{127m}Te / Mg_3TeO_6（1.6 GBq，半減期 109 d）は，^{126}Te から調製した $Mg_3{}^{126}TeO_6$ を JRR-3M BR-1 で 1 サイクル照射，2 ヶ月クーリング後，Al 箔を用いて密封して作成した．メスバウアース

Table 3 ^{127}I Mössbauer parameters and valence electron populations for iodonium ylides and related iodine compounds.

comp.	δ mm s^{-1}	e^2qQ mm s^{-1}	η	N_s	N_x	N_y	N_z	N_t	Z_I
VIII	–0.51	39.4	0.51	1.91	1.34	1.07	2.00	6.31	+0.69
				1.86	1.24	0.97	1.90	5.96	+1.04
IX	–0.45	39.4	0.45	1.86	1.26	0.99	2.00	6.11	+0.89
				1.81	1.16	0.89	1.90	5.76	+1.24
X	–0.53	39.4	0.51	1.93	1.34	1.07	2.00	6.32	+0.69
				1.86	1.24	0.97	1.90	5.97	+1.03
Ph_2ICl	=0.64	42.8	0.40	1.93	1.25	1.02	2.00	6.19	+0.81
Ph_2IBr	–0.66	42.8	0.38	1.93	1.24	1.02	2.00	6.19	+0.81
$PhICl_2$	–0.87	54.0	0.75	1.93	1.18	0.63	2.00	5.74	+1.26

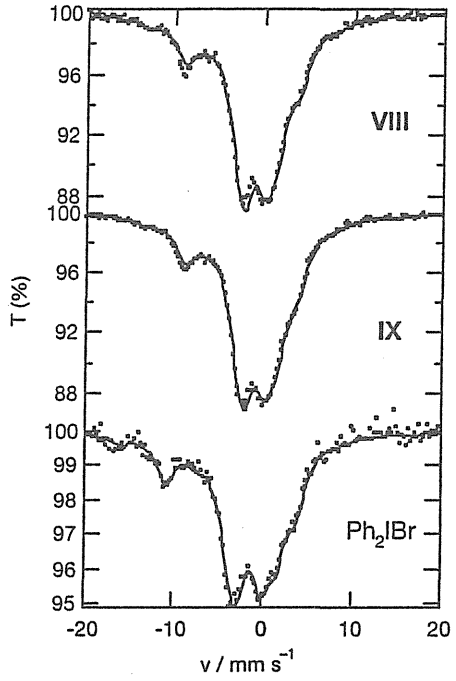


Fig. 4 ^{127}I Mössbauer spectra for iodonium ylides and diphenyliodonium bromide

ペクトルの測定は，大学開放研の低温メスバウアー測定装置を用いて行なった．

［研究成果］

20 K でのメスバウアースペクトルを図4に示す．これらのスペクトルは互いに似ているが，またジフェニルヨードニウムハライド Ph_2IX とも似ている．これはヨードニウムイリド中のヨウ素の電子状態がV 字形をした Ph_2I^+ に近いことを示唆している．解析によって得られたメスバウアーパラメータと Towns–Dailey の取り扱いにより見積もったヨウ素原子の価電子のポピュレーションを表 3 にまとめた．表から VIII—X の電子分布は I—C 結合を二つもつ Ph_2IX に近いことが再確認できる．このことはヨードニウムイリドのヨウ素と炭素原子の結合には二重結合性がほとんどないことを示している．表の価電子のポピュレーションの計算にあたっては，面外方向の軌道の孤立電子対で空孔がないとして計算している．I—C 間に二重結合性があると，p_z 軌道にホールが存在することになるので，仮に 0.1 個の電子が 2 重結合に関与しているとして，価電子のポピュレーションを再計算してみると，ヨウ素原子上の電荷 Z_I が+1.04 — 1.24 となった．この Z_I は $PhICl_2$ のように電子吸引性の基がヨウ素原子に結合しているときに見られるものであり，配位原子には炭素原子しかない VIII — X では，考えにくいことである．したがって，ヨードニウムイリドにおけるヨウ素ー炭素原子間の二重結合性は高々0.1 e 分ということになり，重要でないことが明らかになった．

成果の公表

学術雑誌

1. S. K. Bhargava, F. Mohr, M. Takahashi, M. Takeda, *Bull. Chem. Soc. Jpn.*, **74**, 1051 – 53 (2001): ^{197}Au Mössbauer spectroscopy studies of some cyclometalated gold dimers.
2. J. Wang, M. Takahashi, M. Takeda, *Bull. Chem. Soc. Jpn.*, **75**, 735 – 740 (2002): Crystal structures and ^{166}Er Mössbauer spectrafor some β-diketonatoerbium(III) complexes.
3. J. Wang, J. Abe, T. Kitazawa, M. Takahashi, M. Takeda, *Z. Naturrforsch.*, **57a**, 581 – 585 (2002): ^{155}Gd Mössbauer spectroscopic study of $GdM(CN)_6{\cdot}4H_2O$ (M = Cr^{III}, Fe^{III} and Co^{III}) and $GdM(CN)_6{\cdot}3H_2O$ (M = Fe^{II} and Ru^{II}).
4. J. Wang, M. Takahashi, T. Kitazawa, M. Takeda, *J. Radioanal. Nucl. Chem.*, **255**, 195 – 199 (2003): ^{155}Gd Mössbauer spectra of some Gd(III)–β-diketonato complexes.
5. M. Takeda, M. Takahashi, K.-y. Akiba, S. Kojima, *J. Radioanal. Nucl. Chem.*, **255**, 275 – 278 (2003): The relation between Sb–I bond lengths and charges on iodine atoms determined by ^{127}I Mössbauer

spectroscopy.

6. K. Suzuki, T. Kitazawa, M. Takahashi, M. Takeda, *J. Radioanal. Nucl. Chem.*, **255**, 305 – 309 (2003): ^{161}Dy Mössbauer spectra for cyano coordination polymer compounds.
7. T. Nishimura, H. Iwasaki, M. Takahashi, M. Takeda, *J. Radioanal. Nucl. Chem.*, **255**, 499 – 502 (2003). ^{127}I Mössbauer spectra for phenyliodonium ylides.
8. 高橋　正，王　軍虎，北澤孝史，竹田満洲雄，放射化学ニュース，7，1 – 6 (2002): 希土類化合物のメスバウアー測定.

国際学会講演

1. T. Kitazawa, J. Abe, M. Takahashi, M. Takeda, 2000 International Chemical Congress of Pacific Basin Societies, Honolulu, USA (Dec. 2000): ^{155}Gd Mössbauer spectroscopic study of hexacyanometalates(II and III) compounds containing Gd^{3+}.
2. J. Wang, H. Otobe, A. Nakamura, M. Takeda, 2000 International Chemical Congress of Pacific Basin Societies, Honolulu, USA (Dec. 2000): ^{155}Gd Mössbauer spectroscopic and powder x-ray diffraction studies on $Gd_xZr_{1-x}O_{2-x/2}$ solid solutions.
3. F. Mohr, S. K. Bhargava, M. Takeda, M. Takahashi, 2000 International Chemical Congress of Pacific Basin Societies, Honolulu, USA (Dec. 2000): Novel oxidative addition reactions of binuclear cyclometalated gold compounds studied by ^{197}Au Mössbauer spectroscopy (Invited).
4. M. Takahashi, H. Ikezawa, M. Takeda, H. Sawahata, Y. Ito, XVI International Symposium on Nuclear Quadrupole Interactions, Hiroshima (Sep. 2001): Electronic state for hypervalent oranoiodine(III) compounds (dichloroiodo)benzenes through ^{127}I Mössbauer spectroscopy.
5. J. Wang, J. Abe, T. Kitazawa, M. Takahashi, M. Takeda, XVI International Symposium on Nuclear Quadrupole Interactions, Hiroshima (Sep. 2001): ^{155}Gd Mössbauer spectroscopic study of $GdM(CN)_6{\cdot}4H_2O$ (M = Cr^{III}, Fe^{III} and Co^{III}) and $GdM(CN)_6{\cdot}3H_2O$ (M = Fe^{II} and Ru^{II}).
6. J. Wang, Y. Nomoto, Y. Nemoto, M. Takahashi, M. Takeda, 2001 Asia-Pacific Symposium on Radiochemistry and the Annual Meeting of the Japan Society of Nuclear and Radiochemical Sciences, Fukuoka (Oct. 2001): Erbium-166 Mössbauer spectra of Er(III)-EDTA complexes.
7. J. Wang, M. Takahashi, T. Kitazawa, M. Takeda, 2001 Asia-Pacific Symposium on Radiochemistry and the Annual Meeting of the Japan Society of Nuclear and Radiochemical Sciences, Fukuoka (Oct. 2001): ^{155}Gd Mössbauer spectra of some Gd(III)–β-diketonato complexes.
8. M. Takeda, M. Takahashi, K.-y. Akiba, S. Kojima, 2001 Asia-Pacific Symposium on Radiochemistry and the Annual Meeting of the Japan Society of Nuclear and Radiochemical Sciences, Fukuoka (Oct. 2001): The relation between Sb–I bond lengths and charges on iodine atoms determined by ^{127}I Mössbauer spectroscopy.
9. K. Suzuki, T. Kitazawa, M. Takahashi, M. Takeda, 2001 Asia-Pacific Symposium on Radiochemistry and the Annual Meeting of the Japan Society of Nuclear and Radiochemical Sciences, Fukuoka (Oct. 2001): ^{161}Dy Mössbauer spectra for cyano coordination polymer compounds.
10. T. Nishimura, H. Iwasaki, M. Takahashi, M. Takeda, 2001 Asia-Pacific Symposium on Radiochemistry and the Annual Meeting of the Japan Society of

Nuclear and Radiochemical Sciences, Fukuoka (Oct. 2001): ^{127}I Mössbauer spectra for phenyliodonium ylides.

学会講演

1. 北澤孝史，阿部純子，高橋　正，竹田満洲雄，第 44 回放射化学討論会，神戸（2000.9）：3 次元錯体 $GdM(CN)_6{\cdot}nH_2O$ および $KGdM(CN)_6{\cdot}nH_2O$ の ^{155}Gd メスバウアースペクトル.
2. 王　軍虎，高橋　正，竹田満洲雄，第 37 回理工学における同位元素研究発表会，東京（2000.7）：ガドリニウム(III) β−ジケトン錯体の ^{155}Gd メスバウアースペクトル.
3. 王　軍虎，高橋　正，竹田満洲雄，第 44 回放射化学討論会，神戸（2000.9）：ガドリニウム(III) アセチルアセトン誘導体の ^{155}Gd メスバウアースペクトルと結晶構造.
4. 高橋　正，Mohr F.，Bharagava S.K.，竹田満洲雄，日本化学会第 79 春季年会，神戸（2001.3）：環状二核金錯体の ^{197}Au メスバウアースペクトル.
5. 高橋　正，西村　健，竹田満洲雄，日本化学会第 79 春季年会，神戸（2001.3）：フェニルヨードニウムイリド化合物の ^{127}I メスバウアースペクトル.
6. 西村　健，高橋　正，北澤孝史，竹田満洲雄，日本化学会第 81 春季年会，東京（2002.3）：ポリエチレングリコールを配位子とする硝酸ガドリニウムの大環状錯体の構造と ^{155}Gd メスバウアースペクトル.
7. 鈴木勝也，北澤孝史，高橋　正，竹田満洲雄，日本化学会第 81 春季年会，東京（2002.3）：二核金属錯体 $[Dy(DMF)_4(H_2O)_3Fe(CN)_6]$ (DMF = Dimethylformamide) の ^{161}Dy および ^{57}Fe メスバウアー分光法による研究.
8. 鈴木勝也，北澤孝史，高橋　正，竹田満洲雄，2002 日本放射化学会年会・第 46 回放射化学討論会，札幌（2002.9）：4,4'-ビピリジン *N,N'*-オキシドを架橋配位子にもつ Gd 錯体の構造および ^{155}Gd メスバウアースペクトル
9. 西村　健，高橋　正，竹田満洲雄，2002 日本放射化学会年会・第 46 回放射化学討論会，札幌（2002.9）：非環状配位子ポリエチレングリコール類のガドリニウム錯体の構造と ^{155}Gd メスバウアースペクトル.

研究テーマ：土壌群別分配係数とその変動要因に関する研究
表　　題：青森県の耕作土壌における安定元素の分配係数
3-32

青森県における土壌群別の塩素分配係数

塚田祥文、武田晃、久松俊一、稲葉次郎
環境科学技術研究所　環境動態研究部
青森県上北郡六ヶ所村大字尾駮字家ノ前 1-7

1. 緒言　土壌中放射性核種は、土壌溶液を介して移行し、農作物や地下水へ移行する。そのため、土壌中における固相－液相間の分配係数（土壌中濃度/土壌溶液中濃度の比; Kd 値）は、放射性核種の移行・動態を推測するうえで、極めて重要な環境移行パラメータである。IAEA (1994) によれば、Kd 値は土質に依存した値を示すとされるものの、同類とされる土壌群でも 3～5 桁の変動を示し、移行挙動の評価には、局地域に適した Kd 値を用いることが必要となる。塩素は環境中での移行性に富み、動植物の必須元素である。塩素の放射性同位体のうち ^{36}Cl は超長半減期 (3.0×10^5 y) であり、被ばく線量評価上重要な放射性核種である（核燃料サイクル開発機構, 2000）。しかしながら、塩素の Kd 値に関する報告例は極めて限られており、IAEA (1994) でも取り上げられていない。本研究では、青森県に存在する 12 種類の土壌群から土壌試料を採取し、塩素の Kd 値を求め、比較・検討を行った。

2. 実験　県内に存在する 12 種類の土壌群の耕作土壌を 158 地点から採取した。採取後速やかに高速遠心 (15000 g) により土壌から間隙水を分離し Kd 値を求めた（間隙水法）。また、一般的な分配係数測定法として用いられているバッチ法は、風乾土壌に超純水を固液比 10 の割合で加えて 24 時間接触し、液相を分離して求めた。土壌中塩素濃度は非破壊放射化分析、溶液中塩素濃度はイオンクロマトグラフにより定量した。

3. 結果および考察　岩屑土（1 試料）を除く 11 土壌群について、土壌中塩素濃度を図 1 に示した。我が国における代表的な畑作土壌の火山灰土壌である黒ボク土（青森県における耕作土壌の約 46% を占める）における土壌中塩素濃度の平均値は、270 mg kg^{-1} であり、それと有意な差が認められた土壌群は、灰色低地土、グライ土、褐色森林土および泥炭土であり、黒ボク土より低い値であった。そのうち、褐色森林土を除く 3 種類の土壌群は一般に水田として利用され、一方、黒ボク土が畑土として利用されていることから、これら土壌群に

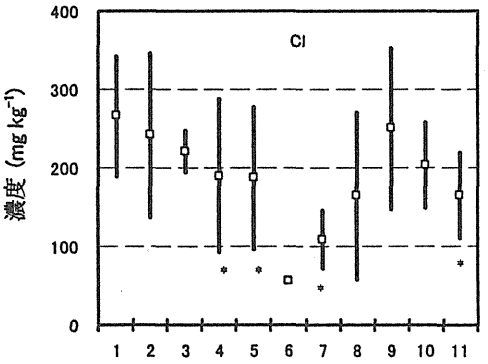


図 1　青森県の土壌群別土壌中塩素濃度
算術平均値±1σ
1. 黒ボク土, 2. 多湿黒ボク土, 3. 黒ボクグライ土, 4. 灰色低地土, 5. グライ土, 6. 砂丘未熟土, 7. 褐色森林土, 8. 黄色土, 9. 褐色低地土, 10. 黒泥土, 11. 泥炭土.
* 黒ボク土と有意な差が認められたもの ($p<0.05$).

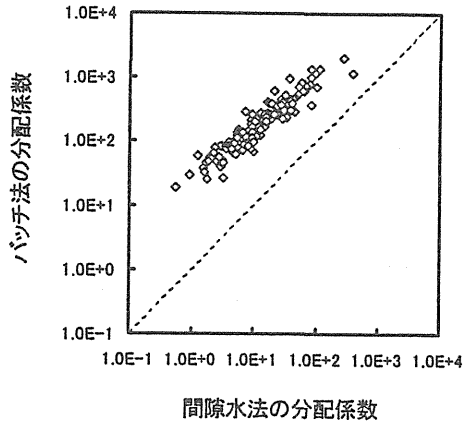


図2 間隙水法とバッチ法による塩素分配係数の比較

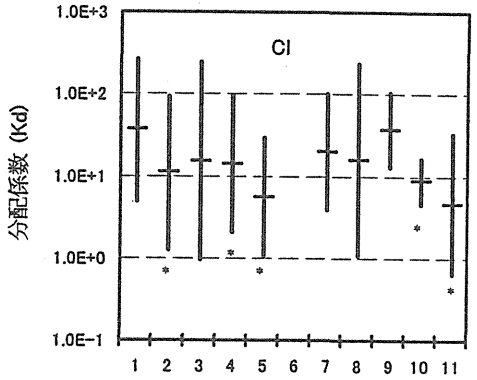


図3 土壌群別塩素の分配係数
幾何平均値および±95%信頼区間
1. 黒ボク土, 2. 多湿黒ボク土, 3. 黒ボクグライ土, 4. 灰色低地土, 5. グライ土, 6. 砂丘未熟土, 7. 褐色森林土, 8. 黄色土, 9. 褐色低地土, 10. 黒泥土, 11. 泥炭土.
* 黒ボク土と有意な差が認められたもの ($p<0.05$).

よる塩素濃度の差は利用形態の違いによることも考えられる。

間隙水法による全試料の Kd 幾何平均値は 12、95%信頼区間は 1.2-130 の 2 桁の変動範囲にあった。一方、バッチ法により求めた Kd 幾何平均値は 190（95%信頼区間; 28-1200）であり、間隙水法とバッチ法による両者の Kd は良い相関を示し、バッチ法の Kd 値が約 1 桁高かった（図 2）。固液比を 10 に補正して両者の Kd 値を比較すると同等な値を示した。土壌中固相から液相に溶出する塩素は、それぞれの土壌で固有の値（0.1～52%）を示すが、固液比に係わらず土壌中塩素の一定量が溶出していると考えられる。

間隙水法による Kd 値を黒ボク土と、各土壌群間で比較すると、多湿黒ボク土、灰色低地土、グライ土、黒泥土および泥炭土で有意な差が認められ（図 3）、土壌の利用形態（特に灌漑水の利用）と密接な係わりがあると思われる。塩素の Kd 値は、IAEA（1994）等で報告されている他の元素と比較すると数桁低い値を示すことから、土壌中での塩素は移行性に富んでいることが示された。

本調査では、土壌中での塩素の移行動態を精度良く評価するために、土壌群別に現実的な Kd 値（間隙水法）とバッチ法による Kd 値を求め比較した。これにより、固液比によらず土壌中塩素の一定量が土壌溶液中に溶出することが明らかになった。塩素は、動植物にとって必須元素であることからも、表層土壌を含む生物圏における分布と挙動を明らかにすることは、被ばく線量評価上極めて重要な課題である。

原子炉：JRR-3・JRR-4　　装置：気送管　　分野：放射化分析（環境科学）

本調査は、青森県からの委託事業により得られた成果の一部である。

3-33 核壊変原子を用いた化学状態分析
－K_2CrO_4 固相中での Cr(Ⅲ)イオンの熱アニーリング反応－

Chemical State Analysis by Means of Nuclear Decay
－ Thermal Annealing Reaction of Cr(Ⅲ) in K_2CrO_4 Solid Phase －

玉木 洋一（宮城教育大学）
Yoichi TAMAKI (Miyagi Univesity of Education)

K_2CrO_4 固相中に Cr(Ⅲ)イオンをドーピングし，加熱により，Cr(Ⅲ)イオンが酸化される熱アニーリング反応について検討した。K_2CrO_4 と Cr(Ⅲ)の成分比を変化させた実験では，酸化反応や Cr(Ⅲ)化学種の成分の変化に違いが見られ，マトリックス効果があることが見いだされた。また，窒素雰囲気下では反応は全く進行せず，熱アニーリング反応は大気中の酸素の関与により進行することが明らかになった。

1．はじめに

K_2CrO_4 固相中に Cr(Ⅲ)イオンを導入し、加熱すると Cr(Ⅲ)イオンは Cr(Ⅵ)に酸化される反応が起こる。この熱アニーリングによる反応はホットアトム反応や^{51}Cr をトレーサーとしたドーピングにより以前から研究されてきている。この反応では、Cr(Ⅲ)イオンの酸化反応は数十分で進む速い反応とその後の遅い反応が起こっており、Cr(Ⅲ)化学種の変化と反応機構についての検討もなされている。

しかし、これまでの熱アニーリング反応では、ホットアトム反応のキャリアーフリーの状態から、^{51}Cr トレーサーを用いたドーピングによる反応までマトリックスである K_2CrO_4 と Cr(Ⅲ)イオンの組成比は大きく変化し、不明確であった。固相中では、組成比の小さい Cr(Ⅲ)イオンはマトリックスである K_2CrO_4 が周囲にあり、Cr(Ⅲ)イオンはこの影響を受けるものと考えられるがこれまでマトリックスの影響についての検討はなされていない。

本研究では、K_2CrO_4 と Cr(Ⅲ)イオンのモル比を変えて熱アニーリング反応を行い，マトリックス効果の存在について検討を行った。また，これまでの研究ではこの反応は大気中で 行われている。熱アニーリングによる酸化反応への空気中の O_2 の寄与について検討するため，反応雰囲気を N_2 に変えて行った結果についても報告する。

2．実験

2．1 試料調製

^{51}Cr 標識化合物は K_2CrO_4 を照射試料として JRR-4 で熱中性子照射を行って得た。この試料を用いて還元反応を行い，所定濃度の^{51}Cr 標識 $Cr(ClO_4)_3$ 溶液を調製した。この溶液では Cr(Ⅲ)イオンは 6 水和物のモノマー及びダイマーとして存在している。ドーピングはマトリックスである K_2CrO_4 粉末に Cr

研究設備 JRR-3 水力照射設備　　研究分野 放射化学 分析化学

$(ClO_4)_3$ 溶液を滴下し，常温で真空乾燥する方法で行った。K_2CrO_4 と Cr(Ⅲ)イオンのモル比は約 3000：1 であった。

モル比の小さい系での実験は非放射性の試料で行った。上記と同様の方法で K_2CrO_4 から $Cr(ClO_4)_3$ 溶液を調製し，ドーピングを行った。K_2CrO_4 と Cr(Ⅲ)イオンのモル比が 100:1 と 10:1 の２種類の試料を作成した。

２．２　熱アニーリングと化学種の分離

大気中での熱アニーリングは恒温槽中でそれぞれ 200，220，240 ℃で行い，時間を追って試料を採取し，化学種分離を行った。窒素雰囲気での熱アニーリングでは，モル比 10:1 の試料を用い，試料を脱気した後，窒素ガスを流しながら 220 ℃で加熱する方法をとった。

熱アニーリング後の試料はカラム法による陽イオン交換分離法を用いて，化学種分離を行った。陽イオン交換樹脂は Dowex 50W-X8 を用い，溶離液を pH=1.5$HClO_4$ 溶液，4M$HClO_4$ 溶液，6M HCl 溶液，2M NaOH 溶液と順次代えて溶離した。それぞれの溶離液では CrO_4^{2-}イオン（Cr(VI)），Cr(Ⅲ)イオンモノマー（Cr(Ⅲ)-M），Cr(Ⅲ)イオンダイマー（Cr(Ⅲ)-D），Cr(Ⅲ)ポリマー（Cr(Ⅲ)-P）が溶離してくる。溶離後，それぞれの溶離成分は，^{51}Cr 標識試料については，壊変に伴う 325keV γ線を NaI(Tl)検出器で測定し，非放射性の試料については，ゼーマン原子吸光分析装置によって定量した。

３．結果と考察

３．１　熱アニーリング反応のマトリックス効果

^{51}Cr 標識試料，240 ℃熱アニーリングよる化学種の時間変化を図１示す。

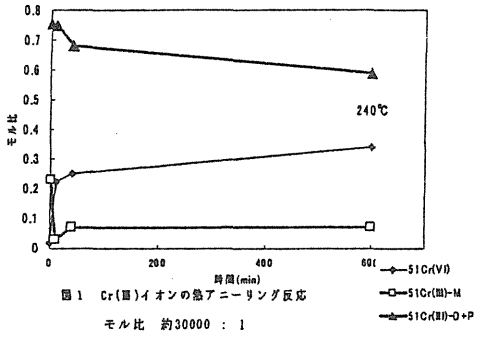


図１　Cr(Ⅲ)イオンの熱アニーリング反応
モル比　約30000　：　1

モル比の大きな系では約 60 分までの速い反応により ^{51}Cr(Ⅲ)-M は急激に減少し，これに対応して ^{51}Cr(VI)が増加している。その後の遅い反応では ^{51}Cr(Ⅲ)-M,D が徐々に減少し，^{51}Cr(VI)が増加している。この変化は他の加熱温度でも同様であった。また，モル比 100:1 でも図１と同様の結果を得た。

モル比 10:1 の結果を示す。

図２は Cr(VI)成分の時間変化を，図３には Cr(Ⅲ)成分の時間変化を示した。

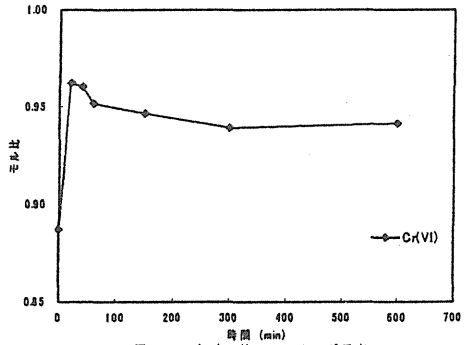


図２　Cr(Ⅲ)の熱アニーリング反応
モル比 10:1　加熱温度 240℃

図２では Cr(VI)成分は速い反応では急に増加するものの，長時間の熱アニーリングでは緩やかに減少しており，モル比の大きい図１とは異なる結果となった。この Cr(VI)成分の減少は図３に示されるように，Cr(Ⅲ)成分のうち Cr(Ⅲ)-D の増加と対応している。この違いは他の加熱温度でも得られている。また、熱アニーリング開始後の速い反応においてもその成分化学種の変化に違いが見られ

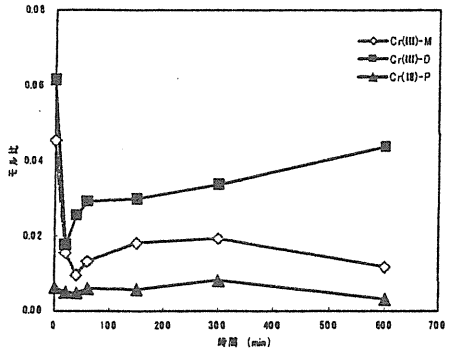


図3 Cr(Ⅲ)の熱アニーリング反応
モル比 10:1 加熱温度 240℃

た。これらの結果より，Cr(VI)成分マトリックスと Cr(Ⅲ)イオンのモル比の違いによりドーピングされた Cr(Ⅲ)イオンの熱アニーリング反応に違いがあり，マトリックス効果があることが示された。

3．2 反応雰囲気の熱アニーリング反応への影響

窒素雰囲気下での熱アニーリング反応の結果を図4に示す。

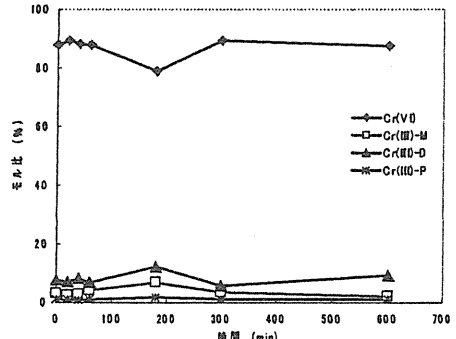


図4 窒素気流中でのCr(Ⅲ)の熱アニーリング反応
モル比10：1 加熱温度220℃

大気中での反応とは全く異なり Cr(VI)成分の増加は見られず，酸化反応は進行していない。また Cr(Ⅲ)化学種全体についても変化はなく，モノマー，ダイマー，ポリマーの成分比もほぼ一定であった。大気中での反応とのこの大きな違いから，熱アニーリング反応は大気中の酸素が関与する反応であり，マトリックスの K_2CrO_4 だけでは反応は進行しないことが明らかになった。

4．まとめ

本研究により，マトリックスとドーピングイオンとの反応はそのモル比によって異なることが示された。また，これまでの同様の系での熱アニーリング反応は空気中で行われており，今回の窒素雰囲気下での結果はマトリックスの K_2CrO_4 との反応だけではなく，空気中の酸素が大きく関わっていることを示している。これまでの実験で障害であったドーピング試料の組成の不確かさなどの問題を解決し，今後，酸素分圧を変化させた反応を行うなどして，固相中での酸化反応の機構を解明して行きたい。

成果発表

玉木他：クロム酸カリウム固相中での Cr(Ⅲ)イオンの熱アニーリング反応，化学系7学協会連合東北地方大会（2000 年 9 月，秋田大学）内容の一部を口頭発表。

研究テーマ：RI 放射線技術者の養成
表　　題：実習　放射化分析

3-34

米の微量元素放射化分析

Neutron activaton analysis of trace elements in rice

櫛田浩平、上沖　寛
国際原子力総合技術センター

国際原子力総合技術センターでは国内向けの各種研修コースの他、主に東南アジア諸外国を対象に原子力・放射線に関する研修事業を行っている。本実験はその中の「指導教官研修」としてベトナムおよびインドネシアからの研修生を対象として行った研修実験である。

研修生は将来自国における指導教官となるべき立場の人であり、本実験を通して放射化分析の基本理論と実験の具体的プロセスを体験し理解してもらうことを目指している。また本実験を通して非密封放射性同位元素の安全取扱いに習熟することも重要な課題である。

この実験では身近な環境試料として玄米および白米（50%精米）を選んだ。試料は予め120℃で乾燥し、JRR-3 PN-3 パイプで 3 分照射した。試料と連続して、中性子フラックスモニター（金）および Mn 標準試料を照射した。

照射後の試料は JRR-3 付属の放射化分析室ですぐに開封し、Ge 測定器で放射能を測定した。今回対象とする元素は短寿命核種であり、7 分から 11 分程度の冷却時間をおいて、500 秒測定した。測定距離は 10 cm。

この照射孔の中性子束は公称 $1.5\times10^{13}/cm^2s$ であるが、モニターによる測定では $1.41\times10^{13}/cm^2s$ という値を得た。

実験データの解析の結果、^{24}Na, ^{27}Mg, ^{28}Al, ^{38}Cl, ^{42}K, ^{49}Ca, ^{56}Mn, ^{59}Fe, ^{66}Cu などを検出した。主な元素の定量結果を表 1 に示す。

金属としては Mg および K が多く含まれ、Al も比較的に多かった。

表 1　米中の微量元素定量結果

元素	ppm（玄米）	ppm（白米）
Na	16	14
Mg	2682	1350
Al	603	374
K	2090	1310
Mn	19	13

解析結果が示すように、米の中の微量元素は白米にしたときよりも玄米の中に多く含まれることが分かる。表中の元素では、玄米／白米の比が 1.2 から 1.9 であった。その他のビタミン類も白米よりも玄米に多く含まれていることが分かっているが、微量金属も同様であることが確認できた。しかし環境汚染物質としての有害金属がある場合は、玄米に多く含まれることになり、注意が必要である。

今回は特に Mn に注目し、その標準試料を用いて定量した。表中の Mn のデータは標準試料による相対法の定量結果であるが、フラックスモニターから得られた中性子束を用いて計算した絶対法による定量結果との違いは 10%ほどであった。

標準的な米の含有量データと比較すると、今回のデータでは Mg、Al の含有量が多く、逆に Mn の量は少ない結果であった。これは今回用いた試料が得られた水田の土壌特性に依存した結果と考えられる。

本実習実験を通して、研修生が放射化分析の基本理論と実験上の主要なプロセスを理解することができたと思われる。

原子炉：JRR-3　　装置：気送管　　分野：放射化分析（環境科学）、教育

4. 原子炉材料照射試験

4. Irradiation Test of Reactor Materials

This is a blank page.

研究テーマ；原子力材料の照射効果の研究
表　　題：固体増殖材からのトリチウム放出挙動

4-1

多孔性 Li 2O焼結体からのトリチウム放出：トリチウムトラップの等温焼鈍

谷藤 隆昭　　八巻大樹　　実川 資朗

日本原子力研究所　　物質科学部

1. はじめに

多孔性のセラミック固体増殖材からのトリチウム放出挙動は内部に存在する閉気孔、開気孔、連結開気孔などの影響を大きく受けるため、気孔内トリチウムの移行挙動 が重要な課題となる。本研究では Li2O 焼結体のトリチウム放出機構の基礎的知見を得るために ,かさ密度71％ＴＤ、76％ＴＤ，81％ＴＤおよび86％ＴＤの4種類の気孔率をもつLi2O 焼結体について　特にトリチウムと照射欠陥の相互作用を明らかにするため、等温加熱実験によりトリチウム放出挙動と照射欠陥の回復との関連性を明らかにする実験を行った。

2. 実験結果

2.1 等温加熱実験

4×10^{16}ｃｍ^{2}まで中性子照射した71％Ｔ.Ｄ.Li2O 焼結体からの等温加熱による代表的なトリチウム放出速度の時間依存性を図1に示す。

放出速度ｄＦ/ｄｔは　Kohlrauch 型の拡張指数関数、

$$dFdt=\exp(-(t/\tau)^{\beta}) \quad \cdots\cdots(1)$$

で表らわされ、βはほぼ0.5に従うことがわっかた。このことはは、トリチウム放出カーブはたくさんの放出過程により構成されていることを意味している。たとえば、試料表面からさまざまな距離にあるコロイド状ＬＩにトラップされているか、あるいは、Ｆ＋ センターにトラップされているなど、さまざまな深さ分布持つトラップからの脱離エネルギーをもっているため 拡張指数関数に従うものと考えられる。拡張 指数関数の係数βは高温側では3桁から4桁にわたりほぼ0.5に従うが、低温領域でのβの値は近似的にほぼ0.5に従うものの、放出速度の変化が1桁前後のため精度よくトラップ滞在時間を評価することができない。

放出速度変化の少ない低温側でもβおよびトラップ滞在時間τの値を評価するために積算放出率Ｆの時間依存性をＪMKA法により解析した。

$$\log(-\log(1-F))=\log(b)+s\log(t) \quad \cdots\cdots(2)$$

この勾配ｓより拡張指数係数βが求められる。4×10^{16}ｃｍ^{2}まで中性子照射した71％Ｔ.Ｄ.，76％Ｔ.Ｄ.，81％Ｔ.Ｄ.および86％Ｔ.Ｄ.焼結体について勾配よりβを求めた。拡張指数係数βは温度に依存し、高温側では約0.5から低温側では約0.8へと変化することがわかった。

またこの切片より平均トラップ寿命時間 τ を求めた。71-86％ＴＤ焼結体の平均トラップ滞在寿命時

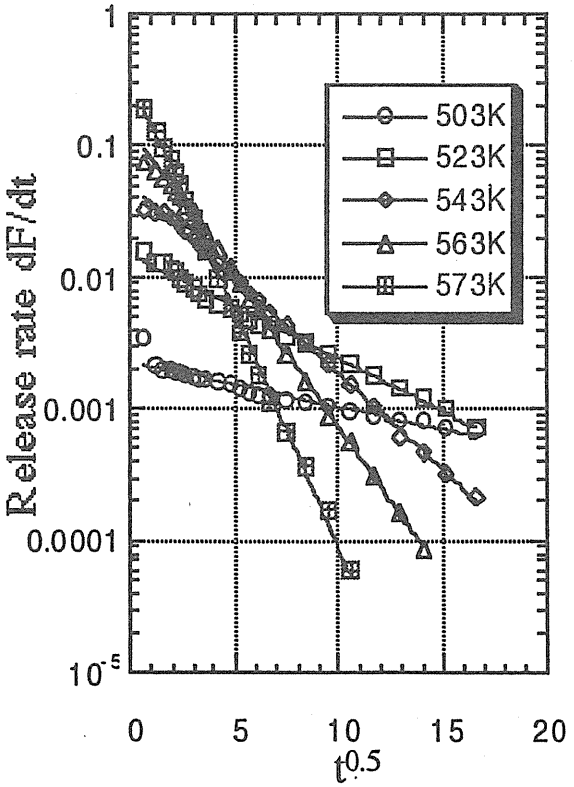


図.1トリチウム放出速度ｄＦ/ｄｔは拡張指数型関数 dF/dt=exp(-(t/τ)$^{\beta}$) に従う。

温度依存性を図2にしめす。トラップ寿命時間間 τ の温度依存性を図2にしめす。トラップ寿命時間 τ は気孔率には依存せず、放出温度のみに依存することがわかる。すなわち、温度の上昇とともに、トリチウム・トラップの存在状態が変化することが考えられる。実験温度に対し20分から2000分と広く分布している。

2.2 活性化エネルギーの解析

温度の逆数にたいしてトラップ寿命時間 τ をプロットしたものを図2に示す。寿命時間は10分から2000分と広く分布しているが、温度の逆数で整理し、あえて直線で近似することにより、活性化エネルギーは低温側では92KJ/mol と求まり、高温側では139KJ/mol と求まった。τ の温度依存性は単純な活性化過程に従うものとみなされる。しかし、2個の活性化エネルギー領域をもつことは少なくとも2種類の活性化過程が存在することを示唆している。

トリチウムの化学形は３８０Ｋから５００ＫではＴ－が増加し、500ｋで最大をしめす。それから６００Ｋにかけて Ｔ－は急激に減少する。これはLi-コロイド の等時昇温加熱による回復実験でもこの温度範囲300Ｋ-590Ｋで回復することと関連しているものと考えられる。すなわち、Li-コロイドと Ｔが作用し LI-T 結合が生成される。440Kから520Ｋまでの低温側のトリチウム放出では動きやすいＴ－ 成分が多くなり、このＬＩ-Ｔ 結合 の解離になどによりトリチウム放出が誘起され、みかけの活性化エネルギー（92KJ/mol ）が小さくなることが考えられる。

またＴの存在化学形は500Ｋ付近より Ｔ－から T+ に急激に変わってゆき、590Ｋではすべてのトリチウムは T+ の化学形となる。のESRの回復もこの温度範囲である。焼鈍によるのF-centerの回復とともにトリチウム化学形がＴ－から T+ への急激な転換が起こし、さらにはO^{2-}-イオン-T+の結合などによりトラップされている。５３０Ｋ以上の加熱によるＴは安定な T+ 種へ転換し、トリチウムのトラップ・サイトとなっている。高温側ではほとんどすべての成分は動きにくいＴ+の化学形で存在しているため、見かけ活性化エネルギーが約１３９ｋＪと大きな値になるものと推定される。

3 結論

(1) 71％から86％Ｔ.Ｄ.の多孔焼結体からのトリチウムは種々の深さ分布を持つ照射欠陥 - トリチウムの複合体にトラップされている。

(2) トリチウム放出速度は dF/dt拡張指数関数 $dF/dt=\exp(-(t/\tau)^{\beta})$ に従う。
β は500Ｋ付近の低温側では約0.8 から580Ｋ付近の高温側では０．５となる。

(3) トリチウム放出の活性化エネルギーは分布をしめすが近似的に493－533Ｋの温度範囲では９２ｋＪ/ mol となり543－583Ｋでは１３９ｋJ/molと評価できた。トリチウム放出は照射欠陥にトラップされたトリチウムのトラップ・サイトからの脱離が律速過程である。すなわち、照射欠陥の回復が律速過程となる。この領域でのトリチウム放出挙動は気孔率には依存性しない。

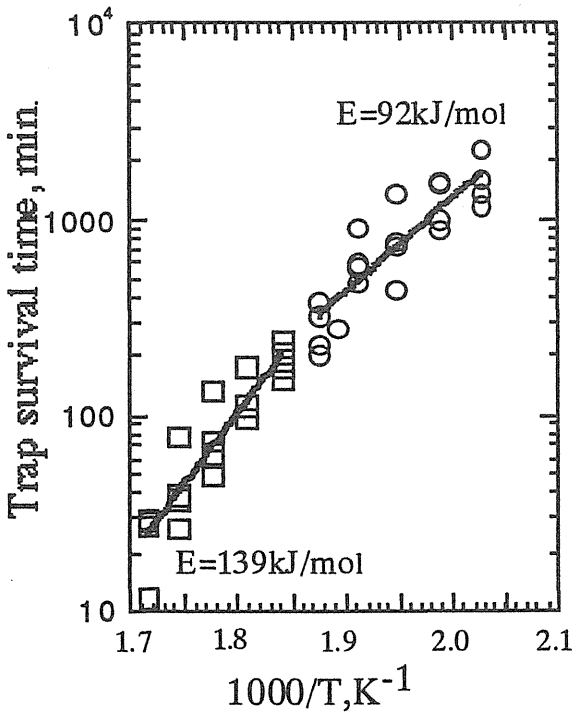


図.2トラップ寿命時間の温度依存性

原子炉: JRR-4 装置: S-パイプ 分野: 核融合炉材料

5. 即発ガンマ線分析

5. Prompt Gamma-ray Analysis

This is a blank page.

5-1 電解および無電解ニッケル合金皮膜中のＢとＰの濃度

Contents of Boron and Phosphorus in the Nickel Alloy Films Deposited by Electroplating and Electroless Plating

森崎　重喜*、長野　龍洋**、春原　弘起**

S.Morisaki*, T.Nagano**, K.Sunohara**

*東京都立大学大学院　理学研究科　　**東京都立大学大学院　工学研究科

*Graduate School of Science, Tokyo Metropolitan University
**Graduate School of Engineering, Tokyo Metropolitan University

---

1、緒言

無電解ニッケルめっき（化学ニッケルめっき）は、非めっき物が複雑な形状であっても膜厚が均一であり、ニッケル本来の耐食性、耐摩耗性、硬さとあいまって産業の各分野で必要不可欠な表面技術となっている。

現在、実用化されている化学ニッケルめっきは主に化学 Ni−P めっきと Ni−B めっきである。前者では、還元剤である次亜リン酸ナトリウム（NaH_2PO_2）により Ni−P 合金が析出する。後者では、還元剤としてジメチルアミノボラン（DMAB：$(CH_3)_2NH \cdot BH_3$）等が用いられ、Ni−B 合金が析出する。

これらのニッケル合金皮膜の特性はめっき浴組成とめっき条件等により多様に変化する。これらの条件の選定、管理により硬度、耐磨耗性などの機械的性質、および電気抵抗、磁性などの電気磁気的特性を制御することができるため近年急速に需要が拡大し、電子機器、半導体産業、自動車産業など様々な分野で使用されている。

両者を比較すると Ni−P は耐食性、耐磨耗性にすぐれ、一方、Ni−B は硬度が高く、半田付け性に優れている。

還元剤としてＰの化合物 NaH_2PO_2 とＢの化合物 DMAB の両方を加えると、３元合金(Ni-P-B)が析出することが知られている。３元合金皮膜は Ni−P と Ni−B の２元合金皮膜の特性を併せ持つことが期待される。

化学めっきの最大の欠点はめっき速度が遅いことである。このためプラスチック等のめっきでは電気の導通性が得られる膜厚になると電気めっきに切りかえることが多い。一方、電解によっても合金めっき皮膜（電気めっき）は得られる。

電解による Ni−P と Ni−B の合金めっきはワッ浴にそれぞれ NaH_2PO_2 と DMAB を加え、直流印加により得られる。また、Ni−P−B 合金めっき皮膜はワット浴に NaH_2PO_2 と DMAB の両方を加えることによって得られる。　電解法の最大の長所は、無電解に比べるとめっき速度が速く低温めっきが可能なことである。低温処理は半導体、プラスチックの表面処理では特に重要である。

2、実験

次の６種類のめっき皮膜（表１）を作成した。被めっき素材は実験目的に応じてガラスまたは銅箔を使用した。ガラスの場合、前処理としてエッチング処理、パラジュウム触媒核付与を行った。

表１　めっき被膜の種類

	３元合金	２元合金
化学めっき	Ni-P-B	Ni-P Ni-B
電気めっき	Ni-P-B	Ni-P Ni-B

これらのめっき皮膜は化学めっきの場合、表２のめっき液に還元剤次亜燐酸ナトリウム（Ni-P）、DMAB（Ni-B）の単独あるいは両方（Ni-P-B）を加え、加温（８０－９０℃）すると得られる。電気めっきの場合にも同様に還元剤を加え、室温で所定の電流密度で電解すると得られる。

研究施設・装置
ＪＲＲ−３．、PGA 装置

研究分野
電気化学

表２　めっき液組成

(g/l)

	電気めっき（ワット浴）	化学めっき
硫酸ニッケル	120	25
塩化ニッケル	45	0
ホウ酸	30	0
クエン酸ナトリウム	0	50

本研究の主たる目的は３元合金の合金組成と皮膜特性の関係の解明にあるので、２元合金は比較検討のため作成した。めっき皮膜中のNi、B濃度はPGA法で、P濃度はICP法で定量した。標準物質としては原子吸光分析用塩化ニッケル、ホウ酸、燐酸二水素カリウムを用いた。
耐摩耗性、硬度等の皮膜特性は合金中のB、Pの含有量と熱処理によって大きく変化する。ここでは非晶質である３元合金の熱処理前後のXRD測定により結晶構造についても検討した。

３、結果

３－１ BとP濃度

３－１－１　電解Ni－P－B合金めっき皮膜

Ni－P－B皮膜中のNi、B、Pの検量線はいずれも良好な直線関係を示した。（図1~３）
図４に電流密度と共析量の関係を示す。電流密度が大きくなるとBとPの共析量がいずれも減少していることがわかる。この傾向は２元合金皮膜（Ni-P、Ni-B）でも同様であった。
図５にめっき液中の還元剤添加量と析出皮膜中のB及びPの含有量の関係を示す。この場合DMABとNaH_2PO_2の添加重量は同じにした。めっき液中のB濃度の増加により皮膜中のB濃度は増大する。この傾向は２元合金でも同様である。一方、皮膜中のPは低濃度領域で著しく減少し、その後一定となる。この傾向は２元合金とは逆になっている。

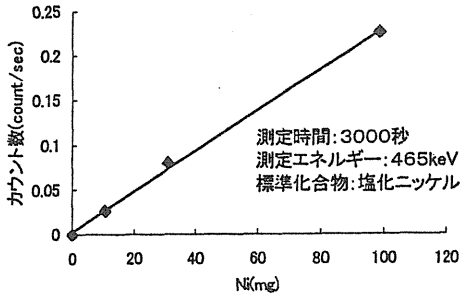


図１　ニッケルの検量線（PGA）

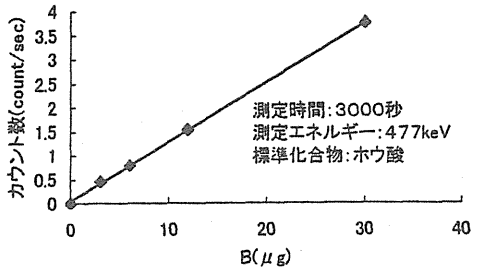


図２　ホウ素の検量線(PGA)

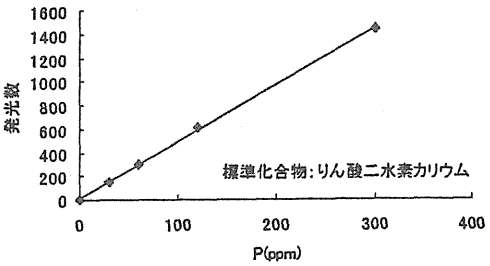
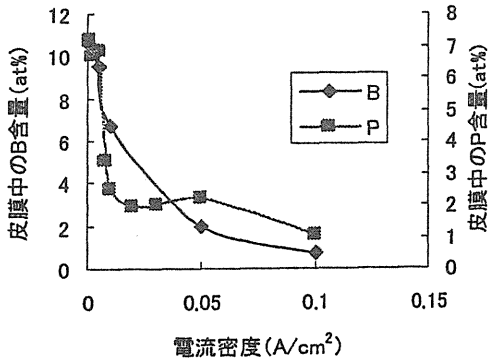


図３　りんの検量線(ICP)



還元剤濃度：[DMAB]＝1g/l、[NaH_2PO_2]=1g/l

図４　３元合金皮膜中のB、P含量と電流密度との関係

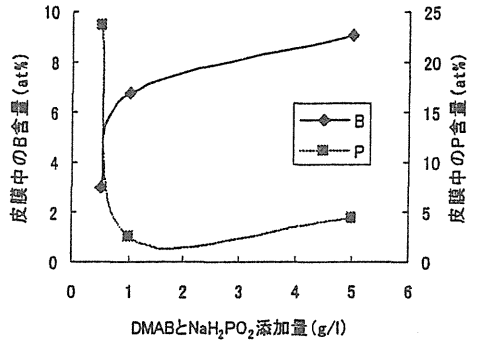


図５　３元合金皮膜中のＢ、Ｐ含量とめっき液中の DMAB、NaH_2PO_2 濃度との関係

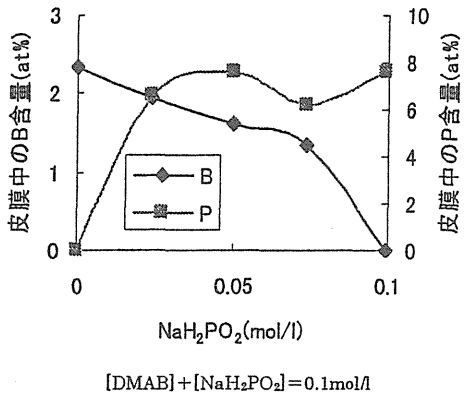


図７　３元合金皮膜中のＢ、Ｐ含量とめっき液中の DMAB、NaH_2PO_2 濃度との関係

３－１－２　化学Ni－Ｐ－Ｂ合金めっき皮膜

３元合金皮膜中のＢとＰの共析量とｐＨの関係を図６に示す。酸性領域でのｐＨの増加につれてＢ、Ｐともに減少傾向をしめした。
還元剤添加量合計を０．１mol/l にした場合の３元合金皮膜中のＢとＰの共析量とめっき液中の DMAB と NaH_2PO_2 濃度の関係を図７に示す。めっき液中のＢの濃度増加につれて皮膜中のＢは２元合金皮膜と同様に単調増加し、共存する NaH_2PO_2 の影響を受けにくいことをしめしている。一方、NaH_2PO_2 の場合、めっき液中の濃度増加は皮膜中のＰの増加に直結していない。この挙動は２元合金の場合と異なる。すなわち、共存する DMAB の影響を受けているようだ。

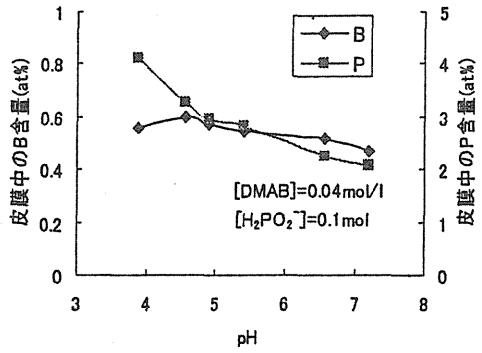


図６　３元合金皮膜中のＢ、Ｐ含量へのｐＨの影響

３－２　熱処理とＸＲＤ測定

２元合金の Ni-B めっき皮膜ではＢ共析量が増加すると非晶質化し、ＸＲＤチャートの Ni（１１１）、（２００）ピーク等はブロードになるが、その存在は認められる。一方、Ni-P 皮膜の場合も同様にＰ含量の増加に伴って非晶質化し、Ni のピークは全く認められなくなる。これらの２元合金を３５０℃程度に加熱するとＢあるいはＰの低濃度領域ではマトリックス Ni のピーク（１１１）、（２００）が明確になると伴に、Ni-B 皮膜の場合化合物 Ni_3B、 Ni-P 皮膜の場合化合物 Ni_3P のピークが出現する。すなわち結晶化が進行し、硬度が著しく向上する。
３元合金の化学めっき皮膜の熱処理前後のＸＲＤチャートを図８に示す。熱処理により Ni メタルのピークが明確化し、化合物 Ni_3B と Ni_3P のピークが出現している。この結果は２元合金でそれぞれ独立して観察された結果の両方をふくんでいる。従って、Ni-P-B 合金皮膜は耐摩耗性良好な Ni-P 合金皮膜と硬度の高い　Ni-B 合金被膜の両方の特性を持つと期待される。

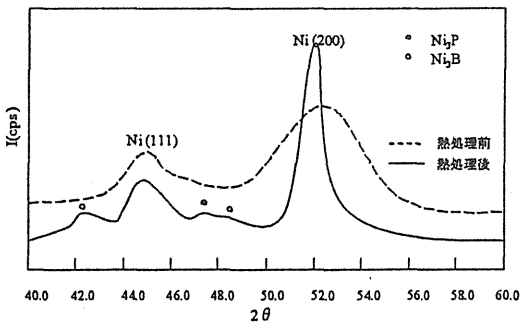


図８　無電解３元合金めっき皮膜のＸＲＤチャート

研究テーマ：環境関連物質の分析高度化研究
表　　題：中性子放射化及び即発γ線分析の研究
5-2

中性子放射化及び即発γ線分析の研究

米沢仲四郎，松江秀明
環境科学研究部 分析科学研究グループ

1. はじめに

報告者らは，これまで中性子放射化分析(NAA)の元素定量法として比較標準試料を必要としないk_0法をいち早く導入するとともに，これを中性子即発γ線分析(PGA)の元素定量法として開発してきた。これまでPGAが有効な27元素のk_0係数を3%以下の精度で測定し，中性子スペクトル特性が異なる海外のPGA装置で測定されたk_0係数との比較や，核データからの計算値等との比較により，得られたk_0係数の正確さを評価した。その結果，数eVの低エネルギー領域に大きな共鳴吸収を持つCd, Sm, Gdの非1/v元素を除く元素のk_0係数の正確さは10%以下であることを明らかにした。また，Cd, Sm, Gdのk_0係数は中性子スペクトルの影響を受けるため，その補正法の検討にも着手した。

本年度は，これまで開発したk_0-PGAとF. De Corteらによって開発されたk_0-NAAにより，独立行政法人産業技術総合研究所計量標準総合センター(NMIJ/AIST)で新たに調製した底質標準物質の多元素定量を行った。また，将来の大強度陽子加速器のパルス中性子によるPGA実験に備え，JRR-3Mの冷及び熱中性子ビームをパルス化するためのビームチョッパーを開発するとともに，PGAによる大学との協力研究も実施した。

2. 底質標準物質の分析

NAAとPGAは，正確さが優れていることや，他の方法では困難な元素の分析が可能であること等から標準物質の調製には不可欠な分析法となっている。本研究では，k_0-NAAとk_0-PGAによりNMIJ/AISTで調製された2種類の底質標準物質(海底質：NMIJ CRM 7302-a，湖底質：NMIJ CRM 7303-a)の多元素定量を行った。k_0-PGAでは元素の絶対濃度を求めることができないため，まず標準添加法により Tiの絶対濃度を定量し，k_0-PGAにより多元素の相対濃度を定量後，標準添加法により求めたTiの絶対濃度から各元素の絶対濃度を求めた。

NAAによる分析：定められた方法によって乾燥させた底質試料約0.1 gを高純度のポリエチレン袋中にはかりとり，三重封入した。中性子モニターとしてAl-Au合金(IRMM-530, Au: 0.1%)0.015 g, Zr板(純度99.7%，厚さ0.1 mm)0.1 gをポリエチレン袋に封入し，中及び長寿命核種測定の場合は試料と同時に，また半減期が分オーダーの短寿命核種測定の場合は，試料とは別に中性子照射をした。分析は測定する核種の半減期に応じ，短寿命，中寿命及び長寿命核種に分けて行った。中性子照射には日本原子力研究所のJRR-4を使用し，短寿命核種測定の場合は気送管で10 sec，中及び長寿命核種測定ではTB-パイプで2及び20 min照射した。γ線スペクトル測定には，あらかじめ検出効率とピーク対全計数(P/T)比測定によって校正した高純度Ge検出器を使用した。得られたγ線スペクトルをHYPERMET-PCプログラムによって解析し，k_0法の解析プログラムKAYZERO/SOLCOIによって元素濃度を定量した。

PGAによる分析：底質試料約0.3 gをFEPフィルム袋中にはかりとり，日本原子力研究所のJRR-3M熱中性子ガイドビームの即発γ線分析装置を用い，

原子炉：JRR-3　-4　　装置：即発γ線分析装置，気送管，水力照射設備　分野：中性子放射化分析(分析化学一般)，即発γ線分析(分析化学一般)

ヘリウム雰囲気中で10000 ～ 50000 sec測定を行った。得られた即発γ線スペクトルをHYPERMET-PC プログラムによって解析し，これまでに測定した k_0 係数を用い，元素の相対濃度を定量した。

k_0-NAAにより，短寿命核種測定ではMg, Al, Cl, Ca, Ti, V, Mnが，中寿命核種測定ではNa, K, As, Br, Laが，そして長寿命核種測定ではSc, Cr, Fe, Co, Zn, Rb, Ba, Cs, Ta, Th等合計22元素が定量された。また，k_0-PGA では軽元素を中心としたH, B, Si, K, Ti, Cr, Mn, Fe, Cd等の15元素が定量された。既に多くの定量値が報告されている池底質（NIES No.2）と河川底質 (NIST SRM1645) 標準物質も分析し，定量値の正確さを評価した。その結果，分析値は認証値及び参考値とほぼ10% 以内で一致した。

3. 中性子ビームチョッパーの開発

将来の大強度パルス中性子によるPGA研究に備え，JRR-3Mの冷及び熱中性子ビームをパルス化するためのビームチョッパー装置を開発した。本装置は，1)中性子飛行時間測定による中性子スペクトル測定と，2)励起原子核の寿命の違いによる即発γ線と壊変γ線の分別測定に使用するため，酸化ガドリニウム(Gd_2O_3)とフッ化リチウム(^6LiF)の2種類の中性子吸収剤の円盤を取り付けることが出来る。これらの円盤を1～3000 rpmの速度で回転することが出来，0.017～100 Hzのパルス中性子ビームを作ることが出来る。

4. 協力研究

JRR-3Mの即発γ線分析装置を使用し，1) 中性子ビームガイドを用いた高速荷電粒子の化学的挙動の研究(大同工業大学工学部)と，2) 廃棄物埋立によるホウ素汚染の機構解明(東京大学大学院新領域創成科学研究科)を大学との協力研究によって実施した。

5. 成果の公表

1) 松江秀明，「中性子共鳴吸収を利用する新しい即発γ線分析」，ぶんせき，**2002**, No. 11, 645.
2) 米沢仲四郎:「原子炉中性子による即発γ線分析」，分析化学，**51**, 61-91 (2002).
3) 吉永淳，松脇崇晃，長谷川陽一，柳沢幸雄，貴田晶子，松江秀明，米沢仲四郎「廃棄物中ホウ素の存在状態と溶出性」，環境化学，**12**, 333-342 (2002).
4) C. Yonezawa, H. Matsue, M. Yukawa: "Non-destructive determination of trace amounts of iodine in biological samples by epithermal neutron activation and Compton suppression gamma-ray spectrometry", J. Radioanal. Nucl. Chem., **255**, 105-109 (2003).
5) H. Matsue, C. Yonezawa: "Neutron spectrum correction of k_0-factors for k0-based neutron-induced prompt gamma-ray analysis, J. Radioanal. Nucl. Chem., **255**, 125-129 (2003).
6) J. A. Liyanage, C. Yonezawa: "A new analytical method for ^{32}P: Liquid scintillation counting with solvent extraction", J. Radioanal. Nucl. Chem., **256**, 279-282 (2003).
7) H. Matsue, C. Yonezawa: "Measurement and evaluation of k_0 factors for PGA at JAERI", J. Radioanal. Nucl. Chem., **257**, 565-571 (2003).

5-3 即発γ線分析の大型試料への適用 (III)

Prompt Gamma-Ray Analysis of Large and Volumious Samples. III

東京都立大学大学院理学研究科
Graduate School of Science, Tokyo Metropolitan University
大浦 泰嗣
Yasuji Ouraa
理化学研究所
The Institute of Physical and Chemical Research (RIKEN)
榎本秀一・蛭沼利江子
Shuichi Enomoto, Eriko Hirunuma

1. はじめに

ガイドビーム型PGA装置は，原子炉外へ中性子を導き照射・測定を行うという構造から二次的特徴を持つ．すなわち，中性子束が小さいため，照射試料中の誘導放射能がごくわずかであること，また，原子炉内へ挿入する必要がないため，試料の大きさの制限が緩いことである．我々はこの特徴に特に注目し，これまでにPGAを大型試料(ここでの「大型」とは，ビームサイズより大きく，厚みのある不定形ということ)に適用するための内標準法を考案し[Sueki96]，考古試料から生体試料まで様々な試料に適用してPGAの有効性を示してきた[Nakahara00].

前期(H9～H11)の後半は生体試料への適用を重点的に行ってきた．一般的に，動物の臓器中の元素濃度を定量するためには屠殺し，摘出された臓器を粉末化あるいは溶液化する必要がある．したがって，例えば，同じ個体を使って臓器中の投与した元素濃度の時間変化を追うことはむずかしい．もし，同じ生きている個体を使ってこの元素分布の時間変化や代謝研究が行うことができれば，個体差による変動のない何かおもしろい情報が得られるに違いない．最終目標は，動物を生かしたまま中性子照射し，各臓器中の元素濃度の時間変化を得ることで，生きたラットの照射試験を行った．当初，散乱中性子の影響は小さいと考えていたが，実際はその影響は大きく，散乱中性子の影響を最小限にする工夫およびその補正法を開発する必要があることがわかった．

今期は生きたラットの照射を中心に行い，実験法を確立する予定であったが，諸条件が整わず一度も行うことができなかった．照射できる見通しも立たなかったため，本課題は2年間で終了とした．本報告では，従来の摘出法により行ったReを投与したラットの臓器中Re濃度の経時変化定量の試みと，比較法での中性子束補正法の試みについて報告する．その他に大型試料ではないが海底土の分析や日本地質調査総合センターから最近発行された岩石標準試料の分析も行ったがこれらの結果についてはここでは割愛する．

2. レニウムの体内分布

レニウムは核医学での利用が非常に多いテクネチウムの同族元素で，最近^{186}Reを核医学的に利用するための検討がさかんに行われている．そこで，PGAでの感度も比較的大きいので，B，Cd，Hgにつづきを対象として体内分布の測定を試みた．

過レニウム酸ナトリウム生理食塩水溶液(136mgReに相当)を3匹のラットに腹腔内投与し，投与1時間後，3時間後，6時間後に肝臓と腎臓を摘出し，ただちに冷凍保存した．さらに，1匹のラットに経口投与し，3時間後に同臓器を摘出・冷凍保存した．

中性子照射は日本原子力研究所JRR-3M実験ホ

JRR-3. 即発γ線分析装置 放射化分析

表1 Reのσb比

	熱中性子	冷中性子
318 keV	5.67 ± 0.10	5.95 ± 0.08
256 keV	15.7 ± 0.7	16.1 ± 0.5
291 keV	10.5 ± 0.5	10.4 ± 0.5

H 2223 keV を1とする.

ールに設置されている即発γ線分析装置で行った. 照射直前に解凍し, 四フッ化エチレン六フッ化プロピレン共重合樹脂フィルムで包み, He雰囲気下でビームサイズ20mm×20mmの冷中性子を照射した. 即発γ線は, BGO検出器で取り囲まれたGe半導体検出器を用いて, コンプトンサプレッションモードで測定を行った.

定量は内標準法によりおこった. まず, 本法に必要なσb比を既知量の試薬を溶解した水溶液を用いて定量した. その結果を表1に示す. 熱中性子での値と冷中性子での値はほとんど等しかった.

図1にRe投与から臓器摘出までの経過時間に対する腎臓と肝臓でのRe/H比を示した. 腎臓を「丸」で, 肝臓を「三角」で示した. また, 経口投与した場合を●と▲で示した. 投与後1時間の腎臓は2回測定を行い誤差内でほとんど等しい定量値が得られた. 再現性の良い定量法であることが確認された.

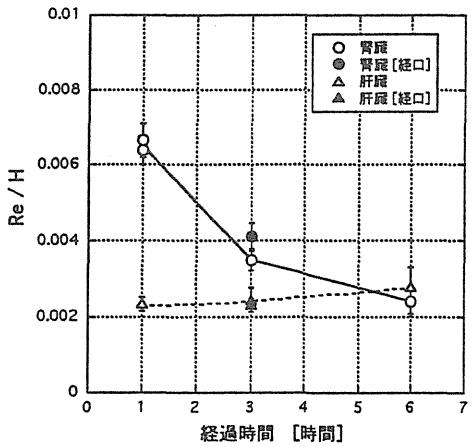


図1 臓器中 Re/H 比の経時変化

腎臓でのRe/H比は時間と共に減少したが, 肝臓では変化が非常に小さかった. 水素濃度を10%(人体での平均濃度)と仮定すると, 投与1時間後に腎臓ならびに肝臓には投与したReのわずか1.3%ならびに2.0%が蓄積していることになる. (肝臓は腎臓の約5倍の重量があるためRe/H比は腎臓の方が大きいが, 絶対量では肝臓の方が大きい.) 一方, 臓器単位重量あたりのRe量は腎臓が0.0013gRe/g, 肝臓が0.00047gRe/gであり, Re/H比は単位重量あたりの濃度の傾向を反映している. 肝臓中のRe濃度は投与6時間後までほぼ一定であった. しかし, 腎臓中では時間と共に減少し, 6時間後には臓器重量あたりの濃度はほぼ等しくなった. また, 腹腔投与と経口投与による明かな差は認められなかった.

矢永ら[Yanaga96]は, マルチトレーサを用いて, 投与したReの80%以上が投与後1日以内に尿として排泄されることを観測した. さらに, 1日をこえると排泄速度が遅くなった. 尿は腎臓を通して排泄されるので, 本研究で得られた結果(投与1日後に腎臓と肝臓内には投与量の数%が残存しており, 腎臓の方が肝臓よりも濃度が高い. また, 腎臓中の濃度は時間と共に緩やかに減少する.) は矢永らによる報告と矛盾しない.

3. 中性子束の補正

PGAは中性子ビームを利用し, 照射しながら即発γ線を測定する必要があるため, 通常の中性子放射化分析法のように多試料を同時に照射することができず, 試料を一つづつ照射しなければならない. 内標準法は各試料での元素濃度比を定量するため, 試料間での中性子束変動の補正は必要な

表2 NaClを用いた中性子束補正の検討

	計数率平均値	補正計数率平均値
Pb (7368 keV)	3.25 ± 1.1%	
Na (472 keV)	3.48 ± 1.5%	3.51 ± 1.7%
Cl (1164 keV)	35.06 ± 1.5%	35.35 ± 1.7%

誤差は相対標準偏差

表3 JB-1を用いた中性子束補正の検討

	計数率平均値	補正計数率平均値
Pb (7368 keV)	2.62 ± 2.0%	
Mn (314 keV)	0.17 ± 13%	0.17 ± 12%
Na+B	4.81 ± 1.6%	4.75 ± 0.77%
K (770 keV)	1.04 ± 1.7%	1.02 ± 0.59%
Ti (1381 keV)	2.22 ± 1.0%	2.19 ± 2.7%
Fe (1725 keV)	0.50 ± 2.8%	0.49 ± 1.4%
Al (1779 keV)	1.35 ± 1.0%	1.34 ± 1.8%
Ca (1942 keV)	1.05 ± 2.5%	1.04 ± 0.77%
Si (3539 keV)	1.17 ± 1.3%	1.16 ± 1.6%

誤差は相対標準偏差

い．一方，絶対量を定量するには通常比較法を用いるが，未知試料と標準試料は同時に照射できないため，厳密にはこれらの中性子束を補正する必要がある．しかし，中性子束をモニターする適当な方法がないため，補正しがたい．そこで，中性子束のモニターとして鉛板が利用できないか試みた．

鉛はPGAではもっとも感度の悪い元素の一つであり，放出される即発γ線は6736 keVと7367 keVの2本だけある．そこで，試料とともに鉛版を照射しても元素定量にはほとんど影響がないと考えられる．そこでNaClまたは岩石標準試料JB-1と鉛板(99.9%，15mm×15mm，2.6 g)をスタック状にして数回照射し，鉛による中性子束変動補正について調べた．なお，NaClの場合は鉛側から，JB-1の場合はJB-1側から中性子を照射した．

表2と表3にそれぞれNaClとJB－1での各測定での生の計数率の平均値と鉛で中性子束を補正した計数率の平均値を示した．誤差は相対標準偏差で示した．JRR-3Mの出力が安定しているため，計数の統計誤差が小さいピークでは計数率の相対標準偏差は2%以下と非常に小さい．鉛で中性子束を補正した計数率の場合この標準偏差よりも小さくなることを期待したが，実際はほとんどかわらなかった．さらに，JB-1のTiの場合のように原因は不明だが逆に大きくなってしまうこともあった．残念ながら，鉛板を利用した中性子束補正は効果が期待できなかった．

4. まとめ

3期，8年に渡りPGA法の大型試料への適用を積極的に行ってきた．内標準法を提案し，特に考古学資料，土器，須恵器，銅鏡を中心にPGA法の優位性を示してきた．後半は，生体試料を中心としてきたが，水素の即発γ線の妨害が大きく，分析対象元素を多量に投与しないと測定は不可能であった．この点は，多重検出器を利用したPGA法で解決できる可能性がある．生きた動物への応用は試験的な実験を一度だけ行い，今後解決すべき問題点を知ることができたが，そのほとんどがまだ未解決である．大型試料への適用を中心とした課題はひとまず今期にて終了とするが，大強度加速器からの中性子を利用したPGAでは新たな発展が期待できるので，これに向けて問題点を解決するよう努力していきたいと思う．

参考文献

桜井94：桜井弘，田中英彦編，「生体微量元素」(廣川書店，1994).

Nakahara00: H.Nakahara et al. *J. Radioanal. Nucl. Chem.* **244**, 405-412 (2000)

Sueki96：K.Sueki et al., *Anal. Chem.* **68**, 2203 (1996).

Yanaga96：M. Yanaga et al., *Appl. Radiat. Isot.* **47**, 235-240 (1996).

成果の公表

・"即発γ線と考古学" 大浦泰嗣，バウンダリー16, 60-61 (2000)

・"Application of prompt gamma ray analysis to biological samples" Y.Oura, S. Enonoto, and H.Nakahara. RIKEN Review No.35, 73-75 (2001)

研究テーマ：リアルタイム非破壊超微量元素分析法の開発

表　　題：多重即発ガンマ線を用いた米に含まれるカドミウムの定量

5-4

多重即発ガンマ線を用いた米に含まれるカドミウムの定量

藤　暢輔、大島真澄、初川雄一、小泉光生、長　明彦、木村　敦、後藤　淳
日本原子力研究所　物質科学研究部　原子核科学研究グループ

食品衛生法により米のカドミウム(Cd)の限界濃度は1.0ppmとされている。コーデックス委員会では、0.2ppmをベースとした引き下げの為の議論がなされている。

日本は火山地帯であり、また鉱山開発が積極的に行われてきた事から、土壌中の濃度が高い傾向にあり、農産物の濃度が比較的高くなる地域が偏在している。日本人のCd摂取は、約50%が米からもたらされているため、米のCd濃度に摂取量が大きく依存している。現在の法定分析法である原子吸光法や一般に広く用いられているICP-MS法においては、煩雑な化学分離が必要であるためその定量に時間がかかり、多数の試料を測定できない。よって、現在の分析法では、全てのCd汚染米を取り除くことは困難である。米に含まれるCd汚染米を例外なく取り除く為に、より迅速で高精度な定量法が望まれている。

米のCd濃度を即発ガンマ線によって分析する場合、多量に含まれる水素が妨害元素となる。Cdは主に558や651keVの即発ガンマ線を放出するが、水素の即発ガンマ線は2223keVと高いエネルギーを持つために、そのコンプトン成分によってCdのガンマ線が覆われ、十分な検出限界が得られない。水素からの影響を取り除く方法の1つに灰化があるが、手間と時間がかかる上に、Cd金属を含む化合物の多くが低い融点を持つために、過小評価してしまう恐れがある。水素が中性子捕獲の際に1本しか即発ガンマ線を放出しないのに対し、Cdは2本以上の強い即発ガンマ線を同時に放出する。即発ガンマ線分析に多重ガンマ線検出法を適用することによって、同時に1本しかガンマ線を放出しない核からの影響を取り除くことができる。これにより米に含まれる水素の影響を取り除き、Cdの定量限界を向上させることが可能である。本研究では、多重ガンマ線検出法による米に含まれるCdの検出限界を求めた。

日本原子力研究所の3号炉C-2ラインにおいて、米に含まれるCdの定量を多重ガンマ線検出法を用いた即発ガンマ線分析によって行った。測定は2台のHPGe検出器を用いた。多重ガンマ線検出法による即発ガンマ線分析での米のCdの測定限界を求める為に、標準Cd試料と米試料を用い、それぞれ1日程度の測定を行った。本研究の結果から絶対効率が10%程度である検出器を用いた場合、10分の測定で0.05ppm以下まで測定が可能であることが見積もられた[1]。この検出器を用いれば、3ヶ月で1万検体以上の米試料が測定可能となり、より詳細で正確な汚染検査が可能になると期待される。

1) The analysis of cadmium-polluted rice by using multiple gamma-raydetecting method
Y.Toh *et. al.*
J. of Nucl. Radiochem. Sci, Vol4,197(2003)

原子炉：JRR-4　　装置：即発ガンマ線分析装置　　分野：放射化分析（農・水産物）

6. その他

6. Others

This is a blank page.

研究テーマ：脳腫瘍に対する中性子捕捉療法の基礎的研究
表題：コメットアッセイによるＢＮＣＴ実験系でのＤＮＡ損傷の検討

6-1 コメットアッセイによる9L腫瘍を用いたBNCT実験系でのＤＮＡ損傷の検討

中井　啓、 吉田文代、遠藤　聖、山本哲哉[1]、松村　明[2]
筑波大学博士課程人間総合科学研究科
[1]茨城県立中央病院脳神経外科
[2]筑波大学　臨床医学系　脳神経外科

目的：ホウ素中性子捕捉療法（BNCT）において、ＤＮＡ損傷の評価を簡便に行うため、細胞、動物を用いたBNCTモデルに、コメットアッセイ法を用いた検討を行った。本手法はSingle strand break（SSB）、Double strand break（DSB）を処理過程で分けることができ、α線の効果を示すには適していると思われる。

方法：9L-gliosarcoma細胞にBSH添加して培養したのち、中性子照射を行った。動物実験ではFisher344ラットに９Ｌ細胞を接種し皮下腫瘍モデルを作成しBSH静注後４時間で全身麻酔下に中性子照射を行った。照射後、細胞懸濁液を調整し、スライドグラス上にゲル包埋した。コメットアッセイにはR&D Systems Inc. のCometAssay Kitを用いた。蛍光顕微鏡を用いた観察で、得られた画像から、Tail Momentをもとめた。

結果：Tail MomentはＤＮＡ損傷の視標として用いられる。細胞実験のTail Momentを図１、２（中性処理およびアルカリ処理）に示す。動物実験におけるTail Momentを図３に示す。細胞実験では、分布が大きく、ボロン濃度および照射時間との相関は傾向を示すにとどまった。アルカリ処理では、主にSSBを、中性処理では、主にDSBを示すといわれ、中性子照射のみの群(neutron)と比較すると、照射時間とともにDSBが増加した。動物実験ではボロン濃度によるDNA障害の増加を示した。細胞個々のＤＮＡ障害は分布が大きく、ＢＮＣＴ治療効果の改善には細胞内の薬物動態、線量分布についてさらに検討を要すると思われた。

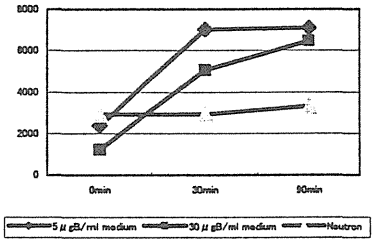


図１:Tail Moment (neutral)

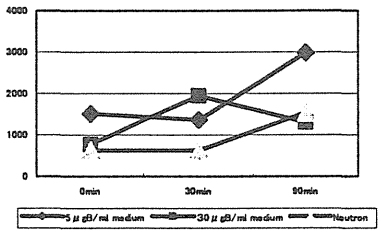


図２: Tail Moment (alkali)

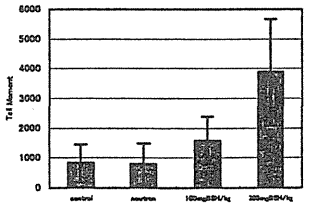


図３　: Tail Moment (in vivo, alkali)

原子炉：JRR-4　　装　置：小動物照射　　分　野：その他

LiAlの電気的性質の中性子照射効果の研究III

6-2

Neutron Irradiation Effects on Electrical Properties of LiAl : III

矢萩正人、橋本恭能（青森大学工学部）
Masahito YAHAGI, Takanori HASHIMOTO (Faculty of Engineering, Aomori University)
栗山一男、浜中廣見（法政大学工学部）
Kazuo KURIYAMA, Hiromi HAMANAKA (College of Engineering, Hosei University)
須貝宏行（日本原子力研究所東海研究所）
Hiroyuki SUGAI (Tokai Research Establishment, Japan Atomic Energy Research Institute)

1．はじめに

Li系IaIIIb金属間化合物は、Li原子空孔(V_{Li})、Al格子点に置換したLi原子(Li_{Al})、複合欠陥(V_{Li}-Li_{Al})等の多量の格子欠陥[1]を有しながら、Li濃度48～56 at.%にわたり均一なβ相（NaTl型結晶構造[空間群:Fd3m]）を保持している。また、この同じ系に属するLiGaにも同様な格子欠陥が多量に存在することが報告されている。[2]これら多量の格子欠陥（特にV_{Li}）の存在はLi系金属間化合物中のLiイオンの自己拡散の活性化エネルギー（0.12～0.15 eV）を小さくしていると予想され、これらの化合物中でのLi^+イオンの容易な移動を考えた場合、これらの化合物は新しいリチウムイオン2次電池の電極材料への適用が期待される。また、中性子照射による$^6Li(n,\alpha)^3H$反応を利用したトリチウム製造試験用のターゲット材料としても研究されている。[1,3]

電子物性の観点から見ると、これらの化合物は通常の金属間化合物には見られない大きな特徴を有している。その特徴は、Li濃度が少ない領域では多量（～10^{21} cm^{-3}）のV_{Li}を含有し、低温（90 K付近）においてV_{Li}の規則-不規則変態に起因する電気抵抗率の異常が観測される。[4]

一方、Li濃度が増加し、50 at.%付近になるとV_{Li}の減少とともに他の欠陥(Li_{Al}とV_{Li}-Li_{Al})が増加し、低温における電気抵抗率の異常が消失する。同様な現象は、Li濃度44～54 at.%にわたり均一なβ相をもつβ-LiGaにおいても観測され、[2] Li濃度48 at.%付近になるとV_{Li}の減少とともにLi_{Al}が増加するが、複合欠陥の存在等の詳細は明らかになっていない。これまで、Li濃度が50at.%付近の組成を有する試料（β-^{6}LiAl）に中性子を照射すると電気抵抗率がLi欠乏相境界(Li濃度48 at.%付近)の値に近くなり、90 K付近に異常抵抗が現れることを報告した。[5]

本研究では、中性子照射後のβ-^{6}LiAl（Li濃度50 at.%付近）について、電気抵抗率が減少し、Li欠乏相境界の値に近くなるメカニズムについて考察し、90 K付近の規則-不規則変態に起因すると思われる比熱の異常が出現するか、同じ系に属するβ-^{6}LiGa（Li濃度48 at.%付近）に中性子を照射した場合、β-^{6}LiAlと同じ現象が発現するか等について明らかにする。さらに、Li系NaTl型金属間化合物β-LiAlおよびβ-LiGaの格子欠陥構造とLi拡散機構の関係を考察する。

2．実験方法

試料は、^{6}Li（99.5% 濃縮）とAl（99.999%）またはGa（99.999%）をタンタル製ルツボに入れ、アルゴンガス中で溶融することにより合成した。[6]合成した試料は、Li濃度50 at.%付近（β-^{6}LiAl）[1]とLi濃度48 at.%付近（β-^{6}LiGa）[2]で、いずれもβ相中間付近のLi濃度のものであり、ほぼ同数のV_{Li}とLi_{Al}を有する。

研究施設と装置名
JRR-3、JRR-4、ラジオアイソトープ製造棟

研究分野
材料科学、放射線損傷

中性子照射は、試料を石英管に真空封入し、JRR-3およびJRR-4を用いて、熱中性子で5×10^{17} n/cm^{2}程度まで行なった。照射条件の詳細はH13年度の報告書を参照されたい。

電気抵抗率は、ヘリウムガスを満たした密閉容器内で、10 Kから室温までの範囲で直流4端子法の一種であるvan der Pauw法によって行なった。

比熱測定は、H13年度に製作したカロリメーター[7]によって、77 Kから室温までの範囲で真空中で測定した。装置の詳細はH13年度の報告書を参照されたい。

3．結果と考察

以前報告したように、β-^{6}LiAl(50.2 at.% Li)の中性子照射前後の電気抵抗率は、図1のようになる。[5] この結果の特徴は、中性子照射後に電気抵抗率が大きく（55 %）減少し、低温（90 K付近）で異常抵抗が観測されることである。この大きな電気抵抗率減少はLi組成が50 at.%付近の試料のみに観測され、Li組成48 at.%および56 at.%付近のβ相境界の試料では観測されない。また、高速中性子や核反応等による照射損傷で起こるはずの抵抗率の増加が観測されなかったことから、大きな中性子断面積をもつ、熱中性子による^{6}Li(n,α)^{3}H反応に起因するβ相内でのLi組成変化[1,8]がこの抵抗率減少の原因であると結論した。詳細はH13年度の報告書を参照されたい。比較のために、β-^{6}LiAlと同時に照射したβ-^{7}LiAlは、熱中性子および高速中性子の照射を受けているにもかかわらず、電気抵抗率の変化がまったくなかったことは、以上の議論を支持している。

H13年度は、図2に示すように、中性子照射前後のβ-^{6}LiGaの電気抵抗率の温度依存性を測定した。また、中性子照射後のβ-^{6}LiGaの比熱測定を行なった。H14年度は、図3に示すように、中性子照射後のβ-^{6}LiGaの電気抵抗率の温度依存性を測定した。H14年度も中性子照射後のβ-^{6}LiGaの比熱測定を継続したが、抵抗率測定における250 K付近の異常抵抗に対応した比熱ピークを観測することはできなかった。今後、用いる試料の量を増やすことやノイズの低減によって測定感度をあげる必要がある。

β-^{6}LiAl(50.2 at.% Li)は中性子照射により、Li濃度48 at.%付近のβ相境界の試料と同じ電気抵抗率の温度依存性を示すようになった。これに対し、β-^{6}LiGa(48 at.% Li)は中性子照射により室温での電気抵抗率は変わらず、温度依存性の傾きが変わったものの、β-^{6}LiAlの場合のような大きな電気抵抗率減少は起こらなかった。しかし、中性子照射後、240 K付近での異常抵抗が観測された点については、Li欠乏相のβ-LiGaの特徴を示すようになった。このような照射効果が生じたのは、β-LiGaがLi欠乏相で12 at.%ものLi原子空孔を含むためと考えられるが、詳細はまだ明らかではない。β-LiGa中のLi原子空孔数は、β-LiAlの場合の約3倍であり、単位胞（16個の原子からなる）当たり2個となる。図2に示す中性子照射後のβ-^{6}LiGaを数ヶ月間ケロシン中に保管しておき、再度、電気抵抗率を測定したものが図3である。同じ試料であるにもかかわらず、図2の金属的な電気抵抗率が、図3では室温から150 K付近まで半導体的な温度依存性を示した。測定前に表面酸化層を取り除くために、十分研磨を行なったにもかかわらず、このような半導体的な性質を示したことから、結晶試料内部にまで酸化が進んだと考えられる。今までの経験では、β-LiAlに比較してβ-LiGaは酸化しやすく試料の劣化が早い。図3の室温から150 K付近までは、降温にともなって電気抵抗率が増加するという半導体的な温度依存性を示したが、240 K付近での異常抵抗は、図2の場合と同様に存在する。

我々が試料を提供したNMR実験[10]によると、室温において、Li欠乏相のβ-LiGa中のLiの拡散係数（1.1×10^{-6} cm^2/c）はβ-LiAl中にくらべて14倍も大きい。これも、β-LiAlに比べて、β-LiGaがLi原子の拡散経路となるLi原子空孔を多量に含むことに起因すると思われる。

4．まとめ

β-LiGaについては十分な実験データを蓄積する

ことが出来なかっが、β-^{6}LiAl(50.2 at.% Li) の場合と同様に、照射前はLi欠乏相近傍の試料にのみ存在する電気抵抗率異常が、中性子照射したβ-^{6}LiGa(48 at.% Li)にも現れることが明らかとなった。Li欠乏相で、単位胞（16個の原子からなる）当たり2個という多量のLi原子空孔を含むβ-LiGaは、β-LiAl以上にその電気的特性やLiの拡散機構が格子欠陥構造に支配される物質である。

大学、原研ともに担当者が多忙になり、本協力研究の遂行が困難になったので、H13年度から開始した本協力研究はH14年度で終了した。しかしながら、我々が提供したβ-LiAl試料が、原研東海研のタンデム加速器で行なわれている ^{8}Li 短寿命核（半減期0.84 s）によるトレーサー拡散実験[11]の標準物質として使われるとともに、^{8}Li 短寿命核によるβ-LiGa中のLi拡散実験が計画される等、今後の展開が期待される。

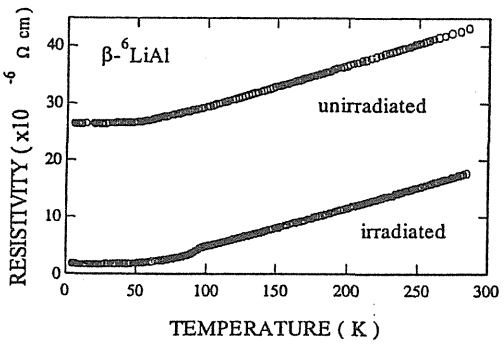


図1．中性子照射前後のβ-^{6}LiAl(50.2 at.% Li)の電気抵抗率と温度の関係

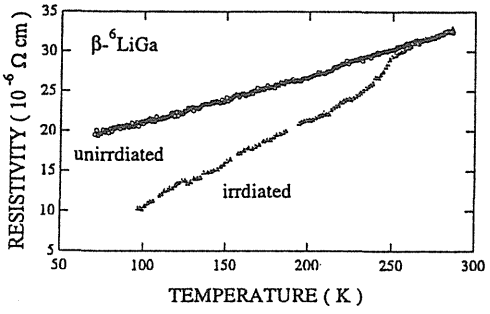


図2．中性子照射前後のβ-^{6}LiGa(48 at.% Li)の電気抵抗率と温度の関係

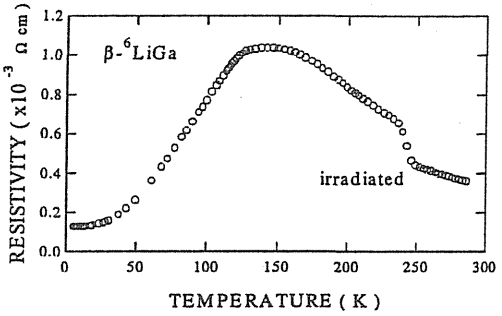


図3．数ヶ月間保管した中性子照射後のβ-^{6}LiGa(48 at.% Li)の電気抵抗率と温度の関係

参考文献

[1] H. Sugai, M. Tanase, M. Yahagi, T. Ashida, H. Hamanaka, K. Kuriyama and K. Iwamura, Phys. Rev. B52, 4050 (1995).

[2] K. Kuriyama H. Hamanaka, S. Kaidou and M. Yahagi, Phys. Rev. B54, 6015 (1996).

[3] H. Sugai, M. Yahagi, H. Hamanaka, K. Kuriyama and T. Hashimoto, Fusion Sci. and Tech. 41, 1030 (2002).

[4] K. Kuriyama T. Kamijoh and T. Nozaki, Phys. Rev. B22, 470 (1980).

[5] 矢萩，須貝，棚瀬，浜中，栗山，日本物理学会秋の分科会講演概要集 23a-N-7 (1997).

[6] M. Yahagi, J. Cryst. Groth 49, 396 (1980).

[7] H. Hamanaka, S. Kaidou, K. Kuriyama and M. Yahagi, Solid State Ionics 113, 69 (1998).

[8] K. Kuriyama, M. Yahagi, T. Nakaya, T. Ashida, K. Satoh and K. Iwamura, Phys. Rev. B29, 5924 (1984).

[9] 橋本，矢萩，須貝，浜中，栗山，日本原子力学会秋の大会予稿集第 III 分冊 K22, 674 (2000).

[10] K. Nakamura, K. Motoki, Y. Michihiro,

T. Kanashiro, K. Kuriyama, H. Hamanaka, and M. Yahagi, J. Phys. Soc. Jpn. 71, 1409 (2002).

[11] S. C. Jeong, I. Katayama, H. Kawakami, H. Ishiyama, H. Miyatake, M. Sataka, A. Iwase, S. Okayasu, H. Sugai, S. Ichikawa, K. Nishio, Y. Sugiyama, M. Yahagi, K. Takada and M. Watanabe, Jpn. J. Appl. Phys. 42, 4576 (2003).

成果の公表

[1] H. Sugai, M. Yahagi, H. Hamanaka, K. Kuriyama and T. Hashimoto, " Tritium and Lithium Diffusion Mechanism in Neutron-irradiated β-^{6}LiAl ", Fusion Sci. and Tech. 41, 1030 (2002).

研究テーマ：フィッション・トラック年代測定
表　　題：FT 年代測定のためのディテクターの開発

6-3

ＤＡＰプラスチックディテクター上のフィッション・トラックの自動計測

岩野英樹[1]・吉岡　哲[1,2]・檀原　徹[1]・鶴田隆雄[2]
[1]:(株)京都フィッション・トラック　[2]:近畿大学原子力研究所

フィッション・トラック（FT）法によるウラン濃度測定は、対象物(鉱物やガラス)に一定の熱中性子線量を照射し、誘導核分裂させた ^{235}U の誘導 FT 密度から求める。一般的に誘導 FT は、鉱物に密着させた外部ディテクター上で測定するが、現在この計数作業は測定者(人間)が行い、自動化が 1 つの重要な課題となっている。

従来外部ディテクターとして天然の鉱物の白雲母が使われてきた。白雲母はバルクエッチング速度が極めて小さく、FT が針状になるため、人間が FT を識別する上では好都合であったが、画像処理をする際には逆に、FT どうしが重なりやすく、自動測定を困難にさせていた。

最近、固体飛跡検出器の新材料としてジアリルフタレート（diallyl phthalate：DAP）樹脂[1,2,3,4,5]が開発された。DAP 樹脂はポリカーボネイトの 1 つで、エッチングに 60℃の PEW-65 溶液（15% KOH, 65% エタノール, 20%水）を用いると、自動測定に適した楕円形のエッチピットが得られる。また FT 密度が $1\times10^5 cm^{-2}$ 程度では、自動測定が十分実用的であると報告された[6,7]。

今回、ウラン入り標準ガラス NIST-SRM612 に密着させた DAP ディテクター上の誘導 FT 密度を、画像処理により自動計測した。熱中性子照射条件は、JRR-4 炉気送管(3.5MW 時)において 90 秒間で、アパタイトの FT 年代測定に用いられる条件である。DAP のエッチングは上述の条件で行った。自動計測は Nikon Eclipse E1000 顕微鏡に接続したハイビジョン CCD カメラ(Nikon HQ-130Ci; 解像度 1920×1080)で取り込んだ静止画を用いた。画像処理には画像解析ソフト(Image-Pro Plus)を使用し、FT は二値化した際の面積を判断基準として用いた。顕微鏡倍率は 1000 倍と 600 倍とし、それぞれの計数粒径として最小ピクセル数 100（およそ $1\mu m^2$）と 50 を採用した[6]。自動計測と測定者による結果を比較するために、自動計測した同一静止画像(1000 倍のみ)を測定し(ビクターHV-M1500 モニターを使用)、さらに別の顕微鏡+モニターシステム(中央無線 THM-14A モニター)でも独立に測定した。

測定結果を表 1 に示す。独立に測定者が測定した 2 回の結果(FT 密度)はほぼ一致した。その 1 つの値を基準とした時、自動測定(1000 倍と 600 倍)はそれぞれ 0.95 倍、0.94 倍となった。個々の FT について画像処理結果を詳しく見ると、測定者の識別基準と全く違いはないことが確かめられた。自動計測の 5～6%の計数ロスについては、1)複数の FT の重なりと 2)角度の浅い FT の読み落としが原因であった。ただし、この計数ロスは同一条件下では一定と考えられることから、補正が可能である。以上のことから、DAP 上の FT 自動計数は簡単かつ正確に行えると結論できる。

参考文献

1) Tsuruta, T. (1999) Radiat. Meas., 31, 99-102.
2) Tsuruta, T. (2000) Radiat. Meas., 32, 289-297.
3) Tsuruta, T. (2001a) Radiat. Meas., 34, 167-170.
4) Tsuruta, T. (2001b) American Society for Testing and Materials, 100, 789-796.
5) 小口・鶴田 (2001) 第 1 回先進放射線応用シンポジウム(大阪大学), 103-106.
6) 吉岡哲・鶴田隆雄・岩野英樹・檀原徹 (2002) FT ニュースレター, 第 15 号, 1-8.
7) Yoshioka, T., Tsuruta, T., Iwano, H. and Danhara, T. (2003) Nucl. Instr. and Meth. B 207, 323-332.

表1. SRM612標準ガラスに密着させたDAPの誘導トラック密度測定

Monitor system	Observer	Magnifi-cation	Area/field ($\times10^{-4}cm^2$)	No. of fields	Counted area	No. of tracks	Density (10^5cm^{-2})	Error ($\pm1\sigma$)	Percent. of error	Ratio
THM-14A	IWANO	×1000	0.800	160	128.0	6343	4.955	0.062	1.3	1.00
Victor	IWANO	×1000	1.259	100	125.9	6202	4.926	0.063	1.3	0.99
Victor	AUTO	×1000	1.259	100	125.9	5955	4.730	0.061	1.3	0.95
Victor	AUTO	×600	3.534	100	353.4	16385	4.636	0.036	0.8	0.94

原子炉：JRR-4　　装　置：気送管　　分　野：その他（放射年代学）

謝　辞

本報告書の発刊にあたり、多くの皆様から多大なご協力を頂きました。編集に際し、ご協力頂いた、東京大学物性研究所吉沢英樹氏、東京大学原子力研究総合センター中沢正治氏、研究炉部長桜井文雄氏、JRR-3管理課鳥居義也氏に深く感謝致します。

This is a blank page.

付　録

Appendix

This is a blank page.

付 録

原研研究炉の利用設備一覧

１．ＪＲＲ－３

１）実験設備

実　験　孔	実　　験　　装　　置
１Ｇ	高分解能粉末中性子回折装置（ＨＲＰＤ）
１Ｇ－Ａ	生体高分子用中性子解析装置（ＢＩＸ－Ⅲ）
１Ｇ－Ｂ	生体高分子用中性子解析装置（ＢＩＸ—Ⅳ）
２Ｇ	三軸型中性子分光器（ＴＡＳ－１）
３Ｇ	中性子トポグラフィ及び精密光学実験装置（ＰＮＯ）
４Ｇ	汎用三軸型中性子分光器（ＧＰＴＡＳ）
５Ｇ	偏極中性子散乱装置（ＰＯＮＴＡ）
６Ｇ	東北大学中性子散乱分光器（ＴＯＰＡＮ）
７Ｒ	中性子ラジオグラフィ装置（ＴＮＲＦ）
Ｔ１－１	中性子偏極回折装置（ＨＱＲ）
Ｔ１－２	単結晶中性子回折装置（ＫＳＤ）
Ｔ１－３	粉末中性子回折装置（ＫＰＤ） （ＨＥＲＭＥＳ）
Ｔ１－４－１	即発ガンマ線分析装置（ＰＧＡ）
Ｔ１－４－１Ａ	化学反応実験装置（ＬＣＥ）
Ｔ１－４－２	多重即発ガンマ線分析装置（ＭＰＧＡ）
Ｔ１－４－３	ＴＯＦ型中性子反射率計（ＴＯＦ）
Ｔ１－４－４	中性子ラウエ回折装置（ＬＡＵＥ）
Ｔ２－１	残留応力測定中性子回折装置（ＲＥＳＡ）
Ｔ２－２	中性子４軸回折装置（ＦＯＮＤＥＲ）
Ｔ２－３	中性子ＩＰ付生体物質中性子回折計（ＢＩＸ－Ⅱ）
Ｔ２－４	高分解能三軸型中性子分光器（ＴＡＳ－２）
Ｃ１－１	高エネルギー分解能三軸型中性子分光器（ＨＥＲ）
Ｃ１－２	二次元位置測定小角散乱装置（ＳＡＮＳ－Ｕ）
Ｃ１－３	超高分解能後方散乱装置（ＵＬＳ）
Ｃ２－１	冷中性子散乱実験デバイス開発装置（ＬＴＡＳ）
Ｃ２－２	中性子反射率計
Ｃ２－３－１	中性子スピンエコー分光器（ＮＳＥ）
Ｃ２－３－２－１	多重即発ガンマ線分析装置（ＭＰＧＡ）
Ｃ２－３－２－２	即発ガンマ線分析装置（ＰＧＡ）
Ｃ２－３－３－１	冷中性子ラジオグラフィ（ＣＮＲＦ）
Ｃ２－３－３－２	パルス中性子機器開発装置（ＣＨＯＰ）
Ｃ２－３－３－３	ＴＯＦ型中性子反射率計（ＴＯＦ）
Ｃ２－３－３－４	中性子ラウエ回折装置(ＬＡＵＥ)
Ｃ３－１－１	高分解能パルス冷中性子分光器（ＡＧＮＥＳ）
Ｃ３－１－２－１	中性子光学システム評価装置（ＮＯＰ）
Ｃ３－１－２－２	多層膜中性子干渉計／反射率計（ＭＩＮＥ）
Ｃ３－２	中性子小角散乱装置（ＳＡＮＳ－Ｊ）

2）照射設備

水力照射設備	HR－1，2
気送照射設備	PN－1，2
放射化分析用照射設備	PN－3
均一照射設備	SI－1
回転照射設備	DR－1
垂直照射設備	VT－1，RG－1～4 BR－1～4，SH－1

2．JRR－4

1）実験設備

プール
中性子ビーム設備
散乱実験設備
冷却水循環ループ
医療照射設備（BNCT）
即発ガンマ線分析装置

2）照射設備

簡易照射筒	Tパイプ（水力）
	Sパイプ
	Dパイプ
	Nパイプ
気送管照射設備	PN

国際単位系（SI）と換算表

表1　SI基本単位および補助単位

量	名称	記号
長さ	メートル	m
質量	キログラム	kg
時間	秒	s
電流	アンペア	A
熱力学温度	ケルビン	K
物質量	モル	mol
光度	カンデラ	cd
平面角	ラジアン	rad
立体角	ステラジアン	sr

表2　SIと併用される単位

名称	記号
分，時，日	min, h, d
度，分，秒	°, ′, ″
リットル	l, L
トン	t
電子ボルト	eV
原子質量単位	u

1 eV=1.60218×10^{-19}J

1 u=1.66054×10^{-27}kg

表5　SI接頭語

倍数	接頭語	記号
10^{18}	エクサ	E
10^{15}	ペタ	P
10^{12}	テラ	T
10^{9}	ギガ	G
10^{6}	メガ	M
10^{3}	キロ	k
10^{2}	ヘクト	h
10^{1}	デカ	da
10^{-1}	デシ	d
10^{-2}	センチ	c
10^{-3}	ミリ	m
10^{-6}	マイクロ	μ
10^{-9}	ナノ	n
10^{-12}	ピコ	p
10^{-15}	フェムト	f
10^{-18}	アト	a

表3　固有の名称をもつSI組立単位

量	名称	記号	他のSI単位による表現
周波数	ヘルツ	Hz	s^{-1}
力	ニュートン	N	m·kg/s^2
圧力，応力	パスカル	Pa	N/m^2
エネルギー,仕事,熱量	ジュール	J	N·m
工率，放射束	ワット	W	J/s
電気量，電荷	クーロン	C	A·s
電位，電圧，起電力	ボルト	V	W/A
静電容量	ファラド	F	C/V
電気抵抗	オーム	Ω	V/A
コンダクタンス	ジーメンス	S	A/V
磁束	ウェーバ	Wb	V·s
磁束密度	テスラ	T	Wb/m^2
インダクタンス	ヘンリー	H	Wb/A
セルシウス温度	セルシウス度	℃	
光束	ルーメン	lm	cd·sr
照度	ルクス	lx	lm/m^2
放射能	ベクレル	Bq	s^{-1}
吸収線量	グレイ	Gy	J/kg
線量等量	シーベルト	Sv	J/kg

表4　SIと共に暫定的に維持される単位

名称	記号
オングストローム	Å
バーン	b
バール	bar
ガル	Gal
キュリー	Ci
レントゲン	R
ラド	rad
レム	rem

1 Å=0.1nm=10^{-10}m

1 b=100fm^2=10^{-28}m^2

1 bar=0.1MPa=10^{5}Pa

1 Gal=1cm/s^2=10^{-2}m/s^2

1 Ci=3.7×10^{10}Bq

1 R=2.58×10^{-4}C/kg

1 rad=1cGy=10^{-2}Gy

1 rem=1cSv=10^{-2}Sv

（注）

1．表1－5は「国際単位系」第5版，国際度量衡局1985年刊行による。ただし，1 eVおよび1 uの値はCODATAの1986年推奨値によった。

2．表4には海里，ノット，アール，ヘクタールも含まれているが日常の単位なのでここでは省略した。

3．barは，JISでは流体の圧力を表わす場合に限り表2のカテゴリーに分類されている。

4．EC閣僚理事会指令ではbar，barnおよび「血圧の単位」mmHgを表2のカテゴリーに入れている。

換算表

力	N(=10^{5}dyn)	kgf	lbf
	1	0.101972	0.224809
	9.80665	1	2.20462
	4.44822	0.453592	1

粘度　1 Pa·s(N·s/m^2)=10 P(ポアズ)(g/(cm·s))

動粘度　1m^2/s=10^{4}St(ストークス)(cm^2/s)

圧力	MPa(=10bar)	kgf/cm^2	atm	mmHg(Torr)	lbf/in^2(psi)
	1	10.1972	9.86923	7.50062×10^3	145.038
	0.0980665	1	0.967841	735.559	14.2233
	0.101325	1.03323	1	760	14.6959
	1.33322×10^{-4}	1.35951×10^{-3}	1.31579×10^{-3}	1	1.93368×10^{-2}
	6.89476×10^{-3}	7.03070×10^{-2}	6.80460×10^{-2}	51.7149	1

エネルギー・仕事・熱量	J(=10^7 erg)	kgf·m	kW·h	cal(計量法)	Btu	ft·lbf	eV
	1	0.101972	2.77778×10^{-7}	0.238889	9.47813×10^{-4}	0.737562	6.24150×10^{18}
	9.80665	1	2.72407×10^{-6}	2.34270	9.29487×10^{-3}	7.23301	6.12082×10^{19}
	3.6×10^6	3.67098×10^5	1	8.59999×10^5	3412.13	2.65522×10^6	2.24694×10^{25}
	4.18605	0.426858	1.16279×10^{-6}	1	3.96759×10^{-3}	3.08747	2.61272×10^{19}
	1055.06	107.586	2.93072×10^{-4}	252.042	1	778.172	6.58515×10^{21}
	1.35582	0.138255	3.76616×10^{-7}	0.323890	1.28506×10^{-3}	1	8.46233×10^{18}
	1.60218×10^{-19}	1.63377×10^{-20}	4.45050×10^{-26}	3.82743×10^{-20}	1.51857×10^{-22}	1.18171×10^{-19}	1

1 cal= 4.18605J（計量法）

= 4.184J（熱化学）

= 4.1855J（15℃）

= 4.1868J（国際蒸気表）

仕事率　1 PS(仏馬力)

= 75 kgf·m/s

= 735.499W

放射能	Bq	Ci
	1	2.70270×10^{-11}
	3.7×10^{10}	1

吸収線量	Gy	rad
	1	100
	0.01	1

照射線量	C/kg	R
	1	3876
	2.58×10^{-4}	1

線量当量	Sv	rem
	1	100
	0.01	1

（86年12月26日現在）

研究炉利用における研究成果集（平成14年度）

R100
古紙配合率100%再生紙を使用しています